



ISSN 1580-3155

Pages 1–348 ■ Year 2020, Vol. 67, No. 1

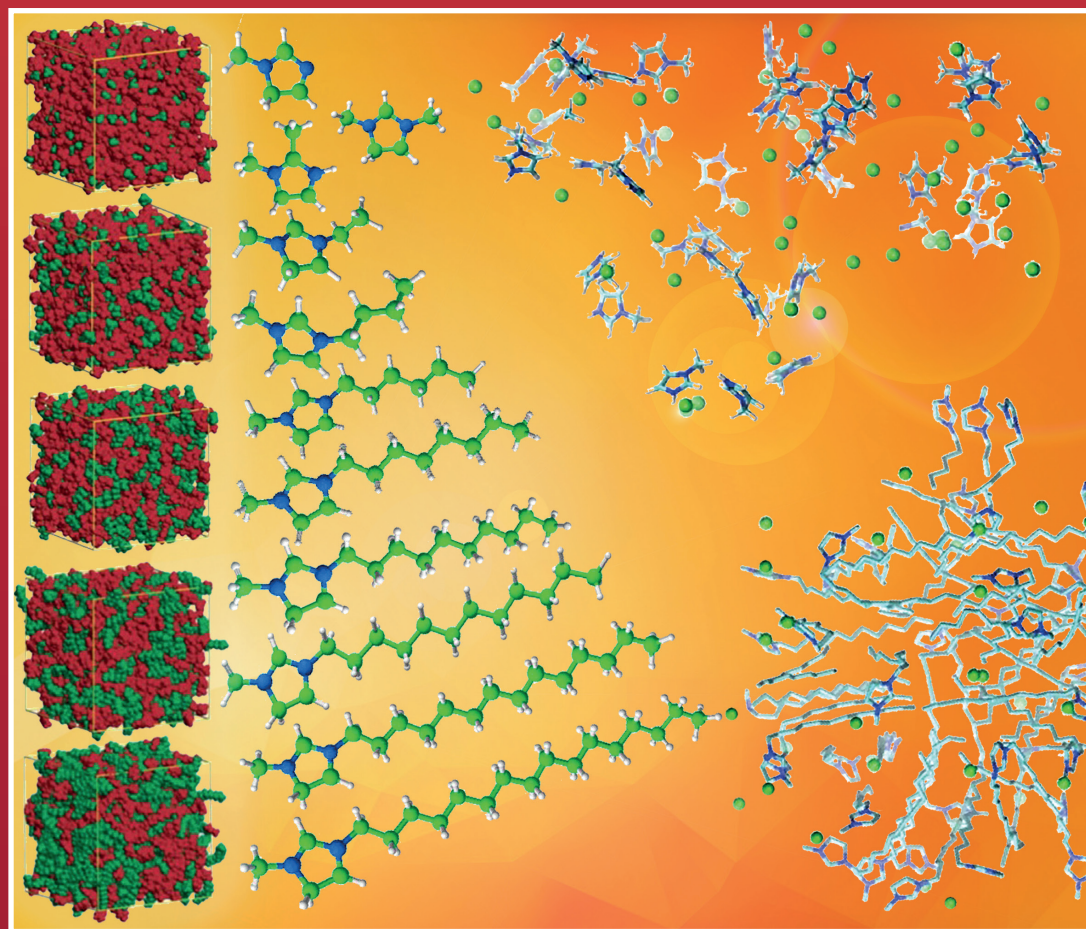
Slovensko kemijsko društvo
Slovenian Chemical Society



Acta Chimica Slo Acta Chimica Slo Slovenica Acta C

1

67/2020



EDITOR-IN-CHIEF

KSENIJA KOGEJ

University of Ljubljana, Faculty of Chemistry and Chemical Technology, Večna pot 113, SI-1000 Ljubljana, Slovenia

E-mail: ACSi@fkk.uni-lj.si, Telephone: (+386)-1-479-8538

ASSOCIATE EDITORS

Aleš Berlec, *Jožef Stefan Institute, Slovenia*
Janez Cerkovnik, *University of Ljubljana, Slovenia*
Mirela Dragomir, *Jožef Stefan Institute, Slovenia*
Ksenija Kogej, *University of Ljubljana, Slovenia*
Krištof Kranjc, *University of Ljubljana, Slovenia*
Matjaž Kristl, *University of Maribor, Slovenia*

Franc Perdih, *University of Ljubljana, Slovenia*
Aleš Podgornik, *University of Ljubljana, Slovenia*
Helena Prosen, *University of Ljubljana, Slovenia*
Irena Vovk, *National Institute of Chemistry, Slovenia*

ADMINISTRATIVE ASSISTANT

Marjana Gantar Albreht, *National Institute of Chemistry, Slovenia*

EDITORIAL BOARD

Wolfgang Buchberger, *Johannes Kepler University, Austria*
Alojz Demšar, *University of Ljubljana, Slovenia*
Stanislav Gobec, *University of Ljubljana, Slovenia*
Marko Goličnik, *University of Ljubljana, Slovenia*
Günter Grampp, *Graz University of Technology, Austria*
Wojciech Grochala, *University of Warsaw, Poland*
Danijel Kikelj, *University of Ljubljana*
Janez Košmrlj, *University of Ljubljana, Slovenia*
Blaž Likozar, *National Institute of Chemistry, Slovenia*
Mahesh K. Lakshman, *The City College and
The City University of New York, USA*

Janez Mavri, *National Institute of Chemistry, Slovenia*
Friedrich Sreenc, *University of Minnesota, USA*
Walter Steiner, *Graz University of Technology, Austria*
Jurij Svete, *University of Ljubljana, Slovenia*
Ivan Švancara, *University of Pardubice, Czech Republic*
Jiri Pinkas, *Masaryk University Brno, Czech Republic*
Gašper Tavčar, *Jožef Stefan Institute, Slovenia*
Christine Wandrey, *EPFL Lausanne, Switzerland*
Ennio Zangrando, *University of Trieste, Italy*

ADVISORY EDITORIAL BOARD

Chairman

Branko Stanovnik, *Slovenia*

Members

Udo A. Th. Brinkman, *The Netherlands*
Attilio Cesaro, *Italy*
Vida Hudnik, *Slovenia*
Venčeslav Kaučič, *Slovenia*
Željko Knez, *Slovenia*

Radovan Komel, *Slovenia*

Stane Pejovnik, *Slovenia*

Anton Perdih, *Slovenia*

Slavko Pečar, *Slovenia*

Andrej Petrič, *Slovenia*

Boris Pihlar, *Slovenia*

Milan Randić, *Des Moines, USA*

Jože Škerjanc, *Slovenia*

Miha Tišler, *Slovenia*

Đurđa Vasić-Rački, *Croatia*

Marjan Veber, *Slovenia*

Gorazd Vesnaver, *Slovenia*

Jure Zupan, *Slovenia*

Boris Žemva, *Slovenia*

Majda Žigon, *Slovenia*

Acta Chimica Slovenica is indexed in: *Academic Search Complete, Central & Eastern European Academic Source, Chemical Abstracts Plus, Chemical Engineering Collection (India), Chemistry Citation Index Expanded, Current Contents (Physical, Chemical and Earth Sciences), Digitalna knjižnica Slovenije (dLib.si), DOAJ, ISI Alerting Services, PubMed, Science Citation Index Expanded, SciFinder (CAS), Scopus and Web of Science*. Impact factor for 2018 is IF = 1.076.



Articles in this journal are published under the
Creative Commons Attribution 4.0 International License

Izdaja – Published by:

SLOVENSKO KEMIJSKO DRUŠTVO – SLOVENIAN CHEMICAL SOCIETY

Naslov redakcije in uprave – Address of the Editorial Board and Administration

Hajdrihova 19, SI-1000 Ljubljana, Slovenia

Tel.: (+386)-1-476-0252; Fax: (+386)-1-476-0300; E-mail: chem.soc@ki.si

Izdavanje sofinancirajo – Financially supported by:

Slovenian Research Agency, Ljubljana, Slovenia

National Institute of Chemistry, Ljubljana, Slovenia

Jožef Stefan Institute, Ljubljana, Slovenia

Faculty of Chemistry and Chemical Technology, University of Ljubljana, Slovenia

Faculty of Chemistry and Chemical Engineering, University of Maribor, Slovenia

University of Nova Gorica, Nova Gorica, Slovenia

Slovensko kemijsko društvo
Slovenian Chemical Society



Acta Chimica Slovenica izhaja štirikrat letno v elektronski obliki na spletni strani <http://acta.chem-soc.si>. V primeru posvečenih številčk izhaja revija tudi v tiskani obliki v omejenem številu izvodov.

Acta Chimica Slovenica appears quarterly in electronic form on the web site <http://acta.chem-soc.si>. In case of dedicated issues, a limited number of printed copies are issued as well.

Transakcijski račun: 02053-0013322846 Bank Account No.: SI56020530013322846-Nova Ljubljanska banka d. d., Trg republike 2, SI-1520 Ljubljana, Slovenia, SWIFT Code: LJBA SI 2X

Oblikovanje ovitka – Design cover: KULT, oblikovalski studio, Simon KAJTNA, s. p. Grafična priprava za tisk: Majanafin, d. o. o.

Dear authors, readers, and reviewers of *Acta Chimica Slovenica*

Thank you for all your contributions to the journal *Acta Chimica Slovenica* (ACSi). In this editorial, I would like to share with you what is new in our journal as well as highlight the activities of the Editorial Board in the past two years.

One of the main accomplishments of the Editorial Board is related to obtaining the seal of the *Directory of Open Access Journals* (the so-called DOAJ Seal; see <https://doaj.org/toc/1580-3155>). This seal is awarded to journals that adhere to best practices in open access publishing. ACSi is a Platinum Open Access Journal, as it enables readers permanent and free access to published scientific works with no publication fees for authors. Importantly, authors retain copyright of their work that may be shared and reused, provided that it is correctly cited. All articles in ACSi are published under the most flexible reuse standard, the Creative Commons Attribution (CC BY) license. Our journal thus fulfills the conditions of the “National strategy of open access to scientific publications and research data in Slovenia 2015–2020”. In addition to the ACSi Editorial Board, the staff of the Central Technical Library of the University of Ljubljana (Mrs. Maja Vihar and Mr. Mitja Vovk Iskrić) participated in the efforts to obtain the DOAJ Seal. Together, we have also upgraded the journal website with additional bibliographic information in hopes that all the necessary information is now available. Nevertheless, we invite your suggestions on how to further enhance the visibility of our journal.

The Editorial Board would especially like to thank the authors of Feature and Review Articles who were willing to share the results of their work with the readership of our journal. We have made nice progress in the publication of our new category of Feature Articles. In the past two years, we have published five Feature Articles from various fields (Biochemistry and Molecular Biology, Chemical and Biochemical Engineering, Material Science, and Physical Chemistry), three Review Articles from various fields (Biochemistry and Molecular Biology, Physical Chemistry, and Analytical Chemistry), and more such articles are in progress. We invite you to read these contributions (<https://acta.chem-soc.si/feature-and-review-articles/>) as well as other papers published in ACSi. Although Feature

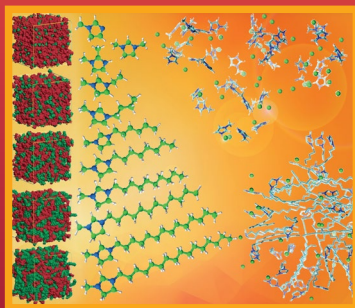
and Review Articles are usually invited contributions, authors are encouraged to send their own proposals, which shall be assessed by the Editorial Board.

The top priority of the Editorial Board is to ensure that papers published in ACSi are subject to rigorous, fair, and critical peer review, as this leads to high-quality publications. We strongly encourage authors and reviewers to adopt a very conscientious approach in their work, as both our editors and authors strive for our journal to have a significant impact in the field of general chemistry in which competition is very high. One critical aspect in this regard is the language quality of manuscripts. We call upon authors to pay special attention to this while disseminating their results to the scientific community. And last, a request for reviewers, whose contributions have a large impact on our journal: when unable to perform a review, please send us a quick reply and possibly a suggestion for an alternative reviewer, as this allows the editor to continue with the review process in a timely manner. This is highly appreciated by both the editors and authors.

Finally, you will notice that the Editorial Board has changed in 2020. In 2019, two long-time associate editors concluded their work with us: Prof. Damjana Rozman, who covered the fields of *Biochemistry and Molecular Biology* and *Biochemical Applications*, and Dr. Melita Tramšek, who covered the fields of *Inorganic Chemistry* and *Materials Science*. On behalf of the Editorial Board, I would like to thank them both for their devoted work for ACSi. To that end, the following associate editors have joined us this year: Assist. Prof. Aleš Berlec (Jožef Stefan Institute, Ljubljana, Slovenia) is responsible for *Biochemistry and Molecular Biology* and *Biochemical Applications*, whilst Dr. Mirela Dragomir (Jožef Stefan Institute, Ljubljana, Slovenia) and Assoc. Prof. Matjaž Kristl (Faculty of Chemistry and Chemical Technology, University of Maribor, Maribor, Slovenia) are responsible for *Inorganic Chemistry* and *Materials Science*. The Editorial Board sincerely welcomes them and wishes them much success.

Ksenija Kogej
Editor-in-Chief
Acta Chimica Slovenica

Graphical Contents



Acta Chimica Slo Acta Chimica Slo Slovenica Acta C

Year 2020, Vol. 67, No. 1

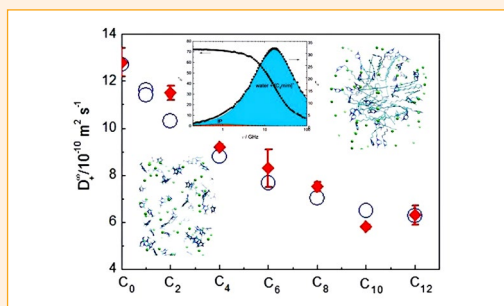
FEATURE ARTICLE

1–14

Feature article

Ionic Liquids: Simple or Complex Electrolytes?

Marija Bešter-Rogač



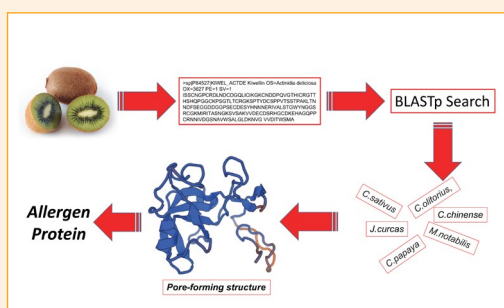
SCIENTIFIC PAPER

15–22

Biochemistry and molecular biology

Identification of Kiwelin-like Proteins in Fruits by Using *In Silico* Tools

Ceylan Turkmen and Levent Cavas

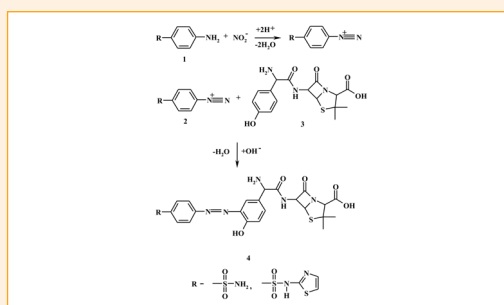


23–35

Analytical chemistry

Development and Validation of the Simple and Sensitive Spectrophotometric Method of Amoxicillin Determination in Tablets using Sulphanilamides

Oksana Kostiv, Olha Korkuna and Petro Rydchuk

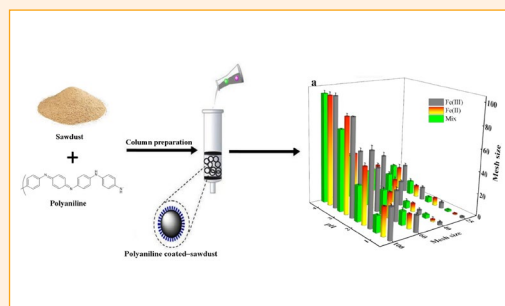


36–46

Analytical chemistry

Adsorption Behavior of Fe(II) and Fe(III) Ions on Polyaniiline Coated Sawdust: Batch and Fixed-Bed Studies

Seyed Jamaledin Mansoor and Fatemeh Abbasitabar

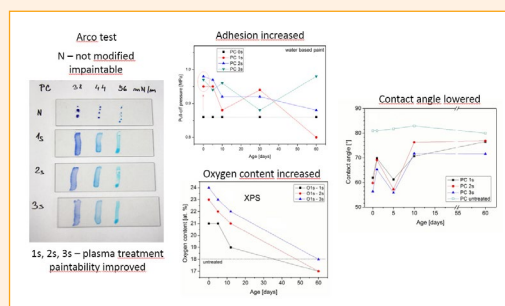


47–54

Materials science

DBD Plasma Influence on the Adhesion of Paints on Polymeric Substrates

Jindřich Matoušek, Pavlína Hájková and Jakub Perner

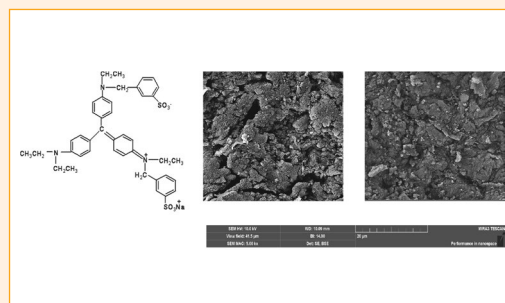


55–69

Chemical, biochemical and environmental engineering

Adsorption of Acid Violet 17 onto Acid-Activated Pistachio Shell: Isotherm, Kinetic and Thermodynamic Studies

İlknur Şentürk and Mazen Alzein

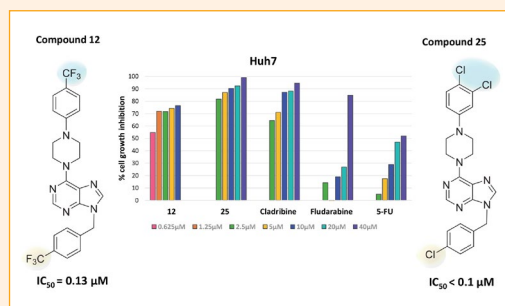


70–82

Organic chemistry

Design, Synthesis and *In Vitro* Cytotoxic Activity of New 6,9-Disubstituted Purine Analogues

Asligul Kucukdumlu, Meral Tuncbilek, Ebru Bilget Guven and Rengul Cetin Atalay

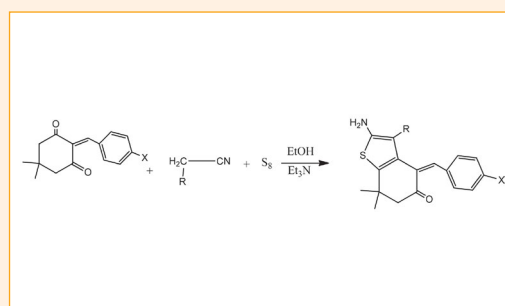


83–95

Organic chemistry

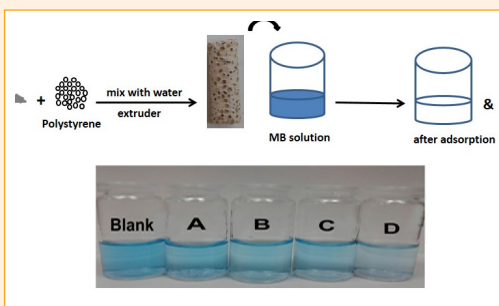
Synthesis of Heterocyclic Compounds Derived From Dimedone and their Anti-tumor and Tyrosine Kinase Inhibitions

Rafat M. Mohareb, Fatma M. Manhi and Amal Abdelwahab



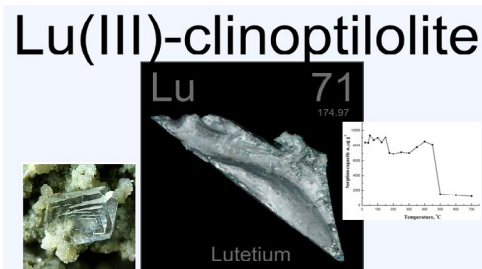
96–104 Chemical, biochemical and environmental engineering
Hybrid Membranes Based on Clay-Polymer for Removing Methylene Blue from Water

Ahmed M. Khalil and Sayed H. Kenawy



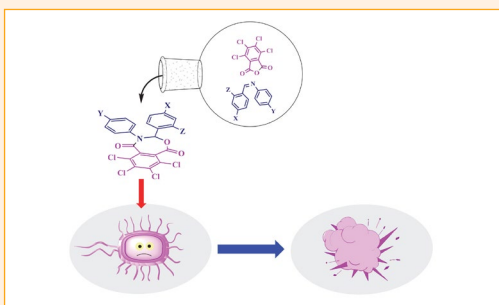
105–112 Applied chemistry
Preconcentration of Lutetium from Aqueous Solution by Transcarpathian Clinoptilolite

Emilia Stechynska, Volodymyr Vasylechko, Galyna Gryshchouk and Ihor Patsay



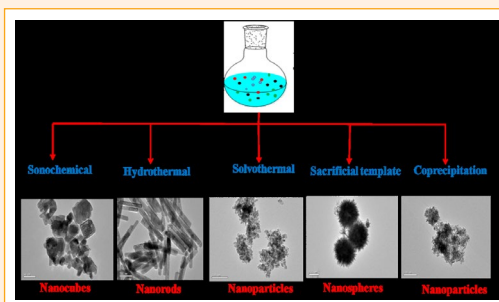
113–118 Organic chemistry
Synthesis and Characterization of Tetrachloro-1,3-Oxazepine Derivatives and Evaluation of their Biological Activities

Abdullah Hussein Kshash



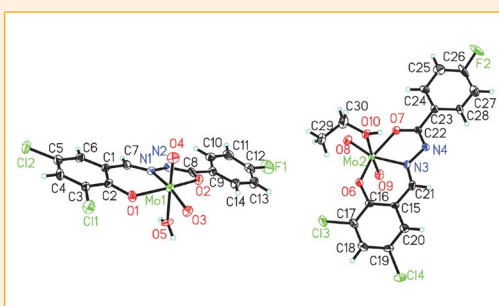
119–129 Materials science
Studies on Morphology and Photoluminescent Properties of Tb³⁺ Doped YbPO₄ Nanostructures Synthesized by Different Synthetic Methods

Heena Khajuria, Manesh Kumar, Lobzang Tashi, Rajinder Singh, and Haq Nawaz Sheikh



130– Inorganic chemistry
Oxidovanadium(V) and Dioxidomolybdenum(VI) Complexes of N³-(3,5-Dichloro-2-hydroxybenzylidene)-4-fluorobenzohydrazide: Synthesis, Characterization, Crystal Structures and Catalytic Property

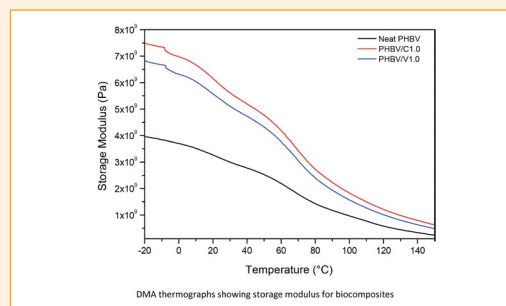
Huan-Yu Liu, Yi-Shu Yin, Luo-Ju Yang, Xiao-Ling Zou and Ya-Fang Ye



137–150 Materials science

Oxygen Barrier and Thermomechanical Properties of Poly (3-hydroxybutyrate-co-3-hydroxyvalerate) Biocomposites Reinforced with Calcium Carbonate Particles

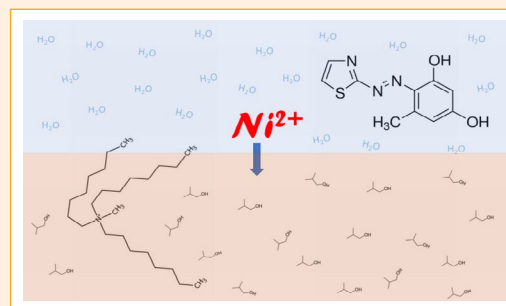
Semra Kirboga and Mualla Öner



151–158 Inorganic chemistry

Extraction-Chromogenic System for Nickel(II) Based on 5-methyl-4-(2-thiazolylazo)resorcinol and Aliquat 336

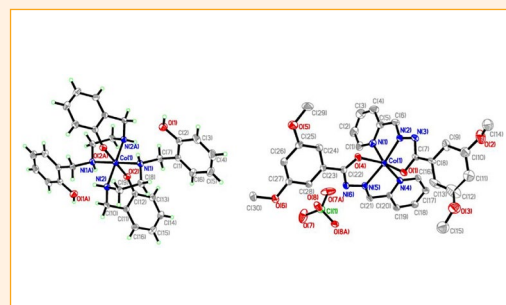
Galya Konstantinova Toncheva, Danail Georgiev Hristov, Nikolina Petkova Milcheva and Kiril Blazhev Gavazov



159–166 Inorganic chemistry

Syntheses, X-Ray Single Crystal Structures and Biological Activities of Cobalt(III) Complexes with Reduced Schiff Base Ligands

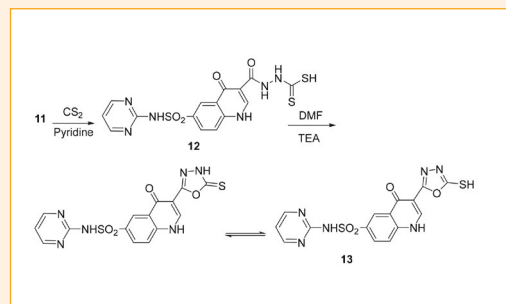
Xiao-Qiang Luo, Qiao-Ru Liu, Yong-Jun Han and Ling-Wei Xue



167–178 Organic chemistry

Some Studies in Sulfadiazine Incorporating Pyridine, Pyrimidine, Oxadiazole, and Azo Moieties Endowed with Pharmaceutical Potency

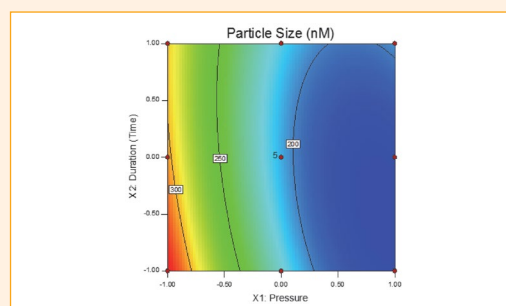
Sherihan A. El-Hadidya and Sraa Abu-Melhab



179–188 Physical chemistry

Formulation and Evaluation of Multidose Propofol Nanoemulsion Using Statistically Designed Experiments

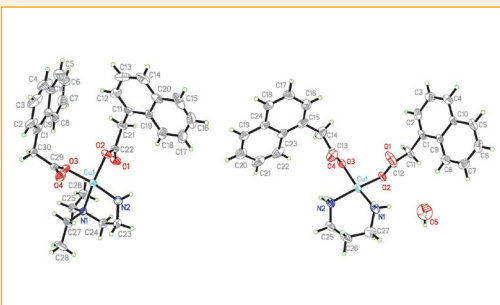
Sidhartha Sankar Hota, Satyanarayan Pattnaik and Subrata Mallick



189–194 Inorganic chemistry

Syntheses, Crystal Structures, Antimicrobial Activity and Thermal Behavior of Copper(II) Complexes Derived from 1-Naphthylacetic Acid and Diamines

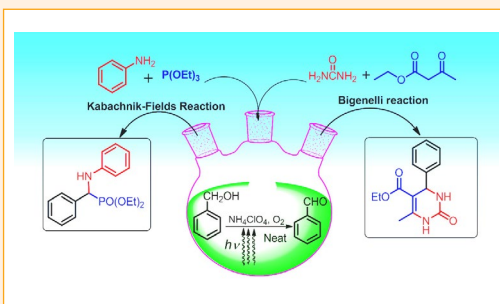
Ling-Wei Xue, Chen Chen, Gan-Qing Zhao and Wei-Chun Yang



195–202 Organic chemistry

Photo-Oxidation Coupled Kabachnik–Fields and Bigenelli Reactions for Direct Conversion of Benzyl alcohols to α -Aminophosphonates and Dihydropyrimidones

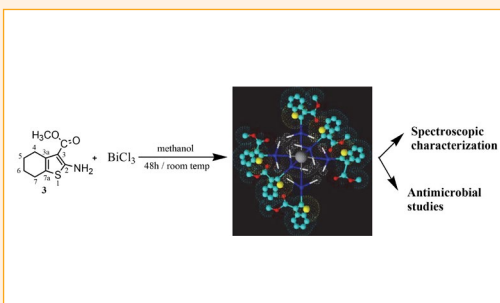
Gazunfor Ali, Nisar A. Dangroo, Shabnam Raheem, Tahira Naqvi, Tabassum Ara and Masood Ahmad Rizvi



203–211 Inorganic chemistry

Room Temperature Synthesis and Characterization of Novel Bi(III) Complex with 2-Amino-3-Carbomethoxy-4,5,6,7-Tetrahydrobenzo[B]Thiophene ...

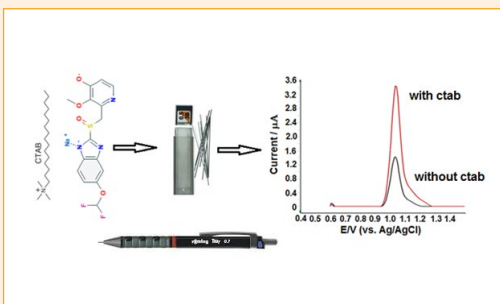
Emmanuel Sopbué Fondjo, Désire André Siéwé, Jean-de-Dieu Tamokou, Steve Endeguele Ekom, Sorel Kamal Dimo Djeukoua, Giscard Doungmo, Mallory E. Walters, Appolinnairé Tsopmo, Peter F. W. Simon and Jules Roger Kuate



212–220 Analytical chemistry

Electrooxidation and Low-tech Determination of Pantoprazole on a Disposable Pencil Graphite Electrode by the use of Cationic Surfactant

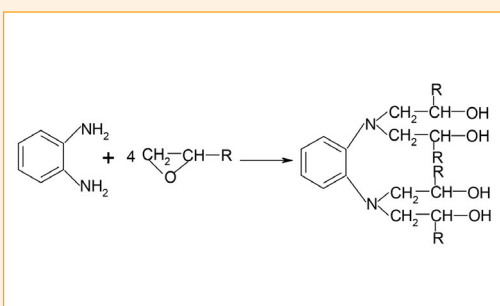
Pınar Talay Pınar



221–234 Applied chemistry

Derivatives of Phenylene-1,2-diamine as Modifiers for Unsaturated Polyester Resins

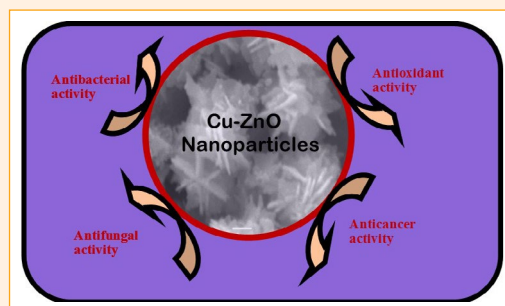
Renata Lubczak and Jerzy Duliban



235–245 Materials science

Synthesis, Characterization and Evaluation of Antimicrobial, Antioxidant & Anticancer Activities of Copper Doped Zinc Oxide Nanoparticles

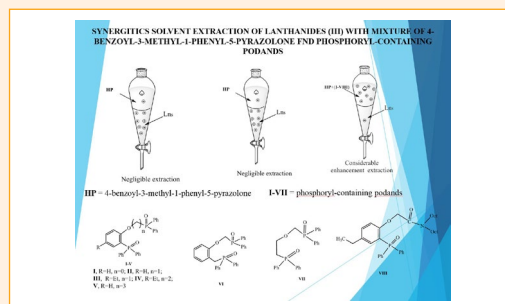
Saranya Rishikesan and Mubarak Ali Muhamath Basha



246–252 Inorganic chemistry

Synergistic Solvent Extraction of Lanthanides(III) with Mixtures of 4-Benzoyl-3-Methyl-1-Phenyl-5-Pyrazolone and Phosphoryl-Containing Podands

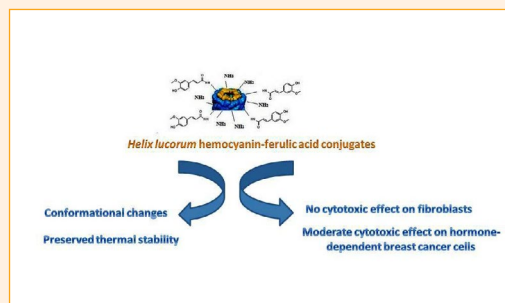
Alexander Nikolaevich Turanov, Vasili Konstantinovich Karandashev, Vladimir Evgenevich Baulin, Dmitriy Vladimirovich Baulin and Aslan Yusupovich Tsivadze



253–259 Biomedical applications

Biophysical Properties and Cytotoxicity of Feruloylated *Helix Lucorum* Hemocyanin

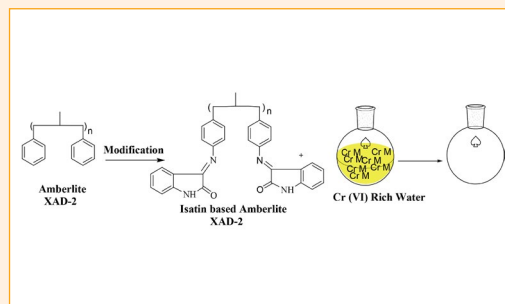
Maya Guncheva, Krassimira Idakieva, Svetla Todinova, Elena Stoyanova and Denitsa Yancheva



260–269 Chemical, biochemical and environmental engineering

Environmental Friendly Synthetic Modification of Amberlite XAD-2 Resin for the Removal of Highly Toxic Hexavalent Chromium from Water

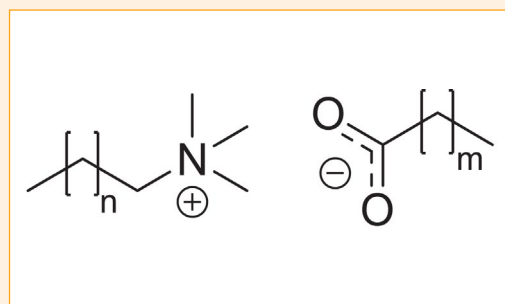
Waqas Jamil, Zunaira Memon, Saima Qayyum Memon, Muhammad Kashif Samon, Muhammad Taha and Khalid Mohammad Khan



270–275 Organic chemistry

Scalable Synthesis of Salt-free Quaternary Ammonium Carboxylate Catanionic Surfactants

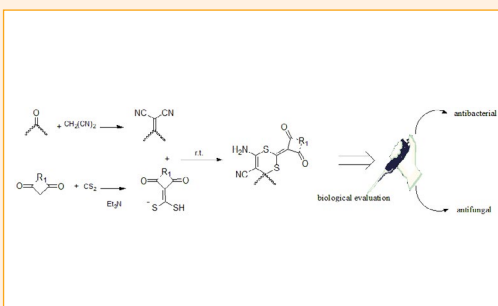
Žiga Medoš, Miha Virant, Urša Štanfel, Boštjan Žener, Janez Košmrlj and Marija Bešter-Rogač



276–282 Organic chemistry

Synthesis, Characterization and Antimicrobial Evaluation of Novel 6'-Amino-spiro[indeno[1,2-*b*]quinoxaline[1,3]dithiine]-5'-carbonitrile Derivatives

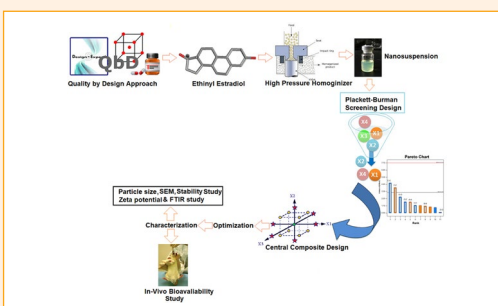
Mohammadreza Moghaddam-Manesh, Dadkhoda Ghazanfari, Enayatollah Sheikhhosseini and Mohammadreza Akhgar



283–303 Materials science

QbD Based Approach to Enhance the *In-Vivo* Bioavailability of Ethinyl Estradiol in Sprague-Dawley Rats

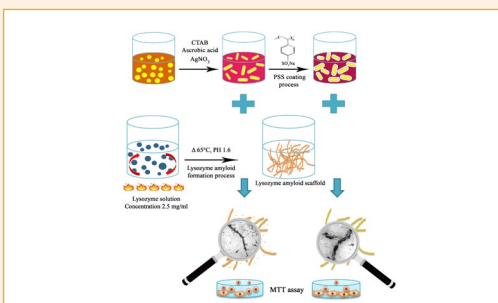
Trupti Ashok Powar and Ashok Ananda Hajare



304–311 Materials science

Surface Functionalization of Gold Nanorods Improves Nanostructure Assemblies on Amyloid Fibril Scaffolds

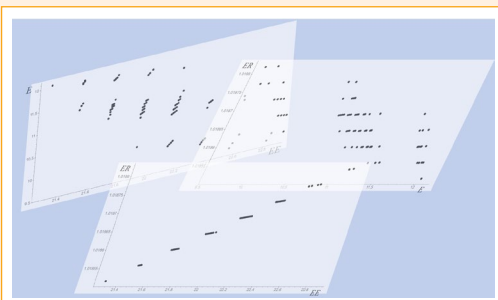
Mani Salimian, Tahereh Tohidi Moghadam and Bijan Ranjbar



312–318 Physical chemistry

On Relationships of Eigenvalue-Based Topological Molecular Descriptors

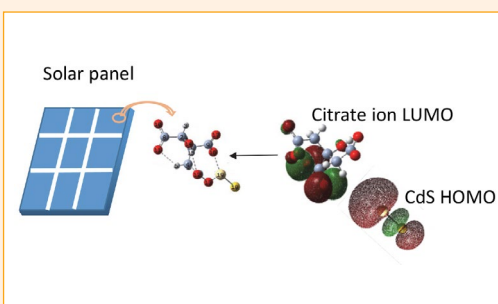
Izudin Redžepović and Boris Furtula



319–324 Materials science

Ab-Initio Study of Citrate Ion as an Oxygen-Rich Complexing Agent

Armando G. Rojas-Hernández, Aned de Leon, Rafael A. Sabory-García, Rafael Ramírez-Bon, Dainet Berman-Mendoza and Santos J. Castillo

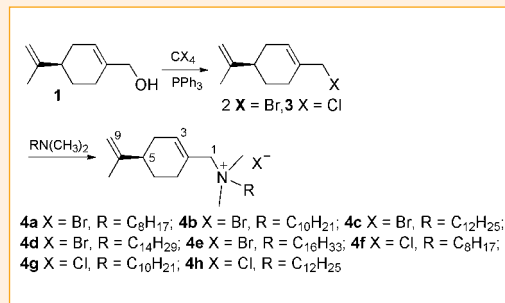


325–335

Organic chemistry

Synthesis of New Quaternary Ammonium Salts with a Terpene Function and Evaluation of their Fungicidal and Herbicidal Activities

Krzysztof Żelechowski, Mirosław Gucma, W. Marek Gołębiewski,
Maria Krawczyk and Alicja Katarzyna Michalczyk

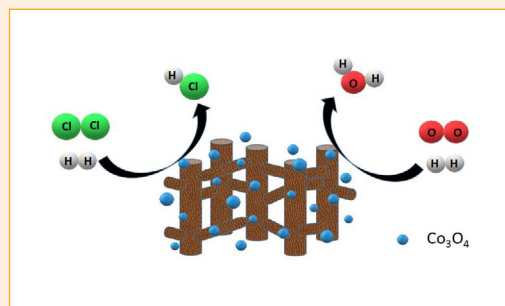


336–347

Applied chemistry

Cobaltic Oxide Catalysts for Catalytically Removing Hydrogen from Tail Chlorine

Tong Zhang, Ling Xue, Jianwei Xue, Fuxiang Li and Zhiping Lv



Feature article

Ionic Liquids: Simple or Complex Electrolytes?

Marija Bešter-Rogač*

University of Ljubljana, Faculty of Chemistry and Chemical technology, Večna pot 113, SI-1000 Ljubljana, Slovenia

* Corresponding author: E-mail: marija.bester@fkkt.uni-lj.si

Received: 01-30-2020

Paper presented as a key-note lecture at the 25th Annual Meeting of the Slovenian Chemical Society, Maribor, 25.–27. 9. 2019 and dedicated to the memory of Professor Josef Barthel, who passed away in February 2019.

Abstract

Ionic liquids belong to the most investigated systems in the recent years and this field is still significantly growing with an increased focus on developing ionic liquids for specific applications, along with fundamental research. In the present featured paper the similarity and differences between common, “classical” electrolytes and common surfactants and ionic liquids along with the surface-active ionic liquids are discussed in order to stress their significance and point out on their weak points. A short survey of the literature data reveals namely that ionic liquids in solutions behave like “classical” electrolytes and can be described by existing models in the range of their validity. There is still a lack of models describing well the concentrated electrolyte solutions and here ionic liquids, less limited by solubility as common electrolytes, can serve as model systems. The micellization of surface-active ionic liquids in aqueous solutions can be described in the same way as for common surfactants, but surface-active ionic liquids offer more possibilities to study specific ion and isomer effects. They are also quite promising systems to study the aggregation processes in non-aqueous solutions.

Keywords: Ionic liquids; surface active ionic liquids; aqueous solutions; non-aqueous solutions

1. Introduction

Ionic liquids (ILs) are molecules composed of anions and cations in which at least one component is an organic molecular structure that hinders efficient close packing. Thus, their melting point temperatures are below 100 °C which differentiate them from typical inorganic salts.

ILs can have useful physical properties, such as low volatility, and are often used as solvents and electrolytes. As suitable systems for a wide range of applications they attracted the attention of many researchers. It turned out² that ILs are more complex than molecular solvents and thus their bulk and interfacial structures are markedly different. They show rich structural diversity both in the nature of ions that can be employed as well as in the organization of these ions in the liquid phase. A sample of representative popular anions and cations chemical structures usually used in ILs is presented in Figure 1.²

By increasing the cationic alkyl side-chain length even the transition from the known spatially heterogeneous structure to a liquid crystal-like phase was observed.³

However, the growing number of reviews dealing with the physicochemical properties of ILs in their pure state has

been extended to investigations of their mixtures with molecular cosolvents. It has been shown that ILs in solutions can serve as excellent model (electrolyte) systems, because they exist in diverse structures and the hydrophobic part of the cation can be varied almost optionally. Investigations of ion association of ILs in diverse organic solvents reveal namely that their ion pairing is entropy-driven and thus associated with cation desolvation, in line with the only moderate strength of cation-solvent interactions.^{4,5} The association of imidazolium based ILs as model 1,1-electrolytes in water solutions is weak but evidently dependent on the molecular structure (alkyl chain length), which also strongly affects the mobility of imidazolium cations.⁶ According to experimental and computational results, hydrophobic hydration of the side chain on the imidazolium ring is most responsible for structure making/breaking properties of investigated imidazolium salts.⁷ Ionic liquids with long alkyl chains behave similar to conventional surfactants forming aggregates in water,⁸ but due to possible variations in the chain length and counter-ions they are extremely appropriate for studying self-assembly processes in solutions.

Thus, ILs exhibit properties from simple salts to liquid crystal-like structures and there are still many unex-

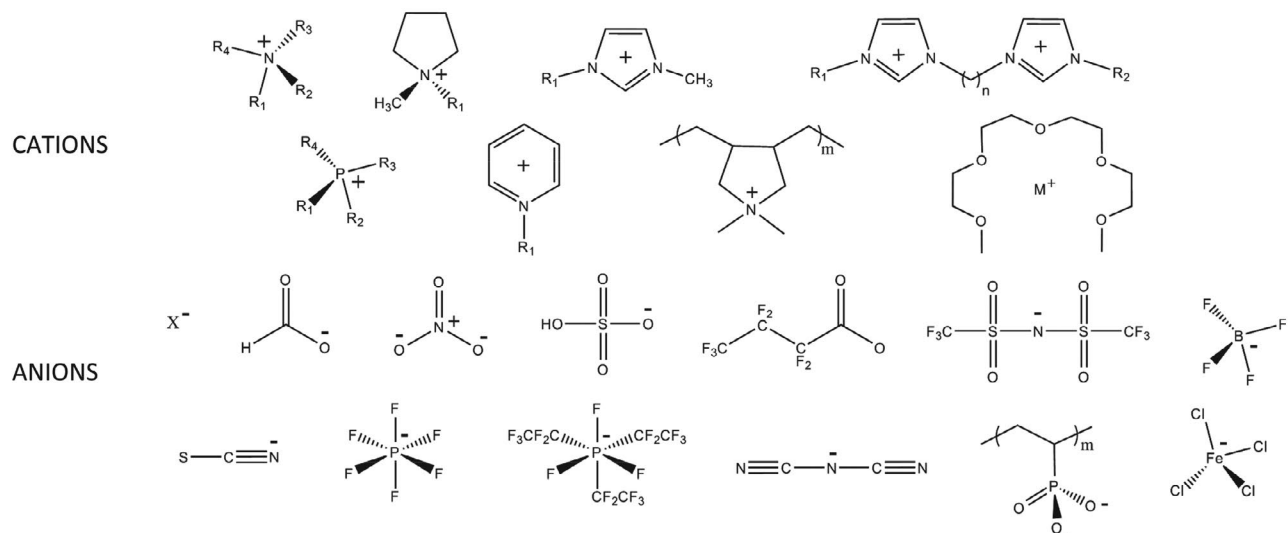


Figure 1. Some chemical structures of representative cations and anions used in ionic liquids. From left to right, the cations (top row) include: ammonium, pyrrolidinium, 1-methyl-3-alkylimidazolium, 1,3-bis[3-methylimidazolium-1-yl]alkane; (second row) phosphonium, pyridinium, poly(diallyldimethylammonium), metal (M^+) tetraglyme. The anions include (third row) halides, formate, nitrate, hydrogen sulfate, heptafluorobutyrate, bis(perfluoromethylsulfonyl)imide, tetrafluoroborate, (bottom row) thiocyanate, hexafluorophosphate, tris(pentafluoroethyl)trifluorophosphate, dicyanamide, poly(phosphonic acid), and tetrachloroferrate. Reprinted with permission from ref.² <https://pubs.acs.org/doi/10.1021/cr500411q>. Further permissions related to the material excerpted should be directed to the ACS.

explored opportunities for manipulating their structure to control their functions and applications.

2. Ionic Liquids in Their Pure State

The large number of cation-anion combinations and the tunability of the cation and/or the anion structure offer possibility to synthesize ILs with targeted properties. In Figure 2 a schematic representation of the different types of possible interactions in an imidazolium-based ionic liquid is presented.⁹ In addition, the hydrophobicity of cation can be varied by the length of side alkyl chains.

Consequently, ILs in their pure state exist in very different structures. Figure 3 shows an example for the struc-

tures in the bulk phase of imidazolium hexafluoro phosphate ($[C_n\text{mim}]\text{PF}_6$), where the increase in the length of side chain from 2 to 12 carbon atoms leads from globular to sponge-like structure.

On the whole – dependent on the composition and building elements of an ionic liquid there are diverse possibilities for structuring – from ion pairs, hydrogen bond networking to ion clusters and – as seen already before – to self-assembled structures (Figure 4).

Thus, ILs even in their pure state form rather complicated and complex structures, whereas for example in sodium chloride, as the simplest electrolyte, the single unit has completely known and unique properties. Sodium and chloride ions have ascribed defined positions and so the structure of the NaCl crystal has no diversity,

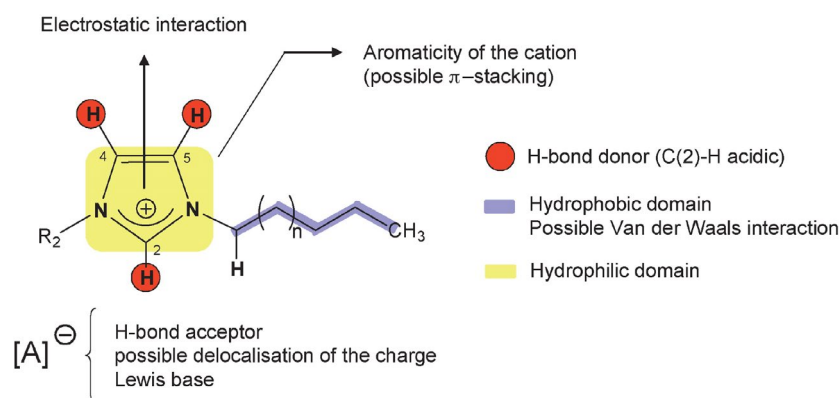


Figure 2. Schematic representation of the different types of interactions present in imidazolium based ILs. Reprinted from ref.⁹ with permission from Elsevier.

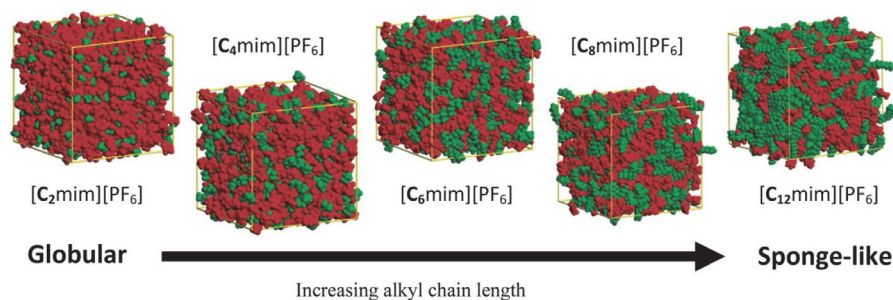


Figure 3. Snapshots of the bulk structure of $[C_n\text{mim}]\text{PF}_6$ ILs for $n = 2\text{--}12$. Each box shows 700 IL ion pairs at equilibrium with polar domains (red, anion + cation imidazolium ring) and nonpolar domains (green, cation alkyl chain) observed. Note that the box dimensions are not of the same length due to differences in ion size and box density. Reprinted with permission from ref.² <https://pubs.acs.org/doi/10.1021/cr500411q>. Further permissions related to the material excerpted should be directed to the ACS.

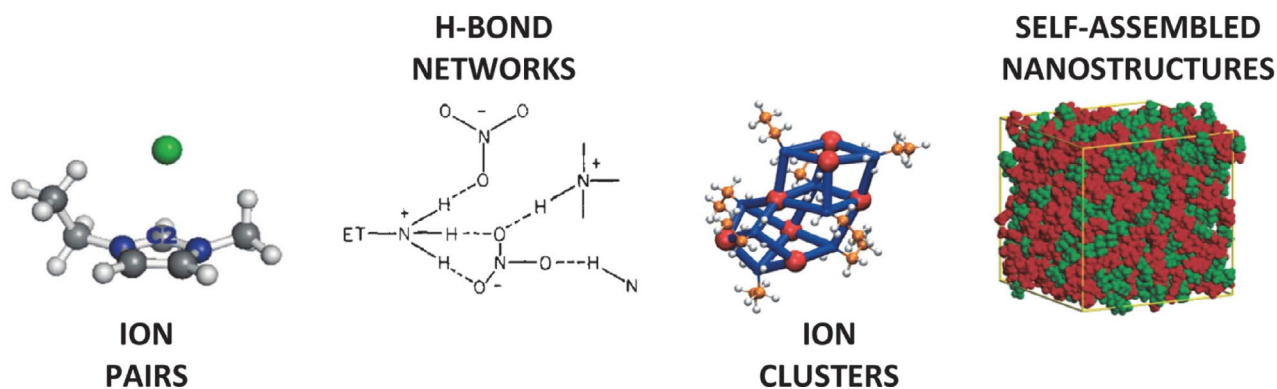


Figure 4. Different models for the bulk structure of ILs. See text for details. Reprinted with permission from ref.² <https://pubs.acs.org/doi/10.1021/cr500411q>. Further permissions related to the material excerpted should be directed to the ACS.

should be easily understood and thus it is simple in comparison to different structures of ionic liquids. Therefore, ionic liquids can without doubt be judged as complex electrolytes in their pure state. The reason for this complexity is – as already mentioned – mainly in the structure of cations.

3. Ionic Liquids in Solutions

Whereas understanding the properties of pure ILs is of fundamental interest, the practical applications generally require the admixture of other compounds, acting either as a reactant or product or as a cosolvent required for process optimization.¹⁰ Some earlier investigations^{11–14} reveal that addition of an IL in an organic solvent enhances the electrochemical and thermal stability of IL/organic solvent binary mixtures which often reflects in higher electrical conductivity and better device performances at low temperature than comparable mixtures of salts with high melting point temperatures.¹⁵

Recently, it has been demonstrated that ILs can serve as an excellent model system for investigating the influence of the ion structure on the mobility and ion pairing even in aqueous solutions, where the interionic interac-

tions are weak.^{6,16,17} It turned out that due to possible variations in the structure of chain length and counter-ions the surface active ionic liquids (SAILs) have a great potential for investigation of micellization process in aqueous solutions.^{8,18,19} Even more, SAILs were used in investigations of aggregation behavior in non-aqueous solvents where solvophobic effect and the hydrogen-bonding interactions were found as the main factors controlling the aggregates formation.^{20,21}

3. 1. Ionic Liquids in Aqueous Solutions

Ion Mobility. Recently, the mobility and the mechanism of ion pairing in aqueous solutions were investigated systematically on nine imidazolium based ILs from 1-methylimidazolium chloride, $[\text{mim}]\text{Cl}$, to 1-dodecyl-3-methylimidazolium chloride, $[\text{C}_{12}\text{mim}]\text{Cl}$, with two isomers 1,2-dimethylimidazolium chloride, $[\text{1,2-mim}]\text{Cl}$, and 1,3-dimethylimidazolium chloride, $[\text{1,3-mim}]\text{Cl}$ in the line.⁶ The values of their molar electric conductivity – as still one of the most suitable quantity for investigation of electrolyte solutions – for diluted solutions of the studied ILs at 298.15 K are presented on Figure 5 together with the data for NaCl aqueous solution for comparison.

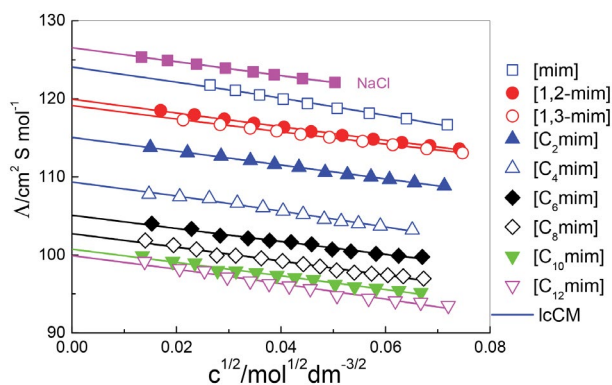


Figure 5. Molar conductivity of investigated imidazole based ILs chlorides⁶ and NaCl²² at 298.15 K in water; symbols denote experiment and lines lCCM calculations.

As one can see here, the values for NaCl are only slightly higher than those for [mim]Cl. So it can be assumed that studied ILs in diluted water solution behave like simple 1,1-electrolytes – molar conductivity is linear dependent on the square root of concentration.

The experimental molar conductivity of diluted IL solutions ($c \approx \leq 0.005$ M) were analyzed in the framework of Barthel's low-concentration chemical model (lCCM) which describes successfully thermodynamic and transport properties of diluted solutions, yielding the molar conductivity of the solute at infinite dilution, Λ^∞ , and the standard-state (infinite dilution) ion association constant, K_A , (details are given in ref.²³). By using the literature value $\lambda_{\text{Cl}^-}^\infty(298.15\text{K}) = 76.35 \text{ S} \cdot \text{cm}^2 \cdot \text{mol}^{-1}$, the limiting molar conductivity was split into separate ionic contributions, λ_i^∞ , and then the values of limiting ionic conductivity were estimated for all cations. Consequently, the diffusion coefficients, D_i^∞ , as the characteristic properties of ionic trans-

port, which are not affected by inter ionic interactions, were calculated by using the relation

$$D_i^\infty = \frac{k \cdot T}{e_o |z_i| F} \lambda_i^\infty \quad (1)$$

Values of D_i^∞ for ILs cations, studied in⁶ at 298.15 K are presented in Figure 6 as a function of the number of C atoms in the alkyl side chain, together with the values that were obtained from MD simulations that were carried out at the same temperature.⁶

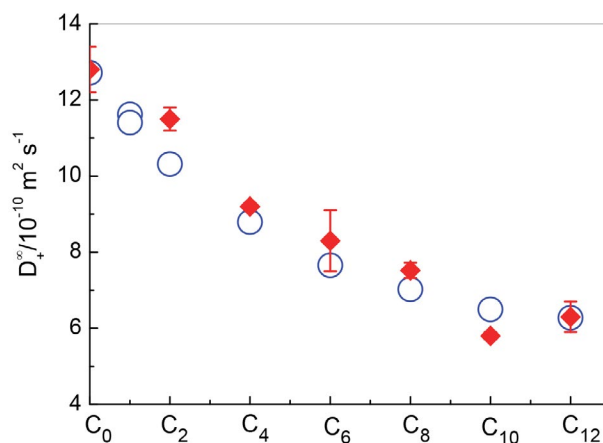


Figure 6. Diffusion coefficients of imidazolium based cations in water at 298.15K as a function of the number of carbon atoms in the side chain: (○) experiment; (◆) MD simulations. Figure reproduced from ref.⁶ with permission from PCCP Owner Societies.

Again, the diffusion coefficient of [mim]⁺ is only slightly lower from that for Na⁺, $D_{\text{Na}^+}^\infty(298.15 \text{ K}) = 13.3 \cdot 10^{-10} \text{ m}^2 \cdot \text{s}^{-1}$, and D_+^∞ is decreasing with increasing length

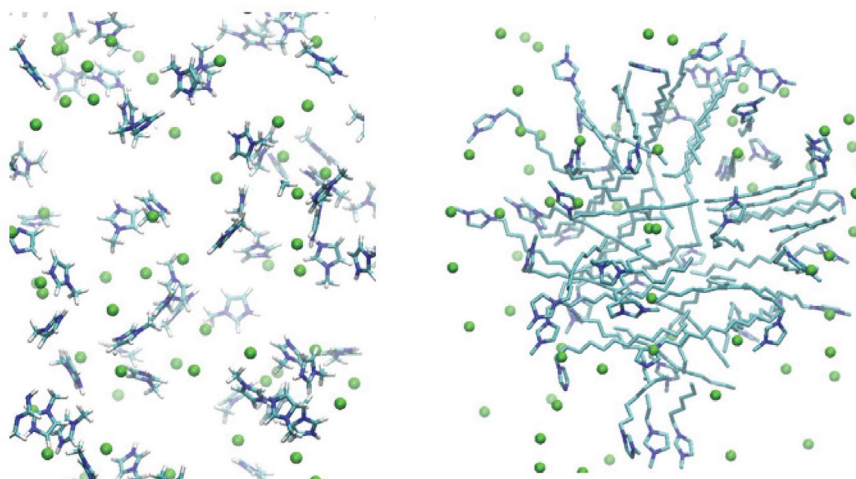


Figure 7. Representative structures of [mim]Cl in solution (left hand side) and [C₁₂mim]Cl (right hand side) taken from equilibrated MD simulations at very high IL concentrations (1.0 M and 1.2 M, respectively). It can be clearly seen that [C₁₂mim]Cl forms micelles in contrast to [mim]Cl, which remained dispersed. The display of water and hydrogens was omitted for clarity. Color code: C = cyan, N = blue and Cl = green. Figure reproduced from ref.⁶ with permission from PCCP Owner Societies.

of alkyl chain (Figure 6), but not linearly with the growing number of C atoms in the side alkyl chain as it has been also obtained by MD simulations.^{6,24} In addition, it was found that the aggregation tendency of cations with long alkyl chains at higher IL concentrations impedes their diffusivity.

This assumption was confirmed by the results of MD simulations at high concentrations. It was observed that within less than 1 ns $[C_{12}mim]^+$ cations formed micelles that remained stable throughout the rest of the simulations as expected. In contrast, $[mim]^+$ cations remained dispersed in water and did not show any signs of aggregation. The cation distribution in water is visualized for these two cases in Figure 7.⁶ The reduction of $[C_{12}mim]^+$ diffusivity is thus also a result of the cation aggregation. $[C_{12}mim]^+$ cations diffuse as members of these micelle aggregates, which move much slower through the solvent than single cations because of the large aggregate sizes.

Recently, for $[C_2mim]Cl$, $[C_4mim]Cl$, $[C_6mim]Cl$ and $[C_8mim]Cl$ the data on conductivity of concentrated aqueous solutions at 298.15 K, presented in Figure 8, were published.²⁵ To reproduce this type of concentration dependence, the empirical Casteel-Amis four-parameter equation²⁶ is widely used. Generally, data fitting is carried out on the molality scale. For the present systems, Casteel-Amis equation can be reasonably applied in the mole-fraction scale of IL, x_{IL} , that is

$$\kappa = \kappa_{max} \left(\frac{x_{IL}}{x_{IL,max}} \right)^n \exp \left[m \left(x_{IL} - x_{IL,max} \right)^2 - n \left(\frac{x_{IL} - x_{IL,max}}{x_{IL,max}} \right) \right] \quad (2)$$

where, κ_{max} is the highest electrical conductance for a given mixture, $x_{IL,max}$ is the mole fraction of IL in which the electrical conductivity of the mixture at a given temperature shows a maximum, and n and m are parameters of the fit. Casteel-Amis parameters are given in Table S1 in the Supplementary data and fitted conductivity values are graphically presented in Figure 8. In the inset of Figure 8, the values for NaCl solutions are added for comparison.

Evidently, in all the here presented systems, conductivity increases sharply in dilute region, due to the increased number of free ions in solutions. But with the addition of ILs, it reaches maximum at nearly the same mole fraction, *i.e.* at around $x_{IL} \cong 0.05$, and then it decreases. This trend is assumed to be the result of the competition between the increasing number of free ions available to contribute to the conductivity and the increasing system viscosity, impeding ion mobility. And here, the conductivity decreases also with the increasing alkyl chain length of the cation, whereas the viscosity is higher for ILs with a longer side chain. As ions are added to the system ion diffusion is hindered by increased viscous forces, resulting in a decrease in ion mobility and, thus, diffusion.

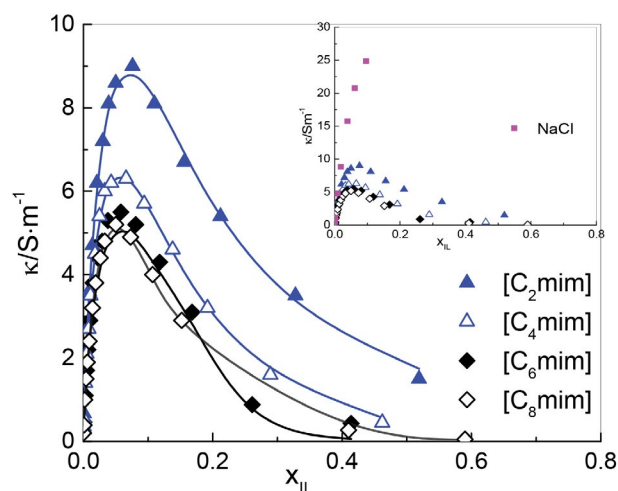


Figure 8. Specific conductivity, κ , of some imidazolium based ILs chlorides at 298.15 K in water as drawn from the literature data.²⁵ Inset: κ of some ILs chlorides and NaCl at 298.15 K in water.²⁷ Symbols represent experimental values and lines the Casteel-Amis-type fitting (Eq. (2)) of the experimental data with parameters reported in Table S1 of the Supplementary data.

Actually, this behavior is not new – the same was observed for “common simple” electrolytes, where the maximum often was not reached due to limited solubility, as it is demonstrated here for NaCl in water (inset in Figure 8). And thus, ILs could be very helpful at studying the concentrated electrolyte solutions, where the reliable theories are still lacking.

Ion association. For in the ref.⁶ studied imidazolium based ILs in water it was found, that K_A values are small ($\sim 2.5 \leq K_A \leq \sim 6$) but distinctly higher than obtained with the same model recently for alkali metal halides in water.²⁸ For $[C_4mim]^+$, $[C_6mim]^+$, and $[C_{12}mim]^+$, the binding free energies with Cl^- , ΔG_{bind}^{MD} , were obtained also from

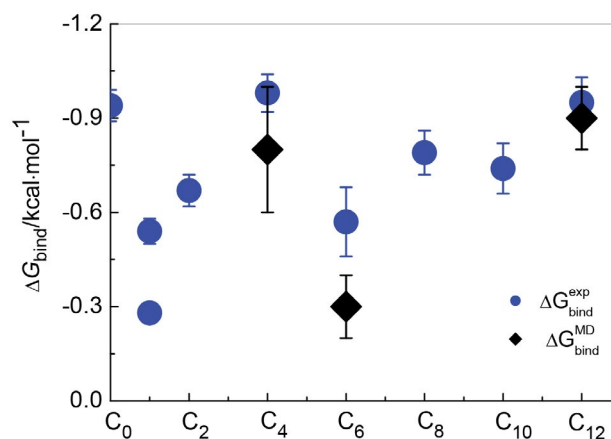


Figure 9. Comparison of binding free energies for imidazolium based chlorides in water as a function of the number of C atoms in the side alkyl chain as obtained from conductivity experiment, ΔG_{bind}^{exp} , and from MD simulations, ΔG_{bind}^{MD} . Adopted from ref.⁶ with permission from PCCP Owner Societies.

MD simulations, using thermodynamic integration as specified in ref.⁶ From the measured values of K_A , binding free energies were calculated using the relation $\Delta G_{\text{bind}}^{\text{exp}} = -RT \cdot \ln K_A$. In Figure 9, the comparison of $\Delta G_{\text{bind}}^{\text{exp}}$ and $\Delta G_{\text{bind}}^{\text{MD}}$ is shown. Evidently, results from MD simulations are in reasonable agreement with the experiment.

Despite the fact that conductivity measurements of dilute electrolyte solutions are probably still the most accurate route to ion-pair association constant, K_A , at least for symmetrical electrolytes,²³ such studies can determine only the overall association and thus yield little information on the nature of the aggregate(s) formed, while conventional spectroscopic techniques, like NMR or Raman spectroscopy, generally detect only contact CIPs.²⁹ On the other hand, dielectric relaxation spectroscopy (DRS) is sensitive to all ion-pair types and allows their identifica-

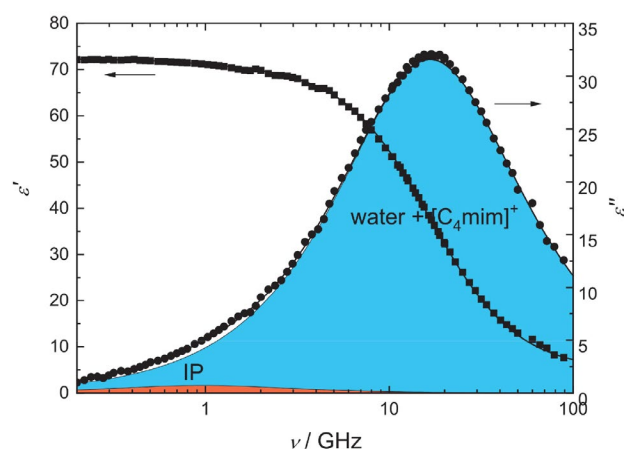


Figure 10. Relative permittivity, $\varepsilon'(\nu)$ (■) and dielectric loss, $\varepsilon''(\nu)$ (●) spectrum of a representative $[\text{C}_4\text{mim}]\text{Cl}$ solution in water ($c = 0.4618 \text{ mol dm}^{-3}$) at 298.15 K. Symbols represent experimental data, lines show the corresponding fit, and the shaded areas indicate the contributions of the individual processes to $\varepsilon''(\nu)$. Adopted from ref.³² with permission from PCCP Owner Societies.

tion and quantification provided reasonably accurate dipole moments, μ_i , of the species formed are available or can be calculated.^{30,31} Having a look on DRS spectra for $[\text{C}_4\text{mim}]\text{Cl}$ solution in water (Figure 10) we can see an area, which corresponds to ion pairs (IP).³²

Thus, MD simulations and experiments reveal that the association of investigated ILs as model 1,1 electrolytes in water solutions is weak but evidently dependent on the molecular structure (alkyl chain length), which also strongly affects the mobility of cations.

3. 2. Ionic liquids in Non-aqueous Solutions

Pure ILs are usually quite viscous and less conductive, whereas the mixing of ILs with molecular liquids (cosolvents) causes a significant decrease of viscosity and a sharp increase of conductivity.^{11–14} A huge number of investigations on conductivity of mixtures of ILs with molecular solvents is available in the literature. Surprisingly, despite the large practical interest for such systems, systematic studies of the transport properties of binary mixtures of ILs and cosolvents in a broad concentration range – from diluted solutions to pure ILs – are still scarce. Thus, in this paper we will focus our attention mainly on those imidazolium based ILs, which are also well investigated in a broader concentration range in aqueous and non-aqueous solutions and thus the comparison of their properties is possible.

Diluted solutions. In Figure 11 a) the molar conductivity of $[\text{C}_4\text{mim}]\text{Cl}$ in acetonitrile (AN),³² methanol (MetOH)⁵ and dimethyl sulfoxide (DMSO)⁵ are presented together with values in water.⁶ Evidently, the mobility of $[\text{C}_4\text{mim}]^+$, as indicated by the ionic limiting conductivity $\lambda_{[\text{C}_4\text{mim}]^+}^\infty$ and the diffusion coefficients $D_{[\text{C}_4\text{mim}]^+}^\infty$, is decreasing with increasing viscosity of the solvents (Table 1).

In Figure 11 b), the molar conductivity of $[\text{C}_4\text{mim}]\text{Cl}$,³² $[\text{C}_4\text{mim}]\text{BF}_4$ ⁴ and – for comparison – tetra-

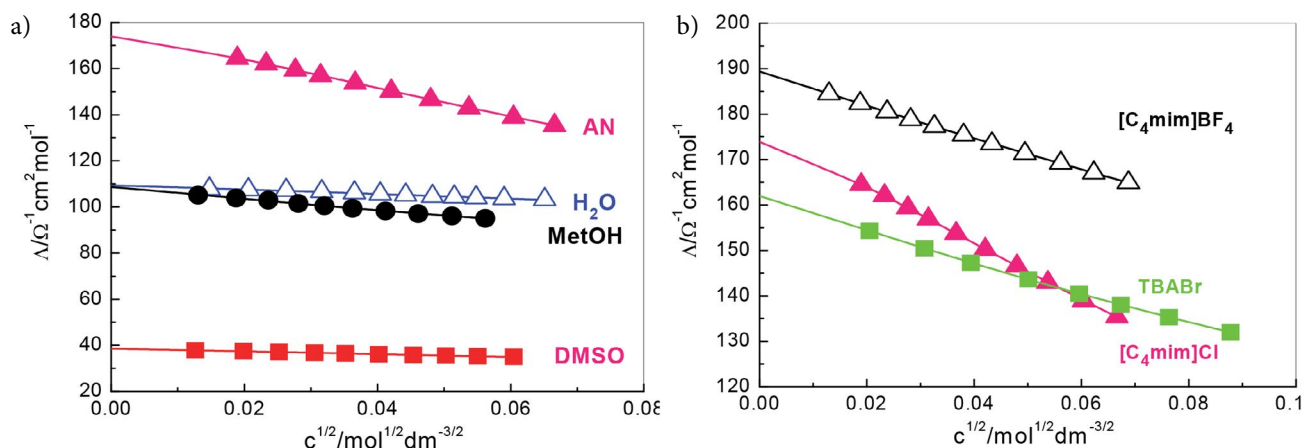


Figure 11. Molar conductivity of a) $[\text{C}_4\text{mim}]\text{Cl}$ in AN,³² water,⁶ MetOH⁵ and DMSO⁵ and b) $[\text{C}_4\text{mim}]\text{Cl}$,³² $[\text{C}_4\text{mim}]\text{BF}_4$ ⁴ and TBABr in AN³³ at 298.15 K; symbols denote experiment and lines lCCM calculations.

Table 1. Literature data on molar limiting conductivity, Λ^∞ , and association constants, K_A , for $[\text{C}_4\text{mim}]\text{Cl}$ and $[\text{C}_4\text{mim}]\text{BF}_4$ in water, DMSO, AN, DMF, MeOH and DCM at 298.15 K as obtained from lcCM model. Where possible, ionic limiting conductivity $\lambda_{[\text{C}_4\text{mim}]^+}^\infty$ and the (average) values of the diffusion coefficients $D_{[\text{C}_4\text{mim}]^+}^\infty$ are given. ϵ and η denote dielectric constant and viscosity of solvents, respectively.^a

	ϵ	η	Λ^∞		K_A		$\lambda_{[\text{C}_4\text{mim}]^+}^\infty$		$D_{[\text{C}_4\text{mim}]^+}^\infty$
			Cl^-	BF_4^-	Cl^-	BF_4^-	Cl^-	BF_4^-	
H ₂ O	78.36	0.8903	109.34 ^b 108.64 ^c		5.2 ^b 6.2 ^c		32.99 ^b 32.29 ^c		8.69
DMSO	46.52	1.9946	38.53 ^d	41.51 ^d	13.4 ^d	4.6 ^d	14.89 ^d	14.53 ^d	3.92
DMF	36.81	0.845		89.83 ^e		10.6 ^e			
AN	35.96	0.3413	173.91 ^c	189.29 ^f 190.37 ^g	63.7 ^c	15.7 ^f 17.8 ^g	81.55 ^c	81.81 ^f	21.75
MetOH	32.63	0.5438	108.64 ^d	121.84 ^d 128.4 ^h	15.5 ^d	37.7 ^d 57.5 ^h	56.25 ^d		14.98
DCM	8.82	0.415		161.08 ⁱ		479 ⁱ			

^aUnits: η , mPa · s; Λ^∞ , $\lambda_{[\text{C}_4\text{mim}]^+}^\infty$, S · cm² · mol⁻¹; $D_{[\text{C}_4\text{mim}]^+}^\infty$, 10⁻¹⁰ m² s⁻¹ ^bref.⁶ ^cref.³² ^dref.⁵ ^eref.³⁴ ^fref.⁴ ^gref.¹⁶ ^href.¹⁷ ⁱref.³⁵

butylammonium bromide (TBABr)³³ as “classical” electrolyte in AN are shown. While in water only weak association was observed ($K_A \cong 5\text{--}6$) for $[\text{C}_4\text{mim}]\text{Cl}$, it is expectedly more expressed in solvents with lower dielectric constants, but evidently depends strongly also on the anion as can be seen in Table 1, where literature data of molar limiting conductivity, Λ^∞ , and association constants, K_A , for $[\text{C}_4\text{mim}]\text{Cl}$ and $[\text{C}_4\text{mim}]\text{BF}_4$ in water, DMSO, AN, N,N-Dimethylformamide (DMF), MeOH and dichloromethane (DCM) at 298.15 K are gathered, as obtained from lcCM model. Where the value of the ionic limiting conductivity $\lambda_{[\text{C}_4\text{mim}]^+}^\infty$ is available, also the (average) values of the diffusion coefficient $D_{[\text{C}_4\text{mim}]^+}^\infty$ are listed.

Whereas values of Λ^∞ are not very “sensitive” on the applied model for the analysis of conductivity data, the opposite is true for K_A . Even more, K_A values are also slightly dependent on the set upper distance limit at which the ions are still treated as ion pairs. However, the abundant different interactions acting together in ILs make them very complex (Figure 2), so that it is not surprising that the dielectric constant is incapable to adequately model the solvent–solute interactions and has often failed in correlating solvent effects qualitatively and quantitatively. It is namely rather surprising, that K_A values for $[\text{C}_4\text{mim}]\text{Cl}$ and $[\text{C}_4\text{mim}]\text{BF}_4$ in AN and MeOH are different despite very similar dielectric constants of these two solvents. However, the obtained K_A values for $[\text{C}_4\text{mim}]\text{BF}_4$ and $[\text{C}_4\text{mim}]\text{Cl}$ in AN are in line with those reported for sodium tetraphenylborate ($K_A = 13.9$ at 298,15 K³⁶) and TBABr ($K_A = 27.5$ at 298.15 K³³).

Having a look on DRS spectra for the $[\text{C}_4\text{mim}]\text{Cl}$ solution in AN (Figure 12) and in water (Figure 10) we can see an area, which corresponds to ion pairs (IP), and this area is much bigger in AN than in water. Thus, evidently the ion pair formation tendency is stronger in AN and the

values of K_A obtained from conductivity data using lcCM model make sense. It could be again concluded that ILs in solutions behave as common (“classical”) simple electrolytes, with more expressed ion association in solvents with lower dielectric constants.

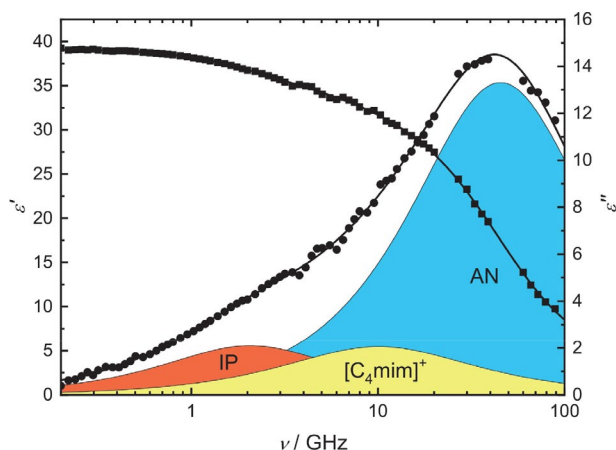


Figure 12. Relative permittivity, $\epsilon'(\nu)$ (■) and dielectric loss, $\epsilon''(\nu)$ (●) spectrum of a representative $[\text{C}_4\text{mim}]\text{Cl}$ solution in AN ($c = 0.4658$ mol dm⁻³) at 298.15 K. Symbols represent experimental data, lines show the corresponding fit, and the shaded areas indicate the contributions of the individual processes to $\epsilon''(\nu)$. Adopted from ref.³² with permission from PCCP Owner Societies.

Concentrated solutions. Despite still growing number of studies and reviews dealing with physicochemical properties of ILs in the pure state and of their mixtures with cosolvents, the systematic studies on transport properties covering entire miscibility range are still scarce. In Figure 13 a) some literature data on conductivity of concentrated solutions of $[\text{C}_4\text{mim}]\text{BF}_4$ in AN, MeOH, DMSO, DCM, and propylene carbonate (PC, $\eta = 2.512$ mPa · s, $\epsilon = 64.96$

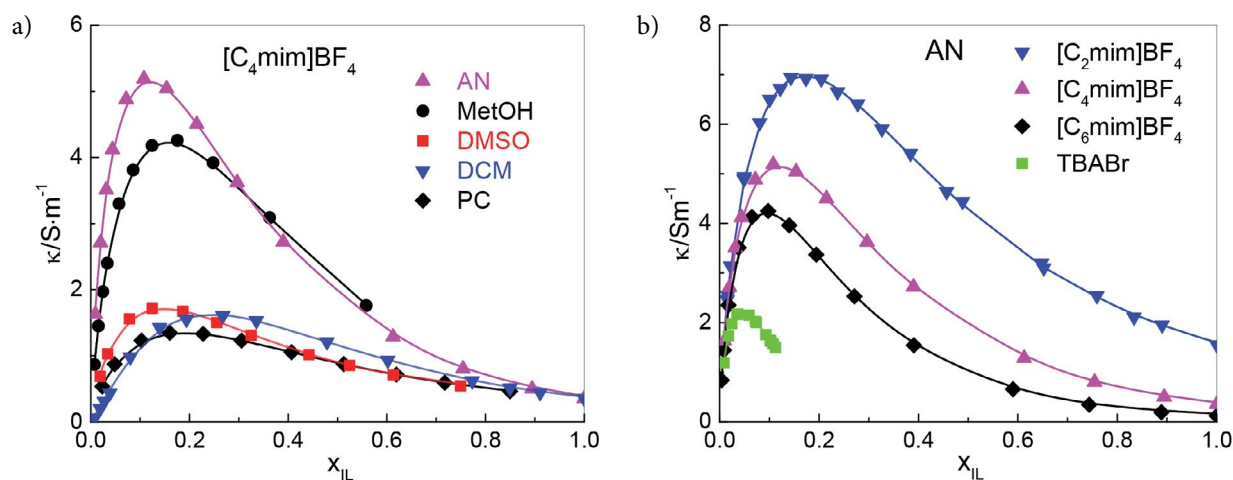


Figure 13. Specific conductivity, κ , of a) $[C_4mim]BF_4$ in AN,³⁷ MetOH,³⁷ DMSO,³⁷ DCM,³⁷ and PC³⁷ and b) $[C_2mim]BF_4$,³⁷ $[C_4mim]BF_4$,³⁷ $[C_6mim]BF_4$ and TBABr³⁸ in AN at 298.15 K as a function of molar fraction of IL, x_{IL} . Symbols represent experimental values and lines the Casteel-Amis-type fitting (Eq. (2)) of the experimental data with parameters reported in Table S1 of the Supplementary data.

at 298.15 K) are presented as determined by Stoppa et al.³⁷ Conductivity of three imidazolium based tetrafluoroborates in AN from the same paper are shown in Figure 13 b) together with data on TBABr in AN³⁸ for comparisons.

From Figure 13 it is evident that conductivity follows the typical pattern of concentrated electrolyte solutions, discussed already in paragraph 3.1. and presented in Figure 8 for aqueous solutions.⁶ After a rapid rise in the low concentration region, κ passes through a well-defined maximum. As it follows from the data, presented in Figure 13 b) and table S1 in Supplementary data, κ for ILs in AN decreases with increasing alkyl chain length of the cation, as it has been observed also for the aqueous solutions of ILs, presented in Figure 8. Whereas in water solution the position of the conductivity maximum was more or less close to the $x_{IL} \cong 0.05$, here the maximum is reached at higher concentration and it moves toward lower x_{IL} with increasing length of the side alkyl chain of cation.

Figure 13 a) reveals clearly that κ for $[C_4mim]BF_4$ depends strongly on the solvent: when the viscosity increases (AN < MetOH < DMSO < PC), κ decreases. But DCM does not follow this order: despite the fact that its viscosity is very low (0.415 mPa s at 298.15 K), the conductivity of $[C_4mim]BF_4$ solutions in DCM is close to that in DMSO and PC with much higher solvent viscosity (Table

1). This behavior can be ascribed to higher ion association in DCM due to the lower dielectric constant. The value, obtained in diluted solutions by Borun and Bald³⁵ ($K_A = 479$ at 298.15 K, Table 1) confirms strongly this assumption. Even more – also in other solvents the decrease of conductivity after the maximum could be ascribed to stronger ion association. Unfortunately, there is no theory to describe this behavior.

3.3. Surface Active Ionic Liquids

Aggregation/micellization in aqueous solutions. As it is already presented in Figure 7, it was confirmed by MD simulations that $[C_{12}mim]Cl$ forms micelles at higher concentrations. Even more, the great potential of surface active ionic liquids (SAILs) at investigating the thermodynamics of micellization process in solutions due to possible variations in the structure of cations, side chain length and counter ions has been demonstrated recently.^{8,18,19} The systems studied recently by Šarac et al.⁸ are presented in Figure 14.

It was found that in many ways the behavior of SAILs is identical to that observed for “classical” cationic surfactants: the critical micelle concentration is decreasing with the length of the hydrophobic chain (Figure 15) and ex-

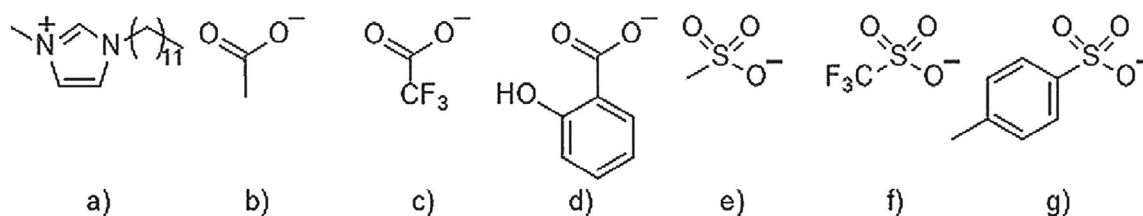


Figure 14. Structures of investigated systems in ref. ⁸: a) $n = 9$ ($[C_{10}mim]$), $n = 11$ ($[C_{12}mim]$), $n = 13$ ($[C_{14}mim]$) and $n = 15$ ($[C_{16}mim]$) cations in $[C_nmim]Cl$ and b) OAc⁻, c) TFA⁻, d) Sal⁻, e) OMs⁻, f) OTf⁻, and g) OTs⁻ anions in $[C_{12}mim]X$ systems. Figure reproduced from ref.⁸ with permission from Elsevier.

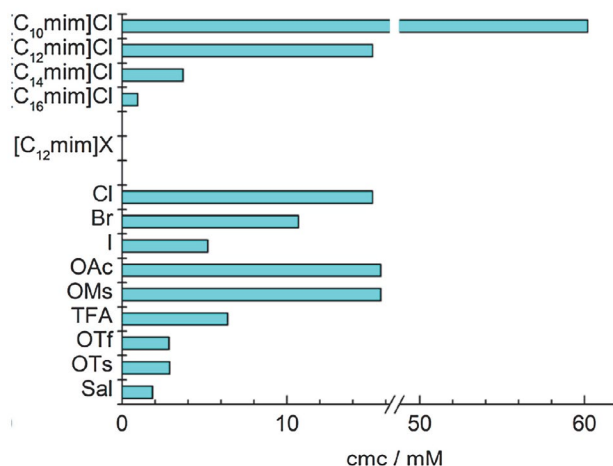


Figure 15. Critical micelle concentrations, cmc, for all systems studied in ref.⁸ at 298.15 K. Figure reproduced from ref.⁸ with permission from Elsevier.

presses a minimum in the temperature dependence, but depends strongly also on the counter ion.⁸

In general, the micellization process for SAILs is as usual endothermic at low temperatures and exothermic at high temperatures, but it was verified that counter ions play an extremely important role.⁸ Even more, it was confirmed, that the hydrophobicity of counter ions evidently contributes to the heat capacity change and the water accessible surface area removal upon burial of non-polar group from the contact with water during the micellization process.

The main driving force for the formation of micelles is presumably the apparent disaffinity of water for the non-polar (interacting) surfaces known as the hydrophobic effect. The parameter that illustrates this effect is the heat capacity of micellization, $\Delta_M c_p^0$, which is always highly negative and can be ascribed to the removal of water molecules from contact with nonpolar surface area upon micelle formation.³⁹ By modeling the micellization processes

as a transfer of surfactant molecules into the micellar phase, the heat capacity can be expressed in terms of the change of water accessible nonpolar and polar surface areas, as derived by Spolar et al.⁴⁰ from the protein folding studies:

$$\Delta_M c_p^0 (\text{J} \cdot \text{K}^{-1} \cdot \text{mol}^{-1}) = -1.34(\pm 0.33) \cdot \Delta A_{\text{np}} (\text{\AA}^2) + 0.59(\pm 0.17) \cdot \Delta A_{\text{p}} (\text{\AA}^2) \quad (3)$$

where ΔA_{p} stands for the loss of water accessible polar and ΔA_{np} for nonpolar surface area upon protein folding. Because the hydrophilic head groups of non-ionic surfactants remain hydrated upon micelle formation, the “theoretical” contribution of water accessible nonpolar surface area change to the heat capacity change upon micelle formation, $\Delta_M c_p^0 (\text{th}_{\text{np}})$, can be assumed to reflect only the change in exposure of the hydrophobic tails to water. Consequently, the Eq. (3) is reduced to

$$\Delta_M c_p^0 (\text{th}_{\text{np}}) (\text{J} \cdot \text{K}^{-1} \cdot \text{mol}^{-1}) = -1.34(\pm 0.33) \cdot \Delta A_{\text{np}} (\text{\AA}^2) \quad (4)$$

This approach turned out as useful for a series of non-ionic surfactants.^{41,42}

According to Richards,⁴³ water accessible surface area of a methylene group is 30 \AA^2 and 88 \AA^2 for a methyl group. Thus, ΔA_{np} of the hydrophobic tails of the surfactants investigated in ref.⁸ is 358, 418, 478 and 538 \AA^2 for the C_{10} , C_{12} , C_{14} and C_{16} alkyl chain, respectively, giving the values of $\Delta_M c_p^0 (\text{th}_{\text{np}}) = -479, -560, -640$ and $-720 \text{ J} \cdot \text{K}^{-1} \cdot \text{mol}^{-1}$ for the same order of alkyl chains. Comparison of $\Delta_M c_p^0 (\text{th}_{\text{np}})$, estimated by Eq. (4) with $\Delta_M c_p^0 (\text{exp})$, as illustrated in Figure 16 a), reveals that there is an evident discrepancy between $\Delta_M c_p^0 (\text{th}_{\text{np}})$ and $\Delta_M c_p^0 (\text{exp})$. This discrepancy was explained in two ways:

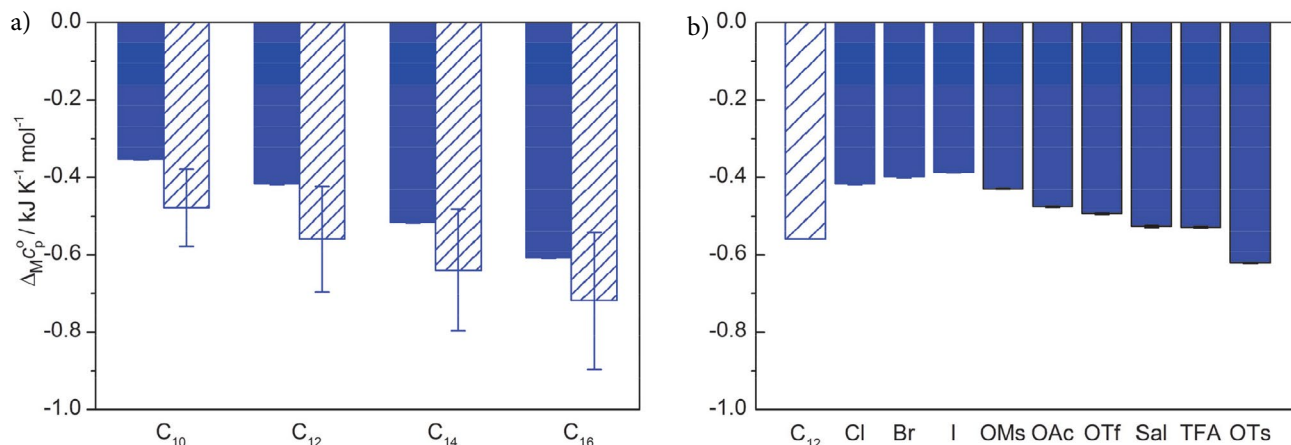


Fig. 16. Comparison of theoretical (shaded) and experimental (full columns) values of heat capacity changes upon micellization process, $\Delta_M c_p^0$, for a) $[\text{C}_n\text{mim}]\text{Cl}$ and b) $[\text{C}_{12}\text{mim}]\text{X}$. Figure reproduced from ref.⁸ with permission from Elsevier.

- a) It can be assumed that there are still water molecules in the interior of the micelle upon micellization and thus the ΔA_{np} estimated by the approach of Richards⁴³ mentioned above is overestimated. That is, the “real” ΔA_{np} is smaller than that according to Richards.
- b) The Eq. (4) holds well for non-ionic surfactants,^{41,42} but it probably is not valid for ionic surfactants. Positive contribution of the removal of water accessible polar surface area to the heat capacity change of micellization should also be considered and cannot be neglected, consistent with the findings for the heat capacity change upon protein folding.⁴⁰

The influence of counterion on $\Delta_M c_p^0$ for $[C_{12}mim]X$ systems⁸ is illustrated in Figure 16 b). For $[C_{12}mim]Cl$, $[C_{12}mim]Br$ and $[C_{12}mim]I$ it is obvious that the difference between $\Delta_M c_p^0$ (exp) and $\Delta_M c_p^0$ (th_{np}) increases along with an increase in the size of the anion. It is plausible to conjecture that the removal of water accessible polar surface area also increases along with an increase in the size of counter ion binding onto the micelle but it can be concluded that the ΔA_p part here cannot be neglected or/and that the hydrophobic parts of counter ions are incorporated in the micelles. In this case the contribution to the $\Delta_M c_p^0$ of the removal of the hydrophobic part of counterion from the contact with water after micellization can be assumed. Thus, the “hydrophobic” anions (OTs^- , OTf^- , TFA^- and Sal^-) can be partially incorporated in the micelle and therefore the hydrophobic part of the anion can contribute to the ΔA_{np} . The incorporation of counterions was already confirmed for $[C_{16}mim]OTs$ by Singh et al. using various methods⁴⁴ and for $[C_{12}mim]OTf$ by DRS.⁴⁵

Recently, it was demonstrated on the dodecyltrimethylammonium chloride (DTACl) in the 0.01 M solutions of sodium *ortho*- (*o*-HBz⁻, denoted previously as Sal⁻), *meta*- (*m*-HBz⁻), and *para*- hydroxybenzoate (*p*-HBz⁻) that even small changes in the structure of anion of the added salt, such as the position of the substituent on an aromatic ring, considerably influence the micellization process.⁴⁶ Howev-

er, it should be kept in mind, that the micellization of DTACl in that case was studied in the presence of NaCl, which also considerably affects the self-aggregation process.⁴⁷ To prove the influence of isomerism of counterions on micellization of surfactant in water without any added compound the study of micellization of $[C_{12}mim]o$ -HBz, $[C_{12}mim]m$ -HBz, $[C_{12}mim]p$ -HBz together with the benzoate salt ($[C_{12}mim]HBz$) (Figure 17) was carried out recently.¹⁹

It was found that the temperature dependence of cmc shows a nearly U-shaped form (Figure 18 a)) but is strongly dependent on the presence and position of the -OH group in the counterion. The micellization process is endothermic at low temperatures and becomes exothermic at higher temperatures – a phenomenon usual for ionic surfactants – for all here investigated systems, only for $[C_{12}mim]o$ -HB it turned out that the micellization is exothermic in the whole investigated temperature range. It is namely well-known that *o*-HBz⁻ provokes the formation of more compact elongated micelles by stronger interaction of *o*-HBz⁻ with surfactant molecule and its subsequent incorporation resulting in the highest exothermicity of micellization process in the case of *o*-HBz⁻. More details are available in ref.¹⁹

Aggregation in non-aqueous solutions. Whereas the aggregation behavior of SAILs in aqueous solutions is relatively well investigated and understood, studies on the aggregation of SAILs in non-aqueous solvents are scarce although they are very important in many applications. Recently, the aggregation behavior and related physiochemical properties of $[C_{12}mim]Br$ in DMSO, AN, DMF and formamide (FA) were investigated by conductivity and density measurements.²⁰ It turned out that the aggregate formation in non-aqueous solvents is not as favored as in water, which is actually similar to the behavior observed for some conventional ionic surfactants by Ray.⁴⁸ The critical aggregation concentration, cac, as a function of the empirical parameters of solvent polarity $E_T^N(30)$ ⁴⁹ is presented in Figure 19.

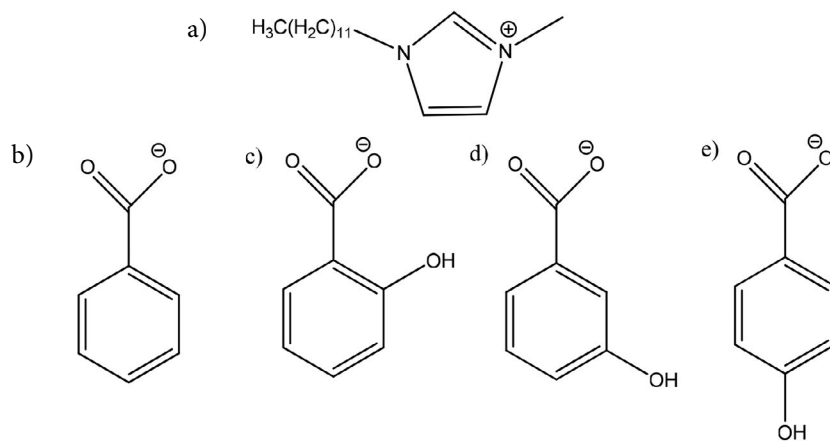


Figure 17. Structures of investigated systems: a) $[C_{12}mim]^+$; b) Bz⁻ c) *o*-HBz⁻; d) *m*-HBz⁻ e) *p*-HBz⁻. Figure reproduced from ref.¹⁹ with permission from Elsevier.

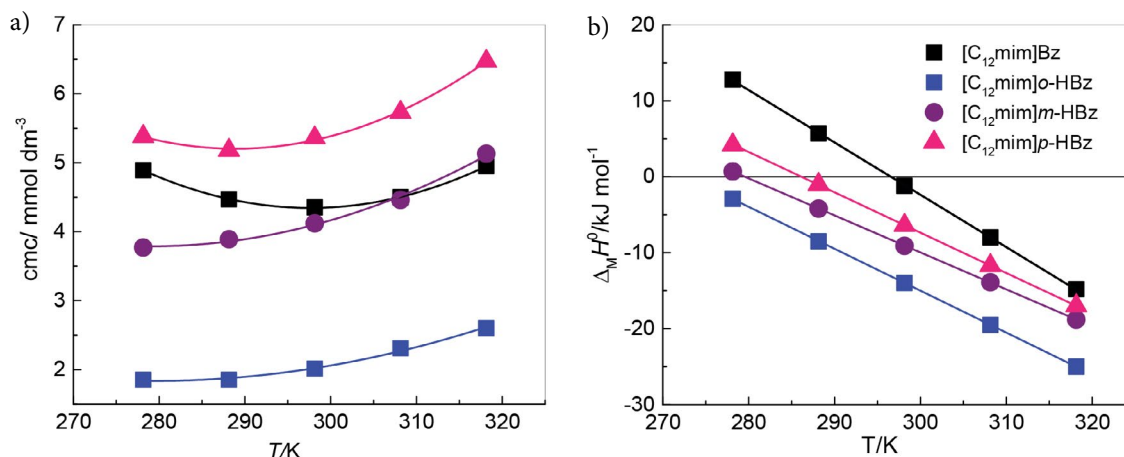


Figure 18. Temperature dependence of a) critical micelle concentration, cmc, and b) the standard enthalpy of micellization, $\Delta_M^0 H^0$ for [C₁₂mim]HBz, [C₁₂mim]o-HBz, [C₁₂mim]m-HBz and [C₁₂mim]p-HBz in water. Solid lines represent in a) the corresponding polynomial fits, $cmc = A + BT + CT^2$ (coefficients are given in Table S2 in Supplementary data); b) linear fits. Figure reproduced from ref.¹⁹ with permission from Elsevier.

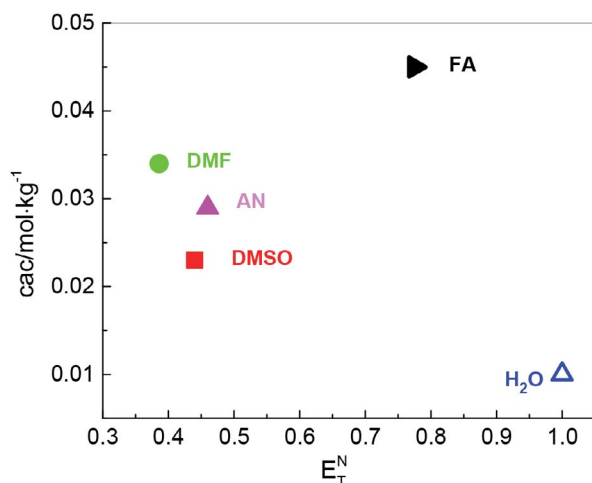


Figure 19. The literature data²⁰ of critical aggregation concentration, cac, for [C₁₂mim]Br in water, DMSO, AN, DMF and FA as a function of empirical parameters for solvent polarity E_T^N (30).

A larger E_T^N (30) value reflects weaker interaction between hydrocarbon and the solvents. Thus, interactions of the SAILs alkyl chain with organic solvents increase with decreasing E_T^N (30) values of the solvents. This reduces the tendency of the SAILs aggregation and increases its cac value, which should increase with decreasing E_T^N (30) values of the solvents. Obviously, the reported data for DMF, AN and DMSO are in line with this prediction, but for FA this is not valid.²⁰ Thus, despite the fact, that “solvophobic effect” of the solvents plays an important role in the aggregation of the classical surfactants^{50,51} and SAILs in non-aqueous solvents, also other factors may be important, as it is demonstrated here for the case of FA.

It is necessary to stress that DMSO, DMF and AN are aprotic solvents, while FA is a protic solvent and capable of forming hydrogen-bonds. Based on molecular dynamics simulations, Hanke et al.⁵² reported that ionic liquids are

strongly solvated by the hydrogen-bonding solvents, principally by forming hydrogen bonds with the anions. This indicates that the stronger hydrogen-bonding interactions of the SAILs anions with protic solvents would result in a decrease of the binding degree of the anions at the aggregates surface. In such a case, the electrostatic repulsion between the head groups of the SAIL cannot be decreased effectively, thus weakening the tendency towards aggregation. Therefore, it seems quite likely that the solvophobic effect and the hydrogen-bonding interactions of the SAIL anions with the solvents are the main factors controlling the aggregates formation of SAILs in non-aqueous solvents. Anyway, the work of Feng and coworkers²⁰ provides some very important new insight into the roles of solvophobic effect and hydrogen-bonding of non-aqueous solvents in the SAILs aggregation and supplies helpful guide how the aggregation of SAILs could be controlled and regulated by solvent properties.

4. Concluding Remarks

It can be concluded that ILs are complex in their pure state, where the structure is strongly dependent on the structures of cations and anions enabling and/or hindering the packaging and/or arrangement of IL molecules. In solutions, ILs behave like simple (“classical”) electrolytes and/or common (“classical”) surfactants, thus they are sharing the “complexity” of electrolyte solutions. But also in solutions, the structures of the ions play a very important role due to the possibility of diverse ion-ion and ion-solvent interactions. Let me mention only two fields, where the great potential of ILs due to their “tunability” of structures and properties can be used:

a) There is still a lack of theories for concentrated electrolyte solutions. Whereas for “classical” electrolytes the limited solubility could be the reason for less effort in

studying concentrated solutions, by applying ILs the whole concentration range from pure solvent to pure electrolyte can be covered. Despite many studies, the observed maximum in the electrical conductivity (Figures 8 and 13) is still not described well and remains the challenge for the theoreticians.

- b) With their wide possibilities of structures in hydrophobic part and counterions, SAILs are promising systems to study the aggregation processes in non-aqueous solutions.

Therefore, ILs can serve as excellent model systems for studying ionic interactions, hydrophobic effect, and specific ion effect to help us at broadening and deepening the knowledge on electrolyte and surfactant aqueous and non-aqueous solutions.

5. Acknowledgements

I would like to thank my colleagues and friends Prof. Dr. Richard Buchner (University of Regensburg, Germany), Prof. Dr. Slobodan Gadžurić (University of Novi Sad, Serbia), Prof. Dr. Milan Vraneš (University of Novi Sad, Serbia), and their Ph. D. students Dr. Johannes Hunger, Dr. Alexander Stoppa, Dr. Sergej Friesen (University of Regensburg, Germany), Dr. Nebojša Zec, Dr. Snežana Papović, and Dr. Aleksandar Tot (University of Novi Sad, Serbia) for the fruitful longstanding collaboration in the field of ionic liquids. Valuable research work of Dr. Bojan Šarac (University of Ljubljana, Slovenia) and Ph. D. students Dr. Martin-Tine Perger, Dr. Ana Kroflič, Dr. Jure Gujt, Dr. Žiga Medoš and Isidora Čobanov is acknowledged.

I am owing my debt to Prof. Dr. Alexander Apelblat (Ben Gurion University of the Negev, Beer-Sheva, Israel) and Dr. Roland Neueder (University of Regensburg, Germany) for sharing his knowledge on electrolyte solutions with me; Prof. Dr. Werner Kunz (University of Regensburg, Germany) for his always optimistic and kind attitude; Dipl. Ing. Herbert Hilbinger (University of Regensburg, Germany) and Dipl. Ing. Dušan Habe (Test and Measurement Technique, Črnomelj, Slovenia) for their permanent and generous technical support.

However, my deepest debt and a profound appreciation go to Professor Josef Barthel, who passed away in February 2019. Not only his friendship, kindness, help, good advice, and pleasant atmosphere in personal relations, but also his long-term support and strong inspiration of my research work encouraged me again and again to follow the – often not easy – scientific way. He supported my application for grant at Alexander von Humboldt foundation and hosted me at the Institute of Physical and Theoretical Chemistry at University of Regensburg (Germany) in 1994/95. After my return, he helped me to build the laboratories at home institution – he supported our application for small-X-ray scattering equipment donation at the Alexander von Humboldt foundation and took care of the

donation of invaluable pieces of cells to the laboratory for electrical conductivity measurements. Without his generous help I would hardly continue my work. He involved me also in the community of solution chemists and put me on the way, where I met people who have been helping me to gather new knowledge and experiences and to overcome many borders. I am deeply grateful for that and for everything I received from him and I am thankful for all the time that was spent together.

Funding

The financial support by the Slovenian Research Agency through Bilateral projects (ARRS-BI-RS/16-17-023 and ARRS –BI-DE/17-19-4) and through Grant No. P1-0201 is gratefully acknowledged. The networking support by the COST Actions CM1206 and CM1101 is appreciated.

Author biography

Marija Bešter-Rogač is a Professor of Physical Chemistry at University of Ljubljana, Faculty for Chemistry and Chemical Technology (UL FCCT), where she earned her Ph.D. in 1988. Since her postdoctoral stay in 1994/95 as a fellow of Alexander von Humboldt Foundation at University of Regensburg, at Institute of Physical and Theoretical Chemistry (Germany) with Professor Josef Barthel, she has been active in the broad field of electrolyte solutions and has been involved in strong international collaborations. As author/co-author she published around 120 papers in peer-review journals, some book chapters, two encyclopaedias in the field of electrolyte solutions and carried out several invited lectures at scientific conferences and universities abroad. She has been taken part in many international (COST) and bilateral projects. Most of her recent work is devoted to ionic liquids as possible functional materials and model systems for investigation interactions in solutions.

As a mentor, she has conducted graduate, master's and doctoral theses. In addition, she has participated in various committees and governing bodies at the Faculty and at the University. In 2013/17 she chaired the Commission for Women in Science at Ministry of Education, Science and Sport Republic of Slovenia, and tried for the implementation of fairer relations in the sphere of science and higher education. Since 2018 she is a member of the European Academy of Science and Arts.

6. References

1. T. L. Greaves, C. J. Drummond, *Chem. Rev.* **2015**, *115*, 11379–11448. DOI:10.1021/acs.chemrev.5b00158
2. R-Hayes, G. G. Warr, R. Atkin, *Chem. Rev.* **2015**, *115*, 6357–6426. DOI:10.1021/cr500411q

3. Y. Ji, R. Shi, Y. Wang, G. Saielli, *J. Phys. Chem. B* **2013**, *117*, 1104–1109. DOI:10.1021/jp310231f
4. M. Bešter-Rogač, A. Stoppa, R. Buchner, *J. Phys. Chem. B*, **2014**, *118*, 1426–1435. DOI:10.1021/jp412344a
5. M. Bešter-Rogač, J. Hunger, A. Stoppa, R. Buchner, *J. Chem. Eng. Data* **2010**, *55*, 1799–1803. DOI:10.1021/je900531b
6. M. Bešter-Rogač, M. V. Fedotova, S. E. Kruchinin, M. Klähn, *Phys. Chem. Chem. Phys.* **2016**, *18*, 28594–28605. DOI:10.1021/je900531b
7. R. Tomaš, A. Tot, J. Kuhar, M. Bešter-Rogač, *J. Mol. Liq.* **2018**, *254*, 267–271. DOI:10.1016/j.molliq.2018.01.076
8. B. Šarac, Ž. Medoš, A. Cognigni, K. Bica, L.-J. Chen, M. Bešter-Rogač, *Colloid Surf. A* **2017**, *532*, 609–617. DOI:10.1016/j.colsurfa.2017.01.062
9. H. Olivier-Bourbigou, L. Magna, D. Morvan, *Applied Catalysis A: General* **2010**, *373*, 1–56. DOI:10.1016/j.apcata.2009.10.008
10. V. V. Chaban, O. V. Prezhdo, *J. Phys. Chem. Lett.* **2013**, *4*, 1423–1431. DOI:10.1021/jz400113y
11. M. Vraneš, S. Papović, A. Tot, N. Zec, S. Gadžurić, *J. Chem. Thermodyn.* **2014**, *76*, 161–171. DOI:10.1016/j.jct.2014.03.025
12. S. Papović, M. Bešter-Rogač, M. Vraneš, S. Gadžurić, *J. Chem. Thermodyn.* **2016**, *99*, 1–10. DOI:10.1016/j.jct.2016.03.034
13. S. Papović, M. Vraneš, B. Kordić, S. Filipović, M. Bešter-Rogač, S. Gadžurić, *J. Chem. Thermodyn.* **2016**, *101*, 260–269. DOI:10.1016/j.jct.2016.06.012
14. S. Papović, N. Cvjetičanin, S. Gadžurić, M. Bešter-Rogač, M. Vraneš, *Phys. Chem. Chem. Phys.* **2017**, *19*, 28139–, 28152. DOI:10.1039/C7CP04478J
15. K. Yuyama, G. Masuda, H. Yoshida, T. Sato, *J. Power Sources*, **2006**, *162*, 1401–1408. DOI:10.1016/j.jpowsour.2006.09.002
16. O. N. Kalugin, I. V. Voroshylova, A. V. Riabchunova, E. V. Lukinova, V. V. Chaban, *Electrochim. Acta* **2013**, *105*, 188–199. DOI:10.1016/j.electacta.2013.04.140
17. I. V. Voroshylova, S. R. Smaga, E. V. Lukinova, V. V. Chaban, O. N. Kalugin, *J. Mol. Liq.* **2015**, *203*, 7–15. DOI:10.1016/j.molliq.2014.12.028
18. I. Čobanov, B. Šarac, Ž. Medoš, M. Vraneš, S. Gadžurić, N. Zec, M. Bešter-Rogač, *J. Mol. Liq.* **2018**, *271*, 437–442. DOI:10.1016/j.molliq.2018.08.152
19. I. Čobanov, B. Šarac, Ž. Medoš, A. Tot, M. Vraneš, S. Gadžurić, N. Zec, M. Bešter-Rogač, *J. Mol. Liq.* **2020**, *301*, 112419. DOI:10.1016/j.molliq.2019.112419
20. Q. Feng, H. Wang, S. Zhang, J. Wang, *Colloid Surf. A* **2010**, *367*, 7–11. DOI:10.1016/j.colsurfa.2010.05.032
21. Y. Pei, Q. Lu, Y. Niu, Y. Zhao, Y. Zhao, Z. Li, H. Wang, J. Wang, *J. Chem. Eng. Data* **2019**, *64*, 4708–4716. DOI:10.1021/acs.jced.9b00040
22. M. Bešter-Rogač, R. Neueder, J. Barthel, *J. Solution Chem.* **1999**, *28*, 1071–1086. DOI:10.1023/A:1022625310402
23. J. M. G. Barthel, H. Krienke, W. Kunz, *Physical Chemistry of Electrolyte Solutions: Modern Aspects*, Springer, New York, **1998**.
24. B. L. Bhargava, M. L. Klein, *Soft Matter*, **2009**, *5*, 3475–3480. DOI:10.1039/b908046e
25. O. Nordness, P. Kelkar, M. A. Stadtherr, J. F. Brennecke, *Mol. Phys.* **2019**, *117*, 23–24. DOI:10.1080/00268976.2019.1635276
26. J. F. Casteel, E.S. Amis, *J. Chem. Eng. Data* **1972**, *17*, 55–59. DOI:10.1021/je60052a029
27. M. Bešter-Rogač, R. Neueder, J. Barthel, *J. Solution Chem.* **2000**, *29*, 51–61. DOI:10.1023/A:1005114500861
28. J. Gujt, M. Bešter-Rogač, B. Hribar-Lee, *J. Mol. Liq.* **2014**, *190*, 34–41. DOI:10.1016/j.molliq.2013.09.025
29. G. Hefter, *Pure Appl. Chem.* **2006**, *78*, 1571–1586. DOI:10.1351/pac200678081571
30. R. Buchner, *Pure Appl. Chem.* **2008**, *80*, 1239–1252. DOI:10.1351/pac200880061239
31. R. Buchner, G. Hefter, *Phys. Chem. Chem. Phys.* **2009**, *11*, 8984–8999. DOI:10.1039/b906555p
32. M. Bešter-Rogač A. Stoppa, J. Hunger, G. Hefter, R. Buchner, *Phys. Chem. Chem. Phys.* **2011**, *13*, 17588–17598. DOI:10.1039/c1cp21371g
33. M. Bešter-Rogač, R. Neueder, J. Barthel, *Electrolyte Data Collection, Part 5c*, in: R. Eckermann, G. Kreysa (Eds.): DECHEMA Chemistry Data Series, Vol XII, Frankfurt, Germany, **2015**, p. 222.
34. A. Borun, A. Bald, *J. Chem. Eng. Data* **2012**, *57*, 475–481. DOI:10.1021/je201014c
35. A. Borun, A. Bald, *Ionics* **2016**, *22*, 859–867. DOI:10.1007/s11581-015-1613-x
36. J. Barthel, L. Iberl, J. Rossmair, H. J. Gores, B. Kaukal, *J. Solution Chem.* **1990**, *19*, 321–337. DOI:10.1007/BF00648139
37. A. Stoppa, J. Hunger, R. Buchner, *J. Chem. Eng. Data* **2009**, *54*, 472–479. DOI:10.1021/je800468h
38. M. Bešter-Rogač, R. Neueder, J. Barthel, *Electrolyte Data Collection, Part 5c*, in: R. Eckermann, G. Kreysa (Eds.): DECHEMA Chemistry Data Series, Vol XII, Frankfurt, Germany, **2015**, pp. 416–417.
39. Z. Kiraly, I. Dekany, *J. Colloid Interface Sci.* **2001**, *242*, 214–219. DOI:10.1006/jcis.2001.7777
40. R. S. Spolar, J. R. Livingstone, M. T. Record Jr., *Biochemistry* **1992**, *31*, 3947–3955. DOI:10.1021/bi00131a009
41. L. J. Chen, Y.-H. Sheu, P.-J. Li, *J. Phys. Chem.* **2004**, *108*, 19096–19098. DOI:10.1021/jp045486a
42. G. C. Kresheck, *J. Phys. Chem. B* **2009**, *113*, 6732–6735. DOI:10.1021/jp9820469
43. a) F. M. Richards, *J. Mol. Biol.* **1974**, *82*, 1–14. DOI:10.1016/0022-2836(74)90570-1
b) F. M. Richards, *Annu. Rev. Biophys. Bioeng.* **1977**, *6*, 151–176. DOI:10.1146/annurev.bb.06.060177.001055
c) F. M. Richards, *Methods Enzymol.* **1985**, *115*, 440–446. DOI:10.1016/0076-6879(85)15032-9
44. G. Singh, T. S. Kang, *J. Phys. Chem. B* **2016**, *120*, 1092–1105. DOI:10.1021/acs.jpcc.5b09688
45. S. Friesen, T. Buchner, A. Cognigni, K. Bica, R. Buchner, *Langmuir*, **2017**, *33*, 9844–9856. DOI:10.1021/acs.langmuir.7b02201
46. B. Šarac, G. Meriguet, B. Ancian, M. Bešter-Rogač, *Langmuir* **2013**, *29*, 4460–4469. DOI:10.1021/la400161n
47. A. Kroflič, B. Šarac, M. Bešter-Rogač, *J. Chem. Thermodyn.* **2011**, *43*, 1557–1563. DOI:10.1016/j.jct.2011.05.015

48. A. Ray, *J. Am. Chem. Soc.* **1969**, *91*, 6511–6512.
DOI:10.1021/ja01051a069
49. C. Reichardt, *Solvents and Solvent Effects in Organic Chemistry*, Third Edition WILEY-VCH Verlag GmbH & Co. KGaA, Weinheim, **2003** pp. 418–424.
50. M. L. Moya, A. Rodriguez, M. D. Graciani, G. Fernandez, *J. Colloid Interface Sci.* **2007**, *316*, 787–795.
DOI:10.1016/j.jcis.2007.07.035
51. M. J. Hollamby, R. Tabor, K. J. Mutch, K. Trickett, J. Eastoe, R.K. Heenan, I. Grillo, *Langmuir* **2008**, *24*, 12235–12240.
DOI:10.1021/la8020854
52. C. G. Hanke, N. A. Atamas, R. M. Lynden-Bell, *Green Chem.* **2002**, *4*, 107–111. DOI:10.1039/b109179b

Povzetek

Ionske tekočine sodijo med najbolj pogosto preučevane sisteme v zadnjih letih in zanimanje zanje – s poudarkom na razvoju ionskih tekočin za posebne namene kot tudi za temeljne raziskave – še vedno narašča. V tem prispevku so opisane podobnosti in razlike med običajnimi, »klasičnimi« elektroliti ter površinsko aktivnimi snovmi (surfaktanti) in ionskimi tekočinami ter površinsko aktivnimi ionskimi tekočinami. Pregled literaturnih podatkov razkrije, da se ionske tekočine v raztopinah obnašajo kot »klasični« elektroliti in jih lahko opišemo z obstoječimi modeli v območju njihove veljavnosti. Še vedno pa nimamo modelov za opis koncentriranih raztopin elektrolitov in tu lahko ionske tekočine, ki so manj omejene s topnostjo kot običajni elektroliti, služijo kot odlični modelni sistemi. Tudi micelizacijo površinsko aktivnih ionskih tekočin v vodnih raztopinah je mogoče opisati na enak način kot za običajne surfaktante, vendar površinsko aktivne ionske tekočine ponujajo več možnosti za proučevanje vpliva specifičnih ionskih in izomernih efektov na proces micelizacije. Prav tako so ionske tekočine zelo obetavni sistemi za proučevanje agreagacijskih procesov v nevodnih raztopinah.



Except when otherwise noted, articles in this journal are published under the terms and conditions of the Creative Commons Attribution 4.0 International License

Scientific paper

Identification of Kiwellin-like Proteins in Fruits by Using *In Silico* Tools

Ceylan Turkmen¹ and Levent Cavas^{1,2,*}

¹ Dokuz Eylül University, Graduate School of Natural and Applied Sciences, Department of Biochemistry,

² Faculty of Science, Department of Chemistry (Biochemistry Division), Kaynaklar Campus, İzmir, Turkey

* Corresponding author: E-mail: levent.cavas@deu.edu.tr

Tel: +90 232 3018701; Fax: +90 232 4534188

Received: 02-01-2019

Abstract

Identification of allergen proteins by using wet-lab technology is a time-consuming and also costly process. In recent years, thanks to the developments in the field of bioinformatics, it is now possible to estimate the allergen proteins by using *in silico* tools. In the present study, it is aimed to find kiwellin-like proteins from different fruits samples by using bioinformatics tools. According to the results of the study, six proteins from *Corchorus olitorius*, *Cucumis sativus*, *Cap-sicum chinense*, *Carica papaya*, *Morus notabilis* and *Jatropha curcas* were defined as the allergens. In conclusion, *in silico* tools developed under the field of bioinformatics can provide a big contribution to the estimation of unknown allergen proteins in different fruits. Based on the *in silico* results, physicians can suggest people who have allergenicity to kiwellin not to consume the fruits that contain kiwellin-like proteins.

Keywords: Allergen; *in silico* tools; kiwellin; kiwi; bioinformatics

1. Introduction

Fruits are very important for public health. On the other hand, some compounds in fruits can cause allergic reactions. Allergens are the substances that immune system recognizes them as foreign molecules and they cause undesirable reactions in the human body.^{1,2} Many external factors such as dust and pollen may cause allergic reactions¹ and it is very difficult to stay away from these natural pollutants. In developed countries, the percentage of hy-

persensitive people for allergen proteins is around 15–20%.³ Food allergy within European population was reported as up to 3.2%.^{3,4,5} Generally, allergens are consisted of proteins and it is very important to investigate three-dimensional structures of the allergen proteins to estimate the possible allergic reactions in different populations.⁶ Actually, studying of allergen proteins in wet lab conditions is a time consuming process and it is costly. On the other hand, the database developed for allergen proteins provides big contribution to the understanding of novel aller-

Table 1. Some selected online bioinformatics tools.

Name of Tool	Web address	Reference
AllergenOnline	http://www.allergenonline.org/	Jin et al 2017
AllerTOP v. 2.0	http://www.ddg-pharmfac.net/AllerTOP/	Wold et al., 1993; Dimitrov et al., 2013
AlgPred	http://crdd.osdd.net/raghava/algpred/	Saha and Raghava, 2006
BIOPEP	http://www.uwm.edu.pl/biochemia/index.php/pl/biopep	Minkiewicz et al., 2008
Allergen Nomenclature	http://www.allergen.org/	Larsen, 2006.
BLAST	https://blast.ncbi.nlm.nih.gov/Blast.cgi	Johnson et al., 2007; Boratyn et al., 2013
ExPASy Bioinformatics Resource Portal	https://www.expasy.org/	Biasini et al., 2014
AllermatchTM	http://www.allermatch.org/	Codex Alimentarius Commission, 2003.

gen proteins and also cross-reactivity. Many tools have so far been developed for estimation of allergen proteins in bioinformatics.⁷ These *in silico* approaches can estimate if the protein can be considered as an allergen proteins or not. *In silico* tools can be used for filtering purposes to eliminate the proteins in a long list. Last developments and tools in this field have been reached to reflect the real results.⁷ The properties used in these tools are protein physicochemical parameters, multiple sequence alignment and also 3 dimensional structure comparisons. Especially homology modelling shows superiority to other techniques inasmuch as there is a direct relationship between protein structures and functions. Some selected online tools for prediction of allergen proteins are given in Table 1.

Kiwelin is the protein that constitutes one-third of the total kiwi proteins.⁸ Although there have been many studies on kiwi fruit on its health effects, kiwi is considered as a strong allergen for some people.^{9,10,11,12} The selection of the protein in this paper is associated with increased consumption of kiwi in Turkey because of increasing planting kiwi along the northern coastline of Turkey.¹³ In this study, it was aimed to find proteins which are similar to kiwelin by using bioinformatic tools.

2. Methods

2.1. Sequences and Tools

In this study, we used database, which is accessible and publicly available on internet. We used WHO/IUIS Allergen Nomenclature Sub-Committee for finding allergen proteins.^{14,15} Basic Local Alignment Search Tool for proteins (BLASTp) search was carried out by BLASTp tool of NCBI.^{16,17} Physicochemical properties of the sequences such as individual amino acid number and percentage, molecular weight, theoretical pI values, total number of negatively and positively charged residues and instability index were calculated by ProtParam tool of ExPasy.¹⁸ Clustal omega was used for multiple sequence alignment.¹⁹ Swiss-MODEL was used for homology modeling.²⁰ Allergenicity estimation was carried out by using AlgPred.²¹ AlgPred

estimates the allergen proteins by using the similarity of known epitope. IgE epitope mapping shows the location of epitope in the searched protein sequence. MEME/MAST allergen motifs are also used in AlgPred. One another feature in AlgPred is based on support vector machine modules which is based on amino acid or dipeptide composition. AlgPred tool also allows users to use above mentioned features together that is mentioned as “hybride systems”.

2.2. The Strategy for Identification of Kiwelin-like Proteins

The sequence of kiwelin kiwi fruit was retrieved from Allergen.org. Then kiwelin-like protein sequences were screened using BLASTp in NCBI website. After BLASTp search, the proteins with high similarity scores were listed in Table 2. These similar proteins were selected from 10 different and commonly used plants. The kiwelin-like proteins in Table 2 were compared by using following tools: 1) Clustal Omega for multiple sequence alignment, 2) ProtParam in ExPasy for physicochemical parameters, 3) SWISS-MODEL for homology modelling, 4) AlgPred is used for *in silico* allergenicity assessment of the proteins.

3. Results and Discussion

Kiwelin is one of the well-defined allergen proteins in *A. chinensis*. However, kiwelin-like proteins in other fruit have not been characterized yet. Developments in the bioinformatics tools can help researchers to find kiwelin-like protein in database easily. In our study, we searched kiwelin-like protein in NCBI database and we found 10 potential proteins which could be considered as candidate allergen proteins (Table 2). Maximum percent identity was found in Barwin-related protein as 95%. On the other hand, minimum identities were observed in the kiwelin like proteins of *C. sativus*, *P. persica* and *C. moschata* as 80%. E-values were maximum when % identity is low and they were minimum when % identity is high.

Table 2. List of kiwelin-like proteins according to the BLASTp analysis.

Species	Name of protein (UniProt)	NCBI Reference Sequence	E-value for BLAST	% identity
<i>Corchorus olitorius</i>	Barwin-related endoglucanase	OMO91533.1	5e-04	95
<i>Vitis vinifera</i>	unnamed protein product, partial (BLASTp)	CBI16343.3	0.007	85
<i>Cucumis sativus</i>	Uncharacterized protein	KGN46853.1	0.16	80
<i>Punica granatum</i>	hypothetical protein CDL15_Pgr026889	OWM73785.1	0.012	90
<i>Capsicum chinense</i>	Ripening-related protein grip22	PHU03889.1	0.012	85
<i>Prunus persica</i>	Receptor-like protein kinase (BLASTp)	XP_020413324.1	0.15	80
<i>Carica papaya</i>	Kiwelin-like (BLASTp)	XP_021896278.1	0.059	85
<i>Cucurbita moschata</i>	Kiwelin-like (BLASTp)	XP_022944715.1	0.22	80
<i>Morus notabilis</i>	Uncharacterized protein	XP_010109489.1	0.063	85
<i>Jatropha curcas</i>	Uncharacterized protein	KDP44018.1	0.064	85

3. 1. Multiple Sequence Alignment and Phylogenetic Tree

We used clustal omega to analyse the similarity of kiwelin-like proteins in this paper. The results were showed in Figure S1.

A first amino acid of kiwelin (I), was same in all candidate proteins except for *Prunus persica*, *Cucumis sativus*, *Carica papaya*. In these species, I was substituted with L. It was very interesting to note that the amino acids at the position of 2,4,6,8,12–14,16,18–20 were same in all studied sequences. It could be said that these regions must have been conserved. 3th amino acid (S) of kiwelin was same in all candidate proteins except for *C. chinense* and *C. olitorius*. S is substituted with Q. 17th amino acid (Q) of kiwelin is R in *C. moschata* and E in *V. vinifera*. The amino acid at the position of 25 is S in kiwelin of *A. chinensis*, however, it is C in other studied sequences. Similarly, the amino acid at the position of 27 is Q in kiwelin of *A. chinensis*, it is D in all studied samples. A phylogenetic tree was constructed based on multiple sequence alignment by clustal omega (Figure 1). Pairwise sequence alignment of P85261 and P84527 was shown in Figure 2. Phylogenetic tree reveals that the sequences can be classified under three clusters. Kiwelin of *A. chinensis* took place in the first cluster with receptor-like protein kinase of *P. persica*, hypothetical pro-

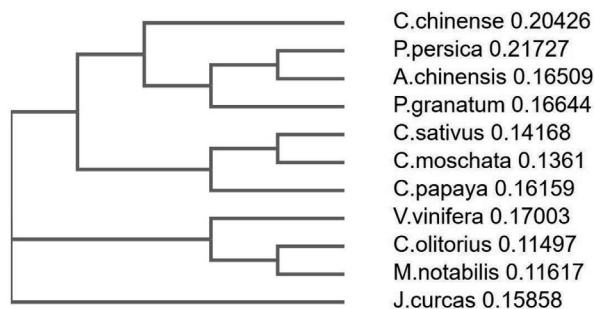


Figure 1. Phylogenetic tree of the studied sequences. (The name of the proteins in these species were given in Table 2).

tein CDL 15_Pgr026889 of *P. granatum* and ripening-related protein grip22 of *C. chinense*. From Figure 1, it could be said that the proteins in *P. persica*, *P. granatum* and *C. chinense* are more close to *A. chinensis*. These three proteins have not been mentioned in allergen.org yet.

3. 2. ProtParam Results

ProtParam tool is used to characterize the physicochemical properties of proteins. The tool is available under expasy.ch developed by Swiss Bioinformatics Institute. By using this tool one can obtain the parameters such as amino acid length, molecular weight, theoretical pI values, negatively and positively charged residues, net charges and instability index (Table 3), number and percentage of amino acids (Table 4) in the studied samples. Kiwelin (P85261 (Uniprot), Act c 5 (Allergen.org)) in *Actinidia chinensis* (Gold Kiwi Fruit) was selected as a model allergen protein in this study. There is also one more kiwelin (P84527 (Uniprot), Act d 5 (allergen.org)) in *Actinidia deliciosa* in allergen.org. We selected P85261 instead of P84527 to find more matched candidate proteins in BLASTp search. Because the length of P85261 is shorter than that of P84527. Therefore, the protparam parameters of P85261 in Table 3 and 4 are quite different compared to other studied proteins because of its length. On the other hand, there is a problem regarding sequence of P85261. Although it is two separated fragments, it seems like it is consisted of just one fragment. According to Table 3, the maximum and minimum number of amino acids were found in *P. persica* and *A. chinensis*, respectively. Theoretical pI value of kiwelin in *A. chinensis* is 5.98 and it was found as 5.83 (data not shown). From this comparison it could be said that theoretical pI values can not be affected by sequence length. The maximum pI value was found in *C. moschata* as 8.54 and minimum value was found from *J. curcas* as 4.12. In Table 3, the net charges were calculated from the subtraction of negatively charged residues from positively charged residues. The net charges of P85261 and P84527 were

CLUSTAL O(1.2.4) multiple sequence alignment

```

sp|P85261|KIWEL_ACTCH      -----ISSCNGPCRDLNDCDGLICG----- 21
sp|P84527|KIWEL_ACTDE      MAQLALLLSLFLTLISLAPPGASISSCNGPCRDLNDCDGLICIKGKCNDPPQVGTHIC 60
                               *****

sp|P85261|KIWEL_ACTCH      --TTHSHQPGGCKPS----- 34
sp|P84527|KIWEL_ACTDE      RGTTPSPQPGGCKPSGTLTCRKGSYPTYDCSPPVTSSTPAKLTNNDFSEGGDDGGPSECD 120
                               ** * *****

sp|P85261|KIWEL_ACTCH      ----- 34
sp|P84527|KIWEL_ACTDE      ESYHNNNERIVALSTGWYNGGSRGCKMIRITASNGKSVSAKVVDCECDSRHGCDKEHAGQP 180

sp|P85261|KIWEL_ACTCH      ----- 34
sp|P84527|KIWEL_ACTDE      PCRNIVDGSNAVWSALGLDKNVGVVDITWSMA 213

```

Figure 2. Pairwise sequence alignment of P85261 and P84527.

Table 4: Amino acid number and percentages in kiwelin-like proteins from different fruits (The name of the proteins in these species were given in Table 2).

	<i>Actinidia chinensis</i>	<i>Corchorus olerius</i>	<i>Vitis vinifera</i>	<i>Cucumis sativus</i>	<i>Punica granatum</i>	<i>Capsicum chinense</i>	<i>Prunus persica</i>	<i>Carica papaya</i>	<i>Cucurbita moschata</i>	<i>Morus notabilis</i>	<i>Jatropha curcas</i>									
	# %	# %	# %	# %	# %	# %	# %	# %	# %	# %	# %									
Ala (A)	0	0.0	18	4.7	10	4.6	13	6.6	10	4.8	53	6.2	11	5.2	11	5.0	13	6.1	12	5.5
Arg (R)	1	2.9	6	2.8	3	1.4	5	2.5	8	3.8	35	4.1	5	2.4	12	5.5	11	5.2	4	1.8
Asn (N)	2	5.9	12	5.6	15	6.9	10	5.1	17	8.1	52	6.1	21	10.0	14	6.4	12	5.6	15	6.9
Asp (D)	3	8.8	16	7.4	16	7.4	13	6.6	15	7.2	40	4.7	13	6.2	14	6.4	19	8.9	19	8.7
Cys (C)	5	14.7	14	6.5	15	6.9	14	7.1	10	4.8	36	4.2	14	6.7	14	6.4	14	6.6	14	6.4
Gln (Q)	2	5.9	9	4.2	7	3.2	4	2.0	5	2.4	22	2.6	4	1.9	5	2.3	5	2.3	7	3.2
Glu (E)	0	0.0	6	2.8	5	2.3	8	4.0	8	3.8	44	5.2	7	3.3	5	2.3	6	2.8	9	4.1
Gly (G)	5	14.7	22	10.2	34	15.7	17	8.6	24	11.5	72	8.4	30	14.3	30	13.7	24	11.3	29	13.3
His (H)	2	5.9	2	0.9	8	3.7	5	2.5	2	1.0	15	1.8	5	2.4	7	3.2	4	1.9	3	1.4
Ile (I)	2	5.9	10	4.7	13	6.0	7	3.5	13	6.2	60	7.0	11	5.2	12	5.5	11	5.2	8	3.7
Leu (L)	2	5.9	13	6.0	17	7.8	13	6.6	13	6.2	58	6.8	13	6.2	15	6.8	14	6.6	15	6.9
Lys (K)	1	2.9	10	4.7	8	3.7	8	4.0	11	5.3	43	5.0	8	3.8	12	5.5	7	3.3	6	2.8
Met (M)	0	0.0	5	2.3	3	1.4	4	2.0	5	2.4	17	2.0	6	2.9	2	0.9	4	1.9	3	1.4
Phe (F)	0	0.0	6	2.8	7	3.2	2	1.0	2	1.0	31	3.6	10	4.8	6	2.7	4	1.9	4	1.8
Pro (P)	3	8.8	12	5.6	10	4.6	13	6.6	13	6.2	47	5.5	12	5.7	10	4.6	9	4.2	9	4.1
Ser (S)	4	11.8	26	12.1	21	9.7	30	15.2	19	9.1	76	8.9	17	8.1	24	11.0	22	10.3	27	12.4
Thr (T)	2	5.9	15	7.0	10	4.6	13	6.6	13	6.2	60	7.0	7	3.3	6	2.7	13	6.1	16	7.3
Trp (W)	0	0.0	3	1.4	3	1.4	2	1.0	4	1.9	7	0.8	3	1.4	4	1.8	3	1.4	3	1.4
Tyr (Y)	0	0.0	4	1.9	1	0.5	4	2.0	3	1.4	28	3.3	1	0.5	1	0.5	6	2.8	4	1.8
Val (V)	0	0.0	12	5.6	11	5.1	13	6.6	14	6.7	58	6.8	12	5.7	15	6.8	12	5.6	11	5.0
Pyl (O)	0	0.0	0	0.0	0	0.0	0	0.0	0	0.0	0	0.0	0	0.0	0	0.0	0	0.0	0	0.0

Table 3. Protein parameters for kiwelin-like proteins in different fruits (The name of the proteins in these species were given in Table 2).

Species	#aa	Mw (KDa)	Theoretical pI	# Negatively Charged Residues (Asp + Glu)	# Positively Charged Residues (Arg + Lys)	Net Charge	Instability Index
<i>Actinidia chinensis</i>	34	3501.86	5.98	3	2	-1	34.23
<i>Corchorus olerius</i>	215	22690.36	4.82	22	16	-8	39.49
<i>Vitis vinifera</i>	382	41391.41	5.18	33	20	-13	44.58
<i>Cucurbita moschata</i>	219	23086.07	8.54	19	24	+5	72.97
<i>Punica granatum</i>	198	20615.93	4.95	21	13	-8	62.58
<i>Capsicum chinense</i>	209	22148.87	5.18	23	19	-4	36.94
<i>Prunus persica</i>	854	92694.39	6.25	84	78	-6	79.79
<i>Carica papaya</i>	210	21995.70	5.06	20	13	-7	38.89
<i>Jatropha curcas</i>	218	22461.42	4.12	28	10	-18	47.05
<i>Morus notabilis</i>	213	22664.24	4.98	25	18	-7	48.58
<i>Cucumis sativus</i>	217	22343.93	5.00	21	11	-10	73.23

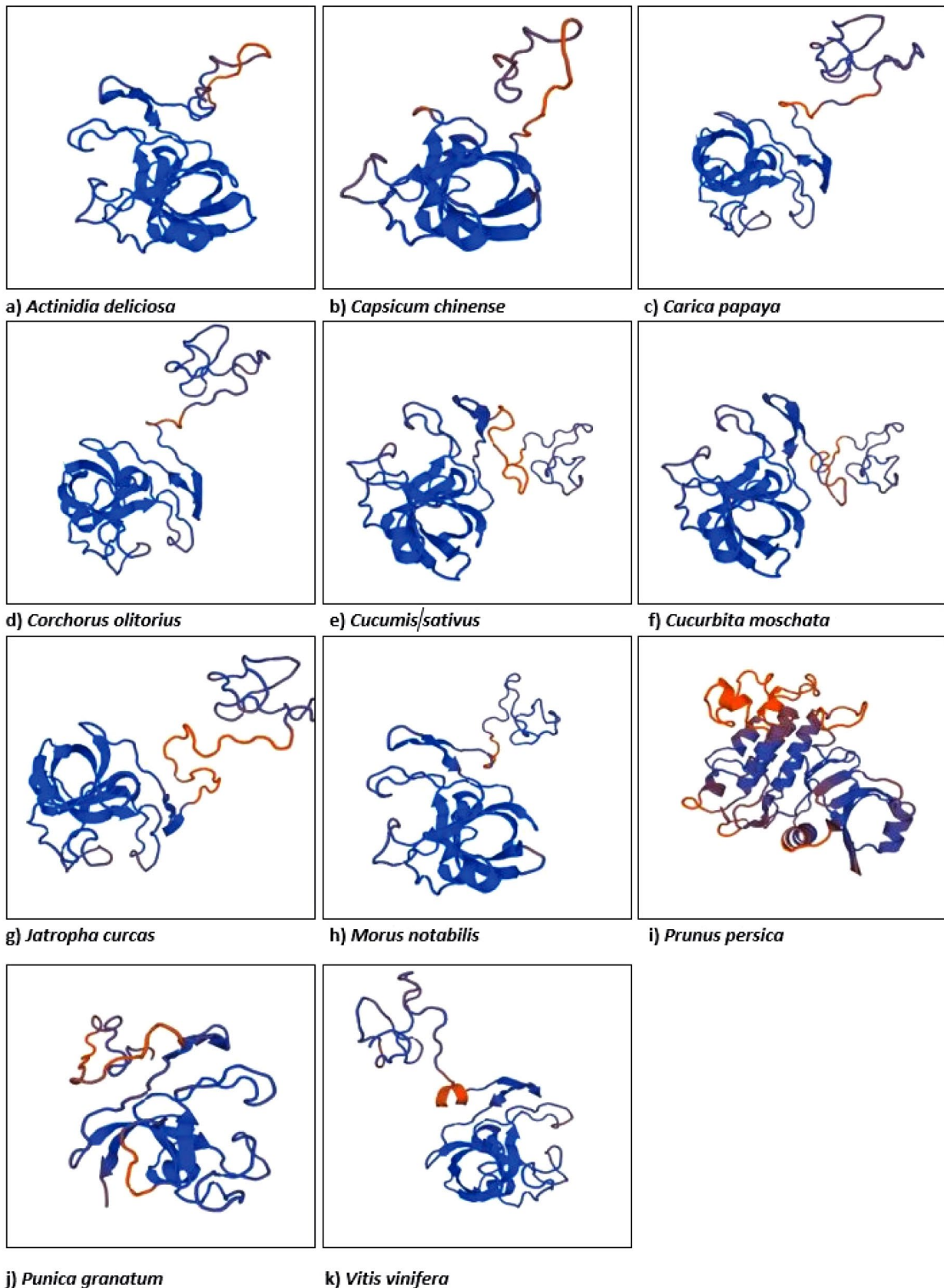


Figure 3. 3-Dimensional visualization of each protein by Swiss-MODEL a) *Actinidia deliciosa*, b) *Capsicum chinense*, c) *Carica papaya*, d) *Corchorus olitorius*, e) *Cucumis sativus*, f) *Cucurbita moschata*, g) *Jatropha curcas*, h) *Morus notabilis*, i) *Prunus persica*, j) *Punica granatum*, k) *Vitis vinifera* (The name of the proteins in these species were given in Table 2).

found as -1 and -4, respectively, which show that kiwellin is a negatively charged protein. Only positive value was observed in *C. moschata* as +5. The highest and lowest instability index were found in the proteins of *P. persica* and *A. chinensis*. The correlation test was carried out for the data in Table 3. But no meaningful correlation was found among the data. When the amino acid numbers and percentages were compared, it was found that glycine and serine were dominant amino acids in the sequences apart from the protein of *V. vinifera*.

3. 3. The Homology Modelling

The homology modelling was carried by using Swiss-MODEL. 3-D structures of proteins are essential and important for understanding biological systems. 3-D homology models also reveal that the kiwellin-like proteins in these species may exhibit similar allergenicity in human. The created 3-D structures were given in Figure 3. Except for the proteins of *P. granatum*, *P. persica* and *V. vinifera*, the proteins include similar barrel-like structure formed by beta-sheets. The pore-forming property of the kiwellin might be associated with these structures. From these homology modelling results, one can estimate the allergenicity of the proteins by comparing the 3-D structures since there is a direct relationship between function and structures of the proteins. Because there is a direct relationship between structure and function in proteins. It is important to note that the structure of kiwellin belongs to P84527 in Figure 3 due to the sequence length of P85261 is shorter than P84527.

3. 4. AlgPred

There are three types prediction algorithms to estimate allergenicity: i) Mapping of IgE epitopes and PID, ii) support vector machine module based on amino acid composition and iii) support vector machine module based on

dipeptide composition. The results of these algorithms are given in Table 5. The mapping of IgE epitopes and PID estimated that none of 10 different proteins were identified as potential allergen. According to SVM based on amino acid results all protein except *V. vinifera* are showed allergen. Considering the SVM based on dipeptide composition results, six protein *C. olitorius*, *C. sativus*, *C. chinense*, *C. papaya*, *M. notabilis* and *J. curcas* were identified allergen. There are six proteins (*C. olitorius*, *C. sativus*, *C. chinense*, *C. papaya*, *M. notabilis*, *J. curcas*) in which the two SVM algorithms give positive results.

It should be noted that % identity might not be used as an important criteria to evaluate if a protein is allergen or not. When we compare all results, we see that only 6 of 10 potential allergens are classified as an allergen. When BLASTp results were examined, the proteins in *C. olitorius* (95%) and *C. sativus* (80%) were classified as allergen proteins. However, even if the protein in *P. granatum* has high similarity (90%), it was not identified as an allergen protein. From these results, it could be said that the similarity index can not be used as a criteria. When Swiss-MODEL results are considered, 3-D structures are different. AlgPred contains different algorithms to evaluate the submitted protein sequences.²¹ Three of them are mapping of IgE epitopes and PID, support vector machine module based on amino acid and dipeptide compositions. So the methods are based on different algorithms. Six proteins in this study were evaluated as allergen proteins inasmuch as they were identified by support vector machine module based on amino acid and dipeptide compositions (Table 5).

4. Conclusions

The aim of the paper is to find kiwellin-like proteins by using allergen based *in silico* tools. Based on the results of the study, it might be said that identified kiwellin-like proteins in this study might show similar allergenicity in

Table 5: AlgPred analysis of different allergens in fruits (The name of the proteins in these species were given in Table 2).

AlgPred Parameters Species	Mapping of IgE epitopes and PID	SVM module based on amino acid Composition				SVM module based on dipeptide Composition			
		Allergen prediction	Score	Positive predictive value (%)	Negative predictive value (%)	Allergen predictive	Score	Positive predictive value (%)	Negative predictive value (%)
<i>Corchorus olitorius</i>	X	√	0.43526052	81.83	74.03	√	-0.048627	63.10	85.56
<i>Vitis vinifera</i>	X	X	-0.74099846	22.82	92.94	X	-0.676397	13.26	74.19
<i>Cucumis sativus</i>	X	√	0.91145594	85.64	67.96	√	0.004279	74.14	79.04
<i>Punica granatum</i>	X	√	-0.14027725	64.55	86.61	X	-0.643383	13.26	74.19
<i>Capsicum chinense</i>	X	√	0.83191078	85.64	67.96	√	-0.034468	63.10	85.56
<i>Prunus persica</i>	X	√	0.37866622	74.81	76.94	X	-0.652229	13.26	74.19
<i>Carica papaya</i>	X	√	0.77608681	87.05	71.53	√	0.320983	85.88	72.01
<i>Cucurbita moschata</i>	X	√	-0.13002118	64.55	86.61	X	-0.256085	39.40	89.34
<i>Morus notabilis</i>	X	√	0.25337214	74.81	76.94	√	-0.028054	63.10	85.56
<i>Jatropha curcas</i>	X	√	0.78994643	87.05	71.53	√	0.304532	85.88	72.01

people who have kiwelling allergenicity. The identification of an unknown protein in a fruit sample by using *in silico* tools is so easier to estimate its allergenicity compared to wet-lab methodology. This strategy can reduce the cost of medicine and/or therapy costs spent for allergenicity. Therefore, there is a great need for development of novel allergenicity tools with better accuracy. Kiwi is an important and highly consumed fruit because of its rich ingredients such as vitamins and antioxidant molecules. Natural production place of kiwi is China. On the other hand, kiwi is also produced in Italy, New Zealand, Iran and Chile. According to FAOSTAT, total production of kiwi is 4,274,840 ton.²² Although kiwi is known as a healthy fruit, it has 13 allergen proteins in it, according to allergen.org. Kiwi has also been started to produce in different country. For example, kiwi trees have been planted in the northern part of Turkey and now the production are significantly increasing. Since some people have not consumed this fruit previously, people should be informed about the possible allergenicity of the allergen proteins of kiwi. In the present study, 10 kiwelling-like proteins have been studied in 10 different plants based on the similarities. It is very important to note that these proteins have still not been taken place in allergen.org. Many scientific studies have been published on kiwi. Tamburrini et al.⁸ purified kiwelling and defined it as an allergen protein. They also mentioned that kiwelling is one third of the total protein of kiwi fruit. In their study, it is selected because of high abundance in kiwi fruit compared to other allergen proteins. They proved its allergenicity by using Scin Prick test, western blot, specific IgE and total IgE tests. Tuppo et al.²³ also showed that kissper part of kiwelling is a proteolysis-resistant protein and also it constitutes pore-forming in lipid membrane of cell. pH dependent and thionine containing Kissper also shows its function in ion-channels. These functions cause allergenicity in human. Ciardiello et al.²⁴ identified two domains in kiwelling. First one is known as kissper consisted of first 39 amino acids and 6 of them is Cys. Kissper is located in the N-terminal. Second domain is known as KiTH and located in C-terminal. The residue number of this location is between 40–189. 8 Cys were also reported for this residue. Ciardiello et al.²⁴ mentioned that kiwelling based ion channel disruption can be associated with cystic fibrosis. Offerman et al.²⁵ reported X-crystallography of kiwelling protein in *A. deliciosa* (Act d 5). Pore forming structure of kiwelling was also explained by Offerman et al.²⁵. Hamiaux et al.²⁶ investigated crystal structure of kiwelling and they found that there is a binding region on the surface of kiwelling for endogenous ligands. Uberti et al.²⁷ studied 13 allergen proteins in kiwi. They defined 3 of them as major allergen proteins (Act d 1, Act d 2, Act d 6). Act d 5 and Act d 8/11 were defined as minor allergen proteins by Uberti et al.²⁷ Jenkins et al.²⁸ analysed the plant genomes to study allergen proteins. It is reported that 65% of the food allergens are originated from 4 different protein family. According to an interesting paper by Ciacci et al.²⁹ they

explained antioxidant and anti inflammatory effects of kissper peptide. In this study, 6 proteins were defined as allergens. by using *in silico* tools in 10 different fruits. From the outputs of this paper and also published papers in this field, it is most likely to be said that *in silico* tools will be of great importance in the life sciences.^{3,7,28,30,31}

In conclusion, kiwelling like proteins can be existed in not only kiwi but also in different fruits. By using *in silico* tools, it is more easier to define possible allergen proteins. Since *in silico* tools have recently been developed, more input will be released in near future. The outputs from *in silico* based investigations will most likely decrease number of allergen based disorders. More scientific researches will be needed for development of new *in silico* tools and also application them to find allergen proteins in foods. Developments in the field of artificial intelligence will most likely to increase the quality of *in silico* tools in near future.

5. References

1. F. Ferreira, T. Hawranek, P. Gruber, N. Wopfner, A. Mari, *Allergy*. **2004**, *59*(3), 243–267. DOI:10.1046/j.1398-9995.2003.00407.x
2. T. Karluss, G. Bannon, S. Hefle, C. Herouet, M. Holsapple, G. Ladics, S. MacIntosh, L. Privalle, *Toxicol. Sci.* **2005**, *88*(2), 307–310. DOI:10.1093/toxsci/kfi277
3. Å. K. Björklund, D. Soeria-Atmadja, A. Zorzet, U. Hammerling, M.G. Gustafsson, *Bioinformatics*. **2004**, *21*(1), 39–50. DOI:10.1093/bioinformatics/bth477
4. J. J. N. Jansen, A. F. Kardinaal, G. Huijbers, B. J. Vlieg-Boerstra, B. P. Martens, T. Ockhuizen, *J. Allergy Clin. Immunol.* **1994**, *93*(2), 446–456. DOI:10.1016/0091-6749(94)90353-0
5. G. Kanny, D. A. Moneret-Vautrin, J. Flabbee, E. Beaudouin, M. Morisset, F. Thevenin, *J. Allergy Clin. Immunol.* **2001**, *108*(1), 133–140. DOI:10.1067/mai.2001.116427
6. J. Cui, L. Y. Han, H. Li, C. Y. Ung, Z. Q. Tang, C. J. Zheng, Z. W. Cao, Y. Z. Chen, *Mol. Immunol.* **2007**, *44*(4), 514–520. DOI:10.1016/j.molimm.2006.02.010
7. M. Hayes, P. Rougé, A. Barre, C. Herouet-Guicheney, P. Rouge, E. L. Roggen, *Drug Discov. Today Dis. Models*. **2015**, *17*, 3–11. DOI:10.1016/j.ddmod.2016.06.001
8. M. Tamburrini, I. Cerasuolo, V. Carratore, A. A. Stanziola, S. Zofra, L. Romano, L. Camardella, M. A. Ciardiello, *Protein J. Vol.* **2005**, *24*, 7–8. DOI:10.1007/s10930-005-7638-7
9. N. Motohashi, Y. Shirataki, M. Kawase, S. Tani, H. Sakagami, K. Satoh, T. Kurihara, H. Nakashima, I. Mucsi, A. Varga, J. Molna, *J. Ethnopharmacol.* **2002**, *81*, 357/364. DOI:10.1016/S0378-8741(02)00125-3
10. M. Gavrović-Jankulović, T. Ćirković, O. Vučković, M. Atanasković-Marković, A. Petersen, G. Gojgić, L. Burazer, R. M. Jankov, *J. Allergy Clin. Immunol.* **2002**, *110*(5), 805–810. DOI:10.1067/mai.2002.128947
11. A. Collins, V. Harrington, J. Drew, R. Melvin, *Carcinogenesis*. **2003**, *24*(3), 511–515. DOI:10.1093/carcin/24.3.511

12. J. S. Lucas, S. A. Lewis, J. H. Hourihane, *Pediatr Allergy Immunol.* **2003**, *14*, 420–428. DOI:10.1046/j.0905-6157.2003.00095.x
13. A. Çavuş, *Atatürk Üniversitesi Sosyal Bilimler Dergisi.* **2016**, *20*, 225–241.
14. M. D. Chapman, A. Poms, H. Breiteneder, F. Ferreira, *J. Allergy Clin. Immunol.* **2007**, *119*, 414–20. DOI:10.1016/j.jaci.2006.11.001
15. J. N. Larsen, Allergen nomenclature: a need for the scientific community. *Arbeitskreis Paul-Ehrlich-Institut (Bundesamt für Sera und Impfstoffe) zu Frankfurt aM*, **2006**, (95), 5–9.
16. G. M. Boratyn, C. Camacho, P. S. Cooper, G. Coulouris, A. Fong, N. Ma, T. L. Madden, W. T. Matten, S. D. McGinnis, Y. Merezhuk, Y. Raytselis, E. W. Sayers, T. Tao, J. Ye, I. Zaretskaya, *Nucleic Acids Res.* **2013**, *41*, W29–W33. DOI:10.1093/nar/gkt282
17. M. Johnson, I. Zaretskaya, Y. Raytselis, Y. Merezhuk, S. McGinnis, T. L. Madden, *Nucleic Acids Res.* **2008**, *36*, W5–W9. DOI:10.1093/nar/gkn201
18. E. Gasteiger, C. Hoogland, A. Gattiker, M. R. Wilkins, R. D. Appel, A. Bairoch, A. Protein identification and analysis tools on the ExPASy server. In *The proteomics protocols handbook*, 2005, 571–607. DOI:10.1385/1-59259-890-0:571
19. F. Sievers, A. Wilm, D. G. Dineen, T. J. Gibson, K. Karplus, W. Li, R. Lopez, H. McWilliam, M. Remmert, J. Söding, J. D. Thompson, D. G. Higgins, *Mol. Syst. Biol.* **2011**, *7*:539. DOI:10.1038/msb.2011.75
20. M. Biasini, S. Bienert, A. Waterhouse, K. Arnold, G. Studer, T. Schmidt, F. Kiefer, T. G. Cassarino, M. Bertoni, L. Bordoli, T. Schwede, *Nucleic Acids Res.* **2014**, *42*, W252–W258. DOI:10.1093/nar/gku340
21. S. Saha, and G. P. S. Raghava, *Nucleic Acids Res.* **2006**, *34*, W202–W209. DOI:10.1093/nar/gkl343
22. FAOSTAT, Kiwifruit production in 2016; Crops/World Regions/Production Quantity from pick lists. UN Food and Agriculture Organization, Statistics Division DOI: <http://www.fao.org/faostat/en/#data/QV> (Retrieved February 20, 2018).
23. L. Tuppo, I. Giangrieco, P. Palazzo, M. L. Bernardi, E. Scala, V. Carratore, M. Tamburrini, A. Mari, M. A. Ciardiello, *J. Agric. Food Chem.* **2008**, *56*(10), 3812–3817. DOI:10.1021/jf703620m
24. M. A. Ciardiello, D. Meleleo, G. Saviano, R. Crescenzo, V. Carratore, L. Camardella, E. Gallucci, S. Micelli, T. Tancredi, D. Picone, M. Tamburrini, *J. Pept. Sci.* **2008**, *14*(6), 742–754. DOI:10.1002/psc.992
25. L. R. Offermann, I. Giangrieco, M. L. Perdue, S. Zuzzi, M. Santoro, M. Tamburrini, J. D. Cosgrove, A. Mari, M. A. Ciardiello, M. Chruszcz, *J. Agric. Food Chem.* **2015**, *63*(29), 6567–6576. DOI:10.1021/acs.jafc.5b02159
26. C. Hamiaux, R. Maddumage, M. J. Middleditch, R. Prakash, D. A. Brummell, E. N. Baker, R. G. Atkinson, *J. struct. biol.* **2014**, *187*(3), 276–281. DOI:10.1016/j.jsb.2014.07.005
27. F. Uberti, E. Peñas, Y. Manzoni, C. Lorenzo, C. Ballabio, A. Fiocchi, L. Terracciano, P. Restani, *Pediatr. Allergy Immunol.* **2015**, *26*(2), 139–144. DOI:10.1111/pai.12345
28. J. A. Jenkins, S. Griffiths-Jones, P. R. Shewry, H. Breiteneder, E. C. Mills, *J. Allergy Clin. Immunol.* **2005**, *115*(1), 163–170. DOI:10.1016/j.jaci.2004.10.026
29. C. Ciacci, I. Russo, C. Bucci, P. Iovino, L. Pellegrini, I. Giangrieco, M. A. Ciardiello, *Clin. Exp. Allergy.* **2014**, *175*(3), 476–484. DOI:10.1111/cei.12229
30. T. C. Tomaš, M. Moškon, M. Mraz, Rozman, D, *Acta Chim. Slov.* **2018**, *65*, 253–265. DOI:10.17344/acsi.2015.1505
31. S. Pleško, H. Volk, M. Lukšič, Č. Podlipnik, *Acta Chim. Slov.* **2015**, *62*(3), 555–564.

Povzetek

Identifikacija alergeni beljakovin z uporabo tako imenovane wet-lab tehnologije je zamuden in tudi drag proces. V zadnjih letih, zahvaljujoč razvoju na področju bioinformatike, je zdaj mogoče oceniti alergene beljakovine z uporabo računskih orodij. V tej študiji je bil cilj, da bi z uporabo bioinformatičnih orodij našli kivelinu podobne beljakovine iz različnih vzorcev sadja. Glede na rezultate študije je bilo šest beljakovin iz *Corchorus olitorius*, *Cucumis sativus*, *Capsicum chinense*, *Carica Papaya*, *Morus notabilis* in *Jatropha curcas* opredeljenih kot alergeni. Skratka, računski orodja, razvita na področju bioinformatike, lahko zagotovijo velik prispevek k oceni neznanih beljakovinskih alergenov v različnih plodovih. Na podlagi teh *in silico* rezultatov zdravniki lahko priporočajo ljudem, ki so alergični na kivelin, da ne uživajo sadja, ki vsebuje kivelinu podobne beljakovine.



Except when otherwise noted, articles in this journal are published under the terms and conditions of the Creative Commons Attribution 4.0 International License

Scientific paper

Development and Validation of the Simple and Sensitive Spectrophotometric Method of Amoxicillin Determination in Tablets using Sulphanilamides

Oksana Kostiv,* Olha Korkuna and Petro Rydchuk

Ivan Franko National University of Lviv, Kyryla & Mefodiya Str., 6, 79005 Lviv, Ukraine

* Corresponding author: E-mail: oksanakostiv73@gmail.com

Received: 05-15-2019

Abstract

A rapid, simple and sensitive spectrophotometric method for the determination of amoxicillin (AM) is described. The method is based on the previous sulphanilamide (SA) and sulphathiazole (STZ) diazotization in the medium of 0.6–0.7 M hydrochloric acid and their subsequent interaction with amoxicillin at pH = 10.5 with formation of yellow-colored azo compounds. Effective molar absorptivities at the absorbance maxima at 445 nm (SA) and 448 nm (STZ) for azo compounds were $(1.74 \pm 0.06) \cdot 10^4 \text{ L} \times \text{mol}^{-1} \times \text{cm}^{-1}$ and $(1.97 \pm 0.05) \cdot 10^4 \text{ L} \times \text{mol}^{-1} \times \text{cm}^{-1}$, respectively. Stoichiometric ratios of the components of azo compounds were determined using continuous variations method. Based on the optimum reaction conditions, new methods were developed. These methods allow to determine the amoxicillin in concentration range 1.3–32.9 mg \times mL⁻¹ with sulphanilamide and 0.7–27.4 mg \times mL⁻¹ with sulphathiazole. The methods were successfully validated for amoxicillin determination in tablets “Amoxil”.

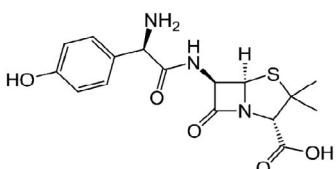
Keywords: Amoxicillin; sulphanilamide; sulphathiazole; spectrophotometry; diazotization; azo-coupling.

1. Introduction

Significant development of medicine, chemistry, and biology result in the increased use of biologically active substances, in particular, antibiotics, which occupy an important place in contemporary medical and veterinary practices. The monitoring of their content to evaluate the quality of finished drugs products and detecting the coun-

terfeits is a very important task. Since antibiotics often cause side-effects and allergic reactions, it is advisable to control their content in biological fluids, as well as in foods (milk, chicken tissues) because of their extensive use in livestock production. It should be noted that the unjustified entry of antibiotics into the body leads to the emergence of microorganisms resistant to the treatment of bacterial infections. Therefore, it is important to control the

Table 1. Molecular structure and characteristics of amoxicillin⁴

Structural formula	Characteristic
(2S,5R,6R)-6-[[[(2R)-2-amino-2-(4-hydroxy-phenyl)-acetyl]amino]-3,3-dimethyl-7-oxo-4-thia-1-azabicyclo[3.2.0]heptane-24-carboxylic acid CAS № 26787-78-0  $M = 365.4 \text{ g} \times \text{mol}^{-1}$; $M = 365.4 \text{ g} \times \text{mol}^{-1}$; $\log K_{ow} = 0.87$	Appearance: white or almost white, crystalline powder. Solubility: slightly soluble in water, very slightly soluble in 96% ethanol, practically insoluble in fatty oils. It dissolves in dilute acids and dilute solutions of alkali hydroxides.

presence of antibacterial substances in the wastewater of the pharmaceutical companies for environmental considerations.

Amoxicillin (AM) is a β -lactam antibiotic belonging to the group of penicillins active against both Gram-positive and Gram-negative bacteria. It is one of the most widely used semi-synthetic penicillins in the treatment of acute bacterial sinusitis and community-acquired pneumonia.^{1,2} The chemical structure of amoxicillin consists of the *d*-4-hydroxyphenylglycine side chain attached to 6-aminopenicillanic acid (6-APA) moiety (Table 1). Amoxicillin, like many other antibiotics, is liable to splitting by β -lactamase, which is produced by certain bacteria. Therefore, it is often used in combination with clavulanic acid, which is an inhibitor of these enzymes.³

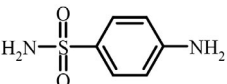
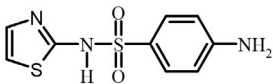
When choosing the analytical procedure for antibiotics assay, the nature of the samples in which they are determined is a priority. For the determination of AM in biological fluids^{6,9,13,15,18} (blood plasma, intestinal fluid, urine), multicomponent drugs,^{5,6,9–11} and food products^{7,8,12,16} (milk, honey, chicken meat), highly efficient liquid chromatography as well as liquid chromatography coupled with tandem mass spectrometry are used.^{5–12} These techniques are expensive, time-consuming and require the use of organic solvent. Furthermore, spectrophotometry, different types of voltammetry,^{13–18} and titrimetry² as well are used for quantification of AM content in medicines and industrial wastewater. The liquid chromatography is the official pharmacopoeia method^{11,19} of AM determination in drug substances, capsules, tablets, boluses, oral and injectable suspension. The microbial assay is used for AM determination in intramammary infusion and the iodometry is used for AM assay in oral suspension in soybean oil.

The advantages of spectrophotometry are rapidity and simplicity, low cost of the analysis, and environmental safety. A number of analytical techniques for the AM spectrophotometric determination based on AM own absorbance in the UV spectrum range (234–302 nm)^{20–22} are used only for pure active pharmaceutical ingredients assay,

because many organic substances absorb light in the same spectrum range. On the other hand, the colored amoxicillin derivatives as analytical forms for AM spectrophotometric determination are often obtained using the azo-coupling reaction. In particular, the spectrophotometric methods of AM determination, which are based on their reaction with diazotized *p*-aminobenzene acid and procaine,²³ *o*-nitroaniline,²⁴ metaclopramid,²⁵ benzocaine,²⁶ and sulphanic acid²⁷ are known. The spectrophotometric methods of the AM determination based on the reactions of chelate and ion-pair complexes formation^{24,28,29} are described. However, many of the known methods of AM determination have a number of disadvantages: long run time, use of organic solvents, and a boiling/ice water bath. All of the above spectrophotometric methods^{23–29} of AM determination were used only for the analysis of pharmaceutical formulations. Moreover, many of the described spectrophotometric methods for AM determination are not validated, although it is required by most world's pharmacopoeia. Among the validated ones are mainly the methods based on measuring their own absorbance in the UV spectrum range.

The azo-coupling reaction is important both for the analysis and the synthesis of new organic substances. Since azo-coupling is widely used for the spectrophotometric AM determination, sulphanilamides can be promising and easily available analytical reagents. They are derivatives of sulphanic acid, which are able to depress the development of Gram-positive and Gram-negative bacteria, some protozoons and pathogenic fungi. The acidic properties of the sulphamide group make it possible to interact with the salts of heavy metals. In this case, colored complexes, soluble or insoluble in water, are formed.³⁰ Besides, due to the presence of the primary aromatic amino group, the sulphanilamides enter into a diazotization reaction with the next azo-coupling with various phenolic compounds. In particular, we have previously studied the conditions for sulphanilamides diazotization and their subsequent azo coupling with hydroxy-substituted azo compounds, namely,

Table 2. Structural formula and some characteristics of investigated sulphanilamides

Reagent	Characteristics
Sulphanilamide (SA), streptocidum <i>p</i> -aminobenzenesulfonamide,  $M = 172.2 \text{ g} \times \text{mol}^{-1}$; $\text{p}K_{\text{a}1} \text{ NA}; \text{p}K_{\text{a}2} = 10.1$ $\log K_{\text{ow}} = -0.62$	Appearance: white crystalline powder. It is odorless, slightly bitter with a sweet after-taste. Solubility: highly soluble in boiling water (1:2), hardly in ethanol (1:37), soluble in solutions of hydrochloric acid, caustic alkalis, acetone (1:5), glycerol, propylene glycols; practically insoluble in ether, chloroform, benzene, petroleum ether.
Sulphathiazole (STZ), 2-(<i>p</i> -aminobenzenesulfonamido)-1,3-thiazol, CAS 72-14-0  $M = 255.3 \text{ g} \times \text{mol}^{-1}$; $\text{p}K_{\text{a}1} = 2.62; \text{p}K_{\text{a}2} = 7.37$ $\log K_{\text{ow}} = 0.05$	Appearance: white or white with a slightly yellowish tint, odorless crystalline powder. Solubility: very slightly soluble in water, slightly soluble in ethanol, soluble in dilute mineral acids and alkaline solutions.

NA – not available.

with the acid monoazo dye Tropaeolin O (TrO)^{30,31} and heterocyclic azo reagents 4-(2-pyridylazo)-resorcinol^{30,32} (PAR) and 4-(2-thiazolylazo)-resorcinol (TAR).^{30,33} The absorbance maxima of the obtained nitroso disazo compounds at the spectrum range 590–620 nm^{30–33} have been successfully used for the sulphanilamides determination in dosage forms.

Sulphanilamides are not used as reagents. In our investigation the simple members of this class, sulphanilamide and sulphathiazole (Table 2), were explored as reagents for the first time.

2. Materials and Methods

2.1. Apparatus

UV-VIS measurements were performed with UV-VIS scanning spectrophotometer SPECORD M-40 (Carl Zeiss Jena, Germany) using 1 cm cuvettes. All absorbance measurements were performed at 20–25 °C.

The pH value was measured by pH-meter model pH 150M (Gomelsky Plant of Measuring Devices, Belarus), equipped with a combination electrode, which incorporates both glass and reference silver chloride electrodes into one body. The required pH of each solution was adjusted using diluted HCl and NaOH solutions.

2.2. Reagents

All aqueous solutions were prepared using distilled water.

Solutions of amoxicillin (Sigma-Aldrich, Germany) were prepared by dissolving the appropriate amounts of the reagent of pharmacopoeia grade ($\geq 99\%$) in a 0.1 M HCl solution. The working solutions were stored at a room temperature in a dark place no longer than two days.

Sulphanilamides (SA, STZ) were purchased from Sigma (USA). Solutions of sulphanilamide and sulphathiazole were prepared by dissolving appropriate amounts of the reagents of pharmacopoeia grade in 0.1 M sodium hydroxide solution. Solutions of amoxicillin were prepared by dissolving appropriate amounts of the reagent of pharmacopoeia grade in 0.1 M hydrochloric acid. All solutions were stored at a room temperature in a dark place.

The solutions of hydrochloric acid, phosphoric acid, acetic acid, boric acid, sodium hydroxide, sodium nitrite, sodium tetraborate, sodium acetate, sodium phosphate, sodium pyrophosphate, and sodium carbonate, were prepared from chemicals of the analytical grade.

2.3. Procedure

Procedure for tablets or powder preparation for the AM determination

Twenty tablets were weighed and finely powdered in a porcelain mortar. The accurate amount of powder, con-

taining ~ 250 mg AM, was placed into a 50 mL volumetric flask and was dissolved in 25 mL 0.1 M HCl for obtaining AM extract. Then solution was mixed for 60 min and 0.1 M HCl was added to complete the volume to 50 mL. Obtained solution was mixed again and was filtered through the folded filter of medium porosity. The filtrate was 10-fold diluted. Furthermore 5.0 mL of filtrate was placed into a 50 mL volumetric flask and diluted with 0.1 M HCl solution to the full volume 50 mL. Nominal AM content in solution obtained in such way was $250 \mu\text{g} \times \text{mL}^{-1}$. For the assay an aliquot of 1 mL of the solution was taken and then treated as described below in the recommended procedure for the amoxicillin determination.

General procedure of AM determination with SA and STZ

5.0 mL of 0.6 M or 0.7 M hydrochloric acid solution was placed into a 25 mL volumetric flask, then 2.0 mL $5.5 \cdot 10^{-3}$ M SA or $4.5 \cdot 10^{-3}$ M STZ were added, respectively. Next, 1.75 mL 0.1 M sodium nitrite solution was added into the flask. Obtained solution was stirred and allowed to stand for 20 min at a room temperature. Then sample of amoxicillin solution containing $1.3\text{--}32.9 \mu\text{g} \times \text{mL}^{-1}$ (in the method with sulphanilamide) or $0.7\text{--}27.4 \mu\text{g} \times \text{mL}^{-1}$ (in the method with sulphathiazole) of AM (in the final volume) was added. Then 10.0 mL 0.25 M sodium tetraborate solution was added, next the obtained mixture was neutralized by adding 3.0 mL 2.0 M sodium hydroxide solution and the pH value was adjusted to pH = 10.5 and distilled water was added to the full volume 25 mL. Then the solution was mixed thoroughly and the absorbance measurements (at the room temperature ~20 °C) were carried out against all corresponding reagents blank solution at 445 nm (AM+SA) and 448 nm (AM+STZ) in 1.0 cm cuvettes. Amoxicillin concentration was calculated using the methods of calibration curve and single-point calibration.

3. Results and Discussion

3.1. Absorption Spectra

The conditions of amoxicillin interaction with sulphanilamide and sulphathiazole have been studied.

Experimental data revealed that AM does not directly interact with sulphanilamides. However, diazonium salts of SA and STZ azo-couple with AM and form colored azo compounds. As follows from their absorption spectra, new absorbance maxima at $\lambda_{\text{max}} = 445$ nm and $\lambda_{\text{max}} = 448$ nm appear, respectively (Fig. 1), the absorbance value of which linearly depends on the AM concentration. These maxima are not characteristic for the absorption spectrum of the amoxicillin own absorbance in the alkaline medium ($\lambda_{\text{max}} = 250$ nm), nor for diazotized reagents in the alkaline medium: $\lambda_{\text{max}} = 263$ nm for SA and $\lambda_{\text{max}} = 265$ nm for STZ. However, in the case of diazotized STZ compared to SA in

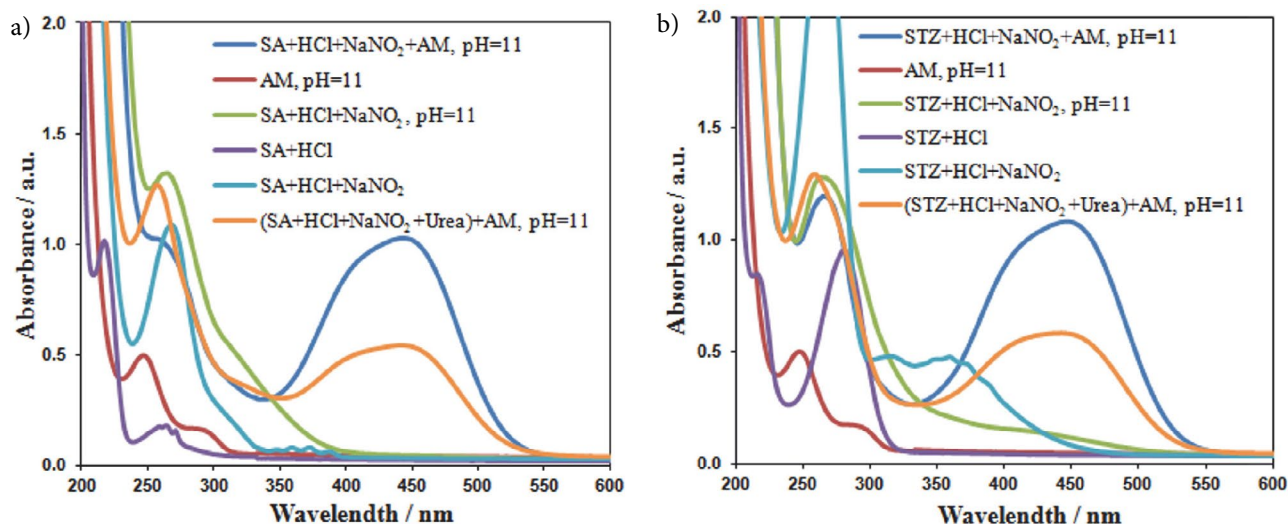


Fig. 1. Absorption spectra of aqueous solutions of AM interaction products with a) SA and b) STZ diazonium salt. $C_{SA} = 1.0 \cdot 10^{-4}$ M, $C_{STZ} = 1.0 \cdot 10^{-4}$ M, $C_{AM} = 5.0 \cdot 10^{-5}$ M, $C_{NaNO_2} = 1.0 \cdot 10^{-3}$ M, $C_{HCl} = 1.0$ M.

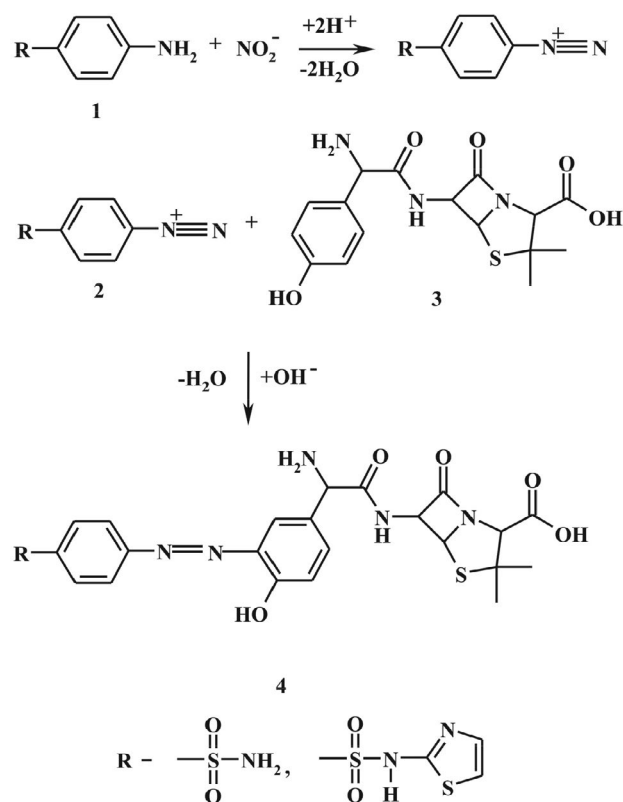
the alkaline medium, a negligible absorbance is observed at 440–450 nm due to the azo compound, which is probably slowly formed by the diazotized STZ's own azo-coupling. This compound has a stronger chromophore system due to the presence of sulphathiazole heterocycle substituent in the sulphanilamide molecule. Though, in subsequent studies, the effect of the competing reaction of the

diazotized STZ's own azo-coupling is compensated, since all measurements were made versus blank solution. In addition, the broad absorbance maxima in the spectrum range 250–270 nm (Fig. 1) are observed on the absorption spectra of both obtained products as a result of the additive absorbance of the fragments of both reagents in the newly formed products.

As follows from the absorption spectra (Fig. 1), it is inappropriate to destroy the excess of unreacted nitrite ions during the SA and STZ diazotization using urea, since the absorbance of their azo-coupling products with AM is significantly reduced.

The obtained water soluble colored products of AM interaction with the diazotized SA and STZ are used for the quantitative determination of amoxicillin (Scheme 1).

Nitrite-ions diazotize primary aromatic amino group of the reagent (SA, STZ) (1) in acid media with the formation of the corresponding diazonium salt (2), which interacts with AM in alkaline media to form yellow-colored product (4).



Scheme 1. Scheme of amoxicillin interaction with sulphanilamide and sulphathiazole

3. 2. Conditions of Sulphanilamides Diazotization

3. 2. 1. Effect of Acid Nature and Concentration

According to literary sources the primary aromatic amino group, which is included in the structure of the investigated reagents, is diazotized in a strongly acidic medium³⁴ and the nature of the acid affects the yield of the following azo-coupling reaction product.

The conditions of SA diazotization described in the literature are rather contradictory (either hydrochloric acid in the concentration range from 0.1 M³⁵ to 5 M^{36–38} or 10 M sulfuric acid³⁹ or a mixture of phosphoric and acetic acid⁴⁰ is used), therefore we have investigated the influ-

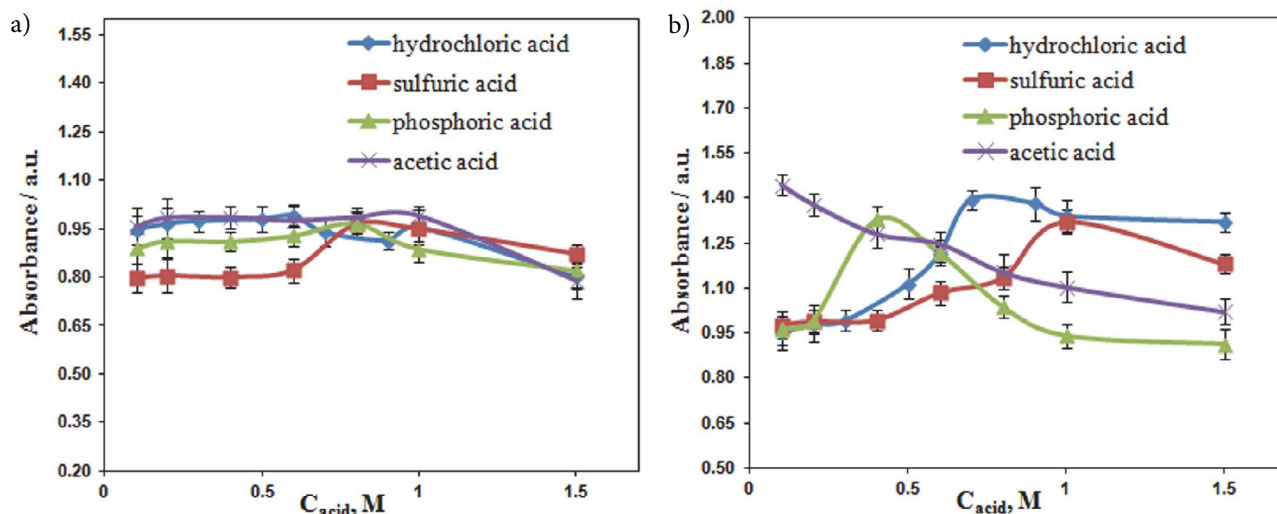


Fig. 2. Effect of nature and concentration of acid on the a) SA and b) STZ diazonium salt formation and the product of its interaction with the AM. $C_{SA} = 2.0 \cdot 10^{-4}$ M, $C_{STZ} = 2.0 \cdot 10^{-4}$ M, $C_{NaNO_2} = 2.0 \cdot 10^{-3}$ M, $C_{AM} = 5.0 \cdot 10^{-5}$ M, $n = 5$.

ence of hydrochloric, sulfuric, phosphoric, and acetic acid concentration on the SA and STZ diazonium salts yield and the following formation of their azo-coupling products with AM.

As follows from the experimental data (Fig. 2), the maximum efficiency of the products of AM interaction with SA and STZ diazonium salts is observed at SA diazotization in acetic acid medium but the use of hydrochloric acid allows to achieve a comparative yield of diazonium salts and azo-coupling products, therefore, we chose 0.6 M and 0.7 M hydrochloric acid for the SA and STZ diazotization, respectively. The differences can be caused by different acids strength as well as by different intermediates activity, which are formed during the SA diazotization. According to the mechanism of diazotization, the reaction occurs in several stages, as a result, depending on the type of the acid used, various diazotizing agents are formed. One of the important steps is the formation of a nitrosyl cation, which at the next stage interacts with a nitrite ion, forming nitrogen(III) oxide, which is the most active diazotizing agent. Depending on the used mineral acid, the actual diazotizing reagent may be nitrosyl chloride, nitrosyl sulfate, nitrosyl acetate, or nitrosyl phosphate, which enter into the next reaction with different activity level.⁴¹

3. 2. 2. Effect of Sodium Nitrite Concentration and Time of Diazotization

The influence of sodium nitrite concentration as diazotizing reagent on the yield of sulphanilamide and sulphathiazole diazonium salts, as well as their azo compounds with AM accordingly has been investigated. As it is shown on Fig. 3, optimum for sulphanilamides diazotization is to use more than 15-fold excess of sodium nitrite towards the concentration of SA and STZ ($C_{reagent} : C_{NaNO_2} = 2.0 \cdot 10^{-4} M : 3.0 \cdot 10^{-3} M = 1 : 15$) when the analyti-

cal signal does not change with the increase in nitrite ions concentration. The excess sodium nitrite towards the SA is explained by the diazotization mechanism, according to which two molecules of nitric acid interact with one aromatic amino group,³⁴ besides, as it is known, the excess of the reagent shifts the reaction equilibrium toward the reaction products.

For obtaining maximal yields of sulphanilamide and sulphathiazole diazonium salts, the effect of time of diazotization was investigated (Fig. 4). The maximal yields of diazonium salts and azo-coupling products with AM have been observed at 20 min of diazotization of reagents at a room temperature. The further increase of diazotization time did not result in any significant increase of azo com-

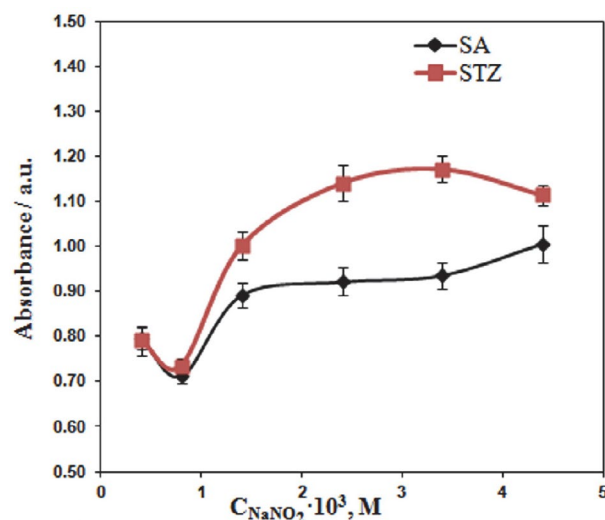


Fig. 3. Effect of sodium nitrite concentration during SA and STZ diazotization on the SA and STZ interaction with AM. 1. $C_{SA} = 2.0 \cdot 10^{-4}$ M, $C_{HCl} = 0.6$ M; 2. $C_{STZ} = 2.0 \cdot 10^{-4}$ M, $C_{HCl} = 0.7$ M; $C_{AM} = 5.0 \cdot 10^{-5}$ M, $C_{Na_2B_4O_7} = 0.1$ M, $n = 5$.

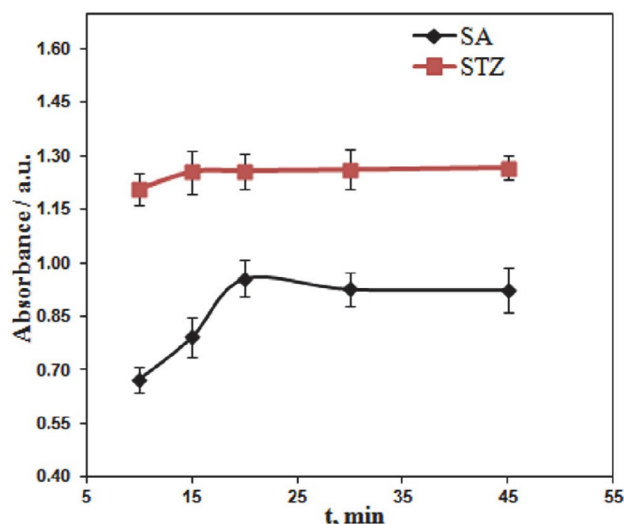


Fig. 4. Effect of time of the SA and STZ diazotization on the yield of the product of their interaction with AM. 1. $C_{SA} = 2.0 \cdot 10^{-4}$ M, $C_{HCl} = 0.6$ M; 2. $C_{STZ} = 2.0 \cdot 10^{-4}$ M, $C_{HCl} = 0.7$ M; $C_{AM} = 5.0 \cdot 10^{-5}$ M, $C_{NaNO_2} = 3.0 \cdot 10^{-3}$ M, $C_{Na_2B_4O_7} = 0.1$ M, $n = 5$.

pounds yield, so all following investigations were carried out at a room temperature while duration of diazotization was 20 min.

3. 3. Azo-Coupling Conditions of AM with SA and STZ Diazonium Salts

3. 3. 1. Effect of pH

According to the literature review, the diazonium cation is a relatively weak electrophile which can exist only in acidic medium and is reactive with a phenolate ion in an alkaline medium rather than with a weakly dissociated molecular form of phenol. Therefore, an azo-coupling re-

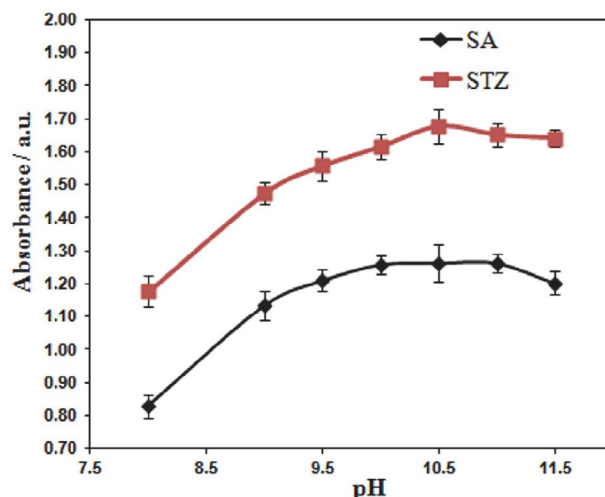


Fig. 5. Effect of medium acidity on SA and STZ diazonium salt azo-coupling with AM. 1. $C_{SA} = 2.0 \cdot 10^{-4}$ M, $C_{HCl} = 0.6$ M; 2. $C_{STZ} = 2.0 \cdot 10^{-4}$ M, $C_{HCl} = 0.7$ M; $C_{NaNO_2} = 3.0 \cdot 10^{-3}$ M, $C_{AM} = 5.0 \cdot 10^{-5}$ M, $C_{Na_2B_4O_7} = 0.1$ M, $n = 5$.

action between diazonium salt and phenolic compounds occurs in an alkaline medium at pH 9–10.³⁴

The influence of acidity on the absorbance of the products of diazotized SA and STZ azo-coupling with amoxicillin were investigated to establish the optimal reaction conditions. As it is shown in Fig. 5, the maximal yield of azo compounds is observed at pH = 10.5, therefore, we used this pH value in the next experiments.

The effect of the nature and concentration of various salts anions on the interaction of AM with the tested reagents has been investigated to study the specificity of the developed methods and the selection of a buffer mixture for stabilization of the conditions of the azo-coupling reaction.

According to the experimental results (Fig. 6), the presence of anions with different nature and concentration

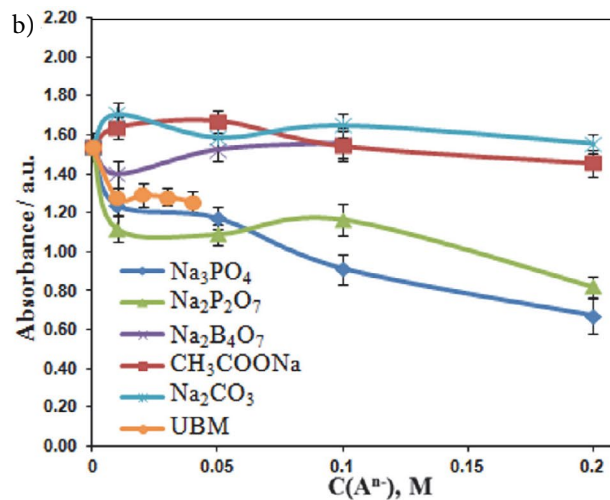
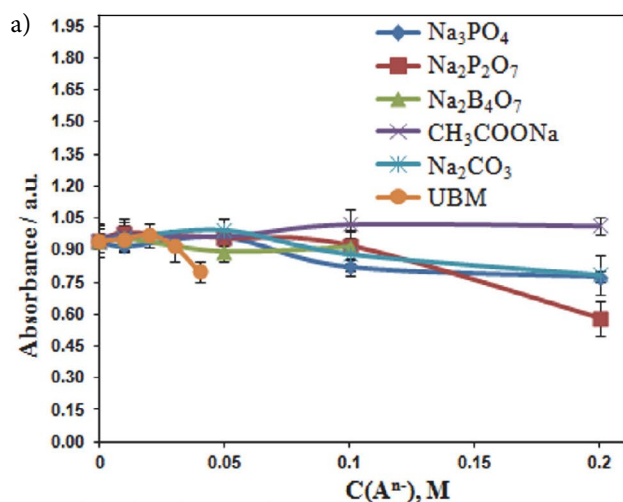


Fig. 6. Influence of nature and concentration of salts anions (acetate, pyrophosphate, carbonate, tetraborate, phosphate) and buffer solution (UBM) on the a) SA and b) STZ interaction with AM. 1. $C_{SA} = 2.0 \cdot 10^{-4}$ M, $C_{HCl} = 0.6$ M; 2. $C_{STZ} = 2.0 \cdot 10^{-4}$ M, $C_{HCl} = 0.7$ M; $C_{NaNO_2} = 3.0 \cdot 10^{-3}$ M, $C_{AM} = 5.0 \cdot 10^{-5}$ M, $n = 5$.

in the solution influence the AM interaction with diazotized reagents. The pyrophosphate and phosphate anions adversely affect the yield of the final product, whereas the use of sodium carbonate slightly increases the analytical signal. The use of sodium tetraborate and universal buffer mixture (UBM: 0.4 M CH_3COOH + 0.4 M H_3PO_4 + 0.4 M H_3BO_3) solutions at low concentrations allows to stabilize the products absorbance. However, the UBM in higher concentration significantly decreases the analytical signal, while sodium tetraborate at low concentrations practically does not affect its value. Therefore, sodium tetraborate with concentration 0.1 M in the final volume has been used as a buffer solution.

3. 3. 2. Effect of SA and STZ Concentration

We investigated the effect of reagents excess on the yield of products of AM azo coupling with SA and STZ dia-

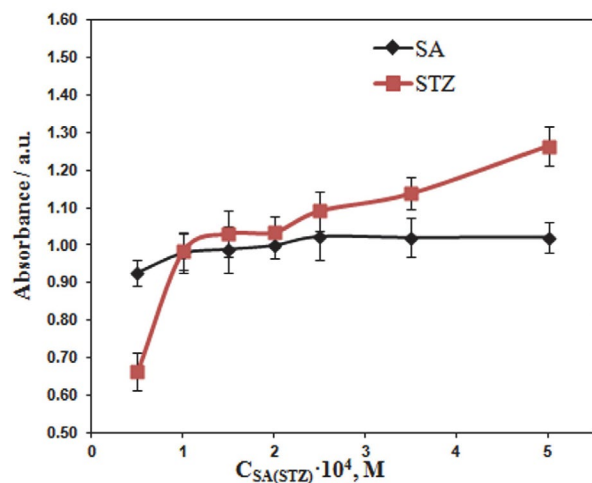


Fig. 7. The mole ratio curve for the product of amoxicillin interaction with SA and STZ diazonium salt. 1. $C_{\text{HCl}} = 0.6 \text{ M}$; 2. $C_{\text{HCl}} = 0.7 \text{ M}$; $C_{\text{AM}} = 5.0 \cdot 10^{-5} \text{ M}$, $C_{\text{HCl}} = 0.6 \text{ M}$, $C_{\text{Na}_2\text{B}_4\text{O}_7} = 0.1 \text{ M}$, $\text{pH} = 10.5$, $n = 5$.

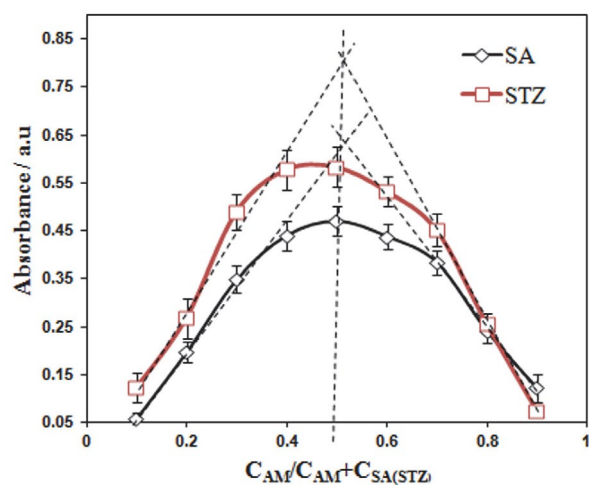


Fig. 8. The method of continuous variations. 1. $C_{\text{SA}} + C_{\text{AM}} = 3.12 \cdot 10^{-4} \text{ M}$, $C_{\text{HCl}} = 0.6 \text{ M}$; 2. $C_{\text{STZ}} + C_{\text{AM}} = 3.12 \cdot 10^{-4} \text{ M}$, $C_{\text{HCl}} = 0.7 \text{ M}$; $C_{\text{NaNO}_2} = 5.6 \cdot 10^{-3} \text{ M}$, $C_{\text{Na}_2\text{B}_4\text{O}_7} = 0.1 \text{ M}$, $\text{pH} = 10.5$, $n = 5$.

zonium salts because certain reagents excess promote a shift of reaction equilibrium toward the formation of reaction products. We found that SA and STZ excess towards AM is required to obtain the maximum yield of the colored analytical forms 5-fold diazotized reagents, while the increase of SA concentrations does not affect the analytical signal (Fig. 7). The experimental results showed a sharp increase in the analytical signal when 10-fold excess of STZ diazonium salts for azo-coupling with AM was used. However, at high concentrations STZ diazonium salts can combine together, therefore, the value of products absorbance also can increase, therefore, the application of a large reagent excess is not required.

The method of continuous variations was used to establish the mole ratio of the components in the compounds of diazotized SA and STZ with amoxicillin (Fig. 8). The stoichiometric SA:AM ratios is equal to 1:1 for both tested sulphanilamides, which indicates the reaction of the azo-coupling of SA and STZ diazonium salts as diazo component with amoxicillin as coupling component to form azo compounds.

The procedure for introducing reagents into the reaction mixture has a significant effect on the yield of colored products. The maximal absorbance of obtained azo compounds is observed if reagents are added in the following sequence. The solution of hydrochloric acid, SA or STZ solution, and sodium nitrite solution are added first. Next, SA diazotization is carried out and only then AM and buffer solutions are added. Finally, the pH of mixture is adjusted to the required value by adding sodium hydroxide solution.

The stability of the analytical form is extremely important for reliable measurement during the assay. Therefore, the stability of absorbance of obtained azo-coupling products of diazotized SA and STZ with amoxicillin was investigated and the results are shown on Fig. 9. The absor-

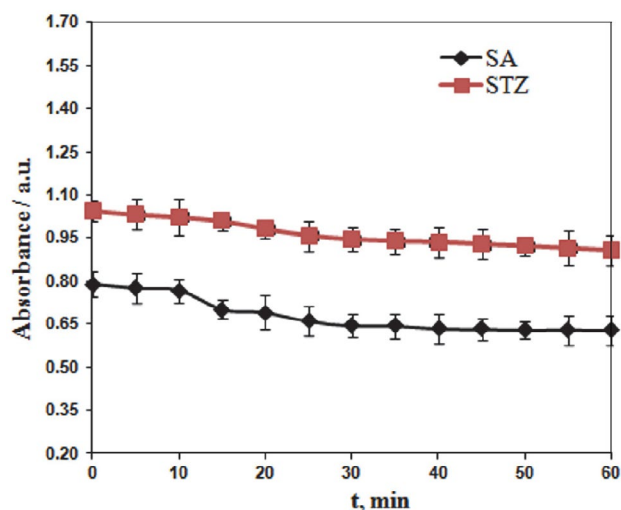


Fig. 9. Effect of the keeping time on the absorbance of azocoupling product of diazotized SA and STZ with AM. 1. $C_{\text{SA}} = 2.0 \cdot 10^{-4} \text{ M}$, $C_{\text{HCl}} = 0.6 \text{ M}$; 2. $C_{\text{STZ}} = 1.9 \cdot 10^{-4} \text{ M}$, $C_{\text{HCl}} = 0.7 \text{ M}$; $C_{\text{NaNO}_2} = 3.0 \cdot 10^{-3} \text{ M}$, $C_{\text{AM}} = 3.75 \cdot 10^{-5} \text{ M}$, $C_{\text{Na}_2\text{B}_4\text{O}_7} = 0.1 \text{ M}$, $\text{pH} = 10.5$, $n = 5$.

bance value of examined azo compounds did not change for 10 min, which is sufficient for the assay (Fig. 9). However, it should be noted that after 20 min the absorbance of solutions of all products slightly decreases, then stabilizes and remains stable for 1 h.

3. 4. Analytical Characteristics of the Developed Method

The new spectrophotometric method of AM determination has been developed based on the optimal condi-

tions of AM interaction with SA and STZ. The absorbance of colored products in systems SA–AM and STZ–AM linearly depends on AM concentration in the solution. Analytical characteristics of AM determination are presented in Table 3.

Characteristics of some available published spectrophotometric methods for the amoxicillin determination are presented in Table 4.

Thus, the elaborated methods for the spectrophotometric determination of amoxicillin with SA and STZ possess wide linear ranges (almost two orders of concentra-

Table 3. Analytical characteristics of the formed azo compound and validation results of AM spectrophotometric determination with SA and STZ. $C_{\text{HCl}} = 0.6 \text{ M}$, $C_{\text{SA}} = 4.5 \cdot 10^{-4} \text{ M}$, $C_{\text{NaNO}_2} = 7.2 \cdot 10^{-3} \text{ M}$, $C_{\text{HCl}} = 0.7 \text{ M}$, $C_{\text{STZ}} = 3.6 \cdot 10^{-4} \text{ M}$, $C_{\text{NaNO}_2} = 5.6 \cdot 10^{-3} \text{ M}$, $C_{\text{Na}_2\text{B}_4\text{O}_7} = 0.1 \text{ M}$, $\text{pH} = 10.5$, $l = 1 \text{ cm}$, $P = 0.95$, $n = 5$.

Parameters/ Characteristics	AM + SA	AM + STZ
λ_{max} , nm	445	448
Stability, h	10	10
Optimum photometric linear range, $\mu\text{g} \times \text{mL}^{-1}$	1.3–32.9	0.7–27.4
Limit of Quantification, $\mu\text{g} \times \text{mL}^{-1}$	1.32	0.76
Limit of Quantification, $\text{M} \times 10^5$	0.36	0.21
Limit of Detection, $\mu\text{g} \times \text{mL}^{-1}$	0.40	0.23
Limit of Detection, $\text{M} \times 10^5$	0.11	0.06
Molar absorptivity, $\epsilon_{\lambda_{\text{max}}} \times 10^{-4}$, $\text{L} \times \text{mol}^{-1} \times \text{cm}^{-1}$	1.74 ± 0.06	1.97 ± 0.05
Regression equation (A) ^a slope (b)	0.059	0.056
Δb	0.006	0.003
Intercept (a)	–0.077	0.043
Δa	0.136	0.034
Correlation coefficient (R)	0.9987	0.9990

^a $A = bC + a$, where C is the concentration of sulphanilamides (SA and STZ) in $\mu\text{g} \times \text{mL}^{-1}$.

Table 4. Spectrophotometric methods for the AM determination using reaction of azo-coupling

Reagent	Reaction conditions	λ_{max} nm	$\epsilon_{\text{max}} \times 10^{-4}$ $\text{L mol}^{-1} \text{ cm}^{-1}$	Limit of detection $\mu\text{g mL}^{-1}$	Linear range, $\mu\text{g mL}^{-1}$
<i>p</i> -aminobenzene acid ²³	$1 \cdot 10^{-3} \text{ M}$ reagent, $1 \cdot 10^{-3} \text{ M}$ NaNO_2 , $1 \text{ M HCl} \rightarrow$ shake	435	1.914	0.1877	0.4–10
procaine ²³	thoroughly \rightarrow AM solution, $2 \text{ M NH}_4\text{OH} \rightarrow$ reaction time 15 min. 10% reagent, 3% NaNO_2 , $1.5 \text{ M HCl} \rightarrow$ reaction time 10 min \rightarrow	450	2.544	0.1916	0.4–14
<i>o</i> -nitroaniline ²⁴	AM solution, $1 \text{ M NaOH} \rightarrow$ reaction time 5 min. AM solution, 0.5 mM diazotized reagent [0.5% reagent, $1 \text{ M HCl} \rightarrow$ reaction time 5 min in ice bath, NaNO_2], $0.5 \text{ M Na}_2\text{CO}_3$, 10% Triton X-114 \rightarrow thermostate (50°C) for 20 min.	435	0.71	0.125	1–5
metaclopramid ²⁵	$2 \cdot 10^{-3} \text{ M}$ reagent, $0.5 \text{ M H}_2\text{SO}_4$, 0.1% $\text{NaNO}_2 \rightarrow$ reaction time 15 min, AM solution \rightarrow reaction time 5 min, triethylamine solution in 40% ethanol \rightarrow reaction time 20 min.	479	23.5	0.083	0.3–3
benzocaine ²⁶	0.5% reagent, 0.2% NaNO_2 , $0.01 \text{ M HCl} \rightarrow$ 455 AM solution, $0.5 \text{ M Na}_2\text{CO}_3$.	455	2.26	0.0156	2–16
sulphanilic acid ²⁷		2.3	0.15	0.3–30	

tion); they are simple, rapid and sensitive. Sensitivity of amoxicillin determination with sulphathiazole is comparable to some sensitive spectrophotometric methods of AM determination (Table 4) and in both cases it is close to most spectrophotometric methods. Our proposed methods do not require the use of an ice bath, the temperature control, or organic solvent and are more rapid when compared to some of the methods presented in Table 4. Additionally, it should be noted that most methods listed in Table 4 were not validated.

3. 5. Analysis of Pharmaceutical Preparations for the AM Content Determination with SA and STZ

Drugs products containing amoxicillin are released in dosage form of tablets and injection solutions. The natural and synthetic excipients are used for obtaining these

dosage forms. The excipients are subdivided into fillers, preservatives, and stabilizers, which usually do not affect the bioactive substances, but may interfere with their determination due to reactions with various reagents. Since a part of amoxicillin dosage forms are combined medicinal products, which besides AM contain other bioactive ingredients, the effect of bioactive substances and common pharmaceutical excipients on the procedure of AM determination by means of SA and STZ was investigated.

Moreover, the selectivity of the developed method was tested for mixtures containing excipients in amounts greatly exceeding their possible content in pharmaceutical preparations. Variability of absorbance value for formed azo compounds SA-AM and STZ-AM in the range $\pm 5\%$ was chosen as the selectivity criterion of AM determination. The research results are presented in Table 5.

The examined excipients and bioactive substance clavulanic acid, which are present in drugs products, do

Table 5. Effect of excipients on the AM assays by SA and STR. $C_{\text{HCl}} = 0.6 \text{ M}$, $C_{\text{SA}} = 4.5 \cdot 10^{-4} \text{ M}$, $C_{\text{NaNO}_2} = 7.2 \cdot 10^{-3} \text{ M}$, $C_{\text{HCl}} = 0.7 \text{ M}$, $C_{\text{STZ}} = 3.6 \cdot 10^{-4} \text{ M}$, $C_{\text{NaNO}_2} = 5.6 \cdot 10^{-3} \text{ M}$, $C_{\text{AM}} = 3.75 \cdot 10^{-5} \text{ M}$, $C_{\text{Na}_2\text{B}_4\text{O}_7} = 0.1 \text{ M}$, $\text{pH} = 10.5$, $l = 1 \text{ cm}$, $P = 0.95$, $n = 5$

Excipient (Exp)	$m(\text{AM}) : m(\text{Exp})^*$	$m(\text{AM}) : m(\text{Exp})^{**}$	SA + AM	STZ+AM
			% Recovery of AM, $\bar{x} \pm S \cdot t_{\alpha} / \sqrt{n}$	% Recovery of AM, $\bar{x} \pm S \cdot t_{\alpha} / \sqrt{n}$
Clavulanic acid	1:0.25	1:0.30	96.4 \pm 2.0	100.6 \pm 1.9
Calcium stearate***	1:0.015	1:10	99.6 \pm 1.9	98.9 \pm 2.1
Povidone***	1:0.03	1:50	100.4 \pm 1.6	100.1 \pm 1.6
Sodium Starch Glycolate Type A***	1:0.47	1:10	96.4 \pm 1.9	97.2 \pm 1.5
Sodium benzoate	1:0.003	1:100	99.5 \pm 1.4	94.5 \pm 1.2
Starch***	1:0.5	1:50	100.4 \pm 1.4	100.1 \pm 2.0
Butylated hydroxytoluene	1:0.007	1:10	95.5 \pm 1.6	97.8 \pm 1.5
Aluminum monostearate***	1:0.1	1:2	99.2 \pm 2.0	99.6 \pm 1.8
Benzyl alcohol	1:0.07	1:0.5	95.4 \pm 2.0	96.4 \pm 2.1
Coconut oil***	1:0.007	1:0.007	94.6 \pm 2.1	94.2 \pm 2.3

*- mass ratios of AM and excipients, which are present in tested drugs products **- maximum mass ratios of AM and excipients examined ***- these substances were insoluble at the experimental conditions. For testing they were pre-mixed with AM and dissolved in 0.1 M hydrochloric acid. Insoluble excipients were filtered from AM extract by the same procedure as for the tablets analysis.

Table 6. Determination of AM in pharmaceuticals. $C_{\text{HCl}} = 0.6 \text{ M}$, $C_{\text{SA}} = 4.5 \cdot 10^{-4} \text{ M}$, $C_{\text{NaNO}_2} = 7.2 \cdot 10^{-3} \text{ M}$, $C_{\text{HCl}} = 0.7 \text{ M}$, $C_{\text{STZ}} = 3.6 \cdot 10^{-4} \text{ M}$, $C_{\text{NaNO}_2} = 5.6 \cdot 10^{-3} \text{ M}$, $C_{\text{Na}_2\text{B}_4\text{O}_7} = 0.1 \text{ M}$, $\text{pH} = 10.5$, $l = 1 \text{ cm}$, $P = 0.95$, $n = 5$

Determined AM (regulated content in preparation)	Amount of found AM $\bar{x} \pm S \cdot t_{\alpha} / \sqrt{n}$ and relative standard deviation (S_r)	
	Spectrophotometric method with SA	Spectrophotometric method with STZ
Amoxicillin (250 \pm 12.5 mg/tab)	"Amoxil" tablets, Corporation "Arterium", JSC "Kyivmedpreparat", Ukraine (excipients – povidone, sodium starch glycolate Type A, calcium stearate)	
	260.4 \pm 1.6 (0.005)	256.4 \pm 4.7 (0.016)
Amoxicillin (500 \pm 25.0 mg/tab)	"Amoksiklav Quicktab" tablets, Sandoz, Lek Pharmaceutical Company D.D., Slovenia (Clavulanic acid (125.5 mg/tab), excipients – aspartame (E 951), iron oxide yellow (E172), talc, cellulose, silicon dioxide)	
	512.5 \pm 8.3 (0.014)	510.3 \pm 5.9 (0.010)

not interfere with the AM determination by the developed method with SA and STZ.

The results of AM determination in these products are given in Table 6. The AM content in tablets “Amoxil” and “Amoksiklav Quicktab” obtained by the developed method using SA and STZ correlates rather well with the content of the AM specified by the manufacturer (with acceptable 5% deviation from regulated content). The high performance liquid chromatography is recommended as an official method for determination of amoxicillin in these drugs products. However, the developed method is much simpler and cheaper. Moreover, it is characterized by high reproducibility and rapidity. The S_r value does not exceed the common values of spectrophotometry errors.

3. 6. Validation Characteristics of the AM Determination in Tablets “Amoxil” Using SA and STZ

Additionally, the validation of the developed methods for amoxicillin determination in tablet “Amoxil”, which contains excipients such as povidone, sodium starch glycolate Type A, and calcium stearate, has been carried out. The following characteristics – the linearity, the accu-

racy, and the precision in the range of 75%–125 % (with SA determination) and 80%–120% (with STZ determination) from the nominal content of AM in the product, and the intermediate precision have been validated according to.^{19,41–43} The results are presented in Tables 7–9.

Calculated validation parameters of AM determination methods in “Amoxil” tablets using sulphanilamide and sulphathiazole satisfied the corresponding criteria, which allows us to suggest that the developed methods are suitable for the quality control of this drug in terms of “Assay”. Although it should be noted that the method of AM determination using SA in tablets “Amoxil” has the better reproducibility, since the calculated value of Δ_{intra} is less than in the case of using STZ.

4. Conclusions

For the first time the formation of azo compounds by the interaction of diazotized sulphanilamide and sulphathiazole with amoxicillin has been established. Optimum conditions for examined sulphanilamides diazotization as well as the following azo-coupling with AM have been investigated. The components ratio in the obtained azo compounds is AM:SA(STZ)=1:1. The azo-coupling occurs due to the phe-

Table 7. The criteria of the linearity, the accuracy, and the precision of AM determination using SA in the preparation of “Amoxil” tablets.

Name of solution	C_p , mg \times mL ⁻¹	$X_i = \frac{C_i}{C_{St}} \cdot 100\%$	A_i	$Y_i = \frac{A_i}{A_{St}} \cdot 100\%$	$D_i = \frac{\text{found}}{\text{added}} \cdot 100\%$
Reference solution	20.00	100.00	1.359	100.00	100.00
No1 (75.0%)	15.05	75.25	1.022	75.20	99.93
No2 (75.0%)	15.05	75.25	1.025	75.42	100.23
No3 (75.0%)	15.05	75.25	1.019	74.98	99.64
No4 (100.0%)	20.01	100.05	1.359	100.00	99.75
No5 (100.0%)	20.01	100.05	1.354	99.63	99.38
No6 (100.0%)	20.01	100.05	1.376	101.25	100.99
No7 (125.0%)	25.15	125.75	1.699	125.02	99.42
No8 (125.0%)	25.15	125.75	1.707	125.60	99.88
No9 (125.0%)	25.15	125.75	1.691	125.42	99.74
		\bar{D}			100.40

Parameters	Criteria of linearity			Conclusion
	Value	Criteria		
b	0.986	–		The first criterion is met
S_b	0.011	–		
a	1.198	1) $\leq 2.064 $ 2) $\leq 2.760 $		
S_a	1.089	–		The criterion is met
R	$ 0.9996 $	$\geq 0.9992 $		

The criteria of the accuracy and the precision			
The relative standard deviation $RSD_0 = 0.489\%$			
Critical values of the one-sided confidence interval, $\Delta x = 0.910\%$		$\Delta x \leq 1.6\%$	Satisfies the requirements
Criterion of the systematic error insignificance, $\delta = 0.12\%$		1. $\delta \leq 0.303\%$ 2. $\delta \leq 0.512\%$	Satisfies the requirements (the first criterion)
The overall conclusion on methods			Is correct

Table 8. The criteria of the linearity, the accuracy, and the precision of AM determination using STZ in the preparation of “Amoxil” tablets.

Name of solution	$C_i, \text{mg} \times \text{mL}^{-1}$	$X_i = \frac{C_i}{C_{St}} \cdot 100\%$	A_i	$Y_i = \frac{A_i}{A_{St}} \cdot 100\%$	$D_i = \frac{\text{found}}{\text{added}} \cdot 100\%$
Reference solution	15.00	100.00	1.246	100.00	100.00
No1 (80.0%)	12.05	80.33	1.021	81.94	81.94
No2 (80.0%)	12.05	80.33	1.015	81.46	81.46
No3 (80.0%)	12.05	80.33	1.019	81.78	81.78
No4 (90.0%)	13.52	90.13	1.119	89.81	89.81
No5 (90.0%)	13.52	90.13	1.122	90.05	90.05
No6 (90.0%)	13.52	90.13	1.125	90.29	90.29
No7 (100.0%)	14.98	99.87	1.246	100.00	100.00
No8 (100.0%)	14.98	99.87	1.240	99.52	99.52
No9 (100.0%)	14.98	99.87	1.242	99.68	99.68
No10 (110.0%)	16.44	109.60	1.353	108.59	108.59
No11 (110.0%)	16.44	109.60	1.381	110.83	110.83
No12 (110.0%)	16.44	109.60	1.362	109.31	109.31
No13 (120.0%)	17.90	119.36	1.471	118.06	118.06
No14 (120.0%)	17.90	119.36	1.482	118.94	118.94
No15 (120.0%)	17.90	119.36	1.475	118.38	118.38
		\bar{D}			100.18

Parameters	Criteria of linearity			Conclusion
	Value	Criteria		
b	0.952	–		The second criterion is met
S_b	0.009	–		
a	4.837	1) $\leq 2.395 $ 2) $\leq 6.072 $		
S_a	0.990	–		The criterion is met
R	$ 0.9993 $	$\geq 0.9973 $		

The criteria of the accuracy and the precision

The relative standard deviation $RSD_0 = 0.667\%$		
Critical values of the one-sided confidence interval, $\Delta x = 1.181\%$	$\Delta x \leq 1.6\%$	Satisfies the requirements
Criterion of the systematic error insignificance, $\delta = 0.18\%$	1. $\delta \leq 0.394\%$ 2. $\delta \leq 0.512\%$	Satisfies the requirements (the first criterion)
The overall conclusion on methods		Is correct

Table 9. Test results of the intermediate precision of AM quantitative determination in “Amoxil” tablets

Analysis No	SA+AM $m_p, \text{mg/tablets}$		STZ+AM $m_p, \text{mg/tablets}$	
	1 st day (experiment 1)	2 nd day (experiment 2)	2 nd day (experiment 2)	1 st day (experiment 1)
1	250.7	250.7	243.7	245.1
2	249.4	245.7	247.8	247.2
3	249.3	245.1	245.8	252.8
4	252.2	248.6	244.8	246.3
5	250.6	249.2	250.4	253.3
average (\bar{m})	250.4	247.9	246.5	248.9
combined average (\bar{m}_{intra})		249.2		247.7
S_m	1.16	2.31	2.67	3.82
$S_{intra}^{44,45}$		1.64		2.31
$\Delta_{intra}^{44,45}$		1.34		1.54

nol group of second component (AM), which has concordantly oriented substituents. The effective molar absorptivi-

ties of obtained azo compounds of amoxicillin with SA and STZ $\epsilon_{445}(\epsilon_{448})$ are $\sim 10^4 \text{ L} \times \text{mol}^{-1} \times \text{cm}^{-1}$. Methods allow to

determine the wide range of AM concentrations (0.7–32.9 $\mu\text{g} \times \text{ml}^{-1}$). Limit of detection for AM determination using SA is 0.40 $\text{mg} \times \text{ml}^{-1}$ and using STZ is 0.23 $\mu\text{g} \times \text{ml}^{-1}$.

The elaborated methods of AM spectrophotometric determination with SA and STZ have been approved during the analysis of single-component and combined commercial pharmaceuticals. Obtained data correlated rather well with the content of the AM specified by the manufacturer. The validation parameters of AM determination in tablets “Amoxil” using SA and STZ clearly indicate the reproducibility ($S_r \leq 0.015$ (SA) or 0.018 (STZ)), the specificity, the robustness, the precision, and the accuracy of both tested methods corresponding to modern requirements of specification.

The proposed method is simple, rapid, sensitive, selective, cost efficient, and competes with most of the spectrophotometric methods available in literature. Therefore, the recommended procedure is well-suited for the assay of drugs to assure high standard of quality control.

5. References

- British Pharmacopoeia (BPh), British Pharmacopoeia Commission, TSO (The Stationery Office), **2019**
- Bird A. E. *Amoxicillin: Analytical Profiles of Drug Substances and Excipients*, G. Brittain – Surrey: Academic Press, **1994**, 23, P.1–52. DOI:10.1016/S0099-5428(08)60599-7
- Belikov V. G. *Pharmaceutical Chemistry: Textbook. 2nd Edition*, MED Press Inform, Moscow, Russia, **2007**, p. 624.
- A.P. Arzamastsev *Pharmaceutical and Toxicological Chemistry*, GEOTAR-MED, Moscow, Russia, **2004**, p. 640.
- M. N. Uddin, S. Das, S. H. Khan, *J. Taibah Univ. Sci.*, **2016**, 10, p. 755–765. DOI:10.1016/j.jtusc.2015.11.005
- S.M. Sabry, M.H. Abdel-Hay, T.S. Belal, A. A. Mahgoub, *Ann Pharm Fr.*, **2015**, 73, p. 351–360. DOI:10.1016/j.pharma.2015.04.008
- H. Li, X. Xia, Y. Xue, S Tang, X Xiao, J Li, J Shen, *J. Chromatogr. B* **2012**, 900, p. 59–63. DOI:10.1016/j.jchromb.2012.05.031
- Ch. Liua, H. Wangb, Y. Jiangb, Z. Du, *J. Chromatogr. B.*, **2011**, 879, p. 533–540. DOI:10.1016/j.jchromb.2011.01.016
- S. M. Foroutan, A. Zarghib, Al. Shafaatib A. Khoddam, H. Movahed, *J. Pharm. Biomed. Anal.*, **2007**, 45, p. 531–534. DOI:10.1016/j.jpba.2007.06.019
- M. Dhoka, V. Gawande, Pr. Joshi, *J. Pharm. Pharm. Sci.*, **2010**, 2, p. 129–133.
- R. V. Rele, and Pr. P. Tiwatane, *Res. J. Recent Sci.*, **2018**, 7, p. 8–13.
- B. Wang M. Pang, X. Xie M. Zhao, *Food Anal. Methods*, **2017**, 10 p. 1–14. DOI:10.1007/s12161-017-0900-8
- H. Karimi-Maleh, F. Tahernejad-Javazmi, V. K. Gupta H. Ahmar, *J. Mol. Liq.* **2014**, 196, p. 258–263. DOI:10.1016/j.molliq.2014.03.049
- A. Pollap, P. Knihnicki, P. Kustrowski, J. Kozak, M. Golda-Cepa, A. Kotarba, J. Kochana, *Electroanalysis*, **2018**, 30, p. 2386–2396. DOI:10.1002/elan.201800203
- R. Ojani, J.-B. Raoof, S. Zamani, *Bioelectrochem.*, **2012**, 85, p. 44–49. DOI:10.1016/j.bioelechem.2011.11.010
- G. Yanga, F. Zhao, *Electrochim. Acta.*, **2015**, 174, p. 33–40. DOI:10.1016/j.electacta.2015.05.156
- B. Norouzi, T. Mirkazemi, *Russ. J. Electrochem.*, **2016**, 52, p. 37–45. DOI:10.1134/S1023193516010067
- Gh. Absalan, M. Akhond, H. Ershadifar, *J. Solid State Electrochem.*, **2015**, 19, p. 2491–2499. DOI:10.1007/s10008-015-2894-8
- United States Pharmacopoeia, USP 41–NF 36 (Convention Inc., Rockville, MD XXVI), **2017**
- S. M. Sinaga, F. Arinawati, M. Bachri, *Int. J. Pharmtech. Res.*, **2016**, 9, p. 79–89.
- R.V. Rele, *Res. J. Pharm. Sci.*, **2017**, 6, P. 1–5.
- R. V. Rele, *Der Pharmacia Lett.*, **2016**, 8, p. 191–196.
- W. A. Al-Uzri, *Iraqi J. Sci.*, **2012**, 53, p. 713–722.
- H. Salem, *Anal. Chim. Acta.*, **2004**, 515, p. 333–341. DOI:10.1016/j.aca.2004.03.056
- Z. A-A. Khammas, H. M. Abdulkareem, *Sci. J. Anal. Chem.*, **2016**, 4, p. 66–76. DOI:10.11648/j.sjac.20160405.12
- S. M. El-Ashry, F. Belal, M. M. El-Kerdawy, D. R. El Wasseef, *Mikrochim. Acta* **2000**, 135, p. 191–196. DOI:10.1007/s006040070010
- H. A. Qader, N. A. Fakhri, *Ibn Al-Haitham Jour. for Pure & Appl. Sci.*, **2015**, 28, p. 142–153.
- G. G. Mohamed, *J Pharm. Biomed. Anal.*, **2001**, 24, P, 561–567. DOI:10.1016/S0731-7085(00)00463-5
- P. B. Issopoulos, *J Pharm. Biomed. Anal.*, **1988**, 6, p. 321–327. DOI:10.1016/0731-7085(88)80060-8
- M. Smolinska, O. Korkuna, I. Kotsyumbas, T. Vrublevska, G. Teslyar, *Methods and objects of chemical analysis*, **2016**, 11, p. 51–81.
- M. Boiko, T. Vrublevska, O. Korkuna, G. Teslyar, *Spectrochim. Acta A*, **2011**, 79A, 325–331. DOI:10.1016/j.saa.2011.02.036
- M. Boiko, T. Vrublevska, O. Korkuna, I. Kotsyumbas, G. Teslyar. *Voprosy Khimii i Khimicheskoi Tekhnologii*, **2012**, 2, 116–126.
- M. Smolinska, O. Korkuna, P. Rydchuk, T. Vrublevska, G. Teslyar. *Open Chem.*, **2015**, 13, 1254–1268. DOI:10.1515/chem-2015-0139
- H. Zollinger, *Chemistry of Azo Dyes*, Goskhimizdat, Leningrad, 1960. (in Russian).
- A. F. Minka, A. F. Shkadova, I. I. Kopychuk, *Farm. Zhurn.*, **1987**, 1, 38.
- A. Calvin Bratton, E.K. Marshall, *J. Biol. Chem.*, **1939**, 128, p. 537–550.
- P. Nagaraja, H. S. Yathirajan, C. R. Raju, R. A. Vasantha, P. Nagendra, M. S. Hemantha Kumar, *Il Farmaco*, **2003**, 58, p. 1295–1300. DOI:10.1016/S0014-827X(03)00093-4
- G. Vijaya Raja, C. Bala Sekaran, P. Siva Kumari, S. K. Parveen, P.V.S. Mahesh, *Oriental J. Chem.*, **2008**, 24, p. 1021–1024.
- P. Nagaraja, K. R. Sunitha, R. A. Vasantha, H. S. Yathirajan, *Eur. J. Pharm. Biopharm.*, **2002**, 53, p. 187–192. DOI:10.1016/S0939-6411(01)00235-1

40. S. M. Sabry, *Anal. Lett.* **2006**, 39, p. 2591–2615.
DOI:10.1080/00032710600824748
41. European Pharmacopoeia (Eur. Ph.). 9-th Ed. (Strasbourg: Council of Europe, 2017)
42. State Pharmacopoeia of Ukraine Add.2 (State Enterprise “Scientific-Expert Pharmacopoeial Centre.” Kharkiv: Rieger, 2008) (in Ukrainian)
43. Note for guidance on validation of analytical procedures: text and methodology (CPMP/ICH/381/95)
44. A. I. Gryzodub, *Farmacom*, **2002**, 3, p. 42. (in Russian)
45. A. I. Gryzodub, N. Zvolynskaya, N. Arkhipova, D.A. Leont’ev et al. *Farmacom*, **2004**, 2, 20. (in Russian)

Povzetek

Opisana je hitra, preprosta in občutljiva spektrofotometrijska metoda za določanje amoksicilina (AM). Metoda je osnovana na začetni diazotizaciji sulfanilamida (SA) in sulfatiazola (STZ) v mediju 0,6–0,7 M klorovodikove kisline ter njuni nadaljnji interakciji z amoksicilinom pri pH 10,5, pri čemer nastaneta rumeno obarvani azo spojini. Efektivna molarna absorptivnost za azo spojine pri absorpcijskem maksimumu 445 nm (SA) je bila $(1,74 \pm 0,06) \cdot 10^4 \text{ L} \times \text{mol}^{-1} \times \text{cm}^{-1}$ in pri 448 nm (STZ) $(1,97 \pm 0,05) \cdot 10^4 \text{ L} \times \text{mol}^{-1} \times \text{cm}^{-1}$. Stehiometrijsko razmerje med obema komponentama azo spojin smo določili z metodo kontinuirne variacije. Pri optimalnih reakcijskih pogojih smo razvili dve novi metodi. Ti dve metodi omogočata določitev amoksicilina v koncentracijskem območju $1,3\text{--}32,9 \mu\text{g} \times \text{mL}^{-1}$ s sulfanilamidom in $0,7\text{--}27,4 \mu\text{g} \times \mu\text{L}^{-1}$ s sulfatiazolom. Metodi smo uspešno validirali za določevanje amoksicilina v tabletah »Amoxil«.



Except when otherwise noted, articles in this journal are published under the terms and conditions of the Creative Commons Attribution 4.0 International License

Scientific paper

Adsorption Behavior of Fe(II) and Fe(III) Ions on Polyaniline Coated Sawdust: Batch and Fixed-Bed Studies

Seyed Jamaledin Mansoor¹ and Fatemeh Abbasitabar^{2,*}¹ Department of Chemistry, Mahshahr Branch, Islamic Azad University, Mahshahr, Iran² Department of Chemistry, Marvdasht Branch, Islamic Azad University, Marvdasht, Iran* Corresponding author: E-mail: fabbasitabar@gmail.com & fabbasitabar@miau.ac.ir
Tel & Fax: +98-37328581

Received: 03-09-2019

Abstract

The aim of this study is to investigate the suitability of polyaniline coated-sawdust (SD/PAni) as an adsorbent for removal of Fe(II) and/or Fe(III) ions from aqueous solutions. The study includes batch and column tests. With column experiments, the influence of different experimental parameters on the adsorption behavior of Fe(II), Fe(III), and a mixture of both ions were studied and it was found that the optimum adsorption conditions for individual iron species and a mixture of them were similar. The optimal values for pH, flow rate, temperature, and adsorbent mesh size were found to be 4.0, 5.0 mL min⁻¹, 25 °C, and 100 BSS mesh, respectively. Batch experiments were carried out to study the adsorption isotherms at ambient temperature. The results demonstrated that the adsorption isotherms for both iron species were best represented by the multilayer adsorption isotherm model. The adsorption-desorption stability performance of the adsorbent was evaluated and confirmed over 5 cycles.

Keywords: Langmuir; Freundlich; Temkin; Multilayer isotherm; Decoration with polyaniline; Solid phase extraction; Continuous adsorption.

1. Introduction

Water pollution by heavy metals remains a serious environmental problem. Their accumulation in numerous plant and animal organisms occurs easily. Hence, one of the most widely researched topics in environmental science which requires extensive study is the removal of heavy metals from aqueous solutions.¹ Iron is a nutrient element required by living cells.^{2,3} Estimates of the minimum daily requirement for iron depend on sex, age, physiological status, and iron bioavailability, and is approximately 10 to 50 mg/day.⁴ Presence of high levels of iron in drinking water is associated with some problems such as bad taste, discoloration, and high turbidity. World Health Organization (WHO) recommends that the iron concentration in drinking water should be less than 0.3 mg L⁻¹.^{5,6} In anaerobic groundwaters, concentration of iron(II) is usually in the range of 0.5–10 mg L⁻¹, but concentrations up to 50 mg L⁻¹ are also reported. The median iron concentration in rivers has been found to be 0.7 mg L⁻¹.⁷ In countries where water is distributed through galvanized iron pipes concentration of iron may be higher than the normal level.⁵ Thus, removal of iron species from aqueous

media to allowable global limits is essential and has led to an increasing interest in developing efficient methods for this purpose.^{8–11}

In recent investigations, adsorption is being extensively employed for separation of metal ions¹² and elaborate efforts have been continued to find an effective and economic adsorbent. Agricultural wastes like corn stalk, rice waste, peanut, straw, sawdust, and sugarcane bagasse have been proved to be low-cost and most efficient adsorbents in this respect.^{13–15} Sawdust was used as an adsorbent in this study. The cell walls of sawdust principally contain cellulose, lignin, and many hydroxyl groups which all are confirmed to have ion exchange capacities.¹⁶ This feature, together with its abundant availability almost free of charge, makes sawdust most suitable for uptake of heavy metal ions or cationic dyes from aqueous solutions.^{17–21} Modification of sawdust using other materials is also considered by some researchers to improve its sorption performance.²² On the other hand, polymers have gained great importance in environmental applications owing to their easy handling, efficiency, and selectivity.²³ Among them is polyaniline which has been used as metal ions adsorbent.^{24–26} Moreover, polyaniline is a suitable candidate polymer for coating of natu-

ral fibers regarding to its flexibility, low cost, and environmentally safe characteristics.^{27,28} The present research was conducted to study the ability of polyaniline-coated sawdust (SD/PAni) for the removal of Fe(II) and/or Fe(III) ions from aqueous solutions. To the best of our knowledge, no reports are available on the application of SD/PAni as adsorbent for iron species. The removal experiments were carried out in a fixed-bed column to study and optimize the operational conditions including pH, temperature, flow rate, and particle size of adsorbent. The possible mechanism of adsorption was also examined in a batch mode through different isotherm models.

2. Experimental

2.1. Chemical Reagents

Aniline was purchased from Merck and distilled twice before use. Ammonium persulfate was ACS grade ($\geq 98\%$) and used as received. The stock solutions (1000 mg L^{-1}) of Fe(II) and Fe(III) were prepared from Merck Titrasol standard solutions in 15% HCl. Working standard solutions were then prepared daily by stepwise dilution of the stock solutions. Other chemicals used in this work were all of analytical reagent grade and prepared in distilled water. pH adjustment was performed using NaOH and HCl solutions. Ammonium acetate buffer solution was prepared by dissolving 38.54 g ammonium acetate in 150 mL distilled water, adding 28.6 mL acetic acid and diluting to 1.0 L with distilled water. Sawdust was obtained from a local carpentry workshop. All vessels used for analysis were kept in dilute nitric acid at least overnight and subsequently washed three times with distilled water.

2.2. Apparatus

Absorbance measurements at 510 nm were performed by spectrophotometer (Perkin Elmer Lambda 25) with a 1.0 cm glass cell. A Metrohm pH meter (model 691) with a combined double junction glass electrode, calibrated against two standard buffer solutions at pH 4.0 and 7.0, was used for pH measurements. Oxford instrument was used to record scanning electron microscopy (SEM) measurements. Perkin Elmer equipment was employed for FTIR recording. TGA curves were recorded on a STA 1500 (Model Rheometric scientific) at the maximum $800 \text{ }^\circ\text{C}$. The specific surface areas of the sawdust and SD/PAni were quantified with the Brunauer, Emmitt and Teller (BET) method from the N_2 adsorption/desorption isotherms with a Quantachrome BET instrument (Quantachrome Corporation, USA).

2.3. Preparation of Sawdust

The raw sawdust obtained from a carpentry workshop was soaked in distilled water for 8 h, followed by rins-

ing with 0.1 mol L^{-1} hydrochloric acid and then with 0.1 mol L^{-1} sodium hydroxide. After that it was thoroughly rinsed with distilled water until the washings showed neutral on litmus paper. To exclude unbound organic materials, the sawdust was washed with 300 mL of acetone and then with 300 mL of methanol. It was then dried at $105 \text{ }^\circ\text{C}$, ground, and sieved to various mesh sizes (100, 60, 40, and 25 BSS mesh).

2.4. Synthesis of Polyaniline Polymer

Polyaniline was prepared by the following procedure.²⁹ 5.0 g freshly distilled aniline was dissolved in 250 mL of 1.0 mol L^{-1} HCl. The solution was placed in an ice bath to cool for 20 min. 250 mL of precooled 0.3 mol L^{-1} ammonium persulfate solution in HCl 1.0 mol L^{-1} was slowly added to the above solution under vigorous stirring. The reaction was then allowed to continue overnight at room temperature without stirring. The dark blue polymer formed was filtered and washed with distilled water and dilute HCl solution until the filtrate became colorless, followed by thorough rinsing with methanol and distilled water. The product was dried ($50\text{--}60 \text{ }^\circ\text{C}$), powdered, and stored for processing.

2.5. Preparation of Polyaniline Coated Sawdust (SD/PAni)

To make PAni soluble in formic acid for coating, it was converted to emeraldine base (EB) form by treating with 0.5 mol L^{-1} NaOH solution for 2 h.³⁰ Following the washing with distilled water, it was dried at $60 \text{ }^\circ\text{C}$. 0.50 g of the as-prepared EB powder was dissolved in 50 mL of formic acid. Undissolved solids were separated by filtration. To prepare polyaniline-coated sawdust (SD/PAni), 5.0 g sawdust with specified mesh size was mixed with 50 mL EB solution ($1\% \text{ w/v}$) and stirred for 2 h at room temperature. It was then kept at room temperature for another 2 h without stirring. After filtration, it was dried at $\sim 60 \text{ }^\circ\text{C}$ to remove residual solvent.³¹

2.6. Fixed-Bed Column Adsorption Experiments

For fixed-bed experiments, 10.0 mg of SD/PAni was packed in a burette column (15 cm length) by keeping glass wool at top and bottom. In order to eliminate dissolvable colored materials in SD/PAni column, it was washed with 100 mL of 5% acetone and then with 0.2 mol L^{-1} sodium hydroxide until the exiting liquid became colorless. The column was then rinsed with distilled water. 50.0 mL of a solution containing Fe(II) and/or Fe(III) with concentration of 20 mg L^{-1} was applied to the column using peristaltic pump at specified flow rate under the optimized conditions. The effluent exiting the column was collected and analyzed for the residual analyte(s) by colorimetric

o-phenanthroline method (3500–Fe iron).³² In the case of Fe(II), 2.5 mL of 1,10-*ortho*-phenanthroline 0.1% (*w/v*) together with 10.0 mL buffer was added to the effluent sample and the absorbance was measured at 510 nm after 10 min.

To evaluate total iron content via the above procedure, reduction of ferric form to the ferrous state is required before the addition of *o*-phenanthroline. Therefore, when ferric ions were present in the effluent sample, reduction to the lower oxidation form was performed by the addition of 2.0 mL hydroxylamine 10% (*w/v*) and 1.0 mL concentrated hydrochloric acid, followed by heating to boiling to ensure a complete conversion. After cooling, it was treated with 2.5 mL of 1,10-*ortho*-phenanthroline 0.1% (*w/v*) and 10.0 mL buffer solution and then the absorbance was measured at 510 nm. Fe(III) could be determined as the difference between total iron and Fe(II). All the absorbance measurements were performed in triplicate. Removal percent and capacity of adsorbent (*q*) were calculated using the following equations:

$$\text{Removal \%} = \frac{(C_0 - C_e)}{C_0} \times 100 \quad (1)$$

$$q = \frac{(C_0 - C_e)V}{m} \quad (2)$$

where C_0 and C_e are the initial and equilibrium concentrations of analyte ion in mg L^{-1} , m and V are mass of adsorbent (g) and volume of the influent (L), respectively.

3. Results and Discussion

In this paper, the potential of polyaniline-coated sawdust as an adsorbent for removal of individual iron species from aqueous solution was investigated through batch and column studies. Simultaneous uptake of ferrous and ferric ions was also examined. Polyaniline was synthesized via an oxidative polymerization approach and then coated on sawdust. The sorbent was characterized by SEM, TGA, and FTIR analysis. The appropriate extraction conditions were estimated by investigating the effect of different parameters by the one-factor-at-a-time approach.

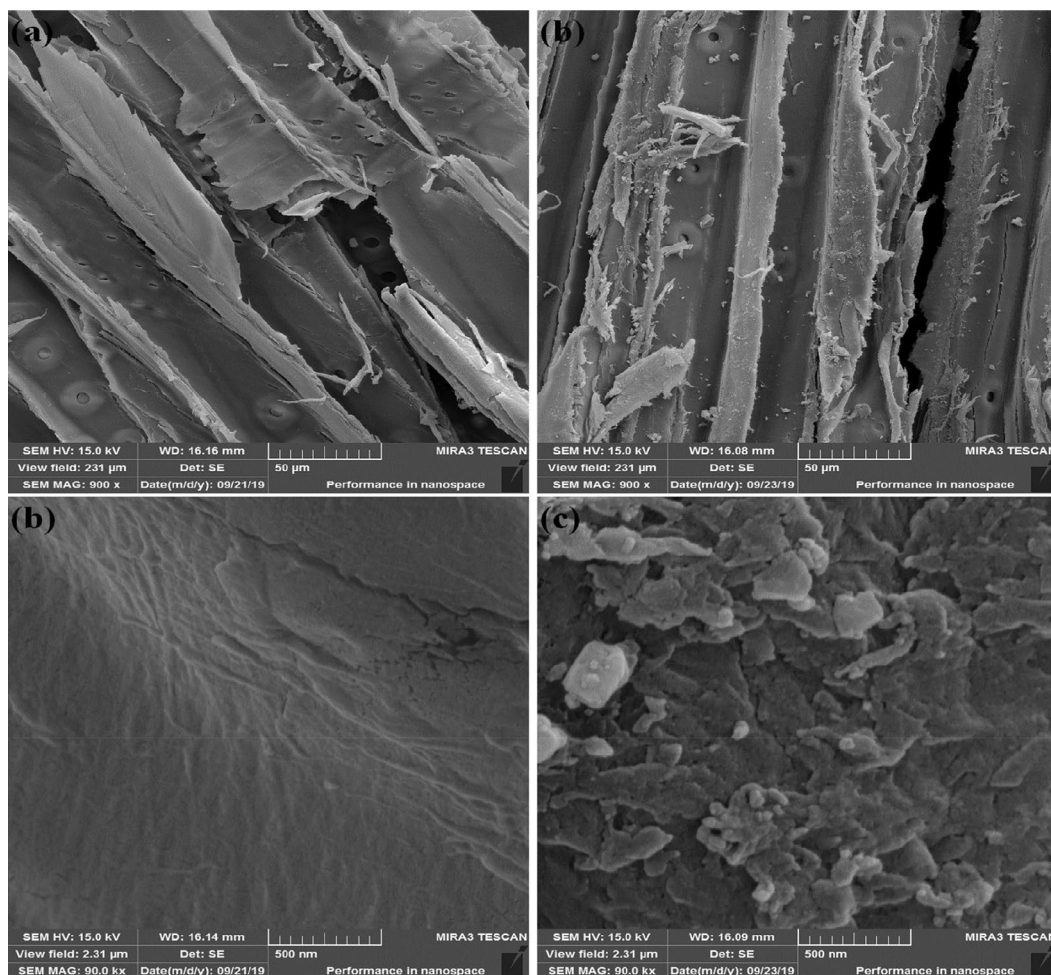


Fig. 1. SEM images of sawdust (a & c) and SD/Pani (b & d).

3. 1. Adsorbent Characterization

SEM measurements of the raw sawdust and SD/PAni are given in Fig. 1. Comparing Figures 1a and 1c with Figures 1b and 1d showed that PAni particles were successfully decorated on the surface of sawdust. Moreover Figures 1b and 1d confirmed that PAni nanoparticles exhibited more or less homogenous shape.

FTIR analysis was carried out to study the surface properties of the raw sawdust and SD/PAni. Fig. 2 shows a broad band at 3287 cm^{-1} for the raw sawdust. This band is related to $-\text{OH}$ stretching vibration. The peak at 2358 cm^{-1} in the same material is stretching vibrations of $\text{N}-\text{H}$ or $\text{C}=\text{O}$ groups probably due to amines and ketones.³³ In the spectrum of SD/PAni, some additional peaks appear, confirming decoration of sawdust with polyaniline. The $\text{N}-\text{H}$ symmetric stretching of polyaniline appears at 3394 cm^{-1} .³⁴ The FTIR spectra of SD/PAni also shows the characteristic peak of nitrogen quinone at 1509 cm^{-1} ,³⁵ and bands appear at 1431 , 1378 , and 1058 cm^{-1} , which correspond to a benzene ring, $\text{C}-\text{N}$ and $\text{C}=\text{N}$ stretching vibrations.³⁶ The peak at 794 cm^{-1} belongs to $\text{C}-\text{H}$ of the polyaniline ring.³⁷

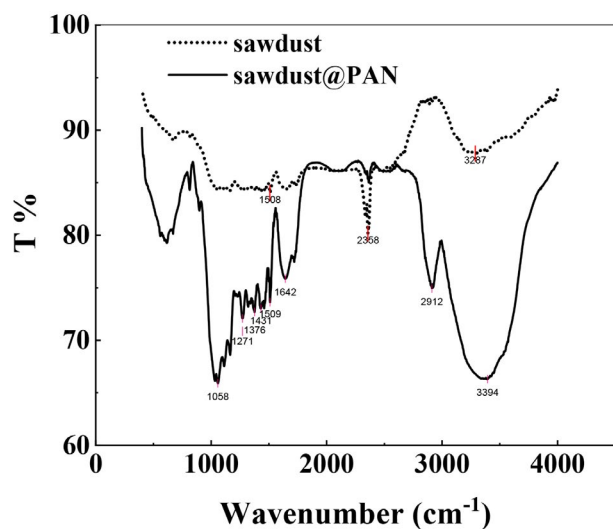


Fig. 2. FTIR spectra of raw sawdust (dot plot) and modified sawdust with polyaniline (solid plot).

The TGA results for the sawdust and SD/PAni presented in Fig. 3 reveal two main steps of weight loss for both adsorbents. The first stage of weight loss for both adsorbents was observed from the beginning of the experiment until the temperature reached about $90\text{ }^{\circ}\text{C}$. This weight loss of around 10% (w/w) was attributed to the loss of physically adsorbed water. The second step occurred between 220 and $400\text{ }^{\circ}\text{C}$, again for both of the adsorbents. This step in the case of raw sawdust was assigned to the transformation of lignin, cellulose, and hemicellulose to gaseous materials and tars.³⁸ For the sawdust decorated with polyaniline, these processes were accompanied with

the production of the facile thermal decomposition of the loaded polyaniline from the surface and, therefore, the weight loss was exacerbated.³⁹ It was also found from TGA results that the surface of sawdust was decorated by PAni with about 5% coating. The specific surface areas for sawdust and SD/PAni were measured using BET surface area analyzer. The values for the specific surface areas and pore diameters for both adsorbents were the same and found to be $0.88\text{ m}^2\text{ g}^{-1}$ and 18.00 nm , respectively.

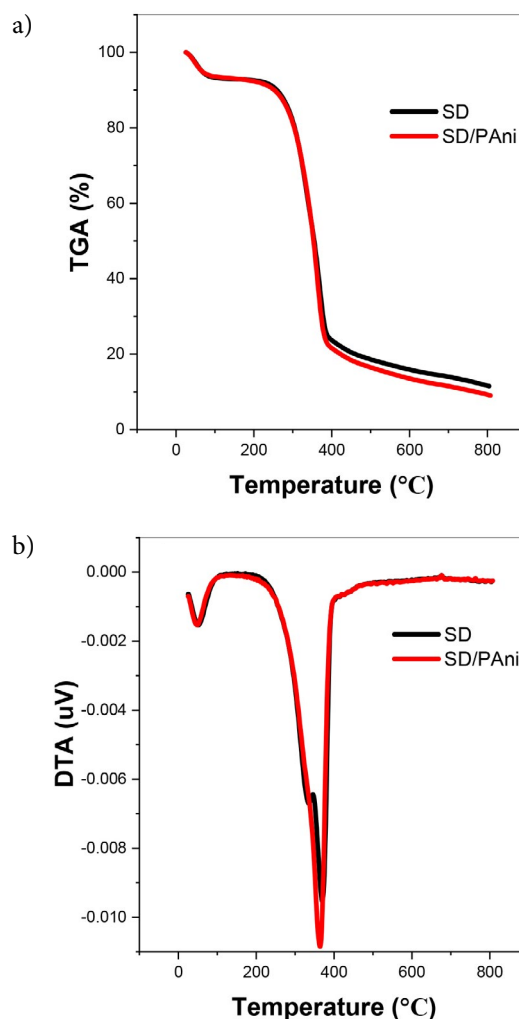


Fig. 3. TGA (a) and DTA (b) curves of sawdust and SD/PAni.

3. 2. Effect of Adsorbent Mesh Size and pH

It is well known that some of the adsorbent properties like its structure, size, and surface chemistry have effect on the adsorption efficiency.⁴⁰ So, the studies were conducted to determine which mesh size of sawdust was suitable to use in the adsorbent preparation step. Fig. 4a depicts the effects of pH and adsorbent mesh size on the removal efficiency. As it is evident, the larger the mesh size of sawdust used for the adsorbent preparation, the

better the adsorption efficiency. This can be contributed to the availability of a larger surface area, providing more adsorption sites which facilitate the adsorption of iron ions.

Another important factor affecting the adsorption process is pH of the sample solution.⁴¹ The effect of pH in the range of 1–4 is depicted in Fig. 4a as well. Higher pH values were not considered due to hydroxide formation of iron ions. In the case of ferrous state, it should be pointed out that iron in the ferrous state can only remain in solution in the absence of oxygen, and generally in acidic media.⁴² Several papers considered only acidic media to prevent the hydroxide formation.^{43,44}

In the present study, optimum pH value was found to be 4.0 for both iron species. At lower pH value, the hydrogen ions compete with the metal ions for the binding sites of the adsorbent. Moreover the protonation of the nitrogen atoms in polyaniline occurred in

acidic solutions.⁴⁵ Consequently, the surface of adsorbent was positive in the highly acidic media and adsorption of the iron ions was suppressed due to the electrostatic repulsion. However, deprotonation of the nitrogen atoms occurs as the pH increases (3–4), leading to the formation of active sites in the adsorbent. Therefore, our further studies were done at pH 4.0. It is worthy to note that the extent of competition of Fe(III) with Fe(II) for the adsorption sites on SD/PAni was also explored. To do this, a solution of mixture of ferric and ferrous ions with initial concentration of 10 mg L^{-1} for each one was passed through the column. Fig. 4b shows that at lower pH values, the extent of competition between iron species was high. However, at optimum pH value, no significant competition might take place. This is mainly due to high adsorption capacity of SD/PAni towards ferrous and ferric ions at $\text{pH} = 4.0$, providing more active sites for the adsorption of the analytes.

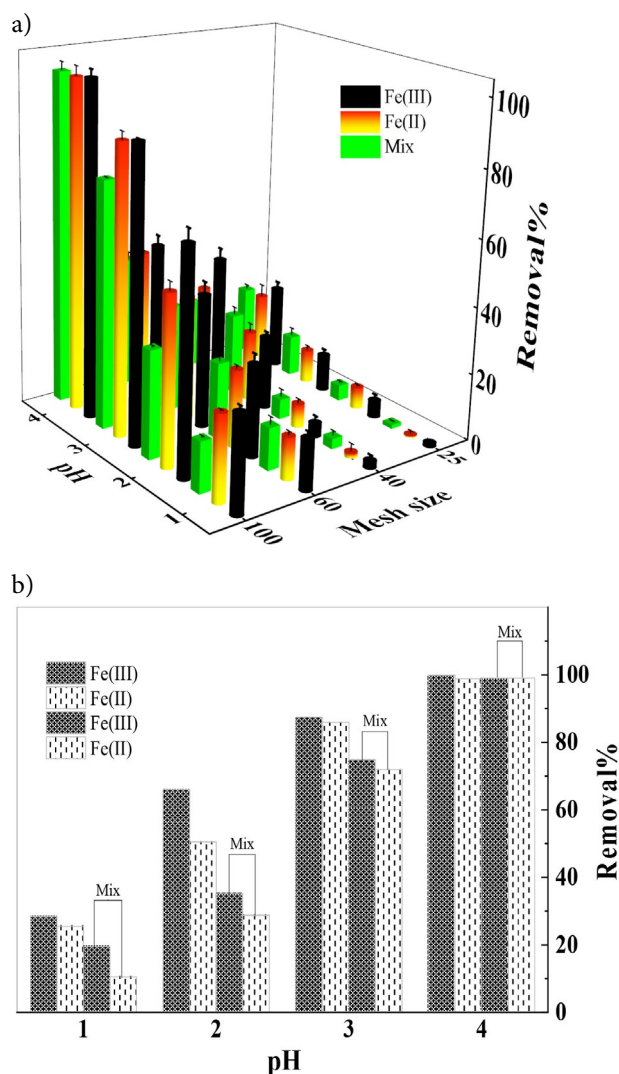


Fig. 4. a) Effect of pH and mesh size on the adsorption of Fe(III) and/or Fe(II); b) pH effect for adsorbent with mesh size of 100. Conditions: $T = 25 \text{ }^\circ\text{C}$; flow rate = 5.0 mL min^{-1} .

3. 3. Effect of Flow Rate

As the adsorption is a time dependent process, the effect of flow rate on the adsorption of iron species was examined at pH 4.0 by passing the influent through packed column at various flow rates. Fig. 5 shows that as flow rate is increased, the adsorption of iron species on SD/PAni decreases. At lower flow rates, there is sufficient contact time between the analyte(s) and the adsorbent and, consequently, the adsorption is brought to completion. In other words, by increasing flow rate the adsorbent has not sufficient time to totally adsorb the analyte(s) well and, as a result, the unretained metal ions leave the column before equilibrium is achieved. Hence, flow rate of 5.0 mL min^{-1} was selected as the best and used in the next experiments. It also can be seen from Fig. 5 that the competition of Fe(I-II) with Fe(II) for the adsorbent is promoted at higher flow rates. Adsorption of Fe(III) becomes most preferable by increasing flow rate.

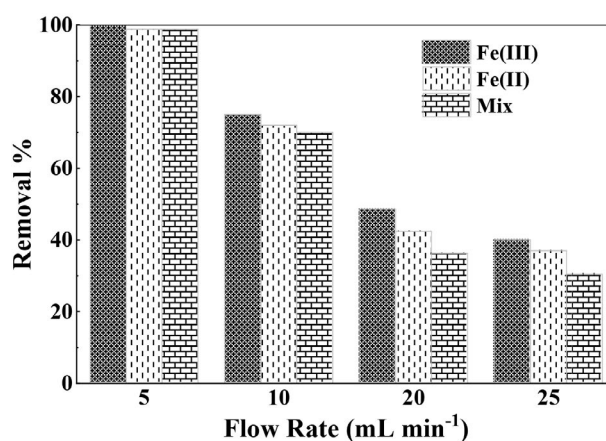


Fig. 5. Effect of flow rate on the adsorption of Fe(III) and/or Fe(II). Conditions: $\text{pH} = 4.0$; $T = 25 \text{ }^\circ\text{C}$; mesh particle size = 100 BSS mesh.

3. 4. Effect of Temperature

The dependence of analytes adsorption on temperature was investigated in the range of 10–75 °C. In accordance to the data shown in Fig. 6, the adsorption increases slightly by increasing in temperature up to 25 °C and then stays at a constant value in the range of 30–55 °C. After that the amounts of removal for both analytes start to decrease, mostly pertaining to the fact that at higher temperature the analyte ions gain more kinetic energy which enables the analytes to overcome the adsorption potential.⁴⁶ Hence, all experiments were performed at ambient temperature. The results in Fig. 6 indicate that ferric ions are favorably adsorbed by SD/PAni at higher temperatures where the experimental conditions are far from optimum.

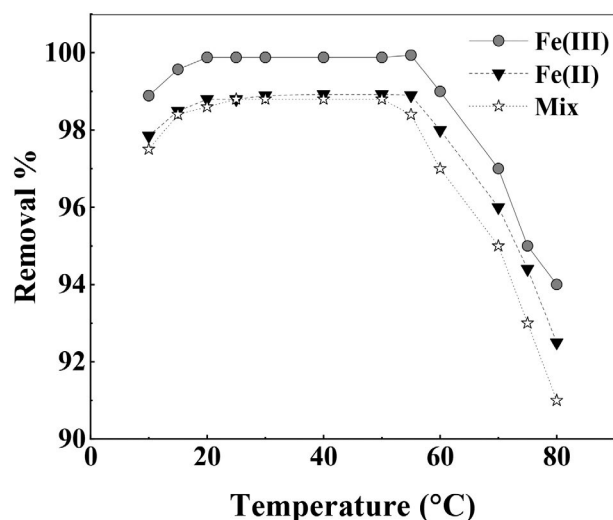


Fig. 6. Effect of temperature on the adsorption Fe(III) and/or Fe(II). Conditions: flow rate = 5.0 mL min⁻¹; pH = 4.0; particle size = 100 BSS mesh.

3. 5. Adsorption Isotherms

Isotherm models are useful to explain the adsorption mechanism and estimate the adsorption capacity of the adsorbent. In other words, the adsorption isotherms explain the relation between the amount of solute adsorbed per unit mass of adsorbent and the amount of the unadsorbed adsorbate at the equilibrium time.⁴⁷

Isotherm experiments were carried out in batch operation by the following procedure: to aliquots of 100 mL solutions of Fe(II)/Fe(III) with initial concentrations ranging from 1 to 7 mg L⁻¹ (pH = 4.0), 10.0 mg SD/PAni was added and the mixture was stirred for 10 min. It should be noted that the adsorption reaches the equilibrium within 10 min. After that, the solution was filtered and residual iron ions was determined. The results are depicted in Fig. 7.

Langmuir adsorption model assumes that adsorption occurs at homogenous monolayer active site of the adsorbent. It also describes that all the adsorption sites have uniform energy and the adsorption takes place at structurally similar sites.⁴⁸ The linearized form of Langmuir adsorption isotherm is given in Eq. 3.

$$\frac{1}{q_e} = \frac{1}{q_m} + \left(\frac{1}{q_m K_L}\right) \frac{1}{C_e} \quad (3)$$

where C_e and q_e are the concentration (mg L⁻¹) and adsorption capacity (mg g⁻¹) at equilibrium, respectively. Langmuir constant (K_L) indicates the affinity of binding sites with the adsorbate. The performance of different adsorbents can be compared using the maximum adsorption capacity (q_m). Langmuir isotherm constants for iron(II) and iron(III) ions were calculated from the intercept and slope of the corresponding

Table 1. Langmuir, Freundlich, Temkin, and multilayer isotherm model constants for the adsorption of Fe(II) and Fe(III) ions

Metal ion	Langmuir isotherm model				
	K_L	q_m	R_L range	R^2	Equation
Fe(II)	0.82	35.29	0.15–0.55	0.9982	$\frac{1}{q_e} = \frac{1}{q_m} + \left(\frac{1}{q_m K_L}\right) \frac{1}{C_e}$
Fe(III)	0.99	40.65	0.12–0.50	0.9889	
	Freundlich isotherm model			R^2	Equation
	K_F	n			
Fe(II)	14.48	1.93		0.9725	$\ln q_e = \ln K_f + \frac{1}{n} \ln C_e$
Fe(III)	18.33	1.77		0.9917	
	Temkin isotherm model			R^2	Equation
	a_t	b_t			
Fe(II)	16.24	8.07		0.9887	$q_e = a_t + b_t \ln C_e$
Fe(III)	20.82	10.33		0.9722	
	Multilayer isotherm model				Equation
	K_1	K_2	q_m	R^2	
Fe(II)	0.94	0.02	31.56	0.9905	$q_e = \frac{q_m K_1 C_e}{(1 - K_2 C_e)[1 + (K_1 - K_2)C_e]}$
Fe(III)	0.88	0.04	39.39	0.9926	

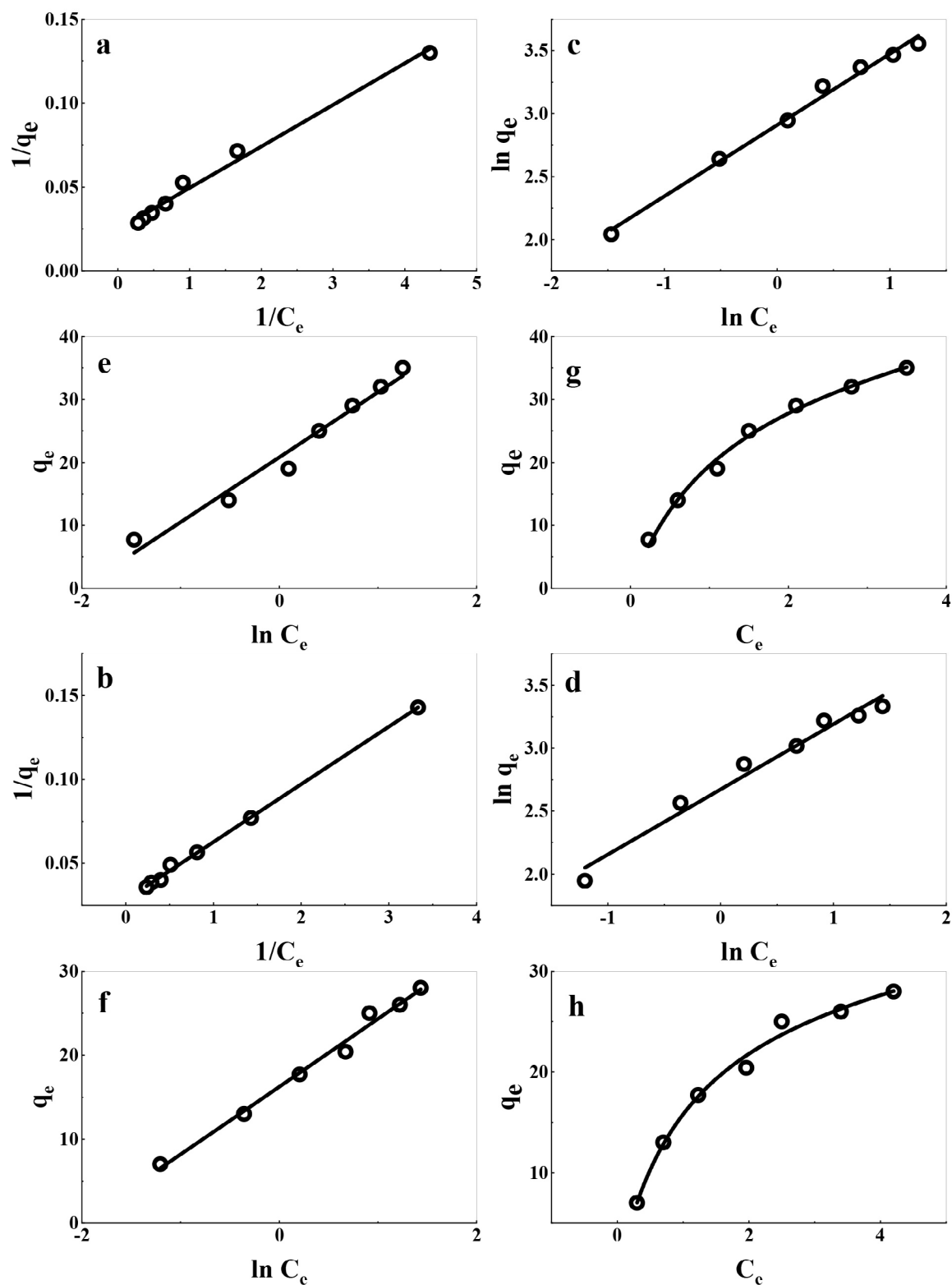


Fig. 7. (a–b) Langmuir; (c–d) Freundlich; (e–f) Temkin and (g–h) multilayer adsorption isotherms for adsorption of Fe(II) and Fe(III) onto SD/PAni; a, c, e, and g represent adsorption data for Fe(III).

linear plot of $1/q_e$ versus $1/C_e$ (Fig. 7a–b). The corresponding parameters are given in Table 1. Both isotherm data sets were well fitted to Langmuir model but

adsorption data of Fe(II) fitted better compared to that of Fe(III). The separation factor which describes the feasibility of the adsorption was calculated by the fol-

lowing equation:⁴⁹

$$R_L = \frac{1}{(1+K_L C_e)} \quad (4)$$

$R_L > 1$ denotes the unfavorable adsorption; $R_L = 0$, the irreversible adsorption, while $0 < R_L < 1$ indicates the energetically favorable adsorption. R_L -value for iron(II) and iron(III) adsorption is less than 1, indicating SD/PAni as a suitable adsorbent for both analytes.

Freundlich isotherm refers to multilayer and heterogeneous adsorption on the adsorbent surface. This model assumes that the highly energetic sites are firstly occupied by the adsorbate ions and adsorption energy decreases exponentially during the adsorption process.⁵⁰ The linearized form of Freundlich isotherm is displayed below.

$$\ln q_e = \ln K_F + \frac{1}{n} \ln C_e \quad (5)$$

where n and K_F are called Freundlich isotherm constants. K_F represents the relative adsorption capacity or the amount of adsorbate adsorbed from a solution with unit concentration. $1/n$ denotes heterogeneity of the adsorbent surface. The value of $1/n$ close to or equal to 1 stands for the homogenous binding sites of the adsorbent.⁵⁰ Freundlich isotherm plots of iron(III) and iron(II) ions are depicted in Fig. 7c–d, respectively. K_F and n values were calculated from the corresponding plots and are given in Table 1. The values of n were found to be 1.93 and 1.77 for iron(II) and iron(III) ions, respectively. These values revealed the favorability of iron(II) and iron(III) ions adsorption onto the SD/PAni, since the n values in the range of 1 to 10 represent favorable adsorption. Comparison between calculated correlation coefficients for Langmuir and Freundlich isotherms (given in Table 1) indicated that the adsorption data of Fe(II) was better fitted to Langmuir whilst the experimental adsorption data for Fe(III) was well modeled by Freundlich isotherm.

The adsorbent–adsorbate interaction and heat of the adsorption were assessed by Temkin isotherm model with the following equation (Fig. 7e–f):

$$q_e = a_t + b_t \ln C_e \quad (6)$$

where b_t stands to the heat of the adsorption (J mol^{-1}) and a_t is related to the equilibrium binding constant. The values of a_t and b_t were calculated as 16.24 and 8.07 for Fe(II) and 20.82 and 10.33 for Fe(III), respectively (Table 1). Regarding to the values of a_t obtained for Fe(II) and Fe(III), it was found that ferric ions were preferably adsorbed on the SD/PAni.

Multilayer adsorption isotherm model was also applied to fit the adsorption data:⁵¹

$$q_e = \frac{q_m K_1 C_e}{(1 - K_2 C_e)[1 + (K_1 - K_2)C_e]} \quad (7)$$

where K_1 and K_2 refers to the adsorption affinity constants for the first layer and for subsequent multilayer, respec-

tively. Eq. (7) is reduced to Langmuir equation if K_2 is negligible. Compared the correlation coefficients given in Table 1 for different isotherm models revealed that both the adsorption data for both iron species are well fitted to the multilayer adsorption isotherm. The constant parameters of the multilayer isotherm calculated for both iron ions are given in Table 1. The corresponding curves are depicted in Fig. 7g–h. The data yielded provide convincing evidence that (i) maximum adsorption capacity for Fe(III) is higher than Fe(II); (ii) the tendency of Fe(III) to be bound in multilayer form is higher than that of Fe(II).

3. 6. Adsorption Mechanism

Study of adsorption efficiency at different pH revealed that the uptake of Fe(III) and Fe(II) onto SD/PAni was lower in highly acidic solutions ($\text{pH} < 2$). The maximum removal of analytes was observed at $\text{pH} = 4$ and minimum removal was seen at $\text{pH} = 1$. The lower adsorption behavior of SD/PAni under the highly acidic condition can be explained by taking into account the protonation of the nitrogen atoms present in polyaniline.⁴⁵ As a result, the surface of adsorbent is positive in the highly acidic media and is not able to uptake the iron ions due to the electrostatic repulsion. However, deprotonation of the nitrogen atoms occur as the pH increases (3–4), leading to the formation of active sites in the adsorbent.

Typically, the adsorption of metal ions onto the surface of adsorbent may follow several approaches including ion exchange, chemisorption, and complexation. Ion exchange is the most dominant mechanism by the reaction of metal ions with surface functional groups. The chemisorptive reaction may be formed by participation of a lone pair of electrons of a donor atom with metal ions. Another mechanism is surface adsorption by which metal ions may be bound to the surface of adsorbent. In this mechanism the surface of adsorbent should have a negative charge. That the adsorption isotherms of iron ions onto SD/PAni are well fitted to the Langmuir equation implies the preferential binding of metal ions on all sites of SD/PAni as homogeneous surfaces. This consideration along with the fact that maximum deprotonation of nitrogen atoms occurs at $\text{pH} = 4$, supports the claim that the adsorption mechanism is chemisorption. This is in accordance with the previous literature.³⁹

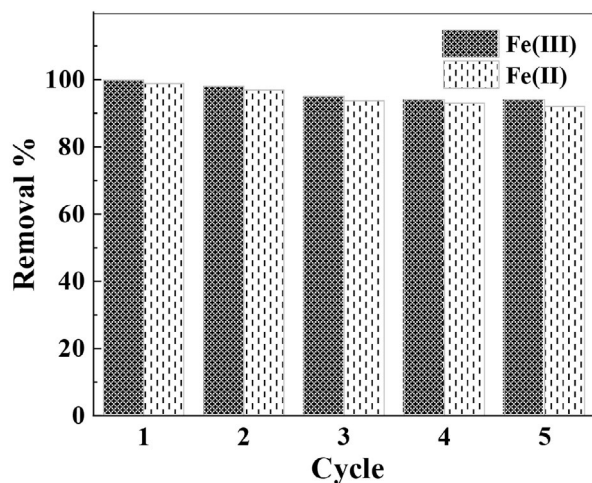
3. 7. Desorption and Reusability

The elution process greatly depends on the type and concentration of the eluent. So, some eluent solutions with different concentrations were employed for desorption of iron(II) and iron(III) ions retained on SD/PAni and the results are given in Table 2. Optimum desorption of both iron ions was observed with 50.0 mL 1.0 mol L⁻¹ HCl. Hence, this solution was considered for regeneration of the used columns.

Table 2. Effect of concentration and type of eluent on the recovery of Fe(II) and Fe(III) ions.

Volume (mL)	Eluent Content	Recovery (%)	
		Fe(II)	Fe(III)
20	0.3 mol L ⁻¹ HCl	87.2	69.0
20	0.3 mol L ⁻¹ HNO ₃	75.7	72.0
20	0.3 mol L ⁻¹ H ₂ SO ₄	63.0	70.3
25	0.5 mol L ⁻¹ HCl	91.2	88.6
30	0.5 mol L ⁻¹ HCl	95.0	94.6
50	1.0 mol L ⁻¹ HCl	98.89	98.3

To check the reusability of SD/PAni for iron ions adsorption, five successive cycles of adsorption and desorption studies were carried out in a batch system. The results are depicted in Fig. 8. The percentage of adsorption of the recycled adsorbent was 98.0% and 96.9% at the first cycle

**Figure 8.** Effect of cycle times on the removal efficiencies of iron ions.**Table 3.** Comparison of the characteristics of the proposed method with the previously published methods.

Adsorbent	Analyte	Adsorption capacity (mg g ⁻¹)	Extraction time (min)	Normalized extraction time (min mg ⁻¹)	Sample volume (mL)	Reference
Fe(III)-IIP	Fe(III)	40.41	15	600	25	9
Fe(III)-imprinted amino-functionalized silica gel	Fe(III)	25.21	150	150000	150	52
Triton X-100-coated PVC	Fe(III)	2.7	80	8000	450	53
Modified silica gel	Fe(III)	25.76	150	150000	150	55
Functionalized activated carbon	Fe(III)	77.8	100	20000	200	56
SDS-coated alumina	Fe(III)	6.3	437.5	8750	1750	57
Pyridinium IL-modified silica	Fe(III)	11.8	100	20000	200	58
Fe(II)-IIP ^a	Fe(II)	1.57 ^a	30	6000	10	59
Polyaniline coated-saw dust	Fe(II)-Fe(III)	31.56-39.39	10	10	50	This work

^a IIP: ion imprinted polymer

for Fe(III) and Fe(II), respectively. After five adsorption-desorption cycles, the adsorption of Fe(III) and Fe(II) decreased by 5.9% and 6.8%, respectively. The results confirm that SD/PAni is an effective and recyclable adsorbent for the removal of iron ions.

3. 8. Comparison with Other Methods

SD/PAni has satisfactory characteristics in comparison to the previously reported methods for removal of iron(II) and iron (III) ions (Table 3). Adsorption capacity is one of the most important characteristics of an adsorbent. The calculated adsorption capacities (q_m) for the SD/PAni were satisfactory and found to be 31.56 and 39.39 mg g⁻¹ for iron(II) and iron(III) ions, respectively. Operation in continuous mode is another major advantage of the presented method. Additionally, the proposed method can handle reasonable sample volume, and has less normalized extraction time than other methods.^{9,52-59} Normalized extraction time is defined as the time required to extract 1.0 mg of the adsorbate by 1.0 g of the adsorbent. It is worth noting that the efficiency of raw sawdust was checked toward the removal of iron ions. It was found that the efficiency of the sawdust decorated with polyaniline was more than 1.5 times greater than the raw sawdust for the removal of iron ions.

4. Conclusions

SD/PAni was synthesized and employed as an effective adsorbent for removal of Fe(II) and/or Fe(III) ions from aqueous solutions in a fixed-bed column system. To our knowledge, this is the first time that SD/PAni has been used for the removal of iron ions. The data gathered in the study suggest that SD/PAni has a good potential for adsorption of iron(II) and iron(III) ions. The greatest adsorption efficiency was observed at pH 4.0, flow rate of 5.0

mL min⁻¹, and temperature of 25 °C with adsorbent mesh size of 100 BSS. A closer look at the results indicated that ferric ions are more adsorbed compared to ferrous ions under conditions far from the optimized conditions. However, under optimal conditions where the adsorption efficiency of SD/PAni is as high as possible, no significant competition of adsorption between Fe(II) and Fe(III) ions takes place. Isotherm data of Fe(II) and Fe(III) adsorption were well fitted to multilayer adsorption isotherm model. Adsorption process of both iron species were temperature-independent in the range of 30–55 °C. 50.0 mL 1.0 mol L⁻¹ HCl was efficiently used as an eluent for regeneration of adsorbent.

Acknowledgements

The authors gratefully acknowledge the financial support of this work provided by Islamic Azad University, Mahshahr branch.

5. References

1. D. Fernández-Calviño, J. A. Rodríguez-Suárez, E. López-Periago, M. Arias-Estévez, J. Simal-Gándara, *Geoderma* **2008**, *145*, 91–97. DOI:10.1016/j.geoderma.2008.02.011
2. G. Khayatian, H. A. V. Kolaie, F. Nasiri, B. Atashkar, S. Hassanpoor, *J. Chin. Chem. Soc.* **2010**, *57*, 118–123. DOI:10.1002/jccs.201000019
3. W. S. W. Ngah, S. Ab Ghani, A. Kamari, *Bioresour. Technol.* **2005**, *96*, 443–450. DOI:10.1016/j.biortech.2004.05.022
4. M. Abbasi, M. Zaghari, M. Ganjkanlo, S. Khalaji, *J. Appl. Anim. Res.* **2015**, *43*, 166–176. DOI:10.1080/09712119.2014.928634
5. World Health Organization, Guidelines for drinking-water quality, 2nd ed. Vol. 2. Health criteria and other supporting information. Geneva, **1996**.
6. S. Vasudevan, J. Lakshmi, G. Sozhan, *Clean Soil Air Water* **2009**, *37*, 45–51. DOI:10.1002/clen.200800175
7. National Research Council. Iron. University Park Press: Baltimore, Maryland, **1979**.
8. M. A. Kassem, A. S. Amin, *Food Chem.* **2013**, *141*, 1941–1946. DOI:10.1016/j.foodchem.2013.05.038
9. M. Roushani, T. M. Beygi, Z. Saedi, *Spectrochim. Acta, Part A* **2016**, *153*, 637–644. DOI:10.1016/j.saa.2015.09.029
10. X. Cai, B. Wei, J. Han, Y. Li, Y. Cui, G. Sun, *Hydrometallurgy* **2016**, *164*, 1–6. DOI:10.1016/j.hydromet.2016.04.010
11. A. Bazmandegan-Shamili, A. M. H. Shabani, S. Dadfarnia, M. Saeidi, M. R. Moghadam, *J. Iran. Chem. Soc.* **2016**, *14*, 843–851. DOI:10.1007/s13738-016-1037-1
12. D. Mohan, C. U. Pittman, *J. Hazard. Mater.* **2007**, *142*, 1–53. DOI:10.1016/j.jhazmat.2007.01.006
13. C. Nieto-Delgado, J. R. Rangel-Mendez, *Water Res.* **2012**, *46*, 2973–2982. DOI:10.1016/j.watres.2012.03.026
14. Q. Manzoor, R. Nadeem, M. Iqbal, R. Saeed, T. M. Ansari, *Bioresour. Technol.* **2013**, *132*, 446–452. DOI:10.1016/j.biortech.2013.01.156
15. I. D. Mall, V. C. Srivastava, N. K. Agarwal, I. M. Mishra, *Chemosphere* **2005**, *61*, 492–501. DOI:10.1016/j.chemosphere.2005.03.065
16. A. Shukla, Y.-H. Zhang, P. Dubey, J. L. Margrave, S. S. Shukla, *J. Hazard. Mater.* **2002**, *95*, 137–152. DOI:10.1016/S0304-3894(02)00089-4
17. H. Alidadi, M. Dolatabadi, M. Davoudi, F. Barjasteh-Askari, F. Jamali-Behnam, A. Hosseinzadeh, *Process Saf. Environ. Prot.* **2018**, *117*, 51–60. DOI:10.1016/j.psep.2018.04.007
18. R. Ansari, Z. Mosayebzadeh, *J. Iran. Chem. Soc.* **2010**, *7*, 339–350. DOI:10.1007/BF03246019
19. D. Božić, V. Stanković, M. Gorgievski, G. Bogdanović, R. Kovačević, *J. Hazard. Mater.* **2009**, *171*, 684–692. DOI:10.1016/j.jhazmat.2009.06.055
20. A. Prado, A. Moura, R. Andrade, I. Pescara, V. Ferreira, E. Faria, A. de Oliveira, E. Okino, L. Zara, *J. Therm. Anal. Calorim.* **2009**, *99*, 681–687. DOI:10.1007/s10973-009-0284-0
21. D. Liu, D. Sun, Y. Li, *Sep. Sci. Technol.* **2010**, *46*, 321–329. DOI:10.1080/01496395.2010.504201
22. A. Ostovan, S. Elhami, *J. Water Wastewater* **2018**, *29*, 29–37. DOI:10.22093/WWJ.2017.62973.2253
23. C. McCullagh, G. C. Saunders, *Water Res.* **2005**, *39*, 2799–2806. DOI:10.1016/j.watres.2005.04.045
24. H. Eisazadeh, *J. Appl. Polym. Sci.* **2007**, *104*, 1964–1967. DOI:10.1002/app.25904
25. M. Kumar, M. A. Khan, Z. A. AlOthman, M. R. Siddiqui, *Desalination* **2013**, *325*, 95–103. DOI:10.1016/j.desal.2013.06.022
26. M. R. Samani, S. M. Borghei, A. Olad, M. J. Chaichi, *J. Hazard. Mater.* **2010**, *184*, 248–254. DOI:10.1016/j.jhazmat.2010.08.029
27. M. Idrees, A. Razaq, A. Islam, S. Yasmeen, K. Sultana, M. H. Asif, M. Nadeem, *Synth. Met.* **2017**, *232*, 138–143. DOI:10.1016/j.synthmet.2017.08.009
28. R. Vallerio, R. Keyer, S. Grabania, M. Landis, S. Jansen, Y. Wei, *MRS Online Proceedings Library Archive* **1995**, *413*, 523–528. DOI:10.1557/PROC-413-523
29. R. Ansari, *Acta Chim. Slovenica* **2006**, *53*, 88–94.
30. H. Li, J. Zhou, X. Lu, J. Wang, S. Qu, J. Weng, B. Feng, *J. Mater. Sci. - Mater. Electron.* **2015**, *26*, 7723–7730. DOI:10.1007/s10854-015-3416-2
31. M. S. Mansour, M. E. Ossman, H. A. Farag, *Desalination* **2011**, *272*, 301–305. DOI:10.1016/j.desal.2011.01.037
32. APHA, Standard methods for the examination of water and wastewater. 21st ed.; Andesite Press: Washington DC, **2005**.
33. F. Gode, E. D. Atalay, E. Pehlivan, *J. Hazard. Mater.* **2008**, *152*, 1201–1207. DOI:10.1016/j.jhazmat.2007.07.104
34. M. Bajpai, N. Rai, S. Bajpai, *J. Appl. Polym. Sci.* **2012**, *125*, 1382–1390. DOI:10.1002/app.35289
35. P. X. Thinh, J. K. Kim, D. S. Huh, *Polymer* **2014**, *55*, 5168–5177. DOI:10.1016/j.polymer.2014.08.011
36. R. Kumar, M. Oves, T. Almeelbi, N. H. Al-Makishah, M. A. Barakat, *J. Colloid Interface Sci.* **2017**, *490*, 488–496. DOI:10.1016/j.jcis.2016.11.082
37. M. Bhaumik, R. McCrindle, A. Maity, *Chem. Eng. J.* **2013**,

- 228, 506–515. DOI:10.1016/j.cej.2013.05.026
38. N. T. Abdel-Ghani, G. A. El-Chaghaby, F. S. Helal, *Desalin. Water Treat.* **2013**, *51*, 3558–3575. DOI:10.1080/19443994.2012.750806
39. M. E. Mahmoud, N. A. Fekry, *J. Polym. Environ.* **2018**, *26*, 3858–3876. DOI:10.1007/s10924-018-1263-y
40. H. Eisazadeh, *Chin. J. Polym. Sci.* **2007**, *25*, 393–397. DOI:10.1142/S0256767907002266
41. A. Ghazali, M. Shirani, A. Semnani, V. Zare-Shahabadi, M. Nekoeinia, *J. Env. Chem. Eng.* **2018**, *6*, 3942–3950. DOI:10.1016/j.jece.2018.05.043
42. S. Chaturvedi, P. N. Dave, *Desalination* **2012**, *303*, 1–11. DOI:10.1016/j.desal.2012.07.003
43. Z. Aksu, Ü. Açikel, *Biochem. Eng. J.* **2000**, *4*, 229–238. DOI:10.1016/S1369-703X(99)00053-4
44. M. Al-Anber, Z. A. Al-Anber, *Desalination* **2008**, *225*, 70–81. DOI:10.1016/j.desal.2007.07.006
45. V. Janaki, K. Vijayaraghavan, B.-T. Oh, K.-J. Lee, K. Muthuchelian, A. Ramasamy, S. Kamala-Kannan, *Carbohydr. Polym.* **2012**, *90*, 1437–1444. DOI:10.1016/j.carbpol.2012.07.012
46. R. Ansari, W. E. Price, G. G. Wallace, *Polymer* **1996**, *37*, 917–923. DOI:10.1016/0032-3861(96)87273-9
47. Z. Hu, H. Chen, F. Ji, S. Yuan, *J. Hazard. Mater.* **2010**, *173*, 292–297. DOI:10.1016/j.jhazmat.2009.08.082
48. R. Nadeem, Q. Manzoor, M. Iqbal, J. Nisar, *J. Ind. Eng. Chem.* **2016**, *35*, 185–194. DOI:10.1016/j.jiec.2015.12.030
49. Y. Yoon, W. K. Park, T.-M. Hwang, D. H. Yoon, W. S. Yang, J.-W. Kang, *J. Hazard. Mater.* **2016**, *304*, 196–204. DOI:10.1016/j.jhazmat.2015.10.053
50. A. Dada, A. Olalekan, A. Olatunya, O. Dada, *IOSR J. Appl. Chem.* **2012**, *3*, 38–45. DOI:10.9790/5736-0313845
51. C.-H. Weng, Y.-F. Pan, *J. Hazard. Mater.* **2007**, *144*, 355–362. DOI:10.1016/j.jhazmat.2006.09.097
52. X. Chang, N. Jiang, H. Zheng, Q. He, Z. Hu, Y. Zhai, Y. Cui, *Talanta* **2007**, *71*, 38–43. DOI:10.1016/j.talanta.2006.03.012
53. M. Ghaedi, K. Niknam, A. Shokrollahi, E. Niknam, H. Ghaedi, M. Soylak, *J. Hazard. Mater.* **2008**, *158*, 131–136. DOI:10.1016/j.jhazmat.2008.01.037
54. X. Zhu, X. Chang, Y. Cui, X. Zou, D. Yang, Z. Hu, *Microchem. J.* **2007**, *86*, 189–194.
55. M. Ghaedi, K. Niknam, A. Shokrollahi, E. Niknam, H. R. Rajabi, M. Soylak, *J. Hazard. Mater.* **2008**, *155*, 121–127. DOI:10.1016/j.jhazmat.2007.11.038
56. Z. Tu, Q. He, X. Chang, Z. Hu, R. Gao, L. Zhang, Z. Li, *Anal. Chim. Acta* **2009**, *649*, 252–257. DOI:10.1016/j.aca.2009.07.042
57. M. Ghaedi, H. Tavallali, A. Shokrollahi, M. Zahedi, M. Montazerzohori, M. Soylak, *J. Hazard. Mater.* **2009**, *166*, 1441–1448. DOI:10.1016/j.jhazmat.2008.12.066
58. H. Abdolmohammad-Zadeh, M. Galeh-Assadi, S. Shabkhi-zan, H. Mousazadeh, *Arabian J. Chem.* **2016**, *9*, S587–S594. DOI:10.1016/j.arabjc.2011.07.006
59. M. Mitreva, I. Dakova, I. Karadjova, *Microchem. J.* **2017**, *132*, 238–244. DOI:10.1016/j.microc.2017.01.023

Povzetek

Cilj te raziskave je bil preučiti primernost žagovine s prevleko iz polianilina (SD/PAni) kot adsorbenta za odstranjevanje Fe(II) in/ali Fe(III) ionov iz vodnih raztopin. Raziskava je obsegala šaržne in kolonske poskuse. Pri kolonskih poskusih smo preučevali vpliv različnih eksperimentalnih parametrov na adsorpcijsko obnašanje Fe(II), Fe(III) in zmesi obeh ionov. Ugotovili smo, da so optimalni adsorpcijski pogoji za posamezno zvrst železa in za njuno zmes podobni. Optimalne vrednosti so bile: pH 4,0; pretok 5,0 mL min⁻¹; temperatura 25 °C in velikost delcev adsorbenta 100 BSS mesh. Za študijo adsorpcijskih izoterm pri sobni temperaturi smo izvedli šaržne eksperimente. Rezultati so pokazali, da se adsorpcijski izotermi za obe zvrsti železa najbolje prilegajo večplastnemu adsorpcijskemu izotermnemu modelu. Preverili smo tudi stabilnost adsorbenta pri ponovitvah adsorpcije–desorpcije ter ugotovili, da je stabilen 5 ciklov.



Except when otherwise noted, articles in this journal are published under the terms and conditions of the Creative Commons Attribution 4.0 International License

Scientific paper

DBD Plasma Influence on the Adhesion of Paints on Polymeric Substrates

Jindřich Matoušek,^{1,*} Pavlína Hájková^{2,3} and Jakub Perner¹¹ University of J.E. Purkyně, Faculty of Science, Department of Physics, České mládeže 8, 400 96 Ústí nad Labem, Czech Republic.² Unipetrol Centre for Research and Education, Revoluční 84, 400 01 Ústí nad Labem, Czech Republic³ Technical University of Liberec, Department of Material Science, Studentská 2, 461 17 Liberec, Czech Republic

* Corresponding author: E-mail: jindrich.matousek@ujep.cz

Received: 04-04-2019

Abstract

The, polyethylene (PE), polypropylene (PP) and polycarbonate (PC) flat substrates were treated by the DBD plasma in air for 1 s, 2 s and 3 s. The adhesion of two types of paints (water based and solvent based) was studied by the pull-off test. The other methods were utilized to gain the information about the surface of the samples. The measurement of contact angle of water and Arcotest (commercial test using set of fluids with defined surface tension) and the XPS technique were used to obtain the chemical composition of the sample surface. The pull-off test confirmed increased adhesion of both types of paints, which is related to oxygen content confirmed by XPS. The aged (60 days) samples keep their enhanced properties although some return to initial state was observed.

Keywords: DBD plasma; polymer; adhesion

1. Introduction

The polymers are known for their low surface energy which then causes low adhesion of various paints to the polymers. These days the polymers production is one of the largest industrial branches and all manufacturers have to deal with the paint adhesion, which can be increased by various ways. Use of chemicals, UV light or flame treatment was described.^{1,2} The use of aggressive chemicals is environmentally unfriendly, although effective. Another possibility is the plasma treatment. Either plasma polymer coating can be created (plasma deposition from gas phase) or plasma itself can be used to create functional groups on the polymeric surface. Many research groups studied the plasma treatment of polymers.^{3–9} The plasma treatment methods usually need to achieve low pressure with the exception of the atmospheric pressure plasma treatment. This is one of the drawbacks of plasma technologies – high initial cost of the equipment. To overcome the need of vacuum equipment installation, the atmospheric plasma can also be used. Although the atmospheric discharges have own specific difficulties – e.g. expensive He is often needed for better discharge stabilisation – it is possible to find ap-

plications, where the helium does not need to be used.^{10,11} This is the case of dielectric barrier discharge (DBD) that can be used for treatment of polymers and for the adhesion improvement. In this study we used DBD discharge for plasma treatment of various polymers to enhance the adhesion of two classes of paints (water based and solvent based) and we characterized the surface chemistry and adhesion by several methods mentioned in following sections.

2. Materials and Methods

2. 1. Substrates

Three different polymers were used. The oxygen containing groups can influence the surface energy and therefore polymers with and without oxygen were selected. Two of them were polyolefins: polyethylene (PE) and polypropylene (PP), the third one was oxygen containing polymer with more complex structure – polycarbonate (PC). These polymers were selected also because they are ones of the most often used polymers in the industry. The samples were supplied by Goodfellow: (UHMW PE, PP, PC sheets) and were 3 mm thick flat pieces that were cut to the same

size (6 cm x 14 cm), cleaned by isopropyl alcohol and let dry. The structure of PE and PP is considered to be known well. The structural formula of PC is given in Fig. 1.

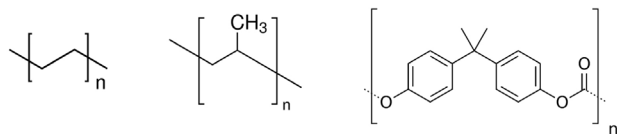


Figure 1. Structural formula of PE, PP and PC.

2. 2. Plasma Treatment

The DBD plasma treatment was performed in air using DBD reactor UniPlasma 140 (from MSV Systems CZ, s.r.o.). This reactor is equipped with two plane parallel electrodes covered by 1 mm thick layer of dielectric. The upper electrode (105 mm x 20 mm x 12 mm) was covered with corundum and the bottom electrode (120 mm x 60 mm x 20 mm) with a rubber conveyor belt. The distance between electrodes was 5 mm, AC source voltage was 20 kV at frequency 3 kHz and power 120 W (PWM modulation was used). The conveyor belt's speed was set to achieve 1 s long treatment in one pass of the sample under the DBD electrode (i.e. each point of the sample spent 1 s under the electrode in the plasma discharge). Multiple passes were used to obtain longer treatments. Three treatments were used: 1 s, 2 s and 3 s long plasma treatment. The treatment was performed in ambient, no other precautions were applied. The relative humidity in the laboratory was between 30–35%.

2. 3. Pull-off Test

The samples were painted by two types of paint. One of them was water based paint (Balakryl UNI from PPG Deco Czech a.s.) and the other one was solvent based paint (Dupli-Color Aerosol ART from Motip Dupli s.r.o.). The substrates were painted immediately after the treatment and also after 5, 10, 30 and 60 days from the plasma treatment. After the paint dried, the test dolly was glued to the surface by epoxy resin and the pull-off test was performed. Automatic adhesion tester PosiTest AT-A (from company DeFelsko) was used to measure the hydraulic pressure applied by the device to pull the test diameter of coating away from the substrate (dolly with diameter 20 mm was used). The pull-off test values are averaged values from 6 measurements. The standard deviation of the data lies between 10–25% of the mean value.

2. 4. Arcotest

The surface energy can be tested by a commercial test – the Arcotest – that consists of set of inks with defined surface tension σ . The surface is wetted when it has at least minimal surface energy which is needed to achieve wet-

ting of the surface by the ink of given surface tension. It is possible to use inks with 1 mN/m resolution, however enormous number of samples would be needed. Therefore it was decided to use 3 of the inks in this study. These 3 inks have surface tensions 38, 44 and 56 mN/m. The surface energy of the surface is usually considered to be good enough when the surface is wetted by the ink with $\sigma = 38$ mN/m or higher.¹² The adhesion of the paints on such surface is then sufficient.

2. 5. Water Contact Angle Measurements

The portable instrument See System from AdveX instruments was used for contact angle measurement by static sessile droplet method. The middle part of the sample was used (approx. 1 cm wide stripe was cut out), 5 μ L of distilled water was dropped on the sample surface and the contact angle was measured. The measurement was repeated 5 times and mean value was then recorded.

2. 6. XPS Measurements

The XPS technique was used to reveal the surface chemistry of the samples and for the polar groups detection as these functionalities influence the surface energy as described in literature.^{13,14} Small piece 1 cm x 1 cm was cut from the middle of the sample and loaded to the XPS chamber. The spectra were recorded using hemispherical analyser Phoibos 100 from Specs operated in FAT mode. Non-monochromatized X-ray beam of Al anode at 200 W with Al K α photon energy 1486.6 eV was used. The survey spectra for binding energies from 1300 eV to 0 eV were recorded with pass energy 40 eV with energy step 0.5 eV and dwell time 0.1 s. For C1s and O1s peaks, high resolution spectra were recorded with pass energy equal to 10 eV, energy step 0.05 eV and the scan was repeated 10 times. The XPS is not equipped with electron gun for charge compensation, so the spectra were referenced to the peak of aliphatic C-H bonds at 285 eV. Quantification was done from high resolution spectra using relative sensitivity factors $RSF_{C1s} = 1$ and $RSF_{O1s} = 2.93$. Software CasaXPS was used for the spectra processing.

2. 7. AFM Measurements

The wettability (and adhesion) of the surfaces is influenced by the chemical changes and also by the surface roughness. Therefore, AFM measurements were performed. The NT-MDT Ntegra Aura was used. The cantilevers used for analysis were HA_FM Etalon cantilevers. These AFM tips have longer and shorter cantilever – the shorter one (183 μ m) in semi-contact mode was used for all AFM images. Images of several sizes were taken – 50 μ m, 30 μ m, 10 μ m and 5 μ m. Each scan had 256 lines. The NT-MDT software was used for flattening the images (fit lines function was used), for noise filtering and for the

roughness evaluation. Values of average roughness (S_a) and root mean square roughness (S_q) were recorded.

The problems with charging of the PP and PC samples caused unwanted artefacts in some of the images. This was solved by using filtering of the images. Low pass 3x3 filter was used in case of PP scans and FFT filtering was needed in case of PC samples. PE scans remained unfiltered.

3. Results and Discussion

3.1. Pull-off Tests

The adhesion is here expressed in terms of hydraulic pressure (pull-off pressure) needed to pull the test dolly from the sample. Better paint adhesion then results in higher pressure needed to pull off the test dolly. Larger

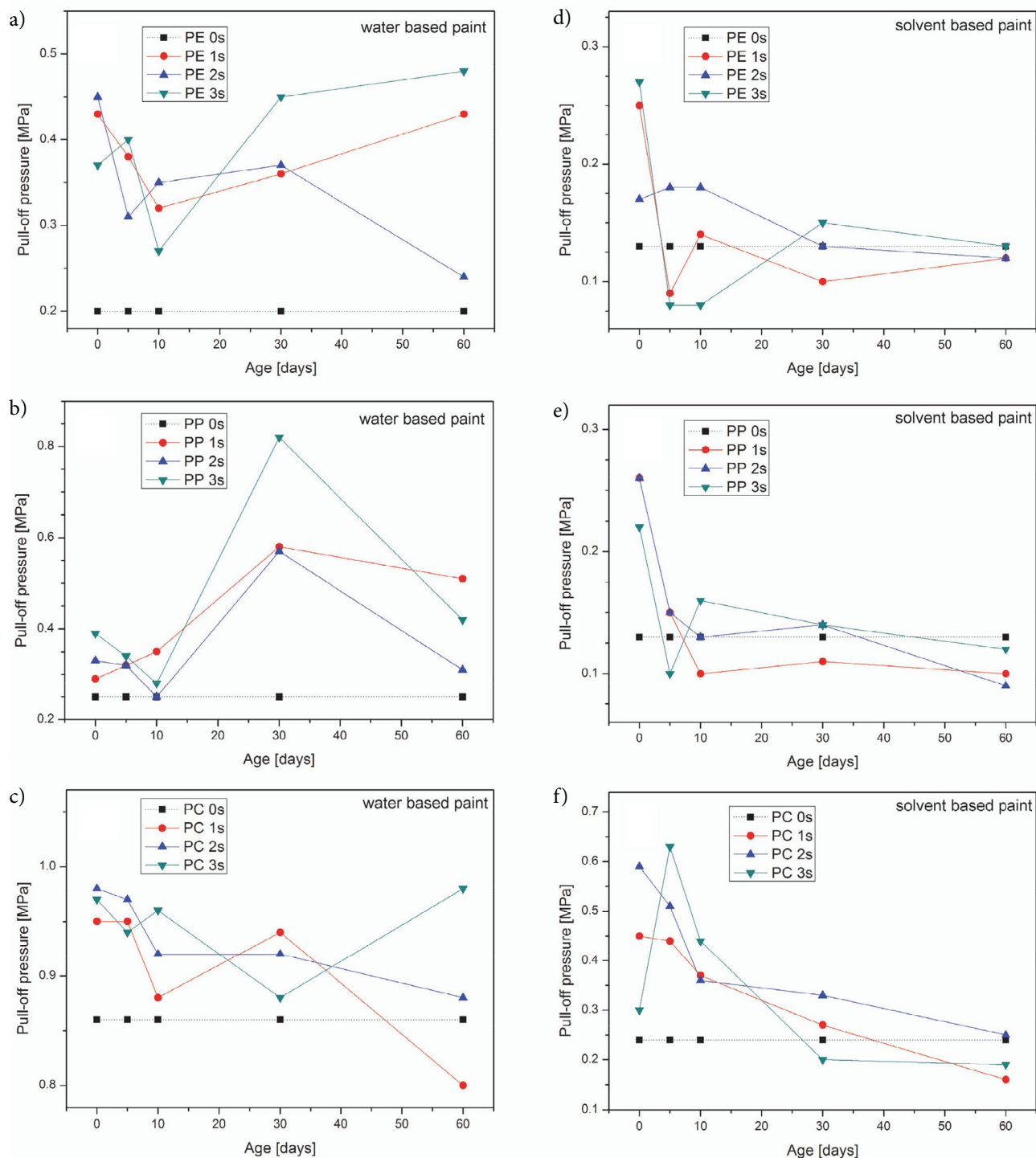


Figure 2. Pull-off test results for water and solvent based paint on the PE, PP and PC substrates. Untreated sample is always labeled “0 s”

standard deviation (10–25% of the value) is the main reason for higher spread of the data and not clear trends, however, the improvements are undoubted.

The pull-off pressure of the water based paint (Fig.2) increased more than 2 times after the plasma treatment in case of PE. Clear trend is not observable during aging, however, the plasma treated PE seems to keep increased pull-off pressure although its decrease can be seen in the first week of aging. In case of PP, the pull-off pressure increase after the treatment is not so strongly pronounced and also the aging seems to have different character compared to the PE – the increase of the pull-off pressure was found. The reason for this behaviour could be explained by existence of reactive species created on the PP surface followed by the oxidation and incorporation of the oxygen from atmosphere into the polymer surface. This difference between PE and PP samples is also supported by contact angle (Fig.3) and XPS (Fig.4) measurements – the contact angles of PE return back almost to the initial values during the first week of aging while the contact angles on PP return much slower. Also the oxygen content given by the XPS decrease back in case of the PE (with the exception of the 3 s treatment) while in case of the PP the oxygen content stays well above the initial value during the aging. That can be caused by creation of the alkyl and alkoxy radicals after the plasma treatment as proposed e.g. by Geyter et al.¹⁸ These radicals can react either with atomic oxygen and ozone in the discharge or with oxygen from atmosphere during the aging. Similar effect was observed, the polar and dispersive fractions of surface energy were measured after atmospheric plasma treatment of PE and PP.¹⁹ For PE increased polar and dispersive fraction directly after the plasma treatment were found contrary to the PP where significant additional increase of polar fraction also after 8 days after the treatment was observed.

In case of the PC, the pull-off pressure on the water based paint is high even for untreated PC. However, after plasma treatment it is increased further and then slowly decreases to approximately initial values. Considering the fact that untreated PC already contains C-O and C=O bonds (and these are believed to be responsible for the good adhesion), this could be expected. The plasma treatment probably changes the two methyl groups (see Fig.1) where hydrogen can be replaced by oxygen containing group and therefore there is still some space for improvement by increasing the amount of oxygen in the polymeric chain.

In case of the solvent based paints both – PE and PP show decrease of the pull-off pressure during first week of aging to almost initial values. The pull-off pressure of untreated PC is low but it is successfully increased by the plasma treatment. It also takes 30 days from the treatment to slowly decrease the values back to the pull-off pressure of untreated PC.

Therefore the adhesion of water based paint is probably governed mainly by the polar groups presence on the surface, while the solvent based paint is not affected that

much by them. The effect on the solvent based paint adhesion can be explained if one considers the composition of the solvent based paint. Its safety data sheet gives the information – the paint contains compounds like acetone (up to 50%), 2-methoxy-1-methylethyl acetate (up to 10%) or butyl acetate (up to 10%). All these compounds contain polar groups and therefore the adhesion of this paint is influenced by the oxidation of the polymer surface.

3. 2. Arcotest

The initial surface energy of all untreated samples was low and the surface was not wetted by any of the used inks (surface tensions $\sigma = 38, 44$ and 56 mN/m). This is considered to be insufficient for good adhesion of any paint and therefore the surface of the samples has to be changed. The DBD plasma treated samples show very interesting increase of the surface energy and all of the above mentioned inks wetted the plasma treated surfaces. The durability of the plasma treatment is also important, therefore all analyses were performed on the aged samples too. The Arcotest was done after 1, 5, 10, 30 and 60 days of aging (see Table 1). The most remarkable effect was observed in case of PP, where all treatments led to surface that was wetted by inks with $\sigma = 56$ mN/m and remained that high for 2 months. That is in agreement with the pull-off tests where increased pull-off

Table 1. Results of the Arcotest *

Arcotest		σ of inks wetting the sample [mN/m]		
		PE	PP	PC
Untreated		<38	<38	<38
1 day	1 s	56≤	56≤	56≤
	2 s	56≤	56≤	56≤
	3 s	56≤	56≤	56≤
5 days	1 s	44<56	56≤	56≤
	2 s	56≤	56≤	56≤
	3 s	56≤	56≤	56≤
10 days	1 s	38<44	56≤	44<56
	2 s	38<44	56≤	44<56
	3 s	38<44	56≤	56≤
30 days	1 s	38<44	56≤	56≤
	2 s	38<44	56≤	44<56
	3 s	38<44	56≤	44<56
60 days	1 s	38<44	56≤	44<56
	2 s	38<44	56≤	56≤
	3 s	38<44	56≤	56≤

*Meaning of the inequality sign: <38 means the surface energy is lower than energy which should the surface have to be wetted by the ink with $\sigma = 38$ mN/m.

56≤ means that the surface energy is equal or higher to the surface energy which should the surface have to be wetted by the ink with $\sigma = 56$ mN/m.

38<44 means that surface energy is between the surface energies that should surface have to be wetted by the inks with $\sigma = 38$ and 44 mN/m. This results in wetting by ink with $\sigma = 38$ mN/m and partial wetting by ink with $\sigma = 44$ mN/m. The 44<56 is similar.

pressure was detected for water based paint. Very positive effect was obtained also for the PC samples, where slight decrease of the surface energy after approx. 2 weeks is observed, but is still good enough to be wetted by ink with $\sigma = 44$ mN/m. The biggest changes are seen in case of PE. In the first week from the treatment, the surface energy keeps the high values (ink with $\sigma = 56$ mN/m) but after one week it drops to the 44–56 mN/m interval and after two weeks of aging drops further to 38–44 mN/m. This behaviour could be ascribed to the hydrophobic recovery described in literature.^{20–22} The functional groups can be rotated along the main chain of the polymer and can be buried into the deeper layers of the polymer. The PE chains are mostly linear and as a consequence the functional groups are easily rotated and buried. The other two polymers have more complex structure and therefore less degrees of freedom, which probably prevents above described mechanism from prevailing. The Arcotest results on PE are in accordance with the pull-off tests and the water contact angle measurements. It is not exactly known to the authors of this article whether the Arcotest is consisting mainly of polar or dispersive components, but from the results of pull-off tests and also the water contact angle measurements it looks like the polar ink is the main component of the testing liquids.

3. 3. Water Contact Angle Measurements

The water contact angle measurement is simple and easy way to gain some information about the polar component of the surface energy.

The untreated samples have contact angle values close to 100° (PE, PP) and 80° (PC). The lower contact angle in case of PC can be attributed to oxygen presence on its surface as mentioned earlier. Directly after the plasma treatment the contact angles decrease significantly by approximately 20–30° (see Fig.3). The trends are similar to those observed for Arcotest and pull-off measurements – the PE recovers almost to the initial values after 1 week of aging, the treatment in case of rest of the samples returns more slowly. The PP contact angles are recovering too, although the surface energy given by the Arcotest remains stable. This is most likely given by low resolution of the Arcotest (only 4 distinguishable values). The longer 3 s treatment is slightly more stable than 1 s or 2 s treatment for all polymers.

3. 4. XPS Measurements

The XPS measurements confirmed the above testing – initial oxygen content is low in case of PE and PP and therefore the contact angles are high and the pull-off pressures low for both polymers (see Fig. 4). The difference is in the speed of the recovery process. The fastest return to initial O content has the PE, where lowest surface energy was found with aging as well as the water contact angle measurements on PE showed the fastest return to almost initial contact angles. The PP has the best retention of the

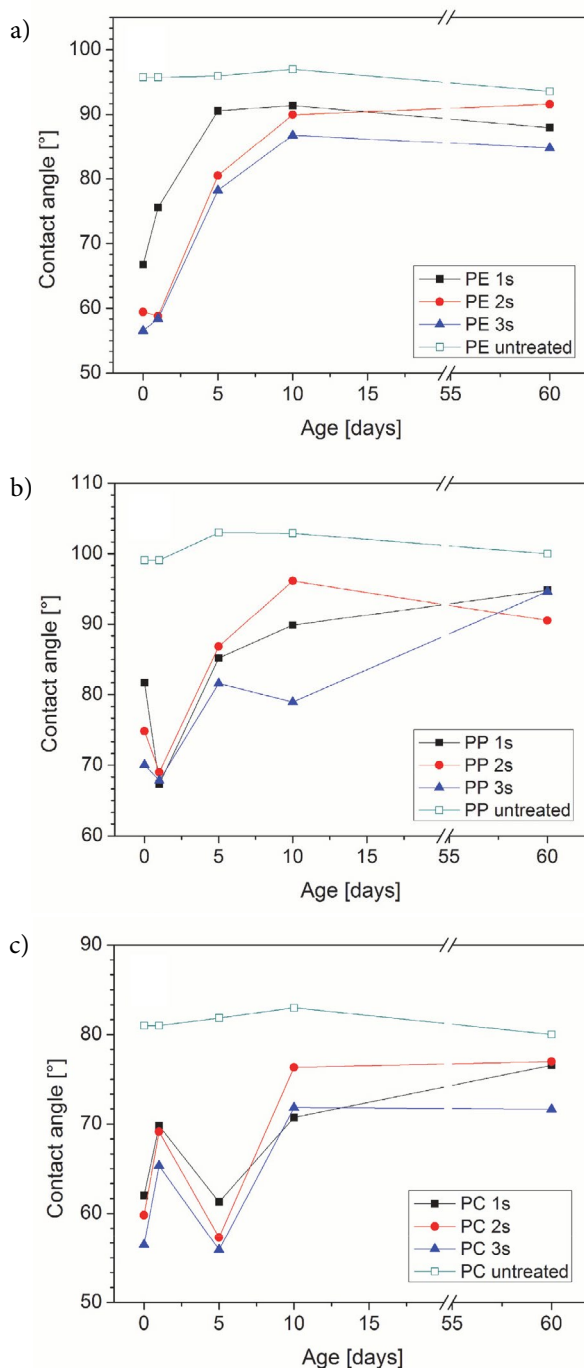


Figure 3. Measurement of contact angle of water on a) PE, b) PP and c) PC substrates after various DBD plasma treatments.

oxygen on the surface from all three studied polymers and therefore the Arcotest measurements show wetting of inks with surface tension above 56 mN/m after the plasma treatment (as already mentioned the Arcotest seems to be based on polar inks). In case of untreated PC, the oxygen content given by XPS begins at higher values and as a consequence the pull-off pressure (of water based paint) is significantly higher than in case of the PE and PP. After the plasma treatment the oxygen contents is increased which

in turn results in increased pull-off pressure and lowered contact angle. The oxygen content then returns to the initial values, however the wetting remains significantly increased (σ over 44 mN/m) after aging. It is possible that some of the polar groups created by the plasma remained on the PC surface, but the XPS is not sensitive enough to distinguish those different conditions of the surface.

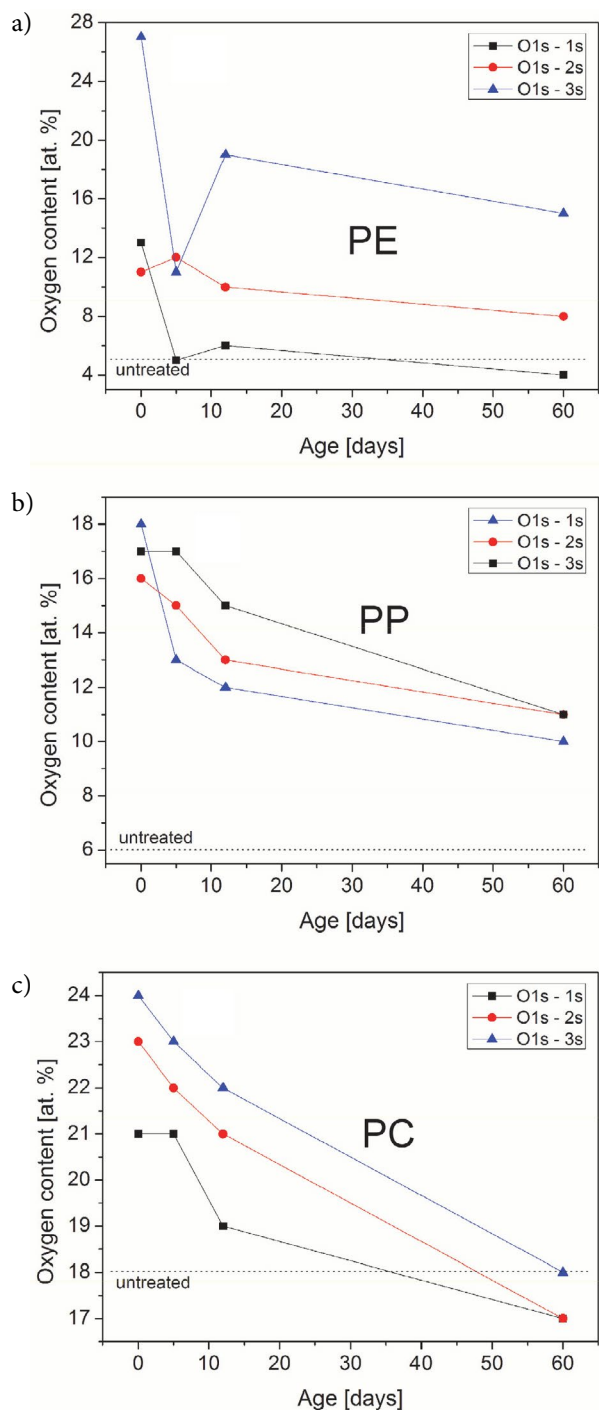


Figure 4. Oxygen contents on plasma treated a) PE, b) PP and c) PC surfaces in atomic % given by XPS. The dashed lines show the oxygen content of untreated polymers.

3. 5. AFM Results

Images of 4 different scan sizes were taken for untreated samples and 3 s long treated ones. Scans with square sides 50 μm , 30 μm , 10 μm and 5 μm were recorded. The roughness differs for all scan sizes for various reasons – the true size of one image point (pixel) differs, the irregular

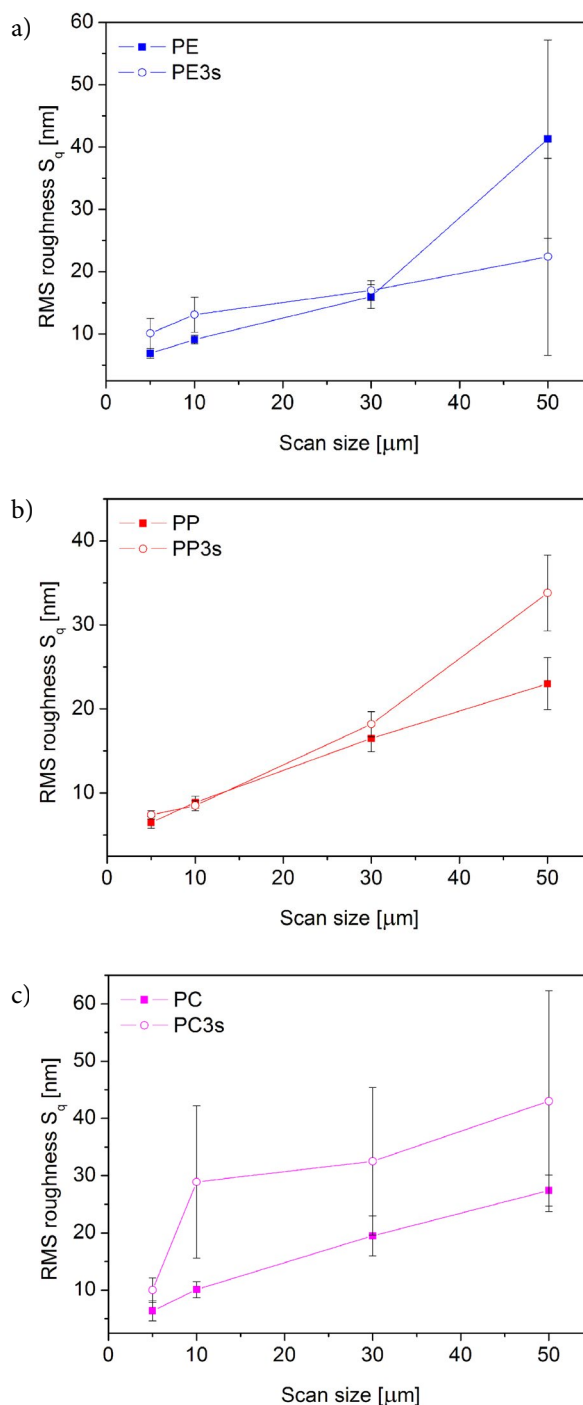


Figure 5. Root mean square roughness calculated from AFM images of untreated (filled squares) and plasma treated samples (circles). 10 μm scan size is optimal.

Table 2. Roughness values and their standard deviations calculated from AFM scans.

	50 μm		30 μm		10 μm		5 μm	
	S_a [nm]	S_q [nm]	S_a [nm]	S_q [nm]	S_a [nm]	S_q [nm]	S_a [nm]	S_q [nm]
PE	25.3 \pm 6.3	41.3 \pm 15.9	12.3 \pm 1.4	16.0 \pm 1.9	7.2 \pm 0.6	9.1 \pm 0.7	5.6 \pm 0.6	6.9 \pm 0.8
PE 3s	15.3 \pm 7.0	22.4 \pm 15.8	13.1 \pm 1.2	17.0 \pm 1.6	10.1 \pm 2.1	13.1 \pm 2.8	7.6 \pm 2.0	10.1 \pm 2.4
PP	18.0 \pm 3.0	23.0 \pm 3.1	12.8 \pm 1.3	16.5 \pm 1.6	6.9 \pm 0.6	8.9 \pm 0.7	4.9 \pm 0.5	6.5 \pm 0.7
PP 3s	26.6 \pm 2.5	33.8 \pm 4.5	14.6 \pm 1.4	18.2 \pm 1.5	6.5 \pm 0.5	8.5 \pm 0.6	5.7 \pm 0.4	7.4 \pm 0.5
PC	20.3 \pm 3.0	27.4 \pm 2.7	14.7 \pm 2.8	19.5 \pm 3.5	7.6 \pm 1.2	10.1 \pm 1.4	5.0 \pm 1.7	6.4 \pm 1.8
PC 3s	30.4 \pm 13.3	43.0 \pm 19.3	23.5 \pm 8.8	32.5 \pm 12.9	24.2 \pm 12.0	28.9 \pm 13.3	7.8 \pm 1.8	10.0 \pm 2.1

surface features can be avoided in case of smaller scan sizes. Roughness values obtained are given in Table 2 together with their standard deviations. Each number (number pair respectively – S_a and S_q are computed from the same image) is calculated as mean value from 3 images. The scan size 10 μm can be considered as optimal. Unwanted features are mostly out of the scan area while the scan is big enough to be representative sample of the surface.

In all cases, small increase of the roughness was observed. Although the difference is not very big compared e.g. to T. Shao or M. Gao, the roughness increase can support the chemical changes induced by the plasma treatment.^{17,23} The roughness difference in case of the PC scan (size 10 μm) is quite large, but the data obtained for plasma treated PC were quite noisy – lots of horizontal streaks had to be removed. The fourier transform filtering helped, but still the quality of the scans on PC was lower and deviation of the values is large. The root mean square roughness can be seen in Figure 5. The average roughness has similar tendency

4. Conclusions

Three polymers (PE, PP, PC) were treated by DBD plasma discharge in air. In all cases, improvement of desired properties was achieved, i.e. pull-off test showed increased adhesion of water based and solvent based paints. The solvent based paint adhesion was probably improved due to presence of oxygen containing compounds in the paint. The results of other techniques are in good agreement with the pull-off tests – oxygen content (XPS) increases after plasma treatment, contact angle decreases and surface energy (Arcotest) is increased and the polymer surface is wetted by testing liquid with $\sigma = 56$ mN/m. The AFM measurements of roughness confirmed, that chemical changes were supported by small increase of roughness. The aging affects all of the polymers and hydrophobic recovery probably takes place. The PE is the polymer most prone to the aging in this case. Most stable behaviour was observed in case of PP, which may be given by its structure where the polymer chains have limited degrees of freedom compared to PE. Adhesion of the water based paint seems to be controlled by the polar groups

while the adhesion of the solvent based paint is not influenced by them.

5. Acknowledgements

The publication is a result of the project Development of the UniCRE Centre (project code LO1606) which was financially supported by the Ministry of Education, Youth and Sports of the Czech Republic under the National Programme for Sustainability I. The publication is a result of the project „Development of textile products from non-combustible and recyclable materials“, registration number CZ.01.1.02/0.0/0.0/16_084/0010282, were obtained through the financial support of the Ministry of Industry and Trade in the framework of the targeted support of the “Application III”, the Operational Programme Enterprise and Innovations for Competitiveness. This research was supported by grant within student grant competition at University of J.E.Purkyně in Ústí nad Labem, project No.: UJEP-SGS-2018-53-006-3.

6. References

1. D. M. Brews, D. Briggs, *Polym.* **1981**, 22, 7–16. DOI:10.1016/0032-3861(81)90068-9
2. Add R. A. Wolf in: *Plastic surface modification: surface treatment, decoration, and adhesion* Hanser Publications, München, Germany, **2010**.
3. C. M. Chan, T. M. Ko, H. Hiraoka, *Surf. Sci. Rep.* **1996**, 24, 1–54. DOI:10.1016/0167-5729(96)80003-3
4. M. R. Wertheimer, A. C. Fozza, A. Holländer, *Nucl. Instrum. Methods Phys. Res. B* **1999**, 151, 65–75. DOI:10.1016/S0168-583X(99)00073-7
5. P. Favia, R. d'Agostino, *Surf. Coat. Technol.* **1998**, 98, 1102–1106. DOI:10.1016/S0257-8972(97)00285-5
6. T. Shen, Y. Liu, Y. Zhu, D.-Q. Yang, E. Sacher, *Appl. Surf. Sci.* **2017**, 411, 411–418. DOI:10.1016/j.apsusc.2017.03.149
7. F. Arefi-Khonsari, J. Kurdi, M. Tatoulian, J. Amouroux, *Surf. Coat. Technol.* **2001**, 142, 437–448. DOI:10.1016/S0257-8972(01)01240-3
8. E. M. Liston, L. Martinu, M. R. Wertheimer, *J. Adhes. Sci. Technol.* **1993**, 7, 1091–1127. DOI:10.1163/156856193X00600

9. M. H. Blees, G. B. Winkelman, A. R. Balkende, J. M. J. den Toonder, *Thin Solid Films* **2000**, 359, 1–13. DOI:10.1016/S0040-6090(99)00729-4
10. M. A. Naveed, A. Qayyum, S. Ali, M. Zakaullah, *Phys. Letters A* **2006**, 359, 499–503. DOI:10.1016/j.physleta.2006.07.002
11. F. J. Andrade, W.C. Wetzel, G. C.-Y. Chan, G. Gamez, S. J. Ray, G. M. Hieftje, *J. Anal. At. Spectrom.* **2006**, 21, 1175–1184. DOI:10.1039/b607544d
12. <https://arcotest.info/wp-content/uploads/2018/06/arcotest-english.pdf> (accessed: April 4, 2019)
13. J. Behnish, A. Holländer, H. Zimmermann, *Surf. Coat. Technol.* **1993**, 59, 356–358. DOI:10.1016/0257-8972(93)90112-2
14. S. H. Park, S. D. Kim, *Colloids Surf. A Physicochem. Eng. Asp.* **1998**, 133, 33–39.
15. J. P. Píchal, L. Aubrecht, J. Hladík, P. Špatenka, *Czech. J. Phys.* **2006**, 56, B1290–B1294. DOI:10.1007/s10582-006-0364-3
16. Ch. Liu, N. Cui, N. M. D. Brown, B. J. Meenan, *Surf. Coat. Technol.* **2004**, 185, 311–320. DOI:10.1016/j.surfcoat.2004.01.024
17. T. Shao, C. Zhang, K. Long, D. Zhang, J. Wang, P. Yan, Y. Zhou, *Appl. Surf. Sci.* **2010**, 256, 3888–3894. DOI:10.1016/j.apsusc.2010.01.045
18. N. De Geyter, R. Morent, C. Leys, L. Gengembre, E. Payen, *Surf. Coat. Technol.* **2007**, 201, 7066–7075. DOI:10.1016/j.surfcoat.2007.01.008
19. N. Encias, B. Díaz-Benito, J. Abenojar, M. A. Martínez, *Surf. Coat. Technol.* **2010**, 205, 396–402. DOI:10.1016/j.surfcoat.2010.06.069
20. T. R. Gengenbach, Z. R. Vasic, R. C. Chatelier, H. J. Griesser, *Plasma Polym.* **1996**, 1, 207–228. DOI:10.1007/BF02532817
21. M. Motrazavi, M. Nosovsky, *Appl. Surf. Sci.* **2012**, 258, 6876–6883. DOI:10.1016/j.apsusc.2012.03.122
22. D. Hegemann, E. Lorusso, M.-I. Butron-Garcia, N. E. Blanchard, P. Rupper, P. Favia, M. Heuberger, M. Vandembossche, *Langmuir* **2016**, 32, 651–654. DOI:10.1021/acs.langmuir.5b03913
23. M. Gao, L. Sun, Y. Guo, J. Shi, J. Zhang, *Chem. Phys. Lett.* **2017**, 689, 179–184. DOI:10.1016/j.cplett.2017.10.009

Povzetek

Substrate iz polietilena (PE), polipropilena (PP) in polikarbonata (PC) smo obdelali z dielektrično barierno razelektrivno plazmo (DBD) na zraku (1 s, 2 s, 3 s). Oprijem dveh vrst barv (na vodni osnovi in na osnovi topil) smo preučevali s preizkusom z odtrganjem (pull-off test). Za pridobivanje informacij o površini vzorcev smo uporabili tudi druge metode. Z meritvami kontaktnega kota vode, Arcotestom (komercialni test z uporabo tekočin z določeno površinsko napetostjo) in rentgensko fotoelektronsko spektroskopijo (XPS) smo pridobili podatke o kemijski sestavi površine vzorca. Preizkus z odtrganjem je potrdil povečan oprijem obeh vrst barv, kar je povezano z vsebnostjo kisika, ki smo jo potrdili z rentgensko fotoelektronsko spektroskopijo (XPS). Tudi po daljšem časovnem obdobju (60 dni) so vzorci ohranili svoje izboljšane lastnosti.



Except when otherwise noted, articles in this journal are published under the terms and conditions of the Creative Commons Attribution 4.0 International License

Scientific paper

Adsorption of Acid Violet 17 onto Acid-Activated Pistachio Shell: Isotherm, Kinetic and Thermodynamic Studies

İlknur Şentürk* and Mazen Alzein

Department of Environmental Engineering, Faculty of Engineering, Sivas Cumhuriyet University, 58140, Sivas, Turkey

* Corresponding author: E-mail: ilknurg.senturk@gmail.com

Tel: +90 2191010/2445; Fax: +903462191165

Received: 04-12-2019

Abstract

The pistachio shell was modified using different chemical agents and utilized as an adsorbent for the adsorption of AV 17 dye in an aqueous solution. Maximum removal of 93.04% was obtained for pistachio shell activated with 10 N H₂SO₄. The physicochemical properties of activated pistachio shell were characterized by pH_{pzc}, FTIR, BET, and SEM-EDX analysis. The results showed that the AV 17 adsorption capacity was positively correlated to the BET surface area. The best fit of kinetic data to pseudo-second-order kinetic was determined. The adsorption follows both the Langmuir and Temkin isotherms. The Langmuir adsorption capacity was determined to be 26.455 mg/g at the initial dye concentration of 160 mg/L. The endothermic nature of adsorption was confirmed by the acquired thermodynamic data. Maximum desorption of 97.33% was achieved in 0.2 M NaOH for AAPS in the first cycle. This is very important for the economic use of the adsorbent. The findings demonstrate that activated pistachio shell may be a good alternative for color removal from industrial effluents.

Keywords: Acid Violet 17; adsorption; chemical activation; regeneration; Akaike's Information Criterion Test (AIC).

1. Introduction

Colored compounds containing pigments and dyes are commonly utilized in the food, textile, pharmaceutical, plastic, paper, leather, and cosmetics industries. These dyes form an aesthetically unacceptable color in the receiving waters. Furthermore, they cause serious environmental problems, carcinogenic and mutagenic effects on aquatic life due to their possible accumulation in the environment and high toxicity even at very high concentrations.^{1,2} Most of these dyes, acid dyes, in particular, are highly soluble in water because of the presence of sulphonic acid groups. Acidic dyes are commonly utilized to color products in the textile, leather, paper, printing and plastic industries.

It is necessary to treat such colored wastewaters to protect the environment and aquatic life. Due to the complex structures they have, it is quite difficult to discolor such wastewaters by conventional chemical and biological wastewater treatment methods (e.g. chemical flocculation, flotation, sedimentation, chemical oxidation and biological techniques).³ Because dyes are resistant to heat, light and microbial attacks due to their complex aromatic mo-

lecular structure and synthetic origin.⁴ Therefore, alternative treatment methods should be considered. Adsorption is a widely preferred method in the treatment of dyed wastewaters due to the absence of hazardous by-product formation, simplicity of design, ease of use, non-sensitivity to toxic substances, the ability to treat dyes in a more concentrated form, being cheaper and more efficient than other methods, and flexibility in operation.⁵ Activated carbon is among the most effective and most common adsorbents used for the adsorption process because of its effect and versatility. Nevertheless, commercially available activated carbon is quite expensive. Agricultural waste-based biomass can be used as an alternative to commercial activated carbon in the treatment of such dyed wastewaters with adsorption because the economic value of such agricultural waste materials is either absent or very little. It is observed that such adsorbents used in many studies provide effective results in color removal originating from dyes.^{1,2,5-7}

Pistachio takes place among the most favorite tree nuts in the world. Pistachio trees naturally grow in dry and desert climate areas and represent native species to Iran, Syria, Greece, Turkey, the United States, China, Afghani-

stan, Pakistan, and Turkmenistan.⁸ In 2016, the United States and Iran were the main producers of pistachio, and they accounted for 68% of the total world production of pistachio, which was 1.1 million tonnes. Turkey and China were determined to be the secondary producers of pistachio. Pistachio shell is generally used as a boiler fuel or sent to landfill as a waste. Thus, it will be useful to develop a new low-cost adsorbent from the pistachio shell, an agricultural waste. In this study, the acid-activated pistachio shell selected after different activation procedures was utilized as an adsorbent for the color removal of Acid Violet 17. The impacts of various operating parameters, including pH, the dosage of adsorbent, time, initial dye concentration, temperature, ionic strength, and desorption, on the extent of adsorption in batch operation were examined, and optimal experimental conditions were determined. This study aimed to evaluate the adsorption capabilities of acid-activated pistachio shell in liquid media against Acid Violet 17 dye that is considered to be a model of acidic dye due to the presence of sulfonic groups in its structure.

2. Material and Methods

2.1. Adsorbent

Pistachio shell utilized in the present research was obtained from pistachios purchased from the local market. Firstly, the shells were washed with tap water and then washed several times with distilled water for the removal of dirt, dust and other impurities on their surface. At the end of washing, they were dried in the oven at 103–105 °C until a constant weight was achieved. The dried shells were then milled and sieved. The particles $-1.0 + 0.71$ mm (USA standard mesh chart) in size were used both as a raw material and in the preparation of acid-activated pistachio shell (activated carbon materials). All adsorbents were washed a few times using distilled water until the neutral pH of the filtrate was achieved. Afterward, the washed materials were dried at a temperature of 80 °C for a period of 24 hours in the oven.

2.1.1. Activation with H₂SO₄

25 mL of 1, 5, 10 and 15 N H₂SO₄ solution was taken, and 4 g of pistachio shell prepared for use in the experiments was added to it and mixed in a 250 mL Erlenmeyer flask. It was kept in a muffle furnace at a temperature of 353 K for a period of 24 h with the closed mouth of the Erlenmeyer flask. Following the treatment, cooling of all the samples to room temperature was performed; they were washed using distilled water until the neutral pH of the filtrate was achieved. The obtained activated carbon materials were dried in the oven at the temperature of 80 °C.⁹ The adsorbent was placed in an airtight container for use in further studies. The obtained material was called as an acid-activated pistachio shell (AAPS).

2.1.2. Activation with NaOH

4 g of pistachio shell ready for use in the experiments and 100 mL of 0.25 M NaOH solution were mixed at 300 rpm at 30 °C for 4 hours. To remove excess NaOH from the adsorbent's surface separated by the filter at the end of the process, it was washed a few times using distilled water until neutral pH was achieved and allowed to dry overnight in the oven at 80°C.¹⁰ The adsorbent was placed in the airtight container for use in further studies.

2.1.3. Activation with CTAB

20 g of pistachio shell ready for use in the experiments and 200 mL of 4% of cetyl trimethyl ammonium bromide (CTAB) solution were mixed at 150 rpm at 30 °C for 24 hours. The adsorbent separated by filtration at the end of the process was washed a few times using distilled water and allowed to dry in the oven at 70 °C.¹¹ The adsorbent was placed in the airtight container for use in further studies.

Furthermore, the adsorption capacity of the new adsorbent obtained by reactivating with 5 and 10 N H₂SO₄ solution as described in section 2.1.1 of the adsorbent activated with CTAB was investigated.

2.2. Pollutant Dye

C. I. Acid Violet 17 (MF, C₄₁H₄₄N₃NaO₆S₂, MA = 761.93 g/mol, λ_{\max} = 542 nm) dye is an anionic azo dye chosen as a model dye in the present research. The dye has a dark purple/dark violet color. The stock dye solution was prepared by weighing the dye and dissolving it in distilled water at the concentration of 1 g/L. Dilutions were made from the stock solution to the desired concentration and used in the studies. The chemical structure of Acid Violet 17 (AV 17) dye is presented in Fig. 1.

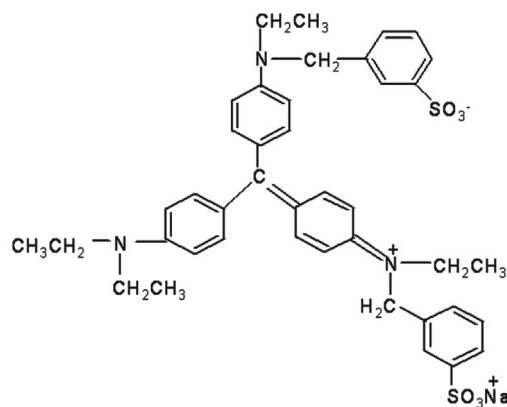


Fig. 1. Chemical Structure of Acid Violet 17.²

2.3. Instruments and Analysis Method

A scanning electron microscope (SEM, Tescan Mira3 XMU) was utilized to determine the morphological

properties and surface characteristics of the acid-activated pistachio shell adsorbent. Fourier transform infrared spectroscopy (FTIR, Bruker Tensor II) was employed to identify functional groups on the adsorbent. The specific surface area and micropore volume of the samples were measured using N_2 adsorption–desorption (AUTOSORB 1C) at -196 °C. Prior to adsorption, the samples were evacuated until a pressure of 66.6 Pa at room temperature was reached, then heated up to 50 °C and evacuated until a pressure of 1.3 Pa was reached. This condition was maintained overnight. The surface area, total pore volume and micropore volume were determined by multipoint BET, DFT (Density Functional Theory) and DR (Dubinin–Radushkevich), respectively.¹² The solid addition method was employed for determining the point of zero charge (pH_{pzc}) of the acid-activated pistachio shell. Preparation of a series of 0.1 M KNO_3 solutions (50 mL each) was performed, and their pH was set in the interval of 1.0–12.0 as a result of adding 0.1 N HCl and NaOH. Addition of 0.1 g of the adsorbent was performed to every solution, and the suspensions were shaken, and the resulting solution was shaken for the period of 48 h. The resulting pH of the solution was recorded, and a graph of the difference between the initial and final pH (ΔpH) (Y-axis) was plotted against the initial pH (X-axis). The point of zero charge was obtained at the point of intersection of the mentioned curve.¹³

The concentration of the residual dye was analyzed by the UV-Visible spectrophotometer (Spectroquant Pharo 300, Merck) at a maximum wavelength of 542 nm. The unknown AV 17 concentration was determined by using the standard curve obtained from the relationship between absorbance and concentration for AV 17. The correlation coefficient, R^2 value, was determined to be 0.9997.

2. 4. Adsorption Experiments

Batch experiments were performed in a thermoshake incubator shaker (Gerhardt, Germany) operating at a constant speed of 125 rpm with a working volume of 75 mL prepared at the desired conditions at 30 °C. The effects of various working parameters such as contact time, pH, adsorbent dose, initial dye concentration, temperature, and ionic strength on AV 17 dye removal were investigated.

The study conditions of the adsorption experiments carried out under different experimental conditions are presented in Table 1.

Dye concentration in supernatant samples after agitating for 4 h was determined spectrophotometrically by monitoring the absorbance change of the dye solution that was separated from the adsorbent by centrifugation of the mixture at 5000 rpm for 10 min for all studies except for determining the equilibrium time. The experiments were performed in duplicate, and the negative controls (without the sorbent added) were conducted at the same time for the purpose of ensuring sorption by the adsorbent material, not by the flask. During the analysis, the values of percentage removal and the amount of dye adsorbed were computed by utilizing the equations presented below:

$$\text{Dye removal (\%)} = \frac{C_i - C_e}{C_i} 100 \quad (1)$$

$$q_e = \frac{(C_i - C_e)V}{m} \quad (2)$$

Where q_e denotes the adsorption capacity (the dye that is adsorbed onto the mass unit of the adsorbent, mg/g), C_i and C_e denote the initial dye concentration and the equilibrium dye concentration, respectively (mg/L), and m denotes the adsorbent dose (g), and V denotes the volume of dye solution (L).

2. 5. Impact of Ionic Strength

Generally, a higher salt concentration is determined in textile wastewater. Therefore, the impacts of ionic strength on the adsorption of dye must be investigated.¹⁴ The additional agents including salts and surfactants are commonly found in the textile industry wastewater. Adsorption is sensitive to the alteration in ionic strength. Two possible impacts of salts during wastewater treatment are as follows: (i) The equilibrium dye removal generally decreases (ii) Contrary to expectations, dye removal increases as the dye dissolution may be increased by the presence of the foreign salts.¹⁴ Hence, the impact of ionic strength on the adsorption efficiency of the adsorbent was investigated in the present research. The impact of ion strength

Table 1. Experimental conditions of the adsorption study.

Process parameter varied	Initial dye conc. (mg/L)	Dose (g/L)	Contact time	Initial pH	Temperature (K)
Contact time	40	10	0–360 min	Solution pH	303
Initial pH	40	10	4 h	2–12	303
Initial dye concentration	40, 80, 160	4–20	4 h	Solution pH	303
Dose	40, 80, 160	4–20	4 h	Solution pH	303
Temperature	20–400	10	4 h	Solution pH	303, 313, 323
Ionic strength (0.05–0.25M)	80	10	4 h	Solution pH	313

on the adsorption of dyes was tested with the addition of NaCl, SDS, and CTAB in the range of 0.05–0.25 M to the solution.

2. 6. Desorption Studies

Desorption studies help to explain adsorbate and adsorbent recovery and the adsorption mechanism. Since the regeneration of the adsorbent makes the treatment process economical, desorption studies were performed to regenerate the spent adsorbent. 75 mL of AV 17 solution with a concentration of 60 mg/L was taken and mixed with 1 g of fresh AAPS until equilibrium was reached (4 h). The AAPS adsorbent was then removed from the medium by centrifugation. 1 g of the dye-loaded adsorbent obtained (0.1, 0.2, 0.4, 0.8 M) was mixed separately with 100 mL of HCl, NaCl, CH₃COOH, NaOH desorption agents prepared at different concentrations (0.1, 0.2, 0.4, 0.8 M) and solvents (ethanol and distilled water) in the orbital mixer operating at 125 rpm. Desorption was performed in two different time periods, 24 and 48 hours. After this process, the solu-

tion was separated by centrifugation, and the concentration of AV 17 that passed to the solution was determined spectrophotometrically. The percentage of the dye desorbed from the adsorbents is computed by means of the following formula:

$$\% \text{ Desorption} = \left(\frac{\text{Amount released to solution (mg/L)}}{\text{Total adsorbed (mg/L)}} \right) * 100 \quad (3)$$

Successive adsorption desorption studies were conducted in three cycles for the purpose of checking the reusability of the regenerated adsorbents. All the experiments, adsorption and desorption, were carried out in a batch set-up in two replicates, and the mean values were acquired.

3. Results and Discussion

3. 1. Adsorbent Characterization

An IR spectrum scan was performed in the wavelength interval of 400–4000 cm⁻¹ to acquire information

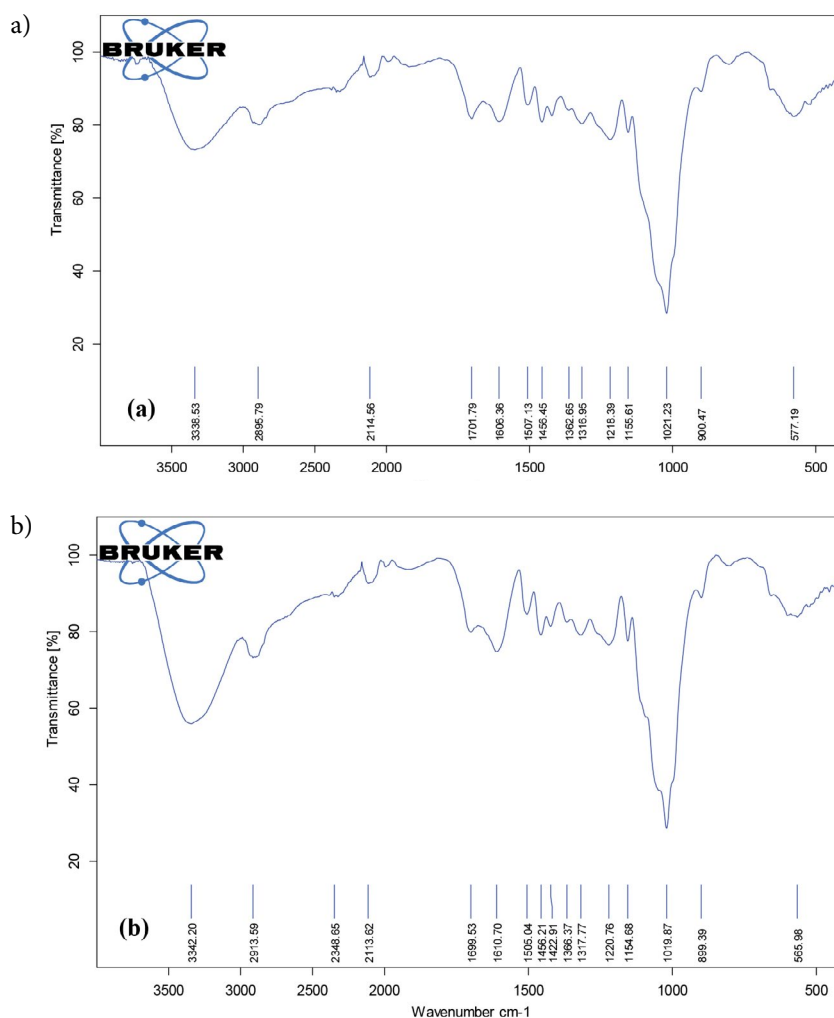


Fig. 2. FTIR spectra of (a) uncoated AAPS and (b) AV 17 coated AAPS.

about the functional groups on the adsorbent's surface and its structure. Figure 2(a,b) demonstrate the FTIR spectra of acid-activated pistachio shell prior to and following its use in the adsorption of AV 17. The peak at a wavelength of 3338.53 cm^{-1} shows that the O-H and N-N (Amines) groups are present on AAPS, which is shifted to a wavelength of 3342.20 cm^{-1} following the dye adsorption. The peak at a wavelength of 2895.79 cm^{-1} originates from C-H stretching vibrations of the alkane, which is shifted to a wavelength of 2913.59 cm^{-1} following the dye adsorption. The peak at a wavelength of 2114.56 cm^{-1} originates from $\text{C}\equiv\text{C}$ stretching, and the peak at a wavelength of 1701.79 cm^{-1} originates from $\text{C}=\text{O}$ (Aromatics) stretching. O-H vibrations at 1606.36 cm^{-1} once again proved the presence of H_2O , which is shifted to a wavelength of 1610.7 cm^{-1} following the dye adsorption. The broad band at a wavelength of 1218.39 cm^{-1} confirms the presence of strong C-O stretching.² A peak at a wavelength of 1021.23 cm^{-1} is obtained as a result of the C-N vibration of ester, which is shifted to a wavelength of 1019.87 cm^{-1} in the adsorbent's image following the dye adsorption. The peak that appeared at 577.19 cm^{-1} originates from the C-X stretching vibrations of alkyl bromide, which is shifted to a wavelength of 565.98 cm^{-1} because of the C-X stretching vibrations of alkyl chloride after the adsorption of the dye. Before (Fig. 2a) and after (Fig. 2b) adsorption, the FTIR spectra of the adsorbent showed similar features, and only peak shifts and changes in peak intensity were observed. Only two new peaks, the one at a wavelength of 2348.65 cm^{-1}

attributed to the $\text{C}\equiv\text{N}$ stretch of alkyne and the other one at a wavelength of 1422.91 cm^{-1} attributed to the C-H stretch of AV 17 dye in Fig. 2b also proved the adsorption of the dye.

The surface texture and morphological characteristics of the H_2SO_4 activated pistachio shell used as an adsorbent were viewed by a scanning electron microscope (SEM). Figure 3(a,b) demonstrate SEM images of acid-activated pistachio shell prior to and following its use in the Acid Violet 17 adsorption. The images presented in Fig. 3a for the adsorbent before adsorption demonstrate that the adsorbent's porous and rough structure was effective in the dye adsorption. Furthermore, the adsorbent's surface appears to be uneven and irregular and have cavities which may promote the interaction of the dye ions with the surface of the adsorbent causing good dye adsorption. An alteration in the rough surfaces of the adsorbent was determined following the usage in the adsorption proving the suggested mechanisms of good dye interactions causing the dye adsorption on the acid-activated pistachio shell.

Energy dispersive X-ray analysis, abbreviated as EDX, represents a common tool for accompanying SEM as well as TEM. The mentioned technique is usually employed for determining relative abundance, the composition of elements, and distribution in a sample.¹⁵ Using EDX, the composition of the acid-activated pistachio shell was studied. Fig. 4 shows that carbon, oxygen, chlorine, sulphur, and bromine atoms are the main chemical elements on the material's surface.

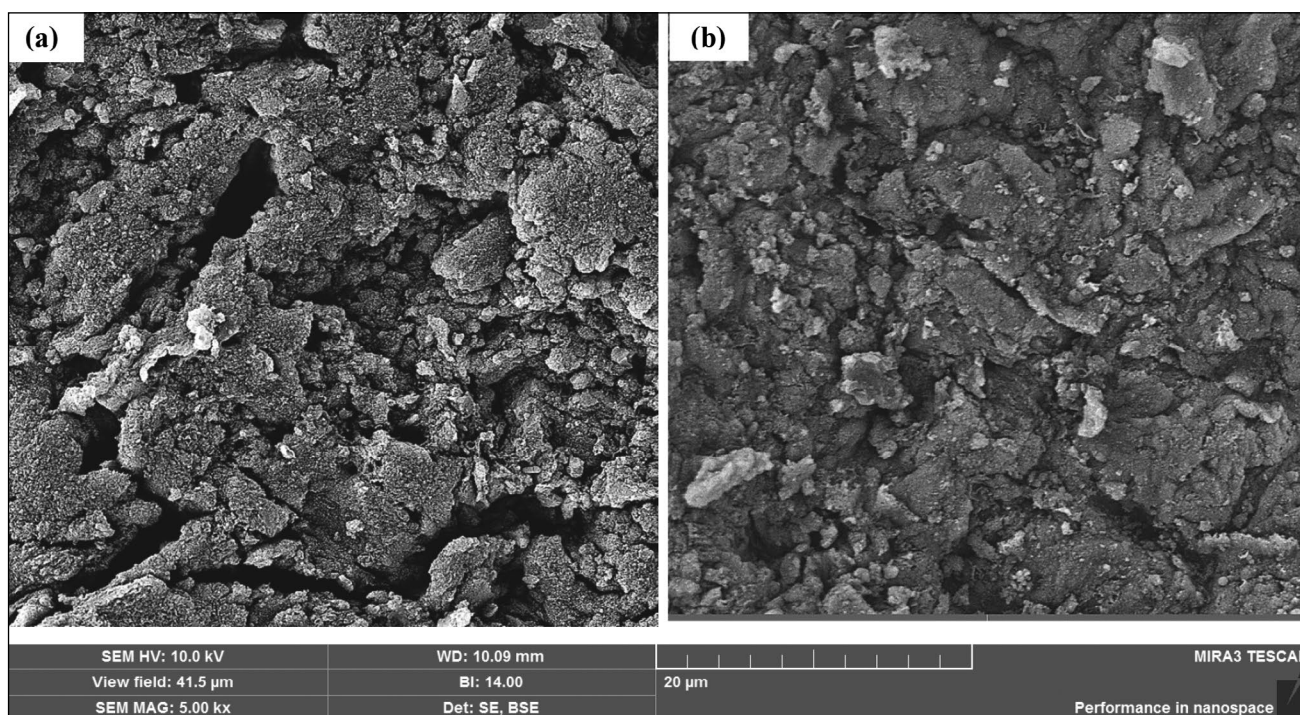


Fig. 3. SEM photograph of (a) uncoated AAPS and (b) AV 17 coated AAPS.

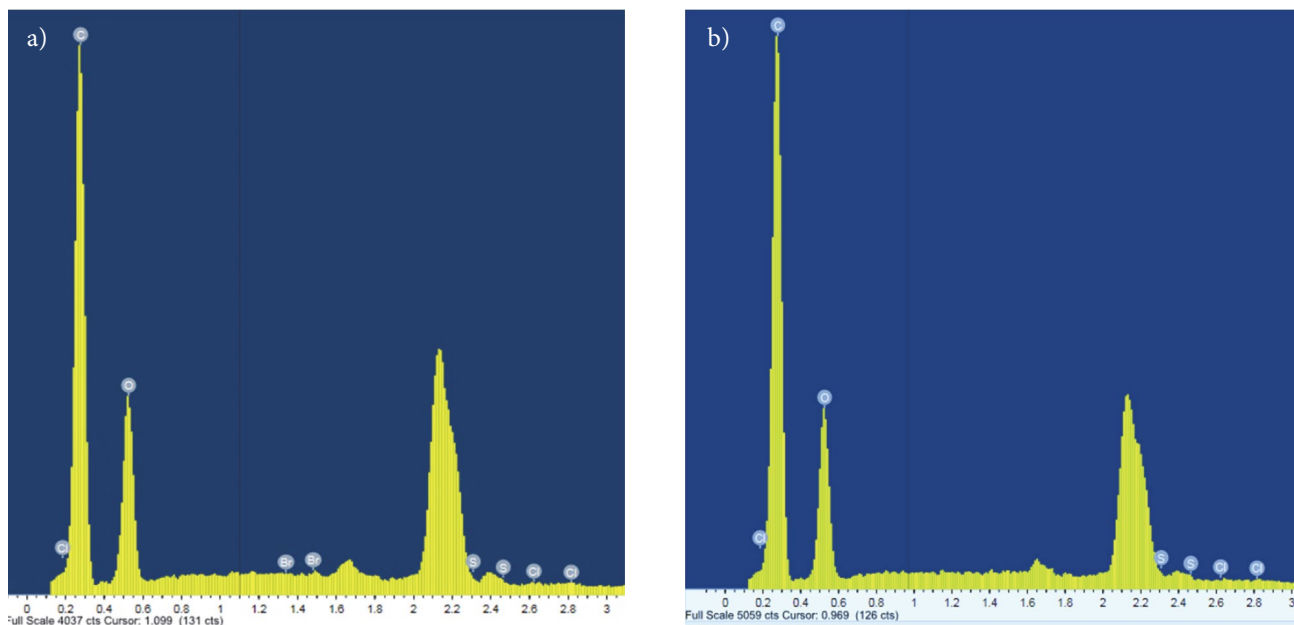


Fig. 4. EDX spectra of AAPS (a) prior to adsorption and (b) following adsorption.

The nitrogen adsorption–desorption isotherms of the natural pistachio shell and acid activated pistachio shell are shown in Fig. 5. The adsorption–desorption isotherms of samples are of type III (BET classification) according to the IUPAC classification,¹⁶ suggesting that samples contain micro- and mesoporous that allow the formation of multiple adsorbent layers with increasing P/P^0 . The acid activated pistachio shells were found to have high surface area and mesopore volumes as compared with natural pistachio shells as seen in Table 2. With the acid activation of pistachio shell, some of the existing bonds might be broken and new bonds may be formed. It might be due to the formation of micropores. As a result, the surface area of activated pistachio shell increased to $55.8 \text{ m}^2/\text{g}$ from $15.3 \text{ m}^2/\text{g}$.

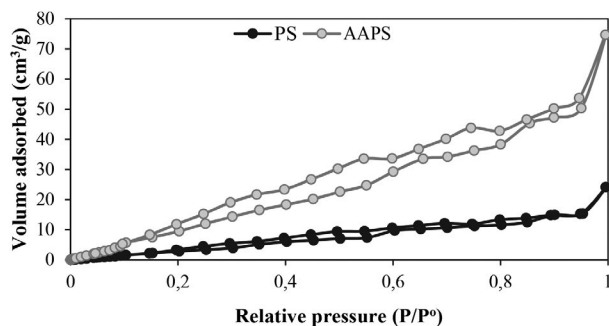


Fig. 5. The nitrogen adsorption–desorption isotherm of PS and AAPS.

The point of zero charge, in physical chemistry, is a concept used to understand the mechanism of adsorption better. As shown in Fig. 6, the point of zero charge, pH_{pzc}

Table 2. The surface area and pore characteristics of natural (PS) and acid activated pistachio shell (AAPS).

	PS	AAPS
$S_{\text{BET}}^{\text{a}}$ (m^2/g)	15.3	55.8
$V_{\text{Total}}^{\text{b}}$ (cm^3/g)	0.02	0.08
$V_{\text{micro}}^{\text{c}}$ (cm^3/g)	0.006	0.010
D_{p}^{d} (Å)	31	28

^aMultipoint BET method; ^bVolume adsorbed at $P/P^0 = 0.99$; ^cMicropore volume calculated by DR method; ^dAverage pore diameter determined by DFT

is 9.6 whereas the adsorption of cations is preferred when $\text{pH} > \text{pH}_{\text{pzc}}$, otherwise, anions are adsorbed.¹⁷ According to the results, since $\text{pH} < \text{pH}_{\text{pzc}}$, AV 17, which is an anionic dye, is preferred by the adsorbent.

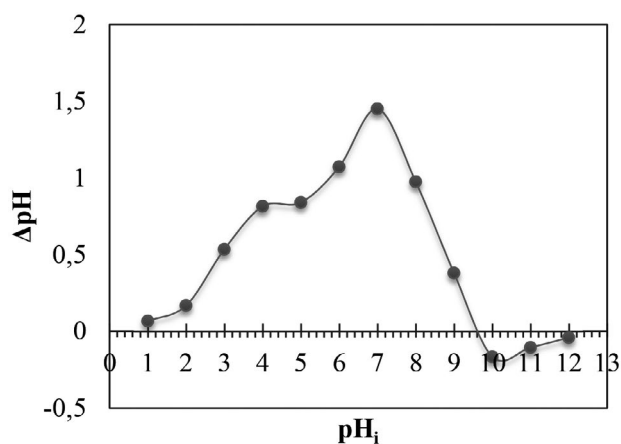


Fig. 6. pH_{pzc} of AAPS.

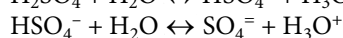
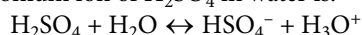
3. 2. Batch Studies

3. 2. 1. Impact of Activation Procedures on Adsorption Efficiency

In the study, the natural pistachio shell, pistachio shell activated with 0.25 N NaOH solution, pistachio shell activated with 1-5-10 and 15 N H₂SO₄, pistachio shell activated with CTAB, and pistachio shells that were again subjected to a chemical activation process with 5 and 10 N H₂SO₄ solutions after activation with CTAB were evaluated in terms of their adsorption efficiency. 75 mL of 40 mg/L AV 17 solution was taken in each Erlenmeyer flask prepared, and 0.75 g of the adsorbent was added to it. The prepared mixture was subjected to adsorption at a stirring rate of 125 rpm at 30 °C for 24 hours at the natural pH of the dye solution. At the end of 24 hours, samples taken from each Erlenmeyer flask were analyzed, and the adsorbent which could be used most efficiently for the removal of AV 17 dye was determined. The results of the study are presented in Table 3.

Activated pistachio shells and natural pistachio shell were used as adsorbent in the adsorption process for AV 17 dye removal. As a result of the studies, it was observed that efficiency of 24.35% was obtained with the natural pistachio shell and activation of the adsorbent was effective in increasing the efficiency. The best results were obtained after activation with H₂SO₄. The efficiency of AV 17 removal after activation with CTAB was 79.5%. In order to increase this efficiency, the adsorbent activated with CTAB was also reactivated with 5 N and 10 N H₂SO₄, and the removal efficiency of the new material was analyzed, and 81.4% and 93.36% efficiency was obtained, respectively.

The general reaction scheme of the distribution of hydronium ion of H₂SO₄ in water is:¹⁸



As we seen from reaction, the HSO₄⁻ and SO₄⁼ are weak bases and can be replaced by the AV 17 ions which is a stronger base. Adsorption efficiency increased with increasing H₂SO₄ activity on adsorbent. Since the same effi-

Table 3. AV 17 removal efficiency and adsorption capacity after activation.

Activation procedures	(%)	q _e (mg/g)
Natural pistachio shell	24.35	1.004
Activation with 0.25 N NaOH	67.81	2.797
Activation with 1 N H ₂ SO ₄	72.99	3.011
Activation with 5 N H ₂ SO ₄	79.43	3.276
Activation with 10 N H ₂ SO ₄	93.04	3.838
Activation with 15 N H ₂ SO ₄	94.23	3.887
Activation with CTAB	79.49	3.279
Reactivating with 5 N H ₂ SO ₄ of the adsorbent activated with CTAB	81.40	3.361
Reactivating with 10 N H ₂ SO ₄ of the adsorbent activated with CTAB	93.36	3.855

ciency was obtained after the activation of the adsorbent with 10 N H₂SO₄, it was decided that it would be appropriate to continue working with pistachio shells activated with 10 N H₂SO₄ in future studies.

Several chemical activating agents are used by researchers such as zinc chloride (ZnCl₂), phosphoric acid (H₃PO₄), potassium hydroxide (KOH), calcium chloride (CaCl₂), sulfuric acid (H₂SO₄), sodium hydroxide (NaOH), hydrochloric acid (HCl), nitric acid etc.¹⁹ This activating agents are used to modify adsorbent to increase its efficiency for adsorption.

Modification with acidic reagents will increase the hydrogen ion content (H⁺) causing increased positive charge on the material surface. This situation leading to enhanced AV 17 removal which is negatively charged. Inorganic (stronger acid) acids (HCl, H₂SO₄ and HNO₃) treatment show that the addition of H₂SO₄ increases adsorbent yield, surface area and porosity.²⁰ The same results were also encountered in our study.

3. 2. 2. Impact of Contact Time (Kinetics Study)

The effect of contact time on the removal of AV 17 by adsorption was studied under the conditions given in Ta-

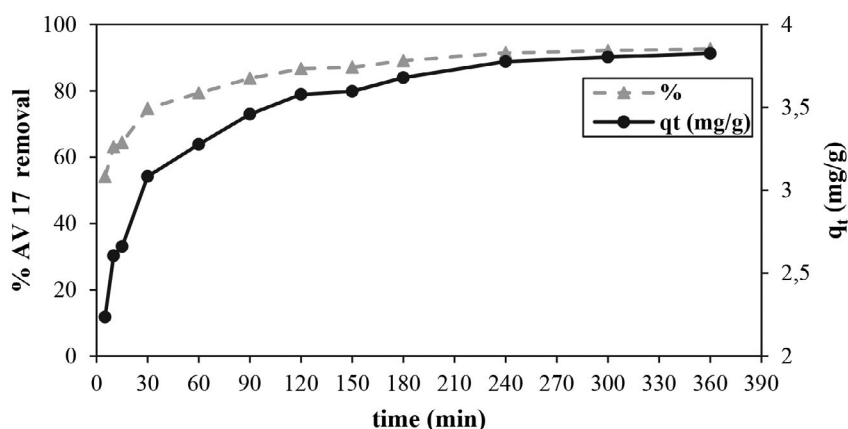


Fig. 7. Impact of agitation time on the adsorption of AV 17 by AAPS.

ble 1, and the relevant data are given in Fig. 7. It is observed from Fig. 7 that the process was initially very rapid and 54% color removal was obtained in the first 5 minutes. 92% removal was achieved at the end of 4 hours. The relative increase in the extent of dye removal following 240 min of contact time was found to be insignificant. This is probably because of the accumulation of dyes on the available adsorption sites on the adsorbent material. Hence, 240 min contact time is fixed as the optimal contact time.

3. 2. 2. 1. Kinetics of Adsorption

The adsorptive uptake of dye at various time intervals was analyzed for the purpose of determining the kinetics of adsorption. The data acquired from adsorption kinetic studies were assessed with the help of various kinetic models selected for the purpose of investigating the adsorption dynamics that control the sorption process, including diffusion control, chemical reaction and mass transfer. The kinetic parameters that can help in predicting the adsorption rate provide significant information to design and model the adsorption process.^{21,22} Thus, models including pseudo-first-order, pseudo-second-order, intra-particle diffusion, and Elovich, which are commonly utilized for the adsorption of pollutants from liquid solutions, were implemented for the data obtained from experimental studies to determine the adsorption kinetics. A summary of the models and constants and the determination coefficients for the linear regression plots of AV 17 dye are presented in Table 4. As is seen in Table 4, higher R^2 values were acquired for pseudo-second-order compared to the other adsorption rate models, which demonstrated that the pseudo-second-order rate could describe the adsorption rates of AV 17 onto the AAPS adsorbent more appropriately in comparison with the other models because of its high correlation coefficient ($R^2 = 0.9995$).

The Δq (the standard deviation between the experimental and computed adsorption capacities) values in Table 4 also prove the perfect fit of experimental results to the pseudo-second-order model. However, the pseudo-second-order kinetic model cannot describe the diffusion mechanism alone. The transfer of the dissolved matter in an adsorption system can be characterized by intra-parti-

cle diffusion or by both models.²³ Therefore, the intra-particle diffusion model was also implemented for the data obtained from kinetic studies for the purpose of explaining the diffusion mechanism. However, the low R^2 value obtained demonstrated that the adsorption process alone does not depend on the intra-particle diffusion model and that the diffusion mechanism can be characterized by both models together.

When C is zero, the intra-particle diffusion represents the sole rate-limiting step, and with an increase in the value of C , the contribution of surface adsorption increases. The plots were determined to be not linear in the whole time range. However, it was possible to separate them into two-three linear regions, indicating the presence of multiple stages to the adsorption process.²¹ The R^2 values are <0.9 (Table 4), which demonstrates that intra-particle diffusion cannot describe the adsorption of AV 17 on AAPS, and due to the fact that the mentioned lines do not pass through the origin, it is possible to conclude that intra-particle diffusion does not represent the sole rate controlling step.

3. 2. 3. Impact of Initial pH

The pH value of the solution is very significant in the process of adsorption since it affects the surface loads of dye and adsorbent materials. The impact of the initial pH of the dye solution on the amount of adsorbed AV 17 dye was investigated by changing the initial pH value between 2–12 while the other parameters were kept constant (Table 1). Dilute HCl or NaOH (0.1 M) solutions were utilized to adjust pH. The results are shown in Fig. 8. After pH 6, some decrease (2%) was observed in the removal efficiency. The change in adsorption capacity was also slight. The pH of the dye solution is 6.1. In accordance with the findings presented above, a pH of 6.1 was selected as the optimum pH to remove AV 17 in the future experiments.

Due to the presence of the sulphonate group, AV 17 carries a negative charge in the aquatic solution. Therefore, for effective dye removal, the adsorbent surface must have positive charges.⁵ Since the AAPS surface has negative charges, it is observed that the removal efficiency increases

Table 4. Modeling of adsorption kinetics.

Model	Pseudo-first-order equation	Pseudo-second-order equation	Weber-Morris	Elovich
Equation	$\ln(q_e - q_t) = \ln q_e - k_1 t$ ²⁴	$t/q_t = (1/k_2 q_e^2) + t/q_e$ ²⁴	$q_t = k_d t^{1/2} + C$ ²⁵	$q_t = \beta \ln(\alpha) + \beta \ln t$ ²⁶
Plot	$\ln(q_e - q_t)$ vs. t	(t/q_t) vs. t	q_t vs. $t^{1/2}$	q_t vs. $\ln t$
Fitted model	$\ln(q_e - q_t) = -0.0146t + 0.2768$	$t/q_t = 2.091 + 0.2573t$	$q_t = 0.0883 t^{1/2} + 2.4123$	$q_t = 0.3766 \ln(\alpha) + 0.3766 \ln t$
R^2	0.9762	0.9995	0.8698	0.9868
Constant	$k_1 = 0.0146 \text{ dk}^{-1}$	$k_2 = 0.0318 \text{ mg}/(\text{g dk})$	$k_d = 0.0883 \text{ mg}/\text{g dk}^{1/2}$	$\alpha = 93.344 \text{ mg}/\text{g dk}$ $\beta = 0.3766 \text{ g}/\text{mg}$
q_e ($q_{e,cal}$)	1.319 mg/g	3.886 mg/g	–	–
q_e ($q_{e,exp}$)	3.776 mg/g	3.776 mg/g	–	–
Δq	1.737	0.077		

when the pH value of the solution is in the range of 5–6 because pH affects the surface characteristics of the adsorbent and dissociation of the dye molecules. The adsorbent's zero-point charge (pH_{zpc}) was found to be 9.6. Fig. 8 shows that the maximum dye removal is at pH 6, i.e. $\text{pH} < \text{pH}_{\text{zpc}}$. In this case, because the positive charge density on the AAPS increases, the adsorption of an anionic dye AV17 also increases. If the exact opposite situation occurred, i.e. $\text{pH} > \text{pH}_{\text{zpc}}$, the adsorption of anionic dyes on AAPS would not be possible due to the propulsive electrostatic force caused by the same charges, since the negative charge density on the adsorbent would increase.

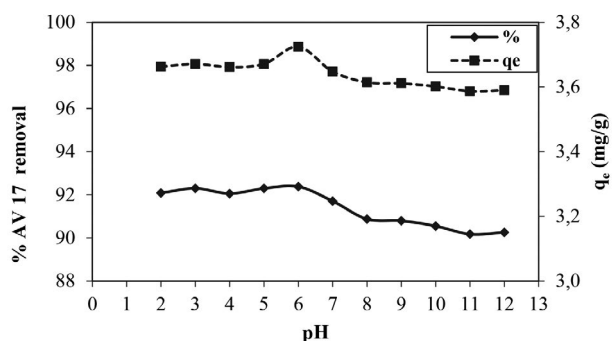


Fig. 8. Impact of pH on the removal of AV 17 onto AAPS.

3. 2. 4. Impact of Dye Concentration and Adsorbent Dosage

Since the adsorbent determines the adsorbent capacity for the given initial concentration, the adsorbent dosage is a significant parameter. The impact of AAPS quantity on the removal of AV 17 was examined, and the findings are presented in Fig. 9. As stated, the amount adsorbed in the unit mass of the adsorbent decreased with an increase in the adsorbent dosage. A decrease in q_e with the increasing dose may be caused by the overlapping of adsorption sites as a result of overloading the adsorbent particles. Likewise, as the concentration of the dye solution increased, the amount of the adsorbed dye also increased. In the adsorbent dosage of 4 g/L, the adsorption capacity was 8.173 mg/g at the dye concentration of 40 mg/L, while this

value became 23.551 mg/g at the concentration of 160 mg/L. Garg *et al.* obtained similar results in 2003. The dye removal data obtained at three different concentrations are presented in Fig. 9. This figure indicates that the AV 17 removal increased up to a 10 g/L adsorbent dosage and then reached saturation. The increase in dye removal with a certain increase in the adsorbent dosage may be related to the availability of more adsorption sites and increased surface area.⁹

The dye removal was not affected by a further increase in the adsorbent dose. Thus, in other parameter experiments, the adsorbent amount of 10.0 g/L was selected. It was determined that, in case of providing sufficient adsorption sites, the removal of AV 17 remains independent of the amount of the adsorbent for AAPS.

The initial dye concentration represents another significant parameter that may influence the process of adsorption. Fig. 9 also presents the findings with regard to removal efficiency versus initial dye concentration. As can be seen in Fig. 9, a slight decrease was observed in AV 17 removal at the initial dosage of 4 g/L from approximately 80% at a 40 mg/L concentration to 60.84% with an increase in the concentration to 160 mg/L. However, when the initial dosage was 10.0 g/L, the removal efficiency was constant at values higher than 93% in the whole range of the studied dye concentrations, which demonstrated that its adsorption was independent of the initial concentration.

3. 2. 4. 1. Adsorption Isotherms

The adsorption isotherm is defined as the equilibrium relation between the quantity of adsorbate per unit of adsorbent (q_e) and its equilibrium solution concentration (C_e) at a constant temperature.²⁷ It is crucial to develop a suitable isotherm model for adsorption for designing and optimizing the processes of adsorption.²⁸ Isotherms are frequently utilized for the purpose of describing the equilibrium behavior of the adsorption process. Equilibrium sorption is generally defined by the isotherm equation characterized by some parameters expressing the interest of the adsorbent in the substance to be adsorbed and the surface properties of the sorbent.²⁹

The equilibrium isotherm of a certain adsorbent demonstrates its adsorptive properties and is crucial for

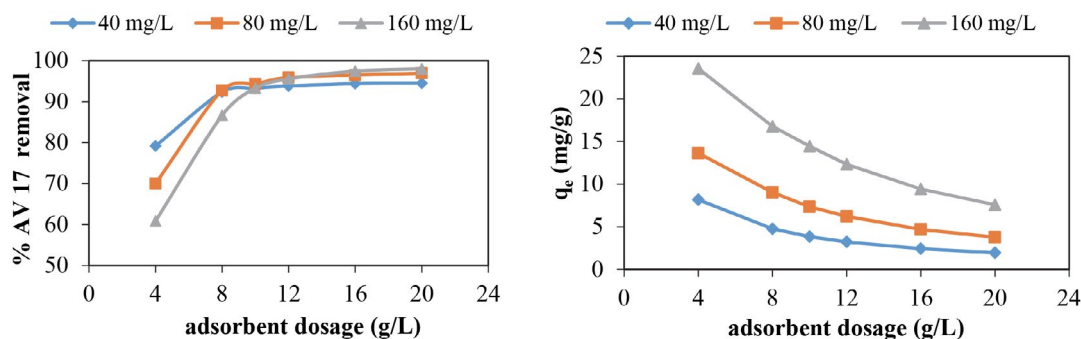


Fig. 9. Impact of adsorbent dosage on the adsorption of AV 17 by AAPS.

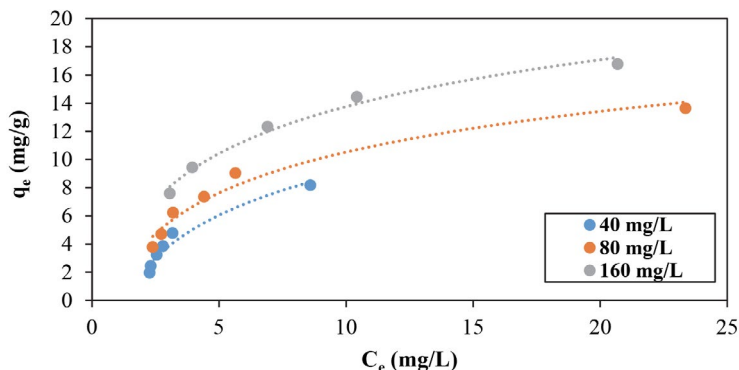


Fig. 10. Adsorption isotherm of Acid Violet 17 at different adsorbent dosages.

designing the adsorption process.³⁰ Experiments to estimate the adsorption isotherms of AV 17 onto AAPS were carried out with the addition of different quantities of AAPS, in the range of 4–20 g/L, to a series of Erlenmeyer flasks, each of which contained dye solution at a concentration of 160 mg/L. The adsorption isotherms were fitted using a few two- and three-parameter isotherms. The two-parameter models are the Langmuir, Freundlich, Dubinin–Radushkevich (D-R), and Temkin isotherms, whereas the three-parameter model is the Redlich and Peterson (R-D) isotherm. Fig. 10 exhibits the adsorption curves of 40, 80, 160 mg/L AV 17 concentration on the different adsorbent dosage (4–20 g/L).

In batch adsorption studies, it is common to fit the equilibrium uptake data to a number of isotherms, afterward to utilize R^2 in order to compare the goodness of fit and choose the best isotherm model. If it is assumed that the best isotherm is determined, findings on the homogeneity of the adsorbent's surface and the adsorption mechanism are generally presented. Nevertheless, a common drawback of certain studies is the use of R^2 for the purpose of comparing two, three, and four-parameter isotherms.³¹

Akaike's information criterion (AIC)³² is a statistical method that is well-established and can be employed for a comparison of models. Information theory and maximum likelihood theory constitute its basis, and therefore, it identifies which model has a higher probability of being correct and quantifies to what extent it is more probable. For a small sample size, AIC is computed for every model using Eq. (3):

$$AIC = N \ln \left(\frac{SSE}{N} \right) + 2N_p + \frac{2N_p(N_p + 1)}{N - N_p - 1} \quad (3)$$

where N represents the number of data points, N_p represents the number of parameters in the model, and SSE represents the sum of the error squares.

A minimization process was applied for the solution of isotherms and kinetic equations as a result of the minimization of the sum of error squared (SSE) between the values predicted and the experimental data.³²

The errors represent the difference between the value observed and the value that the model has predicted (Eq. 4):

$$SSE = \sqrt{\sum (q_{exp} - q_{cal})^2} / N \quad (4)$$

where the subscripts “exp” and “cal” denote the experimental and calculated q values, respectively and N denotes the number of measurements.

It is possible to compare AIC values by utilizing the evidence ratio which is found as in (Eq. 5):

$$\text{Evidence ratio} = \frac{1}{e^{-0.5\Delta}} \quad (5)$$

where Δ represents the absolute value of the difference in AIC between the two models.³¹

Table 5 presents the all isotherm parameters and the results of nonlinear regression. The present research reached a conclusion, based on R^2 comparison, that the D-R isotherm had a smaller R^2 value compared to the other models. The adsorption isotherm fits the Langmuir and Temkin models well. Nevertheless, it is considered to be more suitable to compare the goodness of fit to the Langmuir and Temkin isotherms using AIC. Therefore, AIC values were computed for the Langmuir (–2.908) and Temkin (–3.664) isotherms, respectively. A smaller AIC value indicates that there is a higher probability that the Temkin isotherm will be a better fit. The evidence ratio of 1.459 suggests that there is a 1.459 times higher probability that the Temkin isotherm will be the correct model in comparison with the Langmuir isotherm.

Furthermore, it is possible to determine the parameters of every isotherm equation as a result of minimizing the SSE. The best-fit model is required to have a minimum SSE value. Thus, it is possible to acquire the model in question as a result of comparing the SSE of every model. Table 5 presents a comparison of the SSE values. As a result of a comparison of the SSE of the Langmuir and Temkin isotherm models, the Temkin isotherm appears to be the best fit.

In accordance with the Langmuir model, the adsorption of AV 17 was the monolayer adsorption and occurred

Table 5. Equilibrium modeling for the adsorption of AV 17 by the AAPS.

Isotherm	Unit	Information
Langmuir model		$C_e/q_e = 1/k_L q_{\max} + C_e/q_{\max}$ ²⁴
Plot	–	(C_e/q_e) vs. C_e
Fitted model	–	$C_e/q_e = 0.319 + 0.0378C_e$
q_{\max}	[mg/g]	26.455
k_L	[dm ³ /mg]	0.118
R^2	–	0.994
$R_L = 1/1 + (k_L C_i)$		0.05
SSE		0.974
AIC		-2.908
Freundlich model		$\ln q_e = \ln K_F + 1/n \ln C_e$ ²⁴
Plot	–	$\ln q_e$ vs. $\ln C_e$
Fitted model	–	$\ln q_e = 1.7408 + 0.3586 \ln C_e$
K_F	[mg/g]	5.702
n	[mg/g(dm ³ /mg) ^{1/n}]	2.788
R^2		0.963
SSE		0.907
AIC	–	-3.333
Dubinin–Radushkevich model		$\ln q_e = \ln q_m - K_{DR} \epsilon^2$ ³³
Plot	–	$\ln q_e$ vs. ϵ^2
Fitted model	–	$\ln q_e = 2.8835 - 2E - 06\epsilon^2$
K_{DR}	[mol ² /kJ ²]	2E-06
$E = 1/\sqrt{2}K_{DR}$	[kJ/mol]	0.5
q_m		17.876
R^2		0.848
SSE	–	3.681
AIC		5.069
Temkin model		$q_e = B \ln A + B \ln C_e$ ³⁴
Plot		q_e vs. $\ln C_e$
Fitted model		$q_e = 5.1316 \ln C_e + 2.1246$
A	[dm ³ /g]	1.5129
B	[J/mol]	5.1316
R^2		0.992
SSE		0.485
AIC		-3.664
Redlich-Peterson		$\log \left[\left(\frac{K_R C_e}{q_e} \right) - 1 \right] = \beta \log C_e + \log(\alpha R)$ ³³
Plot		$\log \left[\left(\frac{K_R C_e}{q_e} \right) - 1 \right]$ vs. $\log C_e$
Fitted model		$\log \left[\left(\frac{K_R C_e}{q_e} \right) - 1 \right] = 1.1454 \log C_e - 1.1229$
$K_R = q_{\max} k_L$	[dm ³ /g]	3.1217
β		1.1454
αR		13.27
R^2		0.987
SSE		14.811
AIC		23.422

on a homogenous absorbing surface. The theoretical maximum of adsorption capacity computed by the Langmuir model was found to be 26.455 mg/g. In a study conducted by Kannan and Murugavel,⁷ commercial activated carbon and cashew nut shell carbon were utilized for the removal of AV 17 dye at a concentration of 140 mg/L with adsorption, and q_{\max} was obtained to be 72.01 and 1.975 mg/g, respectively.

Furthermore, the adsorption of AV 17 on the AAPS by utilizing a dimensionless parameter (R_L) that was derived from the Langmuir equation was also evaluated. The R_L value shows that the nature of adsorption is bad in case of $R_L > 1$, linear in case of $R_L = 1$, good in case of $0 < R_L < 1$ and irreversible in case of $R_L = 0$.³⁵ In Table 5, R_L (the separation factor) is $0 < R_L < 1$ indicating that adsorption was good. The amount of “n” in the Freundlich equation was

also shown in Table 5. The n value demonstrates the non-linearity degree between solution concentration and adsorption as presented below: in case of $n = 1$, the adsorption process is linear; in case of $n < 1$, adsorption represents a chemical process; in case of $n > 1$, adsorption represents a physical process. The case of $n > 1$ is the most frequently encountered and may be caused by a distribution of surface sites or any factor that leads to decreased interaction between adsorbent and adsorbate with an increase in surface density, and the n values in the interval between 1–10 indicate favorable adsorption.³⁶ In the current research, the value of n in the Freundlich equation was determined to be 2.788, which suggests the physical adsorption of AV 17 onto AAPS. Furthermore, it confirms that AAPS is appropriate as an adsorbent for AV 17 removal.

The E value for the D-R isotherm is very beneficial for predicting the adsorption type. The values below 8 kJ/mol demonstrate that adsorption is a physical process, and the E value in the range of 8–16 kJ/mol demonstrates that adsorption is caused by the exchange of ions.³⁷ In this research, E was found to be 0.5, so the sorption mechanism was physical.

It is possible to implement the R-P isotherm in homogenous as well as heterogeneous systems.³⁸ There are two restricting behaviors; the Langmuir form for $\beta \geq 1$ and Henry's law for $\beta = 0$. The β value is in the range of 0–1, which indicates favorable adsorption.³⁹ As the exponent, $\beta = 1.1454$ and adsorption is in the Langmuir form.

The Temkin isotherm model estimates that a linear decrease occurs in the adsorption energy with the surface coverage because of interactions between adsorbent and adsorbate.⁴⁰ Linear plots for the Temkin adsorption isotherm, considering chemisorption of an adsorbate onto the adsorbent, fit considerably well with the correlation coefficients of 0.992 (Table 5). This further defends the idea that the adsorption of AV 17 dye onto AAPS represents chemisorption. The Temkin model represents a suitable model for the chemical adsorption on the basis of powerful electrostatic interaction occurring between positive and negative charges.⁴¹

As a result of the evaluation of the coefficients obtained for the isotherms (Table 5), the adsorption process conformed to the Langmuir and Temkin isotherms, so that the physical and chemical adsorption mechanisms were applied together, and since chemical adsorption reached the boundary zone in the adsorption of AV 17 dye at the selected concentration of 160 mg/L by AAPS, adsorption was observed to be affected by both mechanisms.

3. 2. 5. Impact of Temperature

The sorption of AV 17 by AAPS was studied depending on temperature and dye concentration. The research was conducted in the concentration range of 40–400 mg/L at 3 different temperatures, being 303–313–323 K. Fig. 11

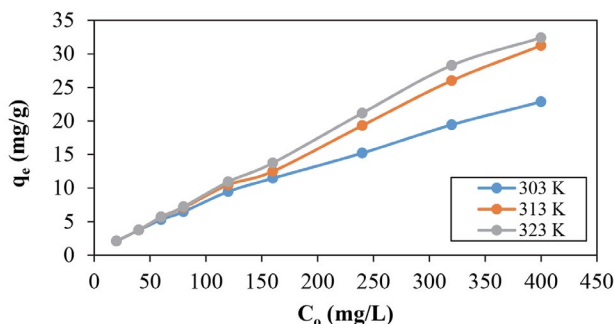


Fig. 11. Impact of temperature on the adsorption of Acid Violet 17 onto AAPS.

shows the sorption capacities obtained at different temperatures. The adsorption capacity of AAPS did not change significantly with increasing temperature at a low dye concentration (≤ 160 mg/L). However, at dye concentrations above 160 mg/L, the increase in temperature caused an increase in adsorption capacity. Probably due to increased mobility of ions at a high concentration and high temperature, the diffusion of dyes into pores increased. Furthermore, the increased adsorption capacity of AAPS with temperature increase may have contributed to the adsorbent surface activation. Therefore, the process was understood to be endothermic and spontaneous, especially at high concentrations. Moreover, there is not a very significant difference between 313 and 323 K. Thus, the adsorption of AV 17 by AAPS appears to be more effective in the mesophilic temperature range.

3. 2. 5. 1. Thermodynamic Parameters

The equations presented below were used to determine the thermodynamic parameters, including a change in standard free energy (ΔG°), enthalpy (ΔH°), and entropy (ΔS°) of adsorption:

$$\Delta G^\circ = -RT \ln K_c \quad (6)$$

$$K_c = q_e / C_e \quad (7)$$

$$\Delta G^\circ = \Delta H^\circ - T \Delta S^\circ \quad (8)$$

$$\ln K_c = \frac{\Delta S^\circ}{R} - \frac{\Delta H^\circ}{RT} \quad (9)$$

where K_c represents the distribution coefficient of the adsorbate, q_e and C_e represent the equilibrium dye concentration on AAPS (mg/g) and in the solution (mg/L), respectively. R denotes the universal gas constant (8.314 J/mol K), and T denotes the temperature (K). It is possible to compute ΔH° and ΔS° parameters from the slope and intercept of the plot $\ln K_c$ vs. $1/T$, respectively (Fig. 12), and the findings are presented in Table 6.

The positive values of ΔH° indicated the endothermic nature of adsorption.² The enthalpy (ΔH°) values above 40 kJ/mol for >160 mg/L dye concentration indicat-

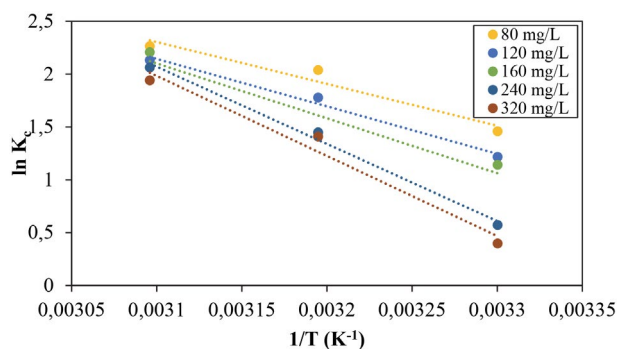


Fig. 12. The estimation of thermodynamic parameters.

ed that the adsorption of AV 17 by AAPS was chemisorption. Furthermore, the positive ΔS° value demonstrates that an increase occurred in the degrees of freedom at the solid-liquid interface in the course of adsorption. Positive ΔS° values also suggested an increase in the randomness and affinity of AV 17 dye toward the AAPS adsorbent.⁴² Therefore, adsorption is favored on AV 17. More negative values of ΔG° were determined at increased temperatures, which indicates that adsorption is feasible and more spontaneous under natural conditions at higher temperatures.⁴³

Table 6. Thermodynamic parameters.

C_0 (mg/L)	ΔG° (kJ/mol)			ΔS° (kJ/mol.K)	ΔH° (kJ/mol)
	303K	313K	323K		
80	-3.673	-5.302	-6.081	0.121	32.956
120	-3.063	-4.627	-5.723	0.134	37.325
160	-2.873	-3.756	-5.926	0.151	43.171
240	-1.439	-3.769	-5.539	0.206	60.768
320	-0.998	-3.663	-5.211	0.212	63.005

3. 2. 6. Impact of Ionic Strength

The effect of ionic strength on the adsorption of AV 17 onto AAPS was studied at different NaCl, SDS and CTAB concentrations. Figure 13 shows that the impact of NaCl salt is weak as the dye removal decreased only a bit (from 93.87% to 92.06%) with an increase in NaCl concentration from 0.05 to 0.25 mol/L. It is possible to attribute the slight decrease mentioned to the competition between AV 17 and chloride anions for the sorption sites. However, studies were also conducted with two different surfactants, anionic and cationic, such as sodium dodecyl sulfate (SDS) and cetyltrimethylammonium bromide (CTAB), respectively. As shown in the Fig. 13, when SDS and CTAB were added, the increase in the ionic charge of the solution caused a decrease in the adsorption percentage of the dye. These findings demonstrate that electrostatic attraction takes a significant part in the removal of AV 17. The reason for this situation can be attributed to the decrease in the affinity of dye molecules and sorption zones. In case electrostatic attraction represents the major adsorption mechanism, ionic strength has a considerable negative impact

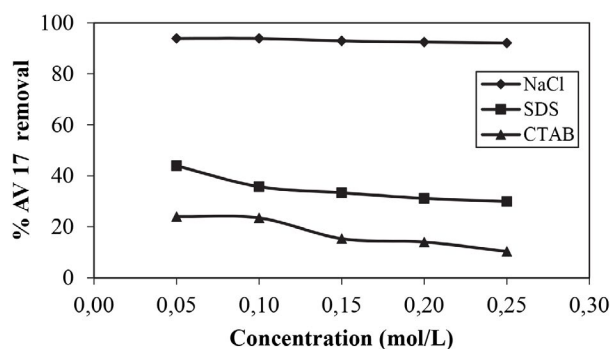


Fig. 13. Influence of ionic strength on efficiency.

on adsorption.²¹ The impact of NaCl concentration on the adsorption of acidic dyes was investigated by using brick kiln ash, and similar results were obtained.⁴

3. 2. 7. Desorption and Recyclability of the Adsorbent

Desorption studies help to explain the recovery of adsorbate and adsorbent and the adsorption mechanism. The regeneration of the adsorbent makes the treatment process economical. It is, therefore, necessary to study whether the adsorbent can be reused after adsorption. 0.05–0.25 M NaCl, SDS, and CTAB solutions were utilized as a desorbing agent for the purpose of determining the desorption behavior of the AAPS. Normally, the addition of 0.1 g of the fresh adsorbent was performed to 75 mL of 60 mg/L AV 17 solution at pH 6.1, and the mixture was shaken for the period of 4 h. Afterward, the AV 17 that was adsorbed by AAPS was separated, and a spectrophotometer was utilized to measure the residual AV 17 concentration. The dye-loaded adsorbent was washed gently using water for the removal of any dye not adsorbed and dried. The desorption process was carried out by mixing the dried adsorbent with 100 mL of water and ethanol as a solvent and solutions prepared at different concentrations. After the mixture was shaken for 24 h and 48 h of contact time, the spectrophotometric determination of the desorbed AV 17 concentration was performed. The results are presented in Figs. 14(a,b). The desorption efficiency was very low in desorption processes performed separately with water and ethanol. Upon examining the results, it was decided to perform regeneration with 0.2 M NaOH for 48 hours. NaOH selected as the regeneration agent has properties such as lower environmental load in its life cycle, less corrosive ability and cheaper chemical cost.⁴⁴

Successive adsorption-desorption studies were conducted in three cycles for the purpose of checking the reusability of the regenerated adsorbents. All the studies, adsorption and desorption, were carried out in a batch setup in two replicates, and the mean values were acquired. Figure 15 shows the simultaneous adsorption-desorption of the dye onto AAPS. The dye-loaded adsorbents were put in 0.2 M NaOH as the stripping solution and mixed for the

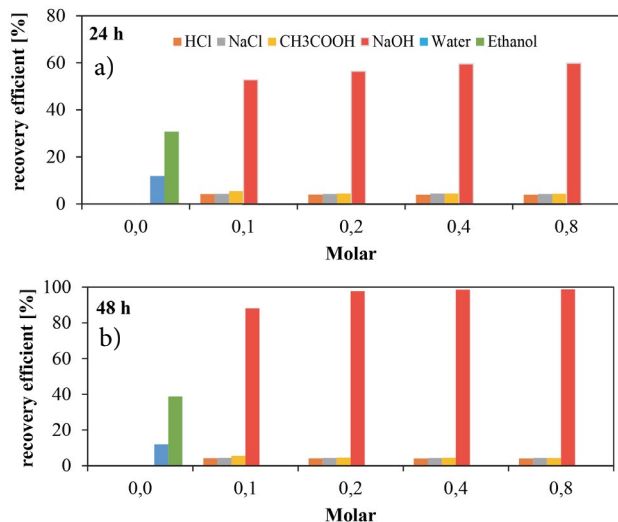


Fig. 14. Desorption of AV 17 dye from the adsorbent using different eluting agents a) 24 h b) 48 h.

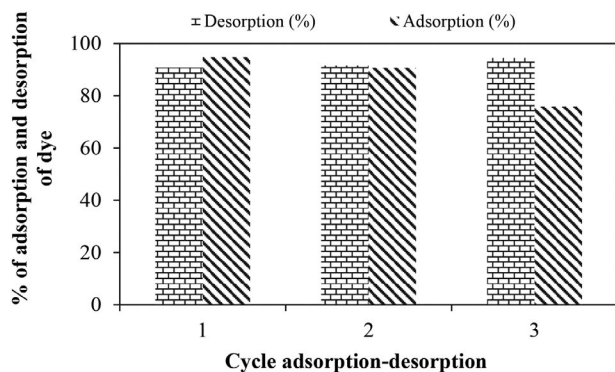


Fig. 15. Simultaneous adsorption-desorption cycles using AAPS.

period of 48 h at the temperature of 303 K to determine the final dye concentration. The percentage of desorption observed for 0.2 M NaOH was 97.73% for AAPS in the first cycle.

The AV 17 dye adsorption efficiency after three cycles of desorption decreased from 94.76 to 75.84%, which represents a promising result for the possible recovery of the adsorbate and re-usage of the adsorbent. The higher desorption percentage may help in recycling the adsorbent spent and also shows that physical forces take the major part in the dye removal for the studied concentration.

4. Conclusion

The present study indicates that it is possible to use the activated carbon prepared from acid-activated pistachio shell efficiently in order to remove Acid Violet 17 from aqueous solution. The use of locally available pistachio shell is cost effective since it is abundantly available in Turkey at a low cost. The AIC value suggests that the Temkin isotherm described adsorption better. The behavior of

adsorption was better described by the pseudo-second-order model. The enhanced sorption at higher temperature indicates an endothermic process and is spontaneous in nature, and the use of acid activated pistachio shell to remove AV 17 from industrial waste solutions at high temperatures would be more efficient. Chemical reagents could increase BET surface area, pore volume and especially surface functional groups that enhance the adsorption of material. The results showed that the AV 17 adsorption capacity was positively correlated to the BET surface area. Desorption study demonstrates that the recycling of adsorbent and adsorbate may be possible for low dye concentrations. However, the mentioned studies should not include only lab-scale batch studies, it is necessary to scale them up to pilot plants for the purpose of assessing their feasibility on a commercial scale.

Acknowledgement

We would like to kindly state that the authors are thanking and feel grateful to Sivas Cumhuriyet University, Scientific Research Project Fund for their financial support [Project number: M-661].

Conflict of interest

As the author(s), we declare that there is no conflict of interest regarding the publication of this article.

5. References

1. N. Thinakaran, P. Baskaralingam, M. Pulikesi, P. Panneerselvam, S. Sivanesan, *J. Hazard. Mater.* **2008**, *151*, 316–322. DOI:10.1016/j.jhazmat.2007.05.076
2. P. Vijayalakshmi, V. S. S. Bala, K. V. Thiruvengadaravi, P. Panneerselvam, M. Palanichamy, S. Sivanesan, *Sep. Sci. Technol.* **2011**, *46*, 155–163. DOI:10.1080/01496395.2010.484006
3. M. Saleem, T. Pirzada, R. Qadeer, *Colloids Surf. Physicochem. Eng. Asp.* **2007**, *292*, 246–250. DOI:10.1016/j.colsurfa.2006.06.035
4. S. Kaur, T. P. S. Walia, R. Kaur, *Online Journal of Health and Allied Sciences.* **2008**, *6* (3), 1–10.
5. S. N. Jain, P. R. Gogate, *J. Mol. Liq.* **2017**, *243*, 132–143. DOI:10.1016/j.molliq.2017.08.009
6. R. Sivaraj, C. Namasivayam, K. Kadirvelu, *Waste Manag.* **2001**, *21*, 105–110. DOI:10.1016/S0956-053X(00)00076-3
7. N. Kannan S. Murugavel, *Glob. NEST J.* **2008**, *10*, 395–403. DOI:10.30955/gnj.000457
8. Z. Zheng, World production and trade of pistachios: The role of the U.S. and factors affecting the export demand of U.S. pistachios, **2011**, 1–67.
9. V. K. Garg, R. Gupta, A. Bala Yadav, R. Kumar, *Bioresour. Technol.* **2003**, *89*, 121–124. DOI:10.1016/S0960-8524(03)00058-0
10. M. A. K. M. Hanafiah, W. S. W. Ngah, S. H. Zolkafly, L. C. Teong, Z. A. A. Majid, *J. Environ. Sci.* **2012**, *24*, 261–268. DOI:10.1016/S1001-0742(11)60764-X

11. H. B. Senturk, D. Ozdes, A. Gundogdu, C. Duran, M. Soylak, *J. Hazard. Mater.* **2009**, *172*, 353–362. DOI:10.1016/j.jhazmat.2009.07.019
12. A. Ates, A. Reitzmann, C. Hardacre, H. Yalcin, *Appl. Catal., A* **2011**, *407*, 67–75. DOI:10.1016/j.apcata.2011.08.026
13. S. Sadaf, H. N. Bhatti, *J. Taiwan Inst. Chem. Eng.* **2014**, *45*, 541–553. DOI:10.1016/j.jtice.2013.05.004
14. N. Gupta, A. K. Kushwaha, M. C. Chattopadhyaya, *Arab. J. Chem.* **2016**, *9*, 707–716. DOI:10.1016/j.arabjc.2011.07.021
15. D. H. K. Reddy, S.-M. Lee, *Adv. Colloid Interface Sci.* **2013**, *201–202*, 68–93. DOI:10.1016/j.cis.2013.10.002
16. K. S. W. Sing, D. H. Everett, R. A. W. Haul, L. Moscou, R. A. Pierotti, J. Rouquerol, T. Siemieniowska, *Pure Appl. Chem.* **1985**, *57*, 603–619.
17. D. Savova, N. Petrov, M. Yardim, E. Ekinci, T. Budinova, M. Razvigorova, V. Minkova, *Carbon* **2003**, *41*, 1897–1903. DOI:10.1016/S0008-6223(03)00179-9
18. S. B. Daffalla, H. Mukhtar, M. S. Shaharun, *Int. J. Chem. Environ. Eng.* **2012**, *3*(3), 192–200.
19. A. Ma, M. Mm, *J. Chromatogr. Sep. Tech.* **2016**, *7:4*, 1–10. DOI:10.4172/2157-7064.1000329
20. R. Thenmozhi, T. Santhi, *Int. J. Environ. Sci. Technol.* **2015**, *12*, 1677–1686. DOI:10.1007/s13762-014-0531-1
21. R. Lafi, A. Hafiane, *J. Taiwan Inst. Chem. Eng.* **2016**, *58*, 424–433. DOI:10.1016/j.jtice.2015.06.035
22. S. Dubey, D. Gusain, Y. C. Sharma, *J. Mol. Liq.* **2016**, *219*, 1–8. DOI:10.1016/j.molliq.2016.01.021
23. F. Deniz, R. A. Kepekci, *J. Mol. Liq.* **2016**, *219*, 194–200. DOI:10.1016/j.molliq.2016.03.018
24. G. Moussavi, B. Barikbin, *Chem. Eng. J.* **2010**, *162* (3): 893–900. DOI:10.1016/j.cej.2010.06.032
25. C. Xiaoli, Z. Youcai, *J. Hazard. Mater.* **2006**, *137* (1): 410–417. DOI:10.1016/j.jhazmat.2006.02.015
26. A. Kuleyin, F. Aydin, *Environ. Prog. Sustainable Energy* **2011**, *30* (2): 141–151. DOI:10.1002/ep.10454
27. S. K. Nadavala, K. Swayampakula, V. M. Boddu, K. Abburi, *J. Hazard. Mater.* **2009**, *162*, 482–489. DOI:10.1016/j.jhazmat.2008.05.070
28. I. A. W. Tan, A. L. Ahmad, B. H. Hameed, *J. Hazard. Mater.* **2008**, *154*, 337–346. DOI:10.1016/j.jhazmat.2007.10.031
29. Z. Rawajfih, N. Nsour, *J. Colloid Interface Sci.* **2006**, *298*, 39–49. DOI:10.1016/j.jcis.2005.11.063
30. G. Moussavi, M. Mahmoudi, *J. Hazard. Mater.* **2009**, *168*, 806–812. DOI:10.1016/j.jhazmat.2009.02.097
31. M. I. El-Khaiary, G. F. Malash, *Hydrometallurgy* **2011**, *105*, 314–320. DOI:10.1016/j.hydromet.2010.11.005
32. I. Senturk, H. Buyukgungor, F. Geyikci, *Desalination Water Treat.* **2016**, *57*, 19529–19539. DOI:10.1080/19443994.2015.1102088
33. S. Sivakumar, P. Muthirulan, M. Meenakshi Sundaram, *Arabian J. Chem.* **2014**, *xx–xx*. DOI:10.1016/j.arabjc.2014.10.028
34. N. A. Oladoja, C. O. Aboluwoye, Y. B. Oladimeji, *Turkish J. Eng. Env. Sci.* **2008**, *32*: 303–312.
35. Dada et al., *IOSR J. Appl. Chem.* **2012**, *3*, 38–45. DOI:10.9790/5736-0313845
36. M. B. Desta, *J. Thermodyn.* **2013**, 1–6. DOI:10.1155/2013/375830
37. M. Ghasemi, M. Naushad, N. Ghasemi, Y. Khosravi-fard, *J. Ind. Eng. Chem.* **2014**, *20*, 2193–2199. DOI:10.1016/j.jiec.2013.09.050
38. E. Alver, A. Ü. Metin, *Chem. Eng. J.* **2012**, *200–202*, 59–67. DOI:10.1016/j.cej.2012.06.038
39. O. Abdelwahab, *Egypt. J. Aquat. Res.* **2007**, *33* (1): 125–143.
40. H. K. Boparai, M. Joseph, D. M. O'Carroll, *J. Hazard. Mater.* **2011**, *186*, 458–465. DOI:10.1016/j.jhazmat.2010.11.029
41. Y. Gao, Y. Li, L. Zhang, H. Huang, J. Hu, S. M. Shah, X. Su, *J. Colloid Interface Sci.* **2012**, *368*, 540–546. DOI:10.1016/j.jcis.2011.11.015
42. S. N. Jain, P. R. Gogate, *Int. J. Environ. Sci. Technol.* **2017**, *14*, 531–542. DOI:10.1007/s13762-016-1160-7
43. V. da Silva Lacerda, J. B. López-Sotelo, A. Correa-Guimarães, S. Hernández-Navarro, M. Sánchez-Báscones, L. M. Navas-Gracia, P. Martín-Ramos, J. Martín-Gil, *J. Environ. Manage.* **2015**, *155*, 67–76. DOI:10.1016/j.jenvman.2015.03.007
44. K. Y. Foo, B. H. Hameed, *Bioresour. Technol.* **2012**, *116*, 522–525. DOI:10.1016/j.biortech.2012.03.123

Povzetek

Luščne pistacije predobdelane z različnimi kemijskimi spojinami smo testirali kot adsorbent za odstranjevanje barvila AV 17 iz vodnih raztopin. Maksimalno odstranitev 93.04 % smo dosegli z luščinami pistacije predobdelanimi z 10 N H₂SO₄. Adsorbent smo okarakterizirali z metodami pH_{pzc}, FTIR, BET in SEM-EDX. Rezultati so pokazali, da je adsorpcijska kapaciteta za AV 17 pozitivno korelirana z specifično površino določeno z BET. Hitrost adsorpcije lahko najbolje opišemo s kinetiko pseudo-drugega-reda. Ravnotežne podatke adsorpcije pa lahko opišemo z Langmuirjevo ali Temkinovo izotermo. Maksimalna kapaciteta vezave določena preko opisa z Langmuirjevo izotermo bi znašala 26.455 mg/g pri koncentraciji barvila 160 mg/L. Termodinamska analiza je pokazala, da je adsorpcija endotermna. Z uporabo 0.2 M NaOH smo v prvem ciklu dosegli 97.33 % desorpcijo, kar je pomembno v primeru ekonomske uporabe adsorbenta. Rezultati kažejo, da bi lahko bile aktivirane luščine pistacij alternativni adsorbent za odstranjevanje barvil iz odpadnih industrijskih odplak.



Except when otherwise noted, articles in this journal are published under the terms and conditions of the Creative Commons Attribution 4.0 International License

Scientific paper

Design, Synthesis and *In Vitro* Cytotoxic Activity of New 6,9-Disubstituted Purine Analogues

Asligul Kucukdumlu,¹ Meral Tuncbilek,^{1,*} Ebru Bilget Guven²
and Rengul Cetin Atalay³

¹ Department of Pharmaceutical Chemistry, Faculty of Pharmacy, Ankara University, 06100 Ankara, Turkey

² Department of Bioinformatics and Genetics, Faculty of Engineering and Natural Sciences, Kadir Has University, 34083, Cibali-Fatih, Istanbul, Turkey

³ Department of Bioinformatics, Graduate School of Informatics, Middle East Technical University, 06800 Ankara, Turkey

* Corresponding author: E-mail: tuncbile@pharmacy.ankara.edu.tr

Received: 04-12-2019

Abstract

A series of new 6,9-disubstituted purine analogs with 4-substituted piperazine at C-6 and 4-substituted benzyl at N-9 were designed and synthesized in four steps. All synthesized compounds (**7–26**) were screened initially for their *in vitro* anticancer activity on Huh7 liver, HCT116 colon and MCF7 breast carcinoma cell lines. Cytotoxic bioactivity studies revealed that all compounds screened, with compound **19** being the exception, were found to have promising cytotoxic activities at IC₅₀ range of 0.05–21.8 μM against cancer cells Huh7, HCT116 and MCF7. Among the prepared purine analogs, two of them (**12** and **22**) exhibited excellent cytotoxic activities, with IC₅₀ 0.08–0.13 μM, on Huh7 cells comparable to camptothecin (CPT) and better than cladribine, fludarabine and 5-FU. Afterwards, the evaluation of cytotoxicity of the most potent purine analogs was screened against further hepatocellular cancer (HCC) cell lines. The 6-(4-(4-trifluoromethylphenyl)piperazine (**12**) and 6-(4-(3,4-dichlorophenyl)piperazine analogs (**25**) displayed a significant IC₅₀ values (IC₅₀ < 0.1–0.13 μM) comparable to CPT and better cytotoxic bioactivity when compared with 5-FU, cladribine and fludarabine on HCC cells (Huh7 and HepG2).

Keywords: Purine; piperazine; benzyl; cytotoxic activity

1. Introduction

The purine nucleus is involved in the biological molecules that play a key role in the signaling pathways of all living organisms.¹ For this reason, the purine structure is an interesting organic moiety included in new drugs. Purine and purine nucleoside analogs exhibit a variety of biological activities. These analogs have been extensively studied as enzyme inhibitors,^{2–5} cytotoxic,^{6–10} antiviral,^{11–14} antihyperglycemic,¹⁵ immunostimulatory,¹⁶ antifungal, and antibacterial^{17–22} agents due to their potential activities, even though their antiviral and anticancer effects are more commonly known. 5-Fluorouracil (5-FU), a well known fluorinated nucleobase analogue, is highly preferred for the treatment of various cancers in clinics.²³ Subsequently, other pyrimidine analogs, such as cytarabine, gemcitabine, capecitabine, decitabine, and 5-fluoro deoxyuridine have been used in solid tumors and hematologic

malignancies.^{24–26} Purine nucleobase analogs such as 6-mercaptapurine and 6-thioguanine, are specifically used in pediatric acute lymphoblastic leukemia as an inhibitor of nucleic acid metabolism.^{27,28} In addition, many purine nucleoside analogs (fludarabine, cladribine, pentostatin, nelarabine, and clofarabine) are clinically administered in the treatment of solid and hematological malignancies.^{29–32}

A large number of investigations indicate that purine nucleobases and purine nucleosides target a series of pathways in chemotherapy-induced cell death mechanisms, such as apoptosis, necrosis, senescence, autophagy, and mitotic catastrophe.^{25,33–35} Also, various purine scaffolds and their analogs have been studied as potential anticancer agents that contain cyclin-dependent kinase and heat shock protein inhibition. Olomoucine,³⁶ roscovitine,³⁷ purvalanol A, B, amino-purvalanol³⁸ (Figure 1) have been synthesized and screened as cyclin-dependent kinase inhibitors. Especially, R-roscovitine is under investigation as

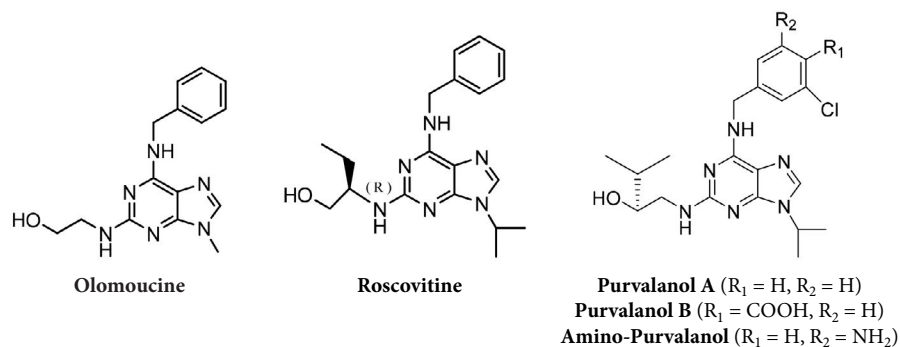


Figure 1. Structures of olomoucine, roscovitine, purvalanol A, B and amino-purvalanol

a chemotherapeutic agent against non-small cell lung cancer and other malignancies. Also, olomoucine with its 2,6,9-trisubstituted purine structure is another purine derivative with antiproliferative effects on cancer cell lines.

In addition to this, various heterocyclic analogs of purines, such as imidazo-pyrazines,³⁹ pyrazolo-pyridazines,⁴⁰ imidazo-pyridines,^{41,42} thieno-pyridines,⁴³ pyrrolo-pyrimidines,⁴⁴ pyrazolo-pyrimidines,^{45,46} thieno-pyrimidines⁴⁷ and triazolo-pyrimidines^{48,49} have been found to possess anticancer activities.

The heat shock protein 90 (Hsp90) has been an existing target in cancer since its inhibition may lead to the

breakdown of many cancer-associated proteins. Furthermore, inhibitors of Hsp90 kill cancer cells at lower concentrations than is required to harm normal human cells. In recent years, purine analogues, which are Hsp90 inhibitors, have entered clinical trials as drugs in the therapy of solid tumors and hematologic malignancies.⁵⁰

In our previous studies,^{51,52} we have reported important cytotoxic activities of 9-(cyclopentyl/ β -D-ribofuranosyl/*para*-toluenesulfonyl)-6-(4-substituted piperazino)purine analogs A, B, C (Figure 2). In this work, we report the synthesis of new analogs of purines A, B, C as 9-(4-substituted benzyl)purines and evaluate their cytotoxic activities against liver (Huh7), colon (HCT116) and breast (T47D) carcinoma cell lines. We further investigate the most active compounds (7–18, 20, 22–26) on a panel of liver cancer cells.

2. Experimental

2.1. Chemistry

Melting points were recorded with a capillary melting point apparatus (Electrothermal 9100) and are uncorrected. NMR spectra were recorded on a VARIAN Mercury 400 FT-NMR spectrometer (400 MHz for ^1H , 100.6 MHz for ^{13}C). TMS was used as internal standard for the ^1H NMR and ^{13}C NMR spectra; values are given in δ (ppm) and J values are in Hz. Mass spectra were taken on Waters Micro-mass ZQ by using the ESI+ method. Elemental analyses (C, H, N) were determined on a Leco CHNS 932 instrument and gave values within $\pm 0.4\%$ of the theoretical values. Column chromatography was accomplished on silica gel 60 (0.040–0.063 mm particle size). The chemical reagents used in the synthesis were purchased from Merck, Fluka, Sigma and Aldrich. 5-Amino-4,6-dichloropyrimidine (**2**) was synthesized according to the reported method.⁵³

2.1.1. General Procedure for the Synthesis of Compounds 3 and 4

5-Amino-4,6-dichloropyrimidine (**2**) (1 mmol) was dissolved in 5 mL of absolute EtOH, and then 4-substitut-

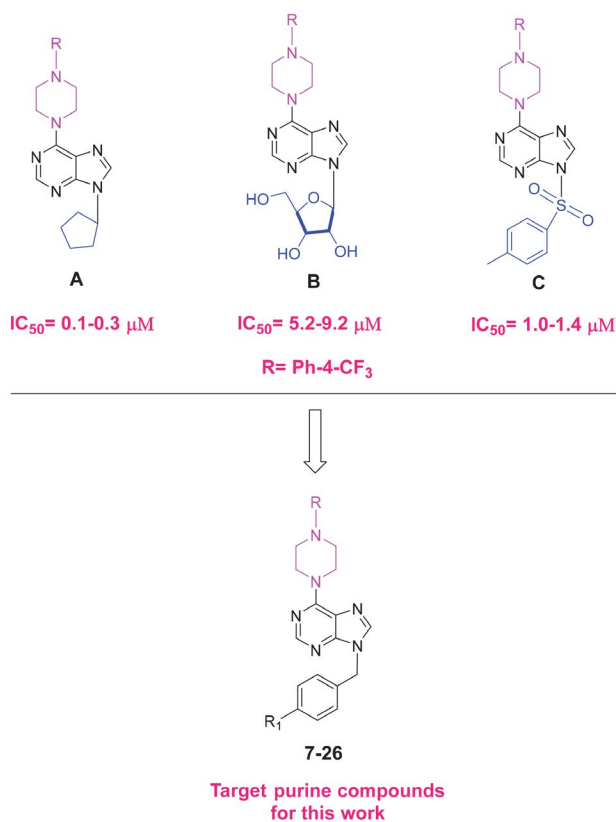


Figure 2. Structures of 9-(cyclopentyl/ β -D-ribofuranosyl/*para*-toluenesulfonyl)-6-(4-substituted piperazino)purine analogs A, B, C and target purine compounds 7–26.

ed benzylamines (2 mmol) and Et₃N (3 mmol) were added. The mixture was refluxed for 15 h. The reaction mixture was concentrated *in vacuo*, and the residue was purified by column chromatography (EtOAc-hexane, 1:4 to 1:2).

2. 1. 1. 1. 5-Amino-6-chloro-4-[(4-trifluoromethylbenzyl)amino]pyrimidine (3)

Yield 120 mg (65%), m.p. 181–183 °C. ¹H NMR (CDCl₃) δ 3.40 (br s, 2H), 4.77 (d, 2H, *J* = 5.6 Hz), 5.24 (s, 1H), 7.46 (d, 2H, *J* = 8 Hz), 7.60 (d, 2H, *J* = 8 Hz), 8.11 (s, 1H). MS (ESI+) *m/z*: 303.34 (100%) (M+H), 305.35 (40%) (M+H+2). Anal. Calcd for C₁₂H₁₀ClF₃N₄: C, 47.62; H, 3.33; N, 18.51. Found: C, 47.63; H, 3.41; N, 18.45.

2. 1. 1. 2. 5-Amino-6-chloro-4-[(4-chlorobenzyl)amino]pyrimidine (4)

Yield 140 mg (88%), m.p. 192–194 °C. ¹H NMR (DMSO-*d*₆) δ 4.58 (d, 2H, *J* = 5.6 Hz), 5.07 (s, 2H), 7.28–7.40 (m, 5H), 7.70 (s, 1H). MS (ESI+) *m/z*: 269.24 (100%) (M⁺), 271.24 (55%) (M+2). Anal. Calcd for C₁₁H₁₀Cl₂N₄: C, 49.09; H, 3.75; N, 20.82. Found: C, 49.14; H, 3.66; N, 20.42.

2. 1. 2. General Procedure for the Synthesis of Compounds 5 and 6

A mixture of 5-amino-6-chloro-4-[(4-substituted-benzyl)amino]pyrimidines (**3**, **4**) (0.29 mmol), 2 mL triethylorthoformate and *para*-toluenesulfonic acid (0.03 mmol) was stirred at room temperature for 72 h. The residue was dissolved with CH₂Cl₂, washed with saturated NaHCO₃ and brine. The extract was dried over Na₂SO₄, the solvent was evaporated *in vacuo*, and the residue was purified by column chromatography (EtOAc-hexane, 1:4 to 1:2).

2. 1. 2. 1. 6-Chloro-9-(4-trifluoromethylbenzyl)-9H-purine (5)

Yield 50 mg (51%), m.p. 131 °C [Lit. 130–132 °C⁵⁴]. MS (ESI+) *m/z*: 313.34 (100%) (M+H), 315.36 (47%) (M+H+2).

2. 1. 2. 2. 6-Chloro-9-(4-chlorobenzyl)-9H-purine (6)

Yield 240 mg (87%), m.p. 133 °C [Lit. 130–133 °C⁵⁴]. MS (ESI+) *m/z*: 279.27 (100%) (M⁺), 281.27 (63%) (M+2).

2. 1. 3. General Procedure for the Synthesis of the Final Compounds 7–26

The appropriate 1-substituted piperazines (1 mmol) and Et₃N (3 mmol) were added to a solution of 6-chloro-purines (1mmol) (**5**, **6**) in 5 mL of absolute EtOH. The mixture was refluxed for 8–16 h. The reaction mixture was concentrated *in vacuo* and the residue was purified by column chromatography (EtOAc-hexane, 1:3 to 1:1).

2. 1. 3. 1. 6-[4-(2-Hydroxyethyl)piperazine-1-yl]-9-(4-trifluoromethylbenzyl)-9H-purine (7)

Yield 270 mg (65%), m.p. 141–143 °C. ¹H NMR (CDCl₃) δ 2.61 (t, 2H, *J* = 5.6 Hz), 2.66 (t, 4H, *J* = 5.2 Hz), 3.68 (t, 2H, *J* = 4.8 Hz), 4.34 (br s, 4H), 5.43 (s, 2H), 7.36 (d, 2H, *J* = 8 Hz), 7.59 (d, 2H, *J* = 8 Hz), 7.74 (s, 1H), 8.37 (s, 1H). ¹³C NMR (CDCl₃) δ 45.12 (CH₂ in piperazine), 46.44 (CH₂), 53.01 (CH₂ in piperazine), 57.77 (CH₂-N), 59.45 (CH₂-OH), 119.77, 122.46, 125.16 (C in phenyl), 125.97 (q, *J*_{CF} = 3.9 Hz), 127.75, 130.57 (q, *J*_{CF} = 32.9 Hz), 137.96 (C-5), 139.78 (C-8), 151.01 (C-6), 152.79 (C-2), 153.87 (C-4). MS (ESI+) *m/z*: 407.65 (100%) (M+H). Anal. Calcd for C₁₉H₂₁F₃N₆O·0.3CH₂Cl₂: C, 53.67; H, 5.04; N, 19.46. Found: C, 53.96; H, 5.08; N, 19.40.

2. 1. 3. 2. 6-[4-Cyclohexylpiperazine-1-yl]-9-(4-trifluoromethylbenzyl)-9H-purine (8)

Yield 360 mg (82%), m.p. 149–148 °C. ¹H NMR (CDCl₃) δ 1.12–1.89 (m, 10H), 2.33 (br s, 1H), 2.72 (t, 4H, *J* = 5.2 Hz), 4.32 (br s, 4H), 5.43 (s, 2H), 7.36 (d, 2H, *J* = 7.6 Hz), 7.59 (d, 2H, *J* = 8.4 Hz), 7.73 (s, 1H), 8.36 (s, 1H). ¹³C NMR (CDCl₃) δ 25.84, 26.25, 28.86 (CH₂ in cyclohexyl), 45.51 (CH₂ in piperazine), 46.41 (CH₂), 49.12 (CH₂ in piperazine), 63.71 (CH in cyclohexyl), 119.71, 122.46, 125.17 (C in phenyl), 125.95 (q, *J*_{CF} = 3.2 Hz), 127.72, 130.53 (q, *J*_{CF} = 32.9 Hz), 137.79 (C-5), 139.85 (C-8), 150.93 (C-6), 152.82 (C-2), 153.82 (C-4). MS (ESI+) *m/z*: 445.86 (100%) (M+H). Anal. Calcd for C₂₃H₂₇F₃N₆·0.05H₂O: C, 62.02; H, 6.13; N, 18.86. Found: C, 62.06; H, 6.13; N, 18.86.

2. 1. 3. 3. 6-[4-(Pyrimidine-2-yl)piperazine-1-yl]-9-(4-trifluoromethylbenzyl)-9H-purine (9)

Yield 380 mg (86%), m.p. 171–173 °C. ¹H NMR (CDCl₃) δ 3.99 (t, 4H, *J* = 5.6 Hz), 4.41 (br s, 4H), 5.45 (s, 2H), 6.54 (t, 1H, *J* = 5.2 Hz), 7.37 (d, 2H, *J* = 8 Hz), 7.60 (d, 2H, *J* = 8 Hz), 7.77 (s, 1H), 8.35 (d, 2H, *J* = 4.4 Hz), 8.41 (s, 1H). ¹³C NMR (CDCl₃) δ 43.75 (CH₂ in piperazine), 44.99 (CH₂ in piperazine), 46.47 (CH₂), 110.24 (C-5 in pyrimidine), 119.89, 122.46, 125.16 (C in phenyl), 125.98 (q, *J*_{CF} = 3.9 Hz), 127.76, 130.57 (q, *J*_{CF} = 32.3 Hz), 138.07 (C-5), 139.78 (C-8), 151.06 (C-6), 152.80 (C-2), 154.04 (C-4), 157.77 (C-4,6 in pyrimidine), 161.68 (C-2 in pyrimidine). MS (ESI+) *m/z*: 441.8 (100%) (M+H). Anal. Calcd for C₂₁H₁₉F₃N₈: C, 57.27; H, 4.35; N, 25.44. Found: C, 57.36; H, 4.24; N, 25.42.

2. 1. 3. 4. 6-(4-Phenylpiperazine-1-yl)-9-(4-trifluoromethylbenzyl)-9H-purine (10)

Yield 430 mg (97%), m.p. 122 °C. ¹H NMR (CDCl₃) δ 3.33 (t, 4H, *J* = 5.2 Hz), 4.82 (br s, 4H), 5.44 (s, 2H), 6.90 (t, 1H, *J* = 7.6 Hz), 6.98 (d, 2H, *J* = 7.6 Hz), 7.29 (t, 2H, *J* = 7.6 Hz), 7.37 (d, 2H, *J* = 8 Hz), 7.59 (d, 2H, *J* = 7.6 Hz), 7.76 (s, 1H), 8.40 (s, 1H). ¹³C NMR (CDCl₃) δ 45.02 (CH₂ in piperazine), 46.47 (CH₂), 49.58 (CH₂ in piperazine), 116.51, 119.85, 120.30, 122.47, 125.17 (C in phenyl), 125.99 (q, *J*_{CF} = 3.8 Hz), 127.76, 129.22, 130.58 (q, *J*_{CF} =

32.8 Hz), 138.06 (C in phenyl), 139.79 (C-5), 151.06 (C-8), 151.20 (C-6), 152.83 (C-2), 153.90 (C-4). MS (ESI+) *m/z*: 439.64 (100%) (M+H). Anal. Calcd for C₂₃H₂₁F₃N₆ · 0.15H₂O: C, 62.61. Found: C, 62.85; H, 4.68; N, 18.66.

2. 1. 3. 5. 6-[4-(4-Methylphenyl)piperazine-1-yl]-9-(4-trifluoromethylbenzyl)-9H-purine (11)

Yield 390 mg (86%), m.p. 156 °C. ¹H NMR (CDCl₃) δ 2.29 (s, 3H), 3.27 (t, 4H, *J* = 5.2 Hz), 4.48 (br s, 4H), 5.44 (s, 2H), 6.90 (d, 2H, *J* = 8.4 Hz), 7.10 (d, 2H, *J* = 8 Hz), 7.37 (d, 2H, *J* = 8 Hz), 7.60 (d, 2H, *J* = 8 Hz), 7.76 (s, 1H), 8.40 (s, 1H). ¹³C NMR (CDCl₃) δ 20.43 (CH₃), 45.12 (CH₂ in piperazine), 46.46 (CH₂), 50.18 (CH₂ in piperazine), 116.89, 119.84, 122.47, 125.18 (C in phenyl), 125.98 (q, *J*_{CF} = 3.9 Hz), 127.75, 129.74, 129.91, 130.58 (q, *J*_{CF} = 32.2 Hz), 138.02 (C in phenyl), 139.80 (C-5), 149.11 (C-8), 151.05 (C-6), 152.82 (C-2), 153.90 (C-4). MS (ESI+) *m/z*: 453.9 (100%) (M+H). Anal. Calcd for C₂₄H₂₃F₃N₆: C, 63.71; H, 5.12; N, 18.57. Found: C, 63.76; H, 5.10; N, 18.43.

2. 1. 3. 6. 6-[4-(4-Trifluoromethylphenyl)piperazine-1-yl]-9-(4-trifluoromethylbenzyl)-9H-purine (12)

Yield 60 mg (18%), m.p. 115–118 °C. ¹H NMR (CDCl₃) δ 3.43 (t, 4H, *J* = 5.2 Hz), 4.48 (br s, 4H), 5.45 (s, 2H), 6.98 (d, 2H, *J* = 8.4 Hz), 7.38 (d, 2H, *J* = 8.4 Hz), 7.52 (d, 2H, *J* = 8.4 Hz), 7.60 (d, 2H, *J* = 8 Hz), 7.77 (s, 1H), 8.40 (s, 1H). ¹³C NMR (CDCl₃) δ 44.72 (CH₂ in piperazine), 46.51 (CH₂), 48.24 (CH₂ in piperazine), 114.85, 119.88, 120.92, 121.24, 123.28 (C in phenyl), 126.01 (q, *J*_{CF} = 3.8 Hz), 126.48 (q, *J*_{CF} = 3.9 Hz), 127.78, 130.47, 138.22 (C in phenyl), 139.71 (C-5), 151.10 (C-8), 152.81 (C-6), 153.15 (C-2), 153.83 (C-4). MS (ESI+) *m/z*: 507.51 (100%) (M+H). Anal. Calcd for C₂₄H₂₀F₆N₆ · 0.1H₂O · 0.3CH₃COOC₂H₅: C, 56.61; H, 4.26; N, 15.71. Found: C, 56.23; H, 3.93; N, 15.43.

2. 1. 3. 7. 6-[4-(4-Fluorophenyl)piperazine-1-yl]-9-(4-trifluoromethylbenzyl)-9H-purine (13)

Yield 240 mg (55%), m.p. 111–113 °C. ¹H NMR (CDCl₃) δ 3.24 (t, 4H, *J* = 5.2 Hz), 4.48 (br s, 4H), 5.45 (s, 2H), 6.91–7.02 (m, 4H), 7.37 (d, 2H, *J* = 8.4 Hz), 7.60 (d, 2H, *J* = 8 Hz), 7.77 (s, 1H), 8.40 (s, 1H). ¹³C NMR (CDCl₃) δ 45.04 (CH₂ in piperazine), 46.48 (CH₂), 50.62 (CH₂ in piperazine), 115.65 (d, *J* = 21.9 Hz), 118.39 (d, *J* = 7.7 Hz), 119.85, 122.46, 125.16 (C in phenyl), 125.99 (q, *J*_{CF} = 3.9 Hz), 127.76, 130.60 (q, *J*_{CF} = 32.8 Hz), 138.08 (C in phenyl), 139.77 (C-5), 147.89 (C-8), 151.07 (C-6), 152.81 (C-2), 153.88 (C-4), 157.50 (d, *J* = 239.3). MS (ESI+) *m/z*: 457.57 (100%) (M+H). Anal. Calcd for C₂₃H₂₀F₄N₆ · 0.2H₂O: C, 60.05; H, 4.47; N, 18.27. Found: C, 59.83; H, 4.30; N, 18.11.

2. 1. 3. 8. 6-[4-(2,4-Difluorophenyl)piperazine-1-yl]-9-(4-trifluoromethylbenzyl)-9H-purine (14)

Yield 420 mg (89%), m.p. 193 °C. ¹H NMR (CDCl₃) δ 3.16 (t, 4H, *J* = 5.2 Hz), 4.49 (br s, 4H), 5.45 (s, 2H),

6.78–6.98 (m, 3H), 7.37 (d, 2H, *J* = 8 Hz), 7.60 (d, 2H, *J* = 8 Hz), 7.76 (s, 1H), 8.40 (s, 1H). ¹³C NMR (CDCl₃) δ 45.21 (CH₂ in piperazine), 46.48 (CH₂), 51.19 (CH₂ in piperazine), 104.84 (t, *J* = 24.5 Hz), 110.78 (dd, *J* = 3.8, *J* = 21.9), 119.81 (dd, *J* = 3.9 Hz, *J* = 10.3 Hz), 122.46, 125.16 (C in phenyl), 125.99 (q, *J*_{CF} = 3.2 Hz), 127.77, 130.59 (q, *J*_{CF} = 32.2 Hz), 136.49 (dd, *J* = 3.8, *J* = 9 Hz), (C in phenyl), 138.05 (C-5), 139.78 (C-8), 151.08 (C-6), 152.81 (C-2), 153.91 (C-4), 155.75 (dd, *J* = 11.6 Hz, *J* = 237.3), 158.22 (dd, *J* = 7.7 Hz, *J* = 232.2 Hz), (C in phenyl). MS (ESI+) *m/z*: 475.82 (100%) (M+H). Anal. Calcd for C₂₃H₁₉F₅N₆: C, 58.23; H, 4.04; N, 17.71. Found: C, 58.29; H, 4.17; N, 17.52.

2. 1. 3. 9. 6-[4-(3,4-Dichlorophenyl)piperazine-1-yl]-9-(4-trifluoromethylbenzyl)-9H-purine (15)

Yield 450 mg (88%), m.p. 136 °C. ¹H NMR (CDCl₃) δ 3.30 (t, 4H, *J* = 4.8 Hz), 4.47 (br s, 4H), 5.45 (s, 2H), 6.79 (dd, 1H, *J* = 9.2 Hz, *J* = 3.2 Hz), 7.00 (d, 3H, *J* = 2.8 Hz), 7.30 (d, 1H, *J* = 9.2 Hz), 7.37 (d, 2H, *J* = 8.4 Hz), 7.60 (d, 2H, *J* = 8 Hz), 7.77 (s, 1H), 8.40 (s, 1H). ¹³C NMR (CDCl₃) δ 44.71 (CH₂ in piperazine), 46.50 (CH₂), 49.02 (CH₂ in piperazine), 115.69, 117.65, 119.88, 122.45, 122.80, 125.16, (C in phenyl), 126.01 (q, *J*_{CF} = 3.8 Hz), 127.78, 130.54, 130.62 (q, *J*_{CF} = 32.9 Hz), 132.90, 138.21 (C in phenyl), 139.71 (C-5), 150.55 (C-8), 151.11 (C-6), 152.80 (C-2), 153.81 (C-4). MS (ESI+) *m/z*: 507.7 (100%) (M⁺), 509.7 (63%) (M+2), 511.9 (5%) (M+4). Anal. Calcd for C₂₃H₁₉Cl₂N₆: C, 54.45; H, 3.77; N, 16.56. Found: C, 54.43; H, 3.70; N, 16.54.

2. 1. 3. 10. 6-[4-(Diphenylmethyl)piperazine-1-yl]-9-(4-trifluoromethylbenzyl)-9H-purine (16)

Yield 340 mg (65%), m.p. 179–182 °C. ¹H NMR (CDCl₃) δ 2.53 (t, 4H, *J* = 5.2 Hz), 4.28 (s, 1H), 4.31 (br s, 4H), 5.40 (s, 2H), 7.17–7.36 (m, 8H), 7.44 (d, 4H, *J* = 7.2 Hz), 7.58 (d, 2H, *J* = 8.4 Hz), 7.67 (s, 1H), 8.33 (s, 1H). ¹³C NMR (CDCl₃) δ 42.82 (CH₂ in piperazine), 43.82 (CH₂), 49.45 (CH₂ in piperazine), 73.53 (CH), 117.19, 119.91, 122.61 (C in phenyl), 123.3 (q, *J*_{CF} = 3.9 Hz), 124.51, 125.17, 125.41, 125.96, 128.95 (q, *J*_{CF} = 32.9 Hz), 135.17 (C in phenyl), 137.28 (C-5), 139.64 (C-8), 148.35 (C-6), 150.24 (C-2), 151.32 (C-4). MS (ESI+) *m/z*: 529.68 (100%) (M+H). Anal. Calcd for C₃₀H₂₇F₃N₆: C, 68.17; H, 5.15; N, 15.90. Found: C, 67.90; H, 5.09; N, 15.71.

2. 1. 3. 11. 6-[4-(2-Hydroxyethyl)piperazine-1-yl]-9-(4-chlorobenzyl)-9H-purine (17)

Yield 290 mg (77%), m.p. 138–141 °C. ¹H NMR (CDCl₃) δ 2.61 (t, 2H, *J* = 5.6 Hz), 2.66 (t, 4H, *J* = 5.6 Hz), 3.68 (t, 2H, *J* = 5.2 Hz), 3.77 (br s, 4H), 5.34 (s, 2H), 7.21 (d, 2H, *J* = 8.4 Hz), 7.31 (d, 2H, *J* = 8.4 Hz), 7.71 (s, 1H), 8.37 (s, 1H). ¹³C NMR (CDCl₃) δ 45.11 (CH₂ in piperazine), 46.34 (CH₂), 53.01 (CH₂ in piperazine), 57.76 (CH₂-N), 59.46 (CH₂-OH), 119.79, 128.98, 129.16, 134.26 (C in phenyl), 134.31 (C-5), 137.99 (C-8), 150.98 (C-6), 152.68 (C-2), 153.84 (C-4). MS (ESI+) *m/z*: 373.61 (100%)

(M+H), 375.62 (33%) (M+H+2). Anal. Calcd for $C_{18}H_{21}ClN_6O \cdot 0.4H_2O$: C, 56.88; H, 5.78; N, 22.11. Found: C, 56.65; H, 5.44; N, 21.88.

2. 1. 3. 12. 6-[4-Cyclohexylpiperazine-1-yl]-9-(4-chlorobenzyl)-9H-purine (18)

Yield 380 mg (93%), m.p. 125 °C. 1H NMR ($CDCl_3$) δ 1.09–1.99 (m, 10H), 2.54 (br s, 1H), 2.86 (br s, 4H), 4.47 (br s, 4H), 5.31 (s, 2H), 7.19 (d, 2H, $J = 8.4$ Hz), 7.29 (d, 2H, $J = 8.4$ Hz), 7.70 (s, 1H), 8.35 (s, 1H). ^{13}C NMR ($CDCl_3$) δ 25.57, 25.82, 28.11 (CH_2 in cyclohexyl), 44.31 (CH_2 in piperazine), 45.78 (CH_2), 48.86 (CH_2 in piperazine), 64.53 (CH in cyclohexyl), 119.80, 129.01, 129.16 (C in phenyl), 134.26 (C-5), 138.20 (C-8), 151.02 (C-6), 152.66 (C-2), 153.55 (C-4). MS (ESI+) m/z : 411.75 (100%) (M+H), 413.74 (30%) (M+H+2). Anal. Calcd for $C_{22}H_{27}ClN_6$: C, 64.30; H, 6.62; N, 20.45. Found: C, 64.28; H, 6.84; N, 20.12.

2. 1. 3. 13. 6-[4-(Pyrimidine-2-yl)piperazine-1-yl]-9-(4-chlorobenzyl)-9H-purine (19)

Yield 280 mg (69%), m.p. 202 °C. 1H NMR ($CDCl_3$) δ 3.99 (t, 4H, $J = 5.6$ Hz), 4.40 (br s, 4H), 5.35 (s, 2H), 6.54 (t, 1H, $J = 4.4$ Hz), 7.21 (d, 2H, $J = 8.8$ Hz), 7.32 (d, 2H, $J = 8$ Hz), 7.74 (s, 1H), 8.34 (d, 2H, $J = 4.4$ Hz), 8.41 (s, 1H). ^{13}C NMR ($CDCl_3$) δ 43.76 (CH_2 in piperazine), 44.98 (CH_2 in piperazine), 46.36 (CH_2), 110.22 (C-5 in pyrimidine), 119.91, 128.99, 129.17, 134.26 (C in phenyl), 134.30 (C-5), 138.12 (C-8), 151.02 (C-6), 152.69 (C-2), 154.01 (C-4), 157.76 (C-4,6 in pyrimidine), 161.67 (C-2 in pyrimidine). MS (ESI+) m/z : 407.77 (100%) (M+H), 409.84 (32%) (M+H+2). Anal. Calcd for $C_{20}H_{19}ClN_8 \cdot 0.43MeOH$: C, 58.34; H, 4.96; N, 27.54. Found: C, 58.73; H, 5.18; N, 26.27.

2. 1. 3. 14. 6-(4-Phenylpiperazine-1-yl)-9-(4-chlorobenzyl)-9H-purine (20)

Yield 120 mg (82%), m.p. 140–143 °C. 1H NMR ($CDCl_3$) δ 3.33 (t, 4H, $J = 5.2$ Hz), 4.48 (br s, 4H), 5.35 (s, 2H), 6.91 (t, 1H, $J = 7.6$ Hz), 6.98 (d, 2H, $J = 8$ Hz), 7.21 (d, 2H, $J = 8.8$ Hz), 7.25–7.34 (m, 4H), 7.73 (s, 1H), 8.40 (s, 1H). ^{13}C NMR ($CDCl_3$) δ 45.04 (CH_2 in piperazine), 46.36 (CH_2), 49.58 (CH_2 in piperazine), 116.50, 119.87, 120.28, 128.99, 129.18, 129.21, 134.28, 134.30 (C in phenyl), 138.10 (C-5), 151.04 (C-8), 151.21 (C-6), 152.73 (C-2), 153.88 (C-4). MS (ESI+) m/z : 405.69 (100%) (M+H), 407.69 (47%) (M+H+2). Anal. Calcd for $C_{22}H_{21}ClN_6$: C, 65.26; H, 5.23; N, 20.76. Found: C, 65.24; H, 5.04; N, 20.70.

2. 1. 3. 15. 6-[4-(4-Methylphenyl)piperazine-1-yl]-9-(4-chlorobenzyl)-9H-purine (21)

Yield 310 mg (75%), m.p. 193 °C. 1H NMR ($CDCl_3$) δ 2.28 (s, 3H), 3.26 (t, 4H, $J = 4.8$ Hz), 4.47 (br s, 4H), 5.34 (s, 2H), 6.90 (d, 2H, $J = 8.4$ Hz), 7.10 (d, 2H, $J = 8$ Hz), 7.21 (d, 2H, $J = 8.8$ Hz), 7.31 (d, 2H, $J = 8$ Hz), 7.73 (s, 1H), 8.40 (s, 1H). ^{13}C NMR ($CDCl_3$) δ 20.44 (CH_3), 45.03 (CH_2 in piperazine), 46.37 (CH_2), 50.23 (CH_2 in piperazine), 116.92, 119.85, 128.99, 129.18, 129.74, 129.97, 134.29 (C in

phenyl), 138.08 (C-5), 149.06 (C-8), 151.01 (C-6), 152.69 (C-2), 153.84 (C-4). MS (ESI+) m/z : 419.78 (100%) (M+H), 421.81 (45%) (M+H+2). Anal. Calcd for $C_{23}H_{23}ClN_6 \cdot 0.2H_2O$: C, 65.38; H, 5.58; N, 19.89. Found: C, 65.94; H, 5.53; N, 20.06.

2. 1. 3. 16. 6-[4-(4-Trifluoromethylphenyl)piperazine-1-yl]-9-(4-chlorobenzyl)-9H-purine (22)

Yield 330 mg (69%), m.p. 162 °C. 1H NMR ($CDCl_3$) δ 3.43 (t, 4H, $J = 4.8$ Hz), 4.48 (br s, 4H), 5.35 (s, 2H), 6.98 (d, 2H, $J = 8.4$ Hz), 7.22 (d, 2H, $J = 8.8$ Hz), 7.31 (d, 2H, $J = 8.4$ Hz), 7.51 (d, 2H, $J = 8.4$ Hz), 7.40 (s, 1H), 8.40 (s, 1H). ^{13}C NMR ($CDCl_3$) δ 44.78 (CH_2 in piperazine), 46.43 (CH_2), 48.22 (CH_2 in piperazine), 114.84, 119.87, 120.89, 121.21, 125.97 (C in phenyl), 126.48 (q, $J_{CF} = 3.8$ Hz), 129.02, 129.21, 134.20 (C in phenyl), 138.31 (C-5), 151.01 (C-8), 152.55 (C-6), 153.13 (C-2), 153.67 (C-4). MS (ESI+) m/z : 473.54 (100%) (M+H), 475.52 (40%) (M+H+2). Anal. Calcd for $C_{23}H_{20}ClF_3N_6$: C, 58.42; H, 4.26; N, 17.77. Found: C, 58.55; H, 4.30; N, 17.60.

2. 1. 3. 17. 6-[4-(4-Fluorophenyl)piperazine-1-yl]-9-(4-chlorobenzyl)-9H-purine (23)

Yield 280 mg (67%), m.p. 186–188 °C. 1H NMR ($CDCl_3$) δ 3.23 (t, 4H, $J = 5.2$ Hz), 4.47 (br s, 4H), 5.35 (s, 2H), 6.91–7.02 (m, 4H), 7.21 (d, 2H, $J = 8.4$ Hz), 7.31 (d, 2H, $J = 8$ Hz), 7.73 (s, 1H), 8.40 (s, 1H). ^{13}C NMR ($CDCl_3$) δ 40.31 (CH_2 in piperazine), 41.62 (CH_2), 45.87 (CH_2 in piperazine), 110.89 (d, $J = 21.9$ Hz), 113.64 (d, $J = 7.7$ Hz), 115.12, 124.24, 124.43, 129.52, 129.54 (C in phenyl), 133.38 (C-5), 143.13 (C-8), 146.28 (C-6), 147.93 (C-2), 149.08 (C-4), 152.75 (d, $J = 239.9$). MS (ESI+) m/z : 424 (100%) (M+H), 425.94 (35%) (M+H+2). Anal. Calcd for $C_{22}H_{20}ClFN_6$: C, 62.48; H, 4.77; N, 19.87. Found: C, 62.55; H, 4.57; N, 19.84.

2. 1. 3. 18. 6-[4-(2,4-Difluorophenyl)piperazine-1-yl]-9-(4-chlorobenzyl)-9H-purine (24)

Yield 410 mg (93%), m.p. 183–185 °C. 1H NMR ($CDCl_3$) δ 3.15 (t, 4H, $J = 4.8$ Hz), 4.48 (br s, 4H), 5.35 (s, 2H), 6.78–6.96 (m, 3H), 7.22 (d, 2H, $J = 8.4$ Hz), 7.32 (d, 2H, $J = 8$ Hz), 7.73 (s, 1H), 8.40 (s, 1H). ^{13}C NMR ($CDCl_3$) δ 40.53 (CH_2 in piperazine), 41.63 (CH_2), 46.44 (CH_2 in piperazine), 100.08 (t, $J = 24.4$ Hz), 106.03 (dd, $J = 21.3$ Hz, $J = 3.9$ Hz), 115.05 (dd, $J = 9.1$ Hz, $J = 3.8$ Hz), 124.25, 124.43, 129.52, 131.71 (dd, $J = 9.1$ Hz, $J = 3.9$), (C in phenyl), 133.35 (C-5), 145.51 (C-8), 146.28 (C-6), 147.90 (C-2), 149.09 (C-4), 151.03 (dd, $J = 240.6$, $J = 11.6$ Hz), 153.46 (dd, $J = 231.6$, $J = 12.2$) (C in phenyl). MS (ESI+) m/z : 441.8 (100%) (M+H), 443.8 (37%) (M+H+2). Anal. Calcd for $C_{22}H_{19}ClF_2N_6$: C, 59.93; H, 4.34; N, 19.06. Found: C, 59.87; H, 4.24; N, 19.11.

2. 1. 3. 19. 6-[4-(3,4-Dichlorophenyl)piperazine-1-yl]-9-(4-chlorobenzyl)-9H-purine (25)

Yield 440 mg (92%), m.p. 198–200 °C. 1H NMR ($CDCl_3$) δ 3.30 (t, 4H, $J = 4.8$ Hz), 4.46 (br s, 4H), 5.35 (s,

2H), 6.79 (dd, 1H, $J = 2.8$ Hz, $J = 9.2$ Hz), 7.00 (d, 1H, $J = 2.8$ Hz), 7.22 (d, 2H, $J = 8.8$ Hz), 7.29–7.33 (m, 3H), 7.74 (s, 1H), 8.40 (s, 1H). ^{13}C NMR (CDCl_3) δ 44.75 (CH_2 in piperazine), 46.41 (CH_2), 49.01 (CH_2 in piperazine), 115.69, 117.64, 119.89, 122.79, 129.01, 129.20, 130.54, 132.90, 134.22, 134.32 (C in phenyl), 138.26 (C-5), 150.56 (C-8), 151.05 (C-6), 152.65 (C-2), 153.75 (C-4). MS (ESI+) m/z : 473.7 (100%) (M^+), 475.8 (90%) ($\text{M}+2$), 477.8 (35%) ($\text{M}+4$). Anal. Calcd for $\text{C}_{22}\text{H}_{19}\text{Cl}_3\text{N}_6$: C, 55.77; H, 4.04; N, 17.74. Found: C, 55.50; H, 4.08; N, 17.86.

2. 1. 3. 20. 6-[4-(Diphenylmethyl)piperazine-1-yl]-9-(4-chlorobenzyl)-9H-purine (26)

Yield 310 mg (62%), m.p. 145–147 °C. ^1H NMR (CDCl_3) δ 2.53 (m, 4H), 4.28 (s, 1H), 4.30 (br s, 4H), 5.28 (s, 2H), 7.14–7.22 (m, 4H), 7.25–7.31 (m, 6H), 7.44 (d, 4H, $J = 7.2$ Hz), 7.63 (s, 1H), 8.34 (s, 1H). ^{13}C NMR (CDCl_3) δ 45.37 (CH_2 in piperazine), 46.28 (CH_2), 52.03 (CH_2 in piperazine), 76.10 (CH), 119.79, 127.06, 127.98, 128.52, 128.98, 129.14, 134.20, 134.36 (C in phenyl), 137.79 (C-5), 142.22 (C-8), 150.89 (C-6), 152.70 (C-2), 153.86 (C-4). MS (ESI+) m/z : 495.67 (100%) ($\text{M}+\text{H}$), 497.66 (39%) ($\text{M}+\text{H}+2$). Anal. Calcd for $\text{C}_{29}\text{H}_{27}\text{ClN}_6$: C, 70.36; H, 5.50; N, 16.98. Found: C, 70.17; H, 5.20; N, 16.92.

2. 2. Biological Evaluation

2. 2. 1. Cells and Culture

The human primary liver cancer cell lines (Huh7, HepG2, Mahlavu and FOCUS) were grown in Dulbecco's Modified Eagle's Medium (DMEM) (Invitrogen GIBCO) with 10% fetal bovine serum (FBS) (Invitrogen GIBCO), nonessential amino acids, and 1% penicillin (Biochrome). It was incubated at 37 °C with 5% CO_2 . DMSO (Sigma) was used as the solvent for the compounds. The concentration of DMSO was always less than 1% in the cell culture medium. The cytotoxic drugs (camptothecin (CPT), 5-fluorouracil (5-FU), fludarabine, and cladribine) used as positive controls were from Calbiochem.

2. 2. 2. Sulforhodamine B (SRB) Assay for Cytotoxicity Screening

Huh7, HCT116, MCF7, HepG2, Mahlavu, and FOCUS cells were inoculated (2000–10000 cells/well in 200 μL) in 96-well plates. The next day, the media was refreshed, and the compounds dissolved in DMSO were applied in concentrations between 1 and 40 μM in parallel with DMSO-only treated cells as negative controls. At the 72nd hour of treatment with compounds 7–26 and the other drugs, the cancer cells were fixed with 100 μL of 10% (w/v) trichloroacetic acid (TCA) and kept at +4 °C in dark for 1 h. TCA fixation was terminated by washing the wells with ddH_2O five times. Air-dried plates were stained with 0.4% sulforhodamine B (SRB) dissolved in 1% acetic acid solution for 10 min in the dark and at room tempera-

ture. The protein-bound and dried SRB dye was then solubilized with 10 mM Tris-Base pH 8. The absorbance values were obtained at 515 nm in a microplate reader. The data normalized against DMSO-only treated wells, which were used as controls in serial dilutions. In all experiments, a linear response was observed, with serial dilutions of the compounds and the drugs.

3. Results and Discussion

3. 1. Chemistry

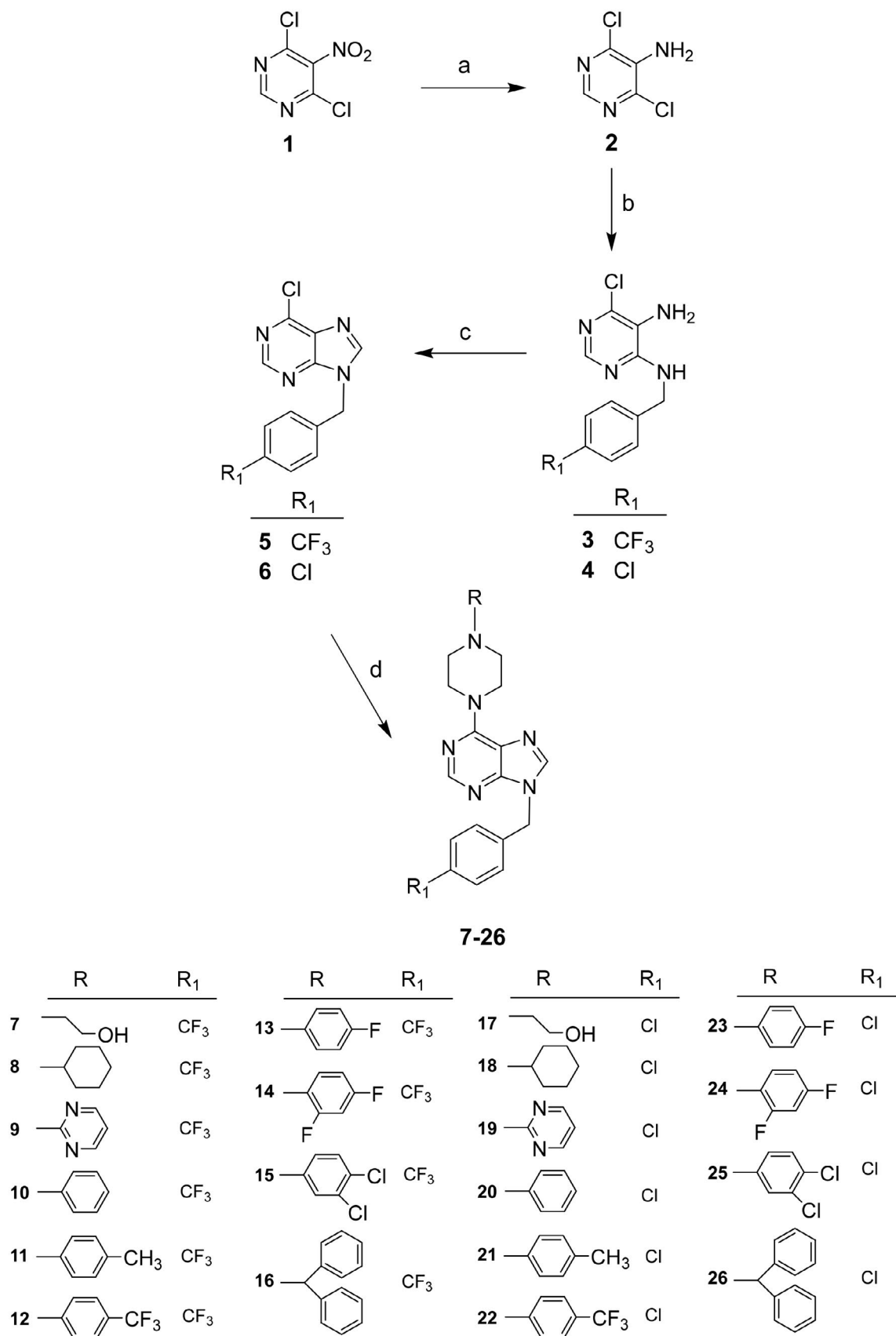
The 6-(4-substituted piperazine-1-yl)-9-(4-substituted benzyl)purine analogs were synthesized in four steps starting with commercially available 4,6-dichloro-5-nitropyrimidine (**1**) (Scheme 1). The dichloronitropyrimidine was reduced to the corresponding dichloroaminopyrimidine (**2**) with stannous chloride and ethanol.⁵³ Amination of 5-amino-4,6-dichloropyrimidine (**2**) with the appropriate benzylamines gave the 4-(4-substituted benzyl)pyrimidines (**3**, **4**). Condensation of compounds **3**, **4** with triethylorthoformate and *para*-toluenesulfonic acid afforded the intermediate 6-chloro-9-(4-substituted benzyl)purines **5**, **6**.⁵⁴ Purines substituted at C-6 (**7**–**26**) were synthesized by nucleophilic substitution of the chlorine of 9-substituted purines (**5**, **6**) with the appropriate 4-substituted piperazines in the presence of base.

3. 2. Biological Evaluation

The antitumor activities of newly synthesized purine analogues were first analyzed on three human cancer cell lines including Huh7 (liver), HCT116 (colon) and MCF7 (breast) cancer cells by using the sulforhodamine B (SRB) method. The IC_{50} values of the purine compounds were calculated in comparison with DNA topoisomerase inhibitor camptothecin (CPT) and the known cell growth inhibitors fludarabine, cladribine, 5-fluorouracil (5-FU). The data are summarized in Table 1.

All synthesized purine derivatives in this study, except for compound **19**, exhibited important cytotoxic activity against cancer cells Huh7, HCT116, MCF7 with IC_{50} from 0.05 to 21.7 μM .

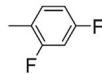
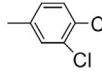
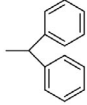
As seen from the data in Table 1, all the 6-(trifluoromethylphenyl)piperazine purines, **12** and **22** exhibited excellent cytotoxic activities with IC_{50} 0.08–0.13 μM on Huh7 cells comparable to CPT and better than cladribine, fludarabine and 5-FU. In addition, compounds **15** and **25** bearing a 3,4-dichlorophenyl group at the piperazine of the purine, presented a higher cytotoxic activity than known nucleoside drugs cladribine, fludarabine and nucleobase drug 5-FU on Huh7 cells. For the 4-fluorophenyl substituted derivatives **13** and **23**, their best activity is observed for the 9-(4-chlorobenzyl) purine derivative **23** with IC_{50} value of 0.57 μM on Huh7. Cytotoxic activity differences were not observed in the nonsubstituted phe-



Scheme 1. (a) $\text{SnCl}_2 \cdot 2\text{H}_2\text{O}$, EtOH; (b) 4-substituted benzylamine, EtOH, Et_3N ; (c) $\text{HC}(\text{OEt})_3$, pTSA; (d) 4-substituted piperazine, Et_3N , EtOH

Table 1. *In vitro* cytotoxicity of compounds 7–26 on different human cancer cell lines

Compound	R	R ₁	Cancer cell lines, IC ₅₀ (μM) ^a		
			Huh7	HCT116	MCF7
7		CF ₃	18.25 ± 0.55	19.14 ± 0.75	17.83 ± 0.56
8		CF ₃	7.86 ± 0.04	7.74 ± 0.08	6.51 ± 0.52
9		CF ₃	9.6 ± 0.6	11.3 ± 2.1	17.8 ± 0.2
10		CF ₃	0.86 ± 0.19	0.28 ± 0.003	0.16 ± 0.037
11		CF ₃	<1.0	<0.1	<1.0
12		CF ₃	0.13 ± 0.12	0.42 ± 0.08	0.4
13		CF ₃	1.54 ± 0.10	1.26 ± 0.13	1.12 ± 0.16
14		CF ₃	5.05 ± 0.52	5.51 ± 0.29	4.24 ± 1.17
15		CF ₃	0.6 ± 0.1	0.74 ± 0.05	<1.0
16		CF ₃	15.55 ± 1.09	12.97 ± 1.11	12.13 ± 0.38
17		Cl	21.8 ± 2.7	18.96 ± 0.06	21.8 ± 4.4
18		Cl	9.26 ± 0.59	8.87 ± 0.35	8.61 ± 0.26
19		Cl	38.0 ± 5.1	57.1 ± 8.8	100.9 ± 28.0
20		Cl	0.56 ± 0.12	0.26 ± 0.17	0.38 ± 0.07
21		Cl	<0.1	0.26 ± 0.35	0.48 ± 0.50
22		Cl	0.08 ± 0.06	0.04 ± 0.004	0.05
23		Cl	0.57 ± 0.12	0.14 ± 0.10	2.80 ± 3.22

24		Cl	9.38 ± 0.65	NI	NI
25		Cl	0.31 ± 0.10	13.0 ± 0.38	7.08 ± 3.03
26		Cl	20.1 ± 6.8	13.15 ± 0.06	14.02 ± 0.67
CPT			<0.1	0.034 ± 0.036	<0.1
5-FU			30.6 ± 1.8	4.1 ± 0.3	3.5 ± 0.7
Fludarabine			28.4 ± 19.2	8.0 ± 3.4	15.2 ± 0.1
Cladribine			0.9 ± 0.7	<0.1	2.4 ± 2.4

^a IC₅₀ values were calculated from the cell growth inhibition percentages obtained with 5 different concentrations (40, 20, 10, 5, and 2.5 μM) of each molecule incubated for 72 h. NI: no inhibition.

Table 2. IC₅₀ values of 7–18, 20, 22–26 against hepatocellular carcinoma (HCC) cell lines Huh7, HepG2, MAHLAVU, FOCUS.

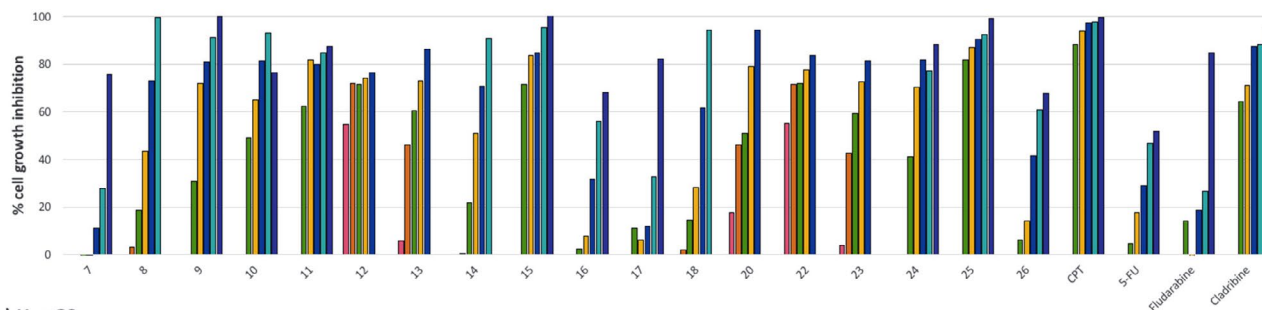
Compound	HCC Cancer cell lines, IC ₅₀ (μM) ^a			
	Huh7	HepG2	Mahlavu	FOCUS
7	28.9 ± 4.0	25.2 ± 4	NI	NI
8	5.36 ± 0.2	6.4 ± 0.5	8.0 ± 0.2	6.4 ± 0.6
9	3.32 ± 1.3	4.3 ± 0.6	6.0 ± 0.1	7.2 ± 1.7
10	1.45 ± 0.2	1.4 ± 0.2	1.9 ± 0.4	1.5 ± 0.5
11	0.29 ± 0.4	<1.0	NI	0.5 ± 0.1
12	0.13 ± 0.1	0.1 ± 0.04	<0.1	<0.1
13	2.13 ± 0.1	1.6 ± 0.2	2.3 ± 0.3	1.9 ± 0.1
14	5.48 ± 0.2	3.8 ± 0.5	4.8 ± 0.2	5.1 ± 0.5
15	0.24 ± 0.1	<0.1	8.2 ± 1.4	1.4 ± 0.3
16	19.4 ± 1.7	32.3 ± 23.9	10.8 ± 0.4	11.6 ± 0.4
17	23.9 ± 0.5	69.4 ± 25.7	85.4 ± 26.9	83.3 ± 14.2
18	6.74 ± 0.3	7.3 ± 1.3	13.1 ± 1.2	9.1 ± 0.9
20	1.89 ± 0.1	1.5 ± 0.2	2.3 ± 0.1	0.2 ± 0.1
22	0.23 ± 0.1	<0.1	<0.1	<0.1
23	2.33 ± 0.2	1.8 ± 0.4	3.2 ± 0.2	4.5 ± 0.5
24	2.22 ± 0.4	1.4 ± 1.1	11.1 ± 1.9	5.1 ± 1.5
25	<0.1	<0.1	5.6 ± 0.1	1.2 ± 0.3
26	16.4 ± 1.7	11.7 ± 1.4	12.1 ± 0.6	1 ± 1
CPT	<0.1	<0.1	<0.1	<0.1
5-FU	30.6 ± 1.8	0.8 ± 0.26	10.0 ± 1.8	3.7 ± 0.5
Fludarabine	28.4 ± 19.2	17.0 ± 5.9	13.5 ± 4.9	13.7 ± 1.2
Cladribine	0.9 ± 0.7	0.4 ± 0.1	<0.1	<0.1

^a IC₅₀ values were calculated from the cell growth inhibition percentages obtained with 5 different concentrations (40, 20, 10, 5, and 2.5 μM) of each molecule incubated for 72 h. NI: No inhibition

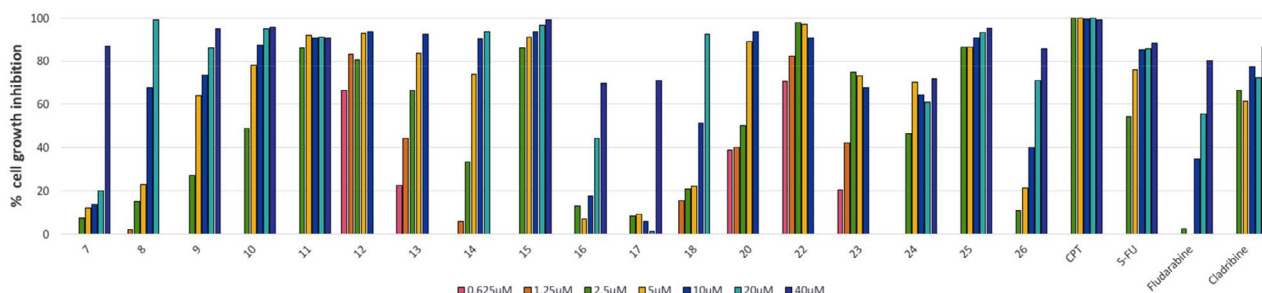
nyl and 4-methyl phenyl group bearing purin derivatives (**10**, **11**, **20**, **21**) and these compounds had significantly higher bioactivity (IC₅₀ < 1.0 μM) compared to 5-FU, fludarabine, cladribine against Huh7 cell.

Within the tested purine analogs on HCT116 cell, compounds **11** and **22** showed superior cytotoxic activity (IC₅₀ < 0.1 and 0.04 μM, respectively) compared to 5-FU (IC₅₀ 4.1), fludarabine (IC₅₀ 8.0 μM), cladribine (IC₅₀ < 0.1

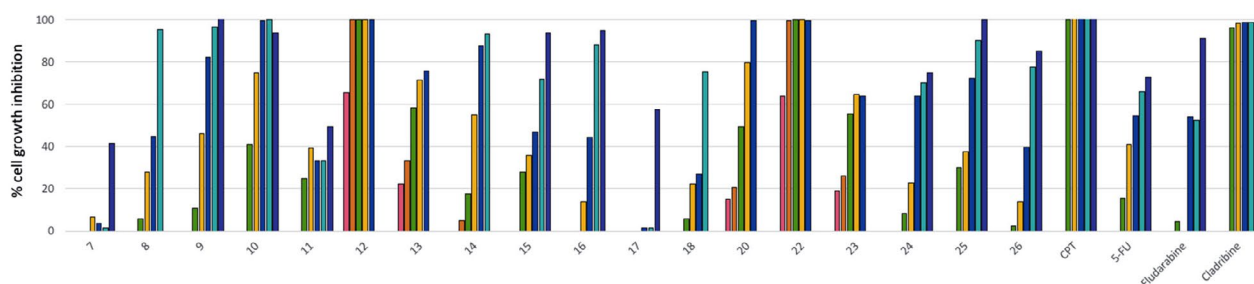
a) Huh7



b) HepG2



c) Mhlavu



d) FOCUS

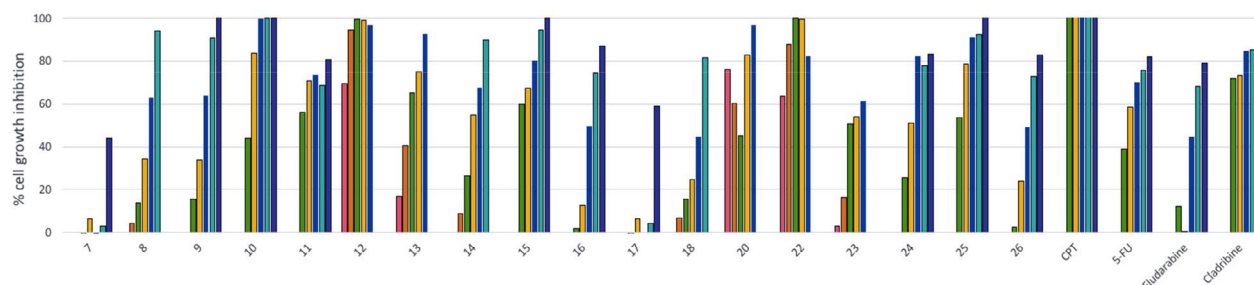


Figure 3. Percent cell death in the presence of most active compounds. Huh7, HepG2, Mhlavu and FOCUS cells were inoculated in 96-well plates. All molecules and their DMSO controls were administered to the cells in triplicate with five different concentrations: 40, 20, 10, 5, and 2.5 μM . After 72 h of incubation, SRB assays were generated, and the cell death percentages were calculated in comparison with DMSO-treated wells.

μM) and CPT (IC_{50} 0.034 μM). Furthermore, compounds **10**, **12**, **15**, **20**, **21**, **23** had a better cytotoxic activity ($\text{IC}_{50} < 1.0 \mu\text{M}$) than 5-FU and fludarabine against HCT116 cell line.

Purine **22**, one of the most cytotoxic molecules, displayed a significant IC_{50} value of 0.05 μM comparable to CPT ($\text{IC}_{50} < 0.1 \mu\text{M}$) on MCF7. Compound **22** also displayed better cytotoxic bioactivities on MCF7 cells with respect to 5-FU (IC_{50} 3.5 μM) and known nucleoside drugs

cladribine (IC_{50} 2.4 μM) and fludarabine (IC_{50} 15.2 μM), on MCF7 cells. In addition, the cytotoxic activity against MCF7 cell line of purines 7–26 was evaluated.

Significant bioactivity was also observed for compounds **10** (IC_{50} 0.16 μM), **12** (IC_{50} 0.4 μM), **20** (IC_{50} 0.38 μM), **21** (IC_{50} 0.48 μM), **11**, **15** ($\text{IC}_{50} < 1.0 \mu\text{M}$) on MCF7 cells.

We then screened the anticancer activity of the most potent purine analogs against further hepatocellular cancer

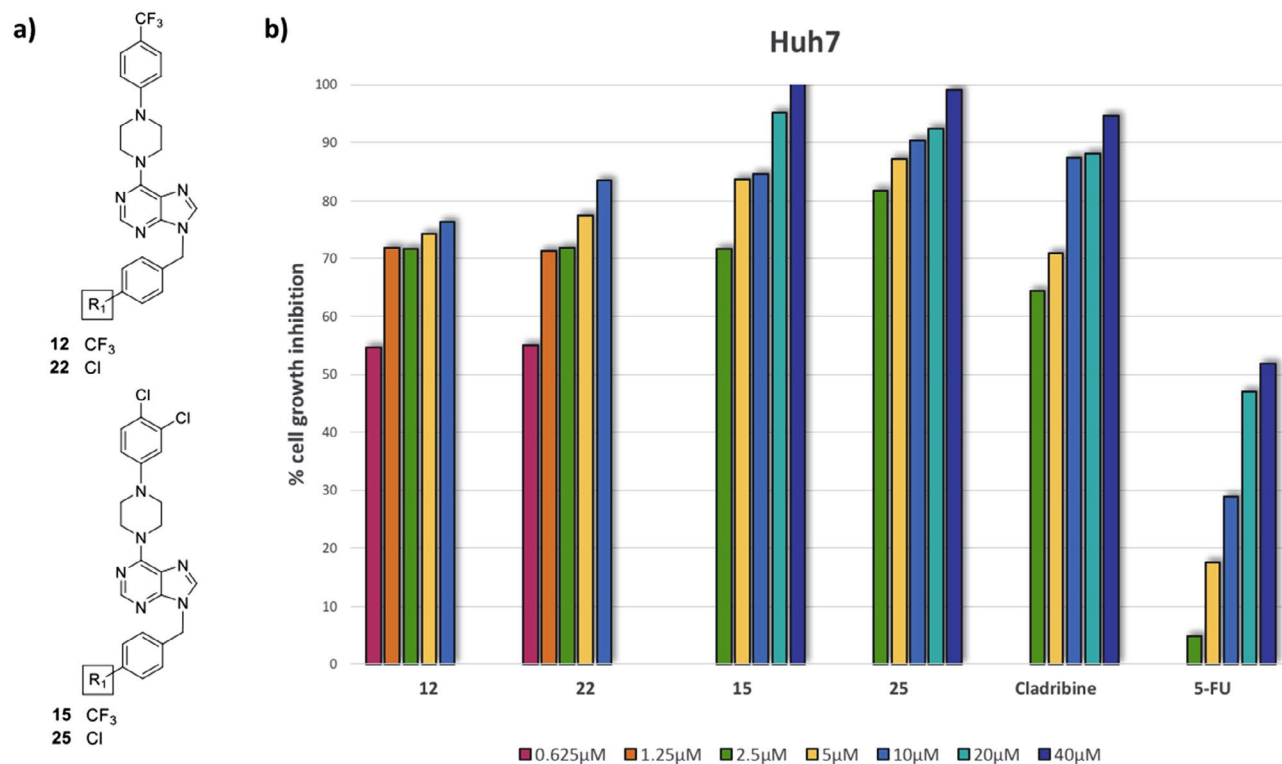


Figure 4. a) Chemical structures of the most active purine analogs **12**, **22**, **15** and **25** b) Percent cell death in the presence of most active compounds (**12**, **22**, **15** and **25**). Huh7 cells were inoculated in 96-well plates. All molecules and their DMSO controls were administered to the cells in triplicate with corresponding different concentrations: 0.625, 1.25, 2.5, 5, 10, 20, and 40 μM. After 72 h of incubation, SRB assays were generated, and the cell death percentages were calculated in comparison with DMSO-treated wells.

(HCC) cells lines (Table 2, Figure 3). We observed that the most important cell growth inhibition in the presence of 6-(4-(4-trifluoromethylphenyl)piperazine)-9-(4-trifluoromethylbenzyl)purine derivative **12** and its 9-(4-chlorobenzyl) analogue **22**, with IC₅₀ values of < 0.1–0.23 μM against all the HCC cell lines. Compounds **12** and **22** also showed comparable cytotoxic effects with CPT and cladribine on these cell lines. Furthermore, **12** and **22** showed a better biological activity than the standard anticancer agents 5-FU and fludarabine in HCC cell lines (Table 2). The 6-(4-(2,4-dichlorophenyl)piperazine) analogs **15**, **25** were also very active (IC₅₀ < 0.1–0.24 μM) against Huh7 and HepG2 cell lines.

4. Conclusion

We designed and synthesized twenty novel purine analogs **7–26** bearing substituted piperazine at the C-6, substituted benzyl group at the N-9, by the multistep reactions, starting from 4,6-dichloro-5-nitropyrimidine. The cytotoxic activities of the compounds were evaluated first in human liver (Huh7), breast (MCF7), colon (HCT116) and then in hepatocellular carcinoma cells (HCC): Huh7, HepG2, Mahlavu and FOCUS. Our results demonstrated that the 6-(trifluoromethylphenyl)piperazine analogs **12**, **22** with IC₅₀ values less than 0.5 μM were promising molecules as cytotoxic agents on Huh7, MCF7 and HCT116

cancer cells. In order to investigate the use of potential cytotoxic agents on HCC, the bioactivity of the purine analogs was also tested in a panel of liver cancer cells. Molecules **12** and **22**, that were synthesized as putative cytotoxic compounds, displayed the best anticancer bioactivities (IC₅₀ < 0.1–0.23 μM) against HCC cell lines (Figure 4). These results indicate that these compounds can be considered as promising lead molecules for the development of potential anticancer agents.

Acknowledgements

This work was supported by the Scientific and Technological Research Council of Turkey-TUBITAK (TBAG-109T987), the KANSIL-2016H121540 (Ministry of Development, Turkey).

5. References

1. M. E. Welsch, S. A. Snyder, B. R. Stockwell, *Curr. Opin. Chem. Biol.* **2010**, *14*, 347–361. DOI:10.1016/j.cbpa.2010.02.018
2. I. Moriguchi, Y. Kanada, *Chem. Pharm. Bull.* **1977**, *25*, 926–935. DOI:10.1248/cpb.25.926
3. A. Brathe, G. Andresen, L. L. Gundersen, K. E. Malterud, F. Rise, *Bioorg. Med. Chem.* **2002**, *10*, 1581–1586. DOI:10.1016/S0968-0896(01)00427-8

4. A. Brathe, L. L. Gundersen, K. E. Malterud, F. Rise, *Arch. Pharm. Chem. Life Sci.* **2005**, *338*, 159–166. DOI:10.1002/ardp.200400951
5. S. F. Laufer, D. M. Domeyer, T. R. Scior, W. Albrecht, D. R. J. Hauser, *J. Med. Chem.* **2005**, *48*, 710–722. DOI:10.1021/jm0408767
6. J. A. Montgomery, K. Hewson, *J. Med. Chem.* **1968**, *11*, 48–52. DOI:10.1021/jm00307a010
7. G. Andersen, L. L. Gundersen, J. Nissen-Meyer, F. Rise, B. Spilberg, *Bioorg. Med. Chem. Lett.* **2002**, *12*, 567–569. DOI:10.1016/S0960-894X(01)00803-4
8. J. F. Wang, L. R. Zhang, Z. J. Yang, L. H. Zhang, *Bioorg. Med. Chem.* **2004**, *12*, 1425–1429. DOI:10.1016/j.bmc.2004.01.005
9. M. Hocek, P. Naus, R. Pohl, I. Votruba, P. A. Furman, P. M. Tharnish, M. J. Otto, *J. Med. Chem.* **2005**, *48*, 5869–5873. DOI:10.1021/jm050335x
10. A. Kucukdumlu, M. Tuncbilek, E. B. Guven, R. C. Atalay, *Acta Chim. Slov.* **2017**, *64*, 621–632. DOI:10.17344/acsi.2017.3419
11. R. W. Sidwell, J. H. Huffman, G. P. Khare, L. B. Allen, J. T. Witkowski, R. K. Robins, *Science.* **1972**, *177*, 705–706. DOI:10.1126/science.177.4050.705
12. E. De Clercq, *Biochem. Pharmacol.* **1987**, *36*, 2567–2575. DOI:10.1016/0006-2952(87)90533-8
13. E. De Clercq, *Nucleosides Nucleotides.* **1998**, *17*, 625–634. DOI:10.1080/07328319808005205
14. E. De Clercq, *Antiviral Res.* **2005**, *67*, 56–75. DOI:10.1016/j.antiviral.2005.05.001
15. B. Y. Kim, J. B. Ahn, H. W. Lee, S. K. Kang, J. H. Lee, J. S. Shin, S. K. Ahn, C. I. Hong, S. S. Yoon, *Eur. J. Med. Chem.* **2004**, *39*, 433–447. DOI:10.1016/j.ejmech.2004.03.001
16. G. Jin, C. C. N. Wu, R. I. Tawatao, M. Chan, D. A. Carson, H. B. Cottam, *Bioorg. Med. Chem. Lett.* **2006**, *16*, 4559–4563. DOI:10.1016/j.bmcl.2006.06.017
17. E. M. Peterson, J. Brownell, R. Vince, *J. Med. Chem.* **1992**, *35*, 3991–4000. DOI:10.1021/jm00100a003
18. A. Gangjee, A. Vasudevan, S. F. Queener, *J. Med. Chem.* **1997**, *40*, 3032–3039. DOI:10.1021/jm970271t
19. G. Gumina, C. K. Chu, *Org. Lett.* **2002**, *4*, 1147–1149. DOI:10.1021/ol025562x
20. F. Bordon-Pallier, N. Jullian, P. Ferrari, A. M. Girard, M. T. Bocquel, J. Biton, N. Bouquin, J. L. Haesslein, *Biochim. Biophys. Acta.* **2004**, *1697*, 211–223. DOI:10.1016/j.bbapap.2003.11.025
21. P. R. Patel, C. Ramalingam, Y. T. Park, *Bioorg. Med. Chem. Lett.* **2007**, *17*, 6610–6614. DOI:10.1016/j.bmcl.2007.09.060
22. M. Tuncbilek, Z. Ates-Alagoz, N. Altanlar, A. Karayel, S. Ozbey, *Bioorg. Med. Chem.* **2009**, *17*, 1693–1700. DOI:10.1016/j.bmc.2008.12.050
23. J. G. Kuhn, *Ann Pharmacother.* **2001**, *35*, 217–227. DOI:10.1345/aph.10096
24. C. M. Galmarini, J. R. Mackey, C. Dumontet, *Lancet Oncol.* **2002**, *3*, 415–424. DOI:10.1016/S1470-2045(02)00788-X
25. D. Sampath, V. A. Rao, W. Plunkett, *Oncogene.* **2003**, *22*, 9063–9074. DOI:10.1038/sj.onc.1207229
26. C. M. Galmarini, F. Popowycz, B. Joseph, *Curr. Med. Chem.* **2008**, *15*, 1072–1082. DOI:10.2174/092986708784221449
27. G. Escherich, S. Richards, L. J. Stork, A. J. Vora, *Leukemia.* **2011**, *25*, 95–959. DOI:10.1038/leu.2011.37
28. P. N. Munshi, M. Lubin, J. R. Bertino, *Oncologist.* **2014**, *19*, 760–765. DOI:10.1634/theoncologist.2014-0178
29. S. A. Johnson, W. Thomas, *Hematol. Oncol.* **2000**, *18*, 141–153. DOI:10.1002/1099-1069(200012)18:4<141::AID-HON666>3.0.CO;2-#
30. S. A. Johnson, *Expert Opin. Pharmacother.* **2001**, *2*, 929–943.
31. W. B. Parker, J. A. 3rd Secrist, W. R. Waud, *Curr. Opin. Invest. Drugs.* **2004**, *5*, 592–596.
32. E. Lech-Maranda, A. Korycka, T. Robak, *Mini-Rev Med Chem.* **2006**, *6*, 575–581. DOI:10.2174/138955706776876212
33. M. S. Ricci, W. X. Zong, *Oncologist.* **2006**, *11*, 342–357. DOI:10.1634/theoncologist.11-4-342
34. M. Collado, M. Serrano, *Nature Rev. Cancer.* **2006**, *6*, 472–476. DOI:10.1038/nrc1884
35. C. Nardella, J. G. Clohessy, A. Alimonti, P. P. Pandolfi, *Nature Rev. Cancer.* **2011**, *11*, 503–511. DOI:10.1038/nrc3057
36. J. L. Haesslein, N. Jullian, *Curr. Topics Med. Chem.* **2002**, *2*, 1037–1050. DOI:10.2174/1568026023393291
37. W. F. De Azevedo, S. Leclerc, L. Meijer, L. Havlicek, M. Strnad, S. H. Kim, *Eur. J. Biochem.* **1997**, *243*, 518–526. DOI:10.1111/j.1432-1033.1997.0518a.x
38. Y. T. Chang, N. S. Gray, G. R. Rosania, D. P. Sutherlin, S. Kwon, T. C. Norman, R. Sarohia, M. Leost, L. Meijer, P. G. Schultz, *Chem. and Biol.* **1999**, *6*, 361–375. DOI:10.1016/S1074-5521(99)80048-9
39. K. Zurbonsen, A. Michel, P. A. Bonnet, L. Gannoun-Zaki, M. N. Mathieu, C. Chevillard, *Eur. J. Pharmacol.* **1997**, *320*, 215–221. DOI:10.1016/S0014-2999(96)00890-4
40. M. F. Brana, M. Cacho, M. L. Garcia, E. P. Mayoral, B. Lopez, B. De Pascual-Teresa, A. Ramos, N. Acero, F. Llinares, D. Munoz-Mingarro, O. Lozach, L. Meijer, *J. Med. Chem.* **2005**, *48*, 6843–6854. DOI:10.1021/jm058013g
41. C. Jaramillo, J. E. Diego, C. Hamdouchi, E. Collins, H. Keyser, C. Sanchez-Martinez, M. Prado, B. Norman, H. B. Brooks, S. A. Watkins, C. D. Spencer, J. A. Dempsey, B. D. Anderson, R. M. Campbell, T. Leggett, B. Patel, R. M. Schultz, J. Espinosa, M. Vieth, F. M. Zhang D. E. Timm, *Bioorg. Med. Chem. Lett.* **2004**, *14*, 6095–6099. DOI:10.1016/j.bmcl.2004.09.053
42. R. M. Mohareb, A. A. Mohamed, A. E. M. Abdallah, *Acta Chim. Slov.* **2016**, *63*, 227–240. DOI:10.17344/acsi.2015.1668
43. R. M. Mohareb, N. Y. M. Abdo, F. O. Al-Farouk, *Acta Chim. Slov.* **2017**, *64*, 117–128. DOI:10.17344/acsi.2016.2920
44. A. Gaagjee, X. Lin, R. L. Kisliuk, J. J. McGuire, *J. Med. Chem.* **2005**, *48*, 7215–7222.
45. S. Schenone, O. Bruno, A. Ranise, F. Bondavalli, C. Brullo, P. Fossa, L. Mosti, G. Menozzi, F. Carraro, A. Naldini, C. Bernini, F. Manetti, M. Botta, *Bioorg. Med. Chem. Lett.* **2004**, *14*, 2511–2517.
46. J. A. Markwalder, M. R. Arnone, P. A. Benfield, M. Biosdir, M. Boisclair, C. R. Burton, C. H. Chang, S. S. Cox, P. M. Czerniak, C. L. Dean, D. Doleniak, R. Grafstrom, B. A. Harrison, R. F. Kaltenbach, D. A. Nugiel, K. A. Rossi, S. R. Sherk, L. M. Sisk, P. Stouten, G. L. Trainor, P. Worland, S. P. Seitz, *J. Med. Chem.* **2004**, *47*, 5894–5911. DOI:10.1021/jm020455u

47. E. H. El-Sayed¹, A. A. Fadda, *Acta Chim. Slov.* **2018**, *65*, 853–864. DOI:10.17344/acsi.2018.4506
48. L. Havlicek, K. Fuksova, V. Krystof, M. Orsag, B. Vojtesek, M. Strnad, *Bioorg. Med. Chem.* **2005**, *13*, 5399–5407. DOI:10.1016/j.bmc.2005.06.007
49. S. Botros, O. M. Khalil, M. M. Kamel, Y. S. El-Dash, *Acta Chim. Slov.* **2017**, *64*, 102–116. DOI:10.17344/acsi.2016.2901
50. M. A. Biamonte, R. Van de Water, J. W. Arndt, R. H. Scannevin, D. Perret, W. C. Lee, *J. Med. Chem.* **2010**, *53*, 3–17. DOI:10.1021/jm9004708
51. M. Tuncbilek, E. Bilget Guven, T. Onder, R. Cetin Atalay, *J. Med. Chem.* **2012**, *55*, 3058–3065. DOI:10.1021/jm3001532
52. Z. Demir, E. B. Guven, S. Ozbey, C. Kazak, R. C. Atalay, M. Tuncbilek, *Eur. J. Med. Chem.* **2015**, *89*, 701–720. DOI:10.1016/j.ejmech.2014.10.080
53. D. L. Romero, C. E. Masse, S. Robinson, J. R. Greenwood, G. Harriman, *PCT Int Appl WO 2015/048281 Al.* **2015**, 1–168
54. A. K. Bakkestuen, L. L. Gundersen, B. T. Utenova, *J. Med. Chem.* **2005**, *48*, 2710–2723. DOI:10.1021/jm0408924

Povzetek

Načrtovali in izvedli smo sintezo serije novih 6,9-disubstituiranih purinskih analogov, ki na položaju C-6 vsebujejo 4-substituiran piperazin, na položaju N-9 pa 4-substituiran benzilni fragment. Vse pripravljene spojine (**7–26**) smo *in vitro* testirali za morebitno protirakavo aktivnost na Huh7 celicah jeter, HCT116 celicah debelega črevesa in MCF7 pljučnih celicah rakavih celičnih linij. Študije citotoksične bioaktivnosti so pokazale, da so vse spojine, z izjemo **19**, obetavno citotoksične z IC₅₀ vrednostmi med 0.05–21.8 μM proti Huh7, HCT116 in MCF7 celičnim linijam. Med vsemi pripravljenimi purinskimi analogi sta dva (**12** in **22**) izkazala posebej odlično citotoksično aktivnost in sicer IC₅₀ 0.08–0.13 μM na Huh7 celicah, kar je primerljivo s kamptotecinom (CPT) in boljše od kladribina, fludarabina in 5-FU. Nato smo raziskali še citotoksičnost najbolj aktivnih purinskih analogov na hepatocelične (HCC) rakave celice ter ugotovili, da spojini 6-(4-(4-trifluorometilfenil)piperazin (**12**) in 6-(4-(3,4-diklorofenil)piperazin (**25**) izkazujeta zelo obetavne IC₅₀ vrednosti (IC₅₀ <0.1–0.13 μM), ki so primerljive z vrednostmi za CPT in boljše kot je citotoksična bioaktivnost 5-FU, kladribina in fludarabina na HCC celice (Huh7 in HepG2).



Except when otherwise noted, articles in this journal are published under the terms and conditions of the Creative Commons Attribution 4.0 International License

Scientific paper

Synthesis of Heterocyclic Compounds Derived From Dimedone and their Anti-tumor and Tyrosine Kinase Inhibitions

Rafat M. Mohareb,^{1,*} Fatma M. Manhi² and Amal Abdelwahab²¹ Department of Chemistry, Faculty of Science, Cairo University, Giza, A. R. Egypt² National Organization for Drug Control & Research, P.O. 29, Cairo, A. R. Egypt

* Corresponding author: E-mail: raafat_mohareb@yahoo.com

Received: 04-25-2019

Abstract

The reaction of dimedone with arylaldehydes gave the benzylidene derivatives **3a–c**, the latter underwent a series of heterocyclization reactions to give fused thiophene, pyrazole isoxazole and pyridazine derivatives. The synthesized compounds were evaluated against different kinds of cancer cell lines together tyrosine kinases and Pim-1 kinase inhibitions. All the synthesized compounds were assessed for the inhibitory activities against A549 (non-small cell lung cancer), H460 (human lung cancer), HT-29 (human colon cancer) and MKN-45 (human gastric cancer) cancer cell lines together with foretinib as the positive control by a MTT assay. The promising compounds were **3c**, **5b**, **5e**, **5f**, **7c**, **7f**, **9c**, **11b**, **12c**, **12d**, **13b**, **13d**, **14b**, **16c** and **16d** among the tested compounds. On the other hand, compounds **5b**, **5e**, **5f**, **7c**, **11b**, **12c**, **12d**, **13d**, **14b**, **16c** and **16d** were the most effective inhibitors against tyrosine kinases and compounds **5b**, **11b**, **12d**, **13d**, **14b** and **16c** were the most potent against Pim-1 kinase.

Keywords: Dimedone; thiophene; pyrazole; isoxazole; antitumor; tyrosine kinase

1. Introduction

As typical reactive 1,3-dicarbonyl compounds, cyclohexane-1,3-dione and its analog 5,5-dimethyl cyclohexane-1,3-dione (dimedone) have been widely used in versatile synthetic reactions.^{1,2} Dimedone is not only a typical reagent for Knoevenagel condensation, but also adds easily to electron-deficient alkenes *via* Michael addition. On the other hand, its one or two carbonyl groups could take part in substitution and cyclization reactions through the tautomeric enolate form. Thus, the cascade reactions of addition, elimination and substitution could be achieved in many reactions involving dimedone. The reactions of cyclohexane-1,3-dione or dimedone with aldehydes have been extensively studied in the past years, from which several types of compounds have been produced according to the reaction conditions.^{3,4} The normal Knoevenagel condensations of cyclohexane-1,3-dione or dimedone with aldehydes have been conducted with numerous methods including promotion *via* amines,⁵ Lewis acids,⁶ surfactants,^{7,8} zeolites,⁹ ionic liquids.¹⁰ The use of environmentally benign methods, such as aqueous medi-

um¹¹ or in the absence of solvents¹² and the usage of ultrasound or microwave heating¹³ have also been developed in recent years. The reactions usually proceed further through Michael addition reaction of the second molecule of dimedone to yield tetraketones as main products.¹⁴ On the other hand, tetraketones could be easily converted to 9-substituted 1,8-dioxoxanthenes by dehydration step.¹⁵ According to our previous work a large number of heterocyclic compounds with anti-proliferative and anti-inflammatory activities were recently synthesized by our research group.^{16,17} Recently, our research group was involved in the synthesis and determination of the anti-proliferative properties of a large number of heterocyclic compounds.^{18,19} In addition, according to our continued interest in the design of new multicomponent reactions and the application in the synthesis of heterocyclic compounds we found some unprecedented reaction patterns in the reaction of dimedone (**1**) with aromatic aldehydes **2a–c**, to produce the benzylidene derivatives **3a–c** and with aromatic diazonium salts **10a,b** to produce products which underwent heterocyclization reactions to give compounds with potential antitumor activities.

2. Experimental

Dry solvents were used throughout this work. All melting points of the synthesized compounds were recorded on Büchi melting point apparatus D-545. The IR spectra (KBr discs) were recorded on Bruker Vector 22 instrument. ^{13}C NMR and ^1H NMR spectra were measured on Bruker DPX200 instrument in $\text{DMSO}-d_6$ with TMS as the internal standard. Mass spectra were measured using EIMS (Shimadzu) and ESI-esquire 3000 Bruker Daltonics instrument. Elemental analyses were measured using the Micro-analytical Data center at Cairo University. All reactions were monitored by TLC on 2×5 cm pre-coated silica gel 60 F254 plates of thickness of 0.25 mm (Merck) for determining when the reactions were complete.

2. 1. General Procedure for the Synthesis of the Benzylidene Derivatives 3a–c

To a solution of dimedone (1.40 g, 0.01 mol) in absolute ethanol (40 mL) containing piperidine (0.50 mL) any of the aldehydes: benzaldehyde (1.05 g, 0.01 mol), 4-methoxybenzaldehyde (1.36 g, 0.01 mol) or 4-chlorobenzaldehyde (1.40 g, 0.01 mol), were added. Subsequently, the mixture was heated using the reflux conditions for 1 h, then poured onto ice/water containing a few drops of hydrochloric acid, the solid was collected by filtration, dried and crystallized from ethanol to get the 3a–c.

2. 1. 1. 2-Benzylidene-5,5-dimethylcyclohexane-1,3-dione (3a)

Orange crystals from ethanol; m.p. 190–192 °C; yield 78%. IR (KBr) cm^{-1} : 3054, 2986, 1689, 1687, 1632. ^1H NMR (300 MHz, $\text{DMSO}-d_6$) δ 7.42–7.23 (m, 5H, C_6H_5), 6.02 (s, 1H, CH), 2.31, 2.28 (2s, 4H, 2CH_2), 1.09, 1.06 (2s, 6H, 2CH_3); ^{13}C NMR ($\text{DMSO}-d_6$, 75 MHz) δ 166.2, 164.8 (C-1, C-3), 127.3, 126.6, 124.3, 121.2 (C_6H_5), 108.6, 103.2 (CH=C), 50.6 (C-4), 36.2 (C-5), 24.4 (2CH_3); EIMS: m/z 228 $[\text{M}]^+$ (28%); Anal. Calcd for $\text{C}_{15}\text{H}_{16}\text{O}_2$ (228.29): C, 78.92; H, 7.06%. Found: C, 78.24; H, 6.83%.

2. 1. 2. 2-(4-Methoxybenzylidene)-5,5-dimethylcyclohexane-1,3-dione (3b)

Pale yellow crystals from ethanol; m.p. 140–142 °C; yield 78%. IR (KBr) cm^{-1} : 3055, 2984, 1689, 1688, 1630. ^1H NMR (300 MHz, $\text{DMSO}-d_6$) δ 7.47–7.26 (m, 4H, C_6H_4), 6.06 (s, 1H, CH), 3.68 (s, 3H, OCH_3), 2.36, 2.24 (2s, 4H, 2CH_2), 1.07, 1.06 (2s, 6H, 2CH_3); ^{13}C NMR ($\text{DMSO}-d_6$, 75 MHz) δ 166.8, 164.5 (C-1, C-3), 127.0, 126.9, 123.7, 121.6 (C_6H_4), 108.3, 103.6 (CH=C), 50.3 (C-4), 50.1 (OCH_3), 36.7 (C-5), 24.2 (2CH_3); EIMS: m/z 258 $[\text{M}]^+$ (32%); Anal. Calcd for $\text{C}_{16}\text{H}_{18}\text{O}_3$ (258.31): C, 74.39; H, 7.02%. Found: C, 74.48; H, 6.95%.

2. 1. 3. 2-(4-Chlorobenzylidene)-5,5-dimethylcyclohexane-1,3-dione (3c)

Pale yellow crystals from ethanol; m.p. 125–127 °C; yield 80%. IR (KBr) cm^{-1} : 3055, 2984, 1690, 1688, 1630. ^1H NMR (300 MHz, $\text{DMSO}-d_6$) δ 7.49–7.22 (m, 4H, C_6H_4), 6.07 (s, 1H, CH), 2.38, 2.21 (2s, 4H, 2CH_2), 1.08, 1.05 (2s, 6H, 2CH_3); ^{13}C NMR ($\text{DMSO}-d_6$, 75 MHz) δ 166.5, 164.2 (C-1, C-3), 128.3, 126.5, 123.2, 121.3 (C_6H_4), 108.8, 103.3 (CH=C), 50.6 (C-4), 36.8 (C-5), 24.5 (2CH_3); EIMS: m/z 262 $[\text{M}]^+$ (28%); Anal. Calcd for $\text{C}_{15}\text{H}_{15}\text{ClO}_2$ (262.73): C, 68.57; H, 5.75%. Found: C, 68.39; H, 6.02%.

2. 2. General Procedure for the Synthesis of the 6,7-Dihydrobenzo[b]thiophene Derivatives 5a–f

To a solution of any of 3a (2.28 g, 0.01 mol), 3b (2.58 g, 0.01 mol) or 3c (2.62 g, 0.01 mol) in 1,4-dioxan (40 mL) containing triethylamine (0.50 mL) each of elemental sulfur (0.32 g, 0.01 mol) and either of malononitrile (0.66 g, 0.01 mol) or ethyl cyanoacetate (1.07 g, 0.01 mol) were added. The reaction mixture was heated under reflux for 1 h then left to cool. The formed solid product was collected by filtration, dried and crystallized from ethanol to give 5a–f, respectively.

2. 2. 1. 2-Amino-4-benzylidene-7,7-dimethyl-5-oxo-4,5,6,7-tetrahydrobenzo[b]thiophene-3-carbonitrile (5a)

Yellow crystals from ethanol; m.p. 199–202 °C; yield 80%. IR (KBr) cm^{-1} : 3487–3348 (NH_2), 3055, 2985, 1688, 1632. ^1H NMR (300 MHz, $\text{DMSO}-d_6$) δ 7.40–7.25 (m, 5H, C_6H_5), 6.06 (s, 1H, CH), 4.30 (s, 2H, D_2O exchangeable, NH_2), 2.32 (s, 2H, CH_2), 1.08, 1.06 (2s, 6H, 2CH_3); ^{13}C NMR ($\text{DMSO}-d_6$, 75 MHz) δ 166.0 (C-1), 138.6, 136.0, 135.2, 130.7, 127.8, 125.4, 124.3, 121.0 (C_6H_5 , thiophene C), 116.9 (CN), 108.9, 103.5 (CH=C), 50.8 (C-4), 36.7 (C-5), 24.6 (2CH_3); EIMS: m/z 308 $[\text{M}]^+$ (22%); Anal. Calcd for $\text{C}_{18}\text{H}_{16}\text{N}_2\text{OS}$ (308.40): C, 70.10; H, 5.23; N, 9.08; S, 10.40%. Found: C, 70.06; H, 5.39; N, 9.29; S, 10.31%.

2. 2. 2. Ethyl 2-Amino-4-benzylidene-7,7-dimethyl-5-oxo-4,5,6,7-tetrahydrobenzo[b]thiophene-3-carboxylate (5b)

Yellow crystals from ethanol; m.p. 117–120 °C; yield 72%. IR (KBr) cm^{-1} : 4682, 3367 (NH_2), 3055, 2985, 1702, 1688, 1632. ^1H NMR (300 MHz, $\text{DMSO}-d_6$) δ 7.43–7.27 (m, 5H, C_6H_5), 6.05 (s, 1H, CH), 4.35 (s, 2H, D_2O exchangeable, NH_2), 4.21 (q, 2H, $J = 7.26$ Hz, OCH_2CH_3), 2.35 (s, 2H, CH_2), 1.12 (t, 3H, $J = 7.26$ Hz, OCH_2CH_3), 1.07, 1.03 (2s, 6H, 2CH_3); ^{13}C NMR ($\text{DMSO}-d_6$, 75 MHz) δ 166.3, 164.2 (C-1, CO ester), 138.3, 136.5, 135.8, 130.3,

127.4, 125.8, 124.1, 121.6 (C₆H₅, thiophene C), 108.6, 103.3 (CH=C), 52.6 (OCH₂CH₃), 50.4 (C-4), 36.3 (C-5), 24.5 (2CH₃), 16.2 (OCH₂CH₃); EIMS: *m/z* 355 [M]⁺ (28%); Anal. Calcd for C₂₀H₂₁NO₃S (355.45): C, 67.58; H, 5.95; N, 3.94; S, 9.02%. Found: C, 67.70; H, 5.64; N, 4.16; S, 8.86%.

2. 2. 3. 2-Amino-4-(4-methoxybenzylidene)-7,7-dimethyl-5-oxo-4,5,6,7-tetrahydrobenzo[*b*]thiophene-3-carbonitrile (5c)

Yellow crystals from ethanol; m.p. 193–196 °C; yield 80%. IR (KBr) cm⁻¹: 3473–3368 (NH₂), 3055, 2985, 2220, 1688, 1630. ¹H NMR (300 MHz, DMSO-*d*₆) δ 7.46–7.21 (m, 4H, C₆H₄), 6.09 (s, 1H, CH), 4.36 (s, 2H, D₂O exchangeable, NH₂), 3.64 (s, 3H, OCH₃), 2.36 (s, 2H, CH₂), 1.07, 1.04 (2s, 6H, 2CH₃); ¹³C NMR (DMSO-*d*₆, 75 MHz) δ 166.3 (C-1), 138.2, 136.4, 135.6, 130.9, 128.5, 126.3, 123.8, 120.8 (C₆H₅, thiophene C), 116.8 (CN), 108.7, 103.5 (CH=C), 52.8 (OCH₃), 50.6 (C-4), 36.5 (C-5), 24.6 (2CH₃); EIMS: *m/z* 338 [M]⁺ (28%); Anal. Calcd for C₁₉H₁₈N₂O₂S (338.42): C, 67.43; H, 5.36; N, 8.28; S, 9.47%. Found: C, 67.72; H, 5.41; N, 8.16; S, 9.63%.

2. 2. 4. Ethyl 2-Amino-4-(4-methoxybenzylidene)-7,7-dimethyl-5-oxo-4,5,6,7-tetrahydrobenzo[*b*]thiophene-3-carboxylate (5d)

Orange crystals from ethanol; m.p. 188–190 °C; yield 67%. IR (KBr) cm⁻¹: 4673, 3359 (NH₂), 3055, 2985, 1689, 1688, 1630. ¹H NMR (300 MHz, DMSO-*d*₆) δ 7.46–7.24 (m, 4H, C₆H₄), 6.03 (s, 1H, CH), 4.38 (s, 2H, D₂O exchangeable, NH₂), 4.22 (q, 2H, *J* = 7.19 Hz, OCH₂CH₃), 3.68 (s, 3H, OCH₃), 2.38 (s, 2H, CH₂), 1.13 (t, 3H, *J* = 7.19 Hz, OCH₂CH₃), 1.08, 1.01 (2s, 6H, 2CH₃); ¹³C NMR (DMSO-*d*₆, 75 MHz) δ 166.6, 164.8 (C-1, CO ester), 138.3, 136.5, 135.8, 130.3, 128.6, 126.2, 123.5, 121.4 (C₆H₅, thiophene C), 108.2, 103.4 (CH=C), 52.8 (OCH₃), 52.6 (OCH₂CH₃), 50.2 (C-4), 36.5 (C-5), 24.8 (2CH₃), 16.2 (OCH₂CH₃); EIMS: *m/z* 385 [M]⁺ (32%); Anal. Calcd for C₂₁H₂₃NO₄S (385.48): C, 65.43; H, 6.01; N, 3.63; S, 8.32%. Found: C, 65.59; H, 5.94; N, 3.80; S, 8.42%.

2. 2. 5. 2-Amino-4-(4-chlorobenzylidene)-7,7-dimethyl-5-oxo-4,5,6,7-tetrahydrobenzo[*b*]thiophene-3-carbonitrile (5e)

Yellow crystals from ethanol; m.p. 170–172 °C; yield 75%. IR (KBr) cm⁻¹: 3480–3359 (NH₂), 3055, 2985, 2220, 1688, 1630. ¹H NMR (300 MHz, DMSO-*d*₆) δ 7.43–7.23 (m, 4H, C₆H₄), 6.05 (s, 1H, CH), 4.34 (s, 2H, D₂O exchangeable, NH₂), 2.38 (s, 2H, CH₂), 1.07, 1.04 (2s, 6H, 2CH₃); ¹³C NMR (DMSO-*d*₆, 75 MHz) δ 166.6 (C-1), 138.3, 135.9, 134.6, 130.3, 128.2, 126.7, 123.5, 120.4 (C₆H₅, thiophene C), 116.9 (CN), 108.3, 103.2 (CH=C), 50.3

(C-4), 36.2 (C-5), 24.7 (2CH₃); EIMS: *m/z* 342 [M]⁺ (35%); Anal. Calcd for C₁₈H₁₅ClN₂OS (342.84): C, 63.06; H, 4.41; N, 8.17; S, 9.35%. Found: C, 63.29; H, 4.69; N, 8.31; S, 9.42%.

2. 2. 6. Ethyl 2-amino-4-(4-chlorobenzylidene)-7,7-dimethyl-5-oxo-4,5,6,7-tetrahydrobenzo[*b*]thiophene-3-carboxylate (5f)

Yellow crystals from ethanol; m.p. 126–128 °C; yield 76%. IR (KBr) cm⁻¹: 4673, 3368 (NH₂), 3055, 2983, 1703, 1688, 1630. ¹H NMR (300 MHz, DMSO-*d*₆) δ 7.46–7.23 (m, 4H, C₆H₅), 6.02 (s, 1H, CH), 4.39 (s, 2H, D₂O exchangeable, NH₂), 4.23 (q, 2H, *J* = 6.72 Hz, OCH₂CH₃), 2.35 (s, 2H, CH₂), 1.13 (t, 3H, *J* = 6.72 Hz, OCH₂CH₃), 1.09, 1.053 (2s, 6H, 2CH₃); ¹³C NMR (DMSO-*d*₆, 75 MHz) δ 166.6, 164.5 (C-1, CO ester), 138.2, 136.3, 135.6, 130.4, 127.3, 125.2, 124.6, 121.3 (C₆H₅, thiophene C), 108.2, 103.5 (CH=C), 52.4 (OCH₂CH₃), 50.6 (C-4), 36.8 (C-5), 24.5 (2CH₃), 16.2 (OCH₂CH₃); EIMS: *m/z* 389 [M]⁺ (32%); Anal. Calcd for C₂₀H₂₀ClNO₃S (389.90): C, 61.61; H, 5.17; N, 3.59; S, 8.22%. Found: C, 61.49; H, 5.36; N, 3.69; S, 8.38%.

2. 2. 7. General Procedure for the Synthesis of the 4,5,6,7-Tetrahydro-2*H*-indazole Derivatives 7a–f

To a solution of any of **3a** (2.28 g, 0.01 mol), **3b** (2.58 g, 0.01 mol) or **3c** (2.62 g, 0.01 mol) in ethanol (40 mL) either of hydrazine hydrate (0.1 mL, 0.02 mol) or phenylhydrazine (3.16 g, 0.02 mol) was added. The reaction mixture, in each case, was heated under reflux for 3 h then was left to cool and the formed solid product was collected by filtration upon pouring onto ice/water mixture containing a few drops of hydrochloric acid.

2. 2. 7. 1. 4-Hydrazono-6,6-dimethyl-3-phenyl-4,5,6,7-tetrahydro-2*H*-indazole (7a)

Pale yellow crystals from ethanol; m.p. 175–177 °C; yield 68%. IR (KBr) cm⁻¹: 3497–3336 (NH, NH₂), 3055, 2985, 1663, 1632. ¹H NMR (300 MHz, DMSO-*d*₆) δ 8.26 (s, 1H, D₂O exchangeable, NH), 7.43–7.26 (m, 5H, C₆H₅), 5.29 (s, 2H, D₂O exchangeable, NH₂), 2.41, 2.38 (2s, 4H, 2CH₂), 1.07, 1.06 (2s, 6H, 2CH₃); ¹³C NMR (DMSO-*d*₆, 75 MHz) δ 172.3 (C-4), 140.6, 138.3, 127.8, 125.4, 124.3, 121.0 (C₆H₅, C-3, C-4), 34.6 (C-6), 36.8, 24.9, (C-7, C-5) 24.3 (2CH₃); EIMS: *m/z* 254 [M]⁺ (28%); Anal. Calcd for C₁₅H₁₈N₄ (254.33): C, 70.84; H, 7.13; N, 22.03%. Found: C, 70.69; H, 6.93; N, 21.79%.

2. 2. 7. 2. 4-Hydrazono-3-(4-methoxyphenyl)-6,6-dimethyl-4,5,6,7-tetrahydro-2*H*-indazole (7b)

Orange crystals from ethanol; m.p. 189–192 °C; yield 70%. IR (KBr) cm⁻¹: 3474–3353 (NH, NH₂), 3055,

2985, 1660, 1630. ^1H NMR (300 MHz, DMSO- d_6) δ 8.28 (s, 1H, D₂O exchangeable, NH), 7.48–7.23 (m, 4H, C₆H₄), 5.27 (s, 2H, D₂O exchangeable, NH₂), 3.52 (s, 3H, OCH₃), 2.46, 2.32 (2s, 4H, 2CH₂), 1.09, 1.06 (2s, 6H, 2CH₃); ^{13}C NMR (DMSO- d_6 , 75 MHz) δ 172.6 (C-4), 140.3, 138.6, 127.4, 126.6, 123.1, 120.8 (C₆H₅, C-3, C-4), 50.2 (OCH₃), 34.8 (C-6), 36.6, 24.8, (C-7, C-5) 24.1 (2CH₃); EIMS: m/z 284 [M]⁺ (30%); Anal. Calcd for C₁₆H₂₀N₄O (284.36): C, 67.58; H, 7.09; N, 19.70%. Found: C, 67.39; H, 6.84; N, 19.66%.

2. 2. 7. 3. 3-(4-Chlorophenyl)-4-hydrazono-6,6-dimethyl-4,5,6,7-tetrahydro-2H-indazole (7c)

Yellow crystals from 1,4-dioxan; m.p. 185–187 °C; yield 77%. IR (KBr) cm⁻¹: 3493–3342 (NH, NH₂), 3057, 2985, 1662, 1630. ^1H NMR (300 MHz, DMSO- d_6) δ 8.27 (s, 1H, D₂O exchangeable, NH), 7.52–7.25 (m, 4H, C₆H₄), 5.25 (s, 2H, D₂O exchangeable, NH₂), 2.43, 2.36 (2s, 4H, 2CH₂), 1.08, 1.03 (2s, 6H, 2CH₃); ^{13}C NMR (DMSO- d_6 , 75 MHz) δ 172.8 (C-4), 140.1, 138.4, 128.3, 125.5, 122.6, 120.2 (C₆H₅, C-3, C-4), 34.6 (C-6), 36.3, 24.5, (C-7, C-5) 24.3 (2CH₃); EIMS: m/z 288 [M]⁺ (24%); Anal. Calcd for C₁₅H₁₇ClN₄ (288.78): C, 62.39; H, 5.93; N, 19.40%. Found: C, 62.58; H, 6.15; N, 19.52%.

2. 2. 7. 4. 6,6-Dimethyl-2,3-diphenyl-4-(2-phenylhydrazono)-4,5,6,7-tetrahydro-2H-indazole (7d)

Pale yellow crystals from ethanol; m.p. 171–173 °C; yield 60%. IR (KBr) cm⁻¹: 3482–3346 (NH, NH₂), 3055, 2985, 1665, 1632. ^1H NMR (300 MHz, DMSO- d_6) δ 8.28 (s, 1H, D₂O exchangeable, NH), 7.46–7.22 (m, 15H, 3C₆H₅), 2.42, 2.38 (2s, 4H, 2CH₂), 1.09, 1.07 (2s, 6H, 2CH₃); ^{13}C NMR (DMSO- d_6 , 75 MHz) δ 172.6 (C-4), 140.4, 138.1, 129.6, 129.3, 128.5, 127.8, 127.4, 126.1, 126.5, 126.9, 125.6, 125.2, 124.0, 121.2 (3C₆H₅, C-3, C-4), 34.8 (C-6), 36.4, 24.7 (C-7, C-5) 24.5 (2CH₃); EIMS: m/z 406 [M]⁺ (24%); Anal. Calcd for C₂₇H₂₆N₄ (406.52): C, 79.77; H, 6.45; N, 13.78%. Found: C, 79.84; H, 6.62; N, 13.53%.

2. 2. 7. 5. 3-(4-Methoxyphenyl)-6,6-dimethyl-2-phenyl-4-(2-phenylhydrazono)-4,5,6,7-tetrahydro-2H-indazole (7e)

Orange crystals from ethanol; m.p. 128–130 °C; yield 76%. IR (KBr) cm⁻¹: 3486–3336 (NH), 3055, 2985, 1660, 1630. ^1H NMR (300 MHz, DMSO- d_6) δ 8.31 (s, 1H, D₂O exchangeable, NH), 7.53–7.26 (m, 14H, C₆H₅, 2C₆H₄), 3.61 (s, 3H, OCH₃), 2.48, 2.36 (2s, 4H, 2CH₂), 1.08, 1.07 (2s, 6H, 2CH₃); ^{13}C NMR (DMSO- d_6 , 75 MHz) δ 172.8 (C-4), 140.7, 138.3, 128.8, 129.3, 128.5, 127.8, 127.3, 126.1, 126.8, 125.9, 125.6, 124.3, 123.7, 120.2 (2C₆H₅, C₆H₄, C-3, C-4), 50.2 (OCH₃), 34.1 (C-6), 36.6, 24.3 (C-7, C-5) 24.2 (2CH₃); EIMS: m/z 436 [M]⁺ (38%); Anal. Calcd for C₂₈H₂₈N₄O (436.55): C, 77.04; H, 6.46; N, 12.83%. Found: C, 77.25; H, 6.58; N, 12.64%.

2. 2. 7. 6. 3-(4-Chlorophenyl)-6,6-dimethyl-2-phenyl-4-(2-phenylhydrazono)-4,5,6,7-tetrahydro-2H-indazole (7f)

Pale yellow crystals from ethanol; m.p. 126–128 °C; yield 66%. IR (KBr) cm⁻¹: 3492–3327 (NH), 3055, 2985, 1660, 1630. ^1H NMR (300 MHz, DMSO- d_6) δ 8.26 (s, 1H, D₂O exchangeable, NH), 7.47–7.21 (m, 14H, 2C₆H₅, C₆H₄), 2.46, 2.38 (2s, 4H, 2CH₂), 1.08, 1.04 (2s, 6H, 2CH₃); ^{13}C NMR (DMSO- d_6 , 75 MHz) δ 172.4 (C-4), 140.1, 138.6, 129.3, 129.1, 128.4, 127.5, 127.4, 126.3, 126.5, 126.7, 125.4, 125.2, 124.0, 121.0 (2C₆H₅, C₆H₄, C-3, C-4), 34.5 (C-6), 36.4, 24.7 (C-7, C-5) 24.8 (2CH₃); EIMS: m/z 440 [M]⁺ (36%); Anal. Calcd for C₂₇H₂₅ClN₄ (440.97): C, 73.54; H, 5.71; N, 12.71%. Found: C, 73.58; H, 5.68; N, 12.86%.

2. 2. 8. General Procedure for the Synthesis of the Dihydrobenzo[c]isoxazole Derivatives 9a–c

To a solution of any of **3a** (2.28 g, 0.01 mol), **3b** (2.58 g, 0.01 mol) or **3c** (2.62 g, 0.01 mol) in ethanol (40 mL) containing sodium acetate (1.00 g) hydroxylamine hydrochloride (1.40 g, 0.02 mol) was added. The reaction mixture was heated under reflux for 2 h then poured onto ice/water and the formed solid product was collected by filtration.

2. 2. 8. 1. 6,6-Dimethyl-3-phenyl-6,7-dihydrobenzo[c]isoxazol-4(5H)-one oxime (9a)

Pale yellow crystals from 1,4-dioxan; m.p. 183–185 °C; yield 68%. IR (KBr) cm⁻¹: 3572–3326 (OH), 3055, 2985, 1663, 1631. ^1H NMR (300 MHz, DMSO- d_6) δ 9.52 (s, 1H, D₂O exchangeable, OH), 7.42–7.26 (m, 5H, C₆H₅), 2.47, 2.33 (2s, 4H, 2CH₂), 1.08, 1.05 (2s, 6H, 2CH₃); ^{13}C NMR (DMSO- d_6 , 75 MHz) δ 175.3 (C-4), 140.1, 137.6, 127.8, 126.5, 124.0, 121.2 (C₆H₅, C-3, C-4), 34.3 (C-6), 36.8, 24.5 (C-7, C-5), 24.8 (2CH₃); EIMS: m/z 256 [M]⁺ (30%); Anal. Calcd for C₁₅H₁₆N₂O₂ (256.30): C, 70.29; H, 6.29; N, 10.93%. Found: C, 70.31; H, 6.37; N, 11.25%.

2. 2. 8. 2. 3-(4-Methoxyphenyl)-6,6-dimethyl-6,7-dihydrobenzo[c]isoxazol-4(5H)-one oxime (9b)

Pale yellow crystals from ethanol; m.p. 177–180 °C; yield 58%. IR (KBr) cm⁻¹: 3529–3336 (OH), 3055, 2985, 1663, 1631. ^1H NMR (300 MHz, DMSO- d_6) δ 9.40 (s, 1H, D₂O exchangeable, OH), 7.48–7.26 (m, 4H, C₆H₄), 3.52 (s, 3H, OCH₃), 2.42, 2.35 (2s, 4H, 2CH₂), 1.09, 1.04 (2s, 6H, 2CH₃); ^{13}C NMR (DMSO- d_6 , 75 MHz) δ 172.8 (C-4), 140.7, 138.1, 126.9, 125.6, 125.6, 120.8 (C₆H₄, C-3, C-4), 50.8 (OCH₃), 34.4 (C-6), 36.9, 24.3 (C-7, C-5) 24.8 (2CH₃); EIMS: m/z 286 [M]⁺ (30%); Anal. Calcd for C₁₆H₁₈N₂O₃ (286.33): C, 67.12; H, 6.34; N, 9.78%. Found: C, 67.26; H, 6.26; N, 9.80%.

2. 2. 8. 3. 3-(4-Chlorophenyl)-6,6-dimethyl-6,7-dihydrobenzo[c]isoxazol-4(5H)-one oxime (9c)

Pale yellow crystals from 1,4-dioxan; m.p. 201–203 °C; yield 77%. IR (KBr) cm⁻¹: 3552–3361 (OH), 3055,

2985, 1664, 1630. ^1H NMR (300 MHz, DMSO- d_6) δ 9.53 (s, 1H, D₂O exchangeable, OH), 7.46–7.23 (m, 4H, C₆H₄), 2.49, 2.31 (2s, 4H, 2CH₂), 1.06, 1.02 (2s, 6H, 2CH₃); ^{13}C NMR (DMSO- d_6 , 75 MHz) δ 175.5 (C-4), 140.3, 137.2, 127.6, 125.8, 123.3, 120.9 (C₆H₅, C-3, C-4), 34.1 (C-6), 36.6, 24.2 (C-7, C-5), 24.3 (2CH₃); EIMS: m/z 290 [M]⁺ (26%); Anal. Calcd for C₁₅H₁₅ClN₂O₂ (290.74): C, 61.97; H, 5.20; N, 9.64%. Found: C, 62.79; H, 4.86; N, 9.80%.

2. 2. 9. General Procedure of the Synthesis of the Hydrazone Derivatives 11a,b

To a cold solution (0–5 °C) of compound **1** (1.40 g, 0.01 mol) in ethanol (40 mL) containing sodium acetate (3.0 g) either 4-methylnaphthalen-1-diazonium salt (0.01 mol) or 4-chloronaphthalen-1-diazonium salt [prepared by the addition of sodium nitrite solution (0.70 g, 0.01 mol) to a cold solution (0–5 °C) of either of 4-methylnaphthalen-1-amine (1.57 g, 0.01 mol) or 4-chloromethylnaphthalen-1-amine (1.77 g, 0.01 mol) with continuous stirring] was added with continuous stirring. The reaction mixture, in each case was stirred at room temperature for an additional 2 h and the formed solid product was collected by filtration.

2. 2. 9. 1. 5,5-Dimethyl-2-(2-(4-methylnaphthalen-1-yl)hydrazono)cyclohexane-1,3-dione (11a)

Pale yellow crystals from ethanol; m.p. 220–223 °C; yield 68%. IR (KBr) cm^{-1} : 3468–3334 (NH), 3055, 2985, 1689, 1687, 1663, 1630. ^1H NMR (300 MHz, DMSO- d_6) δ 8.29 (s, 1H, D₂O exchangeable, NH), 7.48–7.23 (m, 6H, naphthalene H), 2.41, 2.38 (2s, 4H, 2CH₂), 2.89 (s, 3H, CH₃), 1.07, 1.06 (2s, 6H, 2CH₃); ^{13}C NMR (DMSO- d_6 , 75 MHz) δ 172.8 (C-2), 166.2, 164.8 (C-1, C-3), 138.6, 135.2, 133.1, 129.6, 126.5, 126.1, 124.7, 123.9, 122.3, 120.6 (naphthalene C), 34.8 (C-6), 36.5, 32.8 (CH₃), 24.3 (C-7, C-5) 24.5 (2CH₃); EIMS: m/z 308 [M]⁺ (21%); Anal. Calcd for C₁₉H₂₀N₂O₂ (308.37): C, 74.00; H, 6.54; N, 9.08%. Found: C, 73.96; H, 6.82; N, 8.79%.

2. 2. 9. 2. 2-(2-(4-Chloronaphthalen-1-yl)hydrazono)-5,5-dimethylcyclohexane-1,3-dione (11b)

Pale yellow crystals from ethanol; m.p. 211–213 °C; yield 74%. IR (KBr) cm^{-1} : 3493–3358 (NH), 3055, 2985, 1688, 1687, 1663, 1630. ^1H NMR (300 MHz, DMSO- d_6) δ 8.32 (s, 1H, D₂O exchangeable, NH), 7.56–7.25 (m, 6H, naphthalene H), 2.46, 2.33 (2s, 4H, 2CH₂), 1.08, 1.06 (2s, 6H, 2CH₃); ^{13}C NMR (DMSO- d_6 , 75 MHz) δ 172.9 (C-2), 166.7, 164.8 (C-1, C-3), 138.8, 135.6, 134.41, 129.2, 127.8, 125.3, 124.2, 123.7, 122.1, 120.4 (naphthalene C), 34.8 (C-6), 36.8, 24.3 (C-7, C-5) 24.2 (2CH₃); EIMS: m/z 328 [M]⁺ (18%); Anal. Calcd for C₁₈H₁₇ClN₂O₂ (328.79): C, 65.75; H, 5.21; N, 8.52%. Found: C, 65.49; H, 5.06; N, 8.63%.

2. 2. 10. General Procedure for the Synthesis of the 6,7-Dihydrobenzo[b]thiophene Derivatives 12a–d

To a solution of either of **11a** (3.08 g, 0.01 mol), **11b** (3.28 g, 0.01 mol) in 1,4-dioxan (40 mL) containing triethylamine (0.50 mL) each of elemental sulfur (0.32 g, 0.01 mol) and either of malononitrile (0.66 g, 0.01 mol) or ethyl cyanoacetate (1.07 g, 0.01 mol) were added. The reaction mixture was heated under reflux for 1 h then left to cool. The formed solid product was collected by filtration, dried and crystallized from ethanol to give **12a–d**, respectively.

2. 2. 10. 1. 2-Amino-7,7-dimethyl-4-(2-(4-methylnaphthalen-1-yl)hydrazono)-5-oxo-4,5,6,7-tetrahydrobenzo[b]thiophene-3-carbonitrile (12a)

Pale yellow crystals from ethanol; m.p. 218–220 °C; yield 68%. IR (KBr) cm^{-1} : 3480–3350 (NH, NH₂), 3055, 2985, 2220, 1688, 1663, 1630. ^1H NMR (300 MHz, DMSO- d_6) δ 8.37 (s, 1H, D₂O exchangeable, NH), 7.48–7.23 (m, 6H, naphthalene H), 4.85 (s, 2H, D₂O exchangeable, NH₂), 2.86 (s, 3H, CH₃), 2.42 (s, 2H, CH₂), 1.09, 1.06 (2s, 6H, 2CH₃); ^{13}C NMR (DMSO- d_6 , 75 MHz) δ 175.7 (C-2), 166.2, (C-3), 138.8, 136.6, 133.8, 129.3, 126.2, 126.4, 124.2, 123.3, 122.8, 120.2 (naphthalene C), 116.8 (CN), 34.6 (C-6), 32.3 (CH₃), 24.1 (C-7, C-5), 24.8 (2CH₃); EIMS: m/z 388 [M]⁺ (28%); Anal. Calcd for C₂₂H₂₀N₄OS (388.49): C, 68.02; H, 5.19; N, 14.42; S, 8.25%. Found: C, 67.83; H, 5.27; N, 8.39; S, 8.36%.

2. 2. 10. 2. Ethyl 2-Amino-7,7-dimethyl-4-(2-(4-methylnaphthalen-1-yl)hydrazono)-5-oxo-4,5,6,7-tetrahydrobenzo[b]thiophene-3-carboxylate (12b)

Pale yellow crystals from ethanol; m.p. 177–179 °C; yield 73%. IR (KBr) cm^{-1} : 3468–3342 (NH, NH₂), 3055, 2985, 1689, 1687, 1663, 1630. ^1H NMR (300 MHz, DMSO- d_6) δ 8.39 (s, 1H, D₂O exchangeable, NH), 7.56–7.25 (m, 6H, naphthalene H), 4.88 (s, 2H, D₂O exchangeable, NH₂), 4.21 (q, 2H, $J = 6.72$ Hz, OCH₂CH₃), 2.86 (s, 3H, CH₃), 2.41 (s, 2H, CH₂), 1.13 (t, 3H, $J = 6.72$ Hz, OCH₂CH₃), 1.09, 1.07 (2s, 6H, 2CH₃); ^{13}C NMR (DMSO- d_6 , 75 MHz) δ 175.8 (C-2), 166.7, (C-3), 138.2, 137.3, 133.2, 129.7, 126.4, 126.2, 124.1, 123.6, 123.2, 120.0 (naphthalene C), 52.4 (OCH₂CH₃); 34.7 (C-6), 36.8, (CH₃), 32.1, 24.5 (C-7, C-5), 24.4 (2CH₃), 16.2 (OCH₂CH₃); EIMS: m/z 435 [M]⁺ (46%); Anal. Calcd for C₂₄H₂₅N₃O₃S (435.54): C, 66.18; H, 5.79; N, 9.65; S, 7.36%. Found: C, 66.84; H, 5.50; N, 9.19; S, 7.47%.

2. 2. 10. 3. 2-Amino-4-(2-(4-chloronaphthalen-1-yl)hydrazono)-7,7-dimethyl-5-oxo-4,5,6,7-tetrahydrobenzo[b]thiophene-3-carbonitrile (12c)

Pale yellow crystals from ethanol; m.p. 136–139 °C; yield 78%. IR (KBr) cm^{-1} : 3469–3332 (NH, NH₂), 3055, 2985, 2220, 1689, 1663, 1630. ^1H NMR (300 MHz, DMSO- d_6) δ 8.39 (s, 1H, D₂O exchangeable, NH), 7.51–7.23 (m,

6H, naphthalene H), 4.88 (s, 2H, D₂O exchangeable, NH₂), 2.40 (s, 2H, CH₂), 1.09, 1.07 (2s, 6H, 2CH₃); ¹³C NMR (DMSO-*d*₆, 75 MHz) δ 175.7 (C-2), 166.2, (C-3), 138.8, 136.6, 133.8, 129.3, 126.2, 126.4, 124.2, 123.3, 122.8, 120.2 (naphthalene C), 116.8 (CN), 34.6 (C-6), 32.3 (CH₃), 32.6, 24.1 (C-7, C-5), 24.8 (2CH₃); EIMS: *m/z* 408 [M]⁺ (40%); Anal. Calcd for C₂₁H₁₇ClN₄OS (408.90): C, 61.68; H, 4.19; N, 13.70; S, 7.84%. Found: C, 61.93; H, 4.26; N, 13.82; S, 7.94%.

2. 2. 10. 4. Ethyl 2-Amino-4-(2-(4-chloronaphthalen-1-yl)hydrazono)-7,7-dimethyl-5-oxo-4,5,6,7-tetrahydrobenzo[*b*]thiophene-3-carboxylate (12d)

Pale brown crystals from acetic acid; m.p. 205–207 °C; yield 68%. IR (KBr) cm⁻¹: 3442–3329 (NH, NH₂), 3055, 2985, 1689, 1687, 1663, 1630. ¹H NMR (300 MHz, DMSO-*d*₆) δ 8.35 (s, 1H, D₂O exchangeable, NH), 7.53–7.21 (m, 6H, naphthalene H), 4.84 (s, 2H, D₂O exchangeable, NH₂), 4.22 (q, 2H, *J* = 7.41 Hz, OCH₂CH₃), 2.41 (s, 2H, CH₂), 1.13 (t, 3H, *J* = 7.41 Hz, OCH₂CH₃), 1.08, 1.05 (2s, 6H, 2CH₃); ¹³C NMR (DMSO-*d*₆, 75 MHz) δ 175.3 (C-2), 166.5 (C-3), 138.6, 137.6, 133.5, 129.3, 126.1, 126.0, 124.5, 123.2, 122.7, 120.3 (naphthalene C), 52.5 (OCH₂CH₃), 34.8 (C-6), 32.4, 24.2 (C-7, C-5), 24.4 (2CH₃), 16.3 (OCH₂CH₃); EIMS: *m/z* 455 [M]⁺ (22%); Anal. Calcd for C₂₃H₂₂ClN₃O₃S (455.96): C, 60.59; H, 4.86; N, 9.22; S, 7.03%. Found: C, 60.52; H, 5.08; N, 9.13; S, 7.24%.

2. 2. 11. General Procedure for the Synthesis of the Cyclohexane-(1,2,3-triylidene)tris(hydrazine) Derivatives 13a–d

To a solution of either **11a** (3.08 g, 0.01 mol), **11b** (3.28 g, 0.01 mol) in ethanol (40 mL) either of hydrazine hydrate (1.0 mL, 0.02 mol) or phenylhydrazine (3.60 g, 0.02 mol) was added. The reaction mixture in each case was heated under reflux for 3 h then poured onto ice/water containing a few drops of hydrochloric acid and the formed solid product was collected by filtration.

2. 2. 11. 1. (5,5-Dimethyl-2-(2-(4-methylnaphthalen-1-yl)hydrazono)cyclohexane-1,3-diylidene)bis(hydrazine) (13a)

Pale yellow crystals from ethanol; m.p. 220–224 °C; yield 60%. IR (KBr) cm⁻¹: 3473–3326 (NH, NH₂), 3055, 2985, 1665, 1660, 1630. ¹H NMR (300 MHz, DMSO-*d*₆) δ 8.26 (s, 1H, D₂O exchangeable, NH), 7.54–7.26 (m, 6H, naphthalene H), 4.51, 5.16 (2s, 4H, D₂O exchangeable, 2NH₂), 2.80 (s, 3H, CH₃), 2.52, 2.43 (2s, 4H, 2CH₂), 1.08, 1.07 (2s, 6H, 2CH₃); ¹³C NMR (DMSO-*d*₆, 75 MHz) δ 176.1, 172.5, 170.3 (C-1, C-2, C-3), 138.3, 137.2, 133.1, 128.5, 126.6, 126.1, 124.8, 123.1, 122.2, 120.3 (naphthalene C), 50.8 (CH₃), 34.3 (C-6), 32.6 (CH₃), 32.8, 24.3 (C-7, C-5), 24.6 (2CH₃); EIMS: *m/z* 336 [M]⁺ (35%); Anal. Calcd for C₁₉H₂₄N₆ (336.43): C, 67.83; H, 7.19; N, 24.98%. Found: C, 67.61; H, 6.93; N, 25.25%.

2. 2. 11. 2. (2-(2-(4-Chloronaphthalen-1-yl)hydrazono)-5,5-dimethylcyclohexane-1,3-diylidene)bis(hydrazine) (13b)

Pale yellow crystals from ethanol; m.p. 210–212 °C; yield 63%. IR (KBr) cm⁻¹: 3486–3348 (NH, NH₂), 3056, 2985, 1687, 1665, 1660, 1630. ¹H NMR (300 MHz, DMSO-*d*₆) δ 8.23 (s, 1H, D₂O exchangeable, NH), 7.47–7.22 (m, 6H, naphthalene H), 4.53, 5.18 (2s, 4H, D₂O exchangeable, 2NH₂), 2.52, 2.43 (2s, 4H, 2CH₂), 1.08, 1.07 (2s, 6H, 2CH₃); ¹³C NMR (DMSO-*d*₆, 75 MHz) δ 176.1, 172.5, 170.3 (C-1, C-2, C-3), 138.3, 137.2, 133.1, 128.5, 126.6, 126.1, 124.8, 123.1, 122.2, 120.3 (naphthalene C), 34.6 (C-6), 32.8, 24.5 (C-7, C-5), 24.8 (2CH₃); EIMS: *m/z* 356 [M]⁺ (28%); Anal. Calcd for C₁₈H₂₁ClN₆ (356.85): C, 60.58; H, 5.93; N, 23.55%. Found: C, 60.74; H, 6.15; N, 23.68%.

2. 2. 11. 3. 2,2'-(5,5-Dimethyl-2-(2-(4-methylnaphthalen-1-yl)hydrazono)-cyclohexane-1,3-diylidene)bis(1-phenylhydrazine) (13c)

Pale brown crystals from 1,4-dioxan; m.p. 205–207 °C; yield 68%. IR (KBr) cm⁻¹: 3492–3348 (NH, NH₂), 3055, 2986, 1666, 1660, 1630. ¹H NMR (300 MHz, DMSO-*d*₆) δ 8.36, 8.28, 8.25 (3s, 3H, D₂O exchangeable, 3NH), 7.56–7.23 (m, 16H, 2C₆H₅, naphthalene H), 2.83 (s, 3H, CH₃), 2.56, 2.41 (2s, 4H, 2CH₂), 1.09, 1.06 (2s, 6H, 2CH₃); ¹³C NMR (DMSO-*d*₆, 75 MHz) δ 176.6, 172.8, 170.4 (C-1, C-2, C-3), 138.6, 137.1, 133.0, 128.6, 126.4, 126.1, 125.3, 125.1, 124.8, 124.6, 123.6, 123.1, 122.6, 122.2, 121.5, 121.2, 120.3, 119.5 (2C₆H₅, naphthalene C), 50.4 (CH₃), 34.6 (C-6), 32.6, 24.5 (C-7, C-5), 24.7 (2CH₃); EIMS: *m/z* 488 [M]⁺ (40%); Anal. Calcd for C₃₁H₃₂N₆ (488.63): C, 76.20; H, 6.60; N, 17.20%. Found: C, 76.36; H, 6.39; N, 17.48%.

2. 2. 11. 4. 2,2'-(2-(2-(4-Chloronaphthalen-1-yl)hydrazono)-5,5-dimethyl-cyclohexane-1,3-diylidene)bis(1-phenylhydrazine) (13d)

Pale brown crystals from 1,4-dioxan; m.p. 188–191 °C; yield 68%. IR (KBr) cm⁻¹: 3472–3326 (NH, NH₂), 3055, 2985, 1664, 1660, 1630. ¹H NMR (300 MHz, DMSO-*d*₆) δ 8.38, 8.23, 8.22 (3s, 3H, D₂O exchangeable, 3NH), 7.58–7.24 (m, 16H, 2C₆H₅, naphthalene H), 2.54, 2.46 (2s, 4H, 2CH₂), 1.09, 1.03 (2s, 6H, 2CH₃); ¹³C NMR (DMSO-*d*₆, 75 MHz) δ 176.8, 172.5, 170.3 (C-1, C-2, C-3), 138.8, 137.7, 133.1, 128.2, 126.9, 126.3, 125.8, 125.1, 124.3, 124.6, 123.9, 123.3, 122.6, 122.2, 122.0, 121.8, 120.3, 119.5 (2C₆H₅, naphthalene C), 34.8 (C-6), 32.3, 24.7 (C-7, C-5), 24.5 (2CH₃); EIMS: *m/z* 509 [M]⁺ (26%); Anal. Calcd for C₃₀H₂₉ClN₆ (509.04): C, 70.78; H, 5.74; N, 16.51%. Found: C, 70.64; H, 5.59; N, 16.72%.

2. 2. 12. General Procedure for the Synthesis of the Cyclohexane-1,3-dione Dioxime 14a,b

To a solution of either **11a** (3.08 g, 0.01 mol), **11b** (3.28 g, 0.01 mol) in ethanol (40 mL) containing sodium

acetate (2.0 g) hydroxylamine hydrochloride (1.440 g, 0.02 mol) was added. The reaction mixture in each case was heated under reflux for 4 h then poured onto ice/water and the formed solid product was collected by filtration.

2. 2. 12. 1. 5,5-Dimethyl-2-(2-(4-methylnaphthalen-1-yl)hydrazono)cyclohexane-1,3-dione Dioxime (14a)

Pale yellow crystals from 1,4-dioxan; m.p. 212–214 °C; yield 78%. IR (KBr) cm^{-1} : 3563–3347 (OH, NH), 3055, 2985, 1663, 1660, 1630. ^1H NMR (300 MHz, DMSO- d_6) δ 9.68, 10.04 (2s, 2H, D₂O exchangeable, 2OH), 8.28 (s, 1H, D₂O exchangeable, NH), 7.53–7.28 (m, 6H, naphthalene H), 2.83 (s, 3H, CH₃), 2.56, 2.40 (2s, 4H, 2CH₂), 1.09, 1.07 (2s, 6H, 2CH₃); ^{13}C NMR (DMSO- d_6 , 75 MHz) δ 176.8, 173.3, 171.8 (C-1, C-2, C-3), 138.6, 137.4, 133.8, 128.2, 126.1, 125.7, 124.8, 123.6, 122.4, 120.1 (naphthalene C), 34.2 (C-6), 32.6 (CH₃), 32.5, 24.1 (C-7, C-5), 24.8 (2CH₃); EIMS: m/z 338 [M]⁺ (26%); Anal. Calcd for C₁₉H₂₂N₄O₂ (338.40): C, 67.44; H, 6.55; N, 16.56%. Found: C, 67.64; H, 6.41; N, 16.73%.

2. 2. 12. 2. 2-(2-(4-Chloronaphthalen-1-yl)hydrazono)-5,5-dimethylcyclohexane-1,3-dione Dioxime (14b)

Pale yellow crystals from 1,4-dioxan; m.p. 190–193 °C; yield 70%. IR (KBr) cm^{-1} : 3533–3329 (OH, NH), 3055, 2985, 1665, 1662, 1630. ^1H NMR (300 MHz, DMSO- d_6) δ 10.06, 9.65 (2s, 2H, D₂O exchangeable, 2OH), 8.25 (s, 1H, D₂O exchangeable, NH), 7.50–7.24 (m, 6H, naphthalene H), 2.58, 2.43 (2s, 4H, 2CH₂), 1.09, 1.06 (2s, 6H, 2CH₃); ^{13}C NMR (DMSO- d_6 , 75 MHz) δ 176.5, 173.6, 171.8 (C-1, C-2, C-3), 138.8, 137.1, 133.5, 128.0, 126.7, 125.3, 124.8, 123.4, 122.6, 120.1 (naphthalene C), 34.5 (C-6), 32.5, 24.3 (C-7, C-5), 24.5 (2CH₃); EIMS: m/z 358 [M]⁺ (32%); Anal. Calcd for C₁₈H₁₉ClN₄O₂ (358.82): C, 60.25; H, 5.34; N, 15.61%. Found: C, 60.19; H, 5.28; N, 15.80%.

2. 2. 13. General Procedure for the Synthesis of the 2,3,5,6,7,8-Hexahydrocinnoline Derivatives 16a–d

To a solution of either of **11a** (3.08 g, 0.01 mol), **11b** (3.28 g, 0.01 mol) in ethanol (40 mL) containing triethylamine either malononitrile (0.66 g, 0.01 mol) or ethyl cyanoacetate (1.07 g, 0.01 mol) was added. The reaction mixture in each case was heated under reflux for 3 h then poured onto ice/water containing a few drops of hydrochloric acid and the formed solid product was collected by filtration.

2. 2. 13. 1. 3-Imino-6,6-dimethyl-2-(4-methylnaphthalen-1-yl)-8-oxo-2,3,5,6,7,8-hexahydrocinnoline-4-carbonitrile (16a)

Pale brown crystals from 1,4-dioxan; m.p. 188–191 °C; yield 70%. IR (KBr) cm^{-1} : 3478–3337 (NH), 3055,

2985, 2220, 1687, 1666, 1660, 1630. ^1H NMR (300 MHz, DMSO- d_6) δ 8.25 (s, 1H, D₂O exchangeable, NH), 7.53–7.24 (m, 6H, naphthalene H), 2.86 (s, 3H, CH₃), 2.53, 2.42 (2s, 4H, 2CH₂), 1.09, 1.07 (2s, 6H, 2CH₃); ^{13}C NMR (DMSO- d_6 , 75 MHz) δ 176.4 (C-3), 165.8 (C-8), 138.9, 136.3, 135.4, 128.1, 126.5, 125.3, 124.8, 123.6, 122.4, 120.4 (naphthalene C), 117.0 (CN), 34.6 (C-6), 32.8 (CH₃), 32.2, 24.3 (C-7, C-5), 24.8 (2CH₃); EIMS: m/z 356 [M]⁺ (32%); Anal. Calcd for C₂₂H₂₀N₄O (356.42): C, 74.14; H, 5.66; N, 15.72%. Found: C, 74.03; H, 5.79; N, 15.84%.

2. 2. 13. 2. 6,6-Dimethyl-2-(4-methylnaphthalen-1-yl)-3,8-dioxo-2,3,5,6,7,8-hexahydrocinnoline-4-carbonitrile (16b)

Pale yellow crystals from 1,4-dioxan; m.p. 203–206 °C; yield 65%. IR (KBr) cm^{-1} : 3055, 2985, 2220, 1689, 1666, 1660, 1630. ^1H NMR (300 MHz, DMSO- d_6) δ 7.56–7.23 (m, 6H, naphthalene H), 2.84 (s, 3H, CH₃), 2.56, 2.40 (2s, 4H, 2CH₂), 1.09, 1.08 (2s, 6H, 2CH₃); ^{13}C NMR (DMSO- d_6 , 75 MHz) δ 176.6 (C-3), 165.5 (C-8), 138.4, 137.1, 135.2, 127.4, 126.5, 125.1, 124.8, 123.6, 122.2, 120.4 (naphthalene C), 116.8 (CN), 34.6 (C-6), 32.5 (CH₃), 32.0, 24.6 (C-7, C-5), 24.5 (2CH₃); EIMS: m/z 357 [M]⁺ (28%); Anal. Calcd for C₂₂H₁₉N₃O₂ (357.41): C, 73.93; H, 5.36; N, 11.76%. Found: C, 73.61; H, 5.49; N, 11.83%.

2. 2. 13. 3. 2-(4-Chloronaphthalen-1-yl)-3-imino-6,6-dimethyl-8-oxo-2,3,5,6,7,8-hexahydrocinnoline-4-carbonitrile (16c)

Pale yellow crystals from 1,4-dioxan; m.p. 180–183 °C; yield 65%. IR (KBr) cm^{-1} : 3459–3341 (NH), 3055, 2985, 2220, 1689, 1664, 1660, 1630. ^1H NMR (300 MHz, DMSO- d_6) δ 8.23 (s, 1H, D₂O exchangeable, NH), 7.56–7.23 (m, 6H, naphthalene H), 2.56, 2.42 (2s, 4H, 2CH₂), 1.09, 1.07 (2s, 6H, 2CH₃); ^{13}C NMR (DMSO- d_6 , 75 MHz) δ 176.6 (C-3), 165.9 (C-8), 138.5, 137.8, 135.3, 127.6, 126.2, 125.1, 124.8, 123.4, 122.1, 120.5 (naphthalene C), 116.8 (CN), 34.4 (C-6), 32.0, 24.7 (C-7, C-5), 24.5 (2CH₃); EIMS: m/z 376 [M]⁺ (32%); Anal. Calcd for C₂₁H₁₇ClN₄O (376.84): C, 66.93; H, 4.55; N, 14.87%. Found: C, 67.27; H, 4.74; N, 15.04%.

2. 2. 13. 4. 2-(4-Chloronaphthalen-1-yl)-6,6-dimethyl-3,8-dioxo-2,3,5,6,7,8-hexahydrocinnoline-4-carbonitrile (16d)

Pale yellow crystals from 1,4-dioxan; m.p. 210–213 °C; yield 70%. IR (KBr) cm^{-1} : 3055, 2985, 2220, 1689, 1686, 1663, 1660, 1630. ^1H NMR (200 MHz, DMSO- d_6) δ 7.58–7.21 (m, 6H, naphthalene H), 2.54, 2.43 (2s, 4H, 2CH₂), 1.09, 1.08 (2s, 6H, 2CH₃); ^{13}C NMR (DMSO- d_6 , 75 MHz) δ 176.8 (C-3), 165.3 (C-8), 138.6, 137.5, 135.2, 127.8, 126.2, 125.6, 124.3, 123.4, 122.1, 120.1 (naphthalene C), 116.8 (CN), 34.4 (C-6), 32.2, 24.3 (C-7, C-5), 24.5 (2CH₃); EIMS: m/z 377 [M]⁺ (30%); Anal. Calcd for C₂₁H₁₆ClN₃O₂ (377.82): C, 66.76; H, 4.27; N, 11.12%. Found: C, 66.92; H, 4.58; N, 11.43%.

2. 3. Biology Section

2. 3. 1. *In vitro* Cell Assays

All the synthesized compounds were assessed for the inhibitory activities against A549 (non-small cell lung cancer), H460 (human lung cancer), HT-29 (human colon cancer) and MKN-45 (human gastric cancer) cancer cell lines together with foretinib as the positive control by a MTT assay. Furthermore, all compounds were further evaluated against U87MG (human glioblastoma) and SMMC-7721 (human liver cancer) cell lines. The results expressed as IC_{50} are summarized in Table 2. The IC_{50} values are the average of at least three independent experiments. The data listed in Table 2 reveal that the compounds possess moderate to strong cytotoxicity against the five tested cell lines in the single-digit nM range, and high selectivity for inhibition against A549, H460 and MKN-45 cells. The promising compounds were **3c**, **5b**, **5e**, **5f**, **7c**, **7f**,

9c, **11b**, **12c**, **12d**, **13b**, **13d**, **14b**, **16c** and **16d** among the tested compounds.

2. 3. 1. 1. Structure Activity Relationship

From Table 1 it is clear that most of compounds showed high cytotoxicities against the six cancer cell lines. In most cases the high inhibitions was due to the presence of electronegative substituent through the aryl or the heterocyclic rings. Considering the benzylidene derivatives **3a–c**, it is obvious that compound **3a** ($X = H$) is of low inhibitions relative to **3b** ($X = OCH_3$) and **3c** ($X = Cl$). In addition, compound **3b** showed moderate inhibitions and **3a** with highest inhibitions among the three compounds. Considering the thiophene derivatives **5a–f**, it is clear that compounds **5d** ($X = OCH_3$, $R = COOEt$), **5e** ($X = Cl$, $R = CN$) and **5f** ($X = Cl$, $R = COOEt$) were the most cytotoxic compounds. On the other hand, for the 4,5,6,7-tetrahydro-2*H*-indazole derivatives **7a–f**, where compounds **7c**

Table 1. *In vitro* growth inhibitory effects $IC_{50} \pm SEM$ (μM) of the newly synthesized compounds towards cancer cell lines

Compound No	$IC_{50} \pm SEM$ (μM)					
	A549	H460	HT29	MKN-45	U87MG	SMMC-7721
3a	8.32 \pm 2.57	8.68 \pm 2.60	7.93 \pm 2.49	8.73 \pm 2.71	8.48 \pm 2.90	8.29 \pm 2.09
3b	2.63 \pm 1.14	2.64 \pm 0.95	1.63 \pm 0.59	1.47 \pm 0.69	2.16 \pm 0.96	1.53 \pm 0.87
3c	0.29 \pm 0.12	0.34 \pm 0.18	0.62 \pm 0.36	0.26 \pm 0.19	0.35 \pm 0.22	0.41 \pm 0.13
5a	5.23 \pm 1.47	4.82 \pm 1.36	2.58 \pm 0.926	3.62 \pm 1.21	5.78 \pm 1.30	5.39 \pm 1.15
5b	6.88 \pm 1.23	4.83 \pm 2.05	5.64 \pm 2.11	4.52 \pm 2.18	2.38 \pm 2.21	4.20 \pm 1.19
5c	4.56 \pm 1.25	6.72 \pm 1.81	6.23 \pm 2.32	5.88 \pm 1.41	5.22 \pm 2.30	2.34 \pm 1.29
5d	1.20 \pm 0.74	1.47 \pm 0.47	1.23 \pm 0.63	2.22 \pm 1.15	1.60 \pm 0.86	2.96 \pm 1.63
5e	0.41 \pm 0.22	0.87 \pm 0.53	0.52 \pm 0.25	0.43 \pm 0.21	0.39 \pm 0.16	0.48 \pm 0.25
5f	0.26 \pm 0.17	0.31 \pm 0.15	0.42 \pm 0.32	0.26 \pm 0.15	0.40 \pm 0.26	0.38 \pm 0.15
7a	8.90 \pm 3.60	9.53 \pm 2.06	8.31 \pm 2.70	6.16 \pm 1.93	6.49 \pm 2.52	8.24 \pm 3.19
7b	2.36 \pm 1.06	1.48 \pm 0.69	2.40 \pm 1.13	1.05 \pm 0.72	1.28 \pm 0.69	2.59 \pm 1.06
7c	0.43 \pm 0.24	0.57 \pm 0.16	0.42 \pm 0.19	0.58 \pm 0.21	0.35 \pm 0.22	0.28 \pm 0.09
7d	3.25 \pm 1.19	2.36 \pm 0.92	3.50 \pm 1.56	2.87 \pm 1.40	3.42 \pm 1.82	1.92 \pm 0.89
7e	1.28 \pm 0.42	1.67 \pm 0.83	2.61 \pm 0.76	1.88 \pm 0.42	2.26 \pm 0.80	1.53 \pm 0.80
7f	0.24 \pm 0.11	0.31 \pm 0.16	0.38 \pm 0.27	0.41 \pm 0.12	0.25 \pm 0.08	0.52 \pm 0.16
9a	8.38 \pm 2.72	7.29 \pm 2.60	8.53 \pm 2.30	7.93 \pm 2.27	8.09 \pm 1.74	6.92 \pm 1.79
9b	1.18 \pm 0.30	0.86 \pm 0.53	0.69 \pm 0.40	0.83 \pm 0.27	0.59 \pm 0.31	0.63 \pm 0.25
9c	0.32 \pm 0.17	0.52 \pm 0.13	0.44 \pm 0.15	0.23 \pm 0.13	0.23 \pm 0.42	0.63 \pm 0.30
11a	1.03 \pm 0.36	1.43 \pm 0.39	0.96 \pm 1.42	0.78 \pm 0.35	0.68 \pm 0.34	0.80 \pm 0.35
11b	0.28 \pm 0.19	0.36 \pm 0.18	0.41 \pm 0.27	0.31 \pm 0.13	0.28 \pm 0.15	0.50 \pm 0.21
12a	2.25 \pm 0.68	2.70 \pm 0.61	1.09 \pm 0.79	1.17 \pm 0.40	1.58 \pm 0.54	1.80 \pm 0.93
12b	4.27 \pm 1.12	3.55 \pm 1.25	2.38 \pm 1.16	3.42 \pm 1.38	2.25 \pm 1.68	3.51 \pm 1.09
12c	0.46 \pm 0.18	0.39 \pm 0.17	0.72 \pm 0.23	0.84 \pm 0.26	0.34 \pm 0.18	0.34 \pm 0.29
12d	0.63 \pm 0.24	0.22 \pm 0.13	0.47 \pm 0.17	0.68 \pm 0.16	0.37 \pm 0.24	0.52 \pm 0.20
13a	6.09 \pm 1.26	7.83 \pm 1.84	8.39 \pm 2.53	6.73 \pm 1.80	8.53 \pm 2.06	5.27 \pm 1.73
13b	0.98 \pm 0.32	0.45 \pm 0.25	0.69 \pm 0.32	0.38 \pm 0.16	0.50 \pm 0.17	0.68 \pm 0.42
13c	4.48 \pm 1.23	5.59 \pm 1.27	3.27 \pm 1.24	4.25 \pm 1.56	2.82 \pm 1.04	3.53 \pm 1.51
13d	0.34 \pm 0.26	0.39 \pm 0.25	0.60 \pm 0.42	0.52 \pm 0.20	0.28 \pm 0.19	0.26 \pm 0.15
14a	6.23 \pm 1.38	5.39 \pm 1.13	5.09 \pm 1.25	4.78 \pm 2.21	5.42 \pm 2.32	6.26 \pm 2.63
14b	0.79 \pm 0.35	0.85 \pm 0.28	0.84 \pm 0.31	0.59 \pm 0.36	0.80 \pm 0.31	0.48 \pm 0.24
16a	7.28 \pm 2.09	8.26 \pm 3.16	9.26 \pm 2.41	6.27 \pm 1.89	8.47 \pm 2.53	6.61 \pm 1.75
16b	4.33 \pm 1.70	4.16 \pm 1.72	2.46 \pm 1.29	4.59 \pm 1.25	3.72 \pm 1.47	4.64 \pm 1.63
16c	0.28 \pm 0.18	0.43 \pm 0.15	0.34 \pm 0.12	0.45 \pm 0.22	0.39 \pm 0.28	0.39 \pm 0.132
16d	0.23 \pm 0.12	0.44 \pm 0.20	0.32 \pm 0.17	0.28 \pm 0.08	0.20 \pm 0.14	0.19 \pm 0.017
foretinib	0.08 \pm 0.01	0.18 \pm 0.03	0.15 \pm 0.023	0.03 \pm 0.0055	0.90 \pm 0.13	0.44 \pm 0.062

(R = H, X = Cl) and **7f** (R Ph, X = Cl) were the most cytotoxic compounds. For the isoxazole derivatives **9a–c**, compound **9c** (X = Cl) was the most cytotoxic compound among the three compounds. While compound **9b** (X = OCH₃) has high cytotoxicity against the five cancer cell lines H460, HT29, MKN-45, U87MG and SMMC-7721 with IC₅₀ values 0.86, 0.69, 0.83, 0.59 and 0.63 μM, respectively. For the arylhydrazone derivatives **11a,b**, compound **11b** with Y = Cl was more cytotoxic than **11a** with Y = CH₃. Considering the fused thiophene derivatives **12a–d**, it is obvious that compounds **12c** (Y = Cl, R = CN) and **12d** (Y = Cl, R = COOEt) were more cytotoxic than compounds **12a** and **12b** although compound **12a** has moderate cytotoxicity. In case of the trihydrazone derivatives **13a–d**, compounds **13b** (R = H, Y = Cl) and **13d** (R = Ph, Y = Cl) were the most cytotoxic compounds, it is clear that the presence of Cl group was responsible for such high cytotoxicity. The same was also observed in the case of **14a,b** where compound **14b** (Y = Cl) was more cytotoxic than **14a** (Y = CH₃). Finally, for the fused pyridazine derivatives **16a–d**, it is clear that compounds **16c** (Y = Cl, R' = NH) and **16d** (Y = Cl, R' = O) were the most cytotoxic compounds among the four compounds.

2. 3. 2. Inhibition of Tyrosine Kinases (Enzyme IC₅₀ (nM))

Compounds **3c**, **5b**, **5e**, **5f**, **7c**, **7f**, **9c**, **11b**, **12c**, **12d**, **13b**, **13d**, **14b**, **16c** and **16d** were the most potent compounds against the selected six cancer cell lines and were further tested toward the five tyrosine kinases c-kit, Flt-3, VEGFR-2, EGFR and PDGFR and the data are shown in Table 2.

The selection of the five tyrosine kinases was based on the fact that these contain seven, five and three Ig-like domains in the extracellular domain, respectively.²⁰ These RTKs have been implicated in vascular development by

affecting the proliferation and migration of endothelial cells or parricides. Among them, VEGFR is a major regulator of tumor angiogenesis *via* endothelial cell proliferation and the permeability of blood vessels.^{21,22} VEGFR is expressed in most human cancers such as breast, kidney and colon and patients with tumors showing elevated VEGFR expression have a poor prognosis.²³ It is clear that compounds **5b**, **5e**, **5f**, **7c**, **11b**, **12c**, **12d**, **13d**, **14b**, **16c** and **16d** are the most inhibitory compounds.

2. 3. 4. Inhibition of Selected Compounds Towards Pim-1 Kinase

Furthermore, compounds **5b**, **5e**, **5f**, **7c**, **11b**, **12c**, **12d**, **13d**, **14b**, **16c** and **16d** were selected to examine their Pim-1 kinase inhibition activity (Table 3) as these compounds showed high inhibition toward the tested cancer cell lines at a range and high inhibitions toward the five

Table 3. Inhibition of Pim-1 kinase by compounds **5b**, **5e**, **5f**, **7c**, **11b**, **12c**, **12d**, **13d**, **14b**, **16c** and **16d**

Compound	Inhibition ratio at 10 μM	IC ₅₀ (μM)
5b	96	0.31
5e	26	> 10
5f	22	> 10
7c	28	> 10
11b	86	0.68
12c	28	>10
12d	92	0.42
13d	94	0.38
14b	89	0.46
16c	95	0.34
16d	23	>10
SGI-1776	-	0.048

Table 2. Inhibition of tyrosine kinases (Enzyme IC₅₀ (nM)) by compounds **3c**, **5b**, **7c**, **7f**, **9c**, **11b**, **12c**, **12d**, **13b**, **13d**, **14b**, **16c** and **16d**

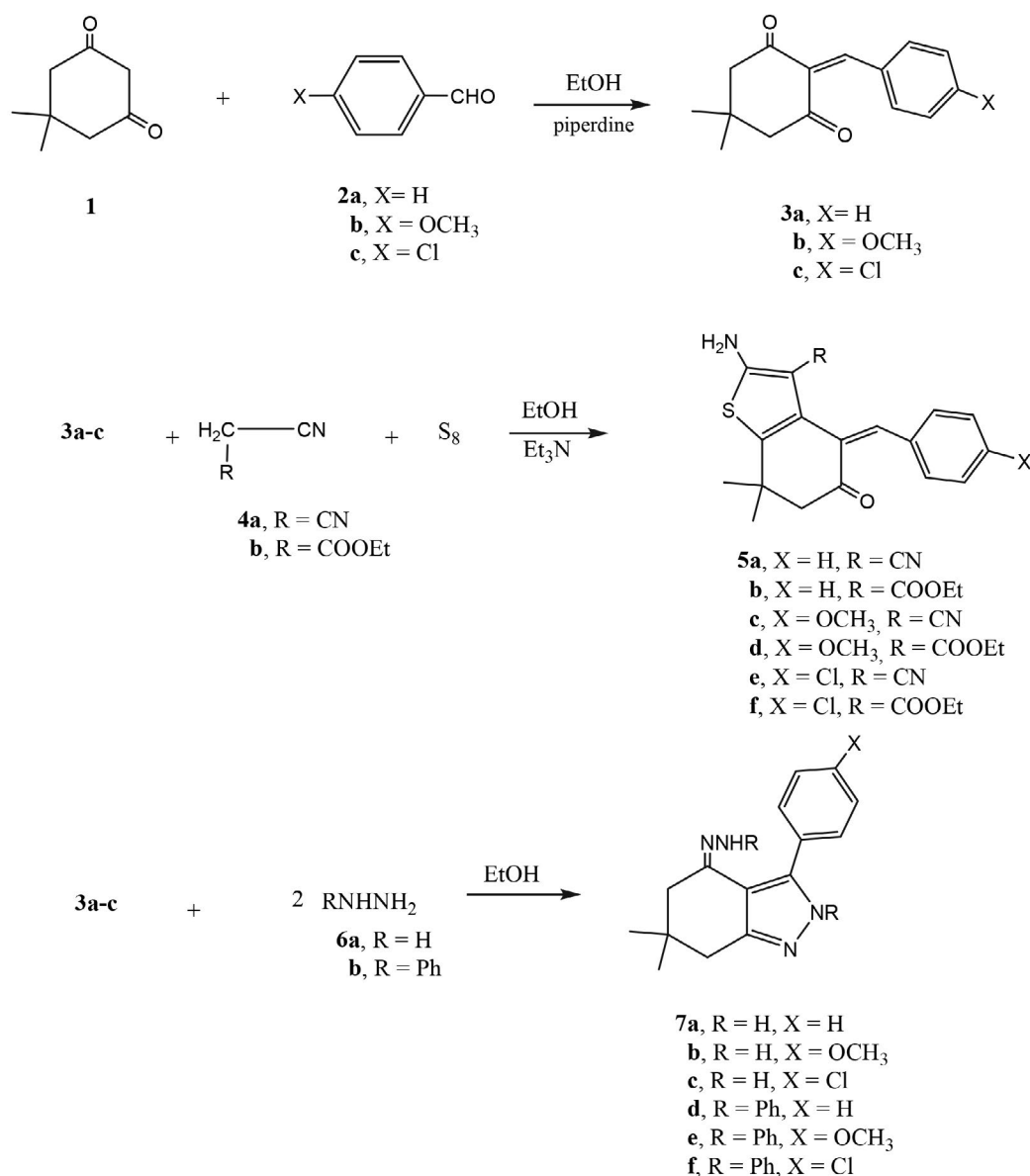
Compound	c-Kit	Flt-3	VEGFR-2	EGFR	PDGFR
3c	1.61	0.96	1.36	1.42	1.17
5b	0.35	0.27	0.21	0.36	0.42
5e	0.28	0.19	0.36	0.25	0.46
5f	0.37	0.24	0.42	0.39	0.48
7c	0.42	0.36	0.51	0.28	0.26
7f	1.09	1.24	1.31	0.96	0.30
9c	1.16	1.27	1.40	1.16	0.52
11b	0.28	0.50	0.19	0.33	0.26
12c	0.26	0.38	0.51	0.39	0.27
12d	0.30	0.35	0.19	0.43	0.60
13b	1.01	0.82	1.07	1.53	1.32
13d	0.38	0.26	0.63	0.62	0.47
14b	0.47	0.56	0.32	0.53	0.61
16c	0.24	0.26	0.38	0.41	0.37
16d	0.72	0.69	0.93	0.52	0.73

tyrosine kinases. Compounds **5b**, **11b**, **12d**, **13d**, **14b** and **16c** were the most potent to inhibit Pim-1 activity with IC_{50} value of 0.31, 0.68, 0.42, 0.38, 0.46 and 0.34 μM , while **7c**, **5e**, **5f**, **12c** and **16d** were less effective ($IC_{50} > 10 \mu\text{M}$). SGI-1776 was used as the positive control with IC_{50} 0.048 μM in the assay. These profiles in combination with cell growth inhibition data of the tested compounds are listed in Table 3 indicating that Pim-1 was a potential target of these compounds.

3. Results and Discussion

The synthetic route to prepare a new class of biologically active molecules using dimedone as the key starting compound is illustrated in Schemes 1–3. The reaction of

dimedone (**1**) with any of the aromatic aldehydes **2a–c** gave the benzylidene derivatives **3a–c**, respectively. Compounds **3a–c** were appropriate for Gewald's thiophene synthesis^{24–26} through the reaction of any of compounds **3a–c** with either of malononitrile (**4a**) or ethyl cyanoacetate (**4b**) and elemental sulfur gave the 6,7-dihydrobenzo[*b*]thiophen-5(4*H*)-one derivatives **5a–f**, respectively. The structures of compounds **5a–f** were based on their analytical and spectral data. Thus, the ^1H NMR spectrum of compound **5a** (as an example) showed the presence of one NH_2 group at δ 4.30 ppm (D_2O exchangeable) and a singlet at δ 2.32 ppm indicating one CH_2 group. The ^{13}C NMR spectrum revealed the presence of a signal at 166.0 due to the presence of $\text{C}=\text{O}$ group and signals at δ 138.6, 136.0, 135.2, 130.7, 127.8, 125.4, 124.3, 121.0 due to the phenyl and thiophene carbons. On the other hand, the reaction of any of



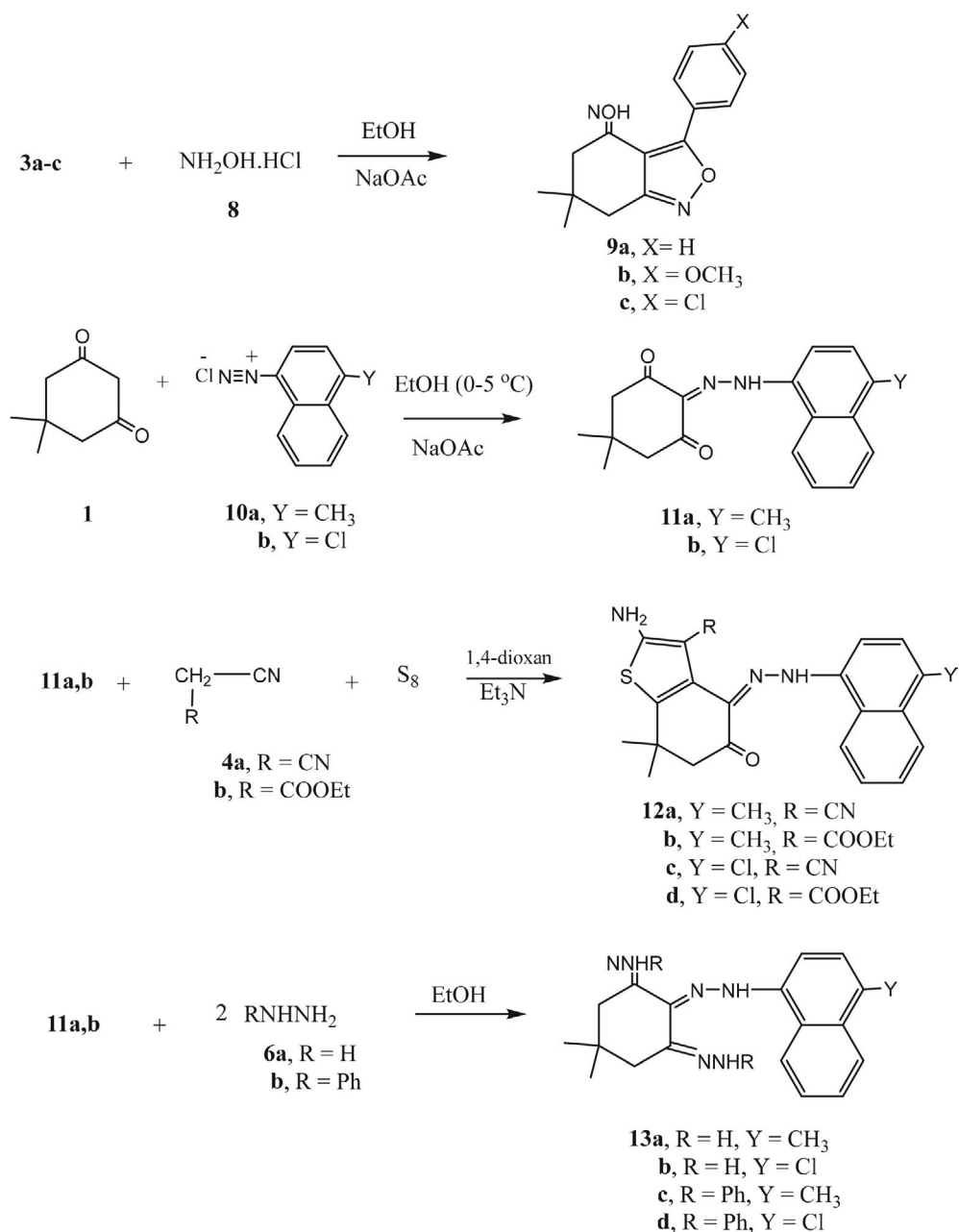
Scheme 1. Synthesis of compounds **3a–c**, **5a–f** and **7a–f**.

compounds **3a–c** with either of hydrazine hydrate (**6a**) or phenylhydrazine (**6b**) gave the 4,5,6,7-tetrahydro-2*H*-indazole derivatives **7a–f**, respectively (Scheme 1).

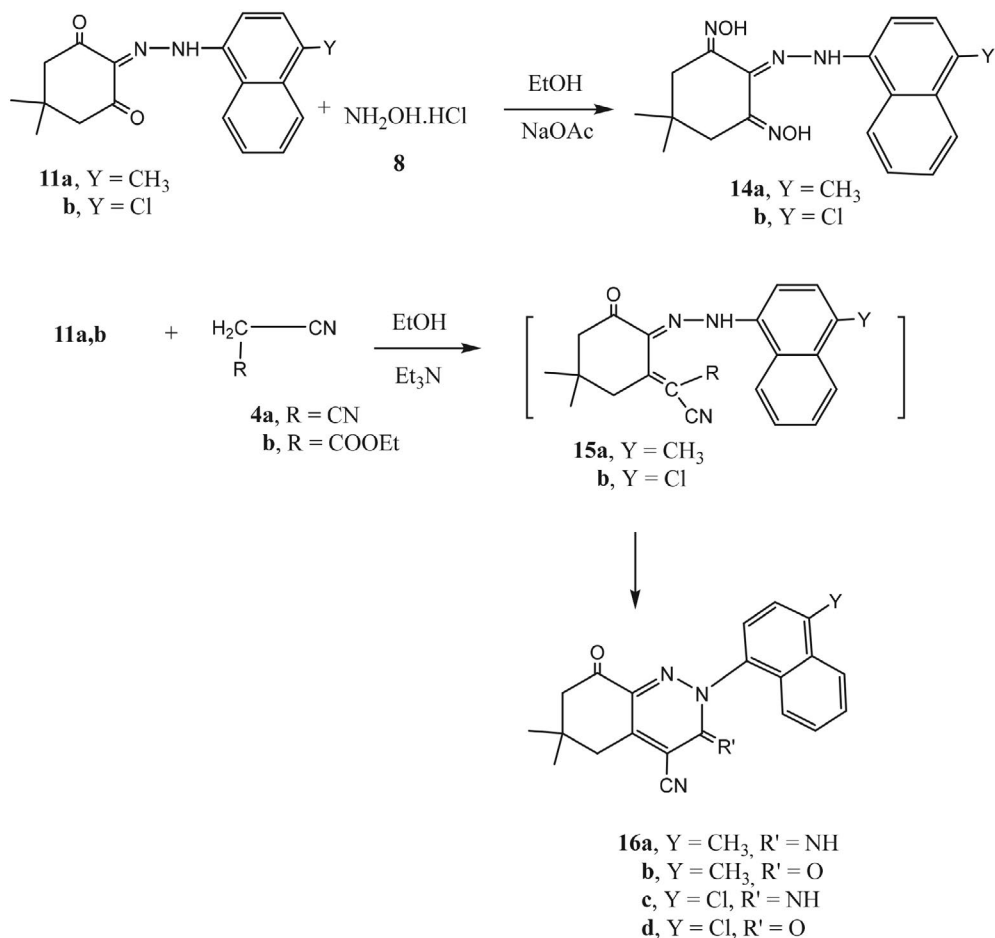
The reaction of any of compounds **3a–c** with two moles of hydroxylamine hydrochloride (**8**) in ethanol containing sodium acetate gave the 4,5,6,7-tetrahydrobenzo[*c*]isoxazol-3-yl)benzene derivatives **9a–c**, respectively. The structures of compounds **9a–c** were established on the basis of analytical and spectral data. Thus, the ¹H NMR spectrum of **9a** (as an example) showed the presence of the OH group at δ 9.52 ppm (D₂O exchangeable) and two singlets at δ 2.47 and 2.33 ppm due to the presence of the two CH₂ groups. On the other hand, the ¹³C NMR spectrum

gave signals at δ 140.1, 137.6, 127.8, 126.5, 124.0, 121.2 due to the phenyl and two isoxazole carbons.

The reaction of compound **1** with either 4-methyl-1-naphthalen-1-diazonium salt (**10a**) or 4-chloro-1-naphthalen-1-diazonium salt (**10b**) gave the naphthylhydrazo derivatives **11a** and **11b**, respectively. Compounds **11a,b** reacted with elemental sulfur and either of malononitrile (**4a**) or ethyl cyanoacetate (**4b**) to give the naphthalen-1-yl)hydrazono)-6,7-dihydrobenzo[*b*]thiophene derivatives **12a–d**, respectively. Compounds **11a,b** were appropriate for Gewald's thiophene synthesis, thus the reaction of either of **11a** or **11b** with elemental sulfur and either of malononitrile (**4a**) or ethyl cyanoacetate (**4b**) gave



Scheme 2. Synthesis of compounds **9a–c**, **11a,b**, **12a–d** and **13a–d**.



Scheme 3. Synthesis of compounds **14a,b** and **16a–d**.

the 6,7-dihydrobenzo[*b*]thiophene derivatives **13a–d**, respectively (Scheme 2).

The reaction of either of **11a** or **11b** with hydroxylamine hydrochloride gave the cyclohexane-1,3-dione di-oxime derivatives **14a** and **14b**, respectively. On the other hand, the reaction of either of compound **11a** or **11b** with either of malononitrile (**4a**) or ethyl cyanoacetate (**4b**) gave the 2,3,5,6,7,8-hexahydrocinnoline derivatives **16a–d**, respectively (Scheme 3). The structures of the latter products were based on their respective analytical and spectral data. Thus, the ¹H NMR spectrum of **16a** (as an example) showed the presence of a singlet at δ 8.25 ppm due to the presence of the NH group, a multiplet at δ 7.53–7.24 ppm due to the presence of the naphthalene protons. In addition the ¹³C NMR spectrum showed the presence of signals at δ 138.9, 136.3, 135.4, 128.1, 126.5, 125.3, 124.8, 123.6, 122.4, 120.4 due to the naphthalene carbons and two signals at δ 32.2, 24.3 for the two CH₂ groups.

4. Conclusion

In conclusion, an efficient and practical synthesis of new series of heterocyclic compounds derived from dime-

done was carried out and the prepared compounds were characterized and their anti-proliferative activities were evaluated against the six cancer cell lines A549, HT-29, MKN-45, U87MG, SMMC-7721 and H460. The results showed that compounds **3c**, **5b**, **5e**, **5f**, **7c**, **7f**, **9c**, **11b**, **12c**, **12d**, **13b**, **13d**, **14b**, **16c** and **16d** were the most potent compounds. On the other hand, compounds **5b**, **5e**, **5f**, **7c**, **11b**, **12c**, **12d**, **13d**, **14b**, **16c** and **16d** were the most inhibitory active compounds against tyrosine kinases and compounds **5b**, **11b**, **12d**, **13d**, **14b** and **16c** were the most potent against Pim-1 kinase.

Acknowledgement

R. M. Mohareb would like to thank the Alexander von Humboldt for affording him regular fellowships in Germany for doing research and completing this work.

5. References

- L. G. Dutra, C. Saibert, D. S. Vicentini, M. M. Sa, *J. Mol. Catal. A: Chemical* **2014**, 386, 35–41.
DOI:10.1016/j.molcata.2014.02.011

2. J. S. Yadav, B. V. Subba, R. Rao, R. Narender, *Tetrahedron Lett.* **2009**, *50*, 3963–3965. DOI:10.1016/j.tetlet.2009.04.088
3. R. Kumar, K. Raghuvanshi, R. K. Verma, M. S. Singh, *Tetrahedron Lett.* **2010**, *51*, 5933–5936. DOI:10.1016/j.tetlet.2010.09.017
4. V. Nadaraj, S. T. Selvi, S. Mohan, *Eur. J. Med. Chem.*, **2009**, *44*, 976–980. DOI:10.1016/j.ejmech.2008.07.004
5. M. L. Deb, P. J. Bhuyan, *Tetrahedron Lett.* **2005**, *46*, 6453–6456. DOI:10.1016/j.tetlet.2005.07.111
6. S. Chassaing, S. Specklin, J. M. Weibel, P. Pale, *Tetrahedron* **2012**, *68*, 7245–7273. DOI:10.1016/j.tet.2012.05.107
7. A. Amoozadeh, E. Tabrizian, S. Rahmani, *Comptes Rend. Chim.* **2015**, *18*, 848–857. DOI:10.1016/j.crci.2014.11.003
8. A. Ilangovan, S. Malayappasamy, S. Muralidharan, *Chem. Cent.* **2011**, *5*, 81. DOI:10.1186/1752-153X-5-81
9. A. M. Al-Majid, M. S. Islam, S. Barakat, N. J. Al-Qahtani, S. Yousef, M. I. Choudhary, *Arab J. Chem.* **2017**, *10*, 185–193. DOI:10.1016/j.arabjc.2014.04.008
10. J. M. Khurana, D. Magoo, *Tetrahedron Lett.* **2009**, *52*, 7300–7303. DOI:10.1016/j.tetlet.2009.10.032
11. H. Naeimi, Z. S. Nazif, *J. Ind. Engin. Chem.* **2014**, *20*, 1043–1049. DOI:10.1016/j.jiec.2013.06.041
12. K. Nikoofar, F. M. Yielzoleh, *J. Saudi Chem. Soc.* **2018**, *22*, 715–741. DOI:10.1016/j.jscs.2017.12.005
13. A. A. Abdelhamid, S. K. Mohamed, A. M. Maharramov, A. N. Khlalilov, M. A. Allahverdiev, *J. Saudi Chem. Soc.* **2014**, *18*, 474–478. DOI:10.1016/j.jscs.2011.10.005
14. M. L. Silva, R. R. Teixeira, L. A. Santos, F. T. Martins, T. C. Ramahho, *J. Mol. Struct.* **2018**, *1156*, 700–711. DOI:10.1016/j.molstruc.2017.11.105
15. C. Jiao, Y. J. Chao-guo, *Chem. Res. Chin. Univ.* **2011**, *27*, 49–53.
16. R. M. Mohareb, T. M. Klapötke, E. Reinhardt, *Med. Chem. Research* **2018**, *27*, 2494–2511. DOI:10.1007/s00044-018-2252-3
17. R. M. Mohareb, F. Al-Omran, M. A. Abdelaziz, R. A. Ibrahim, *Acta Chim. Slov.* **2017**, *64*, 349–364. DOI:10.17344/acsi.2017.3200
18. R. M. Mohareb, P. A. Halim, *Acta Chim. Slov.* **2018**, *65*, 554–568. DOI:10.17344/acsi.2017.4146
19. R. M. Mohareb, N. Y. Abdo, F. O. Al-Farouk, *Acta Chim. Slov.* **2017**, *64*, 117–128. DOI:10.17344/acsi.2016.2920
20. P. B. Jensen, T. Hunter, *Nature* **2001**, *411*, 355–365. DOI:10.1038/35077225
21. J. DiSalvo, M. L. Bayne, G. Conn, P. W. Kwok, P. G. Trivedi, D. D. Soderman, T. M. Palisi, K. A. Sullivan, K. A. Thomas, *J. Biol. Chem.* **1995**, *270*, 7717–7723. DOI:10.1074/jbc.270.13.7717
22. D. R. Senger, S. J. Galli, A. M. Dvorak, C. A. Perruzzi, V. S. Harvey, H. F. Dvorak, *Science* **1983**, *219*, 983–985. DOI:10.1126/science.6823562
23. N. Ferrara, *Nat. Rev. Cancer*, **2002**, *2*, 795–803. DOI:10.1038/nrc909
24. R. M. Mohareb, W. W. Wardakhan, R. A. Ibrahim, *Med. Chem. Res.* **2016**, *25*, 2187–2204. DOI:10.1007/s00044-016-1654-3
25. A. M. Abdallah, R. M. Mohareb, E. M. Khalil, M. A. M. Elshamy, *Chem. Pharm. Bull.* **2017**, *65*, 469–477. DOI:10.1248/cpb.c16-00925
26. W. Zhang, T. Ma, S. Li, Y. Yang, J. Guo, W. Yu, L. Kong, *Eur. J. Med. Chem.* **2017**, *125*, 538–550. DOI:10.1016/j.ejmech.2016.09.068

Povzetek

Pri reakciji dimedona z arilaldehidi so nastali benzilidenski derivati **3a–c**, ki smo jih v naslednji stopnji s heterociklizacijsko reakcijo pretvorili v pripojene tiofenske, pirazol izoksazolske in piridazinske derivate. Pripravljenim spojinam smo določili učinek na različne rakave celične linije ter tudi morebitno inhibicijo tirozin kinaze in Pim-1 kinaze. Za vse sintetizirane spojine smo določili inhibitorno aktivnost na A549 (nemikrocelični pljučni rak), H460 (človeški pljučni rak), HT-29 (rak človeškega debelega črevesa) in MKN-45 (rak človeškega želodca); foretinib smo uporabili kot pozitivno kontrolo pri MTT testiranju. Kot obetavne so se izkazale spojine **3c**, **5b**, **5e**, **5f**, **7c**, **7f**, **9c**, **11b**, **12c**, **12d**, **13b**, **13d**, **14b**, **16c** in **16d**. Po drugi strani so se spojine **5b**, **5e**, **5f**, **7c**, **11b**, **12c**, **12d**, **13d**, **14b**, **16c** in **16d** pokazale kot najbolj učinkoviti inhibitorji tirozin kinaze, spojine **5b**, **11b**, **12d**, **13d**, **14b** in **16c** pa so bile najbolj aktivne proti Pim-1 kinazi.



Except when otherwise noted, articles in this journal are published under the terms and conditions of the Creative Commons Attribution 4.0 International License

Scientific paper

Hybrid Membranes Based on Clay-Polymer for Removing Methylene Blue from Water

Ahmed M. Khalil^{1,*} and Sayed H. Kenawy²¹ Photochemistry Department, National Research Centre, El-Buhouth St., Dokki - 12622, Giza, Egypt² Refractories, Ceramics and Building Materials Department, National Research Centre, El-Buhouth St., Dokki - 12622, Giza, Egypt* Corresponding author: E-mail: akhalil75@yahoo.com
Phone: +202 33371635 Fax: +202 33370931

Received: 04-28-2019

Abstract

Water pollution is a serious environmental problem. Methylene blue is among the dyes that may exist in waste water. Adsorption is an effective process to remove dyes from contaminated water. Hybrid membranes based on clay-polymer; namely kaolin and polystyrene were prepared to absorb the present methylene blue in aqueous solution. These membranes were fired at 1000 °C to degrade polystyrene leaving cavities in the clay matrix with an expanded surface area and porous structure. The membranes were characterized via X-ray diffraction and Infrared spectroscopy. The morphological structure was investigated by using scanning electron microscopy. In this work, we are focusing on facile means represented in UV-Vis spectroscopy, to monitor the adsorption efficiency of the prepared membranes. From the results, the membrane loaded with 20% polystyrene by weight showed the optimum performance in adsorbing methylene blue from water.

Keywords: Clay; polystyrene; membrane; dye removal; methylene blue

1. Introduction

The demand to obtain fresh water increases rapidly with the progressive population growth. The scarcity of potable water is due to environmental degradation resulting from industrial development and its contaminants. To save human health and the environment, water purification is essential to remove turbidity, offensive smell and taste. Purifying water can be achieved by using various methods including coagulation, flocculation, ozonation, reverse osmosis, and adsorption.^{1–4} The kind of pollutant contributes in determining the method of removing it. Chemicals are among the major water contaminants. These chemicals participate in various industries like pharmaceuticals, printing and textiles. Organic compounds are the major pollutants present in the aforementioned industries; mainly in synthetic dyes. Different azodyes are used in textile industries. However, most of these dyes are highly carcinogenic even if they are present in minute quantities. Methylene blue (MB) as a cationic dye is commonly used for coloring, in addition to microbiology, surgery, diagnostics.^{5–7} Though MB is not strongly hazardous, it may have some

harmful effects. Acute exposure to MB leads to an increase in heart rate, shock, cyanosis, jaundice, and tissue necrosis in humans.^{8,9} MB may act as an eye irritant to humans and animals. Hence, the treatment of effluents loaded with MB is interesting to avoid the harmful impacts on the carrying waters.^{10,11} Recently, there is an increasing interest to investigate porous ceramic composite materials. Many products are made of porous ceramic, such as membranes, catalytic substrates and filters. This is due to their notable features such as high temperature stability, high permeability, excellent catalytic activity and low bulk density.

Clays and organic polymers are among the materials that can be employed individually or after mixing to form composites that can be used in adsorption, heavy metal removal, and paper fillings.^{12–14} Clay minerals contribute in various domains such as in preparing polymers nanocomposites and ceramics. The abundance of natural clay minerals of low cost is likely to make them a strong candidate as an adsorbent for the removal of toxic materials from wastewater and other environments. These minerals consist of tetrahedral and octahedral layers. Hence, they are characterized by the ratio of this sheets/layers in the

structure. The clay consisting of 2 tetrahedral sheets and 1 octahedral sheet is known as a 2:1 clay type (3 sheets). Meanwhile, those clays which comprise 1 octahedral sheet and 1 tetrahedral sheet are called 1:1 (2 sheets) clay types.^{15–17} These minerals have an important role in trapping contaminants from water in soil. The commonly used clays include montmorillonite, smectite, kaolinite and illite. They are present in almost all sedimentary rocks. Large ratio of surface area to volume or fine particles gives clay minerals a set of unique adsorption properties for various organic dyes, metals or other environmental pollutants.^{18–20} Furthermore, adsorption using inexpensive and affordable adsorbent would make removal of different dyes or metal pollutants from wastewater feasible. The abundance of natural clay minerals in a low cost permits them to become a strong candidate as an adsorbent for getting rid of toxins from wastewater. Clay-organic interaction is widely investigated. Association of an organic molecule with a clay particle may take place. The organic molecules may be adsorbed onto the clay minerals by ion-dipole forces or it may complex with a counter ion of the clay mineral or it may undergo a cation or anion exchange with original counter ions. Ceramic is produced by firing a mixture of materials for inorganic and non-metallic oxide; nitride or carbide materials. Many types of additives can be used with the ceramic matrix before or after combustion for enhancing its properties. Ceramic membranes are made from clay and waste materials. They are favored as low cost materials. These substrates attract attention for being employed in water treatment applications. Among these membranes, hydrophobic clay-alumina-based capillary membrane was used in desalination application.²⁰ It was prepared from a green silica-based ceramic hollow fiber membrane from waste rice husk. Upon comparing ceramic membranes to polymeric ones, it was found the latter may face some drawbacks. Sometimes, they are unable to proceed in their required processes at high temperature or severe chemical circumstances. Hence, ceramic membranes possess merits over polymeric membranes. This can be correlated to their non-swelling behavior and thermal stability.^{17,18}

Used polystyrene exists as a solid municipal waste through the consumed scrap. Expanded polystyrene (EPS) is substrate which is utilized in large amounts in packaging applications or as an insulator. EPS is a tough, foamy material. It is among the major plastic wastes. It possess a low density, chemical and thermal resistances with a low cost.^{21,22} The augmenting amount of consumed EPS is attracting attention to be recycled.²³ The pellet of EPS is nearly spherical. It consists of approximately 2% polystyrene and the rest percentage is air.²⁴ EPS is hydrophobic. Thereafter, it can be used as a light aggregate for reaching a light weight foam concrete.^{25,26} It can be used producing a walling substrate in construction. Among the disadvantages of EPS is being a non-biodegradable substrate.²⁷ Therefore, inserting it in a wall panel matrix will be beneficial to dispose consumed EPS.

The aim of this work is to prepare hybrid porous membranes based on kaolin and polystyrene to adsorb methylene blue from water. The membranes will possess pores resulting from firing the prepared membranes with degrading the expanded polystyrene. The adsorption changes are proposed to be followed up in an easy and rapid process which is UV-Vis spectral analysis for the resulting solutions after MB adsorption. Kinetics and related isotherms for determining the adsorption capacities are not discussed in the current work.

2. Experimental

2.1. Materials and Instruments

The used raw materials in this study are kaolin and expanded polystyrene. Kaolin was provided from Kalabsha – Egypt. Expanded polystyrene (EPS) pellets with an average diameter 2 mm were obtained by shredding post-consumed polystyrene foam. The polymeric beads were washed with water and dried. Expanded polystyrene has a role in providing cavities in the ceramic matrix as EPS degrades at high temperatures. Methylene blue (MB) powder was purchased from Sigma Aldrich. MB powder was used to prepare an aqueous solution with 250 mg/l concentration at 25 °C. This solution is utilized in carrying out the adsorption investigations. The chemical constituents of the clay were investigated using X-rays Fluorescence equipped by a modern wavelength dispersive spectrometer (Axios PANalytical 2005, Netherlands).

The densification parameters in terms of bulk density (BD), apparent porosity (A. P.), closed – porosity (CP) and total porosity were determined according to the ASTM : C 20-46. This method is based on boiling the sample in water for 2h. The saturated sample were weighed in air and immersed in water. The weight of each dry sample was obtained after drying the saturated samples overnight at 110 °C. The bulk density as well as apparent porosity were calculated using the following equations:

$$\text{Bulk density (BD)} = \frac{W_d}{W_s - W_i} \quad (\text{g cm}^{-3})$$

$$\text{Apparent porosity (A. P.)} = \frac{W_s - W_d}{W_s - W_i} \times 100 (\%)$$

where: W_d = weight of the dry sample

W_s = weight of the saturated sample

W_i = weight of the saturated sample immersed in water

The fired samples were characterized using the scanning electron microscopy (SEM) for microstructure investigations with energy-dispersive spectroscopy (EDX; JEOL JXA-840 A, Electron probe micro-analyzer, Japan). Infrared spectra of the obtained membranes were attained using Fourier transformer infrared spectrophotometer (FT-IR) (model FT/IR-6100 Type A, Germany) before and after adsorption process. X-Ray Diffraction (XRD) patterns were also carried out for the obtained membrane before and after adsorption using (XRD, BRUKER, D8 ADVANCE CuO target, Germany), based generator X-ray dif-

fractometer using CuK_α radiation. The working conditions of the diffractogram was recorded in a 2θ range from 5–70°. UV-Visible spectra were performed by using Agilent Cary 100 UV/VIS spectrophotometer.

2. 2. Methods

2. 2. 1. Steps of Preparing the Membrane

1) *Batching*: It is the process of weighing the clay according to the recipes and preparing them for mixing, weighing different powdered raw materials in different percentages to form the batch composition for different membranes. 2) *Milling*: It is the process by which the size of the clay turns from large particles to smaller ones. It is generally performed mechanically, including attrition. Milling may involve breaking up cemented material (individual particles retain their shape) or pulverization (grinding the particles themselves to a smaller size). 3) *Sieving*: It is a process by which un-milled materials are separated from fine powdered forms. 4) *Mixing*: This step takes place after batching and is performed with ribbon mixer. Kaolin powder was mixed with different percentages of expanded polystyrene (EPS). The amount of expanded polystyrene varied in the five samples in the range of (0, 2.5, 5, 10 & 20%) with respect to kaolin weight. The symbols referring to the prepared membranes are displayed in Table 1. 5) *Membrane preparation*: The main components used in producing the ceramic membranes are clay powder, or-

ganic polymer and water as solvent. Upon selecting the inorganic powder, important factors have to be considered. They are particle size and distribution, as well as the shape of the particles. They affect the porosity, pore size and pore size distribution of the final product. The five membranes were fabricated by means of using extruder. The membranes were prepared as cylinders with 10 mm diameter and 30 mm height.

Kaolin and expanded polystyrene were mixed properly to ensure homogenous distribution in the whole samples. Water was then added in a fixed amount to the samples. The produced membranes were dried at 110 °C to be ready for adsorption experiments. Figure 1 shows a scheme for the preparation steps of the membranes and evaluating them in adsorbing MB from water.

3. Results and Discussion

3. 1. Chemical Composition of Kaolin

From the chemical composition of kaolin material; alumina and silica are found to be the major constituents with other minor ones, while the percentage of manganese (II) oxide²⁸ could not be determined. The loss on ignition (LOI) corresponds to water vapor from hydroxide reaction in the kaolin minerals. Moreover, the burning out of organic matter beside the carbonate decomposition in CO_2 and oxide of the minerals is shown in Table 2.

3. 2. Effect of Polystyrene Content

Expanded polystyrene (EPS) acts as the pore maker in the prepared membranes and affects the physical properties of kaolin which was fired up to 1000 °C. The permeability of these membranes was originated from the burning of the introduced polymer upon preparation. This process forms various kinds of closed cavities like pores with flaky structure. The influence of EPS content is shown in Figure 2. The prepared samples contain various polysty-

Table 1. Composition of the starting materials for preparing the porous ceramic membranes.

Sample	Kaolin (wt. %)	Expanded Polystyrene (wt. %)
Blank	100	0.0
A	97.5	2.5
B	95	5
C	90	10
D	80	20

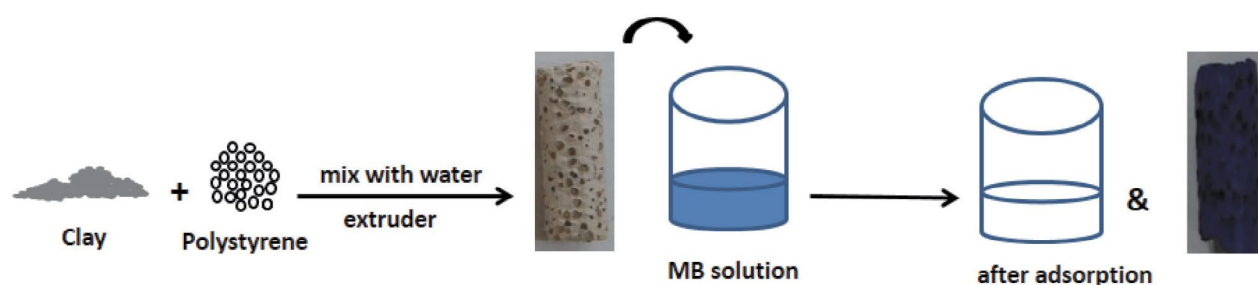


Figure 1. Schematic illustration for the ceramic membrane preparation and using it in adsorbing methylene blue.

Table 2. Chemical composition of Kaolin.

Kaolin components	SiO_2	Al_2O_3	TiO_2	Fe_2O_3	SO_3	MgO	CaO	P_2O_5	K_2O	Na_2O	LOI
Composition %	44.56	37.34	1.98	1.12	0.02	0.39	0.09	0.08	0.02	0.1	14.3

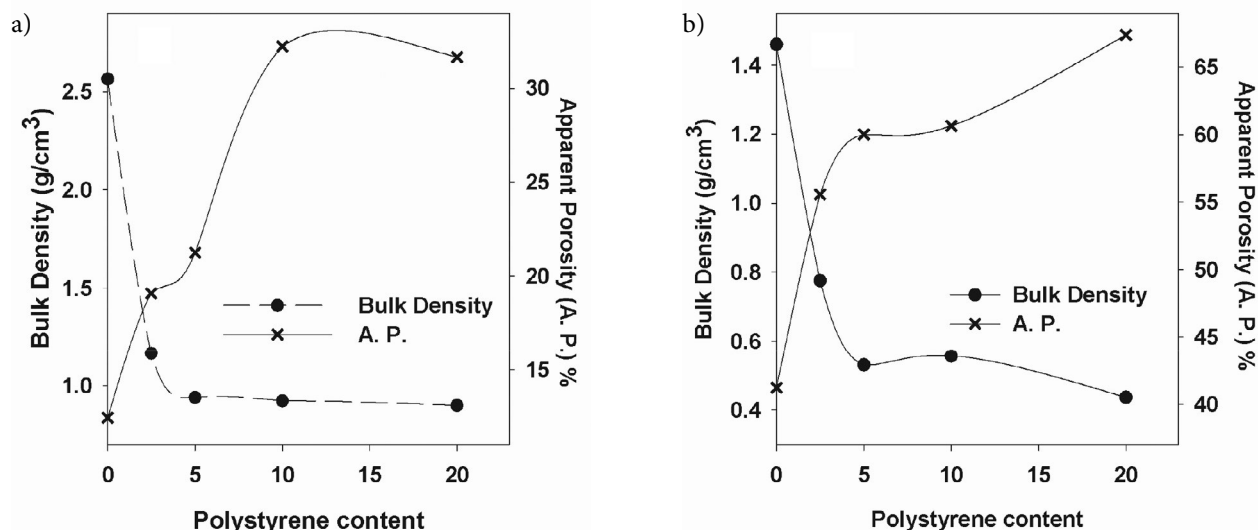


Figure 2. Bulk density and apparent porosity of the prepared membranes (a) before and (b) after MB adsorption.

rene ratios from 0 to 20% by weight. Known percentages of water were added to each of these mixes. The apparent porosity (A. P.) of the ceramic membranes increases proportionally as the polystyrene content in the burnt samples increases. The porosity may be correlated to the formed closed pores during firing the embedded polystyrene inside the clay matrix to produce voids. Meanwhile, the presences of this porosity reduces the bulk density of samples. Sample (D) with 20% polystyrene shows the optimum percentage for adding this polymer. At higher contents of polystyrene, the ceramic membrane tends to be fragile and

inconsistent. After adsorption, sample (D) is more likely to assist in increasing pore volume with decreasing the bulk density. This behavior may be changed due to penetration of the methylene blue dye in closed pores via osmotic pressure through capillary nanopores.

3. 3. UV-Vis Spectral Analysis

UV-Vis spectroscopy measurements were used to monitor the impact of ceramic membrane in adsorbing methylene blue and removing it from water. The ceramic

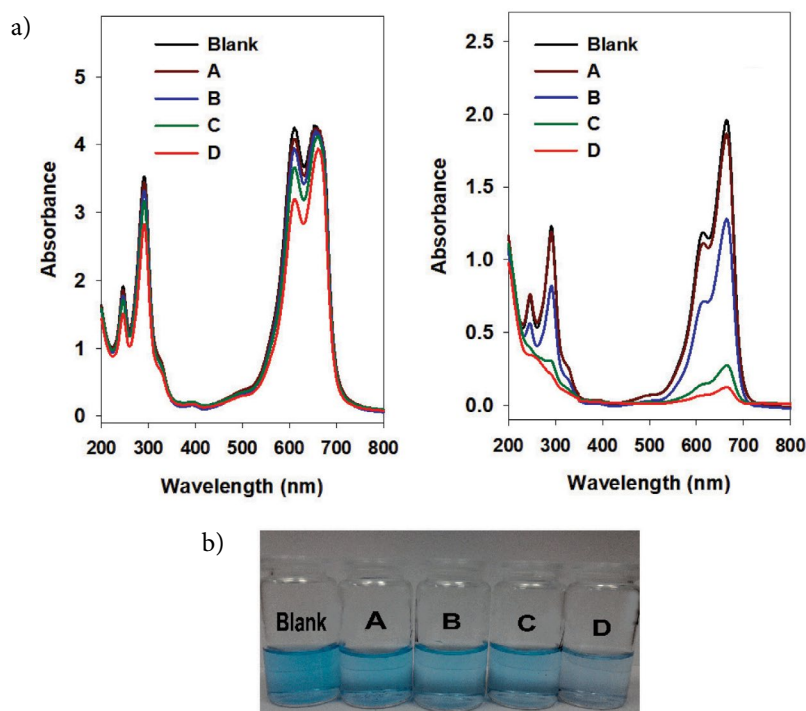


Figure 3. UV-Vis absorption spectra with photos for the collected eluents from the different membranes immersed in MB aqueous solutions resulting from adsorption reactions: a) after 60 min. and b) after 24 hours. An inset photograph for the eluents after 24 hours.

membranes with different pore contents resulting after firing and losing polystyrene; were soaked in aqueous solutions of methylene blue at 25 °C. UV-Vis spectra were recorded at different time intervals from starting the adsorption process. The first obvious change was enrolled after 60 minutes. In Figure 3a, the characteristic peaks of methylene blue appear at 607 and 660 nm. The intensity of the peaks decrease proportionally with increasing the pores amount in the ceramic membranes. This denotes to the increased surface. Upon elapsing the time, it is noticed that the UV-Vis peaks of MB decrease as shown in Figure 3b. After 24 hours, the samples were analyzed to see the changes with gradual fading in the blue color. The results illustrate that the characteristic peaks of MB decreased drastically. The collected eluents from the samples from the tested MB solutions are represented in an inset photograph in Figure 3. They show a gradual decrease in the blue tint of MB. For the membrane sample (D) with 20 % EPS, the membrane adsorbed MB, with almost clear sample of water. This points to the efficiency of the prepared ceramic membrane to remove methylene blue from water after 24 hours at 25 °C. No more samples were analyzed at extra time intervals attempting to detect the estimated time for dye adsorption at certain pore content in the membrane; i.e. to avoid passing or losing the end point as in titration experiments.

3. 4. Morphological Analysis and Spectral Changes Before and after MB Adsorption

SEM micrographs of the ceramic structure, before and after MB adsorption are shown in Figure 4 displaying the cross-sections of ceramic samples fired at 1000 °C. They elucidate an asymmetric morphology, with different size granules of approximately 1 μm (alumina, and silica) and smaller particles (clay) bounded with each other forming the primary vitrified skeletal structure of the alumina-silica with holes, pores or cavity like pores. This kind of ceramic granules have many grooves as well as closed pores on the surface extending to the core of the ceramic matrix.^{14,16} Macro-voids in Figures (4a and b) can be seen. These pores have an extended irregular form. The measure of pores in the ceramic samples are in the range of 1–1.7 mm. Rough surface for the membrane can be noticed before adsorption. After adsorbing methylene blue, the surface became smoother due to the accumulation of methylene blue on the ceramic top with covering some closed pores. The micrographs of Figures (4 c and d) represent higher magnification for the corresponding Figure (4 a and b) respectively. They reveal the heterogeneous nature of surface morphology of the fired kaolin sample. They clarify that crystals possess a foliation like morphology for kaolinite. The typical laminated and layered structure in

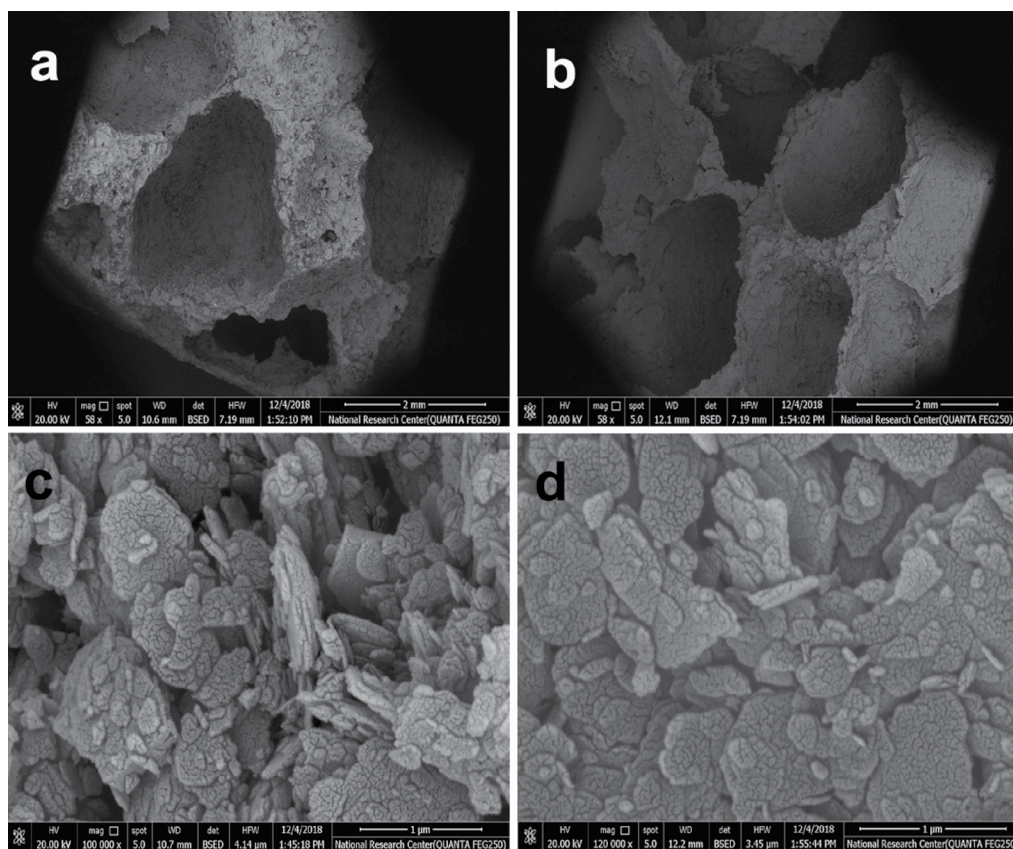


Figure 4. SEM of the ceramic membrane before and after MB adsorption.

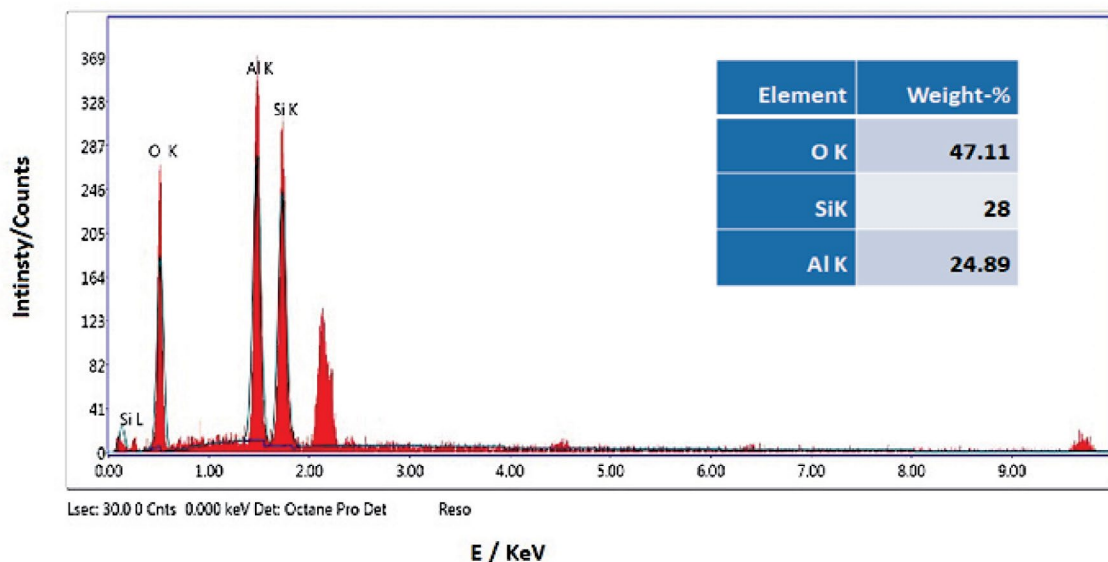


Figure 5. The EDX Microanalysis of mullite sample fired at 1000 °C.

the granules amplified the specific surface area of the ceramic membrane and favored pollutants adsorption into the inner positions of the ceramic body. The augmenting number of pores allows higher adsorption capacity for the dye onto the ceramic surface. The SEM analysis of the MB coated ceramics and uncoated confirmed the results of porosity and density. It can be noticed that expanded polystyrene content 20% in the membrane decreased the bulk density and increased the apparent porosity for sample (D) before and after MB adsorbing MB.

Figure 5 shows the EDX analysis of the ceramic matrix with mullite phase resulting from firing kaolin at 1000 °C. It confirms that mullite does not contain any foreign inclusions.²⁹ The tested sample shows the Al/Si ratio to be ≈ 0.84 as shown in Table 2. It is less than the stoichiometric composition of mullite (Al/Si 3:1).³⁰ However, the surplus silica content may exist as glass. The Al/Si weight ratio confirmed the ratio of the starting materials which was previously determined.

FTIR spectra of the fired samples before and after immersion in methylene blue are plotted in Figure 6. The main characteristic bands of the kaolinite are highlighted as follow, the bands at 3770 to 3714 cm^{-1} which represent the H-O-H stretching free hydroxyl. This result was confirmed by previous work³¹ where the bands at 3694 and 3619 cm^{-1} show (OH stretching vibrations). The membrane sample (before adsorption) shows a broad but weak absorption band in the range 3419–3471 cm^{-1} . The band at 3419 cm^{-1} along with weak band around 1619 and 1637 cm^{-1} are attributed to the stretching vibrations of the free hydroxyl group these may due to moisture accompanied with the sample.¹⁹ FTIR spectra of the two samples show characteristic bands pointing to the formation of metakaolin. A sharp band at 1101 cm^{-1} is attributed to overlap of the double bond at 883 cm^{-1} and 840 cm^{-1} that characterizes Al-O and O-Al-O stretching vibration or correspond-

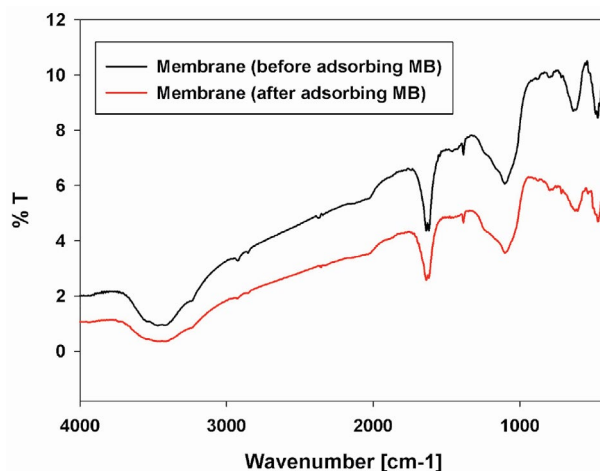


Figure 6. FTIR of a) fired kaolin at 1000 °C before adsorption and b) covered with methylene blue after adsorption.

ing to Si-O-Al bonds. A sharp band with lower intensity is observed at $\sim 412 \text{ cm}^{-1}$ that characterizes Si-O bond. Moreover, sharp bands at $\sim 582 \text{ cm}^{-1}$, 794, 781 and 643 cm^{-1} point to Al-O tetrahedral and Al-O octahedral bonds respectively.³²

The XRD patterns for the membranes before and after MB adsorption are shown in Figure 7. The main peaks for the clay appear at $2\theta = 20.89^\circ$ and 26.65° as displayed in Figure 7a. They are characteristic bands for quartz SiO_2 which is a silica polymorph. It consists of interconnected SiO_2 tetrahedral that build up a rigid three-dimensional network. Two peaks appear at $2\theta = 27.5$ and 60.04° . They may refer to kaolinite clay mineral (Microcline KAlSi_3O_8). The patterns in Figure 7b for the sample loaded with MB showed slight increase in the intensities at $2\theta = 20.6$, 25.8 . However, a new peak appears at $2\theta = 37.22$. It can be referred to the adsorption of MB onto the clay particles. It was concluded that during the adsorption process of MB

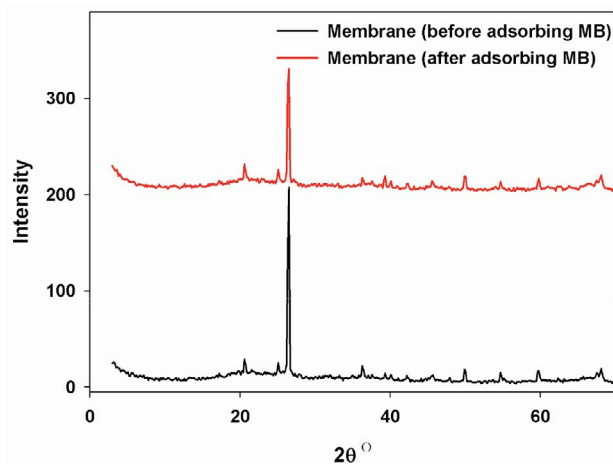


Fig. 7. XRD patterns of the ceramic membrane before and after MB adsorption.

within the clay minerals, MB ions replace alkaline earth cations. This is able to alter the peak intensity of other peaks. MB molecules were adsorbed on the basal spacing of the minerals in aqueous conditions. The d-spacing is too large to be recorded by the diffractometer. It did not show quantified basal reflections of some minerals.⁶

3. 5. Regenerating the Ceramic Membrane

From the previous results, the ceramic membrane loaded with 20% expanded polystyrene; sample (D) showed to be optimum in adsorbing methylene blue from water. Figure 8 illustrates the UV-Vis spectra for the aqueous solution of MB before and after being adsorption onto the surface of ceramic membrane related to sample (D). In addition, it shows the regeneration of the same membrane for 2 cycles. The regeneration cycles took place by immersing the dried membrane after MB adsorption (in the first run) for extra 24 hours to give the eluent (D-R1). This step was followed by drying the membrane then repeating a new cycle for 24 hours to produce (D-R2) eluent. The inset photos show the vials of membrane D in MB solution after 120 minutes from starting the adsorption process in addition to the resulting eluents after 24 hours and the regeneration cycles (D-R1) and (D-R2). The characteristic peaks of MB show a high energy peak at (π - π^* transition) in benzene. Moreover, there is a peak at low energy corresponding to (n - π^* transitions) in N atom of C=N bond and S atom on S=C bond.³³ This peak is located at 660 nm. It may shift according to the change in the pH of the solution. Adsorbing MB on the ceramic surface led to bounding MB to the surface. Hence, MB vanished from the solution and these peaks did not appear. After the first regeneration cycle, it is noticed that the efficiency of the membrane did not lose its capability of adsorbing MB by providing a spectrum with slightly higher MB content than the first cycle of sample (D). However, the absorption capacity of D decreased drastically in the second cycle of re-

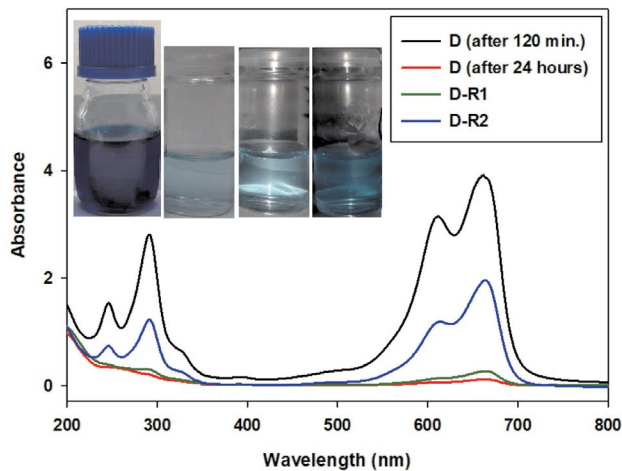


Figure 8. UV-Vis absorption spectra with inset photos for the collected eluents from D membrane immersed in MB aqueous solutions resulting from adsorption reactions after 120 min., 24 hours and regeneration cycles R1 and R2.

generation (D-R2). The eluent showed gradual increase in the blue color after regeneration cycles. This can be correlated to the growing saturation of the free sites in the surface of membrane that started to retard its efficiency towards further adsorption of methylene blue.

4. Conclusions

Ceramic membranes based on kaolin and expanded polystyrene have been prepared in different ratios. These membranes have been employed in removing methylene blue dye from water via adsorption. These membranes were fired at 1000 °C to degrade polystyrene leaving cavities in the clay matrix with an expanded surface area and porous structure. The morphological structure of the membranes have been developed to show the resulting changes onto the surface of the ceramic membranes after adsorbing methylene blue. The adsorption process has been tracked by an easy method which is UV-Vis spectroscopy to follow up the adsorption capacity of the prepared membranes away from adsorption isotherms and kinetic investigations. From the results, the membrane loaded with 20% polystyrene by weight; namely sample (D) membrane showed the optimum performance in adsorbing methylene blue from water. Regenerating this membrane showed a continuous adsorption capacity for the membrane that decrease due to filling the free sites of the membrane surface after using it more than once in adsorption.

5. Acknowledgements

The authors acknowledge the National Research Centre (NRC-Egypt) for funding this work. The authors

also appreciate the helpful input from Dr. Hossam El-Nazer (NRC) for his assistance in performing the UV-Vis experiments.

6. References

1. Y. He, H. Zhang, J. Li, Y. Zhang, B. Lai, Z. Pan, *Environ. Eng. Sci.*, **2018**, 35(5), 501–511. DOI:10.1089/ees.2017.0188
2. G. Crini, E. Lichtfouse, *Environ. Chem. Lett.*, **2019**, 17(1), 145–55. DOI:10.1007/s10311-018-0785-9
3. S. Shanmuganathan, P. Loganathan, C. Kazner, M. A. H. Johir, S. Vigneswaran, *Desalination*, **2017**, 401, 134–141. DOI:10.1016/j.desal.2016.07.048
4. S. Khamparia, D. K. Jaspal, *Front. Environ. Sci. Eng.*, **2017**, 11(1), 8. DOI:10.1007/s11783-017-0899-5
5. S. Afroze, T. K. Sen, M. Ang, H. Nishioka, *Desalin. Water Treat.*, **2016**, 57(13), 5858–5878. DOI:10.1080/19443994.2015.1004115
6. P. T. Hang, G. W. Brindley, *Clays Clay Miner.*, **1970**, 18(4), 203–212. DOI:10.1346/CCMN.1970.0180404
7. A. Rineh, N. K. Dolla, A. R. Ball, M. Magana, J. B. Bremner, M. R. Hamblin, G. P. Tegos, M. J. Kelso, *ACS Infect. Dis.*, **2017**, 3(10), 756–766. DOI:10.1021/acinfed.7b00095
8. O. Duman, S. Tunc, T. G. Polat, B. K. Bozoglan, *Carbohydr. Polym.*, **2016**, 47, 79–88. DOI:10.1016/j.carbpol.2016.03.099
9. S. Wang, L. Li, H. Wu, Z. H. Zhu, *J. Colloid Interface Sci.*, **2005**, 292(2), 336–343. DOI:10.1016/j.jcis.2005.06.014
10. A. M. Khalil, H. A. Hamed El-Nazer, M. M. Badr, A. A. Nada, *J. Vinyl Addit. Technol.*, **2010**, 16(4), 272–276. DOI:10.1002/vnl.20242
11. D. Zhang, F. Zeng, *J. Mater. Sci.*, **2012**, 47(5), 2155–2161. DOI:10.1007/s10853-011-6016-4
12. T. Xu, F. Zheng, Z. Chen, Y. Ding, Z. Liang, Y. Liu, Z. Zhengtao, H. Fong, *Chem. Eng. J.*, **2019**, 360, 280–288. DOI:10.1016/j.cej.2018.11.233
13. M. Karbarz, A. M. Khalil, K. Wolowicz, K. Kaniewska, J. Romanski, Z. Stojek, *J. Environ. Chem. Eng.*, **2018**, 6(4), 3962–3970. DOI:10.1016/j.jece.2018.05.054
14. C. S. C. Chiew, H. K. Yeoh, P. Pasbakhsh, K. Krishnaiah, P. E. Poh, B. T. Tey, E. S. Chan, *Appl. Clay Sci.*, **2016**, 119, 301–310. DOI:10.1016/j.clay.2015.10.032
15. S. K. Hubadillah, M. H. D. Othman, Z. Harun, A. F. Ismail, Y. Iwamoto, S. Honda, M. A. Rahman, J. Jaafar, P. Gani, M. N. M. Sokri, *Ceram. Int.* **2016**, 42(14), 15547–15558. DOI:10.1016/j.ceramint.2016.07.002
16. S. K. Hubadillah, M. H. D. Othman, Z. Harun, A. F. Ismail, M. A. Rahman, J. Jaafar, S. M. Jamil, N. H. Mohtor, *Mater. Lett.* **2017**, 191, 119–122. DOI:10.1016/j.matlet.2016.12.099
17. S. K. Hubadillah, M. H. D. Othman, T. Matsuura, A. F. Ismail, M. A. Rahman, Z. Harun, J. Jaafar, M. Nomura, *Ceram. Int.* **2018**, 44, 4538–4560. DOI:10.1016/j.ceramint.2017.12.215
18. S. K. Hubadillah, M. H. D. Othman, A. F. Ismail, M. A. Rahman, J. Jaafar, *Sep. Purif. Technol.* **2019**, 214, 31–39. DOI:10.1016/j.seppur.2018.04.025
19. Y. Snoussi, A. M. Khalil, B. Strzemiescka, A. Voelkel, M. M. Chehimi, Chapter 11- Surface Analysis of Clay-Polymer Nanocomposites. *Clay-Polymer Nanocomposites*, **2017**, 363–411. Elsevier. DOI:10.1016/B978-0-323-46153-5.00011-2
20. R. Das, K. Sondhi, S. Majumdar, S. Sarkar, *J. Asian Ceram. Soc.* **2016**, 4, 243–251. DOI:10.1016/j.jasc.2016.04.004
21. K. F. El-Nemr, A. M. Khalil, E. S. Fathy, *Int. J. Polym. Anal. Charact.* **2018**, 23(1), 58–69. DOI:10.1080/1023666X.2017.1387447
22. R. V. Sekharan, B. T. Abraham, E. T. Thachil, *Mater. Des.* **2012**, 40, 221–228. DOI:10.1016/j.matdes.2012.03.042
23. M. Lanzon, V. Cnudde, T. De Kock, J. Dewanckele, *Constr. Build. Mater.* **2015**, 94, 817–825. DOI:10.1016/j.conbuildmat.2015.07.086
24. C., Shin, G. G. Chase, D. H. Reneker, *Colloids Surf. A: Physicochem. Eng. Aspects* **2005**, 262, 211–215. DOI:10.1016/j.colsurfa.2005.04.034
25. T. Do, Y. G. Ko, Y. Chun, Y. K. Shin, Y. G. Kim, U. S. Choi, *Polym. Eng. Sci.* **2017**, 57(8), 883–890. DOI:10.1002/pen.24465
26. A. Kaya, F. Kar, *Constr. Build. Mater.* **2016**, 105, 572–578. DOI:10.1016/j.conbuildmat.2015.12.177
27. Y. Xi, J. Li, Z. Lu, J. Jiang, Y. Niu, *Constr. Build. Mater.* **2019**, 195, 505–514. DOI:10.1016/j.conbuildmat.2018.11.091
28. F. Uddin, *Metall. Mater. Trans. A* **2008**, 39(12), 2804–2814. DOI:10.1007/s11661-008-9603-5
29. M. Sardy, A. Arib, K. El Abbassi, M. Gomina, (2012). *New J. Glass Ceram.* **2012**, 2(03), 121–125. DOI:10.4236/njgc.2012.23017
30. S. H. Kenawy, M. Hassan, R. I. Abou-Zeid, G. T. El-Bassouini, *Interceram* **2017**, 66(3–4), 111–116. DOI:10.1007/BF03401207
31. N. Caponia, G. C. Collazzo, S. L. Jahna, G. L. Dotto, M. A. Mazuttia, E. L. Foletto, *Mater. Res. (Sao Carlos, Braz.)* **2017**, 20, suppl.2, 14–22. DOI:10.1590/1980-5373-mr-2016-0673
32. N. M. Khalil, S. H. Kenawy, *Am. Ceram. Soc. Bull.* **2009**, 87(7), 9201–9207.
33. S. Selvam, S., I. Sarkar, *J. Pharm. Anal.* **2017**, 7(1), 71–75. DOI:10.1016/j.jpha.2016.07.006

Povzetek

Onesnaževanje voda predstavlja resen okoljski problem. Med različnimi barvili, ki jih lahko najdemo v onesnaženih vodah, je tudi barvilo metilensko modro. Adsorpcija predstavlja možen učinkovit način njegovega odstranjevanja. S tem ciljem smo pripravili hibridne membrane na osnovi sljude in polimera, bolj natančno kaolina in polistirena. Membrane so bile žgane na 1000 °C, kar povzročilo razgradnjo polimera in ustvarilo praznine v nosilcu iz sljude in povečalo specifično površino ter poroznost. Membrane smo okarakterizirali z rentgensko difrakcijo in infrardečo spektroskopijo, njihovo morfologijo pa z vrstično elektronsko mikroskopijo. Proces adsorpcije smo zasledovali UV-Vis spektroskopijo. Maksimalno adsorpcijo smo dosegli z membrano pripravljeno z 20 % utežnim deležem polistirena.



Except when otherwise noted, articles in this journal are published under the terms and conditions of the Creative Commons Attribution 4.0 International License

Scientific paper

Preconcentration of Lutetium from Aqueous Solution by Transcarpathian Clinoptilolite

Emilia Stechynska,^{1,*} Volodymyr Vasylechko,^{1,2} Galyna Gryshchouk¹ and Ihor Patsay¹

¹ Department of Analytical Chemistry, Ivan Franko National University of Lviv, Kyryla and Mefodiya Str., 6, 79005 Lviv, Ukraine;

² Department of Natural Sciences and Environment Protection, Lviv University of Trade and Economics, Samchuka Str., 9, 79011 Lviv, Ukraine

* Corresponding author: E-mail: milliast10@gmail.com

Received: 05-02-2019

Abstract

Sorptive properties of Transcarpathian clinoptilolite towards trace amounts of Lu(III) were studied under dynamic conditions. It is shown that this lanthanide is sorbed from the weakly alkaline solution (pH 10) most efficiently. The sorption capacity of clinoptilolite under the optimal conditions is equal to 9.37 mg g⁻¹. The distribution of various species of Lu(III) in aqueous solutions at various total concentration of the lanthanide in the pH range from 4 to 13 was calculated. The best desorbent of Lu(III) is the 1 mol L⁻¹ solution of NaCl, preacidified with the solution of HCl to a value of pH 4.0. This desorbent enables 95–100% of Lu(III) removal. The method of Lu(III) trace amounts preconcentration from aqueous samples in a solid phase extraction mode with the further determination of this rare earth element via the spectrophotometric method using arsenazo III was developed. The linearity of the proposed method was observed in the range of 1–12 ng mL⁻¹ with the detection limit of 0.4 ng mL⁻¹.

Keywords: Sorption; lutetium; clinoptilolite; solid phase extraction; dynamic conditions.

1. Introduction

Nowadays lanthanides (Ln) are widely used in many innovative industrial processes: for the preparation of constant magnets, catalysts, powerful lasers, magnetic alloys, and also in machine engineering, radioelectronics, chemical industry, nuclear power, cosmetology, and medicine.^{1–6} That is why the wastes of these metals cause a danger of natural waters contamination, which can lead to a potential risk for the whole environment.

Unlike many other heavy metals, Ln are not considered the priority environmental contaminants. However, it is known that they cause negative consequences for the human health.⁷ That is why the determination of Ln in natural waters is important not only from the point of view of analytical chemistry, but also geochemistry, oceanography, and natural science.^{8–12}

Ln are present in natural objects in small quantities, so often the preliminary treatment of samples is applied for their determination, which in particular includes preconcentration, separation, and exclusion.^{13–16}

The sufficient number of highly sensitive and selective methods of analysis for the detection and quantitative determination of Ln is not available. Among the available methods the sorption should be highlighted due to its simplicity, high efficiency, and low cost. But in the last years the solid phase extraction method with the application of different sorbents has been widely used. This method is in demand even during the sample analysis with such selective and highly sensitive methods as atomic absorption and inductively coupled plasma.¹⁷

There are papers in which the sorption capacity of various nanomaterials (namely metallic, metallic and mixed oxide, magnetic, carbonaceous, silicon, and polymer-based nanomaterials) as efficient sorbents for the preparation of samples before the bioanalysis was investigated,¹⁸ as well as the hybrid nanoadsorbents based on SiO₂ and highly stable nanoparticles γ -Fe₂O₃-SiO₂, that do not behave as adsorptive materials, but function as crystallization nuclei for rare earth elements (REEs) in the form of hydroxides.¹⁹

Authors²⁰ presented the results of Lu(III) accumulation by the Gram-negative bacteria, and in paper²¹ the adsorption of REE with the application of biosorbents was studied.

Natural zeolites are the perspective sorbents for the preconcentration of heavy metals.^{22–28} They are the oxide nanomaterials with the ordered structure,^{29–30} which can sorb trace quantities of substances, possess high sorption capacity and selectivity and are resistant to aggressive media.

The goal of this work is to study the sorptive properties of Transcarpathian clinoptilolite towards trace amounts of lutetium in aqueous solutions and to investigate the possibility of this natural sorbent application in a solid phase extraction method.

2. Materials and Methods

The clinoptilolite from the deposit in the village of Sokyrnytsia in Ukrainian Transcarpathia that contains 85–90 % (mass fraction) of the main component was used for the analysis. Its specific surface area, determined by water sorption, is equal to $59 \text{ m}^2 \text{ g}^{-1}$.³¹ The clinoptilolite formula in the oxide form (mass fraction) is as follows: $\text{SiO}_2 - 67.29\%$; $\text{Al}_2\text{O}_3 - 12.32\%$; $\text{TiO}_2 - 0.26\%$; $\text{Fe}_2\text{O}_3 - 1.26\%$; $\text{FeO} - 0.25\%$; $\text{MgO} - 0.99\%$; $\text{CaO} - 3.01\%$; $\text{Na}_2\text{O} - 0.66\%$; $\text{K}_2\text{O} - 2.76\%$; $\text{H}_2\text{O} - 10.90\%$.³² According to literature³³, the pattern of natural Transcarpathian clinoptilolite samples was indexed in a monoclinic lattice (space group $C2/m$) with the lattice parameters $a=17.64 \text{ \AA}$, $b=17.90 \text{ \AA}$, $c=7.40 \text{ \AA}$, $\beta=116.5^\circ$. Clinoptilolite samples are characterized with rather broad distribution of pores size with the radii values in the range of 1–18 nm with the clearly expressed maximum in the 2.2–2.4 nm range. The energy distribution function of water thermodesorption from the Transcarpathian clinoptilolite surface is described by an asymmetric curve with the maximum near 35 kJ mol^{-1} .³⁴ The difference between the numeric values of sorption characteristics of specific clinoptilolite samples taken from the same batch of sorbent was between 2–3%. If the zeolite samples were used from different batches, then the results of sorption investigations differed less than by 5%. During the implementation of the experimental part of this article the zeolite samples from the same batch were applied.

All reagents were of analytical grade. Standard aqueous solutions of lutetium nitrate (concentration was 1.0 mg mL^{-1}) were prepared by dissolving the metallic lutetium (99.9% purity) in nitric acid (1:1). The working solutions of Lu(III) were prepared by the dilution of the standard solution. The 0.05 % solution of Sulfarsazene was prepared using 0.05 mol L^{-1} aqueous solution of $\text{Na}_2\text{B}_4\text{O}_7$, all other reagent solutions – using bidistillate.

The sorption properties of clinoptilolite towards Lu(III) were studied with the dynamic method in a solid phase extraction mode. The solution of Lu(III) salt was

passed through a cartridge for preconcentration filled with the sorbent using the peristaltic pump at a flow rate of 5 mL min^{-1} . The clinoptilolite with a grain size of 0.20–0.31 mm was used. The investigation techniques under dynamic conditions are described in detail in paper.³⁵ The passage point of lutetium(III) was registered spectrophotometrically using the reaction that leads to a formation of orange complex of lutetium(III) with Sulfarsazene. Sulfarsazene changes its color from yellow to orange starting from the lutetium(III) concentration of 100 ng mL^{-1} . This gave the opportunity to determine the passage moment of Lu(III) using the DR/4000V (HACH) spectrophotometer at 540 nm.

The desorption of Lu(III) preconcentrated on clinoptilolite was carried out by passing 10 mL of a desorbent solution through the preconcentration cartridge with a flow rate of 0.5 mL min^{-1} . The eluate was collected in a 10 mL volumetric flask. As preacidified solutions of alkali metals are the efficient desorbents of Lu(III) from clinoptilolite, then the solutions obtained after the desorption of Lu(III) contain much higher concentration of metals that are constituents of the sorbent than the matrix solutions obtained after Lu(III) sorption on clinoptilolite. That is why the selectivity of Lu(III) spectrophotometric determination with Sulfarsazene proved to be not enough during the analysis of eluates obtained after the desorption of Lu(III). So, in order to determine the content of desorbed Lu(III) in a solution, the spectrophotometric technique based on arsenazo III was applied that despite being less sensitive is much more selective than the technique with the application of Sulfarsazene. In order to eliminate the interfering influence of metal ions that are washed from the zeolite by the desorbent, the Rochelle salt ($\text{C}_4\text{H}_4\text{O}_6\text{KNa} \times 4\text{H}_2\text{O}$), ascorbic acid, and sulfosalicylic acid were additionally added to the system. The solutions absorbance was measured at $\lambda = 650 \text{ nm}$ on the DR/4000 V (HACH) spectrophotometer.

2. 1. Method of Lu(III) Spectrophotometric Determination with Arsenazo III

2 mL of just-prepared 1% solution of ascorbic acid were added to 10 mL of the investigated solution ($\text{pH} \sim 1$). After 2 min 4 mL of 5 % sulfosalicylic acid solution, 1 mL of 0.05 mol L^{-1} EDTA solution, 2 mL of 5% potassium-sodium tartrate solution, 1 mL of the formic buffer solution with $\text{pH} 3.5$, 4 mL of 0.05% arsenazo III solution were mixed and the pH value was adjusted to 2.6 ± 0.1 , then transferred to a 25.0 mL volumetric flask, mixed and the absorbance of the colored solution was measured at $\lambda = 650 \text{ nm}$. As a blank the solution was used that contains all components except Lu(III) (the solution of „idle” experiment).

In order to build the calibration graph a certain amount of Lu(III) standard solution was poured instead of the investigated solution considering that concentrations

of Lu(III) in final solutions are equal to 0.1; 0.2; 0.4; 0.6; 0.8; 1.0; 2.0 $\mu\text{g mL}^{-1}$.

The sorption and desorption studies were conducted at a temperature of $20 \pm 1^\circ\text{C}$. Sorbent for the preconcentration cartridge was prepared as follows: the natural Transcarpathian clinoptilolite was grained in a ball-mill; a zeolite fraction with a grain size of 0.20–0.30 mm was taken, washed with distilled water and dried at room temperature to air-dry condition. To prepare the preconcentration cartridge the amount of the prepared sorbent of 0.6 g was used. Clinoptilolite samples were calcinated at the respective temperature for 2.5 h in a drying oven WSU 200 (Germany) and muffle furnace SNOL 7.2/1100 (Lithuania). The sorbent was cooled in a desiccator.

3. Results and Discussion

The sorption of Lu(III) on clinoptilolite depending on the solution acidity was studied (Fig. 1). The necessary pH values of lutetium salt solutions were adjusted by adding the diluted solutions of NaOH or HNO_3 . The results obtained prove that Lu(III) is sorbed most efficiently from the weakly alkaline solutions. On the curve showing this dependence a clear maximum at pH 10.0 is observed.

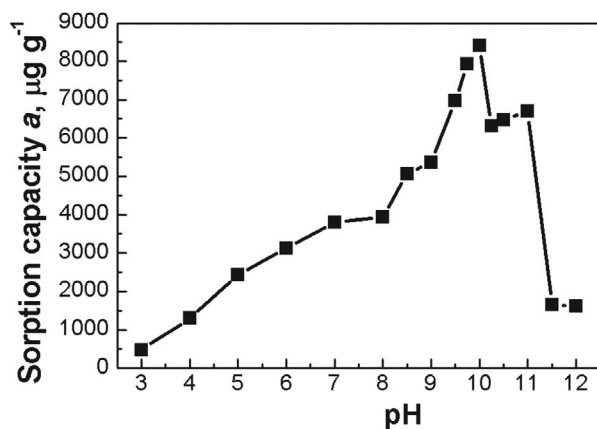


Fig 1. Dependence of sorption capacity of clinoptilolite towards Lu^{3+} ions on the pH value of the aqueous solution under dynamic conditions. $C(\text{Lu}^{3+}) = 1.0 \mu\text{g mL}^{-1}$.

It was established that the sorption capacity of Transcarpathian clinoptilolite depends on the concentration of Lu(III) in the solution (Table 1). Probably, different sorptive capability of the zeolite towards low and high concentrations of Lu(III) is due to the different ability to form hydroxo-complexes at low and high concentrations.

It is known^{26,31,33} that mainly the surface OH-groups of Transcarpathian clinoptilolite are the sorption-active centers towards heavy metal ions. In our opinion, such mode of Lu(III) sorption process is caused by the chemical peculiarities of clinoptilolite surface and by existing forms

Table 1. Dependence of the sorption capacity of clinoptilolite towards Lu(III) on the concentration (clinoptilolite thermally activated at 50°C ; time of heat treatment – 2.5 h; pH of Lu(III) solutions = 10.0)

Concentration of Lu(III), $\mu\text{g mL}^{-1}$	Sorption capacity of clinoptilolite towards Lu(III), $\mu\text{g g}^{-1}$
0.25	6395
0.5	6545
1.0	9365
2.0	6915
5.0	2750
10.0	1400

of Lu(III) in aqueous solutions at different pH. The dissociation of surface hydroxo-groups of the sorbent that first of all are responsible for heavy metals sorption from solutions, is almost completely inhibited at low pH values, which is the reason for the small value of clinoptilolite sorption capacity towards Lu(III). It is known that anionic forms are not sorbed on the zeolite, that is why the sorption capacity of clinoptilolite at high pH values is low. At the same time, on increasing pH from 3.0 to 10.0 the dissociation of surface OH-groups enhances and at the same time the sorption value increases and Lu(III) species in the solution changes too.

Nowadays the hydrolysis of Lu(III) is studied poorly. We have calculated the distribution of Lu(III) in aqueous solutions in the pH range from 4 to 13 at different total concentrations of the metal ion (Fig. 2, 3; Tables 2, 3).

The system of equations that describes equilibria of Lu(III) hydrolysis is the following:

$$K_{11} = \frac{[\text{LuOH}^{2+}][\text{Lu}^{3+}]}{[\text{Lu}^{3+}]}, \quad (1)$$

$$K_{12} = \frac{[\text{Lu}(\text{OH})_2^+][\text{H}^+]^2}{[\text{Lu}^{3+}]}, \quad (2)$$

$$K_{14} = \frac{[\text{Lu}(\text{OH})_4^-][\text{H}^+]^4}{[\text{Lu}^{3+}]}, \quad (3)$$

$$K_{15} = \frac{[\text{Lu}(\text{OH})_5^{2-}][\text{H}^+]^5}{[\text{Lu}^{3+}]}, \quad (4)$$

$$K_{16} = \frac{[\text{Lu}(\text{OH})_6^{3-}][\text{H}^+]^6}{[\text{Lu}^{3+}]}, \quad (5)$$

$$C_M = [\text{Lu}^{3+}] + [\text{LuOH}^{2+}] + [\text{Lu}(\text{OH})_2^+] + [\text{Lu}(\text{OH})_4^-] + [\text{Lu}(\text{OH})_5^{2-}] + [\text{Lu}(\text{OH})_6^{3-}] + [\text{Lu}(\text{OH})_3], \quad (6)$$

$$K_s \geq [\text{Lu}^{3+}][\text{OH}^-]^3 \quad (7)$$

During the calculations it was assumed that total neutral hydroxide $\text{Lu}(\text{OH})_3$ (if it is actually formed) exists in a solution and the formation of a solid phase is not observed.

As it was not clear if the formation of $\text{Lu}(\text{OH})_3$ takes place or not (is the K_s condition fulfilled), then the solution of equations system was carried out in two stages.

At first it was assumed that the condition of $\text{Lu}(\text{OH})_3$ formation is not fulfilled, so the equilibrium state was calculated assuming that $[\text{Lu}(\text{OH})_3] = 0$. At this stage the equilibrium concentration of Lu^{3+} form were found for each pH value. Then the condition of the neutral hydroxide formation ($[\text{Lu}^{3+}] \cdot [\text{OH}^-]^3 \geq K_s$) was checked for each pH value. If the condition was fulfilled, the solution of equations system was carried out taking into consideration the expression for K_s and the equilibrium concentration of $\text{Lu}(\text{OH})_3$ was also determined. The averaged values of constants found at low ionic strength of the solution were used for this purpose.^{36–40}

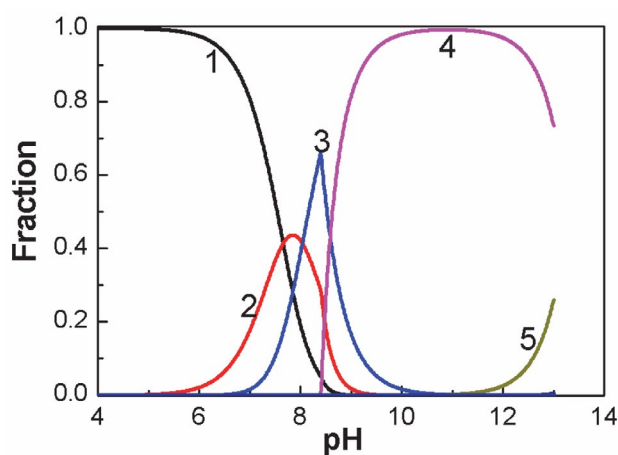


Fig 2. Dependence of the Lu(III) species fraction on pH, concentration of Lu(III) is $1.43 \cdot 10^{-6} \text{ mol L}^{-1}$: 1 – Lu^{3+} , 2 – LuOH^{2+} , 3 – $\text{Lu}(\text{OH})_2^+$, 4 – $\text{Lu}(\text{OH})_3$, 5 – $\text{Lu}(\text{OH})_4^-$

Table 2. Dependence of the Lu(III) species fraction on pH, concentration of Lu(III) is $1.43 \cdot 10^{-6} \text{ mol L}^{-1}$

Fraction	pH ranges*	pH _{max}	W _{max} %
Lu^{3+}	... – 8.64	<4.66	100
LuOH^{2+}	5.30 – 9.31	7.85	43.6
$\text{Lu}(\text{OH})_2^+$	6.79 – 10.40	8.40	66.0
$\text{Lu}(\text{OH})_3$	8.41 – ...	10.25–11.56 (>99 %)	99.6
$\text{Lu}(\text{OH})_4^-$	11.00 – ...	13.0	25.9
$\text{Lu}(\text{OH})_5^{2-}$	12.00 – ...	13.0	0.554
$\text{Lu}(\text{OH})_6^{3-}$	12.34 – ...	13.0	$1.03 \cdot 10^{-2}$

* – extreme pH values correspond to 1% of species maximum

Summarizing the obtained results regarding the formation and distribution of Lu(III) forms, the following conclusions can be made:

1. The pH range where the neutral form $\text{Lu}(\text{OH})_3$ dominates depends significantly on the total concentration of a metal – the higher it is the wider are the limits of its occurrence (Fig. 4).

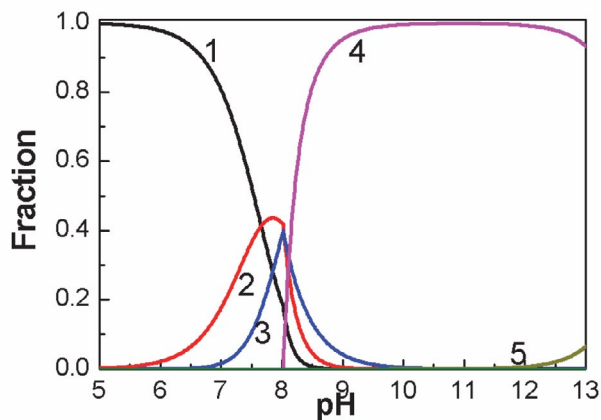


Fig 3. Dependence of the Lu(III) species fraction on pH; concentration of Lu(III) is $5.71 \cdot 10^{-6} \text{ mol L}^{-1}$: 1 – Lu^{3+} , 2 – LuOH^{2+} , 3 – $\text{Lu}(\text{OH})_2^+$, 4 – $\text{Lu}(\text{OH})_3$, 5 – $\text{Lu}(\text{OH})_4^-$

Table 3. Dependence of the Lu(III) species fraction on pH; concentration of Lu(III) is $5.71 \cdot 10^{-6} \text{ mol L}^{-1}$

Fraction	pH *	pH _{max}	W _{max} %
Lu^{3+}	... – 8.44	<4,66	100
LuOH^{2+}	5.30 – 9.01	7.85	43.6
$\text{Lu}(\text{OH})_2^+$	6.67 – 10.02	8.02	39.9
$\text{Lu}(\text{OH})_3$	8.03 – ...	9.64–12.18 (>99 %)	99.9
$\text{Lu}(\text{OH})_4^-$	11.00 – ...	13.0	6.49
$\text{Lu}(\text{OH})_5^{2-}$	12.00 – ...	13.0	0.139
$\text{Lu}(\text{OH})_6^{3-}$	12.34 – ...	13.0	$2.59 \cdot 10^{-3}$

* – extreme pH values correspond to 1% of species maximum

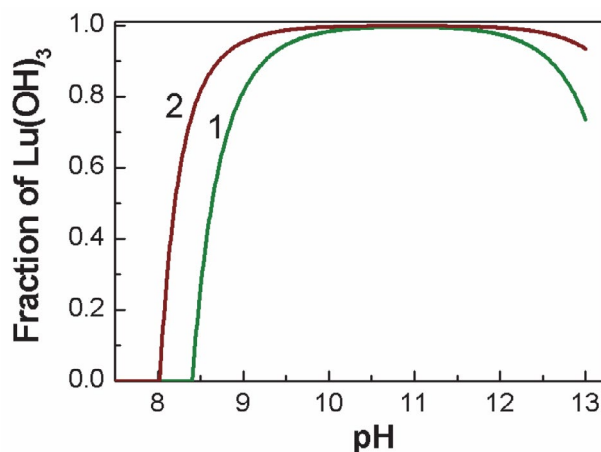


Fig 4. Dependence of the fraction of $\text{Lu}(\text{OH})_3$ on pH, 1 – $C_M = 1.43 \cdot 10^{-6} \text{ mol L}^{-1}$, pH > 8.41; 2 – $C_M = 5.71 \cdot 10^{-6} \text{ M}$, pH > 8.03

2. Among the anionic forms only the species $\text{Lu}(\text{OH})_4^-$ is formed. The contribution of other ions into the pH-distribution of the metal ($\text{Lu}(\text{OH})_5^{2-}$, $\text{Lu}(\text{OH})_6^{3-}$) is negligible.

3. Till pH 4.66 metal remains in the form Lu^{3+} . Then its fraction decreases drastically and after pH 8.44–8.64 (depending on C_M) this form disappears.

4. pH-dependencies of other cationic forms (LuOH^{2+} , $\text{Lu}(\text{OH})_2^+$) have a shape with a pronounced peak. pH ranges of this species are narrower in comparison with the others. pH values that correspond to the maxima of these species are close.

Under the optimal sorption conditions (pH 10.0) trace amounts of Lu(III) usually exist in the soluble hydrolyzed form $\text{Lu}(\text{OH})_3$ (Fig. 2, 3). So, the sorption of Lu(III) on Transcarpathian clinoptilolite takes place under such conditions through the adsorption of the soluble neutral Lu(III) hydroxide on the aluminosilicate surface. Under the optimal conditions of sorption (pH 10.0) trace amounts of Lu(III) mainly exist in the hydrolyzed form $\text{Lu}(\text{OH})_3$ (Fig. 2, 3; Tables 2, 3). So, the sorption of Lu(III) on Transcarpathian clinoptilolite under such conditions mainly takes place through the adsorption of the soluble neutral Lu(III) hydroxide on the aluminosilicate surface.

In the solutions with pH in the range 8–10 trace amounts of Lu(III) remain in a soluble hydrolyzed form $\text{Lu}(\text{OH})_3$, as well as in cationic forms Lu^{3+} , LuOH^{2+} and $\text{Lu}(\text{OH})_2^+$ (Fig. 2, 3; Tables 2, 3). That is why Lu(III) is sorbed from such solutions on clinoptilolite either via the adsorption of soluble neutral Lu(III) hydroxide on the clinoptilolite surface or via the ion-exchange mechanism.

The weakly alkaline (pH 8), neutral and weakly acidic solutions of Lu(III) trace amounts do not contain the hydrolyzed form $\text{Lu}(\text{OH})_3$. In such solutions Lu(III) exists only in the cationic forms (Fig. 2, 3; Tables 2, 3). That is why the sorption of Lu(III) on clinoptilolite from such solutions is carried out through the ion-exchange mechanism. However the sorption capacity of clinoptilolite towards Lu(III) under such conditions is considerably lower in comparison with the optimal conditions, that is when

the sorption of Lu(III) is carried out from solutions with pH 10.0 (Fig. 1).

It is known, that sorptive properties of Transcarpathian clinoptilolite depend significantly on its preliminary thermal treatment.^{22–26, 31, 33, 41}

Natural clinoptilolite samples washed with distilled water were heated at different temperatures for 2.5 h, and after cooling in a desiccator their sorption capacity towards Lu(III) ions was determined. The obtained results are presented on Fig. 5, where it can be seen that the preliminary calcination of the clinoptilolite natural form in the temperature range 50–150 °C causes the increase of sorption capacity towards Lu(III). According to⁴⁰ in this temperature range the elimination of the physically adsorbed water from the clinoptilolite surface takes place.

Authors⁴¹ indicated that in the hydrated zeolite the water molecules can form cyclic hexamers using hydrogen bonds which are stabilized with oxygen atoms of the zeolite frame. That is why in such form the molecules of water do not have free OH-groups. At temperature³ 200 °C during the beginning of ligand water desorption the partial destruction of hydrogen bonds takes place, that is the destruction of the cyclic hexamer, and because of that the free OH-groups appear in that part of destroyed hexamer, which remain bonded with the zeolite frame. In paper⁴³ it was investigated, that at 300 °C the partial transformation of clinoptilolite takes place at which the number of OH-groups in the structure of the zeolite increases according to the scheme:

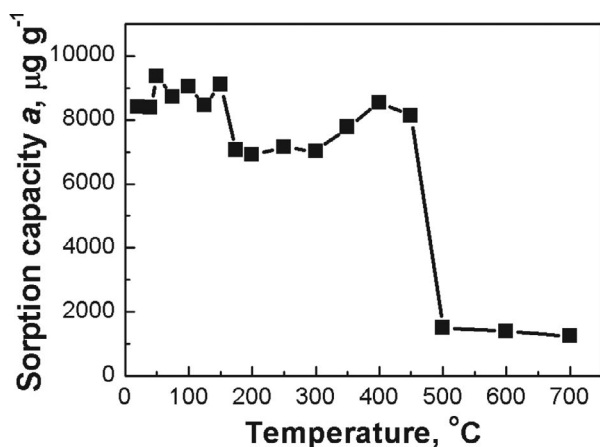
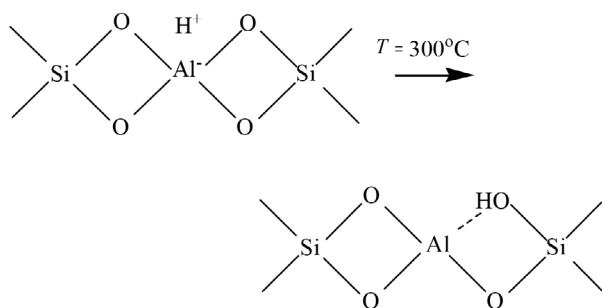


Fig 5. Dependence of the sorption capacity of clinoptilolite towards lutetium(III) on thermal treatment

The increase of sorption efficiency of clinoptilolite samples calcinated in the temperature range 200–400 °C (Fig. 5) is due to the increase of surface OH-groups of water molecules, and also silanol groups (Si–OH). The sorptive properties decrease in clinoptilolite calcinated at temperatures ³500 °C, in our opinion, can be explained by the processes of deep dehydroxylation of the zeolite surface and its amorphization at these temperatures, which was shown in paper.³³

An important stage of the work was the search of effective desorbents for lutetium. For this purpose the acidified solutions of alkali metal salts and mineral acid solutions were tested. The desorption results are given in Table 4, testifying that the best desorbents of lutetium are the alkali metal solutions, acidified to pH 4.0.

Table 4. Desorption effectiveness of Lu(III) from clinoptilolite

Desorbent	Desorption, %
1 mol L ⁻¹ RbNO ₃ (preacidified with HNO ₃ to pH 4.0)	100
1 mol L ⁻¹ NaCl (preacidified with HCl to pH 4.0)	100
1 mol L ⁻¹ KCl (preacidified with HCl to pH 4.0)	98
1 mol L ⁻¹ NaNO ₃ (preacidified with HNO ₃ to pH 4.0)	75
2.0 mol L ⁻¹ HNO ₃	60
2.0 mol L ⁻¹ HCl	50

100 % desorption of Lu from clinoptilolite is achieved with the application of 1 mol L⁻¹ solution of RbNO₃ and 1 mol L⁻¹ NaCl preacidified to pH 4.0. These data confirm that Lu(III) sorption on Transcarpathian clinoptilolite takes place because of the adsorption of the hydrolyzed forms of Lu(III) on the zeolite surface. For the efficient desorption of lutetium sorbed on the zeolite surface under optimal conditions the preliminary dissolution of its hydrolyzed forms with the transformation into the cationic form Lu³⁺ with further desorption mainly through the ion-exchange mechanism is needed. Such process is supplied by the acidified solutions of alkali metal salts (Table 4).

The influence of common ions from natural and waste waters on the preconcentration of lutetium(III) with clinoptilolite was investigated (Table 5). It is shown that the sorption of Lu(III) trace amounts on this natural sorbent takes place on the background of main macrocomponents of waters. Such contents of these cations do not influence on the maximum sorption capacity of clinoptilolite towards Lu(III):

Table 5. The influence of common ions on the maximal sorption capacity of clinoptilolite towards Lu(III) ($C_{Lu(III)}=1.0 \mu\text{g mL}^{-1}$)

Added ion	Maximal ratio $C_{ion}/C_{Lu(III)}$
Na ⁺	100
K ⁺	80
NH ₄ ⁺	30
Mg ²⁺	3
Ca ²⁺	3

Table 6. Determination of lutetium(III) ions in the tap water with an additional introduction of Lu(III) after ions preconcentration with clinoptilolite (n = 3, P = 0.95)

Volume of tap water, mL	Enrichment factor ^a	Concentration of Lu (III), $\mu\text{g mL}^{-1}$		Recovery, %	RSD, %
		Added	Found		
250	25	1.00	0.86 ± 0.02	86	0.83
250	25	0.50	0.48 ± 0.03	97	2.20
500	50	0.50	0.49 ± 0.02	98	1.82
500	50	0.25	0.25 ± 0.01	100	1.72
1000	100	0.25	0.24 ± 0.017	96	2.80
1500	150	0.1	0.095 ± 0.007	95	2.95
2000	200	0.05	0.046 ± 0.004	92	3.06

So, the optimal conditions for Lu(III) sorption are as follows: temperature of the preliminary thermal treatment – 50 °C; zeolite grains size of 0.20–0.31 mm; pH – 10.0; flow rate of Lu(III) solution with the concentration of 1.0 $\mu\text{g mL}^{-1}$ – 5 mL min⁻¹. The maximal sorption capacity of clinoptilolite towards Lu(III) is equal to 9.37 mg g⁻¹.

The ability of Transcarpathian clinoptilolite to sorb trace amounts of Lu(III), its high sorption capacity, the presence of the efficient desorbent give a reason to propose this sorbent for the removal of Lu(III) ions from aqueous solutions and for the preconcentration of Lu(III) during the stage of waters preparation for the analysis.

The method of Lu(III) trace amounts preconcentration in a solid phase extraction mode with further determination of this REE by using the spectrophotometric method was proposed.

3. 1. Preconcentration Method

The sorbent was prepared as follows: the sample of natural Transcarpathian clinoptilolite was grained in a ball-mill; a zeolite fraction with a grain size of 0.20–0.30 mm was taken and washed with distilled water. The dried clinoptilolite at room temperature was calcinated in a drying oven at 50 °C for 2.5 h. The sorbent was cooled in a desiccator. 0.25 – 2.0 L of the investigated water was acidified with nitric acid to pH~1 and heated on the sand bath for 1 h, then filtered through the dense paper filter „blue ribbon”. The solution of NaOH was added to the filtrate to pH~10. Then this solution was passed through the preconcentration cartridge filled with 0.6 g of the sorbent using the peristaltic pump with the flow rate of 5 mL min⁻¹. After that 50 mL of bidistilled water were passed through the cartridge with the same flow rate. The desorption of Lu(III) was carried out in such a way: 10 mL of 1.0 mol L⁻¹ NaCl solution, acidified with HCl to pH 4.0, were passed through the cartridge with a flow rate of 1 mL min⁻¹. The eluate was collected in the 10.0 mL volumetric flask. The Lu(III) content in the solution was determined using the spectrophotometric method with arsenazo III which is described in detail in “Materials and Methods” section. The linearity of the proposed method was observed in the range of 1–12 ng mL⁻¹ with the detection limit of 0.4 ng mL⁻¹.

The proposed method of Lu(III) preconcentration was tested with the analysis of a tap water from the Chemical Department of Ivan Franko National University of Lviv with the additional introduction of Lu(III) ions. The results of the analysis are given in Table 6.

The results of analysis confirm the effectiveness of the proposed method of Lu(III) preconcentration in the sample preparation stage during the analysis of water, because macrocomponents practically do not influence on the removal completeness of trace amount of lutetium that was introduced into the water.

4. Conclusions

Sorptive properties of Transcarpathian clinoptilolite towards trace amounts of Lu(III) were studied under dynamic conditions. The optimal conditions of Lu(III) sorption are as follows: temperature of preliminary thermal treatment of the zeolite – 50 °C; the flow rate of Lu(III) solution with the concentration of 1.0 µg mL⁻¹ through the sorbent – 5 mL min⁻¹; grain size of the zeolite 0.20–0.31 mm; pH 10.0. The maximal value of Transcarpathian clinoptilolite sorption capacity towards Lu(III) under this conditions is equal to 9.37 mg g⁻¹. The efficient desorbent of lutetium is the 1 mol L⁻¹ solution of NaCl preacidified with HCl solution to pH 4. Using this desorbent 96–100 % of lutetium preconcentrated on the zeolite can be removed.

The ability of Transcarpathian clinoptilolite to sorb either low or high concentrations, its high sorption capacity, availability of efficient desorbents give a reason to propose this common natural sorbent for the removal of Lu(III) ions from waters in technological solutions, and also for the preconcentration of Lu(III) ions in the stage of water preparation for the analysis.

The method of Lu(III) trace amounts preconcentration in a solid phase extraction mode during the spectrophotometric analysis of waters was proposed.

Authors' Note: The paper “Preconcentration of lutetium from aqueous solution by Transcarpathian clinoptilolite” was partially presented at the “XVI Polish-Ukrainian Symposium on Theoretical and Experimental Studies of Interfacial Phenomena and Their Technological Applications, Lublin, Poland, 28–31 August 2018”.

Acknowledgments: The author(s) disclosed receipt of the following financial support for the research, authorship, and/or publication of this article: The study was carried out with the support of the Ministry of Education and Sciences of Ukraine.

Conflicts of Interest: The authors declare no conflict of interest.

5. References

1. S. Handa, V. Gnanadesikan, S. Matsunaga, M. Shibasaki, *Am. Chem. Soc.* **2010**, *132*, 4925–4934. DOI:10.1021/ja100514y
2. D. Matsuura, *Appl. Phys. Lett.* **2002**, *81*, 4526–4528. DOI:10.1063/1.1527976
3. D. Haranath, S. Mishra, A.G. Joshi, S. Sahai, V. Shanker, *Nano-Micro Lett.* **2011**, *3*, 141–145. DOI:10.1007/BF03353664
4. M. Pollnau, *Handbook on the Physics and Chem. of Rare Earths*. Bünzli J.-C.; Pecharsky V. North Holland, **2017**, *51*, 111–168. DOI:10.1016/bs.hpcr.2017.04.001
5. R.-N. Zhao, R. Chen, S. Sun, Y.-J. Zhang, Y.-H. Yuan, *J. Mol. Struct.* **2017**, *1141*, 600–606. DOI:10.1016/j.molstruc.2017.04.013
6. Hisao Yamashita, Sadanori Igari, Yu Iino, *Appl. Radiat. Isot.* **1960**, *8(2–3)*, 111–112. DOI:10.1016/0020-708X(60)90076-4
7. F. Zereen, V. Yilmaz, Z. Arslan, *Microchem. J.* **2013**, *110*, 178–184. DOI:10.1016/j.microc.2013.03.012
8. A. Fisher, D. Kara, *Anal. Chim. Acta* **2016**, *935*, 1–9. DOI:10.1016/j.aca.2016.05.052
9. K. Pyrzynska, A. Kubiak, I. Wysocka, *Talanta*. **2016**, *154*, 15–22. DOI:10.1016/j.talanta.2016.03.022
10. F. Zhao, E. Repo, Y. Meng, X. Wang, D. Yin, M. Sillanpää, *J. Colloid and Interface Sci.* **2016**, *465*, 215–224. DOI:10.1016/j.jcis.2015.11.069
11. Q. Fu, L. Yang, Q. Wang, *Talanta* **2007**, *72*, 1248–1254. DOI:10.1016/j.talanta.2007.01.015
12. I. Çelik, D. Kara, C. Karadaş, A. Fisher, S. J. Hill, *Talanta* **2014**, *134*, 476–481. DOI:10.1016/j.talanta.2014.11.063
13. S. U. Yesiller, A. E. Eroglu, T. Shahwan, *J. Ind. Eng. Chem.* **2015**, *19*, 898–907. DOI:10.1016/j.jiec.2012.11.005
14. T. Pasinli, A. A. Eroglu, T. Shahvan, *Anal. Chim. Acta.* **2005**, *547*, 42–49. DOI:10.1016/j.aca.2005.04.076
15. O. I. M. Ali, H. Osmana, S. Sayeda, Shelbie, M. J. Hazard. *Mater.* **2011**, *195*, 62–67. DOI:10.1016/j.jhazmat.2011.08.014
16. R. A. Cranea, D. J. Sapsford, *Chem. Eng. J.* **2018**, *345*, 126–137. DOI:10.1016/j.cej.2018.03.148
17. A. Negrea, A. Gabor, C. M. Davidescu, M. Ciopec, P. Negrea, N. Duteanu, A. Barbulescu, *Sci. Rep.* **2018**, *8:316*, 1–11. DOI:10.1038/s41598-017-18623-0
18. M. Ahmadi, H. Elmongy, T. Madrakian, M. Abdel-Rehim, *Anal. Chim. Acta* **2017**, *958*, 1–21. DOI:10.1016/j.aca.2016.11.062
19. E. P. Legaria, J. Rocha, C.-W. Tai, V. G. Kessler, G. A. Seisenbaeva, *Sci. Rep.* **2017**, *7:43740*, 1–13. DOI:10.1038/srep43740
20. T. Tsuruta, *J. Rare Earths* **2007**, *5:25*, 526–532. DOI:10.1016/S1002-0721(07)60556-0
21. N. K. Gupta, A. Gupta, P. Ramteke, H. Sahoo, A. Sengupta, *J. Mol. Liq.* **2018**, *274*, 148–164. DOI:10.1016/j.molliq.2018.10.134
22. V. O. Vasylechko, E. T. Stechynska, O. D. Stashkiv, G. V. Gryshchouk, I. O. Patsay, *Acta Physica Polonica A* **2018**, *133(4)*, 794–797. DOI:10.12693/APhysPolA.133.794
23. V. O. Vasylechko, G. V. Gryshchouk, V. P. Zakordonskiy, I. O. Patsay, N. V. Len', O. A. Vyviurska, *Micropor. Mesopor. Mat.* **2013**, *167*, 155–161. DOI:10.1016/j.micromeso.2012.08.021

24. V. O. Vasylechko, G. V. Gryshchouk, V. P. Zakordonskiy, O. A. Vyviurska, A. V. Pashuk, *Chem. Central J.* **2015**, *9*, 1:45, 1–7. DOI:10.1186/s13065-015-0118-z
25. V. O. Vasylechko, G. V. Gryshchouk, V. P. Zakordonskiy, L. O. Vasylechko, M. Schmidt, I. M. Leshchack, Ya. M. Kalychak, S. R. Bagday, *Talanta* **2017**, *174*, 486–492. DOI:10.1016/j.talanta.2017.06.052
26. V. Vasylechko, G. Gryshchouk, M. Derev'yanko, Ya. Skorobahatyj, O. Tymoshuk, *Visnyk Lviv Univ. Ser. Chem.* **2008**, *49*, 170–179. http://prima.lnu.edu.ua/faculty/Chem/visnyk_2008/ANALIT/05_Vasylechko.pdf
27. M. Sprynskyy, M. Lebedynets, A. P. Terzyk, P. Kowalczyk, J. Namieśnik, B. Buszewski, *J. Colloid and Interface Sci.* **2005**, *284*, 408–415. DOI:10.1016/j.jcis.2004.10.058
28. M. Sprynskyy, T. Ligor, M. Lebedynets, B. Buszewski, *J. Hazard Mater.* **2009**, *169*, 847–854. DOI:10.1016/j.jhazmat.2009.04.019
29. L.-H. Chen, X.-Y. Li, J. C. Rooke, Y.-H. Zhang, X.-Y. Yang, Y. Tang, B.-L. Su, *J. Mater. Chem.* **2012**, *22*, 17381–17403. DOI:10.1039/c2jm31957h
30. M. E. Davis, *Nature* **2002**, *417*, 813–821. http://image.sciencenet.cn/olddata/kexue.com.cn/bbs/upload/15327Ordered_porous_materials_for_emerging_applications.pdf?fbclid=IwAR0DwCETn6MbCOPRnN7_wJlQvC_tsq6umG9bwqJNIsdq2z27cGsUs5ViMgc DOI:10.1038/nature00785
31. V. O. Vasylechko, G. V. Gryshchouk, L. O. Lebedynets, Yu. B. Kuz'ma, L. O. Vasylechko, V.P. Zakordonskiy, *Adsorp. Sci. Technol.* **1999**, *17(2)*, 125–134. DOI:10.1177/026361749901700206
32. Y. I. Tarasevich, V. E. Polyakov, V. Zh. Penchev, G. N. Kirov, Kh. I. Minchev, I. G. Polyakov, L. I. Badekha, *Khim. Technol. Vody* **1991**, *13(2)*, 132–140.
33. V. O. Vasylechko, G. V. Gryshchouk, Yu. B. Kuz'ma, V. P. Zakordonskiy, L. O. Vasylechko, Lebedynets, M. B. Kalytotov'ska, *Micropor. Mesopor. Mat.* **2003**, *60*, 183–196. DOI:10.1016/S1387-1811(03)00376-7
34. V. P. Zakordonskiy, V. O. Vasylechko, P. Staszczuk, G. V. Gryshchouk, *Visnyk Lviv Univ. Ser. Chem.* **2004**, *44*, 247–256. <http://ua.convdocs.org/docs/index-239615.html>
35. V. O. Vasylechko, L. O. Lebedynets, G. V. Gryshchouk, Yu. B. Kuz'ma, L. O. Vasylechko, T. M. Bernats'ka, *Adsorp. Sci. Technol.* **1996**, *14(5)*, 267–277. DOI:10.1177/026361749601400501
36. L. N. Usherenko, N.A. Skorik, *Zh. Neorgan. Khim.* **1972**, *17(11)*, 2918–2921.
37. E. Rizkalla, G. Choppin, in: Gshneider K.; Jr. and L. Eyring (Eds.) *Handbook of Physics and Chemistry of Rare Earth*. Elsevier. Amsterdam, **1991**, *15*, 393–442. DOI:10.1016/S0168-1273(05)80009-1
38. U. Frolova, V. Kumok, V. Serebrennikov, *Izvestiya VUZ USSR Khim & Khim Technol.* **1966**, *9(2)*, 176–179.
39. V. A. Nazarenko, V. P. Antonovich, Ye. M. N'evskaya, *Hydrolysis of metal ions in dilute solutions*. Atomizdat. Moscow, **1974**.
40. C. F. Baes, R. E. Mesmer, *The Hydrolysis of Cations*; John Wiley & Sons: New York – London – Sidney – Toronto, **1976**.
41. V. O. Vasylechko, G. V. Gryshchouk, I. I. Polyans'ka, Yu. B. Kuz'ma, *Polish J. Chem.* **2008**, *82*, 1–2, 443–451.
42. J. Hunger, I. A. Beta, H. Böhlig, L. Chris, H. Jobic, B. Hunger, *Phys. Chem. B.* **2006**, *110(1)*, 342–353. DOI:10.1021/jp054636u
43. B. Tomazović, T. Čeranić, G. Sijarić, *Zeolites* **1966**, *16*, 301–308. DOI:10.1016/0144-2449(95)00118-2

Povzetek

Pod dinamičnimi pogoji smo preučevali sorpcijske lastnosti transkarpatskega klinoptilolita za Lu(III) v sledovih. Pokazali smo, da se ta lantanid najbolj učinkovito sorbira iz šibko alkalnih raztopin (pH 10). Sorpcijska kapaciteta klinoptilolita pri optimalnih pogojih je enaka 9,37 mg g⁻¹. Izračunali smo porazdelitev različnih zvrsti Lu(III) v vodni raztopini pri različni skupni koncentraciji lantanida v pH območju 4 do 13. Najboljši desorbent za Lu(III) je 1 mol L⁻¹ raztopina NaCl, nakisana z raztopino HCl do pH 4,0. Ta desorbent omogoča 95–100 % odstranitev Lu(III). Razvili smo tudi metodo za predkoncentracijo Lu(III) v sledovih iz vodnih vzorcev v načinu ekstrakcije na trdno fazo z nadaljnjo določitvijo tega redkozemeljskega elementa s spektrofotometrijsko metodo ob uporabi reagenta arsenazo III. Linearnost predlagane metode smo pokazali v območju 1–12 ng mL⁻¹ z mejo zaznave 0,4 ng mL⁻¹.



Except when otherwise noted, articles in this journal are published under the terms and conditions of the Creative Commons Attribution 4.0 International License

Scientific paper

Synthesis and Characterization of Tetrachloro-1,3-Oxazepine Derivatives and Evaluation of their Biological Activities

Abdullah Hussein Kshash

Department of Chemistry, Education College for Pure Science, University Of Anbar,
31001, Ramadi, Anbar, Iraq

* Corresponding author: E-mail: drabdullahkshash@gmail.com
Tel: +964-7830818171

Received: 05-16-2019

Abstract

6,7,8,9-Tetrachloro[1,3]oxazepine-1,5-dione derivatives **1b–10b** have been synthesized by reacting Schiff bases **1a–10a** with tetrachlorophthalic anhydride (TCPA) under (2 + 5 → 7) cycloaddition reaction conditions. All reactions had been monitored using TLC. FT IR and melting points have been used to characterize the Schiff bases; oxazepine compounds **1b–10b** were characterized using FT IR, ¹H NMR and their melting points. Biological activity for oxazepine compounds has been evaluated against bacterial types (*Staphylococcus aureus*, *Escherichia coli*, *Klebsiella spp.*) and against a fungus (*Geotrichum spp.*). Variable activities have been observed against used strains of bacteria and fungi.

Keywords: Oxazepine, tetrachlorophthalic anhydride, Antibacterial activity, Antifungal activity.

1. Introduction

Lately, different heterocyclic compounds were synthesized, using reactions of Schiff bases with various reagents, such as oxazepines. Oxazepines are heterocyclic unsaturated compounds, incorporating two hetero atoms (oxygen and nitrogen). There are many synthetic strategies for synthesis of oxazepines, using gold-, palladium- and rhodium-based catalysts,^{1–3} under microwave irradiation,⁴ and under catalyst-free conditions⁵ as well; all these strategies leading to the formation of 1,3-oxazepines-4,7-diones. Oxazepines were synthesized to be evaluated for their potential activities, e.g. antioxidant and anti-inflammatory activity,⁶ as neuroleptic agents,⁷ kinase inhibitors,⁸ antimicrobial agents.⁹ This paper describes 1,3-oxazepine-4,7-dione derivatives, synthesized by reactions of Schiff bases with TCPA, to provide information of synthetic method and the possible use of 6,7,8,9-tetrachloro[1,3]oxazepine-1,5-dione as an antibacterial (*S. aureus*, *E. coli*, *Klebsiella spp.*) and antifungal agent (*Geotrichum spp.*), in contrast to other routes which use unsubstituted phthalic anhydride for synthesis of 1,3-oxazepines-1,5-dione.

2. Experimental Section

2.1. Materials

Aromatic aldehydes, amines and TCPA were supplied from Sigma-Aldrich Chemical Co. used without further purification. Solvents were supplied from Romil. Instrumentation: infrared spectra were recorded as ATR technique on Bruker-Tensor 27 spectrometer. ¹H NMR spectra were recorded on Bruker 300 MHz spectrometer using DMSO-*d*₆ as the solvent and TMS as the internal standard.

2.2. Procedure for the Preparation of Schiff Bases 1a–10a

To a 100 mL round bottomed flask containing 25 mL absolute ethanol, aromatic aldehyde (4.5 mmol) and 3 drops of glacial acetic acid, equipped with condenser and stirring bar, aromatic amine (4.5 mmol) dissolved in absolute ethanol (10 mL) was added. The reaction mixture was refluxed for 3 h, then cooled down to room temperature. Product was collected as a solid by filtration and recrystallized from ethanol.

2. 3. Characterization of Schiff Bases 1a–10a

1-(4-Bromophenyl)-N-(para-tolyl)methanimine (1a). White solid, yield 1.01 g (82%); m.p. 142–144 °C, IR (ATR) ν 3050 (C-H aromatic), 3025 (ν NC-H), 2982 (ν C-H_{al}), 1617 (ν C=N), 1609, 1502 (aromatic ring) cm⁻¹.

1-(4-Chlorophenyl)-N-(para-tolyl)methanimine (2a).¹⁰ Beige solid, yield 0.9 g (88%); m.p. 125–127 °C (lit. 124–125 °C), IR (ATR) ν 3055 (C-H aromatic), 3026 (ν NC-H), 2976 (ν C-H_{al}), 1623 (ν C=N), 1587, 1499 (C=C aromatic) cm⁻¹.

N-(4-Bromophenyl)-1-(4-chlorophenyl)methanimine (3a).¹¹ White solid, yield 1.13 g (85%); m.p. 120–123 °C (lit. 122–124 °C), IR (ATR) ν 3063 (C-H aromatic), 3027 (ν NC-H), 1617 (ν C=N), 1591, 1566 (C=C aromatic) cm⁻¹.

N-(4-Bromophenyl)-1-(2,4-dichlorophenyl)methanimine (4a). White solid, yield 1.32 g (89%); m.p. 136–138 °C, IR (ATR) ν 3062 (C-H aromatic), 3014 (ν NC-H), 1612 (ν C=N), 1585, 1482 (C=C aromatic) cm⁻¹.

N-(4-Bromophenyl)-1-(para-tolyl)methanimine (5a).¹² White solid, yield 0.93 g (75%); m.p. 130–132 °C (lit. 136.3 °C), IR (ATR) ν 3050 (C-H aromatic), 3023 (ν NC-H), 2972 (ν C-H_{al}), 1621 (ν C=N), 1566, 1473 (C=C aromatic) cm⁻¹.

N-(4-Chlorophenyl)-1-(2,4-dichlorophenyl)methanimine (6a). White solid, yield 1.09 g (80%); m.p. 128–130 °C, IR (ATR) ν 3062 (C-H aromatic), 3021 (ν NC-H), 1613 (ν C=N), 1575, 1484 (C=C aromatic) cm⁻¹.

N,1-Bis(4-chlorophenyl)methanimine (7a).¹⁰ Pale green solid, yield 0.86 g (76%); m.p. 110–112 °C (lit. 110–111 °C), IR (ATR) ν 3056 (C-H aromatic), 3022 (ν NC-H), 1622 (ν C=N), 1591, 1486 (C=C aromatic) cm⁻¹.

N-(4-Chlorophenyl)-1-(para-tolyl)methanimine (8a).¹³ Beige solid, yield 0.76 g (73%); m.p. 109–111 °C (lit. 110 °C), IR (ATR) ν 3052 (C-H aromatic), 3026 (ν NC-H), 2986 (ν C-H_{al}), 1620 (ν C=N), 1565, 1474 (C=C aromatic) cm⁻¹.

N-(4-Chlorophenyl)-1-(4-methoxyphenyl)methanimine (9a).¹³ Beige solid, yield 0.81 g (73%); m.p. 95–97 °C (lit. 95 °C), IR (ATR) ν 3071 (C-H aromatic), 3018 (ν NC-H), 2963 (ν C-H_{al}), 1619 (ν C=N), 1566, 1475 (C=C aromatic) cm⁻¹.

1-(4-Bromophenyl)-N-(4-chlorophenyl)methanimine (10a).¹⁰ Beige solid, yield 1.04 g (78%); m.p. 122–124 °C (lit. 119–120 °C), IR (ATR) ν 3064 (C-H aromatic), 3025 (ν NC-H), 1617 (ν C=N), 1585, 1482 (C=C aromatic) cm⁻¹.

2. 4. Procedure for the Synthesis of 1,3-Oxazepines-4,7-dione derivatives 1b–10b

To a 100 mL round bottomed flask containing 25 mL dry benzene and Schiff bases **1a–10a** (1 mmol) equipped with condenser, was added TCPA (1 mmol) dissolved in 20 mL of dry benzene. The reaction mixture was refluxed for 5 h, then stirred overnight at room temperature. Thereafter, the solid product was collected by filtration and recrystallized from ethanol.

2. 5. Characterization of Schiff Bases 1b–10b

3-(4-Bromophenyl)-6,7,8,9-tetrachloro-4-(para-tolyl)-3,4-dihydrobenzo[1,3]oxazepine-1,5-dione (1b). Pale yellow solid, yield 0.68 g (66%); m.p. 178–180 °C, ¹H NMR (300 MHz, DMSO-*d*₆) δ 7.87 (d, *J* = 8.5 Hz, 2H, H_{11,13}), 7.73 (*J* = 8.4 Hz, 2H, H_{2,6}), 7.49 (d, *J* = 8.4 Hz, 2H, H_{10,14}), 7.22 (s, 1H, H₈), 7.16 (d, *J* = 8.3 Hz, 2H, H_{3,5}), 2.28 (s, 3H, CH₃). IR (ATR) ν 3045 (C-H aromatic), 1726 (ν C=O_{lacton}), 1667 (ν C=O_{lactam}), 1511 (CO-N), 1321 (CO-O) cm⁻¹.

6,7,8,9-Tetrachloro-3-(4-chlorophenyl)-4-(para-tolyl)-3,4-dihydrobenzo[1,3]oxazepine-1,5-dione (2b). Pale yellow solid, yield 0.71 g (63%); m.p. 179–181 °C, ¹H NMR (300 MHz, DMSO-*d*₆) δ 7.95 (d, *J* = 8.5 Hz, 2H, H_{11,13}), 7.59 (d, *J* = 8.5 Hz, 2H, H_{2,6}), 7.54–7.44 (m, 2H, H_{10,14}), 7.21 (s, 1H, H₈), 7.17 (d, *J* = 8.2 Hz, 2H, H_{3,5}), 2.28 (s, 3H, CH₃). IR (ATR) ν 3053 (C-H aromatic), 1726 (ν C=O_{lacton}), 1666 (ν C=O_{lactam}), 1509 (CO-N), 1321 (CO-O) cm⁻¹.

4-(4-Bromophenyl)-6,7,8,9-tetrachloro-3-(4-chlorophenyl)-3,4-dihydrobenzo[1,3]oxazepine-1,5-dione (3b). Pale green solid, yield 0.55 g (55%); m.p. 290 °C dec., ¹H NMR (300 MHz, DMSO-*d*₆) δ 7.97–7.91 (m, 2H, H_{3,5}), 7.76 (d, *J* = 8.7 Hz, 2H, H_{11,13}), 7.67 (d, *J* = 8.4 Hz, 2H, H_{2,6}), 7.28–7.19 (m, 2H, H_{10,14}), 7.21 (s, 1H, H₈). IR (ATR) ν 3063 (C-H aromatic), 1717 (ν C=O_{lacton}), 1669 (ν C=O_{lactam}), 1541 (CO-N), 1312 (CO-O) cm⁻¹.

4-(4-Bromophenyl)-6,7,8,9-tetrachloro-3-(2,4-dichlorophenyl)-3,4-dihydrobenzo[1,3]oxazepine-1,5-dione (4b). White solid, yield 0.49 g (52%); m.p. > 300 °C, ¹H NMR (300 MHz, DMSO-*d*₆) δ 8.16 (d, *J* = 8.5 Hz, 2H, H_{3,5}), 7.81–7.73 (m, 2H, H_{2,6}), 7.57 (s, 1H, H₁₁), 7.37 (s, 1H, H₈), 7.17–7.14 (m, H, H₁₃), 6.56 (d, *J* = 8.6 Hz, 8H, H₁₄). IR (ATR) ν 3060 (C-H aromatic), 1720 (ν C=O_{lacton}), 1670 (ν C=O_{lactam}), 1532 (CO-N), 1313 (CO-O) cm⁻¹.

4-(4-Bromophenyl)-6,7,8,9-tetrachloro-3-(para-tolyl)-3,4-dihydrobenzo[1,3]oxazepine-1,5-dione (5b). Yellow solid, yield 0.691 g (77%); m.p. 260 °C dec., ¹H NMR (300 MHz, DMSO-*d*₆) δ 7.88–7.81 (m, 2H, H_{3,5}), 7.63–7.56 (m, 2H, H_{2,6}), 7.23 (d, *J* = 2.1 Hz, 1H, H₈), 7.15

(d, $J = 8.7$ Hz, 2H, $H_{10,14}$), 6.58–6.51 (m, 2H, $H_{11,13}$), 2.38 (s, 3H, CH_3). IR (ATR) ν 3047 (C-H aromatic), 1721 (ν C=O_{lacton}), 1668 (ν C=O_{lactam}), 1542 (CO-N), 1314 (CO-O) cm^{-1} .

6,7,8,9-Tetrachloro-4-(4-chlorophenyl)-3-(2,4-dichlorophenyl)-3,4-dihydrobenzo[1,3]oxazepine-1,5-dione (6b). Yellow solid, yield 0.64 g (64%); m.p. > 300 °C, 1H NMR (300 MHz, DMSO- d_6) δ 7.70–7.57 (m, 2H, $H_{3,5}$), 7.48–7.41 (m, 2H, $H_{2,6}$), 7.37 (s, 1H, H_{11}), 7.30 (s, 1H, H_8), 7.06 (d, $J = 8.6$ Hz, 1H, H_{13}), 6.62 (d, $J = 8.6$ Hz, 1H, H_{14}). IR (ATR) ν 3062 (C-H aromatic), 1722 (ν C=O_{lacton}), 1667 (ν C=O_{lactam}), 1490 (CO-N), 1312 (CO-O) cm^{-1} .

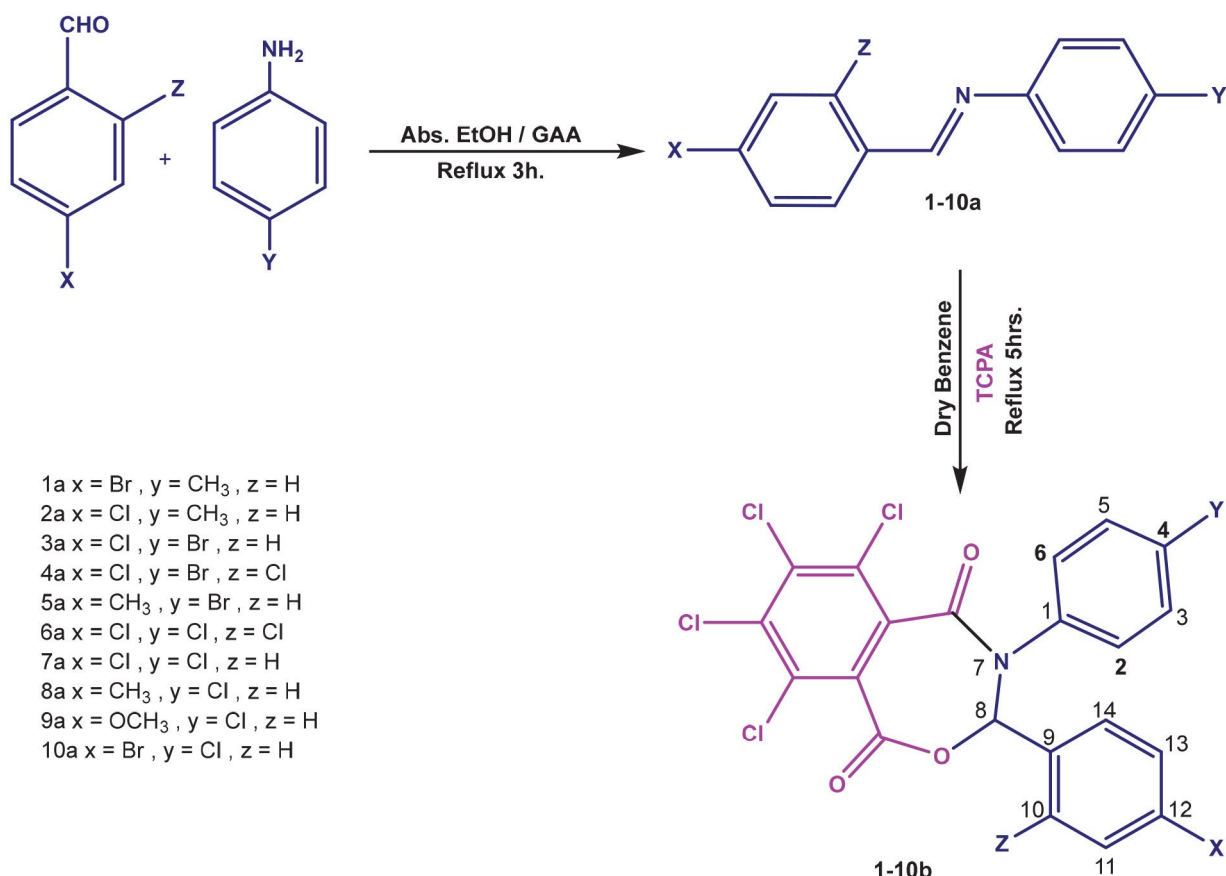
6,7,8,9-Tetrachloro-3,4-bis(4-chlorophenyl)-3,4-dihydrobenzo[1,3]oxazepine-1,5-dione (7b). Pale yellow solid, yield 0.78 g (73%); m.p. 288–290 °C, 1H NMR (300 MHz, DMSO- d_6) δ 7.64 (d, $J = 8.9$ Hz, 2H, $H_{3,5}$), 7.49–7.39 (m, 2H, $H_{11,13}$), 7.30 (s, 1H, H_8), 7.08–6.98 (m, 2H, $H_{2,6}$), 6.58 (d, $J = 8.6$ Hz, 2H, $H_{10,14}$). IR (ATR) ν 3063 (C-H aromatic), 1717 (ν C=O_{lacton}), 1668 (ν C=O_{lactam}), 1541 (CO-N), 1316 (CO-O) cm^{-1} .

6,7,8,9-Tetrachloro-4-(4-chlorophenyl)-3-(*para*-tolyl)-3,4-dihydrobenzo[1,3]oxazepine-1,5-dione (8b).

Pale yellow solid, yield 0.79 g (71%); m.p. 265–267 °C, 1H NMR (300 MHz, DMSO- d_6) δ 7.64 (d, $J = 8.9$ Hz, 2H, $H_{3,5}$), 7.46–7.41 (m, 2H, $H_{2,6}$), 7.27 (s, 1H, H_8), 7.06–7.00 (m, 2H, $H_{10,14}$), 6.57 (d, $J = 8.8$ Hz, 2H, $H_{11,13}$), 2.38 (s, 3H, CH_3). IR (ATR) ν 3062 (C-H aromatic), 1722 (ν C=O_{lacton}), 1666 (ν C=O_{lactam}), 1543 (CO-N), 1327 (CO-O) cm^{-1} .

6,7,8,9-Tetrachloro-4-(4-chlorophenyl)-3-(4-methoxyphenyl)-3,4-dihydrobenzo[1,3]oxazepine-1,5-dione (9b). Pale green solid, yield 1.07 g (74%); m.p. 272–274 °C, 1H NMR (300 MHz, DMSO- d_6) δ 7.67–7.60 (m, 2H, $H_{3,5}$), 7.44 (d, $J = 8.9$ Hz, 2H, $H_{2,6}$), 7.25 (s, 1H, H_8), 7.08 (d, $J = 8.8$ Hz, 2H, $H_{10,14}$), 6.63–6.53 (m, 2H, $H_{11,13}$), 3.84 (s, 3H, OCH_3). IR (ATR) ν 3054 (C-H aromatic), 1723 (ν C=O_{lacton}), 1667 (ν C=O_{lactam}), 1547 (CO-N), 1314 (CO-O) cm^{-1} .

3-(4-Bromophenyl)-6,7,8,9-tetrachloro-4-(4-chlorophenyl)-3,4-dihydrobenzo[1,3]oxazepine-1,5-dione (10b). Yellow solid, yield 0.58 g (60%); m.p. 250–253 °C, 1H NMR (300 MHz, DMSO- d_6) δ 7.88 (d, $J = 8.5$ Hz, 2H, $H_{11,13}$), 7.74 (d, $J = 8.5$ Hz, 2H, $H_{3,5}$), 7.69–7.60 (m, 2H, $H_{2,6}$), 7.44 (d, $J = 8.9$ Hz, 2H, $H_{10,14}$), 7.30 (s, 1H, H_8). IR (ATR) ν 3062 (C-H aromatic), 1723 (ν C=O_{lacton}), 1667 (ν C=O_{lactam}), 1591 (CO-N), 1312 (CO-O) cm^{-1} .



Scheme 1. Synthetic route for synthesis of 1b–10b compounds

3. Results and Discussion

3. 1. Chemistry

Target oxazepine compounds **1b–10b** were synthesized according to the route presented in Scheme 1.

Imines **1a–10a** have been synthesized as precursors for oxazepine compounds by condensation reaction of aromatic aldehydes and primary aromatic amines using absolute ethanol as the solvent. According to the yields obtained, it can be indicated that when the reacting compounds are substituted by electron withdrawing groups (EWG) on benzaldehyde (at the *para* position), greater amount of the product is obtained than was the case with other compounds, this being due to the substituents having $-I$ effect that increase the magnitude of the positive charge (δ^+) on the carbonyl carbon atom. Hence, increasing the reactivity of benzaldehyde to the attack by amine (as a nucleophile).

Oxazepines have been synthesized by reactions of imines with TCPA, using dry benzene as the solvent, in (2 + 5 \rightarrow 7) cycloaddition reaction. This reactions type is controlled by orbital symmetry. Therefore, the frontier molecular orbitals for the reactants have to be taken into consideration. Moreover, orbitals of the reactants (anhydride and imines) have to overlap in the convenient way to afford oxazepines by suprafacial manner.

Synthesis of oxazepines has taken place by overlapping of orbitals for imines and TCPA, through the formation of a four-membered ring as the transition state; increasing this overlap led to the formation of a seven-membered ring compounds, as depicted in Scheme 2.

In general, electron donating groups (EDG) increase HOMO energy levels, therefore, reduce the required energy to accomplish the oxazepine formation reaction; in this study, the reaction progress was in accord with the pericyclic mechanism where FMO of imines serve as HOMO, whereas those of TCPA as LUMO; this expectation is

brought up through the notice that the yield for **5b**, **8b** and **9b** is the highest, due to the precursor imines **5a**, **8a** and **9a** having electron donating groups that increase the HOMO energy level for imines, giving rise to decreasing the required reaction's energy (Figure 1).

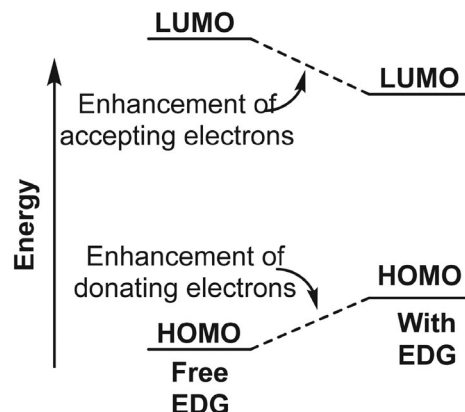
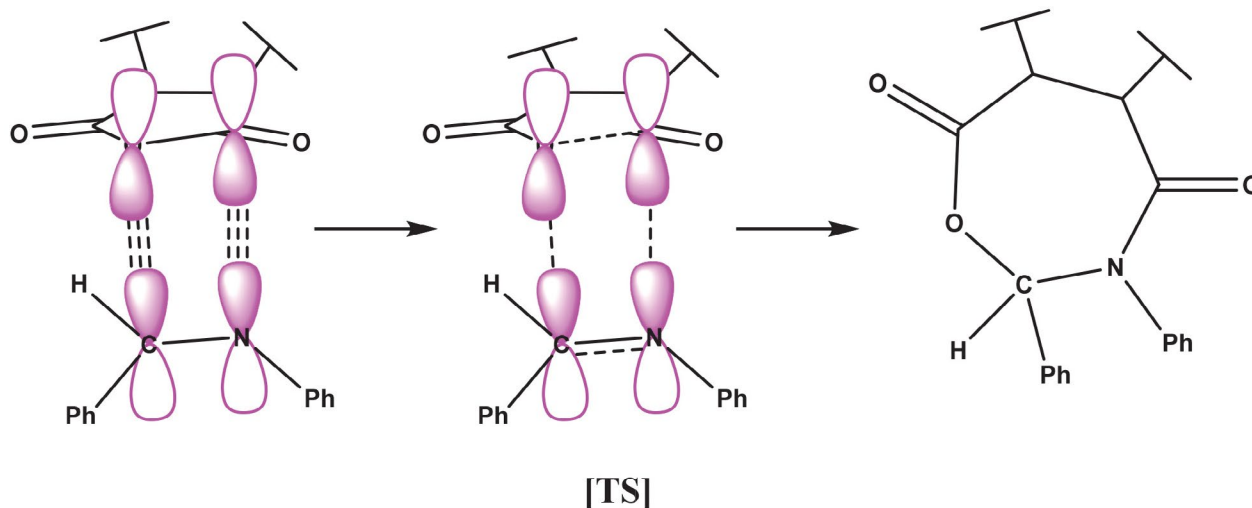


Figure 1. HOMO and LUMO energy level

3. 1. 1. Characterization of Prepared Compounds

Imine compounds **1a–10a** were synthesized by reactions of aromatic aldehydes with amines, using absolute ethanol as the solvent. Color, melting point and R_f changes (TLC analysis) indicated the formation of new compounds, FT IR spectra for compounds **1a–10a** showed the disappearance of stretching vibration bands for NH_2 group for substituted aniline, and $\nu\text{C}=\text{O}$ group absorption band for substituted benzaldehyde, moreover, appearance of strong vibration band at the range $1612\text{--}1623\text{ cm}^{-1}$ can be attributed to the $\nu\text{C}=\text{N}$ azomethine group, beside absorption bands at $3050\text{--}3071\text{ cm}^{-1}$ for aromatic $\nu\text{C-H}$, $3014\text{--}3032\text{ cm}^{-1}$ for $\nu\text{NC-H}$ and $1566\text{--}1609$ and $1473\text{--}1566\text{ cm}^{-1}$ for aromatic rings.



Scheme 2. Formation mechanism of oxazepine compounds

Table 1. *In vitro* zone of inhibition (mm) of target oxazepine compounds.

Strains	Compound									
	1b	2b	3b	4b	5b	6b	7b	8b	9b	10b
<i>Staphylococcus aureus</i>	10	11	15	14.5	13	14	13.5	14.5	14	17
<i>Escherichia coli</i>	8	8	9	8	9.5	8.5	8	0	0	8.5
<i>Klebsiella sp.</i>	8.5	0	10	10	9	0	0	0	0	0
<i>Geotrichum sp.</i>	10	11	14	17	11.5	18	18	15	17	19

Oxazepines **1b–10b** were synthesized by reactions of synthesized imines **1a–10a** and TCPA using dry benzene as the solvent in accord with the mechanism described in Scheme 2. FT IR spectra for oxazepine compounds **1b–10b** showed the disappearance of stretching vibration bands for ν C=N azomethine group, furthermore, appearance of vibration absorption band at 3045–3063 cm^{-1} assigned to the aromatic ν C-H, at 1717–1726 cm^{-1} for ν C=O_{lacton}, 1666–1670 cm^{-1} for ν C=O_{lactam}, 1490–1547 cm^{-1} for ν CO-N and 1312–1327 cm^{-1} for ν CO-O was observed.

3. 2. Biological Activity

3. 2. 1. Antibacterial Activity

Antibacterial activities for oxazepine compounds **1b–10b** were evaluated against *Staphylococcus aureus*, *Escherichia coli* and *Klebsiella spp.* by applying 2 mg/well of the synthesized compounds dissolved in DMSO, then incubated at 37 °C for 24 h. Results indicate *Klebsiella spp.* resistance for compounds **6b–10b**, while *E. coli* was resistant to compounds **8b** and **9b**, other compounds demonstrated good inhibition against microbial tested strains, inhibition zone data in mm are given in Table 1.

3. 2. 2. Antifungal Activity

Antifungal activities for the synthesized oxazepine compounds **1b–10b** were screened against *Geotrichum spp.* by applying 2 mg/well of the synthesized compounds dissolved in DMSO, then incubated at 37 °C for 24 h. Results show that all of the synthesized compounds demonstrate good inhibition against the tested fungus, and no resistance for oxazepine compounds was found; inhibition zone data in mm are given in Table 1.

Data of antibacterial and antifungal activity (Table 1) revealed that compounds with substituents Cl and Br have the highest inhibition zone, particularly against *S. aureus* and *Geotrichum spp.*, whereas compounds with substituents CH₃ and OCH₃ have the lowest inhibition, this can be attributed to van der Waals interaction with chloro and bromo substituent compounds; *para*-Br substituted compounds are more effective than *para*-Cl substituted compounds due to the size of the bromine atom which facilitates halogen bond interactions by supplying van der Waals radii between the donor and the acceptor atom.

4. Conclusion

New tetrachloro[1,3]oxazepine-1,5-diones **1b–10b** were synthesized in good yields, had been characterized by different spectroscopic methods, their anti-bacterial biological activity evaluated against *Staphylococcus aureus*, *Escherichia coli*, and *Klebsiella spp.* and their anti-fungal properties against *Geotrichum spp.*, variable activities were recorded for the tested compounds.

5. References

- K. Goutham, D. A. Kumar, S. Suresh, B. Sridhar, R. Narendar, G. V. Karunakar, *J. Org. Chem.* **2015**, *80*, 11162–11168. DOI:10.1021/acs.joc.5b01733
- Y. Wu, C. Yuan, C. Wang, B. Mao, H. Jia, X. Gao, J. Liao, F. Jiang, L. Zhou, Q. Wang, H. Guo, *Org. Lett.* **2017**, *19*, 6268–6271. DOI:10.1021/acs.orglett.7b02704
- Y. O. Ko, H. J. Jeon, D. J. Jung, U. B. Kim, S. G. Lee, *Org. Lett.* **2016**, *18*, 6432–6435. DOI:10.1021/acs.orglett.6b03328
- N. I. Taha, *Int. J. Org. Chem.* **2017**, *7*, 219–228. DOI:10.4236/ijoc.2017.73016
- A. H. Kshash, M. G. Mokhlef, *Indones. J. Chem.* **2017**, *17*(2), 330–335. DOI:10.22146/ijc.22437
- A. K. Alexander, L. Joseph, M. George, *Eur. J. Pharm. Med. Res.* **2016**, *3*(7), 330–336.
- K. Bajaj, V. K. Srivastava, A. Kumar, *Indones. J. Chem.* **2003**, *42B*, 1149–1155.
- X. Chen, Y. Du, H. Sun, F. Wang, L. Kong, M. Sun, *Bioorg. Med. Chem. Lett.* **2014**, *24*, 884–887. DOI:10.1016/j.bmcl.2013.12.079
- J. Tang, Y.-L. Jiang, B.-X. Wang, Y.-M. Shen, *Z. Naturforsch. C* **2014**, *69*(7-8), 283–290. DOI:10.5560/znc.2014-0029
- J. S. Bennett, K. L. Charles, M. R. Miner, C. F. Heuberger, E. J. Spina, M. F. Bartels, T. Foreman, *Green Chem.* **2009**, *11*, 166–168. DOI:10.1039/b817379f
- H. Naeimi, K. Rabiei, *J. Chin. Chem. Soc.* **2012**, *59*, 208–212. DOI:10.1002/jccs.201100354
- L. Jothi, R. R. Babu, K. Ramamurthi, *J. Miner. Mater. Char. Eng.* **2014**, *2*, 308–318. DOI:10.4236/jmmce.2014.24036
- Y. Algamala, R. M. Ghalib, *Int. J. Sci. Basic Appl. Res.* **2015**, *20*, 53–76. DOI:10.12659/MSMBR.890835

Povzetek

S pomočjo reakcije med Schiffovimi bazami **1a–10a** in tetrakloroftalanhidridom (TCPA) smo s pomočjo (2 + 5 → 7) cikloadicije pripravili 6,7,8,9-tetrakloro[1,3]oksazepin-1,5-dionske derivate **1b–10b**. Reakcije smo spremljali s TLC. S pomočjo FT IR spektroskopije in določitvijo temperature tališča smo karakterizirali pripravljene Schiffove baze; strukture oksazepinskih spojin **1b–10b** smo določili s pomočjo FT IR in ¹H NMR ter z določitvijo temperature tališča. Biološke aktivnosti oksazepinskih derivatov smo določili na bakterijah (*Staphylococcus aureus*, *Escherichia coli*, *Klebsiella spp.*) in glivi (*Geotrichum spp.*). Za različne spojine smo, v odvisnosti od uporabljenega organizma bakterije oz. glive, določili tudi različne aktivnosti.



Except when otherwise noted, articles in this journal are published under the terms and conditions of the Creative Commons Attribution 4.0 International License

Scientific paper

Studies on Morphology and Photoluminescent Properties of Tb³⁺ Doped YbPO₄ Nanostructures Synthesized by Different Synthetic Methods

Heena Khajuria, Manesh Kumar, Lobzang Tashi, Rajinder Singh, and Haq Nawaz Sheikh*

Department of Chemistry, University of Jammu, Jammu 180006, India

* Corresponding author: E-mail: hnsheikh@rediffmail.com

Received: 05-23-2019

Abstract

The morphology dependent optical properties of Tb³⁺ in YbPO₄ host lattice have been investigated. 10 % Terbium doped ytterbium phosphate (YbPO₄:Tb³⁺) nanostructures (NSs) were synthesized by five different synthetic methods i.e. sonochemical method, hydrothermal method, solvothermal method, sacrificial template method and coprecipitation method. Structural facets and optical properties of fabricated nanoparticles were studied in detail by powder X-ray diffraction (PXRD), Fourier transform infrared spectrum (FTIR), scanning electron microscopy (SEM), transmission electron microscopy (TEM), energy dispersive X-ray spectra (EDS), and photoluminescence (PL) techniques. We have investigated the impact of synthetic procedures employed on the morphology and uniformity of synthesized NSs and consequently on the optical properties of the NSs. The intense green emission from the nanophosphor shows that phosphor can be used in IR-sensors, LEDs and as solar spectrum converters.

Keywords: Sonochemical synthesis; hydrothermal synthesis; solvothermal synthesis; sacrificial template synthesis; coprecipitation synthesis; luminescence

1. Introduction

Phosphate compounds are suitable host matrices for lanthanide ions to fabricate luminescent substances. Among LnPO₄, ytterbium phosphate (YbPO₄), is well-known useful host lattice (materials) for lanthanide ions for the synthesis of phosphors.^{1–3} The optical properties of lanthanide based phosphors mostly depend on their shape, size, surface chemistry, uniformity and dimensionality. In general luminescent materials with small particle size have lower luminescence quantum efficiency and shorter fluorescence lifetime than larger particle size materials or their bulk counterparts.^{4,5} This is owing to low crystallinity and large number of surface defects associated with them. Reducing the size of particle to nano dimensions cause increase in the surface-to-volume ratio of the material which leads to dominance of surface effects.^{6–10} In addition to this, the presence of ligands/capping agents and surface-adsorbed ions/molecules (H₂O, CO₂) also lead to luminescence quenching. Molecules in proximity to surface of nanoparticles can diminish the intensity, since the vibrational states of chemical bonds like O-H, C-H or N-H

match the phonon states of the host material resulting in non-radiative relaxation of the excited lanthanide ions.^{11,12} These structural aspects in turn can be controlled by the synthesis methods and reaction conditions.^{13–17} The photoluminescent nanomaterials can be fabricated by various techniques *viz.*, hydrothermal, solvothermal, sonochemical assisted thermal decomposition, and co-precipitation etc. Hydrothermal and solvothermal methods endow some convenient advantages over the conventional methods, such as potential to control over the crystal growth, its simplicity and relatively low temperature for reaction.^{18–20} These methods permit exceptional control over morphology, particle size and crystallinity of material. Among these techniques, sonochemical method is the best method to synthesize nanostructures because it is green synthesis method carried out at room temperature.²¹ It is based on acoustic cavitation resulting from the continuous formation, growth and implosive collapse of bubbles in a liquid. It has become one of the useful, green, simple and fast methods for the synthesis as well as doping of nanostructures. Apart from these, the sacrificial template-directed chemical synthetic method based on the Kirkendall effect

has been established to be an effective approach to obtain the desired hollow inorganic materials.^{22,23} In this method, the shell of desired product forms around the surface of the sacrificial template and takes the shape of the template. Thus, various physicochemical changes evolved in the synthesis of nonmaterial under different synthetic conditions influence the phase, morphology and properties of nanostructures.

In the present work, 10% Terbium doped ytterbium phosphate ($\text{YbPO}_4:\text{Tb}^{3+}$) nanostructures were synthesized by five different synthetic methods such as hydrothermal method, solvothermal method, sacrificial template method, sonochemical method and co-precipitation method to study their effect on morphology and luminescent properties of as prepared nanomaterials. Tb^{3+} is chosen as dopant for doping YbPO_4 host matrices. Yb^{3+} ions act as sensitizer ion for Tb^{3+} ions which shows green emission.^{24–26} $\text{YbPO}_4:\text{Tb}^{3+}$ nanostructures were examined by powder X-ray diffraction (PXRD), Fourier transform infrared spectrum (FTIR), scanning electron microscopy (SEM), transmission electron microscopy (TEM), energy dispersive X-ray spectra (EDS), and photoluminescence (PL) techniques. The effect of synthesis method on the uniformity, structure and the optical properties of the $\text{YbPO}_4:\text{Tb}^{3+}$ nanostructures were studied in detail. Nanostructures of different morphology have been obtained through different synthesis routes. The intense green emission from the nanophosphor shows that phosphor can be used in IR-sensors, LEDs and as solar spectrum converters. The novelty aspect and the significance of the present work with respect to the existing literature reports on related nanostructures lies in the tuning of photoluminescence emission intensity by varying the morphology and grain size of synthesized phosphors via five different synthetic methods.

2. Experimental

2.1. Materials

Ytterbium (III) nitrate pentahydrate $\text{Yb}(\text{NO}_3)_3 \cdot 5\text{H}_2\text{O}$ (99.9 %), terbium(III) nitrate hydrate $\text{Tb}(\text{NO}_3)_3 \cdot \text{H}_2\text{O}$ (99.9 %) and ammonium dihydrogen phosphate were purchased from Alfa Aesar (Massachusetts, United States) and used as received without further purification. Urea was purchased from Himedia (Mumbai, India) and sodium hydroxide from Sigma Aldrich (United States). Deionized water was used throughout.

2.2. Synthesis of $\text{YbPO}_4:\text{Tb}^{3+}$ Nanostructures

2.2. a Sonochemical Method

In a typical synthesis, 20 mL aqueous solution of 0.9 mmol $\text{Yb}(\text{NO}_3)_3 \cdot \text{H}_2\text{O}$ and 0.1 mmol $\text{Tb}(\text{NO}_3)_3 \cdot \text{H}_2\text{O}$ was sonicated for 15 minutes. Thereafter 10 mL aqueous solution of 1 mmol $\text{NH}_4\text{H}_2\text{PO}_4$ was added dropwise to the above mentioned mixture. The pH of solution is main-

tained at 3 by adding ammonia solution. The mixture was then sonicated for additional 1 h. After that, the precipitates were collected and washed with deionised water and ethanol and then dried at 70 °C for 12 hrs.

2.2. b Hydrothermal method

In a typical synthesis, 0.9 mmol (0.344 g) of $\text{Yb}(\text{NO}_3)_3 \cdot 5\text{H}_2\text{O}$ was added to 10 mL aqueous solution of 1 mmol (0.1921 g) citric acid. The reaction mixture was stirred for 10 minutes and after that an aqueous solution of 0.5 mmol (0.057 g) $\text{NH}_4\text{H}_2\text{PO}_4$ was added dropwise. After further vigorous stirring for 30 minutes more, as obtained mixture was transferred into a autoclave, sealed and maintained at 180 °C for 18 hrs. Once the autoclave cooled to room temperature naturally, the precipitates were collected, centrifuged and washed with deionised water and ethanol three times and then dried at 70 °C for 12 hrs. in air.²⁷

2.2. c Solvothermal Method

In a typical synthesis, 0.9 mmol (0.323 g) of $\text{Yb}(\text{NO}_3)_3 \cdot 5\text{H}_2\text{O}$ and 0.1 mmol (0.034 g) $\text{Tb}(\text{NO}_3)_3 \cdot \text{H}_2\text{O}$ were added to mixture of 5 mL oleic acid and 5 mL ethylene glycol. The reaction mixture was vigorously stirred for 10 minutes. After that solution of 0.5 mmol (0.057 g) $\text{NH}_4\text{H}_2\text{PO}_4$ in ethylene glycol was added dropwise to the above mentioned reaction mixture. After further stirring for 30 minutes, the mixture so obtained was transferred into autoclave, sealed and heated at 180 °C for 18 hrs. The autoclave was cool to room temperature naturally; the product was centrifuged, washed with deionised water, followed by ethanol then dried at 70 °C for 12 hrs. in air.

2.2. d Coprecipitation Method

20 mL aqueous solution of 0.9 mmol (0.323 g) of $\text{Yb}(\text{NO}_3)_3 \cdot 5\text{H}_2\text{O}$ and 0.1 mmol (0.034 g) $\text{Tb}(\text{NO}_3)_3 \cdot \text{H}_2\text{O}$ and 20 mL aqueous solution of $\text{NH}_4\text{H}_2\text{PO}_4$ was stirred for 15 min. Two solutions were mixed together and stirred for another 10 minutes. After that solution of NaOH was added to reaction mixture of $\text{Yb}(\text{NO}_3)_3 \cdot 5\text{H}_2\text{O}$, $\text{Tb}(\text{NO}_3)_3 \cdot \text{H}_2\text{O}$ and $\text{NH}_4\text{H}_2\text{PO}_4$. The reaction mixture was vigorously stirred at 80 °C for 30 minutes. The as prepared sample was collected, centrifuged, washed with deionised water and ethanol three times and then dried at 70 °C for 12 h in air.²⁸

2.2. e Sacrificial Template Method

Synthesis of $\text{Yb}(\text{OH})\text{CO}_3$: 10 mol% Tb^{3+} template: The $\text{Yb}(\text{OH})\text{CO}_3:\text{Tb}^{3+}$ precursor was prepared by urea-based homogeneous precipitation process. In a typical synthesis, 0.9 mmol (0.323 g) $\text{Yb}(\text{NO}_3)_3 \cdot 5\text{H}_2\text{O}$ and 0.1 mmol (0.034 g) $\text{Tb}(\text{NO}_3)_3 \cdot \text{H}_2\text{O}$ were dissolved in 50 mL deionized water. Then, 2.0 g of urea was added into the as prepared lan-

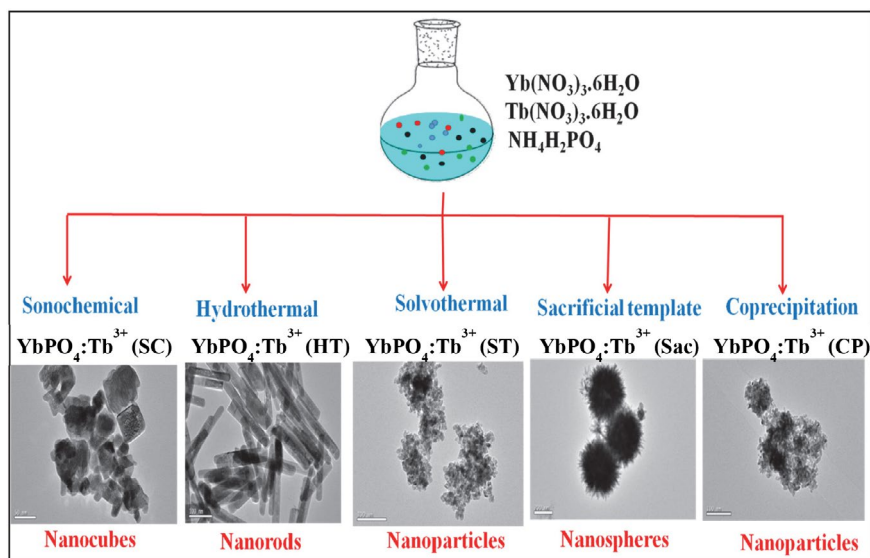


Figure 1. Overview of obtained $\text{YbPO}_4:\text{Tb}^{3+}$ nanostructures

thanide aqueous solution with continues stirring. The solution was stirred vigorously for 2 h at room temperature and heated to 90 °C for another 2 h in an oil bath in order to get the milky-white suspension. The precipitated $\text{Yb}(\text{OH})\text{CO}_3:\text{Tb}^{3+}$ were filtered and then washed with ethanol and deionised water three times.

Synthesis of $\text{YbPO}_4: 10 \text{ mol}\% \text{ Tb}^{3+}$: In a typical synthesis, the as-prepared sample of $\text{Yb}(\text{OH})\text{CO}_3:\text{Tb}^{3+}$ rods acting as template was dispersed into 15 mL deionized water by ultrasonic treatment for 30 min, labelled as solution A. A separate solution B was prepared by dissolving 1 mmol (0.115 g) $\text{NH}_4\text{H}_2\text{PO}_4$ in 15 mL deionised water and mixed with solution A with vigorous agitation. Finally, 30 mL of the resulting reaction mixture was transferred into Teflon lined stainless steel autoclave, seal and heated at 180 °C for 18 hrs. The autoclave was cool down to room temperature naturally. The products were collected, centrifuged and washed with DI water and ethanol three times and dried at 60 °C for 24 hrs in air.²⁹

The samples prepared by sonochemical method, hydrothermal method, solvothermal method, sacrificial template method and coprecipitation method are designated as $\text{YbPO}_4:\text{Tb}^{3+}$ (SC), $\text{YbPO}_4:\text{Tb}^{3+}$ (HT), $\text{YbPO}_4:\text{Tb}^{3+}$ (ST), $\text{YbPO}_4:\text{Tb}^{3+}$ (Sac), $\text{YbPO}_4:\text{Tb}^{3+}$ (CP) respectively as shown in Fig. 1.

2. 3. Characterization

The crystalline structure of the powder samples was assessed by X-ray diffraction using a Panalytical Xpert Pro diffractometer with Cu-K α radiation at 45 kV and 40 mA, and 2 θ ranging from 10° to 70°. The infrared spectra of NRs were measured on a Shimadzu Prestige-21 Fourier Transform spectrometer over the range of wave number 4000 – 400 cm^{-1} , and standard KBr pellet technique was employed. The morphology of the samples was inspected

using a field emission scanning electron microscope (FE-SEM) and transmission electron microscope (TEM). TEM images were taken using a Hitachi (H-7500) transmission electron microscope at an accelerating voltage of 100 kV. To obtain the TEM images, ethanolic solution of the sample is first subjected to sonication to form a very fine suspension. 10 μL of this suspension is then carefully poured onto a carbon copper grid using a micropipette and dried under an electric light. The dried samples are then loaded into the TEM machine. SEM was performed using Nova Nano SEM-450 field emission scanning electron microscope at an accelerating voltage of 5.0 kV. For getting SEM images, the well dried samples are fixed on a metal grid with adhesive, dehydrated and then observed in the microscope. Steady state excitation and emission spectra of the samples were recorded on a Cary Eclipse spectrophotometer equipped with a Xenon lamp as the excitation source. The analysis of optical property of prepared samples was conducted in the powder form, as the lanthanide phosphates are insoluble in most of the solvents. All of the measurements were performed at room temperature.

Particle size determination

Each SEM image has a measurement scale at the bottom left corner for size measurements. Using *Image J software*, particle size of each clearly visible nanoparticle in the image was measured. After size of all of the nanoparticles was measured, a histogram was created in order to show the size distribution of the nanoparticles in each sample.

3. Results and Discussion

3. 1. PXRD Measurements

The crystalline nature and phase purity of the as prepared nanocomposites were explored by PXRD study. Fig.

2 depicts powder X-ray diffraction patterns of the undoped YbPO_4 , $\text{YbPO}_4:\text{Tb}^{3+}$ (SC), $\text{YbPO}_4:\text{Tb}^{3+}$ (HT), $\text{YbPO}_4:\text{Tb}^{3+}$ (ST), $\text{YbPO}_4:\text{Tb}^{3+}$ (Sac) and $\text{YbPO}_4:\text{Tb}^{3+}$ (CP) nanostructures. The PXRD patterns of all prepared phases are in good agreement with the tetragonal phase of YbPO_4 (JCPDS card no. 45-0530) space group ($I4_1/amd$).^{30, 31} No other phase impurity was detected by PXRD analysis, demonstrating the phase purity of as prepared nanostructure. The result indicates that the doping of Tb^{3+} ions in the YbPO_4 nanocrystals has little influence on its crystal structure due to the similar ionic radius of $\text{Tb}^{3+} = (0.104 \text{ nm})$ and $\text{Yb}^{3+} = (0.098 \text{ nm})$. The broadened peaks in PXRD patterns suggest the nano range of as prepared nanomaterials. The broadening of PXRD peaks can be correlated with the particle size measured from SEM images using *Image J software*. The particle size of $\text{YbPO}_4:\text{Tb}^{3+}$ (SC), $\text{YbPO}_4:\text{Tb}^{3+}$ (HT), $\text{YbPO}_4:\text{Tb}^{3+}$ (ST), $\text{YbPO}_4:\text{Tb}^{3+}$ (Sac), and $\text{YbPO}_4:\text{Tb}^{3+}$ (CP) nanostructures is found to be $\sim 170 \text{ nm}$, $\sim 600 \times 80 \text{ nm}$, $\sim 70 \text{ nm}$, $\sim 300\text{-}400 \text{ nm}$, $\sim 100 \text{ nm}$ respectively from SEM images. The observed particle size of nanostructures is in accordance to the broadening of PXRD peaks.

3. 2. FTIR Spectra

The presence of chelating agent and chemical composition on the surface of the nanomaterials have been examined by FT-IR spectra. Fig. 3 shows the FT-IR spectra of undoped YbPO_4 , $\text{YbPO}_4:\text{Tb}^{3+}$ (SC), $\text{YbPO}_4:\text{Tb}^{3+}$ (HT), $\text{YbPO}_4:\text{Tb}^{3+}$ (ST), $\text{YbPO}_4:\text{Tb}^{3+}$ (Sac) and $\text{YbPO}_4:\text{Tb}^{3+}$ (CP) nanostructures. The bands near 1100 cm^{-1} are assigned the stretching modes of the PO_4^{3-} groups of as prepared samples. The splitting of the band indicated the presence of low symmetry crystal phase. The two characteristics bending vibrational modes of the PO_4^{3-} group are at 650 and 520 cm^{-1} .^{32, 33} It can be noted that when YbPO_4 host is

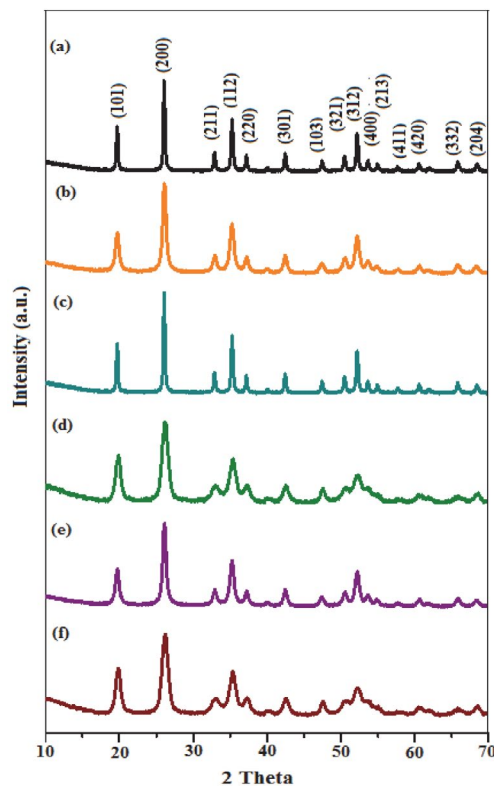


Figure 2. PXRD patterns of (a) undoped YbPO_4 (b) $\text{YbPO}_4:\text{Tb}^{3+}$ (SC) (c) $\text{YbPO}_4:\text{Tb}^{3+}$ (HT) (d) $\text{YbPO}_4:\text{Tb}^{3+}$ (ST) (e) $\text{YbPO}_4:\text{Tb}^{3+}$ (Sac) (f) $\text{YbPO}_4:\text{Tb}^{3+}$ (CP)

doped Tb^{3+} ions the infra red band around 1100 cm^{-1} slightly shifted to higher wave number because of stronger interaction between Tb^{3+} and PO_4^{3-} as compare to Yb^{3+} and PO_4^{3-} units.³⁴ The presence of hydroxyl groups and water molecules on surface of synthesized nanomaterials can be ascertained by infrared bands in the range of $3200\text{-}3600 \text{ cm}^{-1}$ (stretching vibrations) and 1625 cm^{-1} (bend-

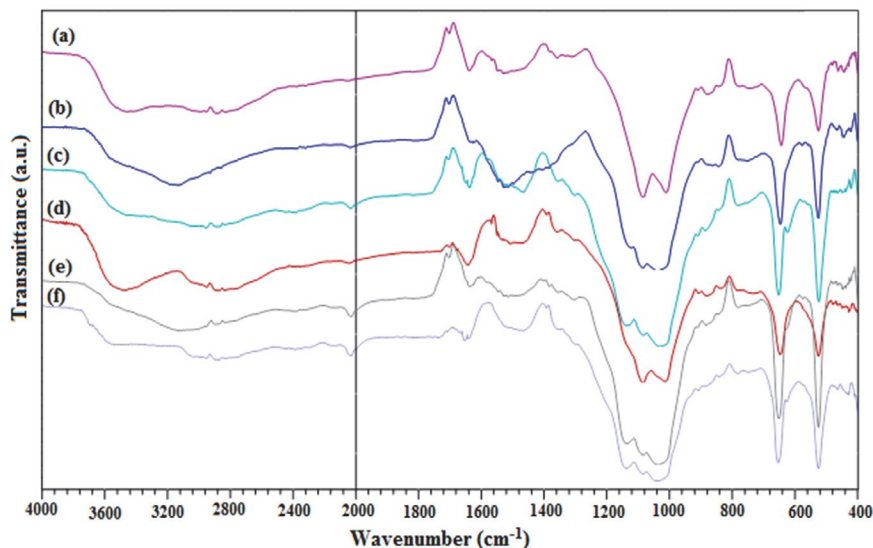


Figure 3. FTIR spectra of (a) undoped YbPO_4 (b) $\text{YbPO}_4:\text{Tb}^{3+}$ (SC) (c) $\text{YbPO}_4:\text{Tb}^{3+}$ (HT) (d) $\text{YbPO}_4:\text{Tb}^{3+}$ (ST) (e) $\text{YbPO}_4:\text{Tb}^{3+}$ (Sac) (f) $\text{YbPO}_4:\text{Tb}^{3+}$ (CP)

ing). The characteristic IR bands (ν_{as} 1680 and ν_s 1384 cm^{-1}) of ligands (citric acid and oleic acid) are not appeared clearly in FTIR spectra of $\text{YbPO}_4:\text{Tb}^{3+}$ (HT) and $\text{YbPO}_4:\text{Tb}^{3+}$ (ST) due to their overlapping with other peaks.

3. 3. SEM and TEM Studies

The structured and morphological facets of the as synthesized nanostructures were probed by the scanning electron microscopy (SEM) and transmission electron mi-

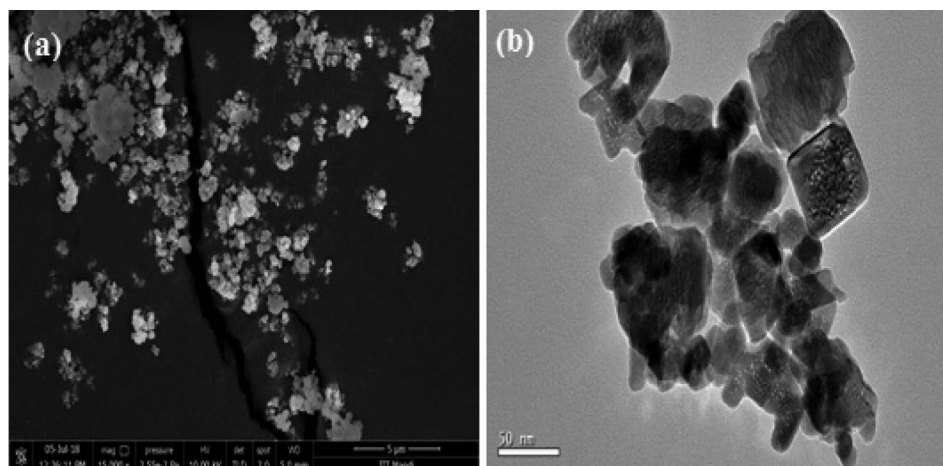


Figure 4. (a) SEM and (b) TEM images of $\text{YbPO}_4:\text{Tb}^{3+}$ (SC)

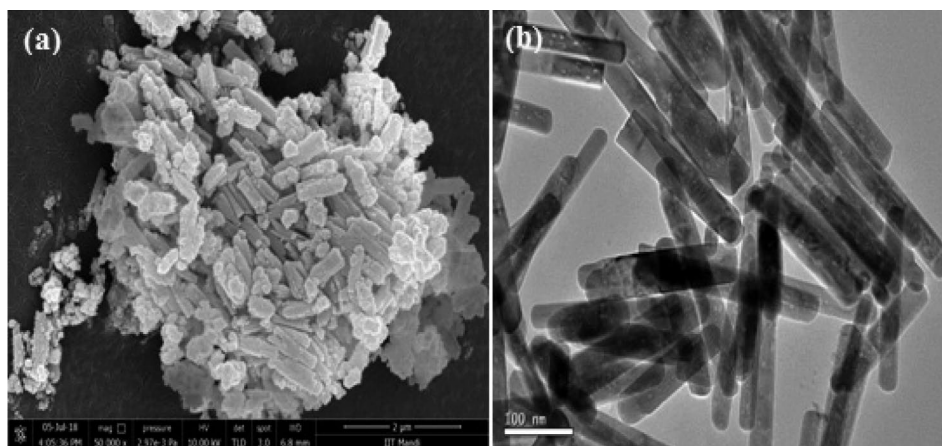


Figure 5. (a) SEM and (b) TEM images of $\text{YbPO}_4:\text{Tb}^{3+}$ (HT)

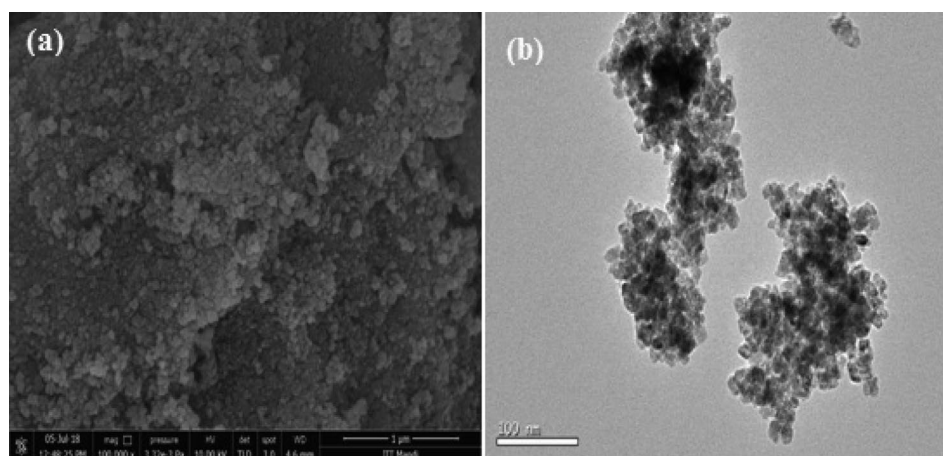


Figure 6. (a) SEM and (b) TEM images of $\text{YbPO}_4:\text{Tb}^{3+}$ (ST)

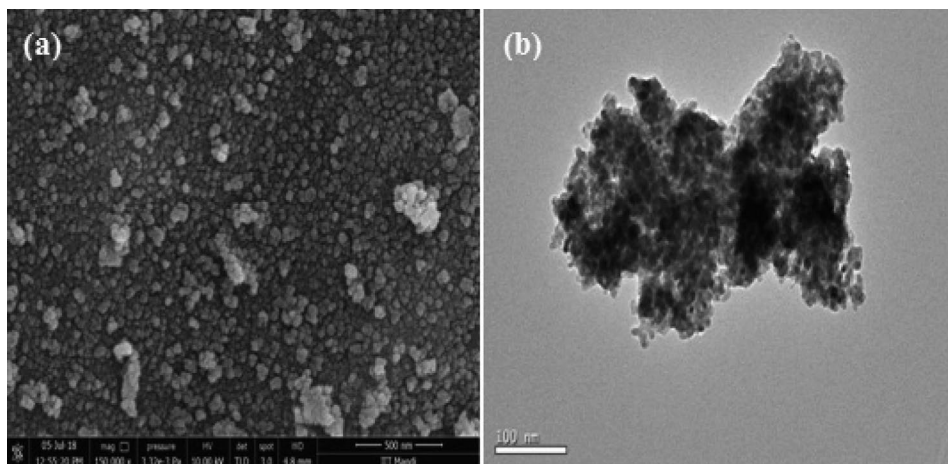


Figure 7. (a) SEM and (b) TEM images of $\text{Yb(OH)CO}_3\text{:Tb}^{3+}$ precursor

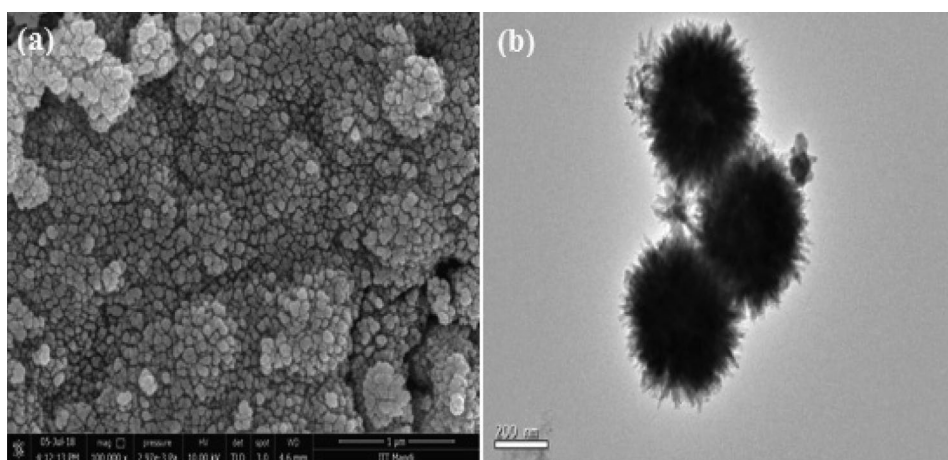


Figure 8. (a) SEM and (b) TEM images of $\text{YbPO}_4\text{:Tb}^{3+}$ (Sac)

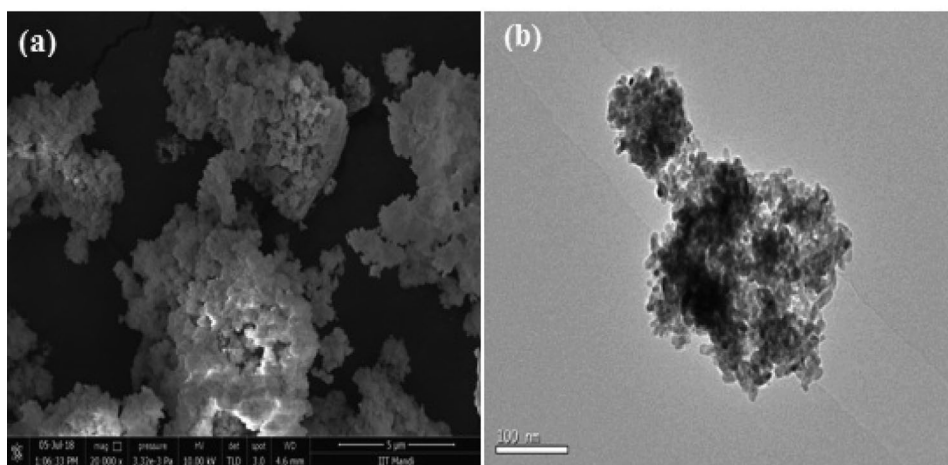


Figure 9. (a) SEM and (b) TEM images of $\text{YbPO}_4\text{:Tb}^{3+}$ (CP)

scopy (TEM) analysis. The scanning electron and transmission electron micrographs of terbium doped ytterbium phosphate nanocomposite as synthesized via different synthetic procedures are shown in Figs. 4–9. SEM images of $\text{YbPO}_4\text{:Tb}^{3+}$ (SC) dispose the square shaped

flakes like morphology of particle size ~ 170 nm. The nanorods like morphology of $\text{YbPO}_4\text{:Tb}^{3+}$ of size 600×80 nm was obtained via hydrothermal method (Fig 5). The $\text{YbPO}_4\text{:Tb}^{3+}$ samples synthesized by solvothermal and co-precipitation method show the nanoparticles like mor-

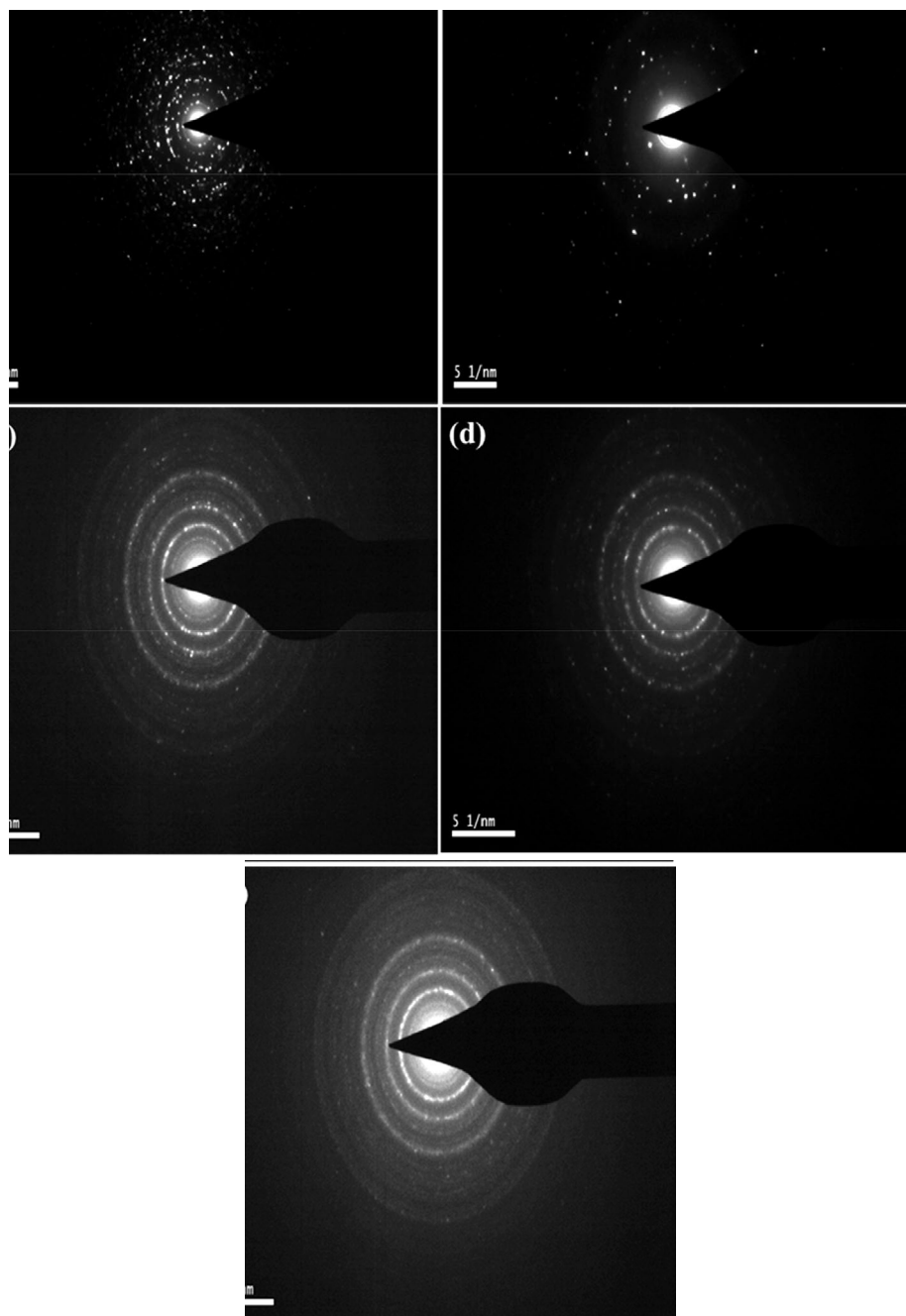


Figure 10. SAED pattern of (a) $\text{YbPO}_4:\text{Tb}^{3+}$ (SC) (b) $\text{YbPO}_4:\text{Tb}^{3+}$ (HT) (c) $\text{YbPO}_4:\text{Tb}^{3+}$ (ST) (d) $\text{YbPO}_4:\text{Tb}^{3+}$ (Sac) (e) $\text{YbPO}_4:\text{Tb}^{3+}$ (CP)

phology with particle size of 70 and 100 nm respectively. The oleic acid and ethylene glycol may play role in the fabrication of nanoparticles. The overall mechanism of their action is such that their molecules embrace the nanocrystals and control their excess growth. Thus, in these syntheses, small sized particles are obtained. Fig. 7 shows $\text{Yb}(\text{OH})\text{CO}_3:\text{Tb}^{3+}$ precursor SEM and TEM micrographs. It shows the spherical morphology of precursor. After its treatment with phosphate source spherical $\text{YbPO}_4:\text{Tb}^{3+}$ nanostructures are formed with diameter 300-400 nm and display rather rough morphological features as compare to the

precursor nanostructures. Thus, nanostructures of different morphology are obtained when synthesis is carried out by different synthetic methods. TEM images also agree well with the SEM results. The selected area electron diffraction (SAED) patterns of as synthesized nanomaterial were shown in Fig. 10. The presence of bright spots in SAED patterns of $\text{YbPO}_4:\text{Tb}^{3+}$ (SC) and $\text{YbPO}_4:\text{Tb}^{3+}$ (HT) indicate their monocrystalline nature (Fig. 10 a, b). However, SAED patterns of $\text{YbPO}_4:\text{Tb}^{3+}$ (ST), $\text{YbPO}_4:\text{Tb}^{3+}$ (Sac) and $\text{YbPO}_4:\text{Tb}^{3+}$ (CP) shows diffuse rings indicating their polycrystalline nature.

3. 4. EDS Analysis

Energy dispersive X-ray spectra were recorded to investigate the presence of dopant (Tb^{3+}) and its concentration in the doped $YbPO_4$ nanoparticles represented in Fig. 11. The EDS results suggest that the nanocrystal fabricated

$YbPO_4:Tb^{3+}$ nanostructures are made up of Yb, Tb, P and O. Table 1 represents the weight percent (Wt. %) and atomic percent (At. %) data for synthesized $YbPO_4:Tb^{3+}$ phases. There is a slight variation in weight and atomic % of constituents is found, as synthesized by different synthetic routes.

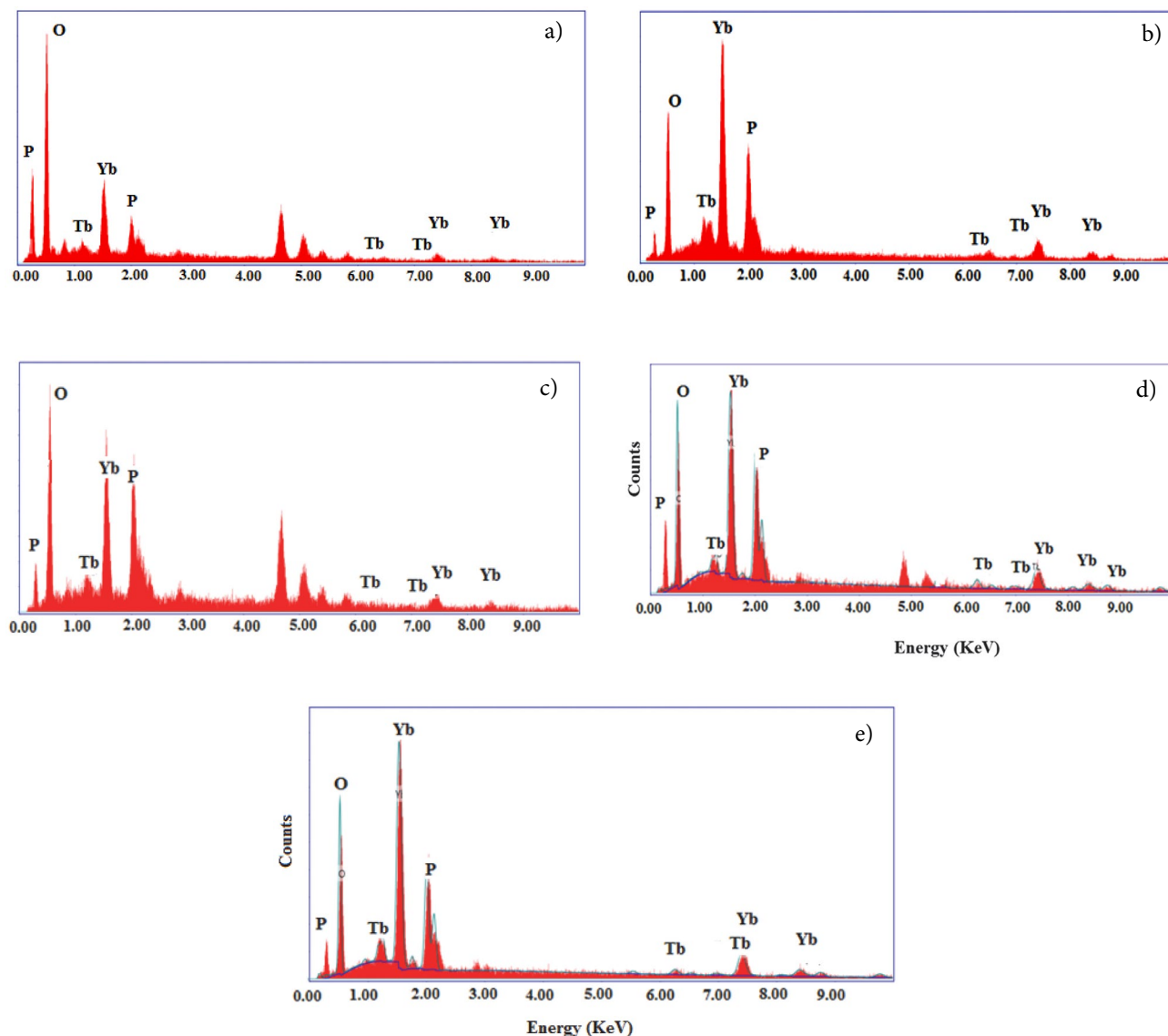


Figure 11. EDS spectra of (a) $YbPO_4:Tb^{3+}$ (SC) (b) $YbPO_4:Tb^{3+}$ (HT) (c) $YbPO_4:Tb^{3+}$ (ST) (d) $YbPO_4:Tb^{3+}$ (Sac) (e) $YbPO_4:Tb^{3+}$ (CP)

Table 1. Atomic and Weight % of elements present in $YbPO_4:Tb^{3+}$ nanostructures

Elements	$YbPO_4:Tb^{3+}$ (SC)		$YbPO_4:Tb^{3+}$ (HT)		$YbPO_4:Tb^{3+}$ (HT)		$YbPO_4:Tb^{3+}$ (HT)		$YbPO_4:Tb^{3+}$ (CP)	
	Wt. %	At. %	Wt. %	At. %	Wt. %	At. %	Wt. %	At. %	Wt. %	At. %
Ytterbium	30.93	4.82	51.48	12.51	34.22	5.34	58.16	16.46	56.39	14.72
Terbium	9.27	1.57	8.48	2.24	0.42	0.07	8.78	2.71	7.53	2.14
Phosphorus	8.91	7.77	15.71	21.32	19.30	16.83	13.73	21.70	13.70	19.98
Oxygen	50.88	85.83	24.33	63.93	46.05	77.75	19.33	59.14	22.37	63.16

3. 5. Photoluminescence

The excitation and emission photoluminescence spectra of $\text{YbPO}_4:\text{Tb}^{3+}$ nanostructures are shown in Fig. 12 and Fig. 13 respectively. We have selectively monitored excitation of Tb^{3+} doped YbPO_4 nanostructures at 543 nm ($^5\text{D}_4 \rightarrow ^7\text{F}_5$ transition). The prominent peaks in the range of 200–280 nm may be attributed to the transitions of $4f^8 \rightarrow 4f^75d^1$ of Tb^{3+} .³⁵ The other weak excitation bands ranging from 300–400 nm can be assigned to the $f-f$ transition of Tb^{3+} . These bands are significant for emission spectra exhibited by UV-Chips.³⁶ The highest intensity peak at 370 nm is due to $^7\text{F}_6 \rightarrow ^5\text{G}_6$ transition of Tb^{3+} . The excitation spectra of $\text{YbPO}_4:\text{Tb}^{3+}$ nanostructures imply that the phosphor can convert ultraviolet wavelength to visible wavelength on emission. Thus the conversion of ultraviolet light into visible light indicates that the fabricated $\text{YbPO}_4:\text{Tb}^{3+}$ can act as ultraviolet light absorber in solar cells to show effective conversion efficiency. In the emission spectrum of $\text{YbPO}_4:\text{Tb}^{3+}$ four prominent peaks near 490, 543, 584 and 621 nm are observed when selectively excited at 394 nm. These emission peaks are assigned to the transitions $^5\text{D}_4 \rightarrow ^7\text{F}_6$ (490 nm), $^5\text{D}_4 \rightarrow ^7\text{F}_5$ (543 nm), $^5\text{D}_4 \rightarrow ^7\text{F}_4$ (584 nm) and $^5\text{D}_4 \rightarrow ^7\text{F}_3$ (621 nm).³⁷ The $^5\text{D}_4 \rightarrow ^7\text{F}_5$ transition is stronger comparing with other transitions and is responsible for green light emission. From the PL spectra, the variation in the emission intensity is observed for $\text{LaPO}_4:\text{Tb}^{3+}$ prepared in different conditions. It is worth noting that $\text{YbPO}_4:\text{Tb}^{3+}$ (Sac) exhibit highest and $\text{YbPO}_4:\text{Tb}^{3+}$ (ST) possess least intense emission.

The difference in photoluminescence intensity can be interpreted from surface area, and particle size aspects of phosphor, as PL intensity is highly affected by these parameters.^{38–41} It is well established fact that the surface area of nanoparticles increases with a decrease in crystallite size. In general, larger the surface area, higher will be the defects into the crystal of a phosphor.^{42, 43} It is seen that defects into phosphor crystal have serious impact on photoluminescence emission of materials. These defects lead to non-radioactive decay of electrons and holes recombination. The number of electron/hole recombinations via radiative pathways must be increased in order to generate intense emission from the material. The efficiency of radiative decay can be enhanced by defects minimizations which in turn can controlled by the degree of crystallinity and surface area. The efficiency of radiative decay can be improved by increasing crystallinity and decreasing surface area. From the SAED and XRD patterns shown in Fig. 2 and Fig. 10, it is clear that the all the prepared samples are highly crystalline. However, they differ in their particle size and morphology. Herein, the particle size for $\text{YbPO}_4:\text{Tb}^{3+}$ in the descending order are $\text{YbPO}_4:\text{Tb}^{3+}$ (Sac) > $\text{YbPO}_4:\text{Tb}^{3+}$ (HT) > $\text{YbPO}_4:\text{Tb}^{3+}$ (SC) > $\text{YbPO}_4:\text{Tb}^{3+}$ (CP) > $\text{YbPO}_4:\text{Tb}^{3+}$ (ST) which is consistent with the luminescence intensity. Highest PL intensity is observed from $\text{YbPO}_4:\text{Tb}^{3+}$ (Sac) which may be due to

its larger particle size, spherical morphology and lower surface area. $\text{YbPO}_4:\text{Tb}^{3+}$ prepared by hydrothermal method possesses nanorods like morphology. The phosphors with nanorod morphology presented directional growth and lower surface area resulting in the enhanced emission intensity. The particle sizes of the samples prepared by sonochemical and coprecipitation methods are lower than that of $\text{YbPO}_4:\text{Tb}^{3+}$ (Sac) and $\text{YbPO}_4:\text{Tb}^{3+}$ (HT) and PL intensity is also less intense than that of $\text{YbPO}_4:\text{Tb}^{3+}$ (Sac) and $\text{YbPO}_4:\text{Tb}^{3+}$ (HT) indicating correlation of particle size and PL intensity. The particle size of the $\text{YbPO}_4:\text{Tb}^{3+}$ (ST) is lowest and thus, surface area will be highest. Therefore, it can be interpreted that a number of holes and electron in the excited state may be expected to return to the ground state through non-radiative decay processes. Thus, it possesses lowest PL intensity. Moreover, another reason for their lowest PL intensity may be the presence of surface adsorbed solvent molecules which quenches the radiative transition.

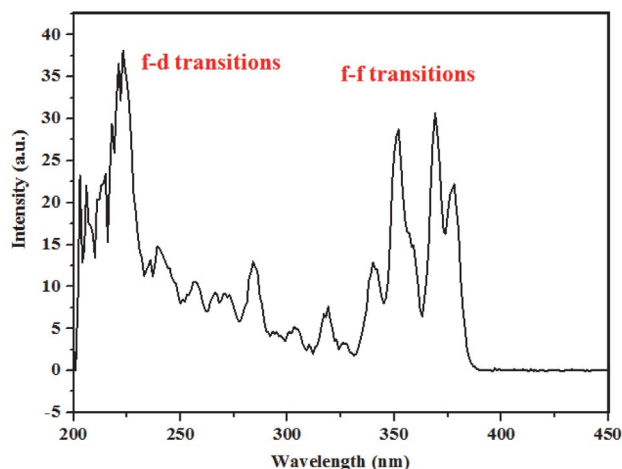


Figure 12. Excitation spectra of $\text{YbPO}_4:\text{Tb}^{3+}$ nanostructures

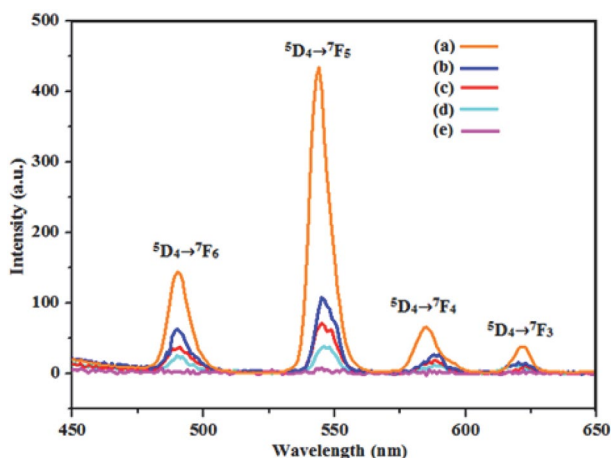


Figure 13. Emission spectra of (a) $\text{YbPO}_4:\text{Tb}^{3+}$ (Sac) (b) $\text{YbPO}_4:\text{Tb}^{3+}$ (HT) (c) $\text{YbPO}_4:\text{Tb}^{3+}$ (SC) (d) $\text{YbPO}_4:\text{Tb}^{3+}$ (CP) (e) $\text{YbPO}_4:\text{Tb}^{3+}$ (ST)

4. Conclusions

YbPO₄:Tb³⁺ nanostructures have been synthesized using five different synthetic methods i.e. sonochemical, hydrothermal, solvothermal, coprecipitation and sacrificial template assisted method. Tetragonal phase of YbPO₄:Tb³⁺ nanostructures have been confirmed by PXRD study. SEM and TEM studies show the nanorods, nanosphere and nanoparticle like morphology of YbPO₄:Tb³⁺ prepared by different methods. Variation in intensity of Tb³⁺ emission peaks is found for YbPO₄:Tb³⁺ nanostructures synthesized by different methods. The difference in photoluminescence intensity can be interpreted in terms of surface area and crystallite size aspects of phosphor. Smaller is the particle size, larger would be the surface area. This results in larger number of defects in the crystal lattice which in turn has negative impact on photoluminescence efficiency. Highly intense Tb³⁺ emission peaks are observed for YbPO₄:Tb³⁺ spheres having diameter 300–400 nm prepared by sacrificial template method and least intense that for YbPO₄:Tb³⁺ nanoparticles obtained by solvothermal method with crystallite size of 70 nm. This shows the dependence of photoluminescence on morphology and particle size. The intense green emission from the YbPO₄:Tb³⁺ phosphor indicates that phosphor can be used in LEDs.

Acknowledgements

We would like to acknowledge Advanced Material Research Centre (AMRC), IIT Mandi, SMVDU Katra for PL studies and Sophisticated Analytical Instrumentation Facility (SAIF), Panjab University for their technical support.

5. References

- Z. Wenyan, N. Yaru, H. Wenjuan, L. Chunhua, X. Zhongzi, *J. Rare Earths* **2010**, *28*, 299–302. DOI:10.1016/S1002-0721(10)60337-7
- Z. Xu, P. Ma, C. Li, Z. Hou, X. Zhai, S. Huang, J. Lin, *Biomaterials* **2011**, *32*, 4161–4173. DOI:10.1016/j.biomaterials.2011.02.026
- S. Lee, K. Teshima, S. Mori, M. Endo, S. Oishi, *Cryst. Growth Des.* **2010**, *10*, 1693–1698. DOI:10.1021/cg9012729
- F. Wang, J. Wang, X. Liu, *Angew. Chem. Int. Ed.* **2010**, *49*, 7456–7460. DOI:10.1002/anie.201003959
- N. K. Sahu, R. S. Ningthoujam, D. J. Bahadur, *Appl. Phys.* **2012**, *112*, 014306 (1–12). DOI:10.1063/1.4731644
- J. C. Boyer, M. P. Manseau, J. I. Murray, F. C. J. M. van Veggel, *Langmuir* **2010**, *26*, 1157–1164. DOI:10.1021/la902260j
- A. Yin, Y. Zhang, L. Sun, C. Yan, *Nanoscale* **2010**, *2*, 953–959. DOI:10.1039/b9nr00397e
- A. Huignard, V. Buissette, A.-C. Franville, T. Gacoin, J.-P. Boilot, *J. Phys. Chem. B* **2003**, *107*, 6754–6759. DOI:10.1021/jp0342226
- X. Bai, H. Song, G. Pan, Z. Liu, S. Lu, W. Di, X. Ren, Y. Lei, Q. Dai, L. Fan, *Appl. Phys. Lett.* **2006**, *88*, 143104 (1–3). DOI:10.1063/1.2187518
- R. S. Loitongbam, N. S. Singh, W. R. Singh, R. S. Ningthoujam, *J. Lumin.* **2013**, *134*, 14–23. DOI:10.1016/j.jlumin.2012.09.026
- Y. Wang, L.P. Tu, J. W. Zhao, Y. J. Sun, X. G. Kong, H. Zhang, *J. Phys. Chem. C* **2009**, *113*, 7164–7169. DOI:10.1021/jp9003399
- H. Schafer, P. Ptacek, K. Kompe, M. Haase, *Chem. Mater.* **2007**, *19*, 1396–1400. DOI:10.1021/cm062385b
- Y. Yang, *Mater. Sci. Eng. B* **2013**, *178*, 807–810. DOI:10.1016/j.mseb.2013.03.017
- T. Grzyb, A. Gruszczyka, R. J. Wiglusz, S. Lis, *J. Mater. Chem. C* **2013**, *1*, 5410–5418. DOI:10.1039/c3tc31100g
- M. Yang, H. You, Y. Huang, G. Jia, Y. Song, N. Guo, K. Liu, Y. Zheng, H. Zhang, *CrystEngComm* **2010**, *12*, 2865–2870. DOI:10.1039/b921258b
- S. Devi, S. Kelkar, V. Kashid, H. G. Salunke, N. M. Gupta, *RSC Adv.* **2013**, *3*, 16817–16828. DOI:10.1039/c3ra43477j
- S. Kar, S. K. Panda, B. Satpati, P. V. Satyam, S. Chaudhuri, *J. Nanosci. Nanotechnol.* **2006**, *6*, 1–6. DOI:10.1166/jnn.2006.532
- K. Byrappa, T. Adschiri, *Prog. Cryst. Growth & Charact.* **2007**, *53*, 117–166. DOI:10.1016/j.pcrysgrow.2007.04.001
- M. Shandilya, R. Rai, J. Singh, *Adv. Appl. Ceram.* **2016**, *115*, 354–376. DOI:10.1080/17436753.2016.1157131
- H. Hayashi, Y. Hakuta, *Materials* **2010**, *3*, 3794–3817. DOI:10.3390/ma3073794
- H. Xu, B. W. Zeiger, K. S. Suslick, *Chem. Soc. Rev.* **2013**, *42*, 2555–2567. DOI:10.1039/C2CS35282F
- G. Li, L. Li, M. Li, Y. Song, H. Zou, L. Zou, X. Xu, S. Gan, *Mater. Chem. Phys.* **2012**, *133*, 263–268. DOI:10.1016/j.matchemphys.2012.01.020
- B. Yan, X. Xiao, *Nanoscale Res. Lett.* **2010**, *5*, 1962–1969. DOI:10.1007/s11671-010-9733-8
- T. Grzyb, R. J. Wiglusz, A. Gruszczyka, S. Lis, *Dalton Trans.* **2014**, *43*, 17255–17264. DOI:10.1039/C4DT02234C
- T. Grzyb, K. Kubasiewicz, A. Szczeszak, S. Lis, *Dalton Trans.* **2015**, *44*, 4063–4069. DOI:10.1039/C4DT03667K
- K. Prorok, M. Pawlyta, W. Stręk, A. Bednarkiewicz, *Chem. Mater.* **2016**, *28*, 2295–2300. DOI:10.1021/acs.chemmater.6b00353
- H. Khajuria, J. Ladol, S. Khajuria, M.S. Shah, H.N. Sheikh, *Mater. Res. Bull.* **2016**, *80*, 150–158. DOI:10.1016/j.materresbull.2016.03.022
- S. Verma, K. K. Bamzai, *J. Rare Earths* **2015**, *33*, 535–544. DOI:10.1016/S1002-0721(14)60453-1
- Z. Yi, W. Lu, C. Qian, T. Zeng, L. Yin, H. Wang, L. Rao, H. Liu, S. Zeng, *Biomater. Sci.* **2014**, *2*, 1404–1411. DOI:10.1039/C4BM00158C
- W. Wang, D. Xu, X. Wei, K. Chen, *Int. J. Nanomedicine* **2014**, *9*, 4879–4891. DOI:10.2147/IJN.S62678
- W. O. Milligan, D. F. Mullica, G. W. Beall, L. A. Boatner, Structures of ErPO₄, TmPO₄, and YbPO₄, *Acta Cryst C* **1983**, *39*, 23–24. DOI:10.1107/S0108270183003467
- M. Ferhi, K. H. Naifer, M. Ferid, *J. Rare Earths* **2009**, *27*, 182–186. DOI:10.1016/S1002-0721(08)60216-1

33. G. M. Begun, G. W. Beall, L. A. Boatner, W. J. Gregor, *J. Raman Spectrosc.* **1981**, *11*, 273–278. DOI:10.1002/jrs.1250110411
34. K. N. Konou, M. Haris, Y. Lare, M. Baneto, K. Napo, *Pramana J. Phys.* **2016**, *87*, 1–7. DOI:10.1007/s10854-017-7857-7
35. M. L. Debasu, D. Ananias, J. Rocha, O. L. Malta, L. D. Carlos, *Phys. Chem. Chem. Phys.* **2013**, *15*, 15565–15571. DOI:10.1039/c3cp52365a
36. W. B. Bu, Z. L. Hua, L. X. Zhang, H. R. Chen, W. M. Huang, J. L. Shia, *J. Mater. Res.* **2004**, *19*, 2807–2811. DOI:10.1557/JMR.2004.0388
37. H. Khajuria, J. Ladol, S. Khajuria, M. S. Shah, H. N. Sheikh, *Mater. Res. Bull.* **2016**, *80*, 150–158. DOI:10.1016/j.materresbull.2016.03.022
38. W. Wang, W. Widiyastuti, T. Ogi, I. W. Lenggoro, K. Okuyama, *Chem. Mater.* **2007**, *19*, 1723–1730. DOI:10.1021/cm062887p
39. L. Bin, J. Li, G. Duan, Q. Li, Z. Liu, *J. Lumin.* **2019**, *206*, 348–358. DOI:10.1016/j.jlumin.2018.10.035
40. T. Han, C. Zhang, X. Cheng, L. Peng, S. Cao, *Nanosci. Nanotechnol. Lett.* **2017**, *9*, 328–332. DOI:10.1166/nnl.2017.2290
41. S. Prashant, K. Sharma, R. K. Dutta, A. C. Pandey, *J. Appl. Phys.* **2012**, *112* 054321(1-5). DOI:10.1063/1.4751335
42. A. Kar, S. Kundu, A. Patra, *J. Phys. Chem. C* **2011**, *115*, 118–124. DOI:10.1021/jp110313b
43. J. Ding, Z. Lian, Y. Li, S. Wang, Q. Yan, *J. Phys. Chem. Lett.* **2018**, *9*, 4221–4226. DOI:10.1021/acs.jpcllett.8b01898

Povzetek

Preučevali smo odvisnost optičnih lastnosti od morfologije YbPO₄ dopiranega s Tb³⁺. Nanodelce s terbijem dopiranega iterbijevega fosfata (YbPO₄:Tb³⁺) smo pripravili s petimi različnimi sintezniimi metodami: sonokemično metodo, hidrotermalno metodo, solvotermalno metodo, z metodo kemijske pretvorbe delcev z ohranitvijo oblike in metodo koprecipitacije. Strukturne in optične lastnosti nanodelcev smo preučevali z rentgensko praškovno difrakcijo (PXRD), infra-rdečo spektroskopijo (FTIR), vrstično elektronsko mikroskopijo (SEM), presevno elektronsko mikroskopijo, energijsko disperzijsko spektroskopijo rentgenskih žarkov (EDS) in meritvami fotoluminiscence (PL). Preučevali smo vpliv uporabljenega sinteznega pristopa na morfologijo in homogenost nanodelcev in posledično na optične lastnosti materiala. Intenzivna emisija zelene svetlobe kaže na to, da bi lahko material uporabili za IR senzorje, LED diode in v fotovoltaiiki.



Except when otherwise noted, articles in this journal are published under the terms and conditions of the Creative Commons Attribution 4.0 International License

Oxidovanadium(V) and Dioxidomolybdenum(VI) Complexes of *N'*-(3,5-Dichloro-2-hydroxybenzylidene)-4-fluorobenzohydrazide: Synthesis, Characterization, Crystal Structures and Catalytic Property

Huan-Yu Liu,* Yi-Shu Yin, Luo-Ju Yang, Xiao-Ling Zou and Ya-Fang Ye

¹ School of Chemistry and Chemical Engineering, Guangdong Pharmaceutical University, Zhongshan 528458, P.R. China

² Guangdong Cosmetics Engineering and Technology Research Center, Zhongshan 528458, P.R. China

* Corresponding author: E-mail: liuhuanyu03@163.com

Received: 05-29-2019

Abstract

N'-(3,5-Dichloro-2-hydroxybenzylidene)-4-fluorobenzohydrazide (H_2L) was used to prepare oxidovanadium(V) complex $[VOL(OEt)(MeOH)]$ (1) and dioxidomolybdenum(VI) complex $[MoO_2L(OH_2)] \cdot [MoO_2L(EtOH)]$ (2). The complexes were characterized by IR, UV-Vis, NMR spectroscopy, and single crystal X-ray diffraction. X-ray analysis indicates that the complexes are mononuclear species with the metal atoms in octahedral coordination. The complexes were studied for catalytic oxidation property on some olefins with *tert*-butyl hydroperoxide as oxidant.

Keywords: Hydrazone; Vanadium complex; Molybdenum complex; Crystal structure; Catalytic property

1. Introduction

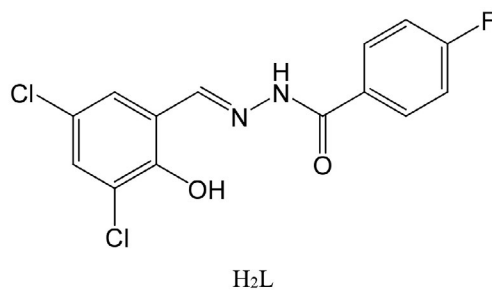
The oxidation of olefins is an important reaction and has received considerable attention in material chemistry. Vanadium and molybdenum complexes with high-valent metal atoms have attracted particular interest due to their important practical applications as efficient catalysts in the sulfoxidation and epoxidation of olefins, and the ammoxidation of propene *etc.*¹ Vanadium and molybdenum can form stable and versatile complexes with various organic ligands. Schiff base vanadium and molybdenum complexes have been reported to have efficient catalytic properties in both homogeneous and heterogeneous reactions.² Recently, we have reported some metal complexes with Schiff bases and their biological applications,³ as well as catalytic properties.⁴ In pursuit of

new catalytic materials based on vanadium and molybdenum complexes, in this work, a new oxidovanadium(V) complex $[VOL(OEt)(MeOH)]$ (1) and a new dioxidomolybdenum(VI) complex $[MoO_2L(OH_2)] \cdot [MoO_2L(EtOH)]$ (2), derived from the hydrazone compound *N'*-(3,5-dichloro-2-hydroxybenzylidene)-4-fluorobenzohydrazide (H_2L) are presented.

2. Experimental

2.1. Materials and Methods

$VO(acac)_2$ and $MoO_2(acac)_2$ and organic materials were purchased from Sigma-Aldrich and used as received. All other reagents were of analytical reagent grade. Elemental analyses of C, H and N were carried out in a Perkin-Elmer automated model 2400 Series II CHNS/O analyzer. FT-IR spectra were obtained on a Perkin-Elmer 377 FT-IR spectrometer with samples prepared as KBr pellets. UV-Vis spectra were obtained on a Lambda 900 spectrometer. X-ray diffraction was carried out on a Bruker APEX II CCD diffractometer. ¹H and ¹³C NMR spectra were recorded on a Bruker FT-NMR 500 MHz spectrometer using *d*⁶-DMSO as solvent. GC analyses were performed on a Shimadzu GC-2010 gas chromatograph.



2. 2. Synthesis of H₂L

To the ethanolic solution (30 mL) of 4-fluorobenzohydrazide (0.010 mol, 1.54 g) was added an ethanolic solution (20 mL) of 3,5-dichlorosalicylaldehyde (0.010 mol, 1.91 g) with stirring. The mixture was stirred for 30 min at room temperature, and left to slowly evaporate to give colorless crystalline product, which were recrystallized from ethanol and dried in vacuum containing anhydrous CaCl₂. Yield 91% (298 mg). Anal. Calc. for C₁₄H₉Cl₂F-N₂O₂: C, 51.40; H, 2.77; N, 8.56%. Found: C, 51.27; H, 2.85; N, 8.72%. IR (KBr; ν_{\max} , cm⁻¹): 3437 w ν (OH), 3329 w ν (NH), 1653 s ν (C=O), 1605 w ν (C=N), 1518 m ν (Ar-O), 1283 m ν (C-O). UV-Vis data (EtOH; λ_{\max} , nm): 220, 285, 337. ¹H NMR (500 MHz, *d*⁶-DMSO; δ , ppm): 12.50 (s, 1H, OH), 12.47 (s, 1H, NH), 8.57 (s, 1H, CH=N), 8.03 (t, 2H, ArH), 7.67 (s, 1H, ArH), 7.61 (s, 1H, ArH), 7.40 (t, 2H, ArH). ¹³C NMR (126 MHz, *d*⁶-DMSO; δ , ppm): 165.40, 163.41, 161.92, 146.97, 130.55, 130.48, 130.22, 128.65, 128.35, 122.89, 121.44, 115.69.

2. 3. Synthesis of Complex 1

The hydrazone compound H₂L (0.10 mmol, 32.7 mg) and VO(acac)₂ (0.10 mmol, 26.5 mg) were mixed in the mixture solvent of methanol and ethanol (20 mL; V:V = 1:1). The mixture was refluxed for 1 h and then cooled to room temperature. Single crystals of the complex, suitable for X-ray diffraction, were grown from the solution upon slowly evaporation within a few days. The crystals were isolated by filtration. Yield 32% (150 mg). Anal. Calc. for C₁₇H₁₆Cl₂FN₂O₅V: C, 43.52; H, 3.44; N, 5.97%. Found: C, 43.37; H, 3.53; N, 5.89%. IR (KBr; ν_{\max} , cm⁻¹): 3440 w ν (OH), 1605 s ν (C=N), 1423 m ν (C=C), 1335 m ν (Ar-O), 1108 m ν (C-O), 947 s ν (V=O). UV-Vis data (EtOH; λ_{\max} , nm): 263, 326, 405.

2. 4. Synthesis of Complex 2

The hydrazone compound H₂L (0.10 mmol, 32.7 mg) and MoO₂(acac)₂ (0.10 mmol, 32.6 mg) were mixed in the mixture solvent of methanol and ethanol (20 mL; V:V = 1:1). The mixture was refluxed for 1 h and then cooled to room temperature. Single crystals of the complex, suitable for X-ray diffraction, were grown from the solution upon slowly evaporation within a few days. The crystals were isolated by filtration. Yield 41% (199 mg). Anal. Calc. for C₃₀H₂₂Cl₄F₂Mo₂N₄O₁₀: C, 37.14; H, 2.29; N, 5.77%. Found: C, 36.33; H, 2.22; N, 5.85%. IR (KBr; ν_{\max} , cm⁻¹): 3406 w ν (OH), 1612 s ν (C=N), 1431 m ν (C=C), 1350 s ν (Ar-O), 1156 m ν (C-O), 944 s, 923 s, 906 s, 876 m ν (Mo=O). UV-Vis data (EtOH; λ_{\max} , nm): 238, 292, 303, 407.

2. 5. X-ray Crystallography

X-ray diffraction was carried out at a Bruker APEX II CCD area diffractometer equipped with MoK α radiation

($\lambda = 0.71073$ Å). The collected data were reduced with SAINT,⁵ and multi-scan absorption correction was performed using SADABS.⁶ The structures of the complexes were solved by direct method, and refined against *F*² by full-matrix least-squares method using SHELXTL.⁷ All of the non-hydrogen atoms were refined anisotropically. The methanol hydrogen atom in complex 1, and the ethanol hydrogen atom in complex 2 were located from electronic density maps and refined isotropically, with O-H distances restrained to 0.85(1) Å, and with *U*_{iso}(H) restrained to 1.5*U*_{eq}(O). The remaining hydrogen atoms were placed in calculated positions and constrained to ride on their parent atoms. The C16-C17 and C15-O4 bonds were restrained to 1.50(1) and 1.45(1) Å, respectively. The crystallographic data and refinement parameters for the compounds are listed in Table 1.

The supplementary crystallographic data for 1 and 2 have been deposited with the Cambridge Crystallographic Data Centre (CCDC nos. 1919016 and 1919017, respectively; deposit@ccdc.cam.ac.uk or <http://www.ccdc.ac.uk/conts/retrieving.html>).

Table 1. Crystallographic and refinement data for the complexes

	1	2
Molecular formula	C ₁₇ H ₁₆ Cl ₂ FN ₂ O ₅ V	C ₃₀ H ₂₂ Cl ₄ F ₂ Mo ₂ N ₄ O ₁₀
Formula weight	469.16	970.20
<i>T</i> , K	298(2)	298(2)
Crystal system	Monoclinic	Monoclinic
Space group	<i>Cc</i>	<i>Pc</i>
<i>a</i> , Å	19.683(2)	7.981(1)
<i>b</i> , Å	15.065(2)	13.610(1)
<i>c</i> , Å	7.633(2)	16.036(1)
β , °	109.145(1)	90.887(2)
<i>V</i> , Å ³	2138.2(7)	1741.6(3)
<i>Z</i>	4	2
ρ_{calcd} , g cm ⁻³	1.457	1.850
μ (MoK α), mm ⁻¹	0.751	1.100
<i>F</i> (000)	952	960
Measured reflections	6136	9783
Unique reflections	3728	5992
Observed reflections (<i>I</i> ≥ 2σ(<i>I</i>))	2522	5092
Parameters	257	473
Restraints	11	3
Goodness of fit on <i>F</i> ²	1.053	1.048
<i>R</i> ₁ , <i>wR</i> ₂ (<i>I</i> ≥ 2σ(<i>I</i>))*	0.0689, 0.1608	0.0486, 0.1211
<i>R</i> ₁ , <i>wR</i> ₂ (all data)*	0.1057, 0.1925	0.0630, 0.1412

$$* R_1 = \sum |F_o| - |F_c| / \sum |F_o|, wR_2 = \{ \sum [w(F_o^2 - F_c^2)^2] / \sum [w(F_o^2)^2] \}^{1/2}$$

2. 6. Catalytic Oxidation Experiment

Catalytic experiment was carried out in a 50 mL glass round-bottom flask fitted with a reflux condenser and placed in an oil bath at 353(2) K under continuous stirring. The catalytic oxidation experiment was carried out as follows: molybdenum(VI) complex (0.032 mmol)

was dissolved in 10 mL 1,2-dichloroethane. Then 10 mmol alkene was added to the reaction mixture and 30 mmol TBHP (*tert*-butyl hydroperoxide) was added. The reaction mixture was refluxed for 1 h. The reaction products were monitored at periodic time intervals using gas chromatography. The oxidation products were identified by comparison with authentic samples (retention times in GC).

3. Results and Discussion

3. 1. Chemistry

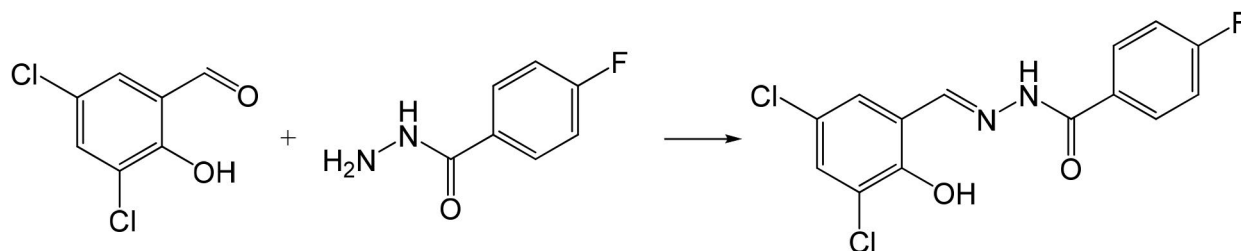
The hydrazone compound H_2L was readily prepared by the condensation reaction of a 1:1 molar ratio of 4-fluorobenzohydrazide with 3,5-dichlorosalicylaldehyde in ethanol (Scheme 1). Complexes **1** and **2** were prepared by the reaction of the hydrazone compound with $VO(acac)_2$ and $MoO_2(acac)_2$ in the mixture solvent of methanol and ethanol, respectively (Scheme 2). Elemental analyses of the compounds are in accordance with the molecular structures proposed by the X-ray analysis.

It is notable that very similar oxidovanadium complex as complex **1** was recently published.⁸ The only difference between the complexes is the presence of one MeOH

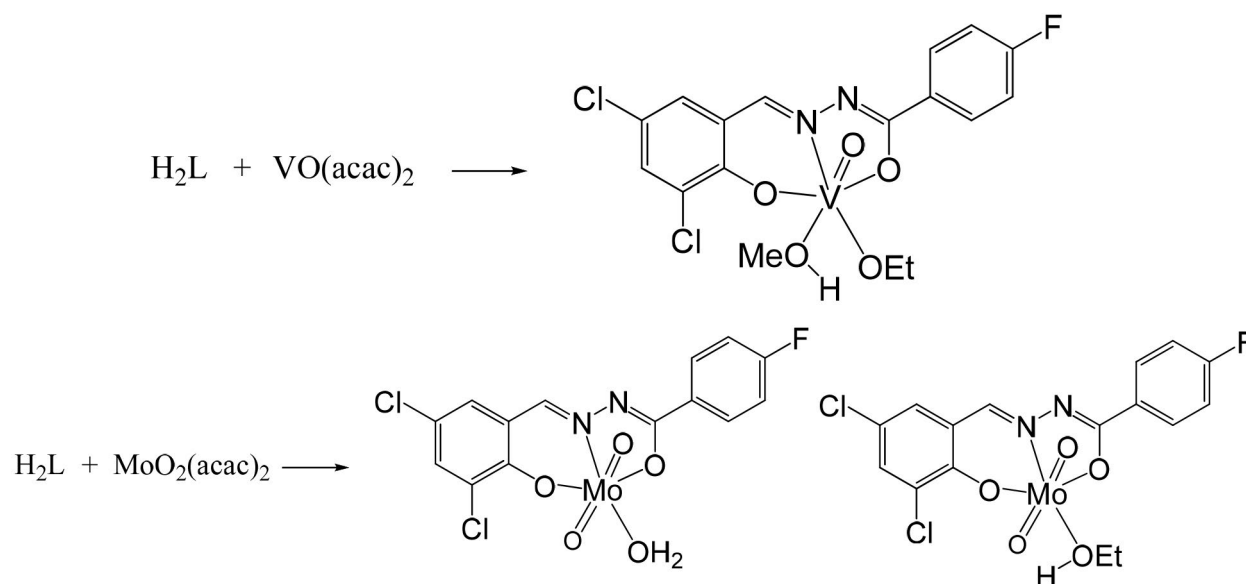
ligand in the present complex instead of EtOH ligand in the published one.

3. 2. IR and UV Spectra

In the IR spectra of the hydrazone compound and the complexes, the weak and broad bands in the region $3400\text{--}3450\text{ cm}^{-1}$ are assigned to the vibration of O–H bonds. The weak and sharp band located at 3329 cm^{-1} of the hydrazone compound is assigned to the vibration of N–H bond. The position of the bands demonstrates that the N–H hydrazone protons are engaged in hydrogen bonding. The intense bands at 1653 cm^{-1} of the hydrazone compound is generated by $\nu(C=O)$ vibration, whereas the band at 1605 cm^{-1} by the $\nu(C=N)$ one. The non-observation of the $\nu(C=O)$ bands, that present in the spectra of the hydrazone compound, indicates the enolization of the amide functionality upon coordination to the V- and Mo-centers. Instead strong bands at 1605 cm^{-1} for **1** and 1612 cm^{-1} for **2** are observed, which can be attributed to the stretching vibration of the C=N groups. The bands at 947 cm^{-1} for **1** is assigned to $\nu(V=O)$,⁹ and the bands in the range of $876\text{--}944\text{ cm}^{-1}$ for **2** are assigned to $\nu(Mo=O)$.¹⁰



Scheme 1. The synthetic procedure of H_2L .



Scheme 2. The synthetic procedure of the complexes.

In the electronic spectra of the complexes, the lowest energy transition band is observed at 405 nm for **1** and 407 nm for **2**, which is attributed to LMCT transition as charge transfer from *p*-orbital on the lone-pair of ligands' oxygen atoms to the empty *d*-orbital of the metal atoms. The other strong bands in the range of 260–330 nm and at about 220 nm in the spectra of both complexes are similar to the absorption band in the spectrum of the hydrazone compound, so they are attributed to the intra-ligand $n \rightarrow \pi^*$ and $\pi \rightarrow \pi^*$ absorption peak of the ligands.

3. 3. Structure Description of Complex 1

Molecular structure of complex **1** is shown in Fig. 1. Selected bond lengths and angles are listed in Table 2. The coordination geometry around the V atom can be described as distorted octahedral with the tridentate hydrazone ligand coordinated in a meridional fashion, forming five- and six-membered chelate rings with bite angles of $73.7(2)^\circ$ and $83.8(3)^\circ$, typical for this type of ligand systems.¹¹ The ethanolato ligand lies *trans* to the hydrazone imino N atom. The methanol O atom *trans* to the oxido group completes the distorted octahedral coordination sphere at a rather elongated distance of 2.355(6) Å due to the *trans* influence of the oxido group.¹² As expected, the hydrazone ligand coordinates in its doubly deprotonated enolate form which is consistent with the observed O2–C8 and N2–C8 bond lengths of 1.304(9) and 1.328(9) Å, respectively. This agrees with reported vanadium complexes containing the enolate form of this ligand type.¹³ The dihedral angle between the two benzene rings of the hydrazone ligand is $4.4(5)^\circ$.

In the crystal packing structure of the complex, the complex molecules are linked by methanol molecules through intermolecular hydrogen bonds of O–H...N (Table 3), leading to the formation of one-dimensional chains along the *c*-axis direction (Fig. 2).

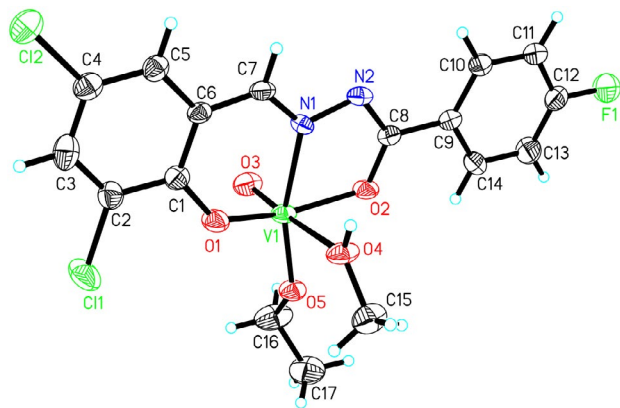


Fig. 1. Perspective view of complex **1** with the atom labeling scheme. Thermal ellipsoids are drawn at the 30% probability level.

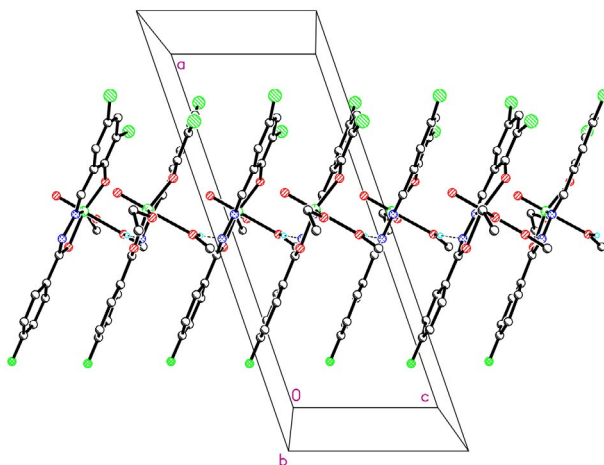


Fig. 2. Molecular packing structure of complex **1**, with hydrogen bonds shown as dotted lines.

3. 4. Structure Description of Complex 2

Molecular structure of complex **2** is shown in Fig. 3. Selected bond lengths and angles are listed in Table 2. The asymmetric unit of the complex contains two independent molecules, $[\text{MoO}_2\text{L}(\text{OH}_2)]$ (A) and $[\text{MoO}_2\text{L}(\text{EtOH})]$ (B). The coordination geometry around the Mo atoms in both molecules can be described as distorted octahedral with the tridentate hydrazone ligand coordinated in a meridional fashion, forming five- and six-membered chelate rings with bite angles of $71.3(3)^\circ$ and $80.9(3)^\circ$ for molecule A, and $70.9(3)^\circ$ and $81.6(3)^\circ$ for molecule B, typical for this type of ligand systems.¹⁴ The oxido groups (O3 and O8) *trans* to the hydrazone imino N atoms form longer bonds with the Mo atoms than the other oxido groups (O4 and O9). The water and ethanol O atoms *trans* to the oxido groups (O4 and O9) completes the distorted octahedral coordination sphere at a rather elongated distances of 2.304(7) and 2.338(6) Å due to the *trans* influence of the oxido groups. As expected, the hydrazone ligands coordinate in their doubly deprotonated enolate form which is consistent with the observed O2–C8, N2–C8, and O7–C22, N4–C22 bond lengths of 1.307(10) and 1.319(11) Å, and 1.296(11) and 1.307(12) Å, respectively. This agrees with reported molybdenum complexes containing the enolate form of this ligand type.¹⁵ The dihedral angles between the two benzene rings of the hydrazone ligand are $5.5(6)^\circ$ for A and $1.2(6)^\circ$ for B.

In the crystal packing structure of complex **2**, the complex molecules A and B are linked by intermolecular hydrogen bonds of O–H...O, O–H...N and C–H...O (Table 3), leading to the formation of 1D chains along the *a* axis. The chains are further linked *via* intermolecular hydrogen bonds of C–H...F (Table 3), to form 2D layers along the *ab* plane (Fig. 4).

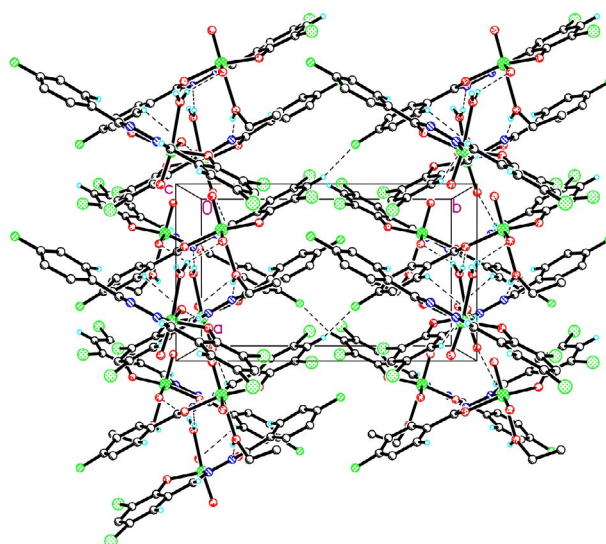
Table 2. Selected bond distances (Å) and angles (°) for the complexes

1			
V1–O1	1.874(6)	V1–O2	1.923(5)
V1–O3	1.576(6)	V1–O4	2.355(6)
V1–O5	1.743(5)	V1–N1	2.135(5)
O3–V1–O5	103.2(3)	O3–V1–O1	98.8(3)
O5–V1–O1	101.7(3)	O3–V1–O2	98.8(3)
O5–V1–O2	94.7(2)	O1–V1–O2	152.4(2)
O3–V1–N1	94.8(3)	O5–V1–N1	160.0(3)
O1–V1–N1	83.8(3)	O2–V1–N1	73.7(2)
O3–V1–O4	174.9(2)	O5–V1–O4	81.8(2)
O1–V1–O4	79.9(3)	O2–V1–O4	80.6(2)
N1–V1–O4	80.2(2)		
2			
Mo1–O1	1.928(6)	Mo1–O2	2.022(6)
Mo1–O3	1.704(6)	Mo1–O4	1.681(7)
Mo1–O5	2.307(7)	Mo1–N1	2.256(7)
Mo2–O6	1.930(6)	Mo2–O7	2.013(6)
Mo2–O8	1.720(7)	Mo2–O9	1.673(7)
Mo2–O10	2.343(6)	Mo2–N3	2.245(7)
O4–Mo1–O3	105.2(3)	O4–Mo1–O1	99.9(3)
O3–Mo1–O1	102.7(3)	O4–Mo1–O2	96.1(3)
O3–Mo1–O2	98.0(3)	O1–Mo1–O2	149.5(3)
O4–Mo1–N1	97.3(3)	O3–Mo1–N1	156.1(3)
O1–Mo1–N1	80.9(3)	O2–Mo1–N1	71.3(3)
O4–Mo1–O5	170.6(3)	O3–Mo1–O5	81.9(3)
O1–Mo1–O5	84.3(3)	O2–Mo1–O5	76.5(3)
N1–Mo1–O5	74.9(2)	O9–Mo2–O8	107.1(4)
O9–Mo2–O6	95.0(4)	O8–Mo2–O6	106.4(3)
O9–Mo2–O7	98.9(3)	O8–Mo2–O7	95.0(3)
O6–Mo2–O7	149.7(3)	O9–Mo2–N3	94.4(3)
O8–Mo2–N3	156.1(3)	O6–Mo2–N3	81.4(3)
O7–Mo2–N3	70.9(3)	O9–Mo2–O10	170.6(3)
O8–Mo2–O10	82.2(3)	O6–Mo2–O10	80.4(3)
O7–Mo2–O10	81.6(2)	N3–Mo2–O10	76.8(3)

Table 3. Geometric parameters of hydrogen bonds for the complexes

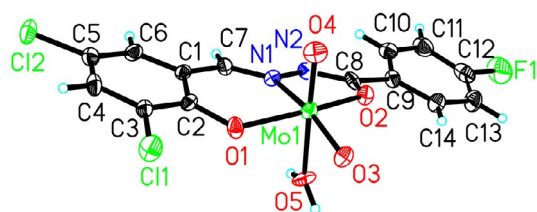
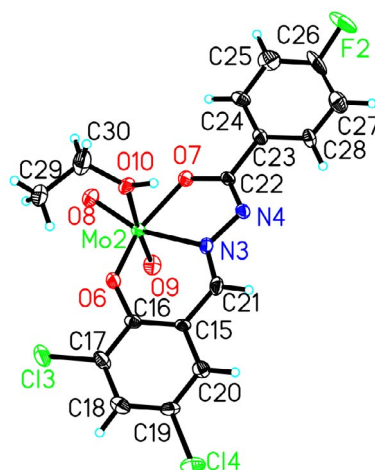
D–H...A	D–H (Å)	H...A (Å)	D...A (Å)	D–H...A (°)
1				
O4–H4...N2 ⁱ	0.85(1)	2.01(2)	2.856(8)	172(6)
2				
O10–H10...N2 ⁱⁱ	0.93	1.92	2.839(9)	169(6)
O5–H5B...O8 ⁱⁱⁱ	0.85	2.06	2.803(10)	145(5)
O5–H5A...N4 ^{iv}	0.85	1.97	2.806(10)	167(5)
C6–H6...O3 ^v	0.93	2.55	3.317(8)	140(6)
C7–H7...O3 ^v	0.93	2.50	3.314(8)	146(6)
C18–H18...F2 ^{vi}	0.93	2.39	3.273(8)	159(6)
C21–H21...O4 ^{vii}	0.93	2.46	3.144(8)	131(6)
C24–H24...O3 ^v	0.93	2.52	3.112(8)	122(6)

Symmetry codes: ⁱ $-x, 1-y, -z$; ⁱⁱ $-x, 1-y, -1-z$; ⁱⁱⁱ $x, -1+y, z$; ^{iv} $-x, 1-y, -z$; ^v $x, -y, 1/2+z$; ^{vi} $-1+x, 1+y, z$; ^{vii} $-1+x, y, z$.

**Fig. 4.** Molecular packing structure of complex 2, with hydrogen bonds shown as dotted lines.

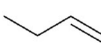


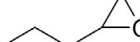
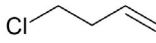
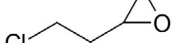
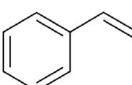
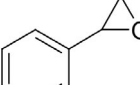
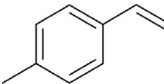
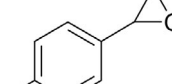
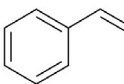
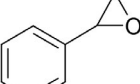
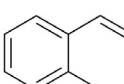
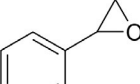
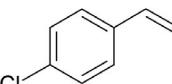
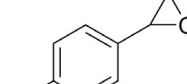
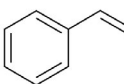
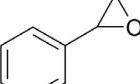
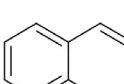
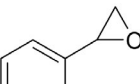
3. 5. Catalytic Property of the Complexes

1-Butene, 1-pentene, 4-chloro-1-butene, phenylene 4-methylphenylene, 3-methylphenylene, 2-methylphenylene, 4-chlorophenylene, 3-chlorophenylene, and 2-chlorophenylene were used as the substrates. The catalytic oxidation results are given in Table 4. The conversions for both aliphatic and aromatic substrates are 100% for either the vanadium complex or the molybdenum complex.

**Fig. 3.** Perspective view of complex 2 with the atom labeling scheme. Thermal ellipsoids are drawn at the 30% probability level.

High epoxide yields (83–89%) are obtained for aliphatic substrates for the molybdenum complex, while somewhat lower yields (76–85%) for the vanadium complex. As for the aromatic substrates, the epoxide yields (93–100%) are

Table 4. Details of the catalytic oxidation of olefins catalyzed by the complexes *

Substrate	Product	Yields, %**	
		1	2
		78.7	85.1
		76.1	83.3
		84.7	88.7
		94.9	96.5
		93.1	93.6
		95.5	94.9
		93.7	95.8
		100	100
		100	100
		100	100

*The molar ratio of catalyst:substrate: TBHP is 1:300:1000. The reaction was performed in mixture of CH₃OH–CH₂Cl₂ (v:v = 3:1).

**The yields (%) were measured relative to the starting substrate after 1 h.

higher than the aliphatic substrates for both complexes. The catalytic oxidation property of the molybdenum complex is comparable to those of the dioxidomolybdenum(-VI) complexes with phloroglucinol and resorcinol derived ligands¹⁶ and with hydrazone ligands.¹⁷ The catalytic oxidation property of the vanadium complex is also similar to those of the oxidovanadium(V) complexes with hydrazone ligands.¹⁸

4. Conclusion

In summary, a new oxidovanadium(V) complex and a new dioxidomolybdenum(VI) complex were obtained from the hydrazone ligand *N'*-(3,5-dichloro-2-hydroxybenzylidene)-4-fluorobenzohydrazide. The V and Mo atoms in the complexes are in octahedral coordination. The complexes have effective catalytic properties on oxidation of various olefins with *tert*-butyl hydroperoxide as the oxidant.

Acknowledgments

We acknowledge the special funds of key disciplines construction from Guangdong and Zhongshan cooperating. Guangdong Pharmaceutical University Cosmetics Talent Practice Teaching Base.

5. References

- (a) I. Gryca, K. Czerwinska, B. Machura, A. Chrobok, L. S. Shulpina, M. L. Kuznetsov, D. S. Nesterov, Y. N. Kozlov, A. J. L. Pombeiro, I. A. Varyan, G. B. Shulpin, *Inorg. Chem.* **2018**, *57*, 1824–1839; DOI:10.1021/acs.inorgchem.7b02684
(b) I. S. Fomenko, A. L. Gushchin, L. S. Shulpina, N. S. Ikonnikov, P. A. Abramov, N. F. Romashev, A. S. Poryvaev, A. M. Sheveleva, A. S. Bogomyakov, N. Y. Shmelev, *New J. Chem.* **2018**, *42*, 16200–16210; DOI:10.1039/C8NJ03358G
(c) D.-L. Peng, *Transit. Met. Chem.* **2016**, *41*, 843–848; DOI:10.1007/s11243-016-0086-8
(d) M. Sutradhar, L. M. D. R. S. Martins, S. A. C. Carabineiro, M. F. C. G. da Silva, J. G. Buijnsters, J. L. Figueiredo, A. J. L. Pombeiro, *ChemCatChem* **2016**, *8*, 2254–2266; DOI:10.1002/cctc.201600316
(e) X. W. Zhu, *Russ. J. Coord. Chem.* **2018**, *44*, 421–424; DOI:10.1134/S1070328418070084
(f) M. R. Maurya, C. Haldar, A. Kumar, M. L. Kuznetsov, F. Avecilla, J. C. Pessoa, *Dalton Trans.* **2013**, *42*, 11941–11962. DOI:10.1039/c3dt50469g
- (a) D. L. Peng, *Russ. J. Coord. Chem.* **2017**, *43*, 404–410; DOI:10.1134/S1070328417060045
(b) S. Gazi, W. K. H. Ng, R. Ganguly, A. M. P. Moeljadi, H. Hirao, *Chem. Sci.* **2015**, *6*, 7130–7142; DOI:10.1039/C5SC02923F

- (c) I. Sheikhsaie, A. Rezaeffard, N. Monadi, S. Kaafi, *Polyhedron* **2009**, 28, 733–738; DOI:10.1016/j.poly.2008.12.044
- (d) S. Rayati, N. Rafiee, A. Wojtczak, *Inorg. Chim. Acta* **2012**, 386, 27–35. DOI:10.1016/j.ica.2012.02.005
3. (a) H.-Y. Liu, *Russ. J. Coord. Chem.* **2013**, 39, 583–587; DOI:10.1134/S1070328413070063
- (b) H. Y. Liu, G. W. Li, Z. L. Li, J. Y. Wu, Y. C. Cai, *Russ. J. Coord. Chem.* **2011**, 37, 668–673;
- (c) H.-Y. Liu, *J. Struct. Chem.* **2014**, 55, 134–138. DOI:10.1016/j.mineng.2013.10.001
4. (a) H. Y. Liu, L. Q. Zhang, J. L. Lv, *Russ. J. Coord. Chem.* **2015**, 41, 451–455; DOI:10.1134/S1070328415070052
- (b) H. Y. Liu, H. H. Yang, Y. X. Diao, Y. F. Ye, X. L. Zou, *Russ. J. Coord. Chem.* **2018**, 44, 572–578. DOI:10.1134/S1070328418090063
5. SMART (version 5.625) and SAINT (version 6.01). Madison (WI, USA): Bruker AXS Inc., 2007.
6. G. M. Sheldrick, SADABS, Program for Empirical Absorption Correction of Area Detector, Göttingen (Germany): University of Göttingen, 1996.
7. G. M. Sheldrick, SHELXTL (version 5.1), Software Reference Manual, Madison (WI, USA): Bruker AXS, Inc., 1997.
8. L.-Y. He, X.-Y. Qiu, J.-Y. Cheng, S.-J. Liu, S.-M. Wu, *Polyhedron* **2018**, 156, 105–110. DOI:10.1016/j.poly.2018.09.017
9. L. Li, K. W. Lv, Y. T. Li, G.-F. Jiang, Y. Xin, L. Ye, Y. Zhang, H. Liu, C.-N. Shang, Z.-L. You, *Chinese J. Inorg. Chem.* **2017**, 33, 905–912.
10. A. Sarkar, S. Pal, *Polyhedron* **2007**, 26, 1205–1210. DOI:10.1016/j.poly.2006.10.012
11. (a) M. Liang, N. Sun, D.-H. Zou, *Acta Chim. Slov.* **2018**, 65, 964–969; DOI:10.17344/acsi.2018.4625
- (b) H. H. Monfared, S. Alavi, R. Bikas, M. Vahedpour, P. Mayer, *Polyhedron* **2010**, 29, 3355–3362. DOI:10.1016/j.poly.2010.09.029
12. (a) S. Guo, N. Sun, Y. Ding, A. Li, Y. Jiang, W. Zhai, Z. Li, D. Qu, Z. You, *Z. Anorg. Allg. Chem.* **2018**, 644, 1172–1176; DOI:10.1002/zaac.201800060
- (b) J. Wang, D. Qu, J.-X. Lei, Z. You, *J. Coord. Chem.* **2016**, 70, 544–555. DOI:10.1080/00958972.2016.1262538
13. (a) R. Bikas, M. Ghorbanloo, S. Jafari, V. Eigner, M. Dusek, *Inorg. Chim. Acta* **2016**, 453, 78–85; DOI:10.1016/j.ica.2016.07.058
- (b) D. Sadhukhan, M. Maiti, E. Zangrando, S. Pathan, S. Mitra, A. Patel, *Polyhedron* **2014**, 69, 1–9; DOI:10.1016/j.poly.2013.11.007
- (c) M. R. Maurya, S. Agarwal, C. Bader, M. Ebel, D. Rehder, *Dalton Trans.* **2005**, 537–544. DOI:10.1039/b416292g
14. (a) L. Xu, Y. Li, M. Duan, Y. Li, M. Han, J. Wu, Y. Wang, K. Dong, Z. You, *Polyhedron* **2019**, 165, 138–142; DOI:10.1016/j.poly.2019.03.016
- (b) Y. Li, L. Xu, M. Duan, J. Wu, Y. Wang, K. Dong, M. Han, Z. You, *Inorg. Chem. Commun.* **2019**, 105, 212–216; DOI:10.1016/j.inoche.2019.05.011
- (c) C. Wang, N. Xing, W. Feng, S. Guo, M. Liu, Y. Xu, Z. You, *Inorg. Chim. Acta* **2019**, 486, 625–635. DOI:10.1016/j.ica.2018.11.020
15. (a) M. Ghorbanloo, R. Bikas, G. Malecki, *Inorg. Chim. Acta* **2016**, 445, 8–16; DOI:10.1016/j.ica.2016.02.018
- (b) V. Vrdoljak, B. Prugovecki, D. Matkovic-Calogovic, T. Hrenar, R. Dreos, P. Siega, *Cryst. Growth Des.* **2013**, 13, 3773–3784; DOI:10.1021/cg400782c
- (c) X.-W. Zhu, *Acta Chim. Slov.* **2018**, 65, 939–945. DOI:10.17344/acsi.2018.4607
16. R. Bikas, V. Lippolis, N. Noshiranzadeh, H. Farzaneh-Bonab, A. J. Blake, M. Siczek, H. Hosseini-Monfared, T. Lis, *Eur. J. Inorg. Chem.* **2017**, 999–1006. DOI:10.1002/ejic.201601359
17. (a) Y.-M. Cui, L. Qiao, Y. Li, Q. Wang, W. Chen, W.-X. Yan, *Transition Met. Chem.* **2017**, 42, 51–56; DOI:10.1007/s11243-016-0105-9
- (b) H. H. Monfared, R. Bikas, P. Mayer, *Inorg. Chim. Acta* **2010**, 363, 2574–2583. DOI:10.1016/j.ica.2010.04.046
18. H. H. Monfared, S. Alavi, A. Farrokhi, M. Vahedpour, P. Mayer, *Polyhedron* **2011**, 30, 1842–1848. DOI:10.1016/j.poly.2011.04.043

Povzetek

Z ligandom N' -(3,5-dikloro-2-hidroksibenziliden)-4-fluorobenzohidrazidom (H_2L) smo sintetizirali oksidovanadijev(V) kompleks [VOL(OEt)(MeOH)] (1) in dioksidomolibdenov(VI) kompleks $[MoO_2L(OH_2)] \cdot [MoO_2L(EtOH)]$ (2). Spojini smo okarakterizirali z IR, UV-Vis in NMR spektroskopijo ter rentgensko monokristalno analizo. Kompleksi so enojedrne zvrsti s kovinskim ionom v oktaedrični koordinaciji. Spojine smo testirali kot katalizatorje pri oksidacijah olefinov s *t*-butil hidroperoksidom kot oksidantom.



Except when otherwise noted, articles in this journal are published under the terms and conditions of the Creative Commons Attribution 4.0 International License

Scientific paper

Oxygen Barrier and Thermomechanical Properties of Poly (3-hydroxybutyrate-co-3-hydroxyvalerate) Biocomposites Reinforced with Calcium Carbonate Particles

Semra Kirboga* and Mualla Öner**Chemical Engineering Department, Yildiz Technical University, 34210, Istanbul, Turkey*** Corresponding author: E-mail: skirboga@yildiz.edu.tr
and muallaoner@gmail.com**Received: 05-31-2019*

Abstract

This study aimed to prepare poly (3-hydroxybutyrate-co-3-hydroxyvalerate), biocomposites with incorporating various percentages of calcium carbonate using extrusion processing. Calcium carbonate was synthesized in the absence and presence of poly(vinyl sulfonic acid). The polymorph and morphology of calcium carbonate changed with the introduction of poly(vinyl sulfonic acid). The rhombohedral calcite was obtained in the absence of poly(vinyl sulfonic acid). Rhombohedral calcite transformed into spherical vaterite with the addition of poly(vinyl sulfonic acid). The influence of filler contents on the properties of poly (3-hydroxybutyrate-co-3-hydroxyvalerate) composites was studied. The structure and properties of poly (3-hydroxybutyrate-co-3-hydroxyvalerate)/ calcium carbonate biocomposites were investigated by XRD, FTIR, TGA, DSC, SEM, OTR and DMA. The nucleation effect of the calcium carbonate on the crystallization of poly (3-hydroxybutyrate-co-3-hydroxyvalerate) was observed in the DSC and XRD measurements by increasing crystallinity of poly (3-hydroxybutyrate-co-3-hydroxyvalerate). It was shown that the variation of the barrier properties of biocomposites was influenced by polymorph and morphology of calcium carbonate. The addition of 0.5 wt% of the rhombohedral calcite and spherical vaterite increased the barrier properties by 25% and 12%, respectively compared to neat polymer. The dynamic mechanical properties of composites based on rhombohedral calcite and spherical vaterite in poly (3-hydroxybutyrate-co-3-hydroxyvalerate) matrix were investigated. The storage modulus increases by adding both particles in the composites over a wide range of temperature (-30 to 150 °C) where the reinforcing effect of calcite and vaterite was confirmed. At the same loading level, rhombohedral calcite led to more increase in the storage modulus, while less increase in storage modulus was observed in the presence of spherical vaterite particles.

Keywords: Poly (3-hydroxybutyrate-co-3-hydroxyvalerate); biocomposite; calcite; vaterite; barrier properties; thermal properties

1. Introduction

Over the past centuries, plastics have been used increasingly because they have many good properties over other materials. The vast majority of plastics are mostly products from the petroleum. They deplete petrochemical feedstock and remain for thousands of years in the environment. Plastics have been accumulating leading to massive waste, which contributes to pollution problems in our ecosystem.^{1,2} All of these burdens have led to tremendous efforts to research and development of environmentally friendly polymers. Many biodegradable materials have been developed as alternatives to conventional nonde-

gradable polymers.³ The Poly(hydroxyalkanoates) (PHAs) are biodegradable polymers produced through the fermentation of sugars, lipids, alkanes, alkenes and alkanolic acids using numerous Gram-positive and Gram-negative bacteria. They can be used in various applications such as biomedical industry, packaging, coatings, films, electronics, sensors, foams, and energy applications because of their remarkable physical properties and biodegradability.^{1,3} Poly (3-hydroxybutyrate, PHB) which is the well-studied polymer is the member of PHAs family. Its application is limited by the poor processability and high brittleness of polymer. The copolymer of PHB like poly (3-hydroxybutyrate-co-3-hydroxyvalerate) (PHBV) was developed to

improve the ductility and processability of the polymer. The mechanical properties of PHBV are better than PHB.² The increase in the composition of HV causes a decrease in the melting point of composites. The presence of polyhydroxyvalerate (PHV) in PHB matrix increases the processability of the polymer. The content of 3-HV in PHBV is effective on the mechanical properties of PHBV composites. However, PHBV has limitations like high crystallinity and a small processing window, which need to be overcome before converting it into useful products. Concerning these shortcomings, fillers can be used in the preparation of poly(3-hydroxybutyrate-co-3-hydroxyvalerate) composites for reducing its production price and enhancing properties.^{2,3}

Composites made from biopolymers and inorganic nanoparticles will find significant potential in many applications due to their enhanced properties and processing characteristics. Braga et al. studied the effect of titanium dioxide particles on properties of PHBV.¹ It was observed that the addition of titanium dioxide in the PHBV matrix decreases the glass transition temperature of the material. PHB/TiO₂ nanocomposites were prepared and characterized by using different techniques. TGA results showed that PHB composites containing TiO₂ particles presented an increment in thermal stability. TiO₂ particles act as a nucleating agent for PHB.¹ Öner et al.^{3,4} studied the effect of h-BN as the potentially interesting material on the enhancement of properties of PHBV. The resulting PHBV nanocomposites showed an increase in oxygen permeability, thermal stability and crystallinity.^{3,4} The effect of adding an electrospun PHBV/CuO coating over compression molded PHBV films on the different properties of nanocomposites were investigated. CuO addition using electrospinning enhanced the nanoparticles dispersion but did not significantly modify the oxygen permeability, mechanical or optical properties.⁵

Thermomechanical behavior of fiber reinforced PHBV was investigated by Adam et al.⁶ The DMA results showed that fibers cause an increase in storage modulus and loss modulus.⁶ Biodegradable nanocomposites were prepared using nanofibrillated cellulose (NFC) as the reinforcement and PHBV as the polymer matrix. DMA results showed that the modulus for 10 wt% NFC reinforced nanocomposite increased 28% compared to neat PHBV at 25 °C, while the storage modulus increased 137% at 100 °C.⁷ Residual lignocellulosic flour was used as a natural filler in PHBV-based composites. A significant increase of rubbery modulus was observed by DMA. The result was ascribed to reinforcing effect of the filler and/or the increase of the degree of crystallinity.⁸ The hybrid composites from wood fiber, talc and PHBV were developed by using extrusion-injection molding. The elastic modulus of the polymer increased by 75% wt. talc loading with the supplementary increase of 120% at additional 20 wt% wood fiber loading below the glass transition temperature. The increase was by 103% and 208%, respectively above the T_g. It was suggested that talc and wood fiber in PHBV were posing a restriction

to the free rotation of the molecular chains above T_g.⁹ The effects of incorporating hyperbranched polymers (HBPs) and different nanoclays on the mechanical properties of PHBV were investigated. Poly(maleic anhydride-alt-1-octadecene) (PA) was used as a crosslinking agent. The storage modulus of PHBV decreased with the addition of 12% (HBP+PA) in the glassy region of the polymer. This result was attributed to the free volume enhancement of the PHBV chains.¹⁰ PHBV/bamboo pulp fiber (BPF) composites were prepared by melt compounding and injection molding. The storage modulus of the composites was found to increase across the whole temperature range from glassy to rubbery states.¹¹ The composites were developed by incorporating agro-residues into PHBV by melt mixing technique. The tensile and storage modulus of PHBV was improved by a maximum of 256% and 308% with the reinforcement of 30 wt% agricultural byproducts.¹² PHBV was reinforced with cellulose nanowhiskers (CNW) using the solvent casting method. DMA results showed that storage modulus of the PHBV increased with the addition of CNW at temperatures higher than the PHBV glass transition temperature.¹³ PHBV and glycerol-plasticized cornstarch blends were prepared by melt extrusion in the presence of an organoclay. The significant increase in the dynamic storage modulus was observed, reaching 251% at 25 °C and 275% at 50 °C.¹⁴ PHBV/husk flour (OHF) were prepared by melt compounding. The surface treatment of OHF by trimethoxyoctadecylsilane (TMOS) was performed by thermo-chemical vapor deposition. The storage modulus of PHBV increase by 36% after adding 20 wt. % of untreated OHF. The effect of silane treatment of filler on PHBV/OHF composites leads to an increase in storage modulus compared to the untreated one.¹⁵ Fabrication of PHBV/natural bamboo fiber was carried out by injection molding. The storage modulus of composites improved by 157% and 173% at 30 and 40 wt% fiber content at 25 °C, respectively.¹⁶ PHBV/multiwalled carbon nanotubes (MWNT) were prepared by melt blending. DMA results showed that CNT's did not affect the T_g but increased storage modulus with an increase in MWNT content.¹⁷

In this study, PHBV composites containing calcite and vaterite particles with different sizes, morphology, and specific surface areas were processed and characterized to elucidate the effects of particles on composite properties. Calcium carbonate (CaCO₃) used in composites was synthesized in the absence and presence of the polymeric additive. Calcium carbonate (CaCO₃) is highly abundant mineral in the earth's crust and is used in many industries such as pigment, cosmetic, plastic, rubber, paper, and electronics.¹⁸ CaCO₃ used in the plastic industry leads to a decrease in surface energy, opacity and surface gloss.¹⁹ The impact strength, elongation at break and stiffness of polymer can be increased with using calcium carbonate with the suitable particle size.¹⁹ CaCO₃ exhibits three polymorphic forms; vaterite, aragonite, and calcite, listed in order of increasing stability.¹⁸ While calcite is the most thermo-

dynamically stable form of calcium carbonate, vaterite and aragonite are thermodynamically unstable forms of calcium carbonate. Unstable forms of calcium carbonate can be stabilized with using additives. Vaterite can be used in biomedical and industrial fields due to its higher solubility and its higher dispersion.²⁰ Calcite used in the plastic industry leads to a decrease in surface energy, opacity and surface gloss. Moreover, the impact strength, elongation at break and stiffness can be increased with using calcite having the suitable particle size.¹⁹

Organic and inorganic fillers have been used in polymeric materials for many years to modify properties, reduce material costs and improving the processing. It is known that understanding the effect of the shape, volume fraction, size and dispersion of particles on the composite's properties is really important.^{21,22} We report here our continuing research effort to design biocomposite with desirable properties by reinforcing calcium carbonate particles with a twin screw extruder. Polymer composites containing particles of two different morphology, rhombohedral calcite and spherical vaterite were prepared through melt processing route with different concentrations to elucidate the role of the particle morphology, on the different properties of the resulting composites. Although the incorporation of calcium carbonate particles into polymers such as polypropylene^{19,23–25} have been carried out, to the best of our knowledge, no information is available on the incorporation of calcite and vaterite particles in PHBV. The study conducted on the effect of spherical and rhombohedral particle shape showed that rhombohedral calcite led to more increase in the storage modulus and oxygen barrier properties, while less increase in storage modulus and barrier properties were observed in the presence of spherical vaterite particles at the same loading level.

2. Experimental Section

2.1. Materials

PHBV, the biopolymer with 8 mol% hydroxyvalerate (HV) content was supplied by ADMajoris Company,

France under the trade name MAJ'ECO FN000HA in a pelletized form suitable for melt extrusion. Calcium chloride (CaCl_2) and sodium carbonate (Na_2CO_3) (reagent grade) were from Merck. Poly(vinyl sulfonic acid) (PVS) of 5000 MW was from Aldrich.

2.2. Preparation of Calcium Carbonate (CaCO_3) Particles

The experiments were conducted in a 0.5 dm^3 water-jacketed reactor providing a constant-temperature at $25 \pm 3 \text{ }^\circ\text{C}$. 100 mM of calcium and 100 mM of carbonate solutions were used to synthesize calcium carbonate. Calcium carbonate was precipitated by mixing equal volumes (100 cm^3) of CaCl_2 and Na_2CO_3 solutions. First, calcium solution was added to the reactor. Sodium carbonate solution and polymer solution were quickly poured into the reactor. The complete experimental procedures were reported previously.^{18,20} The schematic representation of the synthesis of calcium carbonate was given in Figure 1. Ultrasound was applied for 5 minute by use of an ultrasound probe into the reaction. The crystallization solution was subjected to sonication (Sonics Vibra Cell, 20 kHz and 13 mm with threaded end and replaceable tip probe) at room temperature. The amplitude value was 50% whereas polymer concentration was 0.25 g/L. Precipitated crystals were washed with distilled water. The obtained CaCO_3 particles were filtered through a $0.2 \text{ }\mu\text{m}$ cellulose nitrate membrane filter, dried at $100 \text{ }^\circ\text{C}$ for 24 h.

2.3. Preparation of PHBV/ CaCO_3 Composites

PHBV/ CaCO_3 composites were prepared by the melt mixing method. Although there are many different methods to produce composites, melt processing is generally useful due to more economical, more flexible for the formulation. Moreover this process involves compounding and fabrication facilities commonly used in commercial practice.³ A twin-screw extruder (Rondol Microlab, England) with L/D ratio 20 was used for preparing com-

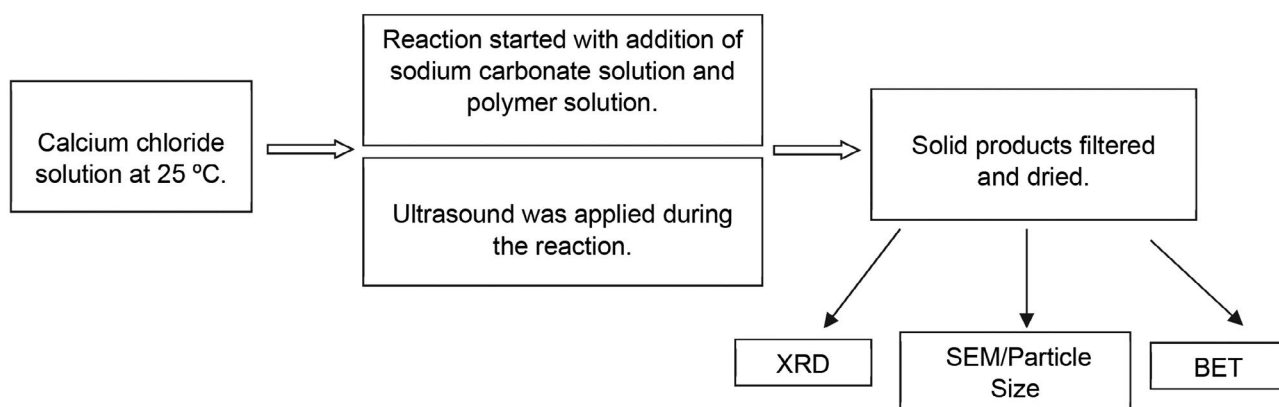


Figure 1. Schematic representation of the synthesis of calcium carbonate.

Table 1. Experimental conditions for obtaining the composites

Sample Code	Particles	Amount of Particles (wt. %)	Sample Code	Particles	Amount of Particles (wt. %)
Neat PHBV	–	–			
PHBV/C0.1	Calcite	0.1	PHBV/V0.1	Vaterite	0.1
PHBV/C0.5	Calcite	0.5	PHBV/V0.5	Vaterite	0.5
PHBV/C1.0	Calcite	1.0	PHBV/V1.0	Vaterite	1.0
PHBV/C3.0	Calcite	3.0	PHBV/V3.0	Vaterite	3.0

posites. The percentages of CaCO_3 used in PHBV/ CaCO_3 composites were 0.1, 0.5, 1 and 3 wt%. The screw speed was 80 rpm, and the operating temperatures of the five extruder zones (from feed to die) were set to 90–135–160–160–155 °C. The extrudate was cooled in air and pelletized for further use. Sheet samples were prepared using a hot-cold press machine (Gülner Makine, Turkey).³ The sheet thickness of the prepared samples was around 0.8 mm. The experimental conditions were given in Table 1 with the sample names carrying the information of synthesis conditions. C (calcite) shows calcium carbonate obtained in the absence of PVS, V (vaterite) indicates calcium carbonate obtained in the presence of PVS. The capital letter shows the species of calcium carbonate used in the composites. The number in the code of composite indicates species amount in the composites (wt. %). For instance, while PHBV/C0.1 denotes composite synthesized in the presence of 0.1 wt. % of calcium carbonate obtained in the absence of PVS, PHBV/V0.1 shows composite synthesized in the presence of 0.1 wt. % of calcium carbonate obtained in the presence of PVS.

2. 4. Characterization of Particles and Composites

X-ray diffraction analysis of the particles and composite samples were carried out using a Panalytical X'pert Pro PW 3040/60 powder diffractometer operating with $\text{Cu K}\alpha$ radiation in operating at 40 mA and 45 kV. The 2θ range was from 5° to 90° at a scan rate of 0.026° step^{-1} . The samples crystal morphology was analyzed by scanning electron microscopy (FEI-Philips, XL 30 ESEM-FEG). PHBV nanocomposite sheet samples were analyzed by scanning electron microscopy (FEI-Philips, XL 30 ESEM-FEG) to evaluate the dispersion of the nanoparticles inside the PHBV matrix. Particle sizes of the particles were investigated using XRD (Scherrer equation), laser diffraction and SEM. We investigated the particle-size distribution of the powders by Laser particle sizer Fritsch Analysette 22-Compact. The Brunauer, Emmett and Teller method was used to investigate the surface area of crystals. Nitrogen sorption isotherms according to the multiple-point BET (Brunauer, Emmett and Teller- COSTECH Kelvin Sorptometer 1042) method was used to determine the specific surface area (SSA) of the CaCO_3 crystals. Calcium carbonate samples were first outgassed at 80 °C. The

nitrogen adsorption isotherm has been performed by additions of gaseous nitrogen to the tube containing the sample at 77 K.¹⁸ FTIR analysis was performed by using BRUKER Alpha-P in the 400–4000 cm^{-1} region at a resolution 4 cm^{-1} . FT-IR analysis was given in ATR-reflectance mode.

2. 5. Dynamic Mechanical Analysis of Samples

Dynamic mechanical analysis (DMA) was carried out with Perkin Elmer DMA8000 (dynamic mechanical analyzer). Film extension mode in the temperature range of –30 °C to 150 °C at a heating rate of 2 °C min^{-1} was applied in order to investigate the dynamic properties of samples in single cantilever mode at 1 Hz. The dimensions of the test samples were 10.40 mm × 10 mm. Storage modulus E' , loss modulus E'' , and $\tan \delta = E''/E'$ were determined and recorded versus temperature during the tests.

2. 6. Thermal Properties of PHBV Composites

Thermo Gravimetric Analyzer (Perkin Elmer Pyris Diamond DTA–TG) was used to characterize the thermal stability of the films. About 10 mg of each film sample was taken in a standard aluminum cup and heated in the temperature ranged from 25 to 800 °C with heating rate of 10 °C/min under a nitrogen flow of 40 mL/min. DSC measurements were performed on Perkin Elmer Diamond DSC. The polymer composites were analyzed in three steps with a heating and cooling rate of 10 °C/min. To determine the thermal properties of the polymer composites, samples of 5 mg mass in an aluminum crucible under 50 mL/min nitrogen atmosphere was used. In the first heating step, samples were heated from 0 °C to 200 °C. In order to erase thermal history of the material, the samples were kept at this temperature for 2 min. In the second step (cooling run), the samples were subsequently cooled to 0 °C at a rate of 10 °C/min. Similarly, the samples were kept at 0 °C for 2 min. In the third step, polymer composites were re-heated from 0 °C to 200 °C. The thermal parameters like melting and the crystallization temperatures (T_m and T_c), the melting and the crystallization enthalpies (ΔH_m and ΔH_c) were obtained from DSC analysis. The following formula was used to calculate the crystallinity of polymer composites:⁴

$$x_c(\%) = \left[\frac{\Delta H_m}{(W_{PHBV} \times \Delta H_m^{ref})} \right] \times 100 \quad (1)$$

Where ΔH_m shows melting enthalpy of sample, ΔH_m^{ref} is theoretical melting enthalpy for 100% crystallized PHBV (146 J/g⁻¹)²⁶ and W_{PHBV} is weight fraction of PHBV in the composite.

2. 7. Barrier Properties of PHBV Composites

Systech Illinois instruments Model 8001 oxygen permeation analyzer was used to measure oxygen transmission rates (OTR) of neat PHBV and PHBV composites films. Polymer composites were analyzed according to continuous-flow cell method approved by ASTM D3985–05. The tests were conducted at 23 °C, 0% relative humidity and 1 atm pressure with highly purified oxygen (99.99%) and nitrogen (99.99%) gases.⁴ Analysis was terminated when OTR graphics reached the steady condition. The permeability (OP) was calculated by multiplying the measured steady state transmission rate by the average sample thickness. At least two separate films were measured for each sample.

3. Result and Discussion

3. 1. Characterization of the Particles

X-ray diffraction pattern of calcium carbonate crystals obtained in the absence of additive and the presence of PVS was given in Figure 2. In the absence of PVS, peaks were observed at scattering angles (2θ) of 29.4° for reflection (104), at 35.9° for reflection (110) and 39.5° for reflection (113).¹⁸ XRD analysis exhibits the characteristic reflections for calcite with scanning angle 23.04, 29.47, 36.05, 39.48, 43.19, 47.54, 48.53, 57.3, 60.61, 64.60 and h k l (012), (104), (110), (113), (202), (018), (116), (122), (214) and (300) respectively.¹⁸ The diffraction peaks of the crystals can be indexed as the (104) reflection of pure calcite. All intensity peaks of XRD patterns of CaCO₃ synthesized in the absence of PVS matched the CaCO₃ described in standards. The main characteristic peaks of vaterite were observed in CaCO₃ sample obtained in the presence of PVS (Figure 2). Vaterite peaks appear at scattering angles (2θ) of 24.92° for reflection (110), at 26.99° for reflection (112) and 32.78° for reflection (114). While a weak peak at 29.26° belongs to calcite was observed, semiquantitative analysis of the XRD results using the Rietveld method with HighScore Plus software showed that the percentage of vaterite was 97%.

It is known that the crystallization mechanism of biominerals can change due to polar functional groups such as -CO₂H, -PO₃H, -SO₃H.^{27,28} Even if the functional groups are present in low concentrations, they have enormous effects on the growth, nucleation, morphology, and polymorphism of the crystals. The required first step of

interaction between functional groups and the crystallizing species is the adsorption of the functional groups onto the pre-nuclear cluster.^{18,20} In this work, the observed changes of the precipitate morphology in the presence of PVS indicate that polymer affects the nucleation and crystal growth calcium carbonate. We can suggest that incorporation of PVS into the crystallization medium slows down the nucleation growth rate of calcium carbonate and therefore calcite growth is poisoned. As the calcite growth is inhibited due to polymer poisoning, formation of vaterite was promoted and PVS stabilized the particles in solution as the vaterite polymorph.

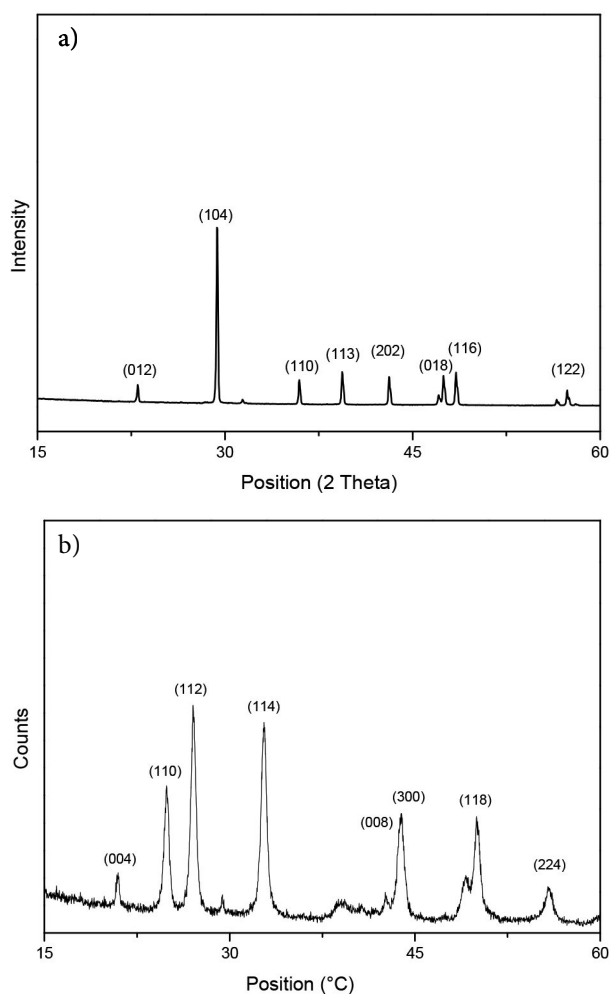


Figure 2. X-ray diffraction patterns of CaCO₃ obtained in the (a) absence and (b) presence of PVS.

SEM analysis also confirmed the morphological changes. Figure 3 shows the morphology of calcium carbonate crystals obtained from SEM investigation. The typical rhombohedral form of calcite was observed in the absence of polymer (Figure 3a). The common shape of calcite is a rhombohedron which consists of (104) faces. It is known both by experiment and by simulation, that the

(104) is the most stable surface of calcite. It is also the most common morphology of the natural calcium carbonate samples.²⁹

The particle size of calcium carbonate was analyzed from SEM micrographs. The dimensions of the minimum of 50 crystals in each sample were measured from SEM photomicrographs. The mean crystal size of rhombohedral calcite was $3.6 \times 3.3 \pm 0.75 \mu\text{m}$. When the particles were produced in the presence of PVS, a significant change in the morphology of calcium carbonate was obtained as evidenced by SEM pictures. PVS lead to the formation of spherical vaterite (Figure 3b). The results of SEM analysis are coherent with the XRD results. The mean crystal size of spherical vaterite was $1.52 \pm 0.47 \mu\text{m}$. The change in the morphology of calcium carbonate could result from the strong interaction of PVS and calcium carbonate. The nucleation and crystal growth of the calcite and vaterite was affected by the introduction of PVS.²⁷ Meng et al. explained morphological changes by the adsorption of sulfonic groups on calcium carbonate.³⁰ The interactions between PVS and crystals may result in the phase transformation of calcite to vaterite.

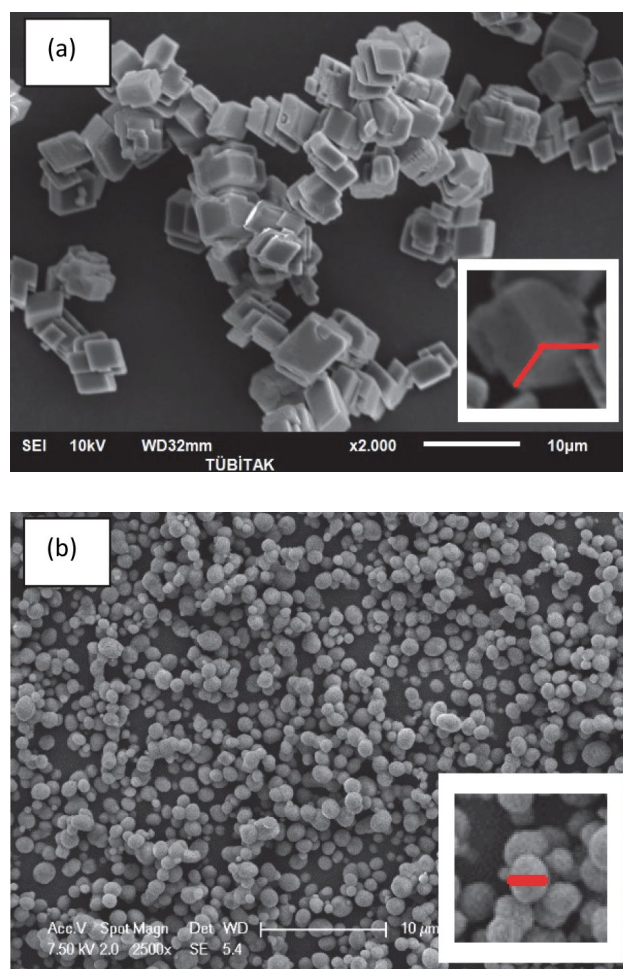


Figure 3. SEM photographs of CaCO_3 obtained in the (a) absence of additive and (b) presence of PVS.

The analysis of particle size and the size distribution of calcium carbonate was carried out with using Fritsch Analysette 22 Compact. The median crystal sizes of were $5.38 \pm 2.22 \mu\text{m}$ and $1.62 \pm 0.66 \mu\text{m}$ for calcium carbonate obtained in the absence of PVS and in the presence of PVS, respectively. A narrow particle size distribution was obtained with the introduction of PVS. The specific surface areas were measured as $0.34 \text{ m}^2/\text{g}$ and $12.08 \text{ m}^2/\text{g}$ for calcium carbonate obtained in the absence of PVS and in the presence of PVS, respectively.

3. 2. SEM Pictures of the Composites

Calcite and vaterite particles were used to produce composites at different particle loadings. The dispersion of the particles achieved in PHBV matrix was observed using SEM for the PHBV/C and PHBV/V composites. Figure 4 shows the cross section SEM images of the surfaces of composites containing 1.0% of PHBV/C and PHBV/V. As shown in Figure 4 for 1.0 wt. % calcium carbonate, the calcite (Figure 4a) and vaterite (Figure 4b) appeared uniformly dispersed and distributed to the individual level in the PHBV

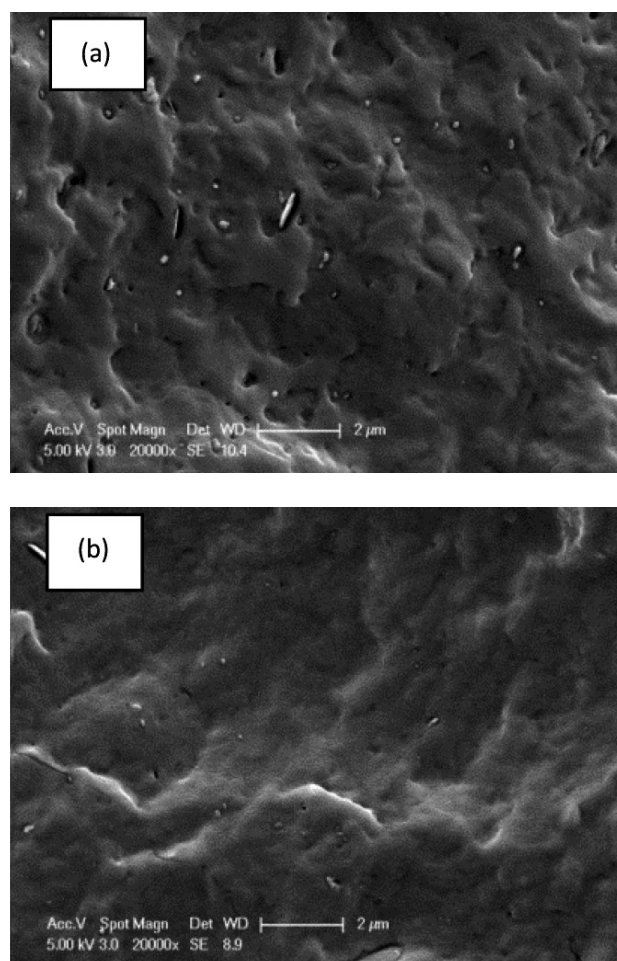


Figure 4. SEM photographs of composites obtained in the presence of (a) 1.0% of calcite and (b) 1.0% of vaterite.

matrix. The edges of individual particles are visible at the fracture surface, and no particle aggregates were observed.

3. 3. XRD and FTIR Analysis of the Composites

XRD analysis is commonly used for the interpretation of composite structure. Figure 5 shows the XRD patterns of biocomposites. The XRD patterns of PHBV exhibited characteristic 2θ peaks at $13.6^\circ(020)$, $17.1^\circ(110)$, $19.9^\circ(021)$, $21.7^\circ(101)$, $22.3^\circ(111)$, $25.5^\circ(121)$, $27.1^\circ(040)$, $30.3^\circ(002)$.³ As shown in Figure 5, all composites show the reflections at the same values for the neat PHBV. It is clear that the unit cell of biopolymer does not change with the addition of calcium carbonate. There is no effect of calcium carbonate on the crystallization of PHBV. The composite can be crystallized in its typical crystalline form. When the intensity of (020) reflection of neat PHBV was compared, the intensity of (020) reflection increased with the addition of calcium carbonate (Figure 5).

XRD of PHBV and CaCO_3 exhibit major peaks around $13\text{--}32^\circ$ scan angle interval. So, in this region, it is

an evident that characteristic peak of neat PHBV can be overlap with characteristic peak of CaCO_3 . However, in the case of composite samples, the intensity of the characteristic diffraction peak located at 2θ of at 55° appear to increase compared to neat PHBV (Figure 6). This result shows the inclusion of the CaCO_3 particles within polymeric matrix.

The peak broadening of XRD reflection can be used to estimate the crystallite size in a direction perpendicular to the crystallographic plane based on the Scherrer's formula as follows:

$$L = \frac{k\lambda}{B\cos\theta} \quad (2)$$

where L is the mean crystallite size in nm, k is the shape factor, B is the broadening of the diffraction line measured at half of its maximum intensity. B was determined by full width at half maximum (FWHM) for the diffraction peak under consideration. The shape factor k becomes 0.9 when FWHM is used for B. λ is the wavelength of monochromatic X-ray beam and θ is the Bragg diffraction angle.² Both the size of the crystallites responsible for the Bragg

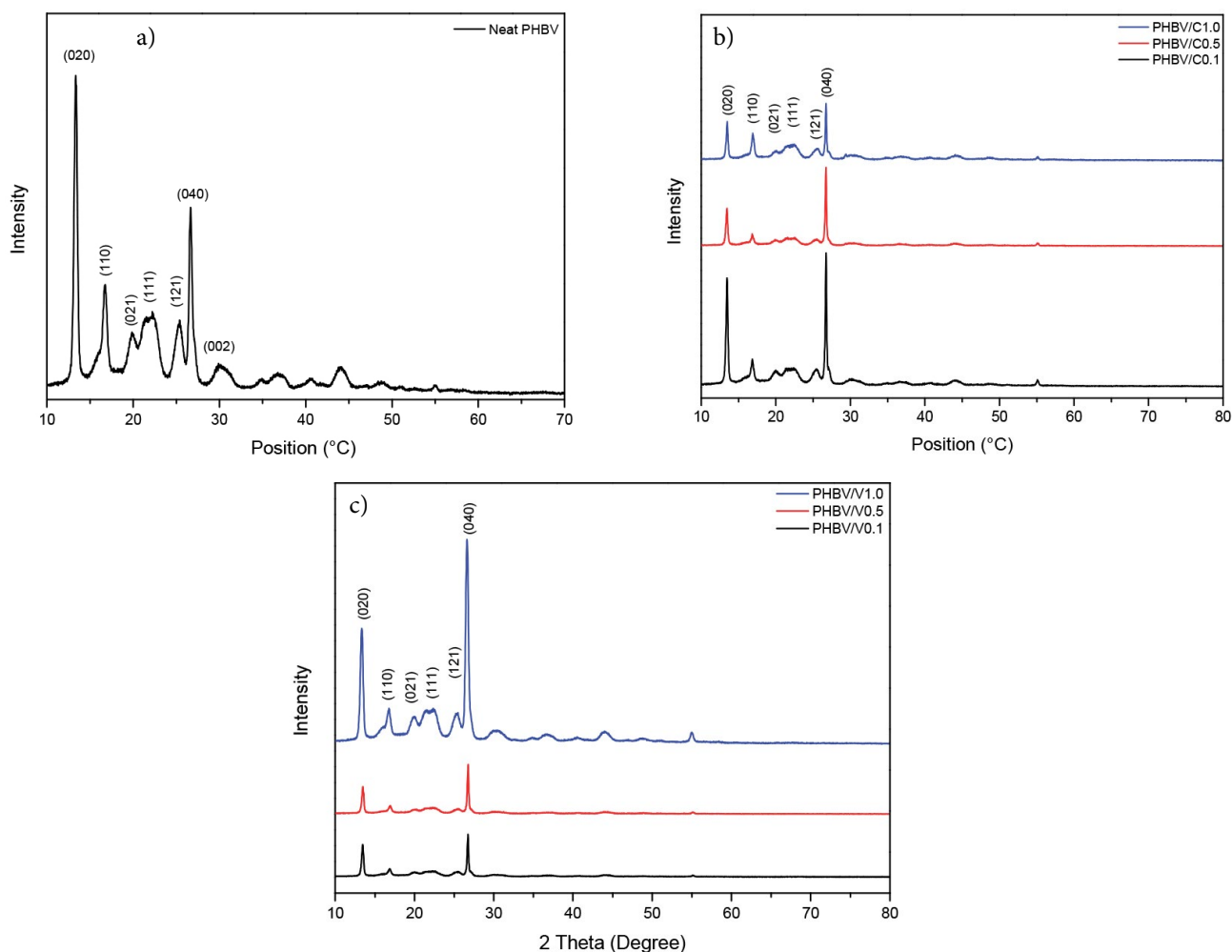


Figure 5. The X-ray diffraction pattern of (a) Neat PHBV, (b) PHBV/C composites and (c) PHBV/V composites.

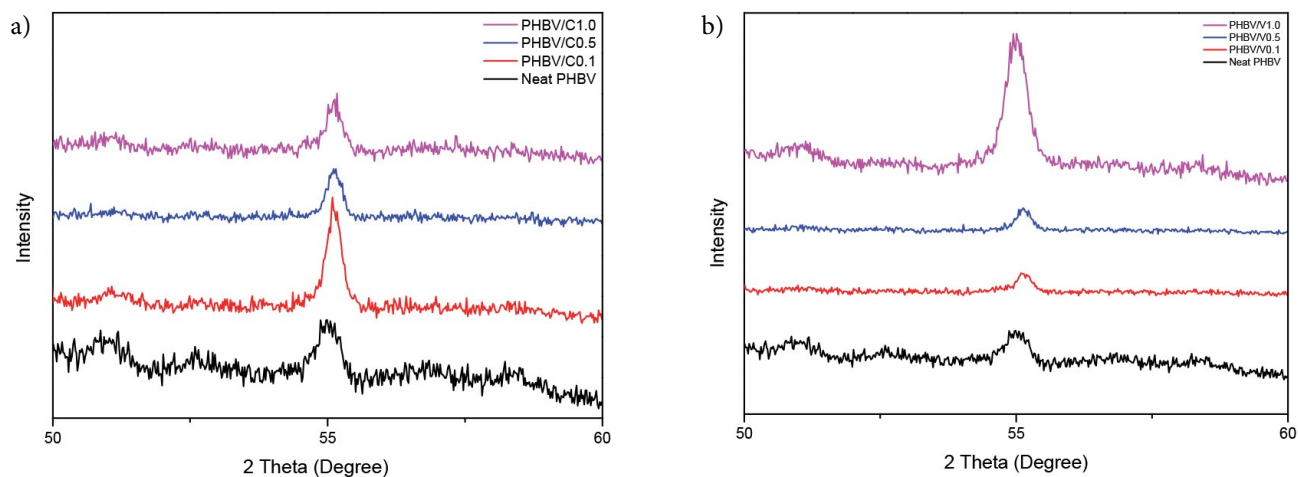


Figure 6. The X-ray diffraction pattern of (a) PHBV/C composites and (b) PHBV/V composites at 2θ of at 55° .

reflection (020) and the ratio of (020)/(110) and (020)/(021) were given in Table 2.

The crystallite size L [nm] calculated for the (020) reflection peak using Scherrer's equation is in the range of 27.10–45.17 nm for composites as opposed to 20.32 nm for neat PHBV. This increase in the crystallite size of (020) crystal plane in the composites with addition of particles shows that nanoparticles provoke the increase in the degree of crystallinity. For this purpose, Crystallinity index (CI) values from XRD measurement were calculated for composite samples based on the (020) peak of PHBV and given in Table 2. The following formula was used for calculating CI :³¹

$$CI = \frac{I_{(020)}}{I_{Total}} \times 100 \quad (3)$$

CI results have shown that the CaCO_3 addition affects the crystallinity of PHBV. The values are higher for all composite samples. The CaCO_3 is known to behave as a nucleating agent and increases the crystallinity of the polymer matrix.³²

Table 2. L (nm), intensity ratios and CI (%) of neat PHBV and its composites from XRD scan

Sample Code	L (nm)	(020)/(110)	(020)/(021)	CI (%)
Neat PHBV	20.32	1.79	8.56	44.70
PHBV/C0.1	36.95	2.51	12.61	48.43
PHBV/C0.5	33.87	3.57	12.05	55.19
PHBV/C1.0	36.95	4.03	22.78	64.47
PHBV/C3.0	24.69	9.21	15.32	69.73
PHBV/V0.1	27.10	2.46	12.07	48.66
PHBV/V0.5	45.17	3.45	13.06	51.34
PHBV/V1.0	36.95	3.38	14.55	54.55
PHBV/V3.0	27.78	2.77	11.60	57.58

Figure 7 shows the FTIR spectra of neat PHBV and the prepared nanocomposites. PHBV exhibited some characteristic peaks as methyl C–H asymmetric stretching at $3015\text{--}2960\text{ cm}^{-1}$, methylene C–H asymmetric stretching at $2945\text{--}2925\text{ cm}^{-1}$, C=O stretching at $1723\text{--}1740$

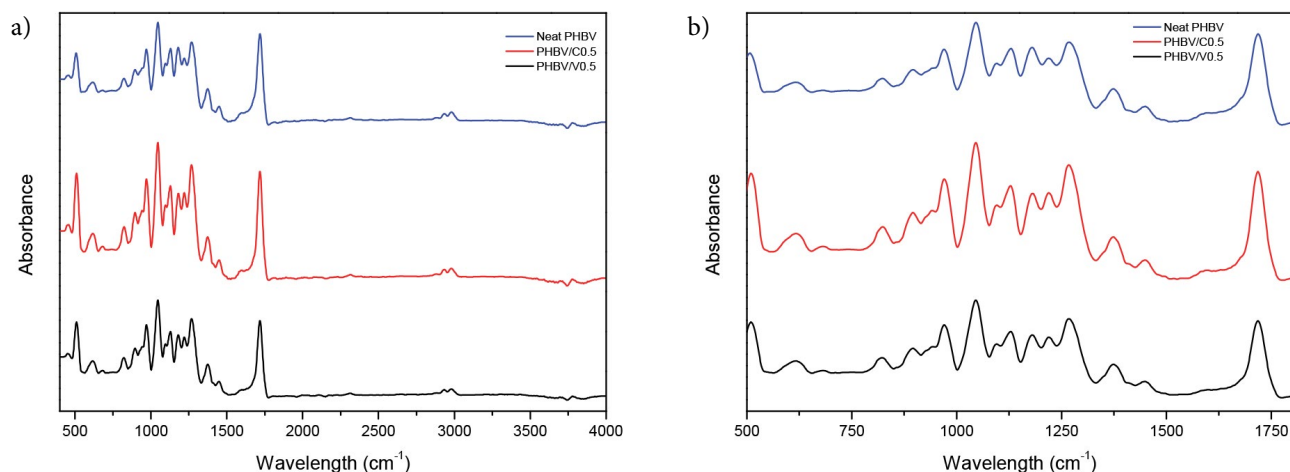


Figure 7. FT-IR spectra of the polymer composites at the (a) $400\text{--}4000\text{ cm}^{-1}$ and (b) $500\text{--}1800$ region.

cm⁻¹, CH₂ wagging at 1320–1159 cm⁻¹, asymmetrical –C–O–C– stretching, symmetrical –C–O–C– stretching at 800–975 cm⁻¹, CH₂ scissoring at 1453–1459 cm⁻¹, C–O stretching at 1065–1030 cm⁻¹ and C–C stretching at 979–980 cm⁻¹, respectively.³³ Calcite and vaterite exhibit main characteristic peaks as 712 cm⁻¹ and 745 cm⁻¹, respectively.¹⁸ While the peaks at ~1420 and ~874 cm⁻¹ indicate the presence of calcite, the peak at ~1070 cm⁻¹ shows the presence of vaterite.¹⁸ The peak of calcium carbonate cannot be observed in the spectra of the nanocomposites due to overlapping with the peak of the PHBV. The bands at 1220 to 1279 cm⁻¹ are crystallinity-sensitive bands for PHBV. The peak intensity in this region is not an absolute measure of the degree of crystallinity but is useful as a comparison criterion.³¹ The intensity of the peak in this region increased in the presence of calcium carbonate as can be seen in Figure 7.

3. 4. TGA Analysis of the Composites

Conventional techniques such as extrusion, injection or compression molding can be used to produce PHBV composites.³ The thermal stability of PHBV is very low so that thermal degradation can take place during the polymer melt processing. Before it was transformed into useful products, the thermal stability of it needs to be developed.³⁴ Therefore, to investigate the effect of the additive on the thermal decomposition of PHBV is vital for industry and science. The thermogravimetric analysis was used to measure the thermal stability of the PHBV and PHBV/CaCO₃ composite. Thermogravimetric analysis was carried out under a nitrogen atmosphere in the temperature range 20–800 °C and the temperature corresponding to initial mass loss (T_i), the temperature of 10% weight loss (T₁₀), the temperature of 50% weight loss (T₅₀) and the temperature of maximum rate of mass loss (T_{max}), were summarized in Table 3. The values of T_i, T₁₀, T₅₀ and T_{max} of composites slightly increased with the addition of calcium carbonate. When the initial weight loss is taken as a point of comparison, the onset degradation temperature (T_i) for neat PHBV is 264.68 °C. The degradation temperature of composite increased to 274.52 °C and

272.01 °C for PHBV/V0.1 and PHBV/C0.1 composites, respectively.

Table 3. TGA values of PHBV/ CaCO₃ composites and neat polymer

Sample Code	T _i (°C)	T ₁₀ (°C)	T ₅₀ (°C)	T _{max} (°C)
PHBV	264.68	280.84	292.20	303.66
PHBV/C0.1	272.01	280.56	290.30	308.76
PHBV/C0.5	268.97	280.14	289.42	307.59
PHBV/C1.0	271.68	280.03	289.41	306.28
PHBV/C3.0	273.29	281.49	291.78	304.62
PHBV/V0.1	274.52	280.68	290.40	306.56
PHBV/V0.5	272.10	280.12	288.39	298.97
PHBV/V1.0	268.61	279.48	284.50	292.11
PHBV/V3.0	272.40	278.18	282.88	288.95

3. 5. DSC Analysis of the Composites

DSC analysis was performed to investigate the effect of calcium carbonate on the thermal characteristic of PHBV. The analysis was carried out in 3 steps. Two heating and one cooling cycles were performed for neat polymer and composites. Figure 8 depicts DSC thermograms of first heating (Figure 8a), cooling (Figure 8b), and second heating (Figure 8c) sequences for neat PHBV and PHBV/CaCO₃ composites. The results calculated from the DSC heating and cooling curves are summarized in Table 4 for composites with different calcium carbonate contents.

The first melting temperature of the nanocomposite samples shifts to slightly lower temperatures compared to neat PHBV. From Table 4, the heat of melting of the bio-composites are seen to increase with increasing calcium carbonate loading up to 3 wt%. ΔH_{m1} values are in the range of 59–85.4 J/g for composites as opposed to 68.8 J/g for neat PHBV. Crystallization temperature (T_{c1}) and heat of crystallization (ΔH_{c1}) were determined from the DSC cooling runs of these samples. There were no significant changes in the cold crystallization temperatures of the nanocomposite samples compared to neat PHBV. The cold crystallization enthalpy values of the composites vary between 77.8–84.5 J/g, while the enthalpy of the PHBV is 80.5

Table 4. Thermal properties obtained from DSC curves for polymer composites

Sample	First Heating		Cooling		Second Heating		
	T _{m1} (°C)	ΔH _{m1} (J/g)	T _{c1} (°C)	ΔH _c (J/g)	T _{m2} (°C)	ΔH _{m2} (J/g)	χc(%)
Neat PHBV	177.06	68.8	126.63	80.5	175.89	74.6	51.1
PHBV/C0.1	174.87	69.5	124.60	79.9	175.18	78.8	54.0
PHBV/C0.5	173.00	74.7	125.72	80.7	172.98	87.5	60.2
PHBV/C1.0	176.69	72.8	125.88	79.5	176.51	82.6	57.1
PHBV/C3.0	176.05	75.2	125.92	79.6	176.99	81.5	57.5
PHBV/V0.1	175.83	85.4	125.41	84.5	175.29	87.0	59.7
PHBV/V0.5	174.81	76.9	124.93	82.2	174.13	82.9	57.1
PHBV/V1.0	177.63	76.3	126.69	77.8	179.47	79.4	54.9
PHBV/V3.0	178.30	59.0	125.68	78.6	176.29	69.3	48.9

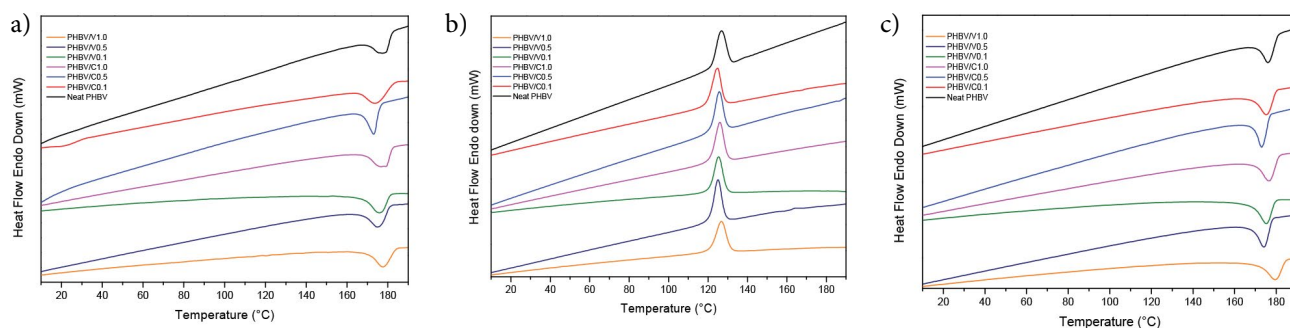


Figure 8. DSC thermograms of polymer composites from the (a) first heating scan, (b) cooling scan, and (c) second heating scan.

J/g. The thermal properties based on the second heating scan of the composites were examined and reported in Table 4. The melting enthalpy and crystallinity of the polymer increased after the incorporation of the calcium carbonate. The values of ΔH_{m2} provide important information about the crystallinity and shows significant variations in the composites. The addition of both calcite and vaterite particles increases the crystallinity of neat PHBV. The addition of calcite increased the degree of crystallinity PHBV from 51.1% to 60.2% at 0.5% wt calcite loading, while addition of vaterite increased from 51.1% to 59.7% at 0.1% wt vaterite loading. This can be explained by the known concept that fillers in a polymer can induce crystal nucleating effects.

3. 6. Oxygen Barrier Properties of the Composites

The oxygen barrier properties of PHBV/ CaCO_3 composites in different CaCO_3 contents were determined by correlating to OTR values of samples with oxygen permeability coefficients. OP is the rate of oxygen transmission through unit area of a flat material of unit thickness induced by unit vapour pressure difference across the material. Relationship between OTR and oxygen permeability were given by the following equation:

$$OP = OTR \times L/\Delta P \quad (4)$$

where OP is the oxygen permeability coefficient ($\text{cc mm m}^{-2} \text{ day}^{-1}$), OTR is the oxygen transmission rate ($\text{cc m}^{-2} \text{ day}^{-1}$), L is the film thickness (mm) and ΔP is the difference (bar) between oxygen partial pressure across the film. As shown in Figure 9, the OP of PHBV has a value of 1.35 ($\text{cc mm m}^{-2} \text{ day}^{-1}$) at 23 °C and the incorporation of calcium carbonate into polymer matrix decreases gas permeability. We can suggest that CaCO_3 particles create a barrier for the diffusing gas molecules. OP of PHBV/C0.5 and PHBV/V0.5 shows 25% and 12% improvements, respectively compared to the neat PHBV. When comparing barrier properties between PHBV/calcite and PHBV/vaterite composites, rhombohedral calcite composites showed higher barrier effect than spherical vaterite composites. Maximum decrease in OP value was observed for PHBV/

C0.5 composite. OP values do not improve with further increasing the particle content.

The presence of particles changes the crystallinity of crystalline polymers that could affect the permeability. The

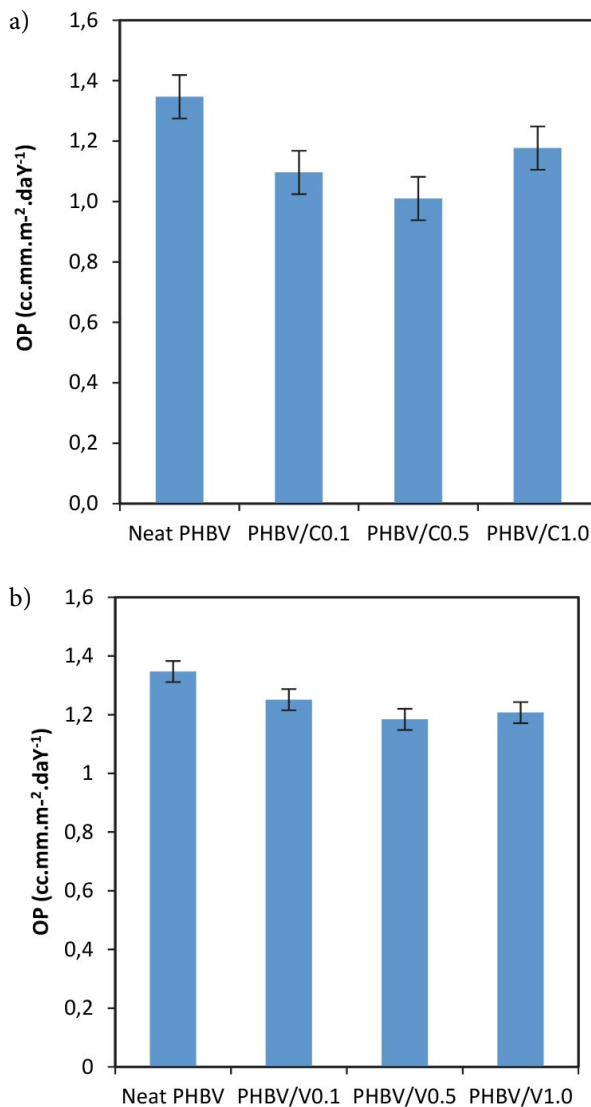


Figure 9. Oxygen permeability (OP) of neat PHBV and PHBV/ CaCO_3 composites with (a) calcite and (b) vaterite.

percentage of crystallinity values determined from DSC is in the range of 54–60.2 for composites as opposed to 51.1 for neat PHBV. All these findings show that the changes in crystallinity can account for the enhanced barrier properties. It is assumed that gas molecules can diffuse through free volumes at amorphous phase of a semi-crystalline material and no gas diffusion takes place in the crystalline phase.³⁵ The nanoparticle reduces the free volume for gas diffusion within the polymer, reducing the diffusivity by a tortuous path mechanism. The improvement can be attributed to the increased tortuosity in the presence of CaCO₃. A tortuous pathway for the diffusion of gas out of the biocomposite matrix may lead to an increase in barrier properties of biocomposites. This increases the effective path length for diffusion of the gas, thereby reducing the rate of diffusion.

3. 7. Dynamic Mechanical Properties

Dynamic mechanical measurements were performed on neat PHBV and composite samples to investigate the effect of the calcite and vaterite particles on their thermo-mechanical properties. The three parameters were measured: the storage modulus (E'), the loss modulus (E''), and tan delta, the ratio of (E''/E'). The storage modulus (E') and loss modulus (E''), represent the elastic and viscous nature of the polymeric material over a range of temperature.

The storage modulus of PHBV and its composites as a function of the temperature are shown in Figures 10a and 10b, respectively for the calcite and vaterite composites. The storage modulus determines the ability of the polymer to absorb or store energy. In addition, storage modulus is often associated with the stiffness (tensile modulus) of the polymer and is proportional to the energy stored during the loading cycle. It was observed that with the increase in temperature, the storage modulus of neat polymer and its composites gradually decreased. This was due to the softening of the matrix phase in composites. This

reduction is expected because of the relaxation of polymer chains as a result of the softening of the matrix phase.

The storage modulus of PHBV in both glassy and rubbery regions is considerably increased after the incorporation of both particles. In Figure 10, it is observed that the storage modulus for nanocomposites is much higher over the whole temperature range compared to neat PHBV. The two particles systems showed different storage modulus values with temperature. Both composites showed reinforcement below and above T_g. The storage modulus enhancement by adding particles can be attributed to the good stress transfer between polymer matrix and particles.

As observed E' , the elastic component of the composites increased by 46% and 91% at 0.5 wt.% and 1 wt.% calcite loading with respect to neat PHBV respectively, at -10 °C. This enhancement was below the glass transition temperature of PHBV. The increase was by 85% and 139%, respectively above the T_g (140 °C) in the rubbery stage with the same loading trend of calcite in PHBV. The DMA analysis of the vaterite composites show that there is a 74% increase in the storage modulus with 1 wt.% vaterite, as compared to the neat PHBV at -10 °C. The storage modulus increased by 91% for PHBV/V1 composite samples with respect to the neat polymer at 140 °C. When comparing reinforcement between the PHBV/calcite and PHBV/vaterite composites, calcite composites showed higher reinforcement than vaterite composites, both below and above T_g of the polymer matrix. The storage modulus partially declined at 3 wt% content owing to the increased agglomeration of particles. The increase in the storage modulus of PHBV nanocomposites can be attributed to the reducing of the mobility of polymer chains in the presence of particles. All composite samples have higher E' values than neat PHBV as a result of the inherent rigidity of particles. The increase of the storage modulus in the rubbery stage of polymer matrix suggesting that the fillers were posing a restriction to the free rotation of the molecular chains above T_g. The rhombohedral shape of the calcite particles has also played a role in the increment of the

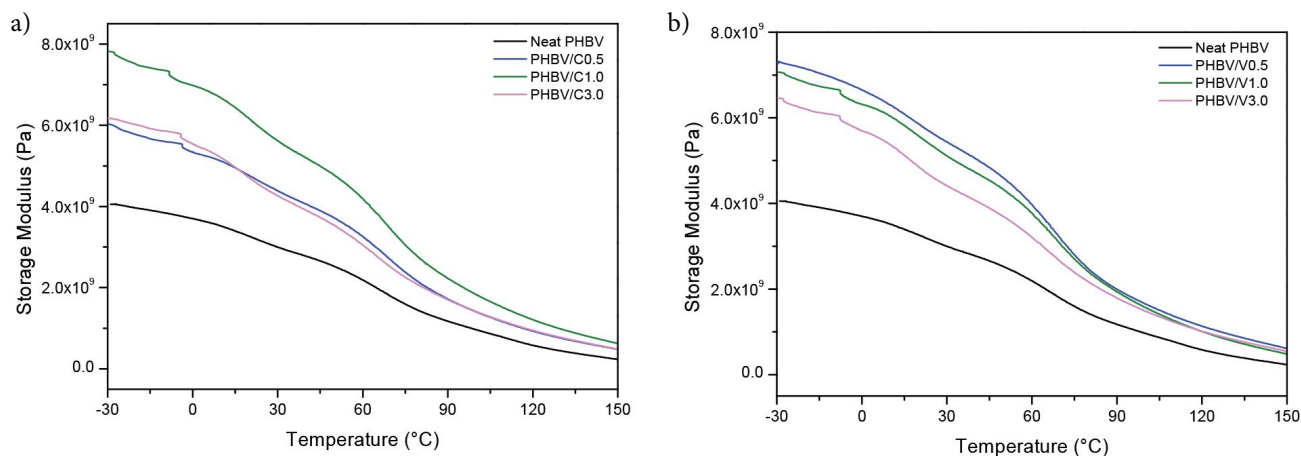


Figure 10. DMA thermographs showing storage modulus for PHBV/CaCO₃ composites with (a) calcite and (b) vaterite.

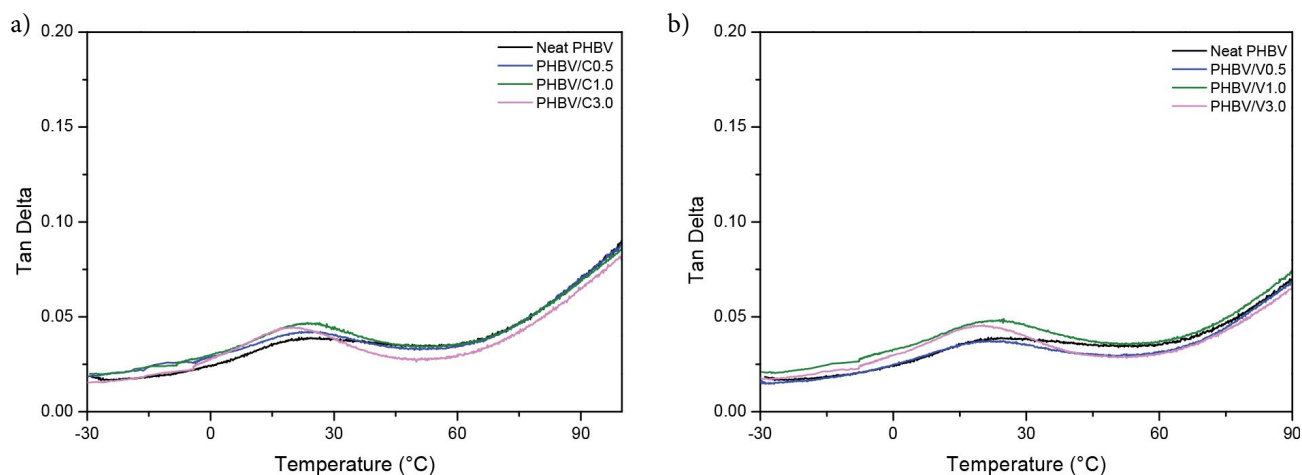


Figure 11. DMA thermographs showing tan delta for PHBV/CaCO₃ composites with (a) calcite and (b) vaterite.

modulus when compared to the increase in the spherical shape of vaterite.

Tan delta is the ratio of loss modulus (E'') to the storage modulus (E'). It is a measure of the energy dissipated and represents internal friction in viscoelastic material. The glass transition (T_g) could be identified as the peak of the tan delta. Figures 11a and 11b show the tan delta curves of the PHBV and its composites as a function of temperature. The T_g value of the neat PHBV is around 26 °C. It is clear that the tan delta peak for both the composites did not shift significantly as the content of particles increases from 0% to 3%. The tan delta peak temperatures for all of the composites samples fell within 2 °C of the neat PHBV. No significant difference was observed between the T_g of PHBV and composite samples which imply particles did not have any specific effect on the glass transition temperature of the polymer.

The previous studies concerning shape have been shown the relationship between nanocomposite properties and particle shape. The incorporation of particles is to promote the time and heat dependent properties of composites. The particle shape was found to influence the mechanical, barrier and thermal properties of the resulting composites.

The nanoparticles have different polymorphic modifications of calcium carbonate particles namely spherical rhombohedral calcite and elongated ortho-rhombic aragonite were used as reinforcement phases of Nylon6. DMTA analysis showed that calcite nanoparticles increase the glass transition temperature of Nylon 6 up to 12 °C, while a less pronounced increase was recorded for aragonite. It was stated that the most significant effect of calcite particles on the glass transition temperature was due to a large interfacial region.³⁶

The effect of filler shape on the nanocomposite reinforcement was investigated by using dynamic-mechanical thermal spectroscopy. Hydroxyapatite (HA) nanofillers with spherical and platelet particle shape were synthesized

and used in poly(vinyl acetate, PVAc) matrix. It was observed that the E' decreased with temperature in case of the neat polymer and nanocomposites but the decrease of the E' was stronger for PVAc filled spherical HA filler than for the nanocomposite with platelet HA particles. It was concluded that the higher is the difference between the mobility of the polymer interface and the bulk chains and, the higher is the portion of the interphase chains the higher is the reinforcement.²¹

The epoxy composites, reinforced by boron nitride spheres (s-BN) and flakes (f-BN) were prepared. The effect of filler morphology on thermal conductivity, thermo-mechanical and dielectric properties were investigated. At the same loading level, s-BN with the larger surface area led to a much more significant increase in glass transition temperature and lower storage modulus. The flake BN (f-BN) composites exhibit much higher E' than the spherical BN (s-BN). It was concluded that the high storage modulus of the f-BN composites could be attributed to the particular two-dimensional flake morphology and larger size of the f-BN, which has more significant potential to resist on the deformation of composites at changing temperatures.³⁷

4. Conclusions

PHBV composites containing calcium carbonate particles with different morphology and shape were prepared and characterized for understanding the effect of particle characteristics on composite properties. The thermal and barrier properties were investigated by using XRD, FTIR, TG, DSC, OTR and DMA analysis. XRD and DSC studies showed an increase in crystallinity due to the addition of particles. TGA analysis revealed improvement in thermal degradation behaviour of the composites. It was found that the gas barrier properties of composites were improved in the presence of particles within the matrix. The nanoparticle shape has been shown to be a con-

tributing factor to the biocomposite properties. The best barrier properties were obtained for rhombohedral calcite particles. Overall, a 25% improvement in barrier properties was obtained for the PHBV/C0.5 biocomposites in comparison to the neat PHBV sample. According to DSC and XRD results, the composite samples show a high level of crystallinity which explains the lowest oxygen permeability. It is also important to note that the rhombohedral calcite particles may increase more the barriers properties of the polymer by creating a maze or tortuous path that retards the diffusion of gas molecules through the polymer matrix compare to spherical shape vaterite particles. The thermo-mechanical properties of the PHBV composites also improved with the incorporation of the calcium carbonate particles within the polymer matrix. However, rhombohedral calcium carbonate particles exhibited the highest modulus increase compared to neat PHBV. The incorporation of calcite and vaterite particles at 1wt% loading into PHBV matrix enhanced the storage modulus equal to 139% and 91%, respectively at 140 °C. In summary, the properties of the PHBV composites were affected by the particles and the composites with improved mechanical, thermal and barrier properties were obtained.

Acknowledgements

This research has been supported by Research Fund of the Yıldız Technical University. Project Number: FAP-2017-3164.

5. References

- N. F. Braga, A. P. da Silva, T. M. Arantes, A. P. Lemes, F. H. Cristovan, *Materials Research Express*, **2018**, *5*. DOI:10.1088/2053-1591/aa9f7a
- M. Oner, B. Ilhan, *Materials Science & Engineering C-Materials for Biological Applications*, **2016**, *65*, 19–26. DOI:10.1016/j.msec.2016.04.024
- G. Keskin, G. Kizil, M. Bechelany, C. Pochat-Bohatier, M. Oner, *Pure and Applied Chemistry*, **2017**, *89*, 1841–1848. DOI:10.1515/pac-2017-0401
- M. Öner, G. Keskin, G. Kızıl, C. Pochat-Bohatier, M. Bechelany, *Polymer Composites*, **2017**.
- J. L. C. Mayorga, M. J. F. Rovira, L. C. Mas, G. S. Moragas, J. M. L. Cabello, *Journal of Applied Polymer Science*, **2017**, *135*.
- A. Jaszkiwicz, A. K. Bledzki, A. Meljon, *Journal of Applied Polymer Science*, **2013**, *130*, 3175–3183.
- Y. Srithep, T. Effingham, J. Peng, R. Sabo, C. Clemons, L. S. Turng, S. Pilla, *Polymer Degradation and Stability*, **2013**, *98*, 1439–1449. DOI:10.1016/j.polymdegradstab.2013.05.006
- A. Dufresne, D. Dupeyre, M. Paillet, *Journal of Applied Polymer Science*, **2003**, *87*, 1302–1315. DOI:10.1002/app.11546
- S. Singh, A. K. Mohanty, M. Misra, *Composites Part a-Applied Science and Manufacturing*, **2010**, *41*, 304–312. DOI:10.1016/j.compositesa.2009.10.022
- A. Javadi, Y. Srithep, S. Pilla, C. C. Clemons, S. Q. Gong, L. S. Turng, *Polymer Engineering and Science*, **2011**, *51*, 1815–1826. DOI:10.1002/pen.21972
- L. Jiang, J. J. Huang, J. Qian, F. Chen, J. W. Zhang, M. P. Wolcott, Y. W. Zhu, *Journal of Polymers and the Environment*, **2008**, *16*, 83–93. DOI:10.1007/s10924-008-0086-7
- S. S. Ahankari, A. K. Mohanty, M. Misra, *Composites Science and Technology*, **2011**, *71*, 653–657. DOI:10.1016/j.compscitech.2011.01.007
- E. Ten, J. Turtle, D. Bahr, L. Jiang, M. Wolcott, *Polymer*, **2010**, *51*, 2652–2660. DOI:10.1016/j.polymer.2010.04.007
- N. F. Magalhaes, K. Dahmouche, G. K. Lopes, C. T. Andrade, *Applied Clay Science*, **2013**, *72*, 1–8. DOI:10.1016/j.clay.2012.12.008
- L. Hassaini, M. Kaci, N. Touati, I. Pillin, A. Kervoelen, S. Bruzard, *Polymer Testing*, **2017**, *59*, 430–440. DOI:10.1016/j.polymertesting.2017.03.004
- S. Singh, A. K. Mohanty, T. Sugie, Y. Takai, H. Hamada, *Composites Part a-Applied Science and Manufacturing*, **2008**, *39*, 875–886. DOI:10.1016/j.compositesa.2008.01.004
- S. Vidhate, L. Innocentini-Mei, N. A. D'Souza, *Polymer Engineering and Science*, **2012**, *52*, 1367–1374. DOI:10.1002/pen.23084
- S. Kirboga, M. Oner, *Powder Technology*, **2017**, *308*, 442–450. DOI:10.1016/j.powtec.2016.11.042
- T. Thenepalli, A. Y. Jun, C. Han, C. Ramakrishna, J. W. Ahn, *Korean Journal of Chemical Engineering*, **2015**, *32*, 1009–1022. DOI:10.1007/s11814-015-0057-3
- S. Kirboga, M. Oner, *Biointerface Research in Applied Chemistry*, **2016**, *6*, 1320–1326.
- J. Kalfus J. Jancar, *Polymer Composites*, **2007**, *28*, 365–371. DOI:10.1002/pc.20273
- P. H. T. Vollenberg, D. Heikens, *Polymer* **1989**, *30*, 1656–1662. DOI:10.1016/0032-3861(89)90326-1
- M. Tanniru, R. D. K. Misra, *Materials Science and Engineering a-Structural Materials Properties Microstructure and Processing*, **2005**, *405*, 178–193. DOI:10.1016/j.msea.2005.05.083
- M. A. Osman, A. Atallah, *Macromolecular Chemistry and Physics*, **2007**, *208*, 87–93. DOI:10.1002/macp.200600435
- Y. Ahn, J. H. Jeon, J. H. Park, T. Thenepalli, J. W. Ahn, C. Han, *Korean Journal of Chemical Engineering*, **2016**, *33*, 3258–3266. DOI:10.1007/s11814-016-0159-6
- R. Thire, L. C. Arruda, L. S. Barreto, *Materials Research-Ibero-American Journal of Materials*, **2011**, *14*, 340–344. DOI:10.1590/S1516-14392011005000046
- A. Neira-Carrillo, P. Vasquez-Quitral, M. Paz Diaz, M. Soledad Fernandez, J. Luis Arias, M. Yazdani-Pedram, *Journal of Solid State Chemistry*, **2012**, *194*, 400–408. DOI:10.1016/j.jssc.2012.05.039
- B. Akin, M. Oner, Y. Bayram, K.D. Demadis, *Crystal Growth & Design* **2008**, *8*, 1997–2005. DOI:10.1021/cg800092q
- S. Kerisit, S. C. Parker, J. H. Harding, *Journal of Physical Chemistry B* **2003**, *107*, 7676–7682. DOI:10.1021/jp034201b
- Q. Meng, D. Chen, L. Yue, J. Fang, H. Zhao, L. Wang, *Macromolecular Chemistry and Physics*, **2007**, *208*, 474–484.

- DOI:10.1002/macp.200600466
31. S. P. Luo, J. Z. Cao, A. G. McDonald, *Acs Sustainable Chemistry & Engineering*, **2016**, 4, 3465–3476.
DOI:10.1021/acssuschemeng.6b00495
32. Z. Wu, Z. Zhang, K. Mai, *Journal of Thermoplastic Composite Materials*, **XX**, **XX**. DOI:10.1177/0892705718807955
33. M. Oner, G. Kızıl, G. Keskin, C. Pochat-Bohatier, M. Bechelany, *Nanomaterials*, **2018**, 8, 940–959.
DOI:10.3390/nano8110940
34. S. K. Swain, S. Dash, C. Behera, S. K. Kisku, L. Behera, *Carbohydate Polymers*, **2013**, 95, 728–732.
DOI:10.1016/j.carbpol.2013.02.080
35. M. H. Klopffer, B. Flaconnèche, *Oil & Gas Science and Technology-Revue D Ifp Energies Nouvelles*, **2001**, 56, 223–244.
DOI:10.2516/ogst:2001021
36. M. Avella, M. E. Errico, G. Gentile, *Macromolecular Symposia*, **2006**, 234, 170–175. DOI:10.1002/masy.200650222
37. L. Huang, P.L. Zhu, G. Li, F.R. Zhou, D.Q. Lu, R. Sun, C.P. Wong, *Journal of Materials Science-Materials in Electronics* **2015**, 26, 3564–3572. DOI:10.1007/s10854-015-2870-1

Povzetek

Namen te študije je bil z metodo ekstruzije pripraviti poli(3hidroksibutirat-ko-3-hidroksivalerat) biokompozite z dodanimi različnimi odstotki kalcijevega karbonata. Kalcijev karbonat smo sintetizirali v odsotnosti in prisotnosti poli(vinil sulfonske kisline). Polimorfizem in morfologija kalcijevega karbonata sta se spremenila z dodatkom poli(vinil sulfonske kisline). Romboedrski kalcit dobimo v odsotnosti poli(vinil sulfonske kisline). Romboedrski kalcit se je z dodatkom poli(vinil sulfonske kisline) preoblikoval v vaterit. Preučevali smo vpliv vsebnosti polnila na lastnosti poli(3-hidroksibutirat-ko-3-hidroksivalerata) kompozitov. Strukturo in lastnosti biokompozitov poli(3-hidroksibutirat-ko-3-hidroksivalerat)/kalcijev karbonat smo preučevali z naslednjimi metodami: XRD, FTIR, TGA, DSC, SEM, OTR in DMA. Vpliv kalcijevega karbonata na kristalizacijo poli(3-hidroksibutirata-co-3-hidroksivalerata) smo opazili pri meritvah DSC in XRD. Pokazalo se je, da sta na lastnosti biokompozitov vplivala polimorfizem in morfologija kalcijevega karbonata. Dodatek 0,5 % (*w*) romboedrskega kalcita in vaterita je v primerjavi s čistim polimerom povečal stopnjo prenosa kisika (OTR) za 25 % oziroma 12 %. Raziskali smo tudi mehanske lastnosti kompozitov, ki so bile izboljšane ob dodatku kalcita oziroma vaterita.



Except when otherwise noted, articles in this journal are published under the terms and conditions of the Creative Commons Attribution 4.0 International License

Scientific paper

Extraction-Chromogenic System for Nickel(II) Based on 5-methyl-4-(2-thiazolylazo)resorcinol and Aliquat 336

Galya Konstantinova Toncheva,¹ Danail Georgiev Hristov,²
Nikolina Petkova Milcheva^{2,3} and Kiril Blazhev Gavazov^{2,3,*}

¹ Department of General and Inorganic Chemistry with Methodology of Chemical Education,
University of Plovdiv Paisii Hilendarski, 24 Tsar Assen St., Plovdiv 4000, Bulgaria

² Department of Chemical Sciences, Medical University of Plovdiv, 120 Buxton Brothers St., Plovdiv 4004, Bulgaria

³ Research Institute at the Medical University of Plovdiv, Vasil Aprilov Bld., Plovdiv 4002, Bulgaria

* Corresponding author: E-mail: kgavazov@abv.bg

Received: 06-07-2019

Abstract

A water–isobutanol extraction-chromogenic system for Ni^{II}, based on the azo dye 5-methyl-4-(2-thiazolylazo)resorcinol (MTAR; H₂L) and the ionic liquid Aliquat 336 (A336), was studied. Under the optimal conditions ($c_{\text{MTAR}} = 2.0 \times 10^{-4}$ mol dm⁻³, $c_{\text{A336}} = 5.6 \times 10^{-3}$ mol dm⁻³, pH 8.5 and extraction time $t = 1$ min), Ni^{II} is extracted as a ternary complex which can be represented by the formula (A336⁺)₂[Ni(L²⁻)₂]. In the absence of A336, or in a slightly acidic medium, a binary complex, [Ni(HL⁻)₂], with an absorption maximum at $\lambda = 548$ nm and a shoulder at 590 nm is formed. The following extraction-spectrophotometric characteristics were determined at the above-mentioned optimal conditions: λ_{max} (545 nm), molar absorptivity (5.0×10^4 dm³ mol⁻¹ cm⁻¹), Sandell's sensitivity (1.2×10^{-3} $\mu\text{g cm}^{-2}$), Beer's law limits (0.05–3.1 $\mu\text{g cm}^{-3}$), constant of extraction (Log $K = 6.1$) and fraction extracted (99.2%). The effect of foreign ions was studied; the most serious interferences were caused by Co^{II}, Cu^{II} and Cr^{III}.

Keywords: Nickel(II); 4-(2-thiazolylazo)resorcinol; ternary complex; solvent extraction; low-toxic solvent; spectrophotometry

1. Introduction

Nickel is a first-row transition metal with many industrial applications¹ and important functions in biology of microorganisms and plants.² It is involved in a variety of products, such as stainless steels, alloys, rechargeable batteries, guitar strings, green colored glasses, permanent magnets and catalysts for large-scale industrial processes. Most of the nickel produced is used in stainless steels, ferrous and non-ferrous alloys and nickel plating.³ The chief criteria of use are its resistance to air oxygen, alkalis and acids, lustrous shine, ductility, malleability, and excellent ability to alloy with both ferrous and nonferrous metals. Over 3000 alloys containing nickel are known. They have more than 250 000 applications.⁴

In the earth's crust, nickel occurs most often in combination with sulfur, iron and arsenic. It is found in all types of soils, in fossil fuels, marine sediments, volcanic emissions and iron meteorites. Anthropogenic activities

that contribute to nickel loadings in the environment include burning of fuel and residual oil, mining, smelting, refining, alloy processing, scrap metal reprocessing, waste incineration and disposal of sewage sludge or application of sludge as a fertilizer.^{4–6}

It is known that nickel may have carcinogenic, mutagenic and allergic properties.⁷ Negative health effects have been documented for respiratory, cardiovascular, gastrointestinal, hematological, musculoskeletal, hepatic, renal, dermal, ocular, immunological, developmental, neurological and reproductive systems.⁶ An allergic skin reaction is a common problem for some people; it is often associated with the presence of nickel in daily-used objects, such as jewelry, keys, jean buttons, children's clothing and toys.^{8,9}

Many analytical techniques, such as atomic absorption spectrophotometry, optical emission spectrometry, X-ray fluorescence analysis, neutron activation analysis, voltammetry and spectrophotometry, have been used for

nickel determination.^{10–14} The methods involving spectrophotometry are simple and low-cost; they can be easily combined with procedures for preliminary separation and concentration, such as cloud point extraction,¹³ solid phase extraction¹⁴ and liquid-liquid extraction (LLE).^{15–20}

5-methyl-4-(2-thiazolylazo)resorcinol (MTAR) is a well-known analytical reagent.^{21–28} It has recently been used in our laboratory for LLE of V^{IV,V}.^{29–32} Here, we describe investigations on a LLE-chromogenic system for Ni^{II} containing MTAR and the ionic liquid Aliquat 336 (A336). The selected organic solvent was isobutanol (2-methylpropan-1-ol). It is characterized by a low toxicity, volatility and corrosivity,^{33,34} can be produced from renewable resources,³⁵ fulfills the so-called “CHON principle”³⁶ and is readily biodegradable and non-bioaccumulative.^{33,37}

2. Materials and Methods

2.1. Reagents and Apparatus

Stock solution of Ni^{II} (1.7×10^{-2} mol dm⁻³; pH ~2) was prepared by dissolving NiSO₄·7H₂O (Sigma-Aldrich, 99.999% trace metals basis) in distilled water containing H₂SO₄. Working solutions (2×10^{-4} mol dm⁻³) were prepared by appropriate dilution of the stock solution. MTAR (95%, Sigma-Aldrich Chemie GmbH) was dissolved in the presence of KOH;³¹ the obtained slightly alkaline aqueous solution (pH 8–9) was at concentration of 2×10^{-3} mol dm⁻³. Aliquat 336 was purchased from Sigma-Aldrich Chemie and dissolved in isobutanol (p. a., Merck). Solutions with concentrations of 1.4×10^{-2} and 5.6×10^{-3} mol dm⁻³ were used; the calculations were based on the average molar mass of A336 (432 g mol⁻¹).³⁸ The acidity of the aqueous medium was set by the addition of buffer solution, prepared by 2 mol dm⁻³ solutions of CH₃COOH and ammonia. The pH of the buffers was measured by a WTW InoLab 7110 (Germany) pH meter with an accuracy of ±0.001 pH units. Absorbance measurements were made with a Camspec M508 and a Ultrospec3300 pro UV-Vis spectrophotometers (UK), equipped with 1 cm path-length glass cells. Distilled water was used throughout the work.

2.2. Determination of the Optimum Conditions

Solutions of Ni^{II}, MTAR and buffer were placed into a separatory funnel. The aqueous phase volume was adjusted to 5 cm³ or 10 cm³ with water. A portion of the A336 solution was added and the organic phase was adjusted to 5 cm³ with isobutanol. Then the funnel was shaken for a fixed time interval (between 5 and 300 seconds). After separation of the phases, the aqueous layer was discarded, and the organic layer was transferred into a beaker. A pinch of anhydrous Na₂SO₄ was added to remove any water and the colored solution was poured into the spectrophotometer cell. The absorbance was measured against isobutanol or simultaneously prepared blank sample.

2.3. Determination of the Distribution Ratio

The distribution ratio D was calculated by the formula $D = A_1/(A_3 - A_1)$, where A_1 is the absorbance obtained after a single extraction under the optimal pH and reagents concentrations (Table 1) and A_3 is the absorbance obtained after a triple extraction.^{30,31} The single extraction and the first stage of the triple extraction were performed with equal volumes of both phases (5 cm³). The organic layers were transferred into two 25-cm³ calibrated flasks and the flask for the single extraction was brought to volume with the isobutanol solution of A336 (5.6×10^{-3} mol dm⁻³). The second stage of the triple extraction was performed by adding a 5-cm³ portion of the A336 solution to the aqueous phase which remained after the first stage. The third stage was performed in the same manner. The two successive organic layers were transferred to the flask with the isobutanol extract obtained after the first stage. The volume was brought to the mark with the A336 solution. Absorbances A_1 and A_3 were measured against corresponding blanks.

2.4. Investigation of the Influence of Foreign Ions

Solutions of Ni^{II} (1 cm³, 2×10^{-4} mol dm⁻³), foreign ion, MTAR (1 cm³, 2×10^{-3} mol dm⁻³) and buffer (1 cm³, pH 8.5) were successively placed into a separatory funnel. The aqueous phase volume was adjusted to 10 cm³ with

Table 1. LLE-spectrophotometric optimization of the Ni^{II} – MTAR – A336 – water – isobutanol system. The volume of the organic phase was 5 cm³.

Parameter	Optimization range	Optimal value
Wavelength, nm	Visible range	545
pH	3.9–9.9	8.5
Volume of the aqueous phase, cm ⁻³	5 and 10	10
Concentration of MTAR, mol dm ⁻³	$(0–1.6) \times 10^{-3}$	2.0×10^{-4}
Concentration of A336, mol dm ⁻³	$(0–1.4) \times 10^{-2}$	5.6×10^{-3}
Extraction time, seconds	5–300	60

water. Then A336 solution (5 cm^3 , $5.6 \times 10^{-3} \text{ mol dm}^{-3}$) was added and the funnel was shaken for 1 min. The organic layer was transferred into a beaker, dried with a pinch of anhydrous Na_2SO_4 and poured into the spectrophotometer cell. The absorbance was measured at 545 nm against isobutanol. For control, samples prepared by the same procedure in the absence of the foreign ion or Ni^{II} were also run.

3. Results and Discussion

3.1. Absorption Spectra of the Isobutanol-Extracted Complexes

Spectra of isobutanol-extracted Ni–MTAR complexes in the presence (1, 3) or absence (2, 4) of A336 are shown in Fig. 1. The spectra 1 and 2 are alike (1: $\lambda_{\text{max}} = 545 \text{ nm}$; 2: $\lambda_{\text{max}} = 548 \text{ nm}$), however in absence of A336 (2) the absorbance is lower, and a shoulder at about 590 nm is observed. Such a shoulder is slightly visible in spectrum 1. There is a tendency for it to become more and more imperceptible with increasing pH and decreasing the MTAR concentration.

At lower pH values (4.7; spectra 3 and 4), nickel is extracted to a negligible extent regardless of the presence or absence of A336. The absorbance of the blanks in the absence of A336 (2' and 4') is lower than that obtained in the presence of A336 (1' and 3', respectively). This can be explained by the formation of an extractable ion pair between the anion of the azo dye (HL^-)^{31,39,40} and the cation of the ionic liquid (A336^+).

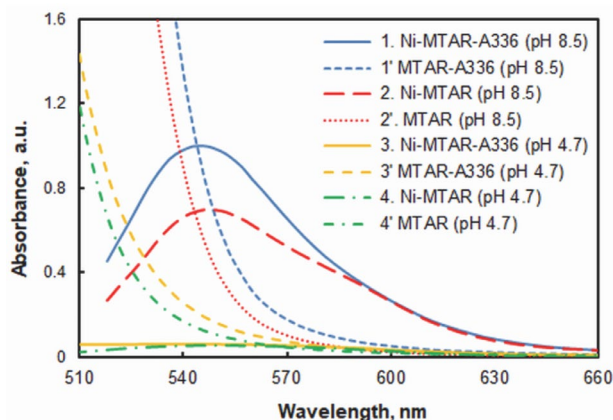


Figure 1. Absorption spectra in isobutanol of complexes against blanks (1 – 4; $c_{\text{Ni}} = 2 \times 10^{-5} \text{ mol dm}^{-3}$, $c_{\text{MTAR}} = 2.7 \times 10^{-4} \text{ mol dm}^{-3}$, $c_{\text{A336}} = 5.6 \times 10^{-3} \text{ mol dm}^{-3}$, $V_{\text{aq. phase}} = 10 \text{ cm}^3$, extraction time $t = 60 \text{ sec}$) and corresponding blanks against isobutanol (1' – 4'). Samples 2, 2', 4 and 4' do not contain A336; pH is given in the legend.

3.2. Effect of pH

The effect of pH on the absorbance obtained in the presence or absence of A336 is shown in Fig. 2. Ammo-

nia-acetate buffer solutions, which have the best buffering action at pH 4.75 (the pK_a of acetic acid) and 9.25 (the pK_a of NH_4^+)⁴¹ were used in all experiments. In the presence of A336 (series 1), maximal absorbance was obtained in slightly alkaline medium. The sharp decrease at $\text{pH} < 6$ can be attributed to incomplete complex formation due to the predominance of doubly protonated MTAR species.⁴² In the absence of A336 (series 2), maximal absorbance was recorded in the slightly acidic region ($\text{pH ca. } 6.5 - 7.0$). It makes sense that the course of series 1 and series 2 is identical in the acidic region (up to $\text{pH ca. } 6$); probably the absorbance obtained in the presence of A336 is due to the simultaneous extraction of two complexes, Ni–MTAR–A336 and Ni–MTAR. However, with the increase in pH, the contribution of the ternary complex to the total absorbance becomes greater.

The decrease in absorbance at $\text{pH} > \text{ca. } 9$ (series 1) can be attributed to two factors: (i) presence of hydrolyzed $\text{Ni}(\text{OH})^+$ species;⁴³ and (ii) a competitive extraction of the $(\text{A336}^+)(\text{HL}^-)$ ion pair which reduces the effective concentrations of the reagents to a larger extent at higher pH values (see spectra 1' and 3' in Fig. 1).

One can conclude from Fig. 2, and from the above mentioned pK_a value of NH_4^+ (9.25), that the optimal pH range for the extraction of Ni^{II} is 8.3–9.0. We performed our further investigations at pH 8.5.

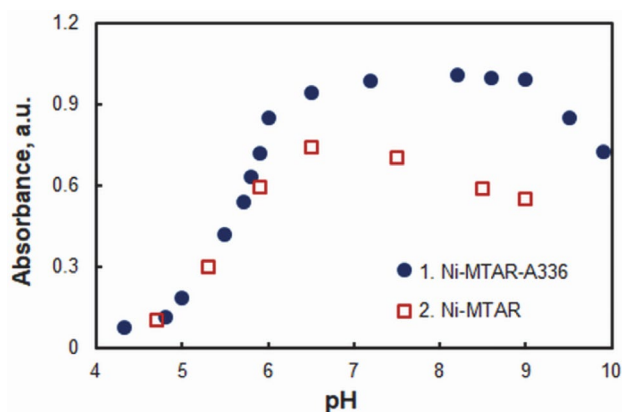


Figure 2. Absorbance of the complex in presence (1) or absence (2) of A336 vs. pH of the aqueous phase. $c_{\text{Ni}} = 2 \times 10^{-5} \text{ mol dm}^{-3}$, $c_{\text{MTAR}} = 2 \times 10^{-4} \text{ mol dm}^{-3}$, $c_{\text{A336}} = 5.6 \times 10^{-3} \text{ mol dm}^{-3}$, $V_{\text{aq. phase}} = 10 \text{ cm}^3$, extraction time $t = 60 \text{ sec}$.

3.3. Effect of the Reagents Concentrations, Volume of the Aqueous Phase and Shaking Time

The effect of the MTAR concentration on the absorbance is shown in Fig. 3 for two different sets of conditions. There is a maximum in both series; at high concentrations of MTAR, the absorption decreases. With a 2:1 volume ratio (series 2; 10 cm^3 aqueous phase / 5 cm^3 isobutanol phase), the apparent molar absorptivity is high-

er. The optimal reagent concentration for this volume ratio appears to be $c_{\text{MTAR}} = 2.0 \times 10^{-4} \text{ mol dm}^{-3}$. It is considerably lower (by almost an order of magnitude) than the MTAR concentration required for the extraction of V^{V} .³¹

The effect of the A336 concentration on the absorbance is shown in Fig. 4. The optimal concentration is $c_{\text{A336}} = 5.6 \times 10^{-3} \text{ mol dm}^{-3}$. It is also lower than that required for the extraction of V^{V} ,³¹ this indicates that the Ni^{II} –MTAR–A336 complex is more stable than the corresponding V^{V} complex.

The effect of shaking time was studied under the optimal pH and reagents concentrations (Table 1). It was found that 50 seconds are enough for a quantitative extraction of Ni^{II} . To avoid accidental errors, induced by the combination of short shaking times and different shaking rates, we shook for 60 seconds in our further experiments.

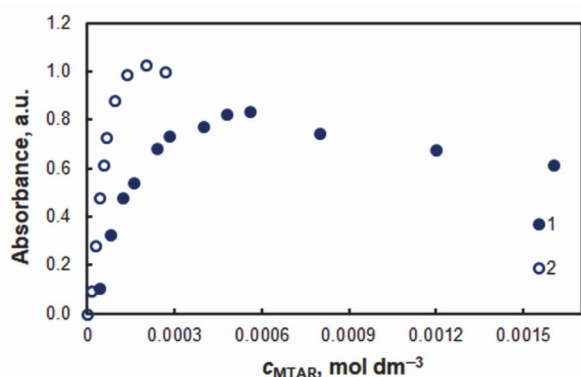


Figure 3. Absorbance vs. concentration of MTAR. (1) $c_{\text{Ni}} = 4 \times 10^{-5} \text{ mol dm}^{-3}$, $c_{\text{A336}} = 1.4 \times 10^{-2} \text{ mol dm}^{-3}$, pH 6, $V_{\text{aq. phase}} = 5 \text{ cm}^3$, extraction time $t = 60 \text{ sec}$; (2) $c_{\text{Ni}} = 2 \times 10^{-5} \text{ mol dm}^{-3}$, $c_{\text{A336}} = 5.6 \times 10^{-3} \text{ mol dm}^{-3}$, pH 8.5, $V_{\text{aq. phase}} = 10 \text{ cm}^3$, extraction time $t = 60 \text{ sec}$.

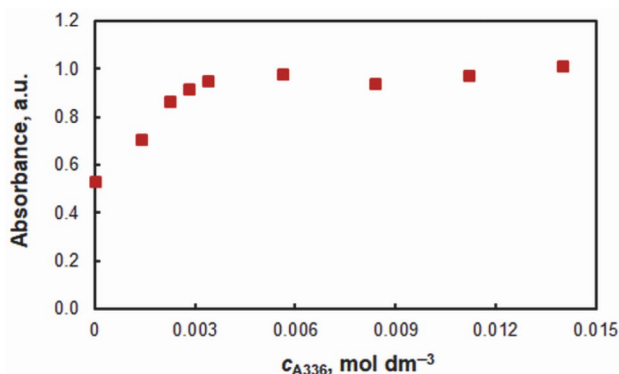


Figure 4. Absorbance vs. concentration of A336. $c_{\text{Ni}} = 2 \times 10^{-5} \text{ mol dm}^{-3}$, $c_{\text{MTAR}} = 2.0 \times 10^{-4} \text{ mol dm}^{-3}$, pH 8.5, $V_{\text{aq. phase}} = 10 \text{ cm}^3$, extraction time $t = 60 \text{ sec}$.

3. 4. Molar Ratios, Structure and Equations of Complex Formation and Extraction

It is known that thiazolylazo- and pyridylazo dyes form 1:1⁴⁴ or 1:2^{45–48} complexes with Ni^{II} . In aqueous medium, at least two different 1:2 Ni-to-PAR complex species

($\text{PAR} = \text{H}_2\text{L} = 4\text{-(2-pyridylazo)resorcinol}$) exist, $[\text{Ni}(\text{HL})\text{L}]^-$ and $[\text{NiL}_2]^{2-}$.⁴⁹ In the presence of a quaternary ammonium salt (tetradecyldimethylbenzylammonium chloride; Q^+Cl^-),⁵⁰ two kinds of complexes can be extracted in chloroform, $[\text{Ni}(\text{HL})_2] \cdot n(\text{Q}^+\text{Cl}^-)$ and $(\text{Q}^+)_2[\text{NiL}_2]$; the second one has a higher molar absorptivity. Karipcin et al. isolated in solid state water-insoluble octahedral 1:2 binary complexes with PAR⁴⁷ or 4-(2-thiazolylazo)resorcinol (TAR);⁴⁸ they can be represented by the general formula $[\text{Ni}(\text{HL})_2]$. The TAR complex is partially soluble in chloroform and readily soluble in alcohols; in ethanol, it shows an absorption maximum at 543 nm and a shoulder at 586 nm.⁴⁸

It is clear from our investigations (see Fig. 1, Fig 2 and Fig. 4) that at least two different Ni^{II} –MTAR isobutanol-extractable complexes exist: (i) a binary Ni–MTAR complex; it is extracted in the absence of A336 (Fig. 1, spectrum 1); and (ii) a ternary Ni–MTAR–A336 complex (Fig. 1, spectrum 2). The MTAR: Ni^{II} and A336: Ni^{II} molar ratios in the ternary complex were determined by the straight-line method of

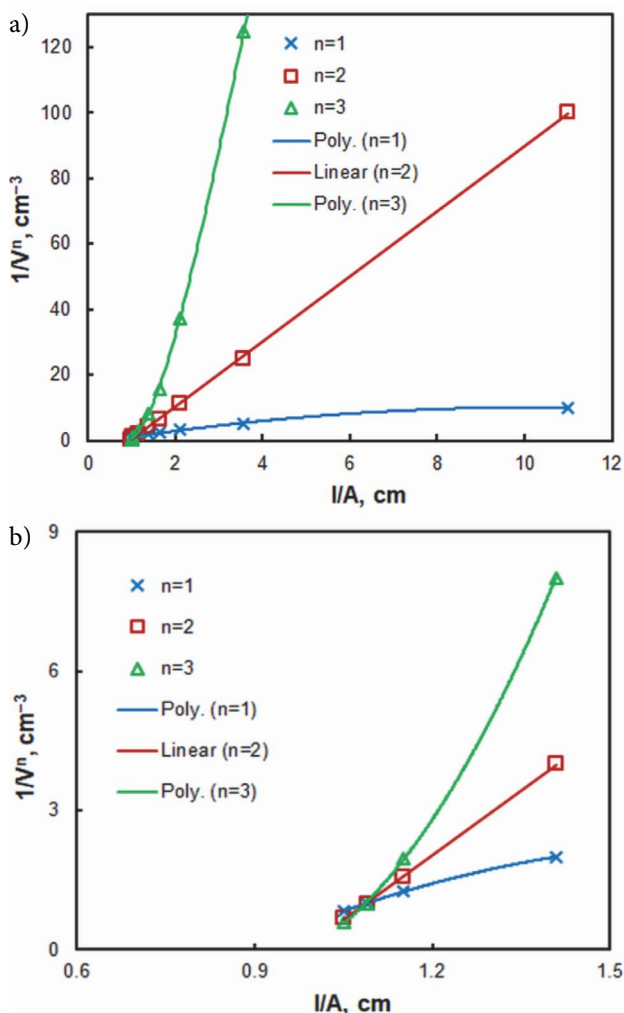
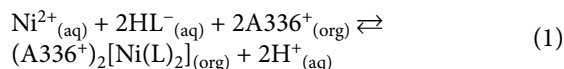
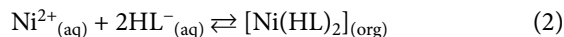


Figure 5. Determination of the MTAR/ Ni^{II} (a) and A336/ Ni^{II} (b) molar ratios by the straight-line method of Asmus. The experimental conditions are given in Fig. 3 (series 2) and Fig. 4, respectively.

Asmus⁵¹ (Fig. 5) and the mobile equilibrium method⁵² (Fig. 6). Its formation and extraction can be represented by Eq. 1.



In the absence of A336, a neutral $[\text{Ni}(\text{HL})_2]$ complex is formed (Eq. 2).



As mentioned above, a complex with the same formula (which is insoluble in water and soluble in alcohols)

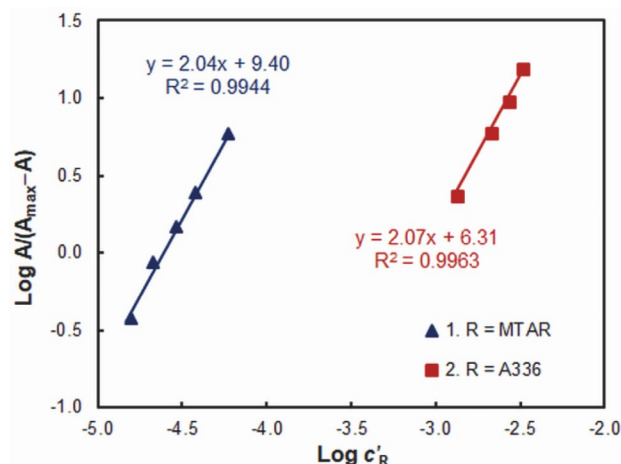


Figure 6. Determination of the MTAR/ Ni^{II} (1) and A336/ Ni^{II} (2) molar ratios by the mobile equilibrium method. The experimental conditions are given in Fig. 3 (series 2) and Fig. 4, respectively.

has been prepared with TAR.⁴⁸ The MTAR complex obtained by us has similar spectral characteristics (an absorption maximum of 548 nm and a shoulder at about 590 nm), indicating that it probably has a similar structure. Most likely, both MTAR complexes, $[\text{Ni}(\text{HL})_2]$ and $(\text{A336}^{+})_2[\text{Ni}(\text{L})_2]$, have an octahedral geometry which is common for Ni^{II} centers.^{47,48,53,54} Donor atoms of each of the tridentate MTAR units should be the o-hydroxyl oxygen (relative to the azo-group) and the two nitrogens (from the thiazole ring and azo-group).^{47,48,55}

As shown in Eqs. 1 and 2, MTAR at the operating conditions exists mainly in its HL^{-} form (with a proton in the OH-group in ortho-position relative to the azo-group).^{42,56} It is known that this form dominates (in aqueous medium) at the pH range of 5.7–11.8.⁴²

3. 5. Beer's Law and Analytical Characteristics

The dependence between the concentration of Ni^{II} in the aqueous phase and the absorbance of the extract was studied under the optimal conditions (Table 1). A good linearity was obtained in the range of 0.05 – 3.1 $\mu\text{g cm}^{-3}$ ($R^2 = 0.9993$, $N = 9$). The linear regression equation was $A = 0.845\gamma - 0.006$, where A is the absorbance and γ is the concentration ($\mu\text{g cm}^{-3}$) of Ni^{II} . The standard deviations of the slope and intercept were 0.008 and 0.013, respectively. The limits of detection (LOD) and quantitation (LOQ), calculated as 3- and 10-times standard deviation of the intercept divided by the slope, were $\text{LOD} = 46 \text{ ng cm}^{-3}$ and $\text{LOQ} = 153 \text{ ng cm}^{-3}$. The molar absorptivity (ϵ) and Sandell's sensitivity (S) at $\lambda_{\text{max}} = 545 \text{ nm}$ were $\epsilon = 5.0 \times 10^4 \text{ dm}^3 \text{ mol}^{-1} \text{ cm}^{-1}$ and $S = 1.2 \times 10^{-3} \mu\text{g cm}^{-2}$, respectively.

Table 2. Effect of foreign ions in determination of 11.7 μg of Ni^{II} .

Foreign ion (FI) added	Added salt	FI : Ni^{II} mass ratio	Amount of Ni^{II} found (μg)	(%)
Al^{III}	$\text{Al}_2(\text{SO}_4)_3 \cdot 18\text{H}_2\text{O}$	8.5	11.4	97.4
Br^{-}	NaBr	850	11.7	100
Cd^{II}	CdCl_2	5	12.3	105
Cl^{-}	NH_4Cl	850	11.8	101
Co^{II}	$\text{CoSO}_4 \cdot 7\text{H}_2\text{O}$	1	17.0	146
Cr^{III}	$\text{Cr}_2(\text{SO}_4)_3$	1	8.42	72.0
Cr^{VI}	K_2CrO_4	500	11.9	101
Cu^{II}	$\text{CuSO}_4 \cdot 5\text{H}_2\text{O}$	1	16.1	138
F^{-}	NH_4F	850	10.6	99.4
Fe^{III}	$\text{Fe}_2(\text{SO}_4)_3$	5	12.3	105
HPO_4^{2-}	Na_2HPO_4	500	11.8	101
I^{-}	KI	250	11.1	95.1
Mg^{II}	MgSO_4	500	11.7	100
Mn^{II}	$\text{MnSO}_4 \cdot 5\text{H}_2\text{O}$	5	11.7	100
Mo^{VI}	$(\text{NH}_4)_6\text{Mo}_7\text{O}_{24} \cdot 4\text{H}_2\text{O}$	100	11.7	100
NO_3^{-}	NH_4NO_3	850	10.4	97.2
Re^{VII}	NH_4ReO_4	400	11.5	98.2
V^{V}	NH_4VO_3	5	12.0	103
W^{VI}	$\text{Na}_2\text{WO}_4 \cdot 2\text{H}_2\text{O}$	500	12.0	103
Zn^{II}	$\text{ZnSO}_4 \cdot 7\text{H}_2\text{O}$	1	12.5	107

The distribution ratio D was calculated from the absorbances obtained after single and triple extractions as described above: $D = 121 \pm 3$ (six replicate measurements). The fraction extracted, $E = 99.2\%$, was found by the formula $E\% = 100 \times D/(D+1)$. The conditional equilibrium constant characterizing Eq. 1 was calculated by the mobile equilibrium method⁵² (Fig. 5, straight line 2; abscissa intercept). The obtained value was $\text{Log } K = 6.1 \pm 0.2$.

3. 6. Effect of Foreign Ions

Various salts were used to test the selectivity of the developed procedure. Their effect is summarized in Table 2. The most significant interferences were those of Co^{II} , Cu^{II} and Cr^{III} which form intensively colored complexes under the specified conditions. Cr^{III} causes a negative error, while Co^{II} and Cu^{II} cause positive errors. Zn^{II} also causes positive errors, however its interfering effect is smaller. A 250-fold excess of I^- ; 100-fold excess of Mo^{VI} ; 8.5-fold excess of Al^{III} ; and 5-fold excess of V^{V} , Fe^{III} , Cd^{II} and Mn^{II} are tolerable. The determination of Ni^{II} is not affected by high concentrations of alkali and alkaline-earth ions, NH_4^+ , Cl^- , Br^- , F^- , NO_3^- , SO_4^{2-} , CrO_4^{2-} , WO_4^{2-} , ReO_4^- and HPO_4^{2-} .

4. Conclusions

The described investigations shed light on the complex formation between Ni^{II} and MTAR in the presence or absence of A336. The conditions of existence of the two main extracted complexes, $(\text{A336}^+)_2[\text{Ni}(\text{L})_2]$ and $[\text{Ni}(\text{HL})_2]$, have been outlined and the differences in their spectra have been highlighted. In a slightly alkaline medium, Ni^{II} predominantly forms a ternary complex. It is intensively colored and readily extractable into isobutanol. This solvent is less toxic than the diluents commonly applied to improve the physico-chemical characteristics of the ionic liquid A336 (e.g., benzene,⁵⁷ carbon tetrachloride,⁵⁸ chloroform,⁵⁸ toluene,⁵⁹ xylene⁶⁰ and kerosene⁶¹) and the organic solvents typically used for LLE-spectrophotometric determination of Ni^{II} (e.g., chloroform).¹⁷⁻²⁰

Acknowledgments

This work was supported by the Research Fund of the University of Plovdiv "Paisii Hilendarski" (Grant No SP19-HF009).

5. References

1. K. K. Chatterjee, *Uses of Metals and Metallic Minerals*, New Age International (P) Ltd. Publishers, New Delhi, India, 2007, pp. 272–275.
2. P. H. Brown, in: A. V. Barker, D. J. Pilbeam (Ed.): *Handbook of Plant Nutrition*, CRC Press, Boca Raton, USA, 2007, pp. 395–409.
3. A. Apostolikas, E. Frogoudakis, J. Bakallbashi, in: *Nickel, World Production and Demand: Proceedings of the 3rd Balkan Mining Congress (Balkanmine 2009)*, The Chamber of Mining Engineers of Turkey, Turkey, 2009, pp. 29–34.
4. Y. Chau, O. Kulikovskiy-Cordeiro, *Environ. Rev.* 1995, 3, 95–120. DOI:10.1139/a95-004
5. S. Sikdar, M. Kundu, *ChemBioEng Rev.* 2018, 5, 18–29. DOI:10.1002/cben.201700005
6. R. Eisler, Nickel hazards to fish, wildlife, and invertebrates: a synoptic review; Geological Survey Washington DC1998, https://www.pwrc.usgs.gov/eisler/CHR_34_Nickel.PDF, (assessed: June 05, 2019)
7. S. Dzugkoev, I. Mozhaeva, O. Margieva, A. Tedtoeva, F. Dzugkoeva, *Sciences of Europe* 2017, 2, 78–81.
8. Position Statement on Nickel Sensitivity (August 22, 2015), <https://www.aad.org/Forms/Policies/Uploads/PS/PS-Nickel%20Sensitivity.pdf> (assessed: June 05, 2019)
9. J. P. Thyssen, *Contact Dermatitis* 2011, 65, 1–68. DOI:10.1111/j.1600-0536.2011.01957.x
10. M. Ghaedi, *Spectrochim. Acta A* 2007, 66, 295–301. DOI:10.1016/j.saa.2006.02.055
11. S. K. Kumar, P. S. Rao, L. Krishnaiah, B. Jayaraj, P. Chiranjeevi, *Anal. Sci.* 2004, 20, 951–953. DOI:10.2116/analsci.20.951
12. Z. Li, J. Pan and J. Tang, *Anal. Lett.* 2002, 35, 167–183. DOI:10.1081/AL-120002369
13. Y. Bazel, A. Tupys, Y. Ostapiuk, O. Tymoshuk, V. Matiychuk, *J. Mol. Liq.* 2017, 242, 471–477. DOI:10.1016/j.molliq.2017.07.047
14. D. Rekha, J. Kumar, B. Jayaraj, Y. Lingappa, P. Chiranjeevi, *Bull. Korean Chem. Soc.* 2007, 28, 373–378. DOI:10.5012/bkcs.2007.28.3.373
15. C. Ramachandraiah, J. Rajesh Kumar, K. Janardhan Reddy, S. Lakshmi Narayana, A. Varada Reddy, *J. Environ. Manage.* 2008, 88, 729–736. DOI:10.1016/j.jenvman.2007.03.033
16. L. S. Sarma, J. R. Kumar, K. J. Reddy, T. Thriveni, A. V. Reddy, *J. Trace Elem. Med. Bio.* 2008, 22, 285–295. DOI:10.1016/j.jtemb.2008.06.003
17. C. Ravichandran, D. Benzil, C. Ramachandraiah, K. Chandrasekhar, *Int. J. Bioassays* 2015, 4, 4468–4472. DOI:10.21746/ijbio.2015.11.005.
18. K. Kuliev, N. Verdizadeh, S. Aliev, G. Suleymanova, *World J. Pharmaceut. Res.* 2018, 7, 61–73. DOI:10.20959/wjpr201819-13762.
19. S. G. Aliyev, R. A. Ismailova, E. I. Suleymanova, L. M. Magararomova, S. S. Sultanzadeh, Z. G. Asgerova, A. Z. Zalov, *Int. J. Innovat. Sci., Eng. Technol.* 2018, 5, 192–206.
20. N. A. Verdizadeh and K. A. Kuliev, *Izv. Saratov Univ. (N.S.), Ser. Chemistry. Biology. Ecology* 2017, 17, 247–262. DOI:10.18500/1816-9775-2017-17-3-247-262
21. M. Tuzen, M. Soylak, D. Citak, H. S. Ferreira, M. G. A. Korn, M. A. Bezerra, *J. Hazard. Mat.* 2009, 162, 1041–1045. DOI:10.1016/j.jhazmat.2008.05.154

22. W. N. L. dos Santos, D. D. Cavalcante, H. S. Ferreira, C. F. das Virgens, A. R. Borges, M. M. Silva, M. G. R. Vale, *Int. J. Environ. Anal. Chem.* **2011**, *91*, 1447–1452. DOI:10.1080/03067319.2010.484885
23. M. Soylyak, M. Tuzen, *J. Hazard. Mat.* **2008**, *152*, 656–661. DOI:10.1016/j.jhazmat.2007.07.027
24. S. A. Rocha and S. L. Ferreira, *Eurasian J. Anal. Chem.* **2007**, *2*, 1–11. DOI:10.12973/ejac/77011
25. Y.-S. Chung, W.-S. Chung, *Bull. Korean Chem. Soc.* **2003**, *24*, 1781–1784.
26. M. A. Zaitoun, A. K. El-Qisairi, K. A. Momani, H. A. Qaseer, W. Alhalasah, *J. Environ. Occup. Sci.* **2014**, *3*, 154–161. DOI:10.5455/jeos.20140909071020
27. M. Zaitoun, K. Momani, Q. Jaradat, I. Momani, I. Qurashi, *Jordan J. Chem.* **2014**, *9*, 81–96. DOI:10.12816/0026472
28. Y. Erdogdu, Ü. C. Başköse and S. Sağlam, *Chem. Pap.* **2019**. DOI:10.1007/s11696-019-00739-4
29. K. B. Gavazov, T. S. Stefanova, *Croat. Chem. Acta* **2014**, *87*, 233–240. DOI:10.5562/cca2436
30. K. B. Gavazov, V. B. Delchev, K. T. Mileva, T. S. Stefanova, G. K. Toncheva, *Acta Chim. Slov.* **2016**, *63*, 392–398. DOI:10.17344/acsi.2016.2431
31. G. K. Toncheva, N. P. Milcheva, K. B. Gavazov, *Acta Chim. Slov.* **2018**, *65*, 847–852. DOI:10.17344/acsi.2018.4491
32. K. B. Gavazov, V. B. Delchev, N. P. Milcheva, G. K. Toncheva, *Open Chem.* **2019**, *17*, 599–608. DOI:10.1515/chem-2019-0071
33. J. Patocka, K. Kuca, *Mil. Med. Sci. Lett.* **2012**, *81*, 142–163. DOI:10.31482/mmsl.2012.022.
34. A. Pal, V. Manish, S. Gupta, N. Kumar, *SAE Tech. Pap.* **2013**, *2013-24-0151*. DOI:10.4271/2013-24-0151
35. S. Atsumi, T. Hanai and J. C. Liao, *Nature* **2008**, *451*, 86–90. DOI:10.1038/nature06450
36. E. Löfström-Engdahl, On the diluent and solvent effects in liquid-liquid extraction systems based on bis-triazine-bipyridine (BTBP) ligands, PhD thesis, Chalmers University of Technology, Gothenburg, Sweden 2014, <http://publications.lib.chalmers.se/records/fulltext/203658/203658.pdf> (assessed: June 05, 2019)
37. C. E. Schaefer, X. Yang, O. Pelz, D. T. Tsao, S. H. Streger, R. J. Steffan, *Chemosphere* **2010**, *81*, 1111–1117. DOI:10.1016/j.chemosphere.2010.09.002
38. J.-P. Mikkola, P. Virtanen, R. Sjöholm, *Green Chem.* **2006**, *8*, 250–255. DOI:10.1039/b512819f
39. K. B. Gavazov, G. K. Toncheva, *Russ. J. Gen. Chem.* **2015**, *85*, 192–197. DOI:10.1134/S1070363215010338
40. K. B. Gavazov, G. K. Toncheva, *J. Adv. Chem.* **2013**, *5*, 641–651.
41. L. Konermann, *J. Am. Soc. Mass Spectrom.* **2017**, *28*, 1827–1835. DOI:10.1007/s13361-017-1739-3
42. N. Menek, E. Eren, S. Topçu, *Dyes Pigm.* **2006**, *68*, 205–210. DOI:10.1016/j.dyepig.2005.01.010
43. D. D. Perrin, *J. Chem. Soc. (Resumed)* **1964**, 3644–3648. DOI:10.1039/jr9640003644
44. A. S. Amin, *Quim. Anal.* **2001**, *20*, 145–151. DOI:10.1023/A:1008799422509
45. A. S. Amin, M. S. Ibrahim, *Ann. Chim. (Rome)* **2001**, *91*, 103–110.
46. K. Ohshita, H. Wada, G. Nakagawa, *Anal. Chim. Acta* **1981**, *124*, 193–200. DOI:10.1016/S0003-2670(01)83913-1
47. F. Karipcin, E. Kabalcilar, *Acta Chim. Slov.* **2007**, *54*, 242–247.
48. F. Karipcin, B. Dede, S. Percin-Ozkorucuklu, E. Kabalcilar, *Dyes Pigm.* **2010**, *84*, 14–18. DOI:10.1016/j.dyepig.2009.06.010
49. D. Nonova and B. Evtimova, *Anal. Chim. Acta* **1972**, *62*, 456–461. DOI:10.1016/0003-2670(72)80058-8
50. H. Hoshino, T. Yotsuyanagi, K. Aomura, *Anal. Chim. Acta* **1976**, *83*, 317–328. DOI:10.1016/S0003-2670(01)84658-4
51. E. Asmus, *Fresenius' J. Anal. Chem.* **1960**, *178*, 104–116. DOI:10.1007/BF00467200
52. Z. Zhiming, M. Dongsten, Y. Cunxiao, *J. Rare Earths* **1997**, *15*, 216–219.
53. R. Vafazadeh, M. Namazian, B. Shahpoori-Arani, A. C. Willis, P. D. Carr, *Acta Chim. Slov.* **2018**, *65*, 372–379. DOI:10.17344/acsi.2017.4096
54. X.-N. Fang, J. Li, X.-G. Yi, Q. Luo, J.-Y. Chen and Y.-X. Li, *Acta Chim. Slov.* **2019**. DOI:10.17344/acsi.2018.4885
55. H. R. Hovind, *Analyst* **1975**, *100*, 769–796. DOI:10.1039/an9750000769
56. K. Pytlakowska, V. Kozik, M. Dabioch, *Talanta* **2013**, *110*, 202–228. DOI:10.1016/j.talanta.2013.02.037
57. W. Wei, C.-W. Cho, S. Kim, M.-H. Song, J. K. Bediako, Y.-S. Yun, *J. Mol. Liq.* **2016**, *216*, 18–24. DOI:10.1016/j.molliq.2016.01.016
58. M. Atanassova, I. L. Dukov, *Separ. Purif. Technol.* **2004**, *40*, 171–176. DOI:10.1016/j.seppur.2004.02.007
59. V. Gardoňová, M. Labaška, I. Antalík, J. Kuruc, *J. Radioanal. Nucl. Chem.* **2013**, *295*, 1353–1360. DOI:10.1007/s10967-012-1955-z
60. A. G. Gaikwad, A. D. Damodaran, *J. Radioanal. Nucl. Chem.* **1992**, *163*, 277–288. DOI:10.1007/BF02034801
61. J. A. López-López, B. Herce-Sesa, C. Moreno, *Talanta* **2016**, *159*, 117–121. DOI:10.1016/j.talanta.2016.06.018

Povzetek

Proučevali smo kromogen sistem ekstrakcije voda-izobutanol za Ni^{II} na osnovi azo barvila 5-metil-4- (2-tiazolilazo) resorcinola (MTAR;H₂L) in ionske tekočine Aliquat 336 (A336). Pri uporabi optimalnih pogojev ekstrakcije ($c_{\text{MTAR}} = 2,0 \cdot 10^{-4} \text{ mol dm}^{-3}$, $c_{\text{A336}} = 5,6 \cdot 10^{-3} \text{ mol dm}^{-3}$, pH 8,5 in čas ekstrakcije $t = 1 \text{ min}$), se Ni^{II} ekstrahira kot ternarna kompleksna spojina, ki jo lahko zapišemo s formulo $(\text{A336}^+)_2[\text{Ni}(\text{L}^{2-})_2]$. V odsotnosti A336 ali v rahlo kislem mediju pride do nastanka binarne kompleksne spojine $[\text{Ni}(\text{HL}^-)_2]$, ki ima absorpcijski maksimum pri $\lambda = 548 \text{ nm}$, v spektru pa je opaziti tudi ramo pri $\lambda = 590 \text{ nm}$. Značilne ekstrakcijske in spektrofotometrične parametre smo določili pri optimalnih pogojih ekstrakcije: λ_{max} (545 nm), molarna absorptivnost ($5,0 \cdot 10^4 \text{ dm}^3 \text{ mol}^{-1} \text{ cm}^{-1}$), Sandellova občutljivost ($1,2 \cdot 10^{-3} \text{ } \mu\text{g cm}^{-2}$), omejitve Beerovega zakona ($0,05\text{--}3,1 \text{ } \mu\text{g cm}^{-3}$), konstanta ekstrakcije ($\text{Log } K = 6,1$) in delež ekstrahirane frakcije (99,2 %). Preučevali smo tudi vpliv dodanih ionov. Namočnejši vpliv v preučevanem sistemu so imeli Co^{II}, Cu^{II} in Cr^{II}.



Except when otherwise noted, articles in this journal are published under the terms and conditions of the Creative Commons Attribution 4.0 International License

Scientific paper

Syntheses, X-Ray Single Crystal Structures and Biological Activities of Cobalt(III) Complexes with Reduced Schiff Base Ligands

Xiao-Qiang Luo,^{1,2} Qiao-Ru Liu,¹ Yong-Jun Han¹ and Ling-Wei Xue^{1,2,*}

¹ School of Chemical and Environmental Engineering, Pingdingshan University, Pingdingshan Henan 467000, P.R. China

² Henan Key Laboratory of Research for Central Plains Ancient Ceramics, Pingdingshan University, Pingdingshan Henan 467000, P.R. China

* Corresponding author: E-mail: pdsuchemistry@163.com

Received: 06-08-2019

Abstract

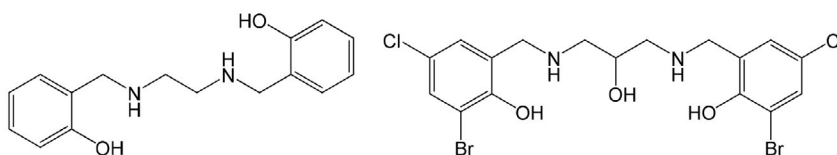
A new mononuclear cobalt(III) complex, $[\text{Co}(\text{HL}^1)_2]\text{Cl}$ (**1**), derived from the reduced Schiff base 2,2'-((ethane-1,2-diylbis(azanediyl))bis(methylene)diphenol (H_2L^1), and a new dinuclear cobalt(III) complex, $[\text{Co}_2(\text{L}^2)_2] \cdot 2\text{H}_2\text{O}$ (**2**), derived from the reduced Schiff base 6,6'-(2-hydroxypropane-1,3-diyl)bis(azanediyl)bis(methylene)bis(2-bromo-4-chlorophenol) (H_2L^2), were synthesized and characterized by infrared and electronic spectroscopy, and single crystal X-ray diffraction techniques. The ligands were synthesized first, and then bound to the Co(III) centre. Compound **1** contains a mononuclear $[\text{Co}(\text{HL}^1)_2]^+$ cation and a chloride anion. The cationic moiety possesses crystallographic inversion center symmetry. Compound **2** contains a dinuclear $[\text{Co}_2(\text{L}^2)_2]$ molecule and two water hydrate molecules. The Co atoms in the complexes are in octahedral coordination. Both complexes showed potential antimicrobial activity.

Keywords: Cobalt complex; reduced Schiff base ligand; crystal structure; antimicrobial activity

1. Introduction

Schiff bases derived from the condensation reactions of carbonyl containing compounds with primary amines have received tremendous attention in coordination chemistry because of their facile coordination ability to a large number of metals.¹ Schiff bases have various biological applications.² A number of complexes with Schiff base ligands have presented interesting biological properties, such as antibacterial, antifungal, antitumor, and enzymatic catalytic property.³ The Schiff bases have good complexing ability and their biological activity increases on complex with metal ions.⁴ Multi-dentate Schiff base ligands containing both nitrogen and oxygen donor atoms,

derived from the condensation of salicylaldehyde and various diamines have intensely been studied, due to their ability to stabilize a great variety of coordination numbers and coordination geometries.⁵ Cobalt(III) Schiff base complexes are also important in bioinorganic chemistry for important biological processes like antibacterial, anti-tumor, and antifungal activities.⁶ However, Schiff bases are not very stable in acid condition due to the azomethine groups. Reduced Schiff bases are in general more stable than Schiff bases. In this paper, two new cobalt(III) complexes, $[\text{Co}(\text{HL}^1)_2]\text{Cl}$ (**1**) and $[\text{Co}_2(\text{L}^2)_2] \cdot 2\text{H}_2\text{O}$ (**2**), where HL^1 and L^2 are the monoanionic form of the reduced Schiff base 2,2'-((ethane-1,2-diylbis(azanediyl))bis(methylene)diphenol (H_2L^1) and the trianionic form of the re-



Scheme 1. H_2L^1 and H_3L^2 .

duced Schiff base 6,6'-(2-hydroxypropane-1,3-diyl)bis(azanediyl)bis(methylene)bis(2-bromo-4-chlorophenol) (H_3L^2 ; Scheme 1), were synthesized and studied on their antibacterial potential.

2. Experimental

2.1. General Methods and Materials

All reagents and solvents were purchased from the commercial sources and used as received. Elemental (C, H and N) analyses were performed on a Perkin–Elmer 2400 II analyzer. IR spectra were recorded in the region 4000–400 cm^{-1} on a Perkin Elmer IR RXI spectrometer with samples as KBr disks. UV-Vis spectra were recorded on a Shimadzu UV-3600 spectrophotometer. Molar conductivity was measured at 25 °C with a DDS-11A conductivity meter. The NMR spectra were recorded on a Bruker spectrometer at 300 MHz. X-ray diffraction was carried out on a Bruker Apex II CCD diffractometer.

2.2. Synthesis of H_2L^1

To salicylaldehyde (1.22 g, 10 mmol) diluted by MeOH (50 mL), 1,2-diaminoethane (0.30 g, 5 mmol) diluted by MeOH (50 mL) was added with stirring. The reaction mixture was refluxed for 1 h and cooled by ice-water bath. Then, $NaBH_4$ (1.0 g, 25 mmol) was added. The mixture was stirred for another 1 h and filtered. The solvent was removed by distillation. The residue was treated with the aqueous solution of 1 M NaOH (50 mL) and extracted by chloroform. The solution was treated with 3 M HCl and the acid phase was made basic by 1 M NaOH. The crude product was then extracted into chloroform. The chloroform extracts were combined and dried over anhydrous Na_2SO_4 . The solvent was removed to give the colorless product. Yield 0.9 g (66%). IR data (ν , cm^{-1}): 3337, 3212, 3061, 2983, 2930, 2855, 1600, 1481, 1075. UV-Vis data (MeOH; λ_{max} , nm): 260, 285. 1H NMR (300 MHz, $CDCl_3$, ppm) δ 7.06 (q, 2H, ArH), 7.03 (d, 2H, ArH), 6.91 (q, 2H, ArH), 6.77 (d, 2H, ArH), 3.85 (s, 4H, CH_2), 2.61 (t, 4H, CH_2). Anal. Calcd. (%) for $C_{16}H_{20}N_2O_2$: C, 70.56; H, 7.40; N, 10.29. Found (%): C, 70.45; H, 7.47; N, 10.23.

2.3. Synthesis of H_3L^2

H_3L^2 was prepared by the same method as described for H_2L^1 , with salicylaldehyde replaced by 3-bromo-5-chlorosalicylaldehyde (2.34 g, 10 mmol), and with 1,2-diaminoethane replaced by 1,3-diaminopropan-2-ol (0.45 g, 5 mmol). Yield 1.6 g (61%). IR data (ν , cm^{-1}): 3382, 3235, 3053, 2977, 2941, 2872, 1597, 1478, 1081. UV-Vis data (MeOH; λ_{max} , nm): 255, 273. 1H NMR (300 MHz, $CDCl_3$, ppm) δ 11.83 (s, 1H, OH), 7.41 (s, 2H, ArH), 7.23 (s, 2H, ArH), 3.71 (d, 4H, CH_2), 3.67 (m, 1H, CH), 2.68 (t, 4H, CH_2). Anal. Calcd. (%) for $C_{17}H_{18}Br_2ClN_2O_3$:

C, 38.59; H, 3.43; N, 5.30. Found (%): C, 38.44; H, 3.52; N, 5.27.

2.4. Synthesis of Complex 1

A solution of H_2L^1 (54.4 mg, 0.20 mmol) in MeOH (10 mL) was added dropwise with stirring at room temperature to a solution of $CoCl_2 \cdot 6H_2O$ (23.8 mg, 0.10 mmol) in MeOH (10 mL). The solution immediately became deep brown and was stirred for 1 h. Single crystals suitable for X-ray diffraction were obtained after 11 days by slow evaporation of the reaction solution. Yield: 23 mg (36%). IR data (ν , cm^{-1}): 3245, 1218, 1073. UV-Vis data (MeOH; λ_{max} , nm): 280, 372. Λ_M (10^{-3} mol L^{-1} in MeOH): 151 $\Omega^{-1} cm^2 mol^{-1}$. Anal. Calcd. (%) for $C_{32}H_{38}ClCoN_4O_4$: C, 60.33; H, 6.01; N, 8.79. Found (%): C, 60.46; H, 6.12; N, 8.76.

2.5. Synthesis of Complex 2

Complex 2 was prepared by the same method as described for complex 1, with H_2L^1 replaced by H_3L^2 (52.9 mg, 0.10 mmol), and with $CoCl_2 \cdot 6H_2O$ replaced by $Co(CH_3COO)_2 \cdot 4H_2O$ (24.9 mg, 0.10 mmol). Single crystals suitable for X-ray diffraction were obtained after 3 days by slow evaporation of the reaction solution. Yield: 23 mg (38%). IR data (ν , cm^{-1}): 3419, 3246, 1587, 1443, 1303, 1274, 1213, 1169, 1085, 861, 730, 605. UV-Vis data (MeOH; λ_{max} , nm): 210, 263, 317, 372. Λ_M (10^{-3} mol L^{-1} in MeOH): 21 $\Omega^{-1} cm^2 mol^{-1}$. Anal. Calcd. (%) for $C_{34}H_{34}Br_4Cl_4Co_2N_4O_9$: C, 33.42; H, 2.80; N, 4.59. Found (%): C, 33.56; H, 2.87; N, 4.47.

2.6. X-ray Crystallography

The crystallographic data for the complexes are summarized in Table 1. Diffraction data of the complexes were collected on a Bruker APEX II CCD diffractometer at 298(2) K using graphite-monochromated Mo $K\alpha$ radiation ($\lambda = 0.71073$ Å). For data processing and absorption correction the packages SAINT and SADABS were used.⁷ The structures were solved by direct and Fourier methods and refined by full-matrix least-squares based on F^2 using SHELXTL and SHELXL-97 packages.⁸ The non-hydrogen atoms were refined anisotropically. The hydrogen atoms on water molecules and the amino groups of complex 2 were located from a Fourier difference map and refined isotropically, with O–H, N–H and H...H distances restrained to 0.85(1), 0.90(1) and 1.37(2) Å, respectively. The structure of complex 2 containing solvent accessible voids of 236 Å³ may accommodate disordered solvent molecules. The remaining hydrogen atoms were inserted on geometrical calculated positions with fixed thermal parameters and were refined isotropically.

CCDC 1906730 and 1946056 contain the supplementary crystallographic data for the complexes 1 and 2, respectively. The data can be obtained free of charge via <http://www.ccdc.cam.ac.uk/conts/retrieving.html>, or from

Table 1. Crystallographic and refinement data for the complexes

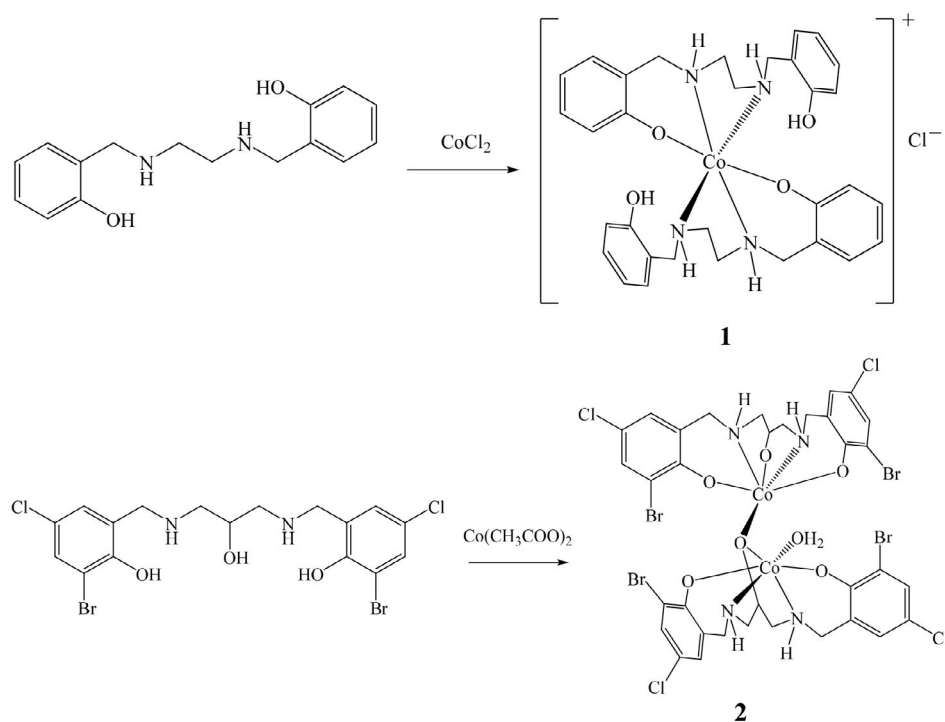
	1	2
Formula	C ₃₂ H ₃₈ ClCoN ₄ O ₄	C ₃₄ H ₃₄ Br ₄ Cl ₄ Co ₂ N ₄ O ₉
FW	637.04	1221.95
Crystal system	Monoclinic	Monoclinic
Space group	C2/c	P2 ₁ /c
a (Å)	23.905(1)	15.732(2)
b (Å)	7.376(1)	12.478(2)
c (Å)	17.745(1)	23.992(3)
β (°)	95.753(1)	103.727(2)
V (Å ³)	3113.2(6)	4575.2(9)
Z	4	4
μ (MoKα) (cm ⁻¹)	0.679	4.504
Collected reflections	8606	26672
Unique reflections	2861	8507
Observed reflections [I ≥ 2σ(I)]	1591	4823
Parameters	192	514
Restraints	0	6
Goodness of fit on F ²	0.947	1.039
R ₁ , wR ₂ [I ≥ 2σ(I)]	0.0532, 0.1031	0.0718, 0.2049
R ₁ , wR ₂ (all data)	0.1275, 0.1307	0.1345, 0.2399

the Cambridge Crystallographic Data Centre, 12 Union Road, Cambridge CB2 1EZ, UK; fax: (+44) 1223-336-033; or e-mail: deposit@ccdc.cam.ac.uk.

2. 7. Antibacterial Activity

The antibacterial activities were tested against *B. subtilis*, *E. coli*, *P. fluorescence* and *S. aureus* using MH medium

(Mueller–Hinton medium). The MICs (minimum inhibitory concentrations) of the test compounds were determined by a colorimetric method using the dye MTT [3-(4,5-dimethylthiazol-2-yl)-2,5-diphenyltetrazolium bromide]. A stock solution of the synthesized compound (50 μg mL⁻¹) in DMSO was prepared and quantities of the test compounds were incorporated in specified quantity of sterilized liquid MH medium. A specified quantity of the



Scheme 2. The synthetic procedure of the complexes.

medium containing the compound was poured into micro-titration plates. A suspension of the microorganism was prepared to contain approximately 10^5 cfu mL⁻¹ and applied to micro-titration plates with serially diluted compounds in DMSO to be tested and incubated at 37 °C for 24 h. After the MICs were visually determined on each of the micro-titration plates, 50 μ L of PBS containing 2 mg of MTT per millilitre was added to each well. Incubation was continued at room temperature for 4–5 h. The content of each well was removed and 100 μ L of isopropanol containing hydrochloric acid was added to extract the dye. After 12 h of incubation at room temperature, the optical density (OD) was measured with a micro-plate reader at 550 nm.

3. Results and Discussion

3.1. Chemistry

The cobalt(III) complexes **1** and **2** were prepared by the reaction of $\text{CoCl}_2 \cdot 6\text{H}_2\text{O}$ with the reduced Schiff base H_2L^1 , and $\text{Co}(\text{CH}_3\text{COO})_2 \cdot 4\text{H}_2\text{O}$ with the reduced Schiff base H_3L^2 , respectively in MeOH (Scheme 2). The aerial oxidation of cobalt(II) to cobalt(III) and metal assisted deprotonation of the phenolic moieties took place during the formation of the complexes. Molar conductivity values of complexes **1** and **2** measured in MeOH indicate the 1:1 electrolytic nature of complex **1** and non-electrolytic nature of complex **2**.⁹

3.2. Spectral Characterization

In the IR spectra of the complexes, the bands corresponding to the azomethine groups ($-\text{CH}=\text{N}-$) are not

observed, instead, new bands indicative of the C–N groups are observed at 1073–1085 cm^{-1} , indicating the reduction of the $-\text{CH}=\text{N}-$ double bonds to the $-\text{CH}_2-\text{NH}-$ single bonds. The complexes show medium bands at 1213–1218 cm^{-1} due to the presence of Ar–O stretching. Weak and sharp bands for the spectra of the complexes located at 3245 cm^{-1} indicates the presence of amino groups. The weak and broad band centered at 3419 cm^{-1} for complex **2** can be assigned to the stretching vibration of water molecules.

The UV-Vis spectra of the complexes were measured in MeOH. There are two bands centered at 280 and 372 nm for **1** and four bands centered at 210, 263, 317 and 372 nm for **2**. The bands arise due to internal ligand transition or ligand to metal charge transfer. The complexes exhibit low intensity bands at 615–630 nm which are due to the $d-d$ transition of Co^{III} center.

3.3. Structure Description of the Complexes

Selected bond lengths and bond angles in the coordination environment of the metal center are listed in Table 2. Complex **1** contains a mononuclear $[\text{Co}(\text{HL}^1)_2]^+$ cation and a chloride anion (Fig. 1). The cationic moiety possesses a crystallographic inversion symmetry. The Co atom, lying on the inversion center, is coordinated by two phenolate O and four amino N atoms from two HL^1 ligands, forming octahedral coordination. The Co–O and Co–N bond lengths in the complex are in the range 1.906(3)–1.991(3) Å, which are very close to those reported in literature.¹⁰ The cisoid ($85.8(1)$ – $94.1(1)^\circ$) and transoid angles (180°) in the complex are almost near to the ideal values.

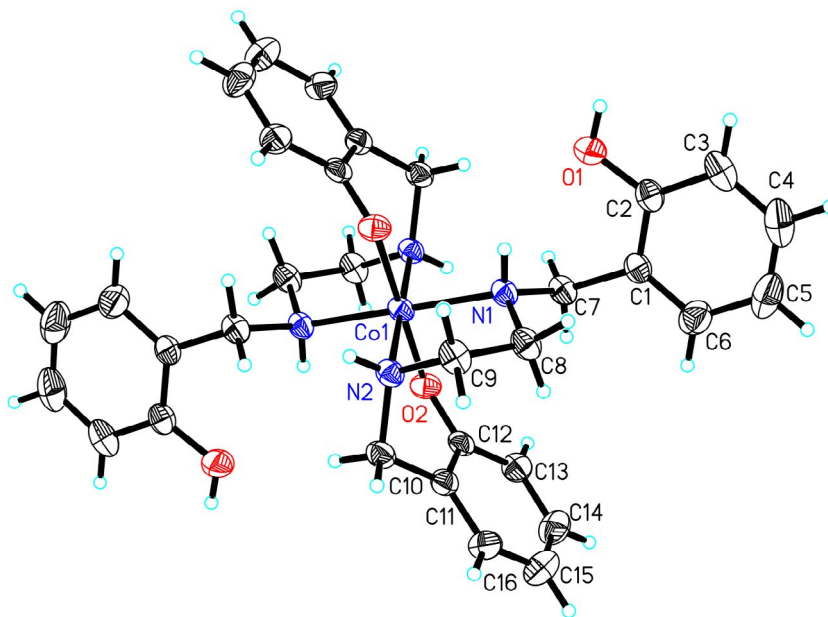


Fig. 1. The mononuclear complex cationic moiety of **1**. The chloride anion is omitted for clarity. Displacement ellipsoids are drawn at the 30% probability level and H atoms are shown as small spheres of arbitrary radii.

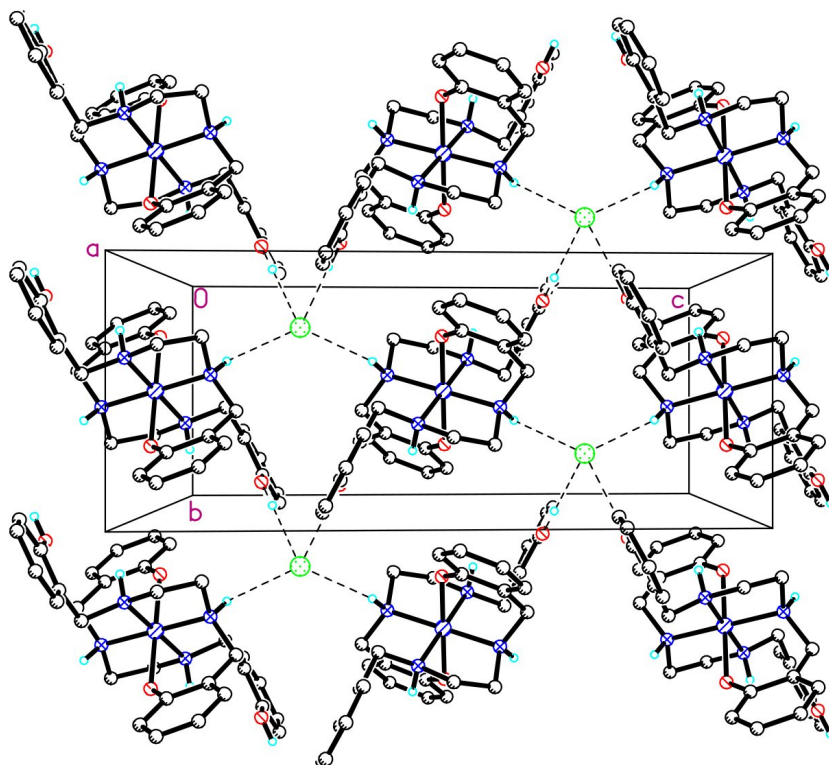


Fig. 2. Molecular packing structure of 1. Hydrogen bonds are shown as dashed lines.

In the crystal structure, the complex cations are linked by chloride anions through intermolecular hydrogen bonds of types N–H...Cl, N–H...O and O–H...Cl (Table 3), to form two-dimensional network along the *bc* plane (Fig. 2).

Complex 2 contains a dinuclear $[\text{Co}_2(\text{L}^2)_2]$ molecule and two water hydrate molecules (Fig. 3). The Co1 atom is coordinated by two phenolate O, two amino N, and two hydroxy O atoms from two L^2 ligands, forming octahedral coordination. The Co2 atom is coordinated by two pheno-

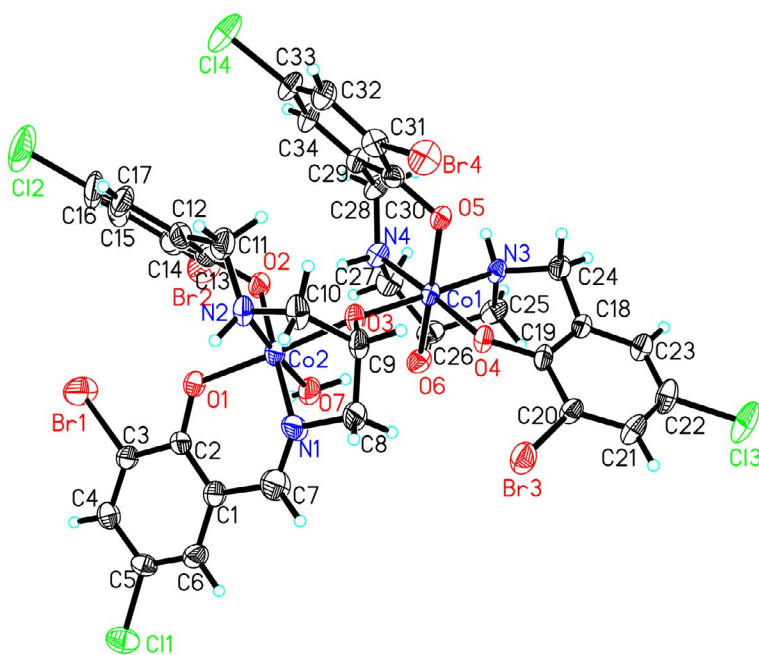


Fig. 3. The dinuclear complex moiety of 2. The two water molecules are omitted for clarity. Displacement ellipsoids are drawn at the 30% probability level and H atoms are shown as small spheres of arbitrary radii.

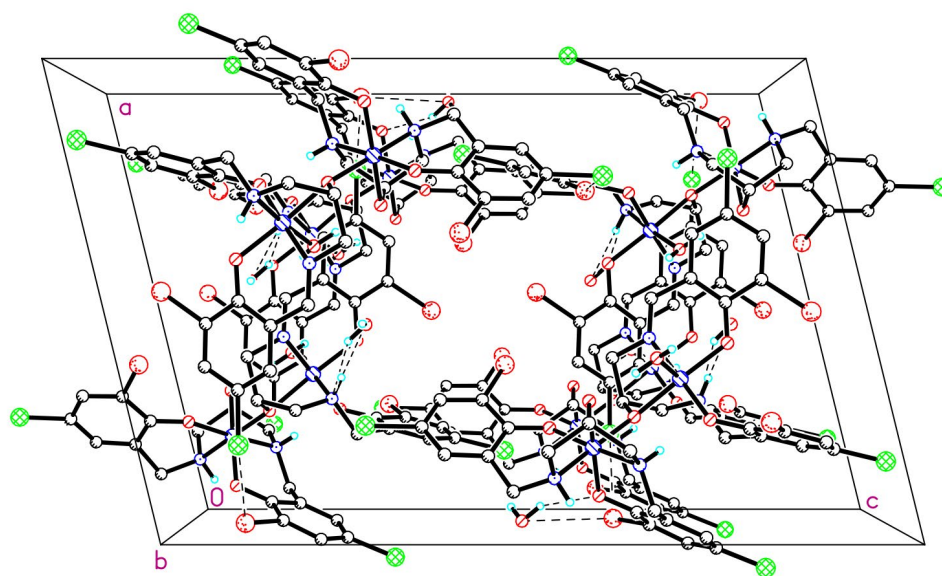


Fig. 4. Molecular packing structure of 2. Hydrogen bonds are shown as dashed lines.

late O, two amino N, and one hydroxy O atoms from one L^2 ligand, and by one water O atom, forming octahedral coordination. The Co–O and Co–N bond lengths in the

Table 2. Selected bond lengths (Å) and angles (°) for the complexes

1			
Co1–O2	1.906(3)	Co1–N2	1.951(3)
Co1–N1	1.991(3)		
O2–Co1–O2 ^{#1}	180	O2–Co1–N2 ^{#1}	85.9(1)
O2–Co1–N2	94.1(1)	N2–Co1–N2 ^{#1}	180
O2–Co1–N1	93.8(1)	O2–Co1–N1 ^{#1}	86.2(1)
N2–Co1–N1 ^{#1}	93.7(1)	N2–Co1–N1	86.3(1)
N1–Co1–N1 ^{#1}	180		
2			
Co1–O4	1.893(6)	Co1–O6	1.905(7)
Co1–N4	1.922(7)	Co1–O5	1.931(6)
Co1–N3	1.942(7)	Co1–O3	1.957(6)
Co2–O1	1.869(7)	Co2–N1	1.895(9)
Co2–O2	1.892(7)	Co2–O3	1.929(6)
Co2–O7	1.932(9)	Co2–N2	1.932(9)
O4–Co1–O6	95.3(3)	O4–Co1–N4	176.9(3)
O6–Co1–N4	81.9(3)	O4–Co1–O5	88.6(3)
O6–Co1–O5	175.8(3)	N4–Co1–O5	94.2(3)
O4–Co1–N3	94.3(3)	O6–Co1–N3	85.5(3)
N4–Co1–N3	87.0(3)	O5–Co1–N3	92.7(3)
O4–Co1–O3	90.1(3)	O6–Co1–O3	91.4(3)
N4–Co1–O3	88.5(3)	O5–Co1–O3	90.1(3)
N3–Co1–O3	174.8(3)	O1–Co2–N1	91.4(3)
O1–Co2–O2	89.4(3)	N1–Co2–O2	175.8(4)
O1–Co2–O3	173.3(4)	N1–Co2–O3	87.5(3)
O2–Co2–O3	92.2(3)	O1–Co2–O7	92.9(3)
N1–Co2–O7	90.3(4)	O2–Co2–O7	85.5(3)
O3–Co2–O7	93.8(3)	O1–Co2–N2	91.2(4)
N1–Co2–N2	89.1(4)	O2–Co2–N2	95.0(3)
O3–Co2–N2	82.1(3)	O7–Co2–N2	175.9(3)

Symmetry code for #1: $-x, -y, 1 - z$.

complex are in the range 1.871(6)–1.957(6) Å, which are very close to those reported in literature.¹⁰ The cisoid (81.9(3)–95.3(3)° for Co1 and 82.1(3)–95.0(3)° for Co2) and transoid angles (174.8(3)–176.9(3)° for Co1 and 173.3(4)–175.9(3)° for Co2) in the complex are almost near to the ideal values.

In the crystal structure, the complex molecules and the water molecules are linked through intermolecular hydrogen bonds of types O–H...O, O–H...N and N–H...O (Table 3), to form two-dimensional network along the *ab* plane (Fig. 4).

3. 4. Antibacterial Activity

The free reduced Schiff base ligands and their cobalt(III) complexes were screened for antibacterial activity against two Gram-positive bacterial strains (*B. subtilis* and *S. aureus*) and two Gram-negative bacterial strains (*E. coli* and *P. fluorescence*) by the MTT method. The MIC values of the compounds against these bacteria are presented in Table 4. Penicillin G and kanamycin were assayed as references. H_2L^1 is inactive against two Gram-positive bacterial strains *B. subtilis* and *S. aureus*, and has weak activity against the Gram-negative bacterial strains *E. coli* and *P. fluorescence* with MIC values of 25 $\mu\text{g mL}^{-1}$. H_3L^2 is inactive against the Gram-negative bacterial strain *P. fluorescence*, and has weak activity against the Gram-negative bacterial strain *E. coli* and the Gram-positive bacterial strain *S. aureus*, with MIC values of 25 $\mu\text{g mL}^{-1}$. H_3L^2 is active against the Gram-positive bacterial strain *B. subtilis*, with MIC value of 12.5 $\mu\text{g mL}^{-1}$. The cobalt(III) complexes, in general, showed a wide range of bactericidal activities against all the Gram-positive and Gram-negative bacteria. Complex **1** has good activity against the Gram-positive bacterial strain *B. subtilis* and medium activity against

Table 3. Hydrogen bond distances (Å) and bond angles (°) for the complexes

D–H...A	d(D–H)	d(H...A)	d(D...A)	∠(D–H...A)
1				
N2–H2...Cl1 ^{#1}	0.89	2.50	3.246(3)	142
N1–H1...O1	0.90	2.45	3.011(4)	120
O1–H1A...Cl1	0.84	2.24	3.068(3)	171
2				
O7–H7A...O6	0.85(1)	1.68(3)	2.507(10)	162(9)
O9–H9A...N2	0.85(1)	2.28(6)	3.048(17)	151(11)
N4–H4...O2	0.90(1)	1.88(4)	2.741(10)	159(11)
N2–H2...O9	0.90(1)	2.15(2)	3.048(17)	177(11)
O8–H8B...O5 ^{#2}	0.85(1)	2.18(5)	2.966(11)	154(10)
N3–H3...O8 ^{#3}	0.90(1)	2.23(7)	2.999(12)	143(10)

Symmetry codes: #1: $-x, -y, 1 - z$; #2: $x, y, 1 + z$; #3: $-x, 3/2 + y, 3/2 - z$.

S. aureus, with MIC values of 3.12 and 12.5 $\mu\text{g mL}^{-1}$, respectively. Complex **2** has good activity against both Gram-positive bacterial strains *B. subtilis* and *S. aureus*, with MIC values of 0.78 and 6.25 $\mu\text{g mL}^{-1}$, respectively. As for the two Gram-negative bacterial strains *E. coli* and *P. fluorescence*, both complexes have excellent activities with MIC values of 1.56 and 0.78 $\mu\text{g mL}^{-1}$ for **1**, and 3.12 and 6.25 $\mu\text{g mL}^{-1}$ for **2**, respectively, which are stronger than the reference drug kanamycin.

Table 4. MIC values ($\mu\text{g mL}^{-1}$) of the compounds

	<i>B. subtilis</i>	<i>S. aureus</i>	<i>E. coli</i>	<i>P. fluorescence</i>
1	3.12	12.5	1.56	0.78
2	0.78	6.25	3.12	6.25
H ₂ L ¹	>100	>100	25	25
H ₃ L ²	12.5	25	25	>100
Penicillin G	0.78	3.13	>100	>100
Kanamycin	0.39	1.56	6.25	6.25

4. Conclusion

Two new cobalt(III) complexes with reduced Schiff base ligands 2,2'-(ethane-1,2-diylbis(azanediyl))bis(methylene)diphenol and 6,6'-(2-hydroxypropane-1,3-diyl)bis(azanediyl)bis(methylene)bis(2-bromo-4-chlorophenol) have been synthesized and structurally characterized. One complex is in mononuclear and the other one is in dinuclear. The Co atoms are in octahedral coordination. The complexes showed potential antimicrobial activities against two Gram-positive bacterial strains (*B. subtilis* and *S. aureus*) and two Gram-negative bacterial strains (*E. coli* and *P. fluorescence*).

5. References

- (a) J. L. Pratihar, P. Mandal, C. K. Lai, S. Chattopadhyay, *Polyhedron* **2019**, *161*, 317–324. DOI:10.1016/j.poly.2019.01.002
- (b) V. S. Zanon, J. A. Lima, T. Cuya, F. R. S. Lima, A. C. C. da Fonseca, J. G. Gomez, R. R. Ribeiro, T. C. C. Franca, M. D. Vargas, *J. Inorg. Biochem.* **2019**, *191*, 183–193. DOI:10.1016/j.jinorgbio.2018.11.019
- (c) M. M. Duan, Y. M. Li, L. Y. Xu, H. L. Yang, F. W. Luo, Y. X. Guan, B. T. Zhang, C. L. Jing, Z. L. You, *Inorg. Chem. Commun.* **2019**, *100*, 27–31. DOI:10.1016/j.inoche.2018.12.009
- (d) A. Banerjee, S. Chattopadhyay, *Polyhedron* **2019**, *159*, 1–11. DOI:10.1016/j.poly.2018.10.059
- (e) S. Kumari, K. Maddipoti, B. Das, S. Ray, *Inorg. Chem.* **2019**, *58*, 1527–1540. DOI:10.1021/acs.inorgchem.8b03031
- (a) F. Tok, B. Kocyigit-Kaymakcioglu, B. N. Saglik, S. Levent, Y. Ozkay, Z. A. Kaplancikli, *Bioorg. Chem.* **2019**, *84*, 41–50. DOI:10.1016/j.bioorg.2018.11.016
- (b) G. Kapoor, D. P. Pathak, R. Bhutani, A. Husain, S. Jain, M. A. Iqbal, *Bioorg. Chem.* **2019**, *84*, 478–492. DOI:10.1016/j.bioorg.2018.11.016
- (c) P. T. Todorov, P. N. Peneva, S. I. Georgieva, R. I. Rusew, B. L. Shivachev, A. H. Georgiev, *New J. Chem.* **2019**, *43*, 2740–2751. DOI:10.1039/C8NJ05748F
- (a) D. Majumdar, D. Das, S. S. Sreejith, S. Das, J. K. Biswas, M. Mondal, D. Ghosh, K. Bankura, D. Mishra, *Inorg. Chim. Acta* **2019**, *489*, 244–254. DOI:10.1016/j.ica.2019.02.022
- (b) O. L. Cifuentes-Vaca, J. Andrades-Lagos, J. Campanini-Salinas, A. Laguna, D. Vasquez-Velasquez, M. C. Gimeno, *Inorg. Chim. Acta* **2019**, *489*, 275–279. DOI:10.1016/j.ica.2019.02.033
- (c) M. Karmakar, T. Basak, S. Chattopadhyay, *New J. Chem.* **2019**, *43*, 4432–4443. DOI:10.1039/C8NJ06549G
- (d) H. Bahron, S. S. Khaidir, A. M. Tajuddin, K. Ramasamy, B. M. Yamin, *Polyhedron* **2019**, *161*, 84–92. DOI:10.1016/j.poly.2018.12.055
- (e) F. Forouzandeh, H. Keypour, M. H. Zebarjadian, M. Mahmoudabadi, L. Hosseinzadeh, R. Karamian, M. A. Khoei, R. W. Gable, *Polyhedron* **2019**, *160*, 238–246. DOI:10.1016/j.poly.2018.12.052
- (f) K. Jana, S. Das, H. Puschmann, S. C. Debnath, A. Shukla, A. K. Mahanta, M. Hossain, T. Maity, B. C. Samanta, *Inorg. Chim. Acta* **2019**, *487*, 128–137. DOI:10.1016/j.ica.2018.12.007

- (g) X.-W. Zhu, *Acta Chim. Slov.* **2018**, *65*, 939–945.
DOI:10.17344/acsi.2018.4607
- (h) D.-L. Peng, N. Sun, *Acta Chim. Slov.* **2018**, *65*, 895–901.
DOI:10.17344/acsi.2018.4543
4. V. Gomathi, R. Selvameena, *Inorg. Chim. Acta* **2018**, *480*, 42–46. DOI:10.1016/j.ica.2018.05.007
5. K. Ghosh, K. Harms, S. Chattopadhyay, *ChemistrySelect* **2017**, *2*, 8207–8220. DOI:10.1002/slct.201701536
6. (a) A. K. Ghosh, C. S. Purohit, R. Ghosh, *Polyhedron* **2018**, *155*, 194–201. DOI:10.1016/j.poly.2018.08.021
(b) P. Nithya, R. Rajamanikandan, J. Simpson, M. Ilanchelian, S. Govindarajan, *Polyhedron* **2018**, *145*, 200–217.
DOI:10.1016/j.poly.2018.02.008
(c) D. Bandyopadhyay, M. Layek, M. Fleck, R. Saha, C. Rizzoli, *Inorg. Chim. Acta* **2017**, *461*, 174–182.
DOI:10.1016/j.ica.2017.02.018
7. G. M. Sheldrick, SAINT (Version 6.02), SADABS (Version 2.03), Bruker AXS Inc., Madison, Wisconsin, 2002.
8. (a) G. M. Sheldrick, SHELXTL (Version 6.10), Bruker AXS Inc., Madison, Wisconsin, 2002.
(b) G. M. Sheldrick, SHELXL-97: A Program for Crystal Structure Solution, University of Göttingen, Göttingen, Germany, 1997.
9. W. J. Geary, *Coord. Chem. Rev.* **1971**, *7*, 81–122.
DOI:10.1016/S0010-8545(00)80009-0
10. (a) E. T. Souza, L. C. Castro, F. A. V. Castro, L. D. Visentin, C. B. Pinheiro, M. D. Pereira, S. D. Machado, M. Scarpellini, *J. Inorg. Biochem.* **2009**, *103*, 1355–1365.
DOI:10.1016/j.jinorgbio.2009.07.008
(b) R. Shakya, C. Imbert, H. P. Hratchian, M. Lanznaster, M. J. Heeg, B. R. McGarvey, M. Allard, H. B. Schlegel, C. N. Verani, *Dalton Trans.* **2006**, *21*, 2517–2525.
DOI:10.1039/B514190G

Povzetek

Sintetizirali smo nov enojedrni kobaltov(III) kompleks, $[\text{Co}(\text{HL}^1)_2]\text{Cl}$ (**1**), z uporabo reducirane Schiffove baze 2,2'-(etan-1,2-diilbis(azandiil))bis(metilen)difenol (H_2L^1), in nov dvojedrni kobaltov(III) kompleks, $[\text{Co}_2(\text{L}^2)_2] \cdot 2\text{H}_2\text{O}$ (**2**), z uporabo reducirane Schiffove baze 6,6'-(2-hidroksipropan-1,3-diil)bis(azandiil)bis(metilen)bis(2-bromo-4-chlorofenol) (H_2L^2). Kompleksa smo okarakterizirali z infrardečo in elektronsko spektroskopijo ter rentgensko monokristalno analizo. Predhodno smo sintetizirali ligande ter jih nato vezali na Co(III) centre. Spojina **1** vsebuje enojedrni $[\text{Co}(\text{HL}^1)_2]^+$ kation in kloridni anion. Kation leži na kristalografskem centru inverzije. Spojina **2** vsebuje dvojedrne $[\text{Co}_2(\text{L}^2)_2]$ molekule in dve molekuli hidratne vode. V kompleksih je Co atom oktaedrično koordiniran. Oba kompleksa izkazujeta potencialne protimikrobne lastnosti.



Except when otherwise noted, articles in this journal are published under the terms and conditions of the Creative Commons Attribution 4.0 International License

Scientific paper

Some Studies in Sulfadiazine Incorporating Pyridine, Pyrimidine, Oxadiazole, and Azo Moieties Endowed with Pharmaceutical Potency

Sherihan A. El-Hadidya^{1,*} and Sraa Abu-Melhab²¹ Department of Engineering Chemistry, Canal High Institute of Engineering and Technology, Sues, Egypt² Department of Chemistry, Faculty of Science, King Khalid University, Abha, Saudi Arabia

* Corresponding author: E-mail: ice_princes52@yahoo.com

Tel: +201001678908

Received: 06-10-2019

Abstract

A set of substituted sulfadiazine compounds was prepared as cytotoxic and antitumor agents by using 4-amino-*N*-(pyrimidin-2-yl)benzenesulfonamide (**1**) as the starting material. Compound **1** was reacted with different reagents to give the corresponding sulfadiazines **2–18** and hydrozoones **19a–h** which were evaluated for their *in vitro* cytotoxicity versus four cancer cell lines. Compounds **3**, **5**, **19d** and **19h** were active against the tested cancer cells.

Keywords: Anticancer; Sulfonamide; Oxadiazole; Pyridine; Thiazole

1. Introduction

Sulfonamides have numerous biological actions, such as antibacterial,¹ hypoglycemia,² diuretic,³ anti-carbonic anhydrase^{3,4} and antithyroid.⁵ Recently, sulfonamides have been notified to exhibit fundamental antitumor action *in vitro* and/or *in vivo*.^{6,7} In addition, pyridine, pyrimidine, oxadiazole, and azo compounds are recognized to have various biological actions containing anticancer activity.^{8–15} So, the first goal in this realization is to synthesis several novel structures having anticancer action and the second goal is to exam the effect of the substitution of pyridine, pyrimidine, oxadiazole, and azo derivatives on the anticancer action and to research their structure action relationships.

2. Experimental

2. 1. Materials and Methods

2. 1. 1. Chemicals and Reagents

All the chemicals and solvents used in this study were obtained from Merck (Germany) and Sigma-Aldrich cheical company (Germany).

2. 1. 2. Instruments

All melting points are measured on Gallenkamp electric melting point apparatus and are uncorrected. The Infrared spectra ν cm⁻¹ (KBr) was measured on (Perkin Elmer Infrared Spectrophotometer Model 157, Grating). The ¹³C and ¹H NMR spectra were run on Varian Spectrophotometer at 400 MHz and 100 MHz using TMS as an internal reference and DMSO-*d*₆ as solvent. The MS (EI) were measured on 70 eV with Kratos MS equipment and/or a Varian MAT 311 A Spectrometer at Cairo University, Giza, Egypt, and were carried on a GC-MS QP-100 EX Shimadzu (Japan). Elemental analyses (C, H, and N) were determined at the Microanalytical Center of Cairo University, Giza, Egypt. The results were in good agreement with the calculated values.

2. 2. Synthesis

2. 2. 1. General Procedure for the Syntheses of (1,3-Dioxoisindolin-2-yl)-*N*-(pyrimidin-2-yl)benzenesulfonamide Derivatives 2–7

A mix of **1** (0.01 mmol) and anhydride derivatives namely; phthalic anhydride (0.01 mmol), 3-nitrophthalic anhydride (0.01 mmol), 4-nitrophthalic anhydride (0.01 mmol), 3,4,5,6-tetrabromophthalic anhy-

dride (0.01 mmol), 1,2,4-benzenetricarboxylic anhydride (trimellitic anhydride), and 1,2,4,5-benzenetetracarboxylic dianhydride (0.01 mmol) in *N,N*-dimethylformamide (15 mL) containing a few drops of triethylamine (3 drops) were boiled for 4 h. The reaction mixture was left to cool to room temperature, and then put into ice-cold water. The insoluble precipitated product was purified and dried to yield sulfonamides 2–7, respectively.

4-(1,3-Dioxoisindolin-2-yl)-*N*-(pyrimidin-2-yl)benzenesulfonamide (2)

Yield (83%), yellow powder, m.p. 288–290 °C; IR (KBr): ν/cm^{-1} 3335 (NH), 1632 (C=O, imidic), 1575 (C=C); ^1H NMR (DMSO- d_6) δ (ppm): 6.76 and 7.71 (dd, 4H, Ar-H AB system), 7.68–8.38 (m, 3H, Ar-H of pyrimidine ring), 9.13 (s, 1H, NH); MS m/z (%) 378 (M^+-2 , 99.90), 347 (67.60), 189 (30.80), 151 (14.50); Anal. calcd. for $\text{C}_{18}\text{H}_{12}\text{N}_4\text{O}_4\text{S}$ (380.06): C, 56.84; H, 3.18; N, 14.73. Found: C, 56.79; H, 3.11; N, 14.72.

4-(4-Nitro-1,3-dioxoisindolin-2-yl)-*N*-(pyrimidin-2-yl)benzenesulfonamide (3)

Yield (89%), white powder, m.p. 297–301 °C; IR (KBr): ν/cm^{-1} 3214 (NH), 1631 (C=O, imidic), 1551, 1337 (NO_2); ^{13}C NMR (DMSO- d_6) δ (ppm): 111.5, 122.3 (2C), 123.6, 127.8, 128.2 (2C), 134.1, 134.9, 135.7, 136.5, 138.3, 146.4, 156.4 (2C), 163.1 (2C), 167.6; MS m/z (%) 423 (M^+-2 , 4.18), 373 (63.15), 244 (100), 73 (20.34), 64 (47.39), 53 (14.39); Anal. calcd. for $\text{C}_{18}\text{H}_{11}\text{N}_5\text{O}_6\text{S}$ (425.04): C, 50.82; H, 2.61; N, 16.46. Found: C, 50.93; H, 2.57; N, 16.41.

4-(5-Nitro-1,3-dioxoisindolin-2-yl)-*N*-(pyrimidin-2-yl)benzenesulfonamide (4)

Yield (86%), yellow powder, m.p. 226–228 °C; IR (KBr): ν/cm^{-1} 3361 (NH), 1721 (C=O, imidic), 1540, 1380 (NO_2); ^{13}C NMR (DMSO- d_6) δ (ppm): 111.5, 122.3 (2C), 123.3, 125.7, 128.2 (2C), 129.5, 133.6, 134.3, 136.5, 138.5, 152.1, 156.4 (2C), 163.1 (2C), 167.6; MS m/z (%) 423 (M^+-2 , 67.35), 373 (82.65), 244 (100), 73 (100); Anal. calcd. for $\text{C}_{18}\text{H}_{11}\text{N}_5\text{O}_6\text{S}$ (425.04): C, 50.82; H, 2.61; N, 16.46. Found: C, 50.73; H, 2.60; N, 16.57.

***N*-(Pyrimidin-2-yl)-4-(4,5,6,7-tetrabromo-1,3-dioxoisindolin-2-yl)benzenesulfonamide (5)**

Yield (80%), pale yellow powder, m.p. 257–260 °C; IR (KBr): ν/cm^{-1} 3360 (NH), 1632 (C=O, imidic), 1330 (SO_2), 760 (C-Br); ^{13}C NMR (DMSO- d_6) δ (ppm): 111.5, 122.3 (2C), 126.1 (2C), 128.2 (2C), 129.4 (2C), 135.5, 136.5, 138.9 (2C), 156.4 (2C), 163.1 (2C), 167.6; MS m/z (%) 691 (M^+ , 12.3), 361 (16.91), 360 (84.34), 330 (7.98), 314 (27.23), 221 (26.41), 185 (13.75), 164 (13.19), 138 (9.36), 103 (53.22), 95 (23.72), 79 (21.64), 75 (71.93), 64 (34.34), 53 (19.52); Anal. calcd. for $\text{C}_{18}\text{H}_8\text{Br}_4\text{N}_4\text{O}_4\text{S}$ (691.70): C, 31.06; H, 1.16; N, 8.05. Found: C, 31.02; H, 1.11; N, 8.17.

1,3-Dioxo-2-(4-(*N*-pyrimidin-2-ylsulfamoyl)phenyl)isoindoline-5-carboxylic acid (6)

Yield (89%), white powder, m.p. 299–301 °C; IR (KBr): ν/cm^{-1} b. 3442 (OH of COOH), 3103 (NH), 1720 (C=O, imidic); ^1H NMR (DMSO- d_6) δ (ppm): 7.51–8.35 (m, 7H, Ar-H), 9.01 (s, 1H, CH of phthalimide), 8.31 and 8.46 (2 s, 2H, 2CH), 9.13 (s, 1H, NH), 12.23 (s, 1H, COOH); MS m/z (%) 426 (M^++2 , 15.26), 425 (M^++1 , 9.17), 361 (39.24), 360 (93.28), 330 (29.17), 314 (37.79), 221 (61.99), 185 (38.54), 164 (41.46), 138 (15.48), 103 (51.84), 95 (28.52), 79 (20.39), 75 (75.23), 64 (23.62), 53 (17.63); Anal. calcd. for $\text{C}_{19}\text{H}_{12}\text{N}_4\text{O}_6\text{S}$ (424.05): C, 53.77; H, 2.85; N, 13.20. Found: C, 53.69; H, 2.91; N, 13.21.

Pyromellitimide Derivative 7

Yield (84%), white powder, m.p. 270–273 °C; IR (KBr): ν/cm^{-1} 3243 (NH), 1646 (C=O, imidic), 1588 (C=N), 1579 (C=C); ^1H NMR (DMSO- d_6) δ (ppm): 7.59–8.31 (m, 14H, Ar-H), 10.18 (s, 2H, 2CH), 9.15 (s, 2H, 2NH); MS m/z (%) 680 (M^+-2 , 22.35), 425 (12.76), 361 (29.18), 360 (85.11), 330 (17.45), 314 (19.28), 221 (34.85), 185 (21.69), 164 (39.22), 138 (26.34), 103 (49.74), 95 (11.47), 79 (27.43), 75 (62.53), 64 (51.46), 53 (19.61); Anal. calcd. for $\text{C}_{30}\text{H}_{18}\text{N}_8\text{O}_8\text{S}_2$ (682.07): C, 52.78; H, 2.66; N, 16.41. Found: C, 52.73; H, 2.72; N, 17.39.

4-(2,4-Dioxo-1,2-dihydroquinazolin-3(4H)-yl)-*N*-(pyrimidin-2-yl)benzenesulfonamide (8)

A mix of **1** (0.01 mmol) and isatoic anhydride (0.01 mmol) in *N,N*-dimethylformamide (15 mL) including a few drops of triethylamine (3 drops) were boiled for 4 h. The reaction mixture was left to cool to room temperature, and then put into ice. The insoluble precipitated product was purified and dried to offer sulfonamide **8**. Yield (79%), white powder, m.p. 296–299 °C; IR (KBr): ν/cm^{-1} 3367 (2NH), 1679 (CO, imidic); ^1H NMR (DMSO- d_6) δ (ppm): 4.28 (s, 1H, NH), 7.61–8.31 (m, 11H, Ar-H), 9.13 (s, 1H, NH); MS m/z (%) 393 (M^+-2 , 41.46), 170 (50.00), 84 (82.32), 56 (100); Anal. calcd. for $\text{C}_{18}\text{H}_{13}\text{N}_5\text{O}_4\text{S}$ (395.07): C, 54.68; H, 3.31; N, 17.71. Found: C, 57.93; H, 3.27; N, 17.71.

2. 2. 2. Syntheses of Diethyl 2-((4-(*N*-Pyrimidin-2-ylsulfamoyl)phenylamino)methylene)malonate (9)

To a solution of **1** (0.01 mmol), diethyl 2-(ethoxymethylene)malonate (0.01 mmol) was added in *N,N*-dimethylformamide (25 mL) including a few drops of trimethylamine. The mixture was boiled for 4 h and left to cool to room temperature, and then put into ice. The insoluble precipitated product was purified, dried to give compound **9**. Yield (82%), yellow powder, m.p. 181–183 °C; IR (KBr): ν/cm^{-1} 3373 (NH), 1689 and 1654 (2 C=O, ester); ^1H NMR (DMSO- d_6) δ (ppm): 1.24, 1.28 (2 t, 6H, 2 CH_3), 4.14, 4.23 (2 q, 4H, 2 CH_2), 8.35 (s, 1H, CH), 7.13–7.77 (m,

7H, Ar-H), 9.07, 10.79 (2 s, 2 H, 2 NH); ^{13}C NMR (DM-SO- d_6) δ (ppm): 26.5, 70.1, 110.5, 115.9 (2C), 117, 122.4, 129.7, 130.8 (2C), 132, 137.2, 142.6, 153.1, 155.4, 164.3, 177.2, 177.8; MS m/z (%) 422 ($M^+ + 2$, 6.50), 232 (29.10), 189 (99.90), 134 (22.90); Anal. calcd. for $\text{C}_{18}\text{H}_{20}\text{N}_4\text{O}_6\text{S}$ (420.11): C, 51.42; H, 4.79; N, 13.33. Found: C, 53.71; H, 2.78; N, 13.21.

2. 2. 3. Syntheses of Ethyl 4-Oxo-6-(N-pyrimidin-2-ylsulfamoyl)-1,4-dihydroquinoline-3-carboxylate (10)

The cyclization reaction was performed by adding portions of **9** (0.01 mmol) to boiling diphenyl ether (15 mL). The reaction mix was boiled for 2 h, cooled to room temperature, then added petroleum ether (10 mL). The obtained insoluble precipitated product was purified, washed with diethyl ether and dehydrated to offer sulfonamide **10**. Yield (70%), gray powder, m.p. charring at 277 °C; IR (KBr): ν/cm^{-1} 3219 (NH), 1681 (C=O, ester), 1623 (α,β -unsaturated C=O), 1516 (C=C); ^1H NMR (DM-SO- d_6) δ (ppm): 1.30 (t, 3H, CH_3), 4.31 (q, 2H, CH_2), 7.24 (s, 1H, $\text{C}_2\text{-H}$ of quinoline), 7.69–7.85 (m, 6H, Ar-H), 8.94, 9.17 (2 s, 2 H, 2 NH); MS m/z (%) 375 ($M^+ + 1$, 69.15), 310 (100), 270 (86.17), 205 (94.68); Anal. calcd. for $\text{C}_{16}\text{H}_{14}\text{N}_4\text{O}_5\text{S}$ (374.07): C, 51.33; H, 3.77; N, 14.97. Found: C, 51.39; H, 3.78; N, 14.81.

2. 2. 4. Syntheses of 3-(Hydrazinocarbonyl)-4-oxo-N-(pyrimidin-2-yl)-1,4-dihydroquinoline-6-sulfonamide (11)

The cyclization reaction was performed by adding portions of **10** (0.01 mmol) to boiling diphenyl ether (15 mL). The mix was boiled for 1 h, cooled to room temperature, then added petroleum ether (10 mL). The obtained insoluble precipitated product was purified, washed with diethyl ether and dehydrated. The resulting insoluble precipitate recrystallized from ethanol to yield sulfonamide **11**. Yield (79%), white powder, m.p. 122–125 °C; IR (KBr): ν/cm^{-1} 3435 (NH_2), 3360 (NH), 1685 (C=O, amidic), 1624 (α,β -unsaturated C=O), 1566 (C=C); ^1H NMR (DM-SO- d_6) δ (ppm): 4.44 (s, 2H, NH_2), 7.36–8.38 (m, 6H, Ar-H), 8.38 (s, 1H, $\text{C}_2\text{-H}$ of quinoline), 9.05, 9.18, 9.74 (3 s, 3 H, 3 NH); MS m/z (%) 361 ($M^+ + 1$, 1.20), 215 (25.50), 103 (31.60), 43 (99.90); Anal. calcd. for $\text{C}_{14}\text{H}_{12}\text{N}_6\text{O}_4\text{S}$ (360.06): C, 46.66; H, 3.36; N, 23.32. Found: C, 56.53; H, 3.27; N, 23.41.

2. 2. 5. Syntheses of 2-(4-Oxo-6-(N-pyrimidin-2-ylsulfamoyl)-1,4-dihydroquinoline-3-carbonyl)hydrazinocarbodithioic acid (12)

To a solution of **11** (10 mmol) in ethanol containing a few drops of glacial acetic acid (4 drops) or in pyridine

(20 mL), carbon disulphide (10 mL) was added and the reaction mixture was boiled for 4 h. The solution was left to cool to room temperature and then put into ice. The insoluble precipitated was purified, dehydrated and recrystallized from ethanol to offer sulfonamide **12**. Yield (81%), white powder, m.p. 221–223 °C; IR (KBr): ν/cm^{-1} 3287 and 3214 (3NH), 1688 (C=O, amidic), 1625 (α,β -unsaturated C=O), 1332 (C=S); ^1H NMR (DMSO- d_6) δ (ppm): 1.93 (s, 1H, SH), 7.61–8.24 (m, 6H, Ar-H), 9.02 (s, 1H, $\text{C}_2\text{-H}$ of quinoline), 9.22 (s, 1H, NH), 10.65, 10.81 (2s, 2H, 2NH); MS m/z (%) 432 ($M^+ - 4$, 2.30), 378 (21.20), 283 (99.90), 165 (31.80); Anal. calcd. for $\text{C}_{15}\text{H}_{12}\text{N}_6\text{O}_4\text{S}_3$ (436.01): C, 41.27; H, 2.77; N, 19.25. Found: C, 41.23; H, 2.86; N, 19.31.

2. 2. 6. Syntheses of 3-(5-Mercapto-4,5-dihydro-1,3,4-oxadiazol-2-yl)-4-oxo-N-(pyrimidin-2-yl)-1,4-dihydroquinoline-6-sulfonamide (13)

A solution of compound **12** in ethanol (25 mL) including TEA (4 drops) was boiled for 4 h. The formed precipitate was purified while heating, dehydrated and washed by ethanol to yield oxadiazole derivative **13**. Yield (85%), white powder, m.p. 271–273 °C; IR (KBr): ν/cm^{-1} 3224 (NH), 2615 (SH), 1615 (α,β -unsaturated C=O), 1561 (C=N), 1332 (C=S); ^{13}C NMR (DMSO- d_6) δ (ppm): 111.5, 117.1, 118.2, 123.6, 131.1, 131.3, 133.7, 142.4, 151.6, 155.3, 156 (2C), 167.1, 167.6, 173.9; MS m/z (%) 402 (M^+ , 45.10), 342 (76.80), 122 (99.90), 43 (87.00); Anal. calcd. for $\text{C}_{15}\text{H}_{10}\text{N}_6\text{O}_4\text{S}_2$ (402.02): C, 44.77; H, 2.50; N, 20.88. Found: C, 44.63; H, 2.66; N, 20.81.

2. 2. 7. Syntheses of 3-(5-(Methylthio)-4,5-dihydro-1,3,4-oxadiazol-2-yl)-4-oxo-N-(pyrimidin-2-yl)-1,4-dihydroquinoline-6-sulfonamide (14)

A mix of oxadiazole **13** (10 mmol), sodium hydroxide solution (10 mmol), and methyl iodide (10 mmol) was stirred in water (15 mL) for 14 h. The forming thioether solution was removed by evaporation, and the residue collected by filtration, washed with water, dehydrated and recrystallized from ethanol to yield sulfonamide **14**. Yield (85%), gray powder, m.p. 172–175 °C; IR (KBr): ν/cm^{-1} 3253 (2NH), 1636 (α,β -unsaturated C=O), and 1581 (C=N); ^1H NMR (DMSO- d_6) δ (ppm): 1.96 (s, 3H, SCH_3), 2.52 (s, 2H, NH_2), 9.02 (s, 1H, $\text{C}_2\text{-H}$ of quinoline), 7.60–8.24 (m, 3H, Ar-H), 10.66 (s, 1H, NH), 10.82 (s, 1H, NH); MS m/z (%) 413 ($M^+ + 3$, 27.5), 258 (16.5), 248 (19.8), 233 (65.9), 209 (16.5), 207 (62.6), 143 (34.1), 115 (26.4), 77 (54.1), 76 (14.3), 69 (11.0), 65 (13.2), 51 (45.1), 50 (14.3); Anal. calcd. for $\text{C}_{16}\text{H}_{12}\text{N}_6\text{O}_4\text{S}_2$ (416.04): C, 46.15; H, 2.90; N, 20.18. Found: C, 46.33; H, 2.86; N, 20.01.

2. 2. 8. Syntheses of 4-Oxo-N-(pyrimidin-2-yl)-3-(5-thioxo-4-((para-tolylamino)methyl)-4,5-dihydro-1,3,4-oxadiazol-2-yl)-1,4-dihydroquinoline-6-sulfonamide (15)

A mix of **13** (10 mmol) and *para*-touluidine (10 mmol) was boiled in ethanol (30 mL) with 30% formaldehyde (20 mmol) for 3 h. The resulting insoluble precipitate was recrystallized from ethanol to yield sulfonamide **15**. Yield (72%), brown powder, m.p. 193–195 °C; IR (KBr): ν/cm^{-1} 3325 (NH), 2969 (CH), 1635 (α,β -unsaturated C=O), 1610 (C=N), 1267 (C=S); ^1H NMR (DMSO- d_6) δ (ppm): 2.16 (s, 3H, CH₃), 4.97 (s, 1H, N-CH₂-NH), 5.85 (s, 2H, N-CH₂-NH), 7.60–8.24 (m, 10H, Ar-H), 8.39 (s, 1H, C₂-H of quinoline), 9.15 (s, H, NH), 11.74 (s, H, NH); MS m/z (%) 521 (M⁺, 17.87), 415 (45.76), 401 (43.51), 301 (21.22), 220 (76.16), 158 (68.25), 120 (28.15), 100 (50.12), 77 (84.41), 76 (19.35), 69 (12.46), 65 (27.35), 50 (28.30); Anal. calcd. for C₂₃H₁₉N₇O₄S₂ (521.09): C, 52.96; H, 3.67; N, 18.80. Found: C, 52.93; H, 3.65; N, 18.71.

2. 2. 9. Syntheses of 2-Cyano-N-(4-(N-pyrimidin-2-ylsulfamoyl)phenyl)acetamide (16)

A mix of **1** (0.01 mmol) and ethyl cyanoacetate (0.01 mmol) was boiled in *N,N*-dimethylformamide (25 mL) for 4 h. The reaction mixture was cooled to room temperature and then put into ice. The precipitated insoluble precipitated product was purified, dried and recrystallized from ethanol to yield sulfonamide **16**. Yield (89%), pale yellow powder, m.p. 237–239 °C; IR (KBr): ν/cm^{-1} 3357 (NH), 2155 (CN), 1647 (C=O, amidic); ^1H NMR (DMSO- d_6) δ (ppm): 4.25 (s, 2H, CH₂), 7.62–8.26 (m, 3H, Ar-H and Ar-H of pyrimidine), 10.94, 11.19 (2s, 2H, 2NH); ^{13}C NMR (DMSO- d_6) δ (ppm): 26.5, 112.7, 117, 122.4, 125.8 (2C), 129.7 (2C), 133.9, 141.2, 143.6, 153.1, 164.3; MS m/z (%) 317 (M⁺, 68.74), 218 (86.32), 126 (88.42), 73 (100); Anal. calcd. for C₁₃H₁₁N₅O₃S (317.06): C, 49.21; H, 3.49; N, 22.07. Found: C, 49.19; H, 3.52; N, 22.81.

2. 2. 10. Syntheses of 4-Amino-2-oxo-N-(pyrimidin-2-yl)-1,2-dihydroquinoline-6-sulfonamide (17)

Compound **1** (0.01 mmol) was boiled in *N,N*-dimethylformamide (30 mL) including trimethylamine for 4 h. The reaction mixture was cooled to room temperature; then put into ice. The insoluble precipitated product was purified, dried and recrystallized from ethanol to offer sulfonamide **17**. Yield (90%), yellow crystals, m.p. 210–213 °C; IR (KBr): ν/cm^{-1} 3357 (NH), 1713 (C=O, amidic), 1651 (α,β -unsaturated C=O), and 1584 (C=C); ^1H NMR (DMSO- d_6) δ (ppm): 4.82 (s, 2H, NH₂), 8.33 (s, 1H, C₂-H of quinoline), 7.58–8.34 (m, 6H, Ar-H), 8.85 (s, H, NH), 10.15 (s, H, NH); MS m/z (%) 322 (M⁺-5, 52.46), 320 (83.59), 231 (100), 135 (35.66); Anal. calcd. for

C₁₃H₁₁N₅O₃S (317.06): C, 49.21; H, 3.49; N, 22.07. Found: C, 49.25; H, 3.43; N, 22.01.

2. 2. 11. Syntheses of 3-Oxo-N-(4-(N-pyrimidin-2-ylsulfamoyl)phenyl)butanamide (18)

A mix of **1** (0.01 mmol) and ethyl acetoacetate (10 mmol) was boiled in *N,N*-dimethylformamide (25 mL) including a few drops of trimethylamine for 3 h. The reaction mixture was cooled to room temperature and then put into ice. The precipitated solid product was purified, dried and recrystallized from ethanol to offer sulfonamide **18**.

Yield (95%), white powder, m.p. 228–230 °C; IR (KBr): ν/cm^{-1} b. 3315 (2NH), 1725 (C=O, amidic), 1689 (C=O), 1567 (C=N), 1549 (C=C); ^1H NMR (DMSO- d_6) δ (ppm): 2.31 (s, 3H, CH₃), 3.33 (s, 2H, CH₂), 7.45–8.21 (m, 7H, Ar-H), 8.47 (s, 1H, NH), 10.16 (s, 1H, NH); ^{13}C NMR (DMSO- d_6) δ (ppm): 25, 29.1, 38.6, 71.3, 110.2, 117, 122.4, 133.9, 137.2, 149.8, 152 (2C), 164.3, 177.8; MS m/z (%) 335 (M⁺+1, 9.80), 180 (87.00), 150 (51.10), 91 (99.90); Anal. calcd. for C₁₄H₁₄N₄O₄S (334.07): C, 50.29; H, 4.22; N, 16.76. Found: C, 50.25; H, 4.34; N, 16.78.

2. 2. 12. General Procedure for the Syntheses of Aryl Hydrazone Derivatives 19a–h

A well stirred solution of aromatic amines (20 mmol) in concentrated HCl (6 mL) and water (4 mL) was cooled in an ice bath and diazotized with a solution of sodium nitrite (1.39 g, 20 mL) in water (5 mL).

The above cooled diazonium salt solution was added drop wise to a well stirred cooled solution of **1** in pyridine (10 mL). The reaction mixture was stirred for 1–2 h until giving a complete coupling reaction. The crude insoluble precipitate was purified, dehydrated well and recrystallized from ethanol to offer compounds **19a–h**, respectively.

(E)-3-Oxo-N-(4-(N-pyrimidin-2-ylsulfamoyl)phenyl)-2-(2-(thiazol-2-yl)hydrazono)butanamide (19a)

Yield (80%), dark gray powder, m.p. charring at 271 °C; IR (KBr): ν/cm^{-1} b. 3250 (3NH), 1700 (C=O, amidic), 1663 (C=O), 1550 (N=N); ^1H NMR (DMSO- d_6) δ (ppm): 2.23 (s, 3H, CH₃), 6.57 (d, 1H, CH of thiazole ring), 7.04 (d, 1H, CH of thiazole ring), 7.82 (d, 2H, Ar-H), 7.93 (d, 2H, Ar-H), 7.65–8.39 (m, 3H, Ar-H of pyrimidine), 8.82 (s, H, NH), 9.04 (s, H, NH), 10.16 (s, H, NH); ^{13}C NMR (DMSO- d_6) δ (ppm): 26.5, 114.7, 117, 122.4, 124.1 (2C), 127.4 (2C), 131.5, 133.9, 141.6, 143.4, 145.6, 153.1, 164.3, 169, 177.8; MS m/z (%) 445 (M⁺, 41.23), 366 (12.34), 287 (24.18), 158 (12.56), 98 (59.76), 84 (69.34), 79 (78.46), 76 (83.76); Anal. calcd. for C₁₇H₁₅N₇O₄S₂ (445.06): C, 45.83; H, 3.39; N, 22.01. Found: C, 45.91; H, 3.33; N, 22.01.

(E)-2-(2-(1,5-Dimethyl-3-oxo-2-phenyl-2,3-dihydro-1H-pyrazol-4-yl)hydrazono)-3-oxo-N-(4-(N-pyrimidin-2-ylsulfamoyl)phenyl)butanamide (19b)

Yield (82%), reddish brown powder, m.p. 213–215 °C; IR (KBr): ν/cm^{-1} b. 3320 (3NH), 1697 (C=O, amidic), 1662 (C=O), 1562 (N=N); $^1\text{H NMR}$ (DMSO- d_6) δ (ppm): 1.77 (s, 3H, CH₃), 2.50 (s, 3H, CH₃), 2.68 (s, 3H, CH₃), 7.47 (d, 2H Ar-H), 7.63 (d, 2H Ar-H), 6.87 and 7.20 (m, 3H, Ar-H), 8.80 (s, H, NH), 9.00 (s, H, NH), 10.19 (s, H, NH); MS m/z (%) 548 (M⁺, 32.27), 469 (17.86), 391 (24.54), 314 (69.33), 202 (61.47), 98 (71.27), 79 (56.84), 76 (81.49); Anal. calcd. for C₂₅H₂₄N₈O₅S (548.16): C, 54.74; H, 4.41; N, 20.43. Found: C, 54.71; H, 4.33; N, 20.41.

(E)-3-Oxo-N-(4-(N-pyrimidin-2-ylsulfamoyl)phenyl)-2-(2-(4-sulfamoylphenyl)hydrazono)butanamide (19c)

Yield (82%), yellow powder, m.p. 162–165 °C; IR (KBr): ν/cm^{-1} 3453 (NH₂), b. 3250 (3NH), 1703 (C=O, amidic), 1667 (C=O), 1551 (N=N); $^1\text{H NMR}$ (DMSO- d_6) δ (ppm): 2.23 (s, 3H, CH₃), 3.95 (s, 2H, NH₂), 7.62 and 7.59 (dd, 4H, Ar-H), 7.82 (d, 2H Ar-H), 7.93 (d, 2H, Ar-H), 7.65–8.39 (m, 3H, Ar-H of pyrimidine), 8.82 (s, H, NH), 9.04 (s, H, NH), 10.16 (s, H, NH); MS m/z (%) 517 (M⁺, 47.37), 438 (26.41), 359 (62.64), 171 (74.91), 158 (69.23), 99 (84.16), 79 (69.65), 77 (85.22); Anal. calcd. for C₂₀H₁₉N₇O₆S₂ (517.08): C, 46.41; H, 3.70; N, 18.94. Found: C, 46.53; H, 3.73; N, 18.89.

(E)-3-Oxo-N-(4-(N-pyrimidin-2-ylsulfamoyl)phenyl)-2-(2-(4-(N-thiazol-2-ylsulfamoyl)phenyl)hydrazono)butanamide (19d)

Yield (84%), dark brown powder, m.p. charring at 300 °C; IR (KBr): ν/cm^{-1} b. 3261 (4NH), 1723 (C=O, amidic), 1663 (C=O), 1580 (N=N); $^1\text{H NMR}$ (DMSO- d_6) δ (ppm): 2.23 (s, 3H, CH₃), 6.51 (s, H, CH of thiazole ring), 7.14 (s, H, CH of thiazole ring), 6.81 and 7.34 (dd, 4H, Ar-H), 7.82 (d, 2H Ar-H), 7.93 (d, 2H Ar-H), 7.65–8.39 (m, 3H, Ar-H of pyrimidine), 8.82 (s, H, NH), 9.04 (s, H, NH), 10.16 (s, H, NH), 10.35 (s, H, NH); MS m/z (%) 600 (M⁺, 74.42), 442 (25.33), 254 (12.03), 171 (16.74), 158 (62.48), 156 (43.64), 85 (82.09), 78 (68.96); Anal. calcd. for C₂₃H₂₀N₈O₆S₃ (600.07): C, 45.99; H, 3.36; N, 18.66. Found: C, 45.93; H, 3.33; N, 18.69.

(E)-2-(2-(Benzo[d]thiazol-2-yl)hydrazono)-3-oxo-N-(4-(N-pyrimidin-2-ylsulfamoyl)phenyl)butanamide (19e)

Yield (74%), brown powder, m.p. charring at 200 °C; IR (KBr): ν/cm^{-1} b. 3341 (3NH), 1714 (C=O, amidic), 1669 (C=O), 1571 (N=N); $^1\text{H NMR}$ (DMSO- d_6) δ (ppm): 2.23 (s, 3H, CH₃), 7.82 (d, 2H, Ar-H), 7.93 (d, 2H, Ar-H), 7.65–8.39 (m, 7H, Ar-H of pyrimidine and benzene rings), 8.82 (s, H, NH), 9.04 (s, H, NH), 10.16 (s, H, NH); MS m/z (%) 495 (M⁺, 42.74), 337 (36.75), 261 (26.82), 249 (29.35), 149 (15.77), 135 (46.44), 99 (75.24), 79 (62.96), 77 (88.57); Anal. calcd. for C₂₁H₁₇N₇O₄S₂ (495.08): C, 50.90; H, 3.46; N, 19.79. Found: C, 50.93; H, 3.33; N, 19.69.

(E)-2-(2-(1H-Imidazol-2-yl)hydrazono)-3-oxo-N-(4-(N-pyrimidin-2-ylsulfamoyl)phenyl)butanamide (19f)

Yield (85%), brown powder, m.p. charring at 232 °C; IR (KBr): ν/cm^{-1} b. 3441 (4NH), 1706 (C=O, amidic), 1664 (C=O), 1563 (N=N); $^1\text{H NMR}$ (DMSO- d_6) δ (ppm): 2.23 (s, 3H, CH₃), 7.03 and 7.05 (d, 2H, 2CH), 7.82 (d, 2H, Ar-H), 7.93 (d, 2H, Ar-H), 7.65–8.39 (m, 3H, Ar-H of pyrimidine), 8.82 (s, H, NH), 9.04 (s, H, NH), 10.16 (s, H, NH), 12.81 (s, H, NH of imidazole ring); MS m/z (%) 433 (M⁺+5, 36.00), 231 (41.10), 202 (99.90), 186 (39.10); Anal. calcd. for C₁₇H₁₆N₈O₄S (428.10): C, 47.66; H, 3.76; N, 26.15. Found: C, 47.63; H, 3.83; N, 26.39.

(E)-2-(2-(1H-Benzo[d]imidazol-2-yl)hydrazono)-3-oxo-N-(4-(N-pyrimidin-2-ylsulfamoyl)phenyl)butanamide (19g)

Yield (78%), pale brown powder, m.p. charring at 251 °C; IR (KBr): ν/cm^{-1} b. 3267 (4NH), 1700 (C=O, amidic), 1668 (C=O), 1573 (N=N); $^1\text{H NMR}$ (DMSO- d_6) δ (ppm): 2.23 (s, 3H, CH₃), 7.82 and 7.93 (dd, 4H, Ar-H), 7.65–8.39 (m, 7H, Ar-H of pyrimidine and benzene rings), 8.82 (s, H, NH), 9.04 (s, H, NH), 10.16 (s, H, NH), 10.81 (s, H, NH); MS m/z (%) 483 (M⁺+5, 1.20), 283 (87.60), 267 (99.90), 171 (82.40); Anal. calcd. for C₂₁H₁₈N₈O₄S (478.1): C, 52.71; H, 3.79; N, 23.42. Found: C, 52.64; H, 3.83; N, 23.35.

(E)-3-Oxo-N-(4-(N-pyrimidin-2-ylsulfamoyl)phenyl)-2-(2-(4-(N-pyrimidin-2-ylsulfamoyl)phenyl)hydrazono)butanamide (19h)

Yield (83%), black powder, m.p. charring at 251 °C; IR (KBr): ν/cm^{-1} b. 3339 (4NH), 1731 (C=O, amidic), 1665 (C=O), 1571 (N=N); $^1\text{H NMR}$ (DMSO- d_6) δ (ppm): 2.23 (s, 3H, CH₃), 7.79–7.96 (dd, 8H, Ar-H), 7.65–8.39 (m, 6H, Ar-H of pyrimidine), 8.82 (s, 2H, 2NH), 9.04 (s, H, NH), 10.16 (s, H, NH); MS m/z (%) 595 (M⁺, 28.63), 249 (59.26), 157 (74.59), 101 (48.42), 98 (64.88), 98 (49.04), 93 (59.69); Anal. calcd. for C₂₄H₂₁N₉O₆S₂ (595.11): C, 48.40; H, 3.55; N, 21.16. Found: C, 48.51; H, 3.43; N, 21.33.

2. 3. Cytotoxicity Activity

RPMI-1640 medium (Sigma Co., St. Louis, USA), Foetal Bovine serum (GIBCO, UK), and the cell lines from ATCC were used.

The cytotoxic activities of the prepared sulfonamides were examined versus HepG2, WI-38, MCF-7, and VERO, carried out according to the previously reported procedure.¹⁶

3. Results and Discussion

3. 1. Chemistry

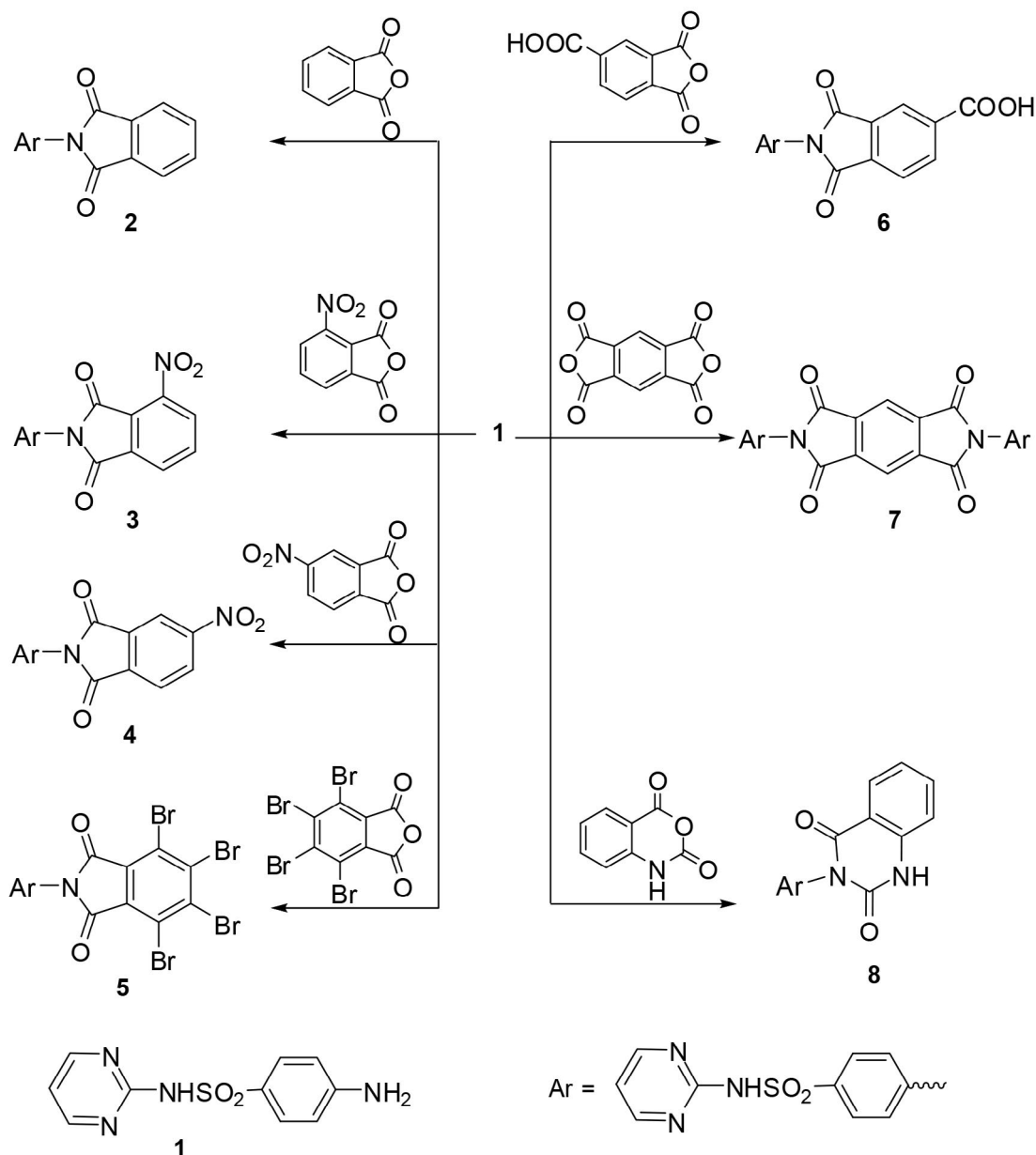
From the above reports in sulfonamide chemistry, we prepared some new heterocyclic compounds containing sulfonamide moiety to evaluate their biological activi-

ties. Condensation of compound **1** with acid anhydrides, namely phthalic anhydride, 3-nitrophthalic anhydride, and 4-nitrophthalic anhydride in refluxing *N,N*-dimethylformamide containing a few drops of triethylamine yielded sulfonamides **2–4**. The infrared spectra of sulfonamides **2–4**, in general, displayed no absorption of NH_2 at 3426 cm^{-1} of sulfonamide **1**, and instead, appeared new bands within the region $1631\text{--}1721\text{ cm}^{-1}$ due to carboximide groups. The MS spectra of sulfonamides **2–4** offered the molecular weight at m/z 378 (M^+-2) and at m/z 423 (M^+-2) corresponding to molecular formulae $\text{C}_{18}\text{H}_{12}\text{N}_4\text{O}_4\text{S}$ and/or $\text{C}_{18}\text{H}_{11}\text{N}_5\text{O}_6\text{S}$, respectively.

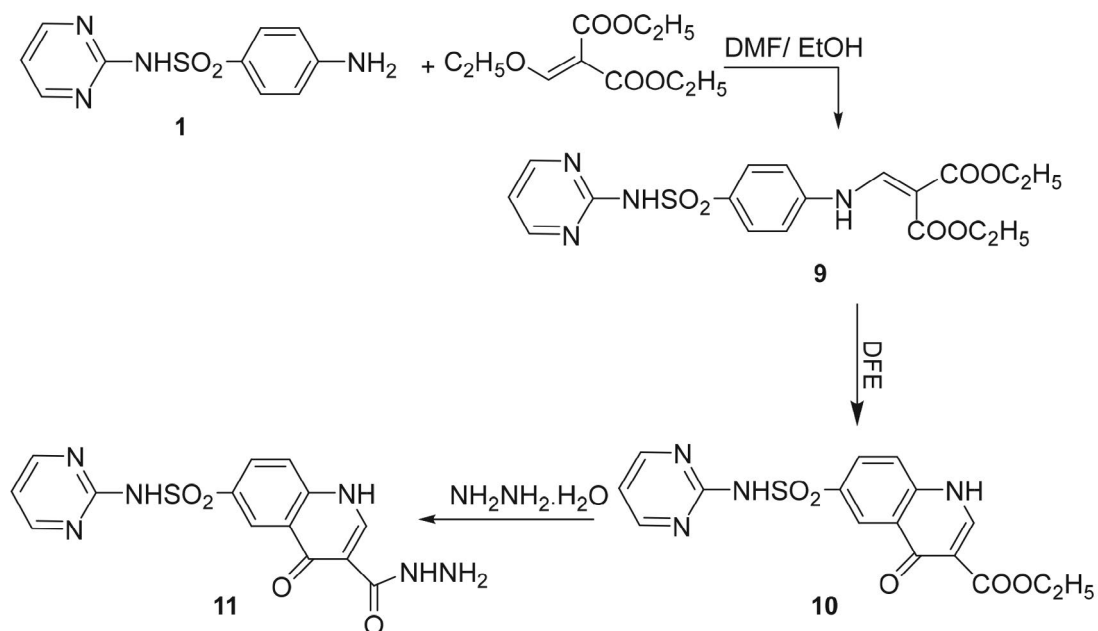
Similarly, condensation of compound **1** with 3,4,5,6-tetrabromophthalic anhydride, and 1,2,4-benzene-

tricarboxylic anhydride (trimellitic anhydride) in boiling *N,N*-dimethylformamide including a few small drops of triethylamine gave sulfonamides **5** and **6**, respectively. Structures **5** and **6** were elucidated by different analyses. The infrared spectra of compounds **5** and **6** exhibited bands at 1720 , 1632 , and 1330 cm^{-1} due to CO groups and SO_2 functional groups. The MS spectra of **5** and **6** offered molecular weight at m/z 691 (M^+) and $426 (M^++2)$, respectively

On the other hand, heating of sulfonamide **1** with pyromellitic anhydride in ethanol with a few drops of triethylamine in a molar ratio 1:2 gave pyromellitimide **7**. The infrared spectrum of compound **7** showed a similar picture to that of **5** and **6**. The MS spectrum of **7** gave molecular



Scheme 1. Synthesis of sulfonamide derivatives **2–8**

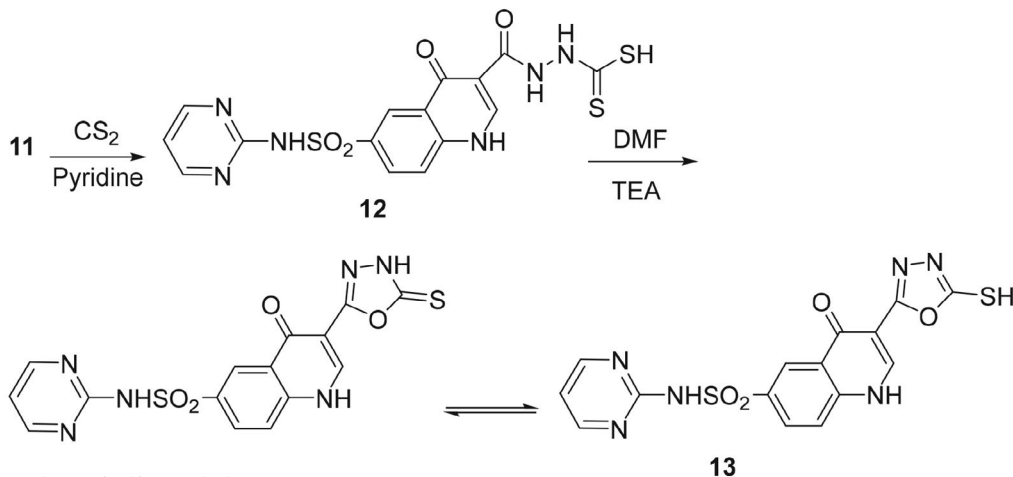


Scheme 2. Synthesis of acid hydrazide 11

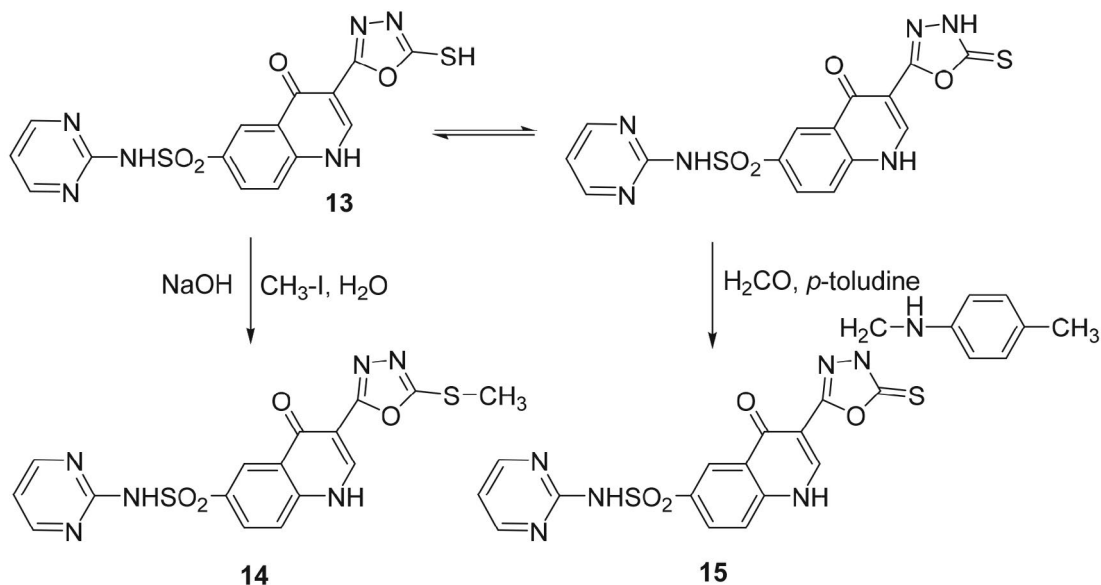
weight at m/z 680 (M^+-2). In addition, stirring of sulfonamide **1** with isoatoic anhydride in ethanol including a few small drops of triethylamine at room temperature yielded compound **8**. The infrared spectrum of sulfonamide derivative **8** displayed band at ν 1679 cm^{-1} corresponding to carboximide functional group. The MS spectrum gave additional confirmation for the correct structure of sulfonamide **8** as it gave a molecular ion peak at m/z 393 (M^+-2).

The starting material **1** was refluxed with diethyl 2-(ethoxymethylene)malonate in a mixture of *N,N*-dimethylformamide and ethanol (1:1 ratio) to give compound **9** in high yield. The infrared spectrum of **9** displayed a band at 1689 cm^{-1} for ester carbonyl functional group, and an absorption frequency at 3373 cm^{-1} corresponding to NH group. The MS spectrum of **9** offered molecular weight at m/z 422 (M^++2) confirming the formula

$\text{C}_{18}\text{H}_{20}\text{N}_4\text{O}_6\text{S}$. Cyclization reaction of compound **9** was performed by boiling in diphenyl ether to give ethyl 4-oxo-6-(*N*-pyrimidin-2-ylsulfamoyl)-1,4-dihydroquinoline-3-carboxylate (**10**) in acceptable yield. The infrared spectrum of **10** displayed the distinctive bands at ν 3219, 1681, 1623, and 1516 cm^{-1} due to NH, C=O of ester, α,β -unsaturated C=O and C=C groups. Its ^1H NMR spectrum revealed a triplet signal at δ 1.30 ppm (CH_3), a quartet signal at δ 4.31 ppm (CH_2), a D_2O exchangeable two NH at δ 8.94 and 9.17 ppm as singlet signals, and a singlet signal for C_2 -H of quinoline ring at δ 7.24 ppm besides the aromatic hydrogens of quinoline and pyrimidine rings at δ 7.69–7.85 ppm. In addition, the MS offered another confirmation for compound **10** as it gave its molecular weight at m/z 375 (M^++1) corresponding to the formula $\text{C}_{16}\text{H}_{14}\text{N}_4\text{O}_5\text{S}$.



Scheme 3. Synthesis of sulfonamide derivative 13



Scheme 4. Synthesis of sulfonamide derivative 14 and 15

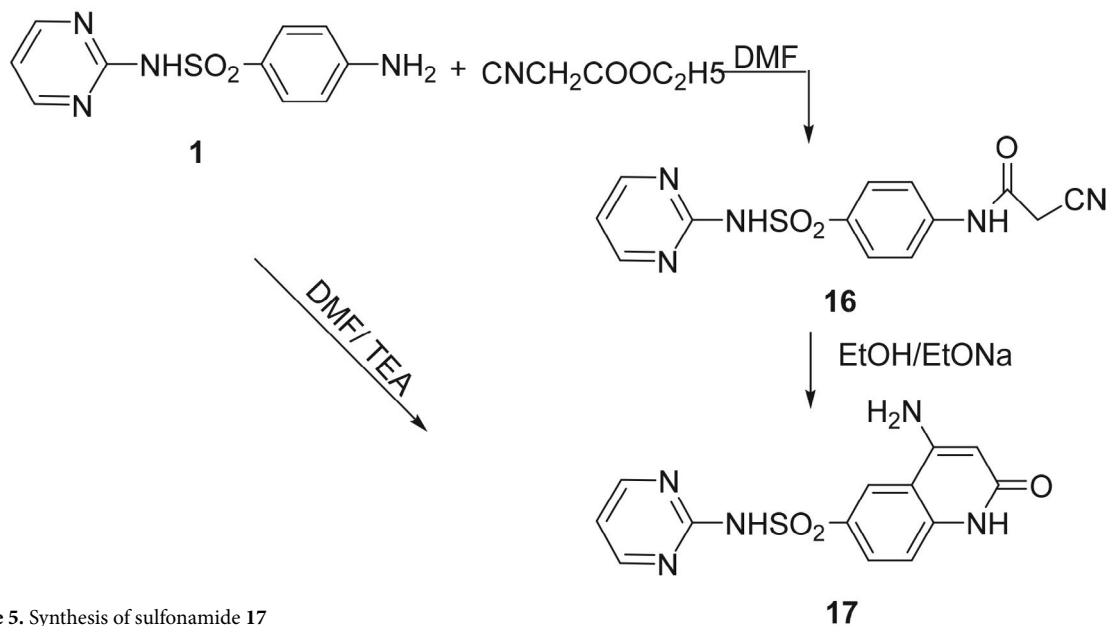
Boiling **10** with hydrazine hydrate in ethanol/DMF solution (1:1 ratio) afforded the corresponding acid hydrazide **11**. The infrared spectrum of **10** displayed bands at ν 3435 and 3360 cm^{-1} due to NHNH_2 group, besides the presence of amide carbonyl group at ν 1685 cm^{-1} .

Reaction of hydrazide **11** with carbon disulphide in refluxing pyridine afforded the thioic acid **12**. The infrared spectrum displayed absorption bands at ν 3287, 3214, 1688, 1625, and 1332 cm^{-1} due to stretching vibration of NH, amide CO, α,β -unsaturated ketone, and C=S groups. The MS spectrum of compound **12** offered a molecular weight at m/z 432 (M^+-4).

When thioic acid derivative **12** was heated under reflux in *N,N*-dimethylformamide containing a few drops of

triethylamine, sulfonamide derivative **13** was afforded. The infrared spectrum of **13** showed a strong band at ν 1332 cm^{-1} due to C=S functional group, and a weak band at ν 2615 cm^{-1} due to SH vibration in a tautomeric mixture as well. The MS spectrum displayed its molecular weight at m/z 402 (M^+).

It has been found that compound **13**, when subjected to react with methyl iodide in sodium hydroxide solution, afforded the SCH_3 derivative **14** (Scheme 4), while when **13** reacted with formaldehyde and *para*-toluidine it afforded the Mannich base **15** (Scheme 4); such reactions were carried out to indicate the thiol-thione tautomerism.



Scheme 5. Synthesis of sulfonamide 17

We have observed that thiol-thione tautomerism exists in compounds **14** and **15**. ^1H NMR of compound **14** showed signal at 1.96 ppm referred to SCH_3 protons, while the infrared spectrum of **15** offered a band at ν 1267 cm^{-1} due to $\text{C}=\text{S}$.

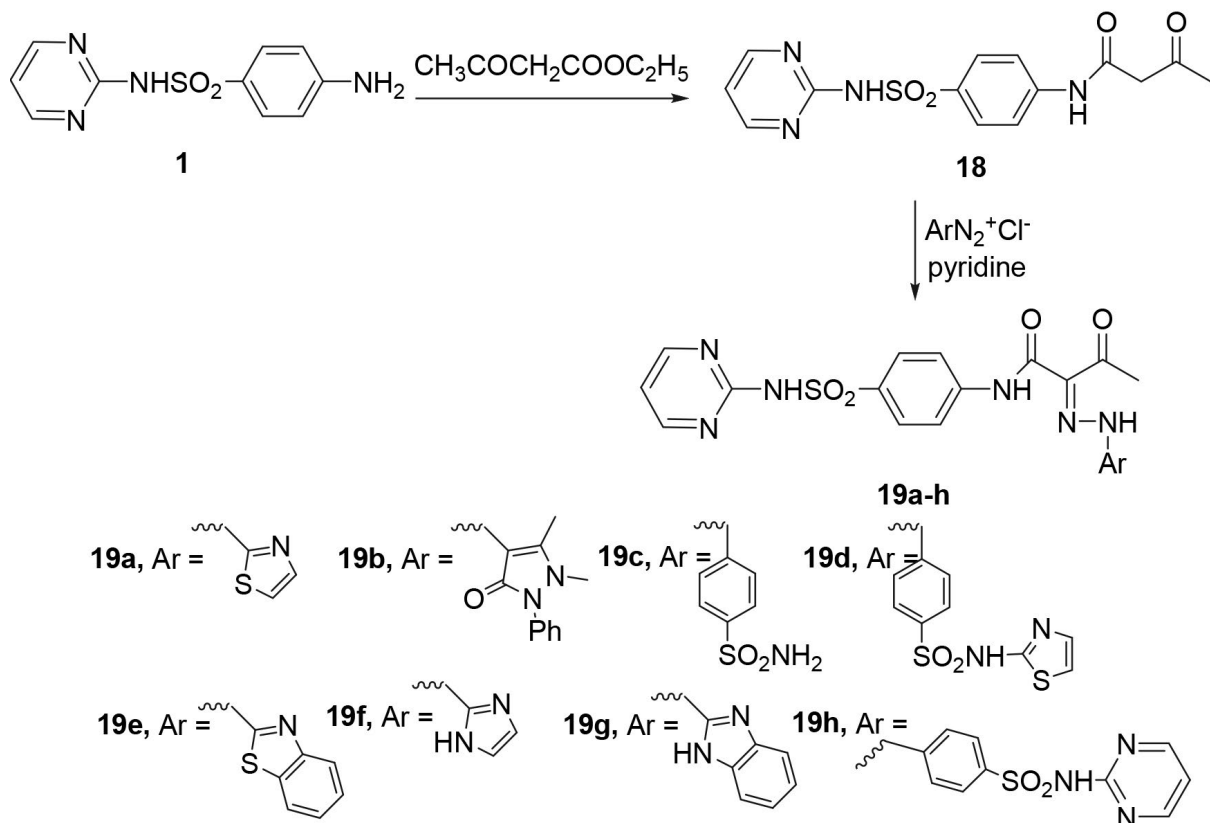
Moreover, it was found that ethyl acetoacetate reacted with compound **1** in refluxing *N,N*-dimethylformamide including a few small drops of trimethylamine to give the acetamide derivative **16**.

The infrared spectrum of sulfonamide **16** gave 3 lines at 1647, 2155, and 3357 cm^{-1} characteristic to amide CO, CN, and N-H groups. Its ^1H NMR spectrum showed signals at δ 4.25 ppm corresponding to CH_2 protons and 11.19 ppm corresponding to amide NH group. The MS spectrum showed additional confirmation to validate the compound as it showed the molecular weight at m/z 317 (M^+). When compound **16** was heated in ethanol containing sodium ethoxide, a cyclization occurred forming the corresponding 4-amino-2-oxo-*N*-(pyrimidin-2-yl)-1,2-dihydroquinoline-6-sulfonamide (**17**). Structure **17** was established based on its correct spectral and elemental analyses. The infrared spectrum displayed lines at 3357, 1713, 1651, and 1584 cm^{-1} corresponding to NH, amidic carbonyl, α,β -unsaturated ketone, and $\text{C}=\text{C}$ groups. ^1H NMR also revealed a very characteristic signal at δ 4.82 ppm due to NH_2 functional group. The MS spectrum offered a molecular weight at m/z 312 (M^+-5). Structure **17** was confirmed also chemically by an alternative preparation. Thus,

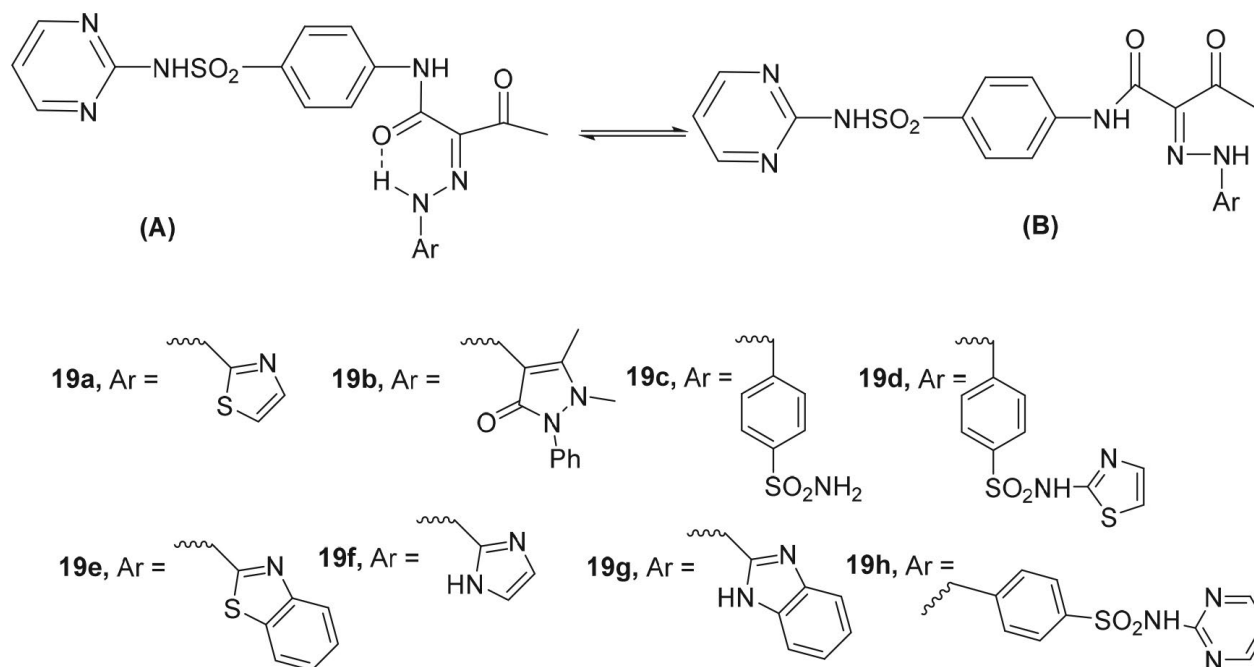
heating of sulfonamide **1** in the presence of *N,N*-dimethylformamide and triethylamine afforded compound conforming in all its properties (m.p., TLC, and infrared spectrum) to the sulfonamide derivative **17**.

When sulfonamide **1** reacted with ethyl acetoacetate in dry boiling xylene, it gave the acyclic intermediate 3-oxo-*N*-(4-(*N*-pyrimidin-2-ylsulfamoyl)phenyl)butanamide (**18**). The infrared spectrum of compound **18** offered new absorption bands at 1689 and 1725 cm^{-1} corresponding to carbonyl of COOR and amide $\text{C}=\text{O}$ functional groups, while the ^1H NMR spectrum of sulfonamide **18** displayed a characteristic signal at δ 2.31 ppm as a singlet for CH_3 protons, δ 3.33 ppm signal for CH_2 protons besides the aromatic protons of pyrimidine ring and benzene ring at δ 7.45–8.21 ppm. The mass spectrometry measurement gave m/z 335 (M^+-1) conforming to the molecular weight of compound **18**.

Coupling of sulfonamide **18** with aromatic amine diazonium salts (namely 2-aminothiazole diazonium salt, 4-aminoantipyrine diazonium salt, sulfanilamide diazonium salt and sulfathiazole diazonium salt, 2-aminobenzthiazole diazonium salt, 2-aminoimidazole diazonium salt, 2-aminobenzimidazole diazonium salt, and sulfadiazine diazonium salt) in pyridine at 0–5 $^\circ\text{C}$ gave the corresponding hydrazone compounds **19a–h**. The spectral and elemental analyses are in harmony with the suggested compound structures. Thus, ^1H NMR spectrum of compound **19a** displayed the disappearance of protons at δ 3.33 ppm



Scheme 6. Synthesis of hydrazone structures **19a–h**



Scheme 7. Intramolecular hydrogen bonding is in support of the hydrazone moieties in sulfonamides **19a–h**

due to CH_2 and the appearance of two doublet signals at δ 6.57 and 7.04 ppm due to two CH of thiazole ring. Similarly, the ^1H NMR of compound **19b** showed two singlet signals appeared at δ 1.77 and 2.68 ppm for CH_3 protons. The infrared spectrum of sulfonamides **19a–h** in general exhibited a band in the area $3200\text{--}3450\text{ cm}^{-1}$ due to NH vibration of the hydrazone moiety and a band at $1550\text{--}1580\text{ cm}^{-1}$ due to the azo form in its tautomeric equilibrium as well. Such shift of NH band was notified by Ramirez and Kerby¹⁷ for these hydrazone derivatives, this being due to the intra-molecular hydrogen bonding as depicted in structure **A** (Scheme 7). These facts indicate that sulfonamide derivatives **19a–h** offer confirmation for intramolecular hydrogen bonding which supports the hydrazone compounds. Infrared spectra of sulfonamides **19a–h** displayed bands at $1662\text{--}1731\text{ cm}^{-1}$ corresponding to vibration of $\text{C}=\text{O}$ functions.

Among the structural factors that make minimizing of the vibration of carbonyl functional group are conjugation and hydrogen bonding. Albeit, even when allowance is exhibited for conjugation, the carbonyl frequencies of the sulfonamides calculated are still much smaller than those in α,β -unsaturated ketones. This marked variance suggests that the carbonyl function of these sulfonamides should participate in hydrogen bonding in the solid state, as demonstrated by the suggested compound **A**. The ultraviolet spectra of the diazonium coupling products gave an extra confirmation that sulfonamides are in the tautomeric equilibrium with monohydrazones. Maximum of the dyes displayed 4 absorption bands at 196–438 nm. The comparatively low variance in λ_{max} may correspond to the polarity

variation of the band due to solvent actions corresponding to the common solvent effect.¹⁸ It has been seen that the ultraviolet spectra of monophenylazo structures differ from those of monophenylhydrazones. The azo structures commonly display two bands at 400–410 and 290–300 nm due to $n\text{--}\pi^*$ and $\pi\text{--}\pi^*$ transitions, respectively.¹⁹

Moreover, monophenylhydrazones display three bands at 220–230, 250–280 and 330–390 nm regions. The ultraviolet spectra of sulfonamides **19a–h** can be explained in terms of the tautomeric mixture. These dyes show four bands, of these, the medium and high wavelength bands appear to be dependent on the type of the polar substituents in the arylazo function, while the low wavelength bands is not affected. The UV spectral data show that both electron withdrawing groups and electron donating groups shift the absorption maxima to longer wavelengths. Moreover, it showed that the presence of this has not caused any observed higher or lower values of λ_{max} in the apparent region and $\log \epsilon$ has stayed nearly constant. This does point to the presence also of hydrazine structure where the resonance actions with the functions in the diazo structure are lower due to steric effects. In addition, the structure of sulfonamides **19a–h** was elucidated by mass spectra which displayed the correct molecular weight.

3. 2. Pharmacology

3. 2. 1. Cytotoxicity

The use of heterocyclic structures has a significant role in the treatment of cancer and in its removal plans.²⁰ Heterocycles are generally used as scaffolds on which

pharmacophores are coordinated to give effective and eclectic drugs. This is especially correct for five membered-ring heterocyclic compounds,²¹ which serve as the core components of a huge number of compounds that have a broad motivating range of biological action.^{22–24} The goal of this study was to prepare new drugs for anti-cancer elucidation as a trial to give novel antitumor agents of a maximum action and minimize side effects. In this paper, the chosen sulfonamides regarding to pyridine, pyrimidine, oxadiazole, and azo compounds were elucidated and screened *in vitro* for prevention of the growth of HepG2 (human hepatocellular liver carcinoma cell lines), WI 38 (human lung fibroblasts), VERO (cell line was initiated from the kidney of a normal adult African green monkey), and MCF-7 (breast cancer cell lines) were compared with the known anticancer drug 5-fluorouracil (5-Fu) and as a trial to get more potent agents with lower toxicity. The collected data are presented as the concentration of sulfonamides that made 50% inhibition of cells growth (IC₅₀).

The *in vitro* elucidation showed that some of the examined sulfonamides displayed (and also that all the modern prepared structures revealed) a certain action against tumor cell lines examined, although the action was commonly maximal towards HepG2 cancer line than the breast cancer one. Compounds **3** and **5** showed an effective antitumor action versus the four tumor cell lines examined (IC₅₀ = 11 and 12.4 against HepG2 and IC₅₀ = 7.3 and 9.32 against VERO, respectively) in contrast to the effective anticancer drug 5-fluorouracil used as the reference standard. So, we found that all examined sulfonamides including electron withdrawing groups (Br or NO₂) in the

Table 1: Cytotoxicity (IC₅₀) of examined sulfonamides on various cell lines^a

Compound No.	IC ₅₀ (µg/mL) ^a			
	HepG2	WI-38	VERO	MCF-7
5-Fu	8.6	3.2	6.5	2.3
2	88	74	90	85.5
3	11	17.1	7.3	10.5
4	23.2	33.7	30.3	26.1
5	12.4	20	9.32	12.5
6	26	40.3	38.1	45
7	102	120	100	200
8	29.5	27.6	36.5	29.9
19a	42	46.1	43.1	42.2
19b	65.2	70.3	86	71.6
19c	26	40.3	38.1	45.5
19d	15.5	16.6	26.5	27.9
19e	33.1	39.8	42.6	45.6
19f	88.2	74	90	85.5
19g	92	99.3	75.2	94.3
19h	10.4	15.1	9.3	11.5

^a IC₅₀ (µg/mL): 1–10 (very strong), 11–25 (strong), 26–50 (moderate), 51–100 (weak), 100–200 (very weak), above 200 (non cytotoxic).
5-FLU = 5-Fluorouracil

benzene ring of phthaliamide moiety displayed a higher to moderate action, so the real effects depend on the existence of thiazole or pyrimidine ring attached to sulfonamide group. It is obvious that compound **19d** showed strong action against two various cell lines and compound **19h** showed strong action versus four various cell lines corresponding to a long π -conjugated system joined to thiazole and pyrimidine rings, besides azo functional group and benzene ring. These outcomes demonstrate that variable molecular structure and orientation could enhance commonly observed antitumor action against the four examined cancer cells.

4. Conclusion

In the current research, fifteen sulfonamides were examined and most of them showed an antitumor action on four cancer cell lines. The most effective compounds **3**, **5**, **19d** and **19h** showed eclectic effect on HepG2 cancer cell line. The gained data exhibit the necessity or further developments to facilitate the future research based on the antitumor potential of the examined sulfonamides.

5. References

1. A. A. Fadda, A. M. Khalil, M. M. El-Habbal, *Pharmazie* **1991**, *46*, 743–744.
2. A. E. Boyd, *Diabetes* **1988**, *37*, 847–850.
DOI:10.2337/diabetes.37.7.847
3. C. T. Supuran, A. Scozzafava, *Exp. Opin. Ther. Patents* **2000**, *10*, 575–600. DOI:10.1517/13543776.10.5.575
4. C. T. Supuran, A. Scozzafava, *Curr. Med. Chem. Immunol. Endocr. Metabol. Agents* **2001**, *1*, 61–97.
DOI:10.2174/1568013013359131
5. C. W. Thornber, *Chem. Soc. Rev.* **1979**, *8*, 563–580.
DOI:10.1039/cs9790800563
6. S. A. Rostom, *Bioorg. Med. Chem.* **2006**, *14*, 6475–6485.
DOI:10.1016/j.bmc.2006.06.020
7. M. S. Al-Said, M. M. Ghorab, M. S. Al-Dosari, M. M. Hamed, *Eur. J. Med. Chem.* **2011**, *46*, 201–207.
DOI:10.1016/j.ejmech.2010.11.002
8. A. A. Fadda, E. M. Afsah, R. S. Awad, *Eur. J. Med. Chem.* **2013**, *60*, 421–430. DOI:10.1016/j.ejmech.2012.11.017
9. A. A. Fadda, K. Elattar, *Med. J. Chem.* **2013**, *2013*, 10.
DOI:10.1155/2013/928106
10. A. A. Fadda, H. A. Etman, A. A. Sarhan, Sherihan A. El-Hadidy, *Phosphorus, Sulfur, Silicon Relat. Elem.* **2010**, *185*, 526–536. DOI:10.1080/10426500902839863
11. A. A. Fadda, M. A. Berghot, F. A. Amer, D. S. Badawy, Nesma M. Bayoumy, *Arch. Pharm. Chem., Life Sci (Archiv der Pharmazie)* **2012**, *345*, 378–355.
DOI:10.1002/ardp.201100335
12. Hanaa Abu-Melha, A. A. Fadda, *Spectrochimica Acta Part A:*

- Molecular and Biomolecular Spectroscopy* **2012**, 89, 123–128.
DOI:10.1016/j.saa.2011.12.054
13. A. A. Fadda, A. A.-H. Abdel-Rahman, W. A. El-Sayed, T. A. Zidan, F. A. Badria, *Chem. Heterocyc. Compd.* **2011**, 47, 856–864. DOI:10.1007/s10593-011-0847-4
14. A. A. Fadda, E. Abdel-Latif, R. E. El-Mekawy, *Pharmacol. Pharm.* **2012**, 3, 148–157.
DOI:10.4236/pp.2012.32022
15. A. El-Shafei, A. A. Fadda, A. M. Khalil, T. A. E. Ameen, F. A. Badria, *Bioorg. Med. Chem.* **2009**, 17, 5096–5105.
DOI:10.1016/j.bmc.2009.05.053
16. A. A. Fadda, A. M. El Defrawy; Sherihan A. El-Hadidy, *Am. J. Org. Chem.* **2012**, 2(4), 87–96.
DOI:10.5923/j.ajoc.20120204.03
17. F. Ramirez, A. F. Kirby, *J. Am. Chem. Soc.* **1954**, 76, 1037.
DOI:10.1021/ja01633a034
18. A. E. Gilman, E. S. Stern, *An introduction to electronic absorption spectroscopy in organic chemistry*, 2nd ed., Edward Arnold Publisher Ltd, London **1957**, pp. 302.
19. A. E. Gilman, E. S. Stern, *Electronic absorption spectroscopy*, Edward Arnold Publisher Ltd, London **1960**, pp. 271.
20. S. Abu-Melha, *Acta Chim. Slov.* **2017**, 64, 910–930.
21. T. Foud, C. Nielsen, L. Brunn, E. B. Pederson, *Sc. J. Az. Med. Fac. (Girls)* **1998**, 19, 1173–1187.
22. E. H. Tawfik, K. S. Mohamed, H. M. Dardeer, A. A. Fadda, *Acta Chim. Slov.* **2018**, 65, 787–794.
DOI:10.17344/acsi.2018.4294
23. E. H. EL-Sayed, A. A. Fadda, *Acta Chim. Slov.* **2018**, 65, 853–864. DOI:10.17344/acsi.2018.4506
24. S. Botros, O. M. Khalil, M. M. Kamal, Y. S. El-Dash, *Acta Chim. Slov.* **2017**, 64, 102–116. DOI:10.17344/acsi.2016.2901
25. R. M. Mohareb, N. Y. M. Abo, F. O. Al-Farouk, *Acta Chim. Slov.* **2017**, 64, 117–128. DOI:10.17344/acsi.2016.2920

Povzetek

Na osnovi izhodne spojine 4-amino-*N*-(pirimidin-2-il)benzensulfonamida (**1**) smo pripravili serijo substituiranih sulfadiazinskih spojin in preučili njihovo citotoksično in antitumorsko delovanje. Spojino **1** smo reagirali z različnimi reagenti in tako pripravili sulfadiazine **2–18** ter hidrazone **19a–h** in preučili njihovo *in vitro* citotoksičnost na štiri rakave celične linije. Ugotovili smo, da so spojine **3**, **5**, **19d** in **19h** aktivne proti preiskovanim rakavim celicam.



Except when otherwise noted, articles in this journal are published under the terms and conditions of the Creative Commons Attribution 4.0 International License

Scientific paper

Formulation and Evaluation of Multidose Propofol Nanoemulsion Using Statistically Designed Experiments

Sidhartha Sankar Hota,^{1,3,*} Satyanarayan Pattnaik² and Subrata Mallick¹

¹ School of Pharmaceutical Sciences, Siksha 'O' Anusandhan (Deemed to be University), Bhubaneswar 751003, Odisha, India.

² Talla Padmavathi College of Pharmacy, Orus, Warangal, Telangana, India.

³ Zenotech Laboratories Ltd., Hyderabad, Telangana, India.

* Corresponding author: E-mail: sshota@rediffmail.com, profsmallick@gmail.com

Received: 08-19-2019

Abstract

Despite of the clinical, scientific, and commercial development, many patients complain about pain on the intravenous injection of propofol. Present work was undertaken to develop a stable multi-dose propofol nano-emulsion using 3² full factorial design which is supposed to be associated with less anticipated pain during intravenous administration. Propofol was incorporated in the mixture of disodium edetate, sodium oleate, thioglycerol, glycerol, egg lecithin, soyabean oil and medium chain triglyceride oil, and homogenization was continued at controlled temperature of 20 °C. The product did not show any significant change in visible extraneous particulate matter, pH, osmolality, bacterial endo-toxin, sterility, high performance liquid chromatography (HPLC) their stability and impurities after exposing at 40 °C for 3 and 6 months. Homogenization at 850 bar pressure of 30 min duration produced 174 nm particles with –53.6 mV zeta potential indicating its stability.

Keywords: Homogenization; nano-emulsion; propofol; statistical design of experiment.

1. Introduction

From the time of World War–II, anesthesiology got its importance for induction in combating casualties. The core objectives in developing injectable formulation are solubility, stability, and systemic tolerability. Osmolality is a potential factor for local tissue tolerability of an injectable drug product which would ideally be similar to that of the body fluid. Propofol is widely used for anesthesia.^{1,2} However, propofol is associated with pain at the administration site of the intravenous (IV) injection which is the substantial setback in clinical anesthesiology for smooth induction of general anesthesia.^{3,4} Various strategies have been reported to diminish the prevalence of pain by the addition of lidocaine, pethidine, fentanyl, alfentanil, remifentanil, butorphanol, thiopental etc. to propofol but no significant success has yet been achieved.^{5–7} The induction of anesthesia needs a single dose of 1–5 mg/kg and maintenance dose of 50–250 mcg/Kg/min. Frequent dosing may be required for the entire operation period of in-

fusion.⁸ Attempts were also taken to minimize the pain by increasing the rate of infusion at 2.5 to 5 ml every 5 seconds compared to the normal rate of infusion (20 drops/minute) but managing pain was still not possible.^{9–11}

Commercially available propofol emulsions vary in particle size and lies somewhere around 300 nm.^{5,12,13} Reduction in particle size of propofol may reduce pain upon its intravenous administration. Particle size reduction presented lower free fraction of propofol and a tendency to a lower incidence of pain.¹⁴ A lot of momentum in the recent past has been observed in fabricating nano-sized drug particles by top-down method using high pressure homogenization. Li et al., formulated microemulsion using pluronic F68, propylene glycol and saline, and produced a droplet size of about 300 nm.¹³ Ethyl butyrate being a short chain fatty (C-4, fewer than six carbons) acid showed higher drug release but deprived stability. Whereas, soybean oil, a larger molecule exhibited lower partitioning with excellent emulsion stability. Propofol emulsions formulated with mixtures of ethyl butyrate and soybean oil

were kinetically stable with reduced aqueous phase drug concentration.^{15–17} No significant differences in pharmacokinetics and sedation properties were observed on comparison to a commercial soy-based propofol emulsion.¹⁸ To decrease the amount of free propofol in the aqueous phase propofol emulsions were fabricated with medium and long-chain triglycerides (MCT/LCT).^{19–22} Heat generated during processing of a propofol product can swiftly induce microbial growth.²⁰ It was evident from a randomized double-blind clinical trial that pain on injection was reduced with small particle size lipid emulsion of propofol.²³ Soybean oil, glycerol, egg lecithin, and disodium edetate are present in the propofol innovator product (Diprivan, Astra Zeneca), and the combination of triglycerides and phospholipids in the formulation reduces the chance of free propofol concentration.^{24–26}

Multi-dose propofol oil in water stable nano-emulsion has been developed complying USP specifications with an intention to decrease the particle size, which is supposed to cause less pain. Propofol nano-emulsions were fabricated with and without sodium oleate using controlled homogenization technique. Process duration and homogenization pressure have been optimized for obtaining stable nano-emulsion of reduced particle size.

2. Experimental

2.1. Materials

Propofol was received as a kind gift sample from Themis Medicare, Gujarat, India. Soybean oil (Lipoid purified soybean oil 700), MCT (medium chain triglycerides) oil, Egg lecithin (Lipoid E80), and sodium Oleate (Lipoid Sodium Oleate B) were collected from Lipoid GMBH, Germany. Glycerols, thioglycerol, benzyl alcohol, disodium edetate, sodium hydroxide were sourced from Sigma Aldrich / Merck India. Capsule and membrane filters were from Millipore, India. Clear tubular glass vials were procured from Schott Kaisha, India and Bromobutyl stoppers were from West Pharma, Singapore. Freshly prepared double distilled water was used whenever required. All other reagents used were of analytic grade.

2.2. Formulation Development and Optimization

Preliminary studies were performed to characterize the active and inactive substances for their various physicochemical properties. Solubility and compatibility of the drug with other excipients were determined. The drug substance was thoroughly mixed with each of the excipients (except sodium hydroxide) in 1:1 ratio and were exposed at 50 °C for 2 weeks and observed for any change due to the impact of temperature and humidity.

The entire work was carried out in a Class-100 area, under the LAF (Lamellar Air Flow, Accumax, India) cabinet,

pre fumigated with H₂O₂. All the containers and accessories were autoclaved at 121 °C, 15 psi of pressure for 15 min prior to use. The dissolution of each and every formulation ingredient was checked. The speed of stirring, temperature and time were recorded. The manufacturing temperature was fixed by observing the solubility of propofol. The formulation pH was observed by checking the pH at each step with reference to pH drift studies performed by adjusting the pH of the bulk to different pH values within the range.

After execution of several trials of process temperature, homogenization time, formulation stability and microbial attributes the optimized formulation was finalized with the inactive ingredients as: soybean oil (50 mg/mL), MCT oil (50 mg/mL), egg lecithin (13 mg/mL), sodium oleate (0.52 mg/mL), glycerol (22.5 mg/mL), benzyl alcohol (1 mg/mL), disodium edetate (0.05 mg/mL), and thioglycerol (1 mg/mL). Disodium edetate, sodium oleate, thioglycerol, glycerol and Egg lecithin were added to water at about 20 °C and stirred for 10 min with an overhead stirrer and filtered using a 0.45 µm PVDF filter (Durapore, Millipore). Soybean oil and MCT oil were mixed with an overhead stirrer for 5 min in a separate beaker and propofol (10 mg/mL) was added to it and mixed further for 5 min. Both these phases were mixed for 5 min and sodium hydroxide was added for pH adjustment to 6.5. Then homogenized using the Lab scale homogenizer (Lark Ultrasonic Cell Crusher, India) until it was filterable through the 0.22 µm PVDF filter (Durapore, Millipore). Throughout the process, the temperature was maintained at about 25 °C. The laboratory scale optimized process was executed in triplicate for reproducibility and to monitor the robustness of the formulae and process with confirmation of various analytical parameters.

Scale up of the manufacturing process of the optimized batch was carried out in a class-100 area (room temperature 20 ± 2 °C) using large scale equipments, e.g., mixing/pressure vessels, homogenizer (Goma Engineering, Mumbai, India), cooling jackets, vertical stirrers, filling and sealing machines. Homogenization^{27,28} was continued for 30, 60 or 90 min at 650, 750 or 850 bar as per the levels of the factorial design (Table 1).

Benzyl alcohol, thioglycerol and disodium edetate were dissolved in water at about 20 °C and egg lecithin was added with continued stirring for 30 min. Other ingredients of the oil phase were properly mixed and filtered through 0.45 µm filter and was poured in to the aqueous phase for homogenisation from 650 to 850 bar pressure for 30–90 min.

Droplet size distributions and zeta potential of emulsion at each interval of time and pressure were obtained using dynamic light scattering (Malvern Nano-ZS, USA).²⁹

2.3. Statistical Design of Experiment

Varieties of factorial designs of experiments can be used in drug development. These different factors and

their interactions should be evaluated to predict their effects on the final formulation and its robustness.³⁰ An appropriate mathematical model (experimental design) can give necessary information for the fabrication process and product development.³¹

A three-level factorial design was used for optimization of the homogenization process. In the present study, pressure during homogenization (X_1) and duration (time) of homogenization (X_2) were chosen as independent variables. The particle size (Z) following homogenization was estimated as dependent response (Table 1). Homogenization pressure was evaluated at 650 bar (-1), 750 bar (0), and 850 bar (+1), while duration of homogenization was evaluated at 30 min (-1), 60 min (0), and 90 min (+1). From the preliminary trials, the levels for these two parameters were finalized. To evaluate the responses incorporating interactive and polynomial terms in a statistical model was explained.

$$Y = b_0 + b_1X_1 + b_2X_2 + b_{12}X_1X_2 + b_{11}X_1^2 + b_{22}X_2^2 + \dots \quad (1)$$

where, Y is the dependent variable, b_0 is the arithmetic mean response of the nine runs, and b_i (b_1, b_2, b_{12}, b_{11} and b_{22}) are the estimated coefficient for the corresponding factor X_i (X_1, X_2, X_1X_2, X_1^2 and X_2^2), in which the average result of changing one factor at a time from its low to high value is represented. The change in response is shown by the interaction term (X_1X_2) when two factors are changed simultaneously. To investigate nonlinearity the polynomial terms (X_1^2, X_2^2) are included. For the generation and evaluation of the statistical experimental design Design-Expert software (Version. 10.0.1, Stat-Ease Inc., Minneapolis, USA) was used.³²

2. 4. Polyvinylidene Fluoride (PVDF) Filter Integrity Test

Sterilizing-grade hydrophilic PVDF disposable filter (Durapore membrane disc, Millipore Corp.) disc (0.45 and 0.22 μm) was used for product integrity test. The filter was incubated with the product in a closed vessel at 40 °C for a contact time of 4 hours. The filter was then investigated for change in the physical characteristics such as bubble point, membrane thickness and burst pressure. The integrity testing of the filter elements were wetted with the optimized formulation.

2. 5. Leachable Extracts

Presence of any leachable extracts and the loss of components due to adsorption were estimated by soaking the filter membrane with the optimized formulation in relation to the fresh formulation.

2. 6. Filling and Sealing

The product was then passed through a membrane filter holder with 2.0 & 0.45 μm filters at 0.3–0.4 bar pressure, filled in 50 mL sterilized vials under nitrogen and sealed.

2. 7. Color and Clarity

The color and clarity parameters were assessed by comparing the test solution with a standard reference suspension. Briefly, standard stock opalescence was prepared by adding 1% (w/v) hydrazine sulphate in water (25ml) to a 10% (w/v) solution of Hexamine in water (25

Table 1. Process variables and the observed response using 3² factorial design

Run	Process factors		Observed response Particle size ^c (Z) in nm
	Pressure (X_1) ^a	Duration (X_2) ^b	
1	1.00	0.00	182 (\pm 8.1)
2	-1.00	-1.00	328(\pm 4.8)
3	-1.00	1.00	302(\pm 6)
4	0.00	0.00	206(\pm 5)
5	-1.00	0.00	302(\pm 5)
6	0.00	0.00	210(\pm 3)
7	1.00	-1.00	176(\pm 3)
8	0.00	0.00	203(\pm 3)
9	0.00	0.00	205(\pm 5)
10	0.00	0.00	209(\pm 3)
11	0.00	1.00	206(\pm 3)
12	1.00	1.00	207(\pm 5)
13	0.00	-1.00	222(\pm 3)

^a Levels of homogenization pressure (X_1) as 650 bars (-1), 750 bars (0) and 850 bars (+1).

^b Levels of homogenization duration (X_2) as 30 min (-1), 60 min (0) and 90 min (+1).

^c Data shown are mean of three determinations and figure in the parentheses indicates standard error of the mean.

ml); mixed well and allowed to stand for 24 hours. Standard opalescence was prepared by diluting 15 ml of the standard stock opalescence solution to 1000 ml with water and further, the reference suspension was prepared by diluting 5ml standard of opalescence with 95 ml of water. Each of 20 ml of test solution and reference suspension was transferred to a colorless, transparent and neutral glass tube, and the absorbance was measured at 430 nm using a UV-visible spectrophotometer (Jasco V-630, USA). The clarity of the solution was compared with standard opalescence produced by hydrazine sulphate in a transparent, neutral glass tube against a black background by viewing in diffused daylight down the vertical axis.³³

2. 8. pH, Osmolality, Particulate Matter Density and Specific Gravity

pH and Osmolality of propofol nano emulsion were measured employing a pH meter (720A; Thermo Orion, USA) and Cryoscopic Osmometer (Osmomat 030; Gonotec GmbH, Germany) respectively. Presence of any particulate matter was observed through the light obscuration counter sensor (APSS-2000 Liquid Particle Counter, Particle Measuring Systems, USA). Density and specific gravity of the emulsion were tested by using a density / specific gravity meter-DA-100 (Kyoto Electronics, Japan).^{33–35}

2. 9. HPLC Assay

For all types of drug estimation the chromatographic procedure was carried out using high performance liquid chromatography (Jasco LC-Net II/ADC, USA). Stainless steel column of 5 mm internal diameter (15 cm × 4.6 mm long), packed with octadecylsilyl silica gel for chromatography R (5 μm) (Nucleosil C18) with a solvent system of orthophosphoric acid, water and acetonitrile at a ratio of 7:200:300 (by volume) was used as mobile phase at a flow rate of 1.2 mL/min. Each solution of 25 μL was injected and the detector of the spectrophotometer was set at 210 nm. Same method was followed taking 10 μL of reference solution and continuing the chromatography for 15 min for the impurities.

2. 10. Multiple Piercing Resistance Study

The final sterile formulation was filled in a sterile 50 mL clear tubular glass vial capped with a sterile bromobutyl stopper. The stopper was punctured with a sterile 22 gauge needle at 0th, 8th, 24th, 32nd, 48th hours with a storage condition of 2–8 °C and sample (2 mL each) was withdrawn for evaluation of sterility and bacterial endotoxin (BET) loads to ensure the products resistance to multiple piercing as BET are lipopolysaccharides associated with pathogenic Gram-negative shock

2. 11. Bacterial Challenge Test

The product was collected from the sealed vials and filtered through a 0.45μ membrane. The membrane was rinsed with 0.1% peptone water and placed over the pre incubated tryptone soya agar plates. The agar plates were incubated at 20–25 °C for 3 days followed by 30–35 °C for further 2 days and the numbers of colonies forming units were counted. Aseptic techniques were followed throughout the process.

Limulus Amoebocyte Lysate (LAL) test was performed to detect the presence of any bacterial endotoxin. All the test tubes, micropipette tips and volumetric pipettes were depyrogenated by autoclaving (121 °C and 15 psi of pressure for 30 min) before testing. Glassware were rinsed with water and are made endotoxin free by dry heat sterilization at 250 °C for one hour. Both NaOH and HCl solution (each 0.1 N) were prepared and autoclaved at 121 °C, 15 psi of pressure for 30 min.⁵¹

2. 12. Stability Studies

Droplet size distribution of the emulsion after 3 freeze–thaw cycles (16 hours at –5 °C, 8 hours at 25 °C) were examined using dynamic light scattering (Malvern Nano-ZS, USA). The hydrodynamic size and zeta potential obtained were compared to that of the freshly prepared samples. Filled and sealed vials (50 mL) were stored at 40 °C ± 2 °C / 75% RH ± 5% RH for 6 months at upright and inverted positions and evaluated for stability. Emulsions were investigated visually at the end of the 3rd and 6th month for any phase separation and creaming and allowed for further testing.¹⁵

3. Results and Discussion

3. 1. Formulation Development

Three reproducible batches of propofol nano-emulsions were developed varying the formulation ingredients and homogenization parameters (Table 1) to optimize the product. Taking the ingredients, pre mixing of oil and water phases with an overhead shaft stirrer resulted in foam formation which hindered a proper mixing of the ingredients. Oil soluble ingredients were mixed and filtered using 0.45 μm filter. Aqueous soluble ingredients were mixed separately and filtered through 2.0 μm filter as egg lecithin micelles cannot be filtered through 0.45 μm filter. Then both phases were mixed separately and then homogenized at up to 850 bar pressure for up to 90 min as per (Table 1). Formulations were fabricated with and without sodium oleate to interpret its interference in BET aggravation. However, sodium oleate was found to be a non-interfering substance. The single dose commercial products may not contain anti-oxidant/preservative; even if the ingredients are susceptible to oxidation and support microbial

Table 2. Stability analysis of the product

Test parameters	Specification	Initial sample	Stability sample	
			3 rd Month	6 th Month
Description	Clear colorless solution free from visible extraneous particulate matter	Complies	Complies	Complies
Absorbance at 430 nm (Color and clarity)	Not more than 0.200	0.108	0.112	0.120
Clarity of the solution	Opalescence not more pronounced than the reference suspension	Complies	Complies	Complies
pH	Between 6.0 and 8.5	6.4	6.5	6.8
Osmolality	Between 260–320 mOsm/Kg	304	306	310
Hydrodynamic size (nm)	–	174	222	227
Zeta potential (mV)	–	– 53.6	– 47.1	– 45.8
Bacterial Endotoxins	Not more than 0.5 EU/mg of Propofol	None detected	None detected	None detected
Particulate matter i) ≥ 10 μ per container ii) ≥ 25 μ	Not more than 6000	120	148	129
	Not more than 600	11	14	11
Sterility	No microbial growth should be observed in the test sample after 14 days of preparation	No growth	No growth	No growth
HPLC assay	Between 90–110	100.02	98.96	96.74
Impurities (%) Total impurities	Not more than 1.0	0.56	0.7	0.71

growth.^{47–48} Formulation trials were also executed incorporating an anti-oxidant and a preservative which are generally recognized as safe (GRAS) for parenteral use. The product characterization data are presented in Table 2.

In the fabrication process addition of egg lecithin to cooled water and stirring for 30 min may promote the growth of microorganisms as egg lecithin is a supportive nutrient.^{36,49} This process was revised by the addition of preservatives first and then egg lecithin. This had a bacteriostatic effect on the liquid and microbial growth was arrested leading to improvement in BET values (Table 3).

With an objective to select a sterilization filter, PVDF capsule and membrane filters were tested to establish a product wetted bubble point values in contrast to the water wetted values. The levels of leachable substances were examined at this part of the study that might be associated with the use of filters in contact with the product.

Initially, the liquid bulk product was tried for sterilization by filtration using capsule filter. However, difficulties were observed in passing this product through the capsule filter. The product was then passed through 2.0 & 0.45 μm membrane filters using a membrane filter holder

at low pressure (0.3–0.4 bar). The bubble point (filter integrity) value was found to be 1.5 bar which was in agreement with its viscosity.^{37,38,46} Based on this confidence levels, the filtered product was filled into vials. Product failed sterility testing as the filtration train with 2.0 & 0.45 μm filter did not meet the usage of a series of filters sufficiently. The microbiological studies for sterility and endotoxin loads confirmed that the product remained intact as of its initial potency.

The sample meets the requirements of the test if the observation of the test is negative when tested at a dilution not exceeding Maximum Valid Dilution (MVD). No microbial growth was observed in the test sample after 14 days of preparation. BET levels were found acceptable in the product i.e., less than the fixed limits of 0.5 EU/mg (Table 2 and Table 3). The addition of the preservative and the method of separate filtration process of the different phases were able to reduce the microbial load of soyabean oil (12 CFU/gm) and egg lecithin (40 CFU/gm). This result enabled the product to resist multiple piercing for up to 48 hours. This confirmed the content integrity of the product for multiple dosing for over a period of 48 hours in a controlled environment.

$$MVD = \frac{\text{Endotoxin limit} * \text{concentration of product} \left(\frac{\text{mg}}{\text{mL}}\right)}{\text{Lysate sensitivity} (\lambda)} \quad (2)$$

Table 3. Bacterial endotoxin testing after multiple piercing of the same vial

Time point of piercing the vial (h)	Endotoxin dilution (EU/mL)				LRW (Negative Control)	End point
	2.0λ (0.06)	1.0λ (0.03)	0.5λ (0.015)	0.25λ (0.007)		
0	+	+	–	–	–	0.12
8	+	+	–	–	–	0.12
24	+	+	+	–	–	0.06
32	+	+	+	–	–	0.06
48	+	+	+	–	–	0.06

Where, λ = labelled sensitivity of LAL Reagent (EU per mL) LRW = LAL (Limulus Amoebocyte Lysate) reagent water

The levels of pH and Osmolality were well in their specific limits and have not changed significantly in accelerated stability condition, and supposed to be in the tolerable level.³⁹ Non appearances of creaming in the product till 1 month were further exposed to freeze thaw cycles and other accelerated conditions. A continuous homogenization with cooling jackets for 30 minutes at 850 bar pressure generated droplets of 174 nm mean diameter and –53.6 mV zeta potential. Under the stressed conditions of freezing and thawing the droplet size distribution of the product remained almost unchanged, and exhibited a size of 175 nm and –47.1 mV zeta potential.

Prior to Bacterial Challenge Test (BCT), a viability test was performed in order to establish the bactericidal effect of the product. The viability test helps determine the most appropriate BCT methodology. After the total exposure time, no more than 1 log reduction of the initial bacterial concentration was observed and hence the product was considered to be non-bactericidal.

3. 2. Homogenization Process Optimization Using DoE

Statistically designed experiments have been exploited widely for pharmaceutical process optimization includ-

ing formulation parameter screening activities.^{40–42} In the present research a 3² full factorial design was used to optimize the homogenization process parameters.⁴³ The homogenization process is very crucial in the development of a stable nano-emulsion, and the key process variables are homogenization duration and pressure. As per DoE software suggestion 13 runs were taken with the selected two numeric continuous process variables. The response variable chosen was the particle size of propofol post homogenization. Since, no aliases were found for quadratic model, response surface quadratic model was used safely for navigation through the model.⁴⁴ The highest order polynomial was selected as the sequential model sum of squares (Type 1) where the additional terms were significant (p<0.05) and the model was not aliased. The cubic model was found to be aliased and hence the model was not selected (Table 4). Quadratic model was fitted to the data (P<0.05) based on the model summary statistics including the adjusted R² and predicted R² for interpretation of the homogenization process response and particle size (Z) (Table 4).

The model and the model terms like X₁, X₁X₂, X₁² and X₂² are significant as understood by the analysis of variance (ANOVA) for the response surface quadratic

Table 4. Statistical model analysis of particle size

Sequential model sum of squares for				
Source	Sum of Squares	Degree of freedom (Df)	F-Value	p-Value
Mean vs Total	6.749E+005	1		
Linear vs Mean	21999.00	2	16.52	0.0007
2FI vs Linear	702.25	1	1.06	0.3298
Quadratic vs 2FI	5813.52	2	144.39	< 0.0001
Cubic ^a vs Quadratic	91.50	2	4.63	0.0728
Residual	49.42	5		
Total	7.035E+005	13		
Design model summary statistics				
Source		Adjusted R ²		Predicted R ²
Linear		0.7212		0.5013
2FI		0.7229		0.0023
Quadratic		0.9916		0.9619
Cubic		0.9959		0.9325

^aCubic model is aliased and hence is not selected.

Table 5. Analysis of variance

Source	Response Surface Quadratic model			Standardized mean effect		
	Sum of Squares	F-Value	p-Value*	Coefficient Estimate	Standard Error	Standardized mean effect
Model	28514.77	283.28	< 0.0001	205.93	1.86	110.71
X1	21961.50	1090.89	< 0.0001	-60.50	1.83	-33.06
X2	37.50	1.86	0.2146	-2.50	1.83	-1.36
X1X2	702.25	34.88	0.0006	13.25	2.24	5.91
X12	3934.09	195.42	< 0.0001	37.74	2.70	13.97
X22	262.09	13.02	0.0086	9.74	2.70	3.60

*p-Values <0.05 indicates significant terms

model (Table 5). The fitted polynomial equations relating to the responses were generated using Design Expert software and are given below.

$$\text{Particle Size} = +205.93 - 60.49 * X_1 - 2.49 * X_2 + 13.24 * X_1X_2 + 37.74 * X_1^2 + 9.74 * X_2^2$$

The coefficient estimate and standardized main effects (SMEs) for the dependent responses are listed in Table 6. SME values were calculated by dividing the main effects by the standard error of the main effects. In addition, three dimensional response surface plots were presented to estimate the effects of the mixture components on each response. Results of multiple regression analysis and SMEs revealed that the process variables had statistically significant influence on the dependent variables ($p < 0.05$, Table 5). The SME values clearly indicated that the homogenization pressure (X_1) is the most influential factor compared to the duration of homogenization (X_2) on the average particle size and can be visualized from the 3D surface plots (Figure 1) and contour plot (Figure 2). The surface response and contour plots are indicative of an op-

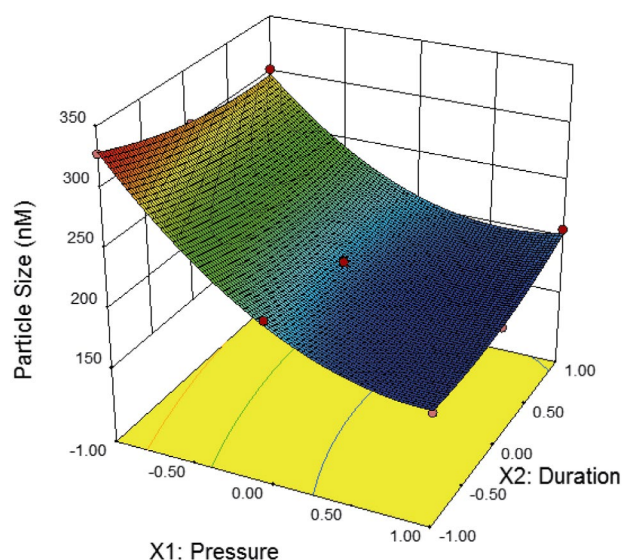


Figure 1. 3D Surface response plot indicates the effect of homogenization pressure (X_1) and the duration of homogenization (X_2) on average particle size.

timal point of resultant particle size beforehand of homogenization. Both the plots of DOE potentially predicted the systematic workflow. Average particle size yield was found to be 174 nm (Figure 3) with 30 min of homogenization at 850 bar pressure. Similar marketed formulations were reported of having much larger particles of around 300 nm⁵ compared to the present formulation and supposed to cause less pain while passing through the arteries.²³

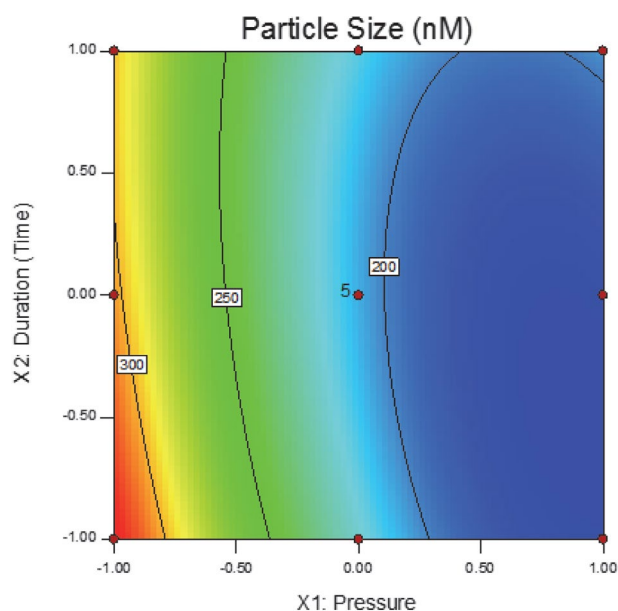


Figure 2. Contour plot indicating that the homogenization pressure (X_1) is the most influential factor compared to the duration of homogenization (X_2) on average particle size.

For parenteral emulsions droplet size and polydispersity index (PI) are vital physicochemical parameters as large particle size is clinically unacceptable. The formulation exhibited PI of 0.096 (Figure 3) which is well below the acceptable limit for parenteral emulsions^{44,45} indicating high stability. The initial zeta potential (-53.6 mV, Figure 4) of the product was found above -40 mV in accelerated stability condition of 6 months, which also implied its better stability. The stability indicating factors of the accel-

erated condition confirmed with those of the initial strategic values and hence can have a better shelf life in controlled environmental conditions.

The HPLC chromatogram of initial formulation are reported in the Figures 5 indicating the retention time of

the active substance and other negligible peaks due to inactive substances and impurities. The assay of the formulation has shown the value in the prescribed range of 90–110 % (Table 3, Figure 5) and the impurity levels (Table 3) remained below the threshold throughout the testing period.

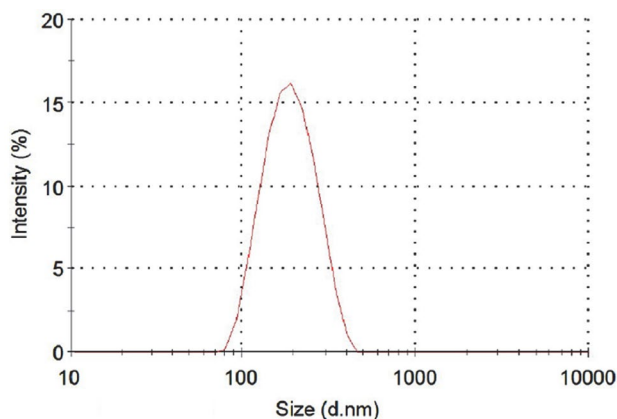


Figure 3. Hydrodynamic size distribution of the initial formulation

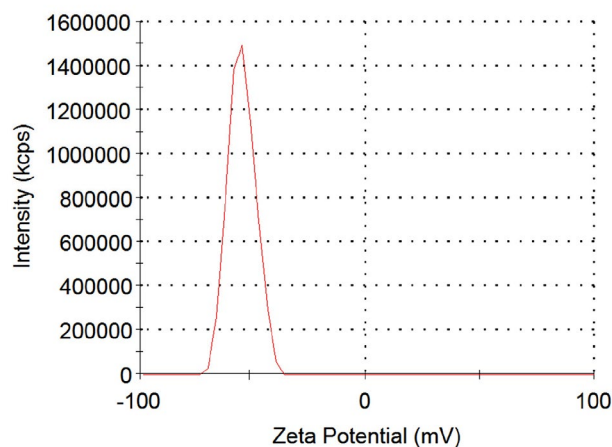


Figure 4. Zeta potential distribution of the initial formulation

4. Conclusions

Multi-dose propofol nano-emulsion was prepared with and without sodium oleate complying USP specifications and evaluated successfully using design of experiments. Controlled homogenization process could unable to influence the particle size significantly. The optimized process of homogenization at 850 bar of 30 min of duration produced 174 nm particles. PI and zeta potential of 0.096 and -53.6 mV respectively indicated highly stable product. The accelerated stress testing including freezing and thawing exhibited no significant change in the product. Further studies could be done to perform preclinical investigations in suitable animal models to assess the product.

5. Acknowledgements

The authors are very much grateful to the Honorable Prof. Manoj Ranjan Nayak, President, Siksha 'O' Anusandhan (Deemed to be University) for providing other facilities and encouragement. The authors are also thankful to Zenotech Laboratories Ltd for providing adequate facilities and support for the research work.

6. References

1. P. Pascale, M. R. Tramer, *Anesth. Analg* **2000**, *90*(4), 963–969. DOI:10.1213/00000539-200004000-00035
2. K. A. Desousa, *Indian J. Pharmacol.* 2016, *48*, 617–23. DOI:10.4103/0253-7613.194845

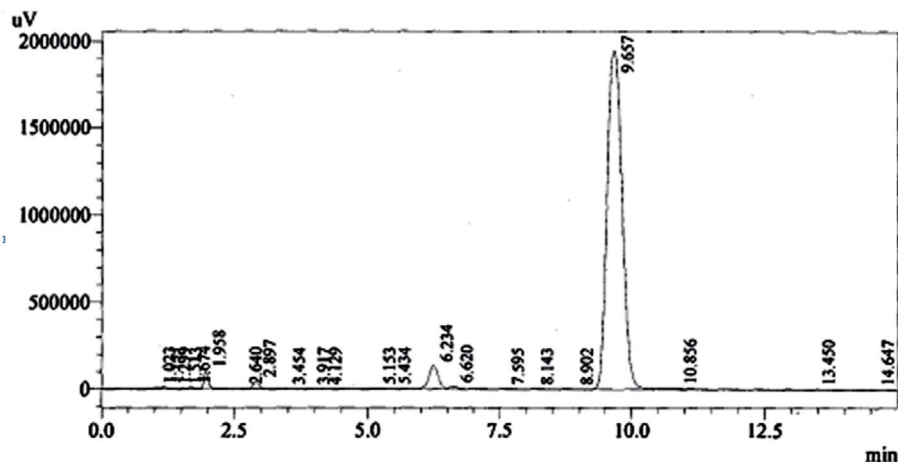


Figure 5. HPLC analysis for assay of the initial formulation

3. E. Liljeroth, J. A. Keson, *Acta. Anaesthesiol. Scand.* **2005**, *49*, 248–251. DOI:10.1111/j.1399-6576.2004.00573.x
4. N. C. H. Sun, A. Y. C. Wong, M. G. Irwin, *Anesth. Analg.* **2005**, *101*, 675–678. DOI:10.1213/01.ANE.0000157564.91910.04
5. W. Gao, B. Sha, Z. Fan, Y. Liu, X. Shen, *J. Nanomater* **2016**, Article ID 8486530, 8 pages.
6. B. Bachmann-mennenga, A. Ohlmer, H. Boedeker, M. Mann, B. Muhlenbruch, M. Heesen, *Eur. J. Anaesthesiol.* **2007**, *24*, 33–38. DOI:10.1097/00003643-200701000-00006
7. E. Kam, M. S. Abdul-Latif, A. McCluskey, *Anaesthesia* **2004**, *59*, 1167–1169. DOI:10.1111/j.1365-2044.2004.03964.x
8. W. S. Jellish, J. P. Leonetti, J. R. Murdoch, S. Fowles, *J. Clin. Anesth.* **1995**, *7*, 292–296. DOI:10.1016/0952-8180(95)00030-L
9. R. P. F. Scott, D. A. Saunders, J. Norman, *Anaesthesia* **1988**, *43*, 492–4. DOI:10.1111/j.1365-2044.1988.tb06641.x
10. C. L. Huang, Y. P. Wang, Y. J. Cheng, L. Susetio, C. C. Liu, *Anesth Analg* **1995**, *81*, 1087–1088. DOI:10.1097/00000539-199511000-00033
11. C. H. Tan, M. K. Onsiong, *Anaesthesia* **1998**, *53*, 468–476. DOI:10.1046/j.1365-2044.1998.00405.x
12. D. F. Driscoll, *Pharm. Res.* **2006**, *23*, 1959–1969. DOI:10.1007/s11095-006-9092-4
13. G. Li, Y. Fan, X. Li, X. Wang, Y. Li, Y. Liu, *Int. J. Pharm.* **2012**, *425(1–2)*, 53–61. DOI:10.1016/j.ijpharm.2012.01.011
14. T. A. Rodrigues, R. A. Alexandrino, M. E. Kanczuk, J. L. Goz-zani, L.A.S.T. Mathias, *Rev Bras Anestesiologia* **2012**, *62*, 325–334. DOI:10.1016/S0034-7094(12)70133-2
15. R. Damitz, A. Chauhan, *Int. J. Pharm.* **2015**, *486(1–2)*, 232–241. DOI:10.1016/j.ijpharm.2015.03.057
16. A. Salman, M. Salman, F. Saricaoglu, *J. Clin. Anesth.* **2011**, *23(4)*, 270–274. DOI:10.1016/j.jclinane.2010.09.008
17. A. Honarmand, M. Safavi, *Acute. Pain.* **2008**, *10(1)*, 23–29. DOI:10.1016/j.acpain.2008.01.001
18. C. Tzagogiorgas, S. Theisinger, E. Heesch, J. Krebs, R. Holm, G. Beck, *Int. J. Pharm.* **2015**, *486(1–2)*, 69–76. DOI:10.1016/j.ijpharm.2015.03.037
19. R. Burimsittichai, K. Kumwilaisuk, S. Charuluxananan, W. Tingthanathikul, P. Premsamran, N. Sathapanawath, *J Med Assoc Thai* **2006**, *89*, 86–91.
20. M. Yamakage, S. Iwasaki, J. Satoh, A. Namiki, *Anesth. Analg.* **2005**, *101(2)*, 385–388. DOI:10.1213/01.ANE.0000154191.86608.AC
21. M. Perlstein, A. Aserin, E. Wachtel, N. Garti, *Colloids Surf., B.* **2015**, *136*, 282–290. DOI:10.1016/j.colsurfb.2015.08.044
22. T. Shimizu, S. Inomata, M. Tanaka, *J. Clin. Anesth.* **2011**, *23(7)*, 540–543. DOI:10.1016/j.jclinane.2011.02.006
23. B. Krobbuaban, S. Diregpoke, S. Kumkeaw, M. Tanomsat, *J. Med. Assoc. Thailand*, **2005**, *88 (10)*, 1401–5.
24. J. Carpenter, Propofol-based Anesthetic and Method of Making Same. U S Patent Number 6,150,423, date of patent November 21, **2000**.
25. C. Jones, J. Platt, Pharmaceutical compositions of propofol and edetate. U S Patent Number 5,731,355, date of patent March 24, **1998**.
26. J. Zhang, J. Ding, M. Luo, Propofol formulation with enhanced microbial inhibition. U S Patent Number 6,399,087, date of patent June 4, **2002**.
27. M. Juttulapa, S. Piriyaarasarth, H. Takeuchi, P. Sriamornsak, *Asian J Pharm Sci*, **2017**, *21*–27. DOI:10.1016/j.ajps.2016.09.004
28. S. Schultz, G. Wagner, K. Urban, J. Ulrich, *Chem Eng Technol*, **2004**, *27*, 361–368. DOI:10.1002/ceat.200406111
29. M. Mlynarczyk, M. Sznitowska, D. W. Swietlikowska, *Drug Dev. Ind. Pharm.* **2008**, *34*, 355–362. DOI:10.1080/03639040701657628
30. S. Pattnaik, K. Swain, P. Manaswini, E. Divyavani, J. V. Rao, V. Talla, S. K. Subudhi, *J. Drug Delivery Sci. Technol.* **2015**, *29*, 199–209. DOI:10.1016/j.jddst.2015.07.021
31. M. Tondar, M J Parsa, Y Yousefpour, A M Sharifi, S V Shetab-Boushehri, *Acta Chim. Slov.* **2014**, *61*, 688–693.
32. S. Bohanec, T. R. Peterka, P. Blazic, R. Jurecic, J. Grmas, A. Krivec, J. Zakrajsek, *Acta Chim. Slov.* **2010**, *57*, 895–903.
33. The United States Pharmacopeia, National Formulary, Rockville (MD), United States Pharmacopeial Convention. **2012**, *1061*, 609–610.
34. The United States Pharmacopeia, National Formulary, Rockville (MD): United States Pharmacopeial Convention. **2012**, *791:343–344*.
35. The United States Pharmacopeia, National Formulary, Rockville (MD): United States Pharmacopeial Convention. **2012**, *785*, 335–336.
36. J. D. Kalen, J. I. Hirsch, K. A. Kurdziel, W. C. Eckelman, D. O. Kiesewetter, *Appl Radiat Isot.* **2007**, *65(6)*, 696–700. DOI:10.1016/j.apradiso.2006.10.015
37. F. Strachan, J. Mansel, R. Clutton, *J. Small Anim. Pract.* **2008**, *49(4)*, 186–190. DOI:10.1111/j.1748-5827.2007.00473.x
38. B. K. Meyer, D. Vargas, *PDA J Pharm Sci Technol* **2006**, *60*, 248–253. DOI:10.2533/000942906777674886
39. I. Wachowski, D. T. Jolly, F. J. Hrazdil, J. C. Galbraith, M. Greacen, A. S. Clanachan, *Anesth Analg* **1999**, *88*, 209–212. DOI:10.1213/00000539-199901000-00039
40. A. Bottino, G. Capannelli, A. Comite, *Desalination* **2005**, *183*, 375–382. DOI:10.1016/j.desal.2005.03.040
41. K. Hayashi, K. Douhara, G. Kashino, *Ann. Nucl. Med.* **2014**, *28*, 586–592. DOI:10.1007/s12149-014-0830-0
42. W. Wang, *Int. J. Pharm.* **2015**, *490*, 308–315. DOI:10.1016/j.ijpharm.2015.05.069
43. S. Pattnaik, K. Swain, J. V. Rao, T. Varun, S. Mallick, *Medicina*, **2015**, *51(4)*, 253–261. DOI:10.1016/j.medici.2015.07.002
44. S. Pattnaik, K. Swain, J. V. Rao, T. Varun, S. K. Subudhi, *RSC. Adv.* **2015**, *5*, 91960–91965. DOI:10.1039/C5RA20411A
45. S. Pattnaik, K. Swain, S. Mallick, *Lat. Am. J. Pharm.* **2009**, *28*, 62–69.
46. B. Jancic, M. Medenica, D. Ivanovic, A. Malenovic, *Acta. Chim. Slov.* **2007**, *54*, 49–54.
47. F. A. Araujo, R. G. Kelmann, B. V. Araujo, R. B. Finatto, H. F. Teixeira, L. S. Koester, *Eur J Pharm Sci* **2011**, *42*, 238–245. DOI:10.1016/j.ejps.2010.11.014
48. R. H. Muller, S. Schmidt, I. Buttle, A. Akkar, J. Schmitt, S. Bromer, *Int. J. Pharm.* **2004**, *269*, 293–302. DOI:10.1016/j.ijpharm.2003.09.019

49. B. K. Meyer, A. NI, B. HU, L. Shi, *J Pharm Sci* **2007**, *96*, 3155–3167. DOI:10.1002/jps.20976
50. The United States Pharmacopeia, National Formulary, Rockville (MD): United States Pharmacopeial Convention. **2012**, 4449–4450.
51. The United States Pharmacopeia, National Formulary, Rockville (MD): United States Pharmacopeial Convention. **2012**, *71*, 69–74.

Povzetek

Kljub kliničnemu, znanstvenemu in komercialnemu razvoju se mnogi bolniki pritožujejo zaradi bolečin pri intravenski injekciji propofola. Pričujoča raziskava je bila izvedena z namenom razviti stabilne večodmerne nano-emulzije propofola z uporabo celovitega 3^2 faktorialnega modela, ki naj bi bil povezane z manj pričakovanimi bolečinami med intravenskim dajanjem propofola. Propofol je bil vgrajen v mešanico dinatrijevega edetata, natrijevega oleata, tioglicerola, glicerola, jajčnega lecitina, sojinega olja in trigliceridnih olj s srednjo dolžino verige. Homogenizacijo smo nadaljevali pri nadzorovani temperaturi 20 °C. Po izpostavitvi temperaturi 40 °C za 3 in 6 mesecev izdelek ni vidno spremenil zunanjega videza, vrednosti pH, osmolalnosti, bakterijskega endotoksina, sterilnosti in določitev nečistoč. Homogenizacija pri tlaku 850 bar je po 30 minutah vodila do delcev velikosti 174 nm in zeta potenciala –63,6 mV, kar kaže na njegovo stabilnost.



Except when otherwise noted, articles in this journal are published under the terms and conditions of the Creative Commons Attribution 4.0 International License

Scientific paper

Syntheses, Crystal Structures, Antimicrobial Activity and Thermal Behavior of Copper(II) Complexes Derived from 1-Naphthylacetic Acid and Diamines

Ling-Wei Xue,^{1,*} Chen Chen,² Gan-Qing Zhao¹ and Wei-Chun Yang¹¹ College of Chemistry and Chemical Engineering, Pingdingshan University, Pingdingshan 467000, P.R. China² Rock and Mineral Testing Center of Henan Province, Zhengzhou 450000, P.R. China

* Corresponding author: E-mail: pdsuchemistry@163.com

Received: 06-15-2019

Abstract

Two copper(II) complexes, [CuL₂(EA)] (1) and [Cu₂L₄(PA)₂] · 2H₂O (2 · 2H₂O), where L is 1-naphthylacetate, EA is *N,N*-diethylethane-1,2-diamine, PA is propane-1,3-diamine, have been prepared and characterized. Structures of the complexes have been characterized by single-crystal X-ray diffraction. Complex 1 is a mononuclear copper(II) compound, with the Cu atoms coordinated in square planar geometry. Complex 2 · 2H₂O is a centrosymmetric dinuclear copper(II) compound, with the Cu atoms coordinated in square pyramidal geometry. Single crystals of the complexes are stabilized by hydrogen bonds. The effects of the compounds on the antimicrobial activity against *Staphylococcus aureus*, *Escherichia coli*, and *Candida albicans*, as well as thermal behavior of the complexes were studied.

Keywords: Copper complex; crystal structure; hydrogen bonding; antimicrobial activity; thermal property

1. Introduction

Carboxylic acids are a kind of interesting ligands for the preparation of metal complexes.¹ Copper is a very important element in biological systems, functions as the active site of hydrolytic enzymes, such as Cu-Zn superoxide dismutase.² Copper complexes with carboxylate ligands have been widely reported for their versatile structures and biological applications.³ Intriguingly, the copper(II) complexes were shown to be significantly more potent than the metal free chelate, leading to the suggestion that the metal complex was the biologically active species.⁴ Copper(II) complexes are known to play a significant role either in naturally occurring biological systems or as pharmacological agents.⁵ 1-Naphthylacetic acid is structurally similar to carboxylic acids. However, very few copper complexes derived from 1-naphthylacetic acid have been reported so far. In the present paper, two new copper(II) complexes, [CuL₂(EA)] (1) and [Cu₂L₄(PA)₂] · 2H₂O (2 · 2H₂O), where L is 1-naphthylacetate, EA is *N,N*-diethylethane-1,2-diamine, PA is propane-1,3-diamine, are reported.

2. Experimental

2. 1. Materials and Measurements

Commercially available 1-naphthylacetic acid, *N,N*-diethylethane-1,2-diamine, and propane-1,3-diamine were purchased from Aldrich and used without further purification. Other solvents and reagents were made in China and used as obtained. C, H and N elemental analyses were performed with a Perkin-Elmer elemental analyser. Infrared spectra were recorded on a Nicolet AVATAR 360 spectrometer as KBr pellets in the 4000–400 cm⁻¹ region. Thermal stability analysis was performed on a Perkin-Elmer Pyris Diamond TG-DTA thermal analyses system.

2. 2. Synthesis of [CuL₂(EA)] (1)

An aqueous solution (10 mL) of CuSO₄ · 5H₂O (0.10 mmol, 24.9 mg) was added to an aqueous solution (10 mL) of 1-naphthylacetic acid (0.20 mmol, 37.2 mg) and *N,N*-diethylethane-1,2-diamine (0.20 mmol, 23.2 mg) with stirring. The mixture was stirred for 1 h at ambient condition

to give a clear blue solution. The resulting solution was allowed to stand in air for several days. Blue block-shaped crystals suitable for X-ray single crystal analysis were formed at the bottom of the vessel. The isolated product was washed three times with water, and dried in a vacuum over anhydrous CaCl_2 . For $\text{C}_{30}\text{H}_{34}\text{CuN}_2\text{O}_4$: anal. calcd., %: C, 65.60; H, 6.23; N, 5.09. Found, %: C, 65.71; H, 6.32; N, 4.98. IR data (ν , cm^{-1}): 3267, 1590, 1460, 1388, 1258, 1119, 1043, 782, 718, 630, 537, 465.

2. 3. Synthesis of $[\text{Cu}_2\text{L}_4(\text{PA})_2] \cdot 2\text{H}_2\text{O}$ ($2 \cdot 2\text{H}_2\text{O}$)

This complex was prepared by the same method as that described for **1**, but with *N,N*-diethylethane-1,2-diamine replaced by propane-1,3-diamine (0.20 mmol, 14.2 mg). For $\text{C}_{54}\text{H}_{60}\text{Cu}_2\text{N}_4\text{O}_{10}$: anal. calcd., %: C, 61.64; H, 5.75; N, 5.32. Found, %: C, 61.50; H, 5.82; N, 5.23. IR data (ν , cm^{-1}): 3309, 3229, 1616, 1367, 1270, 1173, 1110, 1026, 912, 781, 710, 634, 546, 486.

2. 4. X-Ray Diffraction

Diffraction intensities for the complexes were collected at 298(2) K using a Bruker D8 VENTURE PHOTON diffractometer with $\text{MoK}\alpha$ radiation ($\lambda = 0.71073 \text{ \AA}$). The collected data were reduced using SAINT,⁶ and multi-scan absorption corrections were performed using SADABS.⁷ The structures were solved by direct methods and refined against F^2 by full-matrix least-squares methods using SHELXTL.⁸ All of the non-hydrogen atoms were refined anisotropically. The water H atoms in $2 \cdot 2\text{H}_2\text{O}$ were locat-

ed from a difference Fourier map and refined isotropically, with O–H and H...H distances restrained to 0.85(1) and 1.37(2) \AA , respectively. The remaining H atoms were placed in idealized positions and constrained to ride on their parent atoms. The low data completeness of complex **1** (76.2%) is due to the poor-quality data of the crystal. The crystallographic data for the complexes are summarized in Table 1.

2. 5. Antimicrobial Assay

Qualitative determination of antimicrobial activity was done using the disk diffusion method as described in the literature.⁹ Suspensions in sterile peptone water from 24-h cultures of microorganisms were adjusted to 0.5 McFarland. Muller-Hinton Petri dishes of 90 mm were inoculated using these suspensions. Paper disks (6 mm in diameter) containing 10 μL of the substance to be tested (at a concentration of 2048 $\mu\text{g mL}^{-1}$ in DMSO) were placed in a circular pattern in each inoculated plate. Incubation of the plates was done at 37 °C for 18–24 h. Reading of the results was done by measuring the diameters of the inhibition zones generated by the test substance. Tetracycline was used as a reference substance. Determination of MIC was done using the serial dilutions in liquid broth method. The materials used were 96-well plates, suspensions of microorganism (0.5 McFarland), Muller-Hinton broth (Merck) and stock solutions of each substance to be tested (2048 $\mu\text{g mL}^{-1}$ in DMSO). The following concentrations of the substances to be tested were obtained in the 96-well plates: 1024, 512, 256, 128, 64, 32, 16, 8, 4 and 2 $\mu\text{g mL}^{-1}$. After incubation at 37 °C for 18–24 h, the MIC for each tested substance was determined by microscopic observation of

Table 1. Crystallographic and experimental data for complexes **1** and $2 \cdot 2\text{H}_2\text{O}$

	1	$2 \cdot 2\text{H}_2\text{O}$
Formula	$\text{C}_{30}\text{H}_{34}\text{CuN}_2\text{O}_4$	$\text{C}_{54}\text{H}_{60}\text{Cu}_2\text{N}_4\text{O}_{10}$
FW	550.1	1052.1
Crystal system	Monoclinic	Monoclinic
Space group	$P2_1/c$	$P2_1/c$
$a/\text{\AA}$	13.496(2)	11.474(2)
$b/\text{\AA}$	9.111(1)	27.474(2)
$c/\text{\AA}$	22.411(2)	8.409(1)
$\beta/^\circ$	97.331(2)	101.937(2)
$V/\text{\AA}^3$	2733.2(6)	2593.3(6)
Z	4	2
$\mu/\text{mm}^{-1}(\text{Mo-K}\alpha)$	0.836	0.881
$D_c/\text{g cm}^{-3}$	1.337	1.347
Reflections/parameters	3873/336	4493/322
Independent reflections	1669	2316
Restraints	0	3
$F(000)$	1156	1100
Goodness of fit on F^2	1.007	1.011
$R_1, wR_2 [I \geq 2\sigma(I)]^a$	0.0648, 0.1068	0.0647, 0.1298
R_1, wR_2 (all data) ^a	0.2245, 0.1547	0.1625, 0.1599
Largest diff. peak and hole/ $e \text{ \AA}^{-3}$	0.409, -0.728	0.845, -0.500

^a $R_1 = \sum ||F_o| - |F_c|| / \sum |F_o|$, $wR_2 = [\sum w(F_o^2 - F_c^2)^2 / \sum w(F_o^2)^2]^{1/2}$.

microbial growth. It corresponds to the well with the lowest concentration of the tested substance where microbial growth was clearly inhibited.

3. Results and Discussion

3.1. Chemistry

The two copper complexes were prepared by the reaction of $\text{CuSO}_4 \cdot 5\text{H}_2\text{O}$, 1-naphthylacetic acid and *N,N*-diethylethane-1,2-diamine in a molar ratio of 1:2:2 in aqueous solution. Single crystals of the complexes are stable in air at room temperature. The complexes are soluble in water, DMSO, methanol and ethanol, but insoluble in dichloroform and chloroform. 1-Naphthylacetate ligand usually adopt bidentate coordination mode with copper ion,¹⁰ with only two reported examples of monodentate coordination mode.¹¹

3.2. IR Spectra

The infrared spectra of the complexes were consistent with their structures as determined by X-ray diffraction. Features corresponding to naphthyl and benzene ring puckering exist in the region between 800 and 600 cm^{-1} . Asymmetric and symmetric C–O stretching modes of the fully deprotonated, ligated carboxylate groups were substantiated by strong, broadened bands at 1590 and 1389 cm^{-1} for complex **1**, and 1618 and 1369 cm^{-1} for complex **2** · 2H₂O.¹² The lack of bands in the region of about 1710 cm^{-1} is indicative of complete deprotonation of all carboxylate groups in both complexes.

3.3. Structure Description of the Complexes

The molecular structures of complexes are shown in Figures 1 and 2. Selected bond lengths and angles are listed in Table 2. Complex **1** is a mononuclear copper(II) compound. The Cu atom in the complex is coordinated by two N atoms of the diamines, and two carboxylate O atoms from two L, forming square planar geometry. Complex **2** · 2H₂O is a centrosymmetric dinuclear copper(II) compound, and contains two water molecules of crystallization. The Cu atoms in the complex are coordinated by the N atoms of the diamines, and the carboxylate O atoms from L, forming square pyramidal geometry. The bond lengths related to the Cu atoms in both complexes are similar to those observed in comparative copper complexes with carboxylate and amine ligands.^{11,13} The square planar coordination of complex **1** and the basal plane of the square pyramidal coordination of complex **2** · 2H₂O are somewhat distorted, as evidenced from the coordinate bond angles, ranging from 85.3(2) to 93.6(2)° for the *cis* angles and from 167.3(3) to 169.0(3)° for the *trans* angles for **1**, and from 88.7(2) to 93.7(2)° for the *cis* angles and from 162.4(2) to 168.9(2)° for the *trans* angles for **2**.

In the crystal structures of the complexes (Figure 3 for **1** and Figure 4 for **2**), the molecules are linked through intermolecular N–H...O and O–H...O hydrogen bonds (Table 3), to form 1D chains.

Table 2. Selected bond lengths (Å) and angles (°) for **1** and **2** · 2H₂O

1			
Cu1–O2	2.000(5)	Cu1–O3	1.965(5)
Cu1–N1	2.046(5)	Cu1–N2	1.984(5)
O2–Cu1–N1	93.74(17)	O2–Cu1–N2	168.90(18)
N1–Cu1–N2	90.6(2)	O2–Cu1–O3	88.72(15)
N1–Cu1–O3	162.43(18)	N2–Cu1–O3	90.19(17)
2 · 2H ₂ O			
Cu1–O2	1.955(3)	Cu1–O3	2.002(4)
Cu1–N1	1.983(5)	Cu1–N2	1.984(4)
Cu1–O3 ^{#1}	2.467(5)		
O3–Cu1–N2	167.3(3)	O3–Cu1–O2	90.6(2)
N2–Cu1–O2	93.6(2)	O3–Cu1–N1	92.8(2)
N2–Cu1–N1	85.3(2)	O2–Cu1–N1	169.0(3)
O3 ^{#1} –Cu1–N1	115.0(3)	O3 ^{#1} –Cu1–N2	84.5(3)
O3 ^{#1} –Cu1–O2	84.4(3)	O3 ^{#1} –Cu1–O3	82.6(3)

Table 3. Geometrical parameters for hydrogen bonds

Hydrogen bonds	D–H (Å)	H...A (Å)	D...A (Å)	D–H...A (°)
1				
N2–H2B...O1 ^{#1}	0.90	2.14	2.991(10)	157
N2–H2A...O4 ^{#2}	0.90	2.09	2.946(8)	158
2 · 2H ₂ O				
O5–H5B...O4 ^{#3}	0.85(1)	2.03(3)	2.780(8)	148(5)
N2–H1B...O2 ^{#4}	0.90	2.25	3.080(6)	153
N1–H2B...O1 ^{#3}	0.90	2.16	2.971(6)	149
N1–H2A...O5	0.90	2.25	3.119(9)	162

^{#1} 1 – x, ½ + y, ½ – z; ^{#2} 1 – x, –½ + y, ½ – z; ^{#3} 1 – x, –y, 1 – z; ^{#4} 1 – x, –y, –z.

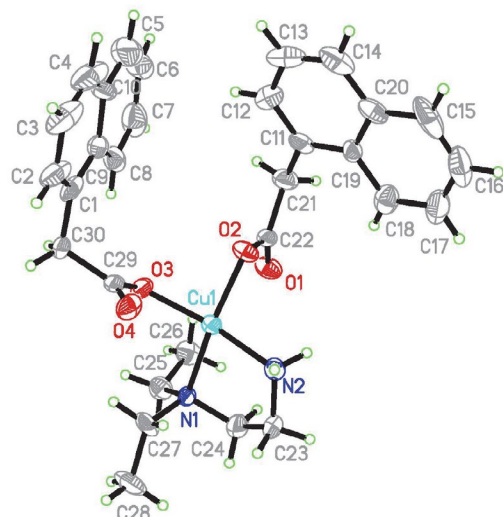


Figure 1. Molecular structure of **1** at 30% probability displacement.

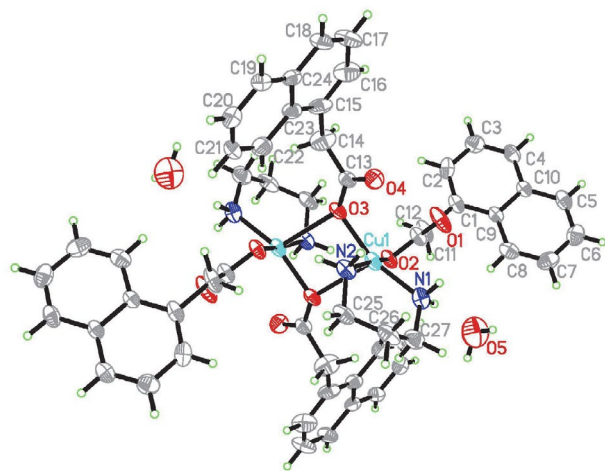


Figure 2. Molecular structure of $2 \cdot 2\text{H}_2\text{O}$ at 30% probability displacement.

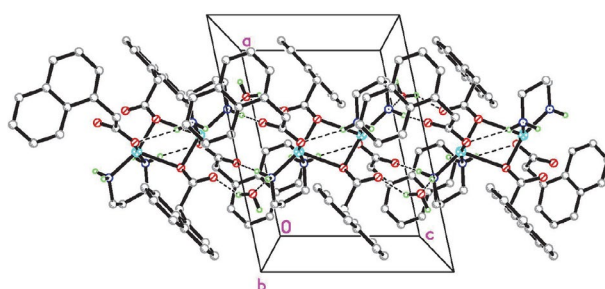


Figure 3. Molecular packing of **1**, viewed along the *a* axis. Hydrogen bonds are drawn as dashed lines. Hydrogen atoms not related to hydrogen bonds are omitted for clarity.

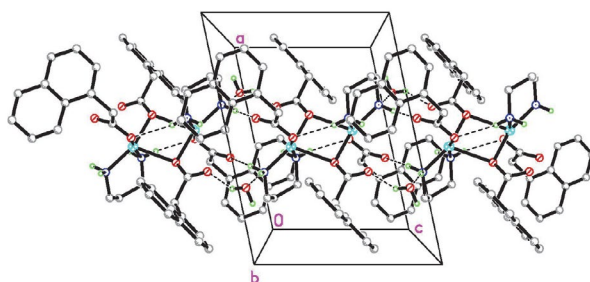


Figure 4. Molecular packing of $2 \cdot 2\text{H}_2\text{O}$, viewed along the *b* axis. Hydrogen bonds are drawn as dashed lines. Hydrogen atoms not related to hydrogen bonds are omitted for clarity.

3. 4. Thermal Stability

Differential thermal (DT) and thermal gravimetric analyses (TGA) were conducted to examine the stability of the complexes. For **1** (Figure 5), the first step started at 166 °C and completed at 320 °C, corresponding to the loss of the *N,N*-diethylethane-1,2-diamine ligand and one 1-naphthylacetate ligand. The observed weight loss of 53.8% is close to the calculated value of 54.5%. The second step, from 320 °C to 526 °C, corresponds to the loss of the other 1-naphthylacetate ligand and the formation of the final

product (CuO). The observed weight loss of 32.1% in this step is close to the calculated value of 30.7%. For $2 \cdot 2\text{H}_2\text{O}$ (Figure 6), the first step slowly started at about 50 °C and was completed at 128 °C, corresponding to the loss of the lattice water molecule. The observed weight loss of 1.8% is close to the calculated value of 1.7%. The second step started at about 128 °C and was completed at 350 °C, corresponding to the loss of the propane-1,3-diamine ligand and one 1-naphthylacetate ligand. The observed weight loss of 49.8% is close to the calculated value of 49.2%. The third step, from 350 °C to 575 °C, corresponds to the loss of the other 1-naphthylacetate ligand and the formation of the final product (CuO). The observed weight loss of 33.9% in this step is close to the calculated value of 32.1%.

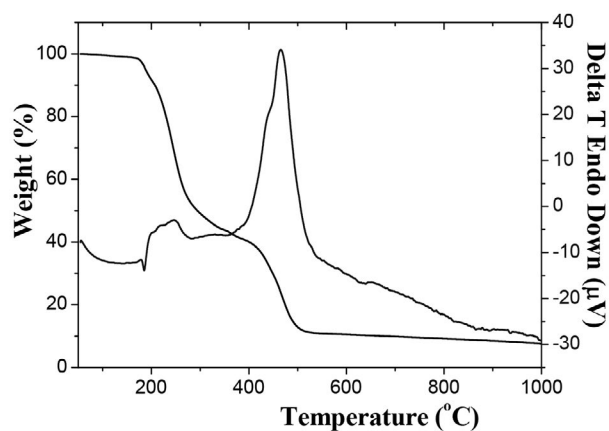


Figure 5. DT-TGA curve of **1**.

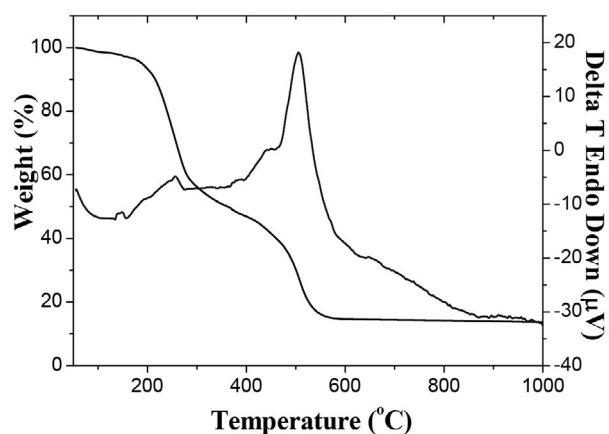


Figure 6. DT-TGA curve of $2 \cdot 2\text{H}_2\text{O}$.

3. 5. Antimicrobial Activity

The antimicrobial activity results are summarized in Table 4. A comparative study of minimum inhibitory concentration (MIC) values of 1-naphthylacetic acid, *N,N*-diethylethane-1,2-diamine, propane-1,3-diamine, and the complexes indicates that the copper complexes have better activity than the free ligands. Generally, this is caused by the greater lipophilic nature of the complexes than the ligand.

Table 4. MIC values ($\mu\text{g mL}^{-1}$) for the antimicrobial activities

Compounds	<i>Staphylococcus aureus</i>	<i>Escherichia coli</i>	<i>Candida albicans</i>
1-naphthylacetic acid	64	128	>512
<i>N,N</i> -diethylethane-1,2-diamine	128	>512	>512
propane-1,3-diamine	128	>512	>512
1	0.5	2.0	32
2 · 2H ₂ O	0.5	2.0	32
Tetracycline	0.32	2.12	>1024

Such increased activity of the metal chelates can be explained on the basis of chelating theory.¹⁴ On chelating, the polarity of the metal atoms will be reduced to a greater extent due to the overlap of the ligand orbital and partial sharing of positive charge of the metal atoms with donor atoms. Further, it increases the delocalization of *p*-electrons over the whole chelate ring and enhances the lipophilicity of the complexes. This increased lipophilicity enhances the penetration of the complexes into lipid membrane and blocks the metal binding sites on enzymes of microorganisms.

From the results, it is obvious that the two complexes have higher antibacterial and antifungal activities against *Staphylococcus aureus*, *Escherichia coli*, and *Candida albicans* when compared to the free ligands. The two complexes have in general the same activities against all the bacteria and fungi strains. The best inhibition on *Staphylococcus aureus* is indicated by the MIC values of $0.5 \mu\text{g mL}^{-1}$, which is similar to tetracycline. The complexes have strong activity against *Escherichia coli*, which is even comparable to tetracycline. It is interesting that both complexes have medium activity against *Candida albicans*, which is rarely seen in metal complexes.

4. Supplementary Material

CCDC-957485 (**1**) and 957486 (**2**·2H₂O) contain the supplementary crystallographic data for this paper. These data can be obtained free of charge at <http://www.ccdc.cam.ac.uk/const/retrieving.html> or from the Cambridge Crystallographic Data Centre (CCDC), 12 Union Road, Cambridge CB2 1EZ, UK; fax: +44(0)1223-336033 or e-mail: deposit@ccdc.cam.ac.uk.

Acknowledgments

This research was supported by the Top-class foundation of Pingdingshan University (no. PXY-BSQD-2018006 and PXY-PYJJ-2018002).

5. References

- (a) M. Das, S. R. Chaudhuri, D. Basak, S. Dasgupta, D. Ray, *Inorg. Chim. Acta* **2019**, 485, 140–154; DOI:10.1016/j.ica.2018.10.018
- (b) E. Echenique-Errandonea, A. Zabala-Lekuona, J. Cepeda, A. Rodriguez-Diequez, J. M. Seco, I. Oyarzabal, E. Colacio, *Dalton Trans.* **2019**, 48, 190–201; DOI:10.1039/C8DT03800G
- (c) I. Galadzhan, R. Kulmaczewski, O. Cespedes, M. Yamada, N. Yoshinori, T. Konno, M. A. Halcrow, *Inorg. Chem.* **2018**, 57, 13761–13771. DOI:10.1021/acs.inorgchem.8b02289
- (a) M. Simunkova, P. Lauro, K. Jomova, L. Hudcova, M. Danko, S. Alwasel, I. M. Alhazza, S. Rajcaniova, Z. Kozovska, L. Kucerova, J. Moncol, L. Svorc, M. Valko, *J. Inorg. Biochem.* **2019**, 194, 97–113; DOI:10.1016/j.jinorgbio.2019.02.010
- (b) S. Bharti, M. Choudhary, B. Mohan, *J. Coord. Chem.* **2018**, 71, 284–310; DOI:10.1080/00958972.2018.1424839
- (c) Y.-F. Kang, X. Q. Liang, X. Wang, T. T. Si, Y. T. Chen, J. H. Zhang, J. Zhao, *Inorg. Chem. Commun.* **2017**, 86, 218–222; DOI:10.1016/j.inoche.2017.10.028
- (d) J. Joseph, G. B. Janaki, K. Nagashri, R. S. Joseyphus, *J. Coord. Chem.* **2017**, 70, 242–260. DOI:10.1080/00958972.2016.1250153
- (a) M. Iqbal, S. Ali, M. N. Tahir, *J. Coord. Chem.* **2018**, 71, 991–1002; DOI:10.1080/00958972.2018.1456655
- (b) Y.-J. Sun, P. Li, Q.-Q. Huang, J.-J. Zhang, S. B. Itoh, *Eur. J. Inorg. Chem.* **2017**, 13, 1845–1854; DOI:10.1002/ejic.201601371
- (c) A. Solanki, M. H. Sadhu, S. Patel, R. Devkar, S. B. Kumar, *Polyhedron* **2015**, 102, 267–275; DOI:10.1016/j.poly.2015.09.012
- (d) R. N. Patel, D. K. Patel, K. K. Shukla, Y. Singh, *J. Coord. Chem.* **2013**, 66, 4131–4143; DOI:10.1080/00958972.2013.862790
- (e) Y.-J. Ren, J.-L. Zhu, L.-X. Zhang, Y.-X. Xu, S.-S. Qian, *Acta Chim. Slov.* **2017**, 64, 825–831;
- (f) A. Mushtaq, S. Ali, M. N. Tahir, H. Ismail, B. Mirza, M. Saadiq, M. A. Haleem, M. Iqbal, *Acta Chim. Slov.* **2017**, 64, 397–408. DOI:10.17344/acsi.2017.3250
- P. B. Sreeja, M. R. P. Kurup, A. Kishore, C. Jasmin, *Polyhedron* **2004**, 23, 575–581. DOI:10.1016/j.poly.2003.11.005
- (a) N. Martini, J. E. Parente, M. E. Toledo, G. E. Escudero, C. H. Laino, J. J. M. Medina, G. A. Echeverria, O. E. Piro, L. Lezama, P. A. M. Williams, E. G. Ferrer, *J. Inorg. Biochem.* **2017**, 174, 76–89; DOI:10.1016/j.jinorgbio.2017.05.012
- (b) E. Ferrari, R. Benassi, M. Saladini, G. Orteca, Z. Gazova, K. Siposova, *Chem. Biol. Drug Des.* **2017**, 89, 411–419; DOI:10.1111/cbdd.12847
- (c) J. Joseph, K. Nagashri, G. B. Janaki, *Eur. J. Med. Chem.* **2012**, 49, 151–163; DOI:10.1016/j.ejmech.2012.01.006

- (d) Y.-L. Sang, X.-S. Lin, *Acta Chim. Slov.* **2019**, *66*, 168–172.
6. Bruker, SMART and SAINT. Bruker AXS Inc., Madison, Wisconsin, USA, 2002.
7. G.M. Sheldrick, SADABS. Program for Empirical Absorption Correction of Area Detector, University of Göttingen, Germany, 1996.
8. G. M. Sheldrick, SHELXTL V5.1 Software Reference Manual, Bruker AXS, Inc., Madison, Wisconsin, USA, 1997.
9. A. Barry, *Procedures and Theoretical Considerations for Testing Antimicrobial Agents in Agar Media*, In: *Antibiotics in Laboratory Medicine*, Lorian, V. (Ed.), Baltimore: Williams and Wilkins, 1991.
10. (a) F.-J. Yin, G. Yu, H. Zhao, D.-S. Bai, *Acta Crystallogr.* **2012**, *E68*, m350; (b) R. E. Marsh, *Acta Crystallogr.* **2005**, *B61*, 359; (c) H.-T. Xia, Y.-F. Liu, S.-A. Li, *Acta Crystallogr.* **2006**, *E62*, m2653; (d) F.-J. Yin, H. Zhao, X.-Y. Xu, X.-J. Yang, *Chin. J. Inorg. Chem.* **2012**, *28*, 1700–1704; (e) Y.-Q. Jiang, X.-F. Yu, *Chin. J. Struct. Chem.* **1992**, *11*, 261–265.
11. (a) F.-J. Yin, L.-J. Han, S.-P. Yang, X.-Y. Xu, Y. Gu, *Acta Crystallogr.* **2011**, *E67*, m1821; (b) F.-J. Yin, L.-J. Han, S.-P. Yang, X.-Y. Xu, *Acta Crystallogr.* **2011**, *E67*, m1772.
12. S. Manna, E. Zangrando, H. Puschmann, S. C. Manna, *Polyhedron* **2019**, *162*, 285–292.
DOI:10.1016/j.poly.2019.01.057
13. (a) D.-Y. Ma, *Inorg. Chim. Acta* **2012**, *392*, 440–445;
DOI:10.1016/j.ica.2012.05.023
(b) R. Carballo, A. Castineiras, S. Balboa, B. Covelo, J. Niclos, *Polyhedron* **2002**, *21*, 2811–2818.
DOI:10.1016/S0277-5387(02)01289-5
14. J. W. Searl, R. C. Smith, S. Wyard, *J. Proc. Phys. Soc.* **1961**, *78*, 1174–1181. DOI:10.1088/0370-1328/78/6/311

Povzetek

Sintetizirali in okarakterizirali smo dva nova bakrova(II) kompleksa, $[\text{CuL}_2(\text{EA})]$ (**1**) in $[\text{Cu}_2\text{L}_4(\text{PA})_2] \cdot 2\text{H}_2\text{O}$ (**2** · 2H₂O), kjer je L 1-naftilacetat, EA je *N,N*-dietiletan-1,2-diamin in PA je propan-1,3-diamin. Strukturi kompleksov smo določili z rentgensko monokristalno analizo. Kompleks **1** je enojedrna bakrova(II) spojina z Cu atomom koordiniranim s kvadratno planarno geometrijo. Kompleks **2** · 2H₂O je centrosimetrična dvojejrna bakrova(II) spojina z Cu atomom koordiniranim s kvadratno piramidalno geometrijo. Kristalna struktura je stabilizirana z vodikovimi vezmi. Antimikrobne aktivnosti obeh spojin smo testirali na *Staphylococcus aureus*, *Escherichia coli* in *Candida albicans*. Proučili smo tudi termične lastnosti spojin.



Except when otherwise noted, articles in this journal are published under the terms and conditions of the Creative Commons Attribution 4.0 International License

Scientific paper

Photo-Oxidation Coupled Kabachnik–Fields and Biginelli Reactions for Direct Conversion of Benzyl alcohols to α -Aminophosphonates and Dihydropyrimidones

Gazunfor Ali,¹ Nisar A. Dangroo,^{1,2,*} Shabnam Raheem,² Tahira Naqvi,³ Tabassum Ara¹ and Masood Ahmad Rizvi^{2,*}

¹ Department of Chemistry, National Institute of Technology, Srinagar 190006, India

² Department of Chemistry, University of Kashmir, Srinagar 190006, India.

³ Department of Chemistry, Government Degree College for Women M. A. Road, Srinagar, J&K, India.

* Corresponding author: E-mail: nisar@nitsri.net, masoodku2@gmail.com

Received: 06-21-2019

Abstract

A tandem one-pot solvent free approach for the direct conversion of benzyl alcohols to α -amino phosphonates and dihydropyrimidones is reported. The method relies on a metal free photo-oxidation of benzyl alcohols to benzaldehydes under UV irradiation using ammonium perchlorate followed by Kabachnik–Fields and Biginelli reactions. The reaction conditions are moderate and metal free with good substrate scope. The control experiments were performed to investigate the role of the ammonium perchlorate and molecular oxygen as oxidants. The quenching experiments in the presence of TEMPO and other radical quenchers suggest radical based mechanism.

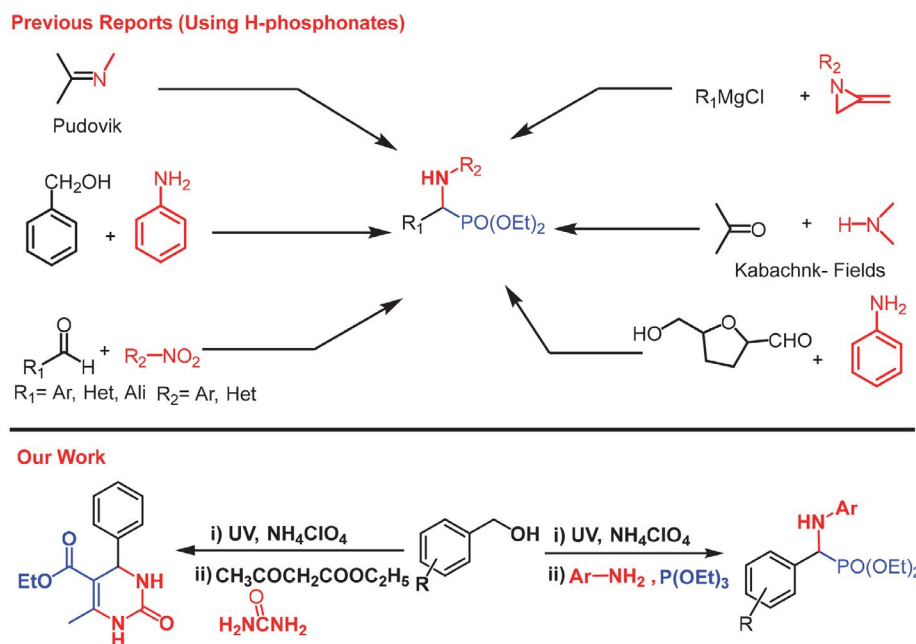
Keywords: One-pot synthesis; photo-oxidation; benzyl alcohol; kabachnik–Fields reaction; biginelli reaction.

1. Introduction

The α -aminophosphonates are core structural components of many pharmacologically active molecules exhibiting diverse range of biological activities such as anti-cancer, HIV protease inhibitors, and serve as surrogates of α -amino acids.^{1–3} The Pudovik reaction⁴ and Kabachnik–Fields reactions⁵ involving nucleophilic addition of phosphite to imines are the most widely used methods for the synthesis of α -aminophosphonates. The aminophosphonates can also be synthesised *via* acid-catalyzed (Lewis/Brønsted),^{6,7} catalyst-free,⁸ microwave assisted⁹ condensation of H-phosphonates with aldehydes or imines. Furthermore, synthesis of α -aminophosphonates has also been achieved from substrates other than aldehydes using methylene aziridines,¹⁰ dehydrogenative α -phosphonation of substituted *N,N*-dialkylanilines,¹¹ reduction of aryl nitro compounds,¹² reductive phosphination of amides,¹³ and biomass-derived hydroxyl methyl furfural.¹⁴ As such, we were particularly intrigued to explore the feasibility of

ubiquitously available benzyl alcohols as substrates for the synthesis of α -aminophosphonates. To the best of our knowledge only report employing the use of benzyl alcohol has been carried out with an expensive gold supported catalyst.¹⁵ Moreover, we wanted to examine if the benzyl alcohol could also serve as a surrogate of benzaldehydes for related reactions like Biginelli reaction leading to the formation of 1,4-dihydropyrimidones. Notably, 1,4-dihydropyrimidones are also a well known class of biologically active compounds with a range of therapeutic properties.¹⁶ The traditional synthesis of dihydropyrimidones involves use of an aldehyde, a β -keto ester or β -diketone, and urea,¹⁷ with most of the advances involving use of a Brønsted acid¹⁸ or base,¹⁹ metal based Lewis acids,²⁰ organocatalysts,²¹ and heterogeneous catalysts.^{22–25}

In this regard, photochemical reactions are undoubtedly greener alternatives to thermal processes, shifting the synthetic path of reaction from its solvo-thermal form to a neat and photochemical form; this has become a major step towards ecofriendly synthetic methodologies. The ap-



Scheme 1. General synthetic pathways and reactions described in this work

lications of photocatalysis have increased significantly in recent times and development of light mediated reactions as sustainable synthetic methodologies is becoming more popular.^{26,27} Besides the intrinsic eco-friendly nature, photochemical reactions are also interesting for introduction of newer reactivities as photon as reagent can interact directly at molecular level and often enables the reactions to take place from excited states unlike the conventional reagents. Thus, in continuation of our work on development of new synthetic methodologies,^{28–30} including photoredox reactions,^{31–33} herein we report a one-pot tandem approach involving oxidation of benzyl alcohols to benzaldehydes under UV-visible light irradiation in the presence of ammonium perchlorate as photocatalyst followed by Kabachnik–Fields and Biginelli reactions for the synthesis of α -aminophosphonates and dihydropyrimidones, respectively (Scheme 1). The reaction besides being photo-catalytic was carried out under neat conditions with a simple work up involving re-crystallization as the product purification step.

2. Experimental

All reactions were carried out in oven-dried glassware. The solvents used were purified by distillation. ¹H and ¹³C NMR spectra were recorded on FT-NMR 500 and 400 MHz instruments. Chemical data for protons are reported in parts per million (ppm, δ scale) downfield from tetramethylsilane and are referenced to the residual proton in the NMR solvent (CDCl₃, 7.26 ppm). Carbon nuclear magnetic resonance spectra (¹³C NMR) were recorded at 125 MHz or 100 MHz: chemical data for carbons are re-

ported in parts per million (ppm, δ scale) downfield from tetramethylsilane and are referenced to the carbon resonance of the solvent. Coupling constants (*J*) are quoted in Hz. Mass spectra were recorded on electron ionization and electrospray ionization (ESI) modes.

2. 1. General Procedure for the Synthesis of α -Aminophosphonates

An equimolar mixture of benzyl alcohol (100 μ L, 1.0 mmol) and ammonium perchlorate (107.6 mg, 1.0 mmol) were taken in oven dried round bottom flask under neat conditions. The reaction mixture was subjected to UV irradiation till complete conversion for benzyl alcohol to benzaldehyde, which was monitored by TLC. Afterwards the UV irradiation was stopped, and to the reaction mixture was added *meta*-bromoaniline (158 μ L, 1.0 mmol) and triethylphosphite (168 μ L, 1.1 mmol). The resulting reaction mixture was stirred at 50 °C on the magnetic stirrer till the completion (monitored by TLC). Upon completion, to the crude reaction mixture was added ice cold water to precipitate the product which was finally recrystallized from ethanol to furnish the desired products **4a–k**. The spectral data for some representative compounds are shown below. The data of the known compounds matches with that of the literature reports³⁴ (please see supporting information for list of known compounds and their references).

Diethyl (((3-Bromophenyl)amino)(phenyl)methyl)phosphonate (**4a**)

Following the general procedure the reaction was carried out by taking benzyl alcohol (100 μ L, 1.0 mmol), ammonium perchlorate (107.6 mg, 1.0 mmol), 3-bro-

moaniline (158 μL , 1.0 mmol) and triethylphosphite (168 μL , 1.1 mmol) to obtain white crystalline compound **4a**^{34g} (342 mg, 93% yield). ¹H NMR (400 MHz, CDCl_3) δ 7.53 (d, $J = 4.8$ Hz, 2H), 7.40–7.31 (m, 3H), 6.96 (t, $J = 8$ Hz, 1H), 6.88–6.81 (m, 2H), 6.56 (d, $J = 4.8$ Hz, 1H), 4.76 (d, $J = 4$ Hz, 1H), 3.99 (m, 4H), 1.34 (t, $J = 8.0$ Hz, 3H), 1.15 (t, $J = 8.0$ Hz, 3H); ¹³C NMR (100 MHz, CDCl_3) δ 170.0, 148.1 (2CH), 135.4, 133.3, 130.6 (2CH), 128.9 (2C), 116.8, 64.0, 55.3, 16.4; EIMS m/z for $\text{C}_{17}\text{H}_{21}\text{BrNO}_3\text{P}$ $[\text{M}+\text{H}]^+$ 397.19.

Diethyl ((3-Bromophenyl)((4-hydroxyphenyl)amino)methyl)phosphonate (4b)

Following the general procedure the reaction was carried out by taking 3-bromobenzyl alcohol (100 μL , 1.0 mmol), ammonium perchlorate (62.5 mg, 1.0 mmol), 4-aminophenol (58 μL , 1.0 mmol) and triethylphosphite (97 μL , 1.1 mmol) to obtain white crystalline compound **4b**^{34b} (201 mg, 91% yield). M.p. 152–155 $^\circ\text{C}$; ¹H NMR (400 MHz, CDCl_3) δ 7.70 (s, 1H), 7.64 (s, 1H), 7.43 (d, $J = 4.0$ Hz, 2H), 7.25 (m, 2H), 6.70 (d, $J = 8$ Hz, 2H), 6.50 (d, $J = 12$ Hz, 2H), 4.70 (m, 1H), 4.18 (m, 4H), 1.34 (t, $J = 8.0$ Hz, 3H), 1.21 (t, $J = 8.0$ Hz, 3H); ¹³C NMR (100 MHz, CDCl_3) δ 149.8 (2CH), 139.5, 138.8, 131.3 (2C), 138.8, 122.9 (2CH), 116.4, 115.8 (2C), 64.1, 56.1, 16.6; EIMS m/z for $\text{C}_{17}\text{H}_{21}\text{BrNO}_3\text{P}$ $[\text{M}+\text{H}]^+$ 414.36.

Diethyl ((3-Bromophenyl)((2-iodophenyl)amino)methyl)phosphonate (4c)

Following the general procedure the reaction was carried out by taking 3-bromobenzyl alcohol (100 μL , 1.0 mmol), ammonium perchlorate (62.5 mg, 1.0 mmol), 3-iodoaniline (116 μL , 1.0 mmol) and triethylphosphite (97 μL , 1.1 mmol) to obtain compound **4c**^{34f} (203 mg, 73% yield). M.p. 145–148 $^\circ\text{C}$; ¹H NMR (400 MHz, CDCl_3) δ 7.72 (d, $J = 8.0$ Hz, 1H), 7.65 (s, 1H), 7.45 (m, 2H), 7.29 (m, 1H), 7.12 (m, 1H), 6.50 (m, 1H), 5.35 (s, NH), 4.75 (m, 1H), 4.12–3.92 (m, 4H), 1.35 (t, $J = 8.0$ Hz, 3H), 1.28 (t, $J = 8.0$ Hz, 3H). ¹³C NMR (100 MHz, CDCl_3) δ 145.7 (2CH), 139.4, 138.1 (2CH), 131.5, 130.5 (2CH), 129.6, 126.5, 123.0, 112.2, 86.4, 64.0, 57.1, 16.6; EIMS m/z for $\text{C}_{17}\text{H}_{20}\text{BrINO}_3\text{P}$ $[\text{M}+\text{H}]^+$ 523.09.

Diethyl (((2-Fluorophenyl)amino)(3-nitrophenyl)methyl)phosphonate (4d)

Following the general procedure the reaction was carried out by taking 3-nitrobenzyl alcohol (100 μL , 1.0 mmol), ammonium perchlorate (76.4 mg, 1.0 mmol), 2-fluoroaniline (72.15 μL , 1.0 mmol) and triethylphosphite (118 μL , 1.1 mmol) to obtain compound **4d**³⁴ⁱ (217 mg, 87% yield). M.p. 185–187 $^\circ\text{C}$; ¹H NMR (400 MHz, CDCl_3) δ 8.89 (s, 1H), 8.21 (d, $J = 8$ Hz, 1H), 7.90 (d, $J = 8$ Hz, 1H), 7.59 (m, 1H), 7.05 (m, 1H), 6.90 (m, 1H), 6.73 (m, 1H), 6.45 (m, 1H), 5.05 (s, NH), 4.96–4.86

(m, 1H), 4.09–3.96 (m, 4H), 1.34 (t, $J = 4.0$ Hz, 3H), 1.26 (t, $J = 8.0$ Hz, 3H); ¹³C NMR (100 MHz, CDCl_3) δ 153.0, 151.1, 148.6, 138.6, 133.8, 129.9, 124.7, 122.9 (2C), 118.9, 115.1, 113.5, 64.1, 56.3, 16.4; EIMS m/z for $\text{C}_{17}\text{H}_{20}\text{FN}_2\text{O}_5\text{P}$ $[\text{M}+\text{H}]^+$ 383.16.

Diethyl (((4-Fluorophenyl)amino)(3-nitrophenyl)methyl)phosphonate (4e)

Following the general procedure the reaction was carried out by taking 3-nitrobenzyl alcohol (100 μL , 1.0 mmol), ammonium perchlorate (76.4 mg, 1.0 mmol), 4-fluoroaniline (72.15 μL , 1.0 mmol) and triethylphosphite (118 μL , 1.1 mmol) to obtain compound **4e**^{34a} (224 mg, 90% yield). M.p. 179–181 $^\circ\text{C}$; ¹H NMR (400 MHz, CDCl_3) δ 8.34 (s, 1H), 8.13 (d, $J = 8$ Hz, 1H), 7.82 (d, $J = 8$ Hz, 1H), 7.50 (d, $J = 8$ Hz, 1H), 6.77 (d, $J = 8.0$ Hz, 2H), 6.50 (d, $J = 8.4$ Hz, 2H), 4.99 (s, NH), 4.83 (m, 1H), 4.15–3.91 (m, 4H), 1.29 (t, $J = 8.0$ Hz, 3H), 1.17 (t, $J = 8.0$ Hz, 3H); ¹³C NMR (100 MHz, CDCl_3) δ 157.7, 155.8, 148.7, 142.2 (2CH), 138.9, 134.0 (2CH), 129.8, 123.0, 116.0, 115.1, 64.0, 55.9, 16.5; EIMS m/z for $\text{C}_{17}\text{H}_{20}\text{FN}_2\text{O}_5\text{P}$ $[\text{M}+\text{H}]^+$ 383.31.

Diethyl ((3-Hydroxyphenyl)((3-nitrophenyl)amino)methyl)phosphonate (4f)

Following the general procedure the reaction was carried out by taking 3-hydroxybenzyl alcohol (100 μL , 1.0 mmol), ammonium perchlorate (94.3 mg, 1.0 mmol), 3-nitroaniline (110 mg, 1.0 mmol) and triethylphosphite (133 μL , 1.1 mmol) to obtain compound **4f** (278 mg, 91% yield). M.p. 165–167 $^\circ\text{C}$; ¹H NMR (400 MHz, CDCl_3) δ 7.49 (m, 1H), 7.40 (m, 1H), 7.26 (s, 1H), 7.19 (s, 1H), 6.96 (d, $J = 8$ Hz, 2H), 6.83 (m, 2H), 5.30 (m, NH), 4.78 (m, 1H), 3.96 (m, 4H), 1.28 (t, $J = 8.0$ Hz, 3H), 1.08 (t, $J = 8.0$ Hz, 3H); ¹³C NMR (100 MHz, CDCl_3) δ 157.1, 156.7, 149.1, 147.2 (2CH), 143.0, 135.9, 130.2, 129.7, 120.2 (2CH), 115.1, 108.0, 64.3, 56.3, 16.3; EIMS m/z for $\text{C}_{17}\text{H}_{20}\text{FN}_2\text{O}_5\text{P}$ $[\text{M}+\text{H}]^+$ 381.10.

Diethyl (((4-Bromophenyl)amino)(4-nitrophenyl)methyl)phosphonate (4k)

Following the general procedure the reaction was carried out by taking 4-nitrobenzyl alcohol (100 μL , 1.0 mmol), ammonium perchlorate (76.4 mg, 1.0 mmol), 4-bromoaniline (112 μL , 1.0 mmol) and triethylphosphite (118 μL , 1.1 mmol) to obtain compound **4k**^{34c} (239 mg, 83% yield). M.p. 182–183 $^\circ\text{C}$; ¹H NMR (400 MHz, CDCl_3) δ 8.18 (d, $J = 8$ Hz, 2H), 7.64 (d, $J = 8$ Hz, 2H), 7.16 (d, $J = 8$ Hz, 2H), 6.41 (d, $J = 8$ Hz, 2H), 5.0 (m, NH), 4.83 (dd, $J = 8.4$ Hz, 1H), 4.17–3.85 (m, 4H), 1.30 (t, $J = 7.0$ Hz, 3H), 1.17 (t, $J = 7.0$ Hz, 3H); ¹³C NMR (100 MHz, CDCl_3) δ 147.7, 144.8 (2CH), 143.6, 132.1, 128.6 (2CH), 123.8, 115.4, 110.9, 63.8, 56.7, 16.4; EIMS m/z for $\text{C}_{17}\text{H}_{20}\text{BrN}_2\text{O}_5\text{P}$ $[\text{M}+\text{H}]^+$ 442.02.

2. 2. General Procedure for the Synthesis of 1, 4-Dihydropyrimidones

An equimolar mixture of benzyl alcohol (100 μ L, 1.0 mmol) and ammonium perchlorate (107.6 mg, 1.0 mmol) were taken in oven dried round bottom flask under neat conditions. The reaction mixture was subjected to UV irradiation till complete conversion of benzyl alcohol to benzaldehyde, which was monitored by TLC. Afterwards the UV light was stopped, and to the reaction mixture was added urea (55.2 mg, 1.0 mmol) and ethyl acetoacetate (143.5 μ L, 1.2 mmol). The resulting reaction mixture was stirred at 80 °C on the magnetic stirrer till the completion of the reaction (monitored by TLC). Upon completion, to the crude reaction mixture was added ice cold water to precipitate the product which was finally recrystallized from ethanol to furnish the desired products in pure form. The spectral data for some representative compounds are shown below. The data of the known compounds matches with that of the literature reports³⁵ (please see supporting information for list of known compounds and their references).

Ethyl 2-Methyl-6-oxo-4-phenyl-1,4,5,6-tetrahydropyridine-3-carboxylate (5a)

Following the general procedure the reaction was carried out by taking benzyl alcohol (100 μ L, 1.0 mmol), ammonium perchlorate (107.6 mg, 1.0 mmol), urea (55.2 mg, 1.0 mmol) and ethyl acetoacetate (143.5 μ L, 1.2 mmol) to obtain white crystalline compound **5a**^{35a} (171 mg, 71% yield). M.p. 204–206 °C. ¹H NMR (400 MHz, CDCl₃) δ 7.28 (s, 1H), 5.28 (d, J = 8 Hz, 2H), 4.03 (d, J = 8 Hz, 2H), 3.37 (s, 1H), 2.15 (m, 2H), 1.13 (q, J = 6.8 Hz, 3H); ¹³C NMR (100 MHz, CDCl₃) δ 165.3, 152.1, 148.3, 144.8, 128.3 (2CH), 127.2 (2CH), 126.2, 99.2, 59.1, 53.9, 17.7, 14.0; EIMS m/z for C₁₄H₁₆N₂O₃ [M+H]⁺ 261.15.

Ethyl 4-(4-Hydroxyphenyl)-2-methyl-6-oxo-1,4,5,6-tetrahydropyridine-3-carboxylate (5c)

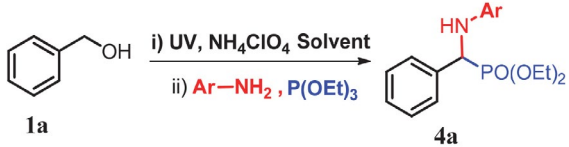
Following the general procedure the reaction was carried out by taking 4-hydroxybenzyl alcohol (100 μ L, 1.0 mmol), ammonium perchlorate (93.6 mg, 1.0 mmol), urea (48 mg, 1.0 mmol) and ethyl acetoacetate (125 μ L, 1.2 mmol) to obtain compound **5c**^{35a} (140 mg, 63% yield). M.p. 197–199 °C; ¹H NMR (400 MHz, CDCl₃) δ 7.14 (d, J = 8 Hz, 2H), 6.75 (d, J = 8 Hz, 2H), 5.28 (s, 1H), 4.06 (m, 2H), 2.34 (s, 3H), 1.18 (q, J = 6.8 Hz, 3H); ¹³C NMR (100 MHz, CDCl₃) δ 165.3, 156.4, 152.1, 147.7, 135.3, 127.3 (2CH), 114.9 (2CH), 99.6, 59.0, 53.3, 17.7, 14.0; EIMS m/z for C₁₄H₁₈N₂O₄ [M+H]⁺ 277.11.

3. Result and Discussion

To begin with we evaluated the possibility of benzaldehyde formation from benzyl alcohols under visible light

(7W blue LED). The reaction of benzyl alcohol (1 equiv) in DMSO in the presence of NH₄ClO₄ (1 equiv) under visible light produced very low yield of product **4a**, due to incomplete conversion of benzyl alcohol **1a** to benzaldehyde (Table 1, entry 6). No substantial enhancement in the percentage yield of the product produced was observed even after employing longer reaction time using (7 W blue LED) illumination (Table 1, entry 7). Interestingly, the same reaction under UV irradiation resulted in the complete oxidation of benzyl alcohol within 3 h which upon addition of *meta*-bromoaniline and triethylphosphite produced α -aminophosphonate **4a** in 89% yields within 4.5 h (Table 1, entry 5). We also evaluated solvents such as acetonitrile (ACN), dichloromethane (DCM), methanol (MeOH) and water. However, these solvents suppressed the reaction yield due to incomplete substrate conversion (Table 1, entries 1–4). Further, water proved to be a poor medium with only 45% yield of product. However, the reaction under neat (solvent free) conditions resulted in complete conversion of **1a** to benzaldehyde within a relatively short time of 2.5 h. The *in situ* generated aldehyde then reacts with *meta* bromoaniline and triethylphosphite (Kabachnik–Fields reaction) furnishing **4a** with 93% yield in a total reaction time of 4 h (Table 1, entry 8). The crude product was purified by simple aqueous recrystallization and hence avoiding the usage of harmful solvents and laborious work up. It was observed that UV irradiation was only important for the oxidation of benzyl alcohol to benzaldehyde in the presence of ammonium perchlorate, the second step involved stirring the reaction mixture at 50 °C

Table 1. Optimization of reaction conditions for the synthesis of α -aminophosphonates

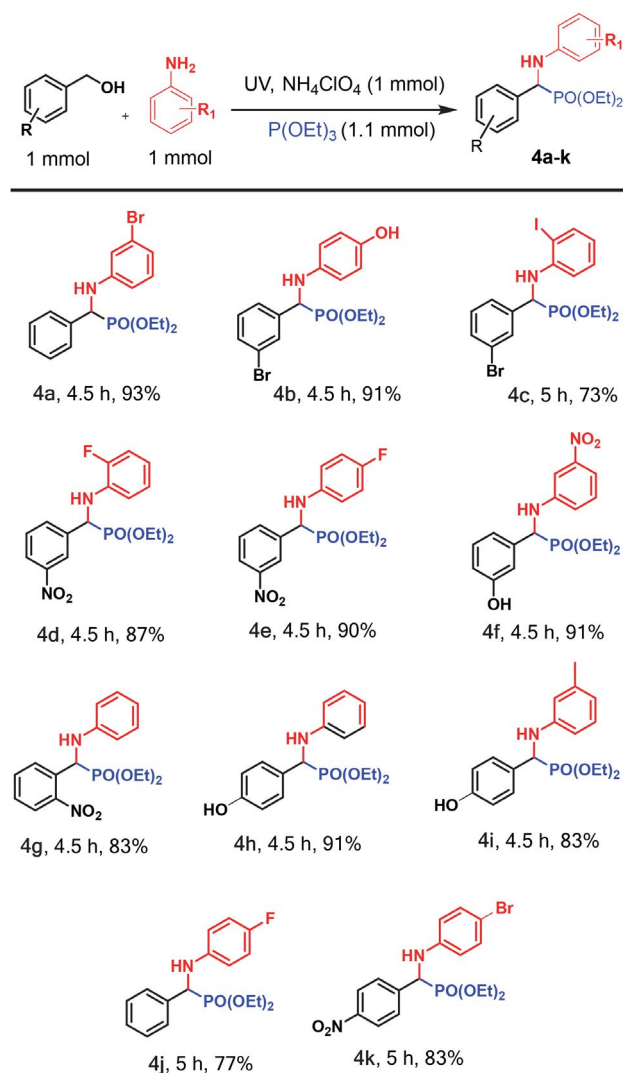


Entry	NH ₄ ClO ₄	Solvent	Yield (%) (4a) ^a	Time (h)
1	1.0 mmol	ACN	73	4.5
2	1.0 mmol	DCM	67	4.5
3	1.0 mmol	MeOH	59	4.5
4	1.0 mmol	Water	41	4.5
5	1.0 mmol	DMSO	89	4.5
6	1.0 mmol	DMSO	13	9 ^c
7	1.0 mmol	DMSO	15	24 ^c
8	1.0 mmol	Neat	93	4
9	0.8 mmol	Neat	67	4.5
10	0.5 mmol	Neat	23	5
11	0.2 mmol	Neat	10	5

^a All the reactions were carried out using 1.0 mmol of benzyl alcohol, 1.0 mmol of *meta*-bromoaniline and 1.1 mmol triethylphosphite. The first step (oxidation) was conducted under UV irradiation followed by Kabachnik–Fields reaction; ^b Isolated yield; ^c The first step (oxidation) was conducted under visible light.

over magnetic stirrer. Decreasing the NH_4ClO_4 loading resulted in attenuation in the conversion rate and the percentage yield of the reaction (Table 1, entries 9–11). In the absence of NH_4ClO_4 only traces of conversion to benzaldehyde were detected. Furthermore, in none of the experimental conditions of these reactions the formation of over-oxidized product (benzoic acid) was observed. In this synthetic methodology, the sequence of reagent addition was also found to be very important. When all the reactants were mixed at once, unnecessary longer reaction time, lower yields and complex mixture of side products were observed. The best synthetic results were obtained when the reaction was performed in a tandem one pot manner using 1.0 equiv NH_4ClO_4 under neat (solvent free) conditions.

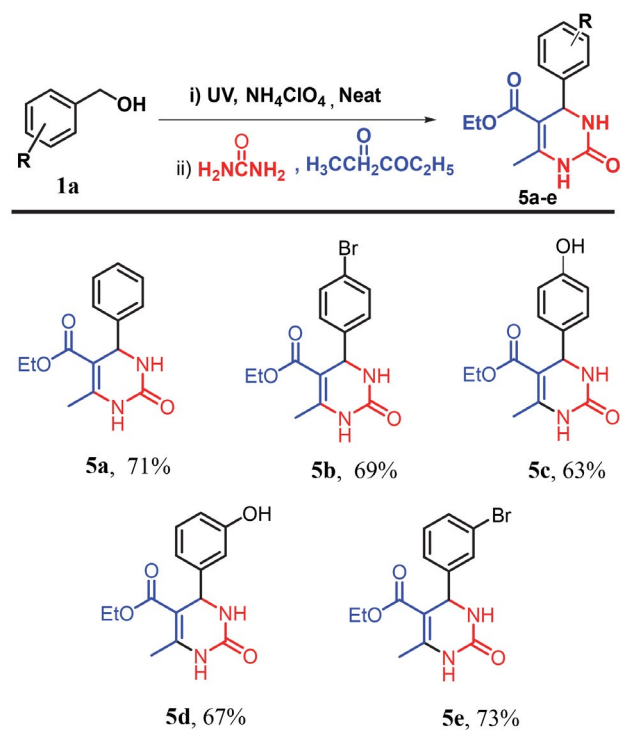
To establish the substrate scope of the developed one-pot three component protocol for the synthesis of α -aminophosphonates, a variety of benzyl alcohols and anilines were evaluated and the results are summarized in



Scheme 2. Substrate scope for one-pot synthesis of α -aminophosphonates from benzyl alcohols

Scheme 2. In all cases reaction proceeded smoothly and furnished the corresponding products **4a-k** in excellent yields. Unsubstituted benzyl alcohols reacted smoothly with good percentage yields (Scheme 2, **4a** and **4j**). Irrespective of the nature of the substituent, whether electron-donating or electron-withdrawing at *para* position (nitro, fluoro, bromo or hydroxyl) on the benzyl alcohols or anilines, the corresponding α -aminophosphonates (**4b**, **4d**, **4e**, **4g**, **4h**) were obtained in good to excellent yields (83–90%). Similar trend was observed in the case of *meta*-substituted anilines, expected to exhibit low electronic impact on their reactivity furnishing a yield of 91% for **4f** and 83% for **4i**. The *ortho*-substituted anilines needed slightly more reaction time even though their yield was comparable to that of *para*- and *meta*-substituted anilines indicating that the substitution on phenyl ring of aniline has not a very significant impact on the reaction, except in the case of *ortho*-iodoaniline producing **4c** with the yield of 73%. Correlating the observed trends in the percentage yields with the structural diversity of the reactants suggested that the synthetic methodology has a wider substrate scope and very little sensitivity towards electronic effects of reactants or their intrinsic reactivities.

Further to expand the applicability of our synthetic methodology, we investigated the synthesis of 1,4-dihydropyrimidones. To our delight, the treatment of benzyl alcohols with urea and ethyl acetoacetate under the previously optimized reaction conditions produced the desired 1,4-dihydropyrimidone products in good yields. The results are summarized in Scheme 3. Benzyl alcohol as well



Scheme 3. One pot synthesis of dihydropyrimidones from benzyl alcohols.

Table 2. Control and quenching experiments for the oxidation of benzyl alcohol to benzaldehyde^a

Entry	Controlled parameter	Comments	Yield (%)
1	Optimum conditions	-	95
2	N ₂ atmosphere	-	Traces
3	No UV light	-	0
4	No NH ₄ ClO ₄	-	0
5	TEMPO (1eq)	radical scavenger	13
6	<i>tert</i> -Butanol (1eq)	hydroxide radical scavenger	91
7	NaN ₃ (1eq)	singlet oxygen scavenger	17
8	Benzoquinone (1eq)	superoxide radical anion scavenger	11
9	TEMPO (1eq)	radical scavenger	13

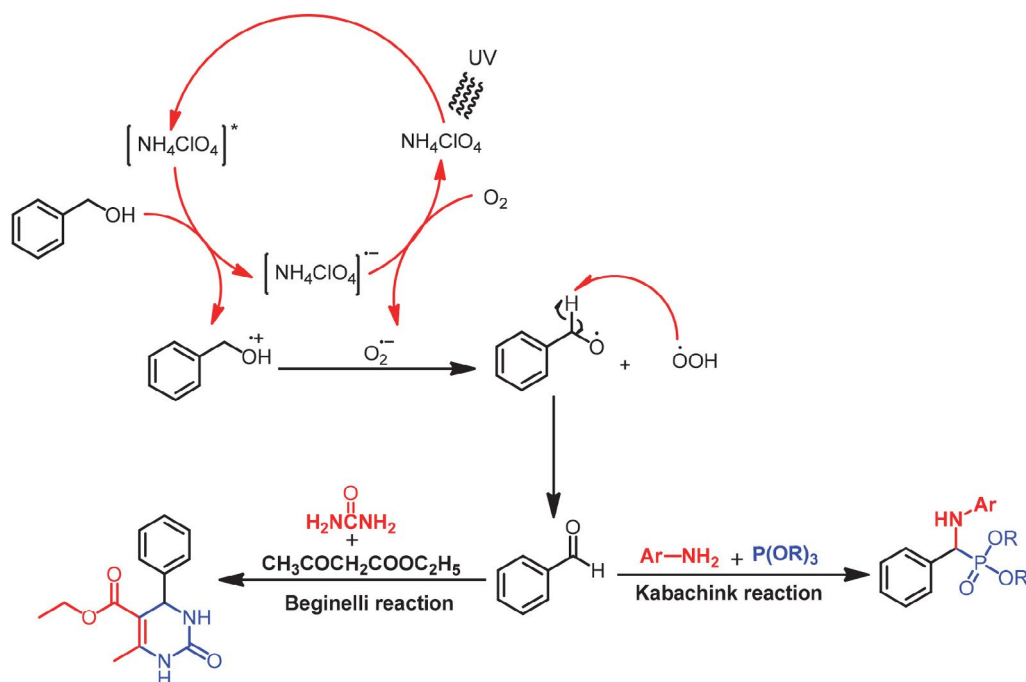
as its substituted derivatives reacted smoothly to furnish the corresponding products in excellent yields **5a–e**.

Having established synthetic scheme for direct conversion of benzyl alcohol to α -aminophosphonates and dihydropyrimidones, we became curious to explore the role of NH₄ClO₄ and the light source on the oxidation of benzyl alcohols. To arrive at mechanistic insight into the photo-oxidation step of benzyl alcohol to benzaldehyde we performed some controlled experiments summarized in Table 2. Under optimized reaction conditions 95% yield of benzaldehyde was achieved. No reaction was observed in the absence of UV light or NH₄ClO₄ (Table 2, entries 3–4). Moreover, only traces of products were formed under N₂ atmosphere, which clearly indicated the significant role of O₂.

The dependence of synthetic reaction on UV light and molecular oxygen was indicative of a possible radical path for the reaction. To explore the radical path, the effect of different quenchers on reaction progress was measured.³⁶ The observed results are summarized in Table 2

(entries 5–9). When (2,2,6,6-tetramethylpiperidin-1-yl)oxyl (TEMPO) was used as a radical scavenger, only 13% benzaldehyde product was formed suggesting that the reaction pathway involved is actually the radical pathway. The use of *tert*-butanol as a hydroxide radical scavenger had no influence on the reaction yield inferring no involvement of the hydroxide radical in the reaction. Use of sodium azide as quencher showed the lowering in the reaction yield highlighting the involvement of singlet oxygen radical in the reaction system. Similarly using the benzoquinone as superoxide radical anion scavenger also lowered the reaction yield significantly suggesting the involvement of superoxide radical participation in the reaction mechanism.

Based on the observations of control experiments, a plausible mechanism as shown in Scheme 4 was proposed. According to the proposed mechanism, upon irradiation of UV light, NH₄ClO₄ gets electronically excited and undergoes single electron transfer (SET) to benzyl alcohol

**Scheme 4.** Plausible mechanism for photocatalytic conversion of benzyl alcohol to α -aminophosphonates and dihydropyrimidones.

generating benzyl alcohol radical cation and in turn gets itself transformed to ammonium perchlorate radical anion. The ammonium perchlorate radical anion generated reacts with molecular oxygen O₂ in air to produce an initial superoxide radical anion. The activated benzyl alcohol radical cation then reacts with superoxide radical O₂⁻ to produce peroxide radical. The generated peroxide radical abstracts hydrogen from the methylene carbon to generate the benzaldehyde molecule. The benzaldehyde then reacts with anilines and triethylphosphite to produce final aminophosphonates. Similarly the *in situ* generated benzaldehyde also reacts with urea and β-keto ester to produce dihydropyrimidones.

4. Conclusion

In summary, we have reported one-pot tandem conversion of benzyl alcohols to α-amino phosphonates and 1,4-dihydropyrimidones. The method is based on the photo-oxidation of benzyl alcohol using NH₄ClO₄ as a commercially available and inexpensive metal-free photocatalyst for the *in situ* generation of benzaldehydes followed by condensation with anilines and trialkylphosphites (Kabachnik–Fields reaction) to furnish α-aminophosphonates and also with urea and β-keto esters (Biginelli reaction) to produce 1,4-dihydropyrimidones. The detailed experimental studies indicate the role of UV light, NH₄ClO₄ and O₂ in the synthetic reaction. Notably, this method avoids the use of harmful organic solvents and involves photo-catalytic action. The results of controlled experiments indicate a radical based mechanism for photo oxidation of benzyl alcohol to benzaldehydes.

5. References

- X.-C. Huang, M. Wang, Y.-M. Pan, G.-Y. Yao, H.-S. Wang, X.-Y. Tian, J.-K. Qin, Y. Zhang, *Eur. J. Med. Chem.* **2013**, *69*, 508–520. DOI:10.1016/j.ejmech.2013.08.055
- Z. Rezaei, H. Firouzabadi, N. Iranpoor, A. Ghaderi, M. R. Jafari, A. A. Jafari, H. R. Zare, *Eur. J. Med. Chem.* **2009**, *44*, 4266–4275. DOI:10.1016/j.ejmech.2009.07.009
- G. Zhang, G. Hao, J. Pan, J. Zhang, D. Hu, B. Song, *J. Agric. Food Chem.* **2016**, *64*, 4207–4213. DOI:10.1021/acs.jafc.6b01256
- J. P. Abell, H. Yamamoto, *J. Am. Chem. Soc.* **2008**, *130*, 10521–10523. DOI:10.1021/ja803859p
- (a) Y.-Q. Yu, D.-Z. Xu, *Synthesis* **2015**, *47*, 1869–1876. DOI:10.1055/s-0034-1380523
(b) G. Keglevich, E. Bálint, *Molecules* **2012**, *17*, 12821–12835. DOI:10.3390/molecules171112821
- (a) I. Essid, S. Touil, *Curr. Org. Synth.* **2017**, *14*, 272–278. DOI:10.2174/1570179413666160624092814
(b) C. Qian, T. Huang, *J. Org. Chem.* **1998**, *63*, 4125–4128. DOI:10.1021/jo971242t
- X.-C. Li, S.-S. Gong, D.-Y. Zeng, Y.-H. You, Q. Sun, *Tetrahedron Lett.* **2016**, *57*, 1782–1785. DOI:10.1016/j.tetlet.2016.03.033
- (a) R. M. N. Kalla, J. Bae, I. Kim, *New J. Chem.* **2017**, *41*, 6653–6660. DOI:10.1039/C7NJ00944E
(b) M. M. Kabachnik, E. V. Zobnina, I. P. Beletskaya, *Synlett* **2005**, 1393–1396. DOI:10.1055/s-2005-868519
(c) X. Mu, M. Lei, J. Zou, W. Zhang, *Tetrahedron Lett.* **2006**, *47*, 1125–1127. DOI:10.1016/j.tetlet.2005.12.027
(d) G. Keglevich, A. Szekrenyi, *Lett. Org. Chem.* **2008**, *5*, 616–622. DOI:10.2174/157017808786857598
(e) E. Bálint, E. Fazekas, P. Pongrácz, L. Kollár, L. Drahos, T. Holczbauer, M. Czugler, G. Keglevich, *J. Organomet. Chem.* **2012**, *717*, 75–82. DOI:10.1016/j.jorganchem.2012.07.031
(f) E. Bálint, E. Fazekas, G. Pintér, A. Szollosy, T. Holczbauer, M. Czugler, L. Drahos, T. Körtvélyesi, G. Keglevich, *Curr. Org. Chem.* **2012**, *16*, 547–554. DOI:10.2174/138527212799499822
(g) E. Bálint, E. Fazekas, L. Drahos, G. Keglevich, *Heteroatom Chem.* **2013**, *24*, 510–515. DOI:10.1002/hc.21126
(h) E. Bálint, E. Fazekas, J. Kóti, G. Keglevich, *Heteroatom Chem.* **2015**, *26*, 106–115. DOI:10.1002/hc.21221
(i) P. Kafarski, M. Górny *vel.* Górniak, I. Andrasiak, *Curr. Green Chem.* **2015**, *2*, 218–222. DOI:10.2174/2213346102666150109203606
(j) E. Bálint, A. Tripolszky, E. Jablonkai, K. Karaghiosoff, M. Czugler, Z. Mucsi, L. Kollár, P. Pongrácz, G. Keglevich, *J. Organomet. Chem.* **2016**, *801*, 111–121. DOI:10.1016/j.jorganchem.2015.10.029
(k) E. Bálint, R. E. Tóth, G. Keglevich, *Heteroatom Chem.* **2016**, *27*, 323–355. DOI:10.1002/hc.21343
(l) E. Bálint, Á. Tajti, D. Kalocsai, B. Mátravölgyi, K. Karaghiosoff, M. Czugler, G. Keglevich, *Tetrahedron* **2017**, *73*, 5659–5667. DOI:10.1016/j.tet.2017.07.060
(m) Á. Tajti, E. Szatmári, F. Perdih, G. Keglevich, E. Bálint, *Molecules* **2019**, *24*, 1640 (13 pages). DOI:10.3390/molecules24081640
(n) A. Tripolszky, L. Zoboki, E. Bálint, J. Kóti, G. Keglevich, *Synth. Commun.* **2019**, *49*, 1047–1054. DOI:10.1080/00397911.2019.1584675
- (a) N. Azizi, F. Rajabi, M. R. Saidi, *Tetrahedron Lett.* **2004**, *45*, 9233–9236. DOI:10.1016/j.tetlet.2004.10.092
(b) E. Bálint, Á. Tajti, A. Ádám, I. Csontos, K. Karaghiosoff, M. Czugler, P. Ábrányi-Balogh, G. Keglevich, *Beilstein J. Org. Chem.* **2017**, *13*, 76–86. DOI:10.3762/bjoc.13.10
- P. M. Mumford, G. J. Tarver, M. Shipman, *J. Org. Chem.* **2009**, *74*, 3573–3575. DOI:10.1021/jo9004958
- W. Han, P. Mayer, A. R. Ofial, *Adv. Synth. Catal.* **2010**, *352*, 1667–1676. DOI:10.1002/adsc.201000092
- M. K. Kolli, P. Elamathi, G. Chandrasekar, V. R. Katta, G. Balvantsinh Raolji, *Synth. Commun.* **2018**, *48*, 638–649. DOI:10.1080/00397911.2017.1385083
- Y. Gao, Z. Huang, R. Zhuang, J. Xu, P. Zhang, G. Tang, Y. Zhao, *Org. Lett.* **2013**, *15*, 4214–4217. DOI:10.1021/ol4019419
- W. Fan, Y. Queneau, F. Popowycz, *RSC Adv.* **2018**, *8*, 31496–31501. DOI:10.1039/C8RA05983G
- H. Sun, F. Z. Su, J. Ni, Y. Cao, H. Y. He, K. N. Fan, *Angew. Chem.* **2009**, *121*, 4454–4457. DOI:10.1002/ange.200900802

16. Á. de Fatima, T. C. Braga, L. da S. Neto, B. S. Terra, B. G. F. Oliveira, D. L. da Silva, L. V. Modolo, *J. Adv. Res.* **2015**, *6*, 363–373. DOI:10.1016/j.jare.2014.10.006
17. H. Qu, X. Li, F. Mo, X. Lin, *Beilstein J. Org. Chem.* **2013**, *9*, 2846–2851. DOI:10.3762/bjoc.9.320
18. Z.-L. Shen, X.-P. Xu, S.-J. Ji, *J. Org. Chem.* **2010**, *75*, 1162–1167. DOI:10.1021/jo902394y
19. S. S. Mansoor, S. S. Shafi, S. Z. Ahmed, *Arab. J. Chem.* **2016**, *9*, S846–S851. DOI:10.1016/j.arabjc.2011.09.018
20. L. M. Ramos, A. Y. Ponce de Leon y Tobio, M. R. dos Santos, H. C. B. de Oliveira, A. F. Gomes, F. C. Gozzo, A. L. de Oliveira, B. A. D. Neto, *J. Org. Chem.* **2012**, *77*, 10184–10193. DOI:10.1021/jo301806n
21. X.-H. Chen, X.-Y. Xu, H. Liu, L.-F. Cun, L.-Z. Gong, *J. Am. Chem. Soc.* **2006**, *128*, 14802–14803. DOI:10.1021/ja065267y
22. M. Moosavifar, *C. R. Chim.* **2012**, *15*, 444–447. DOI:10.1016/j.crci.2011.11.015
23. M. Rahman, A. Majee, A. Hajra, *J. Heterocycl. Chem.* **2010**, *47*, 1230–1233. DOI:10.1002/jhet.415
24. R. Fu, Y. Yang, W. Lai, Y. Ma, Z. Chen, J. Zhou, W. Chai, Q. Wang, R. Yuan, *Synth. Commun.* **2015**, *45*, 467–477. DOI:10.1080/00397911.2014.976346
25. B. Mohammadi, F. K. Behbahani, *Mol. Divers.* **2018**, *1*–42.
26. C. K. Prier, D. A. Rankic, D. W. MacMillan, *Chem. Rev.* **2013**, *113*, 5322–5363. DOI:10.1021/cr300503r
27. J. W. Tucker, C. R. Stephenson, *J. Org. Chem.* **2012**, *77*, 1617–1622. DOI:10.1021/jo202538x
28. N. A. Dangroo, T. Ara, B. A. Dar, M. Khuroo, *Catal. Commun.* **2019**, *118*, 76–80. DOI:10.1016/j.catcom.2018.10.006
29. N. Dangroo, A. Dar, R. Shankar, M. Khuroo, P. Sangwan, *Tetrahedron Lett.* **2016**, *57*, 2717–2722. DOI:10.1016/j.tetlet.2016.05.003
30. N. A. Dangroo, A. A. Dar, B. A. Dar, *Tetrahedron Lett.* **2014**, *55*, 6729–6733. DOI:10.1016/j.tetlet.2014.09.123
31. N. Chalotra, A. Ahmed, M. A. Rizvi, Z. Hussain, Q. N. Ahmed, B. A. Shah, *J. Org. Chem.* **2018**, *83*, 14443–14456. DOI:10.1021/acs.joc.8b02193
32. S. Sultan, M. A. Rizvi, J. Kumar, B. A. Shah, *Chem. Eur. J.* **2018**, *24*, 10617–10620. DOI:10.1002/chem.201801628
33. F. Kouser, V. K. Sharma, M. Rizvi, S. Sultan, N. Chalotra, V. K. Gupta, U. Nandi, B. A. Shah, *Tetrahedron Lett.* **2018**, *59*, 2161–2166. DOI:10.1016/j.tetlet.2018.04.046
34. (a) B. S. Kumara, A. U. Ravi Sankara, C. S. Reddy, S. K. Nayak, C. Naga Rajua, *ARKIVOC* **2007**, (xiii), 155–166. (b) C. Venkateswarlu, P. V. V. Satyanarayana, C. V. Nageswara Rao, C. Naga Raju, C. Sampath, *OCAIJ* **2011**, *7*, 320–324. (c) J. T. Hou, J. W. Gao, Z. H. Zhang, *Appl. Organometal. Chem.* **2011**, *25*, 47–53. DOI:10.1002/aoc.1687 (d) A. A. Jafari, S. Amini, F. Tamaddon, *J. Iran. Chem. Soc.* **2013**, *10*, 677–684. DOI:10.1007/s13738-012-0200-6 (e) M. A. Nasser, M. Sadeghzadeh, *J. Chem. Sci.* **2013**, *125*, 537–544. DOI:10.1007/s12039-013-0403-0 (f) T. Bhattacharya, B. Majumdar, D. Dey, T. K. Sarma, *RSC Adv.* **2014**, *4*, 45831–45837. DOI:10.1039/C4RA08533G (g) S. Sobhani, F. Khakzad, *Appl. Organometal. Chem.* **2017**, *31*, e3877. DOI:10.1002/aoc.3877 (h) S. U. Deshmukh, K. R. Kharat, A. R. Yadav, S. U. Shisodia, M. G. Damale, J. N. Sangshetti, R. P. Pawar, *Chemistry Select* **2018**, *3*, 5552–5558. DOI:10.1002/slct.201800798 (i) S. Poola, M. R. Nadivedhi, S. Sarva, M. Gundluru, S. Nagaripati, M. S. Shaik, P. Kotha, N. Chamarthi, S. R. Cirandur, *Med. Chem. Res.* **2019**, *28*, 528–544. DOI:10.1007/s00044-019-02302-y
35. (a) M. Yadollahi, H. Hamadi, V. Nobakht, *Appl. Organometal. Chem.* **2019**, *33*, e4629 (10 pages). DOI:10.1002/aoc.4819 (b) H. G. O. Alvim, T. B. de Lima, H. C. B. de Oliveira, F. C. Gozzo, J. L. de Macedo, P. V. Abdelnur, W. A. Silva, B. A. D. Neto, *ACS Catal.* **2013**, *3*, 1420–1430. DOI:10.1021/cs400291t (c) E. A. Gilandeh, A. Yahyazadeh, M. A. Hashjin, *RSC Adv.* **2018**, *8*, 40243–40251. DOI:10.1039/C8RA08622B
36. W. Huang, B. C. Ma, H. Lu, R. Li, L. Wang, K. Landfester, K. A. Zhang, *ACS Catalysis.* **2017**, *7*, 5438–5442. DOI:10.1021/acscatal.7b01719

Povzetek

V članku opisujemo tandemsko enolončno neposredno pretvorbo benzil alkoholov v α -aminofosfonate in dihidropirimidone, ki poteka pod pogoji brez uporabe toplil. Metoda temelji na fotooksidaciji benzilnih alkoholov do benzaldehidov pod vplivom UV svetlobe ob uporabi amonijevega perklorata, brez uporabe kovinskih katalizatorjev. Tej prvi reakciji sledi Kabachnik–Fieldsova ali Biginellijeva reakcija. Reakcije potekajo pod zmernimi pogoji, brez dodatkov kovin, s pestrim naborom izhodnih substratov. Kontrolne eksperimente smo izvedli, da bi ugotovili vlogo amonijevega perklorata in molekularnega kisika kot oksidanta. Eksperimenti, izvedeni v prisotnosti TEMPO in ostalih lovilcev radikalov, so pokazali, da reakcijski mehanizem verjetno temelji na radikalskih procesih.



Except when otherwise noted, articles in this journal are published under the terms and conditions of the Creative Commons Attribution 4.0 International License

Scientific paper

Room Temperature Synthesis and Characterization of Novel Bi(III) Complex with 2-Amino-3-Carbomethoxy-4,5,6,7-Tetrahydrobenzo[B]Thiophene as Potential Antimicrobial Agent

Emmanuel Sopbué Fondjo,^{1,*} Désire André Siéwé,¹ Jean-de-Dieu Tamokou,² Steve Endeguele Ekom,² Sorel Kamal Dimo Djeukoua,¹ Giscard Doungmo,³ Mallory E. Walters,⁴ Appolinnaire Tsopmo,⁴ Peter F. W. Simon⁵ and Jules Roger Kuate²

¹Laboratory of Applied Synthetic Organic Chemistry, Department of Chemistry, Faculty of Science, University of Dschang, P.O. Box 67 Dschang, Republic of Cameroon

²Research Unit of Microbiology and Antimicrobial Substances, Department of Biochemistry, Faculty of Science, University of Dschang, PO Box 067 Dschang, Republic of Cameroon

³Institut für Anorganische Chemie, Christian-Albrechts-Universität zu Kiel, Max-Eyth-Str. 2, 24118 Kiel, Germany

⁴Department of Chemistry, Carleton University, 1125 Colonel By Drive K1S 5B6, Ottawa, Canada +1-613-520-260 Ext 3122

⁵Polymer Chemistry Laboratory, Faculty of Live Sciences, Rhine-Waal University of Applied Sciences, Campus Kleve, Marie-Curie Strasse 1, D-47533 Kleve, Germany

* Corresponding author: E-mail: sopbue@yahoo.fr (0000-0002-1077-673X)

Received: 06-27-2019

Abstract

A novel bismuth(III) complex with 2-amino-3-carbomethoxy-4,5,6,7-tetrahydrobenzo[b]thiophene (ACTT) as a ligand have been synthesized. The novel complex was characterized on the basis of its IR, NMR, elemental analysis and MS spectral data. It was found that the ligand behaves as a monodentate chelating agent and bonds to the metal ion through the nitrogen atom of the amino group to form the $[\text{Bi}^{\text{III}}(\text{ACTT})_6]\text{Cl}_3$ complex. The new complex compound displayed significant antimicrobial activity (MIC = 8–32 $\mu\text{g}/\text{mL}$) against *Bacillus subtilis*, *Staphylococcus aureus*, *Escherichia coli*, *Pseudomonas aeruginosa*, *Shigella flexneri*, *Candida albicans*, *Candida tropicalis* and *Cryptococcus neoformans*.

Keywords: Room temperature synthesis; antimicrobial; complexation reaction; 2-aminothiophene; bismuth

1. Introduction

Coordination chemistry is gaining more and more attention nowadays due to the increased demand of new compounds with various properties and functionalities. In fact, combining properties of metal ion like magnetic, optic, conductor, oxydoreduction, biological with the one of an organic chelate compound can lead to new hybrid coordination complexes with enhanced functionalities. There-

fore, many coordination compounds with properties like antimicrobial,^{1–4} AND-binding,⁵ antiviral, anticancerous, cytotoxic,⁶ anti-inflammatory,^{7,8} analgesic,⁹ antioxidant,^{10,11} optoelectronic, superconductor, non-linear optical (NLO),^{12,13} light emitting device (LED),^{14,15} catalyst, antidiabetic,^{16,17} gas storage, metalloenzyme,¹⁸ nanoparticles^{19,20} have been reported.

Heavy metal bismuth is found in group V in the periodic table as the 83rd element. Beside its heavy metal

status, bismuth and derived compounds are relatively non-toxic and can be used as green and effective catalyst^{21,22} in many synthetic reactions to replace toxic catalysts such as compounds of mercury, lead, thallium, arsenic, antimony etc. Other properties of bismuth compounds including antimicrobial,^{23–27} cytotoxic,^{25–30} anti-spermatogenic,³¹ white light emitting diode (WLEDs)³² are also extensively reported. 2-aminotetrahydrobenzo[b]thiophene system and their substituted derivatives have attracted a great deal of interest due to their various electronic,³³ optical,³⁴ dyeing,^{35–37} fluorescence³⁸ and pharmacological properties.^{39–41} On the other hand, to the best of our knowledge, the title 2-aminothiophene derivative (ACTT) used as ligand in this study has not yet been reported in any coordination reaction with bismuth(III) salt.

For all these reasons, we became interested on the investigation of its coordination behavior with bismuth(III) salts. Our expectation was that novel hybrid compounds resulting from the combination in the same molecular framework of the bismuth(III) ion coordinated to one or more 2-aminothiophene ligand and combining the features of its components will exhibit new and improved interesting biological and functional properties.

2. Experimental Part

2. 1. Chemistry

All the reagents mentioned in this work were purchased from Aldrich and Fluka and were used without further purification. Melting points are corrected and were determined with a STUART SCIENTIFIC Melting Point Apparatus Model SMP3 at a heating rate of 1.5 °C / min. The TLCs were carried out on Eastman Chromatogram Silica Gel Sheets (13181; 6060) with fluorescent indicator. A mixture of ethyl acetate and methylene chloride (1:1) was used as eluent and iodine was used to develop the chromatograms. The IR spectra were measured with a Fourier Transform Infrared spectrometer Bruker Alpha. EIMS spectra were recorded on a double focusing mass spectrometer (Varian MAT 311A). ¹H-NMR spectra were recorded in DMSO-*d*₆ on a Bruker DRX spectrometer operating at 300 MHz. ¹³C-NMR spectra were recorded in DMSO-*d*₆ on a Bruker DRX spectrometer operating at 399 MHz with TMS used as internal reference. XRD data was collected on a STOE Stadi-p X-ray powder diffractometer (STOE & Cie GmbH, Darmstadt, Germany) with Cu K_{α1} radiation ($\lambda = 1.54056 \text{ \AA}$; Ge monochromator; flat samples) in transmission geometry with a DECTRIS[®] MYTHEN 1K detector (DECTRIS, Baden-Daettwil, Switzerland). Elemental analyses were performed With a Euro Vector CHNS-O element analyzer (Euro EA 3000) or a vario MICRO Cube (Co. Elementar Analysensysteme).

2. 1. 1. Preparation of 2-amino-3-carbomethoxy-4,5,6,7-tetrahydrobenzo[b]thiophene (3)

A mixture of cyclohexanone (50 mmol, 4.9 g), methyl cyanoacetate (50 mmol, 4.95 g) and sulphur (55 mmol, 1.76 g) in methanol (80 mL) was stirred using a magnetic plate shaker thermostated at 50–60 °C. Ammonia (5 mL) was added drop wise during the first 10 min of the reaction. After 3 h of reaction, the resulting precipitate (8.66 g, 82%) was collected by filtration and crystallized from methanol to yield a yellow powder, mp: 133–135 °C (Lit.⁴² 127–128°C from methanol). IR (neat) $\nu \text{ cm}^{-1}$: 3419, 3310 ($-\text{NH}_2$); 3153 ($-\text{OCH}_3$); 1649 (C=O); 1585, 1575 (C=C); 775; 734 (C–S); 1332 (C–N); 1268 (C–O). ¹H-NMR (400 MHz, DMSO-*d*₆) δ_{H} : 7.17, 3.61, 2.52, 2.46, 2.36, 1.61. ¹³C-NMR (101 MHz, DMSO-*d*₆) δ_{C} : 165.87, 163.41, 131.83, 115.93, 102.90, 50.77, 26.97, 24.41, 23.34, 22.87. Elemental analysis found (calculated): C: 56.87% (56.87%); H: 6.16% (6.16%); N: 6.63% (6.64%); S: 15.17% (15.17%).

2. 1. 2. Preparation of Metal Complex 4

To a magnetically stirred solution of the ligand 3 (0.32 g; 1.5 mmol) in methanol (10 mL) a solution of BiCl₃ (0.315 g; 1 mmol) in methanol (10 mL) was gradually added. After 48 h, the product formed was collected by filtration and crystallized from a mixture water/methanol to give 0.39 g (82%) of 4 as brown precipitate; mp 112 °C. IR (neat) $\nu \text{ cm}^{-1}$: 3480; 3333 ($-\text{NH}_2$); 1653 (C=O); 1576; 1526 (C=C); 1323 (C–N); 1271 (C–O). ¹H-NMR (400 MHz, DMSO-*d*₆) δ_{H} : 7.93, 7.91, 7.74, 7.72, 7.33, 7.22, 7.09, 6.96, 4.63, 3.78, 3.62, 3.59, 3.58, 3.58, 3.45, 3.44, 3.42, 3.38, 3.37, 3.35, 3.33, 1.94, 1.62, 1.19. ¹³C-NMR (101 MHz, DMSO-*d*₆) δ_{C} : 166.65, 165.88, 165.17, 163.92, 163.74, 163.41, 132.03, 131.84, 130.31, 120.99, 116.26, 115.94, 102.06, 101.30, 51.75, 51.06, 50.95, 50.77, 27.77, 26.98, 24.57, 24.41, 24.26, 24.11, 23.34, 22.87, 18.42. Elemental analysis found (calculated): C: 45.53% (45.53%); H: 4.94% (4.93%); N: 5.31% (5.31%); S: 12.14% (12.14%).

2. 2. Biology

2. 2. 1. Microorganisms

A total of six bacteria and three yeasts strains were tested for their susceptibility to the studied compounds. The studied microorganisms include *Staphylococcus aureus* ATCC25923, *Escherichia coli* S2(1), *Bacillus subtilis*, *Staphylococcus aureus*, *Pseudomonas aeruginosa* ATCC27853, *Shigella flexneri* SDINT, *Candida albicans* ATCC10231, *Candida tropicalis* PK233, *Cryptococcus neoformans* H99. These microorganisms were taken from our laboratory collection. The bacterial and fungal species were maintained on agar slant at +4 °C and subcultured at 37 °C on nutrient agar (NA, Conda, Madrid, Spain) and Sabouraud Dextrose Agar (SDA, Conda) slants respectively, prior to any antimicrobial test.

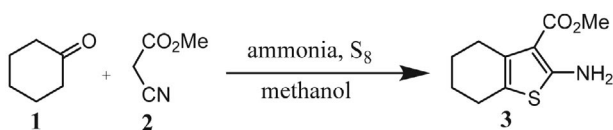
2. 2. 2. Determination of Minimum Inhibitory Concentration (MIC) and Minimum Microbicidal Concentration (MMC)

MIC values were determined by a broth micro-dilution method as described earlier.⁴³ Each test sample was dissolved in dimethyl sulfoxide (DMSO) and the solution was then added to Mueller Hinton Broth (MHB) for bacteria or Sabouraud Dextrose Broth (SDB) for yeasts to give a final concentration of 1024 $\mu\text{g/mL}$. This was serially diluted twofold to obtain a concentration range of 0.25–512 $\mu\text{g/mL}$. Then, 100 μL of each concentration were added in each well (96-well microplate) containing 95 μL of MHB or SDB and 5 μL of inoculum for final concentrations varying from 0.125–256 $\mu\text{g/mL}$. The inoculum was standardized at 1.5×10^6 colony-forming units (CFU)/mL for bacteria and 2×10^5 spores/mL for yeasts using a spectrophotometer (Jenway™ 6305 UV/Visible Spectrophotometer, Fisher scientific, UK). The negative control well consisted of 195 μL of MHB or SDB and 5 μL of the standard inoculum. The MICs were assessed visually and were taken as the lowest compound concentration at which there was no growth or virtually no growth. The lowest concentration that yielded no growth after the sub-culturing was considered as the minimum microbicidal concentrations (MMCs). Ciprofloxacin (Sigma-Aldrich, Steinheim, Germany) and nystatin (Merck, Darmstadt, Germany) were used as positive controls for bacteria and yeasts, respectively. All the tests were performed in triplicate.

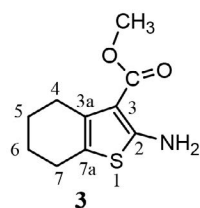
3. Results and Discussion

3. 1. Chemistry

The thiophene compound 2-amino-3-carbomethoxy-4,5,6,7-tetrahydrobenzo[*b*]thiophene (ACTT) (**3**) was prepared by applying one-pot procedure of the second



Scheme 1. Reaction sequence to compound **3**



Scheme 2. Reaction sequence to $\text{Bi}(\text{ACTT})_6\text{Cl}_3$ complex **4**

version of the Gewald technique,⁴² whereby cyclohexanone (**1**), methyl cyanoacetate (**2**) and elemental sulfur were condensed in methanol in the presence of catalytic amount of ammonia (Scheme 1).

The structure of the ligand substrate **3** ($\text{ACTT} = \text{CH}_3\text{O}_2\text{C-Ar-NH}_2$) was confirmed with its physical and spectroscopic data which are in full agreement with those previously reported.⁴²

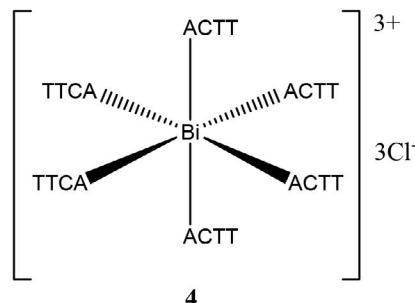
The reaction of compound **3** with bismuth(III) chloride in methanol with constant stirring at room temperature for 48 hours gave the compound **4** (Scheme 2).

3. 1. 1. IR spectrum of the Bismuth Complex **4**

The IR bands of the complex **4** were assigned by comparison with the IR spectrum of the starting 2-aminothiophene ligand **3**. The elongation frequencies $\nu(\text{NH}_2)$ of the aromatic amine which were found in the ligand at 3419 cm^{-1} (more intense) and 3310 cm^{-1} (more intense) in the ligand, respectively, are shifted to higher frequencies at 3480 cm^{-1} (shoulder), 3333 cm^{-1} (shoulder), respectively, in the complex. The presence of these two bands of the amino group in the IR spectrum of the ligand is a clear indication that the complexation occurred without deprotonation of the primary aromatic amine. The modification observed in the shapes of these bands (shoulder) in addition to their important shift ($\Delta\nu = 61$ and 23 cm^{-1}) to higher frequencies may be due to the involvement of the corresponding nitrogen atom to the coordination process.⁴⁴ One can also notice that the strong absorption band of the carbonyl function of the carbomethoxy group which appears at 1649 cm^{-1} in the ligand undergoes a $\Delta\nu = 4$ cm^{-1} shift to higher frequencies and is shown at 1653 cm^{-1} in the complex. This observation indicates that the oxygen atoms of the carbonyl function of the ester groups of the coordinated 2-aminothiophene ligands are involved in various hydrogen bonds interactions with $-\text{NH}_2$ groups.

3. 1. 2. ^1H NMR-Spectrum of Complex **4**

Similarly, the ^1H NMR signals of compound **4** was assigned by comparison with the ^1H NMR spectrum of the ligand **3**. In Table 1 the chemical shifts of both compounds are recapitulated. One can also notice here that each signal



of individual hydrogen or groups of chemically and magnetically equivalent hydrogen atoms in the starting free 2-aminothiophene ligand **3** is splitted into a number of corresponding signals attributed to the six 2-aminothiophene ligands coordinated to the central bismuth(III) ion.

3. 1. 3. ^{13}C NMR-Spectrum of Complex **4**

The assignments of the ^{13}C NMR signals of compound **4** were made by comparison with the ^{13}C NMR spectrum of the ligand **3**. As recapitulated in Table 1, each signal of individual carbon atoms in the starting free 2-aminothiophene ligand **3** is splitted in a number of corresponding signals attributed to the six ligands coordinated to the bismuth(III) ion in the complex compound **4**.

3. 1. 4. 2D NMR Data of Complex **4** and Ligand **3**

The important interactions found in the ^1H , ^1H -COSY; ^1H , ^{13}C -HSQC, ^1H , ^{13}C -HMBC and ^1H , ^1H -NOESY experiments for compounds **3** and **4** are recapitulated in Table 2.

The HSQC spectrum (Figure 1) of the ligand shows five correlation spots corresponding to the five carbon atoms bearing protons. Correlation spots are also observed between methoxyl proton at 3.61 ppm and the corresponding carbon at 50.8 ppm. The assignment of the $-\text{NH}_2$ protons at 7.18 ppm could be rationalized based on the fact that this signal doesn't correlate with any carbon atom. Similar assignments could be done for the complex by comparison (Table 2).

The HMBC experiment shows different correlations' spots that were helpful for the accurate assignments of the

Table 1. Comparison of the ^1H and ^{13}C NMR (DMSO- d_6) chemical shifts of the ligand **3** with those of the complex **4**.

N° C/H	Ligand 3		Complex 4	
	δ_{H} in ppm	δ_{C} in ppm	δ_{H} in ppm	δ_{C} in ppm
2	–	102.91	–	102.89, 102.06, 101.30
3	–	131.83	–	132.03, 131.84, 130.31
3a	–	115.93	–	120.99, 116.26, 115.94
4	1.62	22.87	1.60, 1.66,	22.87, 18.42
5	2.52	26.97	2.55	27.77, 27.76, 26.98
6	2.35	24.41	2.46	24.57, 24.41, 24.26
7	1.62	23.34	1.60, 1.66	24.11, 23.34
7a	–	163.41	–	163.92, 163.74, 163.41
C=O	–	165.88	–	166.65, 165.88, 165.17
$-\text{OCH}_3$	3.62	50.76	4.61, 3.78, 3.73, 3.62, 3.59, 3.44	51.75, 50.95, 50.77, 50.88, 50.86, 50.68
$-\text{NH}_2$	7.18	–	7.73, 7.22	–

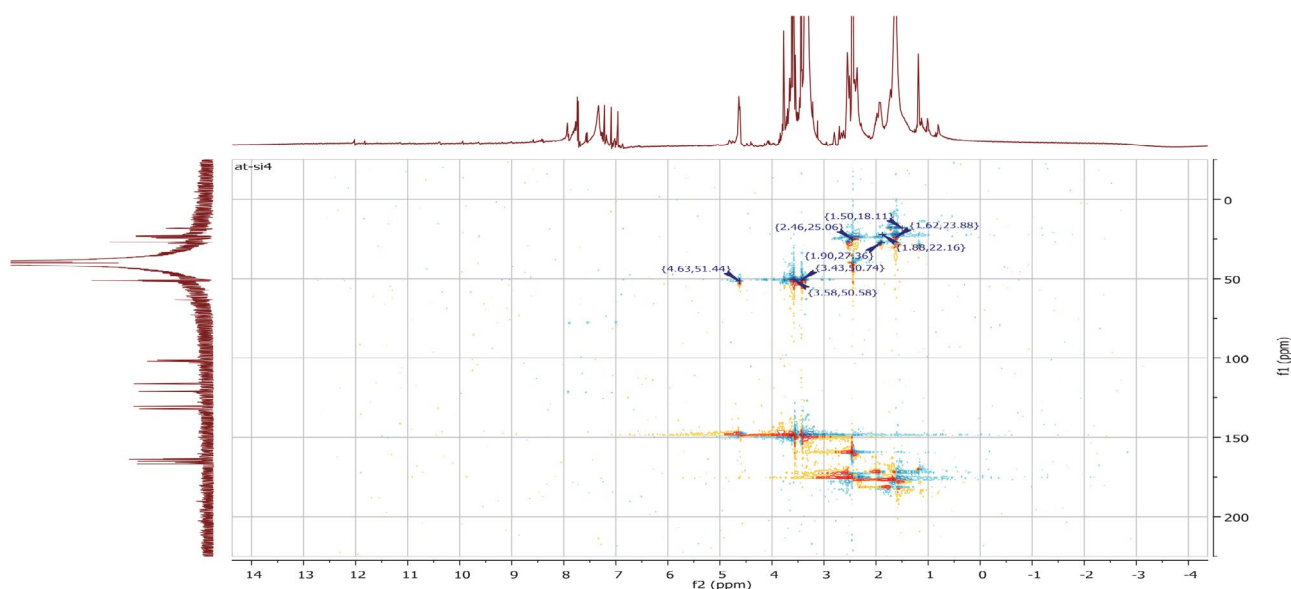


Figure 1. HSQC spectrum of complex with some correlations

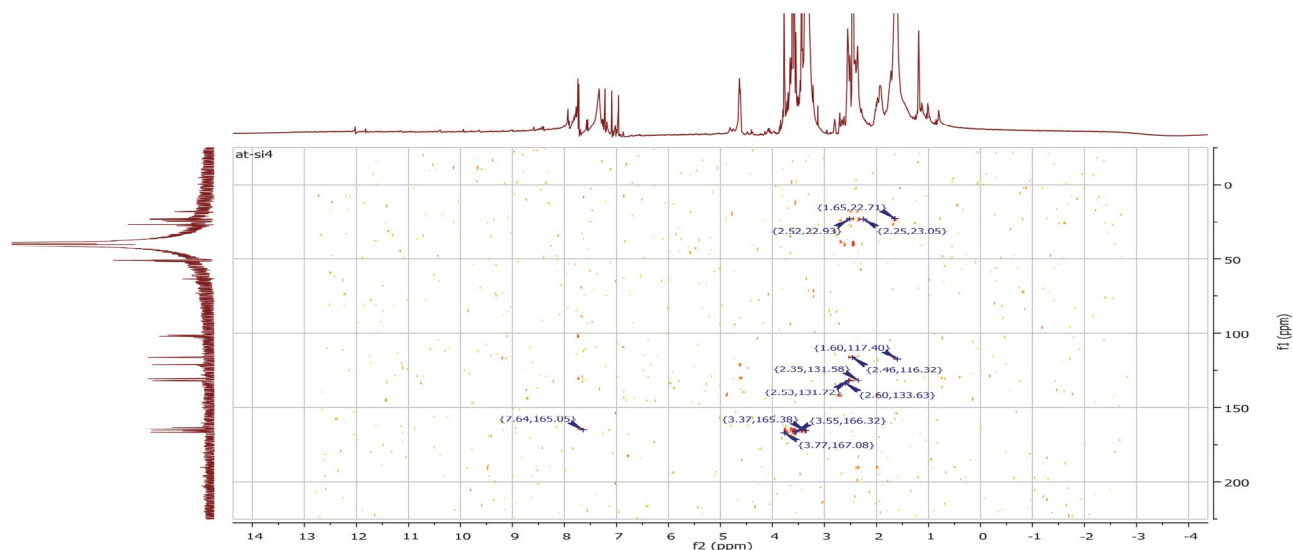


Figure 2. HMBC spectrum of complex with some correlations

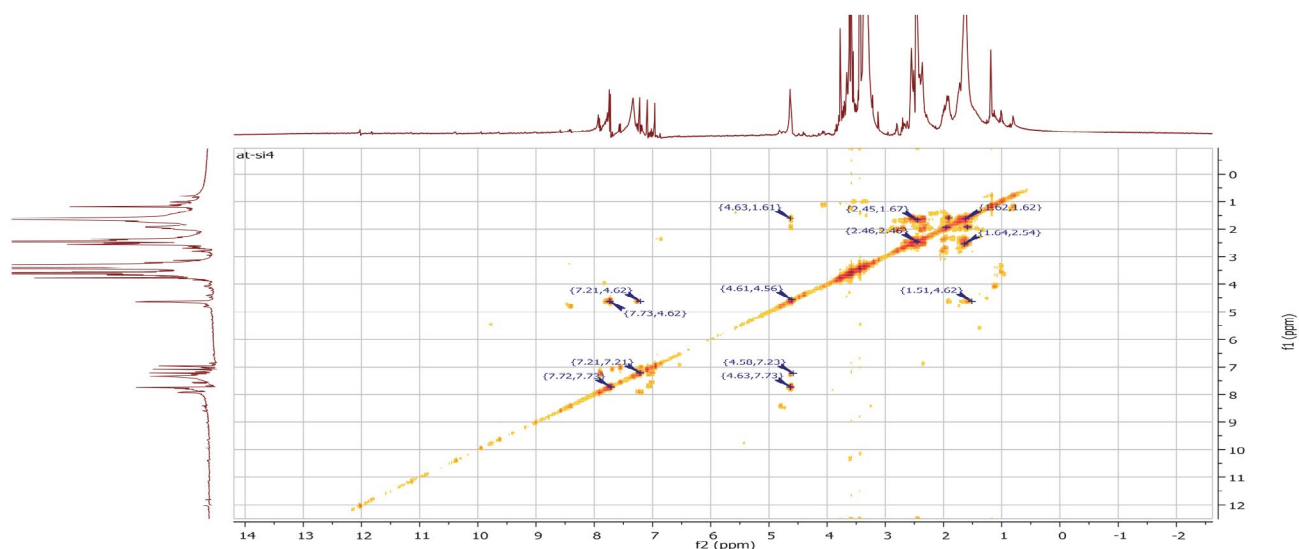


Figure 3. COSY spectrum of complex with some correlations

various carbon atoms in the ligand's molecule (Figure 2). For instance, a correlation between the methoxyl proton appearing at 3.61 ppm and the carbonyl carbon function at 165.9 ppm have been found. Correlations between these methoxyl protons and some carbon atoms of the thiophenic ring at 102.9 ppm have also been observed. A number of these analogous correlations have been found in the HMBC spectrum of compound **4** but their individual assignments to each coordinated ligand could not be conclusive due to high complexity of the overlapping signals caused by the homologous proton systems of the six coordinated ligands.

The COSY experiment of the ligand clearly exhibited the correlation spots between the protons of the cyclohexane ring (Table 2). For the complex (Figure 3), besides the homologous correlations displayed in the COSY experi-

ment, a correlation was observed between the methoxyl protons at 4.62 ppm and the amino protons 7.73 ppm.

The spatial proximity between the methoxyl group and the amino group is confirmed by the NOESY experiment for the ligand and for the complex as well.

3. 1. 5. Mass Spectrum of Complex 4

The mass spectrum of compound **4** exhibited characteristic ion fragments such as $[\text{Bi}(\text{C}_{10}\text{H}_{13}\text{NSO}_2)_2]^{3+}$ ($m/z = 630$), $[\text{Bi}(\text{C}_{10}\text{H}_{13}\text{NSO}_2)]^{3+}$ ($m/z = 419$), Bi (isotope) or $(\text{C}_{10}\text{H}_{13}\text{NSO}_2)^+$ ($m/z = 210$), in agreement with the suggested structure.

Furthermore, one can notice the absence of ion fragments such as $[\text{BiCl}]^+$ or $[\text{BiCl}_2]^+$ proving that chlorine

Table 2: Comparison of the interactions in the ^1H and ^{13}C -2D-NMR ($\text{DMSO}-d_6$) spectra of the ligand **3** with those of the complex **4**

N° C	δ_C	Ligand 3				δ_C	Complex 4				
		HSQC	HMBC	COSY	NOESY		HSQC	HMBC	COSY	NOESY	
2	102.9	–	3.62; 2.52	–	–	102.9; 102.6; 101.3	–	7.74	–	–	
3	131.6	–	2.52; 2.35; 1.62	–	–	132.0; 131.8; 130.3	–	2.55	–	–	
3a	115.9	–	2.52; 2.35; 1.62	–	–	121.0; 116.3; 116.0	–	2.55; 2.45; 1.68; 1.65	–	–	
4	22.9	1.62	1.62	2.52; 2.35	–	22.9; 18.4	1.60–1.66	2.45; 2.38; 2.35; 1.65	1.92; 2.45	–	
5	27.0	2.52	2.35; 1.62	1.62	–	27.8; 27.8; 27.0	2.55; 1.90– 2.40; 1.59	–	1.59; 1.92	–	
6	24.4	2.35	1.62	1.62	–	24.6; 24.4; 24.1	2.79; 2.69; 2.65; 2.45	2.69	1.62; 1.66	–	
7	23.3	1.62	2.52; 2.35; 1.62	2.52; 2.35	–	23.3	1.60–1.66	2.35	1.92; 2.45	–	
7a	163.9	–	–	–	–	163.9; 163.7; 163.4	–	7.74; 7.72;	–	–	
C=O	165.9	–	3.62	–	–	166.7; 165.8; 165.2	–	3.76; 4.62; 3.58; 3.55; 3.43; 3.37	–	–	
OCH ₃	50.8	3.62	–	–	7.18	51.8; 51.1; 51.0; 51.0; 50.9; 50.8	3.76; 3.58; 3.43; 4.62; 3.55; 3.37	–	7.72; 7.74;	7.33	
NH ₂	–	7.18	–	–	3.62	–	7.74; 7.72; 7.33	–	4.62	3.37	

atoms are not directly coordinated to the central metal ion in the complex.⁴⁵

3. 1. 7. Powder XRD Study of Compound 4

X-ray diffraction analysis performed on complex **4** shows a good crystalline structure of the complex formed with well-organized particles (Figure 4). Compound **4** has therefore a stable structure in which there is a good cohesion between atoms.

From the above data and based on various literature reports,^{21,24,46,47} we suggest that in compound $[\text{Bi}(\text{ACTT})_6]\text{Cl}_3$ (**4**), the bismuth atom exhibits a six-fold coordination to the 2-aminothiophene ligands in a tetragonal bipyramidal geometry. Around the central Bi atom, four N atoms occupy the equatorial positions and two N atoms occupy the axial ones. In this representation, the free rotation of the $-\text{Ar}-\text{CO}_2\text{CH}_3$ fragment of each N-coordinated 2-aminothiophene moiety around the Csp^2-N bond enables the formation of various hydrogen bonds between the six oxygen atoms of the carbonyl functions of the six carbomethoxy groups and the hydrogen atoms of the $-\text{NH}_2$ group. These interactions are clearly exhibited in the 3D view of the complex shown in Figure 6.

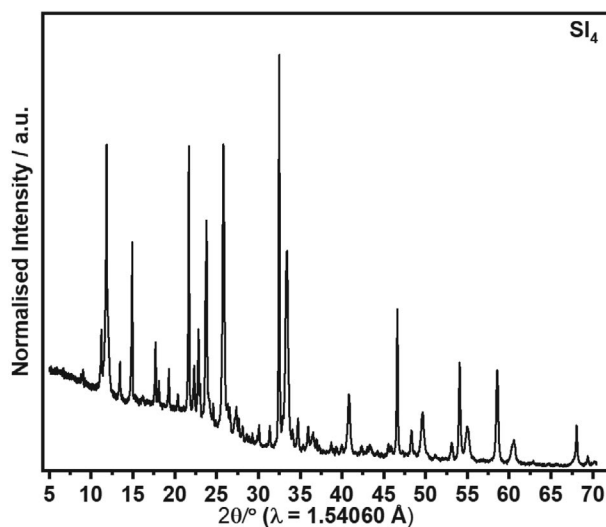


Figure 4. Powder XRD patterns of complex **4**.

3. 2. Antimicrobial Activity

Antimicrobial activity of the ligand, 2-amino-3-carbomethoxy-4,5,6,7-tetrahydrobenzo[*b*]thiophene (**3**) and its bismuth complex **4** was examined *in vitro* against bacterial

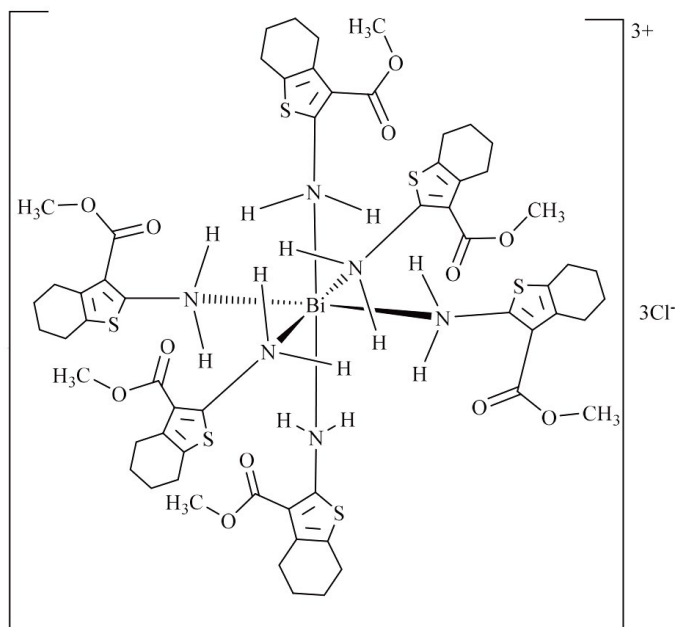


Figure 5. Structural representation of complex 4

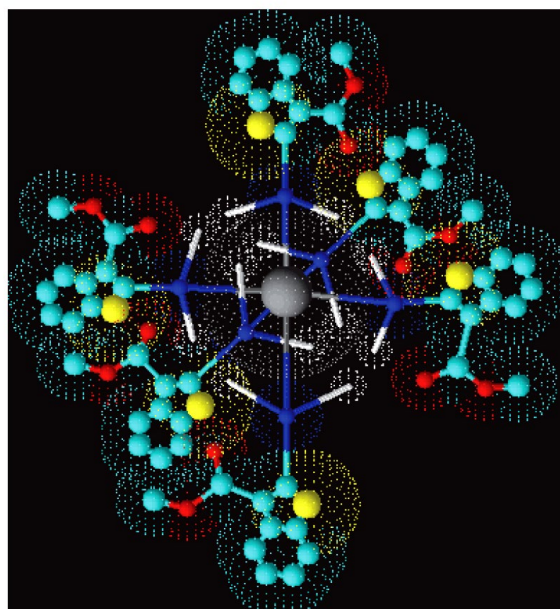


Figure 6. 3D view of the coordination sphere of complex 4 drawn with ACD/Labs 3D viewer (freeware)

Table 4. Antimicrobial activity (MIC, MBC and MFC in $\mu\text{g/mL}$) of compound complex against bacterial and yeast species

Microorganisms	Inhibition	Compound 4 parameters	Reference drugs*
<i>Staphylococcus aureus</i> ATCC25923	MIC	16	2
	MBC	16	2
	MBC/MIC	1	1
<i>Bacillus subtilis</i>	MIC	8	8
	MBC	8	1
	MBC/MIC	1	4
<i>Staphylococcus aureus</i>	MIC	16	4
	MBC	16	4
	MBC/MIC	1	1
<i>Pseudomonas aeruginosa</i> ATCC27853	MIC	16	2
	MBC	32	2
	MBC/MIC	2	1
<i>Escherichia coli</i> S2(1)	MIC	8	4
	MBC	8	4
	MBC/MIC	1	1
<i>Shigella flexneri</i> SDINT	MIC	32	4
	MBC	64	4
	MBC/MIC	2	1
<i>Candida albicans</i> ATCC10231	MIC	32	2
	MFC	32	2
	MFC/MIC	1	1
<i>Candida tropicalis</i> PK233	MIC	32	4
	MFC	32	4
	MFC/MIC	1	1
<i>Cryptococcus neoformans</i> H99	MIC	32	4
	MFC	64	4
	MFC/MIC	2	1

*Ciprofloxacin for bacteria and nystatin for yeasts; MIC: Minimum Inhibitory Concentration; MBC Minimum Bactericidal Concentration; MFC: Minimum Fungicidal Concentration.

and fungal species (Table 4). No activity was noticed for the 2-aminothiophene ligand against all the tested microorganisms (results not shown). However, the bismuth(III) complex showed different degrees of antimicrobial activities against the tested fungal and bacterial species (Table 4).

The bismuth complex showed antibacterial activities against all the tested microorganisms (MIC = 8–32 µg/mL). The lowest MIC value for this compound (8 µg/mL) corresponding to the best antimicrobial activity was obtained on *B. subtilis* and *E. coli*. Interestingly, the antibacterial activity of the complex (MIC = 8 µg/mL) on *B. subtilis* was found to be equal to that of ciprofloxacin (MIC = 8 µg/mL) used as reference drugs; highlighting its good antibacterial potency. The least sensitive microorganism was *Shigella flexneri* SDINT with the highest MIC (32 µg/mL) and MBC (64 µg/mL) values recorded.

The complex compound was more active against bacterial species (MIC = 8–32 µg/mL) than against yeast strains (MIC = 32 µg/mL). The findings of the present study showed that the antimicrobial activities varied with the bacterial and fungal strains. These variations may be due to genetic differences between the microorganisms.

The MBC and MFC values obtained were four fold less than their corresponding MIC values; indicating that this compound has microbicidal effect against the tested microorganisms.⁴⁸ The antimicrobial activity of compound **4** is in agreement with recent findings by Nur Amirah Jamaluddin *et al.* and Latika Dawara *et al.* respectively,^{23,28} who reported the antimicrobial activities of some bismuth(III) complex derivatives against a wide range of microorganisms including *Staphylococcus aureus*, *Bacillus subtilis*, *Escherichia coli*.

3. 3. Effects of Chelation to the Activity of Compounds Complex

Biological screenings' results show that the 2-aminothiophene ligand which was initially non-active yielded a compound with much better biological profile after the complexation with the bismuth. Chelation is certainly responsible of these new properties. Obviously, the polarity of the metal ion will be reduced to greater extent on chelation, due to the overlap of the ligand orbital and partial sharing of the positive charge of the metal ion with donor groups.⁴⁹ The complexation further increases the delocalization of π -electrons over the whole chelating ring which may facilitate the penetration of the complexes into lipid membranes and the blocking of the metal binding sites in the enzymes of microorganisms.⁴⁴ It may be hypothesized that there are other factors such as solubility, conductivity and bond length between the metal and ligand which also increase the activity.⁵⁰

4. Conclusion

In summary, we have synthesized and characterized a coordination complex containing Bi(III) with 2-ami-

no-3-carbomethoxy-4,5,6,7-tetrahydrobenzo[*b*]thiophene at room temperature. Powder XRD confirm the crystalline nature of the complex obtained. Antimicrobial screening's results showed that complex obtained was less antifungal than antibacterial in reference to standard drug, whereas the ligand was found inactive. However, the antibacterial activities of complex on *B. subtilis* were found to be equal to that of ciprofloxacin used as reference drug; highlighting its good antibacterial potency. The overall results of this study indicated that this novel coordination compound exhibited prominent antibacterial and antifungal activities.

Acknowledgements

Emmanuel Sopbué Fondjo gratefully acknowledges the financial support from DAAD (grant N° 91691265). Additional financial supports for the work were obtained from the University of Dschang's research grant committee and the Cameroonian Ministry of Higher Education special research allocation.

5. References

1. S. Bootwala, M. Tariq, S. Somasundaran, K. Aruna, *Int. J. Pharm. Bio. Sci.* **2013**, 3, 345–354.
2. A. K. M. Nur Alam Siddiki, Md. S. Rahman, M. A. Rahman, Md. A. Salam, A. Salam, Md. A. Yousuf, Md. F. Islam, Md. A. Arafat, *Bangladesh Pharm. J.* **2012**, 15, 83–87.
3. K. Y. Gupta, C. S. Agarwal, P. S. Madnawat, R. Narain, *Res. J. Chem. Sci.* **2012**, 2, 68–71.
4. A. D. Kulkarni, S. A. Patil, P. S. Badami, *Int. J. Electrochem. Sci.* **2009**, 4, 717–729.
5. P. S. Bhava, P. Tharmaraj, V. Muthuraj, M. Umadevi, *Int. J. Eng. Sci.* **2013**, 2, 16–25.
6. R. Gomathi, A. Ramu, *Int. J. Innov. Res. Sci. Eng. Technol.* **2013**, 2, 4852–4865.
7. W. Rehman, M. K. Baloch, A. Badshahb, S. Ali, *J. Chin. Chem. Soc.* **2005**, 52, 231–236. DOI:10.1002/jccs.200500034
8. Md. A. Hossain, Md. C. Sheikh, S. K. M. Al Zaheri, Md. A. Alam, *Int. J. Sci. Tech. Res.* **2013**, 2, 233–237.
9. M. R. Karekal, V. Biradar, M. B. H. Mathada, *Bioinorg. Chem. Appl.* **2013**, 2013, 1–16. DOI:10.1155/2013/315972
10. A. A. Al-Amiery, A. A. H. Kadhum, A. B. Mohamad, *Bioinorg. Chem. Appl.* **2012**, 2012, 1–6. DOI:10.1155/2012/795812
11. M. Iyanar, C. Muthamizchelvan, S. Ponnusamy, J. T. J. Prakash, *Rec. Res. Sci. Tech.* **2010**, 2, 97–100.
12. S. Cynthia, B. M. Boaz, *Int. J. Eng. Sci. Invent.* **2013**, 2, 38–43.
13. N. T. Kalyani, S. J. Dhoble, R. B. Pode, *Adv. Mat. Lett.* **2011**, 2, 65–70. DOI:10.5185/amlett.2010.10169
14. Y. Kim, F. W. M. Vanhelmont, C. L. Stern, T. Hupp, *J. Inorg. Chim. Acta* **2001**, 318, 53–60. DOI:10.1016/S0020-1693(01)00400-5
15. P. I. Tripathi, M. M. Kumar, K. Arti, M. Chinmayi, T. Ruchita, S. L. Kant, P. K. Bihari, *Res. J. Chem. Sci.* **2013**, 3, 54–59.

16. R. Shukla, V. Barve, S. Padhyeb, R. Bhonde, *Bioorg. Med. Chem. Lett.* **2004**, *14*, 4961–4965. DOI:10.1016/j.bmcl.2004.07.020
17. B. S. Hammes, M. T. Kieber-Emmons, J. A. Letizia, Z. Shirin, C. J. Carrano, L. N. Zakharov, A. L. Rheingold, *Inorg. Chim. Acta* **2003**, *346*, 227–238. DOI:10.1016/S0020-1693(02)01338-5
18. A. Samadi-Maybodi, S. K. H. Nejad-Darzi, R. Akhoondi, *Int. Nano Lett.* **2011**, *1*, 52–58. DOI:10.9734/ACSJ/2014/12703
19. E. Rasu, *Am. Chem. Sci. J.* **2014**, *4*, 983–991. DOI:10.9734/ACSJ/2014/12703
20. Suresh, J. S. Sandhu, *Rasayan J. Chem.* **2011**, *4*, 73–85.
21. A. A. Frutos, L. F. Sala, G. M. Escandar, M. Devillers, J. M. S. Peregrin, M. G. Sierra, *Polyhedron* **1999**, *18*, 989–994. DOI:10.1016/S0277-5387(98)00384-2
22. P. Mishra, *Int. J. ChemTech Res.* **2009**, *1*, 401–419.
23. N. A. Jamaluddin, I. Baba, N. Ibrahim, *J. Anal. Sci.* **2014**, *18*, 251–259.
24. I. I. Ozturk, C. N. Banti, N. Kourkoumelis, M. J. Manos, A. J. Tasiopoulos, A. M. Owczarzak, M. Kubicki, S. K. Hadjikakou, *Polyhedron* **2014**, *67*, 89–103. DOI:10.1016/j.poly.2013.08.052
25. L. - Z. Zhang, G. - Y. An, M. Yang, M. - X. Li, X. - F. Zhu, *Inorg. Chem. Commun.* **2012**, *20*, 37–40. DOI:10.1016/j.inoche.2012.02.009
26. M. Li, Y. Lu, M. Yang, Y. Li, L. Zhang, S. Xie, *Dalton Trans.* **2012**, *41*, 12882–12887. DOI:10.1039/c2dt31256e
27. M. - X. Li, L. - Z. Zhang, M. Yang, J. - Y. Niu, J. Zhou, *Bioorg. Med. Chem. Lett.* **2012**, *22*, 2418–2423. DOI:10.1016/j.bmcl.2012.02.024
28. L. Dawara; S. C. Joshi, R. V. Singh, *Int. J. Inorg. Chem.* **2012**, *1–9*. DOI:10.1155/2012/372141
29. N. Zhang, Y. Tai, M. Li, P. Ma, J. Zhao, J. Niu, *Dalton Trans.* **2014**, *43*, 5182–5189. DOI:10.1039/c4dt00077c
30. Y. Fang, Y. - T. Wang, M. Zhao, Y. - L. Lu, M. - X. Li, Y. - H. Zhang, *Polyhedron* **2018**, *155*, 254–260. DOI:10.1016/j.poly.2018.08.049
31. A. C. Wibowo, S. A. Vaughn, M. D. Smith, H.-C. Z. Loye, *Inorg. Chem.* **2010**, *49*, 11001–11008. DOI:10.1021/ic1014708
32. K.-T. Wong, R.-T. Chen, *Tetrahedron Lett.* **2002**, *43*, 3313–3317. DOI:10.1016/S0040-4039(02)00520-8
33. V. T. Dubinina, D. V. Dyumaeva, S. A. Trashin, M. V. Sedova, A. B. Karpo, V. I. Krasovskii, L. G. Tomilova, *Macroheterocycles* **2012**, *5*, 149–156. DOI:10.6060/mhc2012.120678d
34. F. A. Mohamed, E. A. El-Alfy, *J. Appl. Sci. Res.* **2013**, *9*, 178–183.
35. H. R. Maradiya, *Turk. J. Chem.* **2001**, *25*, 441–450. DOI:10.1515/labm.2001.25.11-12.450
36. H. Z. Shams, R. M. Mohareb, M. H. Helal, A. M. El-Sayed, *Molecules* **2011**, *16*, 6271–6305. DOI:10.3390/molecules16086271
36. S. A. Khan, A. Y. Obaid, L. M. Al-Harb, M. N. Arshad, A. M. Asiri, M. B. Hursthouse, *Int. J. Electrochem. Sci.* **2015**, *10*, 2306–2323. DOI:10.3390/molecules16086271
38. C. S. Lakshmeeshaa, K. R. V. Reddyb, S. Mohan, *Arch. Appl. Sci. Res.* **2011**, *3*, 556–561.
39. A. Mobinkhaleidi, M. Kalhor, L. Taheri, *Asian J. Chem.* **2010**, *22*, 7399–7404.
40. R. R. Zaky, A. M. Abdelghay, *Res. J. Pharm. Bio. Chem. Sci.* **2011**, *2*, 757–764.
41. G. Saravanan, V. Alagarsamy, C. R. Prakash, *Int. J. Pharm. Pharm. Sci.* **2010**, *2*, 83–86.
42. G. M. Reinecke, A. T. Woodrow, *J. Org. Chem.* **1992**, *57*, 1018–1021. DOI:10.1021/jo00029a046
43. J. D. D. Tamokou, M. F. Tala, H. K. Wabo, J. R. Kuate, P. Tane, *J. Ethnopharmacol.* **2009**, *124*, 571–575. DOI:10.1016/j.jep.2009.04.062
44. S. S. Patil, M. M. Shaikh, *Acta Pol. Pharm.-Drug Res.* **2012**, *69*, 679–686.
45. W. Henderson, J. S. McIndoe, *Mass Spectrometry of Inorganic, Coordination and Organometallic Compounds: Tools-Techniques-Tips*, Chichester, UK: John Wiley & Sons, **2005**. DOI:10.1002/0470014318
46. M. K. Kim, V. Jo, S. K. Kim, I. -W. Shim, K. Min Ok, *Bull. Korean Chem. Soc.* **2008**, *29*, 2273–2276.
47. B. G. Sukhov, S. A. Mukha, I. A. Antipova, S. A. Medvedeva, L. I. Larina, N. N. Chipanina, O. N. Kazheva, G. V. Shilov, O. A. Dyachenko, B. A. Trofimov, *Arkivoc* **2008**, *viii*, 139–149.
48. M. G. Djouossi, J. D. D. Tamokou, D. Ngnokam, J. -R. Kuate, L. A. Taponjoui, D. Harakat, L. Voutquenne-Nazabadioko, *BMC Complementary Altern. Med.* **2015**, *15*, 1. DOI:10.1155/2013/315972 8. DOI:10.1186/s12906-015-0660-1
49. M. Thankamony, K. Mohanan, *Indian J. Chem.* **2007**, *46A*, 247–251.
50. M. Rizzotto, in: Bobbarala V (Eds.), *A Search for Antibacterial Agents*, InTech, Croatia, **2012**, pp. 80–81. DOI:10.5772/1085

Povzetek

Sintetizirali smo nov bizmutov(III) kompleks z 2-amino-3-karbometoksi-4,5,6,7-tetrahidrobenzo[b]tiofenom (ACTT) kot ligandom. Spojina je bila okarakterizirana na podlagi IR, NMR, elementne analize in MS. Ligand je enovezno koordiniran na kovinski ion preko dušikovega atoma ter vodi do nastanka kompleksa $[\text{Bi}^{\text{III}}(\text{ACTT})_6]\text{Cl}_3$. Spojina izkazuje izrazito protimikrobno aktivnost (MIC = 8–32 $\mu\text{g}/\text{mL}$) proti *Bacillus subtilis*, *Staphylococcus aureus*, *Escherichia coli*, *Pseudomonas aeruginosa*, *Shigella flexneri*, *Candida albicans*, *Candida tropicalis* in *Cryptococcus neoformans*.



Except when otherwise noted, articles in this journal are published under the terms and conditions of the Creative Commons Attribution 4.0 International License

Scientific paper

Electrooxidation and Low-tech Determination of Pantoprazole on a Disposable Pencil Graphite Electrode by the use of Cationic Surfactant

Pınar Talay Pinar

Van Yuzuncu Yil University, Faculty of Pharmacy, Department of Analytical Chemistry, 65080 Van, Turkey

* Corresponding author: E-mail: pitalay@gmail.com

Tel: 90 505 7649740

Received: 06-28-2019

Abstract

The electrochemical oxidation of pantoprazole, a selective proton pump inhibitor, was studied in aqueous as well as aqueous/surfactant media at a disposable pencil graphite electrode using cyclic and adsorptive stripping voltammetric techniques. The sensitivity of the stripping voltammetric measurements was significantly improved when the cationic surfactant, cetyltrimethylammonium bromide (CTAB) was present in the neutral electrolyte solution. For analytical purposes, well resolved voltammetric peaks at +1.05 V (versus Ag/AgCl) were obtained in Britton-Robinson buffer at pH 7.0 containing 3×10^{-4} M CTAB using square-wave stripping mode (after 30 s accumulation at open-circuit condition). The process could be used to determine pantoprazole concentrations in the range of 2.4×10^{-8} – 7.1×10^{-7} M (9.2 – $272 \mu\text{g L}^{-1}$) with a detection limit of 7.0×10^{-9} M ($2.7 \mu\text{g L}^{-1}$). The proposed method was applied to the determination of pantoprazole in pharmaceutical formulation and in the spiked human urine samples with acceptable recoveries.

Keywords: Pantoprazole; stripping voltammetry; pencil graphite electrode; cationic surfactant; drug; human urine

1. Introduction

Pantoprazole (PAN) (Fig. 1) is a substituted benzimidazole derivative which belongs to proton pump inhibitors (PPI). PAN inhibits the acid secretion in the stomach via the specific effect on proton pumps of parietal cells. It was developed for the treatment of acid-related gastrointestinal disorders. PAN is a weak base that is converted to its active form by gastric acid before affecting on the proton pump. The stability of the compound in aqueous solution is pH-dependent. Its degradation rate increases with decreasing pH. At ambient temperature, the degradation half-life is approximately 220 h at pH 7.8 while it is approximately 2.8 h at pH 5.0. PAN is extensively metabolized in the liver. The main serum metabolite is formed by demethylation at the 4-position of the pyridine ring, followed by conjugation with sulphate.^{1–4}

Several techniques have been developed to estimate PAN in its bulk form, pharmaceutical and biological matrices, including liquid chromatography with different detectors,^{5–12} UV-spectrophotometry,^{13–15} and capillary electrophoresis.^{16,17}

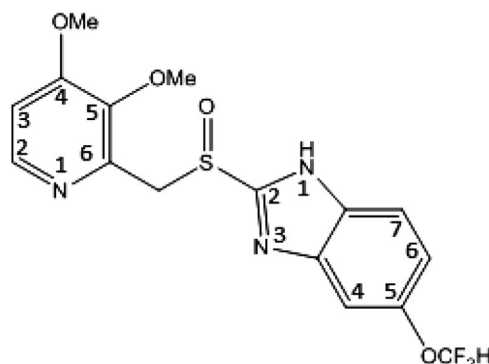


Figure 1. Structure of pantoprazole

Electrochemical assays such as voltammetric methods have been widely used for drug analysis due to their sensitivity, simplicity, cheapness and rapidity. In some studies, hanging mercury drop electrode was applied to the determination of PAN based on its electrochemical reduction.^{18–20} The literature survey states that various bare solid electrodes such as carbon paste electrode,²¹ glassy

carbon electrode,^{22,23} edge-plane pyrolytic graphite electrode,²⁴ and pencil graphite electrode^{25,26} have been exploited for determination of PAN using its oxidative behaviors. On the other hand, some other papers published recently involve the use of modified electrodes for its voltammetric quantification.^{27–29} The analytical performance of the reported electrodes will be discussed later in detail.

In recent years, pencil graphite electrodes (PGEs) have been successfully applied to the electroanalysis of various types of inorganic and organic compounds from very different matrices. In this manner, commercially available graphite pencil leads have been used as electrode materials which present high electrochemical reactivity, good mechanical stability, disposability, low cost, low technology, and ease of modification.^{30–32} The pencil leads are produced by dispersion of natural graphite (major component) into a mixture of clay and polymeric wax followed by heat treatment. Their hardness is commercially modified by varying the graphite and clay ratios. The selection of the correct pencil hardness is also important in the analysis carried out by using PGE.³³

On the other hand, the adsorption features of surfactants can modify and control the properties of electrode surface, and consequently enhance the sensitivity and selectivity of electrochemical response. Additionally, the medium containing surfactant can prevent electrode from fouling.^{34,35}

Keeping the above knowledge in mind, the goal of the current work is to throw more light upon the oxidation behavior of PAN on a PGE. The analytical performance of proposed method will also be demonstrated in the presence of cationic surfactant (cetyltrimethylammonium bromide, CTAB), and applied on quantification of PAN in pharmaceutical and urine samples. Although, in a very recent paper, the voltammetric determination of PAN has been studied on PGE in weakly acid/anionic surfactant solution,²⁶ this approach reports the electrochemical investigation of PAN on the same electrode in the case of neutral solution containing cationic surfactant to enhance the stability of the compound.

2. Experimental

2.1. Chemicals and Apparatus

PAN (as sodium sesquihydrate salt) standard was purchased from Sigma. Tablet dosage form containing the active compound was procured from local pharmacy. Standard stock solutions of PAN (2.4×10^{-3} M) were prepared daily in methanol/water (1:1, v/v) mixture, and kept refrigerated when not in use. All other chemicals used in this study were of reagent grade, and their solutions were prepared in distilled water except uric acid (prepared in 0.1 M sodium hydroxide). Britton-Robinson (BR) buffer solutions (equal volumes of acetic acid, phosphoric acid and boric acid (each 0.04 M) were mixed, and adjusted to

the desired pH between 3.0–10.0 with 3 M NaOH) were used for preparing more diluted solutions of PAN. The surfactants tested were anionic type, sodium dodecylsulfate (SDS), and cationic type, cetyltrimethylammonium bromide (CTAB). They were prepared by dissolving the necessary quantity of reagent in water. Ultra pure water, purified by a Milli-Q system from Millipore, was used to prepare the solutions. All experiments were carried out at the room temperature of the laboratory.

All the voltammetric measurements of cyclic voltammetry (CV) and square-wave adsorptive stripping voltammetry (SW-AdSV) were operated using an Autolab electrochemical analyzer (Metrohm, The Netherlands) controlled with the NOVA 2.1.3 version. A three-electrode-system in a 10-mL one-compartment voltammetric cell was employed consisting of a PGE as working electrode, an Ag/AgCl (3 M NaCl, MF 2012, BASi) as reference electrode, and a Pt wire (MW 1032, BASi) as auxiliary electrode.

For the preparation of PGE,³⁶ a mechanical pencil Model T 0.5 (Rotring, Germany) used as a holder, and pencil leads (Tombo, Japan) with a total length of 60 mm and a diameter of 0.5 mm were purchased from a local bookstore. The electrical contact of the lead was carried out by wrapping a metal wire around the metallic part of the pencil. A total of 7 mm of lead was immersed in solution per measurement. The surface of PGE was pretreated by applying a potential of +1.40 V for 30 s in supporting electrolyte without stirring in order to increase effective surface area of the electrode and typical characteristic of electron transfer. Each measurement was performed using a new pencil surface.

2.2. Sample Preparation

Protonex[®] enteric-coated tablets containing 45.10 mg of PAN sodium sesquihydrate (equivalent to 40 mg PAN), were used in analytical application for this study. Ten tablets were weighed and the average mass per tablet was calculated. The tablets were thoroughly crushed in a porcelain mortar. An adequate amount of the resulting powder was transferred into a 25-mL calibrated dark flask, filled to the mark with a mixed solution of methanol and water (1:1, v/v), and sonicated for about 30 min to achieve the complete dissolution. An aliquot of the supernatant liquid was transferred to the voltammetric cell containing 10 mL of BR buffer, pH 7.0 in the presence of 3×10^{-4} M CTAB.

Drug-free human urine samples were collected from healthy donor (male, age 25 years) before the day of the experiment. 4.90 mL of acetonitrile and 0.1 mL of PAN stock solution (2.4×10^{-3} M) were mixed and completed to 10 mL with the urine sample. The tube was vortexed for about 3 min and then centrifuged at 4500 rpm for 5 min. Appropriate volume of the final mixture was transferred into the voltammetric cell containing 10 mL of same supporting electrolyte mentioned above. All experiments were examined in triplicate, and quantification of PAN

was used by the standard addition method to decrease matrix effects from the urine components.

3. Results and Discussion

At first, CV technique was used at different scan rates to test commercially available pencil leads as tools for the working electrodes. Fig. 2 shows the CV responses of PGE in 0.5 M KCl in the presence of 10 mM $K_3Fe(CN)_6$ as a redox probe. The electroactive surface area of PGE was evaluated by using Randles-Sevcik formula (1).³⁷

$$i_p = (2.69 \times 10^5) n^{3/2} A D_0^{1/2} \nu^{1/2} C_0 \quad (1)$$

where i_p refers to the anodic peak current, n is the number of electrons transferred, A is the dynamic surface area of electrode, D_0 is the diffusion coefficient, ν is the scan rate, and C_0 is the concentration of $K_3Fe(CN)_6$. From the slope of the plot of i_p vs. $\nu^{1/2}$ (Fig. 2), the dynamic surface area of electrode was calculated to be 0.078 cm² for PGE.

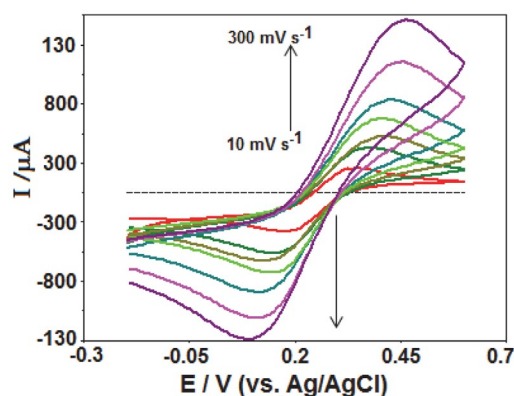


Figure 2. Electroactive surface area of PGE evaluated using cyclic voltammetry. Scan rate; 10–300 mV s⁻¹.

In order to investigate the electrochemical response of PAN at PGE, the experiments were initially executed by means of CV at a scan rate of 100 mV s⁻¹ in BR buffer at pH 7.0 (most suitable medium for analytical purposes, as shown later). As can be seen in Fig. 3, the three consecutive CVs were recorded for 2.4×10^{-5} M PAN within the potential window from +0.5 V to +1.4 V. A cyclic voltammogram without PAN was also plotted in the graphs for comparison. PAN was oxidized in the medium yielding one main oxidation peak (presented as I) at +1.04 V. The presence of barely detectable secondary process (presented as II) was also observed at about +1.2 V (observed more clearly on the original curves). Although such a kind of behavior was described for the oxidation of PAN at pH > 6 on carbon paste electrode,²¹ however, the second oxidation step has not been reported in earlier studies performed by using the bare and modified PGEs. The absence of any peak in the cathodic direction indicates that the oxidation process is irreversible.

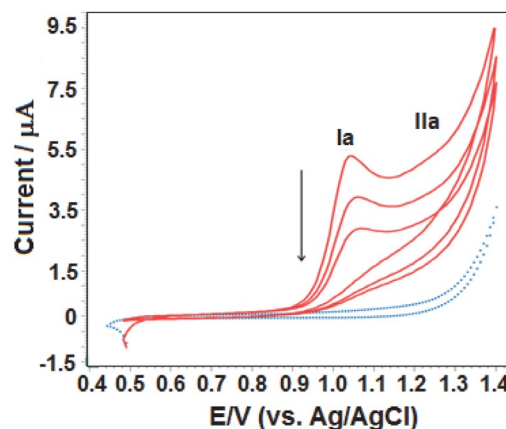


Figure 3. The repetitive cyclic voltammograms of 2.4×10^{-5} M pantoprazole in BR buffer, pH 7.0 at scan rate of 100 mV s⁻¹. Electrode, PGE. Dashed lines represent background current.

From the figure, it is seen that the current intensity of oxidation peak showed a decrease during the successive scans, which may be due to the adsorption of PAN and/or its oxidation products that occurs on the electrode surface.

To examine the influence of scan rate between 25 and 600 mV s⁻¹ on anodic oxidation peak current and potential of PAN, CVs of 2.4×10^{-5} M PAN were recorded in BR buffer at pH 7.0 (Fig. 4). By increasing the scan rate, there was a slight shift of the oxidation peak potentials towards more positive values, confirming that this behavior is characteristic for irreversible processes.³⁸ As seen in Fig. 4, the response of secondary oxidation step IIa was increased at scan rate of 400 mV s⁻¹.

Since the primary oxidation step Ia was sharper and easily measurable, the parameters of this step were determined for further studies.

There was a linear relationship between the oxidation peak current (i_p) and scan rate (ν), which reveals that the electrode process is surface-controlled. The equation is noted below:

$$i_p (\mu A) = 0.015 \nu (\text{mV s}^{-1}) + 0.75 \quad (n = 6; r = 0.998) \quad (2)$$

In order to better understand the PAN oxidation onto PGE, plots were constructed between the logarithm of peak current ($\log i_p$) and logarithm of scan rate ($\log \nu$). In this case, it was also obtained a linear relationship according to the following equation:

$$\log i_p (\mu A) = 0.710 \log \nu (\text{mV s}^{-1}) - 1.017 \quad (n = 6; r = 0.995) \quad (3)$$

As can be seen from the equation, the value of the slope is between the theoretical value of 0.5 for diffusion- and 1.0 for adsorption-controlled process.³⁷ These facts indicate that PAN oxidation process is controlled by adsorption at PGE.

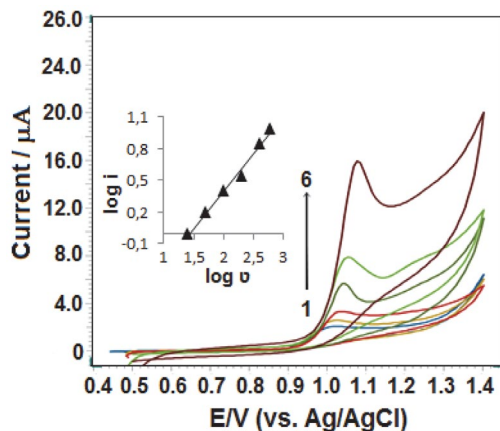


Figure 4. The cyclic voltammograms of 2.4×10^{-5} M pantoprazole in BR buffer, pH 7.0 at different scan rates (1⁻⁶: 25, 50, 100, 200, 400, 600 mV s⁻¹). Electrode, PGE. Inset depicts the plot of $\log i$ vs. $\log v$.

In the light of above outcomes, AdSV studies were performed with an accumulation step to investigate the PAN oxidation process at different pHs. In Fig. 5, this parameter was established in the range from pH 3.0–10.0 of BR buffer by carrying out stripping measurement on 2.4×10^{-6} M PAN, with an open-circuit accumulation at 30 s. It should be noted that at pH values lower than 3.0, well-defined peak shapes were not observed which could be due to the instability of PAN and its decomposition to other degradation products. The plot of the E_p versus pH (Fig. 5, inset) showed a straight line between pH 3.0 and 7.0, which can be expressed by the following equation:

$$E_p \text{ (V)} = -0.062\text{pH} + 1.50 \quad (n = 5; r = 0.993) \quad (4)$$

The slope of this equation was found to be -62 mV/pH units, which is close to the theoretical value of -59 mV. This finding shows that the numbers of electrons and protons participating in the electrode reaction are equal. As can be seen from the figure, the pH did not indicate a significant change in the peak potential between pH 7.0 and 8.0. After that, the peak potential shifted slightly to less positive potential value with increasing pH up to 9.0, and then did not change again remarkably. The intersection point of the curves (\sim pH 7.0 and 8.0) is close to the pK_{a3} (will be given later), and it can be explained by changes in protonation of the acid-base functional groups in the benzimidazole moiety. On the other hand, the clear change in the peak intensity was also observed at about pH 7.0. From the above results, and considering the report dealing with the electrochemical oxidation of a structurally related compound omeprazole at glassy carbon electrode,³⁹ we may assume that the primary oxidation step Ia represents one-electron and one-proton process of PAN to the formation of hydroxylated species.

Since the highest response ($11.33 \mu\text{A}$) was obtained at pH 7.0 with the peak potential of $+1.06$ V, this condition

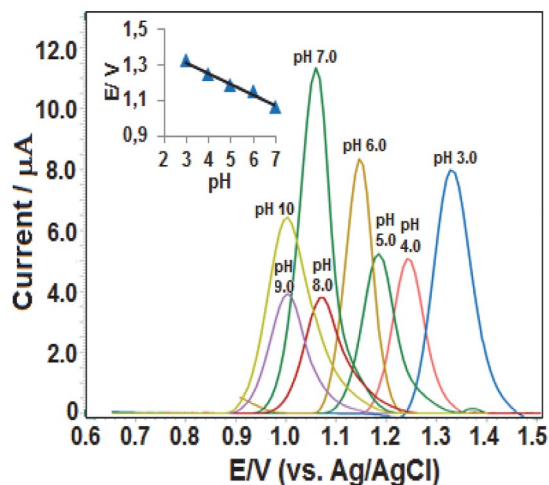


Figure 5. The stripping voltammograms of 2.4×10^{-6} M pantoprazole in BR buffer, pH 3–10. Electrode, PGE. AdSV conditions: accumulation time 30 s at open-circuit condition. SWV parameters: frequency, 50 Hz; step potential, 8 mV; pulse amplitude, 30 mV. Inset depicts the plot of E_p vs. pH.

was selected for further experiments and development of the methodology.

Taking into account the noticeable adsorptive features of PAN at the surface of PGE, the attention was then turned to the effect of pre-concentration/stripping conditions to enhance the sensitivity of analytical methodology. The influence of the accumulation time (t_{acc}) upon the oxidation peak signal was examined in the range 0 – 240 s at open-circuit condition for 2.4×10^{-6} M PAN in BR buffer pH 7.0 (data not shown). The intensity of oxidation peak current increased gradually with t_{acc} until 30 s beyond which the peak current remained nearly constant. This result shows that the electrode surface is saturated with PAN molecules. Next, the dependence of the stripping peak current on E_{acc} was evaluated at open-circuit conditions and over the potential range $+0.1$ to $+0.6$ V with t_{acc} of 30 s. The maximum peak current was achieved at the potential of the open-circuit condition. Therefore, t_{acc} and E_{acc} of 30 s and open-circuit condition were applied in succeeding analytical investigations.

In the following step, to optimize the experimental set-up for PAN determination, the dependence of stripping responses on other parameters such as frequency ($f = 15$ – 125 Hz), scan increment ($\Delta E_s = 4$ – 12 mV) and pulse amplitude ($\Delta E_{sw} = 10$ – 60 mV) were analyzed. Taking into account the repeatability, baseline stability, accuracy, and magnitude of the analytical signal at the PGE for PAN determination, optimal values of f , 50 Hz; ΔE_s , 8 mV; and ΔE_{sw} , 50 mV were obtained.

Finally, the effects of cationic (positively charged) surfactant, CTAB, and anionic (negatively charged) one, SDS were also evaluated on the ease of the oxidation of PAN. Keeping the PAN concentration constant at 2.4×10^{-7} M, surfactants were added to BR buffer, pH 7.0 having different concentrations in the range from 1×10^{-5} M to 5

$\times 10^{-4}$ M. When the solution contained cationic-CTAB, PAN stripping peak current increased with CTAB concentration up to 3×10^{-4} M, after this concentration value a decrease in oxidation peak current was remarked (data not shown). Whereas the electrolyte solution containing anionic-SDS, the peak current was found to decrease with a shift slightly towards more positive values. Fig. 6 shows comparison of stripping voltammograms in the presence of CTAB and SDS having concentrations of 3.0×10^{-4} M and 4.0×10^{-4} M, respectively, at which maximum peak intensities were obtained. To sum up, the concentration of CTAB at 3×10^{-4} M was chosen for the rest of present analytical investigation. In this case, PAN signals were almost 2.5 times higher than those obtained in surfactant-free solution.

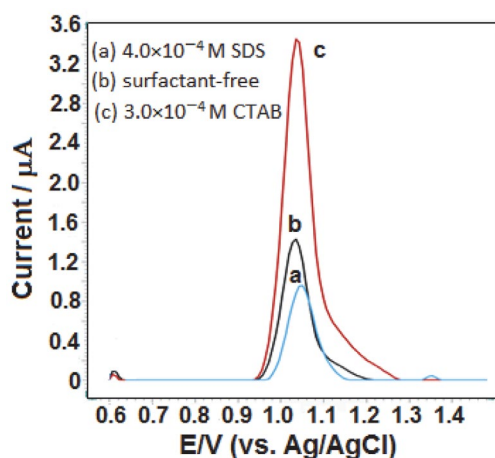


Figure 6. The stripping voltammograms of 2.4×10^{-7} M pantoprazole in BR buffer, pH 7.0 in the absence and presence of surfactants. Electrode, PGE. AdSV conditions: accumulation time 30 s at open-circuit condition. SWV parameters: frequency, 50 Hz; step potential, 8 mV; pulse amplitude, 50 mV.

The estimated pK_a values of PAN have been reported to be $pK_{a1} \approx 0.11$ (for the protonation of the benzimidazole N3), $pK_{a2} \approx 3.9$ (for the protonation of the N-pyridine), $pK_{a3} \approx 8.2$ (for the deprotonation of the benzimidazole-NH).^{40,41} Thus the compound can exist in four different ionic forms in aqueous electrolytes such as dicationic, cationic, neutral, and anionic species. The previously published papers reported that dicationic form of structurally related PPIs is very unstable.⁴² In studied condition (at pH 7.0), PAN molecule exists as a mixture of uncharged (~75%) and partly negatively charged (~25%) forms. Considering the critical micelle concentration of CTAB, $CMC_{CTAB} = 8.7 \times 10^{-4}$ M,⁴³ at relatively higher concentration of surfactant (in our case 3×10^{-4} M) added to the solution, the surface micelles are formed on the electrode surface. Therefore, it is expected that adsorption on the electrode surface is mainly maintained by hydrophobic interaction between neutral PAN molecules (~75%) and long hydrophobic tails of CTAB which dominates the co-adsorption of PAN with CTAB on PGE surface. Addition-

ally, the electrostatic interaction between negatively charged PAN molecules (~25%) and oppositely charged head groups of the CTAB may also occur. Thus, these strong interactions result in a maximum increase in analytical signal. In the case of anionic-SDS, the electrostatic force works in the opposite direction, thus causes the decrease of peak intensity.

It is also important to underline that in a previous study published very recently,²⁶ the voltammetric determination of PAN have been carried out using PGE in supporting electrolyte solutions at pH 6.0 containing anionic surfactant, SDS. In that study, the nature of the interaction between PAN and SDS molecules was ascribed to the effect of electrostatic PAN-SDS. However, at pH 6.0 neutral form of PAN predominates in the supporting electrolyte. In this case, the hydrophobic interactions between PAN and SDS are more pronounced comparing to the electrostatic attractive interaction. The authors reported that in the presence of cationic and non-ionic surfactants, the increase with different degrees in the peak currents was also observed as compared with the value obtained in their absence. These results provide further evidence that the hydrophobicity of PAN induce interaction with all kinds of surfactants that possess a long-chain hydrophobic group.

After optimization of chemical conditions and instrumental parameters, PGE combined with SW-AdSV could allow for analyzing PAN in BR buffer, pH 7.0 containing 3×10^{-4} M CTAB. The stripping responses given in Fig. 7 displayed that the dependence of oxidation peak currents on the PAN concentration was linear, in the range of 2.4×10^{-8} – 7.1×10^{-7} M (9.2 – $272 \mu\text{g L}^{-1}$). The oxidation peak current at a potential of +1.05 V increased continually with its concentration (Fig. 7, inset) to yield a highly linear calibration plot; $i_p (\mu\text{A}) = 27.477 C (\mu\text{M}) + 0.223$ ($r = 0.999$, $n = 7$), where i_p is the stripping peak current, C the

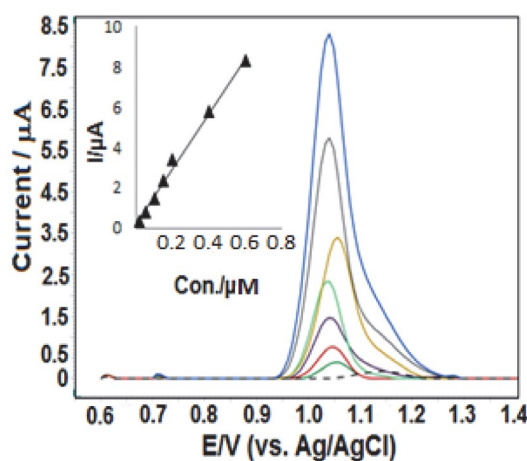


Figure 7. The stripping voltammograms for pantoprazole levels of (1) 0.024, (2) 0.06, (3) 0.12, (4) 0.19, (5) 0.24, (6) 0.48 and (7) 0.71 μM in BR buffer, pH 7.0 in the presence of 3×10^{-4} M CTAB. Dashed lines represent background current. Inset depicts a corresponding calibration plot for the quantitation of pantoprazole. Other operating conditions as indicated in Fig. 6.

Table 1. Comparison of the analytical performance of PGE for the determination of pantoprazole with literature electrodes.

Electrode	Supporting electrolyte	Technique	LOD (M)	Sample	Ref.
HMDE	BR, pH 7.0	SW-AdCSV	5.0×10^{-10}	Pharmaceuticals	18
HMDE	BR, pH 5.0	SWV	1.3×10^{-7}	Pharmaceuticals, human plasma	19
SbF/GCE	BR, pH 5.0	SWV	9.1×10^{-7}	Pharmaceuticals	20
CPE	BR, pH 4.0	DP-AdSV	2.0×10^{-8}	Pharmaceuticals	21
GCE	BR, pH 5.0	DPV	4.0×10^{-7}	Pharmaceuticals, human plasma	22
GCE	BR, pH 8.0	DPV	3.7×10^{-7}	Pharmaceuticals, human urine	23
		SWV	1.8×10^{-7}	Anodized EPPG	
	BR, pH 5.0	DPV	4.1×10^{-9}	Pharmaceuticals, human urine	24
PGE	BR, pH 7.0	Complexation based SW-AdSV	4.0×10^{-11}	Rabbit plasma	25
PGE	BR, pH 6.0 + SDS	SW-AdSV	2.0×10^{-9}	Rabbit plasma	26
EBT/PGE	BR, pH 7.0	SW-AdSV	1.2×10^{-8}	Human serum	27
BCG/PGE	BR, pH 7.0	SW-AdSV	2.2×10^{-8}	Pharmaceuticals, rabbit plasma	28
SWCNTs/CPE	PBS, pH 7.0	SWV	4.9×10^{-10}	Pharmaceuticals, human serum	29
PGE	BR, pH 7.0 + CTAB	SW-AdSV	7.0×10^{-9}	Pharmaceuticals, human urine	This work

Electrode: HMDE, hanging mercury drop electrode; CPE, Carbon paste electrode; GCE, glassy carbon electrode; EPPG, Edge-plane pyrolytic graphite; PGE, pencil-graphite electrode; SbF/GCE, antimony film glassy carbon electrode; EBT/PGE, poly(eriochrome black T) modified pencil graphite electrode; BCG/PGE, poly(bromocresol green) modified pencil-graphite electrode; SWCNTs/CPE, single-walled carbon nanotube modified carbon paste electrode **Supporting electrolyte:** BR, Britton-Robinson buffer; PBS, phosphate buffer solution; SDS, sodium dodecylsulfate; CTAB, cetyltrimethylammonium bromide **Technique:** SW-AdCSV, square-wave adsorptive cathodic stripping voltammetry; SWV, square-wave voltammetry; DP-AdSV, differential pulse adsorptive stripping voltammetry; DPV, differential pulse voltammetry; SW-AdSW, Square-wave adsorptive stripping voltammetry

PAN concentration, r the correlation coefficient, and n the number of experiments.

From this plot obtained by the analytical curves, the limit of detection (LOD) and quantification (LOQ) were calculated using the formulae $3.3 s/m$ and $10 s/m$, respectively, where s is the standard deviation of the response of the lowest concentration of the linearity range (three replicate measurements), and m the slope of the related calibration equation. By using these formulae, the LOD and LOQ were found to be 7.0×10^{-9} M ($2.7 \mu\text{g L}^{-1}$) and 2.1×10^{-8} M ($8.1 \mu\text{g L}^{-1}$), respectively.

Table 1 compares the analytical performance of the PGE with some electrodes (mercury, carbon-based modified and unmodified ones) in previously published papers.

From these data, it can be seen that some electrodes^{19,20–23,27,28} reported in literature declare lower sensitivity than the PGE (used in this study). However, PGE showed a less sensitive voltammetric response than some mercury¹⁸ and carbon-based^{24,25,29} electrodes. Despite the higher sensitivity of HMDE, because of its toxicity mercury electrodes are not environmentally friendly. On the other hand, modified carbonaceous electrodes have a long-time preparation, poor reproducibility, and high costs. Slightly lower LOD value was found for the PGE in acidic/anionic-SDS media (previous study)²⁶ than in the presence of cationic-CTAB (this work). However, the measurement in neutral solutions reduces the risk of decomposition of PAN.

The precision of the developed method was calculated by intra-day repeatability (six experiments within the same day) and inter-day repeatability (three assays for five days from different solutions) by successive measurements of 6.0×10^{-8} M PAN. The relative standard deviation (RSD) values were 2.56% (peak current) and 1.09% (peak potential) for intra-day repeatability, and 3.57% (peak current) and 1.65% (peak potential) for inter-day repeatability.

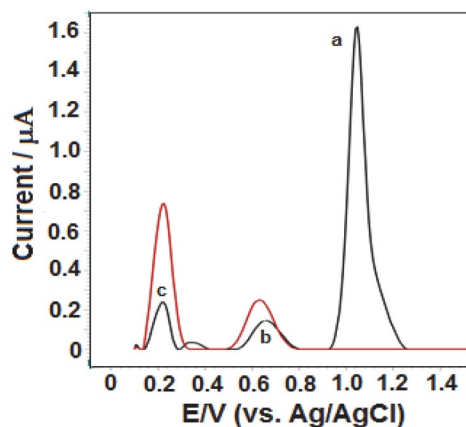


Figure 8. The stripping voltammograms of 1.2×10^{-7} M pantoprazole (a) in the presence of 6.0×10^{-7} M uric acid (b) and 5.3×10^{-7} M dopamine (c). Red line represents the mixture solutions of uric acid at the same concentrations. Supporting electrolyte, BR buffer, pH 7.0 in the presence of 3×10^{-4} M CTAB. Other operating conditions as indicated in Fig. 6.

Taking into account that PAN is fairly unstable at low pHs, working solutions prepared in acidic medium were run and analyzed during a maximum period of 1 h.

The possible interferences of some compounds commonly found in pharmaceutical samples were evaluated via the electrochemical oxidation of 1.2×10^{-7} M PAN in BR buffer solution, pH 7.0. A 10-fold excess of inorganic ions such as K^+ , Na^+ , Ca^{2+} , Cl^- , and I^- , and sugars such as glucose and fructose did not significantly influence the current response of PAN (data not shown).

The interferences of commonly identified biomolecules in urine, such as uric acid (6.0×10^{-7} M) and dopamine (5.3×10^{-7} M) were tested for 1.2×10^{-7} M PAN, and the corresponding stripping curves are depicted in Fig. 8. The oxidation peaks of dopamine and uric acid appeared at about +0.23 and +0.63 V, respectively, thus insignificantly affecting the oxidation signal of PAN at +1.05 V. Taking the results together, the developed method for PAN determination could also be applied to analyze urine samples.

In the light of above findings, proposed methodology was applied to analyze the content of PAN in commercially available tablet form by using calibration method. Samples were prepared as described in the experimental section, without extraction, evaporation or filtration, and adequately diluted. For this formulation, the assay results were in good agreement with the declared content (Table 2). In order to detect the interaction between the excipients and PAN, recovery studies were carried out adding standard PAN solutions to the sample solution in voltammetric cell and followed by analysis using the proposed method. Recovery of PAN was calculated by comparing the concentration obtained from the spiked mixtures with those of the pure compound. As seen in Table 2, the results indicate the absence of matrix interference effect in tablet dosage forms.

Table 2. Pantoprazole content and mean recoveries in tablet dosage form (Protonex® tablets) obtained by SW-AdSV

Labelled claim/mg	40
Amount found ^a /mg	41.05
RSD %	2.8
Bias %	-2.6
Average recovery ^b %	102
RSD of recovery %	3.7
Bias %	-2.0

^a Mean of five experiments ^b Mean of three experiments

The satisfactory analytical sensitivity of the proposed method was also tested in urine sample that is a more complex matrix in comparison with pharmaceutical formulations. To eliminate the effect of interfering substances such as proteins, the urine samples were first treated with acetonitrile, and centrifuged. The determination of PAN in the spiked urine sample was performed by means of the standard addition method (data not shown). An oxidation peak appeared at about +1.07 V which could be due to the oxidation of PAN since its peak current increased after each standard addition of this compound. In the absence of PAN, there were no detectable oxidation peaks in the working potential range where the analytical peak was observed. On the other hand, an unknown oxidation peak at about +0.65 V was observed in blank urine samples due to the oxidation of uric acid. As can be seen in Table 3, the acquired result is consistent with the added amount of PAN, and satisfactory recovery and RSD are the evidence of the accuracy of the method.

4. Conclusion

In the present study, a new electrochemical methodology using modification-free PGE in aqueous and aqueous/surfactant solutions was established, which was rapid, simple, precise, accurate, and having lower risk of decomposition errors. The proposed method was applicable directly to the routine quality control of pharmaceutical formulation after dissolution of the samples, eliminating any use of organic reagents or expensive apparatus. The presented study was also intended to show the possibility of monitoring PAN in human urine samples.

5. References

1. R. Huber, M. Hartman, H. Bliesath, R. Lühmann, and V. W. Steinijans, *Int. J. Clin. Pharmacol. Ther.* **1996**, *35*, 185–194.
2. J. M. Shin, N. Kim, *J. Neurogastroenter. Mot.* **2013**, *19*, 25–35. DOI:10.5056/jnm.2013.19.1.25
3. Q. B. Cass, A. L. G. Degani, N. M. Cassiano, J. Pedrazolli, *J. Chromatogr B* **2002**, *766*, 153–160. DOI:10.1016/S0378-4347(01)00472-8
4. C. J. Shih, Y. T. Chen, S.M. Ou, S. Y. Li, T. J. Chen, S. J. Wang, *Int. J. Cardiol.* **2014**, *177*, 292–297. DOI:10.1016/j.ijcard.2014.09.036

Table 3. The results for addition and recovery of pantoprazole from urine sample using SW-AdSV.

Added/($\mu\text{g mL}^{-1}$)	Found ^a /($\mu\text{g mL}^{-1}$)	Recovery ^a % \pm RSD%
0.025	0.024	96.00 \pm 4.27
0.050	0.048	96.00 \pm 3.90

^a Calculated by the use of standard addition method. Values reported are the average of three independent analysis of the same sample.

5. O. Peres, C. H. Oliveira, R. H. Barrientos-Astigarraga, V. M. Rezende, G. D. Mendes, G. Nucci, *Arzneimittelforschung* **2004**, *54*, 314–319. DOI:10.1055/s-0031-1296977
6. B. Patel, M. Patel, J. Patel, B. Suhagia, *J. Liq. Chrom. Rel. Technol.* **2007**, *30*, 1749–1762. DOI:10.1080/10826070701360368
7. S. Thanikachalam, M. Rajappan, V. Kannappan, *Chromatographia* **2008**, *67*, 41–47. DOI:10.1365/s10337-007-0452-y
8. O. Rahić, E. Vranić, I. Mujezin, J. Hadžiabdić, A. Elezović, *Int. J. Pharm. Teach. Prac.* **2013**, *4*, 793–796.
9. S. Pandey, P. Pandey, D. Mishra, U. K. Singh, *Braz. J. Pharm. Sci.* **2013**, *49*, 175–184. DOI:10.1590/S1984-82502013000100019
10. P. Zhao, M. Deng, P. Huang, J. Yu, X. Guo, L. Zhao, *Anal. Bioanal. Chem.* **2016**, *408*, 6381–6392. DOI:10.1007/s00216-016-9753-z
11. J.B. Nagavi, H. Joshi, B. Gurupadayya, *Int. J. Pharm. Res. Health Sci.* **2018**, *6*, 2690–2700.
12. V. Srinandan, K. Nagappan, S. Patel, K. Yamjala, G. Byran, B. Babu, *Curr. Pharm. Anal.* **2019**, *15*, 17–23. DOI:10.2174/1573412914666180101142646
13. I. Süslü, S. Altınöz, E. Yıldız, *FABAD J. Pharm. Sci.* **2003**, *28*, 85–92.
14. F. Salama, N. Abasawy, S. A. A. Razeq, M. M. F. Ismail, M. M. J. Fouad, *J. Pharm. Biomed. Anal.* **2003**, *33*, 411–421. DOI:10.1016/S0731-7085(03)00233-4
15. N. K. Ramadan, N. A. El-Ragehy, M. T. Ragab, B. A. El-Zeany, *Spectrochim. Acta A Mol. Biomol. Spectrosc.* **2015**, *137*, 463–470. DOI:10.1016/j.saa.2014.09.003
16. J. Guan, F. Yan, S. Shi, S. Wang, *Electrophoresis* **2012**, *33*, 1631–1636. DOI:10.1002/elps.201100650
17. G. Hancu, L. A. Papp, A. Rusu, *Chromatographia* **2015**, *78*, 279–284. DOI:10.1007/s10337-014-2827-1
18. A. Radi, *J. Pharm. Biomed. Anal.* **2003**, *33*, 687–692. DOI:10.1016/S0731-7085(03)00356-X
19. S. Altınöz, I. Suslu, *Anal. Lett.* **2005**, *38*, 1389–1404. DOI:10.1081/AL-200062195
20. B. Nigovic, S. B. Hocevar, *Electrochim. Acta* **2013**, *109*, 818–822. DOI:10.1016/j.electacta.2013.07.173
21. A. Radi, *Il Farmaco* **2003**, *58*, 535–539. DOI:10.1016/S0014-827X(03)00082-X
22. N. Erk, *Anal. Biochem.* **2003**, *323*, 48–53. DOI:10.1016/j.ab.2003.08.023
23. A. M., Elsied, G. G. Mohamed, *Int. J. Electrochem. Sci.* **2015**, *10*, 7147–7158.
24. M. Hadi, A. Ehsani, S. Afr. *J. Chem.* **2016**, *69*, 79–87. DOI:10.17159/0379-4350/2016/v69a10
25. P. Y. Khashaba, H. R. H. Ali, M. M. El-Wekil, *Electroanalysis* **2017**, *29*, 890–897. DOI:10.1002/elan.201600639
26. P. Y. Khashaba, H. R. H. Ali, M. M. El-Wekil, *J. Anal. Chem.* **2019**, *74*, 609–616. DOI:10.1134/S106193481906008X
27. P. Y. Khashaba, H. R. H. Ali, M. M. El-Wekil, *Mat. Sci. Eng. C* **2017**, *75*, 733–741. DOI:10.1016/j.msec.2017.02.092
28. P. Y. Khashaba, H. R. H. Ali, M. M. El-Wekil, *R. Soc. Open Sci.* **2017**, *4*, 170324–170337. DOI:10.1098/rsos.170324
29. P. Manjunatha, Y. Arthoba Nayaka, H. T. Purushothama, R. O. Yathisha, M. M. Vinay, *Ionics* **2019**, *25*, 2297–2309. DOI:10.1007/s11581-018-2624-1
30. I. G. David, D.-E. Popa, M. Buleandra, *J. Anal. Meth. Chem.* **2017**. DOI:10.1155/2017/1905968
31. A.-N. Kawde, N. Baig, M. Sajid, *RSC Adv.*, **2016**, *6*, 91325–91340. DOI:10.1039/C6RA17466C
32. M. R. Akanda, M. Sohail, M. A. Aziz, A.-N. Kawde, *Electroanalysis* **2016**, *28*, 408–424. DOI:10.1002/elan.201500374
33. R. Vittal, H. Gomathi, K. Kim, *Adv. Colloid Interface Sci.* **2006**, *119*, 55–68. DOI:10.1016/j.cis.2005.09.004
34. P. H. C. P. Tavares, P. J. S. Barbeira, *J. Appl. Electrochem.*, **2008**, *38*, 827–832. DOI:10.1007/s10800-008-9518-2
35. G. K. Ziyatdinova, E. R. Ziganshina, H. C. Budnikov, *J. Anal. Chem.* **2017**, *67*, 869–879. DOI:10.1134/S106193481211010X
36. Y. Yardım, Z. Şentürk, *Talanta* **2013**, *112*, 11–19. DOI:10.1016/j.talanta.2013.03.047
37. A. J. Bard, L. R. Faulkner, *Electrochemical methods: Fundamentals and applications*, 2nd ed., John Wiley&Sons, Inc, NewYork, 2000. Wiley&Sons, Inc, NewYork, 2000.
38. A. Levent, Y. Yardim, Z. Senturk. *Electrochim. Acta* **2009**, *55*, 190–195. DOI:10.1016/j.electacta.2009.08.035
39. S. M. A. Jorge, A. D R. Pontinha, A. M. Oliveira-Brett, *Electroanalysis* **2010**, *22*, 625–631. DOI:10.1002/elan.200900377
40. D. Eberl, R. P. Hummel, R. Kuhn, *J. Chromatogr A*, **1997**, *759*, 185–192. DOI:10.1016/S0021-9673(96)00769-8
41. V. F. Roche, *Am. J. Pharm. Educ.*, **2006**, *70*, 1–11. DOI:10.5688/aj7005101
42. R. Yang S. G. Schulman, P. J. Zavala, *Anal. Chim. Acta*, **2003**, *481*, 155–164. DOI:10.1016/S0003-2670(03)00076-X
43. F. Mutelet, M. Rogalski, M. H. Guernouche, *Chromatographia*, **2003**, *57*, 605–610. DOI:10.1007/BF02491736

Povzetek

Preučevali smo elektrokemijsko oksidacijo pantoprazola, selektivnega zaviralca protonske črpalke, v vodnem mediju in v mediju voda/surfaktant na elektrodi iz grafitnega svinčnika (PGE) za enkratno uporabo. Uporabili smo ciklično voltametrijo in adsorptivno inverzno (stripping) voltametrijo. Občutljivost inverznih voltametrijskih meritev se je znatno izboljšala, če je bil v nevtralni raztopini elektrolita prisoten kationski surfaktant cetiltrimetilamonijev bromid (CTAB). Za analizne namene smo uporabili dobro ločene voltametrijske vrhove pri +1,05 V (vs. Ag/AgCl), ki smo jih dobili v Britton-Robinsonovem pufru pri pH 7,0 in s koncentracijo 3×10^{-4} M CTAB ob uporabi inverzne voltametrije s pravokotnimi pulzi (po 30 s akumulacije v kratko sklenjenem tokokrogu). Proces lahko uporabimo za določitev koncentracije pantoprazola v območju $2,4 \times 10^{-8}$ – $7,1 \times 10^{-7}$ M ($9,2$ – $272 \mu\text{g L}^{-1}$) z mejo zaznave $7,0 \times 10^{-9}$ M ($2,7 \mu\text{g L}^{-1}$). Predlagano metodo smo s sprejemljivimi izkoristki uporabili za določitev pantoprazola v farmacevtskem pripravku in v vzorcih človeškega urina z dodanim analitom.



Except when otherwise noted, articles in this journal are published under the terms and conditions of the Creative Commons Attribution 4.0 International License

Scientific paper

Derivatives of Phenylene-1,2-diamine as Modifiers for Unsaturated Polyester Resins

Renata Lubczak* and Jerzy Duliban

Rzeszów University of Technology, Department of Organic Chemistry, Faculty of Chemistry,
Al. Powstańców Warszawy 6, 35-959 Rzeszów, Poland

* Corresponding author: E-mail: rlubczak@prz.edu.pl

Received: 06-30-2019

Abstract

The results are presented on the synthesis of new modifiers for unsaturated polyester resins, obtained by reacting ethylene oxide or propylene oxide with phenylene-1,2-diamine. The effect of the modifiers and cobalt accelerator on the reactivity of resins was also studied. When used in the amount of up to 1.50 wt.-%, the amines substantially (several times) reduced the gelation time of modified unsaturated polyesters. The reactivity of resins, however, improved on the expense of their stability.

Keywords: Unsaturated polyester resins; amine modifiers; modification of polyester resins

1. Introduction

Unsaturated polyesters are most frequently obtained from equimolar amounts of maleic anhydride and phthalic anhydride. Their curing is carried out in copolymerization reactions with vinyl monomers, mostly with styrene. A solution of a polyester in such monomer is called polyester resin. Copolymerization is most frequently carried out as radical reaction initialized with hydroperoxides, peroxides of ketones and acyl peroxides, most commonly benzoyl peroxide. Most of peroxide initiators require elevated temperature in order to start the curing process. To reduce the activation energy of decomposition of peroxides, polymerization accelerators called pre-accelerators are used to cause commencement of the curing reaction, sometimes even at a temperature of 5 °C.¹ Such accelerators include amine compounds. These compounds were initially introduced into the system before the start of the curing process. To avoid dosing the accelerator as a separate packaging, manufacturers began to mix accelerators with unsaturated polyester resin in the production process. Aromatic amines, such as *N,N*-dialkyl derivatives of aniline or *para*-toluidine are most frequently used, as they dissolve in the resin component. Unfortunately, unsaturated resins with amine dissolved in them have poor shelf stability.¹ The disadvantage of this procedure is the deactivation of the pre-introduced accelerator as well as its separation in the form of a separate phase upon long-term storage of the resin. Resins with chemically incorporated accelerators are

characterized by better properties, among others because the accelerator is then evenly distributed in the polyester chain. Some initial information on this topic appeared in 1956 and was related to the incorporation of 2-hydroxyalkyl derivative of aniline (3-phenyl-3-azapentane-1,5-diol)² into the resin structure, which partly replaced diethylene glycol used for the synthesis.

In turn, Li completely replaced glycol with the above mentioned compound, obtaining a resin with a high water resistance.³ In the following years, esters and diesters of aromatic acids substituted at the *meta* or *para* position with tertiary amine were used as pre-accelerators. To ensure their incorporation into the polyester structure they were subjected to transesterification of glycol, followed by reactions with maleic and phthalic anhydrides.^{4,5} Detailed comparative studies on the activity of amine pre-accelerators incorporated into polyester resin and those added as separate ingredients were performed by Jada in the late 1970s and the early 1980s.^{6–8} He found out that resins with incorporated amines exhibited better mechanical properties and a higher thermostability. Jada also described the effect of a metal or amine incorporated into a polyester chain during the polycondensation reaction.^{7,8} Accelerators of the curing are compounds containing metals, e.g. vanadium and cobalt salts, of which the most popular are cobalt(II) naphthenates and 2-ethylhexanoates. Incorporation into the polyester chain of a metal in the form of dimaleate or acetate, cobalt, nickel or manganese in amounts higher than 0.25 mole resulted in curing of the

product during its synthesis. The efficiency of their accelerating effect varied as follows: Co > Mn > Ni. The curing takes place at 20 to 100 °C when solution of cobalt(II) octoate or naphthenate is used. For fast gelation at room temperature, vanadium accelerators are used. Manganese accelerators with ketone peroxides or hydroperoxides yield unsaturated polyester compositions of long life time, but cure quickly at 60–100 °C.¹ Incorporation of cobalt(II) ions into the resin structure is described in a patent.⁹ Cobalt(II) hydroxide was introduced into the unsaturated polyester obtained in reactions of ethylene and propylene glycol with phthalic and maleic anhydrides. The reaction mixtures were held at 140 °C until hydroxide has completely reacted. Finally, the polyester with the incorporated cobalt was dissolved in styrene.

Currently, traditional methods for pre-acceleration of polyester resins presented here are still in use, *i.e.* by mixing the accelerator with the resin before curing,^{10,11} but methods of obtaining stable solutions of accelerators applicable for storage^{12–14} are described increasingly often. Furthermore, studies on incorporation of pre-accelerators into the structure of polyester resins are still carried out. In a publication,¹⁵ the synthesis and the effect of amine modifiers obtained in the reactions of ethylene oxide or propylene oxide with *N,N'*-diphenylethane-1,2-diamine and in the reactions of ethylene oxide with *N,N'*-diphenylhexane-1,6-diamine are described. It was found out that using up to 2 wt.-% of these pre-accelerators reduces curing time of the resins by several times when compared to non-pre-acceler-

ated resins. In turn, another publication¹⁶ describes the reaction between *N,N*-dimethyl-*para*-phenylenediamine and ethylene or propylene oxide which were carried out to obtain 3-[*para*-(*N,N*-dimethylamino)phenyl]-3-azapentane-1,5-diol and 4-[*para*-(*N,N*-dimethylamino)phenyl]-4-azaheptane-2,6-diol, respectively. Prepared diols were incorporated into unsaturated polyester resins. The effect of concentration of the built-in pre-accelerator, the gelation rate and resin stability were investigated.

The results of the study on the activity of amine modifiers for unsaturated polyester resins obtained by reaction of diethanolamine (3-azapentane-1,5-diol) and *N*-phenyl-2-aminoethanol with 2,4-dichloro-6-methoxy-1,3,5-triazine, 2-chloro-4,6-dimethoxy-1,3,5-triazine or with cyanuric chloride are presented in the literature.^{17–19} Effects of the type and amount of amine modifier (in the amount of 0.25 to 2.0 wt.-%), as well as cobalt accelerator on gelation time and stability of the resins were investigated. The effect of the presence of a modifier on the curing behavior of the resulting resin was discussed. In publications^{20,21} obtaining of the pre-accelerators by reaction of ethylene oxide or propylene oxide with phenylene-1,4-diamine and with phenylene-1,3-diamine were presented.

This paper describes the synthesis of pre-accelerators hydroxyalkylation reactions of phenylene-1,2-diamine with ethylene oxide and propylene oxide. Their pre-accelerating properties were analyzed and compared with the properties of hydroxyalkyl derivatives of phenylene-1,4-diamine and phenylene-1,3-diamine.

Table 1. Compounds Used and Their Suppliers.

Compound	Supplier
Accelerator Co-1 (1.0 wt.-% solution of cobalt(II) 2-ethylhexanoate in styrene)	ORGANIKA-SARZYNA, Nowa Sarzyna, Poland
Benzyltriethylammonium chloride	Prepared from triethylamine and benzyl chloride, University of Technology, Faculty of Chemistry
Hydroquinone, pa	POCH, Gliwice, Poland
Luperox K-1, (50 wt.-% solution of peroxide of butanone in dibutyl 1,2-phthalate)	ATOCHEM GmbH, Germany
Interox BP-50-P1, 50 wt.-% solution of benzoyl peroxide in dibutyl 1,2-phthalate	Peroxid Chemie GmbH, Germany
Phthalic anhydride, pure	NITROGEN PLANTS Kędzierzyn, Poland
Maleic anhydride, pure	NITROGEN PLANTS Kędzierzyn, Poland
3-Oxapentane-1,5-diol (diethylene glycol), pure	OIL REFINERY, Płock, Poland
Propane-1,2-diol (propylene glycol), pure	OIL REFINERY, Płock, Poland
Ethylene oxide, pure	Honeywell Research Chemicals, USA
(±)Propylene oxide, pure	Honeywell Research Chemicals, USA
Phenylene-1,2-diamine, pure	SIGMA-Aldrich Chemical, Germany
Styrene, pure	Honeywell Research Chemicals, USA

2. Experimental Section

2. 1. Materials

Table 1 presents a list of the materials used including their suppliers.

2. 2. Synthesis

2. 2. 1. Synthesis of Benzene-1,2-diamine-*N,N,N',N'*-tetraethane-2,2',2'',2'''-tetraol (Modifier A) and Benzene-1,2-diamine-*N,N,N',N'*-tetrapropane-2,2',2'',2'''-tetraol (Modifier B)

To a 100 mL pressure reactor equipped with a magnetic stirrer 16.20 g (0.15 mol) of phenylene-1,2-diamine was placed together with 26.45 g (44.05 mL, 0.60 mol) of ethylene oxide or 34.85 g (42.0 mL, 0.60 mol) of propylene oxide. The content was gradually heated to ca. 95 °C while stirring. The temperature slightly increased as the reaction progressed. It was halted when temperature reached 100 °C. The time of the process was ca. 88 hours for the reaction with ethylene oxide or 95 hours for the reaction with propylene oxide. It was ended when the epoxide number of the reaction mixture was zero. The products of the reaction of phenylene-1,2-diamine with ethylene oxide or propylene oxide had a form resinous mass of dark brown color. Due to the presence of four active hydrogen atoms in the amino groups per 1 mol of the phenylene-1,2-diamine, 4 mol of oxirane were used without any solvent, so the provided products did not have to be isolated from the reaction mixture and as such they were used for polycondensation reactions in the obtained form, hence their yield was 100%. The reaction products of phenylene-1,3-diamine and -1,4-diamine with oxiranes were obtained in the same yield.^{20,21}

The spectra of the substrate of phenylene-1,2-diamine are presented in Figs. 1 and 2, and the description of absorption IR spectra and resonance signals from ¹H NMR are presented in Tables 2 and 3. The chemical structure of the products was confirmed by elemental analysis (Table 4) and by spectroscopic methods: FT-IR (Table 2, Fig. 1) and ¹H NMR (Table 3, Fig. 2).

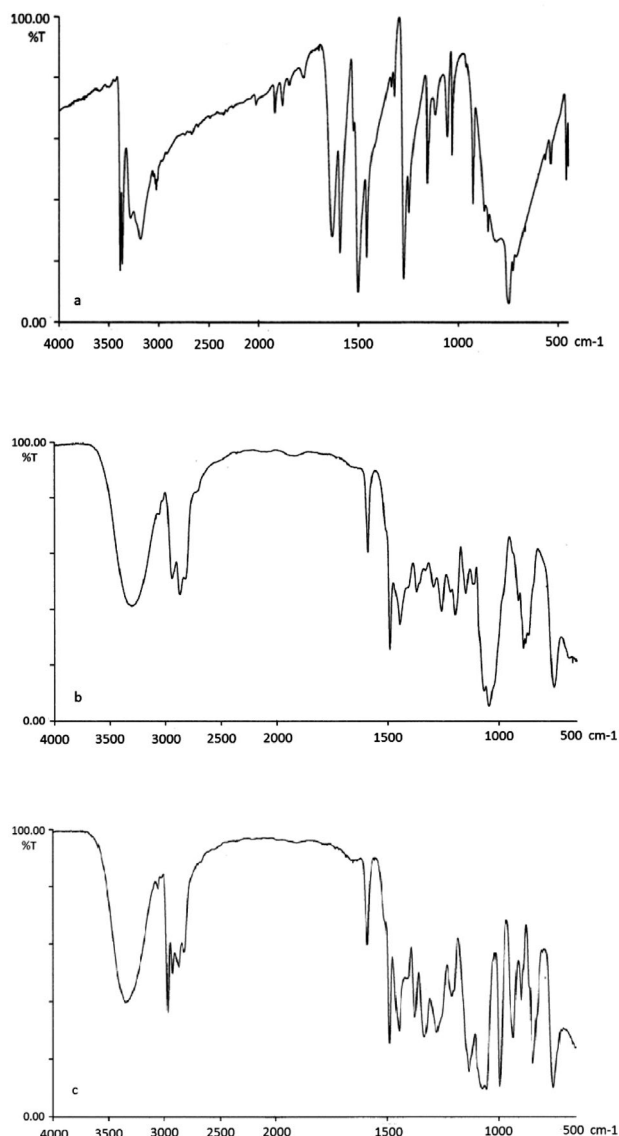


Figure 1. IR spectra of phenylene-1,2-diamine (a), benzene-1,2-diamine-*N,N,N',N'*-tetraethane-2,2',2'',2'''-tetraol (modifier A) (b), and benzene-1,2-diamine-*N,N,N',N'*-tetrapropane-2,2',2'',2'''-tetraol (modifier B) (c).

Table 2. Absorption Bands in IR Spectra of Phenylene-1,2-diamine and obtained Modifiers

Type of vibrations and functional group	Band location (cm ⁻¹)		
	Phenylene-1,2-diamine	Modifier A	Modifier B
ν_{NH_2}	3386, 3364, 3283, 3185	–	–
ν_{OH}	–	3306	3338
$\nu_{\text{C-H}}$ in aromatic ring	3055, 3043, 3015	3031	3061, 3030
ν_{CH_3} , ν_{CH_2}	–	2944, 2873, 2824*	2966, 2930, 2877, 2823
$\nu_{\text{C=C}}$, aromatic ring vibrations	1633, 1592, 1501	1653, 1590, 1491	1647, 1590
δ_{CH_3} , δ_{CH_2}	–	1447, 1418, 1372, 1334	1491, 1448, 1416, 1374, 1335
δ_{NH_2}	1458, 1321, 1274, 1248	–	–
δ_{OH}	–	1150	1133
$\nu_{\text{C-O}}$, in first or second order alcohol	–	1067, 1044	1072, 1054
$\delta_{\text{out of plane}}$, aromatic ring vibrations	928, 872, 852, 808, 748, 712	898, 886, 868, 753	995, 933, 899, 847, 755

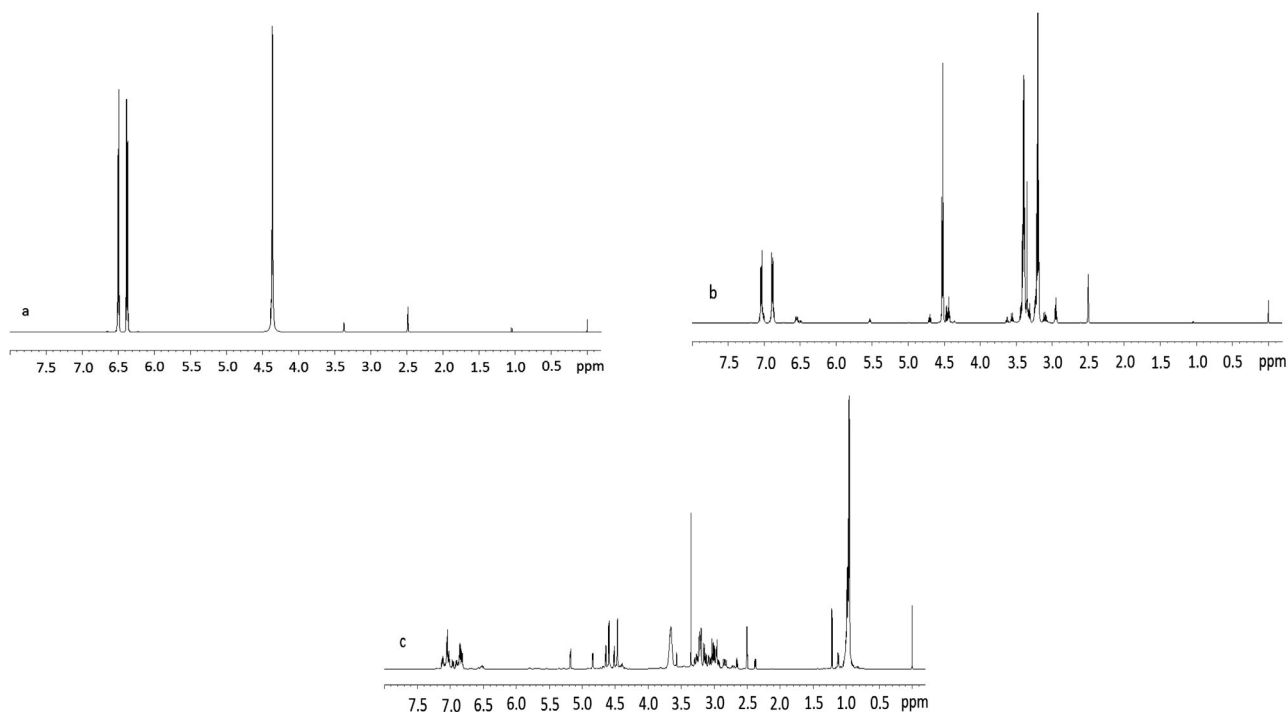
* No bands for ν_{CH_3} or δ_{CH_3} are observed for this compound.

Table 3. Chemical Shifts of Protons in ^1H NMR Spectra of Phenylene-1,2-diamine and obtained Modifiers

Name of chemical compound	Chemical shifts (δ ppm)	Group
Phenylene-1,2-diamine	4.36	$-\text{NH}_2$
	6.37 and 6.48	Aromatic protons
Benzene-1,2-diamine- N,N,N',N' -tetraethane-2,2',2'',2'''-tetraol (modifier A)	3.19	$-\text{CH}_2-\text{O}-$
	3.40	$-\text{CH}_2-\text{N}<$
	4.53	$-\text{OH}$
	6.85–7.10	Aromatic protons
Benzene-1,2-diamine- N,N,N',N' -tetrapropane-2,2',2'',2'''-tetraol (modifier B)	0.95 and 0.96	$-\text{CH}_3$ normal product
	0.97 and 0.98	$-\text{CH}_3$ anomol product
	2.80–3.35	$>\text{N}-\text{CH}_2-\text{C}$
	3.65	$>\text{CH}-\text{O}-$
	4.47 and 4.52	$-\text{OH}$ normal product
	4.90 and 5.18	$-\text{OH}$ anomol product
	6.80–7.10	Aromatic protons

Table 4. Elemental Analysis of Modifiers

Compound	%C		%H		%N	
	Calcd.	Found	Calcd.	Found	Calcd.	Found
Modifier A	59.14	59.25	8.51	8.43	9.85	9.78
Modifier B	63.56	63.74	9.41	9.27	8.23	8.15

**Figure 2.** ^1H NMR spectra of phenylene-1,2-diamine (a), benzene-1,2-diamine- N,N,N',N' -tetraethane-2,2',2'',2'''-tetraol (modifier A) (b), and benzene-1,2-diamine- N,N,N',N' -tetrapropane-2,2',2'',2'''-tetraol (modifier B) (c).

2. 2. Synthesis of Modified Unsaturated Polyester Resins

To a three-necked 500 mL flask equipped with a mechanical stirrer, inlet to inert gas (nitrogen), thermometer, Liebig condenser and calibrated distillate collector, 76.1 g

(0.5 mol) of phthalic anhydride, 49.0 g (0.5 mol) of maleic anhydride, 41.0 g (0.43 mol) of diethylene glycol, 42–44 mL (0.57–0.60 mol) of propylene glycol (depending on the amount of amine-glycol modifier added), and the modifier itself up to 6.4 g (2.0 wt.-% with respect to the total mass of

all substrates) were introduced. The flask was purged with nitrogen for 15 min before heating was switched on. Then 0.18 mL (ca. 12 mg) of 10% solution of hydroquinone in acetone was added and the content heated at 165–200 °C under nitrogen for 9–12 h, until the acid number of the mixture has dropped down to below 50 mg KOH per g of resin.²² The mixture was then cooled down to 90–100 °C and diluted with 125 mL of styrene stabilized with hydroquinone.

2. 2. 3. Curing of Unsaturated Polyester Resins

By using normalized procedures, time of gelation at 25 °C (time until air bubble was arrested in the test tube filled with resin containing initiator)²³ and stability of resins at 70 °C (time until air bubble was arrested in the test tube filled with resin containing no initiator)²⁴ were determined for all unsaturated polyester resins. The time of gelation was measured for the so-called amine-curing system, *i.e.* with benzoyl peroxide as initiator, for cobalt-curing system consisting of butanone peroxide initiator and cobalt(II) 2-ethylhexanoate accelerator. A series of curing experiments with cobalt curing system was performed with an addition of 0.3 wt.-% of benzyltriethylammonium chloride.

2. 3. Analytical Methods

The addition reaction of amine to oxiranes was followed by determining the epoxy number of the reaction mixture using hydrochloric acid solution in dioxane.²⁵ ¹H NMR spectra of the products were recorded at 25 °C in deuterated dimethyl sulfoxide (DMSO-*d*₆) with hexamethyldisiloxane internal standard on a Bruker AM 500 MHz, Germany. IR spectra were recorded as KBr pellets on a Perkin-Elmer PARAGON 1000 FT spectrometer (Wellesley, MA, USA). Elemental analyses were determined on a Vario EL III C, H, N, S and O apparatus (Elementar, Germany).

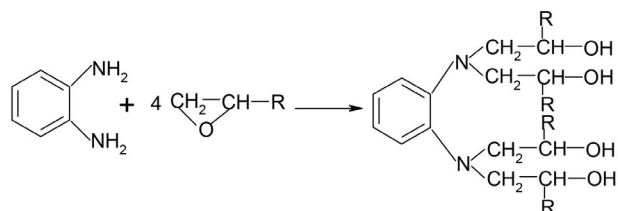
The process of polycondensation leading to unsaturated polyester resins was followed by measuring the amount of water released from the system and, at the end of the reaction, by measuring the acid number (AN) of the reaction mixture. The reaction was ended when AN was smaller than ca. 50 mg KOH per g of resin.²² Hydroxyl numbers (HN) of alkyds used for preparing unsaturated polyester resins were also measured according to the standard procedures.²⁶

3. Results and Discussion

3. 1. Synthesis of Modifiers A and B

The amine-glycol modifiers for unsaturated polyester resins were obtained in a one step reaction between 1 mol of phenylene-1,2-diamine and 4 mol of ethylene oxide or 4 mol of propylene oxide. The reaction yielded alcohols

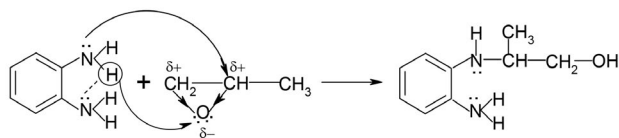
with four hydroxyl groups containing tertiary amino groups with nitrogen atoms linked directly to the aromatic ring (scheme 1).



where: R = -H or -CH₃

Scheme 1. Obtaining modifiers for unsaturated polyester resins

The course of the reaction was confirmed by the vanishing IR absorption bands at 3386, 3364, 3283, 3185 cm⁻¹ due to the stretching vibrations and at 1458 (vibrations in plane), 1321, 1274, and 1248 cm⁻¹ (vibrations out of plane) due to deformational vibrations of amino groups. Appearance of new broad bands was observed due to hydroxyl groups at 3306 and 3338 cm⁻¹ (associated hydroxyl groups). Bands at 1067 and 1044 cm⁻¹ (modifier A) and bands at 1072 and 1054 cm⁻¹ (modifier B) corresponding to stretching vibrations of C–O bonds in primary and secondary alcohols, as well as those at 1198 and 1133 cm⁻¹ due to deformational vibrations of hydroxyl groups were also present (Fig. 1). Similarly, in ¹H NMR spectra (Fig. 2), the signal at 4.36 ppm from amine protons disappeared and appeared instead a signal at 4.53 ppm from hydroxyl protons in 2-hydroxyethyl groups (modifier A) or two signals at 4.47 and 4.52 ppm from OH protons (for the normal product) and also two signals at 4.90 and 5.18 ppm from OH protons (for the regioisomer, anomalous product) in 2-hydroxypropyl groups (modifier B). These four last signals are related to configuration at the chiral carbon atom in the each hydroxypropyl group. In the case of modifier A, a signal from methylene protons appeared at 3.19 and 3.40 ppm, whereas for modifier B three extra peaks from methyl protons could be seen in the spectra in two ranges: the first one at 0.95 and 0.96 ppm for methyl protons in normal product and the second one at 0.97 and 0.98 ppm for methyl protons in anomalous product, beside methylene protons signal from 2.80 to 3.35 ppm, as well as from methine proton at 3.65 ppm. By comparing the signal intensities it was found that ca. 70% of the product of the reaction of phenylene-1,2-diamine with propylene oxide was the normal one, and the rest was the anomalous one. The reason is that proton in amino groups in *ortho* position may form a five-membered ring including H–N hydrogen bond. The weakly linked proton engaged in the hydrogen bond can easily be linked to oxirane oxygen. The result is that a partial positive charge is formed on the most substituted oxirane carbon which can be attacked by the amine electron pair (Scheme 2). This may explain why so much of the anomalous product is formed.



Scheme 2. The formation of the anomalous product.

The anomalous product of addition of propylene oxide to aromatic amine may contribute to the hindering of gelation, as explained later in the text.

The difference between resonance positions of signals from methylene and methine protons in modifier B is a result of strongly electronegative character of the oxygen in hydroxyl group, which is stronger than that from the nitrogen at the aromatic ring. The signals from 6.85 to 7.10 ppm and from 6.80 to 7.10 ppm due to aromatic protons appear in spectra of modifier A and modifier B, respectively.

3. 2. Gelation Time for Modified Unsaturated Polyester Resins

The products modifier A: benzene-1,2-diamine-*N,N,N,N'*-tetraethane-2,2',2'',2'''-tetraol and modifier B:

benzene-1,2-diamine-*N,N,N,N'*-tetrapropane-2,2',2'',2'''-tetraol were built into the structure of an unsaturated polyester resins and their effects on gelation time and stability of the resin were observed. The reference resin was prepared by condensation of phthalic and maleic anhydride with propane-1,2-diol (propylene glycol) and 3-oxapentane-1,5-diol (diethylene glycol).²⁷ This is a typical construction brand resin with 3-oxapentane-1,5-diol (diethylene glycol) acting as the stiffness-reducing monomer of polyester segments. Modification of the resins involved replacing a part of propylene glycol with one of the modifiers. The highest proportion of the modifier was established in the preliminary experiment not to exceed 1.5 mole %. This was a sufficiently small quantity so that no gelation at polyesterification stage was observed in the presence of both four-functional modifiers. The unsaturated polyesters resins were synthesized by carrying condensation of the components at 165–200 °C under nitrogen until the acid number of the reaction mixture dropped down below 50 mg KOH per g of resin.²⁸ As the amount of modifiers increased, the color of modified resins became more and more dark, from yellowish, and yellow at the concentration of modifiers A and B equal about 0.002 to

Table 5. Characteristic of UP Resins with Amine Modifiers Incorporated into Their Chemical Structure

Kind of modifier	Number of resin	Mole of amine accelerating groups/kg resin ($\times 10^{-3}$)	Wt.-% of modifier	AN (mg/KOH/g)	HN (mg/KOH/g)	Stability of resins at 70 °C		Color
						Without ammonium salt (h)	With ammonium salt (h)	
1	2	3	4	5	6	7	8	9
None	1	0.000	0.000	45.23	55.18	824	2658	Colorless
	2	0.023	0.002	43.66	54.22	156	531	Yellowish
	3	0.057	0.005	48.98	56.38	130	471	Yellowish
	4	0.113	0.010	40.24	48.98	114	435	Yellow
	5	0.226	0.020	47.63	56.70	102	372	Dark yellow
	6	0.565	0.050	48.12	58.27	45	165	Dark yellow
	7	1.130	0.100	40.72	47.37	21	120	Light brown
	8	2.825	0.250	46.53	55.97	12	96	Light brown
	9	5.651	0.500	40.67	48.13	9	75	Brown
	10	8.477	0.750	45.76	55.96	9	72	Brown
	11	11.302	1.000	44.83	53.28	9	72	Dark brown
	12	14.128	1.250	47.46	56.67	9	72	Dark brown
	13	16.954	1.500	45.47	55.09	9	72	Brown black
Modifier A	14	0.019	0.002	43.87	52.21	555	1044	Yellowish
	15	0.047	0.005	39.93	48.65	360	972	Yellowish
	16	0.094	0.010	43.36	54.42	234	891	Yellow
	17	0.189	0.020	47.02	57.02	171	765	Dark yellow
	18	0.472	0.050	42.08	51.05	111	612	Dark yellow
	19	0.944	0.100	45.01	55.42	51	309	Light brown
	20	2.35	0.250	45.84	55.76	69	216	Light brown
	21	4.720	0.500	49.69	59.31	90	285	Brown
	22	7.080	0.750	49.29	59.23	105	360	Brown
	23	9.440	1.000	46.03	55.36	126	396	Dark brown
	24	11.800	1.250	44.58	53.26	150	399	Dark brown
	25	14.160	1.500	45.90	55.28	162	399	Brown black

0.010 wt.-% to dark brown and brown black at the concentration from 1.00 to 1.50 wt.-%.

By using normalized procedures, time of gelation at 25 °C (time until air bubble was arrested in the test tube filled with resin containing initiator)²³ and stability of resins at 70 °C (time until air bubble was arrested in the test tube filled with resin containing no initiator)²⁴ were determined for all unsaturated polyester resins. The standard initiator for the cobalt-curing of unsaturated polyester resins was used. Namely, the system consisted of cobalt(II) 2-ethylhexanoate as accelerator and butanone peroxide initiator dispersed in dibutyl 1,2-phthalate (Luperox K-1). The attempt of using benzoyl peroxide dispersed in dibutyl 1,2-phthalate (Interox BP-50-P1) was unsuccessful for too long gelation times. The times of gelation were therefore measured for cobalt-curing system consisting of butanone peroxide (Luperox K-1) initiator and cobalt(II) 2-ethylhexanoate accelerator. A series of curing experiments with cobalt curing system was performed with an addition of 0.3 wt.-% of benzyltriethylammonium chloride. Even in the absence of initiator the resin gelled when heated to 70 °C. The results of stability tests are presented in Table 5.

The shelf stability of the modified unsaturated polyesters reduced with the increasing amount of modifiers A or B added to reaction of polycondensation. This was result of the presence of tertiary amino groups linked to the aromatic ring built into polyester chain, the groups that are known for their significant reduction of threshold energy of double bond decomposition or cleavage. Generally, the modifiers containing 2-hydroxyethyl substituents at the nitrogen atom (such as modifier A) are much more active and show a much shorter gel times than those with 2-hydroxypropyl substituents (modifier B). This can be seen especially for the modified resins increased amount modifier B (from 0.50 to 1.50 wt.-%). For the resins with a built-in modifier A all the gelation times are shorter than the unmodified resin, where for the four series of experiments were made with cobalt solution content of 0.10, 0.15, 0.25, or 0.50 mL per 25 g of resin. For unmodified resin the respective gelation times were 92, 72, 50.5, or 42.5 min for the normative amount of initiator (2 wt.-%).²⁴ However, for unsaturated polyesters with built-in modifier B two ranges of gelation times were observed. The first of the ranges with gelation times shorter than those of unmodified resins, was observed with 0.002 to about 0.25 wt.-% of modifier B built into the resin structure. Then, the modifier acted as a pre-accelerator. The second range of gelation times much longer than those for unmodified resins contained 0.25 to 1.50 wt.-% of modifier B, in this case acting as an inhibitor of gelation times.

Gelation times for the modified resins are shown in Figures 3 and 4. In Figures 5 and 6 the dependence of gelation time is plotted against the amount of cobalt accelerator for resins prepared with different amounts of modifiers A and B. The reactivity and stability measurements were carried out by changing the content of modifiers

built into the structure of unsaturated polyester resins (Figs. 3 and 4) and the amount of cobalt accelerator (Figs. 5 and 6).

To summarize, incorporation of modifier A into the structure of resin in the whole range of concentration from 0.002 to 1.50 wt.-% results in faster gelation of resin com-

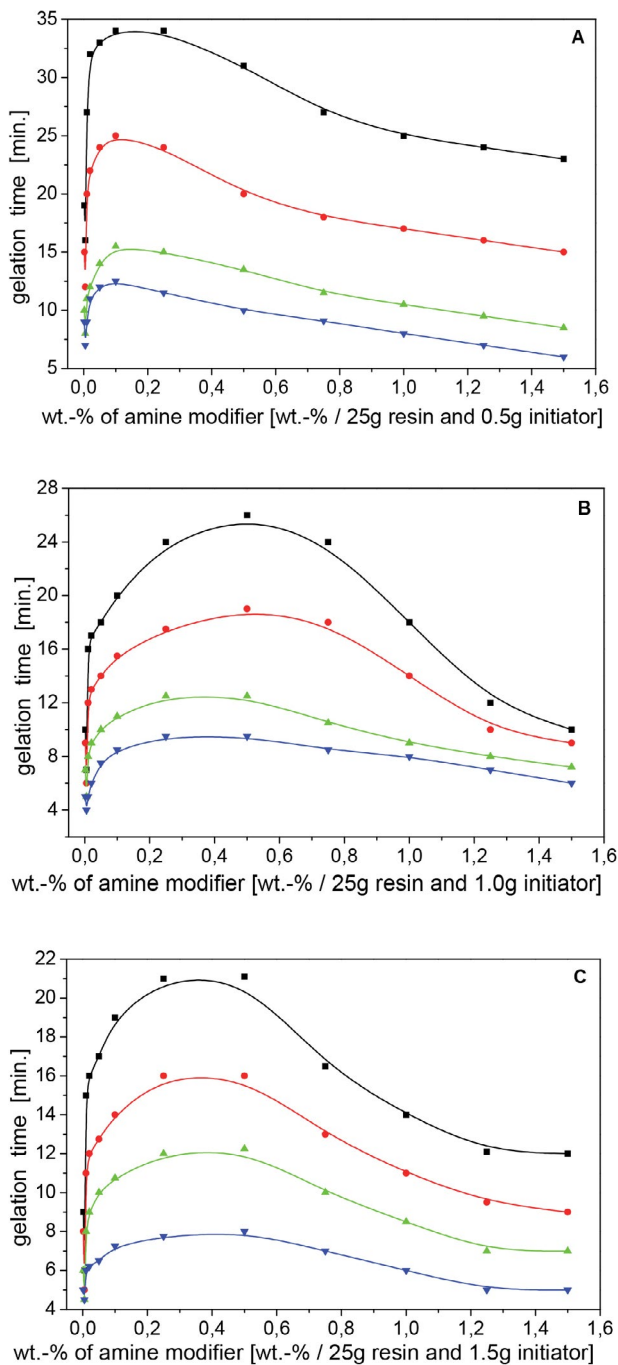


Figure 3. Gelation times of unsaturated polyesters resins with various amount of chemically incorporated modifier A and cobalt accelerator. To 25 g of resin, 0.5 g (plot A), 1.0 g (plot B), and 1.5 g (plot C) of butanone peroxide initiator was added; the amounts of cobalt accelerator: (■), 0.10 mL; (●), 0.15 mL; (▲), 0.25 mL; (▼), 0.50 mL.

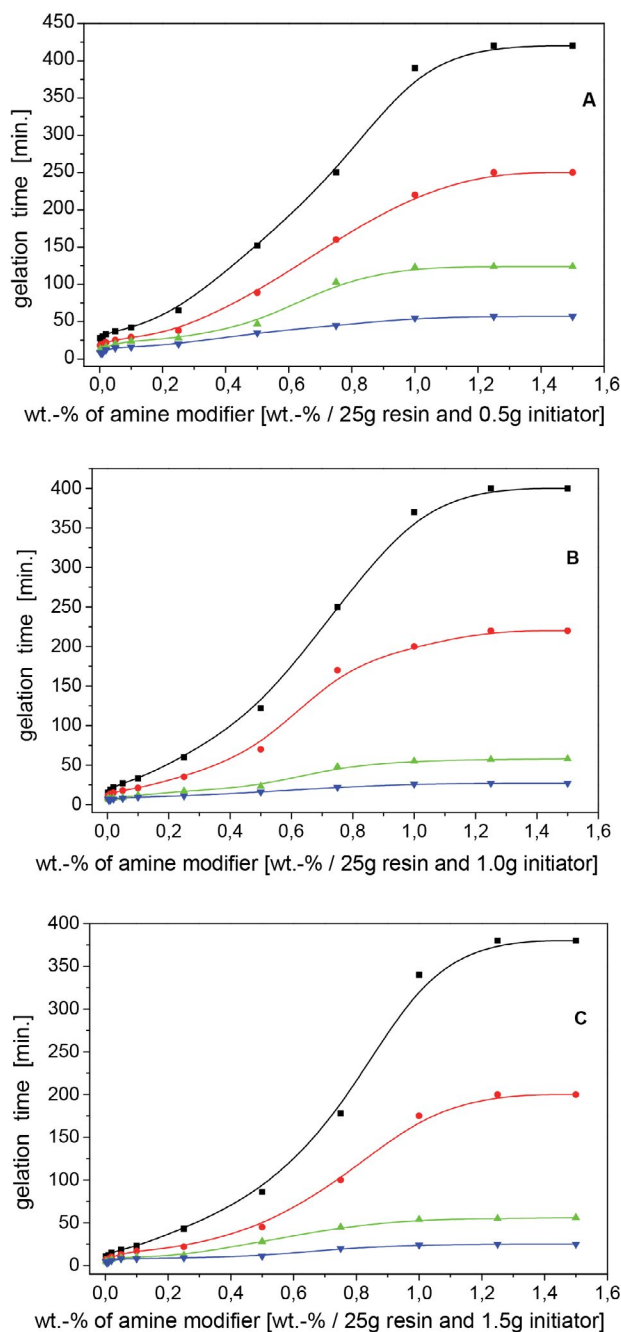


Figure 4. Gelation times of unsaturated polyesters resins with various amount of chemically incorporated modifier B and cobalt accelerator. To 25 g of resin, 0.5 g (plot A), 1.0 g (plot B), and 1.5 g (plot C) of butanone peroxide initiator was added; the amounts of cobalt accelerator: (■), 0.10 mL; (●), 0.15 mL; (▲), 0.25 mL; (▼), 0.50 mL.

pared to the resin without modifier. In the case of modifier B, however, the fundamental effect on gelation time had the addition of cobalt accelerator (1.0% solution of cobalt(II) 2-ethylhexanoate in styrene). When used in the amount of 0.002 to ca. 0.25 wt.-%, modifier B serves as an accelerator. The effect is extended to up to ca. 0.50 wt.-%, when more cobalt accelerator is present in the system (0.50 mL per 25 g of resin at the normative initiator con-

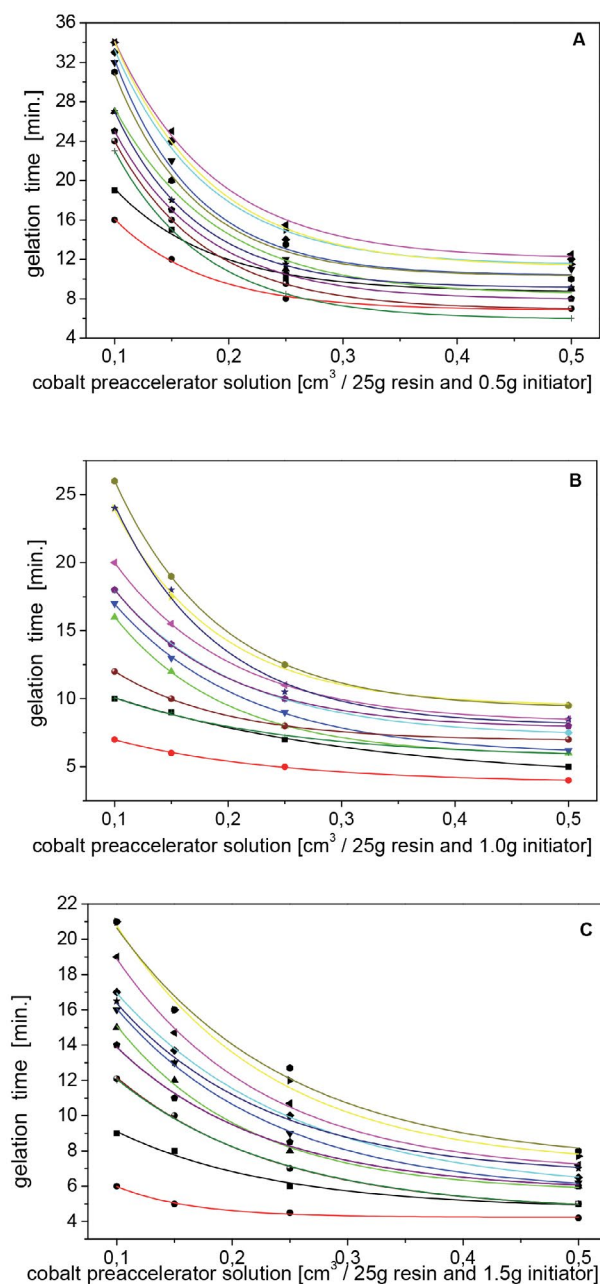


Figure 5. Gelation times of unsaturated polyesters resins with various amount of cobalt accelerator solution and various amounts of chemically incorporated modifier A. To 25 g of resin, 0.5 g (plot A), 1.0 g (plot B), and 1.5 g (plot C) of butanone peroxide initiator was added; the amounts of chemically incorporated modifier A: (■), 0.002 wt.-%; (●), 0.005 wt.-%; (▲), 0.010 wt.-%; (▼), 0.020 wt.-%; (◆), 0.050 wt.-%; (+), 0.100 wt.-%; (●), 0.250 wt.-%; (✱), 0.500 wt.-%; (✱), 0.750 wt.-%; (●), 1.000 wt.-%; (○), 1.250 wt.-%, (+) 1.500 wt.-%.

tent) with an extra amount of initiator, higher than that recommended (1.0 or 1.5 g per 25 g of resin) and 0.5 mL of cobalt accelerator leads to faster gelation of modified resins. This system of curing composition yields shorter gelation times in the whole concentration range of modifiers studied.

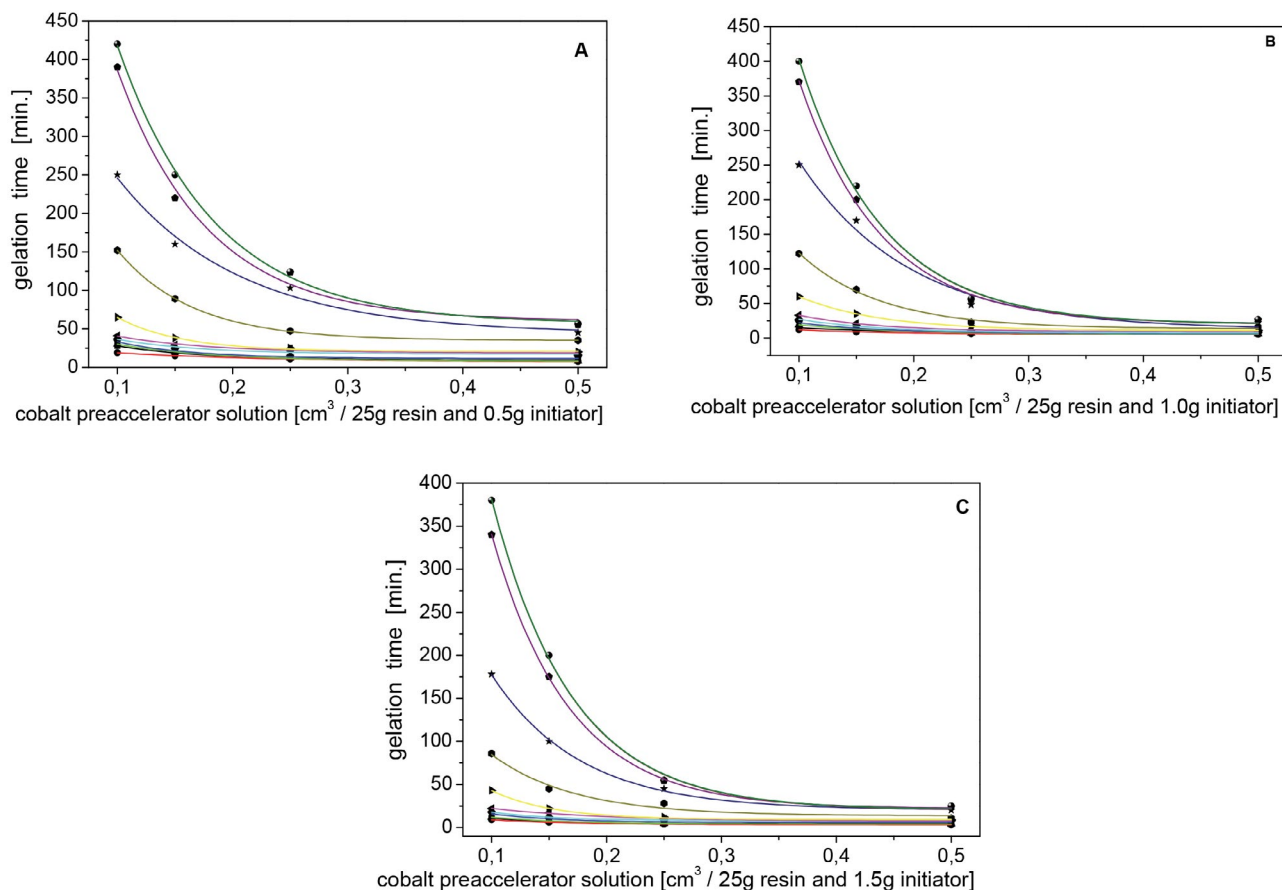
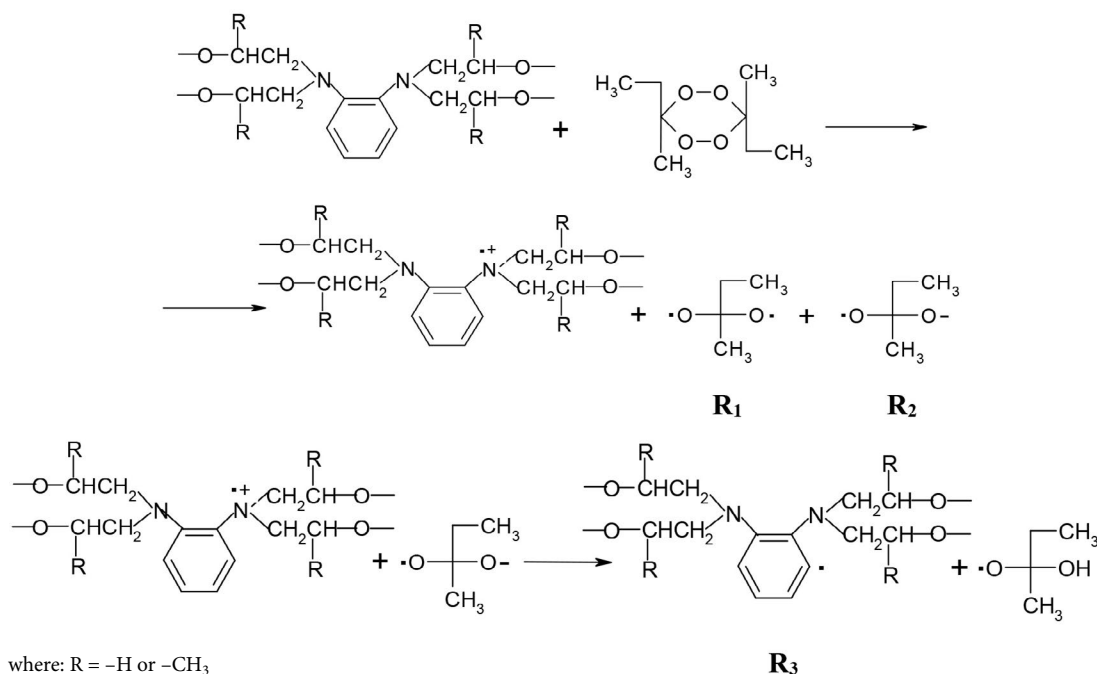


Figure 6. Gelation times of unsaturated polyesters resins with various amount of cobalt accelerator solution and various amounts of chemically incorporated modifier B. To 25 g of resin, 0.5 g (plot A), 1.0 g (plot B), and 1.5 g (plot C) of butanone peroxide initiator was added; the amounts of chemically incorporated modifier B: (■), 0.002 wt.-%; (●), 0.005 wt.-%; (▲), 0.010 wt.-%; (▼), 0.020 wt.-%; (◆), 0.050 wt.-%; (⊕), 0.100 wt.-%; (●), 0.250 wt.-%; (★), 0.500 wt.-%; (*), 0.750 wt.-%; (●), 1.000 wt.-%; (○), 1.250 wt.-%; (+), 1.500 wt.-%.



Scheme 3. The reaction between the built-in amine pre-accelerator in the polyester structure and the peroxide initiator

Based on the analysis of the results one can conclude that incorporation of modifier A into the resin structure in the whole range of concentrations, from 0.002 to 1.50 wt.-%, results in faster gelation of resin compared to that without modifier. However, for modifier B a fundamental effect on the change in gelation time is addition of cobalt accelerator (1.0% solution of cobalt(II) 2-ethylhexanoate in styrene). An increase of gelation time for resins with modifier B can be observed, especially for the system which contains a large amount of cobalt accelerator (0.50 mL per 25 g of modified resins) and for the over-normative amount of initiator (4 and 6 wt.-%).²³

The reason might be the high concentration of amine. The modifier acts as a scavenger of radicals formed from initiator. As follows from the literature data^{1,28,29} amines may act not just as promoters of initiator decomposition, but also as stabilizers preventing radicals formed naturally to propagate into a chain reaction in organic systems. Also the amines built into resin may react with macroradicals thus reducing the rate of polymerization. The process may proceed according to the Scheme 3.

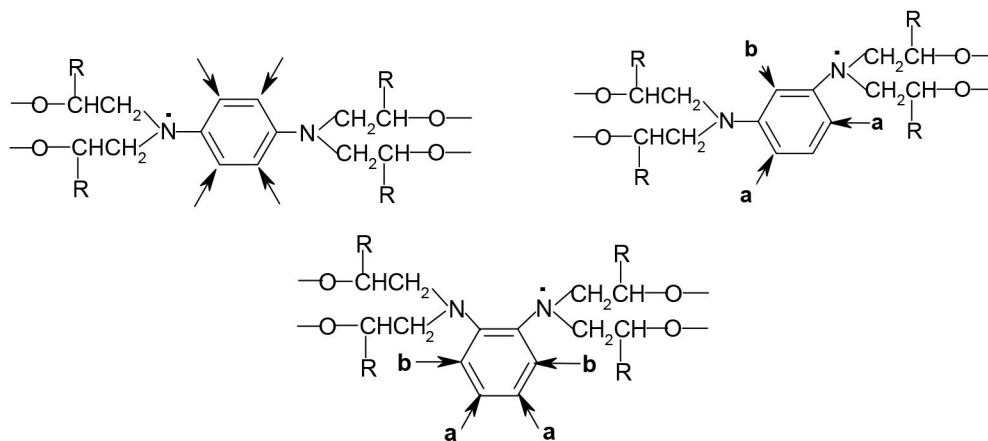
As a result of these reactions diradicals (R_1) and anion radicals (R_2) are formed from peroxide molecule and also mesomerically stabilized radicals are formed from amino-modifier (R_3) built-into the polyester chain. These radicals initiate the process of polymerization of the polyester chain double bonds or those of styrene.

By comparing actions of pre-accelerators of similar structures prepared from phenylene-1,4-amine and phenylene-1,3-amine, as described in the literature,^{20,21} one should note that in the case of hydroxyalkyl derivatives of phenylene-1,2-amine, although in the latter there exist four active sites capable of initiating radical polymerization, but not all are equally accessible.

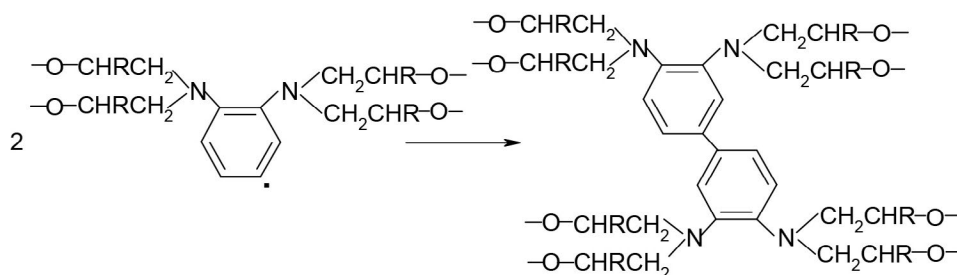
From the point of view of stereochemistry, accessible are only two sites denoted as 'a', while the activity of radicals in position 'b' may be considerably limited by the presence of large and bulky alkyl substituents (this is particularly true for resins containing phenylene-1,3-diamine pre-accelerator).

An extra steric hindrance is exerted by the presence of a methyl group in hydroxyalkyl substituent of modifier B. This seems to be the reason why unsaturated polyester resins modified with benzene-1,2-diamine-*N,N,N',N'*-tetrapropane 2,2',2'',2'''-tetraol (modifier B) exhibit relatively long gelation times, particularly when a small amount of cobalt modifier is applied. The resins modified with benzene-1,2-diamine-*N,N,N',N'*-tetraethane-2,2',2'',2'''-tetraol (modifier A) do gel faster.

The absence of bulky methyl group in 2-hydroxyethyl substituent of modifier A facilitates access to the reactive sites such as 'a' as well as 'b'. The use of higher concentration of cobalt salt significantly accelerates gelation process, as a greater number of aromatic active radicals are used. At



Scheme 4. Active sites in amine pre-accelerators.



Scheme 5. Deactivation of radicals during gelation

the lowest cobalt concentration, on the other hand, (0.10 or 0.25 mL per 25 g of resin) the concentration of aromatic radicals is so high that an inhibiting effect of gelation process is observed according to the reaction presented in Scheme 5.

The gelation times were measured for four different amounts of cobalt accelerator added. For the resin not containing a built-in modifier, gelation times were: 92, 72, 50.5, and 42.5 min. for systems with the normative amount of initiator (*i.e.* 0.5 g of initiator per 25 g of resin) and 0.10; 0.15; 0.25 and 0.50 mL of cobalt accelerator, respectively.²⁹ The graphical dependence of gelation time *vs.* percentage of built-in amine modifier is presented in Figs. 3 and 4.

It follows from the plots presented that the shortest gelation times are observed for unsaturated polyester resins with 0.002 to 1.50 wt.-% of modifier A with the minimum at 0.005 wt.-%. With doubled amount of initiator, relative to the normative one,²³ *i.e.* 4 wt.-% gelation time becomes reduced by ca. 50% at the constant concentration of Co(II) (*cf.* curves A and B in Fig. 3).

With increasing concentration of cobalt accelerator, however, the reduction of gelation times becomes less and less pronounced, so that for resins cured with the normative (0.5 g) (*i.e.* 2 wt.-%) and over-normative (1.0 g) (*i.e.* 4 wt.-%) amounts of peroxide initiator the plots become more and more flat. The differences between the shortest and longest gelation time vanish with increasing amount of cobalt(II) concentration. The most reactive are resins with built-in 0.005% of modifier A.

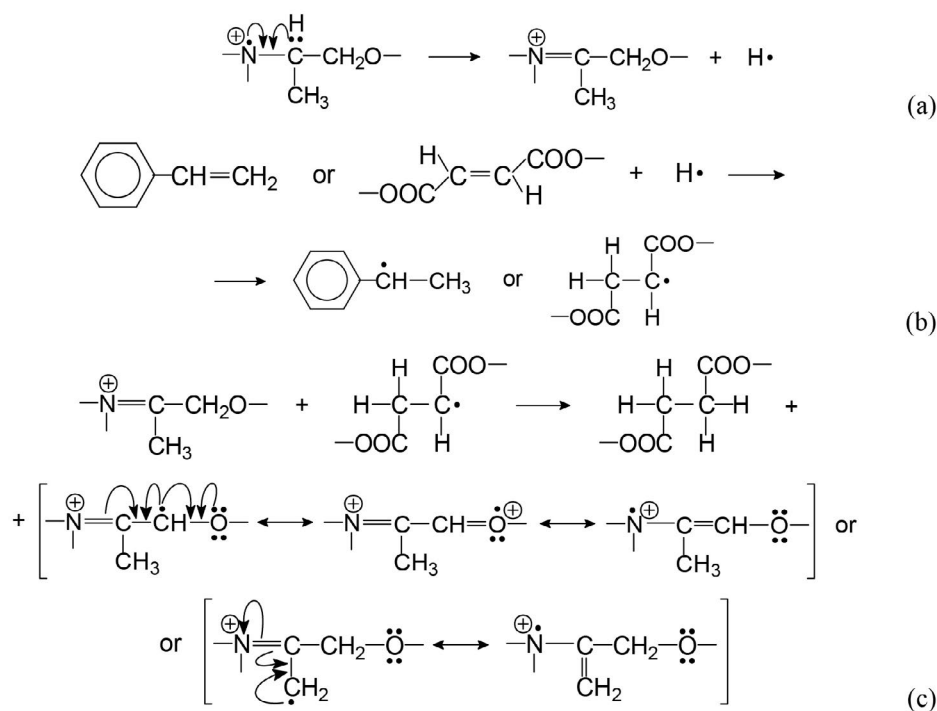
Further increase of initiator content to 1.5 g (6% per resin) did not change gelation time so significantly and,

hence, gelation time got shortened by only about 10% (in relation to the previous system, *i.e.* with 1.0 g of initiator per 25 g of resin). To summarize, one can state that doubling the content of initiator from 2 to 4% results in substantial reduction of gelation time, by as much as 50% (*cf.* curves A and B in Fig. 3), while further increase of initiator content, up to 6%, only slightly reduces gelation time (*cf.* curves B and C in Fig. 3).

The behavior of the resins containing modifier B has been found to be completely different. Gelation times shorter than those for unmodified resin are obtained with 0.002 to ca. 0.25 wt.-% of modifier B built into resin structure with minimum gelation time again corresponding to the content of 0.005 wt.-%, similarly as for modifier A. Above 0.25 wt.-% of modifier B gelation times become much longer than for unmodified resin. Hence, in the range of content from 0.25 to 1.5 wt.-% modifier B acts as an inhibitor of polymerization.

The presence of 30% of anomalous product is probably responsible for the inhibiting effect observed, leading to the increase of gelation time. This could be explained by the following Scheme 6.

The radical formed on nitrogen atom in the reaction between initiator and modifier may form double bond with neighboring carbon atom by removing hydrogen radical (reaction a). Hydrogen radical then breaks the double bond in unsaturated resin or in styrene thus initiating chain reaction (reaction b). The products formed in reactions a and b produce primary or secondary radicals stabilized mesomerically, the reactivity of which (particularly of primary ones) is much higher than that of those



Scheme 6. A reaction cycle explaining the elongation of gelation time.

formed at aromatic ring. As a result, radicals rapidly combine and polymerization process stops without utilizing double bonds of the resin (reaction b). This seems to be the reason why in the plot of gelation time vs. concentration of built-in modifier one observes rapid increase of gelation time.

By applying a higher than normative amount of initiator (*i.e.* 4%) gelation time of resins containing modifier can be reduced by ca. 40%, while still using the same amount of cobalt (*cf.* curves A and B in Fig. 4).²³ Gradual increase of cobalt accelerator up to 0.5 mL per 25 g or resin respond with a similar reduction of gelation times. This effect becomes weaker and weaker as the amount of cobalt increases. Fivefold increase of Co^{2+} content results in three- to six-fold reduction of gelation time at the normative content of initiator. In the case of modifier B, the effect of extra initiator, however, is not as regular as in the case of modifier A. With 4% of initiator, the gelation times change irregularly and depend to a large extent on the amount of cobalt accelerator used. In general, a two-fold increase of initiator content reduced gelation time by 20 to 40% (*cf.* curves A and B in Fig. 4). Further increase of initiator content to 6% brings about 5 to 10% reduction of gelation time (*cf.* curves B and C in Fig. 4).

Reduced shelf stability of the resins as measured according to the appropriate standard procedure²⁴ (*cf.* Table 5, column 7), is a serious disadvantage of the modifiers studied. The presence of tertiary amine built into unsaturated resins reduce not only the gelation time, but also reduce their long-time stability and hence the possibility of storage. This applies particularly to the resins containing 0.05 to 1.50% of modifier A for which the shelf stability were 45 to 9 hours (the time to gelation upon heating the resin without initiator at 70 °C). The resins containing less modifier A, namely 0.002 to 0.02 wt.-%, the stability was in the range 156 to 102 hours (*cf.* Table 5, column 7). Graph-

ically, the relationship between shelf stability of the modified resins and the amount of modifier A resembles a hyperbola. In the case of modifier B the shelf stability time was slightly longer and it was in the range 555 to 51 hours. In this case, the graphical form of the relationship resembles a parabola with minimum at 0.10 wt.-% of modifier B (*cf.* Table 5, column 7).

The stability of unsaturated polyester resin can be improved by using quaternary ammonium salt stabilizers.^{1,30} For the resins containing 0.3 wt.-% benzyltrimethylammonium chloride, the stability at 70 °C (Table 5, columns 7 and 8) improved but to the extent again depending on the amount and kind of amine modifier built into resin.

Generally, the presence of an ammonium salt improved the stability of resins. Its effect was more pronounced for resins containing modifier A, than for resins with modifier B. The stability increased 3.5 to 8 times and 2 to 6 times, respectively. The best stability values were recorded for 0.25 to 1.5 wt.-% content of modifier A and 0.10 wt.-% of modifier B. The latter coincide with the minimum of stability change caused by the presence of modifier B.

Gelation times were also measured for the resins stabilized with benzyltrimethylammonium chloride and initiated with a curing system consisting of 0.25 mL of cobalt accelerator and 0.5 g of peroxide per 25 g of resin. The results are shown in Table 6. For resins containing modifier A, gelation times increased by ca. 2.5 to 10 times as compared to analogous resins not containing quaternary ammonium stabilizer. For the resins containing modifier B, the respective increase of gelation time was ca. 2.5 in the whole range of the content of modifier B (*cf.* columns 2 and 3 as well as column 4 and 5). The character of stability dependence on the amount of amine built into resin did not change in the presence of quaternary ammonium salt.

To summarize the results, for unsaturated polyester resins containing built-in modifier A, much narrower

Table 6. Comparison of Gelation Times for UP Resins with Modifiers A and B Containing or Not the Benzyltriethylammonium Chloride Stabilizer

Wt.-% of modifier	Gelation time (min)			
	Modifier A		Modifier B	
	Without ammonium salt (min)	With ammonium salt (min)	Without ammonium salt (min)	With ammonium salt (min)
1	2	3	4	5
0.002	10.0	95.0	13.0	30.0
0.005	8.0	99.0	11.0	28.0
0.010	11.0	101.0	12.0	32.0
0.020	12.0	94.0	13.0	38.0
0.050	14.0	85.0	22.0	42.0
0.100	15.5	56.0	24.0	46.0
0.250	15.0	36.0	25.0	58.0
0.500	13.5	30.0	47.0	110.0
0.750	11.5	25.0	103.0	233.0
1.000	10.5	23.0	123.0	360.0
1.250	9.5	22.0	124.0	420.0
1.500	8.5	22.0	124.0	420.0

range of gelation times is observed, as compared with those containing modifier B. The gelation times for the former changed from 7 to 34 minutes for the normative content of initiator (2.0 wt.-%) and depended on the amount of cobalt(II) accelerator (0.10–0.50 mL per 25 g resin). In the case of modifier B, the respective gelation times were much longer for the same curing conditions and amounted from 7.5 to 420 minutes. The use of an over-normative amount of initiator (4.0 or 6.0 wt.-%) reduced gelation times, as expected.

Three parameters were found to have a major effect on the rate of gelation of modified unsaturated polyester resins. These are the amount of built-in modifier, the amount of initiator used for curing and the concentration of cobalt accelerator. Each of them influences the time gelation in its specific way. The amount of initiator modifies gelation time only when used in the amount 2 to 4 wt.-%. At the higher amount of 6 wt.-% of butanone peroxide, the reactivity of the resin expressed in terms of gelation time does not increase significantly anymore. Somewhat less important is the amount of cobalt accelerator.

Table 6 summarizes gelation times of the compositions containing ammonium salt stabilizer with 2.0 wt.-% of initiator and 0.25 mL of cobalt accelerator per 25 g of resin. As compared to unstabilized ones the gelation times are from about eight to ten times longer for the resin containing from 0.002 to 0.02 wt.-% as a modifier A or between 2 and 3 times longer for resins containing from 0.05 to 1.50 wt.-%. The gelation times are from two to three times longer for the whole range of concentrations of modifier B (0.002–1.50 wt.-%) used.

4. Conclusions

1. Tertiary amines with aromatic ring were obtained by reacting phenylene-1,2-diamine with ethylene oxide (A) and propylene oxide (B) and used as modifiers for unsaturated polyester resins.

2. The modifier A introduced into resins structure at the stage of polycondensation very strongly reduced gelation time of the resulting unsaturated polyester resin in the cobalt curing system.

3. The modifier B also reduced gelation time in the cobalt curing system, but to a much smaller extent.

4. The gelation time reduction was observed in cobalt curing system in the presence of at least 0.005 wt.-% of the both modifiers. For resins modified with from about 0.25 to 1.50 wt.-% of modifier B an increase of gelation time was observed as compared to that for unmodified resins. The most promising results with regard to the reactivity of resins and their storage stability were observed when 0.005 wt.-% of both modifiers were used.

5. With more than ca. 0.30 mL of cobalt accelerator used per 25 g of resin the resin reactivity does not improve

(i.e. there is no reduction of gelation time), irrespectively of the amount of initiator.

6. By introducing ammonium salt stabilizer (benzyltriethylammonium chloride) to the modified unsaturated polyester resins one can significantly increase their storage (shelf) stability. For both modifiers the presence of ammonium salt changed the reactivity of composition by prolonging the gelation time for resins containing from 0.002 to 0.02 wt.-% modifiers A from about eight to ten times or between 2 and 3 times for resins containing from 0.05 to 1.50 wt.-% and from two to three times for the whole range of used concentrations of the modifier B. Again the reactivity depended on the amount of the built-in amine modifier.

5. References

1. W. Królikowski, Z. Kłosowska-Wółkiewicz, P. Penczek, Polyester resins and laminates (in Polish), WNT, Warsaw 1986, pp. 175–177 and 201–207.
2. A. G. Bayer, Cold-setting Copolymers, GB Patent Number 757,989, date of patent September 26, 1956.
3. P. Z. Li, *Plast. Massy*, **1961**, 12, 11–15. DOI:10.1176/ps.12.5.15
4. Chemische Werke Witten GmbH, Improvements in or relating to hardening of unsaturated polyeter compositions, GB Patent Number 985750, date of patent March 10, 1965.
5. R. Burkhard, H. Wulff, Verfahren zum Haerten von unsaettigte stickstoff- haltige Polyester enthaltende Polyester-Form-massen, DE Patent Number 1196868, date of patent Juli 15, 1965.
6. S. S. Jada, *Makromol. Chem.* **1982**, 183, 1763–1774. DOI:10.1002/macp.1982.021830716
7. S. S. Jada, C. U. Pittman, *Ind. Eng. Chem. Prod. Res. Dev.* **1983**, 21, 281–284. DOI:10.1021/i300006a017
8. S. S. Jada, *Ind. Eng. Chem. Prod. Res. Dev.* **1983**, 22, 14–19. DOI:10.1021/i300009a005
9. B. Gawdzik, T. Matynia, Method of Preaccelerating Unsaturated Polyester Resins, PL Patent Number 305265, date of patent April 1, 1996.
10. A. Motak, A. Kozak, W. Tarnawski, J. Uzar, T. Podulka, G. Rokosz, Method of Pre-acceleration of Unsaturated Polyester Resins, PL Patent number 354814, date of patent January 12, 2004.
11. J. Reijnders, G. M. Martinus, F. Koers, K. Willem, A. G. Talma, Process for the Preparation an Accelerator Solution, US Patent Number 0011966, date of patent January 9, 2014.
12. H. Kamio, Y. Ogino, K. Nakamura, Accelerated Hardening of Unsaturated Polyester Resins, US Patent Number 4348498, date of patent September 7, 1982.
13. F. Koers, K. Willem, J. Meijer, Accelerator Solution, US Patent Number 120977, date of patent May 5, 2010.
14. F. Koers, K. Willem, A. G. Van de Bovenkamp-Bouwman, Storage-Stable Accelerator Solution, US Patent Number 207841, date of patent August 28, 2008.
15. J. Duliban, *Macromol. Mater. Eng.* **2001**, 286, 624–633. DOI:10.1002/1439-2054(20011001)286:10<624::AID-MA-

- ME624>3.0.CO;2-U
16. M. Kucharski, J. Duliban, E. Chmiel-Szukiewicz, *J. Appl. Polym. Sci.* **2003**, *89*, 2973–2976. DOI:10.1002/app.12400
17. J. Duliban, *Polimery* **2004**, *49*, 774–779. DOI:10.14314/polimery.2004.774
18. J. Duliban, *Macromol. Mater. Eng.* **2006**, *291*, 137–147. DOI:10.1002/mame.200500314
19. J. Duliban, *Macromol. Mater. Eng.* **2007**, *292*, 1126–1139. DOI:10.1002/mame.200700146
20. J. Duliban, *J. Appl. Polym. Sci.* **2011**, *120*, 311–321. DOI:10.1002/app.33145
21. J. Duliban, *J. Appl. Polym. Sci.* **2012**, *125*, 3708–3720. DOI:10.1002/app.36721
22. Unsaturated polyester resins - Test methods - Determination of the acid number, Polish (European) Standards PN-EN ISO 2114:2002 – English version, Ed. Polish Committee for Standardization.
23. Unsaturated polyester resins – Test methods – Determination of gelation time after adding the initiating system at 25 and 80 degrees C, Polish (European) Standards PN-EN ISO 2535:2002 - English version, Ed. Polish Committee for Standardization.
24. Unsaturated polyester resins - Test methods - Determination of durability at elevated temperature, Polish Standard PN-C-89082-09: 1986 – Polish version, Ed. Polish Committee for Standardization.
25. Z. Brojer, Z. Hertz, P. Penczek, Epoxy resins, PWN, Warsaw 1972, pp. 448–449.
26. Plastics - Unsaturated polyester resins - Determination of the hydroxyl number, Polish (European) Standards PN-EN ISO 2554:2001 – Polish version, Ed. Polish Committee for Standardization.
27. W. Conrad, Verfahren zum Aushaerten von Polyesteremertel unter Verschiedenen Temperaturbedingungen, DE Patent Number 227711, date of patent October 9, 1984.
28. E. Carleton, N. J. Montclair, Glykol-Maleic Acid Resin and Process of Making Same, US-patent Number 2,195,362, date of patent May 21, 1936.
29. E. Carleton, N. J. Montclair, Ethylenic-Alpha-Beta Synthetic resing and Process of making same, US Patent Number 2,255,313, date of patent September 9, 1941.
30. M. Oleksy, H. Galina, *Polimery*, **2000**, *45*, 541–547. DOI:10.14314/polimery.2000.541

Povzetek

Predstavljamo rezultate sinteze novih modifikatorjev za pripravo nenasičenih poliestrskih smol, ki so nastale z reakcijo med etilen oksidom ali propilen oksidom ter fenilen-1,2-diaminom. Preučili smo učinek modifikatorjev in kobaltnih pospeševalcev na reaktivnost reakcije tvorbe polimernih smol. Kadar smo amine uporabili v količini do 1.50 utežnega %, so se gelacijski časi za nenasičene modificirane poliestre občutno zmanjšali (za večkrat). Vendar se je povečana reaktivnost odražala na račun zmanjšane stabilnosti smol.



Except when otherwise noted, articles in this journal are published under the terms and conditions of the Creative Commons Attribution 4.0 International License

Scientific paper

Synthesis, Characterization and Evaluation of Antimicrobial, Antioxidant & Anticancer Activities of Copper Doped Zinc Oxide Nanoparticles

Saranya Rishikesan¹ and Mubarak Ali Muhamath Basha^{2,*}

¹ Research and Development Centre, Department of Chemistry, Bharathiar University, Coimbatore - 641 046, Tamilnadu, India.

² Department of Chemistry, Chikkaiah Naicker College, Erode - 638 004, Tamil Nadu, India.

* Corresponding author: E-mail: mubarakscience@gmail.com
Contact Number: 091-9443312819

Received: 07-01-2019

Abstract

The present work reveals the influence of copper (Cu) doping in band gap energy level as well as selective cytotoxicity of ZnO nanoparticles against human breast cancer cells (MCF7), human cervical carcinoma (HeLa), and one normal (Vero) cell line. Cu-doped ZnO nanoparticles (Cu-ZnO NPs) were synthesized and validated by UV-Vis, FT-IR, XRD, SEM and EDAX. Cu-doping diminished the band gap energy of ZnO NPs from 3.54 eV to 3.29 eV. Antimicrobial activity has been evaluated against three bacterial and fungal strains. Antioxidant activity was examined using a DPPH free radical, ABTS⁺ radicals, hydroxyl radicals and nitric oxide scavenging assay. Cu-ZnO NPs showed anticancer activity with IC₅₀ value of 219.56 µg/mL against MCF7 and 137.27 µg/mL against HeLa cell lines. The doping of Cu with ZnO improved the selective cytotoxicity of ZnO NPs towards MCF7 and HeLa cells without affecting the normal cells.

Keywords: Cu-ZnO NPs, Antimicrobial activity, Cytotoxicity, MCF7, HeLa and Vero cell lines

1. Introduction

Cancer is a deadly disease which increases the mortality rate in the recent decades. Though the treatment of cancer by chemotherapy, radiation therapy and surgery were efficient towards the killing of cancer cells, it has an adverse effect towards the normal cells also.^{1–3} The importance of these therapies is now gradually diminished due to the advancement of nanomedicine, targeted drug delivery and multi-target inhibitors.⁴ Engineered nanoparticles (NPs) have advanced imaging, therapeutic activity and effective for early detection of cancer and cancer treatment.^{5–8} It has the additional benefits of active/passive targeting, high solubility/bioavailability, biocompatibility and multi-functionality over traditional cancer therapies.⁹ ZnO nanoparticles have multiple properties including favorable band gap, electrostatic charge, large surface area and potentiation of redox-cycling cascades.^{10,11} These characteristics of ZnO nanoparticles are being exploited in biomedical field such as cell imaging, bio-sensing and drug delivery. Recently, ZnO nanoparticles receive much attention for their potential application in can-

cer therapy. ZnO nanoparticles exhibited a preferential ability to kill human cancer cells as compared with normal cells.^{12,13} ZnO nanoparticles have potential to develop as an anticancer candidate. The possible mechanism of cytotoxicity of ZnO NPs was associated with the occurrence of apoptosis.¹⁴ However, for practical therapeutic applications, new strategies are required to further improve the cancer killing ability of ZnO nanoparticles without affecting normal cells. This study focuses on improving the cancer cells killing ability of ZnO nanoparticles by metal ions doping.

As the functionality and efficiency of ZnO nanostructures can be improved by increasing and modifying their surface area by adding some dopants materials i.e. biomolecules and transition metals (Mn, Fe, Cr, Cu) at nanoscale.^{15,16} Through surface modification with biomolecules and transition metals, ZnO nanoparticles could be used as biosensors, antimicrobial, antioxidants, drug delivery systems and bio-imaging materials.^{16–18} Different methods have been developed for the fabrication of ZnO and transition metal doped ZnO nanoparticles.¹⁹ Among all the dopants, doping of ZnO NPs with Cu greatly alter

the optical, morphological structural, magnetic, electrical, and biological properties of the ZnO NPs.^{20,21} ZnO NPs doped with Cu have shown remarkable improvement in different properties i.e. electrical conductivity,²² magnetic,²³ biological,²⁴ gas sensing,²⁵ optical properties and mechanical strength.²⁶ Cu-doped ZnO NPs showed enhanced anticancer activity as compared to Un-doped ZnO NPs.²⁷

The present study aims on improving the anticancer activity of ZnO NPs by cationic doping. Especially, Cu was considered as one of the most effective doping elements for improving the anticancer activity of ZnO NPs. It was found that the doped Cu²⁺ ions with half-filled electronic configuration which contributed to the enhanced anticancer activity of ZnO nanoparticles. In order to verify the efficacy of copper doping with ZnO in various aspects an attempt was taken to investigate elaborately. Herein, we report the synthesis, characterization of ZnO and Cu-ZnO nanoparticles and its antimicrobial, antioxidant and anticancer activities.

2. Experimental

2. 1. Materials

All chemicals used were of analytical grade and used as received. Zinc sulphate heptahydrate (ZnSO₄ · 7H₂O), Sodium hydroxide (NaOH), Copper sulphate pentahydrate (CuSO₄ · 5H₂O) were purchased from Merck and were used as received.

2. 2. Synthesis of ZnO NPs

ZnSO₄ · 7H₂O (0.4 M) and NaOH (0.8 M) were dissolved in distilled water. ZnO nanoparticles was prepared using co-precipitation method by dropwise addition of NaOH to ZnSO₄ · 7H₂O with constant stirring at 80 °C until a white precipitate was formed. After cooling, the precipitate was washed several times with deionized water followed by ethanol and dried in a hot air oven for 5 h at 80 °C. The dried samples were calcined at 350 °C for 3h to obtain the nano sized ZnO.

2. 3. Synthesis of Cu-ZnO NPs

ZnSO₄ · 7H₂O (0.8 M) was dissolved in deionized water. Cu-ZnO NPs were prepared by the drop wise addition of NaOH (0.8 M) solution and CuSO₄ · 5H₂O (0.02 M) solution to ZnSO₄ · 7H₂O with constant stirring. The stirring was continued until the complete precipitation occurs. Before filtration the mother liquid was aged for 12 h. The residue thus obtained was dried at 80 °C for 12 h and calcined at 350 °C for 3 h.

2. 4. Characterization Methods

The Ultra Violet-Visible-Diffuse reflectance spectroscopy (UV-Vis-DRS) measurements were performed

with a JASCO V-550 double beam spectrophotometer with PMT detector. The samples were filled in a quartz cuvette of 1 cm light-path length, and the light absorption spectra were given in reference to deionized water. Surface structure was characterized by a Fourier Transform Infrared (FT-IR) spectrophotometer (JASCO-RT-IR-460 plus). The present study is restricted to the assignment of various vibrational modes of metal oxides compounds within the frequency range 400–4000 cm⁻¹ and IR analysis was carried out for oven-dried samples. The sample for IR analysis was prepared by mixing 0.1 g of KBr with 0.003 g of sample and then pressing into a pellet. X-ray diffraction (XRD) patterns were collected at 25 °C using (XPERT-PRO-X-RAY diffractometer with Cu-Kα radiation and structural assignments were made with reference to the JCPDS powder diffraction files. Scanning electron microscopy (SEM) images were performed by JSM-6701F-6701 instrument in both back scattered electron modes. The elemental analysis was detected by an energy dispersive X-ray spectroscopy (EDX) attached to the SEM.

2. 5. Antimicrobial Activity

Antibacterial and antifungal activities were evaluated for the synthesized ZnO and Cu-ZnO NPs. The salt of ZnSO₄·7H₂O, CuSO₄·5H₂O and the synthesized NPs of ZnO and Cu-ZnO were tested to determine their antimicrobial activities against three bacterial strains namely *E. coli* (1B), *S. aureus* (2B) and *P. aeruginosa* (3B) and three fungal strains namely *Aspergillus flavus* (1F), *Candida albicans* (2F) and *Fusarium* (3F). The samples were dissolved in dimethyl sulphoxide and it was made into the required concentrations. The bacterial strains as well as fungal strain were inoculated separately in 30 mL of nutrient broth in a conical flask and incubated for 24 h to get active strain by using well diffusion method. Muller Hinton agar was poured separately into petri dishes. After solidification 0.25 mL of test strains were inoculated in the media separately and care was taken to ensure proper homogenization. The experiment was performed under strict aseptic conditions. After the medium solidified, a well was made in the plates with sterile borer (5mm). The (40 μL) of the test sample was introduced into the well and plates were incubated at 37 °C for 72 h. All samples were tested in triplicates. Microbial growth was determined by measuring the diameter of zone of inhibition. Amikacin and Ketoconazole were used as control for antibacterial and antifungal activity assay respectively.

2. 5. 1. Determination of Minimum Inhibitory Concentration (MIC)

A sterile 96 well plates were prepared under aseptic conditions. The freshly prepared sample suspensions in DMSO were sonicated using a sonicator. A volume of 100 μL of test material in 10% DMSO (a stock concentration of

1 mg/mL for purified compounds) was pipetted into the first row of the plate. To all the other wells, 50 μ L of nutrient broth was added for bacteria cells and 50 μ L of Sabouraud dextrose broth for fungi cells, and serial dilutions were performed using a multichannel pipette. To each well, 10 μ L of resazurin indicator solution was added. Finally, 10 μ L of bacterial/fungal suspension (5×10^6 cfu/mL) was added to each well to achieve a concentration of 5×10^5 cfu/mL. The commercial drugs Amikacin (against bacteria) and Ketoconazole (against fungi) were used as a positive control. The plates were prepared in triplicate, and placed in an incubator set at 37 °C for 18–24 h and the color change from purple to pink or colorless indicates the reduction of dye by the viable bacteria/fungi. The lowest concentration at which color change occurred was taken as the MIC value. The average of three values was calculated to get MIC values.

2. 6. Evaluation of Antioxidant Properties of the Compounds

The remarkable antibacterial and antifungal activities of the synthesized Cu-ZnO NPs induced us to study its radical scavenging properties. The radical scavenging activities of Cu-ZnO NPs along with standard have been examined with reference to 2,2-diphenyl-1-picrylhydrazyl (DPPH) radicals, 2,2'-azino-bis (3-ethyl benzothiazoline-6-sulfonic acid (ABTS) radicals, hydroxyl radicals (\cdot OH) and nitric oxide ($\text{NO}\cdot$) assay and the determination of 50% activity (IC_{50}) values.

2. 6. 1. DPPH free Radical Scavenging Assay

The DPPH radical scavenging activity of Cu-ZnO NPs was measured according to the method of Blios.²⁸ The DPPH radical is a stable free radical having λ_{max} at 517 nm. A variable concentration of the sample (20–100 μ g/mL) were mixed with 1.0 mL of methanolic solution containing DPPH radicals, resulting in the final concentration of DPPH being 0.2 mM. The mixture was shaken vigorously and left to stand for 30 min, and the absorbance was measured at 517 nm. Vitamin E was used as control. The percentage of inhibition in DPPH radical scavenging activity was calculated as follows;

$$\% \text{ Inhibition} = (A_0 - A_1)/A_0 \times 100$$

2. 6. 2. ABTS Cation Radical Scavenging Assay

ABTS decolorization assay involves the generation of the ABTS^+ chromophore by the oxidation of ABTS with potassium persulphate. It is applicable for both hydrophilic and lipophilic compounds. The scavenging activity of Cu-ZnO NPs on ABTS cation radical was measured at 734 nm.

Equal volume of 7 mM of ABTS was mixed with 2.45 mM potassium persulphate and the mixture was allowed

to stand in the dark at room temperature for 12–16 h before use. ABTS^+ solution was diluted to an absorbance of 0.7 ± 0.05 with ethanol at 734 nm. The reaction was initiated by the addition of 1.0 mL of diluted ABTS^+ to 10 μ L of different concentrations (20–100 μ g/mL) of sample. Vitamin E was used as standard and positive control. The absorbance was read at 734 nm and the percentage inhibitions were calculated. The inhibition was calculated according to the equation,

$$I = (A_0 - A_1)/A_0 \times 100$$

Where, A_0 is absorbance of control reaction, A_1 is absorbance of test compound.

2. 6. 3. Hydroxyl Radical Scavenging Assay

The hydroxyl radical scavenging activities of the compounds have been investigated using Nash method.²⁹ A reaction mixture of 3.0 mL volume contained, 1.0 mL of 1.5 mM FeSO_4 , 0.7 mL of 6 mM hydrogen peroxide, 0.3 mL of 20 mM sodium salicylate and 1.0 mL of different concentrations (50–250 μ g/mL) of Cu-ZnO NPs. After incubation for an hour at 37 °C, the absorbance of the hydroxylated salicylate complex was measured at 562 nm. Vitamin E was used as positive control. The percentage scavenging effect was calculated as,

$$\text{Scavenging activity} = [1 - (A_1 - A_2)/A_0] \times 100$$

Where, A_0 is absorbance of the control, A_1 is absorbance in the presence of the extract; A_2 is absorbance without sodium salicylate.

2. 6. 4. Nitric Oxide (NO) Assay

The amount of nitrite was determined by the literature method.³⁰ The reaction mixture (6.0 mL) containing sodium nitroprusside (4.0 mL), phosphate buffer saline (PBS, 1.0 mL) and different concentrations (50–250 μ g/mL) of a sample (1.0 mL) in DMSO was incubated at 25 °C for 15 minutes. After incubation, 1.0 mL of sulphanilic acid reagent was added, mixed well and allowed to stand for 5 minutes for completion of diazotization and 1.0 mL of N-(1-naphthyl) ethylenediamine dihydrochloride was added, mixed well and allowed to stand for 30 minutes in diffused light. A pink colored chromophore was formed. The absorbance of these solutions was measured at 540 nm against corresponding blank solutions. Vitamin E was used as a standard.

The inhibition was calculated according to the equation, $I = (A_0 - A_1)/A_0 \times 100$

2. 7. Anticancer Activity of Cu-ZnO NPs

The MCF7 and HeLa cells were grown in Eagle's minimum essential medium containing 10% fetal bovine serum (FBS) while Vero cells were grown in Dulbecco's modified Eagle's medium (DMEM) containing 10% FBS. 100 μ L per well of cell suspension were seeded into 96-well

plates at plating density of 10,000 cells/well and incubated to allow for cell attachment at 37 °C, 5% CO₂, 95% air and 100% relative humidity. After 24 h the cells were treated with serial concentrations of the test samples (Cu-ZnO NPs). Cu-ZnO NPs were initially suspended in neat dimethylsulfoxide (DMSO) and an aliquot of the sample solution was diluted to twice the desired final maximum test concentration with serum free medium. Additional four serial dilutions were made to provide a total of five sample concentrations. Triplication was maintained, and the medium without the test sample served as the control. After 24 h, the wells were treated with 20 µL MTT [5 mg mL⁻¹ phosphate buffered saline (PBS)] and incubated at 37 °C for 4 h. The medium with MTT was then removed separately and the formed formazan crystals were dissolved in 100 mL DMSO. The absorbance at 570 nm was measured using an ELISA plate reader. The graph was plotted between the percentage of cell inhibition and the concentration of the complexes. IC₅₀ values were calculated from the percentage of inhibition. The percentage of cell inhibition was determined using the formula which is given below,

$$\% \text{ inhibition} = \left[\frac{\text{mean OD of untreated cells (control)}}{\text{mean OD of treated cells (control)}} \right] \times 100$$

3. Results and Discussion

3.1. Ultra Violet-Visible-Diffuse Reflectance Spectroscopy (UV-Vis –DRS)

Fig. 1 depicts the UV-Vis DRS of ZnO and Cu-ZnO NPs. There are four bands at 213, 255, 358 and 448 nm for ZnO nanoparticles. In Cu-ZnO NPs the bands around 200–360 nm remained unaltered.

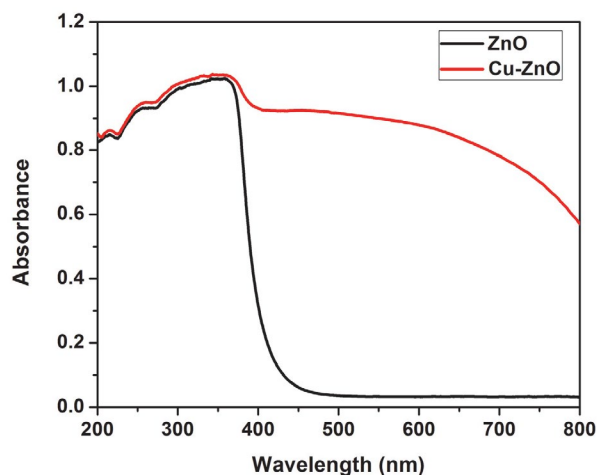


Figure 1. UV-Vis DRS spectra of ZnO and Cu-ZnO NPs

The band which is appeared at 448 nm is shifted to 464 nm. A slight red shift observed in the case of Cu-ZnO is due to the doping of Cu into the crystal lattice of Zn. The

red-shift in absorption peak showed decrease in band gap of ZnO with Cu doping. The band gap of ZnO NPs was decreased from 3.54 to 3.29 eV after doping with copper. Fig. 2 shows the Tauc's plot of ZnO(a) and Cu-ZnO(b). The observed redshift in band gap (E_g) is due to Cu doping-induced band-edge bending. The change in the band gap energy is attributed to two reasons: First, the sp–d exchange interactions between sp and d orbitals of host and dopant, respectively, lead to negative correction in the conduction band and positive correction in valence band, hence overall band narrowing is observed.^{31,32} Secondly, the electronegativity of Cu is 1.9 as compared to ZnO which is 1.6, leading to a chemical affect in the host ZnO crystal which results in decrease in band gap.

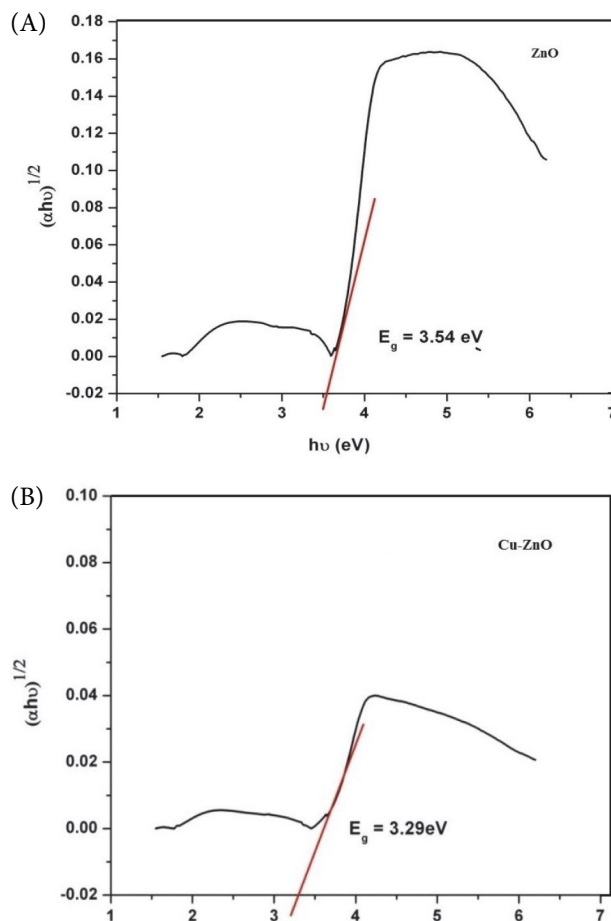


Figure 2. (A) and (B) τ-Plot of ZnO, and Cu-ZnO NPs respectively

3.2. FT-IR Spectral Studies

The FT-IR spectra of ZnO and Cu-ZnO NPs are represented in Fig 3. The peak observed at 3448 and 1132 cm⁻¹ are attributed to O–H stretching vibration of H₂O in the Cu–Zn–O lattice. The peak at 570 cm⁻¹ is attributed to Zn–O^{33,34} whereas in the copper doped ZnO the corresponding peak is observed at 561 cm⁻¹.³⁵

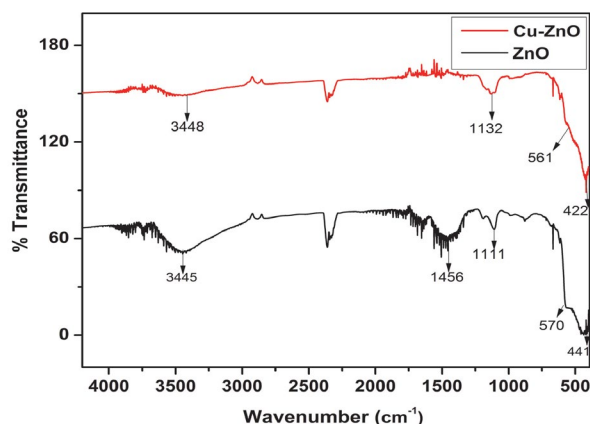


Figure 3. FT-IR data of ZnO and Cu-ZnO NPs

3. 3. X-RAY Diffraction (XRD) Analysis

The XRD pattern of ZnO, Cu-ZnO is depicted in Fig. (4 & 5) All the diffraction peaks can be assigned to the ZnO crystal phase with a hexagonal wurtzite structure (JCPDS-36-1451). The sharp and intensive diffraction peaks indicated that products were well crystallized. The average crystallite size was calculated from Debye-Scherrer formula.³⁶ The average crystallite size of ZnO and Cu-ZnO are 30 nm and 27 nm respectively. From the XRD investigation, the crystal structure of ZnO and Cu-ZnO is wurtzite. The lattice constant for ZnO and Cu-ZnO are $a = 0.3247$ nm, $c = 0.5203$ nm and $a = 0.3249$ nm, $c = 0.5204$ nm respectively. The very slight shift in peak positions

were observed with copper doping in ZnO indicating that all doped copper occupied the substitution sites. No secondary phases viz., Cu_2O , CuO , or other metallic Cu or Zn phases were observed. It is noteworthy that no copper oxide related peak could be observed in the XRD spectra. One probable reason was that the concentration of doped Cu was so low that it cannot be detected by XRD. The other reason was that the radius of Cu-ion (0.073 nm) is similar to that of Zn-ions (0.074 nm) and the Cu-ions may be incorporated into the lattice of ZnO structure.³⁷ Fig. 5 also shows that Cu-ions doping has almost no influence on the phase structure of ZnO. The intensity of XRD peaks of Cu-ZnO NPs was decreased in comparison to that of pure ZnO which indicates a decrease in crystallinity of ZnO with Cu doping. The decrease in crystallite size implies that doping with Cu restrains increase of grain size and refines the crystal size.

3. 4. Scanning Electron Microscope (SEM) Analysis

The morphology of ZnO, Cu-ZnO NPs was elucidated by SEM analysis. SEM micrographs of ZnO, and Cu-ZnO are depicted in Fig.6 (A-D). It was clearly observed that the particles were spherical in shape and well dispersed.

ZnO structure was observed like a stack of vertically aligned thin nanosheets whereas Cu-ZnO possessed rods and grain like structures. The average grain size of all the samples is in the range of 40–60 nm. Cu doping strongly influences the grain size and morphology of ZnO nano-

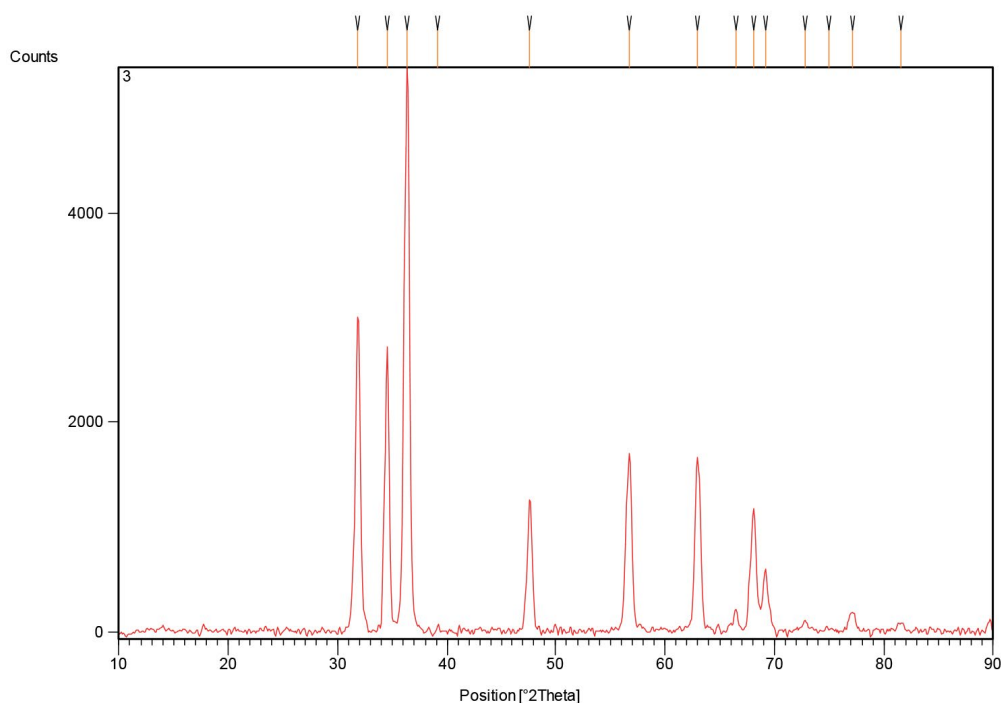


Figure 4. XRD pattern of ZnO NPs

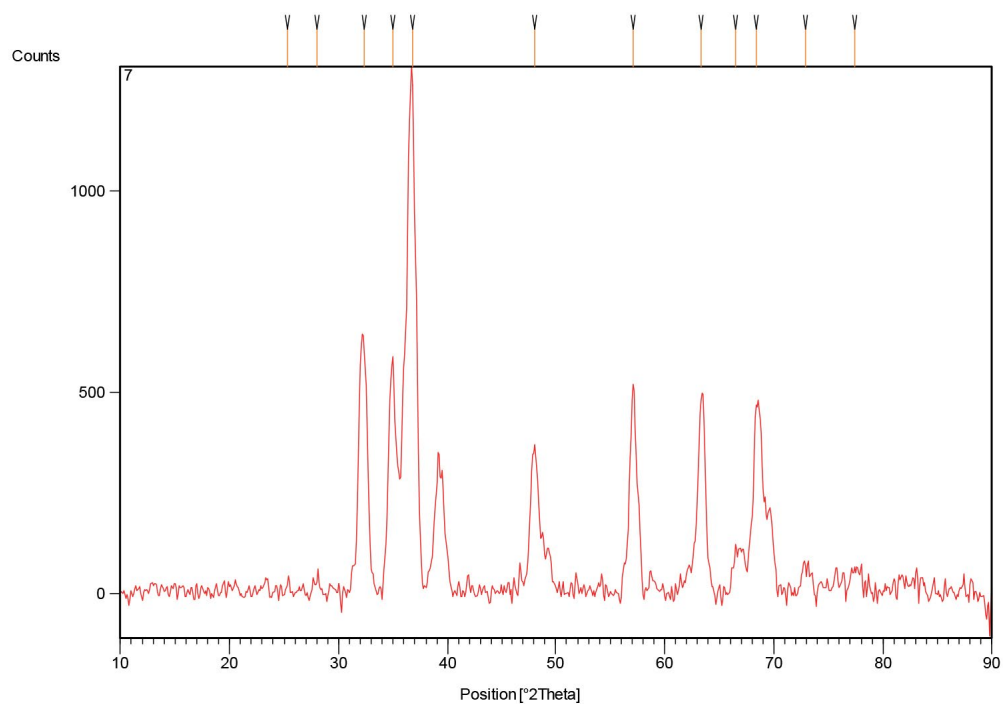


Figure 5. XRD pattern of Cu-ZnO NPs

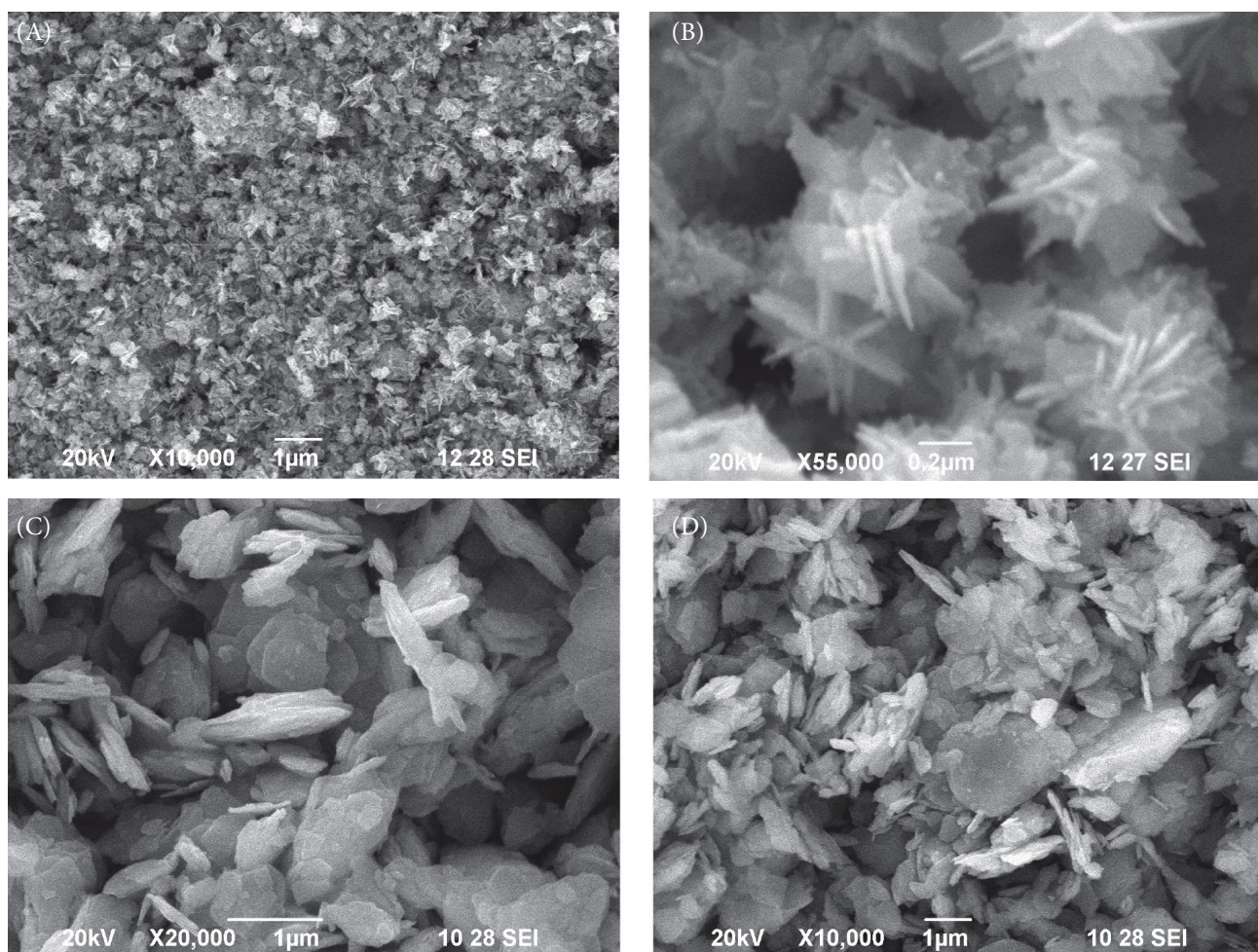


Figure 6. SEM images of ZnO (A) and Cu-ZnO (B-D)NPs at various magnification

particles. The average particle size was found to decrease with the increase in Cu doping into the ZnO matrix. The decrease in the particle size was mostly ascribed to the formation of Cu–O–Zn on the surface of the doped nanoparticles, which prevents the growth of crystal grains and assists separation of particles.³⁸

3. 5. Energy-Dispersive X-ray Analysis (EDAX)

EDAX was carried out to analyze the chemical composition and formation of un-doped ZnO and Cu-ZnO NPs. EDAX was used to confirm the presence of cationic metal ion (Cu^{2+}) dopant in ZnO. Fig. 7 shows the EDAX spectrum of ZnO (a) and Cu-ZnO (b). In addition, the EDAX spectra confirmed the presence of chemical constituents (Zn = 72.96% and O = 27.04% in un-doped ZnO NPs; Cu = 3.21%, Zn = 52.71% and O = 39.12% in Cu-ZnO NPs, it was also found that sample Cu-ZnO was composed only by Zn, Cu and O without any other impurities. The EDAX peak positions were consistent with ZnO, and the sharp peaks of EDAX indicated that the synthesized NPs had crys-

talline structures.^{39,40} The strong intensity and narrow width of ZnO diffraction peaks indicate that the resultant products were highly crystalline in nature. These findings were in close agreement with previous reports⁴¹ but with slight difference due to variations in chemical composition.

3. 6. Antimicrobial Activity

Comparative analysis of the antimicrobial efficacy of ZnO and Cu- ZnO NPs was carried out using well diffusion method and the results are tabulated in Tables 1 and 2. The antibacterial activity of ZnO and Cu-ZnO NPs was studied against three bacterial strains such as 1B, 2B, 3B and three fungal strains 1F, 2F and 3F. The zone of inhibition (mm) was evaluated for three concentrations such as 50 μL , 75 μL and 100 μL . It was clearly indicated that the percentage enhancement of the activity for 1B was 60% in the case of 50 μL . But in the case of 2B and 3B were 70.5% and 75% respectively. The results showed that the Cu-ZnO showed good inhibitory action against 3B. In the second case (75 μL) the percentage of enhancement of 1B, 2B and 3B were 62.5%, 72.2% and 80.9% respectively.

Table 1. Antibacterial activity of Cu-ZnO NPs

Name of the Sample	Zone of inhibition in mm								
	<i>E.coli</i>			<i>Pseudomonas aeruginosa</i>			<i>Staphylococcus aureus</i>		
	50 μL	75 μL	100 μL	50 μL	75 μL	100 μL	50 μL	75 μL	100 μL
ZnO	12 \pm 0.5	13 \pm 0.8	14 \pm 0.2	11 \pm 0.4	12 \pm 0.9	13 \pm 0.7	10 \pm 0.8	12 \pm 0.1	13 \pm 0.6
Cu-ZnO	16 \pm 0.9	17 \pm 0.4	18 \pm 0.1	16 \pm 0.4	17 \pm 0.1	17 \pm 0.9	15 \pm 0.3	16 \pm 0.5	17 \pm 0.2
Amikacin	18 \pm 0.2	20 \pm 0.45	22 \pm 0.3	17 \pm 0.8	19 \pm 0.2	21 \pm 0.5	16 \pm 0.9	18 \pm 0.8	20 \pm 1.2

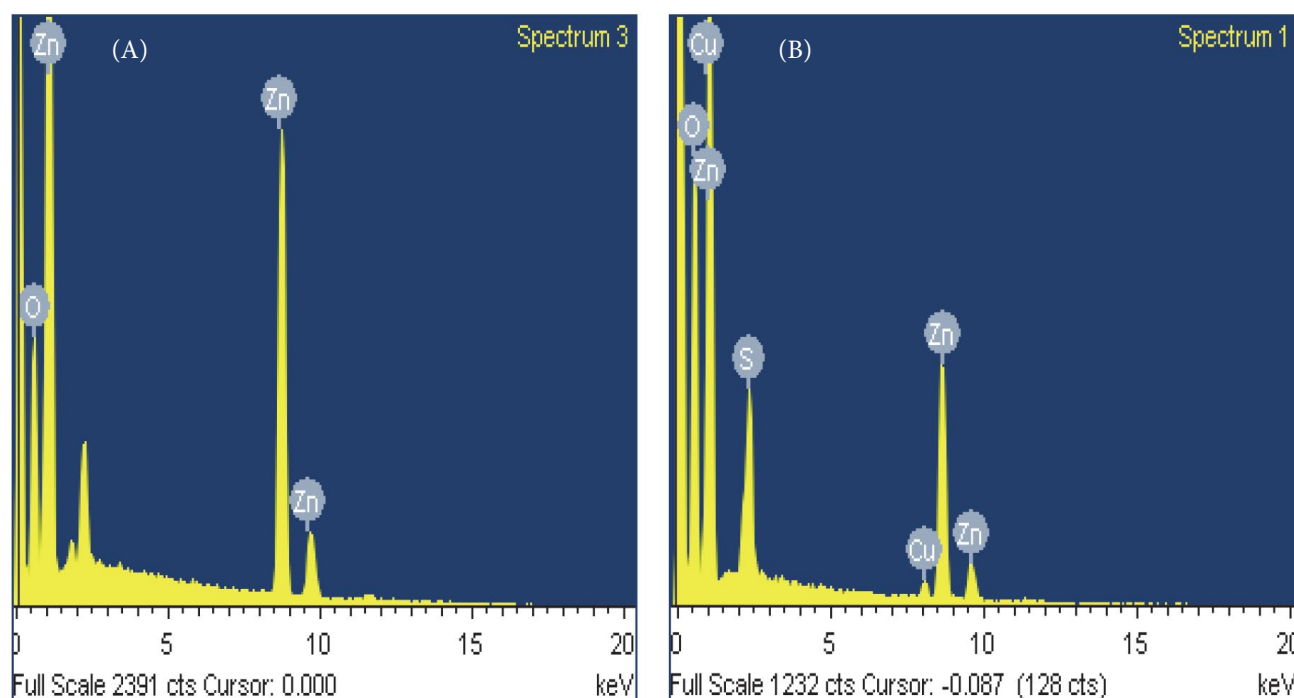


Figure 7. EDAX spectra of (A) ZnO and (B) Cu-ZnO NPs

Table 2. Antifungal activity of Cu-ZnO NPs

Name of the Sample	Zone of inhibition in mm								
	<i>Aspergillus flavus</i>			<i>Candida albicans</i>			<i>Fusarium sp</i>		
	50 μL	75 μL	100 μL	50 μL	75 μL	100 μL	50 μL	75 μL	100 μL
ZnO	13 \pm 0.1	15 \pm 0.4	17 \pm 0.56	12 \pm 0.3	14 \pm 0.2	15 \pm 1.0	12 \pm 0.8	14 \pm 1.0	17 \pm 0.1
Cu-ZnO	17 \pm 0.4	18 \pm 0.7	20 \pm 1.0	16 \pm 0.8	17 \pm 0.9	19 \pm 1.0	17 \pm 0.1	18 \pm 0.3	19 \pm 0.9
Ketoconazole	20 \pm 0.6	22 \pm 0.3	24 \pm 0.4	19 \pm 0.6	21 \pm 0.3	23 \pm 0.1	20 \pm 0.2	22 \pm 0.05	24 \pm 0.3

It was revealed that the zone of inhibition (%) was increased with concentration. If concentration increased to 100 μL , the percentage of enhancement of 1B, 2B and 3B were 64.7%, 73.6% and 86.3% respectively.

Similarly, the antifungal activity of ZnO and Cu-ZnO has been investigated systematically. Additionally, the zone of inhibition (mm) has been evaluated for three kinds of fungal species such as 1F, 2F and 3F. In this connection, three concentrations such as 50 μL , 75 μL and 100 μL were taken for the analysis. The percentage of enhancement was also calculated. From the results, the percentage of enhancement for 1F, 2F and 3F were 76.4%; 7% and 73.3% respectively. On increasing the concentration to 75 μL and 100 μL , the zone of inhibition increases. However, the percentage of enhancement from ZnO to Cu-ZnO was 83.3% (1F), 82.3% (2F) and 75% (3F) respectively. The results indicated that the percentage of enhancement was observed

maximum for Cu-ZnO (100 μL concentration) against 1F.

The results revealed that both ZnO and Cu-ZnO NPs were effective antibacterial agents on gram-positive as well as on gram-negative bacteria. However, percentage reduction in bacterial growth was found to be significantly higher using Cu-ZnO NPs compared to that of the ZnO NPs. Thus, the antibacterial effect of ZnO and Cu-ZnO was more pronounced for gram-positive bacteria as compared to gram-negative bacteria, which was in good agreement with the earlier studies.^{31,42–44} This was explained on the basis of differences in (i) cell membrane structure, (ii) physiology and metabolic activities of the cell, and (iii) degree of contact of gram-positive and gram-negative bacteria.⁴⁵ The antibacterial activity of pure and iron-doped ZnO nanoparticles showed that they were more resistant to gram-negative bacteria than gram-positive bacteria. The results were in good agreement with our results.⁴⁶

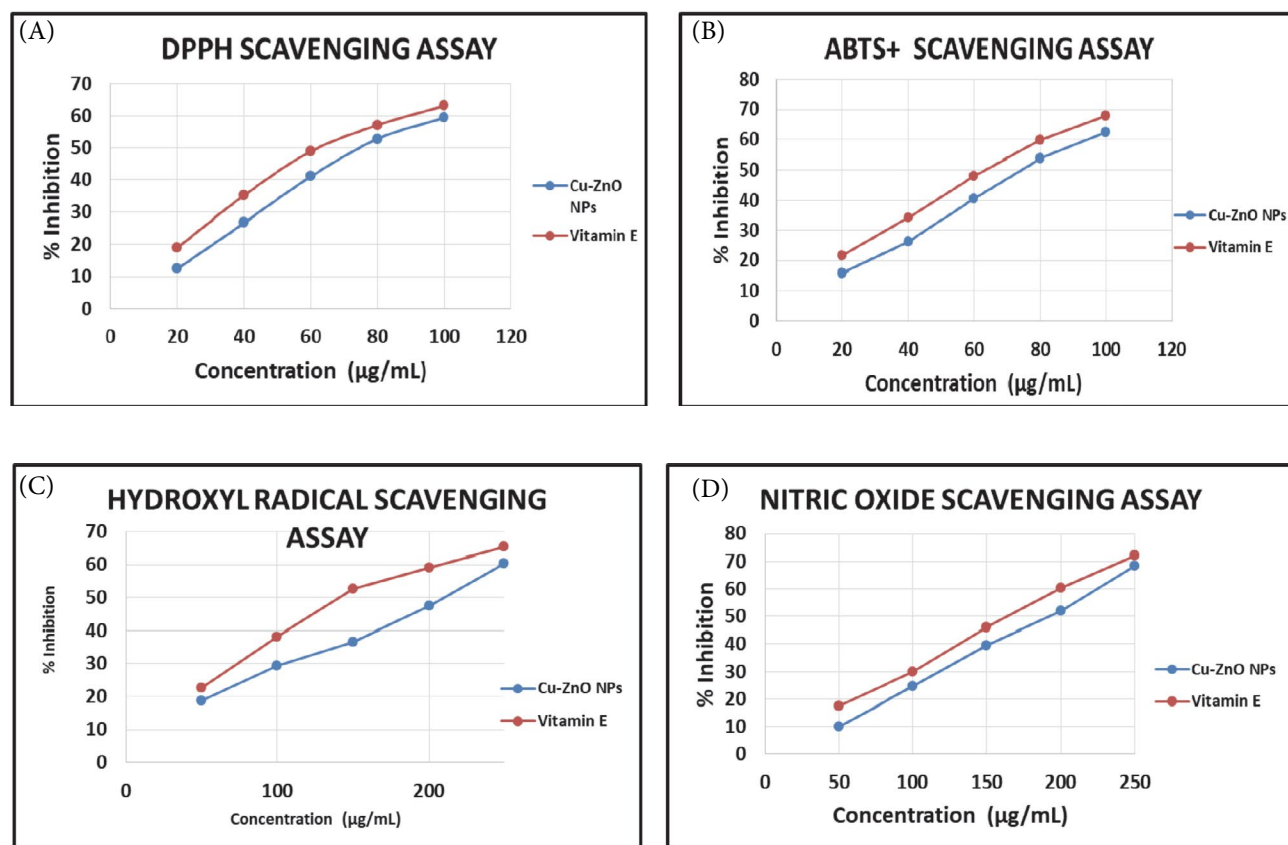


Figure 8. (A) DPPH, (B) ABTS⁺, (C) $\cdot\text{OH}$, (D) $\text{NO}\cdot$ radical scavenging activities of Cu-ZnO NPs and standard at various concentrations.

3. 7. Antioxidant Activity

The antioxidant activity of Cu-ZnO NPs were evaluated in a series of *in vitro* assays involving DPPH radicals, ABTS cationic radicals, hydroxyl radicals, nitric oxide scavenging assay in a dose dependent manner. The antioxidant activities of the Cu-ZnO NPs along with the standard at various concentrations have been shown in Fig.8 respectively. The IC₅₀ values of Cu-ZnO NPs in relevance to DPPH, ABTS⁺, ·OH, NO· assays were 76.29, 74.07, 205.96 and 180.89 µg/mL respectively (Table 3). From the results, the minimum and maximum percentage of inhibition for Cu-ZnO NPs against DPPH radicals for the concentration of 20 µg/mL and 100 µg/mL were 12.54 ± 0.28 and 59.45 ± 0.16 respectively. ABTS⁺ scavenging assay was also carried out to evaluate the free radical scavenging activity of the synthesized Cu-ZnO NPs. The minimum and maximum percentages of inhibition for 20 µg/mL and 100 µg/mL concentrations were 15.75 ± 0.26 and 62.48 ± 0.18 respectively. In the case of hydroxyl radicals scavenging assay, the free radical scavenging activity was investigated using various concentrations such as 50 µg/mL, 100 µg/mL, 150 µg/mL, 200 µg/mL and 250 µg/mL. The scavenging activity was increased with concentration as expected. The minimum and maximum percentage of inhibition at the concentrations of 50 µg/mL and 250 µg/mL were 18.61 ± 0.23 and 60.45 ± 0.55 respectively. Nitric oxide scavenging assay was also carried out for evaluation of free radical scavenging activity of Cu-ZnO NPs. The minimum and maximum percentage of inhibition at the concentration 50µg/mL and 250µg/mL were 10.15 ± 0.61 and 68.36 ± 0.94 respectively. The results indicated that the synthesized Cu-ZnO NPs exhibited appreciable antioxidant activity. The results were compared with the standard Vitamin E. The comparison clearly indicated that the Cu-ZnO NPs exhibited comparable activity with that of the standard. The results revealed that a concentration dependent activity was observed.

Table 3. IC₅₀ values (in µg/mL) calculated from various radical scavenging assays of Cu-ZnO NPs and standard vitamin E

Compound	DPPH	ABTS	·OH	NO·
Cu-ZnO	76.29	74.07	205.96	180.89
Vitamin E	63.32	63.14	147.88	158.13

3. 8. Anticancer Activity

The *in vitro* cytotoxic activity of the compound was determined against human breast (MCF7), human cervical (HeLa) cancer and Vero cell lines using MTT assay. Figure 9 showed the cytotoxicity of the ZnO NPs after 48 h incubation on MCF7, HeLa and Vero cell lines respectively. The results were analyzed by means of cell inhibition expressed as IC₅₀ values. Cu-ZnO NPs showed only mod-

erate activity with IC₅₀ value of 219.56 and 137.27 µg/mL against MCF7 and HeLa cell lines respectively. Fortunately, Cu-ZnO NPs are less toxic towards the normal cell line which was evident from its high IC₅₀ value (> 300 µg/mL). This showed that our Cu-ZnO NPs are particularly toxic towards cancer cell lines.

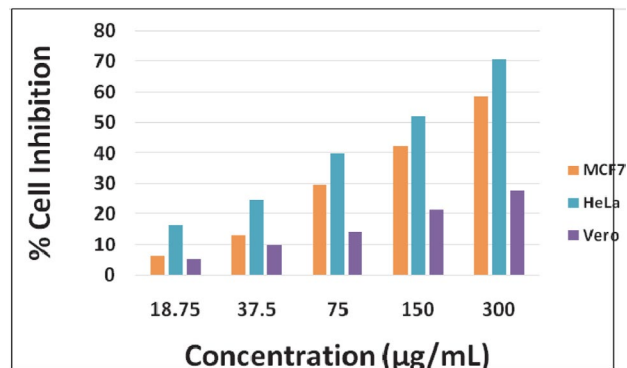


Figure 9. Cytotoxicity of Cu-ZnO NPs in MCF7, HeLa and Vero cell lines

4. Conclusions

In the present work, we have accomplished the synthesis of ZnO and Cu-ZnO nanoparticles. The antibacterial and antioxidant activity of the synthesized ZnO and Cu-ZnO NPs were investigated. The anticancer activity of Cu-ZnO NPs was also evaluated. Cu-ZnO NPs showed superior antibacterial action against gram positive as well as gram-negative bacteria. In addition, doped ZnO NPs had shown appreciable antioxidant activity against DPPH, ABTS⁺, ·OH and NO· assays. The UV-Visible results revealed that band gap undergoes a red-shift in doped ZnO nanorods as compared to pure ZnO. We infer that strong bonding of Cu in the host lattice of ZnO was responsible for the significant reduction of ZnO nanoparticle dissolution. Cu-ZnO NPs exhibited moderate anticancer activity against the tested cell lines. One of the important findings of this study was that Cu-doping unaltered the benign nature of ZnO nanoparticles towards the normal (Vero) cells. Overall, our data suggested a novel approach through which the inherent selective cytotoxicity of ZnO NPs against human breast cancer cells (MCF7) and human cervical carcinoma (HeLa) can be improved by doping of Cu²⁺ ion. Further research on anticancer activity of Cu-ZnO NPs in different types of cancer cells is warranted.

5. Acknowledgements

Author thanks Dr. R. Karvembu, Department of Chemistry, National Institute of Technology, Tiruchirappalli for providing the lab facility.

6. References

- G. Bisht, S. Rayamajhi, *Nanobiomedicine*. **2016**, *3*, 1–11.
DOI:10.5772/63437
- K. S. Smalley, M. Herlyn, *Mini Rev Med Chem*. **2006**, *6*, 387–393. DOI:10.2174/138955706776361402
- R. Langer, *Nature*. **1998**, *392*, 5–10. DOI:10.1038/32020
- R. Gowda, N. R. Jones, *J. Nanomed Nanotechnol*. **2013**, *4*, 184–219.
- I. Baskaran, T. S. N. Sankara Narayanan, A. Stephen, *Mater. Lett.* **2006**, *60*, 1990–1995. DOI:10.1016/j.matlet.2005.12.065
- M. F. Serag, N. Kaji, S. Habuchi, A. Biancod, Y. Baba, *RSC Adv*. **2013**, *3*, 4856–4862. DOI:10.1039/c2ra22766e
- S. Poyraz, I. Cerkez, T. S. Huang, Z. Liu, L. Kang, J. Luo, X. Zhang, *ACS Appl. Mater. Interfaces*. **2014**, *6*, 20025–20034.
DOI:10.1021/am505571m
- R. Wang, P. S. Billone, W. M. Mullett, *J. Nanomater*. **2013**, *2013*, 1–12. DOI:10.1155/2013/629681
- S. E. McNeil, *Nanomed. Nanobiotechnol*. **2009**, *1*, 264–271.
DOI:10.1002/wnan.6
- M. J. Akhtar, H. A. Alhadlaq, A. Alshamsan, M. A. Majeed Khan, M. Ahamed, *Scientific Reports*. **2015**, *5*, 13876.
DOI:10.1038/srep13876
- J. W. Rasmussen, E. Martinez, P. Louka, D. G. Wingett, *Expert Opin. Drug Deliv*. **2010**, *9*, 1063–1077.
DOI:10.1517/17425247.2010.502560
- M. Premanathan, K. Karthikeyan, K. Jeyasubramanian, G. Manivannan, *Nanomed Nanobiotechnol*. **2011**, *7*, 184–192.
DOI:10.1016/j.nano.2010.10.001
- C. Hanley, J. Layne, A. Punnoose, K. M. Reddy, I. Coombs, A. Coombs, K. Feris, D. Wingett, *Nanotechnology*. **2008**, *19*, 295103–295113. DOI:10.1088/0957-4484/19/29/295103
- A. B. Moghaddam, M. Moniri, S. Azizi, R. A. Rahim, A. B. Ariff, M. Navaderi and R. Mohamad, *Genes*. **2017**, *8*, 281–295.
DOI:10.3390/genes8100281
- S. A. Khan, F. Noreen, S. Kanwal, G. Hussain, *Dig J Nanomater Biostruct*. **2017**, *12*, 877–890.
- K. Kalantar, K. Kabir, F. Gharibi, S. Hatami, A. Maleki, *J Med Bacteriol*. **2013**, *2*, 20–26.
- R. Chauhan, A. Kumar, R. P. Chaudhary, *J Chem Pharm Res*. **2010**, *2*, 178–183.
- G. Glaspell, P. Dutta, A. Manivanna, *J. Clust. Sci*. **2005**, *16*, 523–536. DOI:10.1007/s10876-005-0024-y
- A. N. Malika, A. R. Reddy, K. S. Babu, K.V. Reddy, *Ceram. Int*. **2014**, *40*, 12171–12177.
- S. Deka, P. A. Joy, *Solid State Commun*. **2007**, *142*, 190–194.
DOI:10.1016/j.ssc.2007.02.017
- R. Saleh, N. F. Djaja, *Spectrochim Acta A Mol Biomol Spectrosc*. **2014**, *130*, 581–590. DOI:10.1016/j.saa.2014.03.089
- O. G. Jayakumar, H. G. Salunke, R. M. Kadam, M. Mohaparra, G. Yaswant, S. K. Kulshreshtha, *Nanotechnology*. **2006**, *17*, 1278–1285. DOI:10.1088/0957-4484/17/5/020
- M. E. Abrishami, A. Kompany, S. M. Hosseini, N. G. Bardar, *J Solgel Sci Technol*. **2012**, *62*, 153–159.
DOI:10.1007/s10971-012-2701-2
- S. Kim, J. H. Jun, K. Chao, J. Yun, K. S. Suh, T. Y. Kim, *Organic Electron*. **2008**, *9*, 445–451.
DOI:10.1016/j.orgel.2008.02.001
- Y. Lu, J. Zhong, S. Muthukumar, Y. Chen, H. M. Ng, W. Jiang, E. L. Garfunkel, *Appl Phys. Lett*. **2003**, *83*, 3401–3403.
DOI:10.1063/1.1621729
- D. Meng, X. Yu, C. Liu, X. He, Y. Wang, J. Xie, *Material Letter*. **2012**, *86*, 112–114. DOI:10.1016/j.matlet.2012.07.040
- S. A. Khan, F. Noreen, S. Kanwal, A. Iqbal, G. Hussain, *Mater. Sci. Eng. C*. **2018**, *82*, 46–59. DOI:10.1016/j.msec.2017.08.071
- M. S. Blois, *Nature*. **1958**, *29*, 1199–1200.
DOI:10.1038/1811199a0
- T. Nash, *Bihem. J*. **1953**, *55*, 416–421.
DOI:10.1042/bj0550416
- D. J. Stueher, M. A. Marletta, *J. Immunol*. **1987**, *139*, 518–525.
- T. Bhuyan, M. Khanuja, R. Sharma, S. Patel, M. R. Reddy, S. Anand, A. Varma, *J. Nanopart Res*. **2015**, *17*, 1–11.
DOI:10.1007/s11051-015-3093-3
- K. S. Ahn, T. Deutsch, Y. Yan, C. S. Jiang, C. L. Perkins, J. Turner, M. A. I. Jassim, *J Appl Phys*. **2007**, *102*, 23517–23522.
- S. Maensiri, P. Laokul, V. Promarak, *J. Cryst. Growth*. **2006**, *289*, 102–106. DOI:10.1016/j.jcrysgro.2005.10.145
- S. Suwanboon, *Sci. Asia*, **2008**, *34*, 31–34.
DOI:10.2306/scienceasia1513-1874.2008.34.031
- Y. C. Zhang, J. Y. Jang, G. L. Wang, M. Zhang, X. Y. Hu, *J. Cryst. Growth*. **2006**, *294*, 278–282.
DOI:10.1016/j.jcrysgro.2006.06.038
- C. L. Xua, D. H. Qina, H. Li, Y. Guo, T. Xu, H. L. Li, *Mater. Lett*. **2004**, *58*, 3976–3979. DOI:10.1016/j.matlet.2004.08.026
- M. Fua, Y. Li, S. Wu, P. Lu, J. Liu, F. Donga, *Appl Surf Sci*. **2011**, *258*, 1587–1598. DOI:10.1016/j.apsusc.2011.10.003
- A. Samavati, A. F. Ismail, H. Nur, Z. Othaman, M. K. Mustafa, *Chin. Phys. B*. **2016**, *25*, 077803–077809.
DOI:10.1088/1674-1056/25/7/077803
- S. A. Khan, F. Noreen, S. Kanwal, A. Iqbal, G. Hussain, *Mater. Sci. Eng. C*. **2017**, *82*, 46–59.
DOI:10.1016/j.msec.2017.08.071
- S. Y. Pung, C. S. Ong, K. M. Isha, M. H. Othman, *Sains Malays*. **2014**, *43*, 273–281.
- H. R. Ghaffarian, M. Saiedi, M. A. Sayyadnejad, A. M. Rashidi, *Iran. J. Chem. Chem. Eng*. **2011**, *30*, 1–6.
- M. Premanathan, K. Karthikeyan, K. Jeyasubramanian, G. Manivannan, *Nanomedicine*. **2011**, *7*, 184–192.
DOI:10.1016/j.nano.2010.10.001
- K. R. Raghupathi, R. T. Koodali, A. C. Manna, *Langmuir*. **2011**, *27*, 4020–4028. DOI:10.1021/la104825u
- T. Bhuyan, K. Mishra, M. Khanuja, R. Prasad, A. Varma, *Mater Sci Semicond Process*. **2015**, *32*, 55–61.
DOI:10.1016/j.mssp.2014.12.053
- W. K. Jung, H. C. Koo, K. W. Kim, S. Shin, S. H. Kim, Y. H. Park, *Appl Environ Microbiol*. **2008**, *74*, 2171–2178.
DOI:10.1128/AEM.02001-07
- M. Li, S. Pokhrel, X. Jin, L. Madler, R. Damoiseaux, E. M. V. Hoek, *Environ Sci Technol*. **2011**, *45*, 755–761.
DOI:10.1021/es102266g

Povzetek

V prispevku preučujemo, kako dopiran baker (Cu) v nanodelcih cinkovega oksida (ZnO) vpliva na energijsko vrzel ("band gap") in na selektivno citotoksičnost napram celicam raka dojke (MCF7), celicam raka materničnega vratu (HeLa) in napram normalnim celicam (Vero). Nanodelce ZnO dopirane z Cu (Cu – ZnO NPs) smo sintetizirali in karakterizirali z UV-Vis spektroskopijo, infrardečo spektroskopijo (FT-IR), rentgensko praškovo difrakcijo (XRD), vrstično elektronsko mikroskopijo (SEM) in energijsko disperzijsko spektroskopijo rentgenskih žarkov (EDX). Energijska vrzel dopiranih nanodelcev ZnO se je zmanjšala iz 3,54 eV na 3,29 eV. Antimikrobno aktivnost smo ovrednotili napram trem bakterijskim in glivičnim sevom. Antioksidativno delovanje smo preučili z uporabo prostega radikala DPPH, radikalov ABTS⁺, hidroksilnih radikalov in radikalov dušikovega oksida. Rakave celice smo izpostavili nanodelcem in izmerili vrednosti IC₅₀: 219,56 µg/ml (MCF7) in 137,27 µg/ml (HeLa). Dopirani nanodelci ZnO (Cu–ZnO NPs) imajo izboljšano selektivno citotoksičnost napram celicam MCF7 in HeLa, dopiranje pa ne vpliva na normalne celice.



Except when otherwise noted, articles in this journal are published under the terms and conditions of the Creative Commons Attribution 4.0 International License

Scientific paper

Synergistic Solvent Extraction of Lanthanides(III) with Mixtures of 4-Benzoyl-3-Methyl-1-Phenyl-5-Pyrazolone and Phosphoryl-Containing Podands

Alexander Nikolaevich Turanov,¹ Vasilii Konstantinovich Karandashev,^{2,3}
Vladimir Evgenevich Baulin,^{4*} Dmitriy Vladimirovich Baulin⁵
and Aslan Yusupovich Tsivadze⁵

¹ Institute of Solid State Physics, Russian Academy of Sciences, 142432 Chernogolovka, Russia

² Institute of Microelectronics Technology and High Purity Materials, Russian Academy of Sciences, 142432 Chernogolovka, Russia

³ National University of Science and Technology MISiS, 119049, Moscow, Russia

⁴ Institute of Physiologically Active Compounds, Russian Academy of Sciences, Chernogolovka, Moscow Region, 142432 Russia

⁵ Frumkin Institute of Physical Chemistry and Electrochemistry, Russian Academy of Sciences, Moscow, 119991 Russia

* Corresponding author: E-mail: mager1988@gmail.com

Received: 07-02-2019

Abstract

The solvent extraction of La, Ce, Pr, Nd, Sm, Eu, Gd, Tb, Dy, Ho, Er, Tm, Yb, and Lu from weak acidic chloride solutions into an organic phase containing 4-benzoyl-3-methyl-1-phenyl-5-pyrazolone (HP) and phosphoryl-containing podands (L) has been studied. A considerable synergistic effect was observed in the presence of neutral ligands L in the organic phase containing HP. The stoichiometry of the Ln(III) extracted species was determined by slope analysis and the equilibrium constants were calculated. It was found that the lanthanide(III) ions are extracted with mixtures of HP and neutral ligands in toluene from weak acidic solutions as LnLP₃ complexes.

Keywords: Lanthanides(III); synergistic extraction; 4-benzoyl-3-methyl-1-phenyl-5-pyrazolone; phosphoryl-containing podands.

1. Introduction

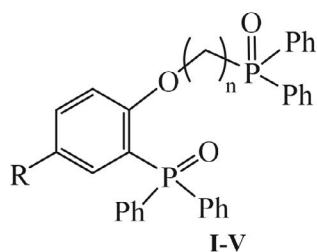
Solvent extraction is a widely used technique for the separation and preconcentration of lanthanide(III) ions. A synergistic effect, a non-additive increase in the distribution ratios of metal ions, is often used to increase the efficiency of the extraction of metal ions.^{1–3} The synergistic effect in solvent extraction systems is due to an increase in the hydrophobicity of extracted species as a result of replacement of water molecules bound to the metal ion by molecules of a synergistic compound.³ The application of mixtures of an acidic chelating extractant and a neutral donor is one of the most thoroughly studied synergistic extraction processes. During the last few decades, the syn-

ergistic extraction of lanthanides(III) with mixtures of acidic chelating extractants such as β -diketones, 4-acylpyrazolones, 4-acyl-5-izoxazolone, etc. and neutral donor extractants (e.g. nitrogen-containing compounds,^{4–6} sulfoxides,^{7,8} crown ethers,^{3,9–11} diglycolamides,¹² neutral mono- and polydentate organophosphorus compounds,^{13–20} etc.) has been studied. Many studies have been carried out using phosphorus-containing calix[*n*]arenes as a synergistic agent at the Ln(III) extraction with various acidic chelating extractants of β -diketone type.^{21–26} The introduction of P(O) functional groups in the calixarene architecture leads to a significant increase in the extraction efficiency.²⁶ The addition of phosphorus-containing calix[6]arene to the chelating extractant, 4-benzoyl-3-

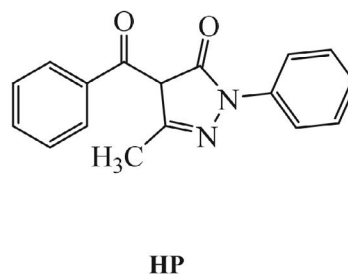
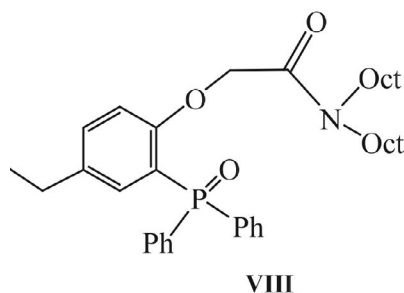
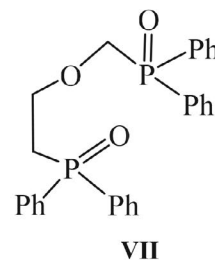
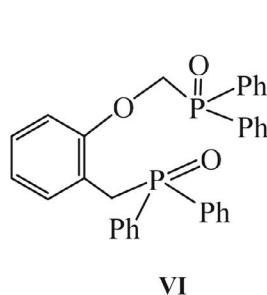
methyl-1-phenyl-5-pyrazolone, improves the Ln(III) extraction and produces very large synergistic effects (more than five orders of magnitude).²⁵

Recently, a great interest has arisen in the use of acyclic analogues of crown ethers (podands), as extractants. The complexation ability of a linear polyether ligand can be markedly increased by replacing its terminal alkyl groups with amide or phosphoryl groups.^{27,28} Phosphoryl-containing podands have high extraction abilities for metal ions due to the ability of flexible podand molecules to acquire pseudo-macrocyclic conformation upon complexation.²⁹ The main factors determining the efficiency of metal ion extraction with phosphoryl-containing podands are the donor ability of phosphoryl oxygen atoms, the length of the polyether chain, and the nature of the moiety linking it to the phosphoryl group.³⁰

In this work, we study the effect of structure of phosphoryl-containing podands I–VII on the extraction of Ln(III) ions with 4-benzoyl-3-methyl-1-phenyl-2-pyrazolin-5-one (HP) in organic diluents and determine the composition of the extracted complexes of Ln(III). The extraction behavior of the above ligands is compared with that of 2-(2-(diphenylphosphoryl)phenoxy)-N,N-dioctylacetamide VIII and monodentate neutral extractant, triphenylphosphine oxide (TPhPO).³¹ The structural formulae of the extractants studied are given below.



I: R = H, n = 0; **II:** R = H, n = 1;
III: R = Et, n = 1; **IV:** R = Et, n = 2;
V: R = H, n = 3



2. Experimental

2.1. Materials and Methods

The commercial products triphenylphosphine oxide (purity > 99%, Chemapol) and 4-benzoyl-3-methyl-1-

phenyl-5-pyrazone (purity > 99%, Vekton) were used as received. Chemical- and analytical-grade chloroform, 1,2-dichloroethane and toluene were used as diluents. (2-((Diphenylphosphoryl)methoxy)phenyl)diphenylphosphine oxide (**II**), (2-((diphenylphosphoryl)-4-ethylphenoxy)methyl)diphenylphosphine oxide (**III**), (2-(2-(diphenylphosphoryl)-4-ethylphenoxy)ethyl)diphenylphosphine oxide (**IV**), (2-(3-(diphenylphosphoryl)propoxy)phenyl)diphenylphosphine oxide (**V**) and ((2-(diphenylphosphoryl)ethoxy)methyl)diphenylphosphine oxide (**VII**) were synthesized as described.^{33–35} Their physical constants and data on elemental analysis and NMR spectra were in agreement with the published data.

2.2. Synthesis of the Extragents

2-(Diphenylphosphoryl)phenyldiphenylphosphinate (I). A mixture of 6.40 g (21.74 mmol) of (2-hydroxyphenyl)diphenylphosphine oxide,³² 1.69 g (21.74 mmol) of dry pyridine, 5.12 g (21.74 mmol) of diphenylphosphinic chloride and 50 mL of dry benzene was mixed on magnetic stirrer at the temperature of 80 °C for 6 h. Then the reaction mixture was poured into water, extracted by benzene (4 × 30 mL), the organic extracts were rinsed with 20% HCl solution (3 × 30 mL), water (3 × 30 mL), dried by

MgSO₄. After evaporation, the residue was crystallized from benzene-hexane mixture. The yield of **I** was 7.23 g (69%), m.p. 175–177 °C. Anal. Calcd. for C₃₀H₂₄O₃P₂ (%): C, 72.87; H, 4.89; P 12.53. Found (%): C, 72.93; H, 4.90; P, 12.56. ¹H NMR (CDCl₃): δ: 7.01–7.28 (2H, m, Ar-H), 7.33–7.56 (12H, m, Ar-H), 7.63–7.90 (10H, m, Ar-H). ³¹P

NMR (CDCl₃): δ: 28.72, 32.25.

(2-((diphenylphosphoryl)methoxy)benzyl)diphenylphosphine oxide (VI). A mixture of 3.22 g (10.00 mmol) 2-(hydroxybenzyl)diphenylphosphine oxide 3.86 g (10.00 mmol) (diphenylphosphoryl)methyl-4-methylbenzenesulphonate and 2.26 g (10.00 mmol) anhydrous cesium carbonate in 35 mL of dry dioxane was heated and stirred at 100 °C for 8 h.³⁶ The reaction mixture was diluted by 75 mL of water, acidified by adding concentrated HCl to pH 1, and extracted by CHCl₃ (3 × 25 mL). The organic layer was separated, washed with water, and evaporated under reduced pressure to give crude product VI. It was purified by column chromatography on silica gel 100–160 mm, the eluents CHCl₃ and CHCl₃/*i*-PrOH (10:1). The yield of VI was 4.04 g (77 %), m.p. 168–169.5 °C. Anal. Calcd. for C₃₂H₂₈O₃P₂ (%): C, 73.56; H, 5.40; P 11.86. Found (%): C, 73.40; H, 5.34; P, 11.69. ¹H NMR (CDCl₃): δ: 3.81 (2H, d, ²J_{H-P} = 7.10 Hz, ArCH₂P), 4.49 (2H, d, ²J_{H-P} = 5.18 Hz, OCH₂P(O)), 7.00–7.32 (2H, m, Ar-H), 7.35–7.56 (12H, m, Ar-H), 7.61–7.92 (10H, m, Ar-H). ³¹P NMR (CDCl₃): δ: 28.15, 32.15.

2. 3. Apparatus

An X-7 mass spectrometer with a quadrupole mass analyzer (Thermo Electron, USA) was used for measurement of lanthanides concentration and pH-150 digital pH meter was used for pH measurements. The ¹H and ³¹P NMR spectra were recorded on a Bruker DXP-200 spectrometer with Fourier transform using tetramethylsilane (¹H, internal) and 85% H₃PO₄ (³¹P, external) as standard. Elemental analyses were performed using a Perkin-Elmer 240C analytical instrument.

2. 4. Solvent Extraction Procedure

Stock solutions of the lanthanide(III) ions were prepared from their oxides by dissolving in concentrated hydrochloric acids and diluting with deionized water to the required volume. All the lanthanides (III) (except Pm) were present in the initial aqueous phase when simultaneous extraction of Ln(III) was studied. The ionic strength was maintained at 0.1 M with NaCl and HCl. The initial lanthanide ions concentration was 2 × 10⁻⁶ M for each element. Extractant solutions in the organic diluents were prepared from precisely weighed amounts of the reagents.

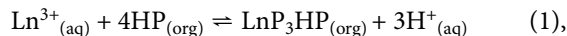
Equal volumes (2 mL) of the aqueous and organic phases were shaken mechanically for 60 min at 22 ± 1 °C, which was sufficient to reach equilibrium. After phase separation, 1 mL of the aqueous solution was taken for further analysis. A portion of the organic phase was transferred to another glass tube, and a specific volume of 1 M HCl solution was added. The mixture was shaken for 30 min and Ln(III) in the organic phase was extracted back into the aqueous phase.

Concentrations of Ln(III) in the initial and equilibrium aqueous solutions after extraction and back-extraction were determined by inductively coupled plasma mass-spectrometry (ICP-MS). The sum of the metal ion concentrations in the two phases agreed well with the initial concentration. The distribution ratios of lanthanides (*D*_{Ln}) were calculated as the ratio of concentrations in the equilibrium organic and aqueous phases. Triplicate experiments showed that the reproducibility of the *D*_{Ln} measurements was generally within 5%. The acidity of the aqueous phase was measured by a pH-meter with an accuracy of 0.01 pH units.

3. Results and Discussion

3. 1. Extraction of Lanthanide(III) Ions with Mixtures of HP and Neutral Ligands I–VIII

There have been many reports on solvent extraction of lanthanide(III) ions with 4-acylpyrazolones.³⁷ The lanthanides(III) extraction with 4-benzoyl-3-methyl-1-phenyl-5-pyrazolone (HP) alone in organic diluents was previously studied by Dukov et al.^{38,39} They found that the metal ions are extracted as self-adducts LnP₃HP and their extraction can be described by the equation:



where the subscripts “aq” and “org” denote the aqueous and organic phases, respectively.

The corresponding extraction constant *K*_p is

$$K_p = D_{\text{Ln}} [\text{H}^{+}]^3_{(\text{aq})} [\text{HP}]^{-4}_{(\text{org})} \quad (2)$$

Preliminary experiments showed that the lanthanides(III) extraction with compounds I–VII and TPhPO alone is negligible under the experimental conditions of the present study. However, a considerable enhancement of the Ln(III) extraction with HP in the presence of these compounds in the organic phase was observed.

To compare the extraction efficiency of neutral donor compounds, a simultaneous extraction of Ln(III) ions from aqueous solutions with mixtures of HP and compounds I–VIII and TPhPO in 1,2-dichloroethane was studied (Figure 1). These experiments showed that the efficiency of Ln(III) synergistic extraction with compounds of phosphine oxide type (II–VII) is higher than that of compound I of phosphinate type. This can be due a weakening donor ability of P(O) group of compound I as compared with compounds II–VII. The efficiency of Ln(III) synergistic extraction with compounds II–VII is higher than that of monodentate TPhPO (Figure 1). Therefore, an increase of a number of P(O) groups in the compounds II–VII molecule leads to an increase in the *D*_{Ln} values.

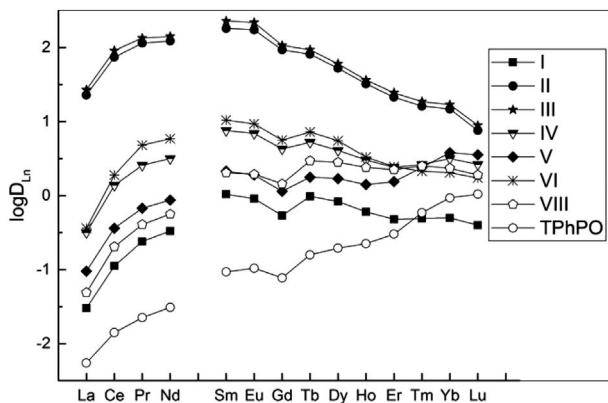


Figure 1. The extraction of lanthanides(III) with HP-compounds I–VIII and TPhPO mixtures in 1,2-dichloroethane at $[HP] = 0.02$ M, $[L] = 0.005$ M and $pH = 2.0$.

The data in Figure 1 suggest that mixtures containing compounds **II** or **III** exhibit the highest synergistic effect. The introduction of ethyl group into the *o*-phenylene fragment of compound **II** is not appreciably influence on the Ln(III) extraction with compound **III**, though is accompanied by an increase of compound **III** hydrophobicity. The replacement of $P(O)Ph_2$ group in the molecule of compound **III** by $C(O)NOct_2$ one leads to a decrease of Ln(III) extraction with compound **VIII**, which suggests that the $P(O)$ group has a higher complexation ability than the $C(O)$ group. The replacement of the *o*-phenylene fragment in the compound **II** molecule by a dimethylene one causes a decrease of Ln(III) extraction with compound **VII**. A higher extraction efficiency of compound **II** as compared with that of podand **VII** was explained both by the delocalization of the electron density from the phenylene group to the metal-connected chelate cycle and an increase in the conformational rigidity of compound **II** molecule, which facilitates the formation of a more stable Ln(III) complex.²⁸ An increase in alkylene bridge between $P(O)$ group and ether oxygen atom (compounds **IV** and **V**) as well as an increase in the distance between the phosphoryl group and the *o*-phenylene fragment (compound **VI**) violates the conditions favorable for the formation of chelate cycles and thus leads to a decrease of the Ln(III) extraction with mixtures of HP and compounds **IV–VI** (Figure 1).

It should be noted that the difference in the synergistic efficiency of compounds **II** or **III** and other studied compounds decreases from La(III) to Lu(III), i.e. with an increase of their atomic number (*Z*). Thus, the ratio $D_{Ln}(I-II)/D_{Ln}(VIII)$ decreases in the lanthanide series from 467 for La(III) to 4.0 for Lu(III) and the ratio $D_{Ln}(II)/D_{Ln}(VII)$ decreases from 57 for La(III) to 1.6 for Lu(III). Evidently, the synergistic extraction of light Ln(III) ions is most sensitive to changes in the neutral synergistic structure.

The effect of an organic diluent on the synergistic extraction of Ln(III) ions with mixtures of HP and compound **III** was also studied. The data in Figure 2 show that

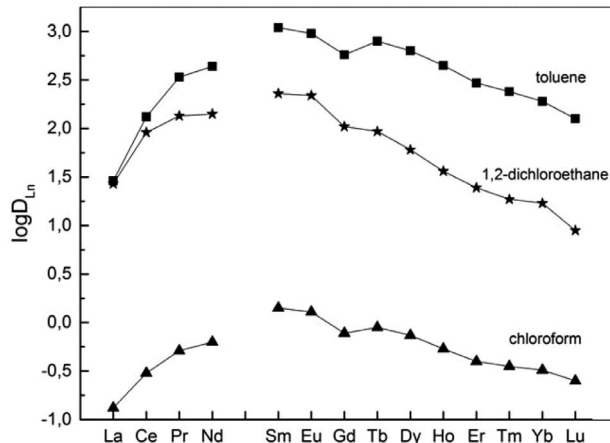


Figure 2. The extraction of lanthanides(III) with HP-compound **III** mixtures in toluene, 1,2-dichloroethane and chloroform at $[HP] = 0.02$ M, $[L] = 0.005$ M and $pH = 2.0$.

the extraction efficiency increased in the order: chloroform < 1,2-dichloroethane < toluene. The same tendency was observed at the metal ions extraction with mixtures of acidic chelating extractants and neutral donor compounds.⁴⁰

3. 2. Extraction of Lanthanide(III) Ions with Mixtures of HP and Neutral Ligand III in Toluene

In the extraction systems with compound **III** and HP, the plots of $\log D_{Ln}$ vs. pH exhibited a series of straight lines with slopes close to three (Figure 3), which means that three H^+ ions were released in the extraction reaction.

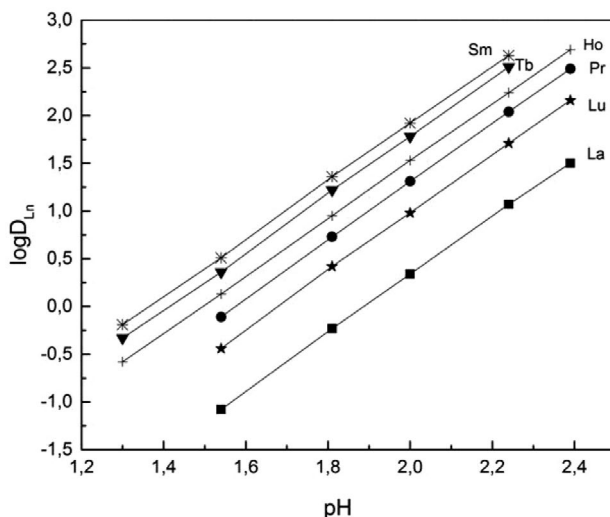


Figure 3. The effect of pH on the extraction of Ln(III) with the mixture of 0.001 M compound **III** and 0.01 M HP in toluene.

The stoichiometry of the Ln(III) extracted complexes in HP–**III** systems was determined by slope analysis. The plots of $\log D_{Ln}$ vs. $\log [HP]$ at a constant pH and neu-

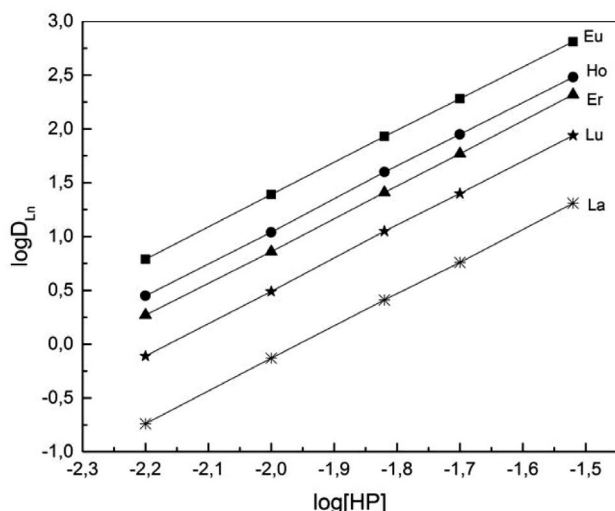
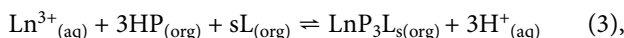


Figure 4. The effect of HP concentration in toluene containing 0.001 M compound **III** on the extraction of lanthanides(III) at pH = 2.0.

tral ligand **III** concentration in the organic phase are straight lines with slopes close to three (Figure 4).

As the Ln(III) extraction from aqueous solutions with compound **III** and HP alone is negligible ($\log D_{Ln} < -2$) at pH = 2, the values of D_{Ln} obtained experimentally are equal to the distribution ratios due to the synergistic effect. Therefore, the synergistic extraction of Ln(III) ions can be described by the equation:



where s is the metal:L stoichiometric ratio.

The variation of D_{Ln} as a function of the compound **III** concentration in toluene containing HP is shown in Figure 5.

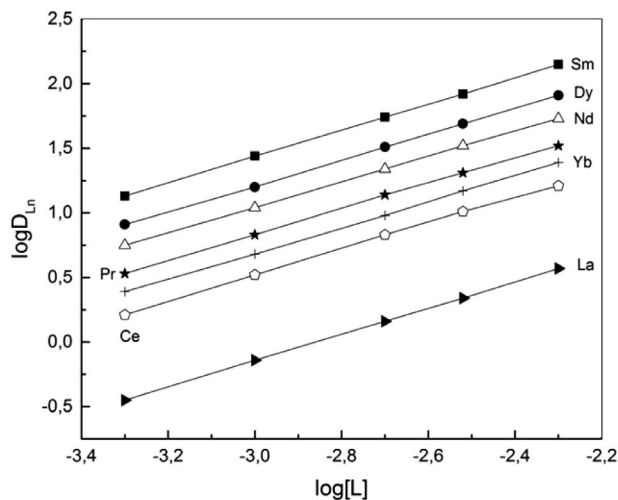


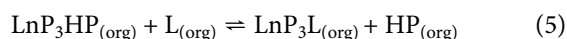
Figure 5. The effect of compound **III** concentration in toluene containing 0.01 M HP on the extraction of lanthanides(III) at pH = 2.0.

The dependence of $\log D_{Ln}$ vs. $\log [L]$ is linear with a slope of 1 ± 0.02 . Hence, one molecule of neutral donor compound **III** is involved in the formation of synergistic Ln(III) complexes. The same stoichiometry of the Ln(III) extracted complexes was observed at the extraction with mixtures of HP and phosphorus-containing calix[6] arene.³¹ On the other hand, in the HP – trioctylphosphine oxide (TOPO) system, the formation of LnP_3TOPO complexes at lower TOPO concentrations and $\text{LnP}_3(\text{TOPO})_2$ at higher TOPO concentrations was observed.¹³

Assuming that the partition of HP and compound **III** towards aqueous phase is very low and the polymerization in the organic phase as well as the hydrolysis in the aqueous phase occur only to a negligible extent,^{37,34} the overall equilibrium constant values $K_{P,L}$ can be determined by the equation:

$$\log K_{P,L} = \log D_{Ln} - 3 \log [\text{HP}]_{(\text{org})} - \log [\text{L}]_{(\text{org})} - 3 \text{pH} \quad (4)$$

The formation of synergistic adducts in the organic phase can be described by the equation:



The equilibrium constant $\beta_{P,L}$ for the adducts formation in the organic phase can be calculated using the expression:

$$\log \beta_{P,L} = \log K_{P,L} - \log K_P \quad (6)$$

The values of K_P for the lanthanides(III) extraction with HP alone in toluene were obtained in the previous work.²⁰ The values of the equilibrium constants $K_{P,L}$ and $\beta_{P,L}$ were calculated from the experimental data and are presented in Table 1. Note that these constants are concentration only because they were calculated on the assumption that the activity coefficients of the species involved do not change significantly under the experimental conditions of the present work.

The data presented in Table 1 show that the addition of neutral donor ligand **III** to the system Ln(III)–HP leads to a very large increase of the efficiency of Ln(III) extraction. The synergistic enhancement produced by mixtures of HP and the studied neutral donor extractant can be determined using a synergistic coefficient $\text{SC} = D_{L,HP}/(D_L + D_{HP})$, where D_L , D_{HP} and $D_{L,HP}$ are the distribution ratios of the Ln(III) ion with the two extractants taken separately and with their mixture. The values of SC for Ln(III) extraction with mixtures of HP and compound **III** is determined by the stability of Ln(III) adducts and dependent on the concentration of HP and compound **III** in organic phase:

$$\log \text{SC} = \log \beta_{P,L} + \log [\text{L}]_{(\text{org})} - \log [\text{HP}]_{(\text{org})} \quad (7)$$

The data presented in Table 1 show that the extraction ability of HP alone for lanthanide(III) ions increases

Table 1. Values of the equilibrium constants K_P , K_{PL} , $\log \beta_{HPL}$ as well as values of synergistic coefficients SC for Ln(III) extraction with HP-compound **III** mixtures in toluene.

Ln(III)	$\log K_P$ [20]	$\log K_{PL}$	$\log \beta_{PL}$	$\log SC^a)$
La	-5.56 ± 0.03	2.86 ± 0.03	8.42 ± 0.06	8.12
Ce	-4.83 ± 0.03	3.51 ± 0.02	8.34 ± 0.05	8.04
Pr	-4.36 ± 0.03	3.91 ± 0.03	8.27 ± 0.06	7.97
Nd	-4.08 ± 0.04	4.03 ± 0.02	8.11 ± 0.06	7.81
Sm	-3.48 ± 0.03	4.43 ± 0.02	7.91 ± 0.05	7.61
Eu	-3.35 ± 0.03	4.37 ± 0.02	7.72 ± 0.05	7.42
Gd	-3.44 ± 0.04	4.15 ± 0.03	7.59 ± 0.07	7.29
Tb	-3.17 ± 0.03	4.29 ± 0.02	7.46 ± 0.05	7.16
Dy	-3.06 ± 0.04	4.19 ± 0.02	7.25 ± 0.06	6.95
Ho	-3.07 ± 0.03	4.04 ± 0.02	7.11 ± 0.05	6.81
Er	-2.94 ± 0.03	3.86 ± 0.03	6.80 ± 0.06	6.50
Tm	-2.67 ± 0.03	3.77 ± 0.02	6.44 ± 0.05	6.14
Yb	-2.43 ± 0.04	3.67 ± 0.03	6.10 ± 0.07	5.80
Lu	-2.46 ± 0.03	3.49 ± 0.02	5.95 ± 0.05	5.65

^{a)} [HP] = 0.01 M, [III] = 0.005 M and pH = 2.0

with the increasing atomic number of lanthanides. This can be connected with an increase of the stability of Ln(I–II) complexes with hard ligands as the Ln^{3+} ions charge density increase owing to decrease of their ionic radii when Z rises. In the lanthanides series, the K_{PL} values increases from La(III) to Sm(III) and then non-monotonic decrease in K_{PL} values is observed due to tetrad effect upon the Ln(III) extraction.⁴¹ The same character of the K_{PL} –Z dependency was observed at the Ln(III) extraction with mixtures of HP and dibutyl-(*N,N*-dibutylcarbamoyl-methoxy)phosphine oxide.²⁰

The data presented in Table 1 show that the values of β_{PL} as well as SC decrease from La(III) to Lu(III). A similar tendency was observed for the adduct formation of LnP_3 with trioctylphosphine oxide,¹³ phosphorus-containing calix[6]arene and dibutyl-(*N,N*-dibutylcarbamoyl-methoxy)phosphine oxide.^{25,20} On the other hand, an increase of the β values from La(III) to Lu(III) was observed by Atanassova and Dukov in the HP–1-(2-pyridylazo)-2-naphthol synergistic system.⁴²

4. Conclusions

Synergetic solvent extraction of lanthanide (III) ions with mixtures of 4-benzoyl-3-methyl-1-phenyl-5-pyrazolone and neutral phosphoryl-containing podands has been studied. The structure of phosphoryl-containing podands has a considerable effect on their extraction efficiency. In combination with HP, compounds **II** and **III** exhibit the highest synergistic effect. A remarkably large synergistic effect (more than 5–8 order of magnitude) was observed for the Ln(III) ions extraction with mixtures of HP and **III** in toluene from weak acidic HCl solutions. This effect is associated with the replacement of HP in self-adducts LnP_3HP by neutral donor ligand **III**. The stoichiometry of the Ln(III) extracted complexes in the HP–**III** system was determined by slope analysis and the equilibrium constants were calculated.

The study was carried out within the framework of a state assignment of the Institute of Solid State Physics, Institute of Microelectronics Technology and High Purity Materials, the Institute of Physiologically Active Compounds the Frumkin Institute of Physical Chemistry and Electrochemistry, Russian Academy of Sciences, and partial supported by the Russian Foundation for Basic Research (project no. 18-29-24069) and program of competitive recovery of National University of Science and Technology MISiS (project no. K2-2016-070).

5. References

1. K. L. Nash, M. P. Jensen, *Analytical separations of lanthanides: basic chemistry and methods*. In *Handbook on the Physics and Chemistry of Rare Earths*; Gschwendner, K.A., Eyring, L. (Eds.). Elsevier Science B.V., **2000**; Vol. 28, 311–371. DOI:10.1016/S0168-1273(00)28008-2
2. G. J. Lumetta, A. V. Gelis, G. F. Vandegrift, *Solvent Extr. Ion Exch.* **2010**, 28, 287–312. DOI:10.1080/07366291003684253
3. A. H. Bond, M. L. Dietz, R. Chiarizia, *Ind. Eng. Chem. Res.* **2000**, 39, 3442–3464. DOI:10.1021/ie000356j
4. S. Nakamura, S. Takai, K. Akiba, *Anal. Sci.* **2002**, 18, 319–323. DOI:10.2116/analsci.18.319
5. I. Matsubayashi, Y. Hasegawa, *Anal. Sci.* **2001**, 17, 221–223. DOI:10.1111/j.1477-9730.2001.tb01580.x
6. M. A. Petrova, *J. Chem. Eng. Data* **2010**, 55, 5791–5796. DOI:10.1021/je100733k
7. S. K. Sahu, V. Chakravorty, M. L. P. Reddy, T. R. Ramamohan, *Radiochim. Acta* **1999**, 85, 107–111.
8. M. Atanassova, I. Dukov, *J. Solution Chem.* **2009**, 38, 289–301. DOI:10.1007/s10953-009-9374-7

9. R. Pavithran, L. R. Varma, M. L. P. Reddy, *Solvent Extr. Ion Exch.* **2003**, *21*, 797–813. DOI:10.1081/SEI-120025924
10. M. Atanassova, I. Dukov, *Sep. Sci. Technol.* **2005**, *40*, 1103–1113. DOI:10.1081/SS-200049855
11. M. Atanassova, I. Dukov, *Acta Chim. Slov.* **2006**, *53*, 457–463.
12. Y. Sasaki, G. R. Choppin, *J. Radioanal. Nucl. Chem.* **1996**, *207*, 383–394. DOI:10.1007/BF02071243
13. H. Mukai, S. Umetani, M. Matsui, *Solvent Extr. Ion Exch.* **2003**, *21*, 73–90. DOI:10.1081/SEI-120017548
14. P. B. Santhi, M. L. P. Reddy, T. R. Ramamohan, A. D. Damodaran, *Solvent Extr. Ion Exch.* **1994**, *12*, 633–650. DOI:10.1080/07366299408918229
15. J. Zhao, S. Meng, D. Li, *J. Chem. Technol. Biotechnol.* **2006**, *81*, 1384–1390. DOI:10.1002/jctb.1572
16. M. A. Petrova, V. Kurteva, L. A. Lubenov, *Ind. Eng. Chem. Res.* **2011**, *50*, 12170–12176. DOI:10.1021/ie201207n
17. M. A. Carey, C. V. Banks, *J. Inorg. Nucl. Chem.* **1969**, *31*, 533–550. DOI:10.1016/0022-1902(69)80497-5
18. A. N. Turanov, V. K. Karandashev, *Solvent Extr. Ion Exch.* **2017**, *35*, 104–116. DOI:10.1080/07366299.2017.1288044
19. L. Rao, Y. Xia, B. R. Rapko, P. F. Martin, *Solvent Extr. Ion Exch.* **1998**, *16*, 913–929. DOI:10.1080/07366299808934560
20. A. N. Turanov, V. K. Karandashev, A. V. Kharlamov, N. A. Bondarenko, *Solvent Extr. Ion Exch.* **2014**, *32*, 492–507. DOI:10.1080/07366299.2014.908584
21. M. Atanassova, V. Lachkova, N. Vassilev, S. Varbanov, I. Dukov, *J. Incl. Phenom. Macrocycl. Chem.* **2007**, *58*, 173–179. DOI:10.1007/s10847-006-9140-z
22. M. Atanassova, V. Lachkova, N. Vassilev, B. Shivachev, S. Varbanov, I. Dukov, *Polyhedron* **2008**, *27*, 3306–3312. DOI:10.1016/j.poly.2008.07.015
23. E. Tashev, M. Atanassova, S. Varbanov, T. Tosheva, S. Shenkov, A.-S. Chauvin, I. Dukov, *Sep. Purif. Technol.* **2008**, *64*, 170–175. DOI:10.1016/j.seppur.2008.09.011
24. M. Atanassova, N. Vassilev, E. Tashev, V. Lachkova, S. Varbanov, *Sep. Sci. Technol.* **2016**, *51*, 49–56. DOI:10.1080/01496395.2015.1078358
25. S. Varbanov, E. Tashev, N. Vassilev, M. Atanassova, V. Lachkova, T. Tosheva, S. Shenkova, I. Dukov, *Polyhedron* **2017**, *134*, 135–142. DOI:10.1016/j.poly.2017.06.013
26. M. Atanassova, V. Kurteva, *RSC Adv.* **2016**, *6*, 11303–11324. DOI:10.1039/C5RA22306G
27. H. Stephan, K. Gloe, J. Beger, P. Muhl, *Solvent Extr. Ion Exch.* **1991**, *9*, 435–458. DOI:10.1080/07366299108918063
28. E. I. Sinyavskaya, *Koord. Khim.* **1986**, *12*, 1155–1161.
29. A. N. Turanov, V. K. Karandashev, V. E. Baulin, *Solvent Extr. Ion Exch.* **1999**, *17*, 1423–1444. DOI:10.1080/07366299908934656
30. A. N. Turanov, V. K. Karandashev, V. E. Baulin, *Russ. J. Inorg. Chem.* **2006**, *51*, 1829–1835. DOI:10.1134/S0036023606110210
31. A. N. Turanov, V. K. Karandashev, D. V. Baulin, V. E. Baulin, A. Y. Tsivadze, *Russ. J. Inorg. Chem.* **2019**, *64*, 407–413. DOI:10.1134/S0036023619030203
32. E. N. Tsvetkov, V. K. Syundyukova, V. E. Baulin, *Bull. Acad. Sci. USSR. Div. Chem. Sci.* **1989**, *38*, 135–149. DOI:10.1007/BF00953718
33. A. N. Turanov, V. K. Karandashev, V. E. Baulin, A. N. Yarkevich, Z. V. Safronova, *Solvent Extr. Ion Exch.* **2009**, *27*, 551–578. DOI:10.1080/07366290903044683
34. S. V. Demin, S. E. Nefedov, V. I. Zhilov, V. E. Baulin, A. Y. Tsivadze, *Russ. J. Inorg. Chem.* **2012**, *57*, 897–902. DOI:10.1134/S0036023612060095
35. E. N. Tsvetkov, V. I. Evreinov, V. E. Baulin, V. V. Ragulin, N. A. Bondarenko, Z. N. Vostroknutova, Z. V. Safronova, *Russ. J. Gen. Chem.* **1995**, *65*, 1300–1307.
36. V. I. Evreinov, V. E. Baulin, Z. N. Vostroknutova, N. A. Bondarenko, V. K. Syundyukova, E. N. Tsvetkov, *Izv. Akad. nauk SSSR, Ser. Khim.* (in Russian) **1989**, *9*, 1990–1997.
37. Y. A. Zolotov, N. M. Kuzmin, *Metal extraction with acylpyrazolones*. Nauka. Moscow. **1977**.
38. V. M. Jordanov, M. Atanassova, I. L. Dukov, *Sep. Sci. Technol.* **2002**, *37*, 3349–3353. DOI:10.1081/SS-120006166
39. M. Atanassova, I. L. Dukov, *Sep. Purif. Technol.* **2004**, *40*, 171–176. DOI:10.1016/j.seppur.2004.02.007
40. K. Akiba, M. Wada, T. Kanno, *J. Inorg. Nucl. Chem.* **1981**, *43*, 1031–1034. DOI:10.1016/0022-1902(81)80169-8
41. I. Fidelis, S. Siekierski, *J. Inorg. Nucl. Chem.* **1971**, *33*, 3191–3194. DOI:10.1016/0022-1902(71)80092-1
42. M. Atanassova, I. L. Dukov, *Sep. Purif. Technol.* **2006**, *49*, 101–105. DOI:10.1016/j.seppur.2005.09.001

Povzetek

Proučevali smo ekstrakcijo La, Ce, Pr, Nd, Sm, Eu, Gd, Tb, Dy, Ho, Er, Tm, Yb, in Lu ionov iz šibko kisle raztopine s kloridnimi ioni v organsko fazo, ki vsebuje 4-benzoil-3-metil-1-fenil-5-pirazolon (HP) in fosforil-vsebujoče podande (L). Opažen je bil izrazit sinergistični efekt ob prisotnosti nevtralnega liganda L v organski fazi, ki vsebuje HP. Stehiometrijo Ln(III) ekstrahiranih vrstni smo določili iz naklonskega kota premic v diagramih ter izračunali ravnotežno konstanto. Lantanidni(III) ioni se ekstrahirajo v toluen s prisotnima HP in nevtralnim ligandom iz šibko kisle raztopine kot LnLP₃ kompleksi.



Except when otherwise noted, articles in this journal are published under the terms and conditions of the Creative Commons Attribution 4.0 International License

Scientific paper

Biophysical Properties and Cytotoxicity of Feruloylated *Helix Lucorum* Hemocyanin

Maya Guncheva,^{1,*} Krassimira Idakieva,¹ Svetla Todinova,² Elena Stoyanova³ and Denitsa Yancheva¹

¹ Institute of Organic Chemistry with Centre of Phytochemistry, Bulgarian Academy of Sciences, Sofia 1113, Bulgaria;

² Institute of Biophysics and Biomedical Engineering, Bulgarian Academy of Sciences, Sofia 1113, Bulgaria;

³ Institute of Biology and Immunology of Reproduction, Bulgarian Academy of Sciences, Sofia 1113, Bulgaria

* Corresponding author: E-mail: maiag@orgchm.bas.bg (M. Guncheva)

Received: 07-11-2019

Abstract

For the first time *Helix lucorum* hemocyanin (HIH) has been feruloylated. Two HIH conjugates with 40- and 120- ferulic acid residues were prepared, denoted as FA-HIH-1 and FA-HIH-2. Expectedly, the feruloylation of HIH induced a rearrangement of the protein molecule, a decrease in the α -helical structure at the expense of β -structures was observed. Besides, the FA-HIH conjugates were more prone to aggregation, which is probably due to the stabilization of the partially unfolded protein molecules by non-covalent bonding. Interestingly, the thermal stability of HIH was not affected by the modification. The native and feruloylated HIH were not toxic to normal fibroblasts (BJ cells). We observed a decrease in cell viability of breast cancer MCF-7 cells to about 66% after a 48h exposure to 70 μ g/well of FA-HIH-2.

Keywords: Hemocyanin conjugates; ferulic acid; conformational stability; thermal stability; cytotoxicity

1. Introduction

Ferulic acid (FA) is a naturally occurring antioxidant, radical scavenging and photoprotective agent with huge therapeutic potential. It has been reported that FA has also strong hepatoprotective activity.¹ Much attention has been paid in the literature on the beneficial role of FA in the treatment and prevention of Alzheimer's disease, a serious neurodegenerative disorder.² In addition, FA inhibits melanin production, therefore can be involved in formulations for skin depigmentation.³ Interestingly, graft copolymers containing ferulic and hyaluronic acid exhibit wound healing properties and can be involved in medicines for the treatment of chronic and acute wounds.⁴ FA is also considered to have potential as an anti-inflammatory drug for curing endometritis. It has been shown that FA reduces the level of the lipopolysaccharide-induced pro-inflammatory cytokines released by bovine endometrial epithelial cells if they are pretreated with the compound.⁵ On the other hand, chitosan-FA conjugates are proposed as novel drug delivery system based,⁶ while FA-modified glycol chitosan exhibited remarkable neuroprotective activity and can be applied in functional resto-

ration of the traumatically injured spinal cord, a life-threatening trauma.⁷ Recently, Caia et al. have reported the preparation of functional foods based on FA grafted curdlans, water-insoluble linear beta-1,3-glucans.⁸ In addition, Liu et al. have shown that daily supplements of a sodium ferulate increased the relative abundance of *Lactobacillus* and *Parabacteroides* in mice model of transverse aortic constriction and the changes in the gut microbiota resulted in an improved cardiac function in the tested animals.⁹

Here we report the preparation of two FA-hemocyanin conjugates. Hemocyanins (Hc) are large complex respiratory proteins freely dissolved in the hemolymph of arthropods and mollusks.¹⁰ Hc isolated from *Keyhole limpet* (KLH) is commercialized and is applied as an immunotherapeutic in case of prostate cancer for several decades.¹¹ Currently, many other vaccines against non-Hodgkins lymphoma, cutaneous melanoma, breast and bladder cancer, that are based on KLH undergo clinical trials. In addition, the whole protein or its subunits are used protein carriers or adjuvants.¹¹ Many other Hcs have been isolated and structurally characterized, some exhibit anticancer, immunostimulatory, antiviral, antifungal activities in in vitro and in vivo assays.^{12,13,14} At present,

KHL- β -1,2-mannan-peptide conjugates are tested as anti-fungal vaccines against *C. albicans*, *C. tropicalis*, *C. lusitanae*, and *C. glabrata*.^f Based on KHL-conjugates are developed easy and fast ELISA methods for detection neurotoxins, vaccines against drugs of abuse and vaccines administrated by new routes.^{15,16,17} Hc from *Helix lucorum* (HIH) has been recently isolated and characterized.¹⁸ Lately, it has been reported that HIH and its structural subunits are cytotoxic to bladder carcinoma cells.¹⁹

The aim of the study is to prepare FA-HIH conjugates and to assess the effect of the feruloylation on the HIH conformation and thermal stability. Cytotoxic effect of the FA-HIH conjugates against fibroblasts (BJ cells), hormone-dependent breast cancer cells (MCF-7 cells) and hormone-independent breast cancer cells (MDA-MB-231 cells). Experiments with the native HIH were conducted for comparison.

2. Materials and Methods

2.1. Materials

Ferulic acid (>99%), N-(3-Dimethylaminopropyl)-N'-ethylcarbodiimide hydrochloride (>98%) (EDC), N-hydroxysuccinimide (>98%) (NHS), thiazolyl blue tetrazolium bromide (98%, MTT), Dulbecco's Modified Eagle's (DMEM) low glucose medium, fetal bovine serum, 0.25% trypsin-EDTA solution and penicillin-streptomycin-amphotericin B antibiotic and disposable PD-10 columns were purchased from Sigma-Aldrich.

Hc was isolated from the hemolymph of *Helix lucorum* garden snails as described in.¹⁰ All other used organic solvents and salts were analytical grade.

The human breast carcinoma cell lines (MCF-7 and MDA-MB-231) and normal human skin fibroblasts (BJ cell line) were obtained from the American Type Culture Collection (ATCC).

2.2. Preparation of the FA-HIH Conjugates

At first, FA was stirred with EDC/NHS in 50 mM phosphate saline buffer (PBS)(pH 7.2) at a stoichiometric molar ratio of FA/EDC/NHS = 1:2:2 for 2 h at room temperature. Then, a 100-to 500-fold molar excess of the obtained NHS-ester of FA was added to the native HIH dissolved in PBS. The mixture was stirred at room temperature for 4 h, and then incubated at 4 °C overnight. The FA-HIH conjugates were purified on prepacked PD-10 desalting columns following the manufacturer's instructions.

The concentration of the native and feruloylated HIH was determined using the Bradford assay.²⁰

Absorbance spectra of the protein samples were recorded on Evolution™ 300 UV-Vis Spectrophotometer (Thermo Electron Corporation) equipped with a Peltier temperature control accessory with the highest resolution (1 nm). The degree of feruloylation was estimated using

the differences in the spectra of the native and the feruloylated HIH at 315 nm. The molar extinction coefficient of ferulic acid at 315 nm in PBS (pH 7.2, 50 mM) is 13 740 L · mol⁻¹ · cm⁻¹.

2.3. Fourier-Transform Infrared Spectroscopy (FTIR)

FTIR spectra were recorded on Bruker Vertex 70 spectrometer equipped with a diamond ATR accessory in the frequency region 4000–600 cm⁻¹ with 128 scanings at a resolution of 1 cm⁻¹. Protein samples were dissolved in PBS buffer (pH 7.2, 50 mM) at a concentration of 20 mg/mL. All spectra were obtained after subtraction of the buffer baseline and were strictly collected under the same conditions, after adjusting the subtraction baseline until a flat baseline was obtained in the 2000–1700 cm⁻¹ region. Second derivatives were obtained using the Savitzky-Golay algorithm based on 25 smoothing points. Curve fitting of the amide I band from 1700 to 1600 cm⁻¹, in water, was performed using Opus software version 5.5 according to the Local Least Squares algorithm. The initial bandwidth of all components was set to 12 cm⁻¹ and the components were approximated by mixed Lorentzian/Gaussian functions. Amide I band positions are assigned to the corresponding secondary structures according to the literature.²¹

2.4. Differential Scanning Calorimetry (DSC)

DSC scans were carried out on a high-sensitivity differential scanning microcalorimeter DASM-4 (Biopribor, Pushchino, Russia), with a sensitivity > 0.017 mJ K⁻¹ and a noise level < ± 0.05 μW. The protein samples were dissolved in PBS (pH 7.2, 50 mM) at a concentration of 3 mg/mL. Heat capacity versus temperature profiles were obtained in the range 30–110 °C at scan rate 1K · min⁻¹. Sample scans were buffer-subtracted, concentration normalized and corrected with the progress baseline. DSC curves were analyzed using the ORIGIN (MicroCal Software) program. Experimental deconvolution of heat capacity curves into individual components by a successive annealing procedure was applied following the approach of Idakieva et al.²²

2.5. Cell Culture

BJ, MCF-7, and MDA-MB-231 cells were maintained in a complete growth DMEM low glucose medium supplemented with 10% (v/v) fetal bovine serum and penicillin-streptomycin-amphotericin B antibiotic mixture under a humidified atmosphere of 5% CO₂ at 37 °C. The medium was changed every other day.

2.6. Cell Viability Assay

Methylthiazolyldiphenyl-tetrazolium bromide (MTT) assays were carried out to evaluate the cytotoxic

effect of FA-HIH on BJ, MCF-7, and MDA-MB-231 cells.²³ The cells were seeded in 96-well plate at a density of 1×10^4 cells per well and cultured in complete growth medium for 24 h. Then, cells were incubated with 0–70 $\mu\text{g}/\text{well}$ of native or FA-modified HIH for 24 h and 48 h. The culture medium was changed to 100 μL serum-free medium containing 500 $\mu\text{g}/\text{mL}$ MTT and plates were incubated for 3 h at 37 °C and 5% CO_2 . The formazan salts were dissolved in 120 μL of dimethylsulfoxide (DMSO) and the absorbance was measured at 544 nm on FLUOstar Optima microplate reader (BMG Labtech, Germany). Samples containing only DMSO were used as a blank control. Control experiments containing untreated with FA-HIH or HIH cells were carried out. The survival of the cells, treated with HIHs was presented in percentages from the corresponding control. Two independent experiments were performed for each cell line.

2. 7. Statistical Analysis

Data were analyzed by one-way ANOVA followed by Tukey–Kramer post-hoc test. The values were considered to be significantly different if the p-value was < 0.05 .

3. Results and Discussion

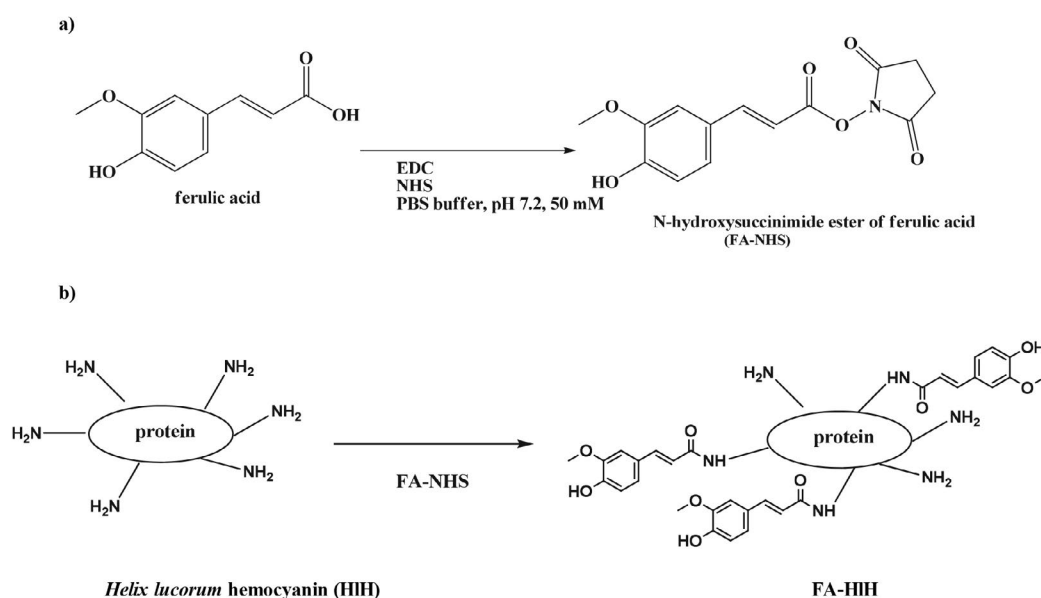
3. 1. Synthesis and Biophysical Characterization of the FA-HIH Conjugates

Ferulic acid was covalently linked to the accessible ϵ -amino groups of lysine residues and N-terminal amino groups of HIH via activated ester method (Scheme 1).

The reaction was conducted under mild reaction conditions in PBS buffer (pH 7.2), at which the primary amino groups are positively charged and exposed to the protein surface. The intermediate, NHS ester of ferulic acid was not isolated and synthesis was performed in one step. An excess of ferulic acid (100- to 500- fold) was used in order to obtain conjugates with a high degree of substitution. Two FA-HIH conjugates containing 40- and 120 ferulic acid residues were prepared and isolated, and were denoted as FA-HIH-1 and FA-HIH, respectively.

We applied ATR-FTIR spectroscopy to assess the effect of the modification on the HIH secondary structure. Spectra of FA-HIH-1, FA-HIH-2, and native HIH were compared in the Amide I band region (1700–1600 cm^{-1}), which is mainly due to C=O stretching vibrations (70–80%) of the amide groups and is known as conformationally sensitive.²¹ For the three protein samples, the original, the second derivative and the deconvoluted spectra scaled to an identical area under Amide I and Amide II (1700–1400 cm^{-1}) are given in the Supplementary (Fig. S1). The spectra were analyzed using 7 (native HIH and FA-HIH-1) or 8 (FA-HIH-2) bands having a centre within 1600–1615; 1615–1640; 1640–1660; 1660–1690; and 1690–1700 cm^{-1} , which are assigned to extended conformations or side-chains residues, β -sheets; α -helical, coiled or disordered structures; β -turns and antiparallel β -sheet structures.²¹ As obtained from the FTIR studies, the conformation of the native and the two feruloylated HIHs are reported in Table 1.

We observed a decrease in the α -helices at expense of the β -structures, which is an indication that HIH is partially unfolded due to the feruloylation. In the spectra of FA-HIH-1 and FA-HIH-2 are found the typical bands that are assigned to protein aggregates, which are probably addi-



Scheme 1: Steps in chemical modification of *Helix lucorum* hemocyanin with ferulic acid: a) activation of the carboxylic group of ferulic acid; b) Conjugation of ferulic acid and primary amino groups of the hemocyanin.

Table 1. Secondary structure band assignments for the native and ferulic acid-conjugated *Helix lucorum* hemocyanin in 50 mM PBS buffer (pH 7.2).

Assignment of the secondary structure components ²¹	HIH native		FA-HIH-1		FA-HIH-2	
	Band position (cm ⁻¹)	Relative area (%)	Band position (cm ⁻¹)	Relative area (%)	Band position (cm ⁻¹)	Relative area (%)
anti-parallel β -sheets	–	–	1609	11.31	1613; 1694	10.91 2.12
β -structures (sheets and turns)	1629; 1633; 1664; 1676 1690	0.15; 8.0; 11.76; 23.31; 7.90	1621; 1633; 1667; 1683	7.31; 14.0; 12.74 10.73	1624; 1632; 1666; 1682	10.28; 14.57; 15.80; 7.74
α -helices	1653	30.39	1651	20.79	1653	23.7
unordered structures/random coils	1642	18.4	1644	23.13	1642	14.57

FA-HIH-1 (40 ferulic acid residues); FA-HIH-2 (120 ferulic acid residues)

tionally stabilized by non-covalent interactions involving the aroma ring of the substituents.

Interestingly, despite of the observed conformational changes of the HIH induced by the modification, the thermal stability of the protein remained mostly unaffected. The DSC profiles of the native HIH, FA-HIH-1, and FA-HIH-2 are depicted in Fig. 1.

The experiment was conducted at a protein concentration of 3 mg/mL in PBS (pH 7.2, 50 mM), and heating rate – 1K/min.

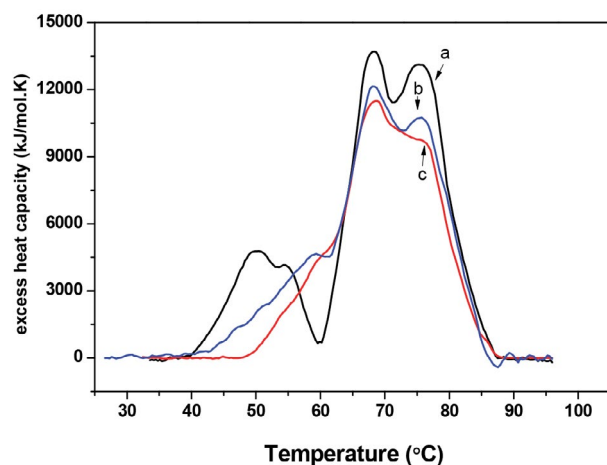


Fig. 1. DSC profiles of the thermal unfolding of native HIH (a) and conjugated with 40 and 120-ferulic acid residues, FA-HIH-1 (b) and FA-HIH-2 (c).

As seen the three DSC curves have an asymmetric shape, which is due to the complex multimeric structure of hemocyanins and is in agreement with the literature data on the thermal denaturation of another Hc in a phosphate-saline buffer.¹⁶ The thermal denaturation temperatures of the feruloylated HIH are slightly shifted toward the higher temperatures (by up to 5 °C) in comparison to denaturation temperatures of the native HIH. DSC curves were experimentally deconvoluted using a successive annealing procedure as previously described by Idakieva et al,²⁴ which allowed a more precise estimation of the thermodynamic parameters, transition temperature (T_{m_i}) and calorimetric enthalpy (ΔH_i) (Table 2). Apparently, the thermal stability of HIH was preserved after the modification.

3. 2. Comparison of the Cytotoxicity of the Native and the Feruloylated HIH

The effect of FA-HIH-1 and FA-HIH-2 on the cell viability of human fibroblasts (BJ cells) was tested in a concentration range between 25 and 200 $\mu\text{g}/\text{well}$ (Fig 2).

We observed a slight increase in proliferation or no effect after a 24h exposure of the BJ cells to 25 or 50 $\mu\text{g}/\text{mL}$ of the native or feruloylated HIH. For the same samples, not evidence of any sign of toxicity was observed even after longer incubation time. Reduction in BJ cell growth was observed after a 24h-treatment with 200 $\mu\text{g}/\text{well}$ ($18.4 \pm 5\%$, $P < 0.001$) of FA-HIH-1, a similar effect was produced

Table 2. The thermodynamic parameters of the native and ferulic acid-modified HIH thermal denaturation.

Sample	T_{m1} (°C)	ΔH_1 (kJ mol ⁻¹)	T_{m2} (°C)	ΔH_2 (kJ mol ⁻¹)	T_{m3} (°C)	ΔH_3 (kJ mol ⁻¹)	T_{m4} (°C)	ΔH_4 (kJ mol ⁻¹)	T_{m5} (°C)	ΔH_5 (kJ mol ⁻¹)	ΔH_{total} (kJ mol ⁻¹)	ΔH_{cal} (kJ mol ⁻¹)
native HIH	49.9	38080	55.2	10752	67.6	92858	75.7	99308	79.8	22263	263261	279337
FA-HIH-1			60.4	40802	68.3	79585	75.4	77372	80.4	20111	217870	214977
FA-HIH-2			58.9	72399	68.5	70882	75.5	67464	81.0	27466	239091	245351

FA-HIH-1 (40 ferulic acid residues); FA-HIH-2 (120 ferulic acid residues)

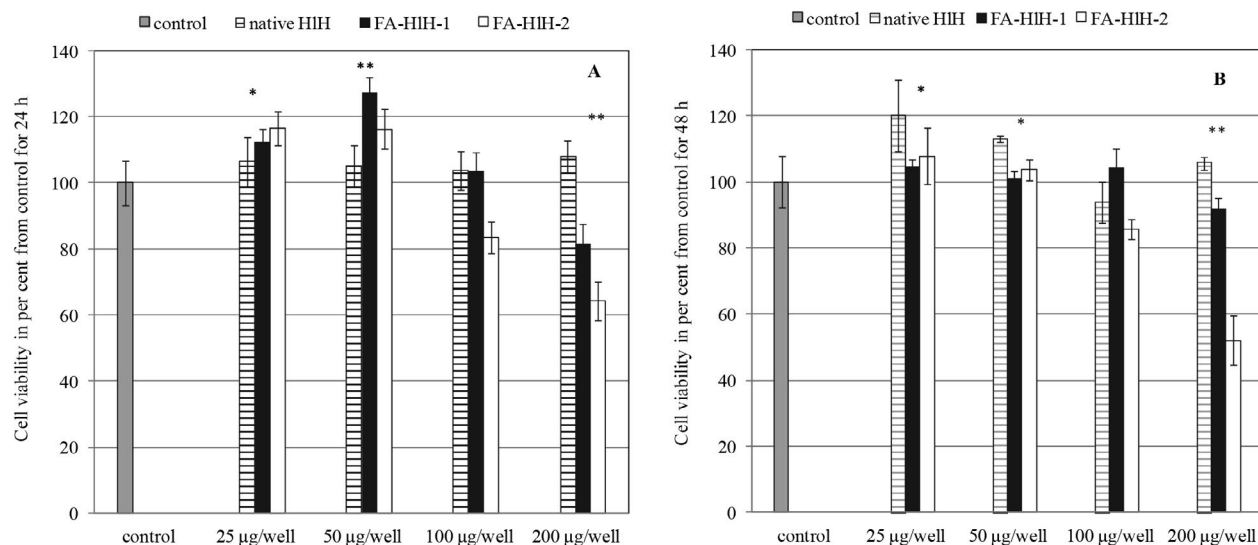


Fig. 2. Antiproliferative effect of native and ferulic acid conjugated HIH on normal fibroblasts (BJ cells) after 24 h (A) and 48 h (B) incubation. Data are presented as mean \pm SD, *($p < 0.05$), ** ($p < 0.01$), $n = 3$.

by 100 µg/well of FA-HIH-2. The lowest cell viability of the BJ cells, 64.1 and 51.1%, was detected after 24 and 48 h, respectively of incubation with 200 µg/mL FA-HIH-2.

Cytotoxicity of the feruloylated HIH against two breast cancer cell lines, a hormone-dependent (MCF-7) and a hormone-independent (MDA-MB-231), was esti-

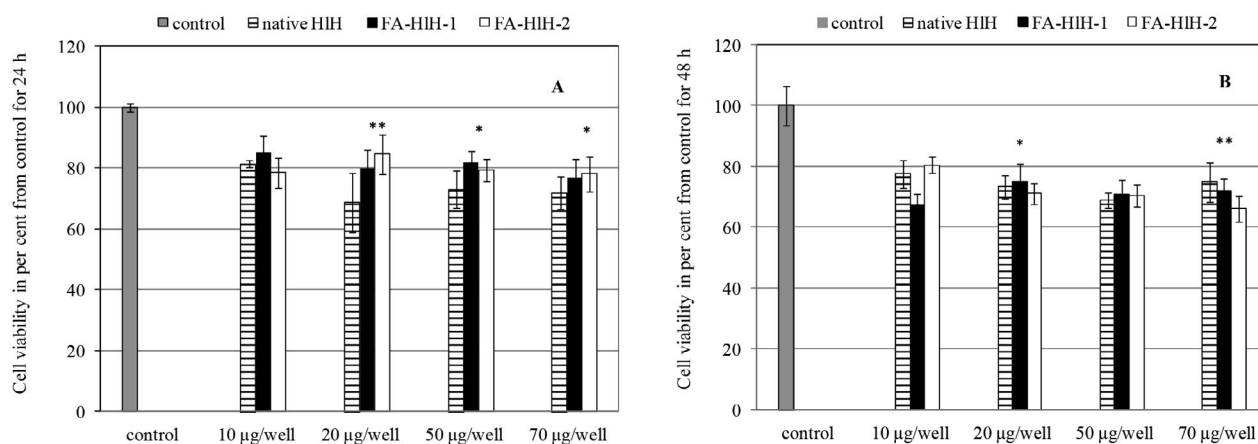


Fig. 3. Effect of native HIH and ferulic acid conjugated HIH on MCF-7 cell viability after 24 h (A) and 48 h (B) incubation. Data are presented as mean \pm SD, *($p < 0.05$), ** ($p < 0.01$), $n = 3$.

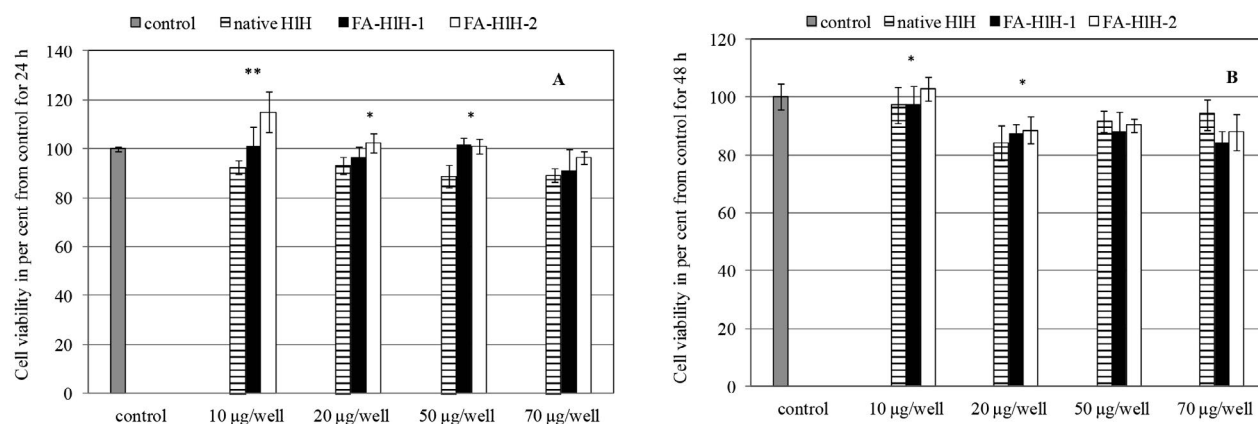


Fig. 4. Effect of native HIH and ferulic acid conjugated HIH on MDA-MB-231 cell viability after 24 h (A) and 48 h (B) incubation. Data are presented as mean \pm SD, *($p < 0.05$), ** ($p < 0.01$), $n = 3$.

mated at concentrations from 10 to 70 µg/well, which are not toxic for normal fibroblasts. The native and the two feruloylated HHs produce a similar effect within one and the same cell line. The effect was more pronounced for FA-HH-2, especially for the MCF-7 cells, for which we noticed concentration dependence (Fig. 3). The three Hcs had negligible cytotoxic effects on MDA-MB-231 cells, even at a concentration of 70 µg/well, the highest tested concentration (Fig. 4).

4. Conclusions

For the first time, two conjugates of *Helix lucorum* hemocyanins with ferulic acid have been successfully prepared. The modified Hcs is likely to adopt more extended β conformations and are apparently additionally stabilized by π - π stacking interactions that involve the ferulic acid residues and aromatic amino acid residues of the protein, which on the other hand explains their increased thermal stability in comparison to that of the native protein. At a concentration of 50 µg/well, FA-HH-1, the sample containing 40 ferulic acid residues, appears to stimulate the growth of the fibroblasts. The moderate to excellent activity and selectivity of the native and the feruloylated HH towards MCF-7 cells makes them promising for future studies because of their biopharmaceutical potential.

5. Supplementary Materials

The supplementary PDF file contains the original, second derivative and deconvoluted in the Amide I band region FTIR spectra of the native and the two feruloylated (FA-HH-1 and FA-HH-2) hemocyanins. A graphic illustration of the experimental annealing procedure for the DSC experiment is also given.

Acknowledgement

The financial support of the Bulgarian National Science Fund (Project: ДКОСТ 01/27) is gratefully acknowledged.

6. References

- R. Rukkumani, K. Aruna, P. S. Varma, V. P. Menon, *J. Med. Food* **2004**, *7*, 456–461. DOI:10.1089/jmf.2004.7.456
- S.F. Nabavi, K. P. Devi, D.S. Malar, A. Sureda, M. Daglia, S.M. Nabavi, *Mimi-Rev. Med. Chem.* **2015**, *15*, 776–788. DOI:10.2174/1389557515666150522102545
- H. Maruyama, F. Kawakami, T. T. Lwin, M. Imai, F. Shamsa, *Biol. Pharm. Bull.* **2018**, *41*, 806–810. DOI:10.1248/bpb.b17-00892
- G. Valacchi, G. Grisci, C. Sticozzi, Y. Lim, M. Paolino, G. Giuliani, R. Mendichi, G. Belmonte, R. Artusi, A. Zanardi, P. Garofalo, G. Giorgi, A. Cappelli, L. Rovati, *J. Mat. Chem. B* **2015**, *3*, 7037–7045. DOI:10.1039/C5TB00661A
- P. Yin, Z. Zhang, J. Li, Y. Shi, N. Jin, W. Zou, Q. Gao, W. Wang, F. Liu, *Res. Vet. Sci.* **2019**, *126*, 164–169. DOI:10.1016/j.rvsc.2019.08.018
- C. Li, J.-B. Li, *Int. J. Biol. Macromol.* **2017**, *105*, 1539–1543. DOI:10.1016/j.ijbiomac.2017.04.103
- W. Wu, S.-Y. Lee, X. Wu, J. Y. Tyler, H. Wang, Z. Ouyang, K. Park, X.M. Xu, J.X. Cheng, *Biomaterials* **2014**, *35*, 2355–2364. DOI:10.1016/j.biomaterials.2013.11.074
- W.-D. Caia, J. Zhu, L.-X. Wu, Z.-R. Qiao, L. Li, J.-K. Yan, *Food Chem.* **2019**, *300*, 125221. DOI:10.1016/j.foodchem.2019.125221
- Z. Liu, Z. Ma, H. Zhang, B. Seel, S. Haiyue, L. D. An, Q. Zhan, W. Lai, Q. Zeng, H. Rend, D. Xu, *Biomed. Pharmacother.* **2019**, *120*, 109482. DOI:10.1016/j.biopha.2019.109482
- C. Gatsogiannis, O. Hofnagel, J. Markl, Stefan Raunser, *Structure* **2015**, *23*, 93–103. DOI:10.1016/j.str.2014.10.013
- J. R. Harris, J. Markl, *Micron* **1999**, *30*, 597–623. DOI:10.1016/S0968-4328(99)00036-0
- C. J. Coates, J. Nairn, *Dev. Comp. Immunol.* **2014**, *45*, 43–55. DOI:10.1016/j.dci.2014.01.021
- H. K. Kang, H. Ho Lee, C. H. Seo, Y. Park, *Mar. Drugs* **2014**, *17*, 350.
- A. Dolashki, L. Velkova, W. Voelter, P. Dolashka, *Z. Naturforsch. C* **2019**, *74*, 113–123. DOI:10.1515/znc-2018-0084
- S. Sato, S. Takaishi, K. Yasumoto, S. Watabe, *Toxins* **2019**, *11*, 551. DOI:10.3390/toxins11100551
- F. Baruffaldi, M. D. Raleigh, S. J. King, M. J. Roslawski, A. K. Birnbaum, C. Hassler, F. I. Carroll, S. P. Runyon, S. Winston, P. R. Pentel, M. Pravetoni, *Mol. Pharmaceutics*, **2019**, *16*, 2364–2375. DOI:10.1021/acs.molpharmaceut.8b01296
- Z. Oreskovic, K. Nechvatalova, J. Krejci, V. Kummer, M. Faldyna, *PLoS One*, **2019**, *14*, e0211896. DOI:10.1371/journal.pone.0211896
- L. Velkova, I. Dimitrov, H. Schwarz, S. Stevanovic, W. Voelter, B. Salvato, P. Dolashka-Angelova, *Comp. Biochem. Physiol. B Biochem. Mol. Biol.* **2010**, *157*, 16–25. DOI:10.1016/j.cbpb.2010.04.012
- A. Dolashki, P. Dolashka, A. Stenzl, S. Stevanovic, W. K. Aicher, L. Velkova, R. Velikova, W. Voelter, *Biotechnol. Biotechnol. Equip.* **2019**, *33*, 20–32. DOI:10.1080/13102818.2018.1507755
- M. Bradford, *Anal. Biochem.* **1976**, *72*, 248–254. DOI:10.1006/abio.1976.9999
- A. Barth, *Biochim. Biophys. Acta.* **2007**, *1767*, 1073–1101. DOI:10.1016/j.bbabi.2007.06.004
- K. Idakieva, C. Gielens, N. Siddiqui, L. Doumanova, B. Vasseva, Kostov, V.L. Shnyrov, *Z. Naturforsch. B.* **2007**, *62a*, 499–506. DOI:10.1515/zna-2007-0906
- T. Mosmann, *J. Immunol. Meth.* **1983**, *65*, 55–63. DOI:10.1016/0022-1759(83)90303-4
- K. Idakieva, K. Parvanova, S. Todinova, *Biochim. Biophys. Acta.* **2005**, *1748*, 50–56. DOI:10.1016/j.bbapap.2004.12.004

Povzetek

Ferulacija hemocianina (HIH) *Helix lucorum* je opisana prvič. Pripravili smo dva HIH konjugata z 40-in 120-ostanki ferulične kisline, označena kot FA-hlh-1 in FA-hlh-2. Po pričakovanjih je ferulacija HIH povzročila preureditev beljakovinske molekule, opaženo je tudi zmanjšanje α -spiralne strukture na račun β -struktur. Poleg tega so bili konjugati FA-HIH bolj nagnjeni k agregaciji, ki je verjetno posledica stabilizacije delno neprepognjenih beljakovinskih molekul z ne-kovalentnimi povezavami. Zanimivo je, da spremembe niso vplivale na toplotno stabilnost HIH. Nativne in ferulirane HIH niso strupene za normalne fibroblaste (celice BJ). Opazili smo zmanjšanje preživetja celic raka dojke MCF-7 na približno 66 % po 48 h izpostavljenosti 70 $\mu\text{g}/\text{žep}$ FA-HIH-2.



Except when otherwise noted, articles in this journal are published under the terms and conditions of the Creative Commons Attribution 4.0 International License

Scientific paper

Environmental Friendly Synthetic Modification of Amberlite XAD-2 Resin for the Removal of Highly Toxic Hexavalent Chromium from Water

Waqas Jamil,^{1,*} Zunaira Memon,¹ Saima Qayyum Memon,² Muhammad Kashif Samon,³ Muhammad Taha⁴ and Khalid Mohammad Khan^{4,5}

¹ Institute of Advanced Research Studies in Chemical Sciences, University of Sindh, Jamshoro, 76080, Pakistan

² Dr. M. A. Kazi Institute of Chemistry, University of Sindh, Jamshoro, 76080, Pakistan

³ Centre for Pure and Applied Geology, University of Sindh, Jamshoro, 76080, Pakistan

⁴ Department of Clinical Pharmacy, Institute for Research and Medical Consultations (IRMC), Imam Abdulrahman Bin Faisal University, P.O. Box 1982, Dammam, 31441, Saudi Arabia,

⁵ H.E.J. Research Institute of Chemistry, International Center for Chemical and Biological Sciences, University Karachi, Karachi 75270, Pakistan

* Corresponding author: E-mail: waqas.jamil@usindh.edu.pk, waqasjam2@yahoo.com
Tel. +923322324551

Received: 07-16-2019

Abstract

Amberlite XAD-2 functionalized by coupling through -C=N- spacer with isatin via an environmental friendly protocol. The modified resin was used for the evaluation of its sorption capacity towards toxic Cr (VI) ions using spectrophotometer. pH, volume, sorbent amount, initial concentration of Cr(VI) ions, and agitation time were optimized. The Freundlich and Dubinin-Radushkevich models gave better fit to isotherm data than Langmuir model. The evaluation of kinetic data indicated pseudo-first-order kinetics followed by sorption process. Thermodynamic parameters were also evaluated. Maximum recovery was obtained at 10 mL of 0.1M NaOH. Spiking methodology was used to confirm the validity of proposed method. The results revealed that developed method can be used for the removal of Cr(VI) ions efficiently from water, as well as reused for three cycles.

Keywords: Amberlite XAD-2; environmental Friendly; toxicity; chromium VI; isatin

1. Introduction

Heavy metals are continuously discharged into the natural environment. The rapid industrialization and their growth in the world pollution cause trouble to all forms of life. Most of the industries discharge wastewater and their effluents containing toxic metals without proper treatment and it becomes a major risk for human health.¹⁻³

Chromium is a commonly used metal in various industries, such as chrome plating, leather tanning, dyes, and wood treatment.⁴ Chromium primarily occurs in two different oxidation states, *i.e.* trivalent [Cr (III)] and hexavalent chromium [Cr (VI)]. Cr (III) is considered as a crucial trace mineral and it is essential for normal removal rates of glucose from blood, as well as protein and lipid metabolism,⁵

however Cr(VI) is a well-established carcinogen associated with lung, nasal and sinus cancer. It diffuses into the cell membrane of living organisms owing to its high solubility in water, high oxidation potential and relatively smaller size.⁶ The high levels of Cr (III) may have some adverse health effects, while Cr (VI) is hazardous even at low concentrations. The extensive use of chromium in the industries and improperly treated water effluent introduce environmental concerns.^{7,8} According to World Health Organization (WHO) and US Environmental Protection Agency (EPA), the permissible limit of Cr (VI) is 0.05 and 0.1 mg/L respectively in drinking water.⁹ The continuous elevation of Cr(VI) concentration is one of the prime cause of water toxicity, therefore the elimination of Cr(VI) toxic species from water resources is of current interest to researchers.

Heavy metal ions can be removed from wastewater in order to reduce toxicity by using various methodologies including adsorption, biodegradation, ion exchange, oxidation, solvent extraction *etc.*,¹⁰ as well as reduction process that converts Cr (VI) to Cr (III) has also reported for the remediation of waste water.

Among them, adsorption is the most common technique for the remediation of waste water from pollutants, due to its cost effectiveness and easy to handle. Adsorption technique has capacity for recovery of value added components *via* desorption and regeneration of adsorbent.^{11,12}

Both natural as well as synthetic sorbents gained much attention owing to their metal-binding capacities, such as *Alisma Plantago Aquata* (APA), modified rice bran, coconut shell carbon, and banana pith *etc.* has been reported as natural sorbents for the removal of Cr (III), Cu (II), Zn (II), Cd (II), Pb (II), and Rhodamine-B from water,¹³⁻¹⁶ while synthetic sorbents including new synthetic polymers and modified polymeric material like polystyrene and Amberlite XAD resins have been used to remove chemicals or metal ions from water and soil.¹⁷ Amberlite XAD-2 can be used as sorbent due to high surface area and large pore size, moreover it can be functionalized *via* mild techniques and these modifications make it more selective for the target analytes.¹⁸

2. Experimental

2.1. Instruments

Orion 5 star model pH meter was used to carry out pH measurements. Orbital Incubator Model I-4000 was used for batch experiments. Fourier Transform Infrared Spectroscopy (FT-IR) analysis in each step of synthesis *i.e.* nitration, reduction and isatin based Amberlite XAD-2 resin was made with FT-IR model Nicolet IS10.

Scanning Electron Microscope (SEM) images for confirmation of morphological changes were carried out by using a scanning electron microscope Jeol model JSM-6490 LV. Chromium as Cr(VI)-diphenyl carbazide complex was determined by Hitachi 220 Spectrophotometer.

2.2. Reagents and Solutions

The chemicals used to carried out the experimental work were chemically pure and of analytical grade.

Amberlite XAD-2, Concentrated (Conc.) hydrochloric acid (HCl), Conc. sulphuric acid (H₂SO₄), Conc. nitric acid (HNO₃), sodium hydroxide (NaOH), potassium chloride (KCl), tin (II)chloride (SnCl₂), ethanol (C₂H₅OH), Isatin, sodium acetate (CH₃COONa), acetic acid (CH₃COOH), potassium dichromate (K₂Cr₂O₇), 1,5-diphenylcarbazide, acetone [(CH₃)₂CO], sodium nitrate (NaNO₃), sodium phosphate (Na₃PO₄), cobalt (II) acetate [Co(CH₃COO)₂ · 4H₂O], Sodium Phosphate (Na₃PO₄), copper (II) chloride (CuCl₂), nickel (II) chloride

(NiCl₂ · 6H₂O), manganese sulphate (MnSO₄ · H₂O), magnesium chloride (MgCl₂), Iron (III) Nitrate [Fe(NO₃)₃], sodium carbonate (Na₂CO₃) were purchased from Sigma-Aldrich and Merck (Germany).

The pH was adjusted by using desired buffer solutions of different ratios of 0.1 M HCl/ KCl for pH 2, 0.2 M CH₃COOH/CH₃COONa for pH 4 and 6 and 0.1 M NaOH for pH 8 and 10. The 1000 ppm stock solution of Cr(VI) was prepared by adding 0.2835 g of K₂Cr₂O₇ in 100mL distilled. Dilution method was used for the preparation of various Cr(VI) concentrations such as 100 ppm, 10 ppm, 8 ppm, 6 ppm, 4 ppm and 2 ppm.

2.3. Procedure of Synthetic Modification of Amberlite XAD-2 Resin

Nitration and reduction of Amberlite XAD-2 Resin was done by reported procedure.¹⁹

In final modification step, 2g of aminated resin was grinded with 2g of isatin in the presence of catalytic amount of HCl (1mL) for 15 min in pestle mortar in order to provide appropriate mechanical energy for reaction. The camel brown precipitates were obtained, washed with water and ethanol and subjected for the IR spectroscopy.

2.4. Sorption Procedure

Sorption experiments were conducted through batch technique in an incubated shaker by varying the parameters that can affect sorption of Cr (VI) on to isatin based Amberlite XAD-2 resin. The effect of pH, volume of sorbate, sorbent dosage, shaking time, temperature and initial concentration was studied. In this regard, pH was varied from 2 to 10. The pH was adjusted by using buffer solutions of 0.1 M HCl/KCl for pH 2, 0.2M CH₃COOH/CH₃COONa for pH 4 and 6 and 0.1M NaOH for pH 8 and 10. Sorbate volume, resin amount, shaking time, temperature and initial concentration of potassium dichromate solution were optimized in range of 10-60 mL, 0.05 to 0.35 g, 5 to 320 min, 10 to 50 °C and 5 to 1000 ppm respectively. After the predetermined time, the sorbate solution was withdrawn and filtered to separate the sorbent. For spectrophotometric determination of Cr(VI) 1,5-diphenyl carbazide reagent was used, spectrophotometer was calibrated using Cr(VI) solution (2 to 10 ppm) contained 1 mL of 1,5-diphenyl carbazide and 2 mL of 3 M H₂SO₄. The concentration of metal ions before and after sorption was measured by following procedure.

% sorption was calculated using Eq. (1).

$$\% \text{ sorption} = \left(\frac{C_i - C_f}{C_i} \right) \times 100 \quad (1)$$

Where C_i and C_f are the initial and final concentration of solution before and after sorption in (mg/L) of Cr(VI) respectively.

2. 5. Desorption Experiment

0.25 g of used sorbent was agitated with 5 and 10 mL of 0.1 M HCl, 0.1 M HNO₃ and 0.1 M NaOH respectively. The sorbent was collected from solution by filtration after the recovery experiment and washed with a plenty of distilled water and reused for analysis.

3. Results and Discussion

3. 1. Chemistry and FT-IR Analysis

The synthetic modification was done by three steps *i.e.* Nitration followed by reduction and formation of isatin based Amberlite XAD-2 **Fig. 1**.

In last step of modification a solid state chemistry was used in order to make modification environmental benign. In this regard amino-Amberlite XAD-2 was ground

with isatin in the pestle mortar with different intervals of time *i.e.* 5, 10 and 15 min. After each interval of time IR spectrum was taken to confirm the maximum conversion of amino group into imine group. The 15 min grinding was found to be enough for conversion. After 15 min sharp peaks for imine bond was observed with disappearance of amino group peaks **Table-1**. After 15 min grinding, camel brown precipitates were obtained. These precipitates were washed with distilled water as well as ethanol in order to remove impurities or un-reacted isatin.

Table 1. Grinding Time for Maximum Conversion

Grinding time (min)	Imine Peak Appearance
5	Weak
10	Medium
15	Intense

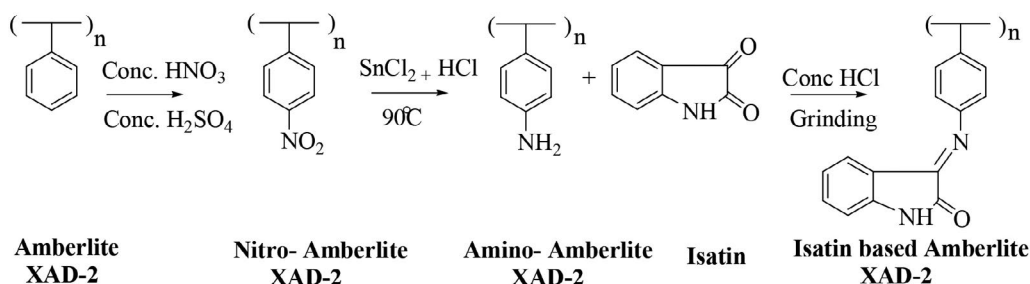


Figure 1. Reaction Scheme for Synthetic Modification of Amberlite XAD-2

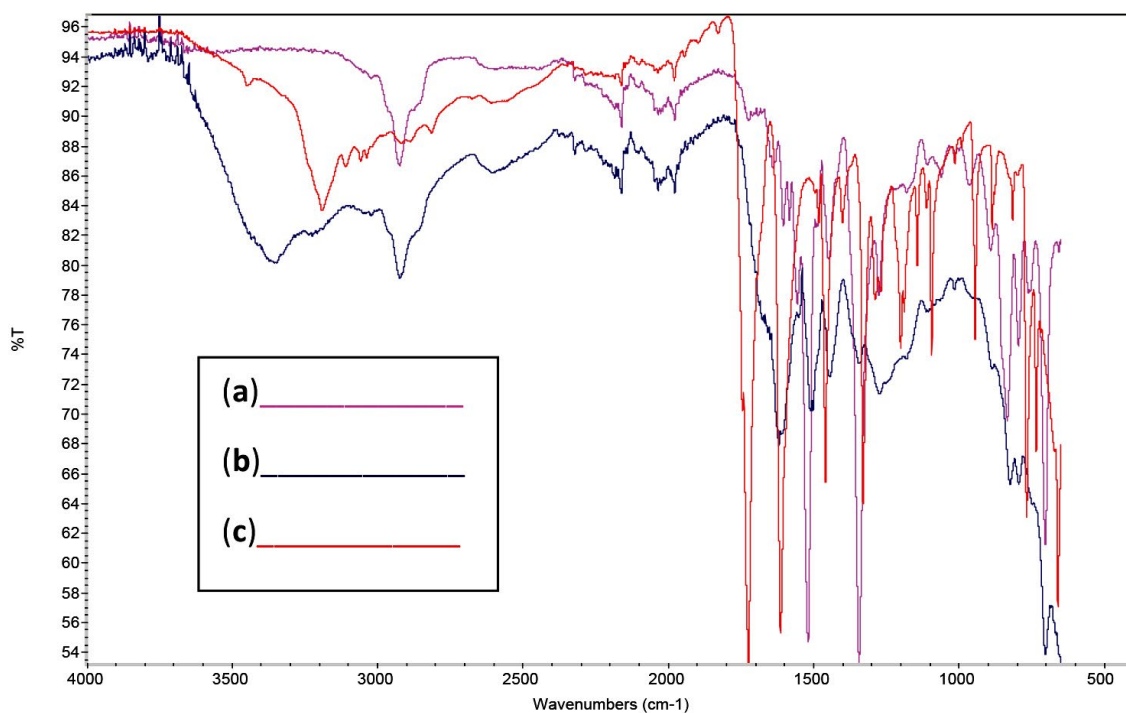


Figure 2. FT-IR Spectra of (a) Nitro- Amberlite XAD-2 (b) Amino- Amberlite XAD-2 (c) Isatin based Amberlite XAD-2

All three products obtained from each step of synthesis were subjected to FT-IR. The presence of two clear peaks at 1519.65 and 1345.19 cm^{-1} which were assigned for N-O asymmetric and N-O symmetric stretching vibration respectively, confirmed that nitration of Amberlite XAD-2 has carried out successfully **Fig. 2. (a)**. The reduction process *i.e.* conversion of nitro into amino group was confirmed by the presence of peaks at 3355.37, 1621.87 and 1272.53 cm^{-1} , assigned for N-H stretching, N-H bending, C-N stretching respectively. Peaks for nitro group were disappeared, that confirmed the successful reduction **Fig. 2. (b)**. The Isatin based Amberlite XAD-2 product was confirmed by the prominent imine ($-\text{C}=\text{N}-$) peak at 1614.68 cm^{-1} , it also showed peak at 3189.40 cm^{-1} and 1725.41 cm^{-1} which are attributed to N-H and C=O of amide group of isatin respectively, shown in **Fig. 2. (c)**.^{20,21}

3. 2. SEM Analysis

SEM analysis was carried out to examine the surface morphology of both modified and free Amberlite XAD-2 resin. **Fig. 3. (a)** is showing SEM photograph of free Amberlite XAD-2 resin and **Fig. 3. (b)** SEM photograph of Isatin based Amberlite XAD-2 resin. Surface modification of Amberlite XAD-2 is confirmed by significant difference in morphology which can be seen in images of free and modified Amberlite XAD-2 resin.

3. 3. pH Effect

pH is considered as a key parameter which influences the surface activity of the resin for the sorption of metal ions. There was a slight increase in % sorption from pH 2–4. The removal of Cr(VI) was then reduced with rising pH which is shown in **Fig. 4**. The sorption of metals is associated to the surface functional groups and chemistry of the sorbate metal ion-solvent interaction that change with the pH. The chromium (VI) ions can exist as hydrogen chromate (HCrO_4^-) or chromate (CrO_4^{2-}) or dichromate ($\text{Cr}_2\text{O}_7^{2-}$) which depends

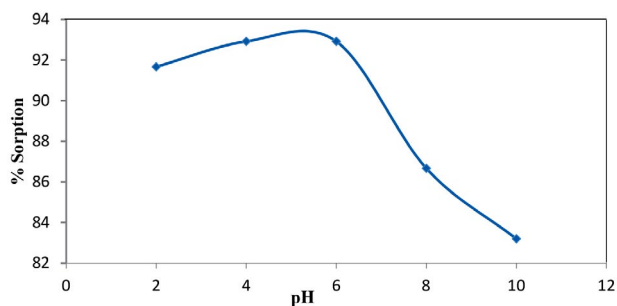


Figure 4. pH Effect for Cr(VI) sorption onto Isatin based Amberlite XAD-2 resin

upon the pH of the solution. The dominant form of Cr(VI) is HCrO_4^- at acidic pH 2, and predominant forms at higher pH are CrO_4^{2-} and $\text{Cr}_2\text{O}_7^{2-}$. Due to strong electrostatic attraction between negatively charged chromium species and positively charged surface groups higher sorption at lower pH is observed and above pH 6 sorption was reduced, which can be attributed to competitive sorption of CrO_4^{2-} and OH^- ions.²²

3. 4. Volume Effect

The volume effect of Cr(VI) on %sorption by isatin based Amberlite XAD-2 was investigated and is shown in

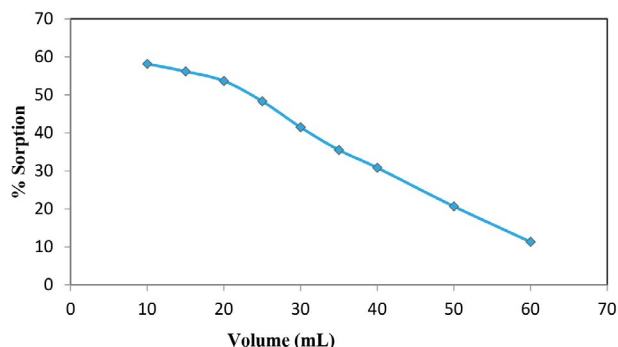


Figure 5. Volume effect for Cr(VI) sorption onto isatin based Amberlite XAD-2 resin

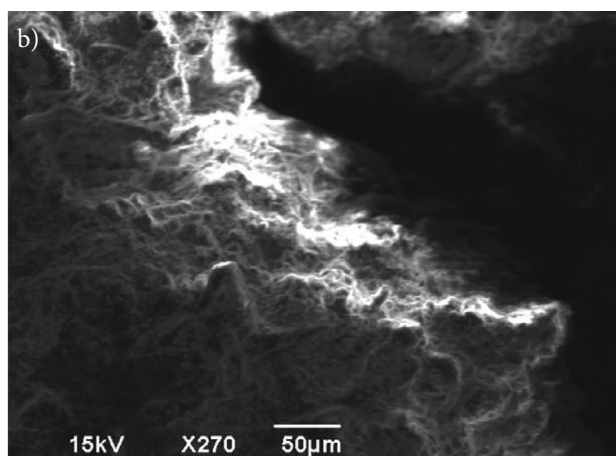
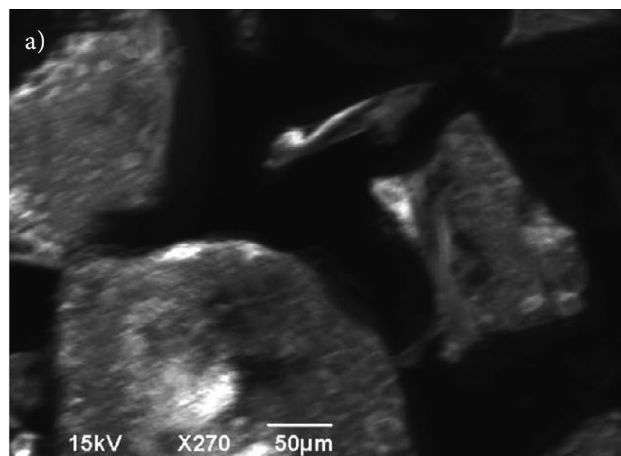


Figure 3. SEM photograph of (a) free Amberlite XAD-2, (b) Isatin based Amberlite XAD-2

Fig. 5. Volume was varied from 10 to 60 mL, maximum response was observed at 10 mL, sorption was decreased with an increase in volume can be attributed to limited availability of sorption sites because Cr(VI) ions were amplified with increase in volume of Cr(VI) solution but resin amount was constant.

3. 5. Resin Dosage Effect

The resin dosage effect on the sorption of Cr(VI) ions were examined in the range of 0.05 g to 0.35 g, sorption was increased with increase in resin amount up to 0.25 g, after which sorption capacity nearly remained constant shown in **Fig. 6**. Due to larger surface area and accessibility of more sorption sites, sorption was increased with resin amount. At higher sorbent dosage there are not enough Cr(VI) ions in the solution to occupy the active sites and as a result the sorption tends to become constant. So 0.25 g of modified Amberlite XAD-2 was chosen as most favorable resin amount for further analysis.

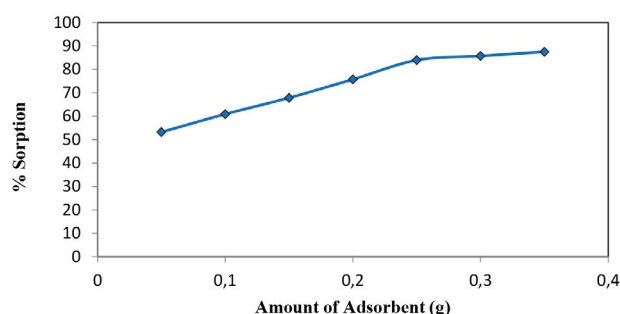


Figure 6. Resin dosage effect for Cr(VI) sorption

3. 6. Kinetic Study

The influence of shaking time on % sorption was examined by varying the time from 5 to 320 min by keeping other optimized parameters constant. It was observed that the sorption was increased till 60 min, after 60 to 320 min no significant change in sorption was observed, and the system attained equilibrium. Kinetic models are of great importance for analyzing the kinetic data, they can give description of what is happening during the sorption process and can also give significant information about the sorbed and residual amount of solute in the solution at any instant of the experiment.²³ The sorption mechanism was identified by subjecting the studied kinetic data to three most commonly used kinetic models, known as Lagergren, Ho and Mckay and Morris-Weber models.

3. 6. 1. Lagergren (Pseudo-First-Order Kinetics)

Lagergren equation is given as;

$$\ln(q_e - q_t) = \ln q_e - k_1 t \quad (2)$$

Where K_1 is the rate constant of pseudo-first-order in (min^{-1}) and q_e ($\mu\text{g/g}$) is the the amount of Cr(VI) ions sorbed on the sorbent at equilibrium were determined from the slope and intercept of linear plot of $\ln(q_e - q_t)$ Vs t shown in **Fig. 7** and q_t ($\mu\text{g/g}$) is the amount of Cr(VI) ions sorbed on the sorbent at time t .²⁴ Kinetic parameters which are obtained in this study of pseudo-first-order model are given in **Table 2**.

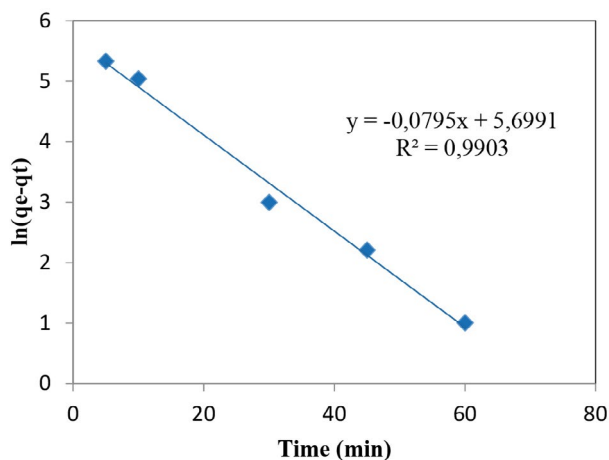


Figure 7. Lagergren kinetic model for Cr(VI) sorption onto isatin based Amberlite XAD-2

3. 6. 2. Ho and Mckay (Pseudo-Second-Order Kinetics)

Ho and Mckay kinetic model is presumably depend on chemisorptions, in which sorption occur because of electron exchange between sorbate and sorbent. The pseudo-second-order rate equation is given as;

$$\frac{t}{q_t} = \left(\frac{t}{k_2 q_e^2} \right) + \left(\frac{1}{q_e} \right) \quad (3)$$

Where, K_2 is rate constant in ($\text{g}/\mu\text{g min}$) of pseudo-second-order and q_e ($\mu\text{g/g}$) is the the amount of Cr(VI) ions sorbed on the sorbent at equilibrium were obtained from the slope and intercept of linear plot of t/q_t against t

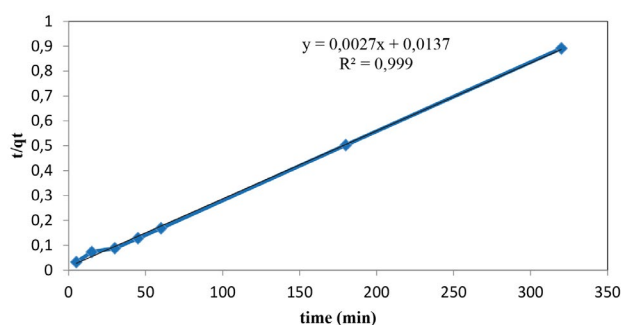


Figure 8. Ho and Mckay kinetic model for Cr(VI) sorption onto isatin based Amberlite XAD-2

Table 2. Kinetic parameters for the Cr(VI) sorption onto isatin based Amberlite XAD-2 resin

K_1 (min^{-1})	Pseudo-first-order kinetic model			Pseudo-second-order kinetic model			
	qe ($\mu\text{g/g}$) Calculated	qe ($\mu\text{g/g}$) Experimental	R^2	K_2 ($\text{g}/\mu\text{g min}$)	qe ($\mu\text{g/g}$) Calculated	qe ($\mu\text{g/g}$) Experimental	R^2
0.079	298.5	357	0.990	0.013	76.92	357	0.999

shown in **Fig. 8** and q_t in ($\mu\text{g/g}$) is the sorbate amount retained at time t .²⁵ Kinetic parameters which are obtained in this study are given in **Table 2**.

Table 2. has summarized the pseudo-first-order and pseudo-second-order kinetic parameters which showed calculated q_e value 298.5 $\mu\text{g/g}$ of Lagergren is more close to experimental value as compared to calculated value of Ho and Mckay 76.92 $\mu\text{g/g}$ which indicated that pseudo-first-order rate equation is more appropriate for explanation of kinetic process.

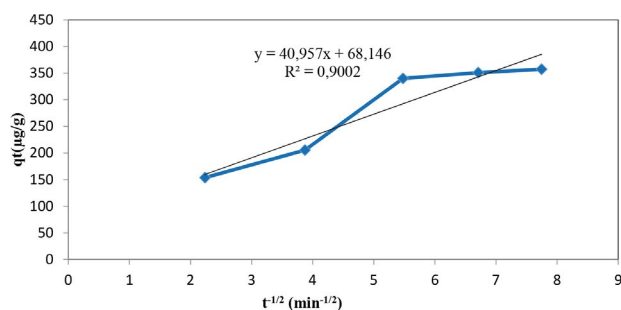
3. 6. 3. Morris-Weber Model (Intra-Particle Diffusion Model)

The diffusion mechanism cannot be recognized only by Lagergren, Ho and Mckay kinetic models, therefore kinetic data was also applied to Morris-Weber model. This model states; if the plot of q_t against \sqrt{t} is straight and passing through origin then the sorption is considered to occur *via* intra-particle diffusion and the rate controlling step only depends upon it, while if it is not passing from the origin it gives the indication that at the same time some other kinetic phenomenon may be responsible for rate-controlling step.²⁶ In current study, plot of q_t against \sqrt{t} is linear but it does not pass through origin shown in **Fig. 9** Which is indicating that sorption rate is controlled by some other kinetic phenomenon and all of which may be operating at the same time.

Equation of this model is given as;

$$q_t = R_d \sqrt{t} \quad (4)$$

Where, the rate constant of intra-particle diffusion is R_d which is calculated from the slope of plot of q_t against \sqrt{t} and q_t is the amount of metal ions sorbed in $\mu\text{g/g}$ at time t in $\text{min}^{-1/2}$.

**Figure 9.** Morris-Weber kinetic model for Cr(VI) sorption onto isatin based Amberlite XAD-2

3. 7. Sorption Isotherm

Sorption isotherm play main role to predict the sorbent capacity for removal of a pollutant. The sorption capability of isatin based Amberlite XAD-2 for removal of Cr(VI) ions has been evaluated by applying Langmuir, Freundlich and D-R isotherms.

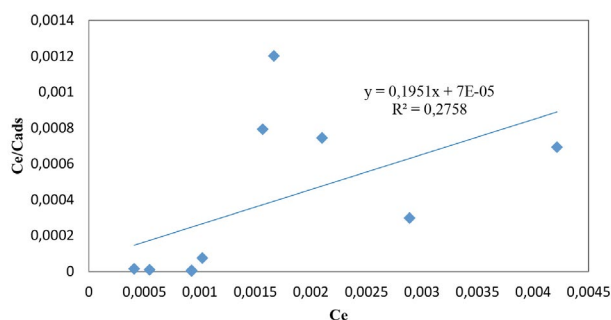
3. 7. 1. Langmuir Isotherm

The Langmuir isotherm is used for the assumption of monolayer surface coverage which shows equal affinity of all binding sites for sorbate molecules and maximum sorption capacity of the sorbent is calculated by using **Eq. (5)**

$$\frac{C_e}{C_{ads}} = \frac{1}{Qb} + \frac{C_e}{Q} \quad (5)$$

The plot of C_e/C_{ads} versus C_e gives $1/Q$ and b as a slope and intercept from which value of Q can be obtained. In this equation b is a constant related to free energy of sorption.²⁷

The non-linear plot of C_e/C_{ads} versus C_e was obtained in current study, which indicated that experimental data does not follow the Langmuir isotherm **Fig. 10**. The regression coefficient was also not fitted to experimental data.

**Figure 10.** Langmuir kinetic model for Cr(VI) sorption onto isatin based Amberlite XAD-2

3. 7. 2. Freundlich Isotherm

The Freundlich isotherm **Eq. (VI)** is applied to predict the probability of multi-layer surface coverage and it is characterized depend on the non-linear energy distribution of the sorption sites for the same sorbent.²⁸

$$\log C_{\text{ads}} = \log A + \frac{1}{n} \log C_e \quad (6)$$

Where, maximum sorption capacity A and heterogeneity factor $1/n$ which are Freundlich constants can be determined from the slope and intercept of plot of $\ln C_{\text{ads}}$ versus $\ln C_e$. In this study the value of $1/n$, <1 , shows that Cr(VI) is favorably sorbed by the resin at lower equilibrium concentration.²⁹ Calculated values are listed in **Table 3**.

The linear plot of $\ln C_e$ versus $\ln C_{\text{ads}}$ and regression coefficient $R^2 = 0.93$ shown in **Fig. 11** has indicated that experimental data gave good fit to Freundlich isotherm.

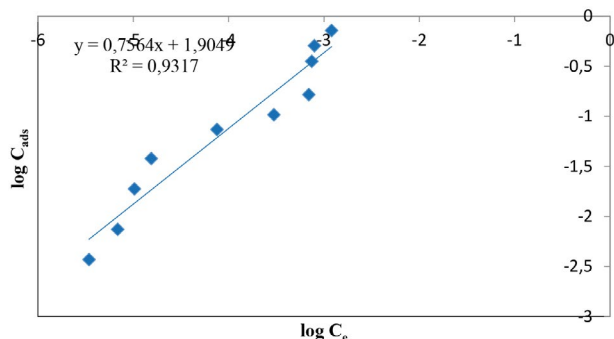


Figure 11. Freundlich isotherm for Cr(VI) sorption of onto isatin based Amberlite XAD-2

3. 7. 3. Dubinin- Radushkevich Isotherm

The D-R isotherm was applied to presume the porosity characteristics and the apparent free energy of sorption. The **Eq. (7)** shows the linearized form of the D-R equation

$$\ln C_{\text{ads}} = \ln X_m - \beta \varepsilon^2 \quad (7)$$

Where C_{ads} is the amount of Cr(VI) ions sorbed per unit mass of sorbent, X_m and β are D-R isotherm constants, and ε is a Polanyi potential which is as given in **Eq. (8)**

$$\varepsilon = RT \ln \left(1 + \frac{1}{C_e} \right) \quad (8)$$

Where R is a gas constant in KJ/mol, T is the temperature in K and C_e is the equilibrium concentration. The linear plot of ε^2 versus $\ln C_{\text{ads}}$ shown in **Fig. 12** gives β and $\ln X_m$ as slope and intercept, energy E can be obtained from the value of slope by using **Eq. (9)**.³⁰

$$E = \frac{1}{\sqrt{-2\beta}} \quad (9)$$

The value of mean free energy E (kJ/mol) suggests that sorption mechanism is either chemical ion exchange or physisorption. According to literature if E value is in the range of 0–8 then sorption mechanism will be considered

as physisorption and the if the value lies in between 8–16 it will correspond to chemisorptions.³¹

In current study, the value of mean free energy E is 3.58 KJ/mol which is calculated from the value of slope given in **Table 3** assuming that sorption mechanism of Cr(VI) onto modified Amberlite XAD-2 follows physisorption.

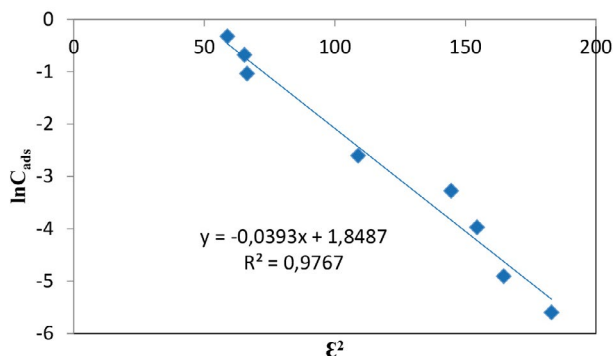


Figure 12. Dubinin-Radushkevich isotherm for Cr(VI) sorption onto isatin based Amberlite XAD-2 resin

Table 3. Isotherm parameters for Cr(VI) sorption on Isatin based Amberlite XAD-2 resin

Parameters	Freundlich	D-R
A ($\mu\text{g/g}$)	6.712	–
X_m ($\mu\text{g/g}$)	–	6.347
$1/n$	0.756	–
E (kJ/mol)	3.58	–
β ($\text{mol}^2 \text{KJ}^{-2}$)	–	–0.039
R^2	0.931	0.976

3. 8. Thermodynamics of Sorption

Sorption of Cr(VI) onto isatin based Amberlite XAD-2 resin was analyzed at different temperatures between 10 and 50 °C and maximum sorption was obtained at 10 °C. It was reported that the sorption capacity reduced with increase in temperature suggests that sorption process is exothermic. Temperature reliance of sorption process is connected with different thermodynamic parameters like change in Gibbs' free energy (ΔG°), entropy (ΔS°) and enthalpy (ΔH°) were analyzed by Van't Hoff equations which are given as follows

$$\Delta G^\circ = -RT \ln K_c \quad (10)$$

$$\ln K_c = \frac{\Delta S^\circ}{R} - \frac{\Delta H^\circ}{RT} \quad (11)$$

Where, R is the gas constant (8.314 J/molK), T is absolute temperature (K) and K_c is the equilibrium constant. The Value of K_c was obtained from the ratio of amount of Cr(VI) sorbed onto modified Amberlite XAD-

2 resin to that of solution phase concentration of Cr(VI). The values of ΔH° , ΔS° and ΔG° are given in Table 4. The variation in enthalpy and entropy were obtained from slope and intercept of the plot of $\ln K_c$ versus $1/T$ respectively Fig. 13.^{32–33}

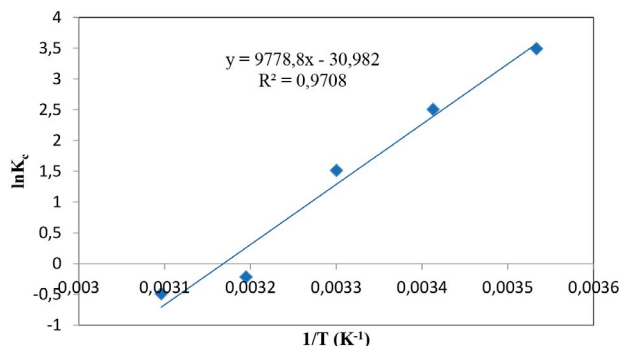


Figure 13. Temperature effect on the sorption of Cr(VI) ions on Isatin based Amberlite XAD-2

Table 4. Thermodynamic parameters of Cr(VI) sorption onto isatin based Amberlite XAD-2 resin

T(°C)	ΔH° (KJ/mol)	ΔS° (J/molK)	ΔG° (KJ/mol)
10	-81.25	-0.257	-8.214
20		-6.102	
30		-3.812	
40		0.565	
50		1.310	

In this study, the negative enthalpy change indicating exothermic nature of the sorption process whereas negative entropy change showed that randomness of Cr(VI) reduces as it passed from solution to sorbed state. The negative free energy changes from 10 to 30 °C indicated the spontaneous nature of the process while from 40 to 50 °C positive value of free energy change was taken as a sign of non-spontaneous sorption process.

3.9. Interference Study

Presence of common ions in solution is reported to have effect on removal efficiency, this may be owing to formation of precipitates or competition for sorption sites.³⁴ Therefore effect of different ions on removal efficiency of Cr(VI) ions onto isatin based Amberlite XAD-2 have been examined using optimized conditions. 1:10 concentration ratio of some anions and cations were added with the Cr(VI) solution. In the presence of sodium nitrate, sodium phosphate, nickel chloride, manganese sulphate, sorption of chromium (VI) was reduced while remaining added electrolytes have no considerable effect on the sorption. The results are shown in the Fig.14.

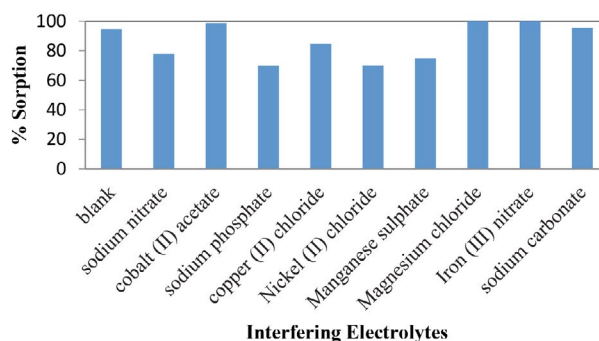


Figure 14. Sorption of Cr(VI) onto isatin based Amberlite XAD-2 resin in the presence of other electrolytes

Table 5. Interference effect of electrolytes on the Cr(VI) removal

Interference Species	% Sorption
Sodium nitrate	78%
Cobalt (II) acetate	98%
Sodium phosphate	70%
Copper (II) chloride	84%
Nickel (II) chloride	70%
Manganese sulphate	75%
Magnesium chloride	100%
Iron (III) nitrate	100%
Sodium carbonate	95%

3.10. Desorption Study

It is necessary to explore the removal efficiency of loaded metal from the isatin based Amberlite XAD resin to make certain their long term use for repeated removal-recovery cycles. The regeneration of the modified resin can be used as an indicator to find its potential capability for commercial application.

The metal ions sorption capacity as well as mechanical stability of the modified Amberlite XAD resin was determined by the three consecutive cycles of sorption-desorption experiments. 0.1M HNO₃, 0.1 M NaOH and 0.1M HCl solutions were used as desorbing agent.

The 0.1 M NaOH was found to be effective eluent to desorb Cr(VI) from resin. The total % sorption efficiency was decreased 25% for at least three cycles. It is revealed from the obtained result that our modified resin has significant potential to sorbed Cr(VI) species from water after recycling for three times.

3.11. Applications of Developed Method

The developed methodology was applied for Cr(VI) removal from well water, RO plant, ground and tap water samples by spiking known concentration of Cr(VI) ions through batch technique using optimized conditions. The % sorption was found to be quantitative as shown in Table 6.

Table 6. Cr(VI) removal from water samples

Sample	% Sorption (spiked amount 10 µg)	% Sorption (spiked amount 20 µg)
Ground water	95%	95%
RO plant	96%	96%
Well water	5%	95%
Tap water	94%	94%

4. Comparison with Other Sorbents

The modified resin were compared with the reported sorbent used for the removal of Cr (VI) species. First of all, the synthetic methodology is very simple and environmental benign. On the other hand, it is clearly seen that the our modified resin have higher surface area with more available binding sites which are capable to remove toxic Cr (VI) ions efficiently. The experimental values also revealed that our modified resin has more sorption capacity with the previously reported resins. The comparison is summarized in Table 7.

Sorbent	Sorption Capacity µg /g	Ref
Isatin Functionalized XAD-2 Resin	7.16	This work(Based on Freundlich isotherm)
Modified Silica MCM-41	–	35
Imidazole-4,5-dicarboxylic acid Modified XAD	1.12	36
Xanthine Functionalized XAD Resin	1.13	37
6-Mercaptopuriny azo XAD Resin	1.06	38
Shellac Modified XAD	0.017	39

5. Conclusion

Isatin based Amberlite XAD-2 was successfully synthesized by green synthesis and sorption capacity of modified resin was examined on highly toxic Cr(VI) removal from water. The Freundlich and D-R models gave better fit to the isotherm data than Langmuir model. The evaluation of kinetic data indicated pseudo-first-order kinetics followed by sorption process. Among thermodynamic parameters, negative enthalpy change indicating that the sorption process is exothermic in nature whereas negative entropy change showed that randomness of Cr(VI) reduces as it passed from solution to sorbed state. The validity of the proposed method was checked in spiked real water samples. Furthermore the synthesized resin can be reused for three cycles.

6. Acknowledgments

Authors are grateful to Institute of Advance Research Studies in Chemical Sciences, and Institute of Pure and

Applied Geology, University of Sindh, Jamshoro for facilitating this study.

Conflict of Interest

The authors declare that they have no conflict of interest.

7. References

- S. S. Banerjee, D. H. Chen, *J. Hazard. Mater.* **2007**, *147*, 792–797. DOI:10.1016/j.jhazmat.2007.01.079
- Y. T. Zhou, H. L. Nie, C. B. White, Zhi Yan He, L. M. Zhu, *J. Colloid Interface Sci.* **2009**, *330*, 29–37. DOI:10.1016/j.jcis.2008.10.026
- N. Kannan, M. M. Sundaram, *Dyes & Pigm.* **2001**, *51*, 25–40. DOI:10.1016/S0143-7208(01)00056-0
- W. Jiang, M. Pelaez, D. D. Dionysiou, M. H. Entezari, D. Tsoutsou, K. O'Shea, *Chem. Eng. J.* **2013**, *222*, 527–533. DOI:10.1016/j.cej.2013.02.049
- S. Kocaoba, G. Akcin, *Talanta*, **2002**, *57*, 23–30. DOI:10.1016/S0039-9140(01)00677-4
- S. Ertul, M. Bayrakci, M. Yilmaz, *J. Hazard. Mater.* **2010**, *181*, 1059–1065. DOI:10.1016/j.jhazmat.2010.05.121
- N. Goyal, S. C. Jain, S. U. C. Banerjee, *Adv. Environ. Res.* **2003**, *7*, 311–319. DOI:10.1016/S1093-0191(02)00004-7
- A. M. Yusof, N. A. Malek, *J. Hazard. Mater.* **2009**, *162*, 1019–1024. DOI:10.1016/j.jhazmat.2008.05.134
- M. I. Qureshi, F. Patel, N. Al-Baghli, B. Abussaud, B. S. Tawabini, T. Laoui, *Bioinorg. Chem. Appl.* **2017**, *2017*, 10–16. DOI:10.1155/2017/1624243
- B. Subramanyam, A. Das, *Int. J. Environ. Sci. Tech.* **2009**, *6*, 633–640. DOI:10.1007/BF03326104
- K. S. Padvamathy, G. Madhu, P. V. Haseena, *Procedia Technol.* **2016**, *24*, 585–594. DOI:10.1016/j.protcy.2016.05.127
- J. C. Igwe, A. Abia, *Afr. J. Biotechnol.* **2006**, *5*, 167–1179.
- A. O. Dada, A. P. Olalekan, A. M. Olatunya, O. Dada, Langmuir, Freundlich, Temkin and Dubinin-Radushkevich, **2012**, *J. Appl. Chem.* *3*, 38–45. DOI:10.9790/5736-0313845
- E. R. Ushakumary, G. Madhu, *Int. J. Environ. Waste Manage.* **2014**, *13*, 75–89. DOI:10.1504/IJEW.2014.058796
- C. Song, S. Wu, M. Cheng, P. Tao, M. Shao, and G. Gao, **2013**, *Sustainability*, *6*, 86–98. DOI:10.3390/su6010086
- H. Ye, Z. Yu, *Nat. Resour.* **2010**, *1*, 104–109.
- C. Namasivayam, N. Kanchana, R. T. Yamuna, *Waste Manage.* **1993**, *13*, 89–95. DOI:10.1016/0956-053X(93)90038-X
- A. Ahmed, J. A. Siddique, M. A. Laskar, R. Kumar, S. H. M. Setapar, A. Khatoon, R. A. Shiekh, **2015**, *J. Environ. Sci.* *31*, 104–123. DOI:10.1016/j.jes.2014.12.008
- M. I. Hoque, D. A. Chowdhury, R. Holze, A. N. Chowdhury, M. S. Azam, *J. Environ. Chem. Eng.* **2015**, *3*, 831–842. DOI:10.1016/j.jece.2015.03.020

20. A. M. Thakre, V. V. Hiwase, A. B. Kalambe, *Arch. Appl. Sci. Res.* **2012**, *4*, 1150–1154.
21. D. L. Pavia, G. M. Lampman, G. S. Kriz. Introduction to spectroscopy, 3rd Ed. Thomson Learning, **2001**, Chapter 2, pp. 26.
22. M. K. Rai, G. Shahi, V. Meena, R. Meena, S. Chakraborty, R. S. Singh, B. N. Rai, *Rai. Resour. Technol.* **2016**, *2*, 563–570.
23. M. P. Leite, L. G. T. Dos Reis, N. F. Robaina, W. F. Pacheco, R. J. Cassella, *Chem. Eng. J.* **2013**, *215*, 691–698.
DOI:10.1016/j.cej.2012.10.087
24. M. Ciopec, C. M. Davidescu, A. Negrea, I. Grozav, L. Lupa, P. Negrea, A. Popa, *Chem. Eng. Res. & Des.*, **2012**, *19*, 1660–1670. DOI:10.1016/j.cherd.2012.01.016
25. U. A. Qureshi, A. R. Solangi, S. Q. Memon, S. I. H. Taqvi, N. Memon, *Clean (Weinh)* **2012**, *40*, 630–639.
DOI:10.1002/clen.201100287
26. S. M. yakout, E. Elsherif, *Carbon-Sci. Tech.* **2010**, *1*, 144–153.
27. V. Srihari, A. Das, *Ecotoxicol Environ. Safe.* **2008**, *71*, 274–283.
DOI:10.1016/j.ecoenv.2007.08.008
28. S. Q. Memon, M. I. Bhangar, S. M. Hasany, M. Y. Khuhawar, *Talanta*, **2007**, *72*, 1738–1745.
DOI:10.1016/j.talanta.2006.12.017
29. S. Q. Memon, M. I. Bhangar, M. Y. Khuhawar, *Anal. Bioanal. Chem.ww* **2005**, *383*, 619–624.
DOI:10.1007/s00216-005-3391-1
30. U. A. Qureshi, A. R. Solangi, S. Q. Memon, S. I. H. Taqvi, *Arab J. Chem.* **2014**, *7*, 1166–1177.
DOI:10.1016/j.arabjc.2013.08.018
31. A. A. Bhatti, S. Memon, N. Memon, A. A. Bhatti, I. B. Solangi, *Arab J. Chem.* **2017**, *10*, S1111–S1118.
DOI:10.1016/j.arabjc.2013.01.020
32. S. O. Owalude, A. C. Tella. Beni-Suef, *Univ. J. Appl. Sci.* **2016**, *5*, 377–388. DOI:10.1016/j.bjbas.2016.11.005
33. Z. Yu, T. Qi, J. Qu, L. Wang, J. Chu, *J. Hazard. Mater.* **2009**, *167*, 406–412. DOI:10.1016/j.jhazmat.2008.12.140
34. J. R. Memon, S. Q. Memon, M. I. Bhangar, M. Y. Khuhawar, G. C. Allen, G. Z. Memon, A. G. Pathan, *Eur. Polym. J.* **2008**, *44*, 1501–1511. DOI:10.1016/j.eurpolymj.2008.02.018
35. M. R. Ganjali, L. H. Babaei, A. Badiei, K. Saberian, S. B. Abu-reihan, G. M. Ziarani, M. Salavati-Niasari, *Quim. Nova*, **2006**, *29*, 440–443. DOI:10.1590/S0100-40422006000300007
36. D. Banerjee, B. C. Mondal, A. K. Das, *J. Indian Chem. Soc.*, **2003**, *80*, 769–772.
37. D. D. Banerjee, A. K. Das, *J. Indian Chem. Soc.*, **2006**, *83*, 479–484.
38. B. C. Mondal, A. K. Das, *Bull. Chem. Soc. Jpn.*, **2003**, *76*, 111–114. DOI:10.1246/bcsj.76.111
39. Y. Sibel, A. Resat, *Int. J. Environ. Anal. Chem.*, **2006**, *86*, 915–929.

Povzetek

Amberlit XAD-2 smo funkcionalizirali z izatinom preko -C=N- ročic z uporabo okolju prijaznega postopka. Tako pripravljenu nosilcu smo določili adsorpcijsko kapaciteto toksičnih Cr (VI) ionov s pomočjo spektrofotometra. Optimizirali smo pH vrednost, volumen, količino adsorbenta, začetno koncentracijo Cr (VI) ionov in čas mešanja. Izkazalo se je, da adsorpcijske podatke bolje opišemo z Freundlichovo in Dubinin- Radushkevichovo kot pa z Langmuirjevo izotermo. Ovrednoteni so bili termodinamski parametri, kinetični podatki so pokazali, da hitrost adsorpcije lahko opišemo z modelom pseudo-prvega reda. Maksimalni izkoristek je bil dosežen pri 10 ml v 0.1 M NaOH. Ustreznost metode smo preverili z metodo standardnega dodatka. Rezultati so pokazali, da lahko z razvito metodo učinkovito odstranjujemo Cr (VI) ione iz vode in lahko adsorbent uporabimo vsaj trikrat.



Except when otherwise noted, articles in this journal are published under the terms and conditions of the Creative Commons Attribution 4.0 International License

Scientific paper

Scalable Synthesis of Salt-free Quaternary Ammonium Carboxylate Catanionic Surfactants

Žiga Medoš, Miha Virant, Urša Štanfel, Boštjan Žener, Janez Košmrlj*
and Marija Bešter-Rogač*

Faculty of Chemistry and Chemical Technology, Večna pot 113, University of Ljubljana, SI-1000 Ljubljana, Slovenia

* Corresponding author: E-mail: janez.kosmrlj@fkkt.uni-lj.si

Tel: +386 1 479 8558

E-mail: marija.bester@fkkt.uni-lj.si

Tel: +386 1 479 8537

Received: 07-16-2019

Abstract

Surfactants in commercial products commonly contain catanionic mixtures thus many studies of aqueous surfactant mixtures have been carried out. However, hardly any studies have been dedicated to pure catanionic surfactants often termed salt-free catanionic surfactants. One of the difficulties is in acquirement of samples with required purity due to difficult separation of these compounds from inorganic salts. In this work we present an alternative method of synthesis using dimethyl carbonate as the alkylating agent in order to obtain alkyl trimethylammonium alkanecarboxylates with medium alkyl chain lengths (6–10).

Keywords: Synthesis; surfactants; salt-free; catanionics; quaternization

1. Introduction

Commercial surfactants are commonly a mixture of cationic, anionic and non-ionic surfactants due to their enhanced performance as mixtures.^{1,2} Therefore, along the studies of non-ionic and ionic surfactants in their pure form as well as in binary aqueous solutions, significant focus has been dedicated to aqueous mixtures of cationic and anionic surfactants – catanionic mixtures. An interesting group of catanionic surfactants are salt-free catanionics, where often the challenge of preparing these surfactants in their pure form is the removal of all inorganic salts upon mixing the parent cation and anion salts. There are three main methods to remove inorganic salts from equimolar catanionic mixtures: (1) ion-exchange columns are used to prepare acids and hydroxides and subsequently mixed; (2) liquid-liquid extraction in organic phase and (3) precipitation method.³ When surfactants are poorly soluble in organic solvents precipitation is generally easily achieved. On the contrary, if solubility is limited in polar solvents liquid-liquid extraction is possible. However, many surfactants, especially those interesting for application, are soluble in both, organic and aqueous media. This limits the separa-

tion techniques to ion-exchange columns or the precipitation of silver halides from water solutions. Unfortunately, these two approaches are not economically viable and some contamination with inorganic salt can still occur. This can have significant impact on some of the surfactant's properties and can crucially affect studied physical and aggregation properties of aqueous solutions.^{4–6} Thus, the development of novel and more effective methods of synthesis is required.

In this work we present two synthetic procedures to prepare alkyltrimethylammonium alkanecarboxylate catanionic surfactants (Figure 1). Generally, the synthesis of quaternary ammonium surfactants starts with ammonia or substituted amine precursor. It is alkylated in two or more steps with the last step being quaternization. Most studied and produced quaternary ammonium surfactants are alkyltrimethylammonium halides followed by dialkyldimethylammonium halides (gemini surfactants).⁷ Their aqueous solutions are generally more stable than quaternary ammonium surfactants with remaining hydrogen(s) on quaternary ammonium. Quaternization can be achieved by the Menshutkin reaction where tertiary amine is reacted with haloalkane. However, halide free methods are preferred for industrial application.

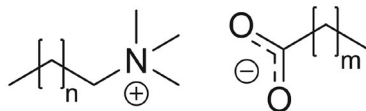


Figure 1. N-alkyl-N,N,N-trimethylammonium alkanecarboxylates.

Recently, Jiang *et al.* presented a synthetic procedure for the preparation of salt-free quaternary ammonium carboxylates using dimethyl carbonate (DMC) as alkylating agent of appropriate tertiary amines, with one or two alkyl chains exceeding 12 carbon atoms and a short-chain carboxylate anion (acetate, propionate, lactate).⁸ They expanded the scope to long-chain cationic surfactants in the follow-up papers, namely tetradecyltrimethylammonium alkanecarboxylates (hexanoate, octanoate, decanoate, dodecanoate, tetradecanoate)⁹ and alkyl (decyl, dodecyl, tetradecyl, hexadecyl, octadecyl) trimethylammonium decanoates.¹⁰ DMC represents an attractive eco-friendly alternative to methyl halides.¹¹

However, additional challenges emerge when both alkyl chains are shorter than 10 carbon atoms. Mainly, due to increased solubility in majority of polar and non-polar solvents the usual purification methods of precipitation, recrystallization and liquid-liquid extraction become less efficient or impossible. Additionally, the commercial price of tertiary amines, required in the most common synthesis approach, increases with shorter chains. Therefore, in this work we present low cost synthetic alternative starting with a secondary amine to produce quaternary ammonium carboxylate surfactants with alkyl chains between 6 and 10 carbon atoms long.

Synthesis of decyltrimethylammonium alkanecarboxylates (acetate, butanoate, hexanoate, octanoate, nonanoate, decanoate, undecanoate) has also been reported by reacting quaternary ammonium halides with silver hydroxide. After precipitation of the silver halide salts, the resulting hydroxide solutions were reacted with carboxylic acid.¹² For large scale application silver salts are not economically viable, therefore we present a competitive approach through precipitation of KCl from ethanol. We compare the thermal properties of products obtained by both procedures.

2. Experimental

2.1. General Information

The reagents and solvents in general procedures were used as obtained from the commercial sources (Merck), unless noted otherwise. Octanoic acid (**4b**) and decanoic acid (**4c**) were recrystallized from ethanol by addition of acetone. IR spectra were obtained with a Perkin-Elmer Spectrum 100, equipped with a Specac Golden Gate Diamond ATR as a solid sample support. High resolution mass spectra (HRMS) were recorded on Agilent 6224 time-of-flight (TOF) mass spectrometer equipped with a double orthogo-

nal electrospray source at atmospheric pressure ionization (ESI) coupled to an HPLC instrument. ¹H, ¹³C and ¹⁵N NMR spectra were recorded with a Bruker Avance III 500 MHz NMR (at 500 MHz, 126 MHz and 51 MHz, respectively) instrument at 296 K in DMSO-*d*₆ using TMS as an internal standard. Proton and carbon spectra were referenced to the residual chloroform shifts of 7.26 ppm and 77.16 ppm, respectively.¹³ Assignments of proton, carbon and nitrogen resonances were performed by 2D NMR techniques (¹H-¹H *gs*-COSY, ¹H-¹³C *gs*-HSQC, ¹H-¹³C *gs*-HMBC and ¹H-¹⁵N *gs*-HMBC). Carbon resonances without labels belong to the chain carbons and could not have been differentiated. Thermogravimetric (TG) measurements were performed on a Mettler Toledo TGA/DSC1 Instrument in the temperature range from 25 to 400 °C under dynamic air flow (100 cm³ min⁻¹) with a heating rate of 5 K min⁻¹. Approximately 3–5 mg of sample was weighed into a 150 μL platinum crucible and the baseline was subtracted. Differential scanning calorimetry (DSC) measurements were performed separately on a Mettler Toledo DSC 1 Instrument in 40 μL aluminium crucibles under the same conditions.

2.2. Synthesis

Alkyltrimethylammonium Chlorides **3a–c**

In a 200 mL autoclave chloroalkanes **2a–c** (0.21 mol, 1 eq) were mixed with 33% trimethylamine solution in ethanol (**1**, 100 mL, 2 eq). The mixture was stirred in an oil bath at 80 °C for 3 days. Excess **1** and solvents were removed under reduced pressure. Products were dissolved in minimal amount of ethanol required (approx. 5 mL) and recrystallized by addition of ethyl acetate (100 mL). The precipitates were filtered and washed with diethyl ether (50 mL) and subsequently dried under reduced pressure to yield products in 50% average yield. Products **3** are very hygroscopic which reduces the yield of recrystallization in open air (**3a** 26%, **3b** 53%, **3c** 55%).

Alkyltrimethylammonium Carboxylates **5a–e** According to Procedure A

In the next step, alkyltrimethylammonium chlorides **3a–c** as prepared above (0.07 mol) were dissolved in ethanol (20 mL) and weighed precisely. The exact amount of chloride ions was determined by AgNO₃ titration of small samples and the required equimolar amounts of carboxylic acids **4a–c** were weighed and added. 95% of KOH, required for neutralization, was weighed as solid pellets. After all of the added solid KOH dissolved and KCl precipitated (1 hour), the remaining KOH was titrated as an approximate 0.25 M solution of KOH in ethanol until potential of glass electrode dropped below -250 mV which was previously determined as the potential of the inflection point. Solutions were filtered to separate the filtrate containing the products from the precipitated KCl. Filtrates were concentrated under reduced pressure subsequently precipitating more KCl which was filtered to obtain filtrate

containing desired alkyltrimethylammonium carboxylates **5a–e** in quantitative yields. Solutions were dried first under reduced pressure and followed by high vacuum. However, due to increased solubility of KCl in the presence of the products up to 3% of KCl remains in the final product as determined by AgNO₃ titration and TG analysis.

Alkyldimethylamines **8a–c**

Bromoalkanes **7** (bromohexane (**7a**) 2.3 mol; bromooctane (**7b**) 1.9 mol; bromodecane (**7c**) 1.6 mol; 1 eq) were mixed with toluene (300 mL) in a 3 L autoclave. Then 40% *N,N*-dimethylamine (**6**) solution in water (500 mL, approx. 2 eq) was added. An excess amount of NaOH (200 mL) was added as a 50% aqueous solution. The mixtures were stirred and heated to 60 °C for 3 days. After the reaction was completed the reaction mixture separated in two layers. The organic phase containing products was separated from water phase and concentrated under reduced pressure. The products were washed several times with water (5 × 20 mL) and distilled under reduced pressure to ensure separation from inorganic byproducts and to remove toluene (**8a** 70%, **8b** 90%, **8c** 95%). While amine **8c** can be dried on a vacuum line with minimal loss due to evaporation, the distillation results in better overall yield. The presence of toluene in product is not problematic, as it is removed in the following steps.

Alkyltrimethylammonium Methylcarbonates **9a–c**

In a 50 mL autoclave alkyldimethylamines **8a–c** as prepared above (0.2 mol, 1 eq) were mixed with dimethyl carbonate (Me₂CO₃, 0.3 mol, 1.5 eq) and methanol (20 mL) as solvent. Mixtures were stirred at 120 °C for 2 days or 110 °C for 3 days. Excess Me₂CO₃ and solvent were removed under reduced pressure. Alkyltrimethylammonium methyl carbonates with traces of hydrogencarbonate analogues were recrystallized from ethyl acetate. The pure products **9** were obtained after recrystallization (**9a** 50%, **9b** 70%, **9c** 90%). Yields are primarily lowered by loss during purification however it should be noted that recrystallization in this step is not strictly necessary as the organic impurities are also successfully removed by recrystallization in the final step of the procedure B thus potentially increasing yield.

Alkyltrimethylammonium Carboxylates **5a–f** According to Procedure B

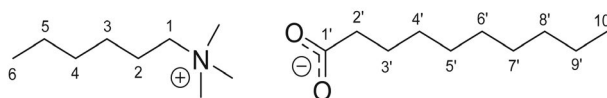
In a round-bottomed flask alkyltrimethylammonium methylcarbonates **9a–c** (0.03 mol) and carboxylic acids **4** (0.03 mol) were weighed. Small amount of methanol (2 mL) was added to increase solubility and speed up the reactions. After stirring for an hour at room temperature, methanol was removed under reduced pressure and the products isolated as white solids. For analysis and further research application, the products were recrystallized using acetonitrile. If significant excess of **4** (more than 2%) was used or methanol was not completely removed the mixture dissolved fully in acetonitrile. The longer the alkyl chains

on cation and anion the better the yield due to the poorer solubility in acetonitrile and lower hygroscopicity (**5a** 70%, **5b** 90%, **5c** 80%, **5d** 40%, **5e** 60%, **5f** 15%). The attempt to make decyltrimethylammonium acetate was unsuccessful because of the complete solubility in acetonitrile.

2. 3. Characterization of

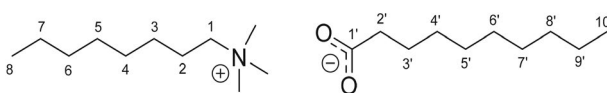
Alkyltrimethylammonium Carboxylates

N-Hexyl-*N,N,N*-trimethylammonium Decanoate (**5a**)



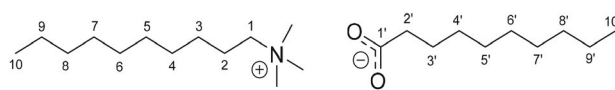
Prepared according to the general procedure B. White solid (11.5 g, 35%). IR 3473, 3393, 3020, 2920, 2852, 1572, 1377, 1055, 963, 643 cm⁻¹. ¹H NMR (500 MHz, CDCl₃) δ 3.42–3.35 (m, 2H, CH₂-1), 3.32 (s, 9H, NMe₃), 2.14–2.06 (m, 2H, CH₂-2'), 1.75–1.64 (m, 2H, CH₂-2), 1.59–1.48 (m, 2H, CH₂-3'), 1.38–1.15 (m, 18H, CH₂-chain), 0.92–0.78 (m, 6H, CH₃-10' and CH₃-6). ¹³C NMR (126 MHz, CDCl₃) δ 179.8 (COO), 66.9 (30.21), 53.2 (NMe₃), 39.4 (C-2'), 32.0, 31.4, 30.2, 29.9, 29.8, 29.50, 27.3, 26.0, 23.2, 22.8, 22.5, 14.2 (CH₃-6/CH₃-10'), 14.0 (CH₃-6/CH₃-10'). ¹⁵N NMR (51 MHz, CDCl₃) δ 49.5 (NMe₃). HRMS (ESI+): calcd. for C₉H₂₂N⁺ [M⁺] 144.1747, found 144.1749. HRMS (ESI-): calcd. for C₁₀H₁₉O₂⁻ [M⁻] 171.1391, found 171.1389.

N-Octyl-*N,N,N*-trimethylammonium Decanoate (**5b**)



Prepared according to the general procedure B. White solid (14.7 g, 63%). IR 3317, 3119, 3032, 2919, 2851, 1657, 1569, 1380, 972, 756 cm⁻¹. ¹H NMR (500 MHz, CDCl₃) δ 3.43–3.38 (m, 2H, CH₂-1), 3.38–3.31 (m, 9H, NMe₃), 2.19–2.05 (m, 2H, CH₂-2'), 1.76–1.61 (m, 2H, CH₂-2), 1.60–1.49 (m, 2H, CH₂-3'), 1.41–1.13 (m, 22H, CH₂-chain), 0.89–0.79 (m, 6H, CH₃-8 and CH₃-10). ¹³C NMR (126 MHz, CDCl₃) δ 179.6 (COO), 66.9 (C-1), 53.2 (NMe₃), 39.2 (C-2'), 32.0, 31.7, 30.2, 29.8, 29.8, 29.5, 29.3, 29.1, 27.3 (C-3'), 26.4, 23.2 (C-2), 22.8, 22.7, 14.2 (CH₃-8/CH₃-10'), 14.1 (CH₃-8/CH₃-10'). ¹⁵N NMR (51 MHz, CDCl₃) δ 49.7 (NMe₃). HRMS (ESI+): calcd. for C₁₁H₂₆N⁺ [M⁺] 172.2060, found 172.2057. HRMS (ESI-): calcd. for C₁₀H₁₉O₂⁻ [M⁻] 171.1391, found 171.1386.

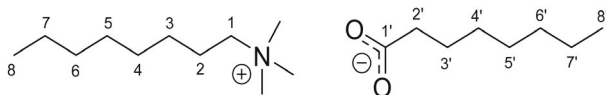
N-Decyl-*N,N,N*-trimethylammonium Decanoate (**5c**)



Prepared according to the general procedure B. White solid (25.3 g, 72%). IR 3429, 3348, 3195, 3119, 3032,

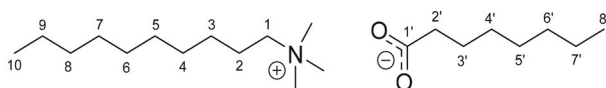
2916, 2850, 1656, 1566, 1387 cm^{-1} . ^1H NMR (500 MHz, CDCl_3) δ 3.42–3.35 (m, 2H, CH_2 -1), 3.32 (s, 9H, NMe_3), 2.16–2.07 (m, 2H, CH_2 -2'), 1.74–1.63 (m, 2H, CH_2 -2), 1.54 (p, $J = 7.2$ Hz, 2H, CH_2 -3'), 1.38–1.14 (m, 26H, CH_2 -chain), 0.91–0.79 (m, 6H, CH_3 -10 and CH_3 -10'). ^{13}C NMR (126 MHz, CDCl_3) δ 179.6 (COO), 66.9 (C-1), 53.2 (NMe_3), 39.0 (C-2'), 32.0, 31.9, 30.2, 29.9, 29.8, 29.54, 29.51, 29.4, 27.2 (C-3'), 26.4, 23.3 (C-2), 22.79, 22.75, 14.22 (CH_3 -10/ CH_3 -10'), 14.19 (CH_3 -10/ CH_3 -10'). ^{15}N NMR (51 MHz, CDCl_3) δ 49.5 (NMe_3). HRMS (ESI+): calcd. for $\text{C}_{13}\text{H}_{30}\text{N}^+$ [M^+] 200.2373, found 172.2373. HRMS (ESI-): calcd. for $\text{C}_{10}\text{H}_{19}\text{O}_2^-$ [M^-] 171.1391, found 171.1388.

N-Octyl-*N,N,N*-trimethylammonium Octanoate (5d)



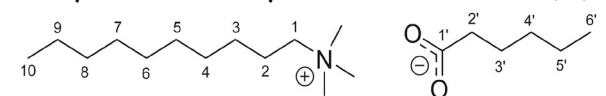
Prepared according to the general procedure B. White solid (10.8 g, 28%). IR 3510, 3022, 2919, 2851, 1657, 1573, 1378, 974, 918, 773 cm^{-1} . ^1H NMR (500 MHz, CDCl_3) δ 3.43–3.36 (m, 2H, CH_2 -1), 3.35–3.25 (m, 9H, NMe_3), 2.16–2.05 (m, 2H, CH_2 -2'), 1.74–1.61 (m, 2H, CH_2 -2), 1.59–1.46 (m, 2H, CH_2 -3'), 1.35–1.12 (m, 14H, CH_2 -chain), 0.89–0.75 (m, 6H, CH_3 -8 and CH_3 -8'). ^{13}C NMR (126 MHz, CDCl_3) δ 179.5 (COO), 66.8 (C-1), 53.1 (NMe_3), 39.1 (C-2'), 32.0, 31.7, 30.1, 29.5, 29.3, 29.1, 27.2 (C-3'), 26.3, 23.2 (C-2), 22.8, 22.6, 14.2 (CH_3 -8/ CH_3 -8'), 14.1 (CH_3 -8/ CH_3 -8'). ^{15}N NMR (51 MHz, CDCl_3) δ 49.4 (NMe_3). HRMS (ESI+): calcd. for $\text{C}_{11}\text{H}_{26}\text{N}^+$ [M^+] 172.2060, found 172.2054. HRMS (ESI-): calcd. for $\text{C}_8\text{H}_{15}\text{O}_2^-$ [M^-] 143.1078, found 143.1076.

N-Decyl-*N,N,N*-trimethylammonium Octanoate (5e)



Prepared according to the general procedure B. White solid (16.7 g, 54%). IR 3464, 3385, 3021, 2919, 2851, 1572, 1380, 915, 772, 722 cm^{-1} . ^1H NMR (500 MHz, CDCl_3) δ 3.45–3.39 (m, 2H, CH_2 -1), 3.40–3.35 (m, 9H, NMe_3), 2.23–2.11 (m, 2H, CH_2 -2'), 1.79–1.67 (m, 2H, CH_2 -2), 1.65–1.53 (m, 2H, CH_2 -3), 1.42–1.18 (m, 22H, CH_2 -chain), 0.93–0.81 (m, 6H, CH_3 -10 and CH_3 -8'). ^{13}C NMR (126 MHz, CDCl_3) δ 180.0 (COO), 67.1 (C-1), 53.4 (NMe_3), 39.3 (C-2'), 32.1, 32.0, 30.2, 29.6, 29.53, 29.49, 29.36, 29.34, 27.3 (C-3'), 26.4, 23.3 (C-2'), 22.9, 22.8, 14.3 (CH_3 -10/ CH_3 -8'), 14.2 (CH_3 -10/ CH_3 -8'). ^{15}N NMR (51 MHz, CDCl_3) δ 49.7 (NMe_3). HRMS (ESI+): calcd. for $\text{C}_{13}\text{H}_{30}\text{N}^+$ [M^+] 200.2373, found 172.2375. HRMS (ESI-): calcd. for $\text{C}_8\text{H}_{15}\text{O}_2^-$ [M^-] 143.1078, found 143.1073.

N-Decyl-*N,N,N*-trimethylammonium Hexanoate (5f)



Prepared according to the general procedure B. White solid (2.2 g, 13%). IR 3359, 3021, 2922, 2854, 1572, 1377, 973, 918, 766, 644 cm^{-1} . ^1H NMR (500 MHz, CDCl_3) δ 3.45–3.37 (m, 2H, CH_2 -1), 3.38–3.30 (m, 9H, NMe_3), 2.21–2.03 (m, 2H, CH_2 -2'), 1.76–1.61 (m, 2H, CH_2 -2), 1.61–1.50 (m, 2H, CH_2 -3'), 1.38–1.15 (m, 18H, CH_2 -chain), 0.92–0.78 (m, 6H, CH_2 -8 and CH_2 -). ^{13}C NMR (126 MHz, CDCl_3) δ 179.6 (COO), 66.9 (C-1), 53.2 (NMe_3), 39.2 (C-2'), 32.4, 31.9, 29.50, 29.46, 29.3, 26.9 (3'), 26.4, 23.3 (C-2), 22.8, 22.7, 14.3 (CH_3 -10/ CH_3 -6'), 14.2 (CH_3 -10/ CH_3 -6'). ^{15}N NMR (51 MHz, CDCl_3) δ 49.8 (NMe_3). HRMS (ESI+): calcd. for $\text{C}_{13}\text{H}_{30}\text{N}^+$ [M^+] 200.2373, found 200.2370. HRMS (ESI-): calcd. for $\text{C}_{10}\text{H}_{19}\text{O}_2^-$ [M^-] 171.1391, found 171.1386.

3. Results and Discussion

A series of quaternary ammonium carboxylates – *N*-alkyl-*N,N,N*-trimethylammonium alkanecarboxylates were prepared according to two general procedures as presented on Figure 2.

In the first step of procedure A, where the reaction mixture was heated at 80 °C for 3 days, alkyltrimethylammonium chlorides (alkyl = hexyl, **3a**; octyl, **3b**; decyl, **3c**) were obtained. Procedure A is followed by a cost effective approach to anion exchange in ethanolic solutions of KOH through precipitation of KCl (see Experimental Section for details) yielding alkyltrimethylammonium alkanecarboxylates (**5a–e**, Table in Figure 2). Even though the reported solubility of KCl in ethanol is very low (0.034%)¹⁴ the final products of procedure A shown in Table 1 contained up to 3% of inorganic salt as determined by AgNO_3 titration ($0.6 \pm 0.5\%$ Cl^-) and TG analysis ($2 \pm 1\%$). Presumably the presence of the product significantly increases solubility of KCl in ethanol. In fact, products are soluble in polar (water, methanol, ethanol, 1-butanol, acetone, ethyl acetate) and most non-polar (diethyl ether, *n*-hexane, toluene, dichloromethane, chloroform) solvents, making complete separation from KCl by precipitation impossible.

Therefore, the procedure B was developed as an alternative. Starting from dimethylamine (**6**) the long alkyl chain is introduced in the step before quaternization. Therefore, the soluble halide salts are easily washed away with water. Quaternization was successfully achieved with dimethyl carbonate (Me_2CO_3), a common methylating agent enabling a facile purification method. The side products, methanol and CO_2 , are easily removed under reduced pressure. Jiang *et al.* used significant excess (5–10 eq) of Me_2CO_3 and relatively short reaction times (5–7 h).^{8,9} We extended the reaction time in attempt to reach quantitative yield with minimal excess of reactant. Anion exchange was performed with carboxylic acid followed by the removal of volatile byproducts. For analysis the products (**5a–f**) were recrystallized from acetonitrile. Surfactants with longer alkyl chains to the ones in this work have been reportedly

For comparison TG/DSC curve of decyltrimethylammonium chloride (**3c**) is also presented on Figures S1 and S2 indicating lower thermal stability of carboxylates. Stability is also somewhat lowered by KCl (Table 1). Melting point or phase transition was observed for some of the products. KCl lowers the temperature of this transition.

4. Conclusions

In the proposed salt-free procedure first alkyl trimethylammonium methylcarbonate is obtained and reacted with carboxylic acid. The side products of methanol and CO₂ are easily removed under reduced pressure. In principle, salts composed of quaternary ammonium cations and most anions can be synthesized with this procedure. Reactants are inexpensive thus the procedure is potentially applicable in industrial production. An alternative procedure applying precipitation method is a viable alternative when inorganic impurities do not affect the application of the surfactant.

Supplementary Material

Copies of the IR and NMR spectra as well as additional figures on thermal analysis are available free of charge.

5. Acknowledgements

The financial support by the Slovenian Research Agency through Grants No. P1-0201, P1-0230 and P1-0134 is gratefully acknowledged. Ž. M. is grateful to Slovenian Research Agency for the position of young researcher enabling him the doctoral study. Dr. Damijana Urankar from the Research Infrastructure Centre at the Faculty of Chemistry and Chemical Technology, University of Ljubljana, is acknowledged for HRMS analyses.

6. References

1. A. Khan, E. Marques, in: I. D. Robb (Ed.) *Specialist Surfactants*. Springer, Dordrecht, **1997**
2. G. Kume, M. Gallotti, G. Nunes, *J. Surfact. Deterg.* **2008**, *11*, 1–11. DOI:10.1007/s11743-007-1047-1
3. P. Jokela, B. Joensson, A. Khan, *J. Phys. Chem.* **1987**, *91*, 3291–3298. DOI:10.1021/j100296a037
4. G. C. Kresheck, *J. Phys. Chem. B* **2009**, *113*, 6732–6735. DOI:10.1021/jp811048d
5. A. Kroflič, B. Šarac, M. Bešter-Rogač, *J. Chem. Thermodyn.* **2011**, *43*, 1557–1563. DOI:10.1016/j.jct.2011.05.015
6. A. Kroflič, B. Šarac, M. Bešter-Rogač, *Langmuir* **2012**, *28*, 10363–10371. DOI:10.1021/la302133q
7. L. L. Schramm, E. N. Stasiuk, D. G. Marangoni, *Annu. Rep. Prog. Chem., Sect. C: Phys. Chem.* **2003**, *99*, 3–48. DOI:10.1039/B208499F
8. Y. Jiang, T. Geng, Q. Li, *J. Surfact. Deterg.* **2012**, *15*, 67–71. DOI:10.1007/s11743-011-1289-9
9. H.-C. Yan, Q. Li, T. Geng, Y. Jiang, Y. Luo, *Tenside Surf. Det.* **2012**, *49*, 211–215. DOI:10.3139/113.110184
10. Y. Jiang, T. Geng, Q. Li, G. Li, H. Ju, *J. Mol. Liq.* **2015**, *204*, 126–131. DOI:10.1016/j.molliq.2015.01.026
11. P. Tundo, M. Selva, *Acc. Chem. Res.* **2002**, *35*, 706–716. DOI:10.1021/ar010076f
12. D. G. Oakenfull, D. E. Fenwick, *Aust. J. Chem.* **1973**, *26*, 2649–2658. DOI:10.1071/CH9732649
13. H. E. Gottlieb, V. Kotlyar, A. Nudelman, *J. Org. Chem.* **1997**, *62*, 7512–7515. DOI:10.1021/jo971176v
14. S. P. Pinho, E. A. Macedo, *J. Chem. Eng. Data* **2005**, *50*, 29–32. DOI:10.1021/je049922y
15. G. A. Kliger, L. S. Glebov, V. P. Ryzhikov, V. E. Shiryaeva, T. P. Popova, S. M. Loktev, *Russ. Chem. Bull.* **1987**, *36*, 1738. DOI:10.1007/BF00960149
16. M. H. S. A. Hamid, C. L. Allen, G. W. Lamb, A. C. Maxwell, H. C. Maytum, A. J. A. Watson, J. M. J. Williams, *J. Am. Chem. Soc.* **2009**, *131*, 1766–1774. DOI:10.1021/ja807323a
17. X. Cui, X. Dai, Y. Deng, F. Shi, *Chem. Eur. J.* **2013**, *19*, 3665–3675. DOI:10.1002/chem.201203417

Povzetek

Površinsko aktivne snovi v komercialnih produktih pogosto vsebujejo mešanice anionskih in kationskih surfaktantov, zato so bile dosedaj večinoma preiskovane vodne raztopine mešanic površinsko aktivnih snovi. Vendar pa so raziskave čistih katanionskih površinsko aktivnih snovi, ki se pogosto imenujejo katanionski surfaktanti brez soli, redke. Ena od težav je pridobivanje vzorcev z zahtevano čistostjo zaradi težkega ločevanja teh spojin od anorganskih soli. V tem delu predstavljamo alternativno metodo sinteze z dimetilkarbonatom kot alkilnim sredstvom za pripravo alkil trimetilamonijevih alkankarboksilatov s srednjimi dolžinami alkilnih verig (6–10).



Except when otherwise noted, articles in this journal are published under the terms and conditions of the Creative Commons Attribution 4.0 International License

Scientific paper

Synthesis, Characterization and Antimicrobial Evaluation of Novel 6'-Amino-spiro[indeno[1,2-*b*]quinoxaline[1,3]dithiine]-5'-carbonitrile Derivatives

Mohammadreza Moghaddam-Manesh, Dadkhoda Ghazanfari,*
Enayatollah Sheikhhosseini and Mohammadreza Akhgar

Department of Chemistry, Kerman Branch, Islamic Azad University, Kerman, Iran

* Corresponding author: E-mail: dadkhodaghbk@yahoo.com

Tel: +98 31321328, fax: +9831321405

Received: 07-23-2019

Abstract

1,3-Dithiin with two sulfurs in its structure is a six-membered, sulfur-containing heterocyclic compound. New derivatives of 6'-amino-2'-(arylidene)spiro[indeno[1,2-*b*]quinoxaline[1,3]dithiine]-5'-carbonitrile were prepared by the multi-component reaction of active methylene compounds, carbon disulfide, malononitrile and multi-ring compounds containing a carbonyl group in the presence of piperidine as a catalyst at room temperature with high efficiency. The antimicrobial effects including antibacterial and antifungal effects based on inhibition zone diameter (IZD), minimum inhibitory concentration (MIC), minimum bactericidal concentration (MBC) and minimum fungicidal concentration (MFC) were studied.

Keywords: Multicomponent reaction; sulfur-containing heterocyclic; spiro[indeno[1,2-*b*]quinoxaline[1,3]dithiine]-5'-carbonitrile; carbon disulfide; antimicrobial activity

1. Introduction

Heterocyclic compounds are highly valuable considering their use as a key ingredient in medications.¹ Sulfur-containing heterocyclic compounds are particularly noteworthy in organic chemistry, medicine, and biochemistry due to their structure.^{2–3} Spiro heterocyclic compounds lead to the biological activity of these compounds because of the commonality of a carbon between the two rings and the lack of symmetry of these compounds due to the asymmetric nature of carbon spiro compounds.^{4–8} Biological activities, such as promising antibacterial, antifungal,^{9–11} anti-hyperglycemic,¹² and anti-tubercular¹³ effects have been reported for spiro heterocyclic compounds.

1,3-Dithiin is a six-membered sulfur-containing heterocyclic ring with two sulfur atoms at positions 1 and 3. This heterocyclic compound has been reported as an anti-thrombotic agent found in *Allium sativum*.¹⁴ Other biological properties have also been reported for synthesized heterocyclic compounds containing 1,3-dithiin ring.^{15–17} These compounds are most often used as a carbon protection groups for the synthesis of heterocyclic compounds.^{18–20}

In this study the new derivatives of 6'-amino-2'-(arylidene)spiro[indeno[1,2-*b*]quinoxaline[1,3]dithiine]-5'-carbonitrile were synthesized using compounds possessing active methylene group, carbon disulfide, malononitrile, 11*H*-indeno[1,2-*b*]quinoxalin-11-one and 1*H*-indene-1,2,3-trione and their biological activities such as antibacterial and antifungal activities were studied.

In our previous report, new derivatives of spiro[indoline-3,4'-[1,3]dithiine] were synthesized by MgO nanoparticles.¹⁷ In this work, the synthesis of derivatives with MgO nanoparticles was investigated but the desired result was not obtained, that could be due to the larger reactant material including 11*H*-indeno[1,2-*b*]quinoxalin-11-one than in the previous work.

2. Experimental

2.1. Chemistry

The ¹H and ¹³C NMR spectra of compounds in DM-SO-*d*₆ were measured using a Bruker Ultra Shield-250 spectrometer (250 and 75 MHz, respectively). The FT-IR

spectra were taken using the KBr disks by a Bruker Tensor 27 FT-IR spectrometer with absorption given in cm^{-1} . Furthermore, elemental analysis was performed for C, H, N, and S by a Thermo Finnigan Flash EA microanalyzer. The melting point of the compounds was recorded on a Kruss type KSP1 N melting point meter. The concentrations of bacterial, fungal suspensions were determined by using Jenway 6405 UV-VIS spectrophotometer. The reaction progression process was monitored using TLC (silica gel, aluminum sheets) obtained from Merck. Moreover, chemicals and solvents were purchased from Merck and Sigma-Aldrich, and no purification was performed prior to their use.

2. 1. 1. General Procedure for the Preparation of Compounds 7a–c and 10a–d

To a solution of active methylene compound **1a–c** (1 mmol) in 2 mL acetonitrile, 2 mmol piperidine (0.1703 g) and 3 mmol carbon disulfide (0.2284 g) were added, and the mixture was stirred for 0.5 h or 1 h (dimedone for 0.5 h and barbituric acid derivatives for 1 h) at room temperature.

In another container, a mixture of 1 mmol malononitrile (0.066 g), 1 mmol piperidine (0.0852 g), and 1 mmol multi-ring compounds containing a carbonyl group (**4, 8a–b**) in 2 mL of acetonitrile were stirred for 0.5 h at room temperature. Then, the two mixtures were mixed and stirred at room temperature for 9–12 h. The reaction was monitored using TLC (hexane/ethyl acetate) and, after completion, the precipitate was filtered and recrystallised from acetonitrile to give the pure compounds.

6'-Amino-7,8-dimethyl-2'-(2,4,6-trioxotetrahydropyrimidin-5(2H)-ylidene)spiro[indeno[1,2-b]quinoxaline-11,4'-[1,3]dithiine]-5'-carbonitrile (7a)

Yield: 70%, m.p. 297–298 °C; IR (KBr, cm^{-1}): 3352, 3275 (NH_2), 2164 (CN), 1718, 1673 (CO); ^1H NMR (250 MHz, $\text{DMSO}-d_6$) δ 0.99 (3H, s, Me), 1.05 (3H, s, Me), 2.01–2.25 (4H, m, 2CH_2), 6.65 (1H, d, $J = 7.5$ Hz, H-Ar), 6.80–7.01 (3H, m, H-Ar), 7.24 (2H, br s, NH_2); ^{13}C NMR (75 MHz, $\text{DMSO}-d_6$) δ 27.8, 27.9, 33.7, 47.6, 51.3, 58.1, 110.4, 111.5, 117.1, 122.7, 123.6, 129.1, 135.3, 143.4, 160.1, 173.9, 177.9, 193.4, 194.6. Anal. Calcd for $\text{C}_{21}\text{H}_{16}\text{N}_2\text{O}_4\text{S}_2$: C, 59.42; H, 3.79; N, 6.59; S, 15.11. Found: C, 59.37; H, 3.83; N, 6.62; S, 15.15.

6'-Amino-2'-(4,6-dioxo-2-thioxotetrahydropyrimidin-5(2H)-ylidene)-7,8-dimethylspiro[indeno[1,2-b]quinoxaline-11,4'-[1,3]dithiine]-5'-carbonitrile (7b)

Yield: 81%, m.p. 273–274 °C; IR (KBr, cm^{-1}): 3129, 3019 (NH_2 , NH), 2175 (CN), 1731, 1669 (CO); ^1H NMR (250 MHz, $\text{DMSO}-d_6$) δ 6.72 (1H, d, $J = 8.25$ Hz, H-Ar), 6.79–6.98 (3H, m, H-Ar), 10.24 (1H, s, NH), 10.52 (1H, s, NH). ^{13}C NMR (75 MHz, $\text{DMSO}-d_6$) δ 53.2, 80.4, 114.6, 117.6, 122.4, 124.1, 127.6, 128.5, 136.4, 143.1, 143.6, 160.2, 162.7, 174.2, 177.8, 179.7, 180.4. Anal. Calcd for $\text{C}_{17}\text{H}-$

$\text{N}_4\text{O}_5\text{S}_2$: C, 49.51; H, 1.95; N, 13.59; S, 15.55. Found: C, 49.32; H, 1.93; N, 13.54; S, 15.57.

6'-Amino-2'-(4,6-dioxo-2-thioxotetrahydropyrimidin-5(2H)-ylidene)-7,8-dimethylspiro[indeno[1,2-b]quinoxaline-11,4'-[1,3]dithiine]-5'-carbonitrile (7c)

Yield: 77%, m.p. 279–281 °C; IR (KBr, cm^{-1}): 3241 and 3164 (NH , NH_2), 2202 (CN), 1725, 1681 (CO); ^1H NMR (250 MHz, $\text{DMSO}-d_6$) δ 6.80 (1H, d, $J = 8$ Hz, H-Ar), 6.84–7.05 (3H, m, H-Ar), 10.36 (1H, s, NH), 10.54 (1H, s, NH). ^{13}C NMR (75 MHz, $\text{DMSO}-d_6$) δ 50.4, 79.3, 111.6, 113.9, 119.2, 124.2, 127.6, 128.2, 132.4, 135.6, 141.9, 161.1, 162.5, 175.1, 178.6, 179.1, 180.2. Anal. Calcd for $\text{C}_{17}\text{H}-$
 $\text{N}_4\text{O}_4\text{S}_3$: C, 47.65; H, 1.88; N, 13.08; S, 22.45. Found: C, 47.61; H, 1.86; N, 13.10; S, 22.41.

6'-Amino-2'-(4,4-dimethyl-2,6-dioxocyclohexylidene)spiro[indeno[1,2-b]quinoxaline-11,4'-[1,3]dithiine]-5'-carbonitrile (10a)

Yield: 85%, m.p. 285–288 °C; IR (KBr, cm^{-1}): 3222 and 3218 (NH_2), 2162 (CN), 1672 (CO); ^1H NMR ($\text{DMSO}-d_6$) δ 0.99 (s, 3H, CH_3), 1.01 (s, 3H, CH_3), 1.99–2.05 (m, 2H, CH_2), 2.57–2.75 (m, 2H, CH_2), 7.30 (br s, 2H, NH_2), 7.49–7.59 (m, 3H, H-Ar), 7.78 (t, $J = 7.75$ Hz, 2H, H-Ar), 8.01–8.16 (m, 3H, H-Ar). ^{13}C NMR ($\text{DMSO}-d_6$) δ 27.4, 28.0, 32.4, 47.5, 50.5, 59.0, 112.3, 117.9, 121.9, 124.9, 129.3, 129.5, 129.8, 130.1, 132.8, 136.6, 141.4, 142.1, 152.3, 154.6, 159.3, 165.3, 159.9. Anal. Calcd for $\text{C}_{27}\text{H}-$
 $_{20}\text{N}_4\text{O}_2\text{S}_2$: C, 65.30; H, 4.06; N, 11.28; S, 12.91. Found: C, 65.34; H, 4.08; N, 11.31; S, 12.95.

6'-Amino-2'-(4,4-dimethyl-2,6-dioxocyclohexylidene)-7,8-dimethylspiro[indeno[1,2-b]quinoxaline-11,4'-[1,3]dithiine]-5'-carbonitrile (10b)

Yield: 81%, m.p. 264–266 °C; IR (KBr, cm^{-1}): 3313 and 3317 (NH_2), 2193 (CN), 1675 (CO); ^1H NMR ($\text{DMSO}-d_6$) δ 0.97 (s, 6H, 2CH_3), 1.97–1.98 (m, 2H, CH_2), 2.63 (m, 2H, CH_2), 3.32 (s, 3H, Me-Ar), 3.35 (s, 3H, Me-Ar), 7.31 (br s, 2H, NH_2), 7.46–7.51 (m, 3H, H-Ar), 7.76 (d, $J = 5.5$ Hz, 1H, H-Ar), 7.89 (d, $J = 5.5$ Hz, 1H, H-Ar), 8.0 (t, $J = 5.5$ Hz, 1H, H-Ar). ^{13}C NMR ($\text{DMSO}-d_6$) δ 20.1, 20.2, 27.5, 27.9, 32.4, 50.6, 112.3, 118.0, 121.7, 124.8, 128.4, 128.5, 129.1, 132.3, 136.9, 139.5, 140.0, 140.2, 140.8, 152.1, 153.6, 159.3, 165.2, 195.4. Anal. Calcd for $\text{C}_{29}\text{H}_{24}\text{N}_4\text{O}_2\text{S}_2$: C, 66.39; H, 4.61; N, 10.68; S, 12.22. Found: C, 66.43; H, 4.89; N, 10.71; S, 12.19.

6'-Amino-2'-(2,4,6-trioxotetrahydropyrimidin-5(2H)-ylidene)spiro[indeno[1,2-b]quinoxaline-11,4'-[1,3]dithiine]-5'-carbonitrile (10c)

Yield: 90%, m.p. 273–275 °C; IR (KBr, cm^{-1}): 3372 and 3375 (NH_2), 2189 (CN), 1660 (CO); ^1H NMR ($\text{DMSO}-d_6$) δ 7.06 (br s, 2H, NH_2), 7.44–7.50 (m, 3H, H-Ar), 7.72–7.74 (m, 2H, H-Ar), 7.99–8.01 (m, 3H, H-Ar), 9.68 (br s, 2H, NH). ^{13}C NMR ($\text{DMSO}-d_6$) δ 52.8, 113.8, 114.3, 121.5, 121.8, 124.9, 125.0, 128.5, 129.0, 129.4, 132.4, 132.6,

136.7, 141.7, 142.0, 149.8, 152.0, 152.9, 161.0, 164.0, 164.9, 166.7. Anal. Calcd for $C_{23}H_{12}N_6O_3S_2$: C, 57.02; H, 2.50; N, 17.34; S, 13.24. Found: C, 57.05; H, 2.53; N, 17.35; S, 13.26.

6'-Amino-2'-(4,6-dioxo-2-thioxotetrahydropyrimidin-5(2H)-ylidene)spiro[indeno[1,2-b]quinoxaline-11,4'-[1,3] dithiine]-5'-carbonitrile (10d)

Yield: 88%, m.p. 254–256 °C; IR (KBr, cm^{-1}): 3172 and 3170 (NH_2), 2194 (CN), 1662 (CO); 1H NMR (DMSO- d_6) δ 7.10 (br s, 2H, NH_2), 7.39–7.54 (m, 2H, H-Ar), 7.75–7.86 (m, 3H, H-Ar), 7.96–8.11 (m, 3H, H-Ar), 10.68 (s, 2H, NH). ^{13}C NMR (DMSO- d_6) δ 57.9, 118.9, 121.6, 125.1, 128.8, 129.2, 129.3, 129.5, 129.6, 129.8, 132.5, 132.7, 136.8, 141.5, 142.1, 153.4, 154.9, 161.0, 162.0, 166.9, 178.9. Anal. Calcd for $C_{23}H_{12}N_6O_2S_3$: C, 55.19; H, 2.42; N, 16.79; S, 19.22. Found: C, 55.23; H, 2.43; N, 16.82; S, 19.19.

2.2. In vitro Antimicrobial Activity

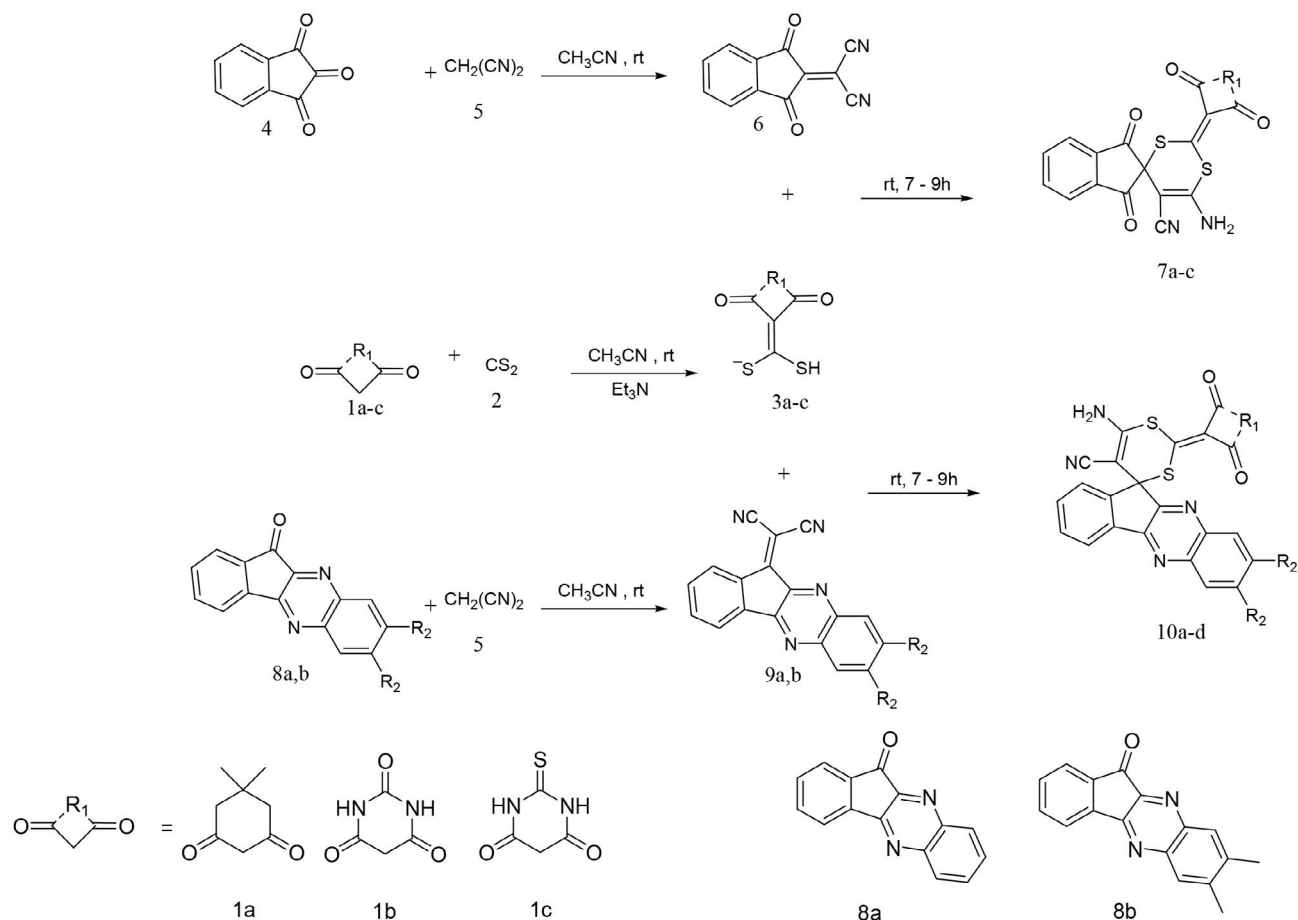
Antimicrobial properties including broth microdilution and time-kill susceptibility were tested based on the IZD, MIC, MBC and MFC values according to the CLSI (the clinical and laboratory standards institute) guidelines M07-A9, M26-A, M02-A11, M44-A and M27-A2.^{17,22–24}

Gram-negative pathogenic bacteria including *Pseudomonas aeruginosa* (PTCC 1310), *Escherichia coli* (PTCC 1399), and *Salmonella enterica* subsp. *enterica* (PTCC 1709); Gram-positive strains including *Staphylococcus aureus* (PTCC 1189) and *Staphylococcus epidermidis* (PTCC 1435); fungi including *Fusarium oxysporum* (PTCC 5115) were prepared from the Persian Type Culture Collection (PTCC), Tehran, Iran.

3. Results and Discussion

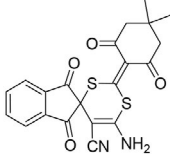
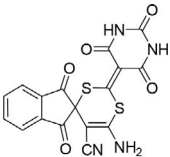
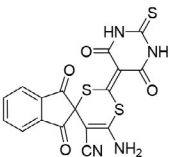
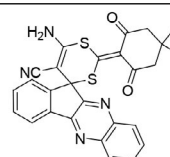
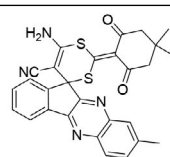
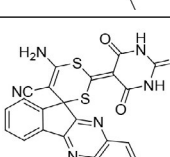
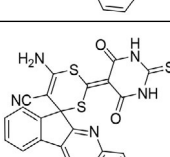
3.1. Chemistry

Seven 6'-amino-2'-(arylidene)spiro[indeno[1,2-b]quinoxaline[1,3]dithiine]-5'-carbonitrile derivatives (Table 1) were synthesized using compounds possessing active methylene groups (e.g. dimedone, barbituric acid and thiobarbituric acid), carbon disulfide, malononitrile, and multi-ring compounds containing a carbonyl group (1H-indene-1,2,3-trione, 11H-indeno[1,2-b]quinoxalin-11-one and 7,8-dimethyl-11H-indeno[1,2-b]quinoxalin-11-one) according to Scheme 1. The presented compounds were synthesized at ambient temperature within the range of yield of 70–90%.



Scheme 1. Multicomponent synthesis of 6'-amino-2'-(arylidene)spiro[indeno[1,2-b]quinoxaline[1,3]dithiine]-5'-carbonitrile derivatives

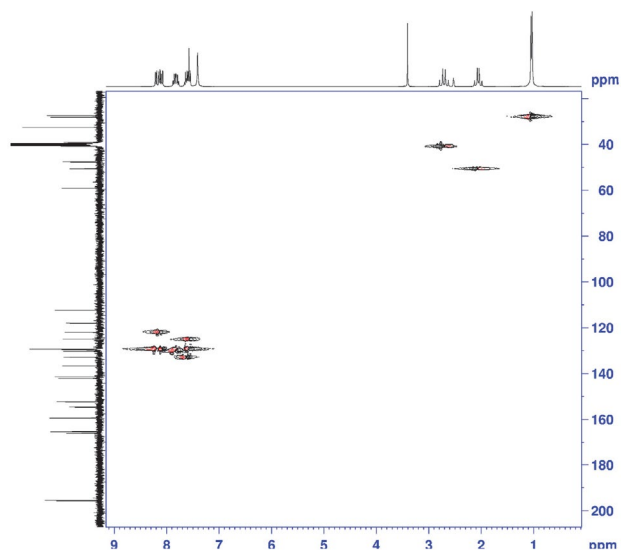
Table 1. Synthesis of 6'-amino-2'-(arylidene)spiro[indeno[1,2-*b*]quinoxaline[1,3]dithiine]-5'-carbonitrile derivatives.

Entry	Structure	Time (h)	Yield (%)	m.p. (°C)
7a		10.5	70	297–298
7b		11	81	273–274
7b		12	77	279–281
10a		9.5	85	285–288
10b		10	81	264–266
10c		10	90	273–275
10d		10.5	88	254–256

The structure of prepared compounds were confirmed by spectroscopic data such as ^1H NMR, ^{13}C NMR and FT-IR. For example, in the derivative **7a**, amine group appeared in regions 3352 , 3275 cm^{-1} , nitrile in 2164 cm^{-1} , and carbonyl in 1718 , 1673 cm^{-1} of the FT-IR spectrum. In the ^1H NMR spectrum, amine groups appeared at δ 7.24 ppm, methyl groups at δ 0.99, 1.05 ppm, and methylidene groups at δ 2.01, 2.25 ppm; and in the ^{13}C NMR spectrum, methyl groups appeared at δ 27.8, 27.9 ppm, spiro carbon at δ 58.1 ppm, and nitrile carbon at δ 117.1 ppm.

In addition, 2D NMR of **10a** is presented in Fig. 1. In this heteronuclear single quantum correlation (HSQC)

spectrum of **10a**, the relationship between the carbons and hydrogens of the dimedone group were visible in aliphatic region along relationship between carbons and hydrogens in the aromatic region.

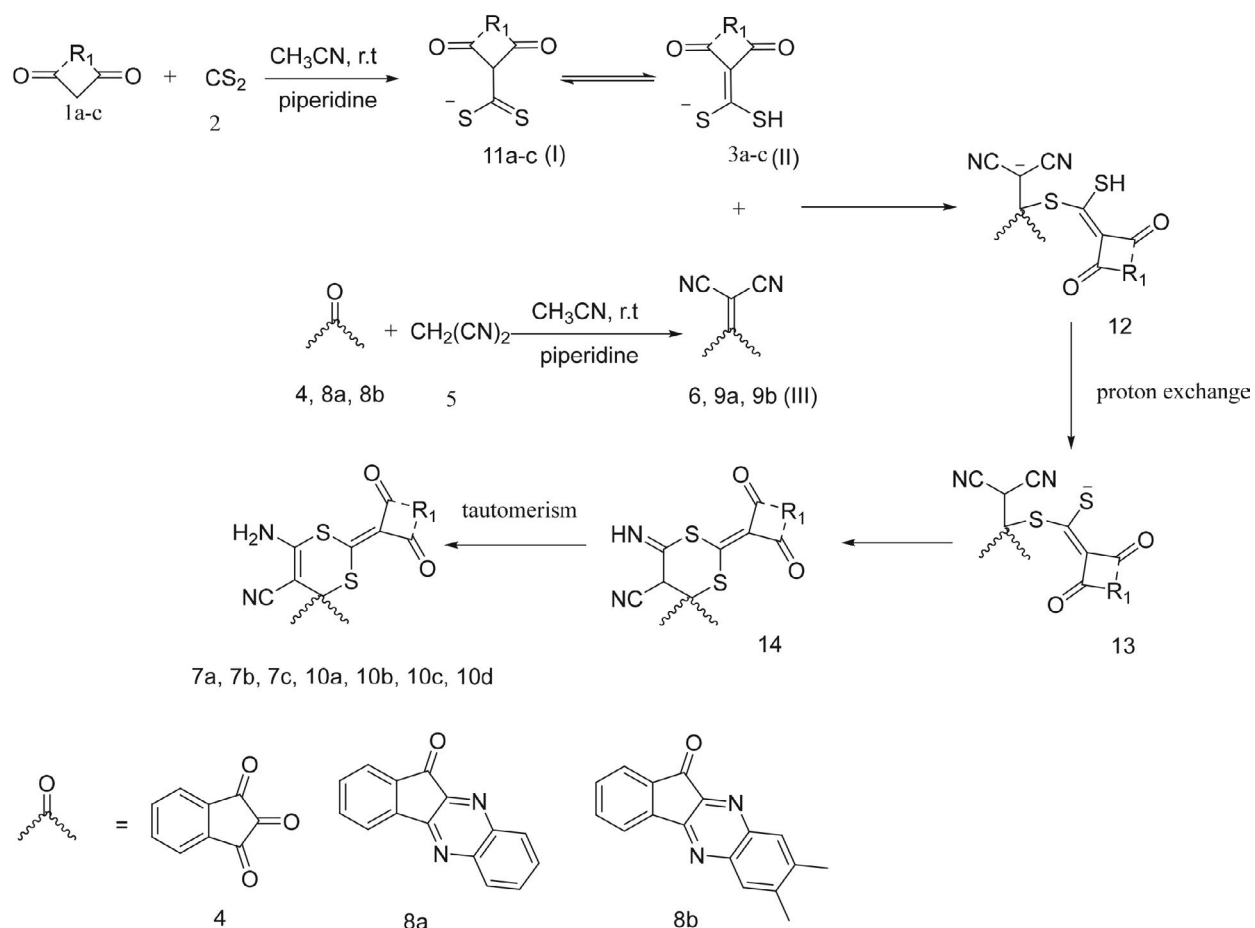
**Fig. 1.** HSQC spectrum of **10a**

The proposed mechanism for the formation of the prepared compounds is presented in Scheme 2.

Carbon disulfide and active methylene compounds in the presence of a base catalyst form species **I** (**11a–c**) that are in equilibrium with **II** (**3a–c**). From the reaction of multi-ring compounds containing a carbonyl group (**4**, **8a** and **8b**) with malononitrile, compounds **III** (**6**, **9a** and **9b**) are formed. Moreover, from the Michael addition reaction of **II** with **III**, intermediate **12** is formed, leading to the creation of **13** by an intramolecular proton exchange. Upon the nucleophilic sulfur attack on the cyanide group, intermediate **14** is formed, and finally with tautomerism, 6'-amino-2'-(arylidin-ylidene)spiro[aryl-[1,3]dithiine]-5'-carbonitrile derivatives are obtained.

3. 2. Antimicrobial Evaluation

Antibacterial activity of synthetic compounds in comparison with gentamicin and penicillin (as reference drugs) was determined against Gram-positive and Gram-negative bacteria. Antifungal activity of synthetic compounds in comparison with terbinafine and tolnaftate (as reference drugs) was investigated as well. According to the results obtained and presented in Table 2 as the IZD, MIC, MBC and MFC values, the following order of decreasing antimicrobial activity can be established: **10d**, **10c**, **10a**, **10b**, **7c**, **7b** and **7a**. Highest effect of the compound **10d** can be due to the presence of sulfur and pyrazine ring in its structure. In general, the presence of the pyrazine ring had the first priority in antimicrobial effects, followed by the presence of thiobarbituric acid which was



Scheme 2. Proposed mechanism for the synthesis of 6'-amino-2'-(arylidene)spiro[indeno[1,2-*b*]quinoxaline[1,3]dithiine]-5'-carbonitrile derivatives

Table 2. Antimicrobial activities of derivatives 7a–c and 10a–d against Gram-negative, Gram-positive pathogenic bacteria and *Fusarium oxysporum*.

Bacteria / fungi ^a		Products								Antibacterial and antifungal ^b	
		7a	7b	7c	10a	10b	10c	10d	A	B	
gram- negative	1310	IZD	17.63	18.37	18.21	20.73	20.91	22.69	22.86	26.42	–
		MIC	1024	512	256	128	256	64	64	0.12	–
		MBC	2048	1024	512	256	256	256	128	0.5	–
	1399	IZD	–	–	–	–	–	10.23	11.47	23.29	–
		MIC	–	–	–	–	–	1024	256	4	–
		MBC	–	–	–	–	–	2048	512	4	–
	1709	IZD	–	9.92	10.18	–	–	10.53	11.51	20.76	13.57
		MIC	–	1024	512	–	–	256	256	4	8
		MBC	–	2048	1024	–	–	512	512	8	16
gram- positive	1189	IZD	13.99	15.49	16.48	18.26	16.37	17.14	17.68	20.03	21.95
		MIC	1024	1024	512	512	512	256	128	4	0.5
		MBC	2048	1024	512	1024	1024	512	128	8	2
	1435	IZD	–	12.56	13.37	13.46	12.79	15.73	16.19	24.43	25.43
		MIC	–	1024	1024	512	1024	256	128	8	1
		MBC	–	2048	1024	512	2048	512	256	16	2
fungi	5115	IZD	–	11.09	12.35	–	–	12.59	14.97	23.31	–
		MIC	–	256	256	–	–	128	64	32	–
		MFC	–	512	256	–	–	256	128	64	–

^a IZD values reported as mm; MIC and MFC values reported as µg/mL ^b For bacteria: A: gentamicin, B: penicillin; for fungi: A: terbinafine, B: tolnaftate

also effective in this property, after that, the barbituric acid and finally, compounds containing dimedone unit having the least effect.

In antibacterial activity, penicillin has no effect on 1310 and 1399, but **10d** with MIC 64, 256 had the highest impact, respectively. In addition, derivative **10c** on 1399 and all other derivatives on 1310 were effective. In antifungal activity too tolnaftate has no effect on *Fusarium oxysporum*, but derivatives **10d**, **10c**, **7c** and **7b** were effective with MIC 64, 128, 256 and 256, respectively.

4. Conclusions

In summary, we succeeded in synthesizing seven novel derivatives of 6'-amino-2'-(arylidene)spiro[indeno[1,2-*b*]quinoxaline[1,3]dithiine]-5'-carbonitrile starting from compounds possessing active methylene group, carbon disulphide, malononitrile and multi-ring compounds containing a carbonyl group using simple process. Antimicrobial activity of these compounds was evaluated against five Gram-negative and Gram-positive pathogenic bacteria. Additionally, antifungal activity against *Fusarium oxysporum* was determined as well. The results of the antimicrobial study show good effects of derivatives investigated and the relationship between their structures and antimicrobial activity was observed. Some derivatives show better antimicrobial activity than commercial drugs such as penicillin and tolnaftate.

The important advantages of the present study were synthesis of novel heterocyclic compounds containing sulfur with antimicrobial activity, high efficiency, perform the reaction at ambient temperature, the availability, cheap and inexpensive materials

5. Acknowledgements

The authors are grateful to Islamic Azad University (Kerman Branch) for its financial assistance.

6. References

- N. C. Sauer, J. G. Leal, S. T. Stefanello, M. T. B. Leite, M. B. Souza, F. A. A. Soares, O. E. D. Rodrigues, L. Dornelles, *Tetrahedron Lett.* **2017**, *58*, 87–91. DOI:10.1016/j.tetlet.2016.11.106
- B. F. Abdel-Wahab, S. Shaaban, G. A. El-Hiti, *Mol. Divers.* **2018**, *22*, 517–542. DOI:10.1007/s11030-017-9810-3
- H. Mehrabi, Z. Esfandiarpour, T. Davodian, *J. Sulfur Chem.* **2018**, *39*, 164–172. DOI:10.1080/17415993.2017.1405959
- A. A. Abu-Hashem, *J. Heterocycl. Chem.* **2014**, *51*, 1020–1026. DOI:10.1002/jhet.2002
- G. Müller, T. Berkenbosch, J. C. J. Benningshof, D. Stumpfe, J. Bajorath, *Chem. Eur. J.* **2017**, *23*, 703–710. DOI:10.1002/chem.201604714
- P. Khloya, P. Kumar, A. Mittal, N. K. Aggarwal, P. K. Sharma, *Org. Med. Chem. Lett.* **2013**, *3*, 1–7. DOI:10.1186/2191-2858-3-9
- E. M. Flefel, W. A. El-Sayed, A. M. Mohamed, W. I. El-Sofany, H. M. Awad, *Molecules* **2017**, *22*, 1–13. DOI:10.3390/molecules22010170
- M. H. Diyanatizadeh, I. Yavari, *J. Sulfur Chem.* **2016**, *37*, 54–60. DOI:10.1080/17415993.2015.1089439
- R. G. Redkin, K. V. Hlebova, *News of Pharmacy.* **2018**, *2(94)*, 24–35. DOI:10.24959/nphj.18.2210
- A. A. Raj, R. Raghunathan, M. R. S. Kumari, N. Raman, *Biorg. Med. Chem.* **2013**, *11(3)*, 407–419. DOI:10.1016/S0968-0896(02)00439-X
- M. Muthukrishnan, M. Mujahid, P. Yogeewari, D. Sriram, *Tetrahedron Lett.* **2011**, *52*, 2387–2389. DOI:10.1016/j.tetlet.2011.02.099
- S. S. Fatahala, S. Mahgub, H. Taha, R. H. A. Hameed, *J. Enzyme Inhib. Med. Chem.* **2018**, *33*, 809817. DOI:10.1080/14756366.2018.1461854
- F. Rouatbi, M. Askri, F. Nana, G. Kirsch, D. Sriram, P. Yogeewari, *Tetrahedron Lett.* **2016**, *57*, 163–167. DOI:10.1016/j.tetlet.2015.11.056
- A. Kamel, M. Saleh, *Studies in Natural Products Chemistry.* **2000**, *23*, 455–485. DOI:10.1016/S1572-5995(00)80135-0
- J. K. DeMartino, I. Hwang, S. Connelly, L. A. Wilson, D. L. Boger, *J. Med. Chem.* **2008**, *51*, 5441–5448. DOI:10.1021/jm800555h
- M. Yamashita, T. Tahara, S. Hayakawa, H. Matsumoto, S. Wada, K. Tomioka, A. Iida, *Bioorg. Med. Chem.* **2018**, *26*, 1920–1928. DOI:10.1016/j.bmc.2018.02.042
- M. Moghaddam-manesh, D. Ghazanfari, E. Sheikhsosini, M. Akhgar, *ChemistrySelect* **2019**, *4*, 9247–9251. DOI:10.1002/slct.201900935
- Z. Li, H. Su, w. Yu, X. Li, H. Cheng, M. Liu, X. Pang, X. Zou, *Org. Biomol. Chem.* **2016**, *14*, 277–287. DOI:10.1039/C5OB02176F
- J. I. Perlmutter, L. T. Forbes, D. J. Krysan, K. Ebsworth-Mojica, J. M. Colquhoun, J. L. Wang, P. M. Dunman, D. P. Flaherty, *J. Med. Chem.* **2014**, *57*, 8540–8562. DOI:10.1021/jm5010682
- M. Yus, C. N. Najera, F. Foubelo, *Tetrahedron* **2003**, *59*, 6147–6212. DOI:10.1016/S0040-4020(03)00955-4
- X. Liu, J. Jia, Y. Jia, H. Gu, J. Luo, X. Chen, *Org. Lett.* **2018**, *20*, 1945–1948. DOI:10.1021/acs.orglett.8b00479
- H. Beyzaei, Z. Motraghi, R. Aryan, B. Ghasemi, M. M. Zaheedi, A. Samzadeh-Kermani, *Acta Chim. Slov.* **2017**, *64*, 911–918. DOI:10.17344/acsi.2017.3609
- H. Beyzaei, M. Moghaddam-Manesh, R. Aryan, B. Ghasemi, A. Samzadeh-Kermani, *Chem. Pap.* **2017**, *71*, 1685–1691. DOI:10.1007/s11696-017-0163-2
- S. Arikan, *Med. Mycol.* **2007**, *45*, 569–587. DOI:10.1080/13693780701436794

Povzetek

1,3-Ditiin z dvema **žveplovima** atomoma v svoji strukturi je **šestčlenska žveplova** heterociklična spojina. S pomočjo multikomponentne reakcije med spojinami z aktivno metilensko skupino, ogljikovim disulfidom, malononitrilom in večkomponentne spojinami, ki vsebujejo karbonylni skupino, smo v prisotnosti piperidina kot katalizatorja pri sobni temperaturi z veliko učinkovitostjo pripravili nove 6'-amino-2'-(ariliden)spiro[indeno[1,2-*b*]kinoksalin[1,3]ditiin]-5'-karbonitrilne derivate. S pomočjo metode merjenja premera cone inhibicije (IZD) in na osnovi tako določenih minimalne inhibitorne (MIC), minimalne baktericidne (MIB) oz. minimalne fungicidne koncentracije (MFC) smo raziskali protimikrobno (t.j. antibakterijsko in antiglivično) učinkovanje pripravljenih spojin.



Except when otherwise noted, articles in this journal are published under the terms and conditions of the Creative Commons Attribution 4.0 International License

Scientific paper

QbD Based Approach to Enhance the *In-Vivo* Bioavailability of Ethinyl Estradiol in Sprague-Dawley Rats

Trupti Ashok Powar¹ and Ashok Ananda Hajare^{1,*}¹Department of Pharmaceutics, Bharati Vidyapeeth College of Pharmacy, Kolhapur Maharashtra-416013, India.* Corresponding author: E-mail: ashok.hajare@bharativedyapeeth.edu
Mobile - 8788409138

Received: 07-24-2019

Abstract

Lyophilized nanosuspension of poorly soluble Ethinyl estradiol (EE) was fabricated to enhance its solubility and bioavailability using a quality-by-design (QbD) approach. With the help of the Ishikawa diagram, prospective risk factors were identified and screened by Plackett–Burman design to investigate the effects of formulation and process variables on dependent variables. The number of cycles (X4), the concentration of soya lecithin (X5) and the concentration of tween 80 (X7) were identified as significant factors ($P < 0.05$), which were further optimized using Central Composite Design. The mean particle size, zeta potential, drug content and entrapment efficiency of optimized lyophilized EE nanosuspension (EENPs) was 220 ± 0.37 nm, -19.3 ± 6.73 mV, $92.23 \pm 0.45\%$, $99.52 \pm 0.52\%$, respectively. Significantly, EENPs enhances C_{max} and AUC_{0-t} by 1.5, 1.7 folds and relative bioavailability by 2-fold with its distribution being at higher concentrations in the liver, spleen, and stomach. Thus, QbD based approach for the development of nanosuspension could be an absolute, optimistic approach to identify the critical process parameters and critical quality attributes.

Keywords: Quality by design; Lyophilized nanosuspension of ethinyl estradiol; Central Composite Design; Plackett–Burman Design; Bioavailability and stability.

1. Introduction

Ethinyl estradiol (EE), (17 α)-19-norpregna-1, 3, 5-(10) trien-20-yne-3, 17-diol is an estrogenic component, which is widely used in hormone replacement therapy and as an oral contraceptive.^{1–3} It is also known for its effectiveness to treat breast cancer, prostate cancer,^{4–9} as high-dose of EE is effective for first-line treatment and also for treatment after endocrine resistance to aromatase inhibitors and tamoxifen.¹⁰ EE is yellow to white crystalline powder, insoluble in water but soluble in ether, ethanol, acetone, chloroform, and dioxane. It is also found to be soluble in dilute alkaline solutions and vegetable oils. It is available in small doses alone or with a combination.¹¹ However, EE has a poor aqueous solubility, which is the biggest hurdle in the clinical application for cancer treatment. Lower solubility leads to complications in drug delivery like unpredictable absorption and thus deplorable oral bioavailability. Due to extensive first-pass hepatic metabolism after oral administration, EE has 40 % of systemic bioavailability due to its initial conjugation with the gut wall.¹¹ There-

fore, solubility enhancement of EE should be considered first for its development.

Various traditional approaches are used to enhance the solubility of poorly soluble drugs which includes micronization, use of cyclodextrin and co-solvents.¹¹ But unfortunately, the problem of bioavailability remains unsolved in many cases. In the case of micronization, sufficient surface area is not produced in order to enhance the dissolution velocity of poorly water-soluble drugs. Thus, industries are moving forward towards nanonization (formulation of nanosuspension) from micronization.¹²

In scientific research, nanomedicines have attained the topmost place and their application as medicines have gained vital place due to its larger surface area as compared to its particle size.^{13,14} In last few decades, new drugs fail to reach the market due to their vital issues related to solubility, dissolution, and bioavailability, maybe due to lack of dose proportionality, uncertain drug absorption, poor dissolution, and inter-intra subject variability. Thus it becomes a complicated task for most of the

scientist in clinical research to fulfill such lacuna.^{15,16,17} Fabrication of practically water-insoluble or very slightly soluble drugs to nanosuspension is in greater demand due to consequences of the previously mentioned problems.¹⁸ Nanosuspension (NS) is a submicron colloidal suspension, which consists of dispersed drug particles in water along with polymer as stabilizer or surfactant through top-down or bottom-up techniques.^{19,20} NS is an emerged potential solubility enhancement technique since last decade's,²¹ in which the poorly soluble drugs without any matrix materials are suspended in dispersion. NS are fabricated using drugs with a small amount of stabilizer below critical micelle concentration (CMC) to stabilize the formulation. Generally, most of the nanoparticle formulations are developed using a larger concentration of excipients but it is not the case with NS, as its most part is a drug. Beyond the use of lower concentration of stabilizers in the formulation of NS, it makes toxicity issues negligible and offers better physical and chemical stability with ease of scale-up as compared to amorphous form. NS enhances the solubility of poorly soluble drugs in aqueous as well as non-aqueous media. Increased solubility leads to an increase in the rate of flooding of drug and hence reaches maximum plasma level at a faster rate. The reduced particle size makes these drugs suitable to be administered by the intravenous route without blocking the blood capillaries. This technique applies to the molecules that have poor permeability, poor solubility, or both (BCS class II and IV drugs).^{22–25} For the productive development of NS, various methods have been reported to be employed that include top-down techniques such as media milling, high-pressure homogenization, and sonication, and bottom-up technique of nanoprecipitation. To enhance the physical stability of NS, numerous solidification techniques have been used which includes lyophilization, spray drying, rotary evaporation and many more based on the physical properties of drugs and characteristics of the final formulation.^{26–29} Out of all techniques listed above, lyophilization is predominately used for solidification of NS, as it offers several merits which include suitability for drying of thermolabile drugs, easy reconstitution of the formulation before use, enhanced storage stability, and production of high-value products without excessive damage.²¹ Thus the development of EE in lyophilized NS form can be a useful tool to tackle the aforesaid problems.

The usage of principles of quality by design (QbD) was proposed by the International Conference on Harmonization (ICHQ8) of technical requirements in the formulation of pharmaceutical products.³¹ The major challenges faced during the formulation of NS are manufacturing variability, due to lack of understanding of the effect of critical material attributes (CMAs) and critical processing parameters (CPPs), attainment of small size, and narrow polydispersity index (PDI). Due to a lack of understanding and manufacturing variabilities, there is an increase in the

cost of a nanoparticulate drug delivery system (NDDS). NDDS is well known for its toxicities due to the faster onset of action, permeability, increased solubility, and bioavailability. Hence, the aim of the present study was to prepare the ethinyl estradiol NS with QbD approach in order to obtain the effect of CMAs and CPPs on critical quality attributes (CQAs), improvement of safety and quality of the formulation, reduction in the manufacturing variability, and controlling the manufacturing cost.³⁰

For the planning of experiments, usage of statistical design of experiments (DOE) is an efficient tool. Plackett Burman (PB) of screening experiment and the Central Composite Design (CCD) of response surface methodology (RSM) are a well-set approach for optimization and development of pharmaceutical formulations, allowing acquisition of maximal data from a lesser number of well-designed experimental batches.¹⁵

Initially, all the potential independent variables were identified using Plackett-Burman design. Then a predictive model for critical response variables was constructed for the determination of optimized value using CCD to develop highly stable and soluble EENPs. Developed EENPs were dried using lyophilizer to stabilize the NS. The resultant EENPs were evaluated for its saturation solubility, zeta potential, particle size, polydispersity index, surface topographical studies, dissolution efficiency, *in-vivo* bioavailability, and stability studies.

2. Experimental

2.1. Materials

EE and Methotrexate were gifted by Cipla Ltd. Goa, (India). Tween 80 and mannitol was procured from Merck Specialities Pvt. Ltd. Mumbai, (India). Soya lecithin (SL) (Phospholipon® 90 H) was gifted by Lipoid GmbH (Germany). HPLC grade methanol was procured from Thermo Fisher Scientific Pvt. Ltd. Mumbai, (India). Double distilled water was prepared in the laboratory and all other reagents used in the study were of analytical grade.

2.2. Methods

2.2.1. Screening of the Stabilizer and Polymers for EENPs

For the preparation of EENPs, suitable stabilizers were screened from 20 stabilizers as follows,

2.2.1.1. Suspending Effect of Stabilizers

Stabilizers and polymers were selected on the basis of suspending concentration of stabilizers namely tween 80, cremophor EL-40, soya lecithin (SL), hydroxypropyl methylcellulose (HPMC), sodium lauryl sulphate (SLS), poloxamer 188 (F68), poloxamer 407, polyethylene glycol (PEG) 6000, sodium deoxycholate (SDS), span 80, polyvi-

nyl pyrrolidone (PVP) K 30, Carbomer 940, and/or their mixtures on EE. About 0.5 mg of EE was added to 0.2 % (w/v) of surfactant solutions, followed by shearing with a high-speed homogenizer (IKA RW 20 Digital, Hyland Scientific, USA) at 3,000 rpm for 1.5 h and centrifugation was done at 4000 rpm for 30 min. The supernatant obtained was diluted with possible solvents and the drug content was determined by ultraviolet-visible spectrophotometer (UV-Vis, Jasco V-530, Japan) at 280 nm. The stabilizers that showed an optimal suspending effect on EE, smaller particle size and lesser sedimentation rate were optimized as the compositions for fabricating NS.^{25,33,34}

2. 2. 1. 2. Docking Tool and Algorithm

Molecular docking was used to predict the virtual interactions between EE, and stabilizers systems. VLife MDS version 4.6 was used for molecular docking studies. The structures of all the stabilizers and drug were drawn in a 2D format which was followed by 3D conversion and was finally optimized for docking study. Biopredicta is a docking algorithm based on the genetic design, and it was used to predict and study modes of interactions between two compounds. The possible interactions were optimized based on receptor-ligand binding geometry within chemical structures. The molecular interaction between EE and stabilizers were analyzed to prove the stabilizers ability to enhance drug solubility and NS stability.

2. 2. 2. Formulation and Lyophilization of EENPs

EENPs were fabricated using high-pressure homogenizer (HPH) (Panda PLUS 2000, GEA Niro Soavi, Germany). To prevent blocking of the homogenizer valve, the coarse powder of EE (0.5 mg/mL) was first eventually dispersed in an aqueous stabilizer solution of tween 80 (0.15% v/v) and SL (30 mg) using digital ho-

mogenizer at 3000 rpm for 1 h to form primary nanosuspension. The primary nanosuspension was further processed through an HPH with three homogenization cycles at 250, 700, and 1200 bars, followed by maximum cycles at 1500 bars. By varying the number of homogenization cycles and keeping process temperature constant at 25 °C different particle size EENPs were obtained.³⁴ Liquid EENPs formulations were processed for lyophilization using laboratory freeze dryer (Freezone12, Labconco, MO, USA) using mannitol (6% w/w) as a cryoprotectant. The formulations were pre-frozen at -30 °C for 12 h. The primary drying was performed at -53 °C and 0.016 mBar for 24 h. The secondary drying was performed at 10 °C for 8 h and was followed by drying at 25 °C for 4 h with a gradual increase in temperature at 1 °C/min. Finally, the temperature of the cold trap was maintained at -53 °C until completion of the drying process. Resultant powder of EENPs was further used for subsequent evaluation studies.³⁴⁻³⁶

2. 2. 3. Design of Experiments

2. 2. 3. 1. Quality Target Product Profile (QTPP)

To determine the quality target product profile (QTPP), risk, regulatory, scientific and practical aspects are considered. The main goal of the study is the determination of target product quality profile (TPQP) and target product profile. Control space can also be helped to establish the region of operability. CMAs and CPPs were selected in this study to achieve the predefined target. The identified QTPP, CMAs, and CPPs are given in Table 1.³⁰

2. 2. 3. 2. Ishikawa Diagram for Risk Assessment

Ishikawa diagram was constructed to identify the formulation variables along with process variables of HPH technique and to evaluate their ability to influence the CQAs

Table 1. Study target with CMAs and CPPs

TPP	QTPP Target	TPQP	CMAs Materials	CPPs Parameters
Formulation type	Nanosuspension	<ul style="list-style-type: none"> • Particle size • PDI Method of assessment: Malvern Zetasizer	Soya lecithin (mg)	No. of cycles
Oral bioavailability	Enhancement of oral bioavailability	<ul style="list-style-type: none"> • Particle shape and morphology • Saturation solubility • In vitro drug release • In vivo studies Method of assessment: SEM Method of assessment: Orbital shaker Method of assessment: USP type II apparatus Method of assessment: an indirect method for the assessment of drug in rat plasma	Tween 80 (% v/v)	

* TPQP = target product quality profile; TPP = target product profile; CMA = critical material attribute; QTPP = quality target product profile; CPP = critical processing parameter; SEM = scanning electron microscopy; USP = United States Pharmacopeia; PCS = photon correlation spectroscopy; PDI = polydispersity index.

of EENPs. This approach helps to enhance the quality, safety and efficacy of the developed formulation. On the basis of prior studies, experimental trials, literature survey and the application of failure mode effect analysis method, the major quality attributes, namely drug content, entrapment efficiency and average particle size, were considered as CQAs of EENPs, which would likely affect the medicinal efficacy of nanoparticles drug delivery. The Ishikawa diagram illustrates the effect of CMAs and CPPs on TPQP. Ishikawa diagram of EENPs showed that formulations and process variables may affect the properties of nanoparticles and thus, such variables should be included in later studies.^{29,30}

2. 2. 3. 3. Plackett–Burman Design for Risk Analysis

Process variables that affect the CQAs of EENPs formulation were screened by a group of experiments using Plackett–Burman (PB) screening design for the formulation of EENPs using HPH. We can screen a large number of factors with a few runs by using the PB design.³⁷ Another important part of PB designs was the option of dummies, the component whose level does not change.³⁸ Only main effects can be estimated by the PB design, as they are the resolution of three designs. From the large set of experimental factors, PB designs are typically used to identify a few but significant factors.³⁷ Design-Expert (Version 11.0.5.0, Stat-Ease Inc., MN), involving eight independent variables, generated 12 experiment trials. The independent variables screened were, speed of high speed homogenizer (primary nanosuspension) (X1), time of homogenizer (primary nanosuspension) (X2), homogenization pressure (X3), number of cycles (X4), concentration of SL (X5), concentration of SLS (X6), concentration of tween 80 (X7) and concentration of EE (X8). The response variables selected were particle size (Y1), drug content (Y2) and en-

trapment efficiency (Y3) based on trials drawn during preliminary batches (Table 2).

According to the runs or trials arranged by design expert software, experiments were performed in randomized order. The values of the response variables were the mean of three measurements. To estimate the significance of interactions and main effects, analysis of variance (ANOVA) was used. Factors that show a negligible effect on the response variables at 95% of significance level were screened and the remaining factors that have an impact on response variables were further optimized by CCD.

2. 2. 3. 4. Central Composite Design for Optimization of EENPs

After identification of critical formulation and process variables using PB screening design, 5³ CCD response surface methods were used to inspect the optimum levels of the variables. This consisted of two groups of design points, which includes two-level factorial design points as -1 and $+1$, axial or star points as $-\alpha$ and $+\alpha$ along with center points as 0. Thus, the effect of three independent variables viz., the concentration of tween 80 (A), the concentration of SL (B) and the number of cycles (C) was studied at five different levels, with the coding of $-\alpha$, -1 , 0, $+1$, and $+\alpha$. Alpha value, 1.6817 fulfills the rotatability in the CC design. Dependent variables selected for the formulation of EENPs by CCD were particle size (Y1), drug content (Y2) and entrapment efficiency (Y3). Table 3 suggests the coded and actual values of variables. The Design Expert[®] software was used to generate a CCD matrix with 20 runs, which includes six replicated center points, one axial point and one replication of fractional point.

To obtain a CCD matrix, the 20 EENPs trial batches were formulated and evaluated for their responses with

Table 2. Plackett–Burman design with independent variables and their responses.

Factors	Levels	
	High	Low
X1 : Speed of Homogenizer (Preliminary Stage) (rpm)	8000	6000
X2 : Time of Homogenizer (Preliminary Stage) (min.)	45	30
X3 : Homogenization Pressure (Bars * 1000)	25	5
X4 : Number of Cycles	25	5
X5 : Concentration of soya lecithin (mg)	30	15
X6 : Concentration of sodium lauryl sulphate (mg)	30	15
X7 : Concentration of tween 80 (% v/v)	0.30	0.15
X8 : Concentration of Ethinyl estradiol (mg)	60	40

Table 3. 5³ Central composite designs with independent variables and their responses.

Factors	Levels				
	$-\alpha$	-1	0	$+1$	$+\alpha$
A : Concentration of Tween 80 (% v/v)	0.10	0.15	0.20	0.25	0.30
B : Concentration of Soya lecithin (mg)	10	15	20	25	30
C : Number of cycles	10	20	30	40	50

model fitting.³⁸ For optimization of the current study, various response surface methodology (RSM) were computed and polynomial models were generated, with interaction and quadratic terms for all the response variables using multiple linear regression analysis (MLRA) approach. Additionally, the output files generated by the Design-Expert software were used to construct 2-D contour plots.⁴⁰

2. 2. 3. 5. Process Analytical Technology (PAT) – Particle Size Analysis, Entrapment Efficiency and Drug Content

Particle size analysis of fabricated EENPs was measured using Zetasizer 300 HAS (Malvern Instruments, Malvern, UK), while entrapment efficiency and drug content was determined using UV-visible spectrophotometer (Jasco V-530, Japan) at 280 nm wavelength, which was used for PAT for particle size, entrapment efficiency and drug content analysis.^{30,35,41}

2. 2. 4. Characterization of Optimized Lyophilized EENPs

2. 2. 4. 1. Particle Size, Polydispersity Index and Particle Charge Analysis

Particle size, zeta potential and polydispersity index (PDI) of optimized EENPs was measured using Zetasizer 300 HAS (Malvern Instruments, Malvern, UK). Prior to size determination, lyophilized nanosuspension was redispersed in distilled water. Data obtained were mean average values of three independent samples that are prepared under same formulation conditions.^{35,41}

2. 2. 4. 2. Scanning Electron Microscopy (SEM)

The SEM was used to study the surface morphology of EENPs which examines sphericity, discreteness and surface properties of NPs. SEM studies were carried out using SEM (JEOL JSM-6360, Japan) at 20 kV accelerating voltage and high vacuum. Before analysis, lyophilized EENPs were first placed on two-sided carbon tape and then, sputtered with gold-palladium alloy up to 3–5 nm of thickness.^{32,34}

2. 2. 4. 3. Saturation Solubility Studies

Saturation solubility was performed by adding an excess quantity of pure drug (EE) and optimized lyophilized EENPs in 10 ml of distilled water. Then, samples were agitated in an orbital shaker (Remi instruments limited, Mumbai) for 48 h at 25 °C. The samples were then centrifuged to remove the solid content as a residue and the amount of drug present in the supernatant layer was analyzed spectrophotometrically using UV-visible spectrophotometer at 280 nm.³⁸

2. 2. 4. 4. Fourier Transform Infrared Spectroscopy (FTIR)

FTIR of a drug (EE), physical mixture (PM) and optimized lyophilized EENPs was analyzed using FTIR spec-

trophotometer (Agilent CARY 630 FTIR) to study the compatibility between drug and stabilizers. Each sample was placed on a diamond ATR crystal and was analyzed using Agilent resolutions pro software. Each spectrum of samples was collected from an average of 21 single scans at 4 cm⁻¹ resolution in the absorption area of 800–4000 cm⁻¹.³²

2. 2. 4. 5. In-Vitro Drug Release

Dissolution studies on EE powder and optimized EENPs were carried out using USP type-II apparatus. Weighed quantities of samples were transferred into dissolution apparatus (Electro lab TDT-08 L, India) containing 900 mL of simulated gastric fluid (SGF) as a medium with pH 1.2. The shaft speed was set to 50 rpm at medium temperature 37 ± 0.5 °C. Samples (5 mL each) were withdrawn at 10, 20, 30, 40, 50 and 60 min time interval and the fresh buffer was added to maintain the sink conditions. The samples were collected and filtered using Whatman filter paper (0.25 µm, Whatman Inc., USA) and analyzed using UV spectrophotometer at 280 nm.³⁴

2. 2. 4. 6. Pharmacokinetic and Biodistribution Study in Sprague- Dawley Rats

The pharmacokinetic (PK) and biodistribution studies were performed using Sprague- Dawley rats, with mean weight 200–220 g, purchased from Global Bioresearch Solutions Pvt. Ltd., Pune. The Institutional Animal Ethics Committee (IAEC) of Bharati Vidyapeeth College of Pharmacy, Kolhapur, Maharashtra, India (BVCPK / CPCSEA / IAEC / 01/14/2017-2020) has approved the study protocol. Prior to the experiment, rats were kept on fast overnight with free access to water *ad libitum*. These rats were randomly divided into three groups (n = 3). The group I was served with optimized EENPs (test group), group II was treated with EEAQD (standard group), whereas group III was given a normal saline solution (control group). On the day of the experiment, samples and dosing (0.5 mg/kg) of optimized EENPs and EEAQD were prepared freshly and administered orally to rats using oral feeding cannula. Under mild anesthesia, blood samples (0.5 mL) were collected at the time intervals of 0, 2, 3, 4, 6, 12, 24, 36 and 48 h from the retro-orbital vein and were transferred into a tube containing EDTA. Immediately blood samples were centrifuged at 3,000 rpm for 10 min at 4 °C to separate plasma and were stored at –20 °C until analysis.

The animals were sacrificed (n = 3) by cervical dislocation. The drug distribution in vital organs is measured after 72 h of dose administration. Tissue samples from liver, spleen, heart, brain, stomach, lungs, and kidney were homogenized quickly followed by centrifugation, and clear tissue samples obtained were stored at –20 °C before analysis. The blood plasma and tissue samples were mixed with 20 µL internal standard (methotrexate) solution (5 µg/mL). Deproteinization was done by adding 100 µL acetonitrile in 50 µL plasma sample, and 300 µL acetonitrile to

200 μL of clear tissue homogenates followed by cold centrifugation at 6,000 rpm for 15 min at 4 °C. Transparent supernatant obtained was filtered using 0.20 μm syringe filter and injected into the HPLC system for determining EE content in blood plasma and tissue samples.^{35,36}

HPLC Analysis

EE content was analyzed using reverse phase-HPLC system with UV detector and with a pump (Model Jasco PU-2080, intelligent HPLC pump). A reverse phase C18 column (150 mm \times 4.6 mm, pore size 5 μm , Phenomenex) was used to achieve chromatographic separation. The mobile phase optimized was 70:30 v/v mixture of water and acetonitrile. The separation was carried out under an isocratic condition with a constant flow rate of 1.0 mL/min, with 20 μL injection volume, at a column temperature of 25 °C, and wavelength of 280 nm. The calibration curve for EE in plasma was linear within the concentration range 15–100 $\mu\text{g}/\text{mL}$ with correlation coefficient $R^2 = 0.9932$, with methotrexate as an internal standard. The experimental data are expressed as mean \pm SD and the level of significance is taken as $P < 0.05$.⁴²

Pharmacokinetic Analysis

The PK analysis of plasma concentration-time profile was carried out by a non-compartmental model using Microsoft Excel (Microsoft office 2016). The PK parameters were directly obtained from plasma data, including AUC_{0-t} (area under the plasma concentration-time curves), C_{max} (maximum plasma concentration), T_{max} (the time to reach

maximum plasma concentration), $t_{1/2}$ (elimination half-life), MRT (mean residence time), K_{el} (elimination rate constant), VD (volume of distribution), Cl (clearance), and F_{rel} (relative bioavailability). F_{rel} of lyophilized EENPs after oral administration was computed according to the following formula with the EEAQD as a reference,

$$F_{\text{rel}} = \frac{\text{AUC}_{\text{test}}}{\text{AUC}_{\text{reference}}} \times 100 \quad (1)$$

All data were expressed as mean \pm SD and the level of significance was taken as $P < 0.05$.³²

2. 2. 4. 7. Stability Studies

The stability studies of optimized lyophilized EENPs and liquid EENPs were performed as per ICH Q1A (R2) guidelines. The formulations were wrapped in aluminum foils and stored at 4 °C (in refrigerator), room temperature (RT) in shadow and 40 ± 2 °C temperature and 75 ± 5 % relative humidity (in the stability chamber) for six months and evaluated at specific time interval for drug content and particle size to study the chemical and physical stability.⁴⁰

2. 2. 4. 8. Statistical Analysis

The data generated as an outcome of experimental work was analyzed using multilinear regression analysis, ANOVA and lack-of-fit tests. To test the statistical significance, wherever applicable, student's t-test was used and expressed as mean \pm SD ($n = 3$).

Table 4. Suspending concentrations and particle size of ethinyl estradiol in different stabilizer systems for formulation of nanosuspension.

Stabilizers*	Conc. of EE** ($\mu\text{g}/\text{mL}$)	Particle size** (nm)	Stabilizers*	Conc. of EE** ($\mu\text{g}/\text{mL}$)	Particle size** (nm)
Tween 80	189.75 \pm 0.05	311.33 \pm 2.56	SL/SDS	19 \pm 0.09	806.65 \pm 1.88
Sodium lauryl sulphate (SLS)	184.60 \pm 0.02	341.23 \pm 2.89	SLS/ Poloxamer 407	183.9 \pm 0.02	456.52 \pm 1.45
Poloxamer 188	155.40 \pm 0.01	389.56 \pm 2.45	Poloxamer 407/ Tween 80	119.66 \pm 0.08	532.02 \pm 1.65
Poloxamer 407	111.14 \pm 0.00	303.56 \pm 2.74	Tween 80/ Carbomer 940	155.4 \pm 0.03	625.78 \pm 2.01
HPMC-K5	15.28 \pm 0.09	896.12 \pm 2.65	Tween 80/ SLS	95.33 \pm 0.04	436.22 \pm 2.01
Soya lecithin (SL)	204.27 \pm 0.01	291.23 \pm 4.25	SDS/ Poloxamer 407	10 \pm 0.04	345.65 \pm 2.42
Cremorphor EL- 40	119.66 \pm 0.04	596.56 \pm 3.56	Tween 80 / HPMC-K5	48.52 \pm 0.06	765.45 \pm 4.56
Sodium deoxycholate (SDS)	15.65 \pm 0.05	356.45 \pm 3.89	Tween 80/ SDS	63 \pm 0.06	456.09 \pm 3.54
Carbomer 940	46.44 \pm 0.09	478.55 \pm 4.23	Tween 80/ SL	77.92 \pm 0.33	346.89 \pm 2.31
PVP K30	54.96 \pm 0.03	689.49 \pm 4.66	Poloxamer 407/ SL	119.56 \pm 0.10	374.88 \pm 2.90
PEG 6000	165.99 \pm 0.54	596.89 \pm 2.96	Tween 80/SDS/ Poloxamer 407	54.66 \pm 0.02	567.09 \pm 3.04
Span 80	175.89 \pm 0.08	665.96 \pm 2.36	Span 80/ Poloxamer 407/SDS	37.49 \pm 0.09	678.02 \pm 2.45
Poloxamer 188/ SLS	180.85 \pm 0.02	459.56 \pm 2.03	Tween 80/Poloxamer 188/ SLS	85.44 \pm 0.02	654.33 \pm 2.41
Tween 80/Poloxamer 188	165.36 \pm 0.17	590.65 \pm 2.14	Tween 80/ SLS/ SL	265.50 \pm 0.49	321.32 \pm 1.62
Poloxamer 407/ Tween 80	119.66 \pm 0.08	788.21 \pm 2.66			

* All the ratios of different stabilizers in one system is represented as 1:1:1 (w/w/w) or 1:1 (w/w), except that the ratio of Tween 80 and Carbomer was 0.5:1 (w/w). ** Results presented as means \pm SD ($n = 3$)

3. Results and Discussion

3. 1. Screening of the Stabilizer for EENPs

3. 1. 1. Suspending Effect of Stabilizers on Drugs

Stabilizers and polymers play a vital role in the fabrication of NS. The absence of appropriate stabilizer induces aggregation of nanosized drug particles due to high surface free energy of nanoparticles. A good stabilizer effectively reduces the surface energy of nanoparticles by dispersing them at an interface between water and particle to prevent particle aggregation in NS. They also prevent the Ostwald's ripening by producing ionic and/or steric barrier. For EENPs system, the appropriate stabilizer was screened by analyzing suspending effects, sedimentation rate and particle size of developed formulation and results obtained are reported in Table 4.

The combination of tween 80/SLS/SL presented superior suspending effect on EE ($265.5 \pm 0.49 \mu\text{g/mL}$) compared to soya lecithin (SL) ($204.27 \pm 0.09 \mu\text{g/mL}$), tween 80 ($189.75 \pm 0.05 \mu\text{g/mL}$) and sodium lauryl sulphate (SLS) ($184.60 \pm 0.02 \mu\text{g/mL}$). While the particle size of the formulation prepared by Tween 80/SLS/SL, SL, tween 80 and SLS was found to be 321.32 ± 1.62 , 291.23 ± 4.25 , 311.33 ± 2.56 , and $341.23 \pm 2.89 \text{ nm}$ respectively. Noteworthy, NS stabilized by SL, tween 80 and SLS did not produce stratification and sedimentation. The high surface free energy of nanosized particles makes NS a highly unstable thermodynamic system. Thus, based on particle size and suspending effect on EE, the combination of tween 80 and SL was selected as a good stabilizer system for fabrication of NS to obtain highest electric repulsion.^{12, 25}

3. 1. 2. Molecular Docking

In the present study, the interaction between EE and stabilizers shows the ability of stabilizers to solubilize drug to enhance its stability. The virtual interactions between EE and stabilizers are shown in Fig. 1. EE and stabilizers con-

tribute stronger interaction with each other by consuming lesser energy for binding, with strong hydrogen, hydrophobic and Vander Waal interactions. Thus, from these results, one can predict that stronger hydrogen bonding interaction between the EE and stabilizers like tween 80 and SL can virtually increase the solubility and stability of NS.

3. 2. Process Analytical Technology (PAT) – Particle Analysis, Entrapment Efficiency and Drug Content

EENPs was prepared using soya lecithin as a polymer and tween 80 as a stabilizer with the applications of the QbD approach. The particle size, entrapment efficiency and drug content of fabricated EENPs was found to be in the range of 221–309 nm, 89.45–98.76 %, and 80.91 to 92.46 %, respectively.³⁰

3. 3. Design of Experiments

3. 3. 1. Ishikawa Diagram

For identification of possible risks of process and formulation variables on the CQAs, viz., drug content, entrapment efficiency and particle size of EENPs, an Ishikawa diagram was established (Fig. 2). Eight possible risk factors were identified based on preliminary experiments and prior knowledge and were further evaluated using experimental designs.¹¹

3. 3. 2. Plackett–Burman Design

PB experimental design is conducted by incorporating eight factors, at two-levels, with twelve-run to screen the most significant formulation and process variables for the fabrication of EENPs. The formulations were piloted and the values of the responses obtained are reported in Table 5. For first response i.e. the particle size (Y1), the most significant and contributed factors were the concentration of tween 80 (X7), the concentration of SLS (X6), and the speed of

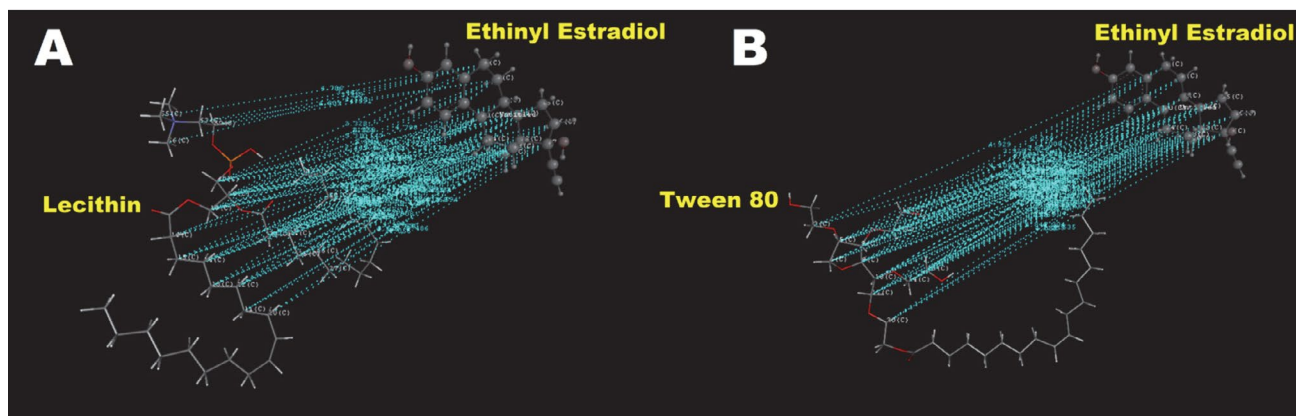


Figure 1. Docking study: a) interaction of ethinyl estradiol with soya lecithin, b) interaction of ethinyl estradiol with tween 80.

*Colour code Light blue: Vander Waal interaction, Green: Hydrogen bonding

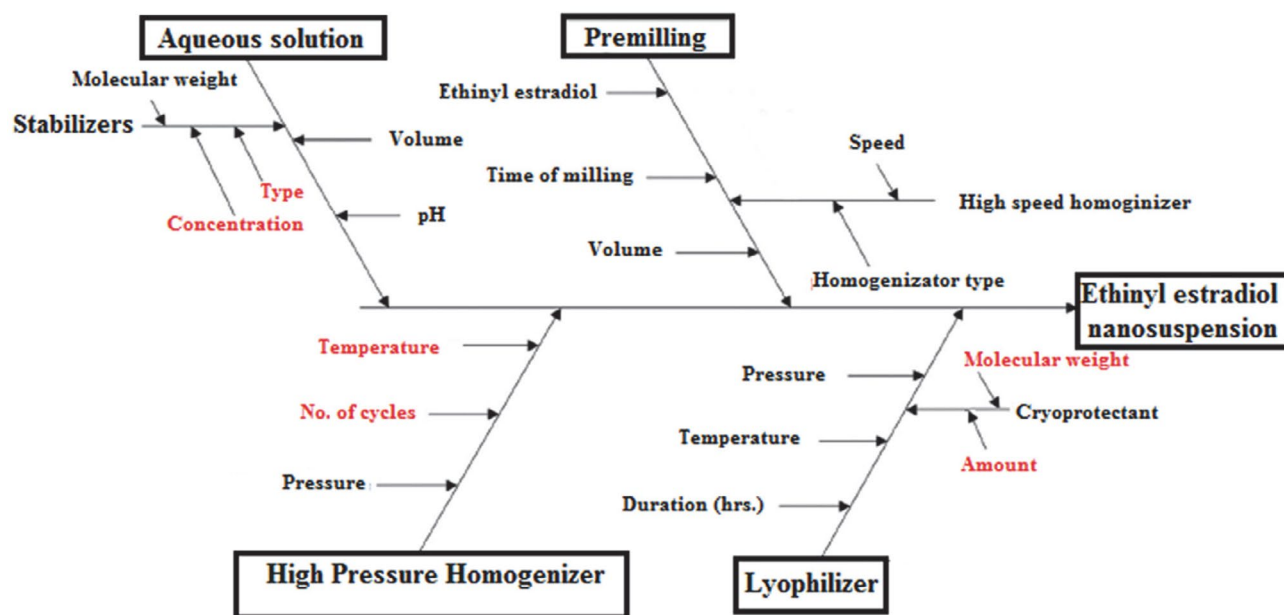


Figure 2. An Ishikawa diagram illustrating process and formulation variables that may influence the properties of NS.

Table 5. Plackett–Burman experimental design matrix with observed values of response variables.

Batch	X1 (rpm)	X2 (min.)	X3 (Bars * 1000)	X4	X5 (mg)	X6 (mg)	X7 (mg)	X8 (mg)	Y1* (nm)	Y2* (%)	Y3* (%)
01	1	-1	1	1	1	-1	-1	-1	221	90.67	90.57
02	-1	-1	-1	-1	-1	-1	-1	-1	324	92.78	92.46
03	-1	-1	1	-1	1	1	-1	1	234	89.99	88.16
04	-1	1	-1	1	1	-1	1	1	351	90.01	89.62
05	1	1	-1	1	1	1	-1	-1	230	95.89	85.61
06	-1	-1	-1	1	-1	1	1	-1	316	94.78	90.61
07	-1	1	1	1	-1	-1	-1	1	298	89.19	85.09
08	-1	1	1	-1	1	1	1	-1	313	90.67	80.91
09	1	1	1	-1	-1	-1	1	-1	309	89.45	85.88
10	1	-1	-1	-1	1	-1	1	1	278	90.11	89.95
11	1	1	-1	-1	-1	1	-1	1	298	98.76	91.7
12	1	-1	1	1	-1	1	1	1	322	90.56	89.09

Table 6. ANOVA analysis for response variables in Plackett – Burman design matrix.

		Y1: Particle size (nm)		Y2: Drug content (%)		Y3: Entrapment efficiency (%)	
		p value	% Contribution	p value	% Contribution	p value	% Contribution
β_0	Constant	0.2454	–	0.0767	–	0.3613	–
A	Speed of homogenizer* (rpm)	0.1747	13.74	0.1869	5.33	0.5725	2.41
B	Time of homogenizer*** (min.)	0.3769	4.69	0.3595	2.14	0.1014	33.02
C	Homogenization pressure** (Bar*1000)	0.3931	4.34	0.0190	39.35	0.1208	27.90
D	Number of cycles	0.8693	0.14	0.8974	0.036	0.8813	0.16
E	Concentration of Soya lecithin* (mg)	0.0969	24.97	0.1806	5.54	0.3659	6.82
F	Concentration of SLS*** (mg)	0.5472	2.00	0.0296	28.16	0.4847	3.82
G	Concentration of Tween 80* (mg)	0.0664	34.97	0.0888	11.33	0.4825	3.86
H	Concentration of Ethinyl estradiol (mg)	0.5472	2.00	0.3183	2.62	0.4804	3.90

*Included in the model of particle size; ** Included in the model of drug content; *** Included in the model of entrapment efficiency.

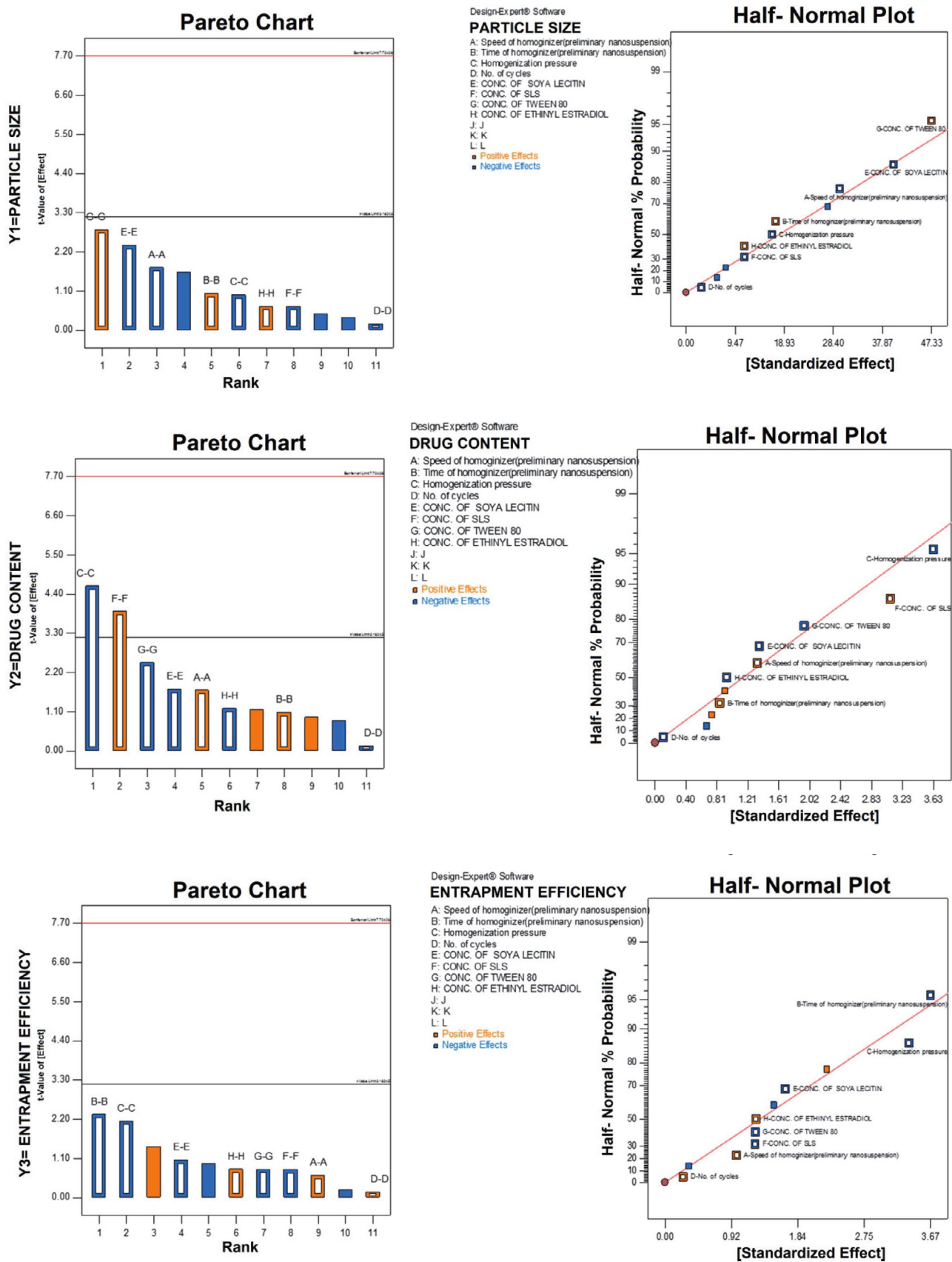


Figure 3. The half-normal plot and Pareto charts showing the significant process and formulation variables on particle size, drug content and entrapment efficiency.

high-speed homogenizer (X1), respectively (Table 6) (Fig. 3a).

The value of R^2 found was 0.8686, which indicates significant model fitting of the tested model. From ANOVA the p-value for main effects obtained was 0.2454, which was not statistically significant; hence, by using CCD most significant factors were further evaluated. Particle size plays an important role for EENPs as it influences the physical stability, cellular uptake, drug release, bioavailability and biodistribution of the drugs.

Following polynomial equation can describe Y1,

$$\begin{aligned} \text{Particle size} = & +291.17 - 14.83 * A + 8.67 * \\ & B - 8.33 * C - 1.50 * D - 20.00 * E - \\ & 5.67 * F + 23.67 * G + 5.67 * H \end{aligned} \quad (2)$$

Polynomial Eq. 2 represents that, upon an increase in the concentration of tween 80 and EE, there is a decrease in average particle size (Y1). It also decreases with decreasing speed of homogenizer in primary NS stage with an increasing number of cycles with higher homogenizer pressure. Thus, from all the process variables, the percentage contribution for average particle size is the concentration of tween 80 (34.97%), the concentration of SL (24.97%) and speed of homogenizer (13.74%), respectively. The smallest particle of 221 nm could be achieved by using 0.15% v/v of Tween 80, 30 mg of SL with homogenization speed of 8000 rpm.

For the Drug content (Y2), the most contributed and significant factors were the concentration of tween 80

(X7), the concentration of SLS (X6), and homogenization pressure (X3), respectively (Table 6) (Fig. 3b). The R^2 value (0.9450) indicate a significant fit to the model being tested. From ANOVA the p-value for main effects obtained was 0.0767, which was not statistically significant; hence, by using CCD most significant factors were further evaluated. Drug content plays an important role in therapeutic activity at a given dose of EE in NS.

Following polynomial equation can describe Y2,

$$\begin{aligned} \text{Drug content} = & +91.91 + 0.67 * A + 0.42 \\ & * B - 1.82 * C - 0.06 * D - 0.69 * E + 1.54 \\ & * F - 0.98 * G - 0.47 * H \end{aligned} \quad (3)$$

Polynomial Eq. 3 represents that, drug content (Y2) was decreased with increasing concentration of SL, speed of homogenizer in primary NS stage with a decreased time of homogenizer. It also decreases with increasing concentration of tween 80, EE and SLS, followed by increasing pressure and number of cycles of homogenizer, respectively. From all the process variables, the percentage contribution of the concentration of tween 80 (11.33%), the concentration of SL (28.16%) and homogenizer pressure (39.35%) influences drug content, respectively. Thus, to achieve 98.76% of drug content in EENPs, experiments can be performed by using 0.15 % (v/v) of Tween 80, 15 mg of SL with homogenization pressure of 25000 Bars.

For the Entrapment efficiency (Y3), the most contributed and significant factors were the concentration of

Table 7. Central composite design matrix with observed and predicted values of responses.

Batch	Independent variables			Dependent variables					
	A (mg)	B (mg)	C	Y1* (nm)	Y2* (%)	Y3* (%)	Y1 (nm)	Y2 (%)	Y3 (%)
01	0	0	-1.68179	225	91.256	99.712	233.17	91.27	98.73
02	0	0	0	215	87.745	99.656	219.93	87.56	99.25
03	0	0	0	204	87.235	99.665	219.93	87.56	99.25
04	-1	1	1	220	93.685	99.99	235.38	94.03	99.61
05	0	0	0	225	87.845	99.662	219.93	87.56	99.25
06	1	-1	1	192	86.231	98.5862	217.90	87.43	98.66
07	0	0	1.68179	228	89.7962	99.764	222.35	89.55	99.77
08	1.68179	0	0	302	92.569	99.436	280.83	92.45	99.11
09	0	-1.68179	0	229	89.321	99.735	240.18	88.19	98.80
10	-1.68179	0	0	225	90.89	99.567	248.69	90.77	99.39
11	-1	-1	-1	235	90.6055	98.263	236.23	91.69	98.69
12	1	-1	-1	278	95.4605	96.675	260.84	95.29	98.28
13	-1	1	-1	233	89.236	97.6064	205.32	88.21	98.75
14	0	0	0	226	87.015	99.669	219.93	87.56	99.25
15	1	1	-1	265	88.4011	99.947	293.43	88.64	100.04
16	0	0	-1.68179	225	91.256	99.712	219.93	87.56	99.25
17	0	0	0	215	87.745	99.656	219.93	87.56	99.25
18	0	0	0	204	87.235	99.665	240.34	89.46	99.70
19	-1	1	1	220	93.685	99.99	248.99	92.42	99.68
20	0	0	0	225	87.845	99.662	267.79	85.87	100.29

* Y1 = Particle size; * Y2 = Drug content; * Y3 = Entrapment efficiency.

Table 8. Results of Quadratic and 2FI model for regression analysis of response variables Y1, Y2 and Y3.

Quadratic model	R ²	Adjusted R ²	Predicted R ²	SD	%CV
Y1	0.6546	0.3437	-1.7414	23.28	9.80
Y2	0.9429	0.8915	0.5597	0.8701	0.9719
2FI	R ²	Adjusted R ²	Predicted R ²	SD	%CV
Y3	0.3462	0.0444	-2.8153	0.8396	0.8460

SL (X5), time of homogenizer (X2), and homogenization pressure (X3), respectively (Table 6) (Fig. 3c). The R² value (0.8189) indicating a significant fit to the model being tested. From ANOVA the p-value for main effects was found to be 0.3613, which was not statistically significant; hence, by using CCD most significant factors were further evaluated. Entrapment efficiency plays an important role for entrapment of EE in stabilizer vesicles to stabilize NPs.

Following polynomial equation can describe Y3,

$$\begin{aligned} \text{Entrapment efficiency} = & +88.30 + 0.50 \\ * A - 1.84 * B - 1.69 * C + 0.13 * D - 0.84 & \quad (4) \\ * E - 0.62 * F - 0.63 * G + 0.63 * H & \end{aligned}$$

Polynomial Eq. 4 represents that, entrapment efficiency (Y3) was decreased with increasing concentration of EE, with increased time of homogenizer and number of cycles of homogenization. It also decreases with increasing concentration of tween 80, SL and SLS, followed by increasing pressure of homogenizer and speed of homogenizer, respectively. From all the process variables, the percentage contribution of the concentration of SL (6.82%), time of homogenizer (33.02%) and homogenizer pressure (27.90%) influences entrapment efficiency, respectively. Thus, to achieve 92.46% of entrapment efficiency in EENPs, experiments can be performed by using 30 min. of homogenization; 15 mg of SL with homogenization pressure of 5000 Bars.

3. 3. 3. Optimization of EENPs by Central Composite Design

3. 3. 3. 1. Model Fitting

By design of expert (DOE), 20 runs were proposed and the input of predicted and observed values for Y1, Y2, and Y3 responses ranges from 192–302 nm, 86.23 to 95.46% and 99.16 to 99.99% respectively (Table 7). The obtained responses were simultaneously fitted to cubic, 2FI, quadratic and linear models. As the R² values were found to be greater than 0.9, and both the observed and predicted values were less comparable with standard deviations (SD) (< 1.0%) and values of precision, thus the best-fitted model for Y1 and Y2 was quadratic and 2FI for Y3. For each response, inputs for linear model parameters are reported in Table 8. As the ratios of maximum to minimum responses values were less than 10, transformation is not necessary (Y1 = 2.51; Y2 = 8.17; Y3 = 1.17).³⁸

3. 3. 3. 2. Analysis of Response Surface Plots

To study the interaction effects of factors on their responses and relationships, response surface plots were used and were constructed for three responses viz., Y1, Y2, and Y3 (Fig. 4 a, b, c).

Effect on particle size (Y1)

The proposed polynomial equation for particle size is as follows,

$$Y1 = +219.93 + 9.56 (A) + 0.0466 (B) - 3.22 (C) \quad (5)$$

where, Y1 is particle size, (A) concentration of tween 80, (B) concentration of SL, (C) number of cycles for EENPs formulation by HPH.

The models were found to be significant as the F value was <0.002, while model terms were significant as the Prob>F, the p-value is <0.0500, hence these model are used to develop the design space. The 3D response surface plots were used to study the impact of independent variables on the particle size (Y1). The predicted values of Y1 response ranges from 205.32 to 293.42 nm. The positive value of coefficient represents increasing Y1. Fig. 4 a, predicts that as the concentration of tween 80 (A) increases from 0.10 to 0.30 (% v/v), the particle starts to aggregate. This may be due to saturation of surfactant in NS, as formed particles are adsorbed by an excess concentration of surfactant. When the concentration of SL (B) increases from 10 to 30 mg respectively, it fails to prohibit reaggregation of dispersed particles leading to the presence of larger bodies in NS thus increased particle size. Hence increased concentration of surfactant and polymer increases the particle size. The number of cycles (C) for HPH shows a direct relationship with particle size: with an increase in the number of cycles of HPH implies a decrease in the particle size. The coefficient with negative value represents decreasing particle size. Increase in the number of cycles leads to particle size reduction by increasing the viscosity of the system, which inhibits the Ostwald ripening. Hence, an increase in no. of cycles leads to an increase in the dynamic pressure with a decrease in the static pressure at room temperature (RT), below the boiling point of water. Hence, water in the system boils at RT by forming the gas bubbles that implode, when the pressure of the system is reached to normal after leaving of

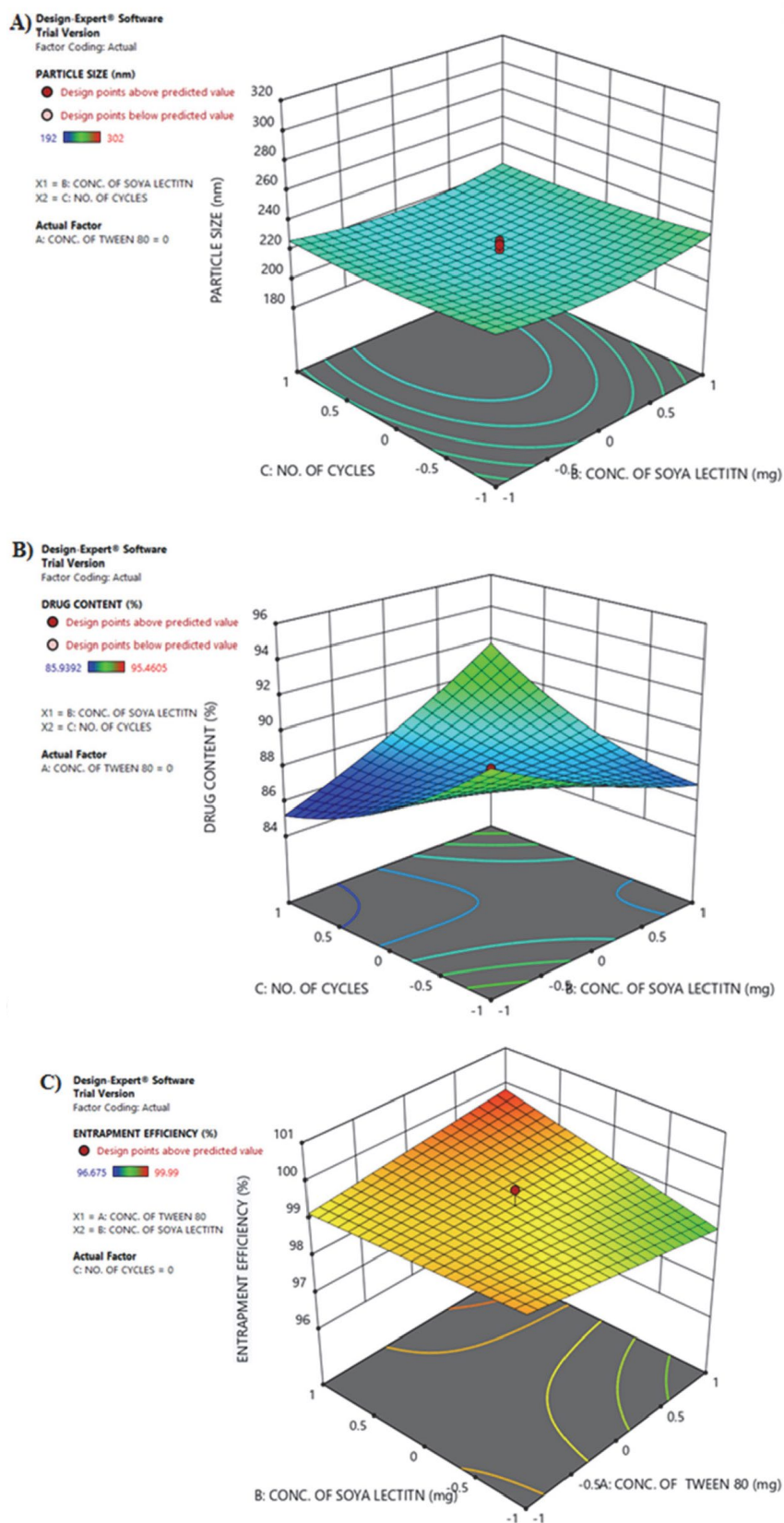


Figure 4. 3D surface response plot showing: a) The effect of factor C (number of cycles) and factor B (concentration of soya lecithin) on response Y1 (particle size).

B) The effect of factor C (number of cycles) and factor B (concentration of soya lecithin) on response Y2 (drug content).

C) The effect of factor B (concentration of soya lecithin) and factor A (concentration of tween 80) on response Y2 (drug content).

NS from the gap. This is the reason for particle size reduction.

Effect on drug content (Y2)

The proposed polynomial equation for drug content is as follows,

$$Y2 = +87.56 + 0.50(A) + 0.38(B) - 0.51(C) \quad (6)$$

The predicted Y2 response values range from 85.87 to 95.29%. The models were found to be significant as the F value were <0.0001, while model terms were significant as the Prob>F, the p-value is <0.0500, hence these model were used to develop the design space. Here the significant model term is 'A' as an increase in the amount of 'A' leads to an increase in drug content. While the concentration of SL 'B' shows the negligible effect on drug content (Fig. 4 b). The drug content also decreases with an increasing number of cycles 'C'. However, drug content had the most important effect on drug dissolution, which directly affects the absorption of the drug and thus bio-availability.

Effect on entrapment efficiency (Y3)

The proposed polynomial equation for entrapment efficiency is as follows,

$$Y3 = +99.25 - 0.08(A) + 0.27(B) + 0.31(C) \quad (7)$$

The predicted values of Y3 are shown in Table 6 and ranges from 96.68– 99.99%. The model was found to be significant as F-value was <0.0001. Here, in this model 'B' & 'C' terms are significant. The 3D surface response plots are shown in Fig. 4c predicts that the % entrapment efficiency increases with an increase in values of 'B' & 'C'. This may be due to significant interaction of SL with EE in NS. Optimum entrapment efficiencies allow control release of EE from NS. Entrapment efficiency increases the drug loading capacity of NS with increased dosing intervals, less toxicity due to the excipients and residual solvents, and more appropriate dosing. Thus, the factors i.e. concentration of SL and number of homogenization cycles that affects entrapment efficiency was optimized by CCD.

3. 3. 4. Optimization Model Validation

To achieve the predicted (software suggestions) composition, targeted criteria were fed into the software. The software-suggested values were selected as a region of interest based on desirability values and were practically used for their verification. The design expert software was used to statistically validate the obtained polynomials by ANOVA.

For the construction of design space graphical method was selected for this study. The desirability values based on selected software suggestion were found to be 0.922, which provides an assurance of 92.20% possibilities to achieve the target with optimized CMAs and CPPs. This indicates higher the value of desirability, more is the possibility to achieve the target.³⁰

The final formulation was prepared with optimized CMAs and CPPs, and its CQAs were analyzed. The actual results and predicted results of CQAs were further used to calculate the residual values to ensure the achievement of design space. The calculation of residual values is also a verification/validation of the model and CQAs. The residual values were calculated as percent residual using the following formula:

$$\text{Percent residual} = \frac{\text{Software suggested results} - \text{Actual obtained results}}{\text{Software suggested results}} \times 100 \quad (8)$$

The optimized CMAs and CPPs with residual values of CQAs are summarized in Table 9.

The residual values were found to be very low (between the range of –1.15 and 0.240) which shows that the obtained results have a very strong correlation with software predicted results. Lower residual value is also an indicator of less variation and more reproducibility of CQAs with the optimized CMAs and CPPs.³⁰ The effect of two independent variables i.e. concentration of SL and no. of cycles of HPH are found to be more predominant from DOE results. The concentration of tween 80 favors the entrapment efficiency of EENPs, thus to enhance the adaptability of the method, the concentration of tween 80 was fixed to 0.15 % (v/v) and by using remaining two factors the design space was developed. The overlay plot obtained from DOE software (Fig. 5) shows the design space to select an optimum concentration of SL and no. of cycles to

Table 9. Residual values of CQAs of optimized formulations.

Response parameters	CMAs/ CPPs			CQAs		
	Conc. of Soya lecithin (mg)	No. of cycles	Conc. of Tween 80 (% v/v)	Particle size (nm)	Drug content (%)	Entrapment efficiency (%)
Software-predicted results	20.68	31	0.15	246.036	89.411	99.36
Actual obtained results	21	31	0.15	220 ± 0.37	92.23 ± 0.45	99.52 ± 0.52
Residual values (%)	–	–	–	–1.15	0.223	0.240

* CMAs= critical material attributes; CPPs =critical processing parameters; CQAs= critical quality attributes.

Table 10. Results of optimized batches obtained from an overlay plot of design expert software.

Optimized batch	Independent variables			Observed value			Dependent variables			Predicted value		
	A	B	C	Y1	Y2	Y3	Y1	Y2	Y3	Y1	Y2	Y3
CCD 21	19.10	28	0.15	222 ± 0.25	89.52 ± 0.55	99.01 ± 0.45	223.553	88.223	98.66	223.553	88.223	98.66
CCD 22	19.08	29	0.15	253 ± 0.31	91.41 ± 0.54	98.68 ± 0.48	255.41	93.785	98.41	255.41	93.785	98.41
CCD 23	20.68	31	0.15	220 ± 0.37	92.23 ± 0.45	99.52 ± 0.52	246.036	89.411	99.36	246.036	89.411	99.36

*A = Concentration of Soya lecithin (mg); B = Number of Cycles; C = Concentration of Tween 80 % (v/v); Y1 = Particle size (nm); Y2 = Drug Content (%); Y3 = Entrapment efficiency (%).

prepare highly stable NS with lesser particle size. The three points that are located in the design space predicts good responses. By changing the composition of factors 'A' and 'B' as per design space and keeping the concentration of tween 80 fix, three formulations, CCD21, CCD22, CCD23 were developed and then characterized for three dependent variables. The plots constructed between predicted and observed responses showed good correlation between the observed (actual) values and theoretical (predicted) values for Y1 (particle size), Y2 (drug content) and Y3 (entrapment efficiency) responses (Table 10 and Figs. 6 a, b, c).

Negligible changes were seen in drug content, entrapment efficiency and particle size of CCD21, CCD22, and CCD23 as compared to above formulations. The CCD23 was selected as optimized EENPs formulation based on the data obtained from the three responses. The optimized formulation showed the particle size of 220 ± 0.37 nm which indicates that cellular uptake of the prepared formulation may be good, as cellular uptake depends upon particle size. Entrapment efficiency is $99.52 \pm 0.52\%$ that confirms increases drug loading capacity of NS with increased dosing intervals, less toxicity due to the excipients and residual solvents. The drug content values

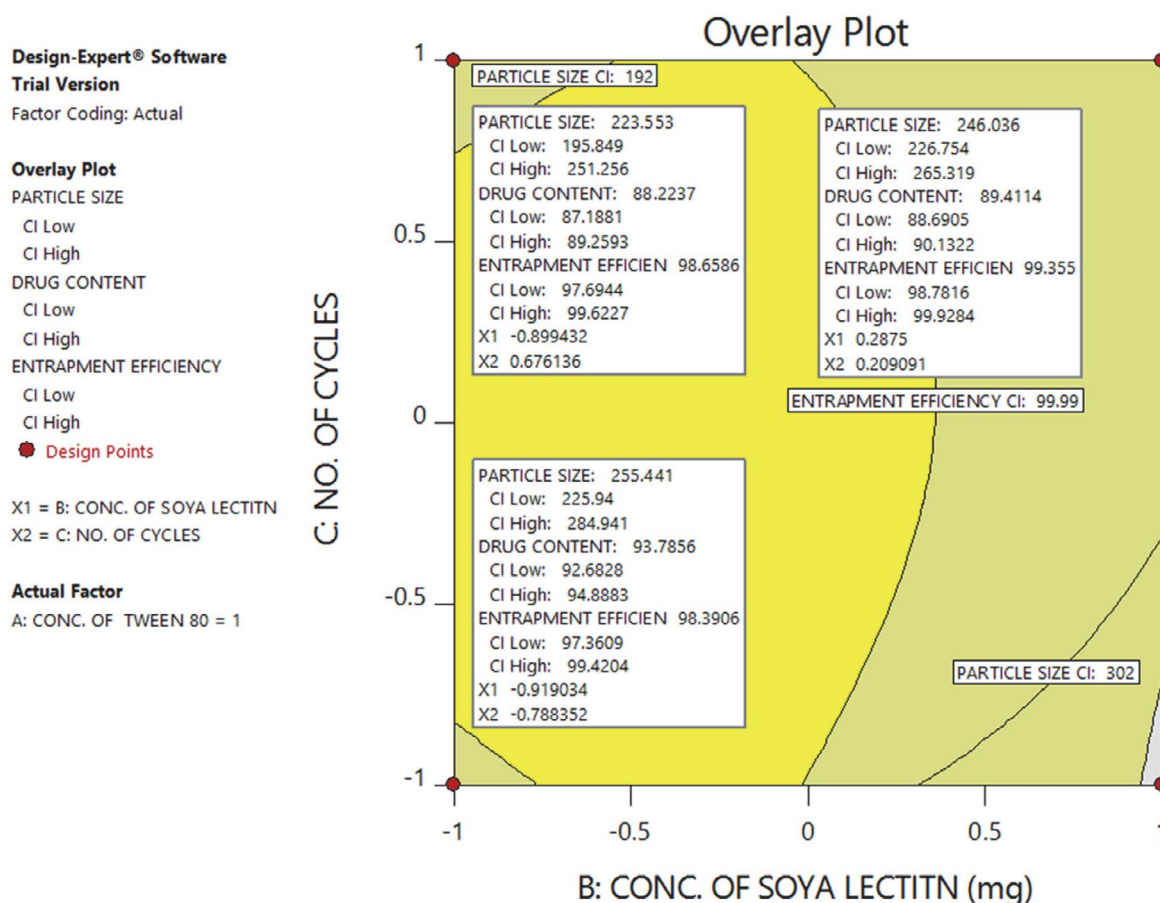


Figure 5. Overlay plot proposed by the design expert software showing design space in yellow colour along with the compositions of selected optimized formulations with the responses.

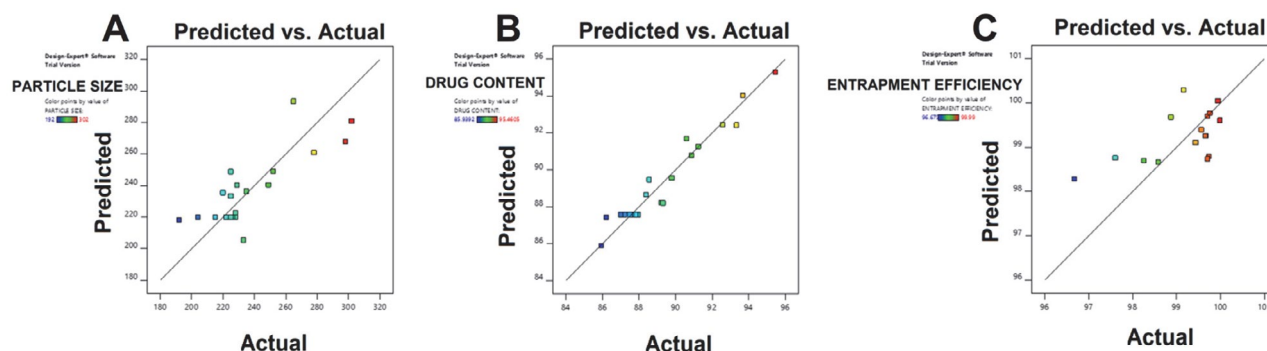


Figure 6. Liner correlation plots between actual and predicted values of responses: a) particle size (nm), B) drug content (%), C) entrapment efficiency (%).

were found to be $92.23 \pm 0.45\%$ which has the most important effect on drug dissolution, which directly affects the absorption of the drug and thus bioavailability. Further, they were dried using lyophilizer with 6% of mannitol as a cryoprotectant to stabilize the system.

3. 4. Particle Size Analysis, Polydispersity Index and Particle Charge (Zeta-potential)

EE is a coarse micronized powder with fine white texture, poor flow properties, and aqueous solubility. The coarse EE particles bear average particle size of 5–7 μm , with 8.38 PDI indicating broad size distribution. The freshly prepared NS was lyophilized to enhance its stability. The lyophilized EENPs powder was smooth in appearance with the particle size 220 ± 0.37 nm (Fig. 7 a), which was easily re-dispersed upon gentle shaking. It has been reported that narrow and uniform particle size distribution favors dissolution enhancement, boosts intestinal absorption and improves oral bioavailability.³⁶ Optimized EENPs showed PDI value equal to 0.22 ± 0.15 indicating the narrow distribution of particles and thus better stability of NS.

Another important significant index is zeta potential, which directly affects the stability of the dispersion

system, as it reflects steric or electrostatic barriers preventing aggregation and agglomeration of nanoparticles. When drug particles possess very low values of zeta potential to provide sufficient steric or electric repulsion between each other, aggregation of particles is likely to occur. Generally, for electrostatically stabilized systems maximum -30 mV of zeta potential or sterically stabilized formulation system at least -20 mV was sufficient for physical stabilization of NS (Fig. 7 b). The zeta potential of reconstituted EENPs was -19.3 ± 6.73 mV indicating physical stability of the optimized NS.³⁶

3. 5. Scanning Electron Microscopy (SEM)

The coarse EE particles bear's average particle size of 5–7 μm with broad size distribution observed (Fig. 8a) in SEM. The SEM (Fig. 8b) of optimized lyophilized EENPs shows that particles were discrete with an absence of agglomeration that may be assigned by the existence of stabilizer.

They had a porous surface and found to be slightly elongated and needle in shape. These pores may be developed due to evaporation of the solvent system from the surface of EENPs during lyophilization. Thus SEM pictures confirm that the larger scaly particles of EE were successfully converted to nearly elongated, smaller sized

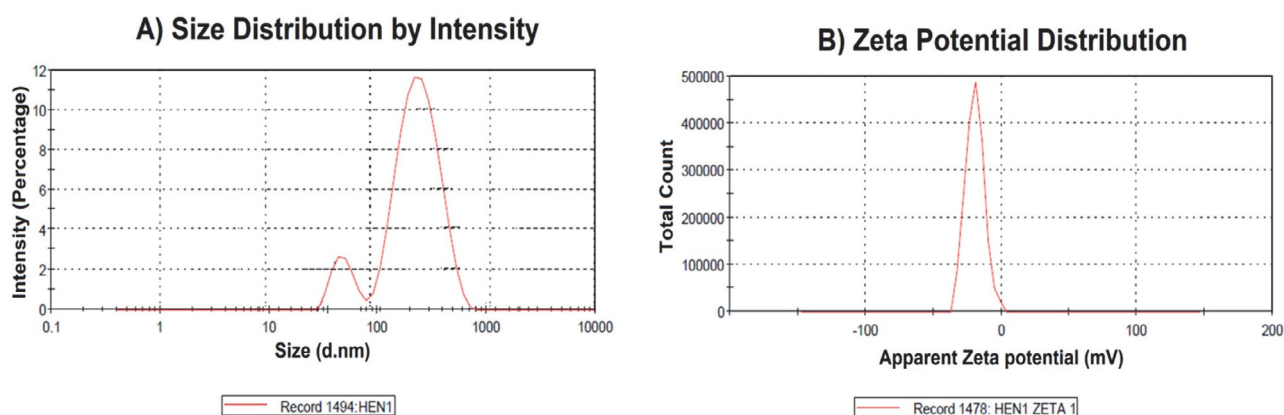


Figure 7. Graph showing: a) average particle size, b) zeta potential.

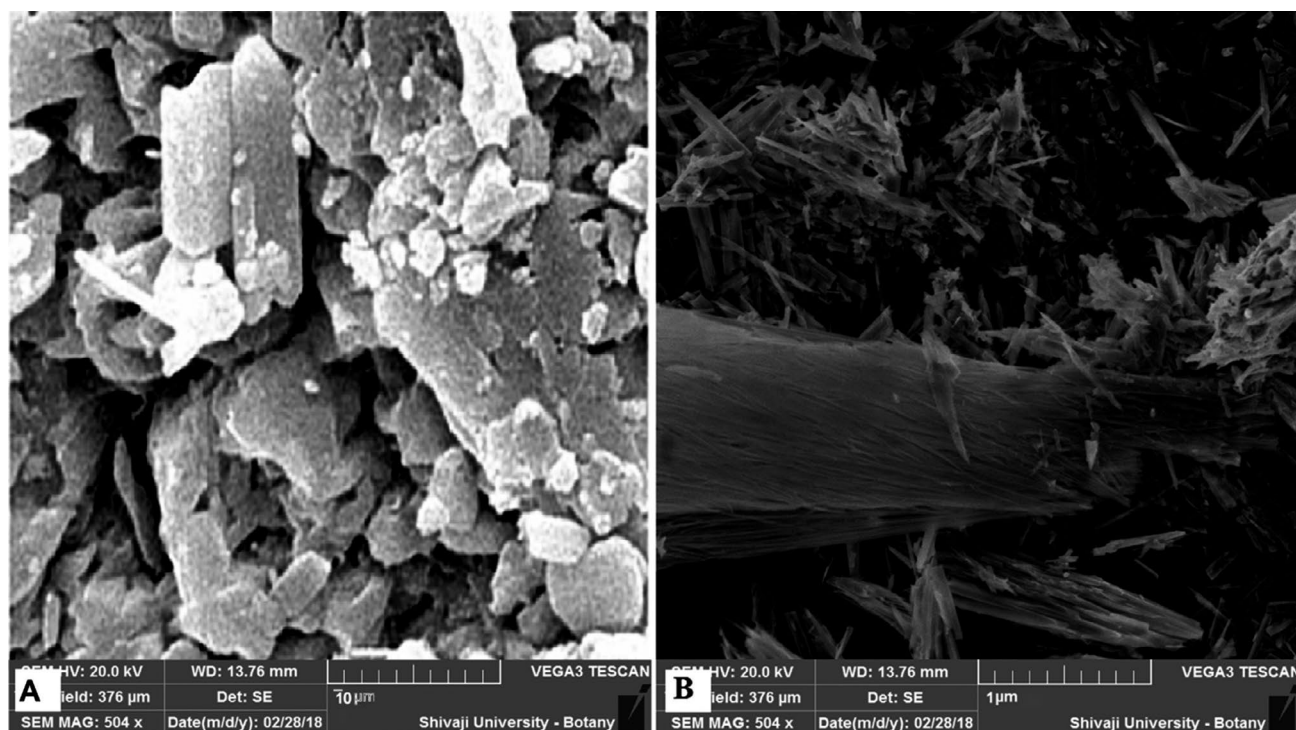


Figure 8. a) SEM images of pure ethinyl estradiol, (b) optimized nanosuspension (EENPs).

nanoparticles with a smoother surface on size reduction. The particle size of EENPs was increased in lesser extent but smaller than EE, after lyophilization.³⁴

3. 6. Saturation Solubility Studies

Saturation solubility studies were carried out for pure drug EE and optimized lyophilized EENPs in double-distilled water. The saturation solubility of EENPs was $805.84 \pm 0.05 \mu\text{g/mL}$ and coarse EE powder was $165.61 \pm 0.02 \mu\text{g/mL}$. Here the saturation solubility of EE in NS form is increased by 4.86 folds over pure EE. This is because of decreased particle size and increased surface area of EENPs as compared to pure drug. Ostwald Freundlich equation states that decreasing particle size increases saturation solubility (C_s)

$$\text{Log} \frac{C_s}{C} = \frac{2sV}{2.303RT r_1 r} \quad (9)$$

where, s = interfacial tension substance, C = solubility of the solid consisting of large particles, R = gas constant, r_1 = density of the solid, C_s = solubility, r = radius, V = molar volume of the particle material, and T = absolute temperature.

Another reason that increases saturation solubility is explained by the Kelvin equation, which suggests that dissolution pressure increases with increasing curvature that occurs with decreasing particle size. When the particle size is reduced to the nanometre range, the curvatures formed are enormous.³⁹

3. 7. Fourier Transform Infrared Spectroscopy (FTIR)

The FTIR spectra of EE coarse powder, physical mixture (PM), and optimized lyophilized EENPs are justified in Fig. 9. The FTIR spectra of EE coarse powder revealed characteristic peaks at 3369.546 and 3288.872 cm^{-1} which is attributed to intermolecular polymeric OH bonding, 2974.151 cm^{-1} peaks is indicating to C-H stretching of $\text{CH}_3\text{-CO-}$ group, 2921.704 and 2853.140 revealed to C-H stretching of $>\text{CH}_2$ group, while 1584.659 is attributed to acids i.e. C = O stretching.

The characteristic peak at 1356.175 cm^{-1} , 1283.928 cm^{-1} and 1058.227 cm^{-1} are attributed to C-H deformation of $-\text{CH}_2\text{-CO-}$ group, C-O stretching and O-H deformation (in-plane) of a secondary alcohol, and C-O stretchings of aralkyl respectively. The FTIR spectra of EENPs shows broadening of peaks at 3269.073 cm^{-1} of OH bonding and C-H stretching at 2935.012 cm^{-1} which could be due to diluting effect of mannitol or may be due to the formation of a hydrogen bond between the N-H group of soya lecithin with the carbonyl group of EE. An extra peak was observed in EENPs at 1732.708 cm^{-1} is the characteristic peak of Tween 80. Absence of characteristics peaks of EE at 2974.151 cm^{-1} , 2921.704 and 2853.140 cm^{-1} in EENPs may be due to overlapping peaks of tween 80 and soya lecithin. Furthermore, the shifting of peaks to its lower wave number and broadening of characteristic peaks of EE which is seen in EENPs may be due to intermolecular hydrogen bonding, while in PM all characteristic peaks of

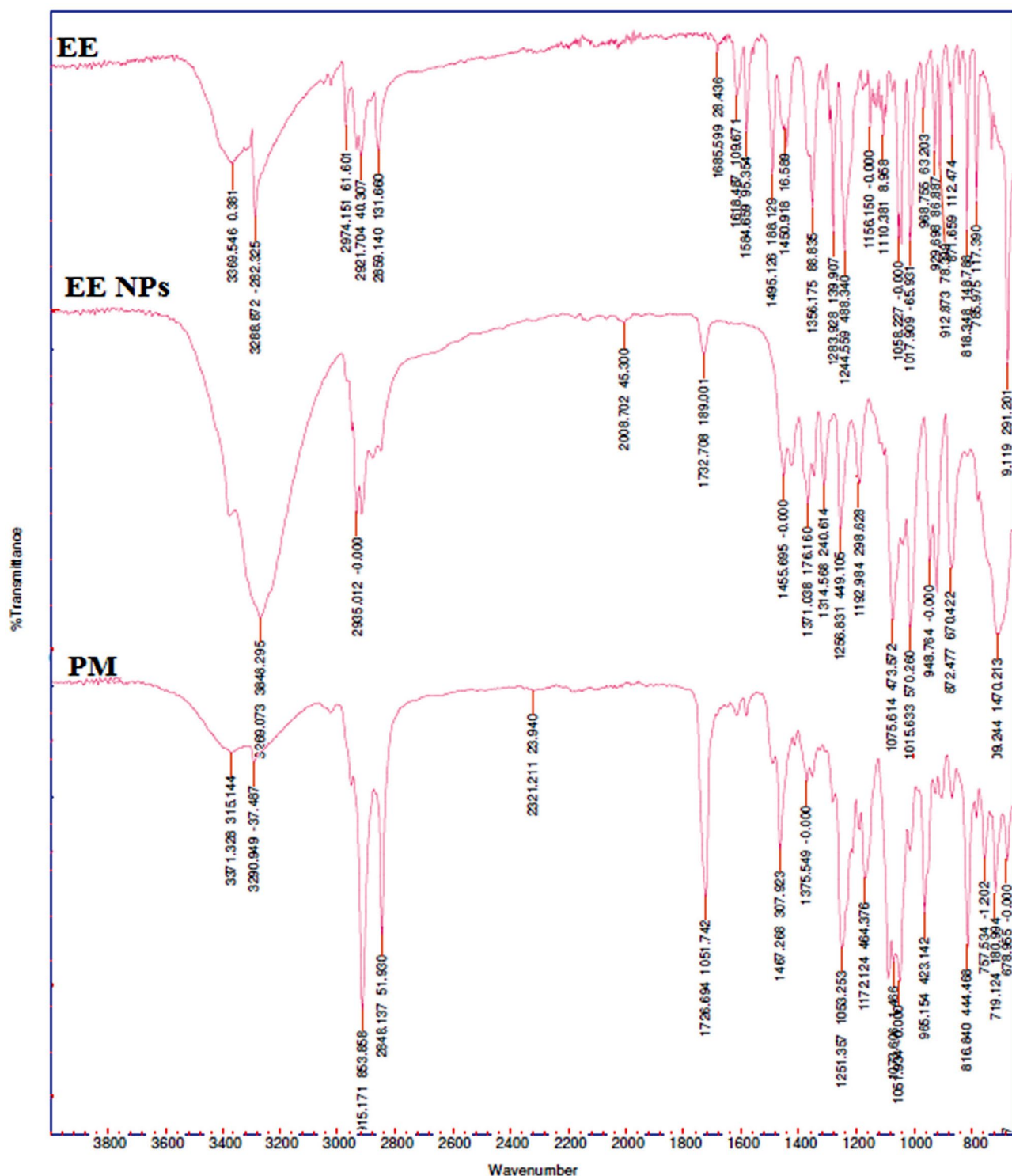


Figure 9. FTIR spectrum of: a) pure ethinyl estradiol, b) optimized nanosuspension (EENPs), c) physical mixture.

EE were retained with the slight shifting of wavenumber. Thus, there may be physical interactions occurring between functional groups of the drug and excipients, probably by the formation of a weak hydrogen bond. The physical interactions found here could be beneficial for the size and shape of the NS and their drug release pattern.

3. 8. *In-Vitro* Drug Release

The dissolution behavior of EE coarse powder and lyophilized EENPs in a simulated gastric fluid is shown in Fig.10. The dissolution rates of EE and EENPs in the simulated gastric fluid were 26.20% and 95.10% respectively.

The EENPs showed a dramatic increase in dissolution rate as compared to EE coarse powder. Moreover, the EENPs displayed a marked increase in dissolution rate, more than 60% as compared to EE coarse powder (15 %) within 60 min.

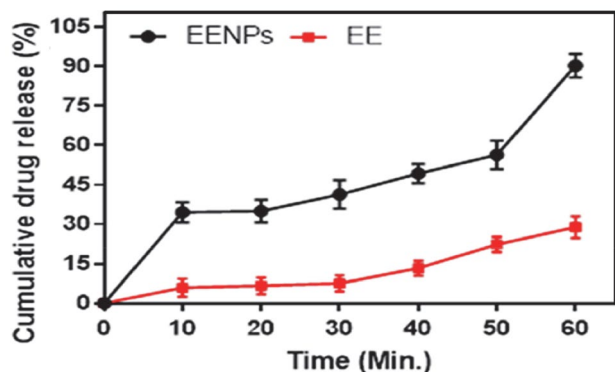


Figure 10. Dissolution profiles of optimized nanosuspension (EENPs) with a pure drug in simulated gastric fluid.

These suggested that the dissolution profile of lyophilized EENPs were distinctly superior as compared to EE. The dissolution enhancement of drug could be initiated to reduced particle size, especially in nanometre range with an effective increase in surface area which is available to get dissolved. This phenomenon is better explained by Noyes–Whitney equation.

$$\frac{dC}{dt} = DS - \frac{C_s - C_t}{h} \quad (10)$$

where h denotes the thickness of the dissolution boundary layer, D is the diffusion coefficient of the solute, C_s is the saturation solubility, S represents the surface area, dC/dt represents the dissolution rate and C_t is the bulk concentration. As the particle size of EENPs was much smaller than that of EE, hence they have a much larger surface area, hence higher dissolution rate.

Besides the particle size, the shape also plays a vital role that may affect the dissolution of the drug. Particles that are irregular, flaky and long may increase its average hydrodynamic thickness at the boundary layer. Thus, the value of h would be increased with a decrease in dissolution rate. The SEM image of EE showed rod-shaped particles in different sizes. Thus concluded enhancement in dissolution was due to the particle size reduction than that of shape alteration.³⁶

3. 9. Pharmacokinetic and Biodistribution Study in Sprague- Dawley Rats

In order to confirm the positive impact of NS on oral bioavailability enhancement of EE, *in-vivo* PK studies of EENPs and EEAQD were carried out in rats, and results obtained were compared with each other. The mean EE

Table 11. Pharmacokinetic parameters of EEAQD and lyophilized EENPs in Sprague- Dawley rats.

Pharmacokinetic parameter	EEAQD	Lyophilized EENPs
C_{max} (ng/ mL)	946.34 ± 1.23	1837.30 ± 1.65**
T_{max} (h)	4.00 ± 1.45	6.00 ± 1.47**
$t_{1/2}$ (h)	20.75 ± 1.36	14.10 ± 1.33**
MRT (h)	29.95 ± 2.01	20.35 ± 2.01**
AUC_{0-t} (ng/mL*h)	12290.12 ± 4.25	0777.17 ± 3.14**
$AUC_{0-\infty}$ (ng/mL*h)	15187.72 ± 4.56	22950.52 ± 3.45**
VD (mL)	0.00588 ± 2.42	0.00122 ± 2.33**
Cl (mL h ⁻¹)	1.97 × 10 ⁻⁵ ± 2.55	6.016 × 10 ⁻⁵ ± 2.65**
KE(h ⁻¹)	0.0334 ± 2.45	0.04915 ± 2.45**
F_{rel}	–	1.70 ± 1.05

**P < 0.01, compared to the corresponding parameters of EEAQD. Results were expressed as the mean ± SD (n = 3)^a

concentration-time profile in the rat plasma is shown in Fig. 11, after oral administration of a single dose of 0.5 mg/kg of EE from EENPs and EEAQD and their PK parameters obtained are reported in Table 11.

Following oral administration of EENPs and EEAQD, the plasma concentration of EE from EENPs in rats was significantly reached to a higher level than that of EEAQD at every time interval. The EENPs exhibited higher C_{max} , which indicates greater drug absorption. The C_{max} of EENPs is increased by ~2 folds. The reduced C_{max} of EEAQD is due to rapid distribution and metabolism of EE. The coating of soya lecithin helps the circulation of formulation in the body for a prolonged period, thus T_{max} of EENPs is higher than EEAQD. The relative bioavailability of EENPs was found to be 1.70 as compared to EEAQD. The area under the curve (AUC) is a vital PK parameter that explains the circulation and exposure time of the drug in bloodstreams.⁴³ The AUC_{0-t} of EENPs and EEAQD were 20777.18 ng/mL*h and 12290.12 ng/mL*h, respectively. These increase in AUC indicated that the EE

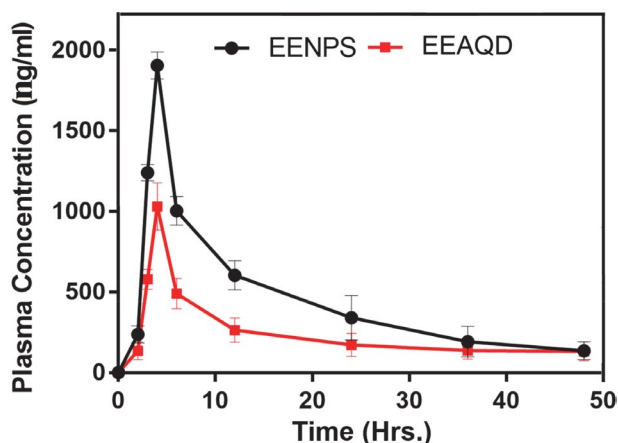


Figure 11. Plasma concentration-time profiles of EE after oral administration of EENPs and the EEAQD formulation in rats. Each value represents the mean ± S.D. (n = 3).

oral absorption in rats was enhanced notably in lyophilized NS form. Thus oral bioavailability of EE was improved by decreased particle size, enhanced membrane permeation and increased dissolution rate. As a stabilizer moreover, soya lecithin (phospholipids) has a thick coat on the surface of EENPs, which also plays a vital role in bioavailability enhancement. It is an amphiphilic surfactant, that may enhances EE penetration ability and thus promote rapid permeation of the EE nanoparticles through the intestinal epithelium, and finally into the systemic circulation.³⁴

After oral administration, biodistribution study of EENPs and EEAQD showed the higher collection of EE in spleen, liver, stomach, and kidney. Fig. 12, revealed the maximum concentration of EE by liver, spleen, stomach, and kidney were 1485.71 ± 5.56 , 1122.43 ± 4.88 , 1323.63 ± 5.62 and 891.16 ± 5.33 ng/g, for EENPs, respectively, after 48 h of oral administration. However, the EEAQD concentration in spleen, liver, stomach, and kidney were 745.62 ± 3.78 , 956.89 ± 4.56 , 821.23 ± 5.02 and 652.35 ± 3.78 ng/g, respectively. This may be due to the faster elimination of EE due to higher particle size as compared to EENPs. The higher uptake of EE in spleen, liver, and stomach is may be

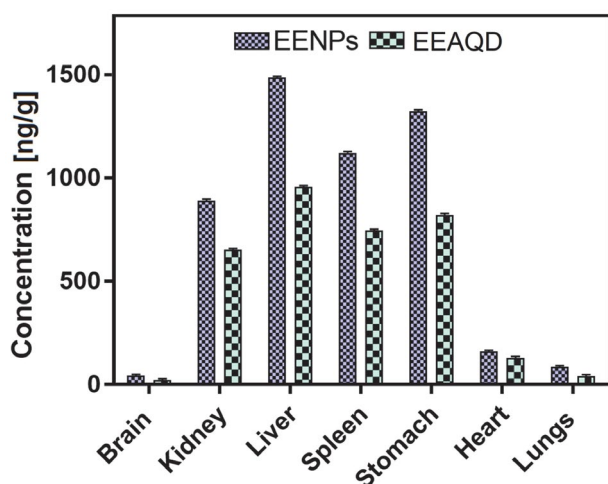


Figure 12. Biodistribution of EENPs and EEAQD after oral administration in rats brain, kidney, liver, spleen, stomach, heart, lungs.

due to enhanced lymphatic uptake. The concentration of EENPs in the brain was 43.56 ± 4.05 ng/g and EEAQD was 22.46 ± 4.35 ng/g, respectively. The concentration of EE in lungs and heart were 86.82 ± 3.02 and 160.48 ± 3.56 ng/g for EENPs, while for EEAQD it was 42.65 ± 4.33 and 130.56 ± 3.98 ng/g respectively. Comparison of EEAQD with EENPs was not statistically significant ($p > 0.05$). Thus, biodistribution studies conclude the accumulation of EENPs in spleen, liver, stomach and kidneys in a larger amount as compared to the brain, lungs, and heart.⁴⁴

3. 10. Stability Studies

The six-month stability data for EENPs and liquid EENPs is presented in Table 12. NS stored at room temperature showed an increased particle size from 220 nm to 316 nm over 6 months. Storage at refrigerated conditions showed a nominal increase from 220 nm to 275 nm indicating better stability. NS stored at 40 ± 2 °C/75 \pm 5 % relative humidity (RH) showed an increased particle size from 220 nm to 315 nm. The observations conclude that temperature influences the aggregation of EE nanoparticles, and hence it was higher at RT and above compared to refrigerator conditions. Significant aggregation was more likely to occur in liquid EENPs compared to lyophilized EENPs at all storage conditions. Refrigerated conditions do not have a significant effect on average particle size, whereas at room temperature and 40 ± 2 °C there was a significant effect. Thus it can be concluded that at higher temperatures particle aggregation takes place which might lead to the increased size of particles and thus makes them less stable. Probably Ostwald ripening may be the second reason resulting from fluctuations at room temperature. The results obtained from the chemical stability of formulation upon storage at different conditions are also presented in Table 10. Results suggest no significant change in EE content of liquid EENPs and lyophilized EENPs when stored at different storage conditions indicating that both the liquid and lyophilized NS are chemically stable at these storage conditions. Noteworthy, for physical stability of liquid EENPs, lyophilization and storage at refrigerated condition are recommended.³⁹

Table 12. Stability data of lyophilized EENPs and EENPs for the six-month stability study.

Formulation	Storage Temperature Conditions	Initial Particle Size	Particle Size			Initial drug content	Drug content		
			2 M	4 M	6 M		2 M	4 M	6 M
Lyophilized EE NPs	4 °C	220.4 ± 10.3	230.5 ± 6.8	255.8 ± 8.2	275.9 ± 4.6	92.23 ± 0.45	91.56 ± 0.89	91.02 ± 0.81	90.59 ± 0.87
	R. T.		256.5 ± 9.1	293.5 ± 4.6	316.2 ± 4.7		90.56 ± 0.56	89.02 ± 0.62	88.63 ± 0.74
	40 ± 2 °C		260.4 ± 8.1	286.9 ± 5.6	315.4 ± 5.6		90.88 ± 0.96	89.45 ± 0.89	88.03 ± 0.97
Liquid EE NPs	4 °C	209.4 ± 10.3	212.5 ± 9.1	225.8 ± 4.6	238.9 ± 7.5	96.48 ± 0.66	95.20 ± 0.58	94.65 ± 0.65	93.33 ± 0.66
	R. T.		268.9 ± 7.7	308.9 ± 7.1	334.8 ± 8.8		93.25 ± 0.47	91.41 ± 0.48	89.63 ± 0.41
	40 ± 2 °C		270.4 ± 8.1	299.2 ± 5.5	322.9 ± 5.6		93.33 ± 0.33	92.00 ± 0.54	90.23 ± 0.38

[†]M = Months

4. Conclusion

Stable lyophilized NS of EE was developed and evaluated using the QbD approach with enhanced bioavailability. The QbD approach was applied to understand the effect of CMAs and CPPs on CQAs and to improve the quality and safety of formulation. The impact of process and formulation variables that affect CQAs of NS, and influence stability and solubility of EE in NS, were optimized using statistical experimental designs viz., Plackett–Burman and Central Composite design within a QbD concept. It was manifested from the design, that the selected variables, i.e. no. of cycles of HPH, the concentration of soya lecithin, and concentration of tween 80 had a keen impact on characteristics of NS. The predicted values obtained from designs were comparable with observed ones. The optimized factors were applied to develop highly stable NS of EE with the remarkable enhancement of dissolution rates and stability. The particle size distribution pattern of optimized product from CCD overlay plot showed an average particle size of 220 ± 0.37 nm with a zeta potential of -19.3 ± 6.73 mV. Dissolution velocity and release rate of EENPs was increased significantly, due to reduced particle size and increased surface area of EE. The lyophilized NS was found to be stable when stored in the refrigerator. The plasma pharmacokinetic parameters including C_{\max} , T_{\max} , and AUC total, of EENPs on rats were significantly higher than those of EEAQD. The relative bioavailability of EENPs was enhanced by more than 2 folds. Biodistribution study suggests that higher concentration of EE was found in the liver within 72 h. Thus, lyophilized EENPS could be a promising aspect in clinical application for cancer as well as contraceptive agents with enhanced bioavailability and stability.

Furthermore, with the application of QbD concept in this study, very few experimental runs are used for the optimization of NS which are the evidence for the reduction of manufacturing cost, while the least values of residual error obtained are the evidence for reduction of manufacturing variability. Small particle size, least PDI values, higher drug content, smooth and spherical particles with higher entrapment efficiency and enhanced bioavailability confirms the desired quality of EE nanosuspension. On the basis of the results obtained as evidence, it can be concluded that QbD is a helpful tool in NDDS to reduce the manufacturing variability, improve the quality and safety, and to reduce the manufacturing cost, which is a primary requirement by USFDA.

5. Acknowledgment

The authors are grateful to Dr. Babasaheb Ambedkar Research and Training Institute (BARTI), Pune for providing funds to carry out the research work smoothly. All authors would like to acknowledge Dr. H. N. More, Principal,

Bharati Vidyapeeth College of Pharmacy, Kolhapur for providing the necessary facilities for the smooth working of the research project.

Conflict of interest

The authors declare no conflict of interest. The authors alone are responsible for the content and writing of the article.

6. References

1. G. Evans, E. L. Sutton EL, *Med. Clin. North. Am.*, **2015**, *99*, 479–503. DOI:10.1016/j.mcna.2015.01.004
2. C. L. Williams, G. M. Stancel, The Pharmacological basis of therapeutics, in : A. G. Gilman, L. S. Goodman, T. W. Rall, F. Murad (Eds.), Estrogens and Progestins, McGraw Hill., New York, **2018**, pp. 1420–1421.
3. L. Speroff, P. D. Darney, Contraception Clinical Guide for Contraception, fifth ed., Wolters Kluwer Health, New York, **2010**.
4. A. Pellegrini, B. Massidda, V. Mascia, M. T. Ionta, M. G. Lippi, A. Muggiano, E. Carboni, G. Robustelli della Cuna, G. Bernardo, M. R. Strada, L. Pavesi, *Cancer Treat. Rep.*, **1981**, *65(1–2)*, 135–6.
5. A. Sueta, M. Hayashi, Y. Fukugawa, H. Shimizu, Y. I. Mutsuko, Y. Yamamoto, H. Iwase H, *Int. Cancer Conf. J.*, **2016**, *5(3)*, 126–130. DOI:10.1007/s13691-015-0241-7
6. J. T. Herjan, C. Bennink, C. Verhoeven, J. Thijssen. *Maturitas.*, **2017**, *95*, 11–23. DOI:10.1016/j.maturitas.2016.10.010
7. H. Iwase, Y. Yamamoto, M. Yamamoto-Ibusuki, K. I. Murakami, Y. Okumura, S. Tomita, T. Inao, Y. Honda, Y. Omoto, K. I. Iyama, *Br. J. Cancer.*, **2013**, *109*, 1537–1542. DOI:10.1038/bjc.2013.520
8. A. Agrawal, J. R. F. Robertson, K. L. Cheung, *World J. Surg. Oncol.*, **2006**, *4*, 44. DOI:10.1186/1477-7819-4-44
9. K. Izumi, Y. Kadono, T. Shima, H. Konaka, A. Mizokami, E. Koh, M. Namiki, *Anticancer Res.*, **2010**, *30(12)*, 5201–5.
10. H. C. Bennink, M. Visser, Estetrol (E4), the forgotten fetal steroid. Proceedings of the 9th European Congress of Endocrinology, Budapest, Hungary, April 28- May 02, 2007. European Society of Endocrinology: **2007**.
11. P. V. Isabela, J. S. Daniel, C. C. Eduardo, J. S. Garcia, M. G. Trevisan., *J. Therm. Anal. Calorim.*, **2015**, *120 (1)*, 573–581. DOI:10.1007/s10973-015-4508-1
12. A. Sattar, D. Chen, L. L. Jiang, Y. Pan, Y. Tao, L. Huang, Z. Liu, S. Xie, Z. Yuan, *Scientific Reports.*, **2017**, *7*, 1–9. DOI:10.1038/s41598-017-02523-4
13. M. Garg, D. Mishra, H. Agashe, N. K. Jain, *J. Pharm. Pharmacol.*, **2006**, *58*, 459–468. DOI:10.1211/jpp.58.4.0005
14. T. Zhang, J. Murowchick, B. B. Youan, *J. Pharm. Sci.*, **2011**, *100 (3)*, 1031–44. DOI:10.1002/jps.22341
15. E. M. Merisko-Liversidge, G. G. Liversidge, *Toxicol. Pathol.*, **2008**, *36 (1)*, 43–8. DOI:10.1177/0192623307310946
16. P. Sharma, W. A. Denny, S. Garg, *Int. J. Pharm.*, **2009**, *380 (1–2)*, 40–8. DOI:10.1016/j.ijpharm.2009.06.029

17. R. Lobenberg, G. L. Amidon, *Eur. J. Pharm. Biopharm.*, **2000**, *50* (1), 3–12. DOI:10.1016/S0939-6411(00)00091-6
18. F. Lai, C. Sinico, G. Ennas, F. Marongiu, G. Marongiu, A. M. Fadda, *Int. J. Pharm.*, **2009**, *373* (1–2), 124–32. DOI:10.1016/j.ijpharm.2009.01.024
19. V. R. Patel, Y. K. Agrawal, *J. Adv. Pharm. Technol. & Res.*, **2011**, *2* (2), 81–87. DOI:10.4103/2231-4040.82950
20. F. Kesisoglou, S. Panmai, Y. Wu, *Adv. Drug. Deliv. Rev.*, **2007**, *59* (7), 631–644. DOI:10.1016/j.addr.2007.05.003
21. D. Gol, S. Thakkar, M. Misra, *Drug Dev. Ind. Pharm.*, **2018**, *44* (9), 1458–1466. DOI:10.1080/03639045.2018.1460377
22. L. Gao, G. Liu, J. Ma, X. Wang, L. Zhou, X. Li, *J. Control Release.*, **2012**, *160* (3), 418–30. DOI:10.1016/j.jconrel.2012.03.013
23. Y. Gao, Z. Li, M. Sun, C. Guo, A. Yu, Y. Xi, J. Cui, H. Lou, G. Zhai, *Drug Deliv.*, **2011**, *18*(2), 131–142. DOI:10.3109/10717544.2010.520353
24. L. Hao, X. Wang, D. Zhang, Q. Xu, S. Song, F. Wang, C. Li, H. Guo, Y. Liu, D. Zheng, Q. Zhang, *Int. J. Pharm.*, **2012**, *433* (1–2), 157–64. DOI:10.1016/j.ijpharm.2012.05.002
25. Q. Huang, H. Yu, Q. Ru, *J. Food Sci.*, **2010**, *75*, 50–57. DOI:10.1111/j.1750-3841.2009.01457.x
26. R. H. Müller, K. Peters, *Int. J. Pharm.*, **1998**, *160*, 229–237. DOI:10.1016/S0378-5173(97)00311-6
27. S. A. Maskarinec, J. Hannig, R. C. Lee, K. Y. C. Lee, *Biophys. J.*, **2002**, *82* (3), 1453–9. DOI:10.1016/S0006-3495(02)75499-4
28. M. Trotta, M. Gallarate, F. Pattarino, S. Morel, *J. Control Release.*, **2001**, *76* (1–2), 119–28. DOI:10.1016/S0168-3659(01)00432-1
29. F. Yerlikaya, A. Ozgen, I. Vural, O. Guven, E. Karaagaoglu, M. A. Khan, Y. Capan, *J. Pharm. Sci.*, **2013**, *102*, 3748–3761. DOI:10.1002/jps.23686
30. N. S. K. Srinivas, R. Verma, G. P. Kulyadi, L. Kumar, *Int. J. Nanomed.*, **2017**, *12*, 15–28. DOI:10.2147/IJN.S122729
31. J. Cook, M. T. Cruaños, M. Gupta, S. Riley, J. Crison, *AAPS Pharm. Sci. Tech.*, **2014**, *15* (1), 140–148. DOI:10.1208/s12249-013-0043-1
32. H. C. Vadlamudi, P. R. Yalavarthi, B. R. Venkata, J. Thanniru, K. R. Vandana, C. R. Sundaresan, *J. Acute. Dis.*, **2016**, *5*(4), 315–325. DOI:10.1016/j.joad.2016.05.004
33. C. P. Dora, S. K. Singh, S. Kumar, A. K. Datusalia, A. Deep, *Acta Pol. Pharm. (dnlm)*, **2010**, *67*(3), 283–290.
34. S. Kalvakuntla, M. Deshpande, Z. Attari, K. Kunnatur, *Adv. Pharm. Bull.*, **2016**, *6*(1), 83–90. DOI:10.15171/apb.2016.013
35. L. Rabelo, N. Monteiro, R. Serquiza, P. Santos, R. Oliveira, A. Oliveira, H. Rocha, A. H. Morais, A. Uchoa, E. Santos, *Mar. Drugs.*, **2012**, *10*, 727–743. DOI:10.3390/md10040727
36. J. He, Y. Han, G. Xu, L. Yin, N. M. Neubi, J. Zhou, D. Yang, *RSC Adv* **2017**, *7*, 13053–13064. DOI:10.1039/C6RA28676C
37. S. R. Shah, R. H. Parikh, J. R. Chavda, N. R. Sheth, *Powder Technol.*, **2013**, *235*, 405–411. DOI:10.1016/j.powtec.2012.10.055
38. P. F. Yue, Q. Zheng, B. Wu, P. Y. Hu, Z. F. Wu, M. J. Yan, *J. Disper. Sci. Technol.*, **2012**, *33*, 213–222. DOI:10.1080/01932691.2011.561162
39. L. Vuppalapati, S. Cherukuri, V. Neeli, R. P. Yeragamreddy, B. R. Kesavan, *Curr. Drug Deliv.*, **2016**, *13*, 143–157. DOI:10.1080/01932691.2011.561162
40. V. M. Pandya, J. K. Patel, D. J. Patel, *Disso. Technol.*, **2011**, *40*–45. DOI:10.14227/DT180311P40
41. A. A. Abdelbary, A. M. Al-mahallawi, M. E. Abdelrahim, M. A. Ali, *Int. J. Nanomed.* **2015**, *10*(1), 6339–6353. DOI:10.2147/IJN.S91631
42. V. Borhade, S. Pathak, S. Sharma, V. Patravale, *Nanomed (Lond.)*, **2014**, *9*(5), 649–66. DOI:10.2217/nnm.13.61
43. I. Ghosh, B. Michniak-Kohn, *AAPS Pharm. Sci. Tech.*, **2013**, *14*(3), 1108–1117. DOI:10.1208/s12249-013-9995-4
44. M. Bagad, Z. A. Khan, *Int. J. Nanomed.*, **2015**, *10*, 3921–3935. DOI:10.2147/IJN.S80706

Povzetek

Liofilizirano nanosuspenzijo slabo topnega etinilestradiola (EE) smo pripravili z namenom izboljšanja topnosti in biološke uporabnosti s pristopom »Quality by Design« (QbD). S pomočjo diagrama Ishikawa smo z načrtovanjem Plackett-Burman identificirali in pregledali potencialne dejavnike tveganja, da bi raziskali učinke formulacijskih in procesnih spremenljivk na odvisne spremenljivke. Število ciklov (X4), koncentracija sojinega lecitina (X5) in koncentracija stabilizatorja »tween 80« (X7) so bili opredeljeni kot pomembni dejavniki ($P < 0,05$), ki smo jih dodatno optimizirali z uporabo »Central Composite Design«. Srednja velikost delcev, zeta potencial, vsebnost zdravila in učinkovitost enkapsuliranja optimizirane liofilizirane EE nanosuspenzije (EENP) je bila $220 \pm 0,37$ nm, $-19,3 \pm 6,73$ mV, $92,23 \pm 0,45\%$, $99,52 \pm 0,52\%$. EENP znatno poveča C_{max} in AUC_{0-t} za 1,5, 1,7 krat in relativno biološko uporabnost za dvakrat, pri čemer je njegova porazdelitev v višjih koncentracijah v jetrih, vranici in želodcu. Razvoj nanosuspenzij, ki temelji na QbD pristopu, bi lahko uporabili za prepoznavanje kritičnih procesnih parametrov in atributov za določanje kakovosti.



Except when otherwise noted, articles in this journal are published under the terms and conditions of the Creative Commons Attribution 4.0 International License

Scientific paper

Surface Functionalization of Gold Nanorods Improves Nanostructure Assemblies on Amyloid Fibril Scaffolds

Mani Salimian,¹ Tahereh Tohidi Moghadam^{2*}
and Bijan Ranjbar^{2,3}

¹ Department of Biomaterials Engineering, Faculty of High Technologies, Tarbiat Modares University, Tehran, Iran

² Department of Nanobiotechnology, Faculty of Biological Sciences, Tarbiat Modares University, Tehran, Iran

³ Department of Biophysics, Faculty of Biological Sciences, Tarbiat Modares University, Tehran, Iran

* Corresponding author: E-mail: t.tohidi@modares.ac.ir

Received: 07-30-2019

Abstract

A hybrid scaffold containing gold nanorods and lysozyme amyloid fibrils has been fabricated, and the effect of surface modification on improving nanostructure assembly on the biological template has been investigated. The nanohybrid system was characterized by monitoring surface plasmon resonance bands, dynamic light scattering spectroscopy, Thioflavin-T assay, and transmission electron microscopy. Surface of gold nanorods (GNRs) was modified with polystyrene sulfonate (PSS), and possible difference in assembly of the pristine and modified nanostructures was compared upon interaction with amyloid fibrils. Analysis of transmission electron microscopy showed that changing the surface charge of GNRs with biocompatible polymer improved electrostatic interactions between the nanostructures and amyloid fibril templates. Analysis of cell viability assays also showed that surface functionalization of GNRs remarkably improved biocompatibility of the nanoscaffold. Results of this study encourage utilization of modification strategies to fabricate a new generation of nanoscaffolds with fruitful applications in regenerative medicine.

Keywords: Gold Nanorods; Surface Plasmon Resonance; Nanoscaffold; Amyloid Fibrils

1. Introduction

Recent developments in nanotechnology have encouraged rapid development of variety of nanomaterials, including quantum dots, carbon nanotubes, plasmonic nanoparticles, etc., to resolve a wide range of medical, biological, catalytic, optical issues. Amongst different structures and materials at nanoscale, plasmonic nanoparticles with typical size in the range of 1–100 nm have received widespread attention due to showing enhanced optical, magnetic, electronic and structural properties. The distinct characteristics of such tiny particles mainly originate from interaction between conductive free electrons of the nanoparticles and the electromagnetic radiation. Surface plasmon is a collective electrons oscillation existing at metal-dielectric interface which responds quickly to the changes of environmental conditions.¹ Such sensitivity to trace changes in the local refractive index, candidates plasmonic nanoparticles for variety of fruitful applications in nanomedicine and biosensing.^{2,3} Upon modifications in

synthesis conditions, shape of gold nanoparticles could be directed to form anisotropic nanoparticles of rod morphology. Gold nanorods (GNRs) with unique ability to scatter light in the near infrared region have been nominated as promising theranostic agents for different biomedical applications, such as biomedical imaging, biosensing, drug delivery, cancer therapy, regenerative medicine etc.^{4,5}

Taking the advantages and applications of plasmonic nanoparticles into consideration, fabrication of hybrid nanoscaffolds with simultaneous exploitation of the optical/electronic properties of the nanoparticles, as well as the functional and structural characteristics of typical biological templates, provides new prospects for nanobiotechnology researchers. Recently, combination of nanoparticles with biomolecules of interest has motivated special attention.^{6,7} An interesting area of research currently involves arranging plasmonic nanoparticles on biological scaffolds with potential application in tissue engineering.^{8,9} The most important issues in tissue engineering is fabrication of structural component that simulates extracellular ma-

trix (ECM) by providing a physical substrate for cellular adhesion, migration, division and transferring differentiation biochemical signals to cells. The biological scaffolds are constructed by several methods; such as self-assembly and thermally induced phase separation and electrospinning from natural proteins, polysaccharides, synthetic and inorganic materials.¹⁰ Self-assembly is an innate feature of some proteins in formation of nanofibers.¹¹ Due to its advantages as a variety of manufacturing processes, low cost, simple and requires laboratory facilities and injectable form a three-dimensional structure, a suitable method to produce nano-scaffolding protein. In this regard, amyloid fibrils are a well-investigated example of self-assembled polypeptides and have been nominated as attractive candidates for applications in materials science and tissue engineering.¹¹ Lysozyme amyloid fibers with high solubility, good mechanical and chemical strength and dimensions at nano scale are particularly attractive choice.

In previous studies, formation of lysozyme amyloid fibrils at low concentrations in an aqueous environment has been examined by using heat, low pH, ionic elements and stirring.^{12,13}

Herein, lysozyme amyloid fibril has been produced using self-assembly method under harsh environment, providing a natural/biological template for the hybrid scaffold. To monitor the efficiency of interaction with amyloid fibrils, assembly of pristine and PSS-modified plasmonic nanostructures of gold with rod morphology (GNRs) was monitored on the nanoscaffold. Formation of the amyloid fibril, anisotropic nanostructure, the surface charge and final nanoscaffold was characterized by UV-Visible, ThT assay, dynamic light scattering, and transmission electron microscopy.

2. Experimental Section

2.1. Materials

Gold (III) chloride trihydrate (HAuCl_4) (>99.9%), sodium borohydride (NaBH_4) (>99%), hexadecyltrimethylammonium bromide (CTAB) (>99%), silver nitrate (>99%), and L-Ascorbic acid (>98%), Sodium phosphate, Polystyrene sulfonate (PSS), sodium hydroxide, hydrochloric acid and Hen egg white lysozyme (HEWL, >99%) were procured from Sigma-Aldrich and used without further purification. All experiments were conducted by deionized water.

2.2. Synthesis, Purification and Modification of Gold Nanorods

2.2.1. Preparation of Au Seeds and Gold Nanorods

Gold nanorods were synthesized via sequential seed mediated growth method, as described previously.¹⁴ Briefly, small spherical gold nanoparticles (seeds) were prepared by mixing aqueous solutions of $\text{HAuCl}_4 \cdot 3\text{H}_2\text{O}$

(250 μL , 0.01 M) and CTAB (7.5 mL, 0.095 M), followed by immediate addition of ice-cold NaBH_4 solution (600 μL , 0.01M). The reactants were mixed rapidly for two minutes and kept undisturbed at room temperature for a minimum of 2 hours. The growth solution was then prepared by sequential addition of CTAB (9.5 mL, 0.095 M), $\text{HAuCl}_4 \cdot 3\text{H}_2\text{O}$ (400 μL , 0.01 M), AgNO_3 (60 μL , 0.01 M) and ascorbic acid (64 μL 0.10 M) solutions, followed by mixing with seed particles (40 μL). It will take several hours for formation of rod-shaped nanostructures.

2.2.2. Purification of Gold Nanorods

The excess cationic surfactant (CTAB) and unreacted gold were decanted by centrifugation process (14,000 rpm, 7 min). The precipitate was diluted by distilled water and the purified sample was sonicated for several minutes to redisperse the nanorods.

2.2.3. Surface Modification of GNRs with PSS

To induce electrostatic interaction between lysozyme fibrils and GNRs, surface of the purified nanostructures was coated by PSS polymer. Working solutions of 1.5 μM and 5 μM PSS were treated with GNRs and the mixture was stirred (100 rpm) at room temperature for 4 hours. Concentration range of the polymer with respect to GNRs was optimized by monitoring the characteristic surface plasmon resonance of the nanostructures upon interaction with PSS. This minimizes the possibility of unwanted aggregation of GNRs at higher concentrations of polymer solution. Excess PSS was removed by centrifugation at 12500 rpm, and total volume of the PSS-modified GNR solution was adjusted to 1 mL.

2.3. Synthesis of Lysozyme Amyloid Fibrils

A stock solution containing 2.5 mg mL^{-1} lysozyme was prepared and adjusted to pH 1.6, using HCl. The solution was then incubated at 65 °C for 9 h with continuous agitation by a stirrer.

2.4. Preparation of the Hybrid Nanoscaffold

Two series of pristine and PSS-modified GNRs were prepared for interaction with amyloid fibrils. The hybrid nanoscaffold consisting of GNRs and the biological template was prepared by treating 5 μL of amyloid fibrils (diluted with 285 mL of deionized water) with 700 μL of GNRs (OD 1). The mixture was incubated for 4 hours.

2.5. Characterization Techniques

2.5.1. Surface Plasmon Resonance of GNRs

To verify the rod morphology of plasmonic nanoparticles the characteristic surface plasmon resonance (SPR)

of GNRs was monitored using UV-Visible spectrophotometer. SPR spectra of both pristine and PSS-modified GNRs were recorded on a Perkin Elmer in the wavelength region of 400–900 nm.

2. 5. 2. Zeta Potential Analysis of PSS-Modified GNRs

Zeta potential of the purified GNRs before and after modification with PSS was recorded using Malvern Zetasizer. Prior to analysis, samples were filtered and sonicated for proper dispersion of the nanostructures.

2. 5. 3. Thioflavin T (ThT) Fluorescence Assay

Kinetics of amyloid fibril formation was studied using ThT assay. During amyloid fibrillation, sampling was carried out each 1h. 20 μ L ThT solution (250 μ M) was incubated with 80 μ L of protein samples. ThT fluorescence was monitored using a spectrofluorimeter (FP-6500; Jasco) with 5 nm slit-width. Intensity of fluorescence was recorded by exciting at 440 nm and recording the emission at 485 nm, at room temperature.

2. 5. 4. Transmission Electron Microscopy of the Hybrid Scaffold

GNRs micrographs were taken by transmission electron microscopy (TEM) (Philips CM200-FEG, USA). Assembly of pristine and PSS-modified GNRs on the amyloid fibril template was imaged, by drop casing 5 μ L of each sample on carbon coated copper grid.

2. 6. Cell Culture and Cell Viability Assay

The HepG2 and fibroblast cells were cultured in DMEM medium supplemented with 1% (v/v) penicillin-streptomycin and 10% (v/v) heat inactivated FBS. Cells were maintained in 5% CO₂ humidified incubator at 37 °C. During subculture, cells were detached by trypsinization when they reached 90% confluency. The cells were harvested and seeded into 96- well plates at a density of 10000 cells per well for experiments.

MTT assay measures the reduction of a tetrazolium component into an insoluble formazan product by the mitochondria of viable cells. The insoluble dye formed in MTT assay was solubilized using DMSO. Cells were seeded in 96-well tissue culture plates (10000 cell/well in 100 μ L DMEM culture medium) and incubated overnight at 37 °C and 5% CO₂. Morphology of cells was then observed by an invert microscope before exposure to Gold nanorods. After overnight growth, 15 μ L of samples containing bare GNRs, GNRs-PSS, bare Amyloid fibrils, GNRs-Amyloid fibrils and GNRs-PSS-Amyloid fibrils were diluted with deionized water to make 0, 1, 2.5, 5, 10, 15, 25 nM of the nanostructures. Samples were ex-

posed to HepG2 and fibroblast cell lines in each well of 96-well tissue culture plates. Treated cells were incubated for 24 and 48 hour at 37 °C and 5% CO₂. Morphology of cells was observed by invert microscope after exposure to different concentrations of nanostructures. After 24 and 48 hours, 10 μ L MTT solution (50 mg/10 mL PBS) was added to each well and the plates were incubated for 4 h. Supernatants were replaced by 100 μ L DMSO and samples were analysed by an ELISA plate reader at 570 nm. All absorbance values were corrected against blank wells containing growth media. Each assay was done in triplicate and mean \pm standard deviation values were calculated.

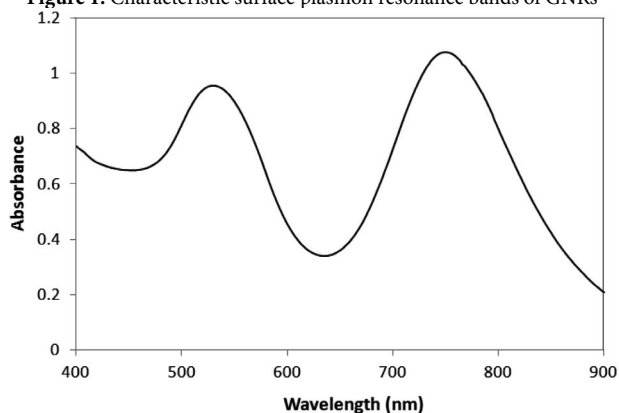
3. Results and Discussion

3. 1. Characterization of the Anisotropic Nanostructures

3. 1. 1. Surface Plasmon Resonance and Transmission Electron Microscopy

Surface plasmon resonance bands of gold nanorods were monitored in the visible and near infrared region, representing oscillation of the conduction band electrons along the short and long axis of GNRs (Fig. 1). Appearance of the strong longitudinal surface plasmon resonance band (LSPR) at 750 nm, along with transverse SPR band of weaker intensity at 531 nm is characteristic of formation of nanostructure with rod morphology. While transverse surface resonance band normally does not show any particular changes upon changes in the refractive index, the longitudinal one (LSPR) shows significant sensitivity to trace changes in the local environment.³ Such response to changes has been exploited in designing novel plasmonic theranostic agents, as well as monitoring biomolecular interactions and molecular binding events.

Figure 1. Characteristic surface plasmon resonance bands of GNRs



Transmission electron microscopy (TEM) image of the purified samples also confirmed formation of the anisotropic nanostructures with rod morphology. Given

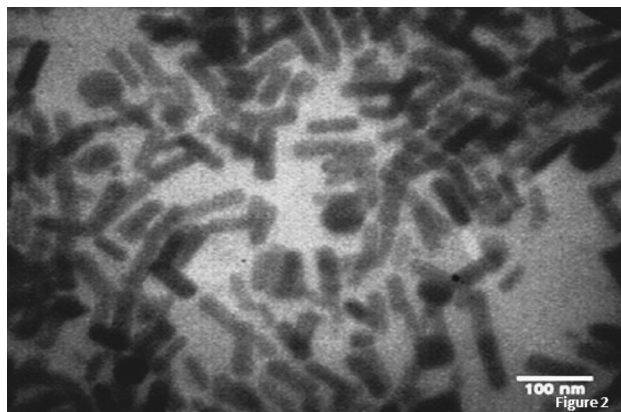


Figure 2. Transmission electron microscopy image of GNRs

the average dimensions by TEM, the mean aspect ratio of GNRs was calculated to be 3.8 ± 0.3 (Fig. 2.)

3. 1. 2. Surface Modification of Gold Nanorods

The position of the SPR peaks, the absorbance intensity and the peaks heights relative to each other are associated with the particle size, population of nanostructures and their aspect ratio, respectively.¹⁵ Surface of GNRs provide a convenient matrix for interaction and/or conjugation with molecules of interest, for various chemical, physical and biological applications. Any changes at nanoparticle interface can be studied by tracing its characteristic SPR spectra in the visible and near infrared region. In this study, surface of GNRs were modified with polystyrene sulfonate (PSS), to reverse the surface charge of the nanostructures and provide opportunity for electrostatic interactions with amyloid fibrils, as well as increasing biocompatibility of the final nanoscaffold for future investigations in tissue engineering.

Upon increasing the PSS concentration (above 5 μM in this investigation), macroscopic aggregates were noticed in GNR samples. This could be attributed to perturbations in morphology of the nanostructure, losing the typical rod shape. To ensure that anisotropy of GNRs is maintained, SPR spectra were monitored in the presence of PSS with different concentrations. Fig. 3a depicts transverse and longitudinal SPR bands of GNRs upon interaction with two selected concentrations of polymer (PSS), i.e. 1.5 and 5 μM of polymer. In the presence of polymer solution, the nanostructures showed redshift in the position, as well as decrease in the intensity of longitudinal SPR. This could be attributed to modification of GNRs' surface with PSS. Although the two counterparts provide opposite surface charge, the characteristic SPR of GNRs has not been perturbed, representing electrostatic interactions, while maintaining the rod morphology within the specified range of polymer concentration. Further experiments, i.e. assembling of PSS-modified GNRs on the biological template were carried out using

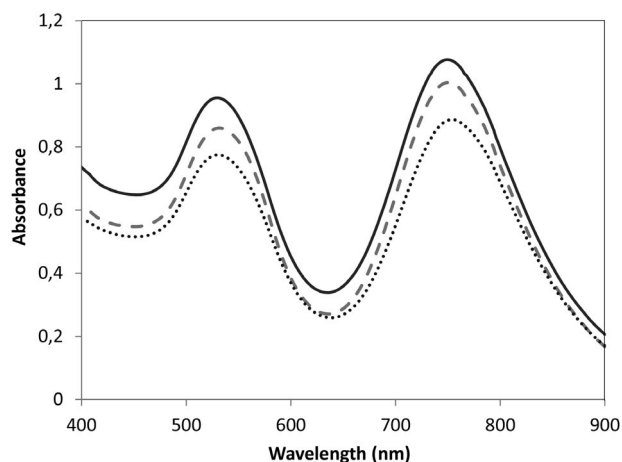


Figure 3. Changes in the SPR bands of GNRs after modification with PSS. From top to bottom: control GNRs, GNRs-PSS (1.5 μM), and GNRs-PSS (5 μM).

5 $\mu\text{g}/\text{ml}$ PSS.

To confirm change in the surface charge of GNRs, dynamic light scattering (DLS) spectroscopy was used. This technique provides useful information about some parameters, including particle size distribution, molecular weight and zeta potential.¹⁵ Fig. 4 depicts zeta potential analysis of GNRs, before and after modification with PSS. Surface of pristine GNRs shows highly positive charge due to presence of cationic surfactant (CTAB), as one of the key chemicals in dictating anisotropy in the nanostructure. Although several rounds of centrifugation are conventionally used to remove excess CTAB molecule from the medium, it still exist after purification processes. Therefore, presence of CTAB provides net positive charge for GNRs. Upon interaction of GNRs with PSS, cationic CTAB is replaced by polymer molecule, reversing the net charge of GNRs from +48 mV to -38 mV.

3. 2. Characterization of the Biotemplate and

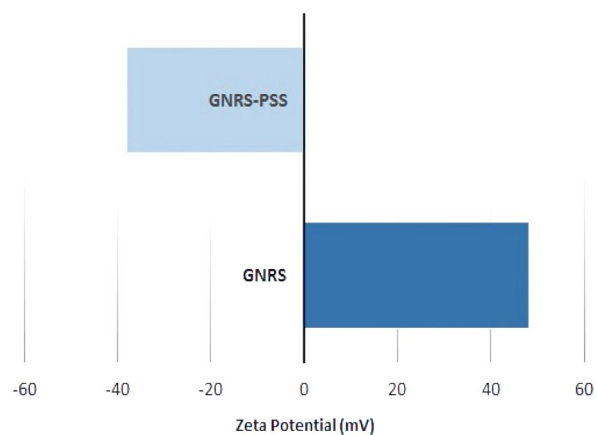


Figure 4. Analysis of zeta potential for pristine and PSS-coated GNRs

the Hybrid Scaffold

3. 2. 1. Thioflavin T (ThT) Fluorescence Assay

To investigate the kinetics of amyloid fibrils formation, Thioflavin T (ThT) Fluorescence assay was used. This method is highly specific and quantitative technique that can clearly show changes in the protein secondary structures. Treated samples were kept away from light for about 5 minutes at room temperature. As shown in Figure 5, intensity of fluorescence emission increased upon formation of β -sheet structures. The increasing trend reaches a plateau upon completion of amyloid formation (data not shown).

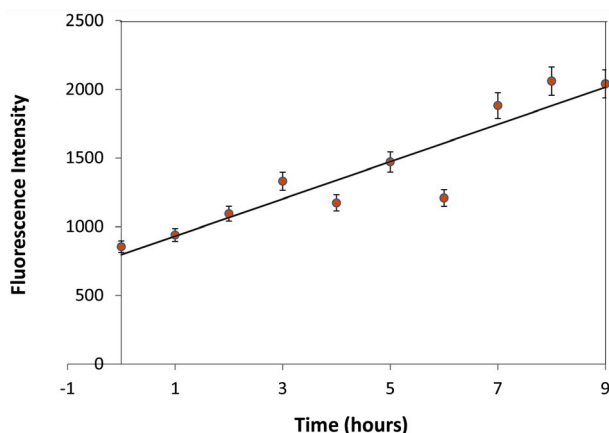


Figure 5. Thioflavin-T Assay of lysozyme upon transformation into amyloid fibril structures

3. 2. 2. Transmission Electron Microscopy of the Hybrid Scaffold

To study possible role of nanostructure surface modification in improving yield of assembly on the biological template, two samples of pristine and PSS-coated GNRs were compared. Fig. 6 depicts transmission electron microscopy images of lysozyme amyloid fibrils treated with

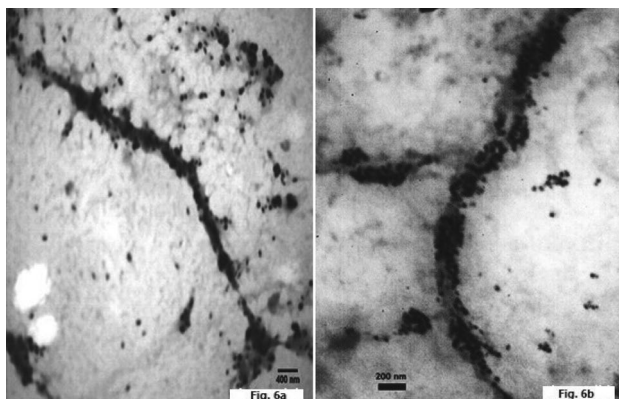


Figure 6. Transmission electron microscopy of plasmonic gold nanoparticle arrays on lysozyme amyloid fibrils, with pristine (a) and PSS-modified (b) plasmonic nanostructures.

pristine and PSS-modified nanostructures. Fig. 6b shows that surface modified plasmonic nanostructures with opposite electrostatic charge have more tendencies to interact with the biological template, as compared to their pristine counterpart (Fig. 6a). Taking the positive zeta potential value of lysozyme amyloid fibrils into consideration, the biotemplate provided opposite electrostatic charge for better interaction with the surface modified GNRs. Assembly of higher population of nanostructures via such strategy could facilitate fabrication of nanohybrid scaffold of more uniformity.

3. 3. Cell Viability Results

Viability percentage measured by MTT assay on HepG2 and fibroblast cell lines exposed to 0, 1, 2.5, 5, 10, 15, 25 nM GNRs in samples containing bare GNRs, GNRs-PSS, bare Amyloid fibrils, GNRs-Amyloid fibrils and GNRs-PSS-Amyloid fibrils for 24 and 48 h represented a dose response pattern as shown in Figs. 7 and 8. Data were reported as mean \pm SD of three independent experiments performed in triplicate for all samples.

As expected from MTT assay results, intact GNRs were severely toxic at higher concentrations, i.e. 25 nM. This due to the fact that the nanostructures are synthesized in the presence of high concentrations of cationic surfactant (CTAB). Although GNRs are purified with several rounds of centrifugation, there still exists the bilayer of CTAB around the bare nanostructures. Upon replacing the cationic bilayer with PSS, cells exposed to GNRs-PSS showed less toxicity as compared to the bare nanostructures. Meanwhile, a glance at cell viability data for the hybrid systems (the nanoscaffolds) shows that PSS-coated GNRs arrays on lysozyme amyloid fibrils have manifested a higher percentage of viability in comparison with the nanoscaffolds containing bare GNRs arrays on amyloid fibrils. Overall, GNRs-PSS and GNRs-PSS-Amyloid fibrils depicted high cell survival at lower concentrations of the nanostructures, with less toxicity at higher concentrations for both cell lines.

Developing biodegradable scaffolds by self-assembly method based on DNA, protein and virus capsid is progressing every day.^{16,17} For example, to support nervous cell regeneration, nanoscaffolds have played an important role in stem cell therapy and brain reconstruction. In this regard, Cass et al. designed bioresponsive nanoscaffolds using engineered self-assembling peptides to connect and grow nervous stem cells.¹⁷

Tissue engineering has great potential to develop and modify patches, meshes, and cell sheets of more similarity to the host tissue. For this reason, bio-based hydrogel are known as suitable options for repairing and reconstructing cardiac cells.

Today, abundant natural and synthesized hydrogels, such as collagen, gelatin, matrigel and PNIPAA are utilized to replace the damaged parts in cardiac muscle.^{18–21}

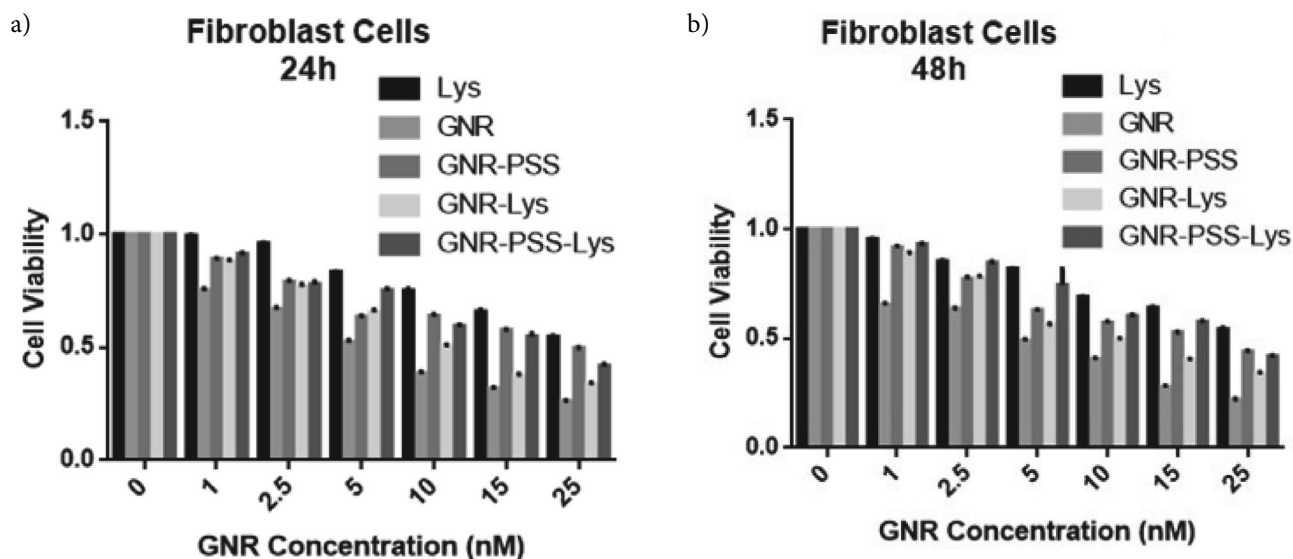


Figure 7. Cell viability assay for fibroblast cell line incubated for 24 h (a) and 48 h (b) with Lys, GNRs, GNRs-PSS, GNRs-Lys and GNRs-PSS-Lys. The abbreviation Lys represents Lysozyme Amyloid Fibrils.

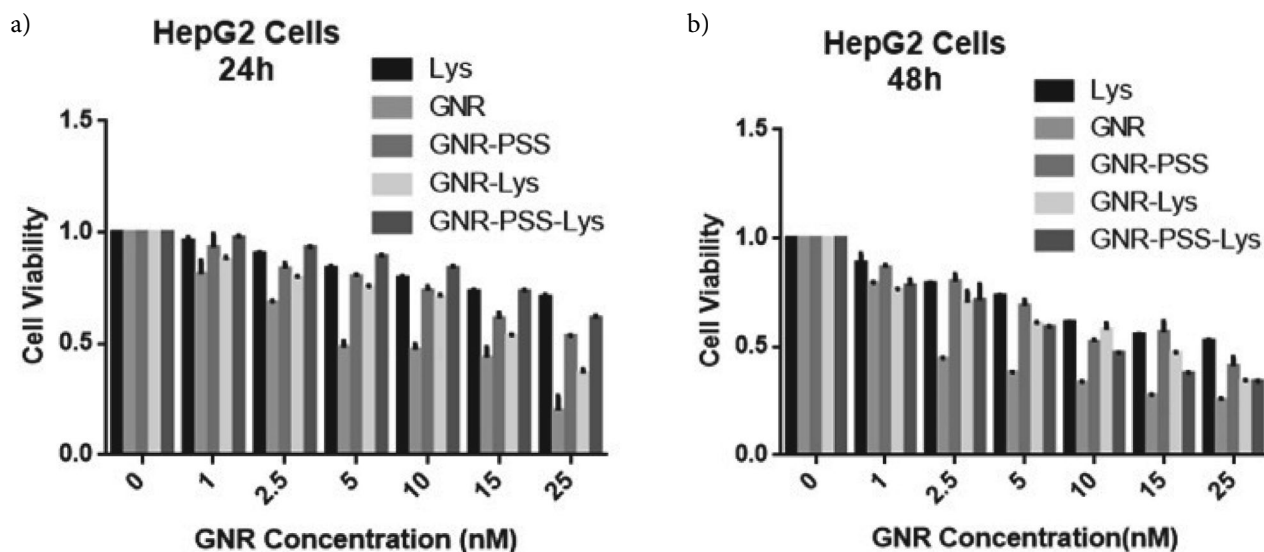


Figure 8. Cell viability assay for HepG2 cell line incubated for 24 h (a) and 48 h (b) with Lys, GNRs, GNRs-PSS, GNRs-Lys and GNRs-PSS-Lys. The abbreviation Lys represents Lysozyme Amyloid Fibrils.

Although hydrogels provide micron-like space similar to ECM to support cardiac function, their electrical conductivity is not very efficient. Especially, the presence of electrical insulations in these hydrogel structures, causes poor cardiac binding and consequently, poor performance in tissue engineering.²² To overcome this issue, nanostructures of good conductivity can be employed. Carbon nanotubes are known to provide electrical conductivity and proper inter-cellular communication. Nevertheless, their tendency to form accumulations on tissue surfaces induces cellular toxicity, which has raised serious concerns about their medical applications.^{23,24} In this regard, coat-

ings and functionalization of nanotubes have been proposed to reduce cell toxicity. However, these changes are expected to affect electrical properties. In addition, insolubility of CNTs in aqueous systems has made it unfavorable to utilize in biological systems. Therefore, replacing CNTs with plasmonic gold nanostructures can be a better idea to overcome toxicity problems in biomedical applications. Plasmonic nanostructures can be produced with various morphologies, e.g. sphericals, rods, prisms, cubes, etc. with promising applications in biomedicine and biosensing. High electrical conductivity, low toxicity, facile synthesis, ease of functionalization and low cost of production

at large scale can be considered as their advantages over other nanoparticles. Amongst gold nanoparticles, gold nanorods have shown remarkable features in biosensing platforms, especially when compared to spherical nanoparticles. The great sensitivity of these rod shaped gold nanostructures to trace changes in the local environment enables their utilization in hybrid scaffolds with superior sensitivity and conductivity.

There are a number of reports on the use of gold nanoparticles in tissue scaffolds, which include several polymers, such as alginate, poly L-caprolactone, Poly (thiol-HEMA) and decellularized omental matrix, showing the potential of these nanoparticles for utilization in conductive scaffolds.^{24–26}

Enhancement in the catalytic activity can also be considered as one of the important and key features of gold nanoparticles due to providing high specific surface area. Mishra et al. reported fabrication of AuFeAg hybrid nanoparticles as an efficient recyclable system with catalytic function. The hybrid nanocatalyst exhibited catalytic activity for the synthesis of α,β - and β,β -dichloroenones, which are important synthetic intermediates in the preparation of natural products.²⁷

Specific features such as electrical conductivity, mechanical strength, and structural integrity are required to improve the function of the cardiac cells. In a recent study, the role of embedded gold nanoparticles in methacrylate gel was shown to improve electrical conductivity and stiffness of the matrix.⁸ The cardiac cells implanted in the matrix have demonstrated the ability to survive and maintain their metabolic function. The uniform dispersion of the specific markers of the cardiac cells confirmed the effect of the nanoparticles concentration.

Researchers at MIT have recently reported fabrication of cardiac patches decorated with tiny gold wires that could be used to create pieces of tissue whose cells all beat in time, mimicking the dynamics of natural heart muscle.²⁸ They used alginate as the base material that is often used for tissue scaffolds and combined it (randomly) with gold nanoparticles. In this study, conduction of the previously designed tissues of pure alginate was compared with its composite scaffold. Combination of alginate and gold nanoparticles provided significant enhancement in signal conduction, i.e. a few hundred micrometers with respect to a scale of millimeters. This idea could notably pave the way for designing conductive systems in muscle cells and vascular constructs as well as neural systems, showing a significant impact on the collective communication of cells. Nevertheless, we believe that assembly of gold nanostructures of rod morphology on fibrillar templates with biological origin might be a better option for such applications. Our group has recently reported synthesis and characterization of assembled gold nanorods on HSA amyloid fibrils.²⁹ Therefore, the fibrillar biotemplate with evidenced mechanical and chemical stability can properly compensate the fibrillar pattern of CNTs and assembly of

GNRs can retrieve its conductivity.

In line with this study, the present effort aimed to improve the interaction and assembly of GNRs on Lysozyme amyloid fibrils via surface functionalization of the nanostructures with polystyrene acetate. Apart from formation of a hybrid nanoscaffold with improved interaction between the nanostructures and the biological template, PSS coating of GNRs can play a significant role in ensuring biocompatibility of the nanostructures, due to the replacement of the cationic surfactant (CTAB) by the biocompatible polymer.

Taking the previous achievements into consideration, the idea of assembling rod-shaped gold nanostructures on biological templates is worth to investigate due to the possibility of developing a new generation of hybrid nanoscaffolds with lower toxicity, promising fruitful applications in various sensing platforms, tissue engineering and regenerative medicine.

4. Conclusion

This effort has focused on fabrication of a nanohybrid scaffold through combination of amyloid fibrils as biotemplates, and plasmonic nanostructures of gold with rod morphology. Amyloid fibrils of lysozyme provided a surface for assembly of gold nanostructures. Gold nanorods were interacted with biotemplates in two different forms of pristine and polymer coated nanostructures. Surface modification of GNRs with biocompatible polymer (PSS) improved electrostatic interactions between the nanostructures and amyloid fibril templates, and facilitated assembly of more GNRs on the biotemplate. Cell viability assays also confirmed an increase of biocompatibility for the nanoscaffold upon surface coating with PSS. Such a modification strategy could pave the way for fabrication of hybrid nanoscaffolds of more uniformity, providing a better chance to produce a new generation of hybrid materials with fruitful applications in biosensing and regenerative medicine.

Declarations

- Availability of data and material
All raw and analyzed data as well as the materials are available in this study.
- Competing interests
The authors do not have any competing interests.
- Funding
The financial grant for chemicals and characterization facilities has been provided by Tarbiat Modares University.
- Authors' contributions
Mani Salimian conducted the experiments, analyzed data and wrote some parts of the manuscript.
Tahereh Tohidi Moghadam designed the experiments,

supervised the project and wrote some parts of the manuscript.

Bijan Ranjbar advised on analysis and interpretation of data.

• Acknowledgements

The authors would like to acknowledge Tarbiat Modars Univrsity for providing characterization facilities.

5. References

1. S. Guo, E. Wang, *Nano Today* **2011**, *6*, 240–264. DOI:10.1016/j.nantod.2011.04.007
2. T. Tohidi Moghadam, B. Ranjbar, *Int. J. Biol. Macromol.* **2015**, *51*, 91–96. DOI:10.1016/j.ijbiomac.2012.04.020
3. S. Shams, B. Bakhshi, *J. Nanobiotechnology* **2019**, *17*, 1–13. DOI:10.1186/s12951-019-0476-0
4. Y. Ma, HX. Xia, YP. Liu, B. Liu, W. Chen, *Chinese Sci. Bull.* **2013**, *58*, 2530–2536. DOI:10.1007/s11434-013-5720-7
5. M. K. Popp, I. Oubou, C. Shepherd, Z. Nager, C. Anderson, L. Pagliaro, *J. Nanomater* **2014**, 1–8. DOI:10.1155/2014/450670
6. W. R. Algar, D. E. Prasuhn, M. H. Stewart, *Bioconjugate Chem.* **2011**, *22*, 825–858. DOI:10.1021/bc200065z
7. S. Ashrafpour, T. Tohidi Moghadam, *Surfaces and Interfaces* **2018**, *10*, 216–221. DOI:10.1016/j.surfin.2017.09.010
8. A. Navaei, H. Saini, W. Christenson, R. T. Sullivan, R. Ros, *Acta Biomater.* **2016**, *41*, 133–46. DOI:10.1016/j.actbio.2016.05.027
9. A. Ito, Y. Takizawa, H. Honda, K. Hata, H. Kagami, *Tissue Eng.* **2004**, *10*, 833–840. DOI:10.1089/1076327041348301
10. B. Dhandayuthapani, Y. Yoshida, T. Maekawa, *Int. J. Polym. Sci.* **2011**, 1–19. DOI:10.1155/2011/290602
11. O. Deschaume, B. De Roo, MJ. Van Bael, *Chem. Mater.* **2014**, *26*, 5383–5393. DOI:10.1021/cm502652t
12. S. Y. Ow, D. E. Dunstan, *Soft Matter* **2013**, *9*, 9692–9701. DOI:10.1039/c3sm51671g
13. E. Takai, G. Ohashi, R. Ueki, Y. Yamada, *Am. J. Biochem. Biotechnol.* **2014**, *10*, 31–39. DOI:10.3844/ajbbbsp.2014.31.39
14. T. Tohidi Moghadam, B. Ranjbar, K. Khajeh, *Int. J. Biol. Macromol* **2012**, *49*, 629–636. DOI:10.1016/j.ijbiomac.2011.06.021
15. M. A. Mahmoud, M. A. El-Sayed, *J. Am. Chem. Soc.* **2010**, *132*, 12704–12710. DOI:10.1021/ja104532z
16. H. Kitching, M. J. Shiers, A. J. Kenyon, *J. Mater. Chem. A* **2013**, *1*, 6985–6999. DOI:10.1039/c3ta00089c
17. T. Scheibel, R. Parthasarathy, *Proc Natl. Acad. Sci.* **2003**, *100*, 4527–4532. DOI:10.1073/pnas.0431081100
18. S. Pedron, S. Van Lierop, P. Horstman, *Adv. Funct. Mater.* **2011**, *21*, 1624–1630. DOI:10.1002/adfm.201002708
19. H. Saini, A. Navaei, A. Van Putten, *Adv. Healthc. Mater.* **2015**, *4*, 1961–1971. DOI:10.1002/adhm.201500331
20. S. Khalil, W. Sun, *J Biomech. Eng.* **2009**, *131*, 1–8. DOI:10.1115/1.3128729
21. M. Radisic, H. Park, H. Shing, T. Consi, *Proc. Natl. Acad. Sci.* **2004**, *101*, 18129–18134. DOI:10.1073/pnas.0407817101
22. J. Zhou, J. Chen, H. Sun, X. Qiu, Y. Mou, Z. Liu, Y. Zhao, *Sci. Rep.* **2014**, *4*, 1–11. DOI:10.1038/srep03733
23. M. Kharaziha, SR. Shin, M. Nikkha, SN. Topkaya, *Sci. Rep.* **2014**, *4*, 7346–7354. DOI:10.1016/j.biomaterials.2014.05.014
24. H. Dumortier, *Adv. Drug Deliv. Rev.* **2013**, *65*, 2120–2126. DOI:10.1016/j.addr.2013.09.005
25. S. Fleischer, M. Shevach, R. Feiner, T. Dvir, *Nanoscale* **2014**, *6*, 9410–9414. DOI:10.1039/C4NR00300D
26. M. Shevach, R. Zax, A. Abrahamov, S. Fleischer, *Biomed. Mater.* **2015**, *10*, 34106. DOI:10.1088/1748-6041/10/3/034106
27. K. Mishra, N. Basavegowda, Y. R Lee, *Appl. Catal. A Gen.* **2015**, *506*, 180–187. DOI:10.1016/j.apcata.2015.09.014
28. T. Dvir, B. P. Timko, M. D. Brigham, SR. Naik, *Nat. Nanotechnol.*, **2015**, *6*, 720–725. DOI:10.1038/nnano.2011.160
29. R. A. Taheri, Y. Akhtari, T. Tohidi Moghadam, B. Ranjbar, *Sci. Rep.* **2018**, *8*, 1–10. DOI:10.1038/s41598-018-26393-6

Povzetek

Na biološkem nosilcu iz amiloidnih vlaken lizocima smo pripravili podlago za nanos nanodelcev zlata («gold nanorods» (GNR)). Za preučevanje tega sistema smo uporabili površinsko plazmonsko resonanco, fluorescenčno spektroskopijo s tioflavinom T in presevno elektronsko mikroskopijo (TEM). Površino nanodelcev zlata (GNR) smo modificirali s polisulfonskim sulfonatom (PSS). Preučevali smo razlike v interakcijah amiloidnih vlaken z nanodelci zlata, bodisi modificiranimi ali nemedificiranimi. Analiza s presevno elektronsko mikroskopijo (TEM) je pokazala, da je površinski naboj GNR z biokompatibilnim polimerom izboljšal elektrostatske interakcije med nanodelci zlata in amiloidnimi fibrili. Analiza opravljena s testi za določanje preživetja celic pa je pokazala, da je površinska funkcionalizacija GNR izjemno izboljšala biokompatibilnost nano kompozita. Rezultati te študije spodbujajo uporabo novih strategij za pripravo prihodnjih generacij materialov, ki bi jih lahko uporabili v medicini.



Except when otherwise noted, articles in this journal are published under the terms and conditions of the Creative Commons Attribution 4.0 International License

Scientific paper

On Relationships of Eigenvalue–Based Topological Molecular Descriptors

Izudin Redžepović and Boris Furtula*

Faculty of Science, University of Kragujevac, P. O. Box 60, 34000 Kragujevac, Serbia

* Corresponding author: E-mail: boris.furtula@pmf.kg.ac.rs

Received: 08-23-2019

Abstract

Three eigenvalue-based topological molecular descriptors are compared using several datasets of alkanes. Two of them are well-known and frequently employed in various QSPR/QSAR investigations, and third-one is a newly derived whose predictive potential is yet to be proven. The relations among them are found and discussed. Structural parameters that govern these relations are identified and the corresponding formulas based on multiple linear regression have been obtained. It has been shown that all three investigated indices are encoding almost the same structural information of a molecule. They differ only by the extent of the sensitivity on a structural branching of a molecule and on the number of non-bonding molecular orbitals.

Keywords: Graph energy, Estrada index, Resolvent energy of a graph, eigenvalues, adjacency matrix.

1. Introduction

Molecular descriptors are the fundamental tools in QSPR/QSAR modeling, which are frequently employed in diverse fields of chemistry.^{1–3} Among them, topological indices are the usual choice, because of their low computational complexity and fairly simple identification of structure–property relationships.^{4–7} There are hundreds of topological descriptors.² A natural way for their classification is by the origin of parameters that are used in their definitions. Thus, one differentiates degree–, distance–, and eigenvalue–based topological molecular descriptors, although there is a couple of them that cannot be strictly designated as members of any of the above-mentioned classes.

Interest for the eigenvalue-based topological molecular descriptors had been aroused after the explanation of the physical meaning of eigenvalues in HMO theory.⁸ This happened in the seventies of the last century. Probably the first eigenvalue-based topological descriptor that had been introduced is the graph energy. This index is defined using the eigenvalues of an “ordinary” adjacency matrix in the following way:

$$E(G) = \sum_{i=1}^n |\lambda_i| \quad (1)$$

where λ_i is the i -th eigenvalue of a graph G .

The graph energy is tightly connected to the total π -electron energy of alternate conjugated molecules. It is a popular research topic both in chemically, and in mathematically oriented investigations. Several books and numerous papers are devoted to this particular topological invariant.⁹ Nowadays, there are numerous eigenvalue-based topological indices, but just a couple of them are based on the eigenvalues that come from the adjacency matrix. These indices have been used as molds for defining almost all other topological invariants belonging to this class. Thus, beside graph energy, one could find indices like Laplacian energy, distance energy, Randić energy, etc. (e.g. see^{10–12}).

Next to graph energy, the second most investigated topological molecular descriptor based on eigenvalues of an adjacency matrix is Estrada index. It was designed to model the folding in some biomolecules.¹³ Estrada index is defined as follows:

$$EE(G) = \sum_{i=1}^n e^{\lambda_i} \quad (2)$$

where λ_i is the i -th eigenvalue of a graph G .

Its undeniable success led to a vigorous research of this quantity (see^{14–16} and references cited therein). This invoked the introduction of many other Estrada-like invariants.^{10,17–19}

Recently, another topological invariant based on “ordinary” eigenvalues has been introduced.²⁰ This descriptor is named resolvent energy after the resolvent matrix which eigenvalues are used in its definition.

$$ER(G) = \sum_{i=1}^n \frac{1}{n - \lambda_i} \quad (3)$$

where $\frac{1}{n - \lambda_i}$ is the i -th eigenvalue of the resolvent matrix of the adjacency matrix of a graph.

Despite its juvenility, this quantity attracted much attention, which led to a couple of its descendants. A question that arises here is, whether there are some relationships among these topological invariants. Since the beginnings of the Estrada index, a connection between it and the energy of a graph has been investigating. Many inequalities, connecting these two descriptors, have been derived. However, the correlation between these two topological molecular descriptors seems to be never investigated. Also, the connections between the resolvent energy and the other two indices have not been tested yet.

This paper is devoted to the relationships among the recently introduced resolvent energy and other two eigenvalue-based topological descriptors. These relationships will shed a light onto relation between graph energy and the Estrada index as well.

2. Results

The results are separated into three parts. In the first subsection, the relation between graph energy and the resolvent energy of a graph will be elaborated. The second subsection is devoted to the relation between the Estrada index and the resolvent energy of a graph, and the last one is reserved for the relation between graph energy and the Estrada index. All relations are investigated in the case of alkanes.

2. 1. Graph Energy Versus Resolvent Energy

The resolvent energy of a graph has emerged in 2016 as a modification of the resolvent Estrada index, which was introduced few years before.¹⁷ Several papers have appeared dealing with the mathematical properties of this quantity.^{21–29}

Due to similar definitions of the resolvent energy (3) and the graph energy (1), the question about their relation naturally occurs. Fig. 1 shows the relation between the resolvent energy and the graph energy.

It is obvious from the Fig. 1 that the values of the graph energy are clustered into three distinct groups. Also, the values of the resolvent energy of graphs lies onto several nearly parallel lines.

We determined, by direct checking, that the values of the energy of acyclic connected graphs are classified into three distinct groups by the number of zeros ($n_0(T)$) in their spectra (number of non-bonding orbitals in a molecule). On the other hand, the values of resolvent energy are separated onto nearly parallel lines by the values of the first Zagreb index ($Zg_1(T)$) (a rough measure of a structural branching in a molecule). The alkanes that are lying on the same line have the same $Zg_1(T)$. Therefore, the correlation between the graph energy and the resolvent energy of a graph should involve these two parameters as well.

$$ER(T) \approx A \cdot E(T) + B \cdot Zg_1(T) + C \cdot n_0(T) + D \quad (4)$$

We made an in-house Python program for testing multiple linear relation shown in (4) using scikit-learn module.³⁰ Results are given in the Fig. 2 and Table 1.

The data presented in the Table 1, as well as the example shown in Fig. 2, demonstrate the remarkably good correlation between the values of the resolvent energy and the values obtained by the model given in (4). The first Zagreb index and the number of zeros in the spectra almost completely explain the dependence between the energy of graph and the resolvent energy in the case of trees.

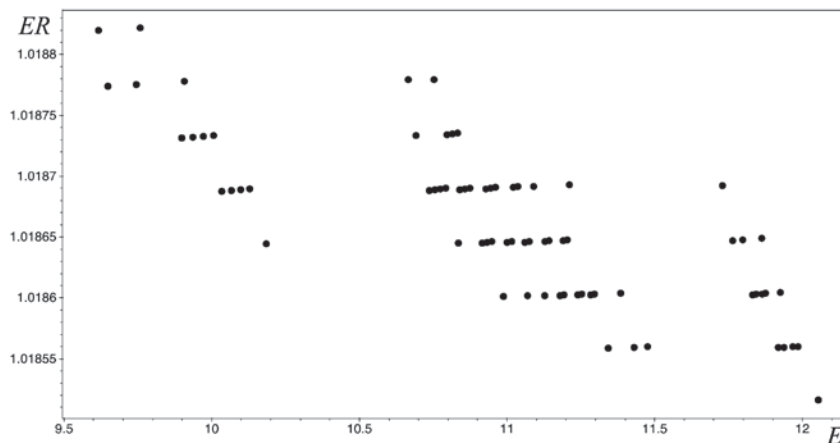


Figure 1. The relation between the resolvent energy of graph (ER) and the graph energy (E) in the case of 75 decanes.

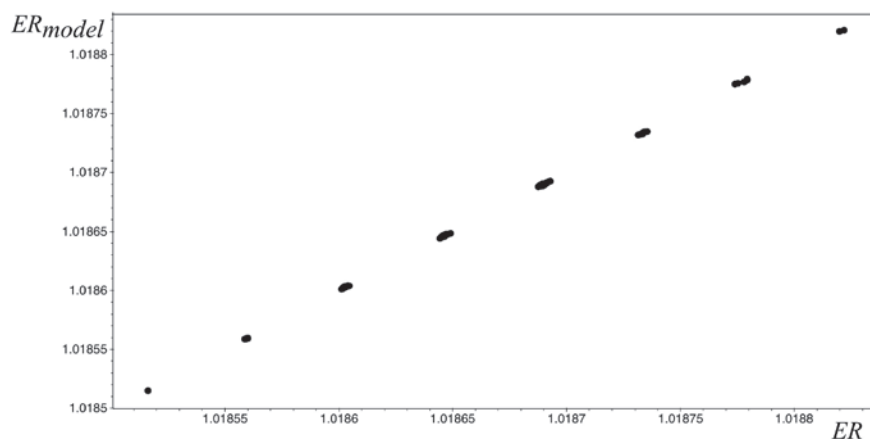


Figure 2. The correlation between the ER-values of chemical trees with 10 vertices and the values of ER calculated using eq. (4).

Table 1. Coefficients A, B, C, and D, in (4), computed to achieve the best correlation coefficient for chemical trees from 6 to 20 vertices. Last two columns contain obtained correlation coefficients and the average relative errors for all data sets used.

n	A	B	C	D	R	ARE
6	-2.21E-05	3.19E-04	-2.13E-05	1.044	1.00000	8.43E-08
7	6.90E-05	1.47E-04	2.11E-05	1.033	0.99999	1.15E-06
8	2.80E-05	7.24E-05	7.48E-06	1.026	0.99996	1.29E-06
9	1.55E-05	3.91E-05	4.56E-06	1.021	0.99998	6.39E-07
10	7.46E-06	2.25E-05	2.05E-06	1.018	0.99997	4.12E-07
11	4.01E-06	1.37E-05	1.15E-06	1.015	0.99998	2.29E-07
12	2.12E-06	8.74E-06	5.71E-07	1.013	0.99998	1.42E-07
13	1.25E-06	5.79E-06	3.48E-07	1.011	0.99998	8.71E-08
14	7.29E-07	3.96E-06	1.94E-07	1.009	0.99999	5.62E-08
15	4.61E-07	2.78E-06	1.25E-07	1.008	0.99999	3.63E-08
16	2.89E-07	2.00E-06	7.65E-08	1.007	0.99999	2.45E-08
17	1.92E-07	1.47E-06	5.11E-08	1.006	0.99999	1.67E-08
18	1.28E-07	1.10E-06	3.35E-08	1.006	0.99999	1.17E-08
19	8.83E-08	8.36E-07	2.32E-08	1.005	1.00000	8.35E-09
20	6.14E-08	6.45E-07	1.60E-08	1.005	1.00000	6.07E-09

2. 2. Estrada Index Versus Resolvent Energy

An illustrative example of correlation between the Estrada index and the resolvent energy of a graph is shown in Fig. 3.

Although the correlation in this example is quite well, it is evident that the points in Fig. 3 are clustered into several nearly parallel lines. It was empirically determined

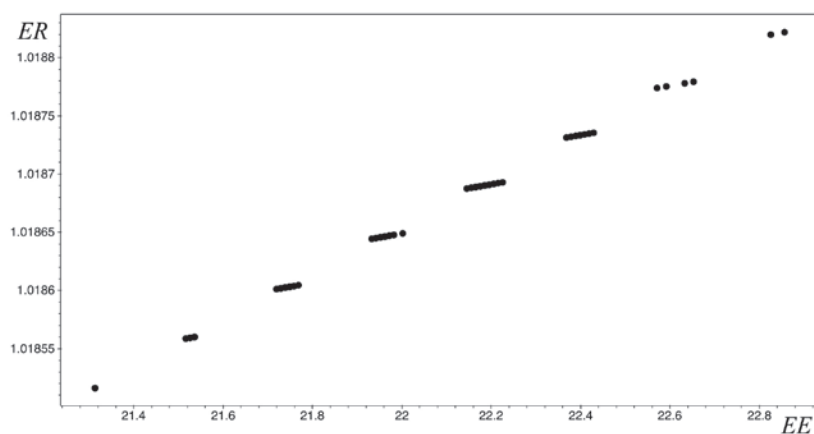


Figure 3. Correlation between the Estrada index and the resolvent energy of graph for all chemical trees with 10 vertices.

that the first Zagreb index is a parameter which governs this classification. Namely, the chemical trees belonging to a cluster have the same first Zagreb index. The relevance of this parameter for the correlation between the resolvent energy of a graph and the Estrada index is mathematically corroborated below. In order to do this, some well-known facts from spectral graph theory need to be outlined. The k -th spectral moment of a graph G is defined in the following manner:³¹

$$M_k(G) = \sum_{i=1}^n \lambda_i^k \quad (5)$$

where k is an integer greater than or equal to 0, and λ_i is the i -th eigenvalue of a graph G . The Estrada index and resolvent energy can be expressed in terms of the spectral moments using Taylor series (e.g.^{15,20}):

$$EE(G) = \sum_{k \geq 0} \frac{M_k(G)}{k!} \quad (6)$$

$$ER(G) = \sum_{k \geq 0} \frac{M_k(G)}{n^{k+1}} \quad (7)$$

Then, using formulas (6) and (7) the following equality can be established:

$$ER(G) = \frac{EE(G)}{n} + \sum_{k \geq 0} \frac{k! - n^k}{k! \cdot n^{k+1}} M_k(G) \quad (8)$$

The odd k -th spectral moments are equal to 0 in the case of bipartite graphs (the chemical trees are bipartite). Using (8), the $ER(T)$ can be approximated in terms of $EE(T)$ and a few of the first spectral moments:

$$ER(T) \approx \frac{\alpha}{n} EE(T) + \frac{1-\alpha}{n} M_0(T) + \frac{2-\alpha \cdot n^2}{2n^3} M_2(T) + \frac{24-\alpha \cdot n^4}{24n^5} M_4(T) \quad (9)$$

where α is a fitting parameter.

Since the k -th spectral moment of a graph is equal to the number of self-returning walks of the length k ,³¹ the relations between spectral moments for $k = 0, 2$, and 4 and some other, easily divisible graph invariants, are derived years ago (e.g. see³²):

$$M_0(T) = n$$

$$M_2(T) = 2(n-1) \quad (10)$$

$$M_4(T) = 2(Zg_1(T) - n + 1)$$

where n , and $Zg_1(T)$ are the number of vertices and the first Zagreb index of a tree T .

Incorporating equations shown in (10) into (9), the formula, relating the resolvent energy of a graph, Estrada index and the first Zagreb index, is obtained:

$$ER(T) \approx \frac{\alpha}{n} EE(T) - \frac{\alpha \cdot n^4 - 24}{12n^5} Zg_1(T) - \frac{11 \cdot \alpha \cdot n^4 - 24n^2 + 24}{12n^5} (n-1) - \alpha + 1 \quad (11)$$

In order to get the fitting parameter α that appears in (11), we made an in-house computer program. This program is written in Python and the α values are obtained for all chemical trees from 6 to 20 vertices. The results are shown in Table 2. The correlation coefficients are so high, and they are equal to 1 rounded to 7 decimals.

Table 2. The values of the fitting parameter α from formula (11) for which the best correlation coefficients are obtained.

n	α	n	α
6	0.0169	13	0.00013
7	0.00631	14	8.20E-05
8	0.00271	15	5.40E-05
9	0.00129	16	3.60E-05
10	0.00066	17	2.60E-05
11	0.00037	18	1.80E-05
12	0.00021	19	1.30E-05
		20	9.00E-06

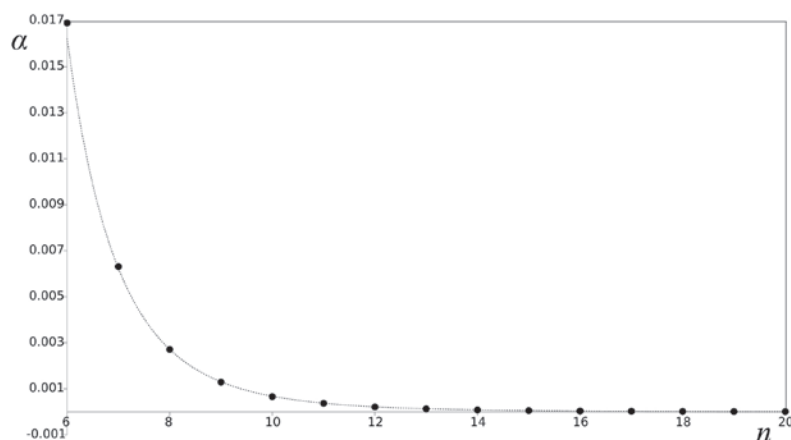


Figure 4. The relation between the fitting parameter α and the number of vertices in chemical trees.

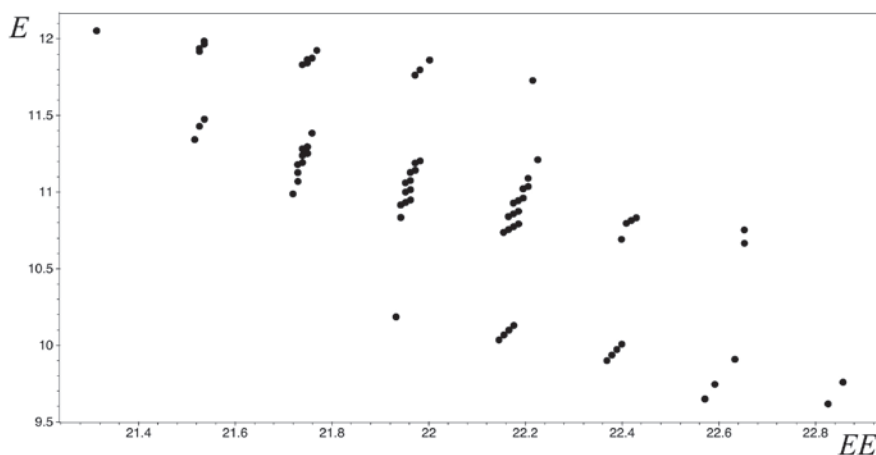


Figure 5. The relation between the Estrada index and the energy of a graph in the case of decanes.

The relation between the α and the number of vertices is given in the Fig. 4. Although this relation is rather complex, the value of α is completely determined by the n . Such finding suggests that the parameter, which solely influences the relation between the resolvent energy and Estrada index of isomeric chemical trees, is the first Zagreb index.

2. 3. Energy of Graph Versus Estrada Index

An introduction of the Estrada index also initiated the investigations of its connection with the energy of a graph. There are several papers presenting various bounds for the Estrada index in terms of the energy of a graph.^{14–16}

However, the relation between these two indices is complex and has never been investigated thoroughly. Fig. 5 shows an illustrative example of the relation between the Estrada index and the energy of a graph. The approximate relations shown in (4) and (11) suggest that the

first Zagreb index and the number of zeros in the spectra of a graph are the parameters who largely influence the relationship between the Estrada index and the graph energy in the case of trees. Thence, we conjectured that the energy of a graph could be modeled by the following formula:

$$E(T) \approx A \cdot EE(T) + B \cdot Zg_1(T) + C \cdot n_0(T) + D \quad (12)$$

We tested the conjecture given in (12) using an in-house built Python program and the results are summarized in the Table 3 and the Fig. 6.

The statistics given in the Table 3 indicate that the model (12) explains more than 98% of the data variations. ARE-values are also considerably small. However, it is evident from Figs. 5 and 6 that beside the first Zagreb index and the number of zeros in the spectra of a graph, some other parameter(s) has an influence on this relation.

Table 3. The coefficients A, B, C, and D, the correlation coefficients and the average relative errors for the model given in (12).

n	A	B	C	D	R	ARE
6	-215.6	22.85	-1.384	2224.4	0.99995	0.07%
7	12.08	-1.388	-0.314	-135.9	0.99936	0.23%
8	7.78	-0.933	-0.31	-96.5	0.99671	0.47%
9	7.48	-0.903	-0.318	-104.3	0.99746	0.36%
10	6.26	-0.771	-0.307	-94.9	0.99563	0.45%
11	5.72	-0.713	-0.322	-94.3	0.99543	0.40%
12	5.53	-0.695	-0.309	-99.1	0.99427	0.42%
13	5.21	-0.659	-0.319	-100.1	0.99423	0.41%
14	5.11	-0.65	-0.31	-105.6	0.99339	0.41%
15	4.93	-0.63	-0.315	-108.5	0.99337	0.39%
16	4.86	-0.623	-0.31	-114	0.99278	0.39%
17	4.74	-0.609	-0.312	-117.6	0.99270	0.38%
18	4.69	-0.604	-0.309	-122.9	0.99229	0.37%
19	4.6	-0.595	-0.31	-127	0.99219	0.36%
20	4.56	-0.59	-0.309	-132.2	0.99189	0.36%

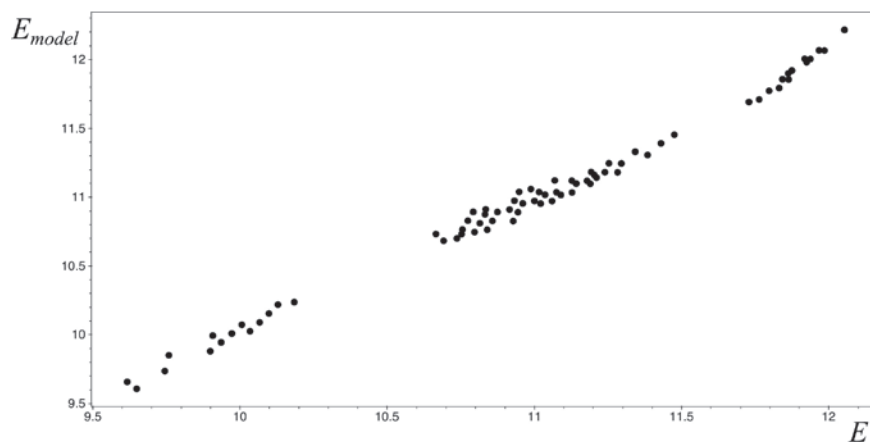


Figure 6. The model given in (12) versus the graph energy in the case of decanes.

3. Conclusion

The approximate relations among three eigenvalue-based topological indices whose definitions are based on the eigenvalues of the adjacency matrix are presented. It is shown that the first Zagreb index, as a measure of structural branching in a molecule, and the number of non-bonding orbitals, are the parameters that significantly influence these relations. In the (4) and (11) these graph invariants almost completely explain the relations between the $ER(T)$ and $E(T)$, and $ER(T)$ and $EE(T)$. The formulas (4) and (11) suggest that the relation between the $E(T)$ and $EE(T)$ can be modeled in terms of the first Zagreb index and the number of zeros in a graph. This model (12) has been tested and it is shown that it explains more than 98% of the data variation in the case of alkanes. However, for the complete description of a relation between the graph energy and the Estrada index, some other parameter(s), beside $n_0(T)$ and $Zg_1(T)$, needs to be involved.

Acknowledgments

This work was supported by the Ministry of Education, Science and Technological Development of the Republic of Serbia through the grant no. 174033.

4. References

1. A. Dudek, T. Arodz, J. Galvez, *Comb. Chem. High Throughput Screen.* **2006**, *9*, 213–228. DOI:10.2174/138620706776055539
2. R. Todeschini, V. Consonni, *Molecular Descriptors for Chemoinformatics*, Wiley-VCH, Weinheim, Germany, **2009**. DOI:10.1002/9783527628766
3. A. Mauri, V. Consonni, R. Todeschini, in: J. Leszczynski, A. Kaczmarek-Kedziera, T. Puzyn, M. G. Papadopoulos, H. Reis, M. K. Shukla (Ed.): *Handbook of Computational Chemistry*, Springer, Cham, Switzerland, **2017**, pp. 2065–2093.
4. J. Devillers, A. T. Balaban (Ed.): *Topological Indices and Related Descriptors in QSAR and QSPR*, Gordon & Breach, Amsterdam, The Netherlands, **1999**.
5. A. Talevi, C. L. Bellera, M. Di Ianni, P. R. Duchowicz, L. E. Bruno-Blanch, E. A. Castro, *Curr. Comput. Aided Drug Des.* **2012**, *8*, 172–181. DOI:10.2174/157340912801619076
6. R. Zanni, M. Galvez-Llompart, R. García-Domenech, J. Galvez, *Expert Opin. Drug Discov.* **2015**, *10*, 945–957. DOI:10.1517/17460441.2015.1062751
7. J. C. Dearden, in: K. Roy (Ed.): *Advances in QSAR Modeling – Applications in Pharmaceutical, Chemical, Food, Agricultural and Environmental Sciences*, Springer, Cham, Switzerland, **2017**, pp 57–88. DOI:10.1007/978-3-319-56850-8_2
8. D. Cvetković, I. Gutman, N. Trinajstić, *Croat. Chem. Acta* **1972**, *44*, 365–374.
9. X. Li, Y. Shi, I. Gutman, *Graph Energy*, Springer, New York, USA, **2012**.
10. G. P. Clemente, A. Cornaro, *MATCH Commun. Math. Comput. Chem.* **2017**, *77*, 673–690.
11. I. Gutman, B. Furtula, *Croat. Chem. Acta* **2017**, *90*, 359–368. DOI:10.5562/cca3189
12. N. J. Rad, A. Jahanbani, I. Gutman, *MATCH Commun. Math. Comput. Chem.* **2018**, *79*, 371–386.
13. E. Estrada, *Chem. Phys. Lett.* **2000**, *319*, 713–718. DOI:10.1016/S0009-2614(00)00158-5
14. A. Ilić, D. Stevanović, *J. Math. Chem.* **2009**, *47*, 305–314. DOI:10.1007/s10910-009-9570-0
15. B. Li, *MATCH Commun. Math. Comput. Chem.* **2017**, *77*, 701–706.
16. W. Wang, Y. Xue, *Appl. Math. Comput.* **2019**, *354*, 32–41. DOI:10.1016/j.amc.2019.02.019
17. X. Chen, J. Qian, *MATCH Commun. Math. Comput. Chem.* **2015**, *73*, 163–174.
18. J. Li, L. Qiao, N. Gao, *Appl. Math. Comput.* **2018**, *317*, 143–149. DOI:10.1016/j.amc.2017.09.015
19. Y. Shang, *Bull. Aust. Math. Soc.* **2013**, *88*, 106–112. DOI:10.1017/S0004972712000676
20. I. Gutman, B. Furtula, E. Zogić, E. Glogić, *MATCH Commun.*

- Math. Comput. Chem.* **2016**, *75*, 279–290.
21. L. E. Allem, J. Capaverde, V. Trevisan, I. Gutman, E. Zogić, E. Glogić, *MATCH Commun. Math. Comput. Chem.* **2017**, *77*, 95–104.
22. M. Bianchi, A. Cornaro, J. L. Palacios, A. Torriero, *MATCH Commun. Math. Comput. Chem.* **2018**, *80*, 459–465.
23. K. C. Das, *MATCH Commun. Math. Comput. Chem.* **2019**, *81*, 453–464.
24. Z. Du, *MATCH Commun. Math. Comput. Chem.* **2017**, *77*, 85–94.
25. A. Farrugia, *Appl. Math. Comput.* **2018**, *321*, 25–36.
DOI:10.1016/j.amc.2017.10.020
26. M. Ghebleh, A. Kanso, D. Stevanović, *MATCH Commun. Math. Comput. Chem.* **2017**, *77*, 635–654.
DOI:10.1007/s11042-017-4634-9
27. I. Gutman, B. Furtula, E. Zogić, E. Glogić, E. in: I. Gutman, X. Li (Ed.): *Energies of Graphs – Theory and Applications*, Univ. Kragujevac, Kragujevac, Serbia, **2016**, pp. 277–290.
28. Z. Zhu, *J. Math. Anal. Appl.* **2017**, *447*, 957–970.
DOI:10.1016/j.jmaa.2016.10.043
29. E. H. Zogić, E. R. Glogić, *Sci. Publ. State Univ. Novi Pazar* **2017**, *9A*, 187–191. DOI:10.5937/SPSUNP1702187Z
30. F. Pedregosa, G. Varoquaux, A. Gramfort, V. Michel, B. Thirion, O. Grisel, M. Blondel, P. Prettenhofer, R. Weiss, V. Dubourg, J. Vanderplas, A. Passos, D. Cournapeau, M. Brucher, M. Perrot, É. Duchesnay, *J. Mach. Learn. Res.* **2011**, *12*, 2825–2830.
31. D. Cvetković, M. Doob, H. Sachs, *H. Spectra of Graphs – Theory and Application*, Johann Ambrosius Barth Verlag: Heidelberg, Leipzig, Germany, **1995**.
32. I. Gutman, K. C. Das, *MATCH Commun. Math. Comput. Chem.* **2004**, *50*, 83–92.

Povzetek

Tri topološke molekularne deskriptorje smo primerjali s podatkovnimi bazami alkanov. Dva od teh deskriptorjev sta dobro znana in pogosto uporabljena v različnih QSPR/QSAR preiskavah, tretji pa je na novo izpeljan in je treba njegove napovedovalne možnosti še dokazati. Našli smo povezave med temi deskriptorji in o njih razpravljali. Z uporabo večkratne linearne regresije smo opredelili strukturne parametre in ustrezne enačbe, ki določajo te povezave. Pokazali smo, da vsi trije preiskovani indeksi kodirajo skoraj iste strukturne informacije o molekuli. Razlikujejo se le po obsegu občutljivosti na strukturno razvejanje molekule in po številu neveznih molekulskih orbital.



Except when otherwise noted, articles in this journal are published under the terms and conditions of the Creative Commons Attribution 4.0 International License

Scientific paper

Ab-Initio Study of Citrate Ion as an Oxygen-Rich Complexing Agent

Armando G. Rojas-Hernández,¹ Aned de Leon,^{2,*} Rafael A. Sabory-García,¹ Rafael Ramírez-Bon,³ Dainet Berman-Mendoza¹ and Santos J. Castillo¹

¹ Departamento de Investigación en Física, Universidad de Sonora, Blvd. Luis Encinas y Rosales S/N, Col. Centro, Hermosillo, Sonora, México

² Centro de Investigación y Estudios Avanzados del IPN. Unidad Querétaro. Apdo. Postal 1-798, 76001, Querétaro, Qro. México

³ Departamento de Ciencias Químico-Biológicas, Universidad de Sonora, Blvd. Luis Encinas y Rosales S/N, Col. Centro, Hermosillo, Sonora, México

* Corresponding author: E-mail: aned.deleon@unison.mx

Received: 08-29-2019

Abstract

Theoretical studies on conformational analysis, geometry optimizations and frequencies for citrate at the MP2/LANL2DZ level portrait it as a promising candidate for a complexing agent for cadmium (II) ion (Cd^{2+}) and cadmium sulfide (CdS). Natural Bond Orbital (NBO) charges, Delocalization Indices, HOMO/LUMO gaps and surfaces along with absolute electronegativity values were employed to analyze the interactions among the configurations obtained. The most stable structures involved the interaction between the LUMO of Cd^{2+} /CdS and the most dense region of the HOMO of the citrate ion.

Keywords: HOMO/LUMO surfaces; complexing agent; CdS; citrate ion

1. Introduction

The synthesis of CdS films, which are used on solar cells through a cheap technique such as chemical bath deposition (CBD) [1] is highly dependable on the complexing agent used. The optimum semiconductor films are produced modulating temperature [2], pH [3] and reactive concentration [4]. In this technique, the thin films are deposited on substrates in contact with dilute chemical baths containing metallic ions. Thus, the morphology of the film is highly dependent on the precipitation of the solid phase. Therefore, the complexing agents play a crucial role on the structure of the thin film being deposited. One of the complexing agents used experimentally is ammonia [5]. However, its volatility and toxicity have contributed to a search for other materials. Among them, are ethylene-diamine (ED) [6], ethylenediaminetetraacetic acid (EDTA) [6], polyethyleneimine [7], acetylacetone [8] and glycine [9]. There are only a handful of complexing agents proposed and few studies on the interactions involved between complexing agents and CdS. Our aim is to propose new com-

plexing agents that can show a good affinity with CdS to enhance the homogeneity of the morphology and structure of the film. We propose citrate ion as a complexing agent for CdS based on our previous studies [9,10] that show a high relationship between the stability of CdS and an oxygen-rich complexing agent. The main goal of this paper is to analyze the participation of the oxygens in the citrate ion on the interaction between it and Cd^{2+} /CdS through charges, delocalization indices, HOMO/LUMO and absolute electronegativity.

2. Methodology

We employed Gaussian 09 [11] software for ab-initio quantum mechanical calculations at the second order perturbation Møller Plesset MP2 [12] level of theory in conjunction with the LANL2DZ [13] basis set. We used global orbital cutoffs and fine convergence criteria. We examined the Hessian matrix to confirm the energy minima configurations had only positive vibrational frequencies which

pertain to energy minima and not transition states. Basis set superposition error (BSSE) [14] calculations and zero-point energies were employed to correct the energies.

Dissociation energies (ΔE) were obtained from:

$$\Delta E = E_{\text{system}} - E_{\text{citrate ion}} - E_{\text{Cd}^{2+}/\text{CdS}}, \quad (1)$$

where system refers to the system formed by Cd^{2+} or CdS and the citrate ion. The terms $E_{\text{citrate ion}}$ and $E_{\text{Cd}^{2+}/\text{CdS}}$ refer to the energy in kcal/mol of the optimized structures of the citrate ion, Cd^{2+} and CdS on an individual level, respectively. In the first set of results, we studied the systems Cd^{2+} -citrate ion, while the second set of results pertain to the CdS-citrate ion systems. For all the systems, we calculated the difference between the Lowest Unoccupied Molecular Orbital (LUMO) and the Highest Occupied Molecular Orbital (HOMO) referred to as GAP in eV in Table 1.

We calculated absolute electronegativity, χ , for all the systems [15],

$$\chi = \frac{I + A}{2} \quad (2)$$

where $-\epsilon_{\text{HOMO}} = I$ and $-\epsilon_{\text{LUMO}} = A$.

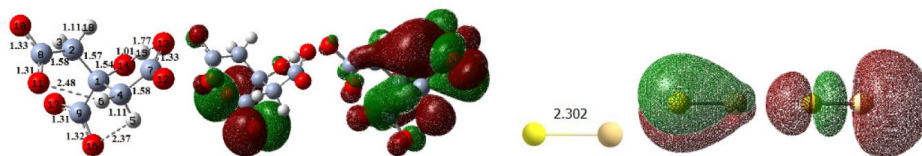


Figure 1. Selected geometrical parameters of citrate ion and CdS whereby bond lengths are in angstroms (Å). HOMO and LUMO surfaces are depicted for both substances.

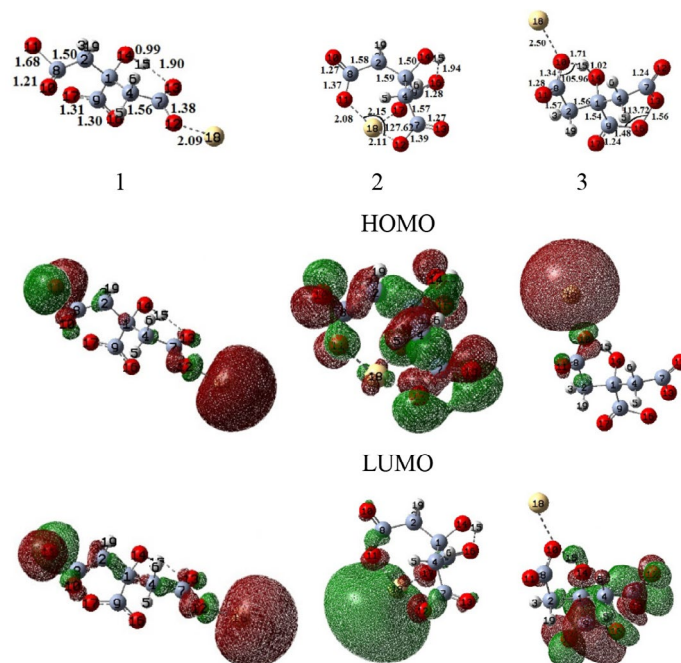


Figure 2. Selected geometrical parameters of the systems citrate ion-Cd whereby bond lengths are in angstroms (Å) and angles in °. HOMO and LUMO surfaces are depicted for all the configurations.

In addition, we report charges in au obtained via Natural Bond Orbital (NBO) analyses [16] using Gaussian 09. Delocalization indices, DI(A,B) between atoms A and B, were calculated through the AIMALL software [17] to analyze bonds and interactions between the atoms in the molecular species.

3. Results and Discussion

The interaction between citrate ion and cadmium (pale yellow) can be considered an acid-base one. The calculated values of χ for the citrate ion and cadmium were of 4.78×10^{-20} J and 1.87×10^{-20} J, respectively. It is expected that Cd^{2+} attracts electrons and the citrate ion donates them. This is confirmed by NBO charges and delocalization indices.

Figure 1 shows the optimized geometry of citrate ion and the CdS in conjunction with their HOMO and LUMO surfaces. The energy minima configurations formed by the interaction between citrate ion and Cd^{2+} are depicted in Figure 2 in order of stability whereas the first structure is the most stable.

In structure 1, the citrate ion displays 3 hydrogen bonds involving its deprotonated carboxyl groups with de-

localization indices of $DI(H6,O11) = 0.04$, $DI(O13,H15) = 0.10$ and $DI(H5,O16) = 0.04$ and distances of 2.48 Å, 1.77 Å and 2.37 Å, respectively. The first structure of Fig. 2 has a dissociation energy of -1065.20 KJ/mol. To form this structure, C4 and C7 moved their attached atoms to interact with cadmium. It shares one hydrogen bond with citrate ion from Fig.1, yet with a smaller $DI(O13,H15) = 0.06$. The transfer of electrons from the citrate ion to cadmium is confirmed by its decrease in charge to 0.85 au and $DI(O12,Cd18) = 0.51$. Structure 2 has a dissociation energy of -798.36 KJ/mol. It does not retain any of the hydrogen bonds the lone citrate ion had, which could account for an increase in energy compared to structure 1. However, its high stability is most likely supported by the interaction of Cd with the ion on the region where most of the citrate ion's HOMO is located. It forms 1 hydrogen bond with $DI(H15,O16) = 0.06$ and shows charge transfer between Cd and 3 oxygens with DI values of $DI(O11,Cd18) = 0.47$, $DI(O12,Cd18) = 0.48$, $DI(O17,Cd18) = 0.39$ and

Table 1. MP2/LANL2DZ dissociation energies with zero point corrections, HOMO/LUMO gaps and absolute electronegativity (X) are listed under $\Delta E(0K)$ in kJ/mol; GAP and χ in ($\times 10^{-19}$ J), respectively, shown on Figs. 1–3.

System	ΔE	GAP	X
1	-1065.20	2.40	0.16
2	-798.36	17.6	0.15
3	-283.34	2.68	0.15
4	-518.36	14.7	0.38
5	-514.16	14.8	0.38
6	-506.40	14.7	0.38
7	-499.44	14.8	0.31
8	-478.53	14.9	0.32
9	-470.91	14.9	0.32
10	-241.98	18.0	0.33

Table 2. Delocalization Indices of citrate ion and structures 1–3.

A	B	DI(A,B) citrate	1	2	3
C8	O10	1.24	1.51	1.41	1.14
H6	O11	0.04	-	-	-
C8	O11	1.28	0.75	1.04	1.38
C7	O12	1.28	1.02	1.05	1.53
C7	O13	1.21	1.34	1.44	0.82
O10	H15	-	-	-	0.10
O13	H15	0.10	0.06	-	-
H5	O16	0.04	-	-	-
C9	O16	1.25	1.30	1.37	0.83
O13	O16	-	-	-	1.08
H15	O16	-	-	0.06	-
C9	O17	1.27	1.30	1.11	1.54
O10	Cd18	-	-	-	0.26
O11	Cd18	-	-	0.47	-
O12	Cd18	-	0.51	0.48	-
O17	Cd18	-	-	0.39	-

distances of 2.08 Å, 2.11 Å and 2.15 Å, leaving Cd with a charge of 1.65 au. Structure 3 is the least stable system. It does not retain any of the lone citrate ion's hydrogen bonds. It forms a hydrogen bond with $DI(O10,H15) = 0.10$. It also forms a single bond between 2 oxygens, with $DI(O13,O16) = 1.08$ which increases the repulsion between them, rising

Table 3. NBO charges in a.u. for citrate ion and systems 1–3.

	citrate	1	2	3
C1	0.28	0.28	0.25	0.25
C2	-0.54	-0.57	-0.54	-0.53
H3	0.23	0.32	0.24	0.25
C4	-0.56	-0.53	-0.56	-0.54
H5	0.23	0.25	0.21	0.24
H6	0.25	0.22	0.27	0.28
C7	1.00	1.08	0.98	0.99
C8	1.00	1.01	0.99	0.99
C9	1.00	0.95	0.97	0.98
O10	-0.98	-0.64	-0.76	-1.00
O11	-0.93	-0.47	-1.05	-0.80
O12	-0.93	-1.05	-1.04	-0.64
O13	-0.97	-0.84	-0.74	-0.34
O14	-0.93	-0.88	-0.87	-0.87
H15	0.52	0.54	0.53	0.56
O16	-0.95	-0.89	-0.79	-0.38
O17	-0.93	-0.88	-1.00	-0.63
Cd18	-	0.86	1.65	-0.02
H19	0.20	0.24	0.26	0.23

Table 4. Delocalization Indices of structures 4–10

A	B	DI(A,B)						
		4	5	6	7	8	9	10
H6	O10	-	-	-	0.04	-	-	-
C8	O10	1.27	1.27	1.10	1.20	1.25	1.19	1.54
H6	O11	0.04	0.04	-	-	-	-	-
C8	O11	1.27	1.27	1.35	1.19	1.27	1.22	0.91
C9	O11	-	-	-	-	-	-	0.76
H3	O12	-	-	0.05	-	-	-	-
C7	O12	1.29	1.33	1.27	1.28	1.16	1.25	1.27
C7	O13	1.15	1.09	1.26	1.23	1.24	1.28	1.06
O10	H15	-	-	-	-	0.07	-	-
O12	H15	0.06	-	-	-	-	-	-
O13	H15	-	-	-	0.09	-	-	-
C9	O16	1.09	1.34	1.37	1.24	1.24	1.30	0.54
O13	O16	-	-	-	-	-	-	1.04
H15	O16	-	-	-	-	-	-	-
C9	O17	1.36	1.10	1.08	1.31	1.32	1.24	1.29
H15	O17	-	0.07	0.05	-	-	0.07	-
O10	Cd19	-	-	0.33	0.28	-	0.30	-
O11	Cd19	-	-	-	0.30	-	0.27	-
O12	Cd19	-	-	-	-	0.30	-	0.30
O13	Cd19	0.30	0.31	-	-	0.30	-	-
O14	Cd19	-	-	-	-	-	-	0.30
O16	Cd19	0.32	-	-	-	-	-	-
O17	Cd19	-	0.30	0.31	-	-	-	-
S18	Cd19	1.22	1.23	1.22	1.33	1.32	1.32	1.02

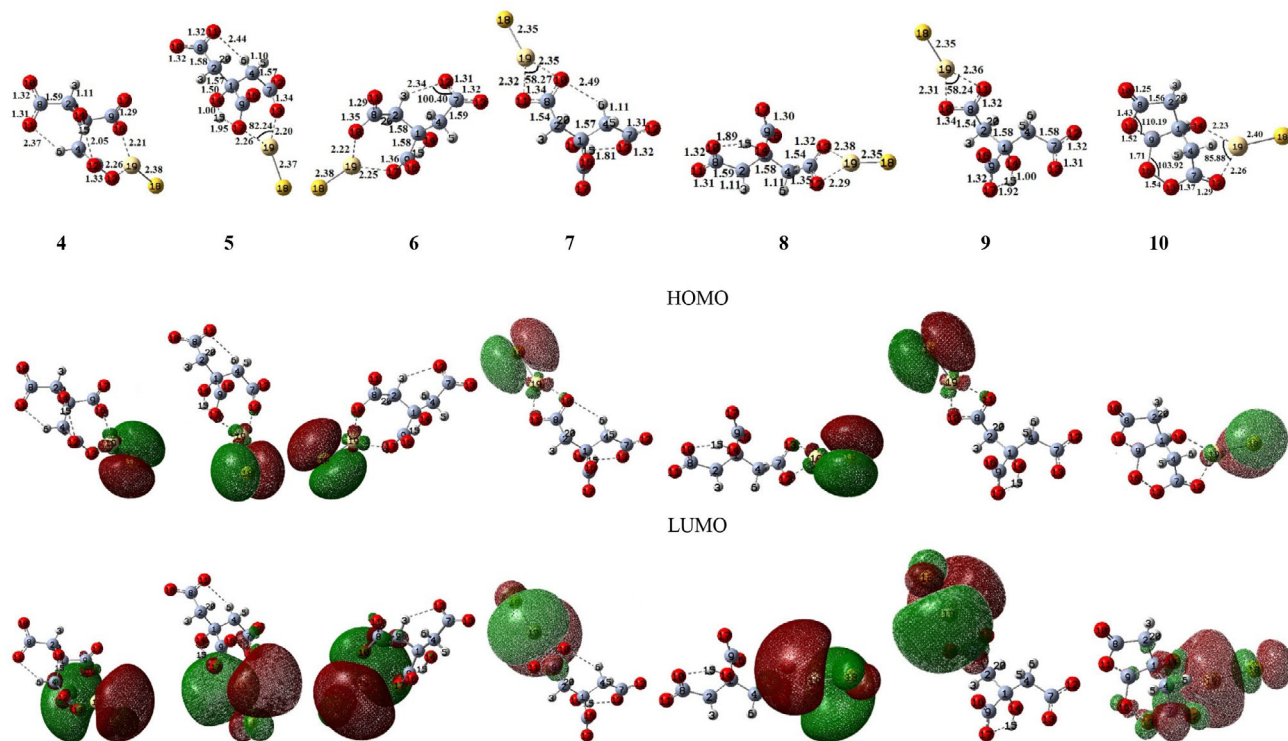


Figure 3. Selected geometrical parameters of the systems citrate ion-CdS whereby bond lengths are in angstroms (Å) and angles in °. HOMO and LUMO surfaces are depicted for all the configurations.

the dissociation energy to -283.34 KJ/mol and the charge of Cd to -0.02 au. Structures 1–3 all showed similar absolute electronegativity values of 1.60×10^{-20} J, 1.53×10^{-20} J and 1.52×10^{-20} J, respectively. HOMO/LUMO gaps of structures 1 and 3 were very similar, with values of 2.40×10^{-19} J and 2.68×10^{-19} J, respectively, while that of structure 2 was of 1.76×10^{-18} J indicating its lower ability as a conductor in comparison.

The next set of structures (4–10) are the energy minima geometries of the interaction between citrate ion and CdS. As in structures 1–3, the transfer of electrons happens from the citrate ion to CdS. Observing Fig. 1, the LUMO is denser on Cd, which indicates it is prone to accepting electrons. It can also be seen that the HOMO of the citrate ion lies mostly on the deprotonated carboxyl groups from $(\text{O}16\text{-C}9\text{-O}17)^-$, to a lesser extent on $(\text{O}10\text{-C}8\text{-O}11)^-$ and on $(\text{O}12\text{-C}7\text{-O}13)^-$. The most stable structures of this set (4–6) show interactions between Cd19 and the $(\text{O}16\text{-C}9\text{-O}17)^-$ group.

Configuration 4 is the most stable structure of this set with a dissociation energy of -518.36 KJ/mol. The interaction of Cd19 is with O13 and O16, with delocalization indices of $\text{DI}(\text{O}13, \text{Cd}19) = 0.30$ and $\text{DI}(\text{O}16, \text{Cd}19) = 0.32$. The charges of Cd and S were of 1.21 au and -1.38 au, respectively. Structure 5 has a dissociation energy of -514.16 KJ/mol, very close to that of structure 4. Its interactions also occur with oxygens of different deprotonated carboxyl groups. Its DI values were of $\text{DI}(\text{O}13, \text{Cd}19) = 0.31$ and $\text{DI}(\text{O}17, \text{Cd}19) = 0.30$. The charges of Cd and S

Table 5. NBO charges in a.u. for systems 4–10.

	4	5	6	7	8	9	10
C1	0.29	0.28	0.29	0.28	0.28	0.29	0.15
C2	-0.52	-0.52	-0.53	-0.52	-0.53	-0.51	-0.27
H3	0.22	0.21	0.27	0.23	0.19	0.23	0.14
C4	-0.54	-0.53	-0.53	-0.55	-0.51	-0.53	-0.27
H5	0.21	0.21	0.22	0.22	0.25	0.23	0.15
H6	0.27	0.26	0.22	0.23	0.20	0.20	0.12
C7	1.01	1.03	1.00	1.00	1.05	1.00	0.52
C8	1.00	0.99	1.00	1.05	1.00	1.04	0.48
C9	0.98	0.99	0.98	0.96	0.96	0.97	0.50
O10	-0.94	-0.94	-1.00	-0.94	-0.93	-0.95	-0.32
O11	-0.93	-0.93	-0.84	-0.94	-0.93	-0.92	-0.34
O12	-0.89	-0.86	-0.93	-0.92	-0.96	-0.96	-0.42
O13	-0.97	-1.02	-0.95	-0.94	-0.90	-0.92	-0.20
O14	-0.87	-0.88	-0.87	-0.90	-0.90	-0.91	-0.49
H15	0.51	0.51	0.50	0.54	0.54	0.53	0.29
O16	-1.02	-0.84	-0.81	-0.96	-0.96	-0.90	-0.16
O17	-0.82	-1.01	-1.02	-0.89	-0.88	-0.94	-0.43
S18	-1.38	-1.38	-1.38	-1.33	-1.34	-1.33	0.27
Cd19	1.21	1.21	1.20	1.14	1.15	1.15	0.66
H20	0.20	0.21	0.19	0.24	0.23	0.22	0.13

showed the same values as in structure 4. In structure 6, Cd interacts with 2 oxygens of different groups, with DI values of $\text{DI}(\text{O}10, \text{Cd}19) = 0.33$ and $\text{DI}(\text{O}17, \text{Cd}19) = 0.31$. Its dissociation energy is very close to that of structures 4 and 5, with a value of -506.40 kcal/mol. The charges of Cd

and S were almost the same as in the last two structures, with values of 1.20 and -1.38 au, respectively. Structures 4–6 had similar values of HOMO/LUMO gaps and absolute electronegativities.

Configuration 7, with a dissociation energy of -499.44 KJ/mol depicts the interaction between Cd19 and two oxygens of the same functional group with $DI(O10, Cd19) = 0.28$ and $(DI(O11, Cd19) = 0.30$. It shows two hydrogen bonds with $DI(H6, O10) = 0.04$ and $DI(O13, H15) = 0.09$. The charges of Cd and S were of 1.14 au and -1.33 au. Configuration 8 interacts with two oxygens of the functional group $(O12-C7-O13)^-$ with $DI(O12, Cd19) = 0.30$ and $DI(O13, Cd19) = 0.30$ but only has one hydrogen bond with $DI(O10, H15) = 0.07$. This could account for a smaller dissociation energy of -478.53 KJ/mol. The charges of Cd and S are similar to those of structure 7, with values of 1.15 au and -1.34 au, respectively. For Structure 9, similarly as in structure 7, the interaction between Cd and citrate is with the same functional group, with $DI(O10, Cd19) = 0.30$ and $DI(O11, Cd19) = 0.27$. It only has one hydrogen bond with $DI(H15, O17) = 0.07$ with a dissociation energy of -470.91 KJ/mol. Absolute electronegativity for systems 7–9 have similar values of electronegativity (1.48×10^{-18} J for 7 and 1.49×10^{-18} J for structures 8 and 9). Their HOMO/LUMO gaps are quite similar, with values of 3.12×10^{-20} J, 3.20×10^{-20} J and 3.19×10^{-20} J.

The last structure, configuration 10 portrays the least stable structure with a dissociation energy of -241.98 KJ/mol. This great difference in energy could be due to a bond formed between O13 and O16 with $DI(O13, O16) = 1.04$. As for the interactions between Cd and oxygens, $DI(O12, Cd19) = 0.30$ and $DI(O14, Cd19) = 0.30$. The charges of Cd and S were of 0.66 and 0.27, greatly influenced by the O13-O16 bond. This last structure has an absolute electronegativity of 3.28×10^{-20} J and a larger HOMO/LUMO gap of 1.80×10^{-18} J.

4. Conclusions

The oxygens in the citrate ion played on important role on the interaction between it and Cd^{2+}/CdS . This was described by NBO charges, delocalization indices, HOMO/LUMO surfaces, gap and electronegativity. The transfer of electrons occurs from the citrate ion to Cd^{2+} or CdS. The most stable structures are formed when the deprotonated carboxyl groups on the citrate ion with greater HOMO density participate. The calculations that support this were dissociation energies, charges, delocalization indices, HOMO/LUMO and electronegativity.

The most stable structure for citrate ion- Cd^{2+} was formed from the interaction $DI(O12, Cd18) = 0.51$, portraying 3 hydrogen bonds. The most stable structure for citrate ion-CdS displayed $DI(O13, Cd19) = 0.30$ and $DI(O16, Cd19) = 0.32$ with also 3 hydrogen bonds. The

least stable structures 3 and 10 both show the formation of a O13-O16 bond with DI's of 1.08 and 1.04 au, respectively and no hydrogen bonds.

Acknowledgements

CONACyT and ACARUS of the University of Sonora are thanked for their support.

5. References

- G. Hodes, Chemical Solution Deposition of Semiconductor Films, Marcel Dekker Inc., New York, Basel, **2003**. DOI:10.1201/9780203909096
- Rabeel, Z.; Abbas, M.; Basit, M.; Shah, N. A.; Ahmad I.; Ul Hassan, M. S. U. J. Adv. Nanomater. **2017**, 2, 112–120.
- J. Barman, J. P. Borah, K. C. Sarma, Chalcogenide Letters **2008**, 5, 265–271.
- H. Khallaf, I. O. Oladeji, G. Chai, L. Chow, Thin Solid Films **2008**, 516, 7306–7312. DOI:10.1016/j.tsf.2008.01.004
- J. L. Chen, S. F. Yang, C. C. Wu, S. Ton, Separation and Purif. Tech. **2011**, 79, 157–163. DOI:10.1016/j.seppur.2011.02.029
- S. Soundeswaran, O. Senthil Kumar, R. F. Dhanasekaran, Mater. Lett. **2004**, 58, 2381–2385. DOI:10.1016/j.matlet.2004.02.012
- A. de Leon, M. C. Acosta-Enrriquez, A. F. Jalbout, A. Apolinar-Iribe, S.J. Castillo, J. Mol. Struct: THEOCHEM **2010**, 957, 90–93. DOI:10.1016/j.theochem.2010.07.013
- A. de Leon, F. Rocha-Alonso, E. F. Velázquez, S. J. Castillo, A. Apolinar-Iribe, Chalcogenide Letters, **2013**, 10, 555–564.
- A. de Leon, M. C. Acosta-Enrriquez, S. J. Castillo, D. Berman-Mendoza, A. F. Jalbout, J. Mol. Struct: THEOCHEM **2010**, 951, 34–36. DOI:10.1016/j.theochem.2010.04.003
- A. de Leon, M. Ruiz-Preciado, M. A. Quevedo-Lopez, A. G. Rojas-Hernandez, A. de Leon, A. Apolinar-Iribe, R. Ochoa-Landin, G. Valencia-Palomo, S. J. Castillo, Digest J. Nanomater. Biostruct. **2017**, 4, 1057–1067.
- Gaussian 09, Revision A.02, M. J. Frisch, G. W. Trucks, H. B. Schlegel, G. E. Scuseria, M. A. Robb, J. R. Cheeseman, G. Scalmani, V. Barone, G. A. Petersson, H. Nakatsuji, X. Li, M. Caricato, A. Marenich, J. Bloino, B. G. Janesko, R. Gomperts, B. Mennucci, H. P. Hratchian, J. V. Ortiz, A. F. Izmaylov, J. L. Sonnenberg, D. Williams-Young, F. Ding, F. Lipparini, F. Egidi, J. Goings, B. Peng, A. Petrone, T. Henderson, D. Ranasinghe, V. G. Zakrzewski, J. Gao, N. Rega, G. Zheng, W. Liang, M. Hada, M. Ehara, K. Toyota, R. Fukuda, J. Hasegawa, M. Ishida, T. Nakajima, Y. Honda, O. Kitao, H. Nakai, T. Vreven, K. Throssell, J. A. Montgomery, Jr., J. E. Peralta, F. Ogliaro, M. Bearpark, J. J. Heyd, E. Brothers, K. N. Kudin, V. N. Staroverov, T. Keith, R. Kobayashi, J. Normand, K. Raghavachari, A. Rendell, J. C. Burant, S. S. Iyengar, J. Tomasi, M. Cossi, J. M. Millam, M. Klene, C. Adamo, R. Cammi, J. W. Ochterski, R. L. Martin, K. Morokuma, O. Farkas, J. B. Foresman, and D. J. Fox, Gaussian, Inc., Wallingford CT, 2016.

12. M. Head-Gordon, J. A. Pople, M.J. Frisch, *J. Chem. Phys. Lett.* **1988**, 153, 503–506. DOI:10.1016/0009-2614(88)85250-3
13. T. H. Dunning, Jr., P. J. Hay, In *Modern Theoretical Chemistry*; Schaefer III, H. F., Ed. Vol. 3, Plenum Press: New York, **1976**; pp. 1–28.
14. S. Simon, M. Duran, J. J. Dannenberg. *J. Chem. Phys.* **1996**, 105, 11024–11031. DOI:10.1063/1.472902
15. R. G. Pearson *Inorg. Chem.* **1988**, 27, 734–740. DOI:10.1021/ic00277a030
16. F. Weinhold, “Natural Bond Orbital Methods,” in *Encyclopedia of Computational Chemistry*, Schleyer, P.v.R.; Allinger, N. L.; Clark, T.; Gasteiger, J.; Kollman, P. A.; Schaefer III, H. F.; Schreiner P. R. (Eds.), (John Wiley & Sons, Chichester, UK, **1998**), Vol. 3, pp. 1792–1811.
17. T.A. Keith, AIMALL (Version 19.02.13), TK Gristmill Software, Overland Park KS, USA, **2019** (aim.tkgristmill.com)

Povzetek

Teoretične študije o konformacijski analizi, geometrijski optimizaciji in frekvencah na ravni MP2/LANL2DZ predstavljajo citrat kot obetavnega kandidata za kompleksirajoče sredstvo za kadmijev (II) ion (Cd^{2+}) in kadmijev sulfid (CdS). Za analizo medsebojnih vplivov med pridobljenimi konfiguracijami so bili uporabljeni naravni naboji orbital (Natural Bond Orbital or NBO), indeksi delokalizacije, HOMO/LUMO vrzeli in površine ter absolutne vrednosti elektronegativnosti. Najbolj stabilne strukture so vključevale interakcijo med LUMO Cd^{2+} /CdS in najbolj gostim območjem HOMO citratnega iona.



Except when otherwise noted, articles in this journal are published under the terms and conditions of the Creative Commons Attribution 4.0 International License

Scientific paper

Synthesis of New Quaternary Ammonium Salts with a Terpene Function and Evaluation of their Fungicidal and Herbicidal Activities

Krzysztof Żelechowski, Mirosław Gućma, W. Marek Gołębiewski,*
Maria Krawczyk and Alicja Katarzyna Michalczyk

Lukasiewicz Research Network - Institute of Industrial Organic Chemistry, Annopol 6, 03-236 Warsaw, Poland

* Corresponding author: E-mail: golebiewski@ipo.waw.pl

Telephone: 48 22 811 1231; fax: 48 22 811 0799

Received: 09-18-2019

Abstract

A series of new quaternary ammonium salts (QASs) containing a terpenoid moiety derived from perillyl alcohol, citronellol, and geraniol was synthesized. Structures of all novel compounds were confirmed by spectral methods and elemental analyses. Fungicidal activity of the obtained compounds against six plant pathogens, against four fungi destroying wood and technical materials as well as herbicidal activity against ten species of temperate climate weeds has been examined. Several salts showed a higher antifungal and herbicidal activity than activity of the reference compounds.

Keywords: Ammonium salts; fungicides; herbicidal activity; NMR spectroscopy; terpenoids

1. Introduction

Quaternary ammonium salts (QASs) are cationic surfactants widely used to combat microorganisms in clinical and industrial applications for the disinfection of surfaces. They are amphoteric compounds containing a quaternary nitrogen atom which is bound to at least one major hydrophobic substituent, such as alkyl, and an anion. The ability to reduce the surface tension facilitates adsorption of the cation on the cell surface and penetration of hydrophobic residues of microbicidal action to the cell membrane of microorganisms. QASs are also used as *inter alia* fabric softeners,^{1,2} antistatic and wood protection agents.³ It was found that salts with alkyl chain length of $n = 12-14$ had the greatest activity against Gram-positive bacteria and yeasts,⁴ while salts with $n = 14-16$, had a maximum activity against Gram-negative bacteria. QASs with aromatic spacers and alkyl groups of different length and different number of charged nitrogen atoms were examined.⁵ The structure-activity relationship (SAR) and modes of action of bis QASs have been discussed.⁶

Few biocides can fight both fungi and insects. These agrochemicals include quaternary ammonium salts, such as didecyltrimethylammonium chloride (DDAC) and benzalkonium chlorides (BAC), having a low toxicity to warm-blooded organisms.⁷

Antimicrobial activity of quaternary ammonium pyridinium (QPy) salts was examined addressing the problem of increasing resistance of microorganisms caused by misuses of QASs.⁸ pH sensitive QPy salts were prepared which activity was controlled by adjusting pH to low values.⁹ QASs containing other heterocyclic systems such as benzofuroxan,¹⁰ pyridobenzodiazepine were also prepared.¹¹

Another approach to avoid microbial resistance was an application of gemini QASs (double head – double tail type).^{12,13}

An effect of organic counterions on antibacterial activity was discussed.¹⁴

Conjugates of QASs with steroids were prepared and shown to exhibit a broad spectrum of antimicrobial activity.¹⁵

Antimicrobial polymers were developed to increase efficiency, selectivity and durability of the low molecular weight agents.¹⁶ Another examples were QASs immobilized on dendrimers,¹⁷ hydroxy QASs as components of polyurethane foams¹⁸ or natural modified polymers (chitosan).¹⁹

Another new group of organic biocides were ionic liquids: pyridinium,²⁰ imidazolium,²¹ ammonium and triazolium.²²

Terpenes are regarded as defensive compounds in plants, offering them protection against herbivores.²³ Terpenes are used in control of termites and other urban pests.^{24,25} Terpenes as residual plant material are used also in composite products resistant to termite degradation.²⁶ Terpene-baited traps are applied to control the pine sawyer beetle.²⁷ Hinokitiol, a natural monoterpenoid found in the wood of trees in the family Cupressaceae, displays insecticidal and fungicidal activities against wood-rotting fungi.²⁸ Essential oils isolated from the leaves and twigs of *Litsea acutivena* plant show antimicrobial and anti-wood-decay fungal activities.²⁹

Application of QASs in dentistry and oral care was reviewed.³⁰ Some QASs inhibited humane androgenic and estrogenic receptors.³¹

The antimicrobial activity of quaternary ammonium salts increased with the presence of the terpene fragment in the molecule.³²

QASs with a carbamate group were incorporated into polyurethane coatings *via* crosslinking with terpene-based polyol and polyisocyanate and showed antimicrobial activity.³³

QASs are readily biodegradable involving mainly microorganisms of *Pseudomonas* genera.³⁴ Ease of QASs biodegradation decreases with increasing length and the number of alkyl chains.⁷

Recently herbicidal activity of QASs was reported. These compounds were synthesized from aminoacetanilides prepared from known herbicides alachlor and acetochlor.³⁵

Application of Inverse QSAR/QSPR analysis for pesticides structures generation has been recently presented. The authors described the relations of pesticide structures to their *n*-octanol–water partition coefficients affording potential new pesticide structures.³⁶

Molecular docking analysis including several known targets indicated that the *N*-myristoyltransferase is a likely site of interaction with fungicides.³⁷

These results induced us to prepare a series of ammonium salts containing a terpene-derived moiety and to test their biological activity which was disclosed in our patent application.³⁸ The rapid emergence of resistance in pathogenic organisms justifies the search for new, selectively acting preparations. The proposed new ammonium salts with a terpenoid fragment may prove to be effective, readily biodegradable wood preservatives.

2. Experimental Section

2.1. Materials and Physical Measurements

Reagent grade chemicals were used without further purification unless otherwise noted. Spectra were obtained as follows: ¹H and ¹³C NMR spectra on Varian 300 UNITY plus 300 spectrometer in deuterated chloroform using TMS as internal standard. Chemical shifts are given in

ppm (δ) relative to tetramethylsilane (TMS) as an internal standard, coupling constants are reported in Hz. Flash chromatography was carried out using silica gel S 230–400 mesh (Merck) and hexane–ethyl acetate mixtures as eluents. *logP* was calculated using EPI SuiteTM 4.1.1 Estimation Program Interface developed by Syracuse Research Corp., Syracuse, NY, USA. Elemental analyses (C, H, N) were conducted using the Elemental Analyser XBO, their results were found to be in good agreement ($\pm 0.3\%$) with the calculated values.

2.2. Chemistry

1-(Bromomethyl)-4-(prop-1-en-2-yl)cyclohexene (2)

Bromide **2** was prepared by the published method and its ¹H NMR spectrum was found to be identical with the one described.³⁹

1-(Chloromethyl)-4-(prop-1-en-2-yl)cyclohexene (3)

Chloride **3** was prepared by the published method and its ¹H NMR spectrum was found to be identical with the one described.⁴⁰

General Procedure for Preparation of Quaternary Ammonium Bromides 4a–e, 7a–e, 10a–e

Bromide **2** (1.0 mmol) was placed in the flask, then anhydrous benzene and tertiary amine (1.1–1.3 mmol) were introduced. The reaction was carried out at reflux for 4–6 hours and stirred overnight at room temperature. The reaction mixture was evaporated and after dissolving the residue in a small amount of benzene the product was precipitated with ethyl ether. The operation was repeated depending on the derivative from two to three times. Yields ranged from 70% for reactions with long chain amines up to 98% for shorter chain amines.

(4R)-N,N-Dimethyl-N-[[4-(prop-1-en-2-yl)cyclohex-1-en-1-yl]methyl]octylammonium Bromide (4a)

This salt was prepared as a yellowish wax (0.354 g, 95%). ¹H NMR (300 MHz, CDCl₃) δ 6.31 (s, 1H, H3), 4.74 (d, *J* = 24 Hz, 2H, H9), 4.24 (s, 2H, H1), 3.51–3.48 (m, 2H), 3.30 (s, 6H, Me₂N), 2.63 (bs, 1H), 2.35–2.05 (m, 5H), 1.74–1.65 (m, 2H), 1.74 (s, 3H, H10), 1.58–1.46 (m, 1H), 1.4–1.12 (m, 10H), 0.88 (t, *J* = 6 Hz, 3H, H₃CCH₂); ¹³C NMR (75.5 MHz, CDCl₃) δ 148.0, 139.4, 126.0, 109.0, 70.2, 64.0, 50.5, 50.4, 39.3, 31.3, 30.8, 30.3, 28.9, 28.8, 27.0, 26.0, 22.6, 22.3, 20.5, 13.8; Anal. Calcd for C₂₀H₃₈BrN: C, 64.50; H, 10.28; N, 3.70. Found: C, 64.41; H, 10.39; N, 3.64.

(4R)-N,N-Dimethyl-N-[[4-(prop-1-en-2-yl)cyclohex-1-en-1-yl]methyl]decylammonium Bromide (4b)

This salt was similarly prepared as above as a yellowish wax (0.368 g, 92%). ¹H NMR (300 MHz, CDCl₃) δ 6.32 (s, 1H, H3), 4.77 (s, H, H9a), 4.69 (s, H, H9a), 4.25 (s, 2H, H1), 3.50 (m, 2H), 3.30 (s, 6H, Me₂N), 2.38–2.05 (m, 5H), 1.87–1.74 (m, 2H), 1.74 (s, 3H, H10), 1.56–1.47 (m, 1H),

1.40–1.23 (m, 14H), 0.88 (t, $J = 6.9$ Hz, 3H); ^{13}C NMR (75.5 MHz, CDCl_3) δ 147.9, 139.2, 125.9, 108.9, 70.0, 63.8, 50.3, 50.2, 39.1, 31.4, 30.6, 29.0, 28.8, 26.8, 25.9, 22.5, 22.2, 20.3, 13.6; Anal. Calcd for $\text{C}_{22}\text{H}_{42}\text{BrN}$: C, 65.98; H, 10.57; N, 3.50. Found: C, 66.05; H, 10.67; N, 3.38.

(4R)-N,N-Dimethyl-N-[[4-(prop-1-en-2-yl)cyclohex-1-en-1-yl]methyl]dodecylammonium Bromide (4c)

This salt was similarly prepared as the salt **4a** as a yellowish wax (0.386 g, 90%). ^1H NMR (300 MHz, CDCl_3) δ 6.32 (s, 1H, H3), 4.77 (s, 1H, H9a), 4.69 (s, 1H, H9a), 4.29 (s, 2H, H1), 3.53 (m, 2H, CH_2N), 3.32 (s, 6H, Me_2N), 2.38–2.25 (m, 2H, H4), 2.25–2.05 (m, 3H), 1.87–1.72 (m, 3H), 1.74 (s, 3H, H10), 1.58–1.45 (m, 1H), 1.42–1.20 (m, 18H), 0.88 (t, $J = 6.6$ Hz, 3H); ^{13}C NMR (75.5 MHz, CDCl_3) δ 148.0, 139.4, 126.0, 109.0, 70.2, 63.9, 50.5, 50.4, 39.3, 31.6, 30.8, 30.3, 29.3 (2C), 29.2, 29.1, 29.0, 29.0, 27.0, 26.1, 22.7, 22.4, 20.5, 13.8; Anal. Calcd for $\text{C}_{24}\text{H}_{46}\text{BrN}$: C, 67.27; H, 10.82; N, 3.27. Found: C, 67.51; H, 10.71; N, 3.17.

(4R)-N,N-Dimethyl-N-[[4-(prop-1-en-2-yl)cyclohex-1-en-1-yl]methyl]tetradecylammonium Bromide (4d)

This salt was similarly prepared as the salt **4a** as a wax (0.343 g, 75%). ^1H NMR (300 MHz, CDCl_3) δ 6.32 (s, 1H, H3), 4.77 (s, 1H, H9a), 4.69 (s, 1H, H9b), 4.28 (s, 2H, H1), 3.53 (m, CH_2N), 3.32 (s, 6H, Me_2N), 2.38–2.22 (m, 2H, H4), 2.25–2.05 (m, 3H), 1.87–1.72 (m, 2H), 1.74 (s, 3H, H10), 1.58–1.45 (m, 1H), 1.40–1.20 (m, 23H), 0.88 (t, $J = 6.6$ Hz, 3H); ^{13}C NMR (75.5 MHz, CDCl_3) δ 147.9, 139.4, 126.0, 109.0, 70.1, 63.9, 50.4, 50.3, 39.2, 31.5, 30.7, 30.2, 29.3, 29.3, 29.3, 29.1, 29.1, 29.0, 28.9, 26.9, 26.7, 26.0, 25.6, 22.6, 22.3, 20.4, 13.8; Anal. Calcd for $\text{C}_{26}\text{H}_{50}\text{BrN}$: C, 68.39; H, 11.04; N, 3.07. Found: C, 68.24; H, 10.91; N, 3.20.

(4R)-N,N-Dimethyl-N-[[4-(prop-1-en-2-yl)cyclohex-1-en-1-yl]methyl]hexadecylammonium Bromide (4e)

This salt was similarly prepared as the salt **4a** as a wax (0.388 g, 80%). ^1H NMR (300 MHz, CDCl_3) δ 6.32 (s, 1H, H3), 4.77 (s, 1H, H9a), 4.69 (s, 1H, H9b), 4.28 (s, 2H, H1), 3.52 (m, 2H, CH_2N), 3.31 (s, 6H, Me_2N), 2.38–2.23 (m, 2H, H4), 2.23–2.05 (m, 3H), 1.87–1.72 (m, 2H), 1.74 (s, 3H, H10), 1.58–1.47 (m, 1H), 1.40–1.20 (m, 27H), 0.88 (t, $J = 6.6$ Hz, 3H) ppm; ^{13}C NMR (75.5 MHz, CDCl_3) δ 147.7, 139.1, 125.8, 108.7, 69.8, 63.7, 50.1, 50.0, 39.0, 31.3, 30.5, 29.1 (3C), 28.9, 28.9, 28.8, 28.7, 25.8, 22.4, 22.1, 20.2, 13.5; Anal. Calcd for $\text{C}_{28}\text{H}_{54}\text{BrN}$: C, 69.39; H, 11.23; N, 2.89. Found: C, 69.30; H, 11.41; N, 2.78.

(4R)-N,N-Dimethyl-N-[[4-(prop-1-en-2-yl)cyclohex-1-en-1-yl]methyl]octylammonium Chloride (4f)

The flask was charged with 1-(chloromethyl)-4-(prop-1-en-2-yl)cyclohexene (2.0 g, 11.8 mmol) and 25 mL of anhydrous benzene. Anhydrous *N,N*-dimethyl-*N*-octylamine (3.5 mL, 17.1 mmol) was then added. The reaction was carried out for 6 hours at reflux and stirred overnight at room temperature. The reaction mixture was

evaporated *in vacuo*, benzene was added to dissolve the residue followed by diethyl ether. The product which separated in the refrigerator as a wax was dried in a vacuum desiccator over anhydrous CaCl_2 to give the ammonium salt (3.0 g, 87%). ^1H NMR (300 MHz, CDCl_3) δ 6.30 (s, 1H, H3), 4.76 (s, 1H, H9a), 4.69 (s, 1H, H9b), 4.29 (m, 2H), 3.50 (m, 2H), 3.29 (s, 6H, Me_2N), 2.35–2.24 (m, 2H, H4), 2.24–2.03 (m, 3H), 1.86–1.70 (m, 2H), 1.73 (s, 3H, H10), 1.58–1.46 (m, 1H), 1.40–1.20 (m, 11H), 0.88 (t, $J = 6$ Hz, 3H, H_3CCH_2); ^{13}C NMR (75.5 MHz, CDCl_3) δ 147.3, 127.3, 125.5, 108.2, 69.3, 63.1, 49.6, 49.5, 39.6, 30.6, 30.1, 29.5, 28.1, 28.0, 26.3, 25.3, 21.9, 21.5, 19.7, 13.0; Anal. Calcd for $\text{C}_{20}\text{H}_{38}\text{ClN}$: C, 73.24; H, 11.68; N, 4.27. Found: C, 73.41; H, 11.55; N, 4.09.

(4R)-N,N-Dimethyl-N-[[4-(prop-1-en-2-yl)cyclohex-1-en-1-yl]methyl]decylammonium Chloride (4g)

This salt was similarly prepared as the salt **4f** as a wax (0.650 g, 70%). ^1H NMR (300 MHz, CDCl_3) δ 6.31 (s, 1H, H3), 4.76 (s, 1H, H9a), 4.69 (s, 1H, H9b), 4.27 (s, 2H, H1), 3.52 (t, $J = 8.1$ Hz, 2H, CH_2N), 3.31 (s, 6H, Me_2N), 2.38–2.03 (m, 5H), 1.85–1.74 (m, 3H), 1.74 (s, 3H, H10), 1.45–1.10 (m, 15H), 0.88 (t, $J = 6.9$ Hz, 3H); ^{13}C NMR (75.5 MHz, CDCl_3) δ 147.7, 138.9, 125.8, 108.7, 69.8, 63.6, 49.9, 49.9, 39.0, 31.2, 30.5, 29.9, 28.8 (2C), 28.6 (2C), 26.6, 25.8, 22.3, 22.0, 20.1, 13.5; Anal. Calcd for $\text{C}_{22}\text{H}_{42}\text{ClN}$: C, 74.22; H, 11.89; N, 3.93. Found: C, 74.03; H, 11.75; N, 4.08.

(4R)-N,N-Dimethyl-N-[[4-(prop-1-en-2-yl)cyclohex-1-en-1-yl]methyl]dodecylammonium Chloride (4h)

This salt was similarly prepared as the salt **4f** as a wax (3.00 g, 73%). ^1H NMR (300 MHz, CDCl_3) δ 6.29 (s, 1H, H3), 4.77 (s, 1H, H9a), 4.69 (s, 1H, H9b), 4.23 (s, 2H, H1), 3.48 (m, 2H, CH_2N), 3.30 (s, 6H, Me_2N), 2.38–2.25 (m, 2H, H4), 2.25–2.05 (m, 3H), 1.87–1.72 (m, 3H), 1.74 (s, 3H, H10), 1.58–1.45 (m, 1H), 1.42–1.17 (m, 18H), 0.88 (t, $J = 6.6$ Hz, 3H); ^{13}C NMR (75.5 MHz, CDCl_3) δ 147.8, 127.9, 126.0, 108.9, 70.0, 63.7, 50.2, 50.1, 39.2, 31.4, 30.1, 29.1 (2C), 29.0, 29.0, 28.9, 28.8, 26.9, 25.9, 22.5, 22.2, 20.4, 20.3, 13.6; Anal. Calcd for $\text{C}_{24}\text{H}_{46}\text{ClN}$: C, 75.05; H, 12.07; N, 3.65. Found: C, 75.21; H, 12.18; N, 3.47.

3,7-Dimethyloct-6-en-7-yl Bromide (6)

Bromide **6** was prepared by the published method from citronellol and its ^1H NMR spectrum was found to be identical with the one described.⁴¹

(3S)-N-Octyl-N,N,3,7-tetramethyloct-6-en-1-ammonium Bromide (7a)

This salt was similarly prepared as the salt **4a** as a wax (0.338 g, 90%). ^1H NMR (300 MHz, CDCl_3) δ 5.06 (m, 1H, H6), 3.63–3.40 (m, 4H, H1, CH_2N), 3.38 (s, 6H, Me_2N), 2.07–1.93 (m, 2H), 1.77–1.68 (m, 3H), 1.68, (s, 3H), 1.60 (s, 3H), 1.60–1.56 (m, 2H), 1.38–1.26 (m, 14H), 0.99 (d, $J = 6.3$ Hz, 3H), 0.88 (t, $J = 6.3$ Hz, 3H, CH_3CH_2); ^{13}C NMR (75.5 MHz, CDCl_3) δ 31.2, 123.7, 63.5, 62.3,

51.3, 51.2, 36.5, 31.1, 29.7, 29.5, 29.0, 28.8, 25.9, 25.7, 25.4, 23.5, 23.3, 19.4, 17.6, 14.0; Anal. Calcd for $C_{20}H_{42}BrN$: C, 63.81; H, 11.25; N, 3.72. Found: C, 64.01; H, 11.37; N, 3.58.

(3S)-N-Decyl-N,N,3,7-tetramethyloct-6-en-1-ammonium Bromide (7b)

This salt was similarly prepared as the salt **4a** as a wax (0.343 g, 85%). 1H NMR (300 MHz, $CDCl_3$) δ 5.07 (m, 1H, H6), 3.65–3.40 (m, 4H, H1, CH_2N), 3.39 (s, 6H, Me_2N), 1.99 (m, 2H), 1.72 (m, 3H), 1.68, (s, 3H), 1.60 (s, 3H), 1.60–1.56 (m, 2H), 1.38–1.26 (m, 18H), 0.99 (d, $J = 6.3$ Hz, 3H), 0.88 (t, $J = 6.3$ Hz, 3H, CH_3CH_2); ^{13}C NMR (75.5 MHz, $CDCl_3$) δ 131.5, 123.5, 63.4, 62.2, 51.2, 51.1, 36.4, 31.5, 30.0, 29.1 (2C), 29.0, 28.9, 28.8, 26.3, 25.9, 25.4, 24.9, 22.4, 22.3, 19.0, 17.4, 13.7; Anal. Calcd for $C_{22}H_{46}BrN$: C, 65.32; H, 11.46; N, 3.46. Found: C, 65.49; H, 11.37; N, 3.41.

(3S)-N-Dodecyl-N,N,3,7-tetramethyloct-6-en-1-ammonium Bromide (7c)

This salt was similarly prepared as the salt **4a** as a wax (0.389 g, 90%). 1H NMR (300 MHz, $CDCl_3$) δ 5.06 (m, 1H, H6), 3.78–3.68 (m, 4H, H1, H1'), 3.39 (s, 6H, Me_2N), 2.06–1.93 (m, 2H), 1.68 (m, 3H), 1.60 (s, 3H), 1.60–1.56 (m, 2H), 1.38–1.26 (m, 20H), 1.00 (d, $J = 6.3$ Hz, 3H), 0.88 (t, $J = 6.3$ Hz, 3H, CH_3CH_2); ^{13}C NMR (75.5 MHz, $CDCl_3$) δ 131.7, 123.6, 63.6, 62.4, 51.3 (2C), 36.6, 30.2, 29.4 (2C), 29.3, 29.3, 29.2, 29.0, 28.9, 26.0, 26.0, 25.5, 25.1, 22.6, 22.4, 19.1, 17.6, 13.9; Anal. Calcd for $C_{24}H_{50}BrN$: C, 66.64; H, 11.65; N, 3.24. Found: C, 66.58; H, 11.79; N, 3.13.

(3S)-N-Tetradecyl-N,N,3,7-tetramethyloct-6-en-1-ammonium Bromide (7d)

This salt was similarly prepared as the salt **4a** as a wax (0.368 g, 80%). 1H NMR (300 MHz, $CDCl_3$) δ 5.08 (m, 1H, H6), 3.65–3.39 (m, 4H, H1, CH_2N), 3.42 (s, 6H, Me_2N), 2.05–1.94 (m, 2H), 1.68 (m, 3H), 1.61 (s, 3H), 1.66–1.58 (m, 2H), 1.40–1.23 (m, 24H), 0.99 (d, $J = 6.3$ Hz, 3H), 0.88 (t, $J = 6.3$ Hz, 3H, CH_3CH_2); ^{13}C NMR (75.5 MHz, $CDCl_3$) δ 131.9, 123.7, 63.6, 62.5, 51.4 (2C), 36.7, 30.3, 29.6, 29.5, 29.5, 29.5, 29.4 (2C), 29.3, 29.3, 29.2, 29.1, 26.2, 25.6, 25.2, 22.7, 22.6, 19.3, 17.7, 14.0; Anal. Calcd for $C_{26}H_{54}BrN$: C, 67.80; H, 11.82; N, 3.04. Found: C, 67.61; H, 11.91; N, 3.15.

(3S)-N-Hexadecyl-N,N,3,7-tetramethyloct-6-en-1-ammonium Bromide (7e)

This salt was similarly prepared as the salt **4a** as a wax (0.391 g, 80%). 1H NMR (300 MHz, $CDCl_3$) δ 5.06 (tt, $J_1 = 6.9$ Hz, $J_2 = 1.5$ Hz, 1H, H6), 3.63–3.44 (m, 4H, H1, CH_2N), 3.41 (s, 6H, NMe_2), 2.05–1.88 (m, 2H), 1.69 (m, 3H), 1.60 (s, 3H), 1.66–1.52 (m, 2H), 1.40–1.23 (m, 28H), 0.99 (d, $J = 6.3$ Hz, 3H), 0.88 (t, $J = 6.3$ Hz, 3H, CH_3CH_2); ^{13}C NMR (75.5 MHz, $CDCl_3$) δ 131.9, 123.7, 63.7, 62.5, 51.3 (2C), 36.7, 30.3, 29.6, 29.6, 29.5, 29.4, 29.4, 29.4, 29.3, 29.3, 29.3, 29.1, 29.0, 26.1, 25.6, 25.2, 24.8, 22.7, 22.6, 19.2,

17.7, 14.0; Anal. Calcd for $C_{28}H_{58}BrN$: C, 68.99; H, 11.90; N, 2.87. Found: C, 68.81; H, 11.90; N, 2.76.

3,7-Dimethyloctadien-2,6-enyl Bromide (9)

Bromide **9** was prepared by the published method from geraniol and its 1H NMR spectrum was found to be identical with the one described.⁴²

(2E)-N-Octyl-N,N,3,7-tetramethylocta-2,6-dien-1-ammonium Bromide (10a)

This salt was similarly prepared from geraniol (**8**) as the salt **4a** as a wax (0.356 g, 95%). 1H NMR (300 MHz, $CDCl_3$) δ 5.32 (t, $J = 8.1$ Hz, 1H, H2), 5.01 (m, 1H, H6), 4.27 (d, $J = 8.1$ Hz, 2H, H1), 3.54–3.48 (m, 2H, CH_2N), 3.30 (s, 6H, Me_2N), 2.23–2.09 (m, 4H, H4, H5), 1.90 (s, 3H), 1.82–1.68 (m, 2H), 1.68 (s, 3H), 1.60 (s, 3H), 1.42–1.26 (m, 10H), 0.88 (t, $J = 6.3$ Hz, 3H, CH_3CH_2); ^{13}C NMR (75.5 MHz, $CDCl_3$) δ 151.5, 131.9, 122.6, 110.2, 62.6, 61.2, 53.2, 49.3 (2C), 42.3, 39.5, 31.1, 28.6, 28.5, 25.8, 25.5, 25.2, 22.3, 22.0, 17.2, 17.2, 13.5; Anal. Calcd for $C_{20}H_{40}BrN$: C, 64.15; H, 10.77; N, 3.74. Found: C, 64.28; H, 10.89; N, 3.69.

(2E)-N-Decyl-N,N,3,7-tetramethylocta-2,6-dien-1-ammonium Bromide (10b)

This salt was similarly prepared as the salt **4a** as a wax (0.382 g, 95%). 1H NMR (300 MHz, $CDCl_3$) δ 5.31 (t, $J = 8.1$ Hz, 1H, H2), 5.02 (m, 1H, H6), 4.26 (d, $J = 8.1$ Hz, 2H, H1), 3.58–3.45 (m, 2H, CH_2N), 3.29 (s, 6H, Me_2N), 2.23–2.10 (m, 4H, H4, H5), 1.90 (s, 3H), 1.87–1.70 (m, 2H), 1.68 (s, 3H), 1.60 (s, 3H), 1.42–1.20 (m, 14H), 0.88 (t, $J = 6.3$ Hz, 3H, CH_3CH_2); ^{13}C NMR (75.5 MHz, $CDCl_3$) δ 151.1, 131.5, 122.3, 109.9, 62.3, 60.8, 56.9, 53.0 (2C), 48.9, 42.0, 39.1, 30.9, 28.5, 28.3, 25.5, 25.1, 24.9, 21.7, 16.9, 15.8, 13.2; Anal. Calcd for $C_{22}H_{44}BrN$: C, 65.65; H, 11.02; N, 3.48. Found: C, 65.51; H, 10.91; N, 3.34.

(2E)-N-Dodecyl-N,N,3,7-tetramethylocta-2,6-dien-1-ammonium Bromide (10c)

This salt was similarly prepared as the salt **4a** as a wax (0.387 g, 90%). 1H NMR (300 MHz, $CDCl_3$) δ 5.30 (m, 1H, H2), 5.00 (m, 1H, H6), 4.22 (d, $J = 8.1$ Hz, 2H, H1), 3.48–3.42 (m, 2H, CH_2N), 3.28 (s, 6H, Me_2N), 2.20–2.14 (m, 2H), 1.90 (s, 3H), 1.89–1.80 (m, 2H), 1.68 (s, 3H), 1.60 (s, 3H), 1.43–1.22 (m, 16H), 0.88 (t, $J = 6.3$ Hz, CH_3CH_2); ^{13}C NMR (75 MHz, $CDCl_3$) δ 152.2, 132.4, 122.8, 110.2, 63.1, 61.6, 57.7, 53.3, 49.7, 42.6, 39.8, 31.6, 29.3, 29.3, 29.2, 29.1, 29.1, 28.8, 26.4, 24.1, 22.6, 17.6, 17.5, 13.9; Anal. Calcd for $C_{24}H_{48}BrN$: C, 65.65; H, 11.02; N, 3.48. Found: C, 65.51; H, 10.91; N, 3.33.

(2E)-N-Tetradecyl-N,N,3,7-tetramethylocta-2,6-dien-1-ammonium Bromide (10d)

This salt was similarly prepared as the salt **4a** as a wax (0.390 g, 85%). 1H NMR (300 MHz, $CDCl_3$) δ 5.28 (t, $J = 7.8$ Hz, 1H, H2), 5.01 (m, 1H, H6), 4.26 (d, $J = 8.1$ Hz,

2H, H1), 3.52–3.44 (m, 2H, CH₂N), 3.31 (s, 6H, Me₂N), 2.20–2.14 (m, 2H), 1.90 (s, 3H), 1.80–1.70 (m, 2H), 1.68 (s, 3H), 1.60 (s, 3H), 1.43–1.22 (m, 20H), 0.88 (t, $J = 6.3$ Hz, CH₃CH₂); ¹³C NMR (75 MHz, CDCl₃) δ 151.8, 132.2, 122.8, 110.3, 62.8, 61.4, 53.3 (2C), 42.6, 39.7, 31.6, 29.3, 29.3 (2C), 29.2, 29.1, 29.0, 28.0, 29.9, 26.4, 24.1, 22.6, 17.6, 17.5, 13.9; Anal. Calcd for C₂₆H₅₂BrN: C, 68.09; H, 11.43; N, 3.05. Found: C, 68.30; H, 11.56; N, 2.92.

(2E)-N-Hexadecyl-N,N,3,7-tetramethylocta-2,6-dien-1-ammonium Bromide (10e)

This salt was similarly prepared as the salt **4a** as a wax (0.389 g, 80%). ¹H NMR (300 MHz, CDCl₃) δ 5.30 (t, $J = 7.8$ Hz, 1H, H2), 5.02 (m, 1H, H6), 4.27 (d, $J = 8.1$ Hz, 2H, H1), 3.54–3.48 (m, 2H, CH₂N), 3.30 (s, 6H, Me₂N), 2.22–2.12 (m, 3H), 1.90 (s, 3H), 1.84–1.70 (m, 2H), 1.67 (s, 3H), 1.60 (s, 3H), 1.42–1.22 (m, 24H), 0.88 (t, $J = 6.6$ Hz, CH₃CH₂); ¹³C NMR (CDCl₃, 75 MHz) δ 151.3, 131.7, 122.5, 110.1, 62.5, 61.0, 53.1 (2C), 42.2, 39.3, 31.1, 29.0 (2C), 29.0 (2C), 28.9, 28.8, 28.8, 28.7, 28.6, 25.7, 25.3, 25.1, 22.2, 22.0, 17.1, 17.1, 13.5; Anal. Calcd for C₂₈H₅₆BrN: C, 69.10; H, 11.60; N, 2.88. Found: C, 69.28; H, 11.63; N, 2.79.

2.3. Fungicidal Testing

The compounds were screened *in vitro* for antifungal activity against the following five plant pathogens: *Fusarium culmorum* Sacc., *Phytophthora cactorum* Schroek, *Alternaria alternata* Keissl.(Fr.), *Rhizoctonia solani* Kuhn, and *Botrytis cinerea* Pers. Ex Fr and mold pathogens *Chaetomium globosum* Kunze, *Aspergillus terreus* Thom, *Aspergillus niger* Van Tieghem, and *Penicillium ochrochloron* Biourge. Pathogenic plant fungal strains came from the Institute of Plant Protection in Poznań, Poland and strains of mold fungi came from the Collection of Pure Cultures of Industrial Microbes of the Institute of Technology and Microbiology of the Faculty of Food Chemistry and Biotechnology of the Łódź University of Technology, Poland.

The test involved determination of mycelial growth retardation in agar medium: Potato Dextrose Agar (PDA; Difco) for phytopathogenic fungi and Sabouraud Dextrose Agar (SDA; Biocorp) for mold fungi. Stock solutions of test chemicals in acetone were added to agar medium to give a concentration of 200 mg/L (phytopathogenic fungi) and 10000 mg/L, 5000 mg/L, 2500 mg/L (mold fungi) and dispersed into sterile Petri dishes. Plates were inoculated within 24 h after they were poured. Four discs (5 mm diameter) were cut from the margins of actively growing 2 week old colony and were placed in equal distances from each other on the surface of the solidified agar. PDA or SDA with addition of acetone was used as the negative control. The plates were incubated in the growth chamber at 25 ± 1 °C (phytopathogenic fungi) and 28 ± 1 °C (mold fungi). The radial growth of the fungal colonies was measured after 3–5 days depending on the growth rate of the

control samples. The growth was determined by calculating the mean of two colony diameters of four replicate colonies. The fungicidal activity was expressed as the percentage of fungi growth inhibition compared to that of the untreated control. The relative growth inhibition of the treatment compared to the untreated control was calculated as percentage, using the following formula:

$$\text{inhibition rate (\%)} = \frac{x - y}{x} \cdot 100 \quad (1)$$

where x is fungal colony diameter on untreated PDA/SDA (mm) and y fungal colony diameter in treated PDA/SDA (mm).

2.4. Herbicidal Testing

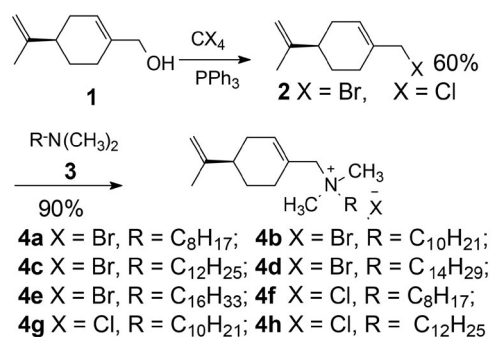
Studies on potential herbicidal activity were carried out in pot experiments under greenhouse conditions using the post-emergence tests (foliar application). As bioindicators, ten common species of weeds belonging to the monocotyledons and dicotyledons classes were used: *Galium aparine*, *Polygonum nodosum*, *Papaver rhoeas*, *Apera spica-venti*, *Galinsoga parviflora*, *Chenopodium album*, *Plantago lanceolata*, *Brassica nigra*, *Amaranthus retroflexus*, and *Stelaria media*. The dilutions of the tested compounds at the dose of 2 kg/ha in the spray volume 500 L/ha were sprayed on approximately 2-week seedlings of plants at the stage of two true leaves. Temperature during vegetation: night/day 15–25 °C. The evaluation of the effects of the compounds was carried out separately for each plant species 2 weeks after the application, recording the degree of damage of the plants in percentage compared to the untreated control.

3. Results and Discussion

3.1. Chemistry

Synthesis of Perillyl Alcohol Derivatives with the Function of Ammonium Salt

The starting material in this synthesis was the reactive derivative of limonene - perillyl alcohol (**1**) which was

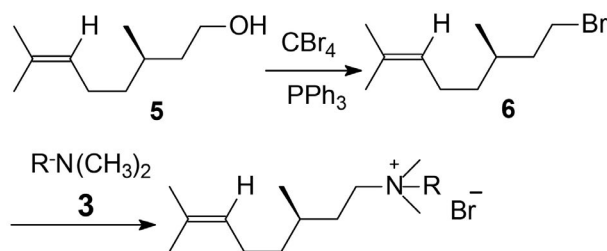


Scheme 1. The synthesis of perillyl ammonium salts **4a-h**

converted to the bromine derivative **2** using carbon tetrabromide and triphenylphosphine,³⁹ and to the chlorine derivative **3** using the classic Appel reaction conditions, *i.e.* carbon tetrachloride and triphenylphosphine in anhydrous DMF.⁴⁰ The next step was alkylation by the resulting halides **2** and **3** of tertiary amines thus obtaining quaternary ammonium bromide salts **4a–e** and corresponding chlorides **4f–h** (Scheme 1).

Synthesis of Citronellol Derivatives with the Function of Ammonium Salt

The starting monoterpene citronellol (**5**) occurs in nature and is used as repellent of mosquitoes and in perfumery. Conversion to a bromine derivative **6** and alkylation of tertiary amines yielded five new quaternary ammonium salts **7a–e** (Scheme 2).

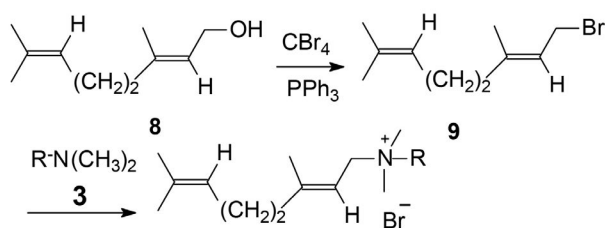


7a R = C₈H₁₇; **7b** R = C₁₀H₂₁; **7c** R = C₁₂H₂₅;
7d R = C₁₄H₂₉; **7e** R = C₁₆H₃₃

Scheme 2. The synthesis of citronellyl ammonium salts **7a–e**

Synthesis of Geraniol Derivatives with the Function of Ammonium Salt

Geraniol (**8**) is a component of essential oils of fruits and herbs with a broad spectrum of activity including repelling mosquitoes and chemoprevention of colon tumors. Analogously as described above, bromide **9** and five ammonium bromides **10a–e** were obtained (Scheme 3).



10a R = C₈H₁₇; **10b** R = C₁₀H₂₁; **10c** R = C₁₂H₂₅;
10d R = C₁₄H₂₉; **10e** R = C₁₆H₃₃

Scheme 3. The synthesis of geranyl ammonium salts **10a–e**

Antifungal Activity Assays of the Ammonium Salts

Fungicidal activity of three sets of compounds: derivatives of perillyl alcohol (**4a–h**), citronellol (**7a–e**), and

geraniol (**10a–e**), was evaluated using *in vitro* poisoned food technique, assaying the degree of inhibition of mycelial growth on the agar medium at the basic concentration of 200 mg/L. For the selected active compounds tests were also carried out at the concentration of 20 mg/L. The following important phytopathogenic fungi were used for the biological assays: *Alternaria alternata* (A. a.), *Botrytis cinerea* (B. c.), *Fusarium culmorum* (F. c.), *Phytophthora cactorum* (Ph. c.), *Phytophthora infestans* (Ph. i.), and *Rhizoctonia solani* (Rh. s.).

The results of the first stage of screening tests revealed a good fungistatic effect of all quaternary salts at the concentration of 200 ppm against six tested pathogenic strains. It is worth noting that geranyl salts **10a–e** exhibited 100% activity against *Ph. cactorum*. The highest effectiveness—100% inhibition of mycelial growth of five species of fungi—was shown for three compounds: **4a**, **4b** (a derivative of perillyl alcohol with a C₈ and C₁₀ side chain) and **10a** (a derivative of geraniol with a C₈ side chain). As outlined in Table 1 the compounds possess more potent antifungal activities than commercial fungicides. Compound **4b** showed also high activity at lower concentration of 20 ppm against two fungal strains (*B. cinerea* and *Ph. cactorum*).

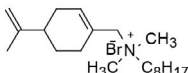
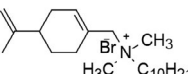
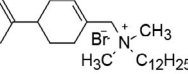
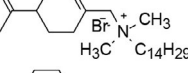
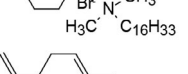
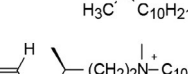
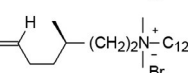
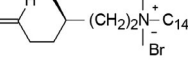
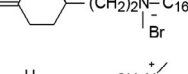
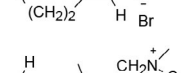
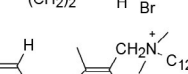
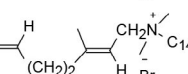
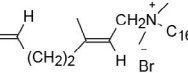
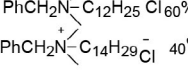
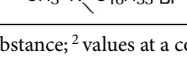
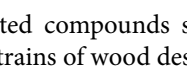

Salts **4a**, **4b**, **4g** exhibited a broad spectrum antifungal activities against above mentioned phytopathogenic fungi, and showed more potent activities than the reference compound **11**. Salts **7b–e** were more active than the reference compound **11** against two fungus strains and compounds **10a** and **10b** surpassed potency of the reference compound **12** against four fungus strains.

It is well known that biological activity of a molecule depends apart from electrophilic parameters on its lipophilicity. A majority of correlation between structure and different displays of biological activity reported in literature are ascribed mainly to hydrophobic-lipophilic character of substances.^{43,44} We have compared for the inspected compounds a fungistatic concentration and such lipophilic parameter of molecules as log *P* (partition coefficients *P* (*n*-octanol-water)).

The optimal range of log *P* values for the examined compounds was 3.2–4.4. It means that in the group of inspected compounds there is an optimal hydrophobic-hydrophilic character corresponding to salts with C₈–C₁₀ *N*-substituent.

In another studies we used microorganisms *Chaetomium globosum* (C. g.) ŁOCK 0476, *Aspergillus terreus* (A. t.) ŁOCK 0451, *Aspergillus niger* (A. n.), and *Penicillium ochrochloron* (P. o.). These filamentous fungi are characterized by low nutritional requirements, they are easily spread in various environments and are responsible for biodeterioration of technical materials including lignocellulosic products. They represent types of filamentous fungi (*Aspergillus*, *Penicillium*, *Chaetomium*) capable of producing cellulase, an enzyme responsible, among others, for the decomposition of paper and wood.

Table 1. Antifungal activity of compounds 4a–h, 7a–e and 10a–e against plant pathogens *in vitro* at conc. 200 mg/L

No.	Structure	Antifungal activity (inhibition rate in %)					Rh. s.	log P
		A. a.	B. c.	F. c.	Ph. c.	Ph. i.		
4a		100 30.0 ²	100 11.1 ²	100 19.2 ²	100 16.0 ²	100 26.5 ²	100 12.1 ²	3.25
4b		100 66.6 ²	100 88.8 ²	83.7 30.7 ²	100 100 ²	100 59.1 ²	100 59.4 ²	4.23
4c		75	75.6	32.4	85.7	60.5	69.8	5.22
4d		66.7	75.6	10.8	85.7	50.0	44.8	6.20
4e		77.8	75.6	27.0	57.1	50.0	47.9	7.18
4g		100	100	45.2	100	–	100	4.23
7b		86.1	87.8	100	100	73.7	72.9	4.43
7c		80.6	78.0	16.2	85.7	50.0	71.9	5.41
7d		77.8	65.9	29.7	100	47.4	66.7	6.39
7e		77.8	73.2	32.4	85.7	52.6	62.5	7.37
10a		80.0	100	100	100	100	100	3.36
10b		86.0	100	37.0	100	69.5	84.8	4.34
10c		83.0	86.0	11.1	100	52.6	63.0	5.32
10d		76.0	80.0	0	100	66.3	45.7	6.30
10e		66.7	65.5	0	100	56.3	34.8	7.29
11 ¹		86.0	87.0	7.4	100	35.8	71.7	– ³
12 ¹		60.0	72.4	0	80.0	72.1	25.0	3.18

¹ Reference substance; ² values at a concentration of 20 mg/L; ³ log P for a mixture of two salts is not reliable.

The tested compounds showed very good activity against two strains of wood destroying fungi *Chaetomium*

globosum and *Penicillium ochrochloron*. The salts **4a**, **7a**, **7c** were particularly active against the two above strains, salt

Table 2. Efficacy of test compounds **4a–h**, **7a–e** and **10a–e** [%] against fungi destroying wood and technical materials

No.	Compound	Conc. [mg/L]	C. g.	A. t.	A. n.	P. o.	log P
4a		10000	100	51.03	40.16	100	3.25
		5000	88.04	37.77	29.34	100	
4c		10000	86.89	70.62	67.55	100	5.22
		5000	86.89	69.91	–	100	
4d		10000	61.82	74.11	61.06	57.14	6.20
4e		10000	40.33	63.62	–	–	7.18
4g		10000	100	74.11	–	–	4.23
7a		10000	100	41.96	40.85	100	3.44
		5000	100	2.77	33.66	79.59	
		2500	82.09	0	–	79.59	
7b		10000	100	71.34	65.38	65.31	4.43
		5000	97.13	63.62	55.99	65.31	
		2500	62.96	51.74	42.32	51.02	
7c		10000	100	58.04	63.95	100	5.41
		5000	100	48.26	48.81	79.59	
		2500	88.04	43.35	30.76	44.9	
7d		10000	78.51	68.53	45.17	51.02	6.39
		5000	78.51	58.75	NB	42.86	
7e		10000	100	72.01	–	–	7.37
10b		10000	100	71.34	56.73	100	4.34
		5000	100	52.45	43.01	100	
		2500	100	41.96	33.66	100	
10e		10000	45.06	60.84	48.07	48.98	7.29
		5000	41.47	46.16	39.42	40.82	
		2500	33.17	15.36	29.34	34.69	
11 ¹		10000	94.12	56.20	70.66	100	
		5000	92.15	55.66	70.34	100	
		2500	76.47	55.66	68.66	71.88	

¹ Reference substance

4c against *P. ochrochloron*, and salts **7b** and **7e** against *C. globosum*. These were ammonium salts of perillyl alcohol (**4a** and **4c**) and citronellol (**7a**, **7b**, **7c** and **7e**).

Salts **4a,c–e** were more active against one fungal strain than the reference compound, while salt **4g** was more potent against *Ch. globosum* and *A. terreus* than reference compound **11**. Salts **7b**, **7c**, and **7d** were more active against two fungal strains than the reference compound **11**, while salts **7a** and **7c** surpassed the activity of the reference compound against one fungal strain. Salt **10b** was more active against two fungal strains (*Ch. globosum* and

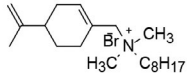
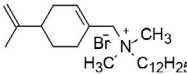
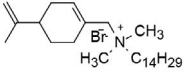
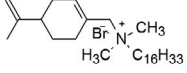
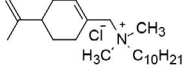
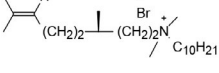
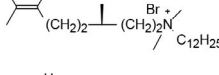
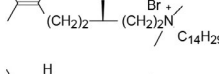
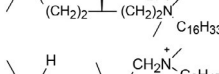
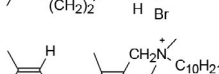
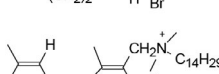
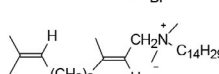
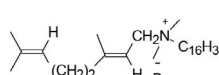
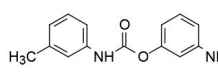
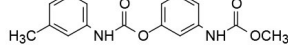
A. terreus) than the reference compound **11** and salt **10e** was more active against one fungal strain (*A. terreus*) than the reference compound. The optimal range of log *P* values for the examined compounds was 3.2–5.4 corresponding to salts with C₈–C₁₂ *N*-substituent.

Using the least squares linear regression method we have compared the activity of all the investigated compounds with their log *P* values. The comparison was done separately for the perillyl ammonium salts (**4a–g**), citronellol derivatives (**7b–e**), and geranyl derivatives (**10a–e**). For the set of the phytopathogenic fungi (Table 1) the ob-

served activity for all the compounds apparently decreased with the increased length of an alkyl chain. On

the other hand for the set of the fungi destroying wood and technical materials (Table 2) the dependence of the

Table 3. Herbicidal activity of quaternary ammonium salts 4a–h, 7a–e and 10a–e (dose: 2 kg/ha)

No.	Compound	<i>Galium aparine</i>	<i>Polygonum nodosum</i>	<i>Papaver rhoeas</i>	<i>Apera spica-venti</i>	<i>Galinsoga parviflora</i>	<i>Chenopodium album</i>	<i>Plantago lanceolata</i>	<i>Brassica nigra</i>	<i>Amaranthus retroflexus</i>	<i>Stelaria media</i>
4a		70	100	100	20	70	100	20	70	100	70
4c		20	40	100	20	20	100	40	40	40	0
4d		20	70	100	40	40	100	70	100	100	20
4e		20	40	100	40	70	100	70	100	70	0
4g		20	70	100	40	70	100	55	100	100	20
7b		30	70	100	40	70	100	55	100	100	20
7c		30	100	100	70	100	100	70	100	100	20
7d		10	100	70	20	70	100	70	100	100	20
7e		40	100	100	70	100	100	70	100	100	40
10a		40	40	100	0	70	100	40	70	70	20
10b		20	20	40	0	20	20	20	20	20	20
10c		40	40	70	0	20	40	20	40	40	20
10d		20	20	20	0	20	20	20	20	20	0
10e		20	20	40	0	20	40	20	20	20	0
13 ¹		70	100	100	40	100	100	70	70	40	40

¹ Reference substance phenmedipham

activity on the length of an alkyl chain was not distinctly observed.

Herbicidal Activity Assays

Ten common species of weeds belonging to one monocot and nine dicot families were used as bioindicators for potential herbicidal activity testing: *Galium aparine*, *Polygonum nodosum*, *Papaver rhoeas*, *Apera spica-venti*, *Galinsoga parviflora*, *Chenopodium album*, *Plantago lanceolata*, *Brassica nigra*, *Amaranthus retroflexus*, and *Stelaria media*.

Most compounds showed herbicidal activity at the dose of 2 kg/ha (*via* leaves), the weeds were destroyed in the range of 20 to 100% depending on the species (Table 3). The most active salts were derivatives of perillyl alcohol (with C₈–C₁₄ side chain) and derivatives of citronellol (with C₁₀–C₁₆ side chain), where two salts showed 100% activity against six weeds and two salts showed 100% activity against four weeds. High activity of all perillyl salts **4a–h** against two species *Papaver rhoeas* and *Chenopodium album* was found. Compound **4a** with the shortest side chain was the most active against weeds *Galium aparine* and *Polygonum nodosum*. For *Galinsoga parviflora* a parabolic dependence was observed with the lowest activity for C₁₂–C₁₄ derivatives and a higher potency for C₈ and C₁₆ salts. On the other hand for weeds *Plantago lanceolata* and *Brassica nigra* the highest activity was noticed for a long chain C₁₄ and C₁₆ ammonium bromides. A higher activity of the tested compounds than one of the reference compound **13** was shown by salts **4d–g** against weed *Plantago lanceolata*, by compounds **4a**, **4d**, and **4g** against *Amaranthus retroflexus*, and compound **4a** against *Stelaria media*.

High activity of all citronellyl salts **7b–e** against three herbs *Chenopodium album*, *Brassica nigra* and *Amaranthus retroflexus* was found. Again higher activity than potency of the reference compound was noticed for salts **7c** and **7e** against monocot species *Apera spica-venti*, for salts **7b–e** against weeds *Brassica nigra* and *Amaranthus retroflexus*.

In case of geranyl derivatives **10a–e** the highest activity of C₈ salt was found against all weeds. Salt **10b** was more potent against *Amaranthus retroflexus* than the reference compound.

4. Conclusions

Eighteen novel quaternary ammonium salts (QASs) with a terpenoid moiety have been synthesized. Most compounds showed a broad spectrum of biological activity including both fungistatic and herbicidal activity. A favourable effect of terpene group introduction was shown by a higher potency of many synthesized salts than that of reference compound **11** and **12** being pure quaternary alkylammonium compounds. Some dependence of fungistatic activity on log *P* was demonstrated.

5. Acknowledgements

This work was supported in part by the Polish Ministry of Science and Higher Education (Research Grant NR EMC: 0/17/005/K), which is gratefully acknowledged.

Conflict of Interest: The authors declare that they have no conflict of interest.

6. References

- P. P. Raichurkar, V. G. Nadiger, T. Ranjit, G. S. Nadiger, *Colourage* **2017**, *64*, 43–51.
- S. Zhang, X. Yang, B. Tang, L. Yuan, K. Wang, X. Liu, X. Zhu, J. Li, Z. Ge, *Chem. Eng. J.* **2018**, *336*, 123–132.
- K. Rajkowska, A. Koziróg, A. Otlewska, A. M. Piotrowska, P. Nowicka-Krawczyk, B. Brycki, A. Kunicka-Styczyńska, B. Gutarowska, *Acta Biochim. Pol.* **2016**, *63*, 153–159.
- N. N. D. Daoud, N. N. Dickinson, P. Gilbert, *Microbios* **1983**, *37*, 75–85.
- B. Brycki, A. Koziróg, I. Kowalczyk, T. Pospieszny, P. Materna, J. Marciniak, *Molecules* **2017**, *22*, 1810. DOI:10.3390/molecules22111810
- M. Tischer, G. Pradel, K. Ohlsen, U. Holzgrabe, *Chem. Med. Chem.* **2012**, *7*, 22–31. DOI:10.1002/cmdc.201100404
- J. Zabielska-Matejuk, K. Czaczuk, *Wood Sci. Technol.* **2006**, *40*, 461–475. DOI:10.1007/s00226-005-0065-2
- B. Brycki, I. Małecka, A. Koziróg, A. Otlewska, *Molecules* **2017**, *22*, 130. DOI:10.3390/molecules22010130
- Y. Yang, V. Reipa, G. Liu, Y. Meng, X. Wang, K. P. Mineart, V. M. Prabhu, W. Shi, N. J. Lin, X. He, J. Sun, *ACS Appl. Mater. Interfac.* **2018**, *10*, 8566–8573. DOI:10.1021/acsami.8b01089
- E. A. Chugunova, N. I. Akyzbekov, E. M. Mahrous, A. D. Voloshina, N. V. Kulik, V. V. Zobov, A. G. Strel'nik, T. P. Gerasimova, A. B. Dobrynin, A. R. Burilov, *Monatsh. Chem.* **2018**, *149*, 119–126. DOI:10.1007/s00706-017-2052-3
- W. Seebacher, F. Belaj, J. Faist, R. Saf, F. Bucar, I. Turek, A. Brantner, M. Alajlani, M. Kaiser, P. Mäser, R. Weis, *Monatsh. Chem.* **2017**, *148*, 263–274. DOI:10.1007/s00706-016-1864-x
- E. Obłąk, A. Piecuch, J. Rewak-Soroczyńska, E. Paluch, *Appl. Microbiol. Biotechnol.* **2018**, 1–8.
- S. Q. Fu, J. W. Guo, X. Zhong, Z. Yang, X. F. Lai, *RSC Advances*, **2016**, *6*, 16507–16515.
- C. Zhang, Y. Jiang, H. Ju, Y. Wang, T. Geng, *J. Mol. Liquids* **2017**, *241*, 638–645. DOI:10.1016/j.molliq.2017.06.062
- B. Brycki, H. Koenig, T. Pospieszny, *Molecules* **2015**, *20*, 20887–20900. DOI:10.3390/molecules201119735
- G. De Luca, R. Amuso, A. Figoli, R. Mancuso, L. Lucadamo, B. Gabriele, *Appl. Sci. (Switzerland)* **2018**, *8*, 1972.
- A. Madhusudhan Reddy, P. Srinivasa Babu, *Research J. Pharm. Technol.* **2016**, *9*, 322–332. DOI:10.5958/0974-360X.2016.00058.5
- F. Demirci, K. Yildirim, H. B. Kocer, *J. Appl. Polym. Sci.* **2018**, *135*, 45914. DOI:10.1002/app.45914
- J. Hoque, V. Yadav, R. G. Prakash, K. Sanyal, J. Haldar, *ACS Biomaterials Sci. Engineer.* **2019**, *5*, 81–91.

20. M. Stasiewicz, A. Fojutowski, A. Kropacz, J. Pernak, *Holz-forschung* **2008**, 62, 309–317. DOI:10.1515/HF.2008.028
21. J. Pernak, J. Zabielska-Matejuk, A. Kropacz, J. Foksowicz-Flaczyk, *Holzforschung* **2004**, 58, 286–291.
22. J. Zabielska-Matejuk, A. Stangierska, M. Kot, *J. Wood Chem Technol.* **2015**, 35, 178–192. DOI:10.1080/02773813.2014.909852
23. E. A. Courtois, C. Baraloto, C. E. T. Paine, P. Petronelli, P.-A. Blandinieres, D. Stien, E. Höuel, J.-M. Bessire, J. Chave, *Phytochemistry* **2012**, 82, 81–88. DOI:10.1016/j.phytochem.2012.07.003
24. A. A. Santos, B. M. S. de Oliveira, C. R. Melo, A. P. S. Lima, E. D. R. Santana, A. F. Blank, M. C. Picanço, A. P. A. Araújo, P. F. Cristaldo, L. Bacci, *Ecotox. Environ. Safety* **2017**, 145, 436–441. DOI:10.1016/j.ecoenv.2017.07.057
25. Y. Xie, M. Li, Q. Huang, C. Lei, *Nat. Prod. Commun.* **2014**, 9, 719–722.
26. F. S. Nakayama, *Industr. Crops Prod.* **2005**, 22, 3–13. DOI:10.1016/j.indcrop.2004.05.006
27. F. Xu **2008**. In: B. G. Zhao, K. Futai, J. R. Sutherland, Y. Takeuchi (Eds: Pine Wilt Disease, Springer, Japan, p 323.
28. J. Hu, Y. Shen, S. Pang, Y. Gao, G. Xiao, S. Li, Y. Xu, *J. Environ. Sci. (China)* **2013**, 25(S1), S32–S35.
29. C.-L. Ho, P.-C. Liao, E. I.-C. Wang, Y.-C. Su, *Nat. Prod. Commun.* **2011**, 6, 1755–1758.
30. P. Makvandi, R. Jamaledin, M. Jabbari, N. Nikfarjam, A. Borzacchiello, *Dental Mater.* **2018**, 34, 851–867.
31. K. Michalíková, L. Linhartová, M. Ezechiáš, T. Cajthaml, *Chemosphere* **2019**, 534–541. DOI:10.1016/j.chemosphere.2018.11.006
32. E. Novotná, K. Waisser, J. Kuneš, K. Palát, V. Buchta, J. Stolaříková, R. Beckert, V. Wsöl, *Arch. Pharm.* **2014**, 347, 381–386. DOI:10.1002/ardp.201300407
33. G. Liu, G. Wu, C. Jin, Z. Kong, *Progr. Org. Coatings* **2015**, 80, 150–155. DOI:10.1016/j.porgcoat.2014.12.005
34. A. H. Khan, E. Topp, A. Scott, M. Sumarah, S. M. Macfie, M. B. Ray, *J. Hazard. Mater.* **2015**, 299, 595–602.
35. Q. Wu, C. Liu, J. Yang, A. Guan, H. Ma, *Pestic. Biochem. Phys.* **2017**, 143, 246–251. DOI:10.1016/j.pestbp.2017.05.006
36. B. Souyei, A. H. Seyd, F. Zaiz, A. Rebiai, *Acta Chim. Slov.* **2019**, 66, 315–325. DOI:10.17344/acsi.2018.4793
37. L. Antypenko, F. Meyer, Z. Sadykova, L.-A. Garbe, K. Stefens, *Acta Chim. Slov.* **2018**, 65, 836–841. DOI:10.17344/acsi.2018.4440
38. W.M. Gołębiowski, M. Gucma, K. Żelechowski, M. Krawczyk, A. Michalczyk **2018**, Pochodne czwartorzędowych soli amoniowych z funkcją terpenową i ich zastosowanie. Pl Patent Application 425314, April 04, 2018.
39. A. F. Barrero, M. M. Herrador, J. F. Quílez del Moral, P. Arteaga, J. F. Arteaga, H. R. Diéguez, E. M. Sánchez, *J. Org. Chem.* **2007**, 72, 2988–2995. DOI:10.1021/jo062630a
40. M. Longhi, S. Arnaboldi, E. Husanu, S. Grecchi, I. F. Buzzi, R. Cirilli, S. Rizzo, C. Chiappe, P. R. Mussini, *Electrochim. Acta* **2019**, 298, 194–209. DOI:10.1016/j.electacta.2018.12.060
41. S. Sankaranarayanan, A. Sharma, S. Chattopadhyay, *Tetrahedr. Asymm.* **2002**, 13, 1373–1378.
42. S. Combemale, J.-N. Assam-Evoung, S. Houaidji, R. Bibi, V. Barragan-Montero, *Molecules* **2014**, 19, 1120–1149. DOI:10.3390/molecules19011120
43. M. Mellado, A. Madrid, M. Reyna, C. Weinstein-Oppenheim, J. Mella, C. O. Salas, E. Sánchez E, M. Cuella, *Med. Chem. Res.* **2018**, 27, 2414–2425. DOI:10.1007/s00044-018-2245-2
44. S. Combemale, J.-N. Assam-Evoung, S. Houaidji, R. Bibi, V. Barragan-Montero, *Molecules* **2014**, 19, 1120–1149. DOI:10.3390/molecules19011120

Povzetek

Sintetizirali smo serijo novih kvarternih amonijevih soli (QAS), katerih terpenoidni fragment izvira iz perilih alkohola, citronelola in geraniola. Strukture novih spojin smo potrdili s spektroskopskimi metodami in z elementno analizo. Fungicidno aktivnost pripravljenih spojin smo preučili na šestih rastlinskih patogenih organizmih, štirih glivah, ki uničujejo les in druge tehnične materiale; herbicidno aktivnost pa smo raziskali na desetih vrstah plevelov, ki uspevajo v pasu zmernega podnebja. Nekaj pripravljenih soli je izkazalo višjo aktivnost proti glivam in herbicidno aktivnost kot so bile ugotovljene za referenčne spojine.



Except when otherwise noted, articles in this journal are published under the terms and conditions of the Creative Commons Attribution 4.0 International License

Scientific paper

Cobaltosic Oxide Catalysts for Catalytically Removing Hydrogen from Tail Chlorine

Tong Zhang, Ling Xue, Jianwei Xue,* Fuxiang Li and Zhiping Lv

College of Chemistry and Chemical Engineering, Taiyuan University of Technology, Taiyuan 030024, China.

* Corresponding author: E-mail: xuejianwei@tyut.edu.cn

Received: 09-19-2019

Abstract

Cobaltosic oxide has been used as catalysts in dehydrogenation for tail chlorine due to the advantages of low price and security. The $\text{Co}_3\text{O}_4/\text{ZSM-5}$ was synthesized by the volume impregnation method. The catalytic dehydrogenation performance of $\text{Co}_3\text{O}_4/\text{ZSM-5}$ was investigated, the catalytic reaction of hydrogen with oxygen and chlorine was carried out in a fixed-bed, and the mixed reactant gases were prepared according to the composition and content of tail chlorine in industry: Cl_2 (65%–80%), N_2 (6–16%), O_2 (8%–10%) and H_2 (1.5%–4%). The catalytic efficiency and stability of $\text{Co}_3\text{O}_4/\text{ZSM-5}$ in dehydrogenation for tail chlorine were better than that of Co_3O_4 . After the calcination on 300 °C, the $\text{Co}_3\text{O}_4/\text{ZSM-5}$ with 1 %wt. Co_3O_4 shown excellent catalytic performance at 50 °C, and the average conversion of hydrogen can reach up to 99.59%.

Keywords: Cobaltosic oxide; $\text{Co}_3\text{O}_4/\text{ZSM-5}$; tail-chlorine; dehydrogenation

1. Introduction

The chlor-alkali industry plays a very important role in the basic chemical industry owing to the critical position in the manufacture of thousands of downstream chemicals.¹ Chlorine and sodium hydroxide are two major products of the chlor-alkali industry, which are the most important inorganic commodities and widely used as raw materials for other processes (handbook of chemical economics, 2018).² Due to the recent development, the production of chlor-alkali and the scale of industrial equipment have made great breakthroughs. By the end of 2016, there are more than 500 chlor alkali producers in the world. The world caustic soda production capacity is about 94.7 Mt, and the output is close to 70 Mt/a. China has the largest caustic soda production capacity in the world.^{3,4} There are 161 caustic soda enterprises with a total output of 42.59 Mt in China at the end of 2016.⁵ Based on market data in this year, the demand for caustic soda is still increasing. The by-product tail chlorine in the chlorine tail gas will inevitably become a more important issue in the industrial production of chlor-alkali. Tail chlorine comes from chlor-alkali industry, which is a process of compressed liquefaction preparation liquid chlorine enriched in chlorine gas, including chlorine gas, nitrogen, oxygen and hydrogen etc. The mixed gas may explode due to hydrogen accumulation when it is used in the downstream. The hydrogen in the mixed gas has been a great po-

tential safety hazard.⁶ Therefore, it is very urgent to develop environment-friendly and effectively methods for the dehydrogenation in chlorine tailings.

There are four common industrial methods for dehydrogenation of tail chlorine: synthetic hydrochloric acid, absorption-desorption, lye absorption and PSA pressure swing adsorption.^{7,8} The synthesis of hydrochloric acid by burning hydrogen and chlorine at high temperature to produce hydrochloric acid,⁹ while tail chlorine is consumed. This is a mature method in industry, but at present the economic benefit of this method is too poor. Dehydrogenation with green catalysts is in line with the national energy conservation and emission reduction and green development concept, which can reduce hydrogen content and even completely dehydrogenate. In the 1950s, it was discovered that hydrogen and chlorine could be catalyzed into hydrogen chloride to remove hydrogen. Kulcsar and Geza scholars for the first time in 1957 used activated carbon as a carrier of load type catalyst under 250 °C, chlorine and hydrogen for hydrogen chloride. Subsequently,¹⁰ Allen and Coolen et al. investigated that the reaction should be controlled within a certain temperature range, otherwise the side reaction occurred at an excessively high reaction temperature.^{11,12} Researchers showed that some precious metals (platinum, palladium, rhodium, etc.) and its alloys, as well as cheap manganese metals reduced the hydrogen content in tail chlorine to less than 10^{-6} in a certain temperature range

(200–400 °C). Pieters et al. with SiO₂ carrier load K, La and Cu chloride preparation as a catalyst, when residual hydrogen content in the best conditions of PPM level, they then used the activated alumina catalyst carrier load the precious metal Pt made around 260 °C catalytic reaction.¹³

The previous studies on the dehydrogenation performance of tail chlorine have also made some progress. Zhou investigated Ce/Pt/SiO₂ as catalyst for low-temperature catalytic tail-chlorine dehydrogenation. She found the optimal reaction condition was 1%wt. Pt loaded on SiO₂ catalyst with 2%wt. of additive Ce(NO₃)₃. The total conversion rate of Ce/Pt/SiO₂ was 92% at the reaction temperature of 60 °C.¹⁴ Later, the Au-Ag / Al₂O₃ bimetallic catalyst prepared by Lu has a hydrogen conversion rate of 94.58% with the calcination temperature of 500 °C under the reaction temperature of 100 °C.¹⁵ Subsequently, Wang et al. continued to developed the catalytic effects of Pd/Al₂O₃ and Pd/SiO₂, a 97% conversion of hydrogen achieved at 60 °C. The noble metal catalyst not only reduced the reaction temperature, but also greatly improved the dehydrogenation rate, but they were not only expensive, but also had a low repetition rate, which is not suitable for industrial use.¹⁶ Therefore, Chen selected to use cheap metal. CuO/Al₂O₃ calcined at 550 °C was used as a catalyst with a load content of 8%wt., Its average hydrogen conversion rate catalyzed at 110 °C was 90.03%. However, the catalyst with poor stability made the conversion rate decrease rapidly.¹⁷ Liu employed cheap metal Fe₂O₃/Al₂O₃ to obtain the superior catalytic performance with conversion rate of hydrogen of 84.11% at reaction temperature of 70 °C and calcination temperature of 500 °C. Among that route, it was found that production of the ferric chloride of by products. This method can not only achieve dehydrogenation effect, but also prepare ferric chloride products.¹⁸

In this article, the cobalt-based catalyst was prepared by using high specific surface area ZSM-5 as supporter. ZSM-5 zeolite has lot of advantages such as thermal stability, unique channel structure, large surface, acidity and shape-selectivity. As is known to us, it has been proverbially used as the support in various moderate acid-catalyzed reactions.¹⁹ This method for catalyst preparation has low energy consumption and simple process, While using this catalyst, safety problem of tail chlorine

can be solved fundamentally, and secondary pollution to the environment will not happen.

2. Experiment

2. 1. Catalyst Preparation

ZSM-5-supported Co₃O₄ catalysts was synthesized by using the volume impregnation method with Co(NO₃)₂·6H₂O. A series of cobalt nitrate aqueous solutions with different mass fractions were prepared, and then the cobalt nitrate aqueous solution with the same volume was soaked for 24h with 1g ZSM-5 at room temperature. After that, it was dried in a oven at 100 °C for 12h, and finally calcined for 6 hours at 300 °C–700 °C.²⁰ Then put it into the sample bag and label it for later use.

2. 2. Catalyst Characterization

After reaction, the product mixture content detection of 1 ml was quantitatively analyzed by gc-900 gas chromatograph with a 3mm*3m 5A molecular sieve stainless steel packed column and a thermal conductivity cell detector. Argon was used as a carrier gas with a gas velocity of 15ml/min (0.05mpa). The temperature of vaporization chamber and detector were 100 °C accompanied by column temperature of 55 °C and bridge current of 60 mA. The X-ray diffraction (XRD) patterns of the catalyst were obtained by using a diffractometer XRD-6000), operating at 40 kv and 30 ma with Cu-ka palladium and nickel filtering. Scanning electron microscope (SEM) pattern of the catalysts was taken by JSM-6300 of Nicocet company in Japan, which was conducted to investigate the morphology of samples with treating by gold spray. Element analysis (EDS) was used to assist in the analysis of the SEM electron micrograph. The N₂ adsorption–desorption was employed to measure the surface area and pore volume by using a NOVA 2000e analyzer.

2. 3. Experimental Steps

The experimental procedure is as follows: Firstly, 0.5g catalyst was put into the fixed-bed reactor system as shown

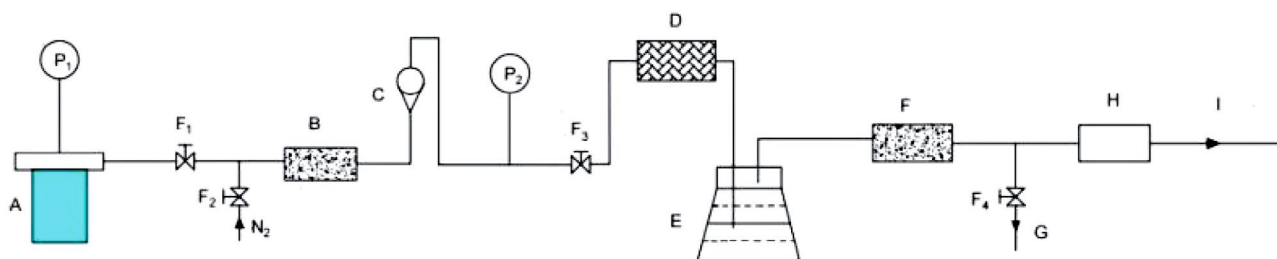


Figure 1. The device for removing hydrogen from the tail chlorine A Gas tank; B. Calcium chloride dryer; C. Flowmeter; D. Quartz tube reactor; E. Sodium hydroxide solution; F. Calcium oxide dryer; G. Sampling device; H. Tail gas treatment; I. Tail gas outlet; F₁,F₂,F₃,F₄. The valve; P₁,P₂. Vacuum manometer

in Figure 1, and the whole pipeline was purged with nitrogen to remove water. Then, the tail chlorine mixture simulated according to the composition of industrial tail chlorine (3.97% H₂, 9.93% O₂, 13.25% N₂ and 72.85% Cl₂) was put into the reactor.^{21,22} The hydrogen content of the tail chlorine after dehydrogenation was analyzed by gas chromatography and the conversion rate of hydrogen was calculated to detect its catalysis and properties of chemical agents.

2. 4. Calculation Method of Hydrogen Conversion

The above figures show the changes of gas flow rate before and after the reaction, respectively. The conversion rate of each reactant was defined as eq 1,

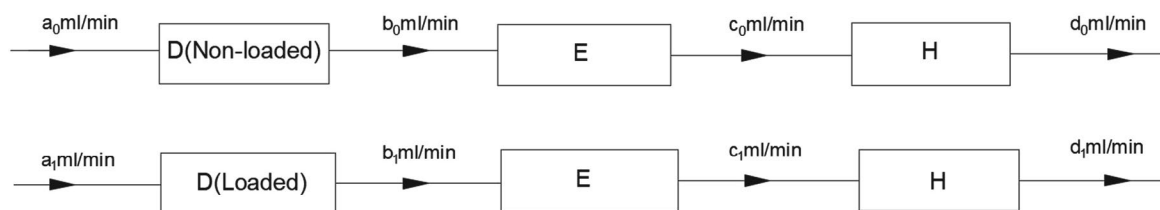


Figure 2. Calculation of hydrogen content in a gas mixture

$$Con = (d_0 \times c_0 - d_1 \times c_1) / (d_0 \times c_0) \quad (1)$$

Where the initial velocity is described as a_0 and a_1 . After reaction, it's b_0 and b_1 . c_0 and c_1 are exhibited with the absorption of chlorine and d_0 and d_1 are the velocity after reaction with sodium carbonate. Hence, the hydrogen conversion rate and oxygen conversion rate are set as eq 2 and eq 3 severally,

$$Con_{H_2} = (d_0 \times c_{0H_2} - d_1 \times c_{1H_2}) / (d_0 \times c_{0H_2}) \quad (2)$$

$$Con_{O_2} = (d_0 \times c_{0O_2} - d_1 \times c_{1O_2}) / (d_0 \times c_{0O_2}) \quad (3)$$

Where c_{0H_2} , c_{0O_2} and c_{0N_2} are respectively the volume concentrations of hydrogen, oxygen, and nitrogen in the mixture before the reaction, while c_{1H_2} , c_{1O_2} and c_{1N_2} are after the reaction. Since the hydrogen is only about 4% and the proportion of chlorine gas is higher, it is reasonable to assume that the gas velocity is basically unchanged after the reaction. As suggested by eq 4 and eq 5,

$$a_0 = a_1 = b_0 \approx b_1 \quad (4)$$

$$c_0 = d_0 \approx c_1 = d_1 \quad (5)$$

Eq 6 and eq 7 can be obtained by substituting the above formula into the conversion rate formula,

$$Con_{H_2} = (c_{0H_2} - c_{1H_2}) / c_{0H_2} \quad (6)$$

$$Con_{O_2} = (d_0 \times c_{0O_2} - d_1 \times c_{1O_2}) / (d_0 \times c_{0O_2}) \quad (7)$$

It would found that hydrogen – oxygen reaction and hydrogen – chlorine are involved in the reaction. The selectivity of hydrogen – oxygen is calculated as eq 8,

$$\begin{aligned} Sel_{(H_2-H_2O)} &= 2 \times (d_0 \times c_{0O_2} - d_1 \times c_{1O_2}) / (d_0 \times c_{0H_2} - d_1 \times c_{1H_2}) \\ &= 2 \times (c_{0O_2} - c_{1O_2}) / (c_{0H_2} - c_{1H_2}) \end{aligned} \quad (8)$$

the selectivity of hydrogen – chlorine, as a consequence, can be reckoned as eq 9,

$$\begin{aligned} Sel_{(H_2-HCl)} &= 1 - Sel_{(H_2-H_2O)} \\ &= 1 - 2 \times (c_{0O_2} - c_{1O_2}) / (c_{0H_2} - c_{1H_2}) \end{aligned} \quad (9)$$

3. Results and Discussion

3. 1. X-ray Diffraction

As suggested by Figure 3, the characteristic diffraction peaks of Co₃O₄ were obtained at 19.0°, 31.3°, 36.9°, 38.6°, 44.8°, 55.7°, 59.4°, and 65.3°. After the reaction, a weak characteristic diffraction peaks of catalyst presented at 75.8°, which indicated that a trace of cobalt chloride was generated in the catalytic reaction process.

The XRD analysis of Co₃O₄/ZSM-5 at different reaction temperature was presented in Figure 4, which was

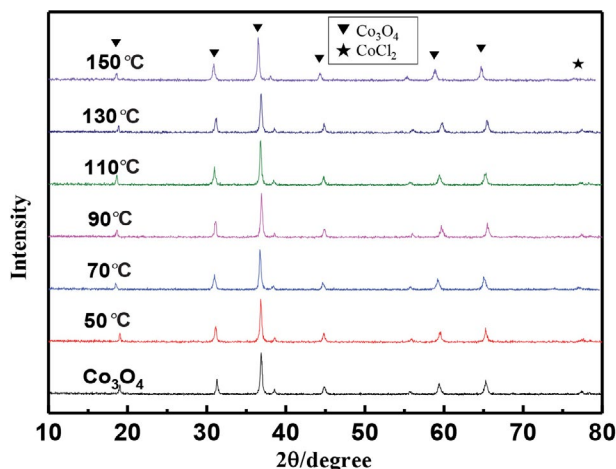


Figure 3. XRD patterns of Co₃O₄ at different reaction temperature

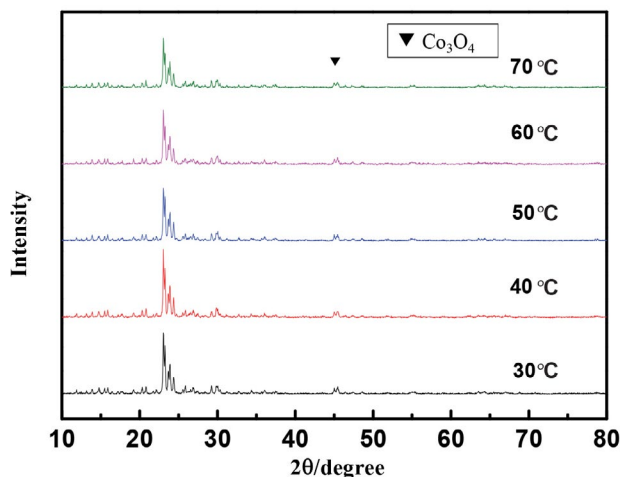


Figure 4. XRD patterns of $\text{Co}_3\text{O}_4/\text{ZSM-5}$ at different reaction temperature

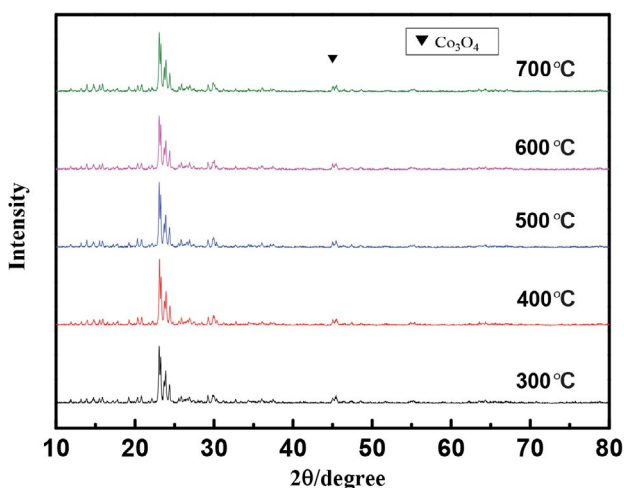


Figure 5. XRD patterns of $\text{Co}_3\text{O}_4/\text{ZSM-5}$ at different calcination temperature

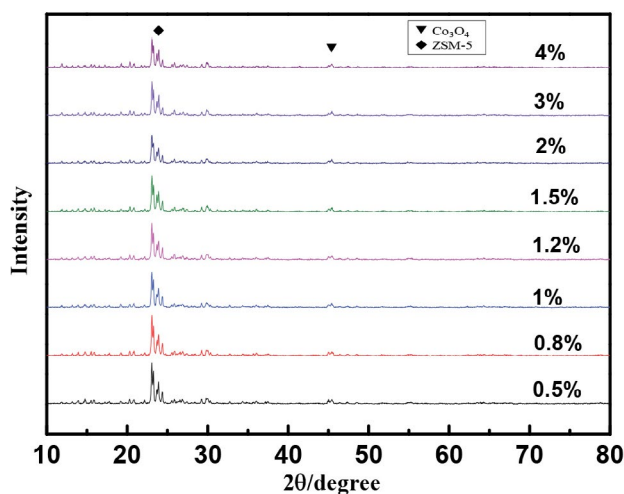


Figure 6. The XRD patterns of $\text{Co}_3\text{O}_4/\text{ZSM-5}$ at different loading

loaded with 1 %wt. and calcined at 600 °C. Compared with unloaded cobaltic oxide, the characteristic diffraction peak of cobaltic oxide also presented at about 45° in Figure 4, exhibiting that the presence of cobalt element in the form of Co_3O_4 . It was assumed that the catalyst had good stability due to there is no diffraction peak of cobalt chloride. Maybe It's because the generation of cobalt chloride rarely not detected. The characteristic peak of Co_3O_4 was found in different load, and the intensity of the peak increased with the increase of load.

The XRD analysis of $\text{Co}_3\text{O}_4/\text{ZSM-5}$ at different calcination temperature was set as Figure 5, which are loaded with 1 %wt. and participated in reaction at 50 °C. From Figure 5, it can be seen that the characteristic diffraction peak corresponding to cobaltic oxide all presented at about 45° at different calcination temperature. However, the strength of peak decreased indistinctly with increase of calcination temperature, which illustrated that the enhanced temperature was unfavorable to the crystallization of cobaltic oxide. The consecutive high-intensity peaks of ZSM-5 having a specific 2θ value of 23°–25° were commonly found in each catalyst sample, indicating that after calcination as well as reaction ZSM-5 structure clearly preserved.

For various Co_3O_4 loadings, the XRD analysis of catalysts were set as Figure 6, which were calcined at 300 °C and participated in reaction at 50 °C. As suggested by Figure 6, all the catalysts revealed characteristic peaks of ZSM-5 crystal in the ranges of $2\theta = 23\sim 25$ which were evident that the crystalline framework of the ZSM-5 was retained after the loading in all the catalysts.²³ With increasing loading of $\text{Co}_3\text{O}_4/\text{ZSM-5}$, the characteristic diffraction peak of ZSM-5 became weaker. This is due to the introduction of Co_3O_4 , which leads to the decrease of the order degree of the molecular sieve structure, indicating that some cobalt ions are exchanged to the internal control surface of the molecular sieve.²⁴

3. 2. SEM Analysis

Figure 7 shows the SEM images of Co_3O_4 samples before and after catalytic reaction. As can be seen from figure a and b, cobaltic oxide particles with hexagonal structure and smooth surface, which was arranged neatly, loose and fine before reaction. In contrast to figure a and c, the phenomenon of agglomerating occurred in the catalyst after the reaction. With the destruction of some hexagonal structure of particles, the particle size became larger, and there seemed to be traces of corrosion of hydrogen chloride and water on the surface. It was performed that the SEM images of Co_3O_4 supported on ZSM-5. Co_3O_4 supported on ZSM-5 showed irregular shape and good dispersity on the ZSM-5 support. The distribution of samples after reaction was loose, but the overall change is not significant.

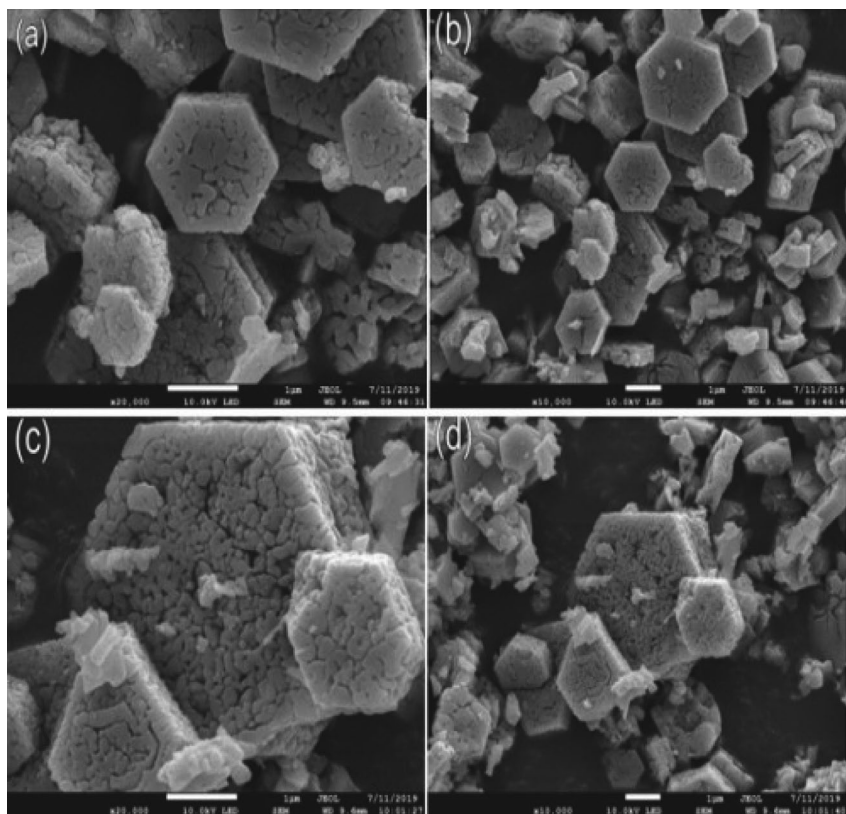


Figure 7. SEM of Co_3O_4 before (a,b) and after reaction(c,d)

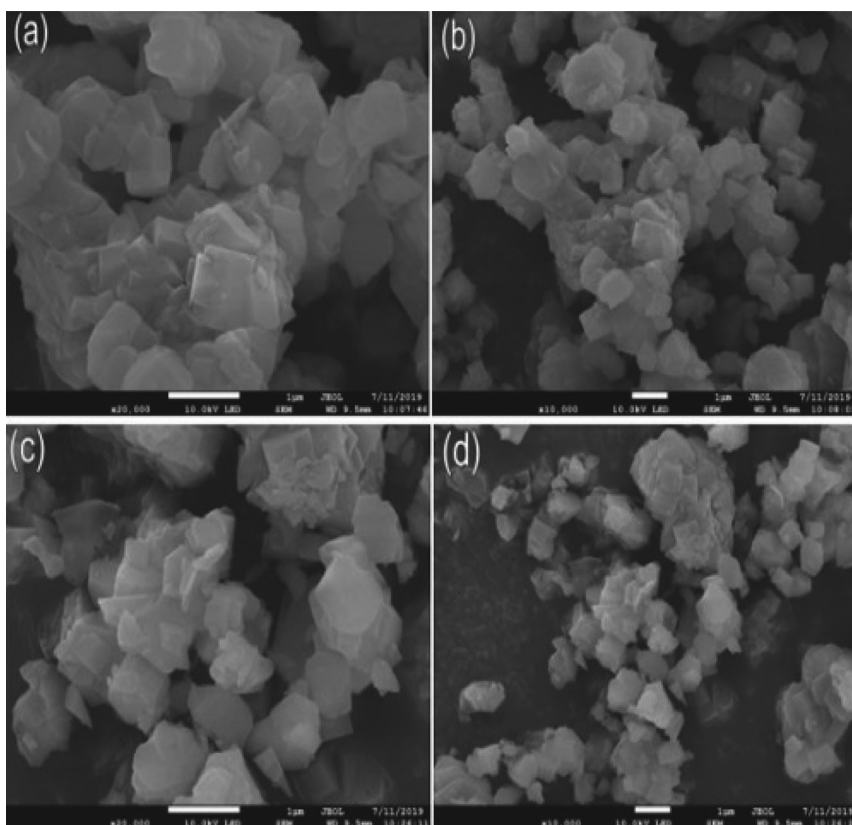


Figure 8. SEM images of $\text{Co}_3\text{O}_4/\text{ZSM-5}$ before (a,b) and after reaction(c,d)

3. 3. EDS Analysis

The analysis of EDS test results exhibited that there was no drastic change of the elements before and after the reaction, no matter cobaltous oxide or cobaltous oxide

loaded, which can also be supported by the SEM results. The morphology of pure cobaltous oxide changed after reaction, while the cobaltous oxide after loading was basically the same. This further revealed that $\text{Co}_3\text{O}_4/\text{ZSM-5}$

Table 1. Elemental analysis of Co_3O_4 catalyst

Element	C	O	Co
Co_3O_4 (before) (w%)	1.00	24.93	74.07
Co_3O_4 (before) (at%)	2.87	53.76	43.37
Co_3O_4 (after) (w%)	1.05	24.46	74.49
Co_3O_4 (after) (at%)	3.03	53.09	43.88

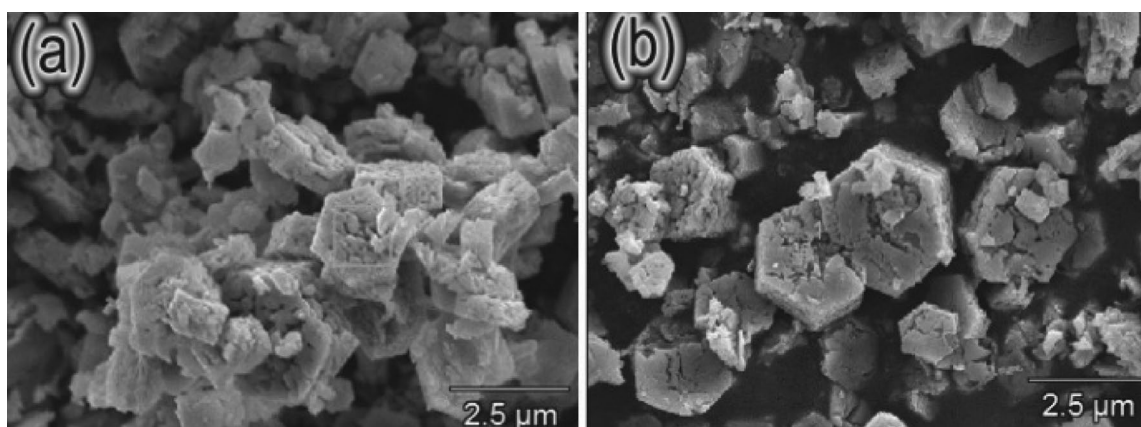


Figure 9. EDS spectra of Co_3O_4 catalyst before (a) and after (b) reaction

Table 2. Elemental analysis of $\text{Co}_3\text{O}_4/\text{ZSM-5}$ catalyst

Element	C	O	Al	Si	Co
$\text{Co}_3\text{O}_4/\text{ZSM-5}$ (before) (w%)	1.46	47.19	2.53	35.33	13.49
$\text{Co}_3\text{O}_4/\text{ZSM-5}$ (before) (at%)	2.67	65.06	2.07	27.74	2.45
$\text{Co}_3\text{O}_4/\text{ZSM-5}$ (after) (w%)	2.77	48.84	2.49	34.54	11.35
$\text{Co}_3\text{O}_4/\text{ZSM-5}$ (after) (at%)	4.91	64.99	1.96	26.18	1.95

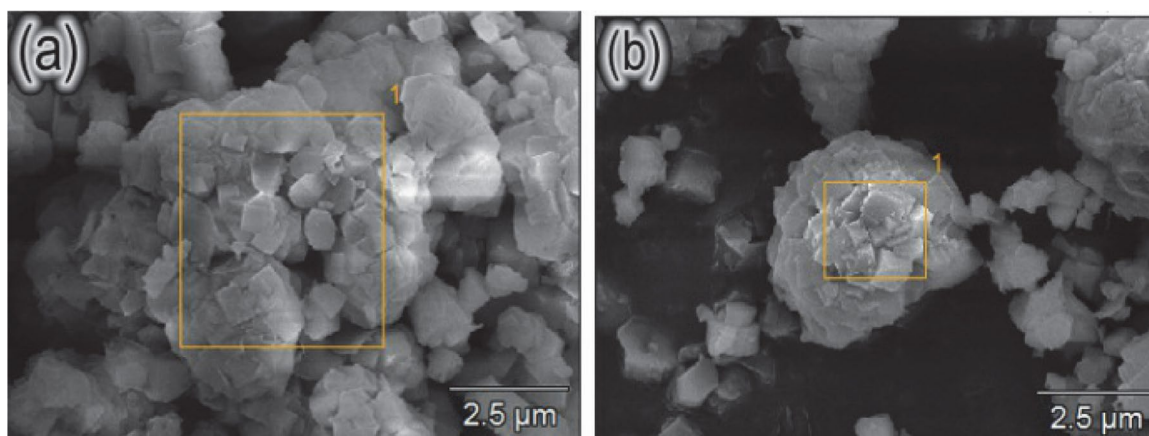


Figure 10. EDS spectra of $\text{Co}_3\text{O}_4/\text{ZSM-5}$ catalyst before (a) and after (b) reaction

made more excellent performance in terms of catalytic activity and stability.

3. 4. Nitrogen Adsorption-Desorption

Figure 11 shows the textural properties of ZSM-5, 1%Co₃O₄/ZSM-5, 1%Co₃O₄/ZSM-5 after reaction, 3% Co₃O₄/ZSM-5 and 4%Co₃O₄/ZSM-5, which were presented by nitrogen adsorption-desorption isotherm. Accord-

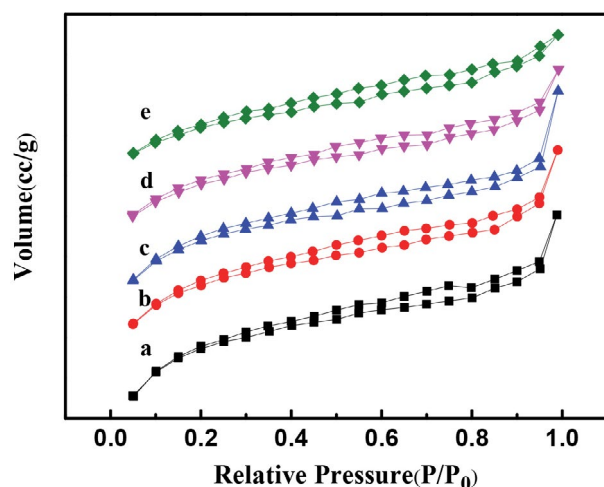


Figure 11. N₂ adsorption-desorption equilibrium curves

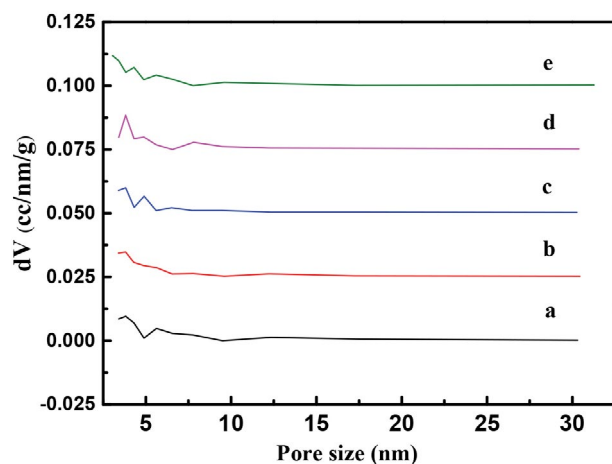


Figure 12. The pore dimension distribution (a)ZSM-5; (b)1%Co₃O₄/ZSM-5; (c)1%Co₃O₄/ZSM-5 after reaction; (d)3%Co₃O₄/ZSM-5; (e)4%Co₃O₄/ZSM-5

ing to the classification of IUPAC and the characteristics of curves in Figure 11, the isotherms of both curve exhibited type-IV isotherm with the H3 hysteresis type of loop, which indicates that it is monolayer saturated adsorption. What is more, the material has a slit structure and uneven interior, and the loading of active components was composed of lamellar particles. By comparing the shape characteristics of the five curves in the figure, it can be determined that the pore structure of the catalyst has not changed significantly before and after the loading and reaction, indicating that the internal structure of ZSM-5 was relatively stable.

The pore size distribution was analyzed by the BJH model. Combined with the comprehensive analysis of Figure 12 and Table 3 above, it was found that a decrease in specific surface area as well as pore volume by impregnation of Co₃O₄ might be owing to the occupation of the pores of ZSM-5 by active metals. Through the diffusion of the carrier, Co²⁺ diffused to the active site of the catalyst, partially replacing Al³⁺ in the ZSM-5 skeleton, as the ionic radius of Co²⁺ is larger than that of Al³⁺.²⁵ Compared with catalysts b and c before and after catalytic dehydrogenation, due to the formation of H₂O and the loose active components on the surface of the catalyst resulted in the decrease of pore diameter and increase of specific surface area after the reaction.

3. 5. Catalytic Performance at different temperature of Co₃O₄

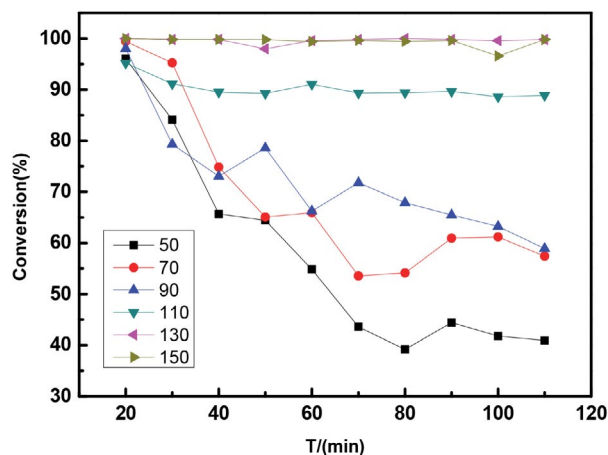
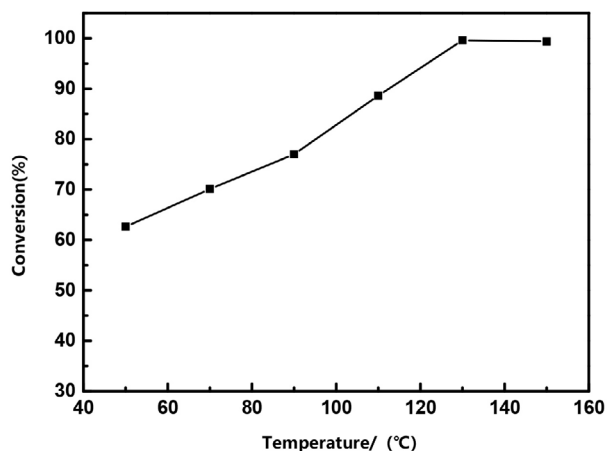
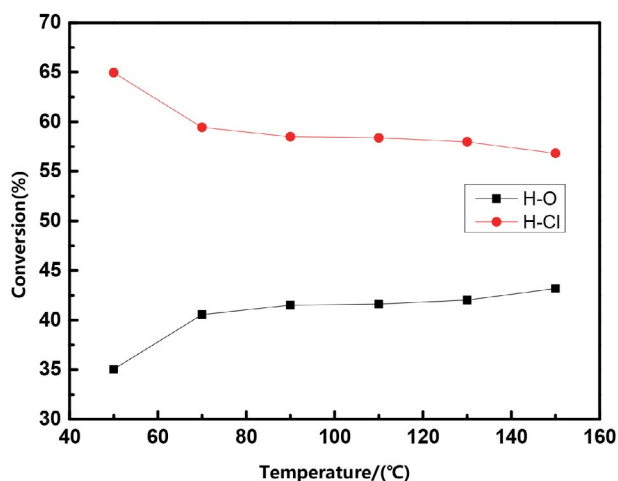


Figure 13. The overall conversion rate of Co₃O₄

Table 3. The pore size and surface area distribution of ZSM-5, Co₃O₄/ZSM-5 and Co₃O₄/ZSM-5 after reaction

Sample	Surface Area/m ² ·g ⁻¹	Pore Volume/cc·g ⁻¹	Pore Diameter/nm
ZSM-5	362.648	0.035	3.83
1%Co ₃ O ₄ /ZSM-5	319.814	0.033	3.816
1%Co ₃ O ₄ /ZSM-5 after reaction	322.807	0.03	3.819
3%Co ₃ O ₄ /ZSM-5	303.363	0.031	3.817
4%Co ₃ O ₄ /ZSM-5	283.703	0.035	3.053

Figure 14. The average conversion rate of Co_3O_4 Figure 15. The average selectivity of Co_3O_4

Combining with Figure 13 and 14, it can be observed that the hydrogen conversion increased with increasing temperature. Especially it increased up to surpass 99% with relative stability when the reaction temperature enhanced above 130 °C. The overall conversion rate dropped with the time developed as presented in figure 13, which suggested that the performance of catalytic dehydrogenation reaction decreased gradually. Cobalt chloride was formed in the reaction by analysis of XRD. Consequently, it is the reason that the formation of cobalt chloride, hydrogen chloride and water has damaged the catalyst including reducing the surface area and weakening the activity of catalyst. On the one hand, the water vapor reacts with the active components on the surface of the catalyst to form other components, reducing the oxygen activity level on the surface and thus reducing the activity of the catalyst. On the other hand, Co_3O_4 was partially inactivated after being chlorinated to cobalt chloride, and the deactivation of catalyst was accelerated by the formation of hydrochloric acid solution from hydrogen chloride gas and water.^{26,27} Nevertheless, the total conversion rate of

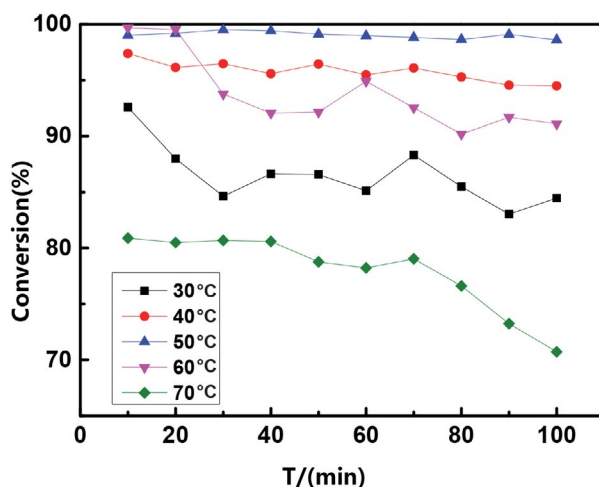
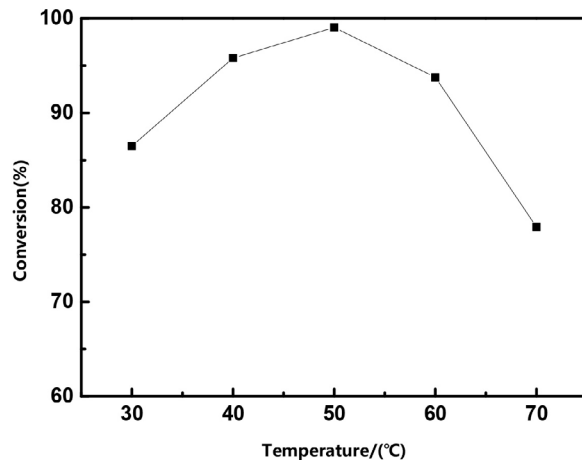
hydrogen increased with the rise of temperature and the catalyst of Co_3O_4 had good stability.

As demonstrated in figure 15, the selectivity of hydrogen and chlorine reactions was obviously higher than that of hydrogen and oxygen reactions at different reaction temperatures. With the rise of temperature, the selectivity of hydrogen-chlorine reaction decreased gradually, while the selectivity of hydrogen-oxygen reaction increased generally. To sum up, the optimal reaction temperature for chlorine removal of hydrogen from tail was 130 °C, which was more favorable for hydrogen and oxygen reactions.

3. 6. Catalytic Performance of $\text{Co}_3\text{O}_4/\text{ZSM-5}$

3. 6. 1. Effect of Different Reaction Temperatures

The catalytic performance of $\text{Co}_3\text{O}_4/\text{ZSM-5}$ at different reaction temperature was acquired in Figure 16, which was loaded with 1 %wt. and was calcined at 600 °C. The average conversion rate of hydrogen removal catalyzed by catalyst increased first and then decreased with the rise of

Figure 16. The overall conversion rate of $\text{Co}_3\text{O}_4/\text{ZSM-5}$ Figure 17. The average conversion rate of $\text{Co}_3\text{O}_4/\text{ZSM-5}$

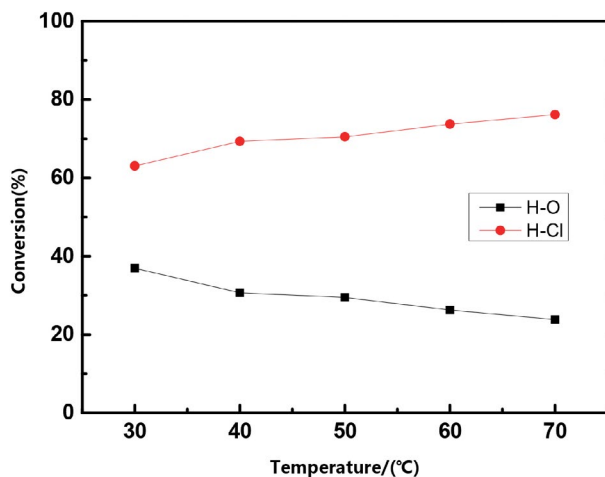


Figure 18. The average selectivity of $\text{Co}_3\text{O}_4/\text{ZSM-5}$

temperature. Samples exhibited an average conversion rate of 99.04% at the reaction temperature of 50 °C, which shows the enhanced catalytic performance. The reduction of hydrogen conversion rate demonstrated that hydrogen removal performance was gradually weakened as illustrated in Figure 16. This is because the formation hydrogen chloride and water has damaged the catalyst like reduced the surface area and weakened the activity of catalyst. It can be presented from the Figure 17 that the average hydrogen conversion first increased and then fell with the enhancement of temperature. First of all, the performance of catalytic dehydrogenation was obviously advanced from 30 °C to 50 °C for the reason that the velocity of gas molecule increased with the enhancement of temperature. The corrosion of catalyst by chlorine gas was accelerated at surpass 50 °C, resulting in unsatisfactory catalytic dehydrogenation of catalyst. Therefore, the optimum reaction temperature for the removal of hydrogen from tail chlorine catalyzed by $\text{Co}_3\text{O}_4/\text{ZSM-5}$ catalyst is 50 °C.

As suggested by figure 18, the selectivity of hydrogen and chlorine reactions was obviously higher than that of hydrogen and oxygen reactions at different reaction temperatures. With the rise of temperature, the selectivity of hydrogen-chlorine reaction increased gradually, while the selectivity of hydrogen-oxygen reaction decreased generally. To sum up, the optimal reaction temperature for chlorine removal of hydrogen from tail was 50 °C, which was more favorable for hydrogen and chlorine reactions.

3. 6. 2. Effect of Different Calcination Temperature

The catalytic performance of $\text{Co}_3\text{O}_4/\text{ZSM-5}$ at different calcination temperature was set as Figure 19, which are loaded with 1 %wt. and participated in reaction at 50 °C. It can be obviously seen that the best performance for catalyzing the dehydrogenation was obtained under the calcination temperature of 500 °C, with the average conversion

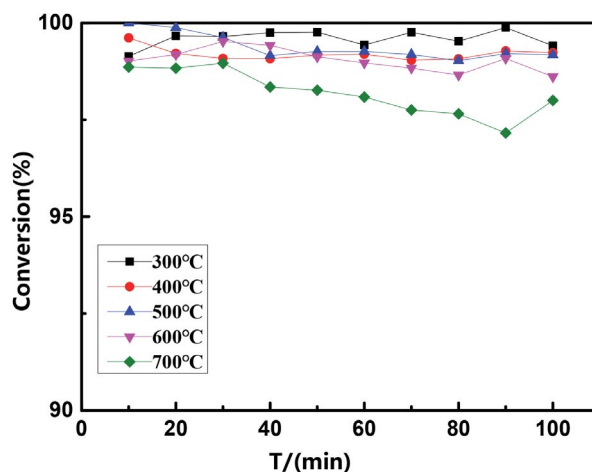


Figure 19. The overall conversion of $\text{Co}_3\text{O}_4/\text{ZSM-5}$

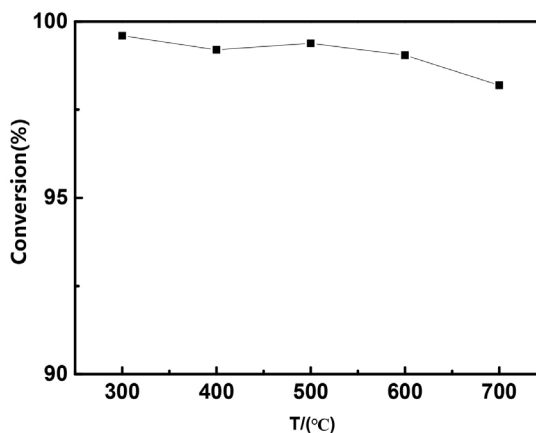


Figure 20. The average conversion of $\text{Co}_3\text{O}_4/\text{ZSM-5}$

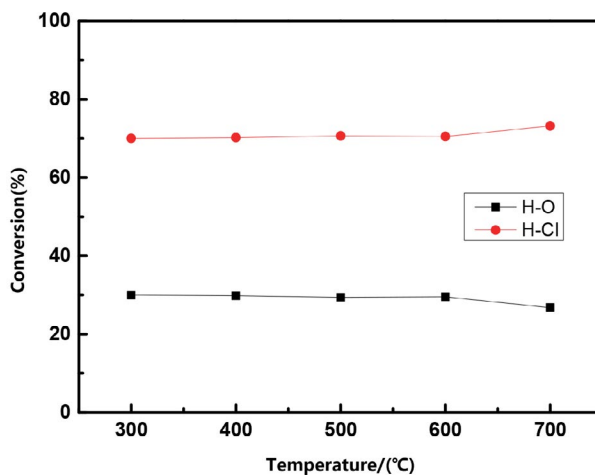


Figure 21. The average selectivity of $\text{Co}_3\text{O}_4/\text{ZSM-5}$

rate of $\text{Co}_3\text{O}_4/\text{ZSM-5}$ reached to 99.59%. It can be revealed that hydrogen removal performance was gradually weakened with increasing of calcination temperature. Combined with the analysis of XRD, the optimum calci-

nation temperature of the catalytic dehydrogenation is 300 °C.

Can see clearly from Figure 21, selectivity of hydrogen chloride reaction were higher than that of hydrogen and oxygen reaction selectivity under different calcination temperature. With the increase of calcination temperature, hydrogen and chloride reaction selectivity was slightly elevated, while hydrogen and oxygen reaction selectivity was reduced somewhat, which is more inclined to the reaction of hydrogen and chlorine.

3. 6. 3. Effect of Loading Amounts on Catalytic Performance

The catalytic performance of $\text{Co}_3\text{O}_4/\text{ZSM-5}$ at loading amount was illustrated in Figure 22, which was calcined at 600 °C and participated in reaction at 50 °C. Next, the loading amount of $\text{Co}_3\text{O}_4/\text{ZSM-5}$ was investigated in the catalytic dehydrogenation reaction as shown in the fig-

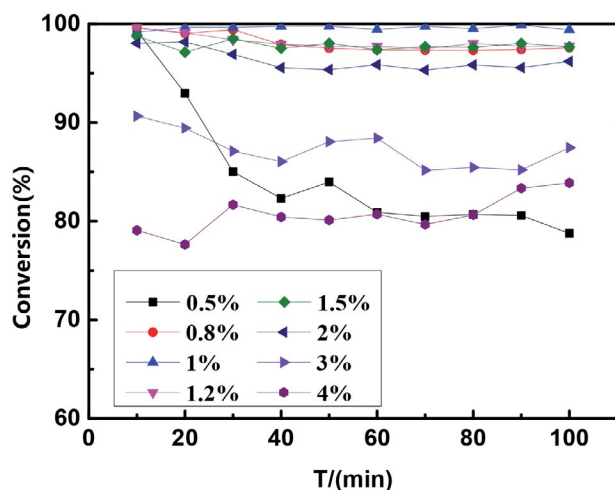


Figure 22. The overall conversion of $\text{Co}_3\text{O}_4/\text{ZSM-5}$

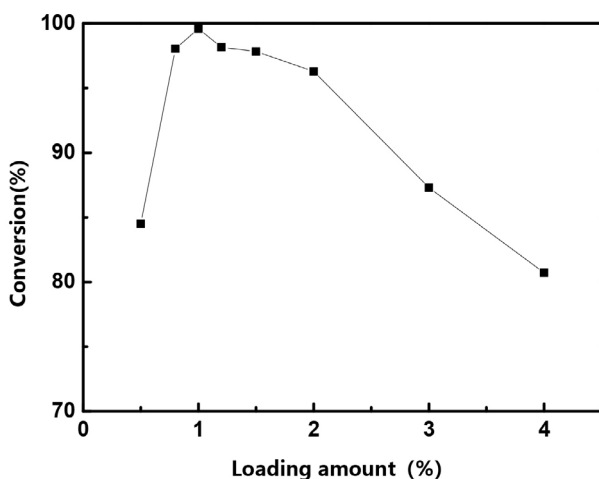


Figure 23. The average conversion of $\text{Co}_3\text{O}_4/\text{ZSM-5}$

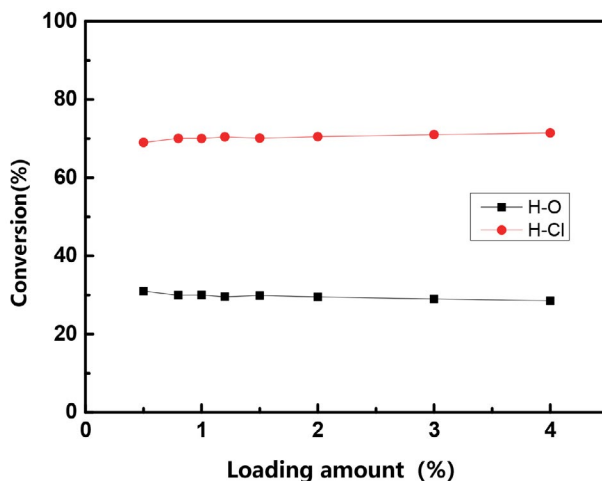


Figure 24. The average selectivity of $\text{Co}_3\text{O}_4/\text{ZSM-5}$

ure. It can be seen obviously that the change of average hydrogen conversion rate can be divided into four stages. First of all, the average conversion of hydrogen advanced dramatically with the load amount less than 0.8%. And then the average conversion of hydrogen slowed down as the load increased from 0.8% to 1%. After that, when the loading of Co_3O_4 is between 1% and 2%, the conversion of hydrogen began to decline tardily. Finally, the conversion of hydrogen fell rapidly with the loading amount of cobaltic oxide exceeding 2%. It is the reason that the amount of catalyst loading corresponds to the active component. Less active components with lower loading, leading to poor catalytic performance of the catalyst. So catalytic activity increased greatly with the increase of the Co_3O_4 loading of the ZSM-5 catalyst. Afterwards, excessive loading will not bring about good results, which blocked the pores and holes of the carrier and reduced the reaction surface area, the catalytic effect of the catalyst decreased rapidly. Based on analysis of the experimental data, the active components were evenly dispersed on the surface of the carrier and the catalytic activity was the highest when the average hydrogen conversion rate reached 99.60% with the loading amount of 1%.

As presented in figure 24, with elevating loading of catalyst, the selectivity of hydrogen-oxygen reaction and hydrogen chloride reaction was not observed the significant change, indicating that loading has little impact on the selectivity of hydrogen.

3. 7. Activity Test

In this experiment, $\text{Co}_3\text{O}_4/\text{ZSM-5}$ was used as catalyst, which was loaded with 1%wt. and calcined at 300 °C. and reacted continuously for 540 minutes at 50 °C, with a sampling interval of 30 minutes each time.

From Figure 25, it can be seen that the catalytic dehydrogenation effect was relatively stable during the reaction time of 120 minutes, which total conversion rate of

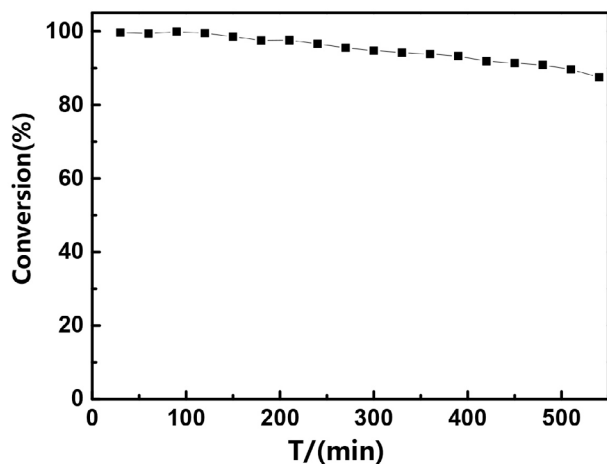


Figure 25. Total conversion rate of hydrogen in the catalytic reaction of $\text{Co}_3\text{O}_4/\text{ZSM-5}$ over time

hydrogen in the catalytic reaction of $\text{Co}_3\text{O}_4/\text{ZSM-5}$ achieved above 99%. After that, the catalytic activity decreased gradually. After the reaction time of 540 minutes, total conversion rate of hydrogen only dropped at 88.48%, meaning that excellent catalytic stability was significantly exhibited. The excellent catalytic activity of $\text{Co}_3\text{O}_4/\text{ZSM-5}$ catalysts can be attributed to the easy reducibility of Co^{3+} , higher Co^{3+} content, higher surface content of lattice oxygen, and fast migration of oxygen ions in the lattice of cobaltous oxide.²⁸

4. Conclusion

Combined with the performance characterization analysis and experimental data of hydrogen removal catalyst, we can see that $\text{Co}_3\text{O}_4/\text{ZSM-5}$ catalyst not only dropped the reaction temperature but also exhibited excellent catalytic performance than Co_3O_4 . The analysis of XRD characterization and SEM images illustrated that Co_3O_4 catalyst produced small amounts of cobalt chloride. After the reaction, the catalyst agglomerated and the surface became rough, which reduced the surface area of the catalytic reaction and the active center involved in the reaction, leading to the gradual decrease of catalytic performance. However, the morphology of supported catalyst $\text{Co}_3\text{O}_4/\text{ZSM-5}$ remained basically unchanged before and after the reaction, and its excellent catalytic activity can be attributed to the easy reducibility of Co^{3+} , higher Co^{3+} content, higher surface content of lattice oxygen, and fast migration of oxygen ions in the lattice of cobaltous oxide.

By comparing the catalytic dehydrogenation effect of Co_3O_4 at different reaction temperatures, the optimum temperature of 130 °C showed the best stability. The preparation method was observed to influence the catalytic performance of the $\text{Co}_3\text{O}_4/\text{ZSM-5}$ catalysts. We also find the optimal reaction condition is 1 %wt. Co_3O_4 loads on $\text{Co}_3\text{O}_4/\text{ZSM-5}$ catalyst with the calcination temperature of

300 °C under the reaction temperature of 50 °C. Its average hydrogen conversion rate catalyzed within 110 minutes of reaction was 99.59%, and only decreased to 88.48% after 540 minutes, which still showed certain catalytic activity. The N_2 adsorption and desorption characterization showed that the part of pore structure of the catalyst might be blocked and the active components were separated from the surface of the carrier, which was consistent with the reduction of catalytic performance of the catalyst in the experiment.

Cobaltous oxide is a kind of catalytic active component in catalytic dehydrogenation. Through the analysis of the selectivity of Co_3O_4 and $\text{Co}_3\text{O}_4/\text{ZSM-5}$, the selectivity of hydrogen and chlorine reaction is greater than the selectivity of hydrogen and oxygen. It could be confirmed that Co_3O_4 is more advantageous to catalyze the reaction of hydrogen and chlorine.

5. Acknowledgement

The authors thank the National Natural Science Foundation of China (No. 50972097) and the Natural Science Foundation of Shanxi (No.2008011025) for supporting this work.

Conflict of Interest

The authors declare no conflict of interest

6. Reference

- H. Khasawneh, M. N. Saidan, M. Al-Addous, *Energy Explor. Exploit.* **2019**, *37*, 1053–1072. DOI:10.1177/0144598719839767
- J. I. Otashu, M. Baldea, *Comput. Chem. Eng.* **2019**, *121*, 396–408. DOI:10.1016/j.compchemeng.2018.08.030
- D. H. Wang, W. Z. Pan, *China Chlor-Alkali.* **2017**, *7*, 1–5. DOI: 10.3969/j.issn.1009-1785.2017.07.001
- Y. Luo, *China Chlor-Alkali.* **2017**, *1*, 1–3.
- P. C. Zhang, *China Chlor-Alkali.* **2019**, *2*, 1–3. DOI:10.3969/j.issn.1009-1785.2019.02.001
- S. Peantong, S. Tangjitsitcharoen, IOP Conference Series: Materials Science and Engineering. **2017**, *215*, 012018. DOI:10.1088/1757-899X/215/1/012018
- J. P. Zhang, D. S. Li, Y. Z. Chen, *Environ. Prot.* **2004**, *12*, 22–24. DOI:10.3969/j.issn.0253-9705.2004.12.005
- K. T. Chue, J. N. Kim, Y. J. Yoo, S. H. Cho, R. T. Yang, *Ind. Eng. Chem. Res.* **1995**, *34*, 591–598. DOI:10.1021/ie00041a020
- K. Kato, M. Kawaguchi, Method and apparatus for purifying polluted soil, and apparatus for emitting chlorine-containing gas and apparatus for decomposing polluted gas using the same, US Patent Number 20000741332, date of parent January 24, **2002**.
- G. J. Kulcsar, M. Kulcsar-Novakova, *Stud. Cercet. Chim.* **1957**, *8*, 221–230.

11. G. C. Allen, G. P. Butt, Removal of hydrogen from chlorine, GB Patent Number 1388292, date of parent March 26, 1975.
12. H. Coolen, Catalytic removal of hydrogen from chlorine, ZA Patent Number 6804493, date of parent January 12, 1970.
13. W. J. M. Pieters, F. Wenger, Removal of low concentrations of hydrogen from chlorine gas, US Patent Number 4224293, date of parent September 23, 1980.
14. H. L. Zhou, Study on Catalytic Dehydrogenation Performance of Hydrophobic Catalyst and Platinum Metal Catalyst in the Tail Chlorine at Low Temperature. Dissertation. Taiyuan: Taiyuan University of Technology, 2015.
15. T. T. Lu, Research on Catalytic Dehydrogenation Performance of Au and Au-Ag Double Metals Supported on Al₂O₃ in Tail Chlorine at Low Temperature. Dissertation. Taiyuan: Taiyuan University of Technology, 2016.
16. H. H. Wang, T. T. Lu, Y. N. Li, B. Wu, J. W. Xue, F. X. Li, Z. P. Lv, *J. Chemistry* 2016, 2090–9063. DOI:10.1155/2016/5620316
17. X. Q. Chen, Study on Performance of Dehydrogen Removal from Tail Chlorine Catalyzed by Copper and Copper Oxide Catalysts at Low Temperature. Dissertation. Taiyuan: Taiyuan University of Technology, 2018.
18. X. Liu, L. Xue, X. Q. Chen, J. S. Liu, H. H. Wang, J. W. Xue, F. X. Li, Z. P. Lv, *Quim. Nova* 2019, 42, 319–328. DOI:10.21577/0100-4042.20170322
19. T. Kanazawa, *Appl. Catal., B* 2006, 65, 185–190. DOI:10.1016/j.apcatb.2006.01.001
20. B. Zhang, X. B. Zhang, L. Y. Xu, Y. J. Zhang, Y. H. Qin, C. F. Liang, *React. Kinet., Mech. Catal.* 2013, 110, 207–214. DOI:10.1007/s11144-013-0589-7
21. S. J. Luo, *Chlor-Alkali Ind.* 1991, 2, 23–25.
22. G. K. Liu, F. J. Lin, *Chlor-Alkali Ind.* 2006, 3, 24–26. DOI:10.3969/j.issn.1008-133X.2006.03.009
23. X. T. Zhang, Y. Yan, *R. Soc. Open Sci.* 2018, 5, 8. DOI:10.1098/rsos.180587
24. G. S. Qi, R. T. Yang, *Appl. Catal., A* 2005, 287, 25–33. DOI:10.1016/j.apcata.2005.03.006
25. X. W. Zou, J. Z. Yao, X. M. Yang, W. L. Song, W. G. Lin, *Chin. J. Process Eng.* 2007, 6, 1107–1113. DOI:10.1016/S1001-6058(07)60030-4
26. D. L. Mowery, M. S. Graboski, T. R. Ohno, R. L. McCormick, *Appl. Catal., B* 1999, 21, 157–169. DOI:10.1016/S0926-3373(99)00017-X
27. D. N. Gao, S. Wang, C. X. Zhang, Z. S. Yuan, S. D. Wang, *Chin. J. Catal.* 2008, 29, 1221–1225. DOI:10.1016/S1872-2067(09)60027-9
28. Z. Z. Zhu, G. Z. Lu, Z. G. Zhang, Y. Guo, Y. L. Guo, Y. Q. Wang, *ACS Catal.* 2013, 3, 1154–1164. DOI:10.1021/cs400068v

Povzetek

Co₃O₄/ZSM-5 je bil uporabljen za dehidrogenacijo rezidualne klorove plinske mešanice iz klor-alkalne industrije zaradi svoje nizke cene in varnosti. Co₃O₄/ZSM-5 je bil sintetiziran z volumsko impregnacijsko metodo. Dehidrogenacijske lastnosti Co₃O₄/ZSM-5 smo preučili s katalitično reakcijo vodika s kisikom in klorom, ki je bila izvedena v strnjem sloju, pri čemer je bila mešanica plinov pripravljena skladno s sestavo in vsebnostjo klorove plinske mešanice v industriji: Cl₂(65%–80%), N₂(6–16%), O₂(8%–10%) in H₂(1.5%–4%). Katalitična učinkovitost in Co₃O₄/ZSM-5 stabilnost pri dehidrogenaciji klorove plinske mešanice je bila boljša kot pri čistem Co₃O₄. Po kalcinaciji na 300 °C je Co₃O₄/ZSM-5 z 1 ut.% vsebnostjo Co₃O₄ izkazal pri 50 °C odlične katalitične lastnosti s povprečno konverzijo vodika do 99.95%.



Except when otherwise noted, articles in this journal are published under the terms and conditions of the Creative Commons Attribution 4.0 International License

DRUŠTVENE VESTI IN DRUGE AKTIVNOSTI SOCIETY NEWS, ANNOUNCEMENTS, ACTIVITIES

Vsebina

Kemijski slovar	S3
Doktorska in magistrska dela, diplome v letu 2019	S5
Koledar važnejših znanstvenih srečanj s področja kemije, kemijske tehnologije in kemijskega inženirstva	S31
Navodila za avtorje	S36

Contents

Chemical Dictionary	S3
Doctoral theses, master degree theses, and diplomas in 2019	S5
Scientific meetings – chemistry, chemical technology and chemical engineering	S31
Instructions for authors	S36

KEMIJSKI SLOVAR

Peter Glavič¹, Andrej Šmalc, Leon Čelik, Anton Stušek

Dopisni član skupine avtorjev:

peter.glavic@um.si

Slovenska kemijska terminologija je razmeroma mlada. Za prvi resnejši prispevek na tem področju lahko štejemo Cigaletovo *Znanstveno terminologijo za srednja učilišča* iz leta 1880. Po nastanku slovenske univerze leta 1919 je potreba po domačem izrazoslovju na področju kemije narastla, tako da je leta 1921 izšla Ferjančičeva *Začasna nemško-slovenska kemijska terminologija*. V šestdesetih letih prejšnjega stoletja je bila ustanovljena Komisija za slovensko kemijsko terminologijo in nomenklaturu, ki je sodelovala s kemijskim izrazjem pri pripravi 2. izdaje Splošnega tehniškega slovarja – izšel je v letih 1978–1981.

Do resnejšega dela v zvezi s pripravo slovarja posebej za področje kemijske terminologije je prišlo leta 2004, ko je začela delovati komisija, ki so jo sestavljali avtorji tega referata in do leta 2013 še Sonja Malej. Pri izdelavi slovarja, ki je do leta 2013 nastajal v okviru delovnega programa Inštituta za slovenski jezik Frana Ramovša ZRC SAZU, sta do tedaj sodelovala terminologa Cvetana Tavzes in Simon Atelšek. Komisija objavlja kratka letna poročila o delu v Acti Chimici Slovenici.

Financiranje dela je po letu 2011 začelo usihati, dokler ni leta 2014 povsem prenehalo. Zato je komisija po letu 2013 zaprosila za pomoč nekatere ustanove in tovarne. Odzvali sta se obe Fakulteti za kemijo in kemijsko tehnologijo (FKKT) v Ljubljani in Mariboru ter tovarne Krka, Helios, Lek in Melamin. Poleg naštetih sta prvo leto s prispevkom sodelovali tudi družbi Yulon in Savatech. Tako je komisija lahko v zadnjih štirih letih krila vsaj najnujnejše stroške. V letu 2018 smo dobili od ARRS sredstva za ureditev in objavo slovarja na medmrežju.

Slovar obsega okrog okoli 7500 gesel in zajema izrazje s področja kemije, kemijske tehnologije in procesne tehnike. Namenjen je kot pomoč strokovnjakom s tega področja in študentom, saj je ob vsakem geslu tudi osnovna informacija o njem oz. kratka razlaga. Omeniti velja tudi angleške in nemške ustreznike ob vsakem geslu, ki omogočajo uporabnikom angleške oz. nemške strokovne literature poiskati ustrezen slovenski izraz. Za zdaj je predvidena samo elektronska izdaja na spletni strani, ki sta jo za slovar prijazno dali na razpolago Slovensko kemijsko društvo, <https://slovar.chem-soc.si/> in FKKT Maribor, <https://www.fkkt.um.si/kslovar/index.php> uvod, navodila in življenjepise avtorjev najdete v dnu vsake strani, <https://www.fkkt.um.si/kslovar/avtorji.php>. Do slovarja je mogoče najbolj enostavno priti, če v Google vtipkate *Kemijski slovar*. Pri pripravi spletne izdaje slovarja sta sodelovala

prof. dr. Milan Ojsteršek s Fakultete za elektrotehniko, računalništvo in informatiko Univerze v Mariboru in njegov študent Klemen Andrejc Kac, ki je opravil tehnično delo.

Druga izdaja je namenjena tudi pripombam k razlagam in predlogom za nova gesla, ki jih bomo upoštevali pri sprotne popravljanju. Računalniški program nam v glavi preglednice omogoča različno iskanje: po črkah abecede, po pojmu (geslu, iztočnici), po pomenu (razlagi), po angleškem ali nemškem pojmu ali po simbolu. Spletna izdaja dopušča sprotne popravljanje ter dopolnjevanje slovarja na podlagi prejetih pripomb in predlogov. Te bo zbirala komisija in jih je mogoče poslati na naslednja e-naslova: peter.glavic@um.si ali andrej_smalc@t-2.net.

UNIVERZA V LJUBLJANI
FAKULTETA ZA KEMIJO IN KEMIJSKO TEHNOLOGIJO

1. januar – 31. december 2019

DOKTORATI

DOKTORSKI ŠTUDIJSKI PROGRAM KEMIJSKE ZNANOSTI

KEMIJA

Maja PORI

VPLIV SINTEZNIH PARAMETROV NA UČINKOVITOST
KATALIZATORJEV NA OSNOVI BAKRA IN CINKOVEGA
OKSIDA ZA REAKCIJE TVORBE METANOLA

Mentor: izr. prof. dr. Marjan Marinšek
Somentor: viš. znan. sod. dr. Goran Dražič
Datum zagovora: 23. 4. 2019

Matic POBERŽNIK

KVANTNO MEHANSKO MODELIRANJE OKSIDACIJE
ALUMINIJEVIH POVRŠIN IN NJIHOVIH INTERAKCIJ S
KOROZIJSKIMI INHIBITORJI

Mentor: viš. znan. sod. dr. Anton Kokalj
Somentor: prof. dr. Tomaž Urbič
Datum zagovora: 25. 4. 2019

Urša PETEK

KATALIZATORJI S POSAMIČNIMI ATOMI KOVIN NA
OGLJIKOVH SUBSTRATIH

Mentor: prof. dr. Miran Gaberšček
Datum zagovora: 13. 5. 2019

Dunja GUSTINČIČ

ADSORPCIJA AZOLNIH MOLEKUL NA OKSIDIRANO
POVRŠINO BAKRA IN NJIHOVA INHIBICIJA KOROZIJE
BAKRA

Mentor: viš. znan. sod. dr. Anton Kokalj
Somentorica: prof. dr. Ksenija Kogej
Datum zagovora: 5. 6. 2019

Ida KRAŠEVEC

RAZVOJ ANALIZNIH METOD ZA DOLOČANJE
BENZOTRIAZOLNIH SPOJIN V OKOLJSKIH VZORCIH

Mentorica: prof. dr. Helena Prosen
Datum zagovora: 19. 9. 2019

Boštjan ŽENER

OPTIMIZACIJA PRIPRAVE IN STRUKTURNE LASTNOSTI
DOPIRANEGA NANODIMENZIONIRANEGA
TITANOVEGA DIOKSIDA

Mentorica: izr. prof. dr. Romana Cerc Korošec
Datum zagovora: 30. 9. 2019

Žiga MEDOŠ

TERMODINAMSKE RAZISKAVE MICELIZACIJE
ALKALIJSKIH IN KVATERNIH AMONIJEVIH ALKIL
KARBOKSILATOV TER NJIHOVIH PREKURZORJEV

Mentorica: prof. dr. Marija Bešter Rogač
Datum zagovora: 30. 9. 2019

Miha VIRANT

RAZVOJ HOMOGENIH PALADIJEVIH KATALITSKIH
SISTEMOV ZA IZBRANE PRETVORBE TERMINALNIH
ACETILENOV

Mentor: prof. dr. Janez Košmrlj
Datum zagovora: 28. 11. 2019

Matija GATALO

RAZVOJ SINTEZE NANODELCEV BINARNIH IN
TERNARNIH ZLITIN PLATINE NA OGLJIKOVEM
NOSILCU KOT ELEKTROKATALIZATORJU

Mentor: prof. dr. Miran Gaberšček
Datum zagovora: 29. 11. 2019

Jernej BOBNAR

MODIFIKACIJA POVRŠINE LITIJA ZA AKUMULATORSKE
APLIKACIJE

Mentor: doc. dr. Boštjan Genorio
Somentor: izr. prof. dr. Robert Dominko
Datum zagovora: 29. 11. 2019

Špela GRADIŠAR

SINTEZA DOBRO DEFINIRANIH POLIPEPTIDOV IN
POLIPEPTIDNIH HIBRIDNIH POLIMEROV Z UPORABO
HIDROKSILNIH SKUPIN ZA INICIACIJO

Mentorica: znan. svet. dr. Ema Žagar
Somentor: izr. prof. dr. Uroš Grošelj
Datum zagovora: 6. 12. 2019

BIOKEMIJA**Urška SLAPŠAK**

ŠTUDIJA PROSTORSKIH STRUKTUR, DINAMIKE IN INTERAKCIJ PRIONSКИH PROTEINOV Z JEDRSKO MAGNETNO REZONANCO
Mentor: prof. dr. Janez Plavec
Datum zagovora: 16. 5. 2019

Mateja REBERNIK

IDENTIFIKACIJA IN KARAKTERIZACIJA ALOSTERIČNIH MODIFIKATORJEV DIPEPTIDIL-PEPTIDAZE I
Mentor: izr. prof. dr. Marko Novinec
Datum zagovora: 6. 11. 2019

Anita KOTAR

STRUKTURNE ŠTUDIJE Z GVANINI BOGATIH ZAPOREDIJ V PROMOTORSКИH REGIJAH PROTOONKOGENOV
Mentor: prof. dr. Janez Plavec
Datum zagovora: 3. 10. 2019

KEMIJSKO INŽENIRSTVO**Marko TRAMPUŽ**

MATEMATIČNO MODELIRANJE ŠARŽNE KRISTALIZACIJE UČINKOVINE PRI RAZLIČNIH POGOJIH OBRATOVANJA
Mentor: doc. dr. Blaž Likozar
Datum zagovora: 8. 10. 2019

Špela HAJDUK

MODIFICIRAN CINKOV OKSID KOT KATALIZATOR ZA PRIDOBIVANJE KISIKA IN VODIKA
Mentor: izr. prof. dr. Marjan Marinšek
Somentor: viš. znan. sod. dr. Marjan Bele
Datum zagovora: 24. 10. 2019

INTERDISCIPLINARNI DOKTORSKI ŠTUDIJSKI PROGRAM VARSTVO OKOLJA**Predrag KORICA**

DOLOČITEV FAKTORJEV VPLIVA IN POSLEDIC RAVNANJA Z ODPADKI S POUČENOM NA PREPREČEVANJU NJIHOVEGA NASTAJANJA
Mentorica: izr. prof. dr. Andreja Žgajnar Gotvajn
Somentorica: prof. dr. Andreja Cirman
Datum zagovora: 10. 10. 2019

MAGISTRSKI ŠTUDIJI**MAGISTRSKI ŠTUDIJSKI PROGRAM 2. STOPNJE – KEMIJA****Tina GRUBAR**

RAZVOJ METODE ZA DOLOČEVANJE PESTICIDOV V TLEH
Mentorica: prof. dr. Helena Prosen
Datum zagovora: 24. 1. 2019

Klemen BERLEC

TVORBA HALOGENSKIH VEZI V SOLEH HALOGENIRANIH DERIVATOV SALICILNE IN IZOFTALNE KISLINE
Mentor: izr. prof. dr. Franc Perdih
Datum zagovora: 22. 2. 2019

Nina PAVLOVIČ

BAKROVE(II) SPOJINE Z ANIONOM 2-ACETILSALICILNE KISLINE
Mentorica: doc. dr. Nives Kitanovski
Datum zagovora: 18. 2. 2019

Urša KOŠAK

OVREDNOTENJE GRADIENTNEGA IN PULZNEGA NAČINA V PRETOČNI ANALIZI
Mentorica: doc. dr. Nataša Gros
Datum zagovora: 22. 2. 2019

Maja GREGORC

OPTIMIZACIJA REAKCIJE PRIPAJANJA PO SONOGASHIRI S Pd-NHC KATALIZATORJEM
Mentor: prof. dr. Janez Košmrlj
Datum zagovora: 22. 2. 2019

Žan TESTEN

UPORABA ARILIDENSKIH DERIVATOV PIROLONA V STEREOSELEKTIVNIH ORGANOKATALIZIRANIH TRANSFORMACIJAH
Mentor: izr. prof. dr. Uroš Grošelj
Datum zagovora: 1. 4. 2019

Žan HRIBAR

SINTEZA IN UPORABA IZBRANIH TERMINALNIH ACETILENOV

Mentor: prof. dr. Janez Košmrlj

Datum zagovora: 25. 4. 2019

Ema SLEJKO

VPLIV POLI(ETILEN GLIKOLA) NA KOEFICIENT AKTIVNOSTI NATRIJEVEGA KLORIDA V VODNIH RAZTOPINAH

Mentorica: prof. dr. Barbara Hribar Lee

Datum zagovora: 24. 5. 2019

Sara TOMŠIČ

FUNKCIONALIZACIJA MONOLITNIH KROMATOGRFSKIH NOSILCEV ZA NAMENE UČINKOVITE IZOLACIJE LAKTOFERINA IZ SIROTKE

Mentor: prof. dr. Darko Dolenc

Datum zagovora: 30. 5. 2019

Natalija POGORELC

SINTEZA IN KARAKTERIZACIJA KOORDINACIJSKIH SPOJIN S KVERCETINOM

Mentorica: doc. dr. Nives Kitanovski

Datum zagovora: 14. 6. 2019

Polona ŠKRINJAR

ŠTUDIJA SORPCIJE POTENCIALNO STRUPENIH ELEMENTOV NA BIOGLJE

Mentorica: doc. dr. Marija Zupančič

Datum zagovora: 14. 6. 2019

Luka CIBER

SINTEZA PIROLONSKIH DERIVATOV IN NJIHOVA UPORABA V ORGANOKATALIZIRANIH REAKCIJAH

Mentor: izr. prof. dr. Uroš Grošelj

Datum zagovora: 3. 7. 2019

Jernej EKAR

SINTEZA HIDRAZINILPIRIDINOV IN VEZAVA SUBSTITUIRANIH HIDRAZINOV NA BICIKLO[2.2.2] OKTENSKI SKELET

Mentor: doc. dr. Krištof Kranjc

Datum zagovora: 11. 7. 2019

Jaka ŠTIRN

VPLIV POLIETILEN GLIKOLA NA STRUKTURNE LASTNOSTI NATRIJEVEGA POLIMETAKRILATA V VODNIH MEŠANICAH

Mentor: prof. dr. Jurij Reščič

Datum zagovora: 11. 7. 2019

Luka RIFELJ

ENTALPIJE MEŠANJA RAZTOPIN FULERENATNIH SOLI Z RAZTOPINAMI ENOSTAVNIH SOLI

Mentor: izr. prof. dr. Janez Cerar

Datum zagovora: 23. 7. 2019

Simona GRIČAR

SINTEZA IN BIOLOŠKA AKTIVNOST RUTENIJEVIH KOORDINACIJSKIH SPOJIN Z IZBRANIMI O,O-, N,O- IN N,N-VEZNIMI LIGANDI

Mentor: prof. dr. Iztok Turel

Datum zagovora: 29. 8. 2019

Rok MARINIČ PODBRŠČEK

OPTIMIZACIJA REAKCIJSKIH PARAMETROV SUZUKI-MIYAUURA REAKCIJE

Mentor: doc. dr. Martin Gazvoda

Datum zagovora: 30. 8. 2019

Jan GNIDOVEC

ORGANOKATALIZIRANA SPIROHETEROCIKLIZACIJA ARILIDENSKIH DERIVATOV PIROLONA Z 1,4-DITIAN-2,5-DIOLOM

Mentor: izr. prof. dr. Uroš Grošelj

Datum zagovora: 2. 9. 2019

Tisa ŽEVART

PRIPRAVA IN REAKTIVNOST PALADIJEVIH KOMPLEKSOV Z NUKLEOFILNIMI LIGANDI

Mentor: doc. dr. Martin Gazvoda

Datum zagovora: 5. 9. 2019

Nataša ŽIGANTE

TERMODINAMIKA KONFORMACIJSKIH SPREMENB G-KVADRUPLEKSOV Z ZAPOREDJEM D(G4T4G4)

Mentor: doc. dr. Iztok Prislan

Datum zagovora: 6. 9. 2019

Nataša PLUTŠTUDIJA INTERAKCIJ MED PROTEINOM FimH IN α -D-MANOZNIMI GLIKOKONJUGATI

Mentor: doc. dr. Črtomir Podlipnik

Datum zagovora: 6. 9. 2019

Tjaša PAVČNIK

RAZVOJ METODE ZA GEM-DIMERIZACIJO TERMINALNIH ACETILENOV

Mentor: prof. dr. Janez Košmrlj

Datum zagovora: 6. 9. 2019

Blaž ZDOVC

VISKOZNOST VODNIH RAZTOPIN GOVEJEGA SERUMSKEGA ALBUMINA

Mentor: izr. prof. dr. Miha Lukšič

Datum zagovora: 9. 9. 2019

Tjaša RIJAVEC

OPTIMIZACIJA DERIVATIZACIJE NEKATERIH AMINOV IN IDENTIFIKACIJA NJIHOVIH RAZGRADNIH PRODUKTOV

Mentorica: izr. prof. dr. Irena Kralj Cigić

Datum zagovora: 9. 9. 2019

Dejan MARJANOVIČ

UPORABA RAZLIČNIH SPEKTROSKOPSKIH TEHNIK (ICP-MS, ICP-OES IN AAS) PRI DOLOČEVANJU KOVIN V BEZGU

Mentor: izr. prof. dr. Mitja Kolar

Datum zagovora: 16. 9. 2019

Katarina DOLES

KATALITSKO ARILIRANJE C-H VEZI 2,3-DISUBSTITUIRANIH PIRAZINSKIH DERIVATOV

Mentor: izr. prof. dr. Franc Požgan

Datum zagovora: 16. 9. 2019

Bibi ERJAVEC

SINTEZA NOVIH FLUORESCENTNIH OZNAČEVALCEV BIOMOLEKUL NA OSNOVI Z CuO KATALIZIRANE CuAIAC REAKCIJE

Mentor: prof. dr. Jurij Svete
Datum zagovora: 16. 9. 2019

Anja KRAMER

ENTALPIJE MEŠANJA RAZTOPIN ALKALIJSKIH HALIDOV KOT TEST ZAKONA O UJEMANJU AFINITET IONOV DO VODE

Mentor: izr. prof. dr. Janez Cerar
Datum zagovora: 30. 9. 2019

Amela MEHANOVIČ

DOLOČANJE VSEBNOSTI IZBRANIH KOVIN V LASEH

Mentor: izr. prof. dr. Mitja Kolar
Datum zagovora: 8. 10. 2019

Nika SIMONIČ

PREUČEVANJE OKSIDACIJE OLJČNEGA IN ARAŠIDOVEGA OLJA PRI SEGREVANJU Z METODAMI TERMIČNE ANALIZE

Mentorica: izr. prof. dr. Romana Cerc Korošec
Datum zagovora: 17. 10. 2019

Tjaša BLATNIK

DOLOČANJE 1-HIDROKSICIKLOHEKSIL FENIL KETONA IN SOLI TRIARILSULFONIJEVEGA HEKSAFLUOROANTIMONATA V POLIMERNIH MATERIALIH

Mentorica: izr. prof. dr. Irena Kralj Cigić
Datum zagovora: 25. 10. 2019

Jan PETROVČIČ

OBNOVLJIVI REAGENTI ZA NUKLEOFILNO FLUORIRANJE NA OSNOVI IMIDAZOLIJEVEGA FLUORIDA

Mentor: izr. prof. dr. Jernej Iskra
Sommentor: viš. znan. sod. dr. Gašper Tavčar
Datum zagovora: 28. 10. 2019

Domen JERONČIČ

SINTEZA TIOHIDROKSAMSKIH KISLIN TER NJIHOVIH NIKLJEVIH IN RUTENIJEVIH KOMPLEKSOV

Mentor: doc. dr. Jakob Kljun
Datum zagovora: 27. 11. 2019

Hana HACE

STEREOSELEKTIVNE PRETVORBE IZATINSKIH DERIVATOV Z BIFUNKCIONALNIMI ORGANOKATALIZATORJI

Mentor: izr. prof. dr. Bogdan Štefane
Datum zagovora: 29. 11. 2019

Rok TOMŠIČ

DOLOČANJE NEONIKOTINOIDNIH PESTICIDOV V PROPOLISU

Mentorica: prof. dr. Helena Prosen
Sommentorica: viš. znan. sod. dr. Ester Heath
Datum zagovora: 11. 12. 2019

Tjaša PODLOGAR

STRUKTURA IN REAKTIVNOST PALADIJEVIH KOMPLEKSOV Z RAZLIČNIMI TRIAZOLILIDENSKIMI LIGANDI

Mentor: doc. dr. Martin Gazvoda
Datum zagovora: 12. 12. 2019

Lea KASTELEC

POTENCIOMETRIČNO DOLOČANJE IN ŠTUDIJ INTERAKCIJ KALCIJEVIH IONOV S TRINATRIJEVIM CITRATOM IN HUMANIM ALBUMINOM

Mentor: izr. prof. dr. Mitja Kolar
Sommentor: doc. dr. Gregor Novljan
Datum zagovora: 16. 12. 2019

Tomaž KOTNIK

SINTEZA IN LASTNOSTI RAZGRADLJIVIH IN SORODNIH POLIMEROV

Mentor: prof. dr. Jurij Svete
Datum zagovora: 20. 12. 2019

MAGISTRSKI ŠTUDIJSKI PROGRAM 2. STOPNJE – KEMIJSKO INŽENIRSTVO**Erik STARC**

PRIPRAVA ZAMREŽENIH POLIESTROV NA OSNOVI POLIKAPROLAKTONA S POLIMERIZACIJO Z ODPIRANJEM OBROČA

Mentor: doc. dr. Aleš Ručigaj
Datum zagovora: 8. 1. 2019

Damjan KODER

ČIŠČENJE MODELNIH FARMACEVTSKIH ODPADNIH VOD S KONTINUIRNO OZONACIJO

Mentorica: izr. prof. dr. Andreja Žgajnar Gotvajn
Datum zagovora: 17. 1. 2019

Milan OBRADOVIČ

VPLIV MIKROPLASTIKE NA KOPENSKE ORGANIZME

Mentorica: doc. dr. Gabriela Kalčikova
Sommentorica: doc. dr. Anita Jemec Kokalj
Datum zagovora: 14. 2. 2019

Timotej GALUN

REAKCIJE PRETVORBE MODELNIH DIMEROV LIGNINA

Mentor: prof. dr. Igor Plazl
Sommentor: doc. dr. Blaž Likozar
Datum zagovora: 18. 3. 2019

Polona STARAŠINIČ

UPORABA ŠARŽNEGA POSTOPKA OZONACIJE ZA ČIŠČENJE ODPADNE VODE IZ PROIZVODNJE ANTIBIOTIKOV

Mentorica: izr. prof. dr. Andreja Žgajnar Gotvajn
Datum zagovora: 14. 6. 2019

Dominika ZORMAN

ADSORPCIJA SREBRA NA MIKROPLASTIKO V VODNEM OKOLJU

Mentorica: doc. dr. Gabriela Kalčikova
Datum zagovora: 12. 7. 2019

Blaž PERIČ

EKSTRAKCIJA V MINIATURIZIRANEM PRETOČNEM
SISTEMU Z INTENZIVNIM KONTAKTIRANJEM FAZ
Mentorica: prof. dr. Polona Žnidaršič Plazl
Datum zagovora: 19. 7. 2019

Blaž REGINA

RAZVOJ KONTINUIRNEGA PROCESA SINTEZE IN
EKSTRAKCIJE IZBRANE AKTIVNE FARMACEVTSKE
UČINKOVINE
Mentorica: prof. dr. Polona Žnidaršič Plazl
Datum zagovora: 19. 7. 2019

Nina KUZMIČ

SPREMINJANJE PRODUKTIVNOSTI PRIDOBIVANJA
BAKTERIOFAGOV V KONTINUIRNEM SISTEMU
Mentor: prof. dr. Aleš Podgornik
Datum zagovora: 26. 8. 2019

Ana OBERLINTNER

RAZGRADNJA BIOPLASTIKE NA OSNOVI HITOZANA V
KOPENSKEM OKOLJU
Mentorica: doc. dr. Gabriela Kalčikova
Somentor: doc. dr. Blaž Likozar
Datum zagovora: 30. 8. 2019

Ula ROZMAN

ADSORPCIJA IZBRANIH TEŽKIH KOVIN NA ODPADNO
GLIVNO BIOMASO
Mentorica: doc. dr. Gabriela Kalčikova
Datum zagovora: 30. 8. 2019

Marko FIRM

PRIPRAVA KOMPOZITNIH ANOD ZA MAGNEZIJEVE
AKUMULATORJE
Mentor: izr. prof. dr. Robert Dominko
Datum zagovora: 13. 9. 2019

Luka PAVKO

POSTAVITEV IN OPTIMIZACIJA CVD SISTEMA ZA RAST
GRAFENA NA SUBSTRATIH IZ BAKRA IN NIKLJA
Mentor: doc. dr. Boštjan Genorio
Datum zagovora: 13. 9. 2019

Tine PLAVČAK

RAZVOJ MEMBRANSKEGA MIKROSEPARATORJA
Mentor: prof. dr. Igor Plazl
Datum zagovora: 16. 9. 2019

Žan KOVAČIČ

MEHANSKE LASTNOSTI IN KINETIKA ZAMREŽEVANJA
AROMATSKIH EPOKSIDOV Z AMINOMALEIMIDOM
Mentor: doc. dr. Aleš Ručigaj
Datum zagovora: 16. 9. 2019

Domen OTOREPEC

IPSO-SUBSTITUCIJE ORTO LITIIRANIH DERIVATOV
BENZENA Z RAZLIČNIMI ELEKTROFILI V CEVNEM
MIKROREKTORJU
Mentor: prof. dr. Igor Plazl
Datum zagovora: 20. 9. 2019

Miha IVANETIČ

VPLIV SESTAVE HIDROGELOV NA OSNOVI TEMPO
MODIFICIRANIH NANOCELULOZNIH VLAKEN IN
SKLEROGLUKANA NA REOLOŠKE LASTNOSTI IN
SPROŠČANJE SPOJIN
Mentorica: prof. dr. Urška Šebenik
Datum zagovora: 26. 9. 2019

Barbara REPIČ

SINTEZA ORGANSKO-ANORGANSKIH HIBRIDNIH
HALOGENID PEROVSKITOV
Mentor: izr. prof. dr. Marjan Marinšek
Datum zagovora: 27. 9. 2019

Mojca ZALOKAR

VREDNOTENJE VPLIVOV ANTIBIOTIKOV NA VODNE
BOLHE IN SOLINARSKÉ RAKE
Mentorica: doc. dr. Gabriela Kalčikova
Datum zagovora: 27. 9. 2019

Klemen PLAHUTA

GRAFENSKI NANOTRAKOVI IN NJIHOVA UPORABA V
KOMPOZITNIH MATERIALIH
Mentor: doc. dr. Boštjan Genorio
Datum zagovora: 19. 12. 2019

MAGISTRSKI ŠTUDIJSKI PROGRAM 2. STOPNJE – BIOKEMIJA**Jakob RUPERT**

PRIPRAVA IN KRISTALIZACIJA REKOMBINANTNEGA
ANEKSINA A11
Mentorica: doc. dr. Vera Župunski
Datum zagovora: 23. 1. 2019

Ana KRIŠELJ

PRIMERJAVA VPLIVA RAZLIČNIH ANTIOKSIDANTOV NA
SIGNALNE POTI, KI JIH SPROŽI MENADION NA CELIČNI
LINIJI IMORTALIZIRANIH MIŠJIH EMBRIONALNIH
FIBROBLASTOV
Mentor: prof. ddr. Boris Turk
Datum zagovora: 11. 2. 2019

Ema GUŠTIN

LIPIDNE KAPLJICE IN TRANSPORT MAŠČOBNIH KISLIN
V CELICAH RAKA DOJKE
Mentor: znan. sod. dr. Toni Petan
Somentor: doc. dr. Miha Pavšič
Datum zagovora: 11. 2. 2019

Anja HERCEG

POGOSTOST OKUŽBE Z VIRUSOM BHANJA PRI
PROSTOŽIVEČIH GLODAVCIH IN KLOPIH V SLOVENIJI
Mentorica: prof. dr. Tatjana Avšič Županc
Datum zagovora: 8. 3. 2019

Bojana LAZOVIĆ

VPLIV SPREMEMBE ZUNAJCELIČNE KONCENTRACIJE KALIJA NA ZNOTRAJCELIČNO RAVEN cAMP, L-LAKTATA IN KALCIJA V PODGANJH ASTROCITIH

Mentorica: doc. dr. Nina Vardjan

Somentor: prof. dr. Robert Zorec

Datum zagovora: 13. 3. 2019

Tjaša GRUM

DOLOČANJE STOPNJE METILACIJE DNA PRI SAMOMORILNEM VEDENJU

Mentorica: doc. dr. Alja Videtič Paska

Datum zagovora: 28. 3. 2019

Vanna IMŠIROVIĆ

KLONIRANJE IN IZRAŽANJE AMILOIDNEGA FRAGMENTA ČLOVEŠKEGA KATEPSINA K V ESCHERICHIA COLI

Mentor: izr. prof. dr. Marko Novinec

Datum zagovora: 8. 4. 2019

Dominik DEKLEVA

TARČNA DOSTAVA UČINKOVIN V RAKAVE CELICE UROTELIJA SEČNEGA MEHURJA

Mentor: prof. dr. Peter Veranič

Datum zagovora: 23. 4. 2019

Julija MAZEJ

INTERAKCIJSKI PROFIL PROTEINA TDP-43 PRI DIVJEM TIPU IN PRI DELECIJI JEDRNEGA LOKALIZACIJSKEGA SIGNALA

Mentor: prof. dr. Boris Rogelj

Datum zagovora: 29. 5. 2019

Nina ROŠTAN

OPREDELITEV GENETSKIH VZROKOV PRI BOLNIKI S SINDROMOM PODALJŠANE QT-DOBE

Mentorica: doc. dr. Maruša Debeljak

Somentor: doc. dr. Gregor Gunčar

Datum zagovora: 2. 7. 2019

Tina LEKAN

VPLIV LEKTINA CNL NA IZBRANE HUMANE TUMORSKE CELIČNE LINIJE

Mentorica: znan. sod. dr. Jerica Sabotič

Somentor: doc. dr. Gregor Gunčar

Datum zagovora: 5. 7. 2019

Simon BOLTA

ANALIZA KOMPLEKSOV DNA-APTAMEROV S PROTEINOM EPCAM

Mentorica: prof. dr. Brigita Lenarčič

Datum zagovora: 9. 7. 2019

Tajda BUH

PRIPRAVA AVKSOTROFNIH MUTANT KVASOVKE AUREOBASIDIUM PULLULANS S TEHNOLOGIJO CRISPR-Cas9

Mentorica: doc. dr. Martina Turk

Datum zagovora: 28. 8. 2019

Tina ŠIMUNOVIĆ

MEHANSKO OBČUTLJIV IONSKI KANAL TRPV6 IN PRENAŠALEC CorA TER NJUNA UMESTITEV V TRANSFICIRANIH CELICAH HEK293T

Mentorica: doc. dr. Mojca Benčina

Somentor: doc. dr. Gregor Gunčar

Datum zagovora: 28. 8. 2019

Uroš ZAVRTANIK

STRUKTURNE IN TERMODINAMSKE OSNOVE INTERAKCIJ GLOBULARNIH IN INTRINZIČNO NEUREJENIH PROTEINOV

Mentor: prof. dr. Jurij Lah

Datum zagovora: 29. 8. 2019

Toni NAGODE

SEKRETORNA FOSFOLIPAZA A2 VPLIVA NA PROTEOMSKO SESTAVO LIPIDNIH KAPLJIC PRI CELICAH RAKA DOJKE

Mentor: znan. sod. dr. Toni Petan

Somentor: doc. dr. Miha Pavšič

Datum zagovora: 29. 8. 2019

Katja MALOVRH

LIPIDI IN CIRKADIANA URA: IZSLEDKI NA HUMANIH CELIČNIH LINIJAH U2OS IN HUH7

Mentorica: prof. dr. Damjana Rozman

Datum zagovora: 9. 9. 2019

Neža BREZOVAR

VPLIV SURFAKTANTOV, TREHALOZE IN TEMPERATURE NA STABILNOST VEZIKLOV IZ JAJČNEGA LECITINA

Mentorica: prof. dr. Ksenija Kogej

Datum zagovora: 10. 9. 2019

Urška ČERNE

VPLIV NANOTELESA M33 NA CELIČNO SMRT POVZROČENO S PROTEINOM MLKL

Mentor: doc. dr. Gregor Gunčar

Datum zagovora: 10. 9. 2019

Marija SRNKO

VPLIV MUTACIJ V PLAŠČNEM PROTEINU VIRUSA Y KROMPIRJA NA BIOKEMIJSKE IN BIOFIZIKALNE LASTNOSTI TER ZGRADBO VIRUSOM PODOBNIH DELCEV

Mentorica: doc. dr. Marjetka Podobnik

Somentor: prof. dr. Janez Plavec

Datum zagovora: 11. 9. 2019

Špela MALENŠEK

IMUNOTERAPIJA RAKA: REGULACIJA T-CELIC Z DIZAJNIRANIM TRANSKRIPCISKIM FAKTORJEM NFAT

Mentor: prof. dr. Roman Jerala

Somentor: prof. dr. Janez Plavec

Datum zagovora: 11. 9. 2019

Peter PEČAN

VLOGA ZUNAJCELIČNIH VEZIKLOV, KI SE SPROSTIJO PO OKSIDATIVNEM STRESU, PRI AKTIVACIJI ADAPTIVNEGA ODGOVORA

Mentorica: viš. znan. sod. dr. Mateja Manček Keber

Somentorica: doc. dr. Vera Župunski

Datum zagovora: 11. 9. 2019

Maja GRDADOLNIK

SINTEZA KONJUGATOV LEKTIN-KOLOIDNO ZLATO ZA LOKALIZACIJO SLADKORNIH PREOSTANKOV V UROTELIJSKIH CELICAH

Mentorica:izr. prof. dr. Daša Zupančič

Datum zagovora: 12. 9. 2019

Fran KRSTANOVIČ

DOLOČITEV KANABIDOIDNIH RECEPTORJEV V CELIČNIH LINIJAH RAKA DOJKE

Mentorica:izr. prof. dr. Nataša Debeljak

Somentorica: prof. dr. Tamara Lah Turnšek

Datum zagovora: 12. 9. 2019

Anja TANŠEK

PRIPRAVA IN KARAKTERIZACIJA NAČRTOVANIH PROTEINSKIH MREŽ Z RAZLIČNO GEOMETRIJO

Mentorica: znan. sod. dr. Andreja Majerle

Somentor: prof. dr. Jurij Lah

Datum zagovora: 19. 9. 2019

Amadeja LAPORNIK

ODKRIVANJE FLEBOVIRUSOV V PEŠČENIH MUHAH, VZORČENIH NA IZBRANIH LOKACIJAH PO SLOVENIJI

Mentorica: prof. dr. Tatjana Avšič Županc

Datum zagovora: 23. 9. 2019

Tadej ULČNIK

PRIPRAVA VEKTORJEV Z ZAPISI ZA PROTEINSKE NANOSTRUKTURE Z METODO SESTAVLJANJA GOLDEN GATE

Mentorica: znan. sod. dr. Helena Gradišar

Somentor:izr. prof. dr. Marko Dolinar

Datum zagovora: 23. 9. 2019

Zala GLUHIČ

RAZVOJ METODE ZA SPREMLJANJE TRANSPORTA PROTEINOV S KLATRINSKIMI VEZIKLI PRI PARAZITU PLASMODIUM BERGHEI

Mentorica: prof. dr. Janja Marc

Somentor: prof. dr. Andrew P. Waters

Datum zagovora: 25. 9. 2019

Nastja MARONDINI

GENOMSKA IN EVOLUCIJSKA ANALIZA AEROLIZINOV IN AKTINOPORINOV PRI NAJSTAREJŠIH VRETENČARJIH

Mentor:izr. prof. dr. Dušan Kordiš

Somentorica: doc. dr. Vera Župunski

Datum zagovora: 25. 9. 2019

Ana CIRNSKI

IZRAŽANJE IN KARAKTERIZACIJA NEKATERIH MUTANTNIH OBLIK ČLOVEŠKEGA KATEPSINA S

Mentor:izr. prof. dr. Marko Novinec

Datum zagovora: 25. 9. 2019

Jernej VIDMAR

PRIPRAVA IN STRUKTURNA KARAKTERIZACIJA TUMORSKEGA OZNAČEVALCA TROP2 Z UPORABO DELNO GLIKOZILIRANIH MUTIRANIH OBLIK

Mentor: doc. dr. Miha Pavšič

Datum zagovora: 30. 9. 2019

Gašper MARINŠEK

OPREDELITEV DELECIJ GENA IKZF1 PRI OTROCIH Z B-CELIČNO AKUTNO LIMFOBLASTNO LEVKEMIJO

Mentorica: doc. dr. Maruša Debeljak

Somentor:izr. prof. dr. Marko Novinec

Datum zagovora: 1. 10. 2019

Anita KUSTEC

HETEROLOGNO IZRAŽANJE GENOV ZA ZUNAJCELIČNE ENCIME GLIVE AUREOBASIDIUM PULLULANS V KVASOVKI SACCHAROMYCES CEREVISIAE

Mentorica: prof. dr. Nina Gunde Cimerman

Datum zagovora: 22. 10. 2019

Sara Kimm FUHRMANN

PRIPRAVA IN KARAKTERIZACIJA OD KALCIJA ODVISNEGA TRANSKRIPCIJSKEGA DEJAVNIKA NA OSNOVI KALMODULINA IN OD KALCIJA IN KALMODULINA ODVISNE PROTEIN KINAZE II

Mentorica: doc. dr. Mojca Benčina

Somentor:izr. prof. dr. Marko Dolinar

Datum zagovora: 4. 11. 2019

Mojca HUNSKI

PRIPRAVA IN KARAKTERIZACIJA IZOOLIKE DELTA PROTEIN KINAZE C

Mentor: doc. dr. Miha Pavšič

Datum zagovora: 29. 11. 2019

Helena POPLAŠEN

DOLOČITEV SEKRETORSKEGA STATUSA NA PODLAGI PRISOTNOSTI ALELOV SEKRETORSKEGA GENA FUT2 IN DOLOČITEV GENOTIPA KRVNOSKUPINSKEGA SISTEMA LEWIS (FUT3) IZ VZORCA PERIFERNE KRVI

Mentorica: prof. dr. Vladka Čurin Šerbec

Datum zagovora: 5. 12. 2019

Tadej SATLER

PRIPRAVA IN KARAKTERIZACIJA BIPIRAMIDALNE PROTEINSKE KLETKE IZ OBVITIH VIJAČNIC ZA VEZAVO NANOTELES

Mentor: prof. dr. Roman Jerala

Somentor: prof. dr. Janez Plavec

Datum zagovora: 11. 12. 2019

Helena JAKŠE

RAZVOJ ANALIZNIH METOD ZA DOLOČEVANJE ANALITOV V MEDU

Mentor:izr. prof. dr. Mitja Kolar

Somentor:izr. prof. dr. Marko Novinec

Datum zagovora: 16. 12. 2019

Inge SOTLAR

OPREDELITEV LASTNOSTI MUTANTOV PERFRINGOLIZINA O S SPREMENBAMI V HOLESTEROL- PREPOZNAVANEM DELU

Mentor: prof. dr. Gregor Anderluh

Somentor:izr. prof. dr. Marko Novinec

Datum zagovora: 20. 12. 2019

Sabina ŠTUKELJ

FILOGENOMSKA ANALIZA LIZOCIMOV PRI
EVKARIONTIH

Mentor: izr. prof. dr. Dušan Kordiš

Somentorica: doc. dr. Vera Župunski

Datum zagovora: 20. 12. 2019

MAGISTRSKI ŠTUDIJSKI PROGRAM 2. STOPNJE – TEHNIŠKA VARNOST**Maja PORENTA**

EMISIJE OGLJIKOVEGA MONOKSIDA PRI TLENJU
DREVESNE GOBE

Mentor: izr. prof. dr. Simon Schnabl

Datum zagovora: 11. 4. 2019

Karin ŽERTEK

SPROŠČANJE OGLJIKOVEGA OKSIDA PRI GORENJU
BIOETANOLA

Mentor: izr. prof. dr. Simon Schnabl

Datum zagovora: 29. 5. 2019

Tajda AHČIN

MERJENJE KONCENTRACIJ PRAHU V
LESNOPREDELOVALNEM OBRATU IN VARNO DELO Z
LESNIM PRAHOM

Mentorica: izr. prof. dr. Alenka Franko

Datum zagovora: 6. 6. 2019

Nina RESNIK

TVEGANJA V LABORATORIJU PRI DELU Z BIOLOŠKIMI
DEJAVNIKI

Mentor: doc. dr. Mitja Robert Kožuh

Datum zagovora: 30. 8. 2019

Urška KOŽELJ

UČINKOVITOST PROTIHRUPNIH PREGRAD

Mentor: doc. dr. Mitja Robert Kožuh

Datum zagovora: 6. 9. 2019

Martina ZADNIK

GASILCI IN INTERVENCIJE

Mentor: izr. prof. dr. Simon Schnabl

Datum zagovora: 6. 9. 2019

Nik RUS

VARNOSTNI KONCEPT ZBIRALNICE RAZLIČNIH VRST
NEVARNIH ODPADKOV

Mentor: doc. dr. Mitja Robert Kožuh

Datum zagovora: 13. 9. 2019

Manca AHAČIČ

ANALIZA GORENJA TALNIH OBLOG

Mentor: izr. prof. dr. Simon Schnabl

Datum zagovora: 30. 9. 2019

Matija KURNIK

NEVARNOSTI POVEZANE Z UPORABO BREZPILOTNIH
ZRAKOPLOVOV (DRONOV)

Mentor: doc. dr. Mitja Robert Kožuh

Datum zagovora: 27. 11. 2019

DIPLOME - UNIVERZITETNI ŠTUDIJI**KEMIJA – 1. STOPNJA****Alenka KRIŽAN**

VPLIV POGOJEV HIDROTERMALNE
SINTEZE NA FOTOKATALITSKO AKTIVNOST
NANOSTRUKTURIRANIH MIKRODELCEV TiO₂

Mentorica: prof. dr. Urška Lavrenčič Štangar

Datum zagovora: 1. 7. 2019

Lara LAVRENČIČ

NAČRTOVANJE IN SINTEZA 1,5-DIMETIL-7-OKSO-3-
FENILTETRAHIDRO-1H,5H-PIRAZOLO[1,2-A]PIRAZOL-1-
KARBOKSAMIDOV KOT POTENCIALNIH INHIBITORJEV
PLASMIDIUM FALCIPARUM DIHIDROOROTAT
DEHIDROGENAZE

Mentor: prof. dr. Jurij Svete

Datum zagovora: 4. 7. 2019

Urška GAZDAG

PROUČEVANJE SORPCIJSKIH SPOSOBNOSTI BIOOGLJA V
VODNIH RAZTOPINAH SVINCA IN KADMIJA

Mentorica: doc. dr. Marija Zupančič

Datum zagovora: 12. 7. 2019

Martin LJUBIČ

FAZNI DIAGRAM BINARNE MEŠANICE METANOL-
KLOROFORM

Mentor: prof. dr. Andrej Jamnik

Datum zagovora: 12. 7. 2019

Matevž SCHWEIGER

SINTEZA AMINALOV NA OSNOVI FENILALANINA

Mentor: izr. prof. dr. Uroš Grošelj

Datum zagovora: 8. 8. 2019

Ana GORENC

SINTEZA ZAVIRALCEV BUTIRILHOLINESTERAZE IZ
HETEROCIKLIČNIH α -AMINOKISLIN

Mentor: izr. prof. dr. Uroš Grošelj

Datum zagovora: 12. 8. 2019

Mišel HOZJAN

SINTEZA IN PRETVORBE TETRAMSKIH KISLIN IZ GLICINA

Mentor: izr. prof. dr. Uroš Grošelj

Datum zagovora: 19. 8. 2019

Neža DROFENIK

POIZKUS IZOLACIJE NIKOTINA, MATRICINA, KAMAZULENA, KANABIDIOLA IN KANABIDIOLNE KISLINE IZ NARAVNIH VIROV

Mentor: doc. dr. Krištof Kranjc

Datum zagovora: 22. 8. 2019

Tamara ILIOSKA

MODIFIKACIJA 1,2,4,5-TETRAOKSANA ZA VEZAVO NA POLISAHARIDNI TRDNI NOSILEC

Mentor: izr. prof. dr. Jernej Iskra

Datum zagovora: 23. 8. 2019

Klemen KOZLOVIČ

SINTEZA IZBRANIH AMIDOV PIRUVIČNE KISLINE

Mentor: doc. dr. Krištof Kranjc

Datum zagovora: 4. 9. 2019

Jernej IMPERL

ŠTUDIJA UPORABE KOMPAKTNIH POTENCIOMETRIČNIH SENZORJEV

Mentor: izr. prof. dr. Mitja Kolar

Datum zagovora: 4. 9. 2019

Eva JANČIGAJ

DOLOČEVANJE HIDROGENTARTRATA V VZORCIH VINSKEGA KAMNA S POTENCIOMETRIČNO TITRACIJO

Mentor: izr. prof. dr. Drago Kočar

Datum zagovora: 4. 9. 2019

Klara KOČEVAR

DOLOČANJE KOVIN V VZORCIH VINSKEGA KAMNA

Mentor: izr. prof. dr. Drago Kočar

Datum zagovora: 4. 9. 2019

Luka JAMŠEK

PRIPRAVA ESTRSKIH DERIVATOV PIRUVIČNE IN BROMOPIRUVIČNE KISLINE

Mentor: doc. dr. Krištof Kranjc

Datum zagovora: 5. 9. 2019

Petra LAPAJNE

VISKOZNOST ČOKOLADE

Mentorica: prof. dr. Barbara Hribar Lee

Datum zagovora: 5. 9. 2019

Peter ROBIČ

REAKCIJE BAKROVIH(2+) IONOV Z 1-(PIRIDIN-2-IL) TIOSEČNINO

Mentor: doc. dr. Andrej Pevec

Datum zagovora: 5. 9. 2019

Žiga VIČIČ

SINTEZE IN KARAKTERIZACIJE KARBONILNIH RUTENIJEVIH SPOJIN

Mentor: prof. dr. Iztok Turel

Datum zagovora: 5. 9. 2019

Vid RAVNIK

VPLIV VELIKOSTI IONOV NA RAZPOREDITEV ELEKTROLITA OB NABITI STENI. PRIMERJAVA POISSON-BOLTZMANNOVE TEORIJE IN SIMULACIJ MONTE CARLO.

Mentor: izr. prof. dr. Miha Lukšič

Datum zagovora: 5. 9. 2019

Martin TUŠEK

MODELIRANJE VODE S POTENCIALOM VRTNICE

Mentor: izr. prof. dr. Miha Lukšič

Datum zagovora: 5. 9. 2019

Anja KOROŠEC

PREGLED KEMOINFORMACIJSKIH METOD ZA NAPOVED METABOLITOV

Mentor: doc. dr. Črtomir Podlipnik

Datum zagovora: 5. 9. 2019

Peter OGRIN

MONTE CARLO SIMULACIJE MERCEDES-BENZ MODELA VODE

Mentor: prof. dr. Tomaž Urbič

Datum zagovora: 5. 9. 2019

Uroš RAPUŠ

SINTEZA ŽELEZOVIIH IN BAKROVIH KOORDINACIJSKIH SPOJIN TIOHIDROKSAMSKIH KISLIN

Mentor: doc. dr. Jakob Kljun

Datum zagovora: 5. 9. 2019

Aleš MARSEL

SINTEZA FLUOROFOROV S 4-AMINOBIFENILNIM SKELETOM

Mentor: doc. dr. Martin Gazvoda

Datum zagovora: 6. 9. 2019

Uroš VEZONIK

SINTEZA IN APLIKACIJA TRIPROPARGILAMINA V PRIPRAVI NOVIH LIGANDOV ZA KOVINE PREHODA

Mentor: prof. dr. Janez Košmrlj

Datum zagovora: 6. 9. 2019

Marjeta SPASOVIĆ

LASTNOSTI BINARNIH MEŠANIC ETANOLA IN N-PROPANOLA

Mentorica: prof. dr. Marija Bešter Rogač

Datum zagovora: 6. 9. 2019

Maša LOGAR

NANOTEHNOLOGIJA SREBRA IN UPORABA SREBROVIH NANOŽIČK V SENZORIKI

Mentor: izr. prof. dr. Matija Tomšič

Datum zagovora: 6. 9. 2019

Tjaša KOŽELJ

RENTGENSKA PRAŠKOVNA DIFRAKCIJA PROTIBOLEČINSKIH ZDRAVIL

Mentor: prof. dr. Anton Meden

Datum zagovora: 6. 9. 2019

Petra RAZINGERPRIPRAVA SPOJIN S TIOCIANATOM IN OVREDNOTENJE
NJIHOVIH INFRARDEČIH SPEKTROV

Mentorica: doc. dr. Barbara Modec

Datum zagovora: 6. 9. 2019

Zala DREŠARPRISOTNOST HALOGENSKIH VEZI V KOKRISTALIH IN
SOLEH DIATRIZOIČNE KISLINE

Mentor: izr. prof. dr. Franc Perdih

Datum zagovora: 6. 9. 2019

Aleksander KRAVOSAEROBNO JODOHALOGENIRANJE ALKENOV
KATALIZIRANO Z DUŠIKOVIMI OKSIDI

Mentor: izr. prof. dr. Jernej Iskra

Datum zagovora: 9. 9. 2019

David VODOPIVEC

UPORABA PAMETNEGA TELEFONA V ANALIZNI KEMIJI

Mentorica: doc. dr. Nataša Gros

Datum zagovora: 9. 9. 2019

Klara GABER

MERILNA NEGOTOVOST PRI ODMERJANJU VOLUMNA

Mentorica: doc. dr. Nataša Gros

Datum zagovora: 9. 9. 2019

Jan HOČEVARKARBOKSIMETILIRANJE CELULOZE PRIDOBLENE IZ
KMETIJSKIH OSTANKOV

Mentor: izr. prof. dr. Jernej Iskra

Datum zagovora: 9. 9. 2019

Kristjan MEŽAKEMIJSKE PRETVORBE AEROSOLOV α -PINENA

Mentor: prof. dr. Matevž Pompe

Datum zagovora: 9. 9. 2019

Dunia SAHIRKRATEK VPOGLED V UNIVERZALNOST HOFMEISTROVE
VRSTE IN ONKRAJ NJE

Mentor: izr. prof. dr. Janez Cerar

Datum zagovora: 9. 9. 2019

Jan JELENSINTEZA NUKLEOFILNEGA IN DEOKSIFLUORIRNEGA
REAGENTA NA OSNOVI IMIDAZOLIJEVIH
POLIFLUORIDOV V VODNEM MEDIJU

Mentor: izr. prof. dr. Jernej Iskra

Datum zagovora: 10. 9. 2019

David SIMONIČVPLIV STARANJA NA TRDOTO VOLFRAMA IN
VOLFRAMOVEGA KOMPOZITA S KARBIDNIMI
VKLJUČKI.

Mentorica: doc. dr. Saša Petriček

Datum zagovora: 10. 9. 2019

Marko GABROVŠEKSINTEZA FLUOROFOROV S 4-FENILAZO-ANILINSKIM
SKELETOM

Mentor: prof. dr. Janez Košmrlj

Datum zagovora: 10. 9. 2019

Nika ŽNIDERŠIČSINTEZA FLUOROFOROV S 4-FENILETINIL-
FENILAMINSKIM SKELETOM

Mentor: doc. dr. Martin Gazvoda

Datum zagovora: 10. 9. 2019

Martin CVIKL

SINTEZA IZBRANIH GEMINALNIH DIBROMOALKENOV

Mentor: prof. dr. Janez Košmrlj

Datum zagovora: 10. 9. 2019

Alenka ZUPANČIČ

VODIKOVA VEZ V VODNIH RAZTOPINAH

Mentor: izr. prof. dr. Janez Cerar

Datum zagovora: 17. 12. 2019

KEMIJSKO INŽENIRSTVO – 1. STOPNJA**Jernej IZDA**MEMBRANSKO INŽENIRSTVO ZA INOVATIVNE
TEKSTILNE IZDELKE

Mentorica: prof. dr. Urška Šebenik

Datum zagovora: 31. 1. 2019

Tadej POLJANŠEKUPORABA SODOBNIH METOD KARAKTERIZACIJ
MATERIALOV NA ARHEOLOŠKIH VZORCIH

Mentor: doc. dr. Boštjan Genorio

Datum zagovora: 11. 2. 2019

Lana MIKECVPLIV KRISTALIZACIJSKIH PARAMETROV NA
MORFOLOGIJO KRISTALOV FARMACEVTSKIH
UČINKOVIN

Mentor: prof. dr. Aleš Podgornik

Datum zagovora: 11. 2. 2019

Urška KOVAČIČ

HIERARHIČNE KRISTALNE STRUKTURE

Mentor: prof. dr. Aleš Podgornik

Datum zagovora: 11. 2. 2019

Luka SMAJILA

SODOBNI MATERIALI ZA DENTALNO KERAMIKO

Mentor: izr. prof. dr. Marjan Marinšek

Datum zagovora: 18. 2. 2019

Žan LAVRIČ

BIOFILMI V MIKROREAKTORJIH

Mentorica: prof. dr. Polona Žnidaršič Plazl

Datum zagovora: 20. 3. 2019

Blaž JAKLIČ

UPORABA GRAFENA V FOTOVOLTAIKI

Mentor: doc. dr. Boštjan Genorio

Datum zagovora: 3. 4. 2019

Jernej KADIVNIKOSKRBOVALNA VERIGA LI-ION BATERIJSKIH
KOMPONENT

Mentor: doc. dr. Boštjan Genorio

Datum zagovora: 14. 5. 2019

Martin MAROVT

KEMIJSKO INŽENIRSTVO IN TRAJNOSTNI RAZVOJ

Mentor: prof. dr. Igor Plazl

Datum zagovora: 26. 6. 2019

Maja NOVAKODSTRANJEVANJE FARMACEVTSKIH UČINKOVIN IZ
ODPADNIH VOD Z OZONACIJO

Mentorica: izr. prof. dr. Andreja Žgajnar Gotvajn

Datum zagovora: 28. 6. 2019

Erik HARTMANVPLIV GEOMETRIJE LISTIČEV BIKOMPONENTNEGA
ŠOBNEGA PAKETA NA KONČNO STRUKTURO VLAKNA

Mentor: prof. dr. Igor Plazl

Datum zagovora: 2. 7. 2019

Patrik LIKARKOMPOZIT TRDE POLIURETANSKE PENE S SILIKO IN
STEKLENIMI VLAKNI

Mentorica: prof. dr. Urška Šebenik

Datum zagovora: 8. 7. 2019

Luka SKUBICVNETLJIVOST POLIMERNIH KOMPOZITOV Z
OGLJIKOVIMI VLAKNI

Mentorica: prof. dr. Urška Šebenik

Datum zagovora: 8. 7. 2019

Teja URBANCDOLOČANJE VSEBNOSTI RAZTOPLJENIH IN
NERAZTOPLJENIH PLINOV V VODI

Mentor: izr. prof. dr. Marko Hočevar

Datum zagovora: 30. 8. 2019

Mojca LEGAN

BIOLOŠKI PROCESI SAMOPRAVLJIVOSTI BETONA

Mentorica: izr. prof. dr. Andreja Žgajnar Gotvajn

Datum zagovora: 30. 8. 2019

Žiga SKOČIRUPORABA GRAFENA V KOMPOZITIH ZA ZAVORNE
OBLOGE

Mentor: doc. dr. Boštjan Genorio

Datum zagovora: 30. 8. 2019

Petra BAJECSTRUPENOST IN BIORAZGRADLJIVOST
2-PROPENAMIDA IN NJEGOVIH KOPOLIMEROV

Mentorica: doc. dr. Gabriela Kalčikova

Datum zagovora: 2. 9. 2019

Luka GORŠENAČRTOVANJE MIKROFLUIDNE NAPRAVE ZA TOK
KOMPLEKSNIH FLUIDOV

Mentor: prof. dr. Igor Plazl

Datum zagovora: 5. 9. 2019

Sanja BAKIČ

ORGANSKI ANORGANSKI PEROVSKITNI MATERIALI

Mentor: izr. prof. dr. Marjan Marinšek

Datum zagovora: 6. 9. 2019

Vid MODIC

BIOKATALITSKI PROCESI V PRETOČNIH SISTEMIH

Mentorica: prof. dr. Polona Žnidaršič Plazl

Datum zagovora: 6. 9. 2019

Matija PIRCTERMODINAMSKE OSNOVE DVOFAZNIH VODNIH
SISTEMOV

Mentor: prof. dr. Aleš Podgornik

Datum zagovora: 6. 9. 2019

Urban KOŠIRORGANSKI POLIMERNI MATERIALI KOT KATODE ZA AL-
ORGANSKE AKUMULATORJE

Mentor: izr. prof. dr. Robert Dominko

Datum zagovora: 6. 9. 2019

Elfi BIRSA

BIOBETON

Mentor: izr. prof. dr. Marjan Marinšek

Datum zagovora: 6. 9. 2019

Žiga LIPOVŠEK

HIBRIDNI DENTALNI MATERIALI

Mentor: prof. dr. Aleš Podgornik

Datum zagovora: 6. 9. 2019

Borut ŠKETAUPORABA MIKROFLUIDIKE ZA RAZISKAVE
CIANOBAKTERIJ

Mentorica: prof. dr. Polona Žnidaršič Plazl

Datum zagovora: 6. 9. 2019

Benjamin BOŽIČ

NASTANEK IN UPORABA DENDRITNIH STRUKTUR

Mentor: prof. dr. Aleš Podgornik

Datum zagovora: 6. 9. 2019

Petra JAGODIČ

KRISTALNI KOSITROV OKSID: NASTANEK IN UPORABA

Mentor: prof. dr. Aleš Podgornik

Datum zagovora: 6. 9. 2019

Leja ZALETELOPTIMIZACIJE KOMPONENT ZA MAGNEZIJ-ŽVEPLOVE
AKUMULATORJE

Mentor: izr. prof. dr. Robert Dominko

Datum zagovora: 6. 9. 2019

Samo SOTLAR

CIANOBAKTERIJE KOT PROIZVODNI ORGANIZMI

Mentorica: prof. dr. Polona Žnidaršič Plazl

Datum zagovora: 6. 9. 2019

Urban SAJEVIC

SINTEZA IN ELEKTROKEMIJSKA KARAKTERIZACIJA BOROGENOV

Mentor: doc. dr. Boštjan Genorio

Datum zagovora: 6. 9. 2019

Janja ŠUSTER

VPLIV RAZLIČNIH ANIONOV NA DELOVANJE MAGNEZIJEVIH AKUMULATORJEV

Mentor: izr. prof. dr. Robert Dominko

Datum zagovora: 9. 9. 2019

Katja POMBERG

NASTAJANJE RADIKALOV PRI KAVITACIJI

Mentor: prof. dr. Matevž Dular

Datum zagovora: 10. 9. 2019

Monika NEDVEŠ

REOLOŠKE LASTNOSTI SLADOLEDA

Mentorica: doc. dr. Lidija Slemenik Perše

Datum zagovora: 10. 9. 2019

Jan GALE

HIBRIDNI KOMPOZITI NA OSNOVI NARAVNIH VLAKEN ZA NAPREDNE APLIKACIJE

Mentorica: prof. dr. Urška Šebenik

Datum zagovora: 10. 9. 2019

Klara MERŠE

PREUČEVANJE MEHANSKIH LASTNOSTI IN OBLIKOVNEGA UČINKA BIO-OSNOVNIH POLIBENZOKSAZINOV

Mentor: doc. dr. Aleš Ručigaj

Datum zagovora: 10. 9. 2019

Erik GREGORI

FOTODISOCIACIJA DUŠIKOVIH OKSIDOV V TROPOFERI

Mentorica: doc. dr. Gabriela Kalčikova

Datum zagovora: 10. 9. 2019

Matevž ZUPAN

SAMOCELJENJE POLIMERNIH MATERIALOV NA OSNOVI MIKROKAPSUL

Mentor: doc. dr. Aleš Ručigaj

Datum zagovora: 19. 9. 2019

Tjaš CVEK

IZDELAVA SISTEMA ZA MERJENJE REGRESIJE PARAFINSKIH GORIV V HIBRIDNIH MOTORJIH

Mentor: izr. prof. dr. Robert Dominko

Datum zagovora: 19. 9. 2019

Janja KRAMARIČ

SPREMENBE STRUPENOSTI PRI OZONACIJI ODPADNE VODE

Mentorica: doc. dr. Gabriela Kalčikova

Datum zagovora: 19. 9. 2019

Žan PLEČKO

TOK NEMEŠLJIVIH KAPLJEVIN V MIKROFLUIDNI NAPRAVI

Mentor: prof. dr. Igor Plazl

Datum zagovora: 24. 9. 2019

Jan CVELBAR

VPLIV STRUKTURE NA RAZGRADLJIVOST BIOPOLIMEROV

Mentorica: doc. dr. Lidija Slemenik Perše

Datum zagovora: 30. 9. 2019

Maja KOZOLE

VPLIV MIKROPLASTIKE NA RAST LISTOV IN KORENIN MALE VODNE LEČE

Mentorica: doc. dr. Gabriela Kalčikova

Datum zagovora: 22. 10. 2019

Andraž KOŠIR

OPTIMIZACIJA KONTINUIRNEGA CEVNEGA KRISTALIZATORJA Z LAMINARNIM TOKOM: VPLIV PROCESNIH PARAMETROV NA KRITIČNO DEPOZICIJSKO HITROST

Mentor: doc. dr. Aleš Ručigaj

Datum zagovora: 20. 11. 2019

BIOKEMIJA – 1. STOPNJA**Tina IVANČIR**

DOKAZOVANJE ALFAVIRUSOV V KOMARJIH, UJETIH V SLOVENIJI V LETU 2017

Mentorica: prof. dr. Tatjana Avšič Županc

Datum zagovora: 6/10/2019

Janja MURN

OPTIMIZACIJA METODE TOČKOVNEGA NANOSA ZA DOLOČANJE RECEPTORJEV ZA KANABINOIDE IN ESTROGENE NA CELIČNIH LINIJAH RAKA DOJKE

Mentorica: izr. prof. dr. Nataša Debeljak

Datum zagovora: 6/12/2019

Lana VOGRINEC

FENOTIPSKA ANALIZA MODELNE CIANOBAKTERIJE SYNECHOCYSTIS SP. PCC 6803 Z NAMENOM DOLOČITVE FUNKCIJE ORTOKASPAZE SyOC IN VIVO

Mentorica: doc. dr. Marina Klemenčič

Datum zagovora: 6/28/2019

Uroš PREŠERN

ANALIZA INTERAKCIJE MED ZUNAJCELIČNIMA DOMENAMA EpCAM IN EGFR

Mentorica: prof. dr. Brigita Lenarčič

Datum zagovora: 7/12/2019

Maša ZORMAN

SINTEZA ZAVIRALCEV BUTIRILHOLINESTERAZE

Mentor: izr. prof. dr. Uroš Grošelj

Datum zagovora: 8/22/2019

Ana OBAHA

KARAKTERIZACIJA VPLIVA AMINOKISLINSKIH

DERIVATOV SUKGINIMIDA NA AKTIVNOST KATEPSINA L

Mentor: izr. prof. dr. Marko Novinec

Datum zagovora: 8/29/2019

Andreja HABIČ

RAZVOJ SISTEMA ZA ISKANJE INTERAKCIJSKIH

PARTNERJEV DNA NA OSNOVI OZNAČEVANJA BLIŽNJIH

MOLEKUL Z BIOTINOM

Mentor: doc. dr. Miha Pavšič

Datum zagovora: 8/30/2019

Andrej IVANOVSKI

VEZAVA KALCIJEVIH IONOV IN NJIHOVA

POTENCIALNA VLOGA PRI REGULACIJI AKTIVNOSTI

ALFA-AKTININA 4

Mentor: doc. dr. Miha Pavšič

Datum zagovora: 8/30/2019

Milica JANKOVIČ

VPLIV KOVINSKIH IONOV NA AKTIVNOST KATEPSINA K

Mentor: prof. dr. Iztok Turel

Datum zagovora: 9/3/2019

Jerneja NIMAC

MERITVE ZNOTRAJCELIČNE RAVNI cAMP V

ASTROCITIH V KULTURI PO AKTIVACIJI α 2-

ADRENERGIČNIH RECEPTORJEV

Mentorica: doc. dr. Nina Vardjan

Datum zagovora: 9/4/2019

Ines MEDVED

RAZPOREDITEV MIKROTUBULOV V EPITELNIH

CELICAH RAZLIČNIH REGIJ PREBAVNE CEVI PRI

NEVRETENČARSKIH MODELNIH ORGANIZMIH

Mentorica: doc. dr. Nada Žnidaršič

Datum zagovora: 9/5/2019

Tanja ZUPAN

VPLIV AGONISTOV G-PROTEINSKIH RECEPTORJEV NA

SPREMEMBE CITOSOLNEGA LAKTATA V PODGANJIH

NEVRONIH V KULTURI

Mentorica: izr. prof. dr. Helena Haque Chowdhury

Datum zagovora: 9/6/2019

Tomaž ŽIGON

MERJENJE STRESNIH IN VNETNIH BIOMARKERJEV

V AKUTNI FAZI ISHEMIČNEGA MOŽGANSKEGA

INFARKTA

Mentor: doc. dr. Uroš Kovačič

Datum zagovora: 9/9/2019

Ajda LENARDIČ

AKTIVACIJA IZRAŽANJA GENA Tst Z METODO CRISPR/

dCas9-VPR V MIŠJI CELIČNI LINIJI

Mentor: prof. dr. Simon Horvat

Datum zagovora: 9/9/2019

Ana MAKLIN

PRIPRAVA REKOMBINANTNEGA ANEKSINA A11 V

BAKTERIJAH E. COLI Z UPORABO EKSPRESIJSKIH

VEKTORJEV NA OSNOVI pMCSG7

Mentorica: doc. dr. Vera Župunski

Datum zagovora: 9/9/2019

Katja DOBERŠEK

RAZVOJ IN VALIDACIJA TEHNIKE CRISPR-Cas9 ZA

HKRATNO CILJANJE VEČ MEST V GENOMU KVASOVKE

SACCHAROMYCES CEREVISIAE

Mentor: izr. prof. dr. Uroš Petrovič

Datum zagovora: 9/9/2019

Urban HRIBAR

KARAKTERIZACIJA VPLIVA AMINOKISLINSKIH

DERIVATOV SUKGINIMIDA NA AKTIVNOST KATEPSINA V

Mentor: izr. prof. dr. Marko Novinec

Datum zagovora: 9. 9. 2019

Tina TUREL

KARAKTERIZACIJA VPLIVA AMINOKISLINSKIH

DERIVATOV SUKGINIMIDA NA AKTIVNOST KATEPSINA B

Mentor: izr. prof. dr. Marko Novinec

Datum zagovora: 9. 9. 2019

Luka LAVRIČ

SIGNALNE POTI V GLIOBLASTOMSKIH CELICAH

OB PRISOTNOSTI KANABIDIOLA V KOMBINACIJI S

KEMOTERAPIJO

Mentorica: prof. dr. Tamara Lah Turnšek

Datum zagovora: 9. 9. 2019

Anže JENKO

ODZIV IN PREŽIVETJE MODELNEGA ALGNEGA

ORGANIZMA CHLAMYDOMONAS REINHARDTII

OB IZPOSTAVITVI NATRIJEVEMU KLORIDU IN

VODIKOVEMU PEROKSIDU

Mentorica: doc. dr. Marina Klemenčič

Datum zagovora: 9. 9. 2019

Daria LATYSHEVA

PRIPRAVA REKOMBINANTNE ZUNAJCELIČNE DOMENE

PROTEINA EGFR IN NJEGOVEGA INTERAKCIJSKEGA

PARTNERJA EGF

Mentorica: prof. dr. Brigita Lenarčič

Datum zagovora: 9. 9. 2019

Samo PURIČ

PREVERJANJE NAPOVEDI HELIČNOSTI

NESTRUKTURIRANIH PEPTIDOV Z

EKSPERIMENTALNIMI PODATKI

Mentor: prof. dr. Jurij Lah

Datum zagovora: 9. 9. 2019

Peter ŠKRINJAR

OPTIMIZACIJA IZRAŽANJA REKOMBINANTNEGA

PROTEINA FHL2

Mentorica: prof. dr. Brigita Lenarčič

Datum zagovora: 9. 9. 2019

Veronika RAZPOTNIK

PRIPRAVA PIRIDINSKIH DERIVATOV
DIAZENKARBOKSAMIDA KOT LIGANDOV ZA
KOORDINACIJSKE SPOJINE S PROTITUMORSKIM
DELOVANJEM

Mentor: prof. dr. Janez Košmrlj
Datum zagovora: 10. 9. 2019

Luka GREGORIČ

PRIPRAVA AKTIVIRANIH DERIVATOV AROMATSKIH
KARBOKSILNIH KISLIN KOT LIGANDOV V
PROTITUMORSKIH PLATINSKIH KOMPLEKSIH

Mentor: doc. dr. Martin Gazvoda
Datum zagovora: 10. 9. 2019

Katja MALENŠEK

AKTIVACIJA SILILIRANIH KISLINSKIH DERIVATOV
SIMVASTATINA ZA PRIPRAVO PLATINOVH(IV)
KOMPLEKSOV S PROTITUMORSKIM DELOVANJEM

Mentor: doc. dr. Martin Gazvoda
Datum zagovora: 10. 9. 2019

Ajda CAFUN

OPTIMIZACIJA LIGACIJE INTEINSKIH KONSTRUKTOV
ZA PRIPRAVO SEGMENTNO OZNAČENEGA
 α -AKTININA-1

Mentorica: prof. dr. Kristina Djinović Carugo
Datum zagovora: 10. 9. 2019

Nika ZAVERŠEK

PRIPRAVA IN KARAKTERIZACIJA NANOTELES 4T5, 3T1

Mentor: doc. dr. Gregor Gunčar
Datum zagovora: 10. 9. 2019

TEHNIŠKA VARNOST – 1 STOPNJA**Lea VALJAVEC**

PRISTOJNOSTI IN UKREPI INŠPEKTORATA REPUBLIKE
SLOVENIJE ZA DELO

Mentor: doc. dr. Luka Tičar
Datum zagovora: 25. 1. 2019

Ula ZLATE

MONOTONIJA IN STRES NA DELOVNEM MESTU

Mentorica: doc. dr. Klementina Zupan
Datum zagovora: 4. 7. 2019

Mirna ŠAFRANKO

ANALIZA EVAKUACIJSKIH POTI FAKULTETE ZA
ARHITEKTURO

Mentor: doc. dr. Domen Kušar
Datum zagovora: 2. 9. 2019

Nika ZAKRAJŠEK

ŠKODLJIVI VPLIVI SVINCA

Mentorica: doc. dr. Barbara Novosel
Datum zagovora: 4. 9. 2019

Klara KOŠIR

OSEBNA VAROVALNA OPREMA IN INFORMACIJSKA
TEHNOLOGIJA

Mentor: izr. prof. dr. Matija Tomšič
Datum zagovora: 4. 9. 2019

Vesna PODGRAJŠEK

AEROBNE BAKTERIJE V POSVEČENI VODI KATOLIŠKIH
CERKVA NA ŠIRŠEM OBMOČJU LJUBLJANE

Mentorica: doc. dr. Martina Turk
Datum zagovora: 11. 9. 2019

Domen VAUPOTIČ

MODELIRANJE CELIČNE RASTI

Mentor: izr. prof. dr. Miha Lukšič
Datum zagovora: 13. 9. 2019

Andrej RACE

OPTIMIZACIJA METOD KOLOKALIZACIJE ZA
FUNKCIONALNO ANALIZO GENOV KROMPIRJA,
KI SODELUJEJO PRI OBRAMBEM ODZIVU NA
KROMPIRJEV VIRUS Y

Mentorica: prof. dr. Kristina Gruden
Datum zagovora: 13. 9. 2019

Aljaž BOŽIČ

VPLIV ZAVIRALCEV JAK NA INZULINSKO
SIGNALIZACIJO V SKELETNIH MIŠICAH

Mentor: prof. dr. Tomaž Marš
Datum zagovora: 16. 9. 2019

Luka KRMPOTIČ

SEKUNDARNE STRUKTURE DNA V TOPILIH Z
RAZLIČNO DIELEKTRIČNO KONSTANTO

Mentor: prof. dr. Janez Plavec
Datum zagovora: 29. 10. 2019

Lea GRENC

VPLIV GOSPODARSKIH DEJAVNOSTI IN SPOLA NA
BOLNIŠKI STALEŽ

Mentor: prof. dr. Tomaž Urbič
Datum zagovora: 5. 9. 2019

Mateja ŠKEDELJ

ERGONOMSKA ANALIZA DELOVNEGA MESTA PRI
POKLICU ŽERJAVIST

Mentorica: doc. dr. Klementina Zupan
Datum zagovora: 6. 9. 2019

Peter KOČMAN

VPLIV KLIMATSKIH SPREMENB NA POŽARNO VARNOST
GOZDOV

Mentor: izr. prof. dr. Simon Schnabl
Datum zagovora: 6. 9. 2019

Tilen ŠEBALJ

NASTANEK IN LASTNOSTI NANODELCEV TER NJIHOV
VPLIV NA OKOLJE

Mentorica: prof. dr. Marija Bešter Rogač
Datum zagovora: 6. 9. 2019

Timotej GRČAR

PRAŠNE EKSPLOZIJE LESNEGA PRAHU

Mentor: izr. prof. dr. Simon Schnabl

Datum zagovora: 6. 9. 2019

Erik Janez SPITZER

SEŽIG KOMUNALNIH ODPADKOV KOT NAČIN
RAVNANJA S KOMUNALNIMI ODPADKI
Mentorica: doc. dr. Klementina Zupan
Datum zagovora: 9. 9. 2019

Tomaž PURGAR

EVAKUACIJSKE POTI IN EVAKUACIJSKI ČASI IZ
ŠPORTNEGA OBJEKTA
Mentor:izr. prof. dr. Simon Schnabl
Datum zagovora: 9. 9. 2019

Alen ALIDŽANOVIČ

OCENA POŽARNE VARNOSTI V OBJEKTU LEKARNE
Mentor:izr. prof. dr. Simon Schnabl
Datum zagovora: 9. 9. 2019

Zala REMEC

PSIHOLOŠKI VIDIK VPLIVA BARVE SVETLOBE NA
ČLOVEKA
Mentor: prof. dr. Grega Bizjak
Datum zagovora: 9. 9. 2019

Petra JERAJ

DOLOČITEV EKSPLOZIJSKIH PARAMETROV
PŠENIČNEGA IN RIŽEVEGA ŠKROBA
Mentorica: doc. dr. Barbara Novosel
Datum zagovora: 9. 9. 2019

Štefan ČOP

ERGONOMIJA IGRANJA VIDEO IGER
Mentorica: doc. dr. Klementina Zupan
Datum zagovora: 9. 9. 2019

Sara HODŽIČ

VPLIV KOVINSKIH IONOV NA ZVRSTI CITRONSKE
KISLINE V ODVISNOSTI OD pH
Mentor: doc. dr. Bojan Kozlevčar
Datum zagovora: 17. 9. 2019

Davor LIPAR

MERITVE IN SANACIJA HRUPA V LESNI INDUSTRIJI
Mentor: doc. dr. Mitja Robert Kožuh
Datum zagovora: 30. 9. 2019

Katarina ILIČ

VPLIV OVIR NA EVAKUACIJSKO ČAS S PROGRAMOM
PATHFINDER
Mentor:izr. prof. dr. Simon Schnabl
Datum zagovora: 10. 12. 2019

Žiga ZUPANČIČ

VARNOSTNA KULTURA V JEDRSKIH ELEKTRARNAH
Mentor:izr. prof. dr. Simon Schnabl
Datum zagovora: 10. 12. 2019

DIPLOME – VISOKOŠOLSKE STROKOVNE ŠTUDIJE

KEMIJSKA TEHNOLOGIJA – 1. STOPNJA

Nina AVSEC

IZOLACIJA IN KEMIJSKE PRETVORBE KANABIDIOLA
Mentor:izr. prof. dr. Bogdan Štefane
Datum zagovora: 3. 1. 2019

Vid ZAGORC SIRK

TRIDIMENZIONALNI TISK MOLEKULSKIH MODELOV
Mentor: doc. dr. Črtomir Podlipnik
Datum zagovora: 28. 1. 2019

Kaja ČERNE

BAKROVE(II) SPOJINE Z ANIONOM
4-HIDROKSIBENZOJSKE KISLINE
Mentor: doc. dr. Bojan Kozlevčar
Datum zagovora: 29. 1. 2019

Polona ŠKERBEC

REAKCIJE BAKROVEGA(II) KINALDINATA S CIKLIČNIMI
AMINI
Mentorica: doc. dr. Barbara Modec
Datum zagovora: 11. 2. 2019

Sara KONČEK

SINTEZA IN REAKTIVNOST NEKATERIH KARBONILNIH
SPOJIN
Mentor: prof. dr. Marjan Jereb
Datum zagovora: 13. 2. 2019

Kristijan KOVAČIČ

SINTEZA IN KARAKTERIZACIJA NEKATERIH
BIPRIDINIJEVIH HEKSAFLUORIDOTITANATOV
Mentor: doc. dr. Andrej Pevec
Datum zagovora: 19. 3. 2019

Gregor JEZERŠEK

MERJENJE NIVOJA KAPLJEVIN IN SIPKIH MATERIALOV Z
ULTRAZVOČNIM MERILNIKOM RAZDALJ
Mentor:izr. prof. dr. Janez Cerar
Datum zagovora: 22. 3. 2019

Teja KMET

SINTEZA KOVINSKO-ORGANSKIH (MOF) MATERIALOV
MODIFICIRANIH Z AMINSKIMI SKUPINAMI
Mentorica:izr. prof. dr. Amalija Golobič
Datum zagovora: 26. 3. 2019

Jernej DOVJAK

KEMIJSKA KARAKTERIZACIJA NEKATERIH VRST
ODPADNE LIGNOCELULOZNE BIOMASE
Mentorica:izr. prof. dr. Irena Kralj Cigić
Datum zagovora: 2. 4. 2019

Erika PLESTENJAK

OPTIMIZACIJA SINTEZE ANALOGOV LIGANDA SALEN
NA OSNOVI VITAMINA B6 IN NJIHOVIH KOMPLEKSOV
PREHODNIH KOVIN

Mentor: doc. dr. Jakob Kljun

Datum zagovora: 25. 4. 2019

Blaž KRIŽAJ

PRIMERI UPORABE RAZVOJNE PLOŠČICE ARDUINO V
KEMIJI

Mentor: doc. dr. Črtomir Podlipnik

Datum zagovora: 26. 4. 2019

Urška MEDVEŠEK

TERMOKROMNI MATERIALI IN NJIHOVA UPORABA

Mentorica: prof. dr. Urška Lavrenčič Štangar

Datum zagovora: 6. 5. 2019

Luka JURŠE

GRAFEN: SINTEZA, LASTNOSTI IN UPORABA

Mentor: izr. prof. dr. Miha Lukšič

Datum zagovora: 15. 5. 2019

Mateja LUZAR

SINTEZA KORO-IN BROMOACETILENSKIH
PRODUKTOV

Mentor: doc. dr. Martin Gazvoda

Datum zagovora: 21. 5. 2019

Sara KOZJAN

STRUKTURNE ZNAČILNOSTI LIZOCIMA IZ JAJČNEGA
BELJAKA

Mentor: doc. dr. Bojan Šarac

Datum zagovora: 14. 6. 2019

Jure KUSTER

OPTIMIZACIJA KINETIKE SINTEZE MIKOFENOLAT
MOFETILA V REAKCIJI DIREKTNE ESTERIFIKACIJE

Mentor: prof. dr. Marjan Jereb

Datum zagovora: 17. 6. 2019

Blaž MIKLAVC

KOMPLEKSI BAKROVEGA(II) NITRATA IN PIRIDIN-2-
ONA

Mentorica: doc. dr. Saša Petriček

Datum zagovora: 18. 6. 2019

Simon BERCKO

ACETILPIRIDINI KOT KATIONI V
HEKSAFLUORIDOTITANATNIH SOLEH

Mentor: doc. dr. Andrej Pevec

Datum zagovora: 18. 6. 2019

Milan BIJELJAC

UPORABA AKRILAMIDNIH HIDROGELOV V BETONU

Mentor: viš. pred. dr. Branko Alič

Datum zagovora: 28. 6. 2019

Matija LEBAN

MERJENJE PRETOKA V POSEBNIH OKOLIŠČINAH

Mentor: viš. pred. dr. Andrej Godec

Datum zagovora: 28. 6. 2019

Urška KOŠIR

VLOGA POLIMEROV IN POVRŠINSKO AKTIVNIH SNOVI
V FARMACEVTSKIH IZDELKIH

Mentorica: prof. dr. Ksenija Kogej

Datum zagovora: 2. 7. 2019

Benjamin MALOVRH

VLOGA IN ANALIZA MEMBRANSKIH VEZIKLOV

Mentorica: prof. dr. Ksenija Kogej

Datum zagovora: 4. 7. 2019

Katja BOKALIČ

VREDNOTENJE UČINKOVITOSTI KOMUNALNE
ČISTILNE NAPRAVE

Mentorica: prof. dr. Helena Prosen

Datum zagovora: 5. 7. 2019

Nina ZUPAN

DOLOČANJE TOKOFEROLOV V OLJIH S HPLC

Mentorica: prof. dr. Helena Prosen

Datum zagovora: 5. 7. 2019

POTOKAR Anton

UPORABA IZKLJUČITVENE KROMATOGRAFIJE PRI
ŠTUDIJI PRISILNE RAZGRADNJE MONOKLONSKEGA
PROTITELESA

Mentor: prof. dr. Matevž Pompe

Datum zagovora: 5. 7. 2019

Blaž KONČAN

ELEKTRIČNI POTENCIAL NEVRONSKE CELICE

Mentor: viš. pred. dr. Andrej Godec

Datum zagovora: 5. 7. 2019

Polona KLEMENČIČ

VPLIV IZBRANIH PEPTIDNIH IN PROTEINSKIH
INHIBITORJEV NA AKTIVNOST NEKATERIH ALGNIH
METAKASPAZ TIPOV I, II IN III

Mentorica: doc. dr. Marina Klemenčič

Datum zagovora: 5. 8. 2019

Maja SELAK

MODIFIKACIJA KARBOKSILMETIL CELULOZE

Mentor: izr. prof. dr. Jernej Iskra

Datum zagovora: 12. 8. 2019

Patrik KOŠIR

AVTOMATIZACIJA POTENCIOMETRIČNIH TITRACIJ ZA
DOLOČANJE KISLIN V TEHNOLOŠKIH PROCESIH

Mentor: izr. prof. dr. Mitja Kolar

Datum zagovora: 26. 8. 2019

Erika KRIVIC

KOMPLEKS ŽELEZOVEGA(III) KLOORIDA S PIRIDIN-2-
ONOM

Mentorica: doc. dr. Saša Petriček

Datum zagovora: 26. 8. 2019

Matic PERME

MIKROPLASTIKA V ODPADNIH VODAH

Mentorica: doc. dr. Lidija Slemenik Perše

Datum zagovora: 27. 8. 2019

Klavdija BENDAFLUORIDOOKSIDOVANADATI NEKATERIH
HALOPIRIDINOV

Mentor: doc. dr. Andrej Pevec

Datum zagovora: 29. 8. 2019

Tina STRAŽIŠARFLUORIDOOKSIDOVANADATI NEKATERIH
NUKLEINSKIH BAZ

Mentor: doc. dr. Andrej Pevec

Datum zagovora: 29. 8. 2019

Urška ROČNIKDOLOČITEV FOSFATOV V ŠTIRIH VZORCIH ŽIVIL Z
MOLEKULSKO ABSORPCIJSKO SPEKTROFOTOMETRIJO

Mentorica: viš. pred. dr. Tatjana Zupančič

Datum zagovora: 30. 8. 2019

Meta COLNAROPTIMIZACIJA SINTEZE ORGANORUTENIJEVEGA(II)
KOMPLEKSA S PIRITIONOM IN PTA

Mentor: prof. dr. Iztok Turel

Datum zagovora: 30. 8. 2019

Tanja BUH

SAMOPOPRAVLJIVI BETONI

Mentorica: izr. prof. dr. Romana Cerc Korošec

Datum zagovora: 30. 8. 2019

Katarina JENKOOBČUTLJIVOST IREVERZIBILNIH TISKARSKIH BARV NA
SEGREVANJE

Mentor: izr. prof. dr. Franc Perdih

Datum zagovora: 30. 8. 2019

Jan ŠPINDLERDOLOČITEV EKSPLOZIJSKIH LASTNOSTI IN
KARAKTERISTIK KROMPIRJEVEGA TER KORUZNEGA
ŠKROBA

Mentorica: doc. dr. Barbara Novosel

Datum zagovora: 2. 9. 2019

Tina ANDREJČIČSINTEZA KOMPLEKSA NIKLJEVEGA(II) NITRATA S
PIRIDIN-2-ONOM

Mentorica: doc. dr. Saša Petriček

Datum zagovora: 3. 9. 2019

Živa Hayat ZUPANČIČ

FIZIKALNE OSNOVE POTAPLJANJA

Mentor: viš. pred. dr. Andrej Godec

Datum zagovora: 4. 9. 2019

Kristina HRIBARDOLOČANJE MAGNEZIJA V PREHRANSKIH
DOPOLNILIH

Mentor: izr. prof. dr. Mitja Kolar

Datum zagovora: 4. 9. 2019

Leja ŠENICA

DOLOČANJE KOFEINA V PREHRANSKIH DOPOLNILIH

Mentorica: viš. pred. dr. Tatjana Zupančič

Datum zagovora: 4. 9. 2019

Alja LESAR

ODGOVORNA RABA KEMIKALIJ V INDUSTRIJI

Mentorica: doc. dr. Barbara Novosel

Datum zagovora: 4. 9. 2019

Nina BAHČIČSPREMLJANJE REAKCIJE BAKROVEGA(II) KINALDINATA
S PIPERIDINOM

Mentorica: doc. dr. Barbara Modec

Datum zagovora: 5. 9. 2019

Jure AVSENIKIONSKE SISTEMI Z DELNO ZAMRZNJENIMI
PROSTOSTNIMI STOPNJAMI

Mentor: izr. prof. dr. Miha Lukšič

Datum zagovora: 5. 9. 2019

Goran KRAGOLNIKANALIZA SINTETIČNIH IN NARAVNIH KANABINOIDOV
V VZORCIH PREPOVEDANIH DROG IN IZDELKIH IZ
KONOPLJE

Mentor: izr. prof. dr. Mitja Kolar

Datum zagovora: 6. 9. 2019

Rok TOMŠIČIONSKE KROMATOGRAFIJE ZA DOLOČEVANJE
ANIONOV

Mentor: izr. prof. dr. Mitja Kolar

Datum zagovora: 6. 9. 2019

Nataša VUKADINOVIČRAZVOJ IN VALIDACIJA HPLC METODE ZA DOLOČANJE
RESVERATROLA

Mentorica: viš. pred. dr. Tatjana Zupančič

Datum zagovora: 6. 9. 2019

Doroteja ŠOŠTARIČFIZIKALNO-KEMIJSKE LASTNOSTI IONSKE
TEKOČINE 1-BUTIL-3-METILIMIDAZOLIJEVEGA
TETRAFLUOROBORATA

Mentor: doc. dr. Bojan Šarac

Datum zagovora: 6. 9. 2019

Amadej MUROVECDOLOČANJE KOVINSKIH IONOV Z ICP/OES V
MEDVRSTNIH KRIŽANCIH BEZGA

Mentor: izr. prof. dr. Mitja Kolar

Datum zagovora: 6. 9. 2019

Nika STANIŠADOLOČANJE SLADKORJA V PIJAČAH Z MOLEKULSKO
ABSORPCIJSKO SPEKTROFOTOMETRIJO

Mentorica: viš. pred. dr. Tatjana Zupančič

Datum zagovora: 6. 9. 2019

Anamarija PIRNATREGULACIJA PROCESOV IN UPORABA KRMILNE
PLOŠČICE ARDUINO

Mentor: viš. pred. dr. Andrej Godec

Datum zagovora: 6. 9. 2019

Patricija FRANKO

PRIPRAVA IN KARAKTERIZACIJA KOKRISTALOV
PIRIDIN-N-OKSIDA IN BENZOJSKE KISLINE

Mentorica: izr. prof. dr. Amalija Golobič

Datum zagovora: 9. 9. 2019

Katja KLOBUČAR

PRETVORBE HALOGENIRANIH ORGANSKIH SPOJIN

Mentor: prof. dr. Marjan Jereb

Datum zagovora: 9. 9. 2019

Nastja ŠADL

VPLIV RAZLIČNIH STABILIZATORJEV NA STABILNOST
VODIKOVEGA PEROKSIDA

Mentor: izr. prof. dr. Janez Cerkovnik

Datum zagovora: 11. 9. 2019

Pia DOLINAR

SINTEZA MANGANOVH OKSIFLUORIDOV ZA LITIJEVE
AKUMULATORJE

Mentor: izr. prof. dr. Robert Dominko

Datum zagovora: 13. 9. 2019

Nina KRŽAN

FAZNA RAVNOTEŽJA V DVOKOMPONENTNIH SISTEMIH

Mentor: prof. dr. Andrej Jamnik

Datum zagovora: 16. 9. 2019

Anja LEBAR

KARAKTERIZACIJA IN SINTEZA $[\text{Cu}(\text{NH}_3)_4(\text{H}_2\text{O})](\text{SO}_4)$

Mentorica: doc. dr. Nives Kitanovski

Datum zagovora: 16. 9. 2019

Tinkara MEZGEC

KONDUKTOMETRIČNE TITRACIJE

Mentorica: doc. dr. Nataša Gros

Datum zagovora: 18. 9. 2019

Martina Tina PUCELJ

HIDROGELI Z LASTNOSTMI LEPIL OBČUTLJIVIH NA
PRITISK

Mentor: viš. pred. dr. Branko Alič

Datum zagovora: 19. 9. 2019

Katja RAŠL

DOLOČITEV STOPNJE TOPLOTNE MODIFIKACIJE
JESENOVINE

Mentorica: izr. prof. dr. Romana Cerc Korošec

Datum zagovora: 19. 9. 2019

Edisa ABDIĆ

PRETVORBE KETONOV PRI POGOJIH BREZ TOPILA

Mentor: prof. dr. Marjan Jereb

Datum zagovora: 19. 9. 2019

Teja VRŠČAJ

ANALIZA KREM ZA SONČENJE Z RENTGENSKO
PRAŠKOVNO DIFRAKCIJO

Mentor: prof. dr. Anton Meden

Datum zagovora: 20. 9. 2019

Matija OMERZEL

KARAKTERIZACIJA NEZNANEGA VZORCA: NASTALEGA
PRI REAKCIJI KOBALTOVEGA(II) KLORIDA IN
AMONIAKA

Mentorica: doc. dr. Nives Kitanovski

Datum zagovora: 24. 9. 2019

Miha ZAKOTNIK

VPLIV RAZLIČNIH TIPOV MATIRNIH SREDSTEV
NA FIZIKALNE LASTNOSTI DVOKOMPONENTNIH
POLIURETANSKIH PREMAZOV ZA LES

Mentor: viš. pred. dr. Andrej Godec

Datum zagovora: 25. 9. 2019

Ivana TUCELJ

POMEN VISKOZNOSTI ZA UPORABO ADHEZIVOV TER
VPLIVI NANJO

Mentorica: prof. dr. Barbara Hribar Lee

Datum zagovora: 26. 9. 2019

Urban ZUPANČIČ

PRIPAJANJE NA CELULOZNA VLAKNA

Mentor: viš. pred. dr. Branko Alič

Datum zagovora: 26. 9. 2019

Janja DEBEVC

STABILNOST ALFA-AMILAZE V RAZLIČNIH
ORGANIZMIH

Mentor: prof. dr. Jurij Lah

Datum zagovora: 26. 9. 2019

Ana ŠKLANDER

NITRIRANJE FENOLOV

Mentor: izr. prof. dr. Bogdan Štefane

Datum zagovora: 30. 9. 2019

Maja TEODORVIČ

MERILNIKI OSVETLJENOSTI

Mentor: izr. prof. dr. Janez Cerar

Datum zagovora: 30. 9. 2019

Marko CUJNIK

SUPERKRITIČNE TEKOČINE

Mentor: prof. dr. Andrej Jamnik

Datum zagovora: 30. 9. 2019

Anže VESEL

IZOTROPNI IN ANIZOTROPNI MAGNETI NA OSNOVI
SM2CO17

Mentor: doc. dr. Bojan Kozlevčar

Datum zagovora: 30. 9. 2019

Žiga SERAFIN

DESALINACIJA MORSKE VODE Z REVERZNO OSMOZO

Mentor: viš. pred. dr. Andrej Godec

Datum zagovora: 10. 10. 2019

Maja DREMELJ

SINTEZA IN KARAKTERIZACIJA DVOJEDERNEGA
KOMPLEKSA NIKLJEVEGA(II) KLORIDA S PIRIDIN-
ZONOM

Mentorica: doc. dr. Saša Petriček

Datum zagovora: 15. 10. 2019

Janez GERDENC

REGENERACIJA DEVTERIRANEGA Kloroforma

Mentor: prof. dr. Janez Košmrlj

Datum zagovora: 15. 10. 2019

Anita STUPAR

MERITVE GOSTOT RAZTOPIN KOT PREIZKUS TEORIJE O UJEMANJU AFINITET IONOV DO VODE

Mentor:izr. prof. dr. Janez Cerar

Datum zagovora: 18. 10. 2019

Janez PROSEN

FIZIKALNO KEMIJSKE LASTNOSTI IN KEMIJSKO TRETIRANJE NARAVNIH KAMNIN

Mentor:izr. prof. dr. Matija Tomšič

Datum zagovora: 28. 10. 2019

Lucija GROJZDEK

MINERALNA SESTAVA KAMNIN IN PRSTI S PODROČJA PODGORICE

Mentorica:izr. prof. dr. Amalija Golobič

Datum zagovora: 28. 10. 2019

Marko ANĐELKOVIĆ

UGOTAVLJANJE USTREZNOSTI REGENERACIJE IN ČIŠČENJA KROMATOGRAFSKIH KOLON V PROCESU IZOLACIJE BIOLOŠKE UČINKOVINE

Mentorica: prof. dr. Polona Žnidaršič Plazl

Datum zagovora: 15. 11. 2019

Maša STARAŠINIČ

RAZISKAVE SORPCIJE KOVIN NA BIOOGLJE S SEM/EDS ANALIZO

Mentorica: doc. dr. Marija Zupančič

Datum zagovora: 29. 11. 2019

Karmen KUŽNIK

PRIPRAVA IN KARAKTERIZACIJA KOKRISTALOV 4-NITROPIRIDIN-N-OKSIDA IN BENZOJSKE KISLINE

Mentorica:izr. prof. dr. Amalija Golobič

Datum zagovora: 16. 12. 2019

Maruša PETRIČ

NIKLJEVE SPOJINE Z BENZOJSKO KISLINO

Mentor: doc. dr. Bojan Kozlevčar

Datum zagovora: 20. 12. 2019

UNIVERZA V MARIBORU
FAKULTETA ZA KEMIJO IN KEMIJSKO TEHNOLOGIJO
1. januar – 31. december 2019

DOKTORATI

DOKTORSKI ŠTUDIJ – 3. STOPNJA

Dušica MIRKOVIĆ

OBLIKOVANJE, PRIPRAVA IN KARAKTERIZACIJA
NANOEMULZIJ ZA PARENTERALNO PREHRANO

Datum zagovora: 15. 5. 2019

Žan ZORE

CELOVITA SINTEZA TRJNOSTNIH (BIO)KEMIJSKIH IN
DRUGIH PROCESNIH OSKRBOVALNIH MREŽ

Datum zagovora: 21. 3. 2019

Tinkara MASTNAK

OPTIČNI SENZORSKI RECEPTORJI NA OSNOVI AZO
BARVIL

Datum zagovora: 15. 4. 2019

Barbara PETOVAR

RAZVOJ MODIFICIRANIH ELEKTROD IZ STEKLASTEGA
OGLJIKA ZA DOLOČEVANJE TEŽKIH KOVIN V

SLEDOVIH IN ANALIZO VODIKOVEGA PEROKSIDA

Datum zagovora: 14.10.2019

MAGISTERIJI

MAGISTRSKI ŠTUDIJ – 2. STOPNJA

Nika KODBA

VPLIV SUPERKRITIČNEGA OGLJIKOVEGA DIOKSIDA NA
AKTIVNOST IMOBILIZIRANE TRANSGLUTAMINAZE

Datum zagovora: 9. 7. 2019

Amadeja KOKOL

SINTEZA SUBSTITUIRANIH POLI(P-FENILEN
ETINILENOV) IN POLI(P-FENILEN VINILENOV) Z
EMULZIJSKIM TEMPLATIRANJEM

Datum zagovora: 20. 11. 2019

Tina OPREŠNIK

KOIMOBILIZACIJA ALKOHOL DEHIDROGENAZE
IN NIKOTINAMID ADENIN DINUKLEOTIDA NA
MAGNETNE NANODELCE

Datum zagovora: 27. 6. 2019

Ksenija RUTNIK

IZOLACIJA KERATINA IZ PERJA S HIDROTERMIČNIMI
POSTOPKI

Datum zagovora: 4. 9. 2019

Suzana STOKIĆ

ANALIZA BIOLOŠKIH POTI POVEZANIH Z
ODGOVOROM NA BIOLOŠKO TERAPIJO PRI BOLNIKI
Z MULTIPLO SKLEROZO Z UPORABO ORODIJ GENSKE
ONTOLOGIJE

Datum zagovora: 23. 8. 2019

Urša STRADOVNIK

SUSPENZIJE NARAVNIH BARVIL: VPLIV SUROVIN,
HIDROKOLOIDOV TER ANTIOKSIDANTOV NA
KVALITETO KONČNIH PRODUKTOV

Datum zagovora: 18. 12. 2019

Nina ŠENEKAR

VOLNA KOT UČINKOVIT SORBENT ZA
ODSTRANJEVANJE TEŽKIH KOVIN IZ ODPADNE VODE

Datum zagovora: 23. 10. 2019

Jadranka ŠVIGELJ

ANTIMIKROBNI UČINEK KOMERCIALNIH IN NARAVNIH
KONZERVANSOV V KOZMETIČNIH IZDELKIH

Datum zagovora: 24. 9. 2019

Ivo URH

VPLIV DINAMIČNEGA KOVALENTNEGA ZAMREŽENJA
NA LASTNOSTI PREPLETENIH POLIMERNIH MREŽ

Datum zagovora: 23. 10. 2019

Sašo BJELIĆ

VPLIV EKSTRAKTOV IZ LISTOV NAVADNEGA NETRESKA
(SEMPERVIVUM TECTORUM) NA METABOLNO
AKTIVNOST ČLOVEŠKIH MELANOMSKIH CELIC

Datum zagovora: 4. 9. 2019

Jan DROFENIK

IZKORIŠČANJE ODVEČNE TOPLOTE INDUSTRIJSKIH IN
KOGENERACIJSKIH HLADILNIH SISTEMOV
Datum zagovora: 23. 10. 2019

Patricia GRUŠOVNIK

SINTEZA IN SIMULACIJA SEPARACIJSKIH ALTERNATIV
ZA SEPARACIJO N-BUTANOLA IZ ZMESI FORMALDEHID,
METANOL, IZOBUTANOL, N-BUTANOL IN VODA
Datum zagovora: 12. 9. 2019

Jure JANEŽIČ

OCENA POTENCIALA VODNE, TOPLOTNE IN
ENERGETSKE INTEGRACIJE BIOPLINSKEGA PROCESA IN
DRUGIH OBRATOV
Datum zagovora: 21. 1. 2019

Sabina JURAK

UPORABA TERMOGRAVIMETRIČNE ANALIZE PRI
DOLOČANJU LASTNOSTI JAJČNIH LUPIN GLEDE NA
NAČIN VZREJE KOKOŠI
Datum zagovora: 28. 2. 2019

Leon LANG

MODELIRANJE PROCESOV ANAEROBNE IN AEROBNE
RAZGRADNJE Z MODELOMA ADM1 IN ASM1
Datum zagovora: 17. 4. 2019

Aljaž MARIN

ŠTUDIJA PROIZVODNOSTI HIDROLIZE SAHAROZE Z
ENCIMOM VEZANIM NA ODPADNA STEKLENA VLAKNA
Datum zagovora: 22. 5. 2019

Maja MEŽNAR

RAZVOJ ALTERNATIVNE RECEPTURE ZA IZDELAVO
PORCELANSKE PLOŠČICE V PODJETJU GORENJE
KERAMIKA
Datum zagovora: 17. 4. 2019

Maja PRESKAR

PROUČEVANJE MIKROFILTRACIJSKE KERAMIČNE
MEMBRANE NA PREPUSTNOST SIROTKINIH
PROTEINOV
Datum zagovora: 4. 9. 2019

Sandi SKRBINŠEK

RAZVOJ IN ANALIZA HIDROFOBNIH PREMAZOV NA
ALUMINIJEVI ZLITINI
Datum zagovora: 17. 4. 2019

Anita SOVIČ

SINTEZA OMREŽIJ TOPLOTNIH PRENOSNIKOV S
SIMULTANIM UPOŠTEVANJEM VARNOSTI
Datum zagovora: 24. 9. 2019

Tina Melisa ŠIMIČ

OPTIMIZACIJA NABORA INVESTICIJSKIH PROJEKTOV Z
UPORABO MATEMATIČNEGA PROGRAMIRANJA
Datum zagovora: 4. 9. 2019

Rok ŠPINDLER

IZKORIŠČANJE ODPADNE TOPLOTE S TRIKOTNIM
EKSPANZIJSKIM CIKLOM
Datum zagovora: 24. 9. 2019

Nina URBIČ

FORMULIRANJE PARACETAMOLA V POLIMERE S
SUPERKRITIČNIMI PLINI
Datum zagovora: 20. 3. 2019

Aljoša VOUK

OPTIMIZACIJA PROCESA NEVTRALIZACIJE V OBRATU
KEMIČNE NEKOVINSKE PROIZVODNJE
Datum zagovora: 23. 10. 2019

Matic BROZ

VPLIV POLIMORFIZMA POSAMEZNEGA NUKLEOTIDA
RS4880 NA GENU SOD2 NA SEKUNDARNO STRUKTURU
ENCIMA MANGANOVE SUPEROKSID-DISMUTAZE
Datum zagovora: 12. 9. 2019

Amanda FERLEŽ

VPLIV ADITIVOV ZA SAMOUGASLJIVOST NA
LASTNOSTI POLIURETANSKIH PEN
Datum zagovora: 13. 2. 2019

Kristina GLUHAK

DOLOČITEV OPTIMALNEGA MARKERJA
HOMOGENOSTI KRMNIH MEŠANIC
Datum zagovora: 12. 9. 2019

Barbara GRABROVEC

INTERAKCIJE BIOTEHNOLOŠKO RELEVANTNIH
ENCIMOV
Datum zagovora: 1. 10. 2019

Sara KRAMBERGER

NiCu NANODELCI V MATRICI SILIKE Z VGRAJENO
ZDRAVLNO UČINKOVINO ZA POTENCIALNO
ZDRAVLJENJE KOŽNEGA RAKA
Datum zagovora: 22. 5. 2019

Stanko KRAMER

POROZNA ZRNA IZ MULTIPLIH EMULZIJ S TIOL-EN
POLIMERIZACIJO
Datum zagovora: 4. 9. 2019

Tina RAJH

NOVI KOMPOZITI NANODELCEV Fe₂O₃ IN POLIMERNIH
NOSILNIH MATERIALOV- RAZŠIRJANJE MOŽNOSTI
BIOMEDICINSKE UPORABE
Datum zagovora: 20. 2. 2019

Nermin SINANOVIĆ

SINTEZE V SISTEMU Bi₂O₃/MOO₃ Z UPORABO
RAZLIČNIH METOD IN TERMIČNA KARAKTERIZACIJA
PRODUKTOV
Datum zagovora: 20. 11. 2019

Jan ŠTOS

RAZVOJ IN VALIDACIJA GC -FID/MS ANALIZNEGA
POSTOPKA ZA DOLOČITEV MAŠČOBNIH KISLIN V ŽIRU
IN POLHOVI MASTI
Datum zagovora: 20. 2. 2019

Jaka ŠTURM

SINTEZA BAKROVIH KOORDINACIJSKIH SPOJIN S
HIDROKSIPIRIDINI
Datum zagovora: 18. 12. 2019

Sara VINKOVIČ

STOPNJA MAŠENJA MEMBRANE PRI FILTRACIJI
RAZLIČNIH ONESNAŽIL

Datum zagovora: 20. 3. 2019

DIPLOME – UNIVERZITETNI ŠTUDIJ

UNIVERZITETNI ŠTUDIJ – 1. STOPNJA

Melisa GJURA

RAZGRADNJA LIGNINA MED PRERAŠČANJEM GOBE
PLEUROTUS OSTREATUS NA LIGNOCELULOZNEM
SUBSTRATU

Datum zagovora: 24. 9. 2019

Maja GLOBOČNIK

PRECIPITACIJA IN AKTIVNOST TRANSLUTAMINAZE V
SUPERKRITIČNEM OGLJIKOVEM DIOKSIDU

Datum zagovora: 4. 9. 2019

Rene GOLE

SINTEZA $Mg_{1+x}Fe_{2-2x}Ti_xO_4$ NANODELCEV Z
MIKROEMULZIJSKO TEHNIKO

Datum zagovora: 4. 9. 2019

Ivana GORIČAN

DOLOČANJE OPTIMALNIH POGOJEV ZA
RAZMNOŽEVANJE BIOMASE VODNEGA KEFIRJA

Datum zagovora: 10. 7. 2019

Anja HRIBERNIK

EKSTRAKCIJA ARTEMIZININA IZ SLADKEGA PELINA
ARTEMISIA ANNUA L.

Datum zagovora: 4. 9. 2019

Špela KOČAR

MODELIRANJE HLAJENEGA NEIZOTERMNEGA
MEŠALNEGA REAKTORJA

Datum zagovora: 17. 4. 2019

Žan KOŠTOMAJ

REDOKS INICIACIJA STIRENSKIH MONOMEROV V
EMULZIJAH

Datum zagovora: 12. 9. 2019

Jan MARKO

FAZNA INVERZIJA V EMULZIJSKIH SISTEMIH Z
MONOMERI TIOLOV IN ALKENOV

Datum zagovora: 12. 9. 2019

Tibor MLAKAR

PRIMERJAVA IZRAČUNANIH IN NUMERIČNIH
REZULTATOV PRI OBRAVNAVI MOLEKULE VODIKA

Datum zagovora: 4. 9. 2019

Vanja MLINARIČ

VPLIV IONOV HOFMEISTER-JEVE VRSTE NA PREMIK
KRITIČNE MICELNE KONCENTRACIJE POVRŠINSKO
AKTIVNIH SNOVI (IONSKEGA TIPA)

Datum zagovora: 27. 3. 2019

Ela PINTAR

IMOBILIZACIJA ENCIMA ALKOHOL DEHIDROGENAZE
NA DEKSTRANSKE MAGNETNE NANODELCE

Datum zagovora: 20. 3. 2019

Jan POLAK

MIKROEMULZIJSKA POLIMERIZACIJA ZA PRIPRAVO
NANOPOROZNIH MATERIALOV

Datum zagovora: 12. 9. 2019

Helena PRIMEC

PRIPRAVA TEKOČINSKIH FORMULACIJ ZA
KONTROLIRANO SPROŠČANJE PESTICIDOV

Datum zagovora: 30. 9. 2019

Nika PROJE

PREVERJANJE USTREZNOSTI ANALITSKE METODE ZA
DOLOČANJE VSEBNOSTI AKTIVNIH UČINKOVIN

Datum zagovora: 4. 9. 2019

Maša STOPINŠEK

SOČASNO DOLOČANJE RAZLIČNIH FENOLNIH SPOJIN V
EKSTRAKTIH ČAJEV S TEKOČINSKO KROMATOGRAFIJO
Z UV ZAZNAVO

Datum zagovora: 17. 4. 2019

Rahil BAJRA

ODSTRANJEVANJE TEŽKIH KOVIN S POMOČJO
MAGNETNIH NANODELCEV

Datum zagovora: 24. 9. 2019

Klara BERLAN

BIOLOŠKA AKTIVNOST EKSTRAKTOV ORIGANA
(ORIGANUM VULGARE)

Datum zagovora: 12. 9. 2019

Janina Gea CVIKL

OPTIMIZACIJA IZOLACIJE DNK IZ TKIVNIH VZORCEV
TER ANALIZA SOMATSKIH MUTACIJ PRI BOLNICAH Z
RAKOM DOJK

Datum zagovora: 10. 7. 2019

Mitja ČUŠ

MODIFICIRANJE ZEOLITOV ZA IZBOLJŠANJE
SELEKTIVNOSTI PRI SEPARACIJI PLINOV

Datum zagovora: 12. 9. 2019

Martin ČERANIČ

VPLIV STRUKTURE IN ZAMREŽENJA poli(HEMA) NA
VODNO ABSORPTIVNE LASTNOSTI

Datum zagovora: 12. 9. 2019

Neža HOZJAN

REFORMIRANJE ZEMELJSKEGA PLINA ZA TRDNO
OKSIDNE GORIVNE CELICE
Datum zagovora: 19. 6. 2019

Robert HREN

UPORABA RAZLIČNIH METOD PREDOBDELAVE
ODPADNIH MATERIALOV TER DOLOČANJE NEKATERIH
PARAMETROV MED PREDOBDELAVO
Datum zagovora: 12. 9. 2019

Mihael IRGOLIČ

ADSORPCIJA KOVINSKIH IONOV NA ŽLINDRO
Datum zagovora: 4. 9. 2019

Jernej JELENKO

EKSTRAKCIJA IN ANALIZA BIOLOŠKO AKTIVNIH SPOJIN
IZ OVSA
Datum zagovora: 4. 9. 2019

Ana JURGEC

FUNKCIONALIZIRANI MAGNETNI NANODELCI ZA
ODSTRANJEVANJE TEŽKIH KOVIN IZ ODPADNIH VOD
Datum zagovora: 4. 9. 2019

Anja KONAJZLER

VPLIV SESTAVE GOJIŠČA NA AKTIVNOST ENCIMOV IZ
PLEUROTUS OSTREATUS
Datum zagovora: 12. 9. 2019

Martina KRUŠIČ

VLOGA GENOV IZ DRUŽINE DEJAVNIKA TUMORSKE
NEKROZE PRI NASTANKU IN POTEKU MULTIPLE
SKLEROZE
Datum zagovora: 12. 9. 2019

Teo MAKOTER

EKSTRAKCIJA BIOLOŠKO AKTIVNIH KOMPONENT IZ
INDUSTRIJSKE KONOPLJE
Datum zagovora: 10. 7. 2019

Mateja MARINIČ

VPLIV ROŽMARINA NA KVALITETO ROŽMARINOVIH
EKSTRAKTOV IN NJIHOVIH FORMULACIJ
Datum zagovora: 4. 9. 2019

Tina MIHELČIČ

ENKAPSULACIJA ADITIVOV S PROTIKOROZIJSKIM
DELOVANJEM
Datum zagovora: 4. 9. 2019

Jan OPARA

UPORABA ENCIMSKIH SKUPKOV ZA ODSTRANJEVANJE
DIKLOFENAKA IZ ODPADNIH VOD
Datum zagovora: 12. 9. 2019

Tamara SAVEC

VZPOSTAVITEV METODE ZA DOLOČANJE
REAKTIVNOSTI APNENČEVE MOKE
Datum zagovora: 4. 9. 2019

Špela SLAPNIČAR

INHIBICIJSKA UČINKOVITOST MEŠANICE ŠKROBA IN
POVRŠINSKO AKTIVNIH SNOVI V KISLEM MEDIJU
Datum zagovora: 12. 9. 2019

Rok ŠPENDL

INHIBICIJSKE LASTNOSTI MEDU NA JEKLU V
AGRESIVNEM MEDIJU
Datum zagovora: 12. 9. 2019

Kaja TOMAŽIČ

VPLIV POSTOPKOV EKSTRAKCIJE NA VSEBNOST
AKTIVNIH UČINKOVIN V EKSTRAKTU IZ OLJČNIH
LISTOV
Datum zagovora: 4. 9. 2019

Kaja ZADRAVEC

TERMODINAMSKA LASTNOSTI DVOFAZNEGA
SISTEMA POLIMER TRILaurin/SUPERKRITIČNI CO₂ IN
FORMULACIJA ZDRAVILNIH UČINKOVIN
Datum zagovora: 4. 9. 2019

DIPLOME – VISOKOŠOLSKI STROKOVNI ŠTUDIJ

VISOKOŠOLSKI STROKOVNI ŠTUDIJ – 1. STOPNJA

Petra BERLAK

VLOGA POLIMORFIZMOV V GENIH MATRIKSIH
METALOPROTEINAZ PRI RAKU DOJK
Datum zagovora: 12. 9. 2019

Danijela COLE

GENETSKA IN FARMAKOGENETSKA ANALIZA GENOV
IZ DRUŽINE DEJAVNIKA TUMORSKE NEKROZE PRI
REVMAOIDNEM ARTRITISU
Datum zagovora: 24. 9. 2019

David HVALEC

BIOLOŠKA AKTIVNOST KONVENCIONALNIH
EKSTRAKTOV IZ PARADIŽNIKA (SOLANUM
LYCOPERSICUM)
Datum zagovora: 4. 9. 2019

Eva KAUČIČ

UPORABA CO₂ ZA ZNIŽEVANJE KONCENTRACIJE
ALKALIJSKIH IN ZEMELJSKOALKALIJSKIH KOVIN V
ALUMINIJEVEM OKSIDU IN HIDROKSIDU
Datum zagovora: 10. 7. 2019

Martina KODRIČ

VPLIV IZKORIŠČANJA TOPLOTE GEOTERMIČNIH IN
PODTALNIH VOD NA OKOLJE
Datum zagovora: 12. 9. 2019

Kristina KRANJČEC

HIDROTERMIČNA DEGRADACIJA ODPADNE EMBALAŽE
IZ POLIPROPILENA
Datum zagovora: 4. 9. 2019

Denisa KREVIHVSEBNOST HOLEKALCIFEROLA IN ERGOKALCIFEROLA
V ŽIVILIH

Datum zagovora: 12. 9. 2019

Jaka KUGLERBENTONIT KOT ADSORBENT ZA SEPARACIJO
KOVINSKIH IONOV IZ VODNIH RAZTOPIN

Datum zagovora: 12. 9. 2019

Danijel LAVRIČEKSTRAKCIJA AKTIVNIH KOMONENT IZ SEMEN ČRNE
KUMINE (NIGELLA SATIVA)

Datum zagovora: 4. 9. 2019

Andraž PAPEŽAKUMULACIJA SENZIBILNE TOPLOTE S FAZNO
SPREMENLJIVIMI SNOVMI

Datum zagovora: 12. 9. 2019

Tilen PEČEKODSTRANJEVANJE TEŽKIH KOVIN IZ KONTAMINIRANE
ZEMLJE

Datum zagovora: 12. 9. 2019

Anže PEKLARANTIMIKROBNA UČINKOVITOST PUNICA GRANATUM
L. NA ESCHERICHIA COLI

Datum zagovora: 12. 9. 2019

Laura PRŠA

INAKTIVACIJA ENCIMOV V ŽIVILIH

Datum zagovora: 9. 7. 2019

Anita SEVERRECIKLIRANJE ODPADNE PET EMBALAŽE S POD- IN
NADKRITIČNO VODO

Datum zagovora: 10. 7. 2019

Žan SMREKARRAČUNALNIŠKO NAČRTOVANJE TERAPEVTSKIH
PROTEINOV

Datum zagovora: 12. 9. 2019

Katja SVETEKEKSTRAKCIJA ETERIČNIH OLJ IZ INGVERJA (ZINGIBER
OFFICINALE)

Datum zagovora: 12. 9. 2019

Katja ŠEKORANJANAPOVEDOVANJE POSLEDIC OB POŽARU IN IZLITJU
NEVARNIH KEMIKALIJ

Datum zagovora: 24. 9. 2019

Urban ŠKET

ADSORPCIJA IONOV TEŽKIH KOVIN NA ZEOLIT

Datum zagovora: 12. 9. 2019

Žiga ŠROTOPTIMIRANJE KONSTANT PID REGULATORJEV
ZA KASKADNO REGULACIJO NIVOJA TEKOČIN Z
METODOLOGIJO ODZIVNIH POVRŠIN

Datum zagovora: 12. 9. 2019

Anja ŠTRAKLRAZGRADNJA POLIETILENSKIH ODPADKOV V
SUPERKRITIČNI VODI

Datum zagovora: 10. 7. 2019

Martina ŠVAJGERBIOLOŠKA AKTIVNOST EKSTRAKTOV PITAJE
(HYLOCEREUS POLYRHIZUS)

Datum zagovora: 10. 7. 2019

UNIVERZA V NOVI GORICI
FAKULTETA ZA PODIPLOMSKI ŠTUDIJ
1. januar – 31. december 2019

DOKTORATI

PODIPLOMSKI ŠTUDIJSKI PROGRAM ZNANOSTI O OKOLJU – 3. STOPNJA

Nada PAVŠER

ENVIRONMENTAL CRIME TRAINING NEEDS ANALYSIS
OF SLOVENE POLICE FORCES

Mentor: doc.dr. Branko Kontić

Datum zagovora: 25.1.2019

Slavica SCHUSTER

FACTORS INFLUENCING COLLECTED QUANTITIES OF
MUNICIPAL SOLID WASTE

Mentor: prof. dr. Andrej Kržan

Datum zagovora: 30.9.2019

Maja OPALIČKI SLABE

REGIONAL BIODIVERSITY AND SEASONAL DYNAMICS
OF THE BACTERIAL COMMUNITIES IN KARSTIC
SPRINGS OF SLOVENIA

Mentor: prof. dr. Anton Brancelj

Datum zagovora: 26.6.2019

Nives VODIŠEK

PHOTOACTIVE NANOCOMPOSITE THIN FILMS ON
GLASS AND THERMOSENSITIVE SUBSTRATES

Mentorica: prof. dr. Urška Lavrenčič Štangar

Datum zagovora: 15.10.2019

Leja GOLJAT

THE DETECTION OF METAL COMPLEXES AND
ORGANOMETALLIC COMPOUNDS IN ENVIRONMENTAL
SAMPLES BY THERMAL LENS SPECTROMETRY

Mentor: prof. dr. Mladen Franko

Datum zagovora: 3.9.2019

Olena PLIEKHOVA

Zr/Cu-TiO₂ CATALYSTS FOR PHOTOCATALYTIC WATER
TREATMENT

Mentorica: prof. dr. Urška Lavrenčič Štangar

Datum zagovora: 3.12.2019

FAKULTETA ZA ZNANOSTI O OKOLJU

1. januar – 31. december 2019

MAGISTERIJI

ŠTUDIJSKI PROGRAM OKOLJE – 2. STOPNJA

Gaja TOMSIČ

DOLOČEVANJE ŽELEZA V NARAVNIH VODAH S
TEHNIKO FIA-TLS

Mentor: prof. dr. Mladen Franko

Somentorica: prof. dr. Dorota Korte

Datum zagovora: 18. 2. 2019

Merisa KAPIČ

KOMPARATIVNA ANALIZA PROCESA PROIZVODNJE
VENTILATORJEV V PODJETJU HIDRIJA ROTOMATIKA;
PRIMERJAVA TIPOV VENTILATORJEV Z VIDIKA
ŽIVLJENJSKEGA CIKLA

Mentor: prof. dr. Henrik Gjerkeš

Somentorica: Sonja Mlakar, univ. dipl. inž. str.

Datum zagovora: 9. 7. 2019

Monika FERFOLJA

VPLIV BIVALNIH NAVAD NA DINAMIKO RADONA V
DOMOVNIH

Mentorica: prof. dr. Janja Vaupotič

Datum zagovora: 12. 4. 2019

Anja Petra BENCEK

ODVISNOST KONCENTRACIJE NANODELCEV V
ZUNANJEM ZRAKU OD STABILNOSTI ATMOSFERE

Mentorica: prof. dr. Janja Vaupotič

Datum zagovora: 11. 10. 2019

Teja MELINC

UPORABA NARAVNIH SLEDIL ZA DOLOČANJE
ZNAČILNOSTI KRAŠKIH IZVIROV NA OBROBJU
PLANINSKEGA POLJA (JZ SLOVENIJA)

Mentorica: prof. dr. Metka Petrič

Datum zagovora: 21. 11. 2019

Urban ČESNIK

PRISOTNOST BOKONTROLNE AKTIVNOSTI PRI
KVASOVKAH, OSAMLJENIH IZ VINOGRADNIŠKEGA
OKOLJA

Mentorica: doc. dr. Lorena Butinar

Datum zagovora: 29. 11. 2019

Petra GERBEC

OBDELAVA ODPADNE VODE NA VAROVANIH
OBMOČJIH NARAVE V SLOVENIJI: TRENUTNO STANJE
IN MOŽNOSTI RAZVOJA

Mentorica: doc. dr. Andreea Oarga-Mulec

Somentorica: mag. Mojca Zega

Datum zagovora: 9. 12. 2019

DIPLOME

ŠTUDIJSKI PROGRAM OKOLJE – 1. STOPNJA

Klemen COTIČ

PRIHODNJI SCENARIJI RABE TAL NA CELOTNEM
OBMOČJU PARKA ŠKOCJANSKE JAME Z UPORABO
PROSTORSKEGA MODELA DYNACLUE

Mentor: dr. Žiga Malek

Mentor: prof. dr. Matjaž Valant

Datum zagovora: 30. 9. 2019

Matjaž REYA

FOTOELEKTROKEMIČNI RAZKROJ BARVILA RODAMIN
B V ODPADNIH VODAH Z UPORABO NANOSOV S
FLUOROM DOPIRANEGA KOSITROVEGA OKSIDA

Mentor: prof. dr. Saim Emin

Datum zagovora: 21. 10. 2019

KOLEDAR VAŽNEJŠIH ZNANSTVENIH SREČANJ S PODROČJA KEMIJE IN KEMIJSKE TEHNOLOGIJE

SCIENTIFIC MEETINGS – CHEMISTRY AND CHEMICAL ENGINEERING

2020

April 2020

- 22 – 24 AUSTRIAN FOOD CHEMISTRY DAYS 2020
Klagenfurt, Austria
Information: <https://www.goech.at/lebensmittelchemikertage>
- 23 – 25 INTERNATIONAL CONFERENCE ON ECONOMICS, ENERGY AND ENVIRONMENT
Cappadocia, Turkey
Information: <http://www.iceee2020.com>
26. – May 2 XII. INTERNATIONAL MASS SPECTROMETRY CONFERENCE ON PETROCHEMISTRY,
ENVIRONMENTAL AND FOOD CHEMISTRY
Crete, Greece
Information: <https://www.petromass2020.com/>

May 2020

- 4 – 5 ECTN GENERAL ASSEMBLY 2020
Perugia, Italy
Information: http://web.chm.unipg.it/chimgen/mb/theo2/ECTN_GA_2020/Welcome.html
- 4 – 8 14TH EUROPEAN CONFERENCE ON SURFACE CRYSTALLOGRAPHY AND DYNAMICS
(ECSCD-14)
Grainau, Germany
Information: http://ecscd14.com/ecscd14/EN/Home/home_node.html
- 05 – 10 44TH INTERNATIONAL CONFERENCE ON COORDINATION CHEMISTRY
Rimini, Italy
Information: <https://www.iccc2020.com>
- 18 – 22 POLY-CHAR 2020 [VENICE] – INTERNATIONAL POLYMER CHARACTERIZATION
FORUM
Venezia Mestre, Italy
Information: <https://www.poly-char2020.org/>
- 18 – 22 10TH INTERNATIONAL SYMPOSIUM ON MOLECULAR ORDER AND MOBILITY IN
POLYMER SYSTEMS
St. Petersburg, Russian Federation
Information: <http://momps2020.macro.ru/>
- 24 – 27 THE 30TH EUROPEAN SYMPOSIUM ON COMPUTER AIDED PROCESS ENGINEERING
Milano, Italy
Information: <https://www.aidic.it/escape30/enter.php>

- 24 – 29 THE 44TH INTERNATIONAL SYMPOSIUM ON CAPILLARY CHROMATOGRAPHY
Riva del Garda, Italy
Information: <http://iscc44.chromaleont.it/slider.htm>
- 25 – 29 EURACHEM GENERAL ASSEMBLY 2020
Bucharest, Romania
Information: <https://www.eurachem.org/>
- 26 – 27 FOOD CONTAMINATION AND TRACEABILITY SUMMIT
Stadthalle Erding Centre, Erding
Information: <https://contaminationsummit.com/>
- 26 – 30 17TH EUROPEAN POWDER DIFFRACTION CONFERENCE (EPDIC17)
Šibenik, Croatia
Information: <https://www.epdic17.org/>

June 2020

- 2 – 05 14TH MEDITERRANEAN CONGRESS OF CHEMICAL ENGINEERING
Barcelona, Spain
Information: <https://www.mecce.org/>
- 3 – 5 POLYMERS 2020: NEW TRENDS IN POLYMER SCIENCE: HEALTH OF THE PLANET,
HEALTH OF THE PEOPLE
Turin, Italy
Information: <http://polymers2020.sciforum.net>
- 8 – 12 11TH EUROPEAN CONFERENCE ON SOLAR CHEMISTRY AND PHOTOCATALYSIS:
ENVIRONMENTAL APPLICATIONS (SPEA)
Turin, Italy
Information: <http://www.spea11.unito.it/home>
- 14 – 18 12TH EUROPEAN SYMPOSIUM ON ELECTROCHEMICAL ENGINEERING
Leeuwarden, The Netherlands
Information: <http://www.electrochemical-engineering.eu/2020/>
- 23 – 26 16TH INTERNATIONAL CONFERENCE ON SURFACE X-RAY AND NEUTRON
SCATTERING (SXNS16)
Lund, Sweden
Information: <https://www.sxns16.org/>
- 24 – 25 2ND INTERNATIONAL CONFERENCE ON SUSTAINABLE PRODUCTION AND
CONSUMPTION
Edinburgh, UK
Information: <https://www.icheme.org/career/events/2nd-international-conference-on-sustainable-production-and-consumption/>
- 28 – Jul. 1 19TH INTERNATIONAL BIOTECHNOLOGY SYMPOSIUM
Maastricht, Netherlands
Information: <https://www.ecb2020.com/>
- 28 – Jul. 1 ESAT2020 – 31TH EUROPEAN SYMPOSIUM ON APPLIED THERMODYNAMICS
Paris, France
Information: <http://www.esat2020.com/>
- 29 – Jul. 2 26TH INTERNATIONAL SYMPOSIUM ON SEPARATION SCIENCES
Ljubljana, Slovenia
Information: <https://www.iss2020.si/>

July 2020

- 4 – 9 2020 FEBS CONGRESS
Ljubljana, Slovenia
Information: <https://2020.febscongress.org/>

- 5 – 9 48TH WORLD POLYMER CONGRESS – MACRO2020
Jeju Island, Republic of Korea
Information: <http://www.macro2020.org>
- 5 – 10 44TH INTERNATIONAL CONFERENCE ON COORDINATION CHEMISTRY
Rimini, Italy
Information: <https://www.iccc2020.com>
- 6 – 8 EUROPEAN CONFERENCE OF RESEARCH IN CHEMISTRY EDUCATION (ECRICE 2020)
Weizmann Institute of Science, Rehovot
Information: <http://www.weizmann.ac.il/st/blonder/>
- 6 – 10 CHEMISTRY FOR CULTURAL HERITAGE - ChemCH-2020
Ravenna, Italy
Information: <https://eventi.unibo.it/chemch2020>
- 12 – 17 28TH IUPAC SYMPOSIUM ON PHOTOCHEMISTRY
Amsterdam, Netherland
Information: <http://Photoiupac2020.amsterdam>
- 12 – 16 84TH PRAGUE MEETING ON MACROMOLECULES – FRONTIERS OF POLYMER
COLLOIDS
Prague, Czech Republic
Information: <https://www.imc.cas.cz/sympo/84pmm>
- 13 – 17 26TH IUPAC INTERNATIONAL CONFERENCE ON CHEMISTRY EDUCATION (ICCE
2020)
Cape Town, South Africa
Information: <https://www.icce2020.org.za/>
- 19 – 24 XRM 2020. INTERNATIONAL CONFERENCE ON X-RAY MICROSCOPY
Taipei, Taiwan
Information: <https://indico.nsrcc.org.tw/event/4/>

August 2020

- 16 – 21 12TH TRIENNIAL CONGRESS OF THE WORLD ASSOCIATION OF THEORETICAL AND
COMPUTATIONAL CHEMISTS
Vancouver, Canada
Information: <https://watoc2020.ca/>
- 22 – 30 TWENTY-FIFTH CONGRESS AND GENERAL ASSEMBLY OF THE INTERNATIONAL
UNION OF CRYSTALLOGRAPHY
Prague, Czech Republic
Information: <https://iucr2020.org/>
- 23 – 27 24TH INTERNATIONAL CONGRESS OF CHEMICAL AND PROCESS ENGINEERING
Prague, Czech Republic
Information: <https://2020.chisa.cz/>
- 30 – Sept. 2 MMPE 2020 – 4TH INTERNATIONAL SYMPOSIUM ON MULTISCALE MULTIPHASE
PROCESS ENGINEERING
Berlin, Germany
Information: <https://processnet.org/mmpe2020.html>
30. – Sept. 3 ECC8 – 8TH EUCHEMS CHEMISTRY CONGRESS
Centro de Congressos de Lisboa, Lisbon
Information: <https://www.euchems.eu/events/ecc8-8th-euchems-chemistry-congress/>
- 30 – Sept. 4 XXIV INTERNATIONAL CONFERENCE ON CHEMICAL REACTORS
Milan, Italy
Information: <http://conf.nsc.ru/CR-24/en/>

September 2020

- 6 – 9 6TH EUROPEAN SYMPOSIUM ON PHOTOPOLYMER SCIENCE
Sarıyer /İstanbul, Turkey
Information: <http://www.esps2020.org/>
- 6 – 10 14TH INTERNATIONAL CONFERENCE ON SOLID STATE CHEMISTRY
Trenčín, Slovak Republic
Information: <https://funglass.eu/ssc2020/>
- 8 – 11 ISIC 2020 – 21ST INTERNATIONAL SYMPOSIUM ON INDUSTRIAL CRYSTALLIZATION
Potsdam, Germany
Information: https://dechema.de/ISIC_21.html
- 9 – 11 25TH CONFERENCE ON ISOPRENOIDS
Karaganda, Kazakhstan
Information: <http://www.isoprenoids25.phyto.kz/>
- 15 – 19 2020 EFCATS SUMMER SCHOOL
Portorož, Slovenia
Information: <https://skd2020.chem-soc.si/2020-efcats-summer-school/>
- 16 – 18 SCS ANNUAL MEETING 2020
Portorož, Slovenia
Information: <https://skd2020.chem-soc.si>
- 16 – 18 18TH RUŽIČKA DAYS – “TODAY SCIENCE – TOMORROW INDUSTRY”
Vukovar, Croatia
Information: <http://www.ruzickadays.eu/>
- 17 – 20 ESBES 2020 – 13TH EUROPEAN SYMPOSIUM ON BIOCHEMICAL ENGINEERING SCIENCES
Portoroz, Slovenia
Information: <https://esbes2020.meetinghand.com/>

Oktober 2020

- 11 – 14 5TH INTERNATIONAL CONFERENCE ON BIOINSPIRED AND BIOBASED CHEMISTRY & MATERIALS
Nice, France
Information: <http://www.nice-conference.com>
- 18 – 22 9TH IUPAC INTERNATIONAL CONFERENCE ON GREEN CHEMISTRY
Athens, Greece
Information: <http://greeniupac2020.org/>
- 23 – 24 6TH SLOVENIAN CONGRESS OF CLINICAL CHEMISTRY AND LABORATORY MEDICINE
Portorož, Slovenia
Information: <https://www.szklmkongres.si/2020/si/>
- 25 – 29 31TH INTERNATIONAL SYMPOSIUM ON THE CHEMISTRY OF NATURAL PRODUCTS AND 11TH INTERNATIONAL CONGRESS ON BIODIVERSITY (ISCNP31 & ICOB11)
Naples, Italy
Information: <https://www.iscnp31-icob11.org/index.php>

2021**January 2021**

19 – 20 METROLOGY, QUALITY AND CHEMOMETRICS – CORRELATION OF TEST RESULTS AND MASS BALANCE INFLUENCE ON CONFORMITY ASSESSMENT
Tel Aviv, Israel
Information: <https://iupac.org/project/2019-012-1-500>

May 2021

18 – 22 13TH INTERNATIONAL CONFERENCE ON THE HISTORY OF CHEMISTRY (13ICHC)
Vilnius, Lithuania
Information: <https://www.ichc2021vilnius.chgf.vu.lt/>

June 2021

9 – 11 5TH INTERNATIONAL CONFERENCE ON CONTAMINATED LAND, ECOLOGICAL ASSESSMENT AND REMEDIATION – CLEAR 2020
London, UK
Information: <http://clear2020.mdx.ac.uk/>

August 2021

13 – 20 IUPAC WORLD CHEMISTRY CONGRESS 2021 MONTREAL
Montréal, Québec Canada
Information: <http://iupac2021.org>

Acta Chimica Slovenica

Author Guidelines

Submissions

Submission to ACSi is made with the implicit understanding that neither the manuscript nor the essence of its content has been published in whole or in part and that it is not being considered for publication elsewhere. All the listed authors should have agreed on the content and the corresponding (submitting) author is responsible for having ensured that this agreement has been reached. The acceptance of an article is based entirely on its scientific merit, as judged by peer review. There are no page charges for publishing articles in ACSi. The authors are asked to read the Author Guidelines carefully to gain an overview and assess if their manuscript is suitable for ACSi.

Additional information

- Citing spectral and analytical data
- Depositing X-ray data

Submission material

Typical submission consists of:

- full manuscript (PDF file, with title, authors, abstract, keywords, figures and tables embedded, and references)
- supplementary files
 - **Full manuscript** (original Word file)
 - **Statement of novelty** (Word file)
 - **List of suggested reviewers** (Word file)
 - **ZIP file containing graphics** (figures, illustrations, images, photographs)
 - **Graphical abstract** (single graphics file)
 - **Proposed cover picture** (optional, single graphics file)
 - **Appendices** (optional, Word files, graphics files)

Incomplete or not properly prepared submissions will be rejected.

Submission process

Before submission, authors should go through the checklist at the bottom of the page and prepare for submission.

Submission process consists of 5 steps.

Step 1: Starting the submission

- Choose one of the journal sections.
- Confirm all the requirements of the **checklist**.
- Additional plain text comments for the editor can be provided in the relevant text field.

Step 2: Upload submission

- Upload full manuscript in the form of a Word file (with title, authors, abstract, keywords, figures and tables embedded, and references).

Step 3: Enter metadata

- First name, last name, contact email and affiliation for all authors, in relevant order, must be provided. Corresponding author has to be selected. Full postal address and phone number of the corresponding author has to be provided.

- **Title and abstract** must be provided in plain text.
- Keywords must be provided (max. 6, separated by semicolons).
- Data about contributors and supporting agencies may be entered.
- **References** in plain text must be provided in the relevant text field.

Step 4: Upload supplementary files

- Original Word file (original of the PDF uploaded in the step 2)
- **Statement of novelty** in a Word file must be uploaded
- All **graphics** have to be uploaded in a single ZIP file. Graphics should be named Figure 1.jpg, Figure 2.eps, etc.
- **Graphical abstract image** must be uploaded separately
- **Proposed cover picture** (optional) should be uploaded separately.
- Any additional **appendices** (optional) to the paper may be uploaded. Appendices may be published as a supplementary material to the paper, if accepted.
- For each uploaded file the author is asked for additional metadata which may be provided. Depending of the type of the file please provide the relevant title (Statement of novelty, List of suggested reviewers, Figures, Graphical abstract, Proposed cover picture, Appendix).

Step 5: Confirmation

- Final confirmation is required.

Article Types

Feature Articles are contributions that are written on editor's invitation. They should be clear and concise summaries of the most recent activity of the author and his/her research group written with the broad scope of ACSi in mind. They are intended to be general overviews of the authors' subfield of research but should be written in a way that engages and informs scientists in other areas. They should contain the following (see also general directions for article structure in ACSi below): (1) an introduction that acquaints readers with the authors' research field and outlines the important questions to which answers are being sought; (2) interesting, new, and recent contributions of the author(s) to the field; and (3) a summary that presents possible future directions. Manuscripts normally should not exceed 40 pages of one column format (letter size 12, 33 lines per page). Generally, experts in a field who have made important contribution to a specific topic in recent years will be invited by an editor to contribute such an **Invited Feature Article**. Individuals may, however, send a proposal (one-page maximum) for an Invited Feature Article to the Editor-in-Chief for consideration.

Scientific articles should report significant and innovative achievements in chemistry and related sciences and should exhibit a high level of originality. They

should have the following structure:

1. Title (max. 150 characters),
2. Authors and affiliations,
3. Abstract (max. 1000 characters),
4. Keywords (max. 6),
5. Introduction,
6. Experimental,
7. Results and Discussion,
8. Conclusions,
9. Acknowledgements,
10. References.

The sections should be arranged in the sequence generally accepted for publications in the respective fields and should be successively numbered.

Short communications generally follow the same order of sections as Scientific articles, but should be short (max. 2500 words) and report a significant aspect of research work meriting separate publication. Editors may decide that a Scientific paper is categorized as a Short Communication if its length is short.

Technical articles report applications of an already described innovation. Typically, technical articles are not based on new experiments.

Preparation of Submissions

Text of the submitted articles must be prepared with Microsoft Word. Normal style set to single column, 1.5 line spacing, and 12 pt Times New Roman font is recommended. Line numbering (continuous, for the whole document) must be enabled to simplify the reviewing process. For any other format, please consult the editor. Articles should be written in English. Correct spelling and grammar are the sole responsibility of the author(s). Papers should be written in a concise and succinct manner. The authors shall respect the ISO 80000 standard [1], and IUPAC Green Book [2] rules on the names and symbols of quantities and units. The Système International d'Unités (SI) must be used for all dimensional quantities.

Graphics (figures, graphs, illustrations, digital images, photographs) should be inserted in the text where appropriate. The captions should be self-explanatory. Lettering should be readable (suggested 8 point Arial font) with equal size in all figures. Use common programs such as MS Excel or similar to prepare figures (graphs) and ChemDraw to prepare structures in their final size. Width of graphs in the manuscript should be 8 cm. Only in special cases (in case of numerous data, visibility issues) graphs can be 17 cm wide. All graphs in the manuscript should be inserted in relevant places and **aligned left**. The same graphs should be provided separately as images of appropriate resolution (see below) and submitted together in a ZIP file (Graphics ZIP). Please do not submit figures as a Word file. In **graphs**, only the graph area determined by both axes should be in the frame, while a frame around the whole graph should be omitted. The graph area should be white. The legend should be inside the graph area. The style of all graphs should be the same. **Figures and illustrations** should be of sufficient quality for the printed version, i.e. 300 dpi minimum. **Digital images and photographs** should be of high quality (minimum 250 dpi resolution). On submission, figures should be of good enough resolution to be assessed by the referees, ideally as JPEGs. High-resolution figures (in JPEG,

TIFF, or EPS format) might be required if the paper is accepted for publication.

Tables should be prepared in the Word file of the paper as usual Word tables. The captions should appear above the table and should be self-explanatory.

References should be numbered and ordered sequentially as they appear in the text, likewise methods, tables, figure captions. When cited in the text, reference numbers should be superscripted, following punctuation marks. It is the sole responsibility of authors to cite articles that have been submitted to a journal or were in print at the time of submission to ACSi. Formatting of references to published work should follow the journal style; please also consult a recent issue:

1. J. W. Smith, A. G. White, *Acta Chim. Slov.* **2008**, *55*, 1055–1059.
2. M. F. Kemmere, T. F. Keurentjes, in: S. P. Nunes, K. V. Peinemann (Ed.): *Membrane Technology in the Chemical Industry*, Wiley-VCH, Weinheim, Germany, **2008**, pp. 229–255.
3. J. Levec, Arrangement and process for oxidizing an aqueous medium, US Patent Number 5,928,521, date of patent July 27, **1999**.
4. L. A. Bursill, J. M. Thomas, in: R. Sersale, C. Collela, R. Aiello (Eds.), *Recent Progress Report and Discussions: 5th International Zeolite Conference*, Naples, Italy, 1980, Gianini, Naples, **1981**, pp. 25–30.
5. J. Szegezdi, F. Cszimadia, Prediction of dissociation using microconstants, http://www.chemaxon.com/conf/Prediction_of_dissociation_constant_using_microconstants.pdf, (assessed: March 31, 2008)

Titles of journals should be abbreviated according to Chemical Abstracts Service Source Index (CASSI).

Special Notes

- Complete characterization, **including crystal structure**, should be given when the synthesis of new compounds in crystal form is reported.
- Numerical **data should be reported with the number of significant digits corresponding to the magnitude** of experimental uncertainty.
- **The SI system of units and IUPAC recommendations** for nomenclature, symbols and abbreviations should be followed closely. Additionally, the authors should follow the general guidelines when citing spectral and analytical data, and depositing crystallographic data.
- **Characters** should be correctly represented throughout the manuscript: for example, 1 (one) and l (ell), 0 (zero) and O (oh), x (ex), D7 (times sign), B0 (degree sign). Use Symbol font for all Greek letters and mathematical symbols.
- The rules and recommendations of the **IUBMB** and the **International Union of Pure and Applied Chemistry (IUPAC)** should be used for abbreviation of chemical names, nomenclature of chemical compounds, enzyme nomenclature, isotopic compounds, optically active isomers, and spectroscopic data.
- **A conflict of interest** occurs when an individual (author, reviewer, editor) or its organization is involved in multiple interests, one of which could possibly corrupt the motivation for an act in the

other. Financial relationships are the most easily identifiable conflicts of interest, while conflicts can occur also as personal relationships, academic competition, etc. **The Editors** will make effort to ensure that conflicts of interest will not compromise the evaluation process; potential editors and reviewers will be asked to exempt themselves from review process when such conflict of interest exists. When the manuscript is submitted for publication, **the authors** are expected to disclose any relationships that might pose potential conflict of interest with respect to results reported in that manuscript. In the Acknowledgement section the source of funding support should be mentioned. The statement of disclosure must be provided as Comments to Editor during the submission process.

- **Published statement of Informed Consent.** Research described in papers submitted to ACSi must adhere to the principles of the Declaration of Helsinki (<http://www.wma.net/e/policy/b3.htm>). These studies must be approved by an appropriate institutional review board or committee, and informed consent must be obtained from subjects. The Methods section of the paper must include: 1) a statement of protocol approval from an institutional review board or committee and 2), a statement that informed consent was obtained from the human subjects or their representatives.
- **Published Statement of Human and Animal Rights.** When reporting experiments on human subjects, authors should indicate whether the procedures followed were in accordance with the ethical standards of the responsible committee on human experimentation (institutional and national) and with the Helsinki Declaration of 1975, as revised in 2008. If doubt exists whether the research was conducted in accordance with the Helsinki Declaration, the authors must explain the rationale for their approach and demonstrate that the institutional review body explicitly approved the doubtful aspects of the study. When reporting experiments on animals, authors should indicate whether the institutional and national guide for the care and use of laboratory animals was followed.
- To avoid conflict of interest between authors and referees we expect that not more than one referee is from the same country as the corresponding author(s), however, not from the same institution.
- Contributions authored by **Slovenian scientists** are evaluated by non-Slovenian referees.
- Papers describing **microwave-assisted reactions** performed in domestic microwave ovens are not considered for publication in *Acta Chimica Slovenica*.
- *Manuscripts that are **not prepared and submitted** in accord with the instructions for authors are not considered for publication.*

Appendices

Authors are encouraged to make use of supporting information for publication, which is supplementary material (appendices) that is submitted at the same time as the manuscript. It is made available on the Journal's web site and is linked to the article in the

Journal's Web edition. The use of supporting information is particularly appropriate for presenting additional graphs, spectra, tables and discussion and is more likely to be of interest to specialists than to general readers. When preparing supporting information, authors should keep in mind that the supporting information files will not be edited by the editorial staff. In addition, the files should be not too large (upper limit 10 MB) and should be provided in common widely known file formats to be accessible to readers without difficulty. All files of supplementary materials are loaded separately during the submission process as supplementary files.

Proposed Cover Picture and Graphical Abstract Image

Graphical content: an ideally full-colour illustration of resolution 300 dpi from the manuscript must be proposed with the submission. Graphical abstract pictures are printed in size 6.5 x 4 cm (hence minimal resolution of 770 x 470 pixels). Cover picture is printed in size 11 x 9.5 cm (hence minimal resolution of 1300 x 1130 pixels)

Authors are encouraged to submit illustrations as candidates for the journal Cover Picture*. The illustration must be related to the subject matter of the paper. Usually both proposed cover picture and graphical abstract are the same, but authors may provide different pictures as well.

* The authors will be asked to contribute to the costs of the cover picture production.

Statement of novelty

Statement of novelty is provided in a Word file and submitted as a supplementary file in step 4 of submission process. Authors should in no more than 100 words emphasize the scientific novelty of the presented research. Do not repeat for this purpose the content of your abstract.

List of suggested reviewers

List of suggested reviewers is a Word file submitted as a supplementary file in step 4 of submission process. Authors should propose the names, full affiliation (department, institution, city and country) and e-mail addresses of three potential referees. Field of expertise and at least two references relevant to the scientific field of the submitted manuscript must be provided for each of the suggested reviewers. The referees should be knowledgeable about the subject but have no close connection with any of the authors. In addition, referees should be from institutions other than (and preferably countries other than) those of any of the authors.

How to Submit

Users registered in the role of author can start submission by choosing USER HOME link on the top of the page, then choosing the role of the Author and follow the relevant link for starting the submission process. Prior to submission we strongly recommend that you familiarize yourself with the ACSi style by browsing the journal, particularly if you have not submitted to the ACSi before or recently.

Correspondence

All correspondence with the ACSi editor regarding the paper goes through this web site and emails. Emails are sent and recorded in the web site database. In the correspondence with the editorial office please provide ID number of your manuscript. All emails you receive from the system contain relevant links. **Please do not answer the emails directly but use the embedded links in the emails for carrying out relevant actions.** Alternatively, you can carry out all the actions and correspondence through the online system by logging in and selecting relevant options.

Proofs

Proofs will be dispatched via e-mail and corrections should be returned to the editor by e-mail as quickly as possible, normally within 48 hours of receipt. Typing errors should be corrected; other changes of contents will be treated as new submissions.

Submission Preparation Checklist

As part of the submission process, authors are required to check off their submission's compliance with all of the following items, and submissions may be returned to authors that do not adhere to these guidelines.

1. The submission has not been previously published, nor is it under consideration for publication in any other journal (or an explanation has been provided in Comments to the Editor).
2. All the listed authors have agreed on the content and the corresponding (submitting) author is responsible for having ensured that this agreement has been reached.
3. The submission files are in the correct format: manuscript is created in MS Word but will be **submitted in PDF** (for reviewers) as well as in original MS Word format (as a supplementary file for technical editing); diagrams and graphs are created in Excel and saved in one of the file formats: TIFF, EPS or JPG; illustrations are also saved in one of these formats. The preferred position of graphic files in a document is to embed them close to the place where they are mentioned in the text (See **Author guidelines** for details).
4. The manuscript has been examined for spelling and grammar (spell checked).
5. The **title** (maximum 150 characters) briefly explains the contents of the manuscript.
6. Full names (first and last) of all authors together with the affiliation address are provided. Name of author(s) denoted as the corresponding author(s), together with their e-mail address, full postal address and telephone/fax numbers are given.
7. The **abstract** states the objective and conclusions of the research concisely in no more than 150 words.
8. Keywords (minimum three, maximum six) are provided.
9. **Statement of novelty** (maximum 100 words) clearly explaining new findings reported in the manuscript should be prepared as a separate Word file.
10. The text adheres to the stylistic and bibliographic requirements outlined in the **Author guidelines**.
11. Text in normal style is set to single column, 1.5 line spacing, and 12 pt. Times New Roman font is

recommended. All tables, figures and illustrations have appropriate captions and are placed within the text at the appropriate points.

12. Mathematical and chemical equations are provided in separate lines and numbered (Arabic numbers) consecutively in parenthesis at the end of the line. All equation numbers are (if necessary) appropriately included in the text. Corresponding numbers are checked.
13. Tables, Figures, illustrations, are prepared in correct format and resolution (see **Author guidelines**).
14. The lettering used in the figures and graphs do not vary greatly in size. The recommended lettering size is 8 point Arial.
15. Separate files for each figure and illustration are prepared. The names (numbers) of the separate files are the same as they appear in the text. All the figure files are packed for uploading in a single ZIP file.
16. Authors have read **special notes** and have accordingly prepared their manuscript (if necessary).
17. References in the text and in the References are correctly cited. (see **Author guidelines**). All references mentioned in the Reference list are cited in the text, and vice versa.
18. Permission has been obtained for use of copyrighted material from other sources (including the Web).
19. The names, full affiliation (department, institution, city and country), e-mail addresses and references of three potential referees from institutions other than (and preferably countries other than) those of any of the authors are prepared in the word file. At least two relevant references (important papers with high impact factor, head positions of departments, labs, research groups, etc.) for each suggested reviewer must be provided.
20. Full-colour illustration or graph from the manuscript is proposed for graphical abstract.
21. **Appendices** (if appropriate) as supplementary material are prepared and will be submitted at the same time as the manuscript.

Privacy Statement

The names and email addresses entered in this journal site will be used exclusively for the stated purposes of this journal and will not be made available for any other purpose or to any other party.

ISSN: 1580-3155

Koristni naslovi

Slovensko kemijsko društvo
Slovenian Chemical Society



Slovensko kemijsko društvo

www.chem-soc.si

e-mail: chem.soc@ki.si



Wessex Institute of Technology

www.wessex.ac.uk



SETAC

www.setac.org



European Water Association

<http://www.ewa-online.eu/>



European Science Foundation

www.esf.org



European Federation of Chemical Engineering

<https://efce.info/>



I U P A C

INTERNATIONAL UNION OF
PURE AND APPLIED CHEMISTRY

International Union of Pure and Applied Chemistry

<https://iupac.org/>

Novice evropske zveze kemijskih društev EuChemS najdete na:

 **EuChemS**
European Chemical Society

Brussels News Updates

<http://www.euchems.eu/newsletters/>

Sistemi za čisto in ultračisto vodo

Kvaliteta vode 1 do 3*

*v skladu s standardom ISO 3696 in ustreznimi ASTM ter CLSI



DONAU LAB Ljubljana
Member of LPPgroup

Donau Lab d.o.o., Ljubljana
Tbilisjska 85
SI-1000 Ljubljana
www.donaulab.si
office-si@donaulab.com



Že od
3.214€+DDV
(B30 Trace s 25 L Pro rezerv.
Slika je simbolična.)



adrona

Napredek, obarvan v zeleno

V Heliosu načela trajnostnega razvoja in skrbi za okolje vpeljujemo na vsa področja našega delovanja. Nove rešitve in proizvode razvijamo tudi z namenom, da bi zmanjšali porabo vseh vrst virov in ogljični odtis produktov.

Part of  **KANSAI**
PAINT

www.helios-group.eu

 **HELIOS**

Designing Excellence

Izjemen dan se začne z izjemnim spancem.

Odpravite nespečnost in začnite dan spočiti.

Noctiben Mea®

doksilaminijev hidrogensukcinat



Učinkuje hitro – vzame se 15 do 30 minut pred spanjem.



Deluje celo noč.



Izboljša kakovost spanca in naslednjega dne.



NOVO

www.noctibenmea.si

Noctiben Mea®, doksilaminijev hidrogensukcinat, filmso obložene tablete, 15 mg

Kaj je zdravilo Noctiben Mea in za kaj ga uporabljamo Jemanje tega zdravila se priporoča pri občasnih nespečnosti pri odraslih. Če se znaki vaše bolezni poslabšajo ali ne izboljšajo v 5 dneh, se posvetujte z zdravnikom. **Kaj morate vedeti, preden boste vzeli zdravilo Noctiben Mea** Ne jemljite tega zdravila, če ste alergični na doksilamin, antihistaminike ali katerikoli sestavino tega zdravila, če ste imeli v preteklosti akutni glavkom (zvišan očesni tlak), če ste moški in imate težave z odvajanjem vode (zaradi težav s prostato ali drugih težav), če ste mlajši od 18 let. Pred začetkom jemanja zdravila se posvetujte z zdravnikom ali s farmacevtom. Pri starejših je treba zdravilo uporabljati previdno zaradi tveganja za poslabšanje kognitivnih sposobnosti, zaspanost, počasne odzive in/ali omotico, ki lahko poveča tveganje za padce. Tako kot pri drugih uspavalnih in pomirjevalih bo tudi pri jemanju tega zdravila verjetno prišlo do poslabšanja sindroma spalne apneje. Med zdravljenjem ni priporočljivo pitje alkohola. Če imate dolgotrajno jetrno ali ledvično bolezen, se posvetujte z zdravnikom, da bo lahko prilagodil odmerek. Zdravilo vsebuje laktozo. Če ne prenašate nekaterih sladkorjev, se pred jemanjem tega zdravila posvetujte z zdravnikom. Otroci in mladoletniki, mlajši od 18 let, zdravila ne smejo jemati. Da bi se izognili morebitnim interakcijam med različnimi zdravili, morate o kakršnekoli drugem zdravljenju obvestiti svojega zdravnika ali farmacevta. Če ste noseči ali dojite, če menite, da bi lahko bili noseči, ali če načrtujete zanositev, se posvetujte z zdravnikom ali s farmacevtom, preden vzamete to zdravilo. Med nosečnostjo lahko to zdravilo jemljete samo, če vam je tako svetoval zdravnik. Jemanje med dojenjem ni priporočljivo. Zavedati se morate, da sta z jemanjem tega zdravila povezani zaspanost podnevi in zmanjšana pozornost. Med upravljanjem vozil in strojev ni priporočljivo sočasno jemanje drugih sedativnih zdravil, natrijevega oksibata ter seveda pitje alkohola ali jemanje zdravil, ki vsebujejo alkohol. Pri nezadostnem trajanju spanja je tveganje za pojav zmanjšane pozornosti še povečano. **Kako jemati zdravilo Noctiben Mea** Priporočeni odmerek je ½ tablete do 1 tableta na dan, po potrebi se lahko poveča na 2 tableti na dan. Pri starejših in bolnikih z ledvično ali jetrno okvaro se priporoča najmanjši odmerek. Tableta se lahko deli na enaka odmerka. Pogoltnite jo z nekaj vode. Dnevni odmerek vzemite zvečer, 15 do 30 minut pred spanjem. Zdravljenje traja od 2 do 5 dni. Brez posveta z zdravnikom lahko zdravilo jemljete največ 5 dni. Če ste vzeli večji odmerek zdravila, kot bi smeli, se takoj posvetujte z zdravnikom ali s farmacevtom. Če ste pozabili vzeti prejšnji odmerek, ne vzemite dvojnega. Naslednji odmerek vzemite ob običajnem času. **Možni neželeni učinki** Zaspanost podnevi, zaprtje, zastoj urina, suha usta, zmedenost, rabdomioliza, povečane vrednosti kreatin fosfokinaze v krvi, motnje vida, palpitanje srca, sedacija, kognitivne in psihomotorične motnje. **Izglede zdravila Noctiben Mea in vsebina pakiranja** Filmso obložene tablete so blede vijoličasto sive do vijoličasto sive, ovalne, izbočene, z razdelilno zarezo na eni strani. Zdravilo je na voljo v 3katalci z 10 tabletami v pretisnem omotu. **Način izdajanja zdravila** Zdravilo se brez recepta izdaja v lekarnah. **Imetnik dovoljenja za promet z zdravili** Krka, d. d., Novo mesto, Šmarješka cesta 6, 8501 Novo mesto, Slovenija. **Datum zadnje revizije navodila** 17. 5. 2019.

Pred začetkom jemanja zdravila natančno preberite navodilo, ker vsebuje za vas pomembne podatke. Pri jemanju tega zdravila natančno upoštevajte napotke v tem navodilu ali navodila zdravnika ali farmacevta. Če opazite katerikoli neželeni učinek, se posvetujte z zdravnikom, farmacevtom ali drugim zdravstvenim delavcem. O domnevnem neželenem učinku lahko poročate tudi neposredno nacionalnemu centru za farmakovigilanco, na način, kot je objavljeno na spletni strani www.jazmp.si.



KRKA

Pred uporabo natančno preberite navodilo!

O tveganju in neželenih učinkih se posvetujte z zdravnikom ali s farmacevtom.

ActaChimicaSlovenica

ActaChimicaSlovenica

Ionic liquids can be treated as complex electrolytes in their pure state, where the structure is strongly dependent on the structures of cations and anions. In solutions, they behave like "simple" electrolytes and "classical" surfactants, thus they are sharing the "complexity" of electrolyte solutions - from the formation of ion pairs to the larger aggregates (micelles). Parts of the cover picture are reproduced from ref. 6 with permission from PCCP Owner Societies and ref. 2 (<https://pubs.acs.org/doi/10.1021/cr500411q>), further permissions related to the material excerpted should be directed to the ACS (see page 1).



Year 2020, Vol. 67, No. 1

